

SAUPEC

Southern African Universities Power Engineering Conference



**28 – 30 January
2015**



UNIVERSITY
OF
JOHANNESBURG

**Proceedings of the 23rd
Southern African Universities Power
Engineering Conference**

SAUPEC 2015

**University of Johannesburg, Johannesburg, South
Africa
28-30 January 2015**

Review:

Authors were invited to submit full papers to the broad subject “Electrical Engineering”. Each paper was peer reviewed by at least two specialist reviewers. In the case where the reviewers did not agree, a third review was done to decide the outcome. Final acceptance was based on the contribution, scientific and technical merit of the paper.

Disclaimer:

Authors are responsible for the contents of their papers.

Published by the Southern African Universities Power Engineering Conference

School of Electrical Engineering
University of Johannesburg
PO Box 524
2006 Auckland Park
South Africa.

Tel: +27 11 559 4555

ISBN 978-0-86970-786-9

Technical Committee (Reviewers)

M	Adonis	H	Marais
AO	Akumu	A	Marks
K	Awodele	P	Moodley
AA	Beutel	MC	Muteba
E	Boje	J	Naudé
P	Bokoro	DV	Nicolae
T	Booyesen	F	Nicolls
J	Braid	KJ	Nixon
G	Breedt	M	Ntshani
J	Carroll	C	Nyamupangedengu
S	Chan-Wing	BS	Paul
R	Chetty	D	Pentz
S	Chowdhury	PH	Pretorius
WA	Cronje	AK	Raji
IE	Davidson	PJ	Randewijk
A	de Beer	CG	Richards
J	de Kock	AK	Saha
W	Doorsamy	M	Shuma-Iwisi
KA	Folly	N	Smit
CT	Gaunt	G	Stoltz
HJ	Geldenhuys	AG	Swanson
S	Gerber	KV	Thejane
M	Gumede	KR	Uren
R	Gouws	J	van Coller
AJ	Grobler	Fred	van der Merwe
M	Grobler	Frikkie	van der Merwe
N	Gule	B	van Jaarsveld
R	Herman	G	van Schoor
M	Hove	HJ	Vermeulen
H	Hunt	R-J	Wang
AA	Jimoh	R	Wolhuter
ALJ	Joannou	G	Wooding
MJ	Kamper	N	Zabihi
R	Loubser		

Local Organising Committee Members

Dr David Pentz

Dr Arnold de Beer

Ms Aamina Malek

Mr Andrew Joannou

Mrs Lucia Pelser

Ms Daphney Mashamaite

Mr Eduard Basson

Mr Theren Lam

Foreword

It is a privilege to welcome you to the 23rd Southern African Universities Power Engineering Conference, to be hosted by the University of Johannesburg, School of Electrical Engineering. It has been 25 years since the first SAUPEC in 1990 (Stellenbosch). We hope that the papers presented will generate stimulating conversations and that all involved will experience academic growth.

We would like to thank all the reviewers for their huge contribution to the success of the conference. Thank you for the excellent feedback. Your time and efforts are greatly appreciated. Only papers that were accepted by two reviewers are published in the proceedings. Discussion papers were not reviewed and are considered work in progress. Digital copies are included on the USB devices.

We would like to thank everyone that was involved in making this conference a success. A special thank you to all the staff at the University of Johannesburg, Resolution Circle and The South African Institute of Electrical Engineers. Thank you to all the speakers and especially Prof Braham Ferreira for the keynote address.

Enjoy SAUPEC 2015!

The SAUPEC 2015 organising committee.

A special thank you to the sponsors of SAUPEC 2015



resolutioncircle
the ecosystem for technology solutions



TECH EXPO
AFRICA



TINTLEY



GEEP



Solutions (Pty) Ltd

TABLE OF CONTENTS

SESSION 1-A: MEDIUM AND HIGH VOLTAGE 1

SAU003: REAL TIME MONITORING OF HIGH VOLTAGE TRANSMISSION LINE CONDUCTOR SAG USING RFID RADAR SYSTEM T.S. Hlalele	1-6
SAU031: ANALYSIS OF THE INDUCED VOLTAGE ON BURIED PIPELINE IN THE VICINITY OF HIGH AC VOLTAGE OVERHEAD TRANSMISSION LINES K.B. Adedeji, A.A. Ponnle, B.T. Abe and A.A. Jimoh.	7-12
SAU043: PARTIAL DISCHARGE ANALYSIS IN POWER CABLES USING 3D PHASE RESOLVED PATTERNS I.K. Kyere, J.J. Walker and D.V. Nicolae	13-18
SAU030: EXPERIMENTAL INVESTIGATION OF AEOLIAN-VIBRATIONAL LOADS ON COMPOSITE INSULATORS K.A. Ntambwe, R.C. Loubser, P. Moodley and K.O. Papailiou	19-24
SAU014: NATURAL POLLUTION TEST FOR INVESTIGATING LEAKAGE CURRENT EFFECTS ON MEDIUM VOLTAGE WOODPOLE DISTRIBUTION LINE STRUCTURES A. Beutel, M.D. Ntshani, K.V. Thejane, H.J. Geldenhuys, T.D. Mvayo, R.F. Watson, W.L. Vosloo, A. Khatri	25-30
SAU013: DESIGN, TEST AND BASIC EVALUATION OF A TEST RESISTOR FOR USE ON A MEDIUM VOLTAGE DISTRIBUTION NETWORK A.A. Beutel, F. Jooste, H.J. Geldenhuys, A. Khatri	31-35
SAU032: PREDICTING THE REMAINING LIFE OF MEDIUM VOLTAGE VACUUM SWITCHGEAR USED IN DISTRIBUTION NETWORKS J. O'Reilly, J.M. van Coller and N. Smit	36-42
SAU011: APPARENT SOIL STRUCTURES RELEVANT TO BURIED EARTH ELECTRODES IN SOUTH AFRICA - A RESEARCH PROPOSAL P. H. Pretorius	43-48

SESSION 1-B: POWER ELECTRONICS AND MACHINES 1

SAU080: PERFORMANCE EVALUATION OF A NINE-PHASE SELF- EXCITED INDUCTION GENERATOR G.C. Mangena and M. Muteba	49-52
SAU081: MODELLING OF A DC EXCITATION OF A SYNCHRONOUS GENERATOR M. Mtsamane and M. Muteba	53-56
SAU024: STATOR DESIGN FOR A 1.5 kW AXIAL FLUX PERMANENT MAGNET GENERATOR A. Smith and A.J. Grobler	57-62
SAU002: SOFTWARE SIMULATION INTEGRATION IN ENHANCING ENGINEERING DESIGN IN POWER CONVERSION STUDIES A.M. Almaktoof, A.K. Raji and M.T.E. Kahn	63-68
SAU044: SENSOR-LESS OUTPUT CURRENT MEASUREMENT FOR SWITCHING CONVERTERS A.M. Hank, D.J. Cooper, I. Hofsjajer	69-73
SAU048: EXPERIMENTAL EVALUATION OF DELTA MODULATION FOR PWM NINE PHASE INVERTER WITH A TRAPEZOIDAL REFERENCE CURRENT WAVEFORM. L. Gunda and N. Gule	74-79
SAU039: THE FUNDAMENTAL CONSTRAINTS OF CONSTANT VOLTAGE POWER CONVERTERS J.A. Naudé and I.W. Hofsjajer	80-86
SAU008: DEVELOPMENT OF SMART CONTROLLER FOR FUEL CELL AND SUPERCAPACITOR APPLICATION IN ELECTRIC VEHICLES H.J. Rautenbach, R. Gouws, D. Bessarabov, A. Kruger and G. Human	87-92
SESSION 1-C: MICRO- AND SMART-GRID	
SAU028: ENERGY MANAGEMENT SYSTEM IN AUTONOMOUS MICROGRID A.A. Aminou Moussavou, M. Adonis, A.K. Raji	93-97

SAU029: EVALUATION OF SMART TECHNOLOGY FOR THE IMPROVEMENT OF RELIABILITY IN A POWER DISTRIBUTION SYSTEM G.C. Dumakude, .A.G. Swanson, R. Stephen and I.E. Davidson	98-104
SAU056: COST EFFECTIVE SOLUTION FOR A SMART HOUSE ENVIRONMENT D. Horne, Q. Machin, M. Shuma-Iwisi and I. Hofsjer	105-110
SAU084: A SYSTEMS ENGINEERING APPROACH TO ANALYSING MICROGRID CHALLENGES IN SUB-SAHARAN AFRICA W. Doorsamy, L. Lakay-Doorsamy and W.A. Cronje	111-116
SAU108: A DYNAMIC THREE-PHASE LOAD EMULATOR FOR DISTRIBUTED GENERATION STUDIES IN A MICROGRID LOAD TEST-BED T.K. Nkalai, M.V. Mabuyakhulu and W.A. Cronje	117-122
SAU101: DYNAMIC POWER REQUIREMENTS FOR CONTROLLED ENERGY STORE USED FOR STABILIZATION OF THREE-PHASE LOW-VOLTAGE STANDALONE MICROGRID N. Horonga and W. Cronje	123-128
SAU068: SMART MICROGRIDS FOR RURAL ELECTRIFICATION IN SOUTH AFRICA R Chetty	129-133
SAU036: A DATA VISUALISATION SOLUTION FOR SMART ENERGY MONITORING SYSTEMS M.C. Geddes, B.E. Phillips and K.J. Nixon	134-140
SESSION 1-D: RENEWABLE ENERGY 1	
SAU053: MODELLING AND PERFORMANCE ANALYSIS OF A MICRO-HYDROKINETIC RIVER SYSTEM AS COMPARED TO WIND SYSTEM S.P. Koko, K. Kusakana and H.J. Vermaak	141-147
SAU042: ECONOMIC ANALYSIS OF A STAND-ALONE SOLAR PV SYSTEM FOR DIFFERENT SIZES OF MIDDLE INCOME RESIDENTIAL LOAD CLUSTERS IN SOUTH AFRICA M. N. Martin, C. Buque and S. Chowdhury	148-153

SAU034: A CUSTOMIZABLE ENERGY MONITORING SYSTEM FOR RENEWABLE ENERGY SYSTEMS P.E. Hertzog and A.J. Swart	154-159
SAU049: IMPACT OF PV GENERATORS ON POWER SYSTEM VOLTAGE REGULATION FOR DISTRIBUTION NETWORKS WITH VERY LONG BRANCH NETWORKS M. Dlamini and N. Gule	160-163
SAU004: A PRELIMINARY STUDY TO ASCERTAIN THE TECHNO-ECONOMIC VIABILITY OF RESIDENTIAL AIR SOURCE HEAT PUMP WATER HEATER: FORT BEAUFORT, SOUTH AFRICA Stephen L. Tangwe, M. Simon and E.L. Meyer	164-169
SAU010: A TECHNOLOGICAL AND PERFORMANCE COMPARISON OF WASTE-TO-ENERGY THERMAL TECHNOLOGIES W. Maisiri, L. Van Dyk and J. De Kock	170-176
SAU100: PERFORMANCE PREDICTION OF WIND TURBINE BLADES: PRELIMINARY TESTING AND RESULTS J. Braid	177-182
SAU040: ECONOMIC FEASIBILITY ANALYSIS OF RURAL STANDALONE BIOFUEL-BASED ELECTRICITY GENERATION WITH AND WITHOUT ENERGY STORAGE P.M. Seshabela, M.P. Nthontho and S. Chowdhury	183-189
SESSION 2-A: MACHINES 2	
SAU015: THE CHARACTERIZATION AND MODELLING OF A LINE START PERMANENT MAGNET SYNCHRONOUS MACHINE A.J. Grobler and P.E. Plaatjie	190-196
SAU069: POWER FACTOR CORRECTION AND REACTIVE POWER CONTROL OF A SLIP SYNCHRONOUS PERMANENT MAGNET WIND TURBINE USING VARIABLE FLUX. A.S. Erasmus, L.L. Amuhaya and M.J. Kamper	197-202
SAU096: A HIGH PERFORMANCE CONCENTRIC MAGNETIC GEAR A. Mathee, S. Gerber and R-J Wang	203-207

SAU041: IMPLEMENTATION OF A ROTOR ANGLE MEASUREMENT METHOD USING SYNCHROPHASOR TECHNIQUES B.W.D. Berry, M.A. Edwards and K.J. Nixon	208-215
SAU035: OPTIMISATION OF A LINE-START PERMANENT MAGNET SYNCHRONOUS MACHINE FOR A LOAD SPECIFIC APPLICATION A.J. Sorgdrager, R-J Wang and A.K. Pfeffer	216-220
SAU026: ROTOR DESIGN OF A RETROFIT LINE START PERMANENT MAGNET SYNCHRONOUS MOTOR K. Garner and A.J. Grobler	221-226
SAU075: ROTOR DESIGN OF A LINE START PERMANENT MAGNET SYNCHRONOUS MACHINE USING THE TAGUCHI METHOD A.J. Sorgdrager, R. Smith and R-J Wang	227-232
SAU088: THEORETICAL AND FINITE ELEMENT ANALYSIS OF A DOUBLE ROTOR RADIAL FLUX PERMANENT MAGNET EDDY CURRENT COUPLING C.H.O. Lombard and M.J. Kamper	233-238
SESSION 2-B: MEDIUM AND HIGH VOLTAGE 2	
SAU103: LIGHTNING RETURN STROKE MODELLING WITH REFERENCE TO LIGHTNING ELECTROMAGNETIC FIELDS C.W.I. McAfee and K.J. Nixon	239-243
SAU105: CORRELATION BETWEEN IEC 60853 AND F.E. SIMULATIONS FOR TRANSIENT RATINGS OF BURIED CABLES. B.J. le Roux and J.J. Walker	244-249
SAU001: INVESTIGATING THE CONCEPT OF FRAUNHOFER LINES AS A POTENTIAL METHOD TO DETECT CORONA IN THE WAVELENGTH REGION 338.67NM – 405NM DURING THE DAY N. Maistry, J. Van Coller and R.A. Schutz	250-254
SAU076: A COMPARATIVE STUDY OF SURFACE PARTIAL DISCHARGE PARAMETERS AT VERY LOW FREQUENCY (VLF) AND POWER FREQUENCY TEST VOLTAGES S. Chimunda, C. Chidzikwe, C. Nyamupangedengu	255-260

SAU077: A COMPARATIVE STUDY OF CAVITY PARTIAL DISCHARGE PARAMETERS AT VLF AND AT 50 Hz TEST VOLTAGES K. Mosito, M. Dlamini and C. Nyamupangedengu	261-266
SAU012: COGNITIVE EXPLORATION IN SUPPORT OF FORMULATING AN HYPOTHESIS TO EXPLAIN ANOMALOUS FLASHOVERS IN HVDC SYSTEMS P.H. Pretorius	267-280
SAU061: POWER SYSTEM TRANSIENT STABILITY ANALYSIS AND STABILITY IMPROVEMENT OF A LARGE MULTI-MACHINE HVAC NETWORK USING HVDC TECHNOLOGIES K.N.I. Mbangula and I.E. Davidson	281-286
SAU089: SOUTH AFRICAN LOAD MODELS FOR RESIDENTIAL ENERGY CONSUMPTION USING A BOTTOM-UP MODELLING TOOL K.D. Mutamba, M.T. Samanga and K.J. Nixon	287-292
 SESSION 2-C: PROTECTION SYSTEM AUTOMATION AND STABILITY	
SAU067: IMPACT OF SYSTEM EXPANSION ON SPECIFICATION OF PERSONAL PROTECTIVE EQUIPMENT: ARC FLASH ANALYSIS D. Edwards and P. Bokoro	293-296
SAU066: A CASE STUDY OF INDUCED CURRENT UNBALANCE AS A RESULT OF CAPACITOR FAILURE S. Zondi, P. Bokoro and B. Paul	297-300
SAU109: RING MAIN PROTECTION H. Sewnarain and A.K. Saha	301-305
SAU070: PRIME MOVER FAILURE PROTECTION FOR GENERATORS D.N. Ngema and A.K. Saha	306-310
SAU062: STABILITY ENHANCEMENT OF HVAC NETWORKS USING HVDC LINKS S. M'builu Ives, A. Edwards, A.G. Swanson, and N. Parus	311-318

SAU091: SIMULATION OF 100 % STATOR WINDING INTERNAL GROUND FAULT PROTECTION IN RTDS A. Gwala, A.K. Saha	319-324
SAU102: SIMULATION STUDY OF OVERCURRENT PROTECTION COORDINATION OF DISTRIBUTION SYSTEM A.K. Saha	325-330
SAU090: REAL TIME SIMULATION AND TESTING OF LOSS OF FIELD EXCITATION EVENTS IN RTDS A. Gwala, A.K. Saha	331-336
SESSION 2-D: EMC, ARTIFICIAL INTELLIGENCE AND ECONOMICS	
SAU060: PROPOSED MODEL OF THE ELECTROMAGNETIC ENVIRONMENT IN TRACTION SYSTEMS TO PREDICT THE PATH OF RETURN J. Clay and I. Hofsjajer	337-342
SAU058: CURRENT PROBE CALIBRATION FOR MEERKAT LIGHTNING INDUCED CURRENT MEASUREMENT S.L. Combrink and P.G. Wiid	343-348
SAU019: DESIGN AND IMPLEMENTATION OF A DATA ACQUISITION STATION J. Joubert and A.J. Grobler	349-355
SAU059: SHORT TERM LOAD FORECASTING USING PSO AND ANN E. Shezi, K.A. Folly	356-361
SAU071: HYDROCYCLONE SEPARATION EFFICIENCY ESTIMATION USING ARTIFICIAL NEURAL NETWORKS S. van Loggenberg, G. Van Schoor, K.R. Uren and A.F. van der Merwe	362-367
SAU051: MINIMUM COST SOLUTION OF ISOLATED BATTERY-INTEGRATED DIESEL GENERATOR HYBRID SYSTEMS K. Kusakana	368-372
SAU087: COMPARISON OF ECONOMIC LOAD DISPATCH OF NIGERIA THERMAL PLANTS USING GENETIC ALGORITHM AND DIFFERENTIAL EVOLUTION METHODS O.O. Awodiji and K.A. Folly	373-377

SESSION 3-A: CONTROL

- SAU018:** MODELLING AND SIMULATION OF A FUZZY CONTROLLER FOR DOMESTIC BATTERY CHARGING APPLICATIONS
P. Lambert, C. Buque and S. Chowdhury 378-382
- SAU038:** QUADRUPLE TANK PROCESS DEMONSTRATOR
S. van Graan, G. van Schoor and K.R. Uren 383-388
- SAU078:** NONLINEAR STATE SPACE MODELLING OF AN AXIAL-FLOW COMPRESSOR SYSTEM FOR ENERGY VISUALISATION
L.B. Fouché, K.R. Uren, G. van Schoor 389-394
- SAU057:** AERIAL APE: INDUSTRIAL BRACHIATING POWER LINE INSPECTION ROBOT
J. Patel and E. Boje 395-400
- SAU050:** COMPUTER VISION FOR A POWER LINE INSPECTION ROBOT
A. Morarjee , F. Nicolls and E. Boje 401-406
- SAU045:** DEMYSTIFYING INTERCONNECTION AND DAMPING ASSIGNMENT PASSIVITY-BASED CONTROL
P.J. Kruger, K.R. Uren and G. van Schoor 407-412
- SAU072:** THERMAL-FLUID STATE SPACE MODEL OF A COUNTER-FLOW SINGLE PHASE HEAT EXCHANGER FOR ENERGY VISUALIZATION
S.B. Smuts, G. Van Schoor and K.R. Uren 413-418
- ## **SESSION 3-B: ENERGY EFFICIENCY AND RENEWABLE ENERGY 2**
- SAU098:** EFFICIENCY BENCHMARKING AND EVALUATION OF COAL FIRE POWER STATIONS USING DATA ENVELOPMENT ANALYSIS
A. de Villiers and H.J. Vermeulen 419-424
- SAU104:** VOLTAGE PROFILES IMPROVEMENT WITH WIND ENERGY CONVERTER CONNECTED TO A DISTRIBUTION NETWORK
Ayodeji Stephen Akinyemi and Kehinde Awodele 425-430
- SAU047:** AN INTELLIGENT GEYSER WITH WI-FI ACCESS TO SUPPORT DEMAND-SIDE MANAGEMENT
J.W.K. Brown and M.J. Booyesen 431-436

SAU007: DESIGN OF AN INTELLIGENT CONTROLLER FOR A RENEWABLE ENERGY EFFICIENT BULK STORAGE TANK W.A. Pelser and R. Gouws	437-443
SAU022: DESIGN A THERMOELECTRIC COOLING HOLDER SUPPLIED BY PHOTOVOLTAIC PANELS N. Zabihi and R. Gouws	444-449
SAU021: IN-LINE WATER HEATING SYSTEM FOR INDUSTRIAL APPLICATION O. Dobzhanskyi, R. Gouws, N. Zabihi	450-454
SESSION 3-C: NETWORKS AND RELIABILITY	
SAU055: BAYESIAN PARAMETER ESTIMATION FOR POWER ENGINEERS W. Doorsamy, J. Naudé, W.A. Cronje, and I. Hofsjer	455-462
SAU097: ON THE ADEQUACY OF ELECTRICITY RELIABILITY INDICES IN SOUTH AFRICA R. Herman, C.T. Gaunt and L. Tait	463-467
SAU020: INTRA-BUILDING POWER NETWORK NOISE MODELLING IN SOUTH AFRICA A.M. Nyete, T.J.O. Afullo and I.E. Davidson	468-472
SAU107: DISTANCE TO FAULT ACCURACY IN AN ESKOM DISTRIBUTION NETWORK C. Snyman and A. Marks	473-479
SESSION 3-D: TRANSFORMERS	
SAU037: MEASUREMENT OF SWITCHING SURGES AND RESONANCE BEHAVIOUR IN TRANSFORMER WINDINGS C.A. Banda and J.M. van Coller	480-485
SAU052: ADVANCEMENTS IN DISTRIBUTION TRANSFORMER ELECTRICAL TRANSIENTS AND POWER FREQUENCY SIGNAL MONITORING F. A. Netshiongolwe, R. Cormack, J. M. Van Coller	486-491

SAU099: INVESTIGATION AND ANALYSIS OF THE CAUSES OF 11kV/400V DISTRIBUTION TRANSFORMERS' HIGH FAILURE RATE: CASE STUDY- SWAZILAND ELECTRICITY COMPANY M.T. Maziya and K. Awodele	492-496
SAU106: WIDE BAND ANALYTICAL INDUCTANCE CALCULATIONS FOR LARGE POWER TRANSFORMERS USING WILCOX'S APPROACH B.J. van Jaarsveld	497-501
SAU016: APPLICATION OF KEY FAULT GASES AND OIL TESTING FOR EVALUATION OF TRANSFORMER CONDITION AND ITS MAINTENANCE REQUIREMENT G.K. Irungu, A.O. Akumu, J.L. Munda and B. Lubisi	502-507
SAU065: MODELLING AND EVALUATION OF SINGLE-PHASE OPTIMISA POWER TRANSFORMER A. Coetzer and M.J. Kamper	508-513

Real time monitoring of High Voltage Transmission line conductor sag using RFID radar system

Tlotlollo Sidwell Hlalele

University of South Africa, Cnr.Christiaan De Wet & Pioneer Avenue, Florida P.O. Box 392, UNISA 0003 RSA (phone: +27-11-471-2099; fax: 086-540-6292; e-mail: hlalets@unisa.ac.za).

Abstract: There have been developments in real time monitoring of a power transmission line for the past and in recent years. In South Africa detecting such critical infrastructure proactively in real time is still a challenge. This paper characterizes and evaluates various methods developed to measure conductor sag in real time. Some of the methods are still at initial stage of simulation and have not yet been applied in industry. Radio Frequency Identification(RFID) radar system is implemented for sag detection using matlab. Due to uncertainties of environmental factors, high voltage response and the capacitance of the line, the detected range contains significant errors.

Keywords: Power quality, Reliability and Sag

1. INTRODUCTION

Long distance high voltage power lines are very important in electricity power delivery because power stations are normally located at distance. Balance must be constantly maintained to match the power supply and demand. World climatic changes have an impact on our existing electrical transmission line performance. The electric current flowing in the lines should be measured to avoid overloads, phase unbalance and fluctuation. Line positions should be monitored to keep track of the sagging and galloping situations. Sagging can lower the conductor to a usage height above the earth. The oscillations can cause serious transmission problems, such as flashover due to infringed line to line clearance, risk of mechanical failure of transmission tower, and excessive loading stress [7]. Conductors between two transmission towers often suffer sagging and galloping phenomenon. According to IEEE Standard 1159-1995 Recommended Practice for Monitoring Electric Power Quality, sag is a decrease in RMS voltage at the power frequency for durations from 0.5cycles to 1 minute, reported as the remaining voltage [14]. Sagging can lower the conductor to an unsafe height above the earth. It can be caused by oscillations which can result into serious transmission problems, such as flashover due to infringed line-to-line clearance, risk of mechanical failure of transmission tower, and excessive loading stress. Efforts have been made to understand this phenomenon better and develop means of protecting the transmission line against this problem. The low frequency, high amplitude induces vibration on this transmission line conductors as a result, causes serious galloping which result to more sagging. It is valid to interpret galloping as an oscillation of either a single or bundled conductor due to wind force or wind-induced vibration on an iced or wet snow accretion on the conductors. It is also caused by steady crosswind acting upon asymmetrically iced

conductor surface. Large amplitude is normally observed on a vertical position depending on the line construction and the oscillation mode excited [14].

The cost associated with galloping can be due to damaged components which require inspection and repair. It damages the conductor strands which result in to a conductor breakage or sagging and dynamic overload. In the event of this situation, patrolling need to be performed to detect any damage. This requires a helicopter or some sort of physical view, which is costly [10].

The problem of sagging has the impact on system reliability and power quality of service. Swinging suspension points longitudinally to the power line could accompany galloping and act to couple the galloping motions in adjacent spans, resulting to more sagging phenomenon.

2. MATHEMATICAL APPROACH

2.1 Review of sag catenary

The shape of the catenary changes with conductor temperature, ice and wind loading, and time. To ensure adequate vertical and horizontal clearance under all weather and electrical loadings, and to ensure that the breaking strength of the conductor is not exceed, the behavior of the conductor catenary under all conditions must be known before the line is designed. The future behavior of the conductor is determined through calculations commonly referred to as sag-tension. Sag tension calculations predict the behavior of conductor based on recommended tension limits under varying

loading conditions. These tension limits specify certain percentages of the conductors rated breaking strength that is not to be exceeded upon installation or during the life of the line. These conditions, along with the elastic and permanent elongation properties of the conductor, provide the basis for determining the amount of resulting sag during installation and long-term operation of the line. Accurately determined initial sag limits are essential in the line design process. Final sags and tensions depend on initial installed sags and tensions and on proper handling during installation. The final sag shape of conductors is used to select support point heights and span lengths so that the minimum clearances will be maintained over the life of the line. If the conductor is damaged or the initial sags are incorrect, the line clearance may be violated or the conductor may break during heavy ice or wind loading.

The shape of a catenary is a function of the conductor weight per unit length, w , the horizontal component of tension, H , span length, S , and the maximum sag of the conductor, D . Conductor sag and span length are illustrated in Fig.1 for a level span. The exact catenary equation uses hyperbolic functions. Relative to the low point of the catenary curve shown in Fig.1, the height of the conductor, $y(x)$, above this low point is given by the following equation [14]:

$$y(x) = \frac{H}{w} \cosh\left(\left(\frac{w}{H}x\right) - 1\right) = \frac{w(x^2)}{2H} \quad (1)$$

For a level span, the low point is in the center, and the sag, D , is found by

$$D = \frac{H}{w} \left(\cosh\left(\frac{ws}{2H}\right) - 1 \right) = \frac{w(S^2)}{8H} \quad (2)$$

At the end of the level span, the conductor tension, T , is equal to the horizontal component plus the conductor weight per unit length, w , multiplied by the sag, D as shown in the equation below:

$$T = H + wD \quad (3)$$

Considering the conductor length from the low point of the catenary from either direction of the sag can be obtained as follows [7]:

$$L(x) = \left(\frac{H}{w} \text{SINH}\left(\frac{Sw}{2H}\right)\right) = S \left(1 + \frac{x^2(w)^2}{6H^2}\right) \quad (4)$$

For a level span, the conductor length corresponding to $x = S/2$ is the half of the total conductor length and the total length, L , is [6]:

$$L = \left(\frac{2H}{w}\right) \text{SINH}\left(\frac{Sw}{2H}\right) = S \left(1 + \frac{x^2(w^2)}{24H^2}\right) \quad (5)$$

The parabolic equation for conductor length can also be expressed as a function of sag, D , by substitution of the sag parabolic equation, giving [6]:

$$L = S + \frac{8D^2}{3S} \quad (6)$$

Conductor Slack is the difference between the conductor length, L , and the span length, S . The parabolic equations for slack may be found by combining the preceding parabolic equations for conductor length, L , and sag, D .

$$L - S = S^3 \left(\frac{w^2}{24H^2}\right) = D^2 \left(\frac{8}{3S}\right) \quad (7)$$

The slack of the conductor in a span can contribute to the changes in conductor sag, such that:

$$D = \sqrt{\frac{3S(L-S)}{8}} \quad (8)$$

For inclined spans: they may be analyzed using essentially the same equations that are used for level spans. The catenary equation for the conductor height above the low point in the span is the same. However the span is considered to consist of two separate sections, on to the right of the low point and the other to the left of the low point. The shape of the catenary relative to the low point is unaffected by the difference in suspension point elevation. In each direction from the low point, the conductor elevation, relative to the low point is;

$$y(x) = \frac{H}{w} \cosh\left(\left(\frac{w}{H}x\right) - 1\right) = \frac{wx^2}{2H} \quad (9)$$

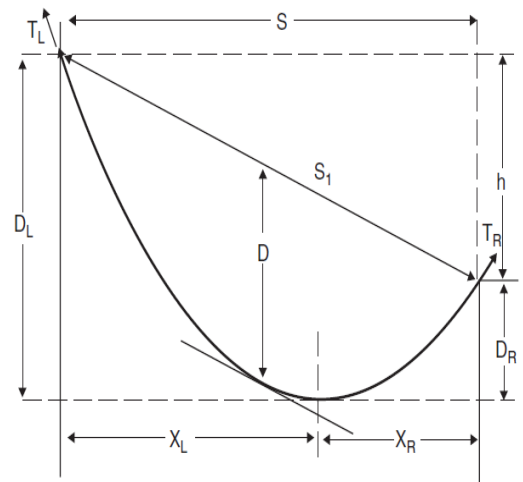


Figure 1: The inclined catenary [7]

The horizontal distance XL from the left support point to the low point in the catenary is given:

$$XL = \frac{S}{2} \left(1 + \frac{h}{4D} \right) \quad (10)$$

The horizontal distance, XR , from the right support point to the low point of the catenary is:

$$Xr = \frac{S}{2} \left(1 - \frac{h}{4D} \right) \quad (11)$$

From the inclined catenary span $S1$ is the straight-line distance between support points, S , horizontal distance between supports, h , vertical distance between support points, D , the sag measured vertically from a line through the points of conductor support to a line tangent to the conductor [6].

The midpoint sag D is approximately equal to the sag in a horizontal span equal to the length to the inclined span, knowing the horizontal distance from the low point to the support in each direction, the preceding equations for $y(x)$, L , D and T can be applied to each side of the inclined span, $S1$. Knowing the horizontal distance from the low point to the support point in each direction, the preceding equations for $y(x)$, L , D , and T can be applied to each side of the inclined span. The total length in the inclined span is equal to the sum of the lengths in XR and XL sub-span sections [7].

$$L = S + (X_R^3 + X_L^3) \left(\frac{w^2}{6H^2} \right) \quad (12)$$

2.2 Conductor position vector

When we review the position of a stretched conductor as presented by author [7], such that the position vector $X(l, t) = (X(l, t), Y(l, t))$ with corresponding tension vector $T(l, t) = T(l, t) (\cos\psi, \sin\psi)$, where ψ is the positively oriented angle between the cable tangent and the horizontal. The tension vector is tangent to the cable or the conductor because of the assumed negligible bending stiffness. Now considering a small cable element under tension dl . Due to gravity, cable tension, and inertial forces, this element is stretched however the mass remain the same. A conductor element is elongated in proportion to tension as indicated according Hooke's law.

$$(dX^2 + dY^2)^{\frac{1}{2}} = \left(1 + \frac{T}{EA} \right) dl.A \quad (13)$$

According to a Newton's law, the internal tension and the external gravity forces are in equilibrium with the inertial forces, such that; $dT = \left(ge_y + \frac{d^2y}{dx^2} \right) m dl$

$$\frac{\partial X}{\partial l} = \left(1 + \frac{T}{EA} \right) \cos\psi, \frac{\partial Y}{\partial l} = \left(1 + \frac{T}{EA} \right) \sin\psi, \quad (14)$$

The equation result in the limit $dl \xrightarrow{\text{yields}} 0$ are given by.

$$\frac{\partial}{\partial l} \left(\frac{T}{1 + \frac{T}{EA}} \frac{\partial X}{\partial l} \right) = m \frac{\partial^2 X}{\partial t^2}, \quad (15)$$

$$\frac{\partial}{\partial l} \left(\frac{T}{1 + \frac{T}{EA}} \frac{\partial Y}{\partial l} \right) = m \frac{\partial^2 Y}{\partial t^2} + mg, \quad (16)$$

$$\left(\frac{\partial X}{\partial l} \right)^2 + \left(\frac{\partial Y}{\partial l} \right)^2 = \left(1 + \frac{T}{EA} \right)^2. \quad (17)$$

For the boundary and coupling conditions in the Figure 2, below

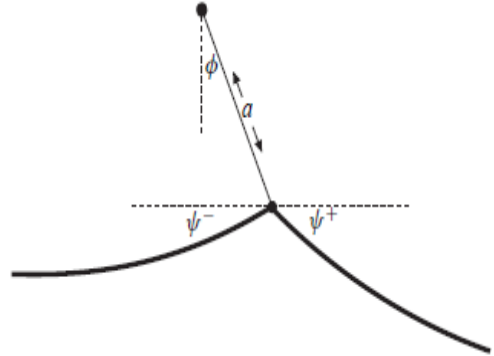


Figure 2: Boundary and coupling conditions [7]

$L = 0$ and $L = NL$ For a fixed support

$$X = 0, Y = 0, (l = 0), \quad (18)$$

$$X = 0, Y = 0, (l = 0), \quad (19)$$

At suspension string

$$[X]_{l=nL-}^{l=nL+} = 0, \quad (20)$$

$$(X - nS)^2 + (Y - a)^2 = a^2, \quad (21)$$

$$[T \cos(\phi - \psi)]_{l=nL-}^{l=nL+} = 0. \quad (22)$$

Where ϕ is the angle of the suspension string.

The mathematical approach help us to understand sag problem more clearly and the behavior of the transmission line under galloping conditions and to reduce various problem parameters in to a single clear problem.

3. CURRENT TRANSFORMERS

They are typically used for current measurement. However, their drawback is a narrow bandwidth and they are expensive and limited by their magnetic core characteristic. The CTs performance under distorted conditions is usually characterized by means of the frequency response test [1].

4. POWER LINE CARRIER

It determines average overhead conductor height variations by correlating sag with measured variations in the amplitude of signals propagating between PLC stations [8], [9]. It is fundamentally based on the theory of natural modes supported by multi-conductor transmission lines. PLC system provides a highly reliable infrastructure for the transmission and reception of data, speech and protection signals between stations. This is not accurate as conductors swing differently in different conditions more specifically when we consider the wind induced vibrations.

5. POWER DONUT

5.1 Considering the Fourier's law of heat conduction

According to Fourier's law of heat conduction presented by authors [2], [3], local heat flow in x direction is such that $q_x = -k \frac{dT}{dx}$ where k is the thermal conductivity ($W/m^\circ C$). Q is the vector quantity and can have x, y and z components. Therefore the heat transfer in a power transmission line conductor cannot determine the vertical movement of the conductor in real time. However it can help in the design of the line rating at initial stage. The power donut is installed on live conductor wires [2]. However, this device measures the conductor surface temperature rather than the core temperature for calculating sag.

6. GLOBAL POSITIONING SYSTEM

Based on a constellation of 24 satellites, which uses the Navigation satellite Timing and Ranging (NAVSTAR) developed, launched and maintained by the United States government [4], [5]. It is a worldwide navigation and positioning resource for both military (i.e., precise positioning service) and civilian (i.e., standard positioning service) applications. This method relies on accurate time-pulsed radio signals in the order of nanoseconds from high altitude Earth orbiting satellites of about 11 000 nautical miles with the satellites acting as precise reference points. These signals are transmitted on two carrier frequencies known as the L1 and L2 frequencies. The L1 carrier is 1.5754GHz and carries a pseudo-random code (PRC) and the status message of the satellites. There is a potential in this technology, although there are some errors contributing to estimates. The differential GPS is generally used in order to decrease the selective availability errors. This mode consists of the base and the rover. The main disadvantage of the DGPS is the requirements of a second GPS receiver and corresponding communication equipment between the base and rover instruments. The accuracy of the direct instrumentation of overhead power line conductor sag measurement is about 19.6 cm range and 70% of the time. In the implementation of this technology, the phenomenon of the corona discharge in a transmission line conductor is a challenge in that it creates potentially intolerable conditions for radio reception in the 930MHz and 1.5 GHz frequency bands. This technique is promising; however the challenge such as electromagnetic interference (EMI) from the phase conductors is questionable.

7. IMAGE PROCESSING

In image processing an edge is the boundary between an object and its background appearance. This represents the frontier for single objects. If the edges of image objects are identified with precision all objects can be located and their properties such as area, perimeter and shape can be calculated. Edge detection is an essential tool for image processing technology. In some instances, image processing technique, uses automatic image analysis techniques for extracting information from the line insulators. This concerns the detection of snow overage on insulators on the line and the detection of swing angles of insulators with respect to the vertical position. It must be clear that no real-time detection of the actual transmission line is made by this technique; hence it cannot be translated or be linked to real time dynamic rating of the line. It is also a costly technique and its installation requires contact with phase conductors for actual placement of the correct point.

8. ELECTROMAGNETIC COUPLING METHOD

It is based on the magnetic field surrounding the conductor [7], [8], [11]. For different line configurations, the grounded wire position and the sag calculation need to be modified. Also, Electro Magnetic Interference from nearby transmission lines cannot be neglected. It calculates the current flow and line positions from the magnetic field emanated from the phase conductors.

9. MAGNETO RESISTIVE SENSORS

Provided the sensitivity of the magnetic sensors is sufficient, the electric and spatial information of the overhead line can be found by inverse calculation from the magnetic field measured at the ground level [6]. These sensors are still in early design, although experiments results are promising. The accuracy of this technique is questionable. Factors such as multiple power conductors, bundle conductors and image current due to a conducting ground have to be taken in to consideration.

10. AUTONOMOUS ROBOT TECHNIQUE

This technique uses electromagnetic energy from the line and run along the conductor while making the inspection [10]. The stability and reliability of this technique is questionable as the magnetic field emanated from the conductors always varies and the storage of such is a challenge.

11. RADIO FREQUENCY IDENTIFICATION

It uses electric coupled propagation properties to transfer energy from the radar to the transponder and from the transponder back to the radar. The radar system measures the path length for signals travelling from the transponder to the radar to determine the range hence the sag. Transponders are here simulated on the transmission line from the ground as Figure 1 depicts.

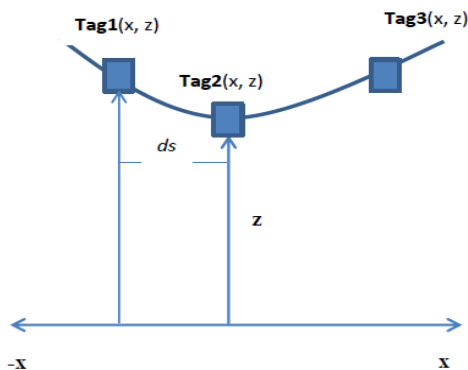


Figure 3: Transponders on the transmission line

Due to the uncertainties of environmental factors and the time spend by the transponder to respond to the radar instructions; the measured ranges contain significant errors. Therefore the distance from the transponder to ground calculated from the measured ranges has big errors. In Figure 5, the blue stare curve denotes the detection error without using the proposed method, and the measurement errors of the proposed method are denoted as circle red curve. The performance is better at Figure's 5 and 6, where the capacitance of the line is considered to be smaller.

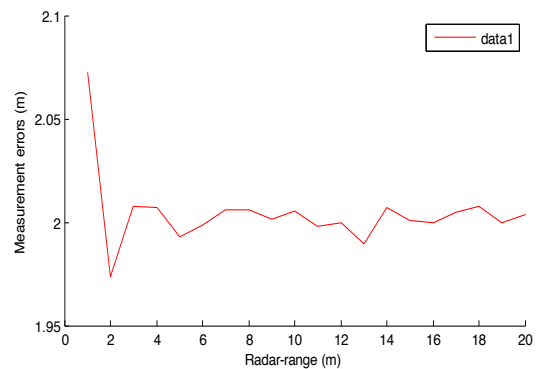


Figure 4: Relative range stability

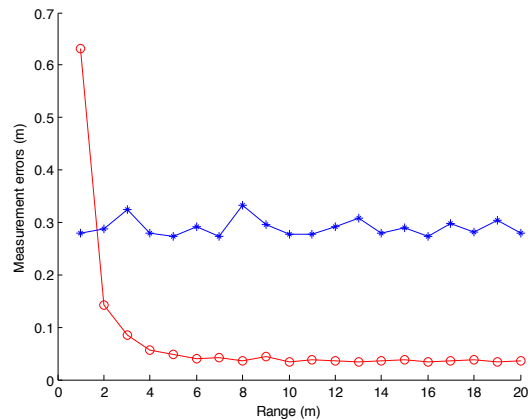


Figure 5: Detection errors

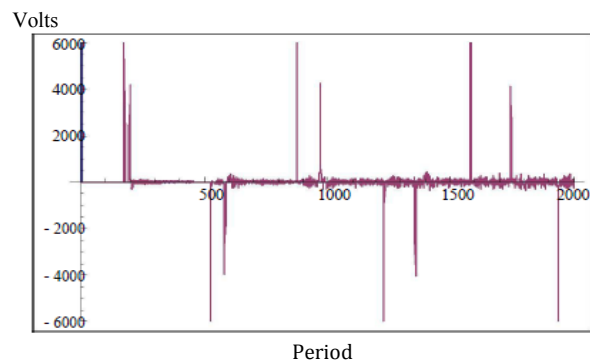


Figure 6: High Voltage response

12. CONCLUSION

The current power system is ideally exposed to different factors such as galloping phenomenon which result in to sagging problem. The methods discussed in this paper mostly do the determination of sag by means of either devices/sensors which require electric field energy to operate. These devices are mounted on the live conductor or the line insulator. Although the PLC method is expensive and does the measurement by comparing average variation of amplitude signals, it is more safe and easy to operate in terms of data processing and monitoring. However the challenge still remains to develop a technique for real-time detection of the conductor itself. RFID radar could be more valuable in future if the errors and EMI challenge is overcome.

13. REFERENCES

- [1] A. Cataliotti et al., "Characterization of current transformers in the presence of harmonic distortion, Presented at the" *IEEE Int. Instrum. Meas. Technol. Conf.*, Victoria, Vancouver Island, Canada, 2008.
- [2] L. Fish, "Low Cost Sensors for Real Time Monitoring of Overhead Transmission Lines". Washington, DC: *Underground Systems Inc.*, 2006.
- [3] G. Thomas Heydt, IEEE, "Application of the Global Positioning System to the Measurement of overhead Power Transmission Conductor Sag," *IEEE Trans. Power Del.*, Vol. 17 NO. 1, pp 273-278, January 2002.
- [4] R.G. Olsen and K.S. Edward, "A new method for real-time monitoring of high-voltage transmission-line conductor sag," *IEEE Trans, Power Del.*, Vol.17 no.4 pp. 1142-1152, Oct. 2002.
- [5] C Mensah-Bonsu, "Novel application of Magnetoresistive Sensors for High-Voltage Transmission-Line Monitoring," *IEEE on Magnetism*, Vol. 47 NO. 10 October 2011.
- [6] S.W. Rienstra, "Nonlinear free vibration of coupled spans". *Power Delivery*, vol. PWRD-2, pp. 851-856, July 1987. spans of overhead transmission lines," in proc. 3rd Eur. Conf. Math. Ind., 1988 pp 133-134.
- [7] R. G. Olsen and K.S. Edwards, "A new method for real-time monitoring of high voltage transmission line conductor sag," *IEEE Trans. Power Del.*, vol.17, no. 4 pp 1142 – 1152, Oct. 2002.
- [8] Wernich de Villiers, and Arthur Burger, "Real-time sag monitoring system for high voltage transmission lines based on power-line carrier signal behaviour" *IEEE Trans. On power del.*, Vol.23, NO.1, January 2008.
- [9] Graham Hall "Maxwell's electromagnetic theory and special relativity" *Phil. Trans. R. Soc. A* 2008, published 28 May 2008.
- [10] Y.H Gu, and S Berlinjn, "Practical applications of automatic image analysis for overhead lines" *22nd Int. Conf. on Electricity distribution*, Stockholm, Norway 10-13 June 2013.

- [11] MJ Tunstal et al., "State of the art of conductor galloping, 2002"
- [12] T.S Hlalele& S Du "Application of a Radio Frequency Identification Technology on High voltage Transmission Line for conductor sag measurement" *ICEET2013 Conf. Proceedings*, 22-23 July 2013.
- [13] *IEEE Std 1159-2009* "IEEE Recommended Practice for Monitoring Electric Power Quality"
- [14] H Saadat "*Power System Analysis*" Second Eedition, 2004 pp 103-135

ANALYSIS OF THE INDUCED VOLTAGE ON BURIED PIPELINE IN THE VICINITY OF HIGH AC VOLTAGE OVERHEAD TRANSMISSION LINES

K.B. Adedeji, A.A. Ponnle, B.T. Abe and A.A. Jimoh.

Department of Electrical Engineering, Faculty of Engineering and the Built-Environment, Tshwane University of Technology, Pretoria, South Africa.
kezman0474@yahoo.com, ponnleAA@tut.ac.za, abeBT@tut.ac.za, jimohAA@tut.ac.za.

Abstract: Continuous growth of electricity and water/oil/gas consumption coupled with environmental factors, has force pipelines to share common corridors with high voltage transmission lines (HVTL), which induce voltage on the pipeline as a result of the magnetic field produced by the current on the lines. This may pose a serious danger to working personnel and even the coating materials of the pipelines. The integrity and safety of pipelines may be compromised, leading to high cost of maintenance and repairs to owners of the pipelines. This paper focuses on the parameters that influence the magnitude of the induced voltage due to inductive coupling between an overhead 275 kV transmission lines and an underground parallel pipeline using Carson's equations for single circuit horizontal and vertical geometry. These parameters include variation in the length of parallelism of the pipeline with the HVTL, the position of the pipeline from the centre of the HVTL tower, the immediate soil resistivity in which the pipeline was laid and depth of the pipeline below the earth surface. The results obtained showed that the induced voltage on the underground pipeline increases with increase in the length of parallelism of the pipeline with the HVTL and the soil resistivity. The results also showed that the induced voltage decreases with increase in the distance of the pipeline from the centre of the tower and the depth of the pipeline below the soil surface.

Keywords: Inductive coupling, Induced voltage, Carson's equation, Ground wire, Underground pipeline, High Voltage Transmission Line.

1. INTRODUCTION

Induced alternating current (AC) degradation has become more widely recognized as a threat to the integrity of underground structures such as pipelines co-located with high voltage transmission lines, electric-powered rail transit systems and other structures where there are stray electric currents [1]. Long term AC interference on the pipelines due to electromagnetic radiation may cause corrosion due to an exchange of AC-induced current and voltages between pipeline and the surrounding soil. This may pose a danger to working personnel and affects the materials of the pipeline's coating. AC affects the performance of cathodic protection (CP) system and shifts the CP potential applied on pipelines to deviate from the design value [2].

The AC carried by High Voltage Transmission Lines (HVTL) conductors create a time varying magnetic field which couples to any structures such as metallic pipelines in the vicinity of the HVTL, according to Flemings right hand rule, resulting in current and voltage being induced on such structures. Whenever electromagnetic lines of force cut through a conductor, a voltage is induced in such a conductor. This effect is shown in Figure 1 in which electromagnetic lines of force produced by HVTL cut through a nearby underground pipeline, thereby inducing voltage in it.

It has been investigated [4-6] that the corrosion rate of most metallic pipelines can be accelerated in the presence of AC interference. AC interference between HVTL and

nearby metallic structures can be divided in to three main types; inductive, conductive and capacitive coupling [7-10].

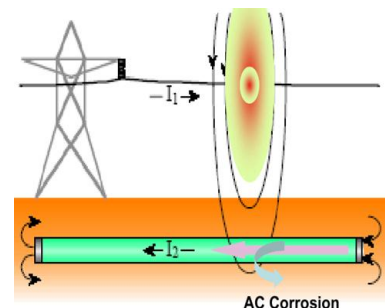


Figure 1: Electromagnetic field from HVTL inducing voltage and current on a nearby underground pipeline as a result of inductive coupling [3].

Inductive coupling affects both aerial and underground pipelines that run parallel to or in the vicinity of HVTL, whereby voltage is induced in to the pipelines due to the time varying magnetic fields produced by the transmission line currents. The induced voltage causes current circulation between the pipeline and the surrounding soil. Capacitive coupling only affects structures located above ground since these have a capacitance to both the HVTL and to the earth [11]. "Resistive coupling between a HVTL and a metallic pipeline is only relevant during ground fault where significant levels of current flows into the ground" [11].

AC corrosion is caused by current exchange between the soil and buried pipelines. This exchange of current

depends on the voltage induced on the pipelines [12]. The magnitude of the induced voltage varies with some parameters such as; the separation between the phase conductors, the height of the HVTL and other varying parameters mentioned earlier. It is then necessary to evaluate and analyze the magnitude of such voltages as the various parameters changes.

Various works have been done to see the effects of magnetic field and induced voltages on pipelines. Lalvani and Lin (1996) worked on a revised model for predicting corrosion of materials induced by alternating voltages [12]. From their work it was concluded that increased peak potential on pipeline always results in corresponding increase in the root mean square current, which in turn increases the absolute ratio of anodic to cathodic Tafel slope, leading to accelerated corrosion. Nelson, (1986) works on Power System in close proximity to pipelines [13]. He calculated the induced voltage on underground pipeline considering horizontal geometry of the line. M'hamed *et al.*, (2014) also present a conference paper on AC corrosion induced by HVTL on cathodically protected pipelines [14]. Their work asserts that current density varies linearly with induced voltage. In view of this, there is need to investigate and analyze the variation in magnitude of induce voltage on pipelines.

In this paper, we use Carson's equation to evaluate the induced voltage on pipeline under inductive coupling. Inductive coupling was chosen because the pipeline of interest is an underground structure in close proximity with a 275kV HVTL. Also both horizontal and vertical geometry of the transmission line were considered.

2. METHODOLOGY

For this study, a single-circuit 275kV, 50Hz with two overhead (shield) ground wires was considered in both horizontal and vertical geometry. The pipeline was a single underground pipeline with 2km length of parallelism with the HVTL. The pipeline position from the centre of the transmission tower was taken to be 30m according to Table 1 [3]. Other parameters used for this work were given in table. The soil resistivity was assumed to be homogenous (100 Ω m) and later varied to see its effects on the induced voltage. The resistance and reactance of the ground wire conductor used were 1.0427 Ω /km and 0.4331 Ω /km according to [13]. Using Carson's equations, the voltage induced on the pipeline considering the effect of both the phase conductors and the overhead ground or shield wire is given by (1)

$$V_p = I_R Z_{Rp} + I_W Z_{Wp} + I_B Z_{Bp} + I_{g1} Z_{g1p} + I_{g2} Z_{g2p} \quad (1)$$

where V_p is the voltage induced on the pipeline; I_R , I_W , and I_B are the full load phase currents in the red, white and blue phase respectively. Z_{Rp} , Z_{Wp} , and Z_{Bp} are the mutual impedance between the phase conductors and the pipeline; I_{g1} and I_{g2} are the current on the ground wires

above the tower; Z_{g1p} and Z_{g2p} are the mutual impedance between the ground wire and the underground pipeline.

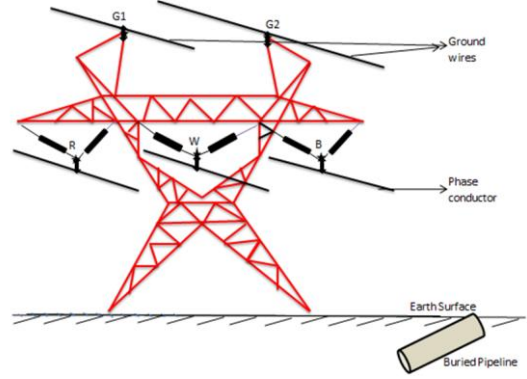


Figure 2: Single circuit horizontal geometry of HVTL and underground pipeline.

Since the overhead ground wire is always connected directly to the ground we can assume that I_{g1} and I_{g2} are zero [13] so that (1) reduces to

$$V_p = I_R Z_{Rp} + I_W Z_{Wp} + I_B Z_{Bp} \quad (2)$$

Considering symmetrical component of a three phase power system, the induced voltage [13] is given by;

$$\begin{aligned} V_p = & \frac{1}{3}(I_R + I_W + I_B)(Z_{Rp} + Z_{Wp} + Z_{Bp}) + \\ & + \frac{1}{3}(I_R + aI_W + a^2I_B)(Z_{Rp} + a^2Z_{Wp} + aZ_{Bp}) + \\ & + \frac{1}{3}(I_R + a^2I_W + aI_B)(Z_{Rp} + aZ_{Wp} + a^2Z_{Bp}) \end{aligned} \quad (3)$$

where $a = e^{j2\pi/3} = \cos 120^\circ + j \sin 120^\circ$

$I_1 = \frac{1}{3}(I_R + aI_W + a^2I_B)$ is the positive sequence current, while $I_2 = \frac{1}{3}(I_R + a^2I_W + aI_B)$ is the negative sequence current and $I_0 = \frac{1}{3}(I_R + I_W + I_B)$ is the zero sequence phase current. According to [13], at a point further away from phase conductors of the line, Z_{Rp} , Z_{Wp} , Z_{Bp} became equal so that, $1 + a + a^2 = 0$, from

$$1 + e^{j2\pi/3} + (e^{j2\pi/3})^2 = 0 \quad (4)$$

So that the voltage induced will be a function of the zero sequence current as,

$$V_p = I_0(Z_{Rp} + Z_{Wp} + Z_{Bp}) \quad (5)$$

Figure 3 shows the equivalent diagram for the horizontal geometry of HVTL and underground pipeline illustrated in Figure 2. It consists of three circuits, the ground wire,

the phase conductors and the pipeline. Individual effects of both the ground wire and the phase conductors on the pipeline are analyzed thus:

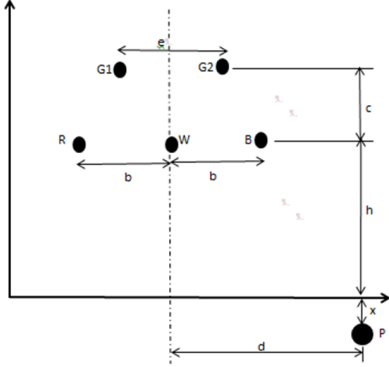


Figure 3: Equivalent diagram for the single circuit horizontal geometry of HVTL and underground pipeline.

The horizontal distance d , between the pipeline and the centre of the HVTL is given in Table 1. For this work, 50 meters was chosen because we are working on 275kV line.

Table 1: Minimum horizontal spacing between HVTL and pipelines

HVTL	Minimum horizontal spacing from pipeline (m)
Voltage less than 69kV, parallel for more than 1.6km	30m
Voltage of 69kV and more, parallel for more than 1.6km	150m
Up to 330kV, parallel for more than 1.6km	30m
Up to 500kV, parallel for less than 1.6km	50m
Up to 1000kV, parallel for less than 1.6km	85m

(Source: [3]).

The coupling factor Z_{CF} , and the mutual impedances (in Ω/km) between the line and the pipeline is given by (6-9) [13].

$$Z_{CF} = Z_{PCP} - \frac{Z_{PCP} \times Z_{gp}}{Z_g} \quad (6)$$

$$Z_{PCP} = r_e + j(X_e - 3X_d(PCP)) \quad (7)$$

$$Z_{PCg} = r_e + j(X_e - 3X_d(PCg)) \quad (8)$$

$$Z_{gp} = r_e + j(X_e - 3X_d(gp)) \quad (9)$$

where Z_{PCP} is the mutual impedance between the phase conductors and the pipeline, Z_{PCg} , mutual impedance between the phase conductors and the ground wires, Z_{gp} , the mutual impedance between the ground wires and the pipeline, r_e and X_e are the earth resistance and reactance factors. These values depend on the operating frequency of the power line and the soil resistivity. For 50Hz, the

values are shown in Table 2 which was calculated using (10-11) [13, 15].

$$r_e = 0.002954 \times f \quad (10)$$

$$X_e = 0.004341 \times f \times \log_{10} \left(4.6656 \times 10^6 \times \frac{\rho}{f} \right) \quad (11)$$

Table 2: Zero sequence resistance and inductive reactance factor

Factor	Soil Resistivity (Ωm)	Factor value (Ω/km)
r_e	All resistivity value	0.1477
X_e	1	1.0787
	5	1.2304
	10	1.2958
	20	1.3611
	30	1.3993
	50	1.4475
	100	1.5128
	150	1.5510
	200	1.5782
300	1.6164	

$X_d(PCP)$, is the mutual reactance between the phase conductors and the pipeline, $X_d(PCg)$ is the mutual reactance between the phase conductors and the overhead ground wire and $X_d(gp)$ is the mutual reactance between the overhead ground wire and the pipeline. The impedance of the ground wire (in Ω/km) is given by (12) [13].

$$Z_g = \frac{3r_a}{n} + r_e + j \left(X_e + \frac{3x_a}{n} - \frac{3(n-1)}{n} X_d(g) \right) \quad (12)$$

where r_a and x_a are the resistance and reactance of the ground wire conductor in Ω/km , $X_d(g)$ is the space reactance of the ground wire and n is the number of ground wires on top of the HVTL tower. The space reactance of the ground wire (in Ω/km) is given (13) [13].

$$X_d(g) = 0.0896 + 0.1736 \log_{10} D_{g1g2} \quad (13)$$

where D_{g1g2} , is the geometric mean distance between the two overhead ground wires. The mutual reactance $X_d(PCP)$, between the phase conductors and the pipeline [13] is given by (14)

$$X_d(PCP) = 0.0896 + 0.1736 \log_{10} D_{PCP} \quad (14)$$

where D_{PCP} , is the geometric mean distance between the phase conductors and the pipeline; is D_{PCg} , is the geometric mean distance between the phase conductors and the two overhead ground wires and D_{gp} , is the geometric mean distance between the two overhead ground wires and the pipeline. D_{PCP} is given by (15)

$$D_{PCP} = \sqrt[3]{D_{Rp} D_{Wp} D_{Bp}} \quad (15)$$

where D_{RP} , D_{WP} , and D_{BP} are the geometric mean distance between red, white and blue phase conductors and the pipeline and these can be evaluated from Figure 3 using Pythagoras theorem. Therefore, the geometric mean distance between red, phase conductors and the pipeline is given by

$$D_{Rp} = \sqrt{(h+x)^2 + (d+b)^2} \quad (16)$$

Other geometric mean distances were also calculated using the same approach. The self-reactance (in Ω/km), between the phase conductors and the overhead ground wire and its geometric mean distance is given by (17-18) [13],

$$X_d(PCg) = 0.0896 + 0.1736 \log_{10} D_{PCg} \quad (17)$$

$$D_{PCg} = \sqrt[6]{D_{Rg1} D_{Rg2} D_{Wg1} D_{Wg2} D_{Bg1} D_{Bg2}} \quad (18)$$

The self-reactance between (in Ω/km) the overhead ground wire and the pipeline and its geometric mean distance is given by (19-20) [13],

$$X_d(gp) = 0.0896 + 0.1736 \log_{10} D_{gp} \quad (19)$$

$$D_{gp} = \sqrt{D_{g1p} \times D_{g2p}} \quad (20)$$

The maximum induced voltage on the pipeline is given by (21)

$$V_p = 3 \times I_0 \times Z_{CF} \times L \times K \quad (21)$$

where L , is the length of parallelism of the pipeline with the transmission line in (km) and K is the shielding factor of the earth wire due to inductive coupling. For Aluminium Conductor Steel Reinforce (ACSR) with dc resistance less than $0.5 \Omega/\text{km}$, $K=0.55$ for two ground wires and 0.77 for one ground wire [16].

For single circuit vertical geometry of the line, Figure 4 shows vertical geometry of HVTL and an underground pipeline. The equivalent diagram for the vertical geometry of the HVTL and the underground pipeline is shown in Figure 5.

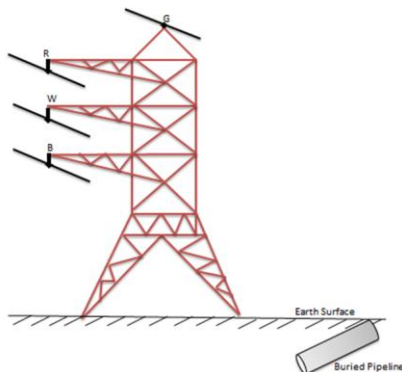


Figure 4: Single circuit vertical geometry of HVTL and underground pipeline.

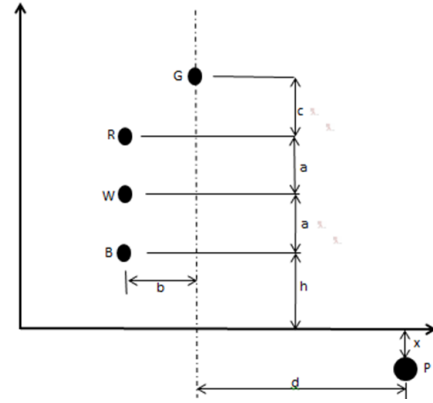


Figure 5: Equivalent diagram for single circuit vertical geometry of HVTL and underground pipeline.

The expression for calculating the induced voltage on pipeline, the coupling factor and the various mutual impedances still holds for single circuit vertical geometry. The geometric mean distances are calculated using the same approach applied in the horizontal geometry. For this case (vertical geometry), the number of overhead ground wire is one as shown in Figure 5. Table 3, shows the varying parameters used for the analysis and the calculations we performed using MATLAB.

Table 3: Operating parameters used for simulations (for 275kV, 50Hz)

S/n	Parameters	Horizontal Geometry	Vertical Geometry
1	Pipeline position from the canter of the HVTL tower.	30m	30m
2	Height of the transmission tower above ground to the last conductor	12m	12m
3	Depth of pipeline beneath the soil surface.	1m	1m
4	Separation between the phase conductors.	*10m	**8m
5	Length of parallelism of the pipeline with the HVTL	2km	2km
6	Soil resistivity in which the pipeline was laid	100 Ωm	100 Ωm
7	Separation between the phase conductors and the overhead ground wires	8m	4m
8	Separation between the overhead ground wires	8m	
9	Resistance and reactance of the ground wire conductor	1.0427 Ω/km and 0.4331 Ω/km	

* Horizontal separation between the phase conductors.

** Vertical separation between the phase conductors.

3. RESULTS AND DISCUSSIONS

Using the parameters in Table 3, the results of the analysis which was simulated in MATLAB are presented in Figure 6 to Figure 9. Figure 6 shows variation of the induced voltage with different pipeline position from the centre of the HVTL for the horizontal and vertical geometry, with 2km length of parallelism and 1m below the soil surface. From this figure it can be seen that the induced voltage has a maximum value at a distance too close to the tower and decreases as its distance from the centre of HVTL increases. This indicates that the underground pipeline should be far away from the centre of HVTL to reduce the voltage that might be induced on the nearby pipelines.

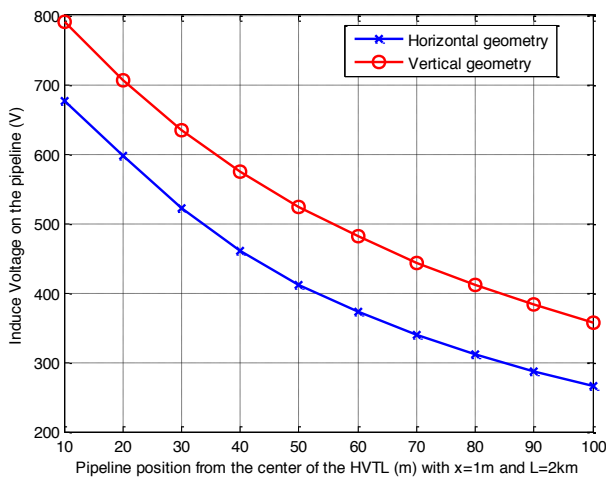


Figure 6: Variation of induced voltage with distance of the pipeline from the centre of HVTL

Figure 7 shows the variation of the induced voltage with depth of the pipeline below the soil surface, with 2km length of parallelism and 30m from the centre of the tower. From the figure, it can be seen that the induce voltage decreases with increase in the depth of pipeline below the soil surface. This means that as the pipeline is buried far below the soil surface, the magnitude of the induce voltage on the pipe decreases.

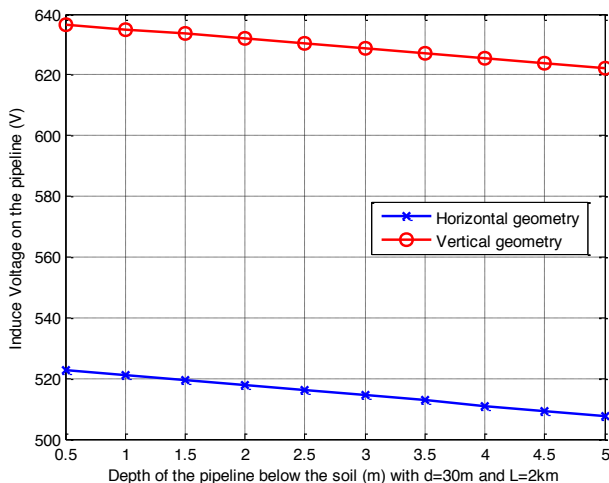


Figure 7: Variation of induced voltage with depth of the pipeline below the soil.

Figure 8 presents the effects of the length of parallelism of the pipeline on the induced voltage on the pipeline, at a distance of 30m from the center of the tower and 1m below the soil surface. It can be observed from the figure that the magnitude of the induced voltage increases as the length of parallelism increases. This means that the induced voltage on the pipeline has a direct proportion relationship with its length of parallelism. It can also be observed from the figure that, the magnitude of the induced voltage is lower for pipeline sharing corridor with transmission line having horizontal geometry than that of vertical geometry.

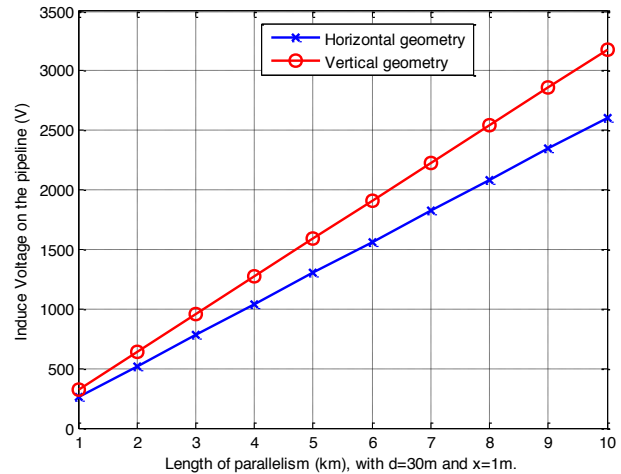


Figure 8: Variation of induced voltage with the length of parallelism of the pipeline.

Figure 9 shows how the induced voltage varies with the soil resistivity in which the pipeline was buried. From the figure it can be observed that, the magnitude of the induce voltage on the pipeline increases as soil resistivity increases. The figure also points out that transmission lines with vertical geometry carrying the same operating voltage with the horizontal geometry induce more voltages on the pipeline than that of the horizontal counterpart.

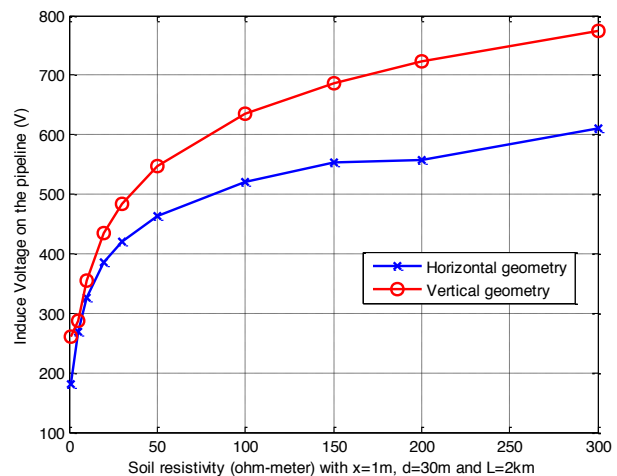


Figure 9: Variation of induced voltage with soil resistivity

4. CONCLUSION

The effects of various parameters on the magnitude of the induced voltage on underground pipelines due to the time varying magnetic field produced by AC current on the HVTL has been analyzed using Carson's equations; and the results were simulated in MATLAB. The results obtained showed that the magnitude of the voltage induced on the pipeline varies as those parameters used changes. The magnitude of the maximum induced voltage on the underground pipeline increases; as the length of parallelism of the pipeline with the HVTL increases and as the soil resistivity increases. The results also showed that the induced voltage decreases as horizontal distance between the pipeline and the HVTL increases and as the depth of the pipeline below the soil surface increases.

It can also be concluded that the magnitude of the induced voltage on the buried pipeline varies with phase geometry on the transmission line tower. Its magnitude is higher for vertical geometry than horizontal geometry of the same transmission potential and load currents. From the analysis described above, if pipeline must share common corridor with high voltage transmission lines, it will be better to share corridor with tower having horizontal phase geometry than the one with vertical phase geometry.

5. ACKNOWLEDGEMENT

This work is based on the research supported by the Rand Water and the National Research Foundation of South Africa. The Grant holder acknowledges that opinions, findings and conclusions or recommendations expressed in any publication generated by the NRF supported research are that of the author(s), and that the NRF accepts no liability whatsoever in this regard.

REFERENCES

- [1] N. Ida, Y. Menach, X. Shan and J. Payer: "A nonlinear model for AC induced corrosion", *Journal of Advanced Electromagnetics*, Vol. 1, No. 1, pp.1-2. 2012.
- [2] L.Y. Xu, X. Su, Y.F. Cheng: "Effect of Alternating Current on Cathodic Protection on Pipelines", *Corrosion Science*, Vol. 66 pp. 263–268, 2013.
- [3] M. Husain: "AC Interference on Pipelines Leading to AC Corrosion", CP Specialist - Saudi Aramco, 2012.
- [4] T.C. Tan and D.T. Chin: "AC Corrosion of Nickel in Sulphate Solutions", *Journal of Applied Electrochemistry*, Vol. 18, Issue 6, pp. 831-838, 1988.
- [5] S. Goidanich, L. Lazzari, M. Ormellese and M. Pedferri: *Corrosion'2005*, NACE, Houston, 2005 Paper No. 05189. 2005.
- [6] J.L. Wendt, and D.T. Chin: "AC Corrosion of Stainless Steel-II; the Breakdown of Passivity of SS304 in Neutral Aqueous Solutions", *Corrosion Science*, Vol. 25, Issue 10, pp. 889-900, 1985.
- [7] E. Collet, B. Delores, M. Gabillard and I. Ragault: "Corrosion due to AC Influence of Very High Voltage Power Lines on Polyethylene-coated Steel Pipelines: Evaluation of Risks Preventive Measures", *Anti-Corrosion Methods and Materials*, Vol. 48, No. 4, pp. 221–227, 2001.
- [8] R.G. Wakelin and C. Sheldon: "Investigation and Mitigation of AC Corrosion on a 300mm Diameter Natural Gas Pipeline", *CORROSION/04*, NACE expo, paper 205, New Orleans, Louisiana, 2004.
- [9] D. Funk, W. Printz and H.G. Schoneich: "Investigation of AC Corrosion in Cathodically Protected Pipes", *3R International*, Vol.31, No. 6, pp. 336–341, 1992.
- [10] I. Ragault: "AC Corrosion Induced by V.H.V. Electrical Lines on Polyethylene Coated Steel Gas Pipelines", *CORROSION/98*, NACE expo, Paper 557, San Diego, California, 1998.
- [11] H. Ahmed, M. Wael and A. Ehab: "Effects of Electromagnetic field from power line on Metallic Objects and Human Bodies", *International Journal of Electromagnetics and Applications* Vol. 2, No.6, pp. 151-158, 2012.
- [12] S.B. Lalvani and X. Lin: "A Revised Model for Predicting Corrosion of Materials Induced by Alternating Voltages", *Corrosion Science*, Vol. 38, No. 10, pp. 1709-1719, 1996.
- [13] J.P. Nelson: "Power System in Close Proximity to Pipelines", *IEEE Transactions on Industry Application*, Vol. 22, No. 3, pp.435-441, 1986.
- [14] O. M'hamed, Z. MouradAicha Z., Omar, T., Rachid I., Saida, B., and Cherif, D. 2014. AC Corrosion Induced by HVTL on Cathodically Protected Pipelines. *Proceedings: International Conference on Control, Engineering and Information Technology (CEIT'14)*, Sousse, Tunisia, pp. 22-26, March, 22-25, 2014.
- [15] ABB Power T & D Company: "Electrical Transmission and Distribution Reference Book", Raleigh, North Carolina, 5th Edition, p. 54, 1997
- [16] Eskom: "Guideline on the Electrical Co-ordination of Pipeline and Power Lines", Paper No. 240-66418968, pp. 25-73.

Partial Discharge Analysis in Power Cables using 3D Phase Resolved Patterns.

I.K. Kyere*, J.J. Walker **and D.V. Nicolae ***

* Vaal University of Technology, Dept. of Power Engineering, Private Bag X021, Vanderbijlpark, 1900, South Africa E-mail:ikyere@gmail.com

** Walmet Technologies (Pty) Ltd. E-mail: jerrywalker@walmet.co.za

***Tshwane University of Technology, Staatsartillerie Road, Pretoria Wes, Pretoria. E-mail:nicolaedy@tut.ac.za

Abstract: The integrity of solid insulation in high voltage system is an important factor to be considered in maintaining the normal operation of the equipment. Thus, this analysis presents partial discharge measurement in artificial defects in 11kV XLPE insulation. The partial discharge measurement was conducted in a solid insulation sample with typical known defects of spherical and slot shapes at specific locations in the insulation. Analysis was done using the phase-resolved measurement principle which determines the partial discharge magnitude (q), phase of partial discharge occurrence (Φ) and partial discharge number (n). As a result, it was found that the generation of partial discharge patterns of the two voids can be separated from each other with the increment of the applied voltage. Hence, the proceeding results obtained in this very examination are detailed via phase-charge-number (Φ -q-n).

Keywords: Partial Discharge, Phase-resolved, Insulation, PD magnitude, PD number.

1. INTRODUCTION

Electric power systems include a large number of expensive and important power cables of different ages manufactured and installed over many decades [1]. Investments in power cables are capital intensive with long life and of great economic importance [2]. This has resulted in higher demands by the electricity industry to create an increased focus on the need to obtain higher performance, reliability, and asset life span [3].

Partial discharge (PD) seems to be a somewhat, inevitable part of the life of most insulating systems for high voltage equipment. Increasing interest arose in 1930s, when its degrading effect on high voltage insulation became problematic. Early studies used ultrasonic detection techniques to assess discharge activity in oil. From 1960, PD was studied intensively in terms of fundamental physics, its effect on insulating systems, and how best to measure and monitor it with time [4].

Partial discharge is defined as a local dielectric breakdown that only partially bridges the insulation system between conductors under high voltage (HV) stress. The main causes for the partial discharge are cavities within the solid and liquid dielectrics [5]. The existence of either a highly non – uniform electric field as in corona discharge, or in a situation where the insulation has a weak point such as a gas-filled void, usually results in the occurrence of a partial discharge, which limits the lifetime of an insulation system

due to its deteriorating effect. High-energy electrons or ions can cause deterioration of the insulation material during partial discharge on the surface or inside an insulation material, thus this bombardment may result in chemical decomposition in the insulation material, which could finally result in the complete breakdown of the insulation [6].

The insulation systems of high-voltage power cables are subjected to different kinds of stresses during their service life, and thus suffer degradation and deterioration that can lead to a reduction of life, which in turn lowering the reliability of electrical power systems [1]. One of these high stress situations occurs when the insulation shield (screen) is removed from a cable resulting in high potential gradients being concentrated at the cutback point, causing high electrical stress [7].

This paper presents partial discharge measurement in artificial defects in an 11kV XLPE insulation system. The partial discharge measurement was conducted in solid insulation sample with known defects of spherical shape and slot shape at specific location in the insulation using the method of phase-resolved measurements technique. The phase-resolved measures the partial discharge magnitude (q), phase of partial discharge occurrence (Φ) and partial discharge number (n). The results obtained are discussed through Φ -q-n.

2. INTERNAL DISCHARGES

The electric field in air-filled cavities is higher than the electric field in the materials because of the difference in their dielectric constants, as well as the shape of the cavity. In solid insulating materials, cavities are of irregular shape. The cavities in solid insulations can be broken down as a result of the presence of certain particles such as metallic particles, the presence of a charge on the cavity, and semi-conducting deposits on the surface of the cavity. Figure 1 shows partial discharge electrode configurations [21].

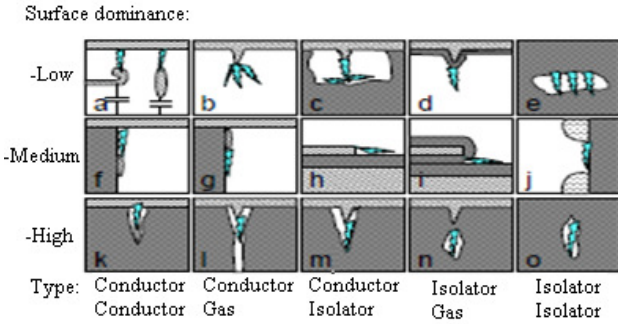


Figure 1: Partial Discharge Electrode Configurations

These remaining charges change the electric field of the cavity and the next discharge takes place at different locations of the cavity. When the alternating voltage is applied, the discharges of opposite polarities are produced alternatively. There are charge clusters of opposite polarities at different sites of the cavity that result in discharge on the cavity's surface inside the insulating materials. A conducting channel is formed between the electrodes that bridge the cavity. It results in insufficient voltage for the breakdown of gas, and at the end, the discharge extinguishes. The extinction voltage is less than the inception voltage because after the initial discharge, a lower voltage is required to maintain the discharge; it can be 25 percent lower in many cases. If cavities are small (< 0.15 mm) and filled with air at atmospheric pressure, discharges cannot be detected by pulse discharge detectors. These types of discharges are called pseudo-glow discharges. The cavities or voids of such small dimensions are not dangerous for solid insulations [8, 9].

3. AGEING AND BREAKDOWN DUE TO PARTIAL DISCHARGE

During manufacturing process, the gas-filled cavities are created within the dielectric or adjacent to the interface between the insulation and the conductor. When a voltage is applied to such insulation, the discharges occur in gas-filled cavities and result in the transfer of charges between two points to cause discharges of cavity capacitance. The

deterioration is produced in insulation from this charge on the dielectric surface and the charge transfer results in forming a dipole moment, and the field in the cavity opposes the applied electric field; therefore, the discharge extinguishes. The degree of ageing depends on inception voltage and discharge magnitude. However, the inception voltage is dependent on the thickness of the cavity and the permittivity of insulation. The electric field stress in the cavity filled with gas is given by [18],

$$E_{\text{cavity}} = \frac{\epsilon_i}{\epsilon_c} \times E \quad (1)$$

Where:

E = the electric field strength of insulation,

ϵ_i = relative permittivity of insulation

ϵ_c = relative permittivity of air in cavity

E_{cavity} = the electric stress in the cavity (Note: it will be more than the breakdown strength of gas in cavity).

For the breakdown of gas in the cavity, the discharge has to start at one end and progress to the other end. The discharge phenomena in small cavities can be modelled by using Townsend's discharge mechanism. According to this theory, the breakdown voltage is a function of pressure in the cavity and the size of the cavity [19].

In uniform fields, the Townsend's criterion for breakdown in electropositive gases is given by the following equation,

$$\gamma (e^{\alpha d} - 1) = 1 \quad (2)$$

$$\text{or } \alpha d = \ln(1/\gamma + 1)$$

where the coefficients α and γ are functions of E/p and are given as follows:

$$\alpha = pf_1 \left(\frac{E_0}{p} \right) \quad (3)$$

and

$$\gamma = f_2 \left(\frac{E_0}{p} \right) \quad (4)$$

where:

E_0 = the applied electric field,

p = the gas pressure,

In a uniform field electrode system of gap distance d ,

$$E_b = \frac{U_b}{d} \quad (5)$$

Where:

U_b is the breakdown voltage and E_b the corresponding field intensity. E_b is equal to the electric strength of the dielectric under given conditions. When the applied field intensity $E_0 = E_b$, the Townsend's criterion for breakdown in electropositive gases in uniform field can be represented in terms of the product of the gas pressure and the electrode gap distance ' pd ' as,

$$f_2 \left(\frac{U_b}{pd} \right) \{ \exp [\text{pdf}_1 \left(\frac{U_b}{pd} \right)] - 1 \} = 1 \quad (6)$$

$$U_b = F (P \times d) \quad (7)$$

From expressions 1 and 7, it is possible to calculate the breakdown voltage and maximum permissible electric field strength of insulating material in order to avoid the partial discharge [20].

4. PARTIAL DISCHARGE ACQUISITION SYSTEM

The *ICMmonitor* is the part of the Power Diagnostix Systems GmbH ICM series of digital partial discharge detectors. It is a compact stand-alone instrument for evaluating the condition of medium and high voltage insulation. The instrument can be used over a range of frequency of applied voltage, including power system frequency (50/60Hz) and very low frequency (0.1Hz). Furthermore, it provides high-resolution, digital, partial-discharge patterns for characterisation of defects in inter alia transformers, cables and bushings.

A wide range of external preamplifiers provides control of the frequency range in which partial discharge activity is detected from 40Hz up to 2GHz. The *ICMmonitor* features various noise handling techniques. The noise-gating module can be connected to an antenna or a current transformer to sense and remove noise without losing significant partial discharge data. Another method available is the simple windowing, in which phase-stable noise is blocked out for portions of each applied high voltage wave. Similarly, a low-level discriminator (LLD) can be set to a certain level in order to reduce noise.

5. EXPERIMENTAL SETUP

Two artificial defects of different shapes and sizes were prepared in one sample in order to determine the influence of applied voltage on partial discharge.

The sample used for these measurements consists of 11 kV XLPE insulated cable with additional heat-shrink insulation applied across the XLPE to form a multi-layer insulation. Artificial defects were introduced in the XLPE and heat-shrink insulation. Figure 2 shows the test sample that was used in the experiment. The first defect (cavity) was artificially created by drilling a 2mm diameter hole in the XLPE insulation of the sample. The cavity was covered with one layer of heat shrink insulation having a longitudinal slot cut into it before being covered by another layer of heat shrink insulation.

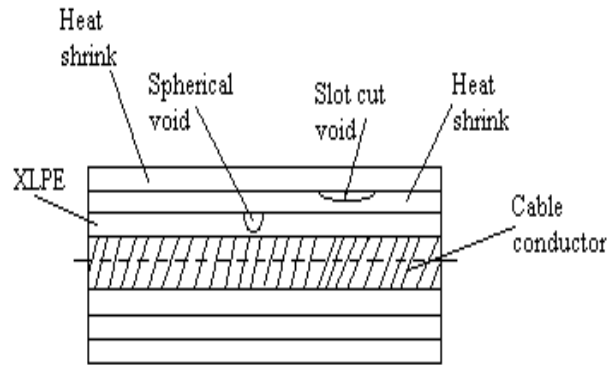


Figure 2: Artificial voids in solid insulation

The circuit arrangement shown in Figure 3 below is the conventional PD test circuit in accordance with IEC 60270 [10] consisting of 50 Hz ac power supply, the test sample, the Coupling Capacitor (C_c), the measuring impedance (Z_m), and the PD measuring device which consist of the *ICMmonitor* from Power Diagnostix and personal computer with software to evaluate and save the data.

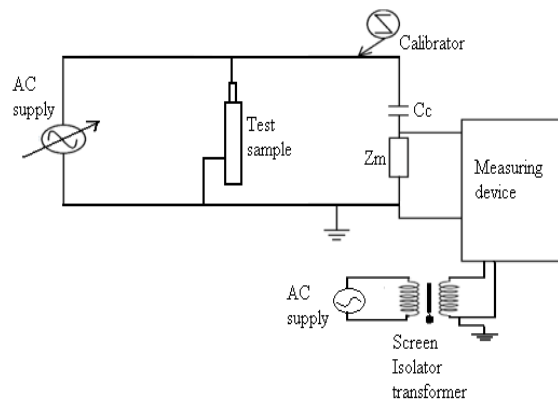
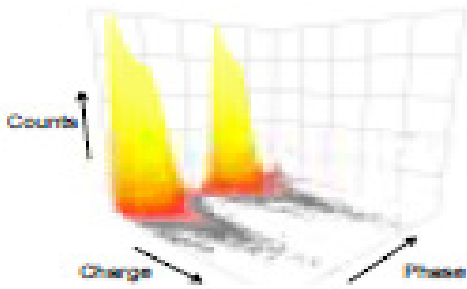


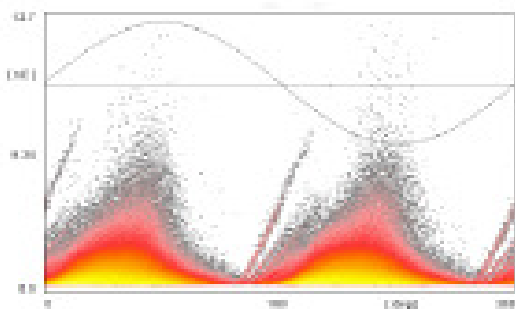
Figure 3. Partial discharge measuring circuit

6. PHASE-RESOLVED PARTIAL DISCHARGE PATTERNS

A phase-resolved partial discharge technique provides comprehensive information to analysed properties of the defects in insulation materials. The Phase-resolved partial discharge (PRPD) pattern indicates the defect's geometry, the availability of the initial detection and the properties of the contributing materials [16]. The horizontal axis is the phase angle where partial discharge pulses occurred while vertical axis is the partial discharge charge magnitude in pC. Each point has a colour, which represents the number of partial discharges that occurred with given amplitude and phase (a brighter colour indicates a higher number) [11, 12]. Figure 1(a) and 1(b) shows the different between the traditional 3D pattern and the 3D PRPD patterns.



(a) Traditional 3D Pattern

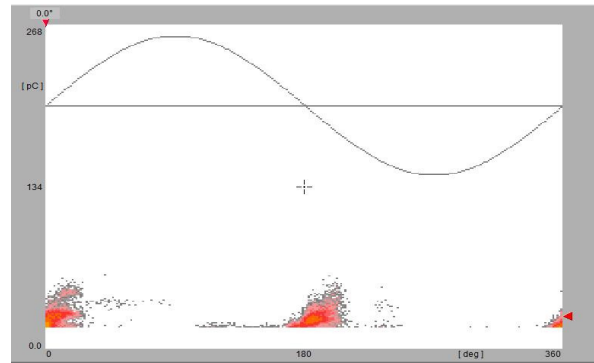


(b) Modern 3D PRPD pattern

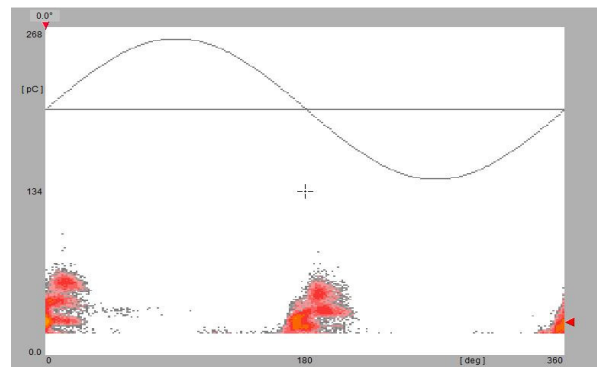
7. RESULTS AND DISCUSSIONS

The measurements were carried out by varying the voltage in different levels. The acquired PD was measured at 2 kV, 2.5 kV, 3.5 kV, 4 kV and 4.5 kV. Figure 4 shows phase

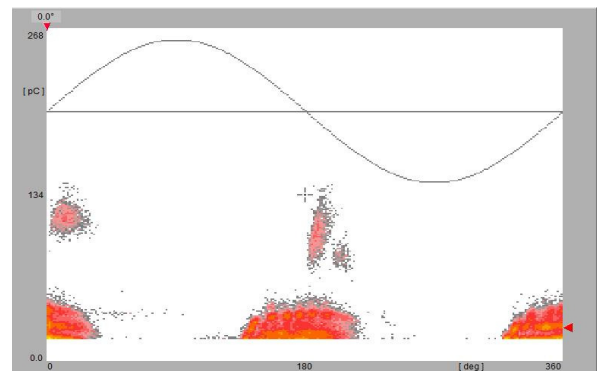
resolved patterns for the partial discharge activities of the test samples in Figure 2 consisting of two cavities positioned on different insulating materials. This phase-resolved plot displays all discharge pulses obtained during a 60-second interval at different magnitudes of applied voltages.



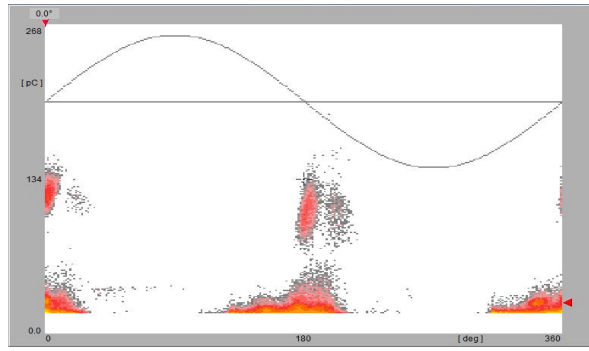
(a) 36.8 pC at 2 kV



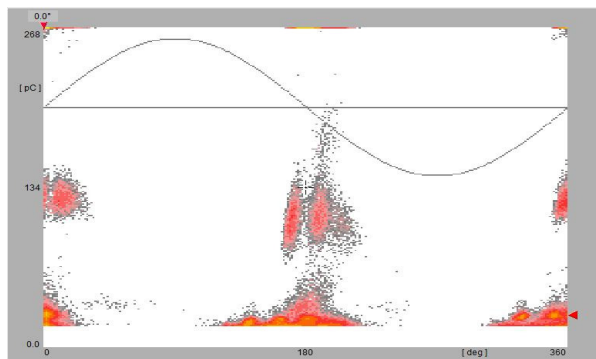
(b) 70.5 pC at 2.5 kV



(c) 121.1 pC at 3.5 kV



(d) 138.8 pC at 4 kV



(e) 268.4 pC at 4.5 kV

Figure4: PRPD patterns obtained at different voltages

When the applied voltage is higher, the numbers of partial discharges per cycle, total charge per cycle and the maximum magnitude of the cavity discharge would be higher. A partial discharge normally occurs in the cavity when the electric field in the cavity is higher than the inception field and there is an initial free electron to start an avalanche process [14]. At higher applied voltage, the electric field in the void increases faster towards the inception field resulting in more discharges in one of the applied voltage cycles.

From these figures, it can be seen that the discharges occur within two voids of different diameters. Figure4 (a) shows the single discharge pattern when 2 kV was applied. However, increasing applied voltage, shows the two voids separating from each other as seen in Figure4 (c, d & e).

Generally, it is seen that partial discharge pulse appears around 30° - 90° phase angle in the positive half cycle, and 150° - 270° phase angle in the negative half cycle of the applied voltage. The non-symmetrical partial discharge pattern indicates either a strongly non-symmetrical electrical field or an interface contributing to the discharge showing different amount of free electrons to be accelerated in the electrical field [15].

When partial discharges occur within two different size voids, discharges can be seen at a higher repetition rate within one of the voids by referring to the pattern that

occurs near the minimum charge magnitude (the bottom pattern) [17].

Referring to figure4(c and d), the number of partial discharge is higher at the bottom than the upper part of the pattern. This is due to higher initial free electrons in the void to initiate discharges, resulting in larger probability of partial discharge to occur. Therefore, within one cycle of the applied voltage, more PDs occur, could be seen by the high density of partial discharge distribution pattern. However, there is a smaller number in the upper part of the pattern due to lower initial free electrons to cause the occurrence of partial discharge in the other void. Hence, most of partial discharges occur after certain time delay when the inception field has been exceeded. Thus, there is a lower number of partial discharges per cycle, which can be seen by the low density of partial discharge distribution in the upper part of the pattern [17].

8. CONCLUSION

A three-dimensional (3D) phase-resolved partial discharge in Power Cables has been studied to analyse the defects in the insulation materials using the electrical method of partial discharge detection [18]. It is inferred that the occurrence of partial discharge is highly depends on the applied voltage. Hence, from the phase-resolved pattern obtained, it is established that partial discharge patterns from two different cavities can clearly be seen as the voltage increases as well as the magnitude of the discharges.

9. REFERENCE

- [1] P. Hyvonen: "Prediction of insulation degradation of distribution power cables based on chemical analysis and electrical measurements". DTech. Thesis, Helsinki University of Technology. 2008.
- [2] E. Peschke and R.V. Olshausen: "Cable system for High and Extra-High Voltage". Germany: MCD Verlag. 1999.
- [3] H. Marazzato, K. Barber, M. Jansen and G. Barnewall: "Cable Condition Monitoring of Improve Reliability". Techcon,14. 2004.
- [4] C. Smith: "Partial discharge & insulation failure". Independent Power Engineering Consultants (IPEC) Ltd., Manchester, United Kingdom, pp. 1 – 11. 2005.
- [5] M. Fidan and H. Ismailoglu: "A novel partial discharge calibrator design via dual microcontroller and high speed DAC". *ELECO 2007*, session A6, High Voltage Engineering, pp. 169-172. 8 December 2007.
- [6] M.G. Niasar: "Partial discharge signatures of defects in insulation systems consisting of oil and oil-impregnated paper". Licentiate thesis, Licentiate thesis, Kungl

- Tekniska högskolan, Stockholm, Sweden, pp. 11; 33-35. 2012.
- [7] B., Gokcen: “*Electric field analysis in stress controlled high voltage cables*”. MTech.Dissertation.Middle East Technical University. 2005.
- [8] D. König and Y. N. Rao: “*Partial Discharges in Electrical Power Apparatus*”. Vdeverlaggbmh, Berlin and Offenbach, pp. 15-26, 106-108. 1993.
- [9] T.J.Gallagher and A.J. Pearmain: “*High Voltage Measurement Testing and Design*”. John Willey and Sons, pp. 163-189. 1983.
- [10] IEC60270: “*Standard. High– Voltage Test Techniques – Partial Discharge Measurements*”.2000.
- [11] M. Conti: “*Development of artificial intelligence systems for electrical insulation defect identification through partial discharge measurements*”. Ph.D. Thesis. Bologna, Italy: University of Bologna. Department of Electrical Engineering, pp. 8-9. 2003.
- [12] S. Suwarno and H. Sutikno: “Measurement, modeling and computer simulation of partial discharges in natural liquid insulation for high voltage transformer”. *Recent Researchers in Computational Techniques , Non-Linear Systems and Control*, Wisconsin, USA, pp. 160 – 165. 2011.
- [13] D.W., Gross and J.G., Herbig: “Partial discharge fault location and diagnosis on HV power cables”. *In Electrical Insulation and Dielectric Phenomena, 2000 Annual Report. Conference on IEEE*, Victoria BC, pp. 630-633. 15-18 October 2000.
- [14] H. Illias, T. S. Yuan, AB H. Abu. Bakar, H. Mokhlis, G. Chen and P. L. Lewin: “Partial Discharge Patterns in High Voltage Insulation”. *In proceedings of IEEE International Conference on Power and Energy (PECon)*, Kota Kinabalu Sabah, Malaysia, pp. 751-755. 2-5 December 2012.
- [15] D.W. Gross and M. Söller: “Strategies to locate partial discharge in large power transformers”. *Draft, submitted to INSUCON 2006, 10th International Insulation Conference*, Birmingham, UK, May 24-26. 2006.
- [16] D.W. GROSS & M. SÖLLER: “Partial discharge diagnosis on large power transformers.” In proceedings of Conference Record of the 2004 IEEE International Symposium on Electrical Insulation, Indianapolis, USA, pp. 186-191, 19-22 September 2004.
- [17] H.A Illias, G Chen, A.H.A, Bakar, H. Mokhlis and M.A., Tunio: “Partial discharges within two spherical voids in an epoxy resin”. 2013 *J. Phys. D: Appl. Phys.* 46 335301, pp. 1-10. 29 July 2013.
- [18] A. Mehta, R.N. Sharma, S. Chauhan and S.D. Agnihotri: “Study the Insulation System of Power Transformer Bushing”. *International Journal of Computer and Electrical Engineering*, Vol.3, No.4; pp. 544-547. August 2011.
- [19] M.S. Naidu and V. Kamaraju: “*High voltage engineering*”. 2nd ed. Tata: McGraw-Hill Publishing, pp. 71 – 76.1995.
- [20] G. Engdahl, H. Edin and R. Eriksson: “*Electrotechnical Modeling and Design*”. KTH, 2006.
- [21] D. W. Gross: “A brief Introduction into the Theory of Partial Discharge”, Power Diagnostix Systems GmbH Bruesseler Ring 95a, 52074 Aachen, Germany,p.1

EXPERIMENTAL INVESTIGATION OF AEOLIAN-VIBRATIONAL LOADS ON COMPOSITE INSULATORS

K.A. Ntambwe*, R.C. Loubser*, P. Moodley* and K.O. Papailiou**

* *Vibration Research and Testing Centre (VRTC), Dept. of Mechanical Engineering, School of Engineering, University Road, Westville, University of KwaZulu-Natal, Durban 4001, South Africa*
E-mails: 212562424@stu.ukzn.ac.za, rloubser@smri.org and moodleypr@ukzn.ac.za

** *Chairman Cigré SC B2 (Overhead Lines) 6102 Malzers, Switzerland*
E-mail: konstantin@papailiou.ch

Abstract: This paper reports on the experimental evaluation of the relationship between mechanical loads and bending amplitudes of overhead transmission lines (OHTL) caused by wind-induced Aeolian vibrations. These loads may have an influence on the long-term performance of insulators which are still under investigation. The methods proposed here are the swept-sine test and the bending amplitude test. By selecting the resonance frequencies in the range of 7-25Hz, the peak-to-peak mechanical loads caused by the vibrating conductors on the insulator were measured by a force transducer, while a displacement transducer was measuring in the range of 0.1 to 1.0 mm the peak-to-peak bending amplitude of the conductor. The dynamical loads caused by two ACSR Aluminium Conductors Steel-Reinforced, i.e. Tern 45Al/7St. and Pelican 18Al/1St. were collected as a function of the bending amplitude. A comparative study between different clamp configurations was completed at four conductor static tensions on levels (15-30%UTS with 5% of increment) for both conductors.

Keywords: Aeolian vibration, bending amplitude, dynamic loads, suspension clamps, composite insulator

1. INTRODUCTION

High-voltage transmission lines are used to transport the electric power from the generation plant to the end-users. Mounted to the towers and held by insulators, the overhead line conductors are exposed to pollution and weather (rain, wind, and ice). In particular, wind, ice loads, temperature variations, and the conductor tensions, impose mechanical loads on the conductors. When a smooth, steady crosswind blows onto a conductor at low wind-speed (1-7m/s), a mechanical phenomenon called Aeolian vibration occurs. This is characterized by low amplitudes (approximately one conductor diameter) and relative high frequencies (5-120Hz) [1, 2].

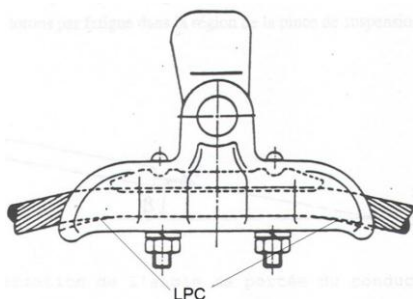


Fig. 1 Suspension clamp/conductor schematic [3]

Aeolian vibration is an unexpected but undesired phenomenon, because of its dynamic character. Different types of vibration-protection fittings (Stockbridge dampers, spiral impact dampers, etc.) are used to reduce and minimise its effects which possibly leads to fatigue failures. The first signs of failure on a conductor usually

appear at the clamp edge (CE). Previous studies have shown that the critical areas of a vibrating conductor were near suspension clamps (Fig.1), but also at Stockbridge-damper and spacer-damper clamps. The mechanical behaviour of the vibrating conductor (i.e. its bending stiffness, bending amplitude, self-damping, etc.) is complex, because of the structure of the conductor, which is an assemblage of different twisted strands from different materials. This dynamical behaviour depends on the tension, vibration frequency, vibration amplitude, and the temperature of the conductor [1]. For the relationship between the bending amplitude and the bending strain of a vibrating conductor, the so-called Poffenberger-Swart (P-S) formula is often used, whereby the conductor is assumed to be a homogeneous and uniform standard beam under tension, whose stiffness is simply the sum of single-wire bending stiffness, thus disregarding inner friction as stipulated by Papailiou [4, 5].

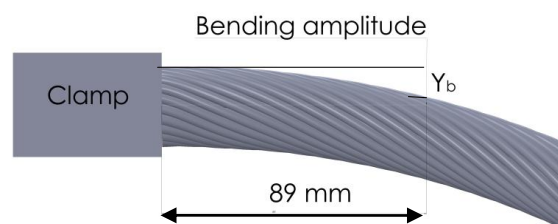


Fig. 2. Bending amplitude method

In this paper, the mechanical loads and stresses which occur during the conductor vibration are evaluated by using the bending amplitude method (Fig. 2) [3, 5, 6].

The main intent of this paper is to determine the mechanical loads acting on composite insulators by two types of Aluminium Conductor Steel-Reinforced (ACSR) as a function of their peak-to-peak bending amplitude. The test set-up is based on international standards [7, 8], and the tests were performed in the VRTC (indoor laboratory facility) on a span 84.6 m long. An anchor tower, on which different clamp configurations and transducers were fixed, was placed at mid-span. Three clamp configurations were used: a blocked clamp, as recommended by the IEEE standard, a pivoted clamp, and a clamp mounted on a suspension insulator which was free to move. In addition, four different static tensions at 15-20-25-30% UTS (ultimate tensile strength) were used during the tests.

2. GENERAL MATHEMATICAL MODEL OF THE CONDUCTOR

2.1 Strouhal number

The winds cause the conductors to vibrate in transverse direction at the same frequency of the so-called von Kármán vortices, which produces a vertical pulsating force. The vibration frequency may be approximately calculated by using a non-dimensional number k_s (0.185), called the STROUHAL number [1, 9]:

$$f = 0.185 \frac{v}{D} \quad (1)$$

with f : the vibration frequency (m/s);
 v : Wind speed (m/s); and
 D : Conductor diameter (m).

2.2 Equation of the Conductor

For building up a mathematical model of the Aeolian vibration of a single conductor, many assumptions have to be adopted. For instance, the conductor is considered to be uniform and inextensible, and the bending stiffness of the conductor is disregarded. Furthermore, the effect of the wind along the span is considered constant and continuous.

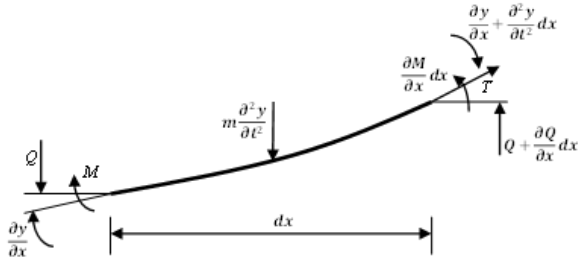


Fig. 3 Infinitesimal force distribution for vibrating conductor

Referring to Fig. 3, $f(x,t)$ is the exciting force of the wind on the conductor, Q is the shear, and M the bending

moment of the conductor differential element. This model leads to the following non-linear partial differential equation of the fourth order for the conductor [9]:

$$EI \frac{\partial^4 y}{\partial x^4} - T \frac{\partial^2 y}{\partial x^2} - f(x,t) = -m \frac{\partial^2 y}{\partial t^2} \quad (2)$$

whereby T : Horizontal conductor tensile force;
 m : Conductor mass per unit length;
 EI : Conductor bending stiffness;
 y : Displacement of conductor under vibration;
 t : Time; and
 x : Axial coordinate.

The bending stiffness of the conductor during its alternative bending motions lies between its minimum and its maximum value; however, since the conductor is composed of twisted wires of aluminium and steel, the calculation of the bending stiffness is quite complex. For high bending amplitude values, the strands of the conductor are considered moving without any friction, and independently, around their own axes [4].

$$EI_{\min} = \frac{\pi}{64} (N_{al} d_{al}^4 E_{al} + N_{st} d_{st}^4 E_{st}) \quad (3)$$

where N_{al} is the number of aluminium strands, N_{st} the number of steel strands, d_{al} and d_{st} the diameters of aluminium and steel strands, respectively, E_{al} and E_{st} the modulus of elasticity of aluminium and steel strands, respectively; while for the upper bending stiffness limit, it has been assumed that the strands form a homogenous body.

$$EI_{\max} = \sum_{i=1}^n \frac{N_i E_i \pi d_i^2}{8} \left(\frac{d_i^2}{8} + R_i^2 \right) \quad (4)$$

with N_i the number of the strands per layer, d_i the diameter of the strands, and R the layer radius.

The following relationship gives the frequencies of a conductor span as a function of its average bending stiffness EI

$$f_n = \frac{1}{2\pi} \sqrt{\left(\frac{n\pi}{L} \right)^2 \frac{T}{m} \left[1 + \left(\frac{n\pi}{L} \right)^2 \frac{EI}{T} \right]} \quad (5)$$

with n the mode number, N_i the number of the strands per layer, m the mass per unit length of the conductor, L the span length, and T the tensile loads.

The bending stiffness is very small, therefore its influence on the resonant frequencies may be ignored. All resonant frequencies are an integer multiple of the resonant frequency corresponding to the first mode shape.

3. EXPERIMENTAL SET-UP & PROCEDURE

3.1 Bending amplitude method

The IEEE Transmission and Distribution Committee has established a standard method called *bending amplitude method* which is considered suitable for assessing conductor vibration (Fig 2) [1, 6, 8]. The EPRI methodology which is based on the P-S formula, assumes direct measurements of the bending amplitude, preferably at 89 mm of the last point of contact (LPC) of the suspension clamps [5]. The bending amplitude has been valuable in establishing a relationship with the bending-dynamic strain, and subsequently with the dynamic stress, and the fatigue of the power line conductors.

3.2 Experiments Description

A schematic depiction of the test bench, including an anchor tower (at mid-span), is shown in Fig 4. The test apparatus is similar to other overhead line test benches; these have been described by the authors elsewhere [8]. The experimental set-up is composed of one conductor line held between two blocks and clamped at each end by rigid clamps. The conductor line is then forced to vibrate at its natural frequencies. In addition, and in order to ensure a constant static tension of the vibrating conductors, an arm loaded with dead-weights, and equipped with load cells (constant tension device), was used to control the tension of the conductor. Additionally, an anchor tower was placed at mid-span. The possibility of having different suspension clamp configurations has been achieved by a movable fixation system which allows maximum of flexibility whether to block or hold the clamp.

Thus, three clamp configurations are considered here:

- Non-articulated, with no suspension insulator;
- Articulated, with no suspension insulator.

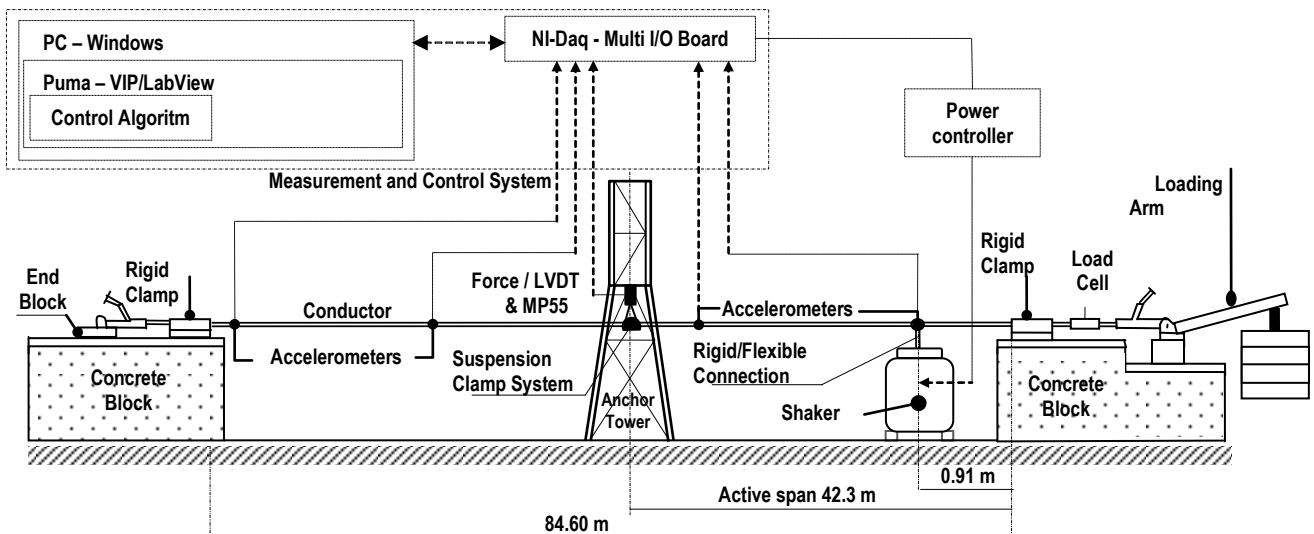


Fig.4 Schematic view of the laboratory set-up for loads measurement

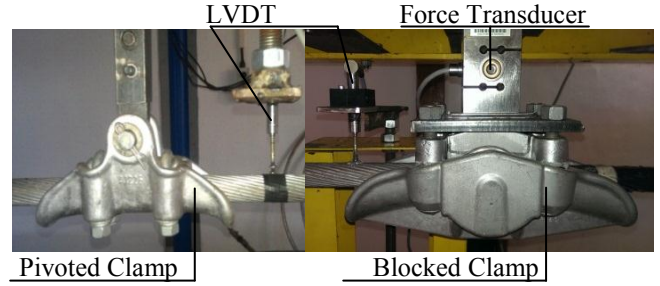


Fig. 5 Montage of the clamp configuration

For these two first configurations, the clamps are fixed directly to the force transducer (Fig. 5); and

- A suspension insulator which was mounted on the force transducer (Fig. 6).

The clamp-configuration using a non-articulated clamp is essentially the approach recommended by IEEE, and considered as standard compared with other support-configurations [8]. An electrodynamic shaker was used to keep the conductor under steady vibrating conditions (both amplitude and frequency) at its natural frequencies. Instrumentation included a force transducer to measure the mechanical loads, while the plunger of a linear variable-displacement transducer (LVDT) placed on the conductor at 89 mm from the mouth of the clamp was measuring the bending amplitude (Fig 5 and Fig 6). Piezo-accelerometers were used to control the dynamic behaviour of the span (velocity, amplitude, accelerations, and displacement).

Two types of exciter-cable connection were used to excite the conductor. The elastic connection equipped with a quartz load-cell was used during the sweep method, and the energy exchange between the shaker and the overhead line conductor was measured.

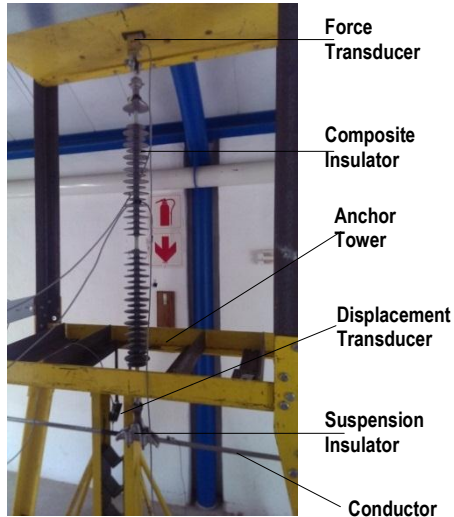


Fig. 6 Setup of the anchor tower with composite insulator

Thermocouples and air-conditioners were continuously controlling and regulating the temperature of the laboratory at $20^{\circ}\text{C} \pm 1$, in order to avoid temperatures variations which would provoke alterations of the length and tension of the conductor. This could have affected the repeatability and quality of the tests. To obtain an accurate picture of the dynamical behaviour of the conductor, all measurement signals were collected using a VIP-Puma control system for the sweep method. These signals were fed into data-acquisition equipment HBM MP55 and DAQ-NI modules, connected to a PC on a LABVIEW programme. The statistical analysis was conducted using Microsoft Excel and Matlab.

3.3 Material & Equipment

The ACSR conductors have been widely accepted in transmission and distribution of power lines, especially in South Africa. The tests were carried out on two ACSR conductors. Table I gives the mechanical characteristics of the conductors used.

TABLE I. TYPES OF THE CONDUCTORS TESTED

ACSR Conductor Size	Masse (kg/m)	Outside Diameter (mm)	Stranding	
			Number and Type	Diameter (mm)
Pelican	0,97	20.70	18 Aluminium 1 Steel	4.14 4.14
Tern	1.34	27.00	45 Aluminium 7 Steel	3.38 2.25

The suspension clamp was made of non-magnetic mould-cast aluminum alloy with 70 kN rated tensile strength (RTS). It comprised an upper and lower clamp with a U-type carbon steel bolt and nut. It was fixed directly to the force transducer for the test, no insulator present (Fig. 5), and later mounted directly onto the suspension insulator (Fig. 6). Fig. 5 shows the suspension clamp which was blocked. The clamps were attached to the conductor by a 50Nm torque applied to the nuts of the U-nuts of the suspension clamp.

The model of the suspension insulator was a silicone long-rod insulator HASDI 725/4500 c/w 16 mm ball & socket. The specified mechanical load (SML) is 120kN. The rating of the ball is in accordance with IEC 60120 (16), while that of the socket is IEC 60120 (16A). The diameter of the FRP rod is 16 mm and the height is 1464 mm. The diameters of the big shed are 120mm and 24, respectively, while the small-shed diameters are 90mm, and 23mm, respectively. The mass of the composite insulator according to the specifications, and according to the information provided by the manufacturer, is 5.29 kg.

3.4 Test Procedure

The swept-sine test, as the most common vibration test, has been used to find the conductor's natural frequencies. The signal, which is a sine wave, changes with time. An elastic connection between the conductor and the shaker was used. The frequency range was from 5Hz to 50Hz for the ACSR Tern conductor, while the range of 5Hz to 70Hz was tested for the ACSR Pelican as per the Strouhal formula (1). The second procedure, which was the steady frequency method, has allowed the direct measuring of dynamical loads and the bending amplitude of the vibrating conductor (Fig. 7-12). The bending amplitude range varied within the acceptable limit of 0.10 mm to 1.00 mm peak to peak (according to IEEE and CIGRE recommendations) [1]. The rigid connection was used to control the bending amplitude easily and safely. The conductors tested were tensioned with four different static tensions as shown in Table II.

TABLE II. ULTIMATE TENSILE STRENGTH (UTS)

Conductor	UTS [kN]	Ultimate Tensile Strength (UTS) [%]			
		15	20	25	30
		Pelican	53.800	8.010	10.500
Tern	98.700	18.405	19.740	24.675	29.610

4. EXPERIMENTAL RESULTANTS & DATA ANALYSIS

Owing to a large number of tests and data (accelerations, velocity, displacement, and frequency) of the vibrating conductor, only the vibrational loads graphs vs. bending amplitude of both conductors at four different static tensions will be presented here (Table II). The results of the sweep-frequency method indicated that the high vibrational loads and peak-bending amplitude could be obtained in the frequency range of 7Hz to 25Hz for most static tensions used, and for both conductors.

4.1 Vibrational loads

The natural frequencies have been chosen experimentally by the sweep method. The peak value of the vibrational loads which were pure sinusoidal waves was recorded at the resonance frequencies.

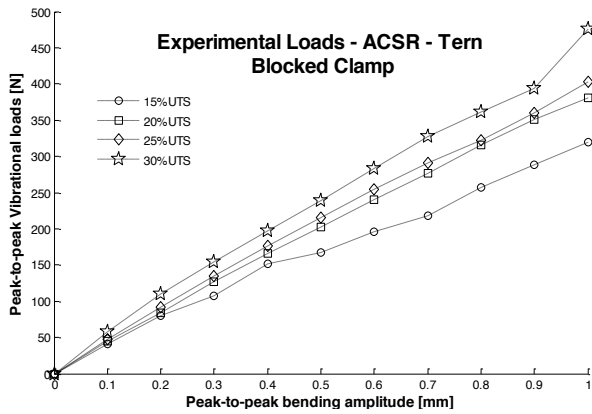


Fig. 7 Bending amplitude and vibrational loads of Tern: Blocked clamp

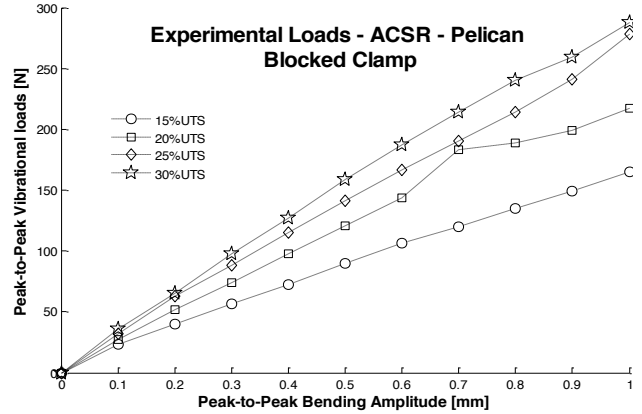


Fig. 10 Bending amplitude and vibrational loads of Pelican: Blocked clamp

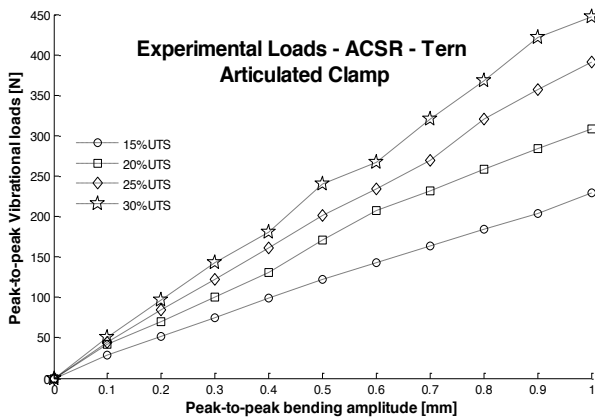


Fig. 8 Bending amplitude and vibrational loads of Tern: Articulated clamp

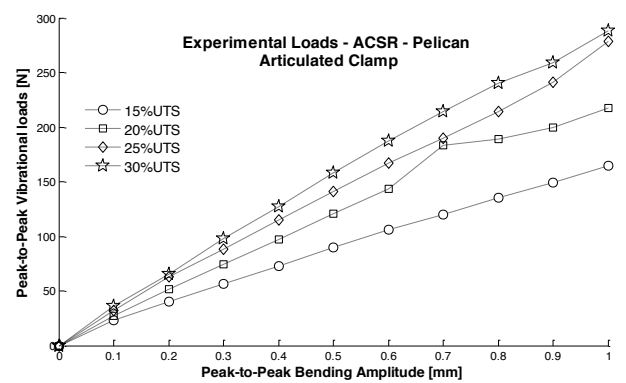


Fig. 11 Bending amplitude and vibrational loads of Pelican: Articulated clamp

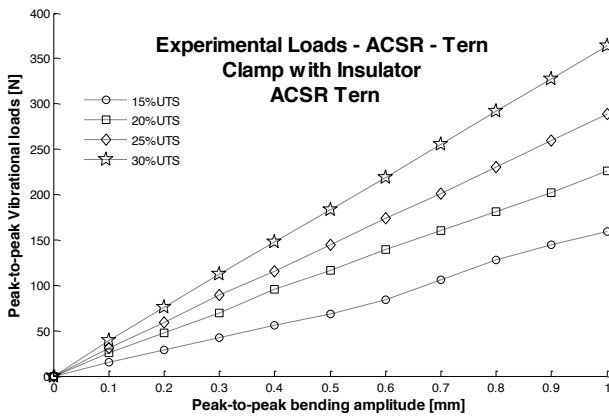


Fig. 9 Bending amplitude and vibrational loads of Tern: Clamp-Insulator

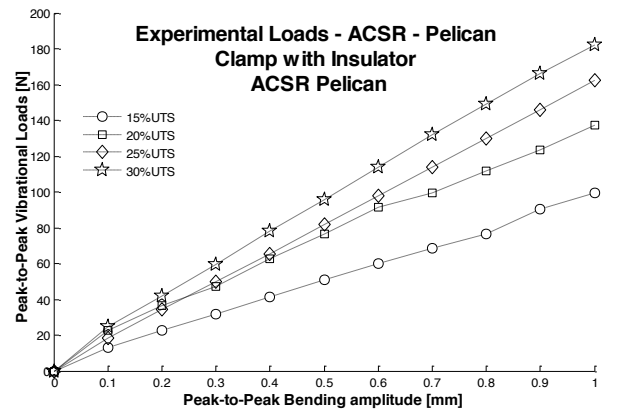


Fig. 12 Bending amplitude and vibrational loads of Pelican: Suspension insulator

Only the mean values were retained to plot the graphs. The standard deviation of all load measurements was inferior to 3 N.

The evolution of the loads according to the bending amplitude seems to be linear; it was approximated by a linear regression. It is shown in Fig.7-12 that for high static tension (30%UTS) for each conductor tested (ACSR Tern or Pelican), the peak-to-peak vibrational loads of the blocked clamp are greater than those of the other two clamp-configurations.

The dynamical loads collected from the vibration of the cable showed that the force generated was acting in compression and in tension at the force transducer. The results of the loads generated during the test suggest that attention must be focused on the high tension of the conductor (30%UTS); the loads created by the Aeolian vibration of the conductor being high compared with the other tensions. This applies to both conductors (Tern and Pelican).

It has been further noticed that, for the Tern conductor tensioned at 15% and 20% UTS, at small bending amplitudes, the difference of the peak values between the

compression force and tensile force at which an articulated clamp system and/or when using a suspension insulator, is high (nearly 11%), while for high tension (25% and 30% UTS), it is significantly lower.

During all tests, the compression loads were permanently greater than the tensions loads. Tables III and IV are summarised results of the mechanical loads at 1.0 mm peak-to-peak of the bending amplitude of both Tern and Pelican conductors.

TABLE III: TERN

UTS [%]	Vibrational loads (N) at 1.0 mm (peak-to-peak)		
	Suspension clamp with insulator	Articulated Suspension clamp	Blocked Suspension clamp
15	187	228	320
20	265	307	380
25	342	390	402
30	435	447	476

TABLE IV: PELICAN

UTS [%]	Vibrational loads (N) at 1.0 mm (peak-to-peak)		
	Suspension clamp with insulator	Articulated Suspension clamp	Blocked Suspension clamp
15	99	105	164
20	137	142	217
25	162	160	278
30	182	180	288

4.2 Static test

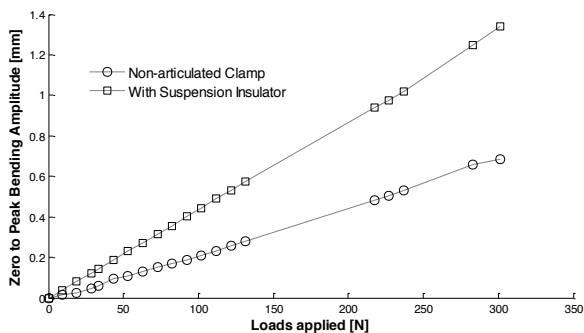


Fig. 13 Static measurement at 25%UTS of Tern at 89mm from clamp edge

The static test was conducted by comparing the dynamical loads of the vibrating conductor at 25%UTS under blocked clamp and insulator clamp configurations, while the conductor was loaded with 10N increment and measurement at 89 mm away from the clamp edge (Fig.2). The static behaviour of the conductor loaded interpreted here by its deflection was linear, and the conductor suspended with a blocked clamp shows little displacement comparing it with the one using the insulator, there being no movement restriction at the suspension clamp (Fig. 13).

5. CONCLUSION

In this paper, the mechanical loads on composite insulators excited by a conductor under Aeolian vibration have been, to the knowledge of the authors, for the first

time measured and analysed in detail. Three clamp-configurations were investigated. It has been shown that the conductor bending amplitude encountered depends upon conductor static tension. There is high probability that greater dynamical loads occur at low frequency (5-12Hz) and it has been found that the vibrational loads generated are considerably lower compared to the specified mechanical load SML of suspension insulator. Aeolian vibration load considerations may be helpful in the mechanical design insulators.

These experimental results show also that the relationship between the bending amplitude and dynamic loads presents some non-linearity at low conductor tensions, which is in accordance with the stick-slip mechanical model for the conductor [3].

6. ACKNOWLEDGEMENTS

This project was supported by VRTC, CEPS, Pfisterer, THRIIP and NRF. This financial support is gratefully acknowledged.

7. REFERENCES

- [1] EPRI, *EPRI Transmission Line Reference Book: Wind-Induced Conductor Motion* second edition ed. Palo Alto, C. A. 1012317, USA: EPRI, 2009.
- [2] O. Nigol, R. C. Heics, and H. J. Houston, "Aeolian Vibration Of Single Conductors And Its Control," *Power Apparatus and Systems, IEEE Transactions on*, vol. PAS-104, pp. 3245-3254, 1985.
- [3] A. Cardou, *Stick-slip mechanical models for overhead electrical conductors in bending (with Matlab applications)*. Université Laval, Québec: GREMCA, 2013.
- [4] K. O. Papailiou, "On the bending stiffness of transmission line conductors," *Power Delivery, IEEE Transactions on*, vol. 12, pp. 1576-1588, 1997.
- [5] J. C. Poffenberger and R. L. Swart, "Differential Displacement and Dynamic Conductor Strain," *Power Apparatus and Systems, IEEE Transactions on*, vol. 84, pp. 281-289, 1965.
- [6] A. Rolim, J. d. Moreira, L. C. M. Veloso, R. de Souza, and J. Araújo, "Differential displacement and strain analysis of transmission line cables," *Journal of the Brazilian Society of Mechanical Sciences and Engineering*, vol. 35, pp. 327-336, 2013/10/01 2013.
- [7] "IEEE Guide for Laboratory Measurement of the Power Dissipation Characteristics of Aeolian Vibration," *IEEE Std 664-1993*, p. i, 1993.
- [8] I. C. Report, "Standardization of Conductor Vibration Measurements," *Power Apparatus and Systems, IEEE Transactions on*, vol. PAS-85, pp. 10-22, 1966.
- [9] F. Kiessling, P. Nefzger, U. Kaintzyk, and J. F. Nolasco, *Overhead Power Lines: Planning, Design, Construction*: Springer, 2003.

NATURAL POLLUTION TEST FOR INVESTIGATING LEAKAGE CURRENT EFFECTS ON MEDIUM VOLTAGE WOODPOLE DISTRIBUTION LINE STRUCTURES

A. A. Beutel*, M. D. Ntshani*, K. V. Thejane*, H. J. Geldenhuys*, T. D. Mvayo*, R. F. Watson*, W. L. Vosloo*, A. Khatri*

* Eskom Holdings SOC Limited, Lower Germiston Road, Rosherville, Gauteng, South Africa.
E-mail: BeutelAA@eskom.co.za

Abstract: It is accepted practice to evaluate insulator pollution performance using leakage current monitoring. These tests are meant to determine expected ageing and pollution performance of insulators to be installed in the field. Leakage current is also the parameter that determines the electrical performance of wood with respect to pollution. At present there is no standardised method for corresponding tests performed on complete powerline structures, including both wood and insulators and other associated hardware, i.e. the extension of insulator leakage current tests to include performance of an entire woodpole structure. The need for doing this is that leakage currents flowing on the surface of the insulators may flow onto or into the wood of the structure, and may cause the wood of the structure to burn. These tests can be used to understand structure leakage current performance and estimate their susceptibility to wood burning. Long term natural pollution tests have been performed on medium voltage structures. The test method is described, selected results are presented and a natural pollution test method is proposed and discussed.

Keywords: Insulators, leakage currents, test site, pole-top fire, pollution, power distribution, wood, pollution.

1. INTRODUCTION

It is accepted practice to evaluate insulator ageing and pollution performance using leakage current monitoring. Such tests may be artificial ageing [1] and pollution [2] tests or natural pollution tests [3]. The aim of these tests is to determine expected performance of insulators installed in the field, primarily in terms of prevention of flashover and material failure. The effect of leakage current on wood has also been studied [4], [5]. Not considering leakage current leads to pole-top fires in conducive conditions. Therefore, to reduce the likelihood of pole-top fires it is advisable to perform appropriate structure tests and inspections.

At present there is no standardised method for ageing and pollution tests performed on complete powerline structures, including both wood and insulators, as well as the other hardware on such structures, i.e. the extension of presently accepted insulator leakage current tests to include performance of an entire wood structure. The need for doing this is that leakage currents flowing on the surface of the insulators may flow onto or into some part of the structure, and may, depending on the circumstances and the design of the structure, cause the wood of the structure to track and then burn [4], [5], [6]. An example of a burnt structure in the field is shown in Fig. 1. These tests can therefore be used to understand issues such as leakage current magnitude, where the leakage current flows on the structure and the effect of atmospheric conditions. Ultimately, leakage current performance of structures can be established and their susceptibility to wood burning can be estimated.

Long term natural pollution tests have been performed on several three-phase medium voltage (MV) woodpole structures (22 kV line-to-line voltage, 50 Hz supply frequency). The tests arose from the need to understand the mechanism and mitigation of pole-top fires [6], and involved measurement and logging of leakage current on at least one point on each structure, simultaneous recording of weather parameters, equivalent salt deposit density (ESDD) measurement, regular visual inspections and ultraviolet (UV) imaging. This was performed at the Koeberg Insulator Pollution Test Station (KIPTS), near Cape Town. The KIPTS site is situated in close proximity to the coast and is therefore subjected to significant levels of marine pollution. Additionally, industrial and



Figure 1: Example of a burnt structure in the field

agricultural pollution sources are on the inland side of the site from the sea [7].

The paper covers the following topics related to natural pollution testing of woodpole distribution line structures: the method employed at KIPTS, the flow of leakage current on three-phase MV wood structures, the significance of thermal and peak leakage current from the pole-top fires perspective and evaluation of the test method. Finally, a test procedure is proposed for natural pollution testing of wood distribution line structures and discussed.

2. KIPTS TEST ARRANGEMENT

For practical (space) reasons the tests are limited to six structures at KIPTS. An example of these structures is shown in Fig. 2. The structures are energised via three phase conductors strung above the test structures. Fuses are connected in series between these supply conductors and the test structures for every connection made. The purpose of the fuses is to minimise the risk of damage to equipment and of the entire site tripping in the event of a short circuit (flashover).

The leakage current measurement and logging system is the same as used for individual insulators; this is described in [7]. One sensor was installed in the earth downwire of each test structure. The sensors are galvanically isolated, and the leakage current is sampled by the logging system at a frequency of 2 kHz. The logging system calculates and stores several leakage current parameters every 10 minutes. These include [7]:

- The highest positive and negative peaks in the -500 mA to 500 mA range,
- Positive and negative average and root mean square values,
- Positive and negative charge accumulated (integrated) over the 10 minute period,

- Integrated leakage current squared,
- Sixteen cycles of the maximum leakage current waveform.

In addition, a sensor was installed in series with each phase insulator (bonding) on one structure, in effect measuring the leakage current of each phase. This was used to study the flow of leakage current on a three-phase structure. This was limited to one structure by the available sensors and to a structure that was fully bonded and earthed, so that all sensors are earthed. A fully bonded and earthed structure refers to a structure where all conductive hardware is electrically bonded together and connected to earth via an earth downwire. All test structures were either fully bonded and earthed or partially bonded, the only difference being that the latter had an insulation coordination gap inserted into the earth downwire. Test structure and leakage current measurement configuration are illustrated in Fig. 3.

3. LEAKAGE CURRENT FLOW ON THREE-PHASE MV WOOD STRUCTURES

Leakage currents flowing through the four sensors on the applicable fully bonded and earthed structure were recorded simultaneously using an oscilloscope. An example of recorded waveforms is shown in Fig. 4. In this example, the insulators connected to phases 1 and 2 conducted measurable leakage current, but the insulator connected to phase 3 did not. The leakage current measured on the earth downwire is clearly the sum of the leakage currents on the three phase insulators, since all current pulses measured on the phases also appear on the downwire, with no additional pulses on the downwire that don't also appear on any of the phases. The current pulses are stochastic in nature.

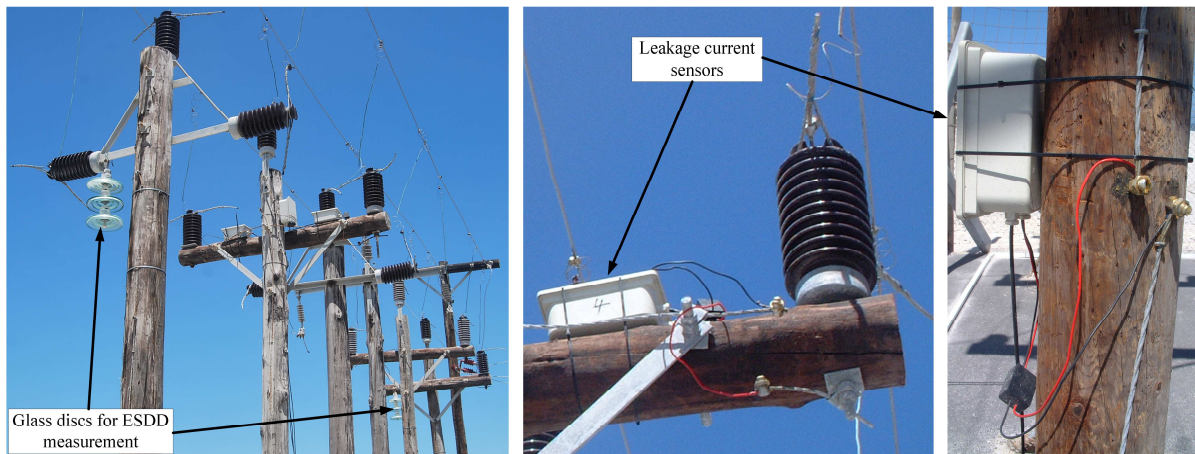


Figure 2: Example of test structures at KIPTS: six structures (left), sensor installed to measure insulator bonding leakage current (centre), leakage current sensor in earth downwire (right)

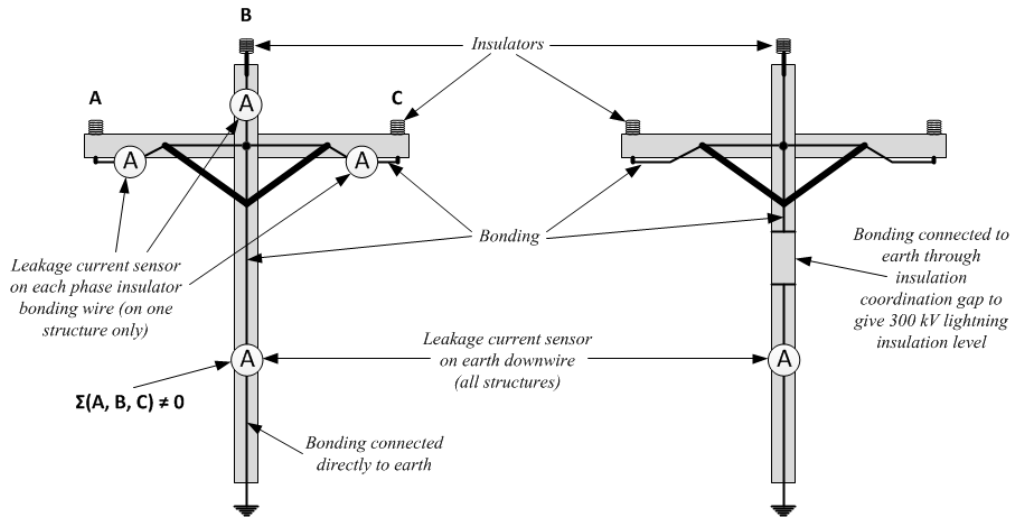


Figure 3: Test structure configuration: fully bonded and earthed (left), partially bonded (right)

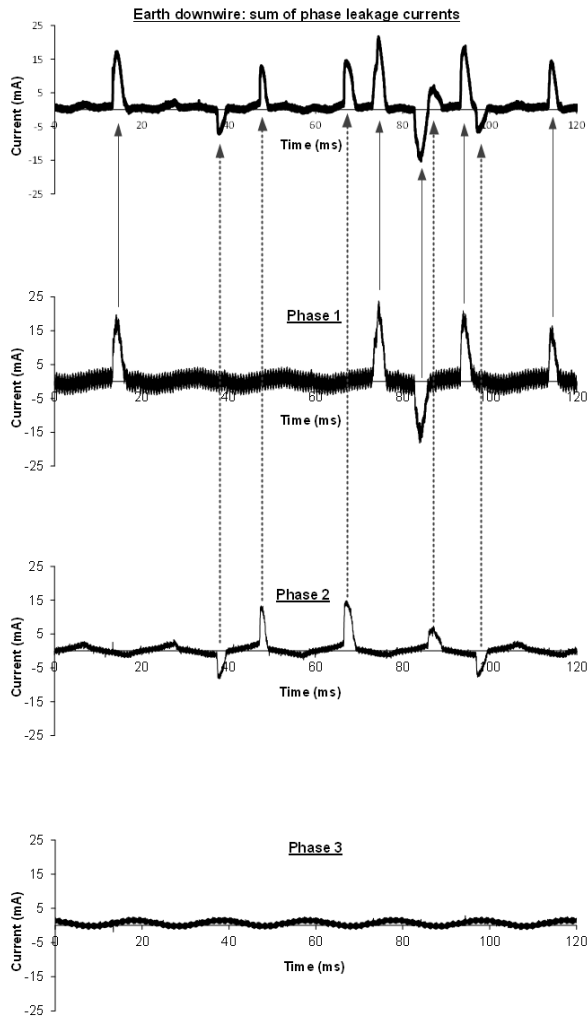


Figure 4: Leakage current waveforms recorded on the test structure with four leakage current sensors by measuring at the appropriate inputs of the logging system with an oscilloscope

Leakage current waveforms were also recorded on the earth downwires of other structures (where only the one earth downwire sensor was installed). An example is shown in Fig. 5. It was surmised that all three insulators were conducting measurable current simultaneously, resulting in a continuous 150 Hz waveform. This is proved and explained in Fig. 6, where a typical leakage current waveform measured on a single insulator was shifted (delayed) by 120° and 240° and the resulting three waveforms were added. The result is also a continuous 150 Hz waveform (for 50 Hz supply frequency).

This therefore indicates that the leakage currents due to the three phase insulators on such structures sum to give the current in the earth downwire. This current is not zero because insulator leakage current is not sinusoidal and its magnitude varies stochastically. Note that it was not possible to determine the amount of leakage current flowing in the wood, as an instrument capable of measuring the relatively low levels of leakage current, but with a sufficiently large aperture, could not be located and would be complex to design and construct. In such a case, artificial pollution tests in a laboratory environment may be beneficial.

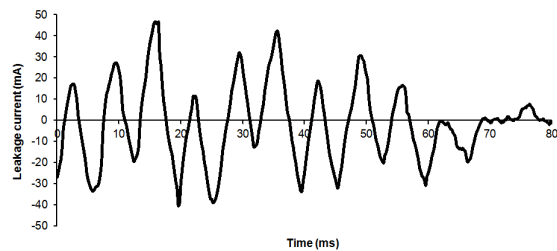


Figure 5: Measured earth downwire leakage current showing three-phase homogenous current at 150 Hz frequency for the case where the three phase insulators conduct leakage current pulses simultaneously (different time scale to Figure 4)

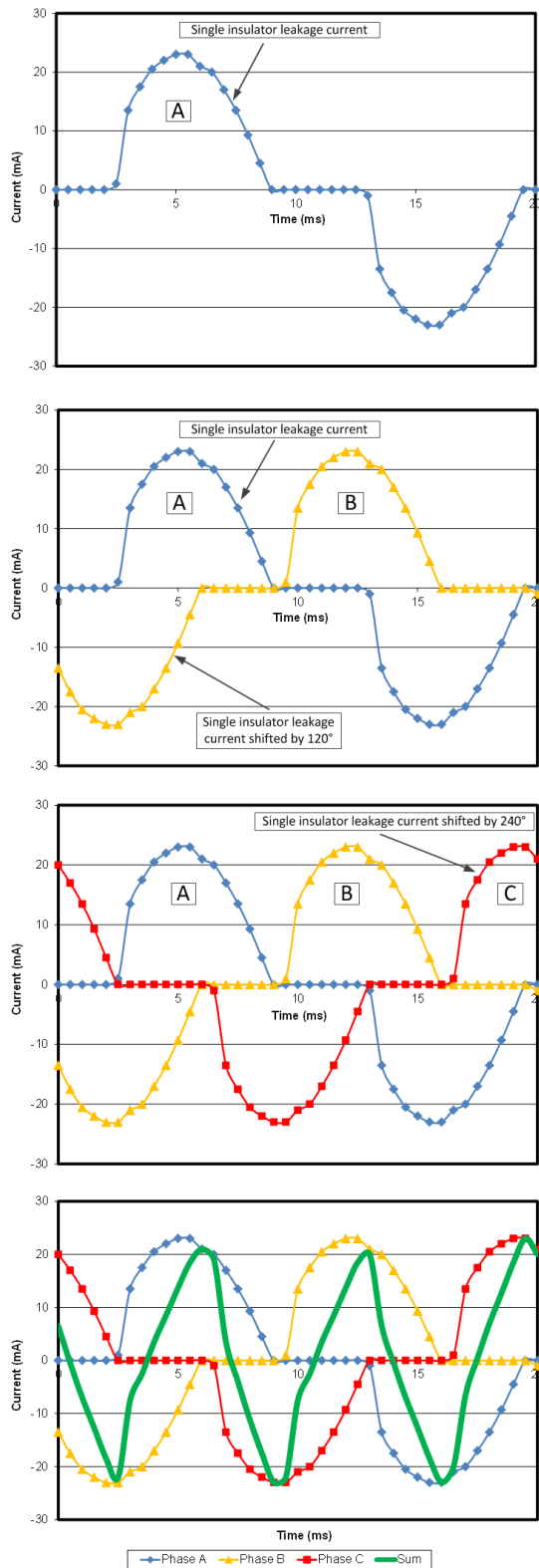


Figure 6: Explanation of 150 Hz earth downwire leakage current: leakage current measured on one insulator (top), addition of the same current shifted by 120° and 240° and inclusion of the sum of the three currents (below)

4. SIGNIFICANCE OF THERMAL AND PEAK LEAKAGE CURRENT WITH RESPECT TO POLE-TOP FIRES

Leakage current is the parameter that determines electrical performance of both insulators [1], [2], [3] and wood [4], [5]. The primary aim for insulators is to prevent flashover and material failure. For wood structures (poles and cross-arms), the purpose is also to prevent tracking, which is the first stage of the process leading to pole-top fires. Tests performed on complete structures at KIPTS revealed a structure that exhibited significant tracking. This structure generally exhibited larger leakage current than other structures tested at the same time. This is true for all of the parameters measured by the logging system when studied over several months, but is not necessarily true for every 10 minute measurement cycle. Tracking occurred on one of the structures during part of this period. Since all recorded parameters showed generally larger values for the structure that tracked, it is not clear which parameter is the most significant. It is suspected that thermal leakage current (approximated by integrated parameters) is more significant in determining pole-top fires performance than peak values. However, it is not clear whether this is indeed the case from data obtained so far [8].

5. EVALUATION OF KIPTS TEST METHOD

The objectives of the tests performed have been to understand the mechanism of pole-top fires, including leakage current flow on typical three-phase structures, and to evaluate various mitigation measures. The advantage of these tests is that the effect of various environmental conditions could be estimated, such as pollution level, wind direction, temperature and humidity. Examples of measured pollution levels (ESDD) are shown in Fig 7. This also allowed for unforeseen discoveries, such as the sometimes large effect of structure location with respect to wind direction and pollution source on the difference in measured ESDD between the two outermost test structures. The ESDD measurements were performed using a set of three glass discs suspended from the cross-arm of each of the outermost test structures, as shown in Fig. 2. The main limitation is that tests must be performed in extremely harsh environmental conditions so that sufficiently large leakage currents can be generated to produce results relatively quickly, and for ease of measurement, in the same way as for testing insulators only. This is the case at KIPTS. The quality of electrical connections therefore had to be checked frequently as corrosion is a significant problem. Also, one is often at the mercy of weather conditions, as conditions conducive to leakage current flow are required to perform many ancillary tests, such as UV imaging and oscilloscope recording of leakage currents. These conditions mostly occur at night, and their occurrence can in most cases not be predicted

beforehand. Leakage currents measured on the same structure on different days can vary widely, even if weather conditions are similar, due to the effect of pollution level, wind direction and wood condition.

6. SUGGESTED NATURAL STRUCTURE POLLUTION TEST METHODOLOGY

Valuable experience has been obtained from the testing of complete woodpole electricity distribution structures at KIPTS. This has informed the recommended procedure described below.

6.1 Objectives

Before commencing with such a test, the objectives should be established. Possible objectives of natural pollution tests are similar to most of those listed by CIGRE for insulators [3]. The general objective of such tests performed on a wood structure could be to evaluate its leakage current performance. Objectives as part of that could be to compare the performance of different structures, including different structure and insulator designs, materials or orientation, or bonding arrangements, as applicable. The associated measurements and observations are important. As a minimum, it is recommended that the leakage current in the earth downwire of a structure be logged and regular surface visual inspections are carried out and the evidence photographed. Other inspections described in this paper may also be carried out, as required. Leakage current may also be measured and logged at other positions on a structure to those described here to aid in understanding the leakage current performance of the structure. The leakage current, weather and pollution parameters that are recorded should be the same as for insulator test stations [3] – the more information that is available the more confidence there is in the conclusions reached.

6.2 Practical considerations

The quality of electrical connections must be frequently confirmed and materials must be suitably corrosion-resistant while still being as representative of the field as

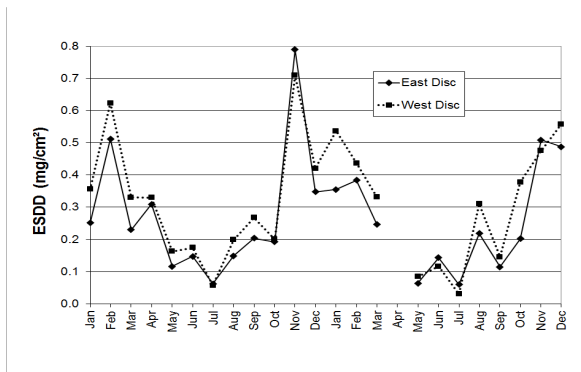


Figure 7: Example of ESDD measured at KIPTS

possible. Also, insulators with higher specific creepage than commonly used in the field should be considered, to minimise the number of disruptions due to flashovers. Even so, fuses should be frequently checked for operation due to overcurrent. The larger the specific creepage of insulators, the less often insulators are likely to flash over and cause the protection to operate, interrupting tests. However, the magnitude of leakage current is then smaller and more difficult to measure. There is therefore a trade-off to be made and consideration needs to be given as to how different the test structures, including the insulators, are from reality, and the effect of this. The choice of insulator material is also important, as this can significantly affect leakage current performance. Insulator profile and orientation (usually vertical or horizontal) should also be carefully chosen, as these may affect results [9]. The intended analysis to be performed with the logged data should also be considered when compiling a test program. Further details are given further on.

6.3 Visual inspections

Visual inspections are important in evaluating the leakage current performance of a structure, and may take various forms. Inspection of the wood surface should be performed regularly. This involves photographing the structure surface in all places where tracking has taken place or where tracking may occur, even if no tracking has been observed. Examples of tracking observed at KIPTS are shown in Fig. 8. This has the advantage of being relatively easy to perform, but has the disadvantage that difficult-to-reach places cannot be inspected. Less frequent, but more thorough, visual inspection is also recommended. This involves dismantling (and reassembling) part or all of the structures. Again, photographs should be taken. This is more thorough than surface inspection, but significantly more time consuming. Also, the inside of the wood, especially where bolts or spindles are located, is not inspected, due to the obvious practical drawbacks. Pole-top fires have been known to start inside the wood, so not being able to inspect there is a necessary trade-off.

6.4 UV imaging

This should also be performed, under relatively active conditions. UV imaging has proved to be useful in illustrating the location of sparking and hence in evaluating structure leakage current performance, as illustrated in [8].

6.5 Insulator condition

All insulators should be in a clean and healthy condition when commencing with a new test, i.e. when energising after modifications have been made to any structure, including after handling any insulator. This is so that all insulators are in the same condition at the start of a test sequence.

6.6 Analysis of results

The correlation between different recorded parameters, i.e. leakage current, visual state, level of activity, weather conditions and pollution level, should be analysed. Test structure location with respect to other structures may also be important, as shown in Fig. 7, as may the condition of the wood at the start of testing. It is ideal to test more than one structure of the same type to minimise effects such as relative location and wood properties. The species of wood may also play a role. Comparison of results from different stations is complex and should be based on guidelines given in [3]. Comparison of results from the same station, but from different times, is also complex. The effect of differences between test structures and those in the field, such as use of insulators with higher than normal specific creepage, should be considered in the analysis.

6.7 Test station

Making use of an existing research station, rather than one of the other types listed in [3], is recommended for the flexibility and more comprehensive support structure.

6.8 Test duration

This should be at least one complete year, but longer may be needed if it is not possible for obtain sufficiently conclusive results after one year.

7. CONCLUSIONS

Natural pollution tests performed on complete medium voltage electricity distribution woodpole structures have been covered in this paper. It has been confirmed that leakage current is the electrical quantity that determines the pollution performance of such structures, as for insulators evaluated on their own. Selected results from performance of such tests have been provided and the test method has been discussed, including practicalities involved with performing such tests.

The leakage current flowing to earth via the earth downwire of a three-phase distribution line structure is the sum of the insulator leakage currents and has a



Figure 8: Examples of tracking recorded at KIPTS

frequency of 150 Hz for a 50 Hz supply frequency. The downwire current is not zero because insulator leakage current is not sinusoidal and its magnitude varies stochastically. A natural pollution test procedure for woodpole structures has been suggested, and reasons for the performance of these and artificial pollution tests have been discussed. The importance of this work lies in providing a test procedure for better understanding pollution performance of woodpole electricity distribution structures and for evaluating mitigation measures, hence providing a way of reducing susceptibility of such structures to pole-top burning and confirming findings.

8. REFERENCES

- [1] Insulators for overhead lines – Composite suspension and tension insulators for a.c. systems with a nominal voltage greater than 1 000 V – Definitions, test methods and acceptance criteria, IEC Standard 61109, Edition 2.0, 2008.
- [2] Artificial pollution tests on high-voltage insulators to be used on a.c. systems, IEC Standard 60507, Edition 2.0, 1991.
- [3] Guide for the establishment of naturally polluted insulator testing stations, CIGRE Guide 333, 2007.
- [4] M. Darveniza: “Electrical resistance of wood and leakage current effects”, in *Electrical properties of wood and line design*, University of Queensland Press, 1980, pp. 115–129.
- [5] A. K. Persadh: *A study of pole top fires on 22 kV wood pole power lines in KwaZulu – Natal*, M. S. thesis, Univ. of KwaZulu-Natal, South Africa, 2007.
- [6] K. V. Thejane, A. A. Beutel, M. D. Ntshani, H. J. Geldenhuys, A. C. Britten, W. Vosloo, T. D. Mvayo, R. Watson, R. Swinny, C. R. Evert, A. Khatri: “Pole Top Fires: Review of Work to Date and a Case for Further Research”, *Proceedings: IEEE PES PowerAfrica Conference*, Johannesburg, Paper 7B-1, July 2012.
- [7] W. L. Vosloo: *A comparison of the performance of high-voltage insulator materials in a severely polluted coastal environment*, PhD dissertation, Stellenbosch Univ., South Africa, 2002.
- [8] M. D. Ntshani, A. A. Beutel, K. V. Thejane, H. J. Geldenhuys, A. C. Britten, T. D. Mvayo, R. Watson, R. Swinny, A. Khatri: “Leakage current performance of woodpole line distribution structures: experiences from Koeberg Insulator Pollution Test Station”, *Proceedings: CIGRE Southern Africa Regional Conference*, Paper CN202, October 2013.
- [9] K. V. Thejane, M. D. Ntshani, H. J. Geldenhuys, J. Van Coller, A. A. Beutel, T. D. Mvayo, R. Watson, W. L. Vosloo and A. Khatri: “Effect of insulator properties on the leakage current performance of woodpole distribution line structures”, *Proceedings: ISH*, Korea, pp. 1222–1227, August 2013.

DESIGN, TEST AND BASIC EVALUATION OF A TEST RESISTOR FOR USE ON A MEDIUM VOLTAGE DISTRIBUTION NETWORK

A. A. Beutel*, F. Jooste*, H. J. Geldenhuys**, A. Khatri*

* Eskom Research, Testing and Development Department, Lower Germiston Road, Rosherville, 2022, South Africa. E-mail: BeutelAA@eskom.co.za

** Eskom Technology Division, Lower Germiston Road, Rosherville, 2022, South Africa. E-mail: GeldenHJ@eskom.co.za

Abstract: The methodology behind the selection, design and basic testing of a high voltage and high power resistor for electrically modelling a human body is described. Practical aspects and limitations were discussed. The resistor is to be used for testing on an electricity distribution network operated at medium voltage.

Keywords: resistor, voltage, current, high voltage, high power, safety, electricity distribution.

1. INTRODUCTION

There are situations when an electricity supply utility wishes to simulate the effect of a person making contact with an energised phase conductor, e.g. to determine the response of protection relays for the purpose of detecting such a contact condition. Such simulations may be performed using digital software simulation packages or via testing. The preferable scenario is to perform both software simulation and full-scale tests on an energised network, so that measurements and simulation results can be compared to verify the simulations, allowing the model developed to be modified for other scenarios. A realistic but practical model of the human body is therefore needed.

SANS 60479-1 [1] provides typical impedances measured of the human body, which can be used for such simulations. The values vary widely, depending on several parameters. When simulations are being performed, this is not a significant problem as it is a simple matter to change the values as required. However, when performing tests this is not so simple. This is compounded in the case presented in this paper by the fact that high voltage and high power are also required, as the test impedance is to be used on a medium voltage (22 kV phase-to-phase) distribution network. Also, impedances are only available for voltages significantly lower than those required for this work. Thermal design, safety considerations, readily available test facilities and practicality all need to be considered.

The purpose of this paper is therefore to describe the process used to determine the impedances required, design the device and perform basic tests. Results are also included. Only modelling of human contact is covered here, animal contact is the subject of SANS 60479-3 [2].

2. PREVIOUS EXPERIENCE

Eskom had previously performed similar tests on a medium voltage (MV) network. The experience gained from these tests was used to design the new resistor. However, the previous design had to be critically analysed as the new device is to be used in a specially constructed test site, whereas previous tests were in effect once-off tests. Also, the latest edition of SANS 60479-1 [1] was published after the original tests were performed.

The following was noted from the original tests regarding the test resistor:

- a. A water resistor of approximately 800 to 1700 Ω was used, it was connected to earth via a crow's foot earthing arrangement.
- b. It was made from PVC pipes filled with distilled water, with salt added as needed to obtain the desired resistance.
- c. Additional contact resistance in the form of a leather mat was also added.
- d. The effect of wet ground was also investigated.
- e. A circuit breaker was placed in series with the resistor and closed for 4 to 6 seconds for each test.

3. DETERMINATION OF IMPEDANCE (RESISTANCE) VALUE FROM SANS 60479-1 [1]

The SANS 60479 series of standards covers effects of electrical current on humans and livestock. SANS 60479-1 includes impedance values of the human body. Due to the obvious safety considerations, impedances are not available for voltages of up to the level required (12.7 kV phase-to-earth for a 22 kV network). Values given at significantly lower voltages therefore had to be extrapolated. In several cases curves (equations) had to be fitted to the values given. Also, the values differ widely with the area of contact made and with the moisture conditions (dry, wet or salt wet). Values provided in [1] were plotted and curves were fitted; examples of the results are shown in the appendix.

SANS 60479-1 provides human body impedance values that are a combination of resistance and capacitance, made up of the internal impedance and that of the skin. The internal impedance of the human body can be considered as mostly resistive. At higher voltages measured, which are still significantly lower than the 12.7 kV designed for in this case, the total impedance of the body approaches that of the internal impedance. Therefore, the total body impedance was considered to be purely resistive for the purposes of this study. Since the arm and leg impedances are assumed to be of the same value, the hand-to-hand values given in [1] can be directly used for hand to foot contacts, which would probably be the most representative of a typical contact situation.

The range of values obtained for a voltage of 12.7 kV is 3 Ω to 3340 Ω , using the curves fitted to the graphs obtained by plotting the values given in [1]. The values previously used are therefore accurate. This large range would be further complicated by whether one hand, both hands, one foot or both feet are in the current path. Any value chosen is therefore an estimate and a range of values would need to be tested. For the development a value of 2 k Ω (approximately) was chosen, but the design needs to be such that the value can be varied widely.

4. DESIGN OF THE RESISTOR

4.1 Summary

A water resistor with plastic housing and fixed electrodes was chosen, for the following reasons:

- Flexibility of resistance is provided. Also, such a resistor has been successfully used at a much higher voltage at Eskom's corona cage facility.
- A fixed-value resistor, or a series of these, would not give the flexibility of resistance attainable with a water resistor.
- Moving electrodes are complex to construct – the resistance is to be set by varying the conductivity of the water by adding salt (one would need to judiciously choose the test regime to avoid having to increase the resistance too often during testing).
- Approximate resistance values obtained are “infinity” (too large to measure) with distilled water only, 30 Ω with 1 kg of salt added and 12 Ω with additional salt added; it is therefore clear that most of the desired range of resistances can theoretically be obtained using this design. Further details are given later.
- Calculated temperature rise is acceptable for the initial value of 2 k Ω .
- Smaller resistances would also likely need to be used, which would result in larger power being dissipated and hence larger temperature rise. Since tests would not last longer than 5 seconds, and 10 seconds was used for the design, a resistance of at least 1 k Ω could safely be used.

- Plastic housing reduces corrosion risk and makes the resistor lighter and hence easier to move around, replacement of the solution is also relatively easy.
- It may be used in phase-to-earth mode (most likely), but may also be used in a way that is not referenced directly to earth (noting that it must be adequately insulated for such tests).

4.2 Basic electrical design and specifications

Voltage

Phase-to-phase voltage = $V_{line} = 22$ kV
 Phase-to-earth voltage = $V_{ph} = 12.7$ kV
 For withstand during a fault, $V_{ph} = 24$ kV

Resistance

Resistance = $R = 2000$ Ω (initial value chosen, as stated above).

Current

Current = $I = V \div R = 12.7$ kV \div 2 k $\Omega = 6.35$ A
 Under fault conditions, $I = V \div R = 24$ kV \div 2 k $\Omega = 12$ A

Power

Power = $P = V^2 \div R = (12.7$ kV)² \div 2 k $\Omega = 80.65$ kW
 Under a fault, $P = V^2 \div R = (24$ kV)² \div 2 k $\Omega = 288$ kW

Energy

Expected duration of each test = $t = 5$ s
 For design purposes, $t = 10$ s
 Energy = $E = P \times t = 80.65$ kW \times 10 s = 806.5 kJ
 Under fault conditions, $E = 288$ kW \times 10 s = 2880 kJ

4.3 Resistor construction

The following materials were used to construct the water resistor:

- 2 m long PVC gutter pipe.
- 10 cm diameter PVC end caps.
- Strap-on fitting with aperture for filling and emptying the resistor, with lid.
- PVC weld glue for joining the various parts.
- Silicon sealer and rubber seal.
- Various nuts, bolts and washers.

The basic design is shown in Fig 1 and the finished resistor is shown in Fig 2. The design is heavily based on the corona cage design.

4.3 Thermal calculations

Calculations were performed to determine whether the resistor can adequately be subjected to the required power of 288 kW from a thermal (temperature rise) point of

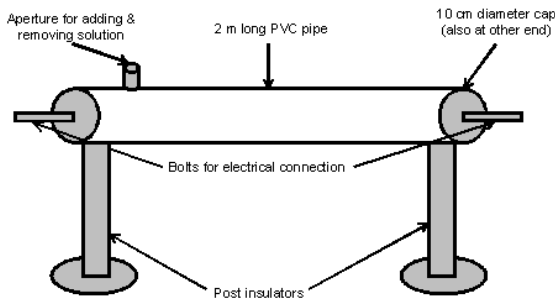


Figure 1: Basic design



Figure 2: Resistor constructed (not mounted on insulators)

view. The applicable outputs of the electrical calculations were used where needed.

Dimensions

Diameter = $\Phi = 10 \text{ cm} = 0.1 \text{ m}$
 Radius = $r = 0.1 \div 2 = 0.05 \text{ m}$
 Length = $h = 2 \text{ m}$

Constants

Specific heat capacity of water = $C = 4180 \text{ J/kg}^\circ\text{C}$ [3].

Resistivity of de-ionised water = $1.8 \times 10^5 \Omega\text{m}$ at 20°C [4] (this value was assumed for distilled water in the absence of other information).

Resistivity of sea water = $2 \times 10^{-1} \Omega\text{m}$ at 20°C [4] (used as an estimate for distilled water with salt dissolved in it).

1 litre (ℓ) = 0.001 m^3 (for water).
 1 $\ell = 1 \text{ kg}$ (for water) [5].

Area, volume and mass

Area = $A = \pi.r^2 = \pi \times 0.05^2 = 0.0079 \text{ mm}^2$.
 Volume = $V = \pi r^2 h = \pi \times 0.05^2 \times 2 = 0.0157 \text{ m}^3 = 15.71 \ell$.

Therefore, mass of water = $m = 15.71 \text{ kg}$.

Resistance

$R = (\rho \times L)/A = (1.8 \times 10^5 \times 2)/0.0079 = 45.57 \text{ M}\Omega$ for de-ionised water.

$R = (\rho \times L)/A = (2 \times 10^{-1} \times 2)/0.0079 = 50.633 \Omega$ for sea water.

This shows that the resistor can theoretically be used for a large part of the range of resistances required. However, the power rating would need to be checked carefully for lower resistances (larger currents). Also, resistor performance for all resistances would need to be experimentally verified.

Temperature rise

Heat energy = $Q = E = 2880 \text{ kJ}$ under fault conditions (worst case).

$Q = m \times C \times \Delta T$; therefore $\Delta T = Q \div (m \times C)$, where $\Delta T =$ temperature rise [5].

Under fault conditions, $\Delta T = 2880 \text{ kJ} \div (15.71 \times 4180) = 43.9^\circ\text{C}$.

The resistor is therefore very likely to survive a fault, from the thermal point of view, especially since a fault is very unlikely to last as long as 10 seconds. The resistor is therefore expected to perform acceptably under normal conditions. However, this would need to be verified by measurement, especially as numerous applications of voltage under normal conditions are expected. Resistances other than $2 \text{ k}\Omega$ also need to be tested.

5. BASIC LABORATORY TESTING

Facilities were not available to test the resistor using a voltage source with the required power rating, since such power can only realistically be obtained at a location such as on a distribution network. Two separate tests were therefore performed. First, a low voltage test was performed, where the resistor was connected to the low voltage (LV) mains supply, to verify its current-carrying ability. Then a high voltage test was performed by subjecting the resistor to rated voltage to verify its voltage withstand ability.

5.1 Low voltage test

LV mains voltage was applied to the resistor and the salt content of the solution was varied to draw various currents. The purpose was to verify the current-carrying capability of the resistor (12 A under fault conditions), verify that there is little temperature rise at such relatively low power, as predicted, and to confirm that the resistor indeed behaves as a resistive load. At the lowest resistance, the current was measured as approximately 18.2 A, and the voltage was measured as 220.1 V. These values were used to calculate the theoretical temperature rise for various durations. The results are shown in Table 1.

Table 1: Temperature rise calculations for LV test

Voltage (V)	Current (A)	Time (s)	Energy (kJ)	Temperature
220.1	18.2	10	40.06	0.61 °C
220.1	18.2	30	120.169	1.83 °C
220.1	18.2	60	240.34	3.66 °C
220.1	18.2	120	480.68	7.35 °C
220.1	18.2	600	2403.38	36.6 °C
220.1	18.2	1200	4806.77	73.2 °C

The test process is summarised here. First, distilled water was poured into the resistor, and the resistance was measured. It was found to be too large to accurately measure without any salt added. Thereafter, salt was gradually added until a sufficiently large current was drawn. The resistor was monitored for excessive heating or other danger signs throughout.

The current was measured using a Tektronix A662 current probe connected to a Tektronix TPS 2023 oscilloscope. The measurement was checked using a LH1040 current probe with digital readout. Voltage was measured using a custom-built voltage divider and the same oscilloscope. The reading was checked using a Fluke 233 digital multimeter. The voltage divider and oscilloscope were only used for voltage measurements at lower water resistance values, to avoid loading the circuit excessively due to the divider’s relatively low resistance (its total resistance is approximately 634 Ω). The resistance was calculated from the measured r.m.s. values determined from the digital multimeter (voltage) and oscilloscope (current).

Test results are listed in Table 2. An example of the voltage and current waveforms obtained from the oscilloscope are shown in Fig 3.

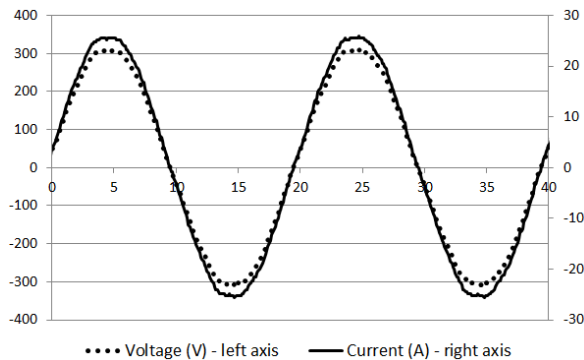


Figure 3: Example of waveforms obtained

Table 2: LV test results (TS = tea spoon)

Voltage (meter)	Current ('scope)	Resistance calculated	Test conditions
235.3 V	227 mA	993 Ω	+ 5 TS salt
236.0 V	404 mA	584 Ω	+ 6 TS salt
235.2 V	555 mA	424 Ω	+ 8 TS salt
235.3 V	744 mA	316 Ω	+ 11 TS salt
234.6 V	1.31 A	179 Ω	+ 20 TS salt
233.7 V	2.37 A	98.6 Ω	+ 40 TS salt
232.7 V	4.40 A	52.9 Ω	+ 80 TS salt
231.3 V	6.10 A	37.9 Ω	+ 120 TS salt
228.7 V	7.63 A	30.0 Ω	±1 kg of salt added
225.7 V	7.68 A	29.4 Ω	Repeat
226.4 V	8.78 A	25.8 Ω	> 1 kg salt added
225.8 V	10.3 A	22.4 Ω	> 1 kg salt added
223.7 V	10.8 A	20.7 Ω	Repeat
224.6 V	12.7 A	17.7 Ω	Repeat
226.0 V	14.3 A	15.8 Ω	Repeat
224.6 V	15.3 A	14.7 Ω	Repeat
220.09 V	18.2 A	12.1 Ω	Repeat

The following was observed from the test results:

- The water resistor is purely resistive, as the voltage and current are in phase with one another.
- Addition of salt decreases the resistance, as expected. However, the current was found to vary with time, most significantly increasing with continued application of voltage (several minutes). This is also in line with previous Eskom experience with throwing faults, and is not expected to be a problem for the application for which it is intended due to the relatively short application of voltage.
- The surface of the resistor increased in temperature over time when left energised for several minutes, as expected; but it did not become too hot to touch.

5.2 High voltage test

This test was performed by applying a voltage of approximately 25 kV a.c. to the test resistor for about two minutes (120 seconds). The resistor was empty to give the highest available resistance so as to not overload the supply. The purpose was therefore to verify the voltage withstand capability of the resistor. The resistor was monitored for excessive heating and other danger signs throughout. The pass criterion was a successful withstand of the applied voltage over the two minute test period. No flashover occurred and no signs of excessive heating or other danger signs were detected. The resistor therefore passed the test.

6. CONCLUSIONS AND RECOMMENDATIONS

The methodology behind selection, design and basic testing of a high voltage and high power resistor for electrically modelling a human body has been described. Practical aspects and limitations were discussed. Further work is required. For example, the earthing arrangement needs to be considered when performing tests, e.g. the use of solid earthing and various means of increasing the contact resistance to ground. The large range of possible resistance values of the human body and its contact with a conductor also need to be considered when performing the tests. It is recommended that a voltage source with sufficient power rating be used to test the prototype resistor to verify its performance before being used on site. Failing that, very large resistances should be used initially when testing on site and the resistor monitored carefully for overheating before reducing the resistance. Since only human body resistance is being considered initially, livestock would need to be considered at a later date.

7. REFERENCES

- [1] SANS 60479-1:2006, "Effects of current on human beings and livestock, Part 1: General aspects", Edition 2 and IEC corr. 1, 2006.
- [2] SANS 60479-3:1998, "Effects of current on human beings and livestock, Part 3: Effects of currents passing through the body of livestock", Edition 1 and nat. amd 1, 1998.
- [3] D. C. Giancoli, "Physics for scientist and engineers", Second edition, 1988, Prentice Hall Englewood, Page 452.
- [4] Wikipedia, Electrical resistivity and conductivity, last accessed 20 Dec 2012, http://en.wikipedia.org/wiki/Electrical_resistivity_and_conductivity.
- [5] Wikipedia, The mass of water vs litres of water, <http://en.wikipedia.org/wiki/Litre>, last accessed 29 Nov 2012.

8. ACKNOWLEDGEMENTS

E. L. Motsei and A. Mangxola are acknowledged and thanked for performing the data analysis and calculations to determine the range of suitable resistance values.

M. Mathebula is acknowledged and thanked for his significant assistance in designing and constructing the resistor, performing laboratory tests and documenting the work. N. Parus is also acknowledged for his assistance with the resistor design.

9. APPENDIX

Examples are shown here of the graphs obtained by plotting the values given in SANS 60479-1:2006 [1].

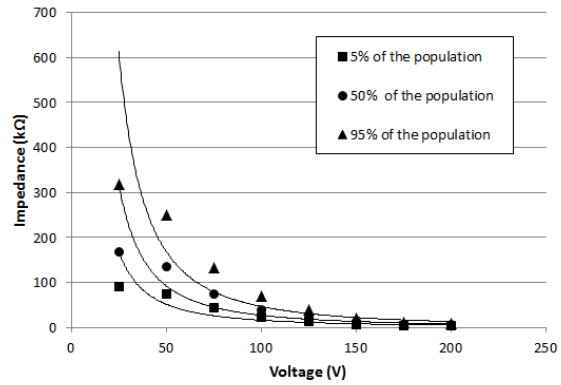


Figure A.1: Body impedance for 50 Hz a.c., hand-to-hand contact, small contact area, dry conditions – plotted from and equations fitted to values given in [1]

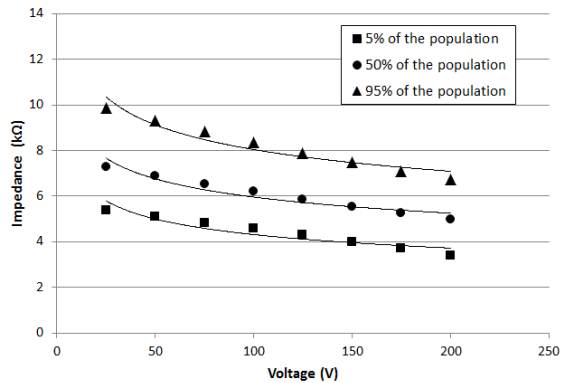


Figure A.2: Body impedance for 50 Hz a.c., hand-to-hand contact, small contact area, saltwater-wet conditions – plotted from and equations fitted to values given in [1]

PREDICTING THE REMAINING LIFE OF MEDIUM VOLTAGE VACUUM SWITCHGEAR USED IN DISTRIBUTION NETWORKS

J. O'Reilly*, J.M. van Coller** and Nico Smit***

* Eskom Power Plant Engineering Institute (EPPEI) – High Voltage (AC), School of Electrical and Information Engineering, Faculty of Engineering and the Built Environment, University of the Witwatersrand, Private Bag 3, Wits 2050, South Africa, E-mail: oreillj@eskom.co.za

** School of Electrical and Information Engineering, Faculty of Engineering and the Built Environment, University of the Witwatersrand, Private Bag 3, Wits 2050, South Africa, E-mail: john.vancoller@wits.ac.za

***Eskom - Private bag. X5012, Kriel 2271 - South Africa E-mail: smitnw@eskom.co.za

Abstract: The medium voltage (MV) electrical distribution network is a very conservative and risk averse sector that has undergone minor changes for the past 30 years when compared to other technologies. This, however, is changing drastically. The arrival of cost effective and reliable telecommunications, in addition to the radical price decrease of wireless communication and sensing technologies, is driving the industry towards an information based era known as Smart Grid. With an emphasis on medium voltage vacuum circuit breakers, the purpose of this research is to identify sensor technologies and analytics that will allow Eskom to assess the health of its medium voltage vacuum circuit breakers and utilize this information for effective maintenance planning. The key areas of research are the condition assessment of interrupter contacts through thermal monitoring, condition monitoring of the circuit breaker mechanism based on coil current diagnosis and vacuum integrity assessment of vacuum interrupters based on the magnetron pressure measuring technique.

Keywords: Medium Voltage, Vacuum Circuit Breakers, Vacuum Interrupters, Electrical Contacts Degradation, Temperature Rise, Wireless Temperature Monitoring, Mechanical Operation, Trip Coil Current Signature, On-line Condition Monitoring and Diagnostics, Condition-based Maintenance.

1. INTRODUCTION

The importance of circuit breakers to electric utilities cannot be overstressed. Circuit breakers have an important role in the delivered power quality and reliability, as well as in the promotion of customer satisfaction. Therefore, the need for improving the performance, reducing the life-cycle costs and most importantly enhancing the reliability and safety of the distribution network is ever increasing. This paper highlights the problem of an ageing infrastructure where the existing assets are becoming more expensive to maintain. The main problem with aged equipment is that, without appropriate maintenance, it is much more prone to failure than new equipment. Investment that has failed to keep up with the increasing demand has led to increased stresses on the existing infrastructure and this is a contributory cause to the acceleration of the ageing phenomenon. The level of investment required to modernise the existing Eskom medium voltage distribution network is prohibitive and alternatives must be found such that the system performs with the same reliability as in the past. Maintenance is essential in order to deliver the

demanding reliability. Condition-based maintenance, intended to “do only what is required, when it is required,” has been reported as the most efficient maintenance strategy for power system circuit breakers [1]. Since utilities have an interest in downscaling (through subcontracting, losing, and retiring their staff), this policy may cause crucial knowledge and skills required for circuit breaker condition assessment and defect diagnosis to be jeopardized [2]. Consequently, all of these point towards the need for intelligent knowledge base circuit breaker diagnostic algorithms and a smart fault detecting method. A vital step in the implementation process of an assessment framework is to understand component reliability and failure modes. International studies have provided exceptional insight into the failure statistics of circuit breaker components. Most common circuit breaker failures observed in the field are related to operating mechanism and auxiliary control circuits. More accurately, 43% to 46% of the main failures are mechanical in nature, 20% to 29% are correlated to auxiliary and control circuits, and 21% to 31% are associated with problems involving the vacuum interrupters [3].

In the medium voltage realm, vacuum interrupters are widely used to interrupt short-circuit currents. A key requirement for vacuum interrupters is to pass continuous current in the closed contacts position within a limited temperature rise range [4]. Although vacuum interrupters spend the vast bulk of their service life in the closed position, they could be subjected to extreme stresses such as short-circuit interruption and high dielectric stress. After short-circuit operations, the resistance across electrical contacts will generally increase due to melting of the contact surface from making and breaking arcs. Direct measurement of the interrupter's electric contact temperature using continuous temperature monitoring of energized equipment provides real information related to the condition of the electrical contact. The advantage of continuously monitoring the condition of energized equipment on-line enables operation and maintenance personnel to determine the operational status of equipment, to assess the present condition of equipment, timely detect any abnormalities, and initiate maintenance preventing impending possible forced outages [5].

With emphasis on the operating mechanism of circuit breakers, one useful parameter to effectively diagnose the health of the mechanism is the trip/close coil current signature. The coil current is easily accessible and measurable, which can be assessed online or offline [6]. One aspect of this research is to focus on trip/close operation of medium voltage vacuum circuit breakers and to provide an intelligent failure detection algorithm based on the results of exploring the characteristics of trip/close coil current signatures of healthy and defective circuit breaker mechanisms. The failure modes within the mechanical mechanism of the circuit breaker that should be investigated are the variation in auxiliary supply voltage, increase in coil resistance, excessive friction of the release mechanism, and faulty auxiliary contacts. The impact of each specific failure on coil current features and operation time of circuit breakers (closing and opening times) needs to be observed to derive the discrepancies in the coil current features during the healthy and faulty conditions.

Focusing on the vacuum integrity of vacuum interrupters, the main disadvantage of vacuum interrupters is the possibility of losing vacuum and the absence of a simple method for effectively monitoring the level of vacuum in the interrupter. Although the lifetime of a modern vacuum interrupter is supposed to be more than twenty years, the possibility of abnormal inner pressure rise due to leakage, long term diffusion and other factors [7] cannot be completely excluded. In order to determine whether the inner pressure of a vacuum interrupter is within its safe operational limits, many techniques and test equipment have been developed [7,8], all of which are functional off-line, and have to demount the vacuum interrupters from the circuit breakers. Consequently, when the interrupters

are to be reinstalled, some of the mechanical parameters of the vacuum interrupters must be calibrated, which is labor intensive and should be performed by qualified technicians. Recently, a pressure diagnostic method known as the leak-rate test has been used by field technicians to detect the vacuum integrity of vacuum interrupters. Leak-rate testing provides results beyond a "pass/fail" result obtained from a high potential test which provides quantifiable data based on the internal pressure and interrupter geometry that allows maintenance personnel to use predictive maintenance procedures and programs that result in higher equipment reliability and improved lifetime compared to reactive maintenance programs [9]. This paper proposes techniques that could enhance the reliability and lifetime of medium voltage vacuum switchgear by means of a real-time condition based monitoring and maintenance approach.

2. BACKGROUND

2.1 Electrical contacts condition diagnostics based on wireless temperature monitoring of energized equipment

With reference to MV circuit breakers, the main source for hot-spots originates from the interrupter's contact surface, which over time will deteriorate and result in increased electrical resistance and temperature. If these parameters are not observed for long durations and deterioration reaches a critical state, arcing across the contact surface will most probably occur. With this understanding, industry saw the need of developing reliable and durable long-life sensors capable of withstanding the harsh conditions that exists in the area directly outside the vacuum interrupter's contact enclosure indicated by the shaded zones in Figure 1.

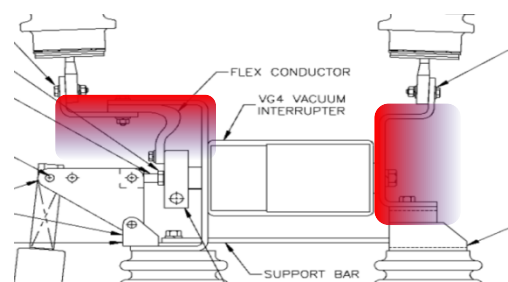


Figure 1: Preferred temperature monitoring areas in MV circuit breakers [10]

Thermal monitoring and analytics:

Continuous monitoring of the interrupter's contact temperature begins with a physical model for the heat energy balance: heat energy supplied to the interrupter generated from its resistance to current must add up to the heat convected to the interrupter's surroundings and the system's absorbed heat – revealed in the equipment's temperature (1) [11].

The heat energy balance equation is given as

$$RI^2 dt = K\theta dt + mCd\theta \quad (1)$$

Where:

$$\theta = T_i - T_e \quad (2)$$

T_i = Interrupter internal temperature [$^{\circ}\text{C}$]

T_e = Interrupter external temperature [$^{\circ}\text{C}$]

R = Interrupter resistance [Ohm]

I = Interrupter current [Ampere]

K = Characteristic constant of heat exchange [Watt/ $^{\circ}\text{C}$]

m = Interrupter mass [kilogram]

C = Interrupter average heat capacity [Watt/kilogram]

t = Time [seconds]

Further manipulation of (1) is possible when an interrupter is in steady state with known temperatures and load current [11].

$$\theta = \frac{RI_n^2}{K} \left\{ \left[\left(\frac{I_{OL}}{I_n} \right)^2 - 1 \right] e^{-t/\tau} \right\} \quad (3)$$

Where:

I_n = nominal current [Ampere]

I_{OL} = overload current [Ampere]

τ = interrupter thermal time constant

Figure 2 shows heat rise H and characteristic term τ as a function of $H = \theta / \theta_n$ as described by (3). From a trending perspective, as the equipment deteriorates and τ decreases, shifts in thermal response times and temperature levels are detectable.

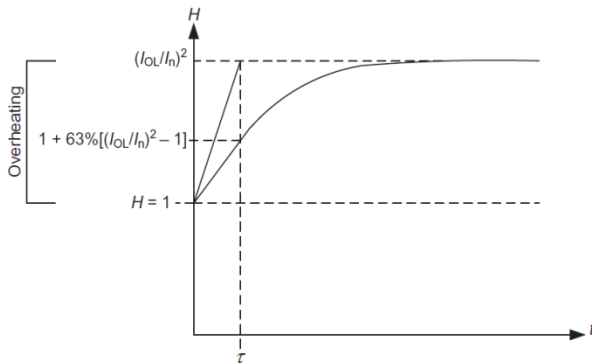


Figure 2: Interrupter heat rise characteristic [11].

The generated heat depends on the load current and the contact resistance. The contact resistance has a tendency to rise over time due to the aging process,

caused by both mechanical and environmental factors. At some stage an aging contact with increased resistance will generate excessive amounts of heat and tip the heat energy balance towards elevated temperatures. As a result, an aging contact temperature will be significantly higher at the same current. Assuming that the heat dissipation means have not significantly changed during the period of observation, the temperature rise over time will depend mainly on the resistance change. Therefore contact temperature change at the same current level over the period of time could serve as the qualitative tool of evaluation of contact conditions. An aging scenario for electrical contact may be roughly presented in Figure 3 as a sequence of three different types of thermal behavior.

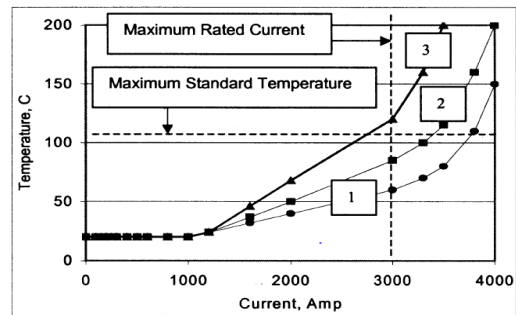


Figure 3: Thermal behavior of an energized contact in different conditions: normal (1), deteriorating (2), and faulty (3) [5].

Wireless surface acoustic wave temperature monitoring system:

Surface Acoustic Wave (SAW) technology provides an ideal solution as it is non-invasive, no power is required to the sensors, highly scalable, and provides continuous real-time monitoring. The SAW temperature monitoring system includes SAW temperature sensors mounted at strategic contact points within the switchgear panel and a reader capable of interrogating multiple SAW temperature sensors simultaneously. Figure 4 shows a layout of the SAW temperature sensing system. The reader antenna is mounted inside the switchgear panel and sends short radio frequency pulses into the panel. If the pulses are at the frequency of the sensor, the sensor receives, modifies and passively returns the pulses. The returned pulses contain information related to equipment temperature.

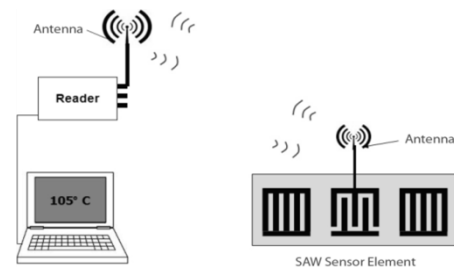


Figure 4: SAW wireless temperature sensing system

2.2 Circuit breaker mechanical operation

The fundamental reason why monitoring of the circuit breaker actuator coil current signature is so effective is that the coil current's behaviour is directly influenced by the physical resistance of all movable parts of the actuator system and therefore, the coil current characteristics can be used as a means of identifying deviations in the mechanical operation of a circuit breaker actuator. By capturing and analysing the circuit breaker's actuation coil current signatures from open and close operations, it is possible to initiate preventive maintenance alarms based on the outcome of the analysis.

Relationship between coil current and circuit breaker mechanism performance:

The trip/close coil consists of a solenoid around a movable iron armature forming an electromagnetic actuator. Once a command signal is initiated and the control circuit receives the signal, the opening or closing operation of the circuit breaker commences. When a voltage is applied to the coil, a current starts to flow through the coil. As a result, the armature slide toward the circuit breaker latch mechanism, and actuates the operating mechanism. The stored energy in the charged opening spring is employed to set all of the mechanical parts in motion and open or close the main interrupting contacts while, at the same time, the coil current reaches its maximum. Finally, after a short delay, auxiliary contacts open and disconnect the coil from the Direct Current (DC) supply and, as a result, the coil current decays to zero (see Figure 5).

Circuit breaker trip/close coil current features:

In order to evaluate the condition of the circuit breaker through its coil current signature, six features reflecting the circuit breaker abnormalities are identified as shown on a typical measured waveform in Figure 5.

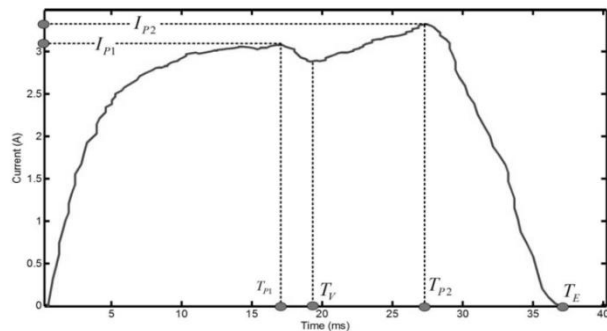


Figure 5: Circuit breaker captured coil current signature [1].

The following terminologies are presented in Figure 5:

I_{p1} = First local maximum current;

T_{p1} = Time from initial pulse current rise to first local maximum value I_{p1} ;

I_{p2} = Second local maximum current;

T_{p2} = Time between circuit breaker relay initiating a trip/close operation and the circuit breaker transitioning to fully open/close state;

T_v = start time of circuit breaker's operation (latching time);

T_e = Total energised time of coil current.

Features and failures:

The most common failure modes that need to be considered during circuit breaker mechanical operation are the variation in auxiliary supply voltage, increase in coil resistance, excessive friction of the release mechanism, and defect of auxiliary contacts. The impact of each specific failure on the coil current features and circuit breaker operation times must be investigated to derive the discrepancies in the coil current features during the healthy and faulty conditions. Figure 6 presents an example of the impact of malfunctions in the voltage supply, latch, and auxiliary contacts on the close coil current of a 72.5 kV circuit breaker.

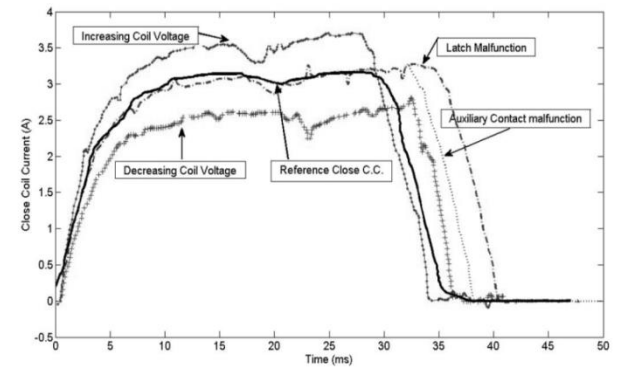


Figure 6: Effect of various malfunctions on the close coil current [1].

Failure detection algorithm:

The failure detection algorithm is explained in the following steps:

1. Coil current capturing and calculation of features

After the circuit breaker has reached its fully opened/closed state, the coil current waveform is recorded in order to calculate the defined features such that their discrepancies can be revealed.

2. Calculation of discrepancy of features and sorting

By comparing the calculated features in Step 1 and the normal features, the percentage deviation can be obtained. Afterwards, these discrepancies are sorted from the highest (most affected) to lowest (least affected) absolute value.

3. Identification of failures and their causes

The mode of failure and their root causes are recognized in this step through a failure detection box presented in Figure 8. The algorithm is shown in Figure 7.

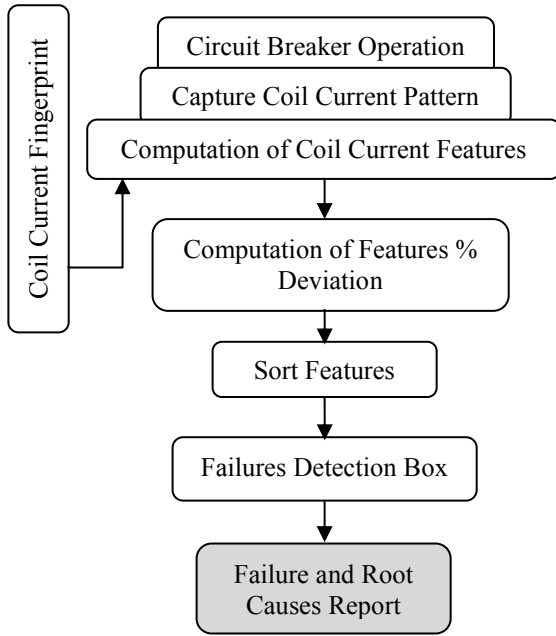


Figure 7: Outline of the proposed failure detection algorithm

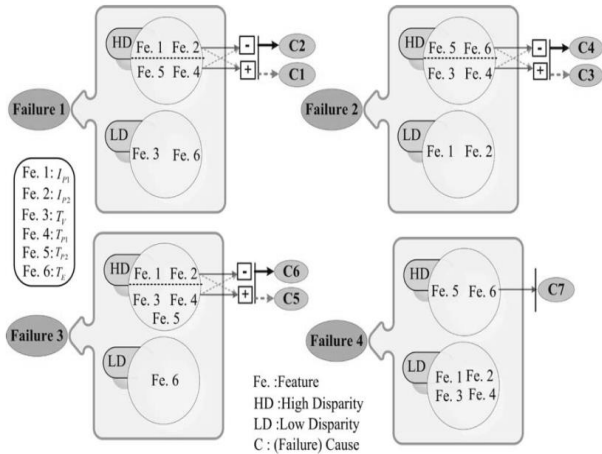


Figure 8: Failures detection box [1].

A broad overview of the main points of analyzed failures and their root causes, as well as the most affected features of coil current, which relate to the core of the detection box, are provided in Table 1.

Table 1: Circuit breaker failures and root causes from a coil current perspective

Failure Cause	Causes Description	Affected Parameters
Voltage Supply (Failure 1)	C1. Voltage Level Increasing C2. Voltage Level Increasing	Circuit Breaker Timing I_{P1} I_{P2} T_V T_{P1}
Latch (Failure 2)	C3. Soft Latch C4. Stiff Latch	Circuit Breaker Timing T_{P2} T_E T_V T_{P1}
Coil (Failure 3)	C5. Resistance Decreasing C6. Resistance Increasing	Circuit Breaker Timing I_{P1} I_{P2} T_V T_{P1}
Mechanism and Auxiliary Contacts (Failure 4)	C7. Auxiliary Bounce, Faulty Operation	Circuit Breaker Timing T_{P2} T_E I_{P2}

In order to differentiate between different failures, the features are classified by their absolute value of discrepancies as High Disparity (HD) and Low Disparity (LD) as in Figure 8. Once the discrepancy of features is calculated in Step 2, the deviations of more than a certain percentage are labeled as HD and the other are regarded as LD. Based on this approach, the algorithm can detect the type of failures by considering Table 1. Finally, the root causes of failures are concluded through the sign of feature discrepancy.

2.3 Vacuum life assessment of vacuum interrupters

Vacuum interrupter operating principles - Paschen's law:

The medium voltage electrical distribution network relies on an ageing population of vacuum interrupters. It is imperative to know what the vacuum integrity is within the interrupters that are in service. Vacuum Interrupters' high interrupting capacity is based on the physical principle discovered by Louis Karl Heinrich Friedrich Paschen (1865-1947).

Paschen did original experimental research and discovered that the dielectric strength/breakdown voltage U_b of a gas is a function of the gas pressure p , the distance between the two electrodes d , and the type of gas [12].

The breakdown voltage in air can be calculated from

$$U_B = \frac{apd}{\ln(pd)+b} \quad (4)$$

Where:

- U_B = breakdown voltage [kV];
- a and b = constants derived for dry air;
- p = gas pressure [Pa]
- d = distance between the two electrodes [mm]

Figure 9 shows a typical Paschen curve for air for a (pd) in the range of $1-10^5$ Pa.

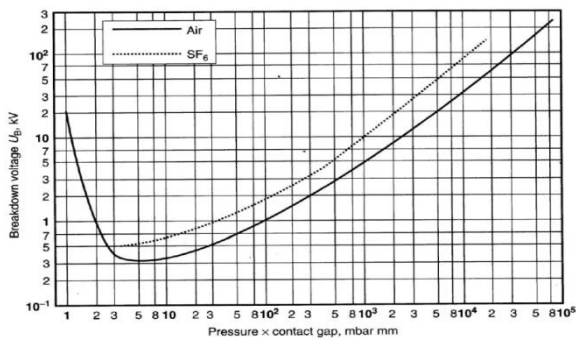


Figure 9: Paschen curves in air and SF₆ for contacts with a uniform electric field between them [12].

The left hand side of the curve in Figure 9 is of interest, which shows an increase in dielectric strength around 3×10^{-1} Pa and then a constant dielectric strength for pressures below 10^{-1} Pa. Any pressure below about 10^{-1} Pa has no effect to the interrupter performance. The pressure within the vacuum interrupter is allowed to increase from the normal manufactured value of about 10^{-6} Pa to an end of life value of 10^{-1} Pa, after which the insulation effect deteriorates very rapidly with rising pressure. Once an interrupter goes beyond this threshold it has failed, as it will quickly reach a point where the Transient Recovery Voltage cannot be withstood and the interrupter would then be unable to interrupt even small currents.

Magnetron pressure measuring technique for vacuum interrupters:

Once the vacuum interrupter is finally assembled, evacuated, and brazed, the final vacuum interrupter has a vacuum below 10^{-6} Pa sealed inside it. The common method for measuring the vacuum level is based on the principle of a Penning discharge. Here a high DC voltage (typically in the range of 10kV) is applied between two suitable electrodes in the presence of a magnetic field. Electrons are drawn from the cathode electrode by field emission and then spiral back and forth around the magnetic flux lines. Their travel path to the anode is thus substantially lengthened. When

these electrons collide with residual gas molecules, ionization can occur and a small current flow in the range of micro-amperes can be measured. The level of current measured is directly proportional to the residual gas pressure. One way of performing this measurement using a vacuum interrupter is by means of a Magnetron pressure measuring technique illustrated in Figure 10.

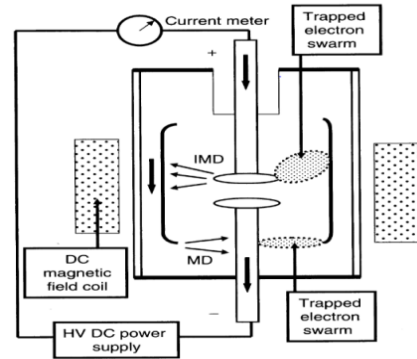


Figure 10: Magnetron pressure measurement technique for vacuum interrupters [12].

The vacuum interrupter is placed inside a magnetic field coil. The contacts are opened and a DC voltage of about 10 kV is applied across them. In this case the trapped electron swarm is captured between the upper contact (in this example the anode) and the floating shield (i.e., an Inverted Magnetron Discharge, IMD). An electron swarm is also trapped between the floating shield and the lower cathode (i.e., a Magnetron Discharge, MD). The current measured in the high voltage circuit thus flows from the anode to the shield and then to the cathode [12]. The actual current/pressure relationship for a specific vacuum interrupter model depends on its internal geometry. Therefore, before the magnetron method can be routinely used as a manufacturing test device, it has to be calibrated for each vacuum interrupter model. One way of performing this calibration is to add a nozzle to a specific vacuum interrupter model and then attach it to a pressure gauge and to a vacuum system. The magnetron current can then be measured for a given vacuum interrupter as a function of the actual pressure inside the interrupter. Figure 11 illustrates an example of the relationship between current and pressure of a vacuum interrupter.

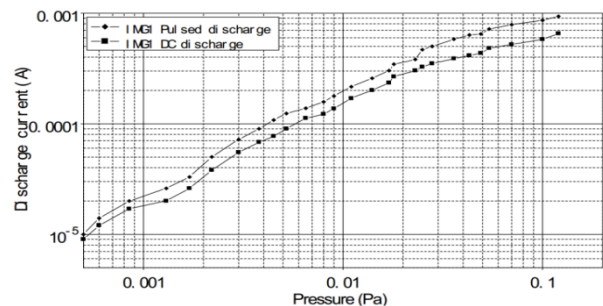


Figure 11: Current-pressure relationship of a vacuum Interrupter [8].

3. SUMMARY OF PROPOSED INVESTIGATION

This paper discusses a data-driven approach to the condition assessment of medium voltage vacuum circuit breakers, operating on thermal monitoring of energized vacuum interrupter contacts, circuit breaker mechanical operation monitoring based on trip/close coil current diagnostics and vacuum integrity monitoring of vacuum interrupters through the Magnetron pressure measurement technique. These condition monitoring techniques should allow utility switchgear technicians and maintenance personnel to identify and establish correlations between circuit breaker healthy and faulty conditions. The main benefits to asset managers envisaged from the introduction of condition monitoring and diagnostic systems are:

- identification of incipient circuit breaker degradation;
- automated and consistent assessment of circuit breaker conditions;
- faster, more informed condition assessment;
- recognition of manufacturing faults;
- provision of diagnostic support for more targeted, condition-based maintenance activity;
- obtaining reliable and characteristic information describing the present asset condition;
- avoiding unnecessary maintenance and consequent faults;
- reduced maintenance costs.

4. FUTURE WORK

The three areas of research previously discussed in this paper will be investigated through extensive laboratory testing and attempt to understand them more clearly such that the theoretical explanation can be validated.

5. ACKNOWLEDGEMENTS

The first author would like to thank Actom MV Switchgear (the circuit breaker manufacturer) for their support in granting permission to perform measurements on their circuit breakers and to provide access to the existing measurement data files on their circuit breakers. The first author also acknowledges the contribution of Eskom for the opportunity to participate in the Eskom Power Plant Engineering Institute (EPPEI) programme.

6. REFERENCES

- [1] A. A. Razi-Kazemi, M. Vakilian, K. Niayesh and M. Lehtonen, "Circuit-Breaker Automated Failure Tracking Based on Coil Current Signature," *IEEE Transactions on Power Delivery*, vol. 29, no. 1, pp. 283-290, Feb. 2014.
- [2] G. Balzer, D. Drescher, F. Heil, P. Kirchesch, R. Meister, and C. Neumann, "Evaluation of failure data of HV circuit-breakers for condition based maintenance," in *Proc. CIGRE Sessions*, 2004.
- [3] CIGRE Working Group 13.06, "Final report of the second international enquiry on high voltage circuit breaker failures and defects in service," Paris, France, Rep. no. 83, Aug./Sep. 1994.
- [4] High-voltage switchgear and controlgear – Part 1: Common specifications, IEC Standard 62271-1, 2011.
- [5] A. Livshitz, B. H. Chudnovsky, "Condition Diagnostics of Energized Electrical Equipment: Case Studies," 1-4244-0493-2/06 ©2006 IEEE.
- [6] S. Strachan, S. Mearthur, J. McDonald, W. Leggat, and A. Campbell, "Providing decision support for the condition-based maintenance of circuit breakers through data mining of trip coil current signatures," *IEEE Transactions on Power Delivery*, vol. 22, no. 1, pp. 178–186, Jan. 2007.
- [7] G. C. Damstra, R. P. P. Smeets and H. B. F. Poulussen, "Pressure estimation in vacuum circuit breakers", *IEEE Transactions on Dielectrics and Electrical Insulation*, Vol. 2, pp. 198-201, 1995.
- [8] H Mao, G. Chang, X. Zhu and Y. Wang, "On-line Monitoring of Pressure in Vacuum Interrupters," *IEEE Transactions on Dielectrics and Electrical Insulation*, vol. 14, no. 1, pp. 179-184, Feb. 2007.
- [9] J. Cadick and F. Ledbetter. "Predicting the Remaining Life of Vacuum Interrupters in the Field," 81st International Conference of Doble Clients, Doble Engineering Company, 2014.
- [10] ABB, MV Circuit Breaker Instruction Manual [Online]. Available: [http://www05.abb.com/global/scot/scot235.nsf/veritydisplay/7e5daa7afc45ac4bc1257574004dd7bc/\\$file/r-mag%20instruction%20book%201val255101-mb%20rev%20e.pdf](http://www05.abb.com/global/scot/scot235.nsf/veritydisplay/7e5daa7afc45ac4bc1257574004dd7bc/$file/r-mag%20instruction%20book%201val255101-mb%20rev%20e.pdf), March 2009.
- [11] A. A. Sallam and O.P. Malik, "Electric Distribution Systems", Piscataway, NJ: John Wiley & Sons, Inc., 2011.
- [12] Paul G. Slade, *The Vacuum Interrupter: Theory, Design, and Application*, CRC Press, 2007.

APPARENT SOIL STRUCTURES RELEVANT TO BURIED EARTH ELECTRODES IN SOUTH AFRICA - A RESEARCH PROPOSAL

P. H. Pretorius

*University of the Witwatersrand, Faculty of Engineering and the Built Environment, School of Electrical and Information Engineering, Private Bag 3, Wits 2050, South Africa.
e-mail: pieter.pretorius@wits.ac.za*

Abstract: Transmission infrastructure development in South Africa, over the period 2015 to 2024, requires a planned total length of 13 396 km of high voltage overhead power lines. This effectively translates into an approximate number of 33 490 towers that require assurance that the tower foot resistance of each tower falls below a specified threshold to allow for optimum lightning performance of the line. Designing a set of tower foot earth electrodes, based on the predominant soil structures expected along the line route, is preferred to the design of individual electrodes for each tower as that is likely to result in a costly design-approach. Soil structure and soil resistivity form an integral part of such design but is currently not generally available and can only be obtained through specific site visits and soil resistivity measurement. An alternative means of obtaining soil resistivity data from existing sources is discussed in this paper. The paper in essence covers a proposal for research that will lead to the development of an information base of typical soil structures in South Africa that can be applied in the design of general earth electrodes, such as those applicable to overhead power line towers and their footings.

Key words: Soil Structure, Earth Electrode, South Africa, Research Proposal.

1. INTRODUCTION

1.1 Electricity Network Expansion in South Africa

With the transmission network expansion in South Africa a total of 13 396 km (3 940 km at 765 kV; 9 097 km at 400 kV and 359 km at 275 kV) of power lines are planned for the period 2015 to 2024 [1]. With an assumed average span length of 400 m, for these lines, a total number of 33 490 towers will be required. Each tower has a foundation that forms an integral part of the tower foot earth electrode. The tower foot electrode impedance is an important parameter in the lightning performance of any power line. Depending on the lightning ground flash density (See Figure 1 [2]) and the soil resistivity at the tower location, the tower foot electrode can be optimised in terms of its electrical performance [3, 17].

Each of the power lines terminates at a substation of which the electrode plays an important part in ensuring both equipment and human safety. Safety is dictated by the earth potential rise during fault conditions in the substation or at the power line tower. Again, the electrode can be optimised from a design perspective with knowledge about the electrical characteristics of the soil that the electrode is buried in.

1.2 Buried Earth Electrodes

Relatively low values are preferred for earth electrodes to allow controlled dispersion of unwanted current into the

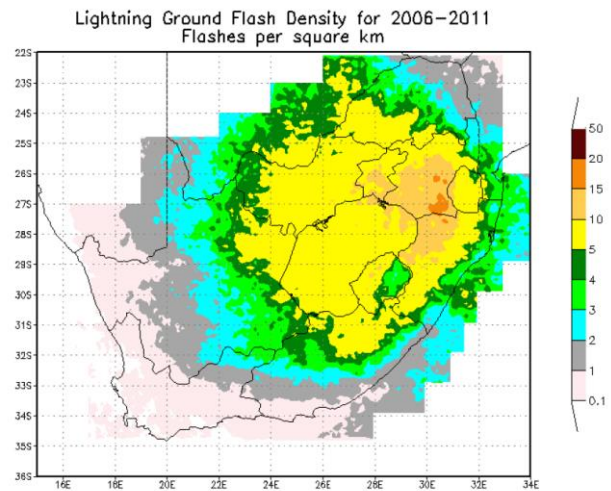


Figure 1: Lightning Ground Flash Density across South Africa - 2006 to 2011 (Taken from [2]).

soil. In its simplest form, an earth electrode can be represented by a driven rod (Figure 2 - left: side view; right: top view) with the resistance of the rod given by

$$R = \frac{\rho}{2\pi L} \ln\left(\frac{2L}{r}\right) \quad (1)$$

where ρ is the soil resistivity ($\Omega\cdot\text{m}$), L is the length (m) of the rod and $2 \times r$ is the diameter (m) of the rod. It is clear

that the rod resistance is directly proportional to the soil resistivity.



Figure 2: Schematic illustration of a rod electrode.

Figure 3 shows a typical conceptual structure of a horizontal two layer soil with the top layer 2 m thick, presenting a high resistivity (1 000 Ω.m), and the deeper layer presenting a lower resistivity of 100 Ω.m.

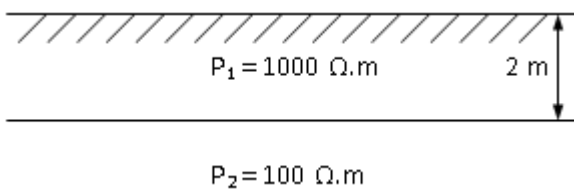


Figure 3: Typical conceptual horizontal two layer soil structure.

Using the soil structure noted in Figure 3, a 0,5 m long rod with 10 mm diameter will effectively be embedded into the 1 000 Ω.m soil layer to present a resistance close to 1 687 Ω. Selecting a longer rod, 3 m in length with the same diameter, will present a resistance of 207 Ω in the average “homogeneous” soil layer of 550 Ω.m. This example conceptually illustrates the importance of information required about the soil structure to lower the electrode resistance through proper design.

2. SOURCES OF SOIL DATA - THE PROBLEM

2.1 General

General: Soil data is available from various sources or can be obtained from various techniques, depending on its application. These include published material, such as, Geophysical Reports, maps from the Department of Agriculture / Agricultural Research Council (ARC), Geological Maps and Soil Resistivity Measurements, to name a few. However, the data available from these sources (other than resistivity measurements) are not suitable for electrode design as discussed below.

2.2 Geophysical Reports

These reports, from a power line perspective, contain data on the type of soil in which the tower foundation will be embedded. Different types of soil are classified, for example, a Type 1 soil is classified as a hard and granular type of soil and is considered a competent engineering soil; Soil Type 2 is a less competent soil comprising of a stiff clay or dense sand; Soil Type 3 is a very incompetent soil based on loose sand or soft clay [4]. This type of soil data does not provide any information about soil strata,

their thickness and resistivity and can at best be guessed from a range, such as, that presented in Figure 4.

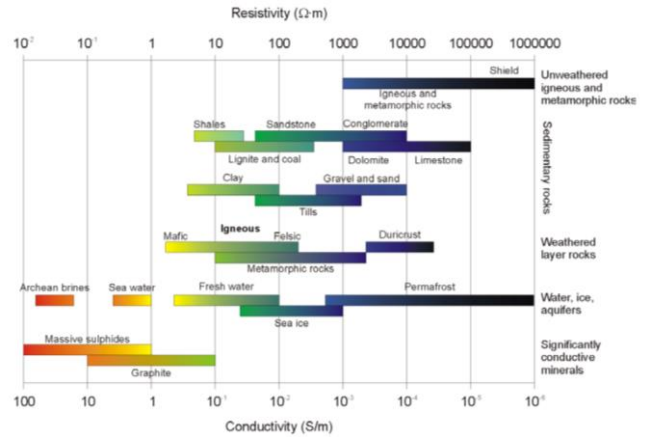


Figure 4: Resistivity of typical earth materials and soils (Taken from [5]).

2.3 Data for Agricultural Application

Soil data available from the Department of Agriculture [6] and the ARC [7] is very useful in the application to agriculture: types of vegetation and grazing that are likely to thrive in the different soil types (See Figure 5 as an example). But again, this type of data does not provide any information about the resistivity of different strata that can be employed in electrode design because it only presents information about the top soil, a few centimeters deep, in a particular area.

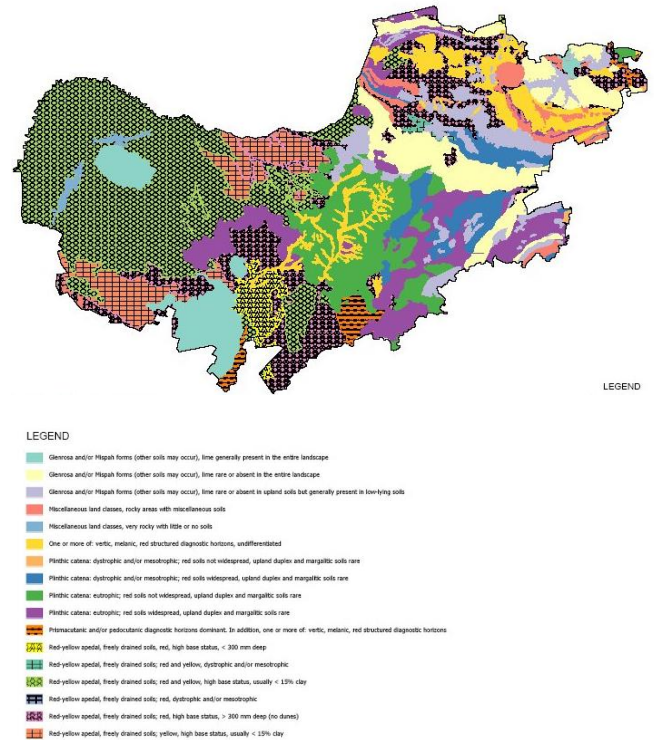


Figure 5: Soil types of the North West Province in South Africa [6, 7].



Figure 9: Traverse near the tower of Figure 7 along which soil resistivity measurements were conducted.

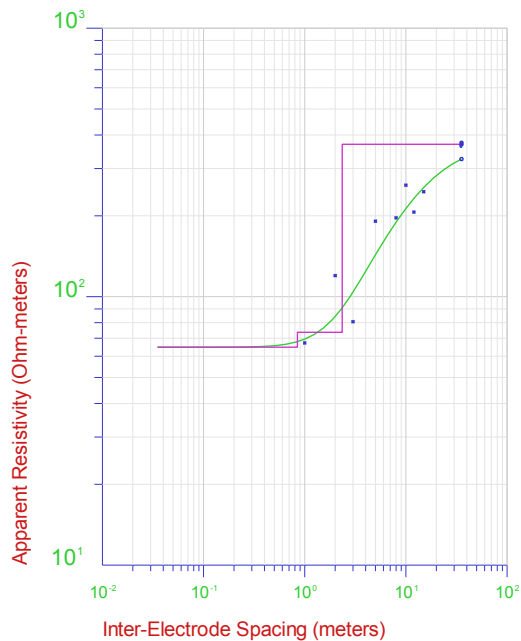


Figure 10: Soil structure obtained from the soil resistivity measurements for the traverse indicated in Figure 9.

Capturing data with the Wenner method requires the despatch of personnel and equipment to the site where the soil data is required. This may take some time and it is effectively required that a resistivity measurement (along one to several traverses) be done at the locations where electrode will be located. The design for each electrode then follows.

Considering the number of towers noted earlier, even assuming that only 10 % of these towers may require modification of the tower foot electrode, it still presents a significant number (3 349) that will demand significant resources to address. A means to overcome this challenge is presented in the following section.

3. UNTAPPED SOURCES OF SOIL DATA - MOTIVATION

Soil resistivity measurements based on the Wenner method have been done for many years in South Africa, particularly as input to the design of substation earth electrodes. In 2011, Eskom dispersed 130,005 MVA and 102,053 MVA respectively through transmission (132 kV and above) and distribution substations [13]. This equates currently to a total of 3665 substations of which 213 are transmission substations [14]. See Figure 11 for a spread of both transmission and distribution substations across the country. Each of these substations required soil resistivity measurements for the design of their earth electrodes. These designs present a “hidden” source of information on soil structures.

Plans are on the table to install a further 181 transformers (81,385 MVA) over the period 2015 to 2024 [1]. Even though these may not necessarily be installed at new substations, their installation may require the refurbishment of some substation electrodes due to elevated fault levels. It is these refurbishments that may require soil resistivity measurements and that may present additional information relevant to this discussion.

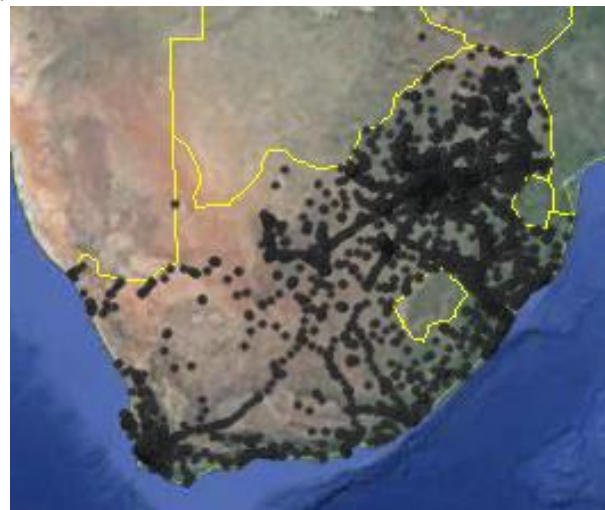


Figure 11: Spread of Transmission and Distribution Substations (Mapped on [15, 16]).

Apart from Eskom, there are several private companies in South Africa that have been providing soil resistivity measurement services for more than a decade. It is these companies that sit with a wealth of historical soil resistivity data.

It is not claimed that all the soil resistivity data is available for all the substations in South Africa but a significant amount of data is likely to exist due to good record keeping by these respectable companies. For example, assume five companies are likely to participate in the sharing of the soil resistivity information and each company holds historical soil resistivity data for 50 substations (that is data from 5 substations per year). This

yields 250 data sets. If it is further assumed that double this number of data sets can be obtained from Eskom, a total of 750 soil resistivity data sets will be available without any expenditure in terms of site visits or measurements.

4. PROBLEM STATEMENT

Both the existing electricity network and expansion thereof presents overhead power line towers with electrodes that need to be optimised in terms of lightning performance. The optimisation of these electrodes requires soil structure data as input to the electrode design and optimisation. In limiting the cost component of such designs, it makes sense not to design individual electrodes for all the towers, but rather to design a set of universal electrodes that can be applied for predominant soil structures present in South Africa. Data on predominant soil structures in the country can be obtained in a cost effective manner from historical soil surveys done mainly for substations electrode designs. This data can be transformed into an information base, in support of electrode design, that can be extended through future soil resistivity measurements.

The abovementioned problem statement raises key research questions that include:

- Can sufficient historically data be obtained in support of statistically significant analyses?
- Is the historical data representative of the larger part of South Africa?
- How should the historical data be screened, analysed and presented to add value to the design of earth electrodes for towers?
- Based on the historical data, what type of soil structures are dominant in South Africa that should be considered in electrode design for power line towers?

5. PROPOSED RESEARCH DIRECTION AND METHODOLOGY

5.1 General

In answering the research questions, the proposed research direction will include the following components: data collection, primary data analysis, development of soil structures and secondary data analysis.

5.2 Data Collection

The initial stage will involve the identification of credible third parties that can contribute to and would like to participate in the sharing of historical soil resistivity data. Initial telephonic attempts by the author to determine whether some parties may participate resulted in positive response received.

The data to be collected will include the location of the site where the measurements were made plus the raw soil resistivity data captured by means of the Wenner method.

Secondary information about the time / season of measurement and the climatic conditions, if available, will further assist in the Primary Data Analysis.

It will be endeavoured to collect at least 1 000 soil resistivity data sets (that is, data from 1 000 sites) that are representative of South Africa, as a target for the project initiation. It is expected that more data sets will be required but these can be grown as network expansion projects, for example, develop. In addition, the third parties noted may also have soil resistivity data available from non-utility projects, such as, mobile base station sites that were surveyed for soil resistivity and that can contribute to the information base.

5.3 Primary Data Analysis

The primary data analysis will involve the screening and preparation of the data to be input-compliant to the software that will be used for the development of the soil structures. In-house developed or commercially available software will be used for this purpose.

As part of the of the primary data analysis, statistical requirements will dictate the number and spread of data required to be representative of soil structures in South Africa. Raw data will be screened according to these requirements.

5.4 Development of Soil Structures

Numerical models will be used to translate the raw data into representative and equivalent horizontally (vertically or otherwise) layered soil structures. Output of the model will reflect the number of layers, the thickness of the layers and the resistivity of the layers. Confidence in the accuracy of the model will form part of the output.

5.5 Secondary Data Analysis

The secondary data analysis will include statistical analysis of the soil structures, yielding the probability for example, that a particular soil structure may be expected at a particular location. Alternatively it may indicate that in 95 % of the cases, the top soil layer is representative of a certain soil resistivity or the depth that electrically attractive (low resistivity) soils are mostly found. These are all specific points that the electrode designer is interested in.

6. EXPECTED BENEFITS

The expected benefits from developing a soil structure information base cover several aspects as noted below. With a database on typical soil structures, it would be possible to:

- Determine the threshold for equivalent soil resistivity at which tower foot electrode modification becomes too expensive. Such a threshold could dictate where and when line surge arrestors become a more attractive solution to improve lightning performance.
- Indicate in which areas the permittivity of soils becomes more important from a perspective of the high frequency behaviour of earth electrodes [3].
- Save cost by developing a set of electrodes applicable to soil structures most frequented in South Africa as opposed to the design of individual electrodes.
- Eliminate accommodation for seasonal variation from the electrode design process if knowledge is available about soil at a depth of typically 1,5 m to 3 m. If, for example a measurement was made in winter (dry season), the database will support information on how the electrode will behave in summer (wet season).
- Design in general for the critical distance along power lines near substations. The critical distance defines the length of the line section within which back-flashovers could result in unacceptably high overvoltages in the substation. This length is determined by considering the arrester protective zone. Earthing requirements can then adequately be addressed for lightning surges originating on the line close to and further away from the substation. For the latter, corona attenuation (reduction of the steepness of the incoming surge) will also be considered with the effect that the lightning surge is likely to pose a lesser threat to the substation equipment.
- To link resistivity with the permittivity of the soil through a universal soil impedance [3].

7. CONCLUDING REMARKS

A means to initiate the development of an apparent soil structure database for South Africa in a cost effective manner has been presented in this paper. The paper, in essence, took on the form of a research proposal that covered: the Motivation to address the problem; the Problem Statement with Research Questions; the proposed Research Direction and Methodology and Expected Benefits.

In considering the expected benefits, it is anticipated that the proposed research will lead to a full understanding of the behaviour of soil based on soil structures in South Africa and that can be applied in effective electrode design of power line towers (and substations).

8. ACKNOWLEDGEMENT

This work was grant-funded by the Eskom Centre for High Voltage Engineering - Project No ECHV001 managed by the University of the Witwatersrand.

9. REFERENCES

- [1] Eskom, "Transmission 10 Year Development Plan: 2015–2024 (TDP 2014)", *Public Forum*, 10 Oct 2014, http://www.eskom.co.za/Whatweredoing/TransmissionDevelopmentPlan/Pages/Transmission_Development_Plans.aspx, Last Accessed 15 Oct 2014.
- [2] Morné Gijben, "Lightning Climatology of South Africa with a Special Focus on Lightning Risk Maps", *22nd International Lightning Detection Conference & 4th International Lightning Meteorology Conference*, Broomfield, Colorado, USA, 2 - 5 Apr 2012.
- [3] P H Pretorius, "Engineering Perspectives on Soil Properties Important to the Design and Performance of Earth Electrodes at Low and High Frequency", *Paper submitted for presentation at the 19th International Symposium on High Voltage Engineering (ISH)*, University of West Bohemia, Pilsen, Czech Republic, 23 - 28 Aug 2015.
- [4] Eskom, *The Planning, Design and Construction of Overhead Power Lines*, Published by Crown Publications cc, ISBN 9780620330428, 2005.
- [5] A M Castells, "A Magneto-telluric Investigation of Geo-electrical Dimensionality and Study of the Central Betic Crustal Structure", *PhD Thesis*, Dept of Geodynamics and Geophysics, University of Barcelona, 2006.
- [6] B de Villiers, S Mangold, "The Biophysical Environment", Chapter 2, <http://www.nwpg.gov.za/soer/FullReport/bio-physical.html>, Last Accessed 16 Feb 2014.
- [7] <http://www.arc.agric.za/arc-iscw/Pages/ARC-ISCW-Homepage.aspx>, Last Accessed 8 Nov 2014.
- [8] "Lithography of South Africa", *Council for Geoscience*, Jul 2000.
- [9] <http://en.wikipedia.org/wiki/Karoo>, Last Accessed 8 Nov 2014.
- [10] Eskom Standard TST 41-321, "Earthing of Transmission Line Towers", Nov 2006.
- [11] IEEE Std 80, "IEEE Guide for Safety in AC Substation Grounding", 2000.
- [12] IEEE Std 81, "Guide for Measuring Earth Resistivity, Ground Impedance, and Earth Surface Potentials of a Ground System", 1983.
- [13] Eskom, "Integrated Report 2011".
- [14] Personal Correspondence with Mr Richard Evert, Senior Engineer, Eskom, 8 Nov 2014.
- [15] R Marais, "Transmission Development Plan (TDP) 2015 - 2024, Transmission Strategic Grid Study 2040", *Public Forum*, John Maree Auditorium, Eskom Academy of Learning, 10 October 2014, http://www.eskom.co.za/Whatweredoing/Transmission_Development_Plans.aspx, Last Accessed 15 Oct 2014.
- [16] Eskom, "Integrated Report 2014".
- [17] L Ekonomou, I F Gonos, I A Stathopoulos, "Lightning Performance Assessment of Hellenic High Voltage Transmission Lines", *Electric Power Systems Research*, Vol 78, p 703 - 712, 2008.

PERFORMANCE EVALUATION OF A NINE-PHASE SELF- EXCITED INDUCTION GENERATOR

G.C Mangena * and M Muteba **

*University of Johannesburg Department of Electrical and electronic engineering Technology, PO Box 17011, Doornfontein, 2023, Johannesburg, South Africa

Abstract. This paper evaluates the performance of a self-excited nine-phase induction generator. The advantages of using Multi-phase system (more than three-phases) are well known such as high power handling capability by dividing the required power between multiple phases, higher reliability, reduced harmonics and fault tolerant. For a nine-phase machine, if failure occurs the machine can still operate since each three phase group can be made independent from each other. In this paper, a mathematical model is developed directly from the equivalent circuit of nine-phase self-excited induction generator by means of nodal admittance method. The stator three-phase winding of a conventional 1.5 kW, 4-pole, 50 Hz three-phase squirrel cage induction machine has been modified to nine-phase winding for experimental evaluation. The excitation is provided by nine capacitors each rated 40 μF and 450 V.

Key Words. Nine-phase, Self-excited induction generator, Performance Evaluation, Renewable Energy.

1. INTRODUCTION

Apart from their general use as motors, three-phase induction machines (IMs) are also used as generators in electric power systems. The induction generator offers advantages for hydro and wind applications in terms of cost and simplicity and it plays an important part in the renewable energy industry today [1, 2, 3]. However, the advantages of using multi-phases system are well known such as high power handling capability by dividing the required power between multiple phases, reduced torque pulsations, higher reliability, reduced harmonics and fault tolerant. The induction generator has its limitations; it generally needs an external power source to provide its excitation. This means that it is difficult to employ in remote areas where there is no electrical power supply network. The possibility of using a Self-excited Induction Generator (SEIG) where a three-phase capacitor bank is connected across the stator terminals to supply the reactive power requirement of a load and generator was discovered by Basset and Potter in the 1930s [5]. When such an induction machine is driven by an external mechanical power source, the residual magnetism in the rotor produces an electromotive force (EMF) in the stator windings. This EMF is applied to the capacitor bank causing current flow in the stator winding and establishing a magnetizing flux in the machine [4, 5]. An induction machine connected and excited in this manner is capable of acting as a standalone generator supplying real and reactive power to a load. In this mode of operation, the capacitor bank supplies the reactive power requirement of the load and generator, and the real power demand of the terminal load is supplied by the prime mover. The use of an induction machine as a generator is becoming more and more popular for renewable energy applications [3, 8, 9, 10, 11]. Squirrel cage induction generators with excitation capacitors (known as SEIGs) are popular in isolated non-conventional energy systems [2, 3, 6, 7]. However, the main drawback of the SEIG system is that the voltage and frequency produced by the system is highly dynamic under variable load conditions. Although many studies have been focused on regulating the voltage and frequency of

the SEIG system under variable loads, the regulation of speed and voltage does not result in a satisfactory level of performance due to the nonlinear behavior of the machine [12]. In this paper some aspects of performance of a nine-phase system are analyzed. The mathematical model using Nodal analysis for nine-phase self-excited induction generator (NPSEIG) is illustrated in details. Furthermore practical measurements were carrying out to evaluate the process of voltage build up in NPSEIG. It should be noted that only no-load results are presented in this paper. Table 1 gives the machine specification and data, while Fig.1 and Fig. 2 show detailed winding arrangement of the NPSEIG and picture of a readily wound 9-phase stator, respectively.

Table 1: Machine Specification and Data

Description	Values
Number of phases	9
Stator external diameter	136 mm
Stator bore diameter	79 mm
Active axial length	112 mm
Number of poles	4
Number of stator slots	36
Number of turns per phase	132
Air-gap length	0.45 mm
Rated kVA	2.205 kVA
Rated phase voltage	127 V
Average flux density	0.65 Wb/m ²
Frequency	50 Hz
Rated current	6.8 A
No-load current	2.78 A

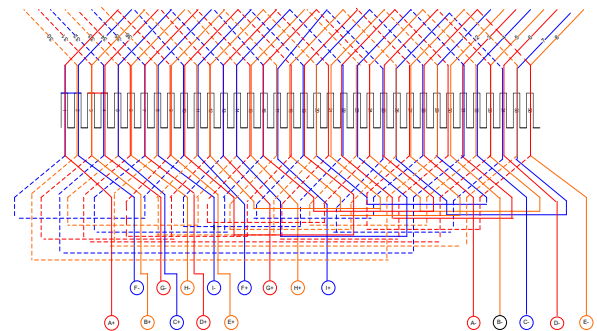


Fig. 1: Complete 9-phases winding housed in 36 slots



Fig. 2: Readily wound 9- phase stator (right) and squirrel cage (left)

2. ANALYSIS OF NPSEIG

The steady-state operation of the self-excited generator may be analysed by using genetic algorithm [13], the equivalent circuit representation is shown in Fig. 3.

Where R_S , R_R and R_L are the stator, rotor and load resistances respectively. X_S , X_R , X_M and X_{sh} are the stator, rotor, and magnetizing and excitation reactance respectively. Y_S , Y_R , Y_M , Y_L and Y_C are the stator, rotor, magnetizing, load and Excitation admittances respectively. F is the p.u frequency. v is the p.u speed which is the ratio of rotor speed to synchronous speed. I_S , I_r , I_M , and I_L , are the stator, rotor, magnetizing and load currents respectively. V_g and V_T are the p.u air gap and terminal voltages at rated frequency respectively.

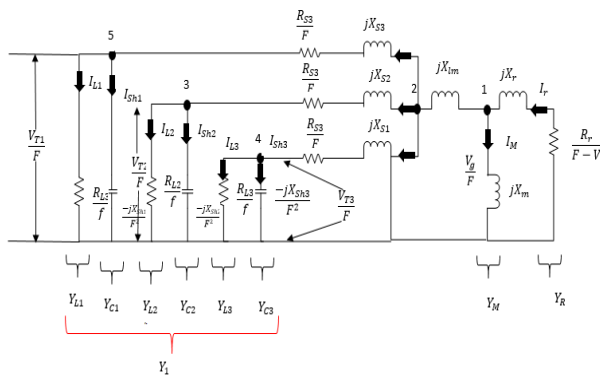


Fig. 3: Per phase equivalent circuit representation of nine-phase self-excited induction generator.

The above equivalent circuit is valid for any per unit speed v . The various elements of equivalent circuit are given from equations (1) to (12).

$$Y_R = \frac{1}{\left[\frac{R_r}{(F-v)} + jX_r \right]} \quad (1)$$

$$Y_M = \frac{1}{jX_M} \quad (2)$$

$$Y_{lm} = \frac{1}{jX_{lm}} \quad (3)$$

$$Y_{s2} = \frac{1}{\left[\frac{R_{s2}}{F} + jX_{s2} \right]} \quad (4)$$

$$Y_{s1} = \frac{1}{\left[\frac{R_{s1}}{F} + jX_{s1} \right]} \quad (5)$$

$$Y_{s3} = \frac{1}{\left[\frac{R_{s3}}{F} + jX_{s3} \right]} \quad (6)$$

$$Y_{c2} = \frac{1}{\left[\frac{-jX_{sh2}}{F} \right]} \quad (7)$$

$$Y_{L2} = \frac{1}{\left[\frac{RL_2}{F} \right]} \quad (8)$$

$$Y_{C1} = \frac{1}{\left[\frac{-jX_{sh1}}{F_2} \right]} \quad (9)$$

$$Y_{L1} = \frac{1}{\left[\frac{RL_1}{F} \right]} \quad (10)$$

$$Y_{C3} = \frac{1}{\left[\frac{-jX_{sh3}}{F_2} \right]} \quad (11)$$

$$Y_{L3} = \frac{1}{\left[\frac{RL_3}{F} \right]} \quad (12)$$

The matrix equation presented based on nodal admittance method for the equivalent circuit can be expressed as in (13).

$$[Y][V] = [IS] \quad (13)$$

Where $[V]$ is the node voltage matrix and $[IS]$ is the source current matrix. $[Y]$ is the nodal admittance matrix. The $[Y]$ matrix can be formulated directly from the equivalent circuit in fig. 3 using nodal admittance method based on inspection and as given in (14).

$$[Y] = \begin{bmatrix} Y_R + Y_M + Y_{lm} & -Y_{s3} & 0 & 0 & 0 \\ -Y_{lm} & Y_{lm} + Y_{s2} + Y_{s1} + Y_{s3} & -Y_{s1} & -Y_{s2} & -Y_{s3} \\ 0 & -Y_{s1} & Y_{s1} + Y_{c1} + Y_{L1} & 0 & 0 \\ 0 & -Y_{s2} & 0 & Y_{s2} + Y_{c2} + Y_{L2} & 0 \\ 0 & -Y_{s3} & 0 & 0 & Y_{s3} + Y_{c3} + Y_{L3} \end{bmatrix} \quad (14)$$

Since, the equivalent circuit does not contain any current sources, $[IS] = [0]$ and hence Equation (13) is reduced as;

$$[Y][V] = 0 \quad (15)$$

For successful voltage build up, $[V] \neq 0$ and therefore from Equation (3), $[Y]$ should be a singular matrix i.e., $\det [Y] = 0$. It implies that both the real and the

imaginary components of $\det [Y]$ should be independently zero. Therefore to obtain required parameter which results $\det [Y] = 0$, genetic Algorithm based approach can be implemented [13].

3. EXPERIMENTAL RESULTS

3.1 Experimental setup

Fig.4 illustrates the experimental setup test rig photo. The dc supply station feeds the field and armature the dc motor which is used as prime mover to mechanically drive the NPSEIG. Star-connected nine capacitors provide excitation to the 9-phase windings of the NPSEIG.

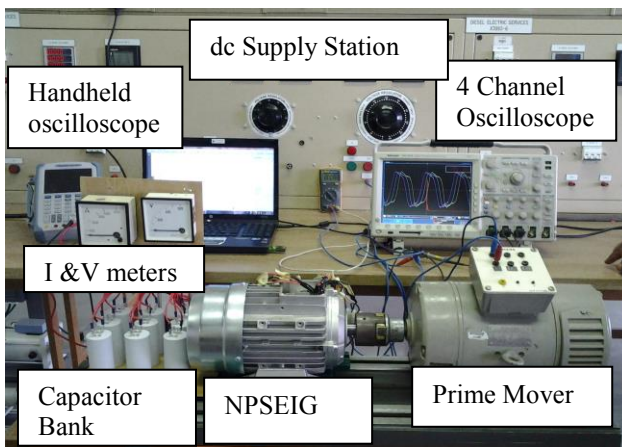


Fig. 4: Experimental setup rig photo

3.2 Analysis of Results

3.2.1 The Initial Self-excitation Process of the Induction Generator; No-load

The stator phase voltage starts building up slowly and reaches a steady-state value while the magnetization current starts from zero rising to a stable steady-state value. Table 2 gives the measured results on no-load with a capacitor of 40 μF per phase.

Table 2: Measured results on no-load

Speed (rpm)	V/phase (V)	I_o (A)	Q_c (VAR)	P (W)
1700	3.00	0.00	0.00	0.00
1800	4.20	0.05	0.63	0.00
1850	75.90	1.32	101	0.00
1900	98.60	1.84	195.1	4.80
2000	102.50	2.11	215.2	7.30
2050	119.50	2.55	295.4	10.10
2100	121.30	2.63	311.8	11.20
2150	127.20	2.28	366.1	17.80
2200	132.80	3.16	421.7	23.00

A stable output voltage could only be obtained once the machine's core is saturated. Another physical explanation of the starting process of the SEIG is that the residual magnetism present in the rotor core

induces a small voltage across the stator windings once the rotor is driven by the prime mover. This produces a delayed current which in turn produces an increased voltage and consequently an increased capacitor current. This phenomenon goes on until saturation of the magnetic flux paths. Fig. 5 illustrates the stator Phase voltage builds up at no-load obtained from computer simulation.

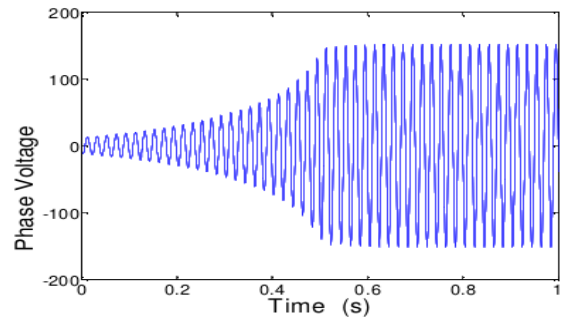


Fig. 5: Stator phase voltage builds up at no-load.

3.2.2 Magnetizing curve

When the machine runs at synchronous speed (1500rpm), the rotor and load parameters of the equivalent circuit can be ignored as the slip is zero. Therefore, the magnetising curve of the machine can be obtained by varying the supply voltage and measuring the stator current. The recorded magnetising current when varying the supply voltage is shown in Fig. 6.

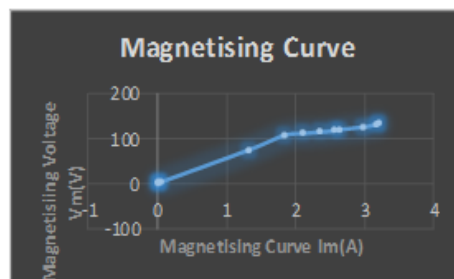


Fig. 6: The magnetising characteristics.

3.2.3 Speed versus Voltage

It is evidenced in Fig.7 that the terminal voltage of NPSEIG depends on change in speed and shunt capacitance. When the NPSEIG is driven above synchronous speed, Voltage start building up at the stator terminals.

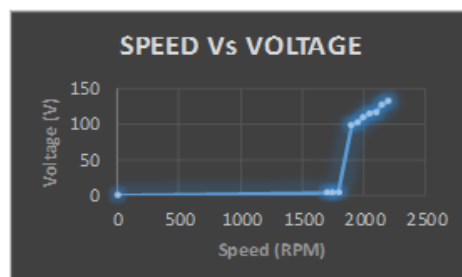


Fig.7: Voltage increase when speed is increased

3.2.4 Phase-Shift

The phase-shift voltages of a NPSEIG is 40 degrees. Measurements using the four channel oscilloscope on one the three distinct three phases is shown in Fig.8.

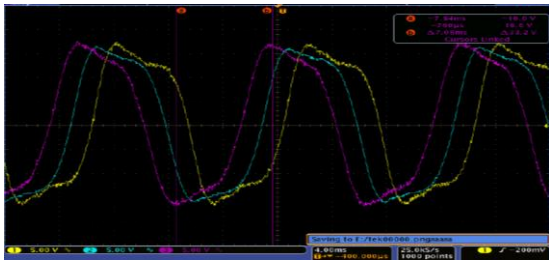


Fig. 8: 3-phase voltages of one group of nine phases with 40° phase shift

4. CONCLUSION

Nine-phase self-excited induction generator is analyzed using a Mathematical model Nodal admittance inspection method derived from the equivalent circuit of a NPSEIG. The method of genetic algorithm can be developed for computer simulation (GA toolbox) to determine the necessary capacitance and VAR requirement to maintain constant terminal voltage for different constant speed. Experimental results were conducted and results show that speed is directly proportional to voltage generated connected to a 40 μ F capacitor bank. Experimental results have evidenced that the process of voltage build up can be possible with zero excitation current as long as there is residual magnetism in the rotor core. Performance of the nine-phase induction generator under load and transient conditions will be presented in subsequent paper.

REFERENCES

- [1] P. K. Sen and J. P. Nelson, "Application Guidelines for Induction Generators," in *IEEE International Conference on Electric Machines and Drives*, Milwaukee, May 1997.
- [2] B. Palle, M. G. Simoes and F. A. Farret, "Dynamic Simulation and Analysis of Parallel Self-excited Induction Generators for Islanded Wind Farm Systems," *IEEE Transactions on Industry Applications*, vol. 41, no. 4, pp. 1099 - 1106, July 2005.
- [3] R. C. Bansal, T. S. Bhatti and D. P. Kothari, "Bibliography on the Application of Induction Generators in Nonconventional Energy Systems," *IEEE Transactions on Energy Conversions*, vol. 18, no. 3, pp. 433-439, September 2003.
- [4] P. K. Shadhu Khan and J. K. Chatterjee, "Three Phase Induction Generators": A Discussion on Performance," *Taylor & Francis on Electric Machines and Power Systems*, vol. 27, no. 8, pp. 813-832, 1999.
- [5] J. M. Elder, J. T. Boys and J. L. Woodward, "Self-excited Induction Machine as a Small Low-cost Generator," *IEE Proceedings C on Generation, Transmission and Distribution*, vol. 131, no. 2, pp. 33-41, March 1984.
- [6] R. C. Bansal, "Three-Phase Self-Excited Induction Generators: An Overview," *IEEE Transactions on Energy Conversion*, vol. 20, no. 2, pp.292-299, June 2005.
- [7] E. D. Basset and F. M. Potter, "Capacitive Excitation for Induction Generators," *Transactions of the American Institute of Electrical Engineers*, vol. 54, no. 5, pp. 540-545, May 1935.
- [8] M. G. Simoes and F. A. Farret, *Renewable Energy Systems: Design and Analysis with Induction Generators*, London: CRC Press, May 2004.
- [9] M. G. Simoes and F. A. Farret, *Alternative Energy Systems: Design and Analysis with Induction Generators*, Bosa Roca: *Taylor & Francis*, December 2007.
- [10] A. F. Zobaa and R. Bansal, *Handbook of Renewable Energy Technology*, Singapore: *World Scientific Publishing*, 2011.
- [11] Singaravelu, S., & Velusami, S., (2007) "Capacitive VAR requirements for wind driven self-excited induction generators", *Energy Convers. And Management*, Vol. 48, pp.1367-1382
- [12] H. S. Timorabadi, "Voltage Source Inverter for Voltage and Frequency Control of a Stand-alone Self-excited Induction Generator," in *Canadian Conference on Electrical and Computer Engineering*, Ottawa, May 2006.
- [13] D. Joshi and K. Sandhu, "Excitation Control of Self Excited Induction Generator Using Genetic Algorithm and Artificial Neural Network," *International Journal of Mathematica Modela and Methods In applied Sciences*, Vol. 3, No. 1, 2009, pp. 68-75

MODELLING OF A DC EXCITATION OF A SYNCHRONOUS GENERATOR

M Mtsamane* and M Muteba**

* University of Johannesburg, Department of Electrical and Electronic Engineering Technology. PO Box 17011, Doornfontein 2028, Johannesburg, South Africa

Abstract. This paper describes the modelling of a DC excitation system of a synchronous generator. The DC excitation system is one of the various methods of excitation that are applied in power systems. Even though the AC excitation methods are commonly used nowadays, this method still has wide usage in many power system industries. A mathematical model is developed using differential equations from the first principles. Transfer functions of the developed equations are presented and implemented in Matlab Simulink. The performance of the DC excitation is analysed under steady state and transient operations.

Key Words. Synchronous Generator, DC Excitation system, Field voltage, System stability.

1. INTRODUCTION

Excitation systems are the basis of power system stability and control. The design of the excitation system and its parameters play a major role in the performance of the power system control and protection [1]. Many power systems fail as a result of poor design of the excitation system. When a fault occurs, it becomes very difficult to troubleshoot if the excitation was not thoroughly and clearly modelled and designed [2]. Therefore, modelling of excitation systems is very crucial and it requires thorough detail of every single part in order to allow quick fault detection. The AC excitation system is the most popular excitation method. However, the AC excitation systems are more complicated in design as opposed to the DC excitation systems. In this paper the DC excitation system is modelled and analyzed in terms of its performance under steady state and transient conditions. This method of excitation is chosen over the other methods owing to its simplicity, reliability and lower design costs. It is easier to troubleshoot simple systems. The most important aspect in DC excitation systems is frequent maintenance since they use brushes and slip-rings.

2. DC EXCITATION MODEL

The complete model of the DC excitation is shown by the transfer function block diagram in Fig 1.

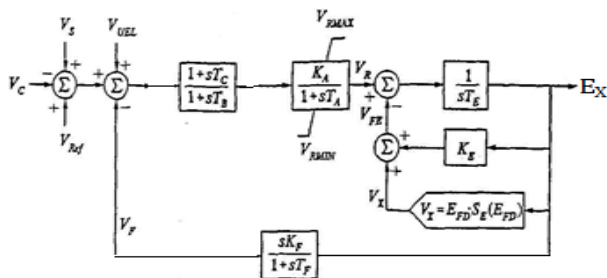


Fig. 1: DC Exciter model.

Where:

V_c - Voltage output from the compensator

V_{ref} - Input reference voltage

V_{UEL} - Under-excitation limit voltage

T_A - Time constant associated with the regulator and firing of the thyristor

K_A - Overall gain constant

E_x - Terminal voltage of the exciter

V_R - Regulator output voltage

S_E - Saturation function

This model is as a result of the building blocks of the excitation system. The transfer function blocks were obtained from equation derivations from the first principles as detailed in section 2.1.

2.1 Mathematical model

DC excitation systems can be either separately excited or self-excited. The excitation model incorporates both separately excited and self-excited; the only difference between the two is on the parameters. When the self-excited system is used the parameters need to be set in such a way that the terminal field voltage is achieved with V_R set to zero. The exciter consists of a field winding and an armature winding. The field winding is composed of a resistor and an inductor as illustrated in Fig. 2. The field winding of the DC exciter is highly inductive; the inductor plays a significant role.

The voltage equation (1) of the field is the basis of the model of a DC excitation system. This equation is applied for both the separately excited and self-excited DC exciter method. Neglecting the flux leakages, the terminal voltage of the DC exciter is proportional to the flux linkage, as shown by equation (2). The proportionality constant is " k_x ". The proportionality constant is dependent on the speed and design of the

DC exciter parameters. The exciter terminal voltage is as in equation (2).

$$E_f = R_{ef} i_f + L_f \frac{di_f}{dt} \quad (1)$$

Where R_{ef} is the field resistance and L_f the field inductance.

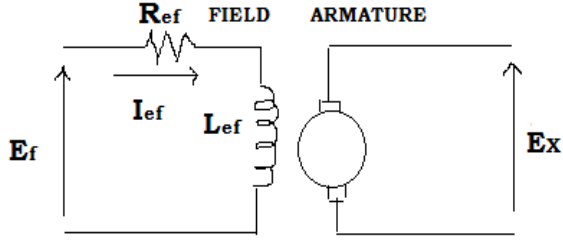


Fig. 2: Separately excited exciter circuit.

$$E_x = k_x \psi \quad (2)$$

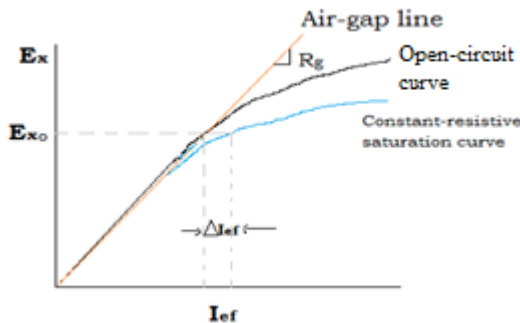
The flux linkage can be expressed as in (3)

$$\psi = L_f i_f \quad (3)$$

$$E_f = R_{ef} i_f + \frac{d\psi}{dt} \quad (4)$$

The load saturation curve in Fig. 3 shows the non-linear characteristics of the field current and the terminal voltage of the exciter. When the exciter is loaded, due to armature reaction, the terminal voltage of the exciter terminals drops. Therefore, when modelling the exciter the loading effect and the saturation effect have to be taken into account. The two armature reaction effects are represented by the two curves, open circuit curve and saturation curve. Tangent to the open-circuit saturation curve is the air-gap line. The slope of the air-gap line denotes the resistance of the field on the air-gap.

Fig. 3: Terminal voltage characteristic curves



R_g denotes the slope of the air-gap line. Therefore, the field current depends on current due to the air-gap line and the current due to the difference between the two saturation curves

$$i_f = \frac{E_x}{R_g} + \Delta i_f \quad (5)$$

Δi_f is a non-linear function of E_x and it is expressed as in (6)

$$\Delta i_f = E_x S_e(E_x) \quad (6)$$

The function $S_e(E_x)$ is a saturation function that depends on E_x . Equation (2) is now written as in (7).

$$E_x = \frac{R_f}{R_g} E_x + R_f S_e(E_x) E_x + \frac{1}{k_x} \frac{dE_x}{dt} \quad (7)$$

In order to obtain the required transfer functions the equation had to be represented in per unit system. Equivalent per unit quantities of the variables are given by their base quantities as expressed in equation (8).

$$\bar{E}_x = \frac{R_f}{R_g} \bar{E}_x [1 + \bar{S}_e(E_x) \bar{E}_x] + \frac{1}{k_x} \frac{d\bar{E}_x}{dt} \quad (8)$$

The saturation function is expressed as in (9).

$$\bar{S}_e(E_x) \bar{E}_x = \frac{\bar{\Delta i}_f}{\bar{E}_x} = R_g S_e(E_x) \quad (9)$$

The proportionality constant k_x is derived from equation (2) and is now written as in (10).

$$k_x = \frac{E_x}{\psi} = \frac{E_x}{L_f I_f} = \frac{R_g}{L_f} \times \frac{E_x}{i_f} \quad (10)$$

For any given values of the field current and the terminal voltage of the exciter, the quantity L_{fu} can be obtained as in (11).

$$L_{fu} = L_f \frac{\bar{I}_{fo}}{\bar{E}_{x0}} \quad (11)$$

Therefore, the proportionality constant is denoted as in (12).

$$k_x = \frac{R_g}{L_{fu}} \quad (12)$$

The derivation of the transfer function equation using the per-unit method yields the final equation (13).

$$\bar{E}_x = K_E \bar{E}_x + \bar{S}_e(\bar{E}_x) \bar{E}_x + T_E \frac{d\bar{E}_x}{dt} \quad (13)$$

The model for the exciter is shown in Fig. 4.

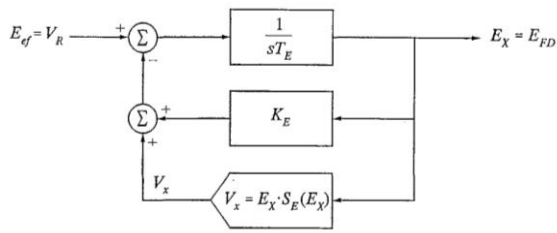


Fig. 4: Exciter Model

3. SIMULATION RESULTS

The excitation system was modeled using Matlab/Simulink with a plant system consisting of a 3.25MVA synchronous generator with a diesel engine governor as its prime mover, and a 1MVA resistive load. The initial condition values of the excitation system and constant values were given as the standard IEEE values [3]. The values of the circuit parameters were simulated in Simulink and analysis was made under transient and steady state conditions.

2.1 Steady-state Operation

The plant was operated on both full load and no-load conditions. The terminal voltage from the synchronous generator was measured and simulated under full load condition as in Fig. 5.

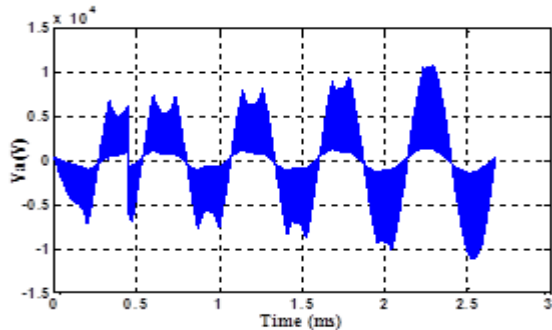


Fig. 5: Terminal voltage on full load.

The terminal voltage increased to almost twice the full load when the system was operating under no-load conditions. The result indicates that the load has a high resistance. Therefore, the voltage regulation was high. The terminal voltage under no-load conditions is shown in Fig. 6.

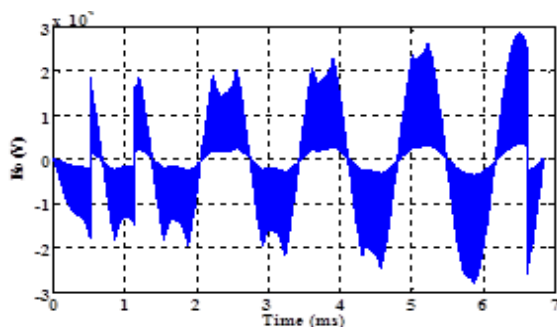


Fig. 6: No-load terminal voltage.

After the synchronous machine was excited by a field voltage, it started off by supplying a constant active power of about half the rated value as shown in Fig 7. After a few seconds the active power dropped instantaneously to a negative value and the machine started supplying an increasing reactive power, as shown in Fig. 8.

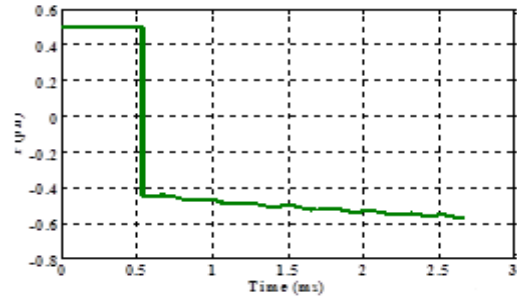


Figure 7: Per unit active power under load conditions.

The reactive power picked up exactly the same instant the active power was dropping as in Fig. 7, and the machine started delivering reactive power to the resistive load.

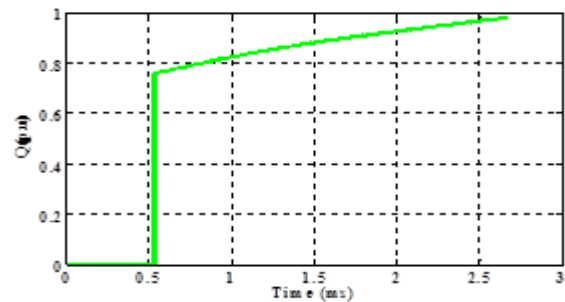


Fig. 8: Reactive power under load conditions

2.2 Transient-state conditions

The reaction of the plant system due to changes in the excitation system was tested by creating a line to ground fault in the excitation system. Looking at Fig. 9, it is observed that the magnitude of generated voltage is very small and dropped down to a very large negative value for about 0.01ms between intervals of about 0.25ms. This drop was as a result of the unbalanced voltages between lines. The system was no longer operating under three phase conditions and the unbalanced phase was affecting the healthy phases.

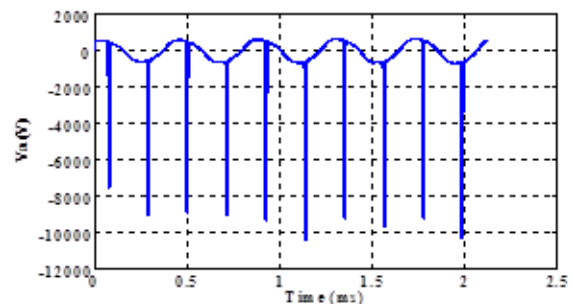


Fig. 9: Transient-state terminal voltage.

The plot in Fig. 10 shows the generated voltage reaches the same maximum amplitude that it reached under healthy conditions, the difference this time is that the voltage could only be seen for a very few milli-seconds (ms) then it drops again. It does the latter for equal interval and it never reaches a steady value. This is still due to the unbalanced voltage phases. The system is not stable enough to retain a high voltage, which is the reason the voltage drops very fast.

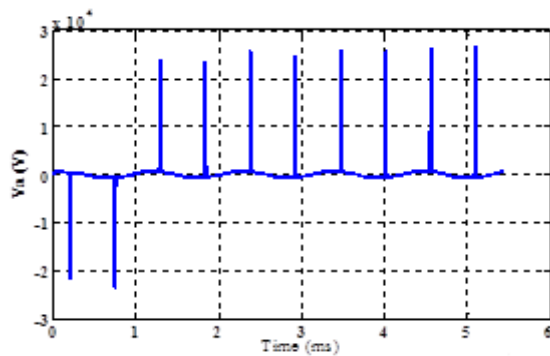


Fig. 10: Transient-state no-load terminal voltage

The system behaved differently under transient conditions as compared to normal (healthy) conditions in terms of the active power. The machine started supplying active power to the load as opposed to the steady-state conditions whereby reactive power was delivered to the load and active power was absorbed in the system.

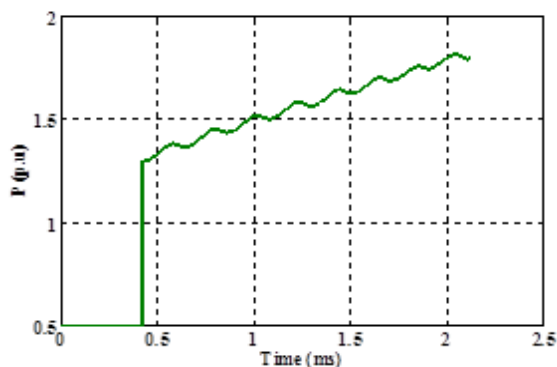


Fig. 11: Transient-state active power.

The reactive power delivered to the load remained the same during the transient state condition. Therefore, both active power and reactive power were delivered during the unhealthy conditions.

4. CONCLUSION

The paper has described and discussed how an excitation system of a synchronous generator is modelled. The results have given conclusive evidence that excitation systems are crucial components of power systems. Changes in the excitation due to faults or unstable conditions affect the whole excitation system. A DC excitation system does not only provide field power to the synchronous generator but it also monitors the system performance and stability. Any

undesired behavior in the system can be corrected through the excitation system feedback. The regulator can sense the terminal voltage, amplify and filter it to acceptable levels for excitation.

REFERENCES

- [1] P. Kundur, "Power System Stability and Control. *McGraw-Hill*, pp.315-375, 1994.
- [2] IEEE committee report, "Excitation models for stability studies", *IEEE transactions on Power Apparatus and Systems*, vol PAS-100, No.2, feb 1981
- [3] IEEE recommended practice for Excitation system models for power system stability studies". *IEEE std* 421, 5-1992

STATOR DESIGN FOR A 1.5 kW AXIAL FLUX PERMANENT MAGNET GENERATOR

A. Smith* and A.J. Grobler**

*Dept of Electrical and Electronic Engineering, North West University, Potchefstroom, South Africa.
E-mail: Andre.Grobler@nwu.ac.za

Abstract: The North-West University has all the components for an Axial Flux Permanent Magnet Generator (AFPMG), apart from the stator. In this paper the design, simulation, manufacturing and implementation of the stator will be discussed. The stator must be tested and if the performance is as desired, the machine can be implemented in the field of alternative energy as a wind turbine.

1. INTRODUCTION

The increasing demand for electricity has strained the natural resources around the world and this led to the greater need to generate energy from renewable sources.

The investigation into wind energy increased the interest in Axial Flux Permanent Magnet Generator (AFPMG) due to their size and unique shape.

The most common generators are radial magnetic flux machines however in the axial flux machines, the flux flows in an axial direction through the air-gap, parallel to the axis, as seen in Figure 1 [1].

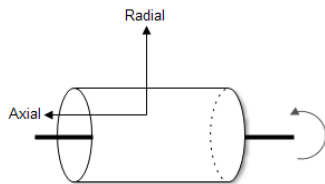


Figure 1: Axial and Radial flux comparison

AFPM machines can be classified by their different topologies. The machine in question is a double sided, internal stator generator; the focus will therefore be on this topology. Figure 2 is a breakdown of the possible topologies for this machine [2].

Various projects have been done on this particular machine with limited success. Since the existing rotor and other hardware will be reused the design, simulation and manufacturing of a stator for the 1.5 kW AFPMG is the aim for this project.

Sizing equations and FEMM 4.2 simulation software will be used to evaluate the design. After manufacturing and implementation, the stator will be tested using Tie-Pie

scopes and T-P multichannel software. The voltage induced in the stator will be measured. A comparison between the simulated and practical results can provide insight into the accuracy of simulations. Power output, voltage regulation and efficiency will be calculated from the practical results.

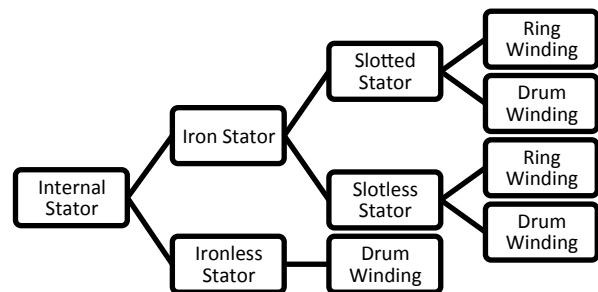


Figure 2: Possible topologies

2. CONCEPTUAL DESIGN

2.1. Possible Topologies

Since the machine is a dual rotor, internal stator generator, the different possibilities can be evaluated by using a simple trade-off.

The criteria identified for the stator topology is efficiency, cost and simplicity. Each criterion has an additive weight. The efficiency of the machine is of great importance for the project and the additive weight of 40% has been assigned to this criterion. Cost and simplicity was chosen since the project is on a budget and the stator was to be manufactured by hand. An additive weight of 33% and 28% has been assigned to these two criterions.

Each stator type has its own advantages and disadvantages.

- Slotted Stator

A slotted stator can accommodate more turns than the slotless stator. The air-gap of a machine can be smaller if a slotted stator is used and the amount of permanent magnets needed to deliver the required output can be reduced.

The greatest disadvantage of a slotted stator is that there is less magnetic material in the stator. Manufacturing these stators is expensive and the effect of cogging torque on the machine can strain its operation [3].

- Slotless Stator

The slotless stator is cheaper since it is simpler to manufacture. The amount of magnetic material in the stator is higher than a slotted stator.

The only disadvantage of the slotless stator is that the air-gap is affected by the windings. There exist a relationship between the number of turns and the size of the air-gap. When the number of turns increases, the length of the air-gap will increase [3].

- Ironless Stator

An Ironless Stator has no permeable material and is constructed with the windings, moulded and set in epoxy resin. Core losses are reduced and the machines can operate at higher efficiencies without cogging torque. One of the biggest advantages of these stators is that the axial forces between the rotor and stator is negligible.

The only disadvantage of these stators is that a larger volume of permanent magnet material is used to reach the desired flux density in the air-gap [3]. All of these characteristics were considered and the results can be seen in Table 1.

Table 1: Stator type_Trade-off

Stator Type						
Criterion	Slotted Iron Stator		Slotless Iron Stator		Ironless Stator	
	Weight	Weight	Weight	Weight	Weight	Weight
Efficiency	7	2.8	6	2.4	7	2.8
Cost	4	1.32	6	1.98	8	2.64
Simplicity	4	1.12	7	1.96	6	1.68
Total:		5.24		6.34		7.12

As seen in Table 1, most suitable stator type for this project is the ironless stator.

The different types of Drum windings must be investigated for this stator type. Figure 3 shows the different winding arrangements.

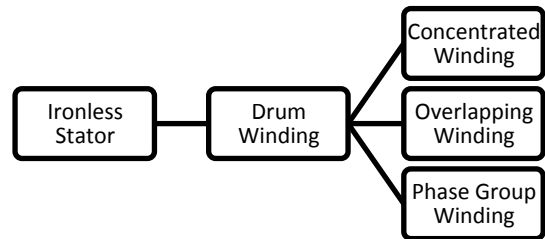


Figure 3: Winding Arrangement

Again three criterions have been chosen; efficiency, possible losses and simplicity. The winding configuration is an important aspect in the efficiency of the stator. An additive weight of 40% has been assigned to this criterion. When using an ironless stator core, losses must be minimised by the winding arrangement and an additive weight of 33% has been assigned to the criterion. Since the coils will be wound by hand, an additive weight of 28% has been assigned to the simplicity of the winding arrangement.

Each possibility must be carefully investigated before a trade-off can be done.

- Concentrated Winding

The fundamental winding factor for concentrated winding is low. The electromagnetic torque is proportional to the winding factor. Concentrated winding is an effective way to minimise losses since they have shorter end windings.

However a disadvantage of concentrated winding is that it can generate odd and even harmonics. These harmonics lead to additional flux in the machine which will result in higher eddy-current losses. Figure 4 shows the concentrated winding configuration [1].

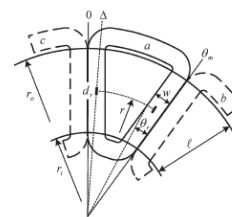


Figure 4: Concentrated winding

- Overlapping Winding

Overlapping or distributed windings use more insulation, since different phases intersect, than concentrated windings and this is seen as a more reliable insulation system. Distributed windings typically have longer end windings since the coils of each phase overlap other phases.

Overlapping/Distributed winding configuration can be seen in Figure 5 [1].

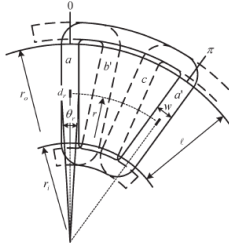


Figure 5: Distributed winding

- Phase group Winding

All the coils of a phase are grouped together. They are spaced on one third of the machine as shown in Figure 6. Phase-group winding is rarely used and its characteristics are not considered for this project.

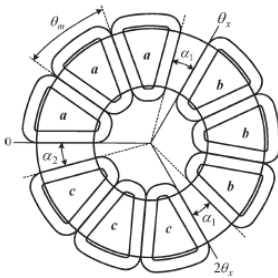


Figure 6: Phase group winding

The trade-off can be seen in Table 2. The comparisons between concentrated and distributed windings result in a small margin for decision making. For this project, the concentrated winding configuration appears most suitable.

Table 2: Winding Configuration_Trade-off

Winding Configuration				
Criterion	Concentrated		Distributed	
		Weight		Weight
Efficiency	7	2.8	6	2.4
Possible losses	5	1.65	7	2.31
Simplicity	7	1.96	6	1.68
Total:		6.41		6.39

2.2. Sizing Equations

Each topology has its own sizing equations relevant to their structure. The equations for an ironless stator are given below.

The relationship between the inner and outer diameter of the stator core can be expressed by:

$$k_d = \frac{D_{in}}{D_{out}}$$

The EMF induced in the stator is then given by:

$$E_f = \pi\sqrt{2} n_s p N_1 k_{w1} \Phi_f$$

$$E_f = \frac{\pi}{4} \sqrt{2} n_s N_1 k_{w1} B_{mg} D_{out}^2 (1 - k_d^2)$$

where n_s is rotational speed (rpm), p is number of poles, k_{w1} is the winding factor (For toroidal type winding, $k_{w1} = 1$), Φ_f is magnetic flux and B_{mg} is magnetic flux density.

2.3. Simulations

When using copper wire with a diameter of 1 mm; the current capacity is 4.7 A when assuming maximum current density of 6 A/mm². To reach an output power of 1.5 kW, a voltage of 320 V must be induced in the stator.

Only 2 of the 16 pole pairs of the generator can be used in simulations since the stator is symmetric. The permanent magnets are aligned N-S, S-N respectively.

The simulation shown in Figure 7 has an effective air-gap length of 8 mm. The red line is used to integrate the flux density of each pole. This value is then multiplied by the length of the magnet to determine the complete flux at the given section.

The machine has a radius of 25mm and 16 pole pairs are distributed uniformly, 12.5° apart. This results in a spacing of 9mm. The length of the magnet at any given point can be calculated by using the radius and spacing of the permanent magnets.

The simulation was repeated for variations in air-gap lengths to determine the amount of turns per phase needed to produce a voltage of 320 V. A rotational speed of 400 r/min is used.

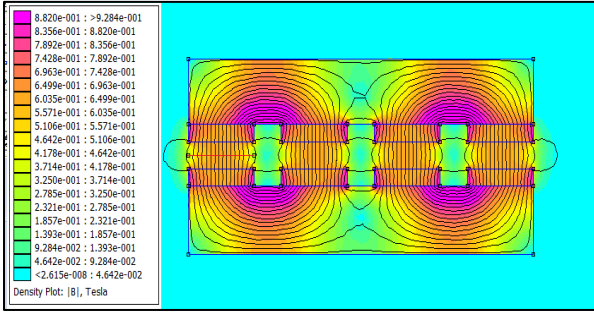


Figure 7: Magnetic flux density plot (8mm air-gap)

The following table shows the results from the simulation data:

Table 3 : Air-gap simulation results

Air-gap length (mm)	Magnetic flux density (T)	Number of turns per coil
8	0.546027	25
10	0.478188	29
12	0.421163	33
14	0.375147	37
16	0.335347	41
18	0.302161	45
20	0.27396	50
22	0.24719	56
24	0.225136	61
26	0.204974	67

When using the data in Table 3, the practical possibility of reaching these air-gap lengths with the desired number of turns per coil must be evaluated.

Choosing an effective (mechanical) air-gap of 16 mm at 400 r/min; 41 turns per pole must be used. The total area for the copper wires is calculated:

$$A = \pi(0.5)^2 \times 41$$

$$= 32.2 \text{ mm}^2$$

Therefore, the length and width of the coils are 5.67 mm when neglecting packing factor. To ensure that the simulation results can be reached practically, the length and width of the coil is increased to 10 mm, resulting in an mechanical air-gap of 3 mm per side.

The induced voltage of the simulated generator for a single coil can be seen in Figure 8 below.

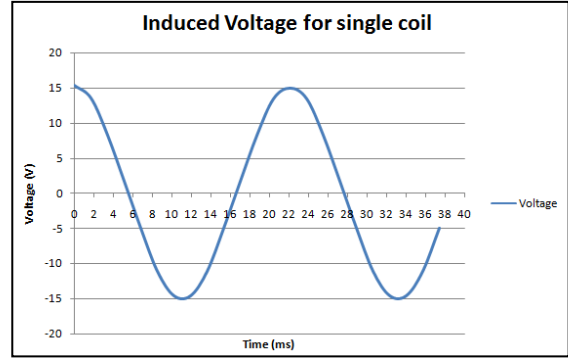


Figure 8: Simulation Results

Since 16 coils will be used the induced voltage will be 240 V. In order to reach the desired voltage of 320V, there must be a total of 57 turns per coil, with an effective air-gap of 16mm. This proved to be practically not realisable.

3. DETAIL DESIGN

The remaining concern is the effect of an added load to the generator. When a load is connected to the generator, the current in the coils will affect the magnetic field, provided by the permanent magnets of the rotors. The current will result in a force that opposes the direction of the magnetic flux and can therefore cause poor voltage regulation.

To ensure that all possible challenges are taken into account, the generator is simulated with current present in the coils.

Figure 9 shows the simulation results of a single coil with 41 turns. A current of 4.7A is present in the coil. A rotational speed of 400r/min is used.

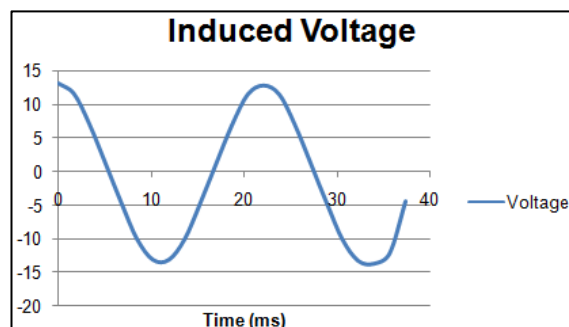


Figure 9: Final Simulation Results

As seen in the results above, the current has a negative effect on the magnetic flux and will therefore reduce the output voltage. The induced voltage is reduced by 2V per coil and is therefore 13% less than the voltage at no load. This reduction is expected in machines with ironless stator cores as a result of leakage flux.

4. IMPLEMENTATION AND EVALUATION

The coils are manufactured by winding each coil on a mould. The mould was designed using SolidWorks software. The stator is wound with 16 coils in series. Each coil has 41 turns. The stator can be seen in Figure 10.

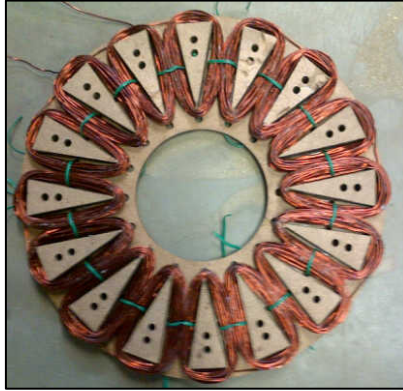


Figure 10: Wound Stator

An epoxy resin is used to set the coils. The resin is a non-magnetic material and ensures a solid structure.

The stator is then installed in the generator to be tested.

Figure 11 shows the output voltage of the generator when no load is added. A rotational speed of 400r/min is used.

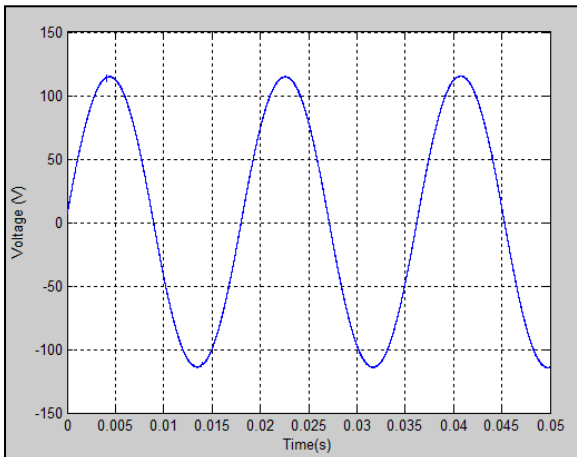


Figure 11: Voltage at no-load

The voltage in the stator is 82.3V (rms) and is significantly less than the simulated results. In the simulations, endspace leakage flux is not taken into account and can explain the lower output voltage.

The generator is tested at various loads to examine the effect of the current on the output voltage of the generator. The performance of the generator can be evaluated by examining the power capabilities and the voltage regulation.

In Figure 12 the power and voltage regulation of the machine can be seen at various currents.

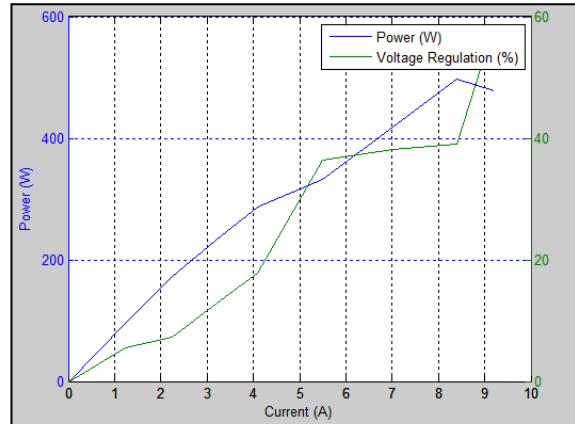


Figure 12: Power and Voltage Regulation

The optimum power of 500 W is achieved at 8.4 A, the voltage regulation at this point is 38%.

5. CONCLUSION

The final design had 41 turns per coil and a mechanical air-gap of 16mm. When adding the current to the coils, the voltage reduction was accepted since an ironless stator is used.

When implementing the design, the size of the air-gap was successfully kept to a minimum. The shape of the coils ensured that a perfect sinusoidal voltage waveform is induced in the stator.

Since leakage flux is not accounted for in the simulations, the voltage at no-load was lower than expected

Although the power capabilities of machine were significantly improved, the results were not as expected. The poor voltage regulation of the machine at smaller loads proved to be problematic. The maximum power the machine can deliver is 500W.

6. REFERENCES

- [1] S. O. Ani, H. Polinder and J. A. Ferreira, "Low Cost Axial Flux PM Generator for Small Wind Turbines", *IEEE International, Electrical power processing*, pp.735-740, 15-18 May 2011.
- [2] J. Gieras, R. Wang and M.J. Kamper, *Axial flux permanent magnet brushless machines*,

Dordrecht, The Netherlands: Kluwer Academic Publishers, 2008.

- [3] M. Cirani, C. Sadarangani, and P. Thelin. “Analysis of an innovative design for an axial flux Torus machine”, *Renewable Energy*, vol. 12, no.3, pp. 245-257, 2007.

SOFTWARE SIMULATION INTEGRATION IN ENHANCING ENGINEERING DESIGN IN POWER CONVERSION STUDIES

A. M. Almaktoof*, A. K. Raji** and M. T. E. Kahn***

***** Centre for Distributed Power and Electronics Systems (CDPES), Electrical Engineering department, Cape Peninsula University of Technology (CPUT), Bellville Campus, 7535, South Africa
E-mail: * 213301091@mycput.ac.za, ** raji@cput.ac.za, *** khant@cput.ac.za

Abstract: PSIM and MATLAB are the most commonly used software packages available for simulation of power electronic systems. The paper presents the simulation of power converters using a SimCoupler Module in MATLAB which provides the link between PSIM and MATLAB/Simulink for Software Simulation Integration (SSI) work. The power electronic system is implemented in PSIM for representing the system model, while the control circuit is implemented in MATLAB/Simulink in a complementary way, so significantly shortening the time to set up and simulate a system which includes electronic circuits. The important step in SSI technique is the time synchronization of the two independent software platforms that is used in this study PSIM and MATLAB/ Simulink. The availability of personal computers with fast microprocessors and ample RAM size makes SSI technique possible. The objective of this paper is to demonstrate how to use the Simcoupler Module for a three-phase, multilevel inverter using model predictive strategy with resistive-inductive load (RL-Load). The paper explains the theoretical approach of the system model and then the simulation results are given in order to show the effectiveness of the system in the SSI arena. The output currents and DC-link capacitor voltages are sampled and predicted for the next sampling time for each valid switching state of the inverter. The error between the predicted and reference current values and also the error between the capacitor voltages with respect to the reference value are obtained to minimize the cost function by choosing the appropriate state's switching signals and then applied the control signals to the switches embedded in the converter under study. The co-simulation results show that the proposed control achieves high performance. As a result, applying SSI tools by using SimCoupler enhances the engineering design efficiency in power conversion studies.

Keywords: Software simulation integration; PSIM; MATLAB/Simulink; SimCoupler Module; Model predictive control; Diode clamped converter.

1. INTRODUCTION

There are various software applications available to analyze power electronic devices and circuits. These programs enable the designer to cover the semiconductor switching characteristics and give accurate information about power electronic circuit behaviors like voltage, current and harmonic distortion. Many studies mainly use languages like SPICE (Simulation Program with Integrated Circuit Emphasis) and ACSL (Advanced Continuous Simulation Language), these programs are useful in the detailed design studies, where time domain analysis is necessary for predicting the detailed circuit performances[1-3].

In the last two decades, simulation tools made a significant contribution to the great progress in the development of power electronics systems. Computer simulation can greatly aid in the analysis, design and education of power electronics applications. PSIM and MATLAB are the most commonly used software packages available for simulation of power electronic systems [4, 5]. PSIM is a simulation software application specifically designed for power electronics systems [6, 7]. With fast simulation and friendly user interface, PSIM provides a powerful simulation environment for power

electronics, control and motor drive system studies [6, 8]. MATLAB is one of the most popular software used in control systems, and MATLAB/Simulink is very suitable for dynamic system simulation because there are plenty of toolboxes and modules for use within the platform. However, it is awkward and cumbersome to simulate electric circuits, especially power electronic circuits [5, 6] in Simulink. The purpose of this paper is to present the ability to simulate predictive control of advanced power converter using a SimCoupler Module which provides the link between PSIM and MATLAB/Simulink for SSI work. The SimCoupler Module uses the SLink nodes to establish the interface between PSIM and Simulink. With the SimCoupler Module, one can make full use of PSIM's capability in power simulation for representing the system model and MATLAB/Simulink's computational capability for control strategy algorithm development in a complementary way.

Research of modern voltage source multilevel converters started with the introduction of Diode-Clamped Converter (DCC) three level inverters in 1981[9]. Pulse Width Modulation (PWM) [10, 11] and Space Vector Modulation [12] are the most modulation techniques that have been proposed for controlling this kind of converters. The diode-clamped balancing problem in this

topology is another subject that has been studied in recent years [13-15]. Early applications of the ideas of Model Predictive Control (MPC) in power electronics can be found from the 1980s considering high-power systems with low switching frequency [16]. The use of higher switching frequencies was not possible at that time due to the large calculation time required for the control algorithm compared to classic control methods. However, with the development of fast and powerful microprocessors, interest in the application of MPC in power electronics has increased considerably over the last decade [4, 17].

To validate the feasibility of the control algorithm that proposed in this study, MATLAB/Simulink and PSIM modeling for SSI work are carried out for different conditions for the current references and loads implemented for three-phase, three-level DCC with RL-Load. The paper starts with overview of SimCoupler Module for SSI with PSIM-MATLAB/Simulink in section two. Section three presents the power converter model which is completely represented in PSIM environment. The theoretical approach of the system model presents firstly the time-continuous model and then discretized to obtain the output currents and DC-link capacitor voltages. The control scheme is developed in section four that is used to control the power converter model and balance the DC-link capacitors. MATLAB/Simulink and PSIM modeling and co-simulation work is presented in the penultimate section. Conclusion is presented in the last section of the paper.

2. SIMCOUPLER MODULE FOR SSI.

The SimCoupler Module allows power electronics designers to simulate control in the MATLAB/Simulink environment [6, 8], thus further enhances PSIM's control simulation capability by providing access to numerous Simulink toolboxes for various applications. For example, one can achieve automatic code generation with the PSIM-MATLAB/Simulink for SSI. First, the power circuit is simulated in PSIM, and the control algorithm in MATLAB/Simulink. Then Simulink toolbox and supporting resources can be used to generate production quality code automatically for a target platform. Figure 1 depicted how the SimCoupler Module provides interface between PSIM and MATLAB/Simulink for SSI. The SimCoupler interface consists of two parts: the SLink nodes in PSIM and the SimCoupler model block in MATLAB/Simulink as shown in Figure 2.



Figure 1: The SimCoupler Module provides interface between PSIM and MATLAB/Simulink.

Three-phase, three-level DCC inverter using model predictive strategy with RL-Load when the power

converter and the load implemented in PSIM and MPC implemented in MATLAB/Simulink as shown in Figure 2. In PSIM as shown in the bottom graph of Figure 2, three-phase load currents, voltages and DC-link capacitor voltages are connected to output SLink nodes to pass these variable values to MATLAB/Simulink, and to receive values back from Simulink, there are three signals that are connected to the input SLink nodes to apply all switching states to the inverter. In Simulink, the proposed control block and reference current are represented and SimCoupler model block (highlighted as depicted in the top graph of Figure 2), which represents the PSIM calculation, connects to the rest of the system through input/output ports as shown in Figure 2.

After the connection of the system model is done, the important step in SSI technique is the time synchronization of the two independent software platforms that is used in this case PSIM and MATLAB/Simulink, by set the solver type to either Fixed-step or Variable-step in MATLAB/Simulink. If the fixed-step type is chosen, the fixed step size should be the same as or close to PSIM's time step (in this study, the PSIM's time step is 2 μ s). The Simulink circuit will look as the bottom graph of Figure 2.

Alternatively, we can use the variable-step solver option. However, in this case, a zero-order-hold [8] must be inserted to each input port of the SimCoupler model block and the sampling time of the zero-order hold must be equal or close to PSIM's time step.

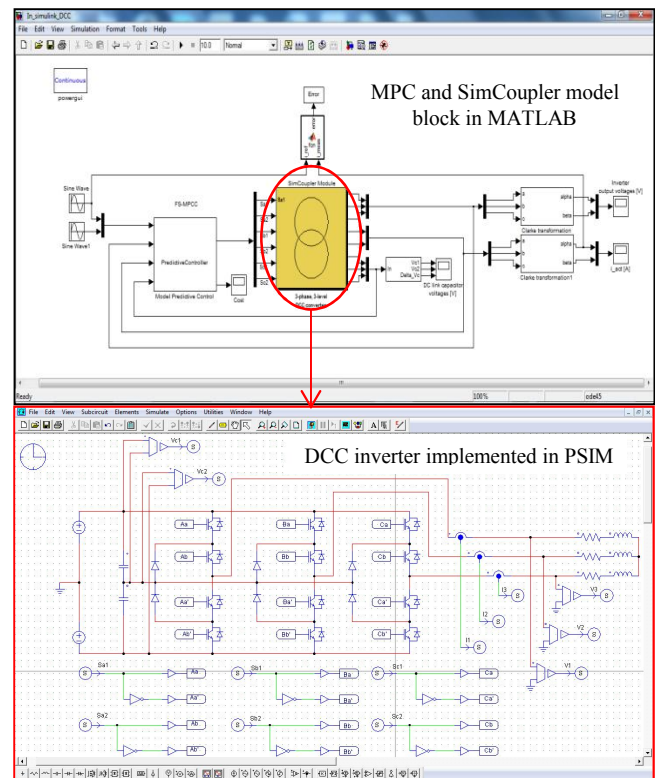


Figure 2: Three-phase DCC inverter with RL-Load implemented in PSIM and MPC and SimCoupler model block implemented in MATLAB/Simulink.

3. POWER CONVERTER MODEL

The concept of the DCC topology was proposed by Nabae in 1981 [9]. Figure 3 shows a three phase DCC multi-level inverter. It consists of two pairs of switches and two diodes in each leg. RL-Load represents the most common applications for this kind of converter as depicted in Figure 3. The output voltage v_{xn} has three states: $v_{DC}/2$, 0, and $-v_{DC}/2$. Switching states of the three-level DCC inverter are summarized in Table 1.

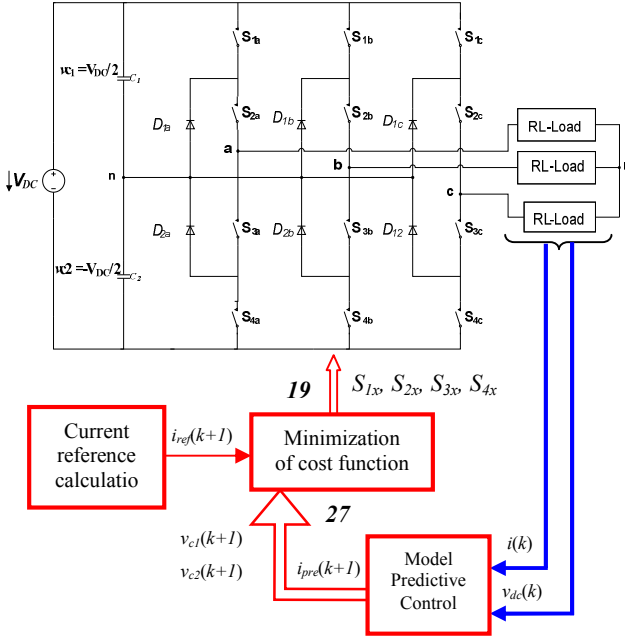


Figure 3: Three-level DCC circuit topology connected to the load and control block diagram.

Table 1. Possible Switching Configurations in a DCC.

#	complementary pair No 1		complementary pair No 2		v_{xn}
	S_{1x}	S_{3x}	S_{2x}	S_{4x}	
1	1	0	1	0	$v_{DC}/2$
2	0	1	1	0	0
3	0	1	0	1	$-v_{DC}/2$

To obtain the continuous-time state-space equations of the load for each phase the differential equation of the load current is applied:

$$v_{DC}(t) = R \cdot i(t) + L \frac{di}{dt}. \quad (1)$$

Applying the Clarke transformation to the load, the load model can be expressed in a simplified coordinate system with linearly independent axes α and β . Then, the continuous-time state-space equation of the load results to

$$\begin{bmatrix} \dot{i}_\alpha \\ \dot{i}_\beta \end{bmatrix} = \begin{bmatrix} -\frac{R}{L} & 0 \\ 0 & -\frac{R}{L} \end{bmatrix} \begin{bmatrix} i_\alpha \\ i_\beta \end{bmatrix} + \begin{bmatrix} \frac{1}{L} & 0 \\ 0 & \frac{1}{L} \end{bmatrix} \begin{bmatrix} v_\alpha \\ v_\beta \end{bmatrix}. \quad (2)$$

A discrete-time equation for the future load current is obtained by using the Euler-forward approximation to obtain a discrete-time system representation as:

$$\begin{bmatrix} i_\alpha(k+1) \\ i_\beta(k+1) \end{bmatrix} = \begin{bmatrix} 1 - T_S \frac{R}{L} & 0 \\ 0 & 1 - T_S \frac{R}{L} \end{bmatrix} \begin{bmatrix} i_\alpha(k) \\ i_\beta(k) \end{bmatrix} + \begin{bmatrix} \frac{T_S}{L} & 0 \\ 0 & \frac{T_S}{L} \end{bmatrix} \begin{bmatrix} v_\alpha(k) \\ v_\beta(k) \end{bmatrix} \quad (3)$$

4. MODEL PREDICTIVE CONTROL OF DCC

DCC converter under MPC, the error between the reference and predicted values is obtained to minimize the cost function and the switching state that minimizes the cost function is chosen is shown Figure 3. The chosen state's switching signals, S , are then applied to the converter. In order to reduce the computational effort [4, 5] which gives rise to the switching possibilities (27 different switching possibilities for one prediction step) the best switching state which delivered the best voltage vector among 19 voltage vectors is determined. The optimal switching state is selected which minimizes the cost function that should be applied in the next sampling instant $k+1$, the simple cost function has to be minimized.

With long prediction horizon the calculation effort raises to multiple possibilities, we still need very powerful computer especially very fast microprocessors and ample RAM size. For that a very powerful and fast computer is used for the SSI, the specifications of the computer used in this study are tabled in Table 2.

Table 2. The specifications of the computer hardware components

Computer hardware	Specifications
Processor	Intel Core i7-3930K (3.2GHz, 12M Cache, 12x Cores) Overclocked to 4.5GHz Per Core
Memory	32 GB Quad Channel (8x4GB) DDR3 1600MHz High Performance Gaming RAM With Heat Spreader
Two Storage Drives	OCZ Vertex 4 128GB SSD Read: 560MB/s Write:430MB/s SATA3 Solid State Drive 4TB

To balance the two DC-link capacitor voltages, voltage balancing algorithm based on predictive control was presented. This algorithm aims to keep the capacitor voltages within the boundary. The mechanism of this algorithm has been presented for the same system model in [18]. The differential equation for the capacitor current which is given by (4)

$$i_C = C \frac{dvc}{dt}. \quad (4)$$

A discrete-time equation for the DC-link capacitor voltage is obtained by using Euler-forward as in (3) in

order to obtain a discrete-time system representation. Then, the discrete-time load model can be to:

$$v_{c1,2}(k+1) = v_c(k) + \frac{1}{C}i_c(k)T_s. \quad (5)$$

Where $v_{c1,2}(k+1)$ is predicted DC-link capacitor voltages, $i_c(k)$ is the current through the capacitor, $v_c(k)$ is its voltage, and C is the capacitance. Equation (5) is used to predict the DC-link capacitor voltage for each switching possibility.

The control block diagram is shown in Figure 3, the future value of the load current $i(k+1)$ and capacitor voltages $v_{c1}(k+1)$ $v_{c2}(k+1)$ are predicted for the 19 switching states generated by the inverter. For this purpose, it is necessary to measure the present load currents $i(k)$ and DC-link capacitor voltages $v_{c1}(k)$ and $v_{c2}(k)$. After obtaining the predictions, a cost function g is evaluated for each switching state as (6). The switching state that minimizes g is selected and applied during the next sampling period. The proposed cost function g is shown in (6).

$$g = f(i_{ref}(k+1), i(k+1)) + \lambda_{DC}|Delta|. \quad (6)$$

Where, delta is the error between $v_{c1}(k+1)$ and $v_{c2}(k+1)$ and λ_{DC} is the weighting factor to be adjusted as shown in (7). A simple cost function can be defined in absolute value term with one prediction step as in (7) for DCC inverter.

$$g = |i_{ref\alpha}(k+1) - i_\alpha(k+1)| + |i_{ref\beta}(k+1) - i_\beta(k+1)| + \lambda_{DC}|v_{c1}(k+1) - v_{c2}(k+1)|. \quad (7)$$

In order to simplify the calculations, it can be assumed that the current reference value is constant as in (8) with the prediction horizon for small sampling time T_s . This approximation is considered in this study.

$$i_{ref}(k+n) \approx i_{ref}(k). \quad (8)$$

The algorithm implemented for three-phase three-level DCC is explained in a flow diagram of SSI presented in Figure 4. The algorithm starts running a DCC inverter circuit with RL-Load in PSIM environment then the algorithm loop begins sampling the required signals. Then, the algorithm measure the output currents and capacitor voltages, and the value of the optimum cost function ($g_{optimal}$) is initialized. Then the strategy enters a loop where, for each possible switching state, the cost function in (7) is evaluated considering output current and capacitor voltage predictions. If, for a given switching state, the evaluated cost function g happens to be lower than $g_{optimal}$, that lower value is stored as $g_{optimal}$ and the switching state number is stored as $x_{optimal}$. The loop ends when all 27 switching states have been evaluated. The state that produces the optimal

value of g (minimal) is identified by variable $x_{optimal}$ and will be applied to the converter during the next sampling interval, starting the control algorithm again.

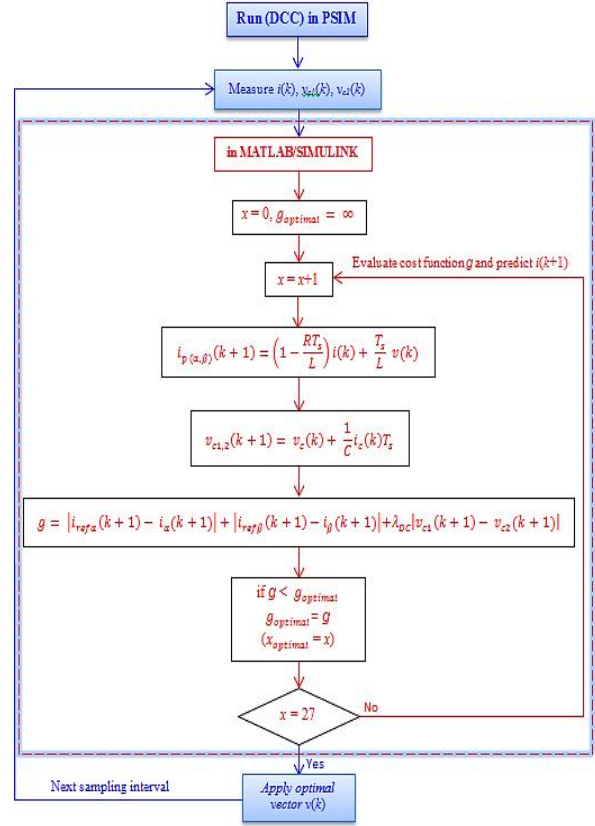


Figure 4: Flow diagram of software simulation integration

5. SSI RESULTS AND DISCUSSION

Modeling and simulation are a key stage in predictive control design for power electronics, since it provides valuable information on the control system performance which is needed to adjust control parameters such as weighting factors in the cost function. In addition, simulation is a preliminary validation required prior to experimenting on a real prototype. The case study analyzed in this paper is selected to show the effectiveness of the system in the simulation arena. MPC strategy for three-phase three-level DCC has been co-simulated with MATLAB/Simulink together with PSIM, in order to evaluate the performance of the proposed control algorithm and check the performance and robustness of the proposed predictive control method. Table 3 shows the parameters used for the SSIs.

Table 3. Parameters used for the SSIs

Parameter	Value
Load resistor, R	10 Ω
Load inductor, L	20 mH
DC-link capacitor	3300 μ F
DC-link voltage, v_{DC}	200 V
Reference amplitude current, i_{ref}	4A
Sampling time, T_s	25 μ s

5.1 DC-link capacitor voltages balancing

DC-link capacitor voltages balancing of DCC has been done in [18]. The SSI provides a better DC-link capacitor voltages balance with smaller steady-state error as shown in Figure 5. In the first two graphs of Figure 5 the DC-link capacitor voltages are kept around their references, the band-limited performance of the controller with less error as shown in the bottom graph of Figure 5.

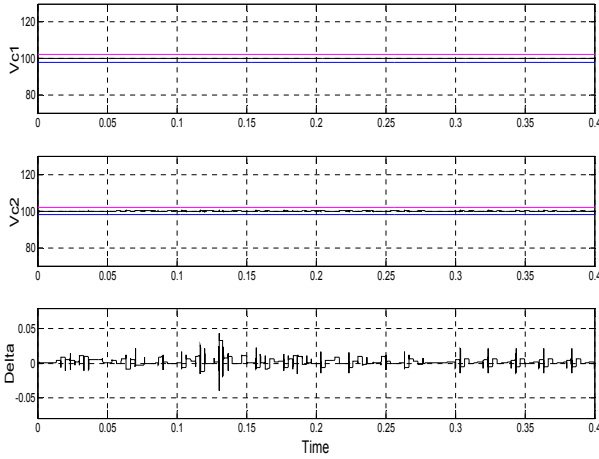


Figure 5: DC-link capacitor voltages v_{c1} and v_{c2} around their references and Delta ($v_{c1} - v_{c2}$).

5.2 Long prediction horizon

In the second simulation the robustness of the proposed control method was tested with four prediction steps, it can be seen in Figure 6 how the output currents are tracking their references with four prediction steps, it can be seen that the control algorithm shows excellent tracking behaviour.

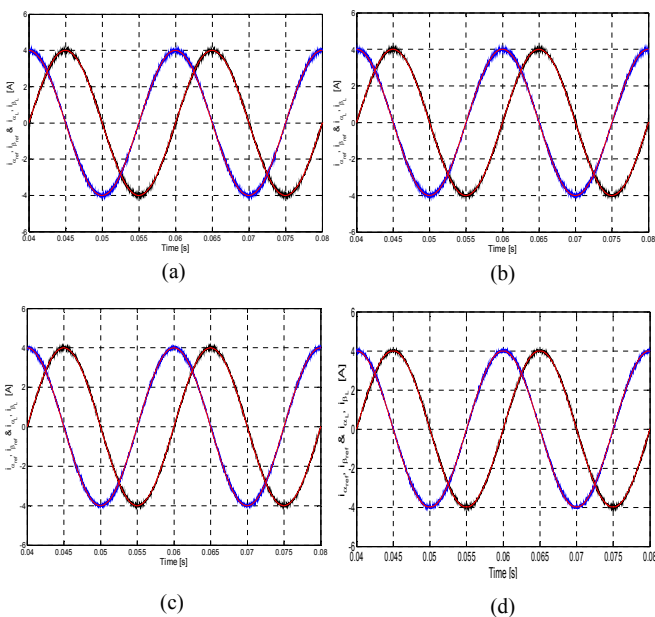


Figure 6: The load current with RL-Load for four prediction steps : a) $n = 1$. b) $n = 2$. c) $n = 3$. d) $n = 4$.

5.3 Square waveform reference

In this simulation the control algorithm was tested with a square waveform in orthogonal coordinates as a reference current. One of the applications of a square waveform is in a stepper motor driver when two things are normally required: a controller to create step and directional signals and that what MPC does. The result for square waveform in the amplitude of the references i_{α} and i_{β} were set to 2 A, $T_S = 25 \mu s$ is shown in Figure 7. In this simulation, the i_{α} and i_{β} currents correctly follows the reference, it can be noticed that there is current ripple in steady state resulting from the finite switching and controller frequency. It can be observed from this simulation that the predictive control method has fast dynamic response. It shows excellent tracking behavior.

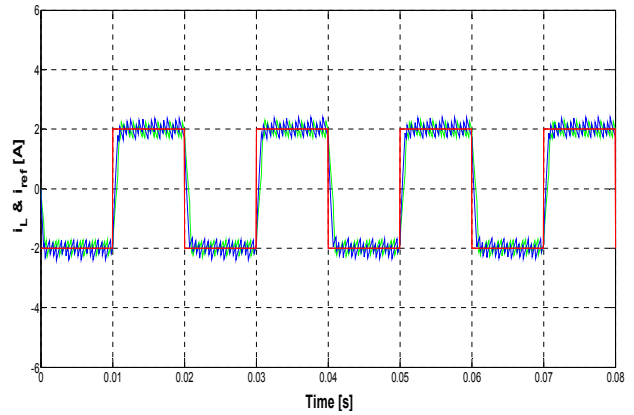


Figure 7: Square waveform reference for load current.

6. CONCLUSIONS

The paper has demonstrated the effectiveness of SSI technique as shown in the DCC case study presented. The SimCoupler Module allows power electronics researchers and engineers to simulate control in the Matlab/Simulink environment, and the SimCoupler Module further enhances PSIM's control simulation capability by providing access to numerous Simulink toolboxes for various applications, at the same time, the SimCoupler Module enables MATLAB/Simulink users to implement and simulate power circuits in the original circuit form, thus greatly shortening the time to set up and simulate a system which includes electric circuits and motor drives. The important step in SSI technique is the time synchronization of the two independent software platforms that is used in this case PSIM and MATLAB/Simulink.

The MPC strategy has been presented as well to control the three-level DCC inverter. The control algorithm has been evaluated with three different cases through SSI results. First of all, balance the DC-link capacitor voltage has been implemented. It has been noticed that the control algorithm provides very good current tracking behavior and the capacitor voltages are also very well balanced with small error. Secondly, the robustness of the

proposed control method with four prediction steps has been assessed. It has been noticed that the control algorithm provides very good current tracking behaviour. Thirdly, with step change in the amplitude of the reference, the control algorithm was tested with a square waveform reference steps. Results show that the predictive control algorithm has fast dynamic response with inherent decoupling between i_a and i_β and gives excellent tracking behavior.

SSI results show that MPC strategy gives very good performance under these conditions. Applying SSI tools by using SimCoupler enhances the engineering design efficiency in power conversion studies.

15. REFERENCES

- [1] B.K., Bose, (editor), *Power Electronics Variable Frequency Drives*, IEEE Press, New York, 1997, pp.400-453.
- [2] PSPICE, *Microsim Reference Manual*, Version 7.1, October 1996.
- [3] SABER, Anolgoy, Inc, 9205 S.W. Gemini Drive, Beaverton, OR 97008, USA, Release 5.0 edition.
- [4] A. M. Almaktoof, A. K. Raji, M. T. E. Kahn, "Finite Set-Model Predictive Current control of three-phase voltage source inverter for Renewable Energy Systems (RES) applications," *Journal of Energy and Power Engineering*, USA, 8 (2014), pp 748-755, 2014.
- [5] J. Rodríguez, and C. Cortés, *Predictive control of Power Converters and Electrical Drives*, 1st ed. New York: Wiley-IEEE, 2012.
- [6] V. Boscaino and G. Capponi (2011). High Accuracy Modelling of Hybrid Power Supplies, MATLAB for Engineers - Applications in Control, Electrical Engineering, IT and Robotics, Dr. Karel Perutka (Ed.), ISBN: 978-953-307-914-1, InTech, Available from: <http://cdn.intechopen.com/pdfs-wm/21224.pdf>.
- [7] PSIM[®] User's Guide, Powersim Inc., PSIM 9.3, June 2014.
- [8] PSIM Software, "Tutorial on How to Use the SimCoupler Module". Powersim Inc. April 2006. Available from: www.psim-europe.com/openload2.php?doc=tutorialSimcoupler.pdf
- [9] A. Nabae, I. Takahashi, and H. Akagi, 1981. A new neutral-point-clamped PWM inverter, *IEEE Trans. Ind. Applicat.*, IA(17):518 – 523, Sept./Oct. 1981.
- [10] G. Carrara, S. Gardella, M. Marchesoni, R. Salutati, and G. Sciutto, "A new multilevel PWM method: a theoretical analysis," *IEEE Transactions on Power Electronics*, vol. 7, no. 3, pp. 497– 505, Jul. 1992.
- [11] B. P. McGrath and D. G. Holmes, "Multicarrier PWM strategies for multilevel inverters," *IEEE Transactions on Industrial Electronics*, vol. 49, no. 4, pp. 858–867, Aug. 2002.
- [12] N. Celanovic and D. Boroyevich, "A fast space-vector modulation algorithm for multilevel three-phase converters," *IEEE Transactions on Industry Applications*, vol. 37, no. 2, pp. 637–641, Mar./Apr. 2001.
- [13] R. Tallam, R. Naik, and T. Nondahl, "A carrier-based PWM scheme for neutral-point voltage balancing in three-level inverters," *IEEE Trans. Ind. Appl.*, vol. 41, no. 6, pp. 1734–1743, Nov./Dec. 2005.
- [14] A. Bendre, G. Venkataramanan, D. Rosene, and V. Srinivasan, "Modeling and design of a neutral-point voltage regulator for a three-level diode-clamped inverter using multiple-carrier modulation," *IEEE Trans. Ind. Electron*, vol. 53, no. 3, pp. 718–726, Jun. 2006.
- [15] V. Yaramasu, B. Wu, M. Rivera, and J. Rodriguez, "Predictive current control and DC-link capacitor voltages balancing for four-leg NPC inverters," *Industrial Electronics (ISIE), 2013 IEEE International Symposium on*, Tehran, pp.1-6, 28-31 May 2013.
- [16] R. Kennel, and D. Schroeder, Predictive control strategy for converters, *Proc. of the third IFAC Symposium*, Lausanne, 1983, pp. 415 – 422, Lausanne, 1983.
- [17] V. Najmi, S. Ebrahimi, and H. Oraee, "Output voltage quality intensification of diode clamped multilevel inverters using FM PWM technique," *Power Electronics and Drive Systems Technology (PEDSTC)*, 2012 3rd, pp.98 – 102, 15-16 Feb. 2012.
- [18] A. M. Almaktoof, A. K. Raji, and M. T. E. Kahn, "Robust Current Control Technique for Variable DC-link Voltage Source Inverters for Renewable Energy Systems" 11th Industrial and Commercial Use of Energy Conference (ICUE2014), pp. 353-360. 18–20 August 2014 in Cape Town, South Africa.

Sensor-less output current measurement for switching converters

*A.M. Hank, *D.J. Cooper, *I. Hofsajer

* School of Electrical and Information Engineering, University of the Witwatersrand 2050, South Africa

E-mail: andrew.hank@students.wits.ac.za douglas.cooper@students.wits.ac.za

ivan.hofsajer@wits.ac.za

Abstract: Measuring current in densely populated power electronic circuit boards is a challenge. A mathematical model to determine the instantaneous output current of a buck converter is presented as a non-invasive current measurement technique. This method removes the dependence of traditional current measurement techniques by applying an average model. A buck converter was designed, modelled in MultiSim, and constructed to validate the mathematical model. The results show that the mathematical model is accurate within 10 % when analysing instantaneous error and using an iterative approach. The mathematical model can be improved by incorporating parasitic components and switching loss.

Keywords: buck converter, instantaneous output current, instantaneous error, non-invasive.

1. INTRODUCTION

The measurement of current within a power electronics circuit is always challenging [1]. The work presented here describes a non-invasive technique to measure the average output current from a switch-mode converter. It is non-invasive in the sense that it does not require a series current measurement sensor. It requires no sensor at all, only an accurate duty cycle measurement and a robust model of the converter specifically including parasitic components.

In a typical DC-DC converter the control loop will monitor the output voltage and adjust the duty cycle so that the output voltage remains essentially constant. As larger load currents are drawn it is reasonable to predict the output voltage will droop because of the parasitic series voltage drops in the converter. The control loop normally compensates for this by increasing the duty cycle. It therefore becomes possible to relate the change in duty cycle to the change in the average output current.

The application of this technique is intended for use in densely populated microprocessor boards where it is difficult to gain access to the processor supply rails to insert a current measurement device. Measuring the current being supplied to a processor can give an indication of the power consumed by the processor and this can be used to optimize computational algorithms for energy efficiency. This is possible as often the processor, or even the processor cores will be supplied from a single DC-DC converter, with the rest of the circuit running off different supplies.

Techniques for measuring the power consumption of microprocessors normally require a modified DC bus structure with a current measuring device of some nature inserted [2],[3]. This however is not suitable for measurements on pre-existing boards.

Although the technique described here has been developed to measure the current supplied to microprocessors, this approach is general in nature and can be used with any switching power supply. The discussion in this paper focuses on a buck converter, and develops an equivalent time averaged model for a buck converter. The model is validated against simulation and experiment. Measurement resolution and model linearity which affect the accuracy of the technique are discussed.

2. MODEL DERIVATION

In an ideal buck converter the output voltage is dependant only on the switching duty cycle. In reality non-ideal characteristics such as diode forward bias voltage; MOSFET on resistance; inductor resistance and resistance throughout the circuit cause losses in the system, especially as load current demand increases. A detailed discussion on some of these non-linear effects is given in [4]. It is these normally undesirable parasitic elements that make this technique possible. The buck converter shown in Figure 1 is used as a point of departure.

For steady state operation, a buck converter circuit model can be developed that accounts for average voltages and currents rather than the exact time dependant waveforms. To develop this model, the effects of the different circuit components when the switch is closed and when it is open are added together and analytically used to determine the equivalent circuit. With this approach each component is reduced to their basic real power element: the diode to a voltage source; the MOSFET to an on resistance; the inductor to a resistance.

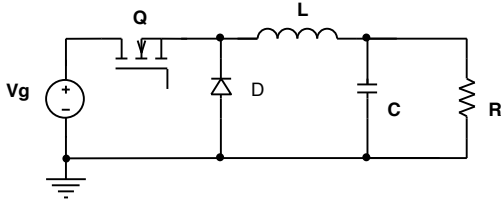


Figure 1: Circuit diagram of a typical buck converter used to derive the model.

Specifically the following assumptions are made:

- The buck converter only operates in continuous conduction mode and the duty cycle is measureable.
- The switching frequency is much higher than the ripple frequency of the converter. This is a requirement that would already need to be in place for a feedback control system to operate correctly.
- The switching signal has a constant frequency and the switching times were fast enough to only permit an on and off state, without reverse recovery for the switches in the buck converter.
- Switching losses were excluded from the model. This can be done if the transition times of the switch are very much faster than the switching period.
- The MOSFET is modelled as a resistor and the diode as a voltage source. The only other parasitic element considered is the series resistance of the inductor.

The modelling done in this paper, as well as the majority of working information regarding power electronics, is based on the work done in [5]. Beyond this basic knowledge, the most similar work done can be found in [6], which describes the use of a Kalman estimator and Linear Quadratic Regulator to control a buck converter's energy transfer with only an output voltage measurement.

Figures 2 and 3 below show the equivalent circuits when the switch is closed and when it is open respectively.

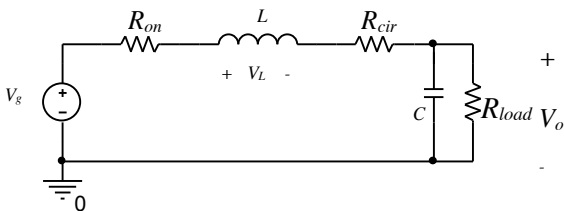


Figure 2: Equivalent circuit of the buck converter when the switch is closed.

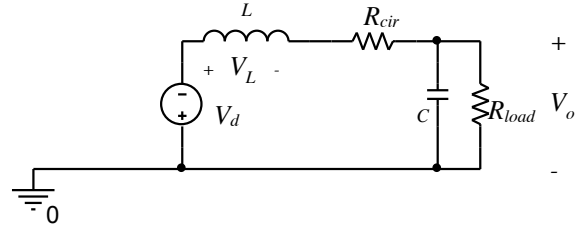


Figure 3: Equivalent circuit of the buck converter when the switch is open.

Where:

- V_L = voltage over the inductor
- V_g = supply voltage
- i_{out} = instantaneous current flowing through the loop
- R_{on} = on resistance of the MOSFET
- R_{cir} = Circuit resistance, including inductor resistance
- V_d = forward bias voltage of the diode
- V_o = output voltage
- D = duty cycle
- D' = inverse duty cycle (1-D)

Describing equations for each of these are added together and scaled to account for the time each equivalent circuit represents the converter, as seen in Equation (1) below. This leads to the simplified voltage loop Equation (2) below. Along with this a current node equation describing current through the capacitor, inductor and load is shown in Equation (3).

$$V_L = D(V_g - iR_{on} - iR_{cir} - V_o) + D'(-V_d - iR_{cir} - V_o) \quad (1)$$

$$V_L = DV_g - DiR_{on} - D'V_d - iR_{cir} - V_o \quad (2)$$

$$i_{out} = i_{inductor} - i_{capacitor} \quad (3)$$

With the averaged nature of this model it is possible to further reduce this equation by noting that the average voltage over the inductor and average current through the capacitor must be zero for the system to be stable. This means that the average current flowing through the inductor is equivalent to the current flowing through the load. Using Equation (2) with the inductor voltage equal to zero allows for a fully averaged equivalent circuit to be developed as a single voltage loop shown in Figure 4.

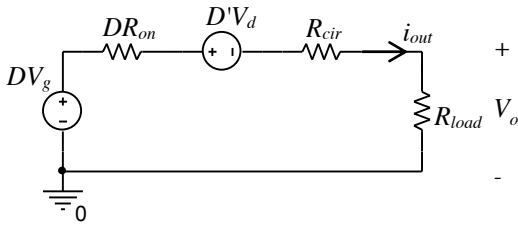


Figure 4: Equivalent averaged circuit to describe output current which combines the on and off models by the duty cycle.

From the work done above, an equation can be developed to describe the behaviour of the output current within the circuit. Equation (4) gives the averaged model used to determine the output current for the buck converter which is independent of switching effects and load resistance.

$$i_{out} = \frac{DV_g - D'V_d - V_o}{DR_{on} + R_{cir}} \quad (4)$$

3. METHODOLOGY AND RESULTS

3.1 Simulation

To validate the model the circuit shown in Figure 1 was firstly modelled in Multisim using an ideal switch for Q and an ideal diode for D. To emulate a closed loop buck converter, the load was changed to observe 100 mA current steps from 100 mA to 2 A, and the duty cycle was changed manually to maintain the output voltage between 5 V and 5.2 V at each step. Figure 5 shows the results for the closed loop simulation. The MOSFET switch and the circuit resistance was modelled as 0.07 Ω and 0.4 Ω respectively. The diode voltage, output voltage, duty cycle and output current were measured to produce the results in Figure 5. It can be seen that the current prediction matches the simulated results closely and verifies the model for the closed loop system. This is to be expected as both the simulation environment and the equivalent circuit model are completely specified. These results demonstrate confidence in the model derivation.

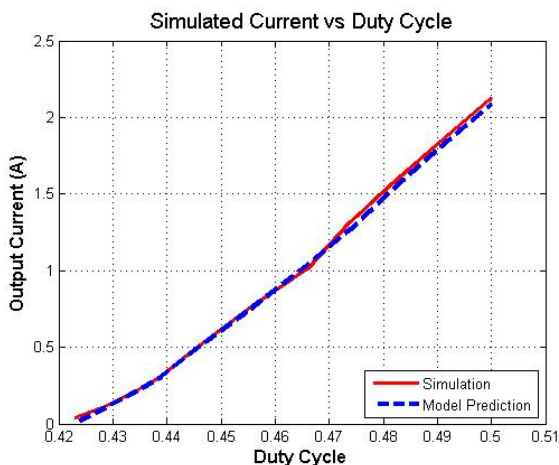


Figure 5: Validation of mathematical model via simulation under closed loop conditions.

3.2 Experimental

In the physical system the inductor, solder track resistance, and MOSFET drain source resistances were measured to account for R_{cir} and R_{on} . A 150 Ω variable resistor was used to model the microprocessor. All other parameters in Equation (4) were measured. The MOSFET is specified as having a total rise and fall time of 61 ns. At the selected switching frequency, these points of operation account for less than 0.25 % of the full switching period. The switching times are thus considered negligible. Similarly, a Schottky diode was selected for its fast switching characteristics as well as the fact that these diodes have effectively zero reverse recovery time. To reduce the effect of temperature rise leading to increased resistance the components selected are rated well above the current expected to flow through the circuit. Figure 6 shows the 10 W, 12 V to 5 V buck converter circuit constructed. It utilises a conventional bootstrap driver and there are no additional complexities.

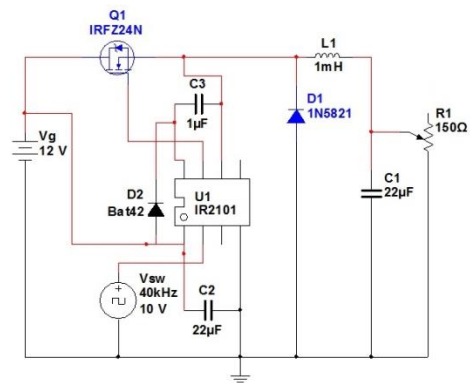


Figure 6: Schematic circuit diagram showing MOSFET driver in buck converter circuit.

The physical converter was found to operate as expected, with a similar trend to that seen in the simulations. Figure 7 shows both the measured and predicted current to duty cycle trend of the experimental closed loop system. Clearly the trend has a non-linear ripple not seen in the simulations. This is because experimental parameters were used in theoretical Equation (4). The measured value for the diode voltage changes at each operational point while the MOSFET and circuit resistances were measured as 0.062 Ω and 0.4 Ω respectively. The model is in good agreement with the measured results. From the simulated and experimental results the effect of each parameter of the model is noted as follows:

- V_d changes the overall trend offset.
- R_{cir} changes the trend slope.
- R_{on} is closely coupled with R_{cir} , and has a higher effect with higher duty cycle.

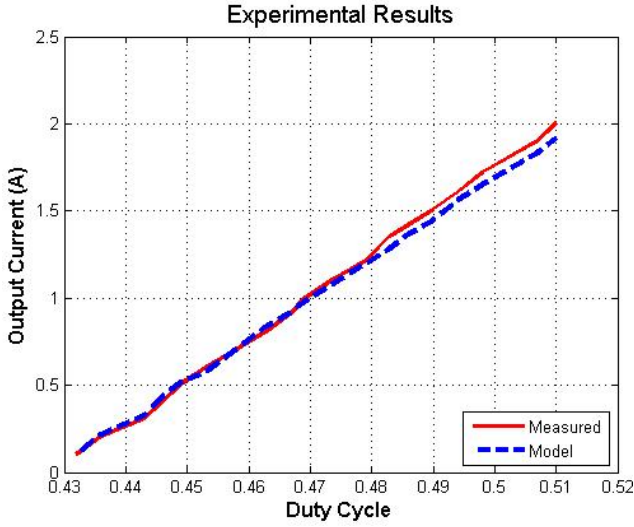


Figure 7: Constructed results validating mathematical results with non-linear ripple under closed loop conditions.

3.3 Error Analysis

An error analysis was performed to determine the instantaneous error (IE) for the model for the constructed model using Equation (5). Additionally this analysis took into account the effect of resolution error of the equipment.

$$E_{inst} = \left| \frac{I_{out} - I_{pred}}{I_{out}} \right| \times 100 \quad (5)$$

Where:

- E_{inst} = the absolute IE
- I_{out} = measured instantaneous output current
- I_{pred} = predicted instantaneous output current

To show the sensitivity of the prediction with regards to the measurement resolution, the various measured parameters of the model were altered by the smallest resolution change and the errors were recorded. Table 1 shows the error for various element value changes and shows that measurement of the diode model has a more significant contribution to the IE compared to the other parameters. The resolution percentage column indicates the percentage of the full scale measurement error. The maximum error due to resolution is shown in the last column of Table 1.

Figure 8 describes the error results using Equation (5) and the maximum error due to resolution. The error analysis shows that while there is error between the model and measured results, the error is mostly under 10 % hence showing good agreement. While the resolution of the equipment increases the IE at the lower currents, on average there does not appear to be a significant contribution at higher currents.

Table 1: Measurement error effects

Element values				Error
Vd (V)	Ron (Ω)	Rcir (Ω)	Resolution (%)	IE (%)
Original	Original	Original		7.9
+0.01	Original	Original	+2.5	16.83
-0.01	Original	Original	-2.5	11.47
Original	+0.001	Original	+1.6	7.78
Original	-0.001	Original	-1.6	8.01
Original	Original	+0.01	+2.5	7.49
Original	Original	-0.01	-2.5	10.48
+0.01	+0.001	+0.01		18.8

Error Comparison

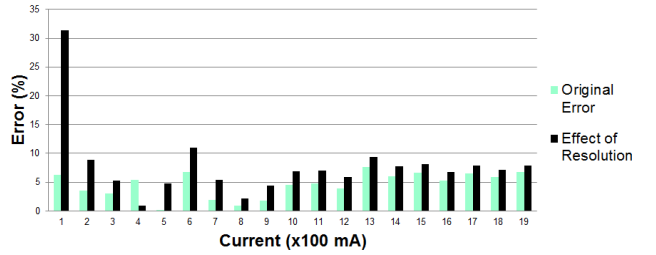


Figure 8: Instantaneous error results for each current step with added effect of resolution.

This is a limited set of the possible errors due to measurement resolution but serves to highlight the limits to which measurements can alter the prediction's accuracy. It is seen that in the worst case, where all three elements have incorrect measurements, it is possible for the error of the prediction to vary by up to 10% for the IE. Even with these errors, the prediction tends to predict the trend of the converter within 5% of measurements and only occasionally predicts the current with an inaccuracy above 10%.

3.4 Iterative Approach

Based on the dependency of the non-linear diode voltage, it was pertinent to determine how well the model performs if there is no access to the diode. This was done by iteratively solving Equation (4) with a diode model. The diode curve was modelled as a polynomial accurate within the bounds of the experimental operation (100 mA to 2 A) shown as Equation (6). The iterative approach involved cycling Equation (4) and Equation (6) with an initial diode voltage of zero. The iterative results of the initial solution as well as the 5th iteration are shown in Figure 9. Provided knowledge of the diode in use either via measurement or datasheet information, the model can be used to iteratively determine the current with accuracy comparable to the non-iterative approach.

$$V_d = 0.0084i_{out}^3 - 0.0481i_{out}^2 + 0.1438i_{out} + 0.25 \quad (6)$$

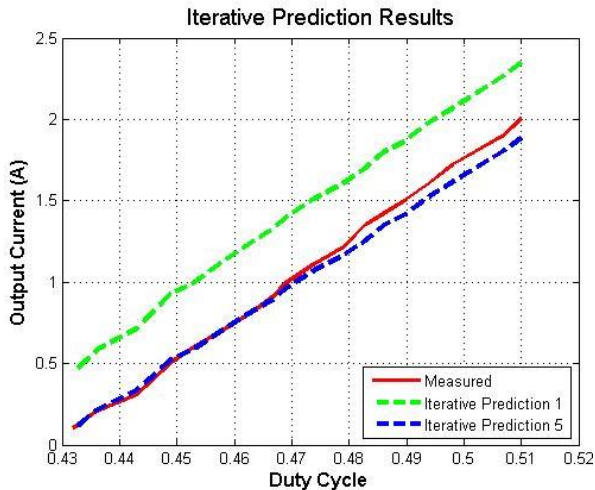


Figure 9: Iterative current prediction results using the 1N5821 datasheet model for five iterations

4. FUTURE WORK

Future investigation should look into the impact different components have; with this it could be determined at what point reverse recovery and switching times influence the converter operation. The iterative approach to solving for unknown diode voltage could possibly be expanded to other unknown elements of the circuit such as the circuit resistance. Beyond these, using the modelling procedure to create models for alternative switched-mode power supplies could be done to further verify the modelling itself. It may be possible to develop a generic current model for all switching power supplies similar to the IEEE transformer model.

5. CONCLUSION

Before the measurement of current within power electronics circuits was a challenge, but now a non-invasive current measurement has been developed and verified with a buck converter. By using the averaged model approach it is possible to determine the current flowing into an unknown load from a buck converter. The results show that this non-invasive current measurement is accurate within 10 %. The effects of each element in the model have been noted, and accurate measurements are needed for all parameters of the model. An iterative prediction can also be used to determine the current, if exact diode voltage measurements are not possible but a diode characterising curve is available. The model can be improved to reduce the error by incorporating parasitic components and switching losses.

REFERENCES

- [1] C. Xiao, L. Zhao, T. Asada, W. G. Odendaal, and J. D. van Wyk, "An overview of integratable current sensor technologies," in *Industry Applications Conference, 2003. 38th IAS Annual Meeting. Conference Record of the*, 2003, vol. 2, pp. 1251–1258 vol.2.
- [2] A. Borovyi, V. Kochan, A. Sachenko, V. Konstantakos, and V. Yaskilka, "Analysis of Circuits for Measurement of Energy of Processing Units," in *4th IEEE Workshop on Intelligent Data Acquisition and Advanced Computing Systems: Technology and Applications, 2007. IDAACS 2007, 2007*, pp. 42–46.
- [3] N. Kavvadias, P. Neofotistos, S. Nikolaidis, C. A. Kosmatopoulos, and T. Laopoulos, "Measurements analysis of the software-related power consumption in microprocessors," *IEEE Trans. Instrum. Meas.*, vol. 53, no. 4, pp. 1106–1112, Aug. 2004.
- [4] Sanjaya Maniktala, "Unraveling Buck Converter Efficiency and Maximizing Performance." Microsemi, Analog Mixed Signal Group, Feb-2013.
- [5] R. W. Erickson, *Fundamentals of power electronics*, 2nd ed. Norwell, Mass: Kluwer Academic, 2001.
- [6] C. O. Moreira, F. A. Silva, S. F. Pinto, and M. B. Santos, "Digital LQR control with Kalman Estimator for DC-DC Buck converter," in *2011 IEEE EUROCON - International Conference on Computer as a Tool (EUROCON)*, 2011, pp. 1–4.

EXPERIMENTAL EVALUATION OF DELTA MODULATION FOR PWM NINE PHASE INVERTER WITH A TRAPEZOIDAL REFERENCE CURRENT WAVEFORM.

L Gunda* and N Gule*

**Stellenbosch University, Department of Electrical and Electronic Engineering, Stellenbosch.*

Abstract: The paper presents the experimental evaluation of delta modulation for a multiphase pulse width modulation (PWM) inverter with trapezoidal reference current which can be used on a Brush-DC Equivalent (BDCE) controlled multiphase induction machine drive. The inverter switches change states many times during one period of the reference signal to produce pulse width modulated voltage pulses across the load. Inverters are used in high power system with switching frequencies above five kilohertz and power electronic switches like insulated gate bipolar transistors (IGBT) with high speed and high power switching capabilities are used. In this paper; delta modulation is evaluated for a nine phase inverter with the delta modulator being implemented in a digital signal processor controller. Experimental results show that conventional linear delta modulation does not produce the required trapezoidal stator currents while a modified delta modulation technique which uses an integrator at the input gives better results.

Key Words: Multiphase PWM inverter, Delta Modulation, trapezoidal reference; experimental evaluation

1. INTRODUCTION

An inverter is a device that converts a low frequency power signal to a higher frequency power signal. The inverter is mainly used to convert a direct current (DC) power to alternating current (AC) power. Industrial applications of inverters include adjustable-speed AC drives, photovoltaic systems, electric vehicles, induction heating, grid connection of wind energy systems, standby aircraft power supplies, uninterruptible power supplies (UPS) for computers and high voltage DC transmission lines.

The inverter operates by supplying pulse width modulated voltage pulses to the load such that the load voltage or load current follows a defined reference signal. The inverter energy efficiency, waveform quality and voltage or current linearity as well as the harmonic distortion is determined by the choice of the modulation method. Carrier based modulation techniques are the most common techniques used because they are easy to implement once the right carrier signal has been generated.

Carrier based sinusoidal PWM is presented in [1] where a single phase sinusoidal PWM microcontroller-based 300VA inverter is designed and tested for fixed modulation index of 0.6 and unipolar voltage switching. The sinusoidal PWM technique was presented for a single phase inverter which gave a maximum efficiency of 89% showing that there was still need for improved design.

In electrical machine drives, space vector modulation is the most commonly used technique because it gives better control of the overall power system. Space vector modulation for sinusoidal output voltage generation with a nine-phase VSI is developed; implemented and verified experimentally using a digital signal processor (DSP) base controller in [2] and unwanted low order harmonics are eliminated.

Delta modulation is also being used where a constant switching frequency is desired and because it has

inherent filtering of current harmonics. Zaogas [3] introduced the use of delta modulation for static PWM inverters. The delta modulation technique is implemented using op-amp circuits on a single phase induction motor. The electronic circuitry is prone to failure and research is being advanced to implement it in software.

Due to the introduction of DSPs and related micro-computers, the delta modulation algorithm can be executed in software thereby removing the need for electronic circuit hardware which can cause unpredictable system failures as presented in [4]. The switching sequences corresponding to specified set of parameters are stored in a look-up table. The parameters used are the reference signal, sampling frequency and filter coefficients. The look up table is used to determine the switching states of the inverter depending on the values of the variables in the look up table. The method proved to be more effective than natural sampling and regular sampling since the reconstructed signal closely followed the reference signal. The method enabled operation optimization by varying the delta modulator parameters in software but has high system memory demand for storing the look up tables and also for looking up the values.

In most delta modulation applications, the reference signal used in delta modulator is a sinusoidal waveform. The use of sinusoidal modulating signals has limited input voltage transfer by utilising only 64% of the available DC voltage [4] and the voltage transfer of a sinusoidal modulating signal is at most 87% [5]. This can be improved by over modulation but with loss of performance because it introduces distortions in the output waveform, causes large sub harmonic currents and reduces the fundamental voltage gain.

However, it has been shown in [6] and [7] that a flat topped modulating signal has better voltage transfer characteristics and less total harmonic distortion than

conventional sinusoidal signals. The next section is a presentation of the multiphase PWM inverter configurations used and the modulation techniques used to generate PWM switching signals.

2. MODULATION TECHNIQUES FOR PWM INVERTERS

PWM techniques used in induction machine control are classified as either carrier based or carrier-less. The carrier based PWM methods involve the comparison of the modulation signal to a separately generated carrier signal to determine the switching state of the inverter. The switching instant occurs at the intersection of the carrier signal and the modulating signal. Sinusoidal PWM (SPWM), space vector PWM (SVPWM) and third (or n th) harmonic injection PWM (THIPWM) are examples of carrier based PWM techniques. Carrier-less modulation techniques involve the generation of a carrier from the system outputs and the properties of the carrier vary with the system outputs. Examples include delta PWM (DPWM), specific harmonic elimination PWM (SHEPWM) and wavelet pulse width modulation (WPWM).

The techniques can be modified and refined to ensure smooth operation of inverters with minimum power losses and less harmonic distortions in the voltages and currents supplied to the machine phases. PWM produces the inverter switching pattern by firing full voltage pulses at high frequencies in order to shape the output voltage and current close to the modulating signal waveform. A PWM signal contains only carrier related harmonics which can be easily filtered off by the machine inductance and the fundamental frequency is the same as the modulating signal frequency. A good PWM technique produces high amplitude of the fundamental component, has lower total harmonic distortions, has low switching losses and does not affect the supply side of the inverter. The technique should allow easy controllability of the inverter and easy implementation.

The use of PWM fed inverters enables the power source to adjust the power supplied to the load and hence reduce the current surges that normally occur when starting high power inductive loads. PWM also highly regulates and controls the inverter output voltage harmonic content [6] by pushing the harmonics to higher frequencies which can be easily filtered off by the inductance of the machine. The performance of the PWM inverter fed load is determined by the inverter switching technique and the current control method used to produce the load current waveforms and this directly affects the harmonic content of the stator currents.

Holtz [7] reviews the application of pulse width modulation for power conversion and notes that the most important performance parameter to be considered when choosing a PWM scheme is the

switching frequency since it is the one which determines the losses as well as the ease of filtering off harmonics by the leakage inductance of the motor. In theory, high switching frequencies are the most desirable, but they are limited by the magnitude of maximum allowed rate of change of voltage across the switching devices.

2.1 Sinusoidal PWM:

SPWM is a modulation technique whereby a sinusoidal modulating signal is compared to a triangular carrier signal to determine the switching instant of the inverter. The object of SPWM is to force the load current waveform to track the sinusoidal modulating signal as closely as economically possible with attenuated lower order harmonics. The pulse width of the switching voltage pulse at a particular time is always proportional to the sine of the angular position of the waveform.

To extend the implementation of SPWM to n -phase systems, n modulating signals are used to generate the PWM signals for the inverters. The modulating signals are spatially spaced by the same angle as the phases of the load. The intersection of the modulating signal and the carrier determines the switching instant for the particular inverter leg corresponding to the modulating signal.

In [8] a carrier based sinusoidal PWM technique is presented for utilization on a seven phase VSI with 7th order harmonic injection. Injection of the zero sequence n th-harmonic into reference signals in case of an n -phase system extends the linear modulation region and does not affect the output voltage waveforms but improves DC voltage utilization. The n th order harmonic injection technique used gives improved performance than ordinary sinusoidal PWM. In general, sinusoidal PWM is simple to implement because there is no need to construct and select the optimum voltage vectors as is required in space vector PWM.

2.2 Space Vector PWM:

Space vector modulation uses space vectors to represent the switching states of an inverter and is popularly applied to three phase systems. A reference signal generated from three separate phase references using the $\alpha\beta\gamma$ transform is sampled at a constant frequency. The three phase modulating signal (reference vector) is transformed to a two dimensional vector ($\alpha;\beta$). The reference voltage vector is calculated and a polygon of vectors representing the switching vectors and the reference voltage vector is produced. The modulation algorithm then selects a set of voltage vectors delimiting the reference voltage vector and these vectors are each applied to the load [9], [10].

Multiphase systems can however not be represented by a single d - q plane and hence are analyzed by using the multidimensional approach for SVPWM

presented in [11]. The identification of the sector in the polygon of $n!$ (mathematical factorial) vectors for a multiphase system is not as simple as the three phase system.

The discussion of SVPWM shows that the analysis of multiphase systems using space vector theory is done based on three phase space vector theory and the use of space vector decomposition transformations which becomes complicated as the number of phases increases.

Delta modulation however can be implemented without a carrier and also without space vectors and that makes it simpler to implement.

3. THE DELTA MODULATION CURRENT CONTROLLER

Delta modulation is a simple analogue to digital conversion method in which an analogue signal is encoded into a sequence of pulses for transmission and the message is easily reconstructed at the receiver using low pass filters [12], [13]. The pulses are sampled at a fixed sampling rate and are fed back to the comparator through a low pass filtering integrator which reconstructs the analogue signal.

Delta modulation has variations which mainly depend on the type of load being supplied with power. Delta modulation works perfectly for inductive loads which

can filter the high frequency switching pulse to reconstruct the reference signal.

3.1 Variations of Delta Modulation

The variations of delta modulation are; linear-delta modulation, sigma-delta modulation, adaptive-delta modulation and asynchronous delta modulation. Linear delta modulation is the simplest technique which is less demanding in implementation. It can be implemented as a sensor-less technique where the load being driven by the inverter has inherent filtering characteristics. However, sensors may be required to improve accuracy and these sensors only have to detect the two signal levels of the output waveform and hence the sensors used are simpler than those required in the hysteresis control scheme.

3.1.1 Linear delta modulation:

Fig. 1 shows the conventional linear delta modulation block with a sample and hold block which dictates the maximum switching frequency. The two-level quantizer uses the signum function to determine the sign of the error. The two levels $+V_{out}$ and $-V_{out}$ are the outputs of the quantizer corresponding to a positive error and to a negative error respectively.

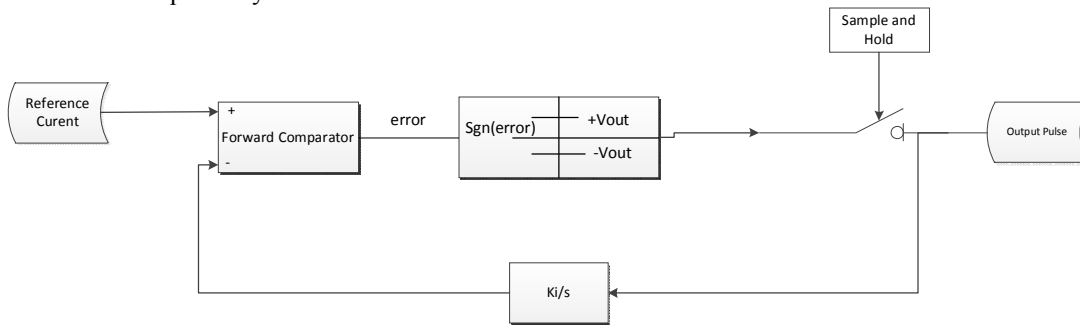


Fig. 1: Linear delta modulation block.

The performance of the delta modulator is determined by the maximum slope of the reference signal S_r ; the two level quantizer output magnitude V_{out} ; the magnitude of the hysteresis band ΔV (if a hysteresis band is used); the sampling frequency of the sample and hold block, F_s and the integrator gain K_i [14]. The expressions for the delta modulator parameters are derived in [14] as follows:

Consider a reference current signal given by:

$$I_r = I \sin \omega_r t, \quad (1)$$

Where:

I is the current waveform amplitude
 ω_r is the signal angular frequency.

The switching frequency is given by [14] as:

$$f_s = \frac{S_c^2 - S_r^2}{4 * \Delta V * S_c}, \quad (2)$$

Where:

$$S_c \text{ is the slope of the carrier wave given by } S_c = K_i * V_{out}, \quad (3)$$

Duty ratio is given as:

$$D = \frac{1}{2} \left(1 + \frac{S_r}{S_c} \right), \quad (4)$$

The slope of the reference signal is given by:

$$S_r = I * \omega_r * \cos \omega_r t, \quad (5)$$

When the reference signal is a constant value, then

$$S_r = I * \omega_r * \cos \omega_r t = 0 \quad (6),$$

and the switching frequency is solely dependent on ΔV and V_{out} and at this instant, f_s is maximum while

$$D = 1/2.$$

For the carrier I_{carr} to track the reference I_{ref} with minimum error,

$$\left| \frac{dI_{ref}}{dt} \right|_{max} \leq \left| \frac{dI_{carr}}{dt} \right|_{max} \quad (7)$$

This implies that

$$|I * \omega_r * \cos \omega_r t|_{max} \leq |K_{int} * V_{out}|_{max} \quad (8).$$

For practical implementation in PWM inverters, it was observed in [15] that good performance is achieved if the switching voltage across the load is fed back and filtered to produce the carrier than when the quantizer output is used. This is because the switching voltage automatically includes the load dynamics which will then not need to be modelled for implementation. The technique also has inherent error detection.

3.1.2 Alternative Linear Delta Modulation:

The conventional linear delta modulation technique described above shows some complications when the reference signal has a constant value in its waveform and when its slope changes in an unpredictable way. Such waveforms present challenges in striking a balance between slope overload and granular noise. To mitigate this problem, the reference is first integrated before being compared to the carrier. The carrier therefore tracks the integral of the reference. Fig. 2 shows the alternative linear delta modulator that is used to reduce the slope overload and granular noise without using an adaptive algorithm. The input to the forward comparator is an integral of the reference and its maximum slope is independent of the frequency of the reference. The input is therefore given by:

$$V_r = V \int \sin \omega_r t dt = -\frac{K_i V \cos \omega_r t}{\omega_r}, \quad (9)$$

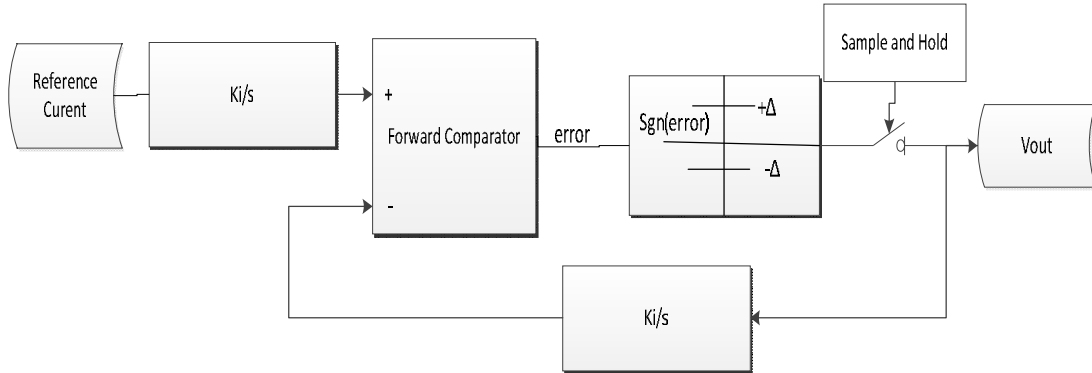


Fig. 2: Alternative linear delta modulator with integrator at the input

Fig. 3 shows the schematic diagram of the nine phase inverter together with its connection to the nine phase induction machine phases used for evaluating the delta modulation technique. The two capacitors are

The slope of V_r is $K_i V \sin \omega_r t$ hence the maximum value of the slope of the reference signal is independent of ω_r . The condition for the desirable slope overload condition is therefore determined by the relative magnitude of the reference signal with respect to the magnitude of the quantizer output. For the alternative delta modulation, the necessary condition for proper operation is that:

$$I * K_i \leq K_i * V_{out} \quad (10).$$

This implies that the integrator gain is no longer a design constraint and hence only the magnitude of the reference signal and that of the quantizer output are monitored. By using the worst case scenario, the two variables can be fixed. By restricting the values of the integrator constant and of the reference signal magnitude, the maximum slope can be restricted and the carrier frequency can be increased to any value without causing undesirable slope overload. This scheme is handy when performing delta modulation where the reference signal has a varying frequency and persistent dc levels and is very simple to design and implement in software without using much computing resources.

Considering maximum values from (8),

$$5.83 * (2\pi * 50) \leq K_{int} * 400 \quad (11)$$

$$\Rightarrow K_{int} \geq 4.8$$

The minimum value of K_{int} is 4.8 and its maximum value is determined by the minimum value of the two-level quantizer output.

The delta modulator is designed, simulated and implemented in a DSP controller board to control the inverter.

used to reduce the voltage ripples in the dc link voltage which is supplied from a rectifier circuit not shown in the figure.

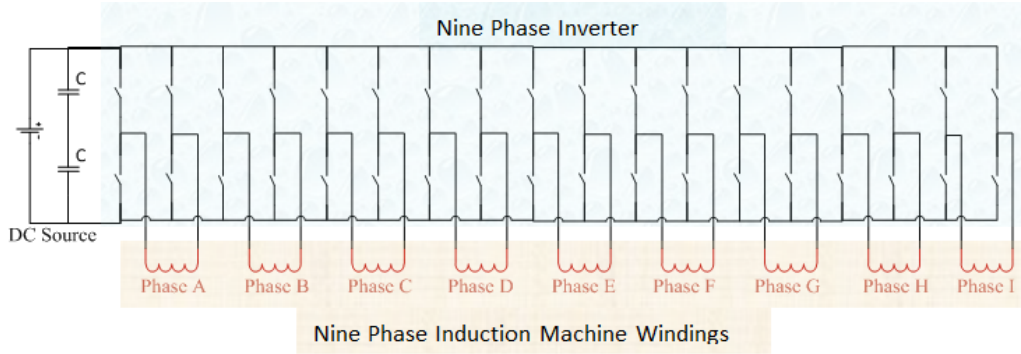


Fig. 3: Nine Phase PWM inverter using full H-bridge configuration.

The delta modulator is implemented in software and the integrator used is represented by Fig. 4. The low pass filter integrator is designed from the Z-transform transfer function and the linear delta modulator is developed from there. The transfer function of an RC integrator is given by:

$$\frac{V_{out}(s)}{V_{in}(s)} = -\frac{1}{RCs} \quad (12).$$

The transfer function for the integrator in the Z-transformation is given by:

$$\frac{V_{out}(z)}{V_{in}(z)} = \frac{T(1+z^{-1})}{2RC(1-z^{-1})} \quad (13),$$

where T is the sampling period of the integrator and RC is the integrator time constant.

Rearranging (13), an expression for the delta modulator can be written as:

$$V_{out}(z) = \frac{T}{2RC}(V_{in}(z) + V_{in}(z-1)) + V_{out}(z-1) \quad (14).$$

For digital implementation, the integrator is developed using unit delays and a complete delta modulation block is shown in Fig. 4.

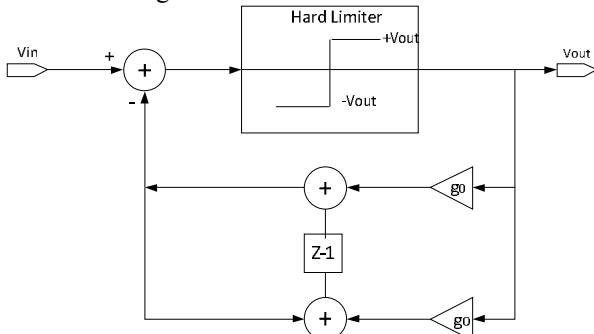


Fig. 4: Delta modulator implementation using Z-transformation.

From [1], the time constant is given by:

$$RC = \frac{4V_s}{\pi * V_{in} * \Omega_{rb}} \quad (15),$$

where Ω_{rb} is the break frequency.

The designed break frequency for the input signal is 55 Hz, hence $\Omega_{rb} = 2 * \pi * 55$. The maximum value of the reference signals is 11.66 and the designed maximum value of the op-amp comparator output is 12 for the delta modulator under consideration. Substitution of these values into the time constant equation in (15) gives a time constant of 0.00381 seconds.

4. EXPERIMENTAL EVALUATION RESULTS

The experimental evaluation is done by programming the DSP controller to execute the current control algorithm and using the PWM signals produced to control the inverter. Fig. 5 show the nine phase inverter used in the evaluation. The optic fibre link transmits PWM signals from the controller to the inverter. The load is a nine phase BDCE controlled induction machine. Phase currents are displayed to show the performance of the delta modulation controller.

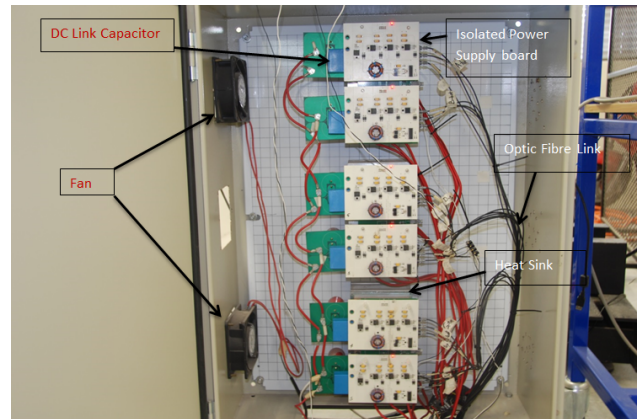


Fig. 5: Nine phase inverter

The hysteresis controller is tested for comparison with the delta modulation controller and the stator waveform produced by the hysteresis controller is shown in Fig. 6. Fig. 7 shows the current switching waveform produced. The results show a varying switching frequency which gives irregular inverter operation.

The conventional linear delta modulation fails to produce the desired stator current waveform leading to the design of an alternative technique. The alternative scheme which uses two integrators is simulated and tested on the inverter. The waveform produced by the alternative delta modulation tends to produce curved portions just before reaching the peak due to the action of the integrator which uses cumulative addition. Fig. 8 and Fig. 9 show the practical results of using the alternative delta modulation technique for the trapezoidal reference waveform. The curved end before the peak can be observed. However, the current switching waveform shows a constant switching frequency which is desirable for regular

inverter operation. This also enables easy design of filters to filter off harmonics.

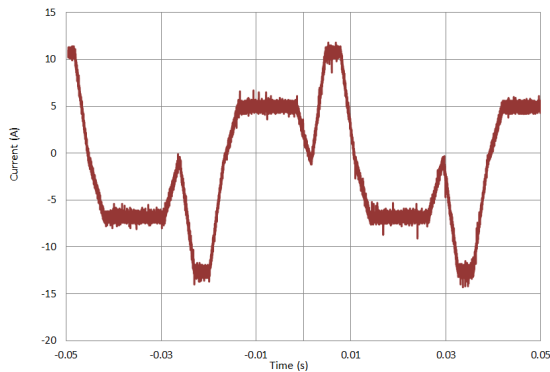


Fig. 6: Waveform produced by the hysteresis controller

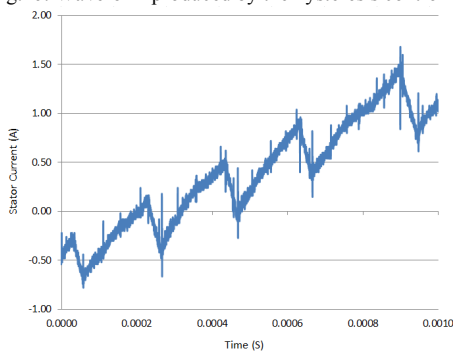


Fig. 7: Hysteresis controller current switching waveform

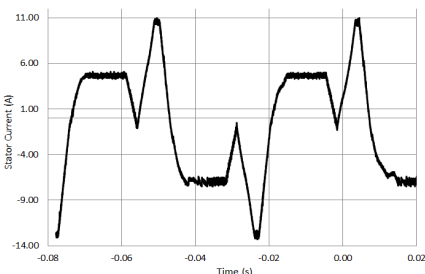


Fig. 8: Stator current waveform produced by alternative linear delta modulation controller

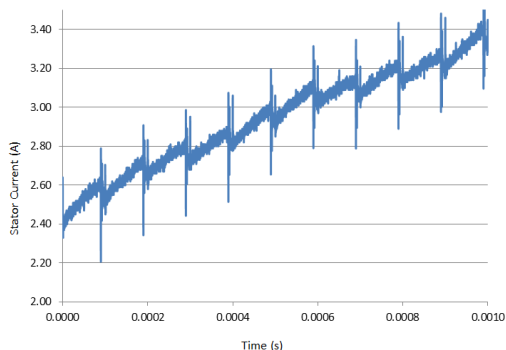


Fig. 9: Delta modulation current switching waveform

5. CONCLUSIONS

The delta modulation PWM technique has been experimentally evaluated and the results obtained have been presented. The conventional linear delta modulation scheme fails to produce trapezoidal current waveforms in the load and the alternative delta modulation scheme gives better results than the conventional technique.

Compared to the alternative delta modulator, the hysteresis controller produces better stator current waveforms. However, the current switching waveforms show that the delta modulator gives a constant switching frequency and this gives regular inverter operation. The results show the possibility of implementing delta modulation PWM scheme on loads that use non-sinusoidal voltages and better results are expected if load voltages are measured.

REFERENCES

- [1] P. H. Zope, P. G. Bhangale, P. Sonare and S. R. Suralkar, "Design and Implementation of carrier based Sinusoidal PWM Inverter," *International Journal of Advanced Research in Electrical, Electronics and Instrumentation Engineering*, Vol. 1, Issue 4, pp. 230-236, 2012
- [2] D. Dujic, M. Jones, and E. Levi. "Space Vector PWM for Nine-Phase VSI with Sinusoidal Output Voltage Generation: Analysis and Implementation," *Proc. of the 33rd Annual Conference of IEEE Industrial Electronics Society (IECON)*, pp. 1524-1529, 2007.
- [3] D. Dujic, E. Levi, M. Jones, G. Grandi, S. Serra and A. Tami. "Continuous PWM Techniques for Sinusoidal Voltage Generation with Seven-Phase Voltage Source Inverters". *IEEE Power Electronics Specialists Conference (PESC)*, pp. 47-52, 2007.
- [4] P.D. Ziogas. "The Delta Modulation Technique in Static PWM Inverters". *IEEE Transactions on Industry Applications*, Vol. 1A-17. No. 2. pp. 199-204, 1981.
- [5] K. Taniguchi and H. Irie. "Trapezoidal Modulating Signal for Three-Phase PWM Inverter". *IEEE Transactions on Industrial Electronics*. Vol.33. No.2. pp. 193-200, 1986.
- [6] R. K. Srivastava, M. A. Rahman, J. E. Quaicoe and M.A. Choudhury. "Software Control of Delta Modulated Inverters". *Proceedings of Annual Conference of Industrial Electronics Society*. Vol. 3. pp. 836-841, 1988.
- [7] J. Holtz. "Pulse Width Modulation for Electronic Power Conversion". *Proceedings of the IEEE*. Vol. 82. No. 8. pp. 1194-1214, 1994
- [8] D. Dujic, E. Levi, M. Jones, G. Grandi, S. Serra and A. Tami. "Continuous PWM Techniques for Sinusoidal Voltage Generation with Seven-Phase Voltage Source Inverters". *IEEE Power Electronics Specialists Conference (PESC)*, pp. 47-52, 2007.
- [9] A. Bellini and S. Bifaretti, "Comparison between Sinusoidal PWM and Space Vector Modulation Techniques for NPC Inverters". *Proc. IEEE Russia Power Tech Conference*. pp. 1-7, 2005.
- [10] A. Lega, M. Mengoni, G. Serra, A. Tani and L. Zarri. "General Theory of Space Vector Modulation for Five-Phase Inverters". *IEEE International Symposium on Industrial Electronics*. pp. 237-244, 2008.
- [11] M. Duran and E. Levi, "Multi-Dimensional Approach to Multi-Phase Space Vector Pulse Width Modulation," *Proc of IECON*. pp. 2103-2108, 2006
- [12] Intersil Corporation. "Delta Modulation For Voice Transmission". *Application Note, AN607.1*, 2000.
- [13] J. Nieznanski. "Performance characterization of vector sigma-delta modulation". *Proceedings of IEEE Annual Conference of the Industrial Electronics Society*. Vol. 1. pp. 531-536, 1998.
- [14] A. I. Maswood and S. Anjum. "Delta Modulation with PI Controller – A comparative Study". *Journal of Electromagnetic Analysis and Applications*. Vol. 3. pp 145-151, 2009.
- [15] S. Sae-Sue, V. Kinnaree, K. Sirichanpong and K. Kleebua. "Design and Analysis of Delta Modulated PWM Inverter with regulated output voltage for 1- ϕ Induction Motor Drives". *Proceedings of the IEEE International Conference on Power Systems*. Vol. 1. pp 317-320, 2000

THE FUNDAMENTAL CONSTRAINTS OF CONSTANT VOLTAGE POWER CONVERTERS

J.A. Naudé* and I.W. Hofsjager†

* School of Electrical and Information Engineering, University of the Witwatersrand, South Africa
E-mail: jacques.naude@wits.ac.za

† School of Electrical and Information Engineering, University of the Witwatersrand, South Africa
E-mail: ivan.hofsajger@wits.ac.za

Abstract: The theoretical understanding of power electronics was severely lacking in the field's infancy. It was Middlebrook who developed the theoretical framework used today. The chief concern, so far, has been in either discovering new circuit topologies or in improving the components and control of existing topologies. The present work aims to address the problems of constant input voltage (CIV) power conversion using fundamental physical theory. It is shown that a CIV power converter with only series components: has an ideal efficiency exactly equal to the voltage gain ratio $G := \frac{V_{out}}{V_{in}}$; and is fundamentally incapable of boost conversion. A T network power converter is the simplest non-trivial CIV power converter which has the possibility of perfect efficiency, $\eta = 1$. The ideal current and voltage relations for $\eta = 1$ are found and these depend on G . It is proved that it is fundamentally impossible to use only passive components in a T network power converter and achieve perfect efficiency. Hence, a switch is a fundamental requirement in any CIV power converter.

Key words: Fundamental Limits, Power Electronics.

1. INTRODUCTION

Power electronics is a mature, technologically driven field with a large number of possible circuit topologies for each of the four main power conversion problems. It is a field that was born out of the space race of the 60's, which required devices which were light weight [1]. Traditional alternating current transformers and generators were too heavy to be practically useful for space electrical power applications [1]. Hence, the switched mode power supply was developed. However, the theoretical understanding of its operation and indeed much of the analysis of performance of switched mode power supplies was severely lacking [1]. It was Middlebrook who developed the theoretical framework upon which to understand the operation and control of switched mode power converters [2, 3]. Given this historical development, the field can be said to be *topologically* founded, in that circuits are known which achieve a particular power conversion result. The primary interest, so far, has been in either discovering new topologies or in improving the components and control of existing topologies. Any comprehensive textbook on power electronics begins with the basic circuit topologies and discusses the design around these topologies as well as practical means to drive them [4, 5].

The present work aims to address the problems of constant input voltage (CIV) power conversion using fundamental physical theory. Instead of choosing from an existing set of circuit topologies, this work is chiefly concerned with how necessary these topologies are in the first place. Is there any fundamental physical reason that a

DC-DC converter needs a shunt path? Is it possible to design a power converter using only components that are in series with the load? Can a power converter be designed using only passive components? These and other important foundations will be addressed in this work. The development of the work was to remain as non-committal as possible to circuit topology and find out the important relationships which must be upheld in the light of the known physical constraints.

Section 2 gives a short description of the model circuit considered in this analysis, this circuit is a constant input voltage CIV power converter. Section 3 graphically depicts the surface in state space on which all physically possible CIV power converters must traverse on. Section 4 discusses the fundamental theoretical possibilities of series only components in CIV power converters. Section 5 discusses the first non-trivial extension of a series only CIV converter, a "T" network power converter. Here the theoretically ideal voltage and current relations which the "T" network must satisfy are developed. The impossibility of a passive CIV power converter is also proved in this section. Section 6 develops the idea that the ideal current relations from Section 5 may be achieved over time, hence necessitating the use of a switch. Recommendations for future work are briefly described before concluding.

2. MODEL CIRCUIT

The model circuit considered for a generic, constant input voltage, power converter is depicted in Figure 1. The input source is modeled as a constant voltage V , with current i_n entering the device. The power converter itself is considered unknown. The output of the power converter

is a current i_o entering a single load resistor R . The only source of power is the constant voltage source, V .

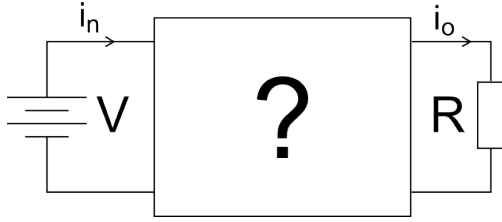


Figure 1: Model Circuit of Constant Input Voltage Power Converter

3. FUNDAMENTAL CONSTRAINT VISUALISATION

The two most important constraints in the model circuit of Figure 1 are power and current. The first constraint is that the input power, P_n is equal to the sum of the stored power, P_s and the output power P_o and is given by equation 1.

$$P_n = P_s + P_o \quad (1)$$

This is nothing more than the first law of thermodynamics. However, given the nature of the input power source and the output power sink, equation 1 may be further constrained resulting in equation 2.

$$Vi_n = P_s + i_o^2 R \quad (2)$$

Equation 2 has further detail of the input and output power in Figure 1 built into it. Now, equation 2 may be rewritten as equation 3

$$i_n = \frac{P_s}{V} + \frac{i_o^2 R}{V} \quad (3)$$

which suggests a family of parabolas if P_s is considered a constant. These may be visualised in a state space of input current against output current and is depicted in Figure 2.

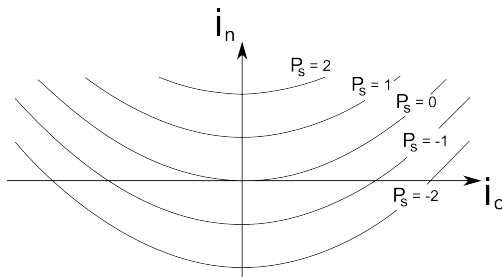


Figure 2: Power and current constraints

The only effect of P_s on this family of parabolas is to offset the input current when the output current is zero.

Of course, if the power stored, P_s is considered as another independent variable, then equation 3 is really a surface in a three dimensional state space of i_n , i_o and P_s . Every physically realisable CIV power converter must traverse the state space on this surface, which is depicted in Figure 3.

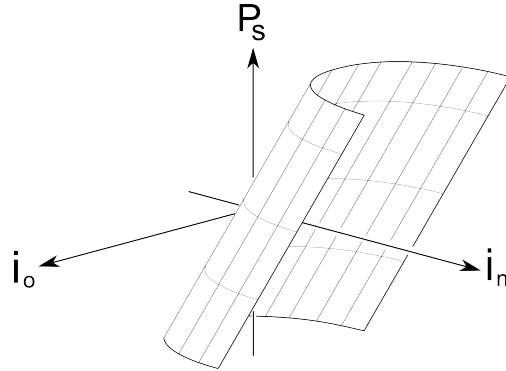


Figure 3: Three Dimensional Rendering of Power Constraint Surface

In terms of analysis, it is simpler to consider the three dimensional surface as a two dimensional state space with a super-imposed family of storage power level curves, as is depicted in Figure 2. What follows next are the implications of various network configurations within the converter in Figure 1.

4. SERIES ELEMENT CONVERTERS

If there are only series elements in the converter then it implies, following the law of conservation of charge, that the input current must equal the output current. The circuit under consideration is depicted in Figure 4 and may contain an arbitrary arrangement of one port circuit elements provided they are all in series with the load resistor R .

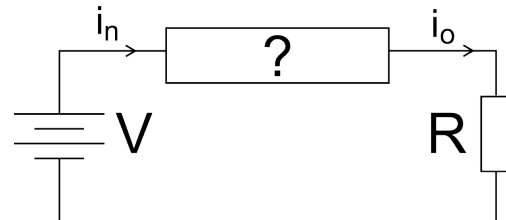


Figure 4: Series element power converter

This relationship, $i_n = i_o$ places an additional constraint in the state space in Figure 2. Now the system in Figure 1 is constrained to move along the straight dashed line in Figure 5. Having the system evolve along the straight line, $i_n = i_o$ has implications for the storage of power during this evolution.

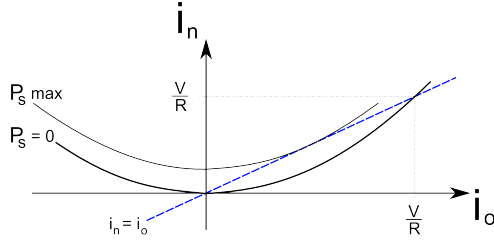


Figure 5: Series Element Only State Space

As a starting point, Figure 5 demonstrates that there are exactly two solutions which have zero storage power and $i_n = i_o$. The one solution is at the origin which means that $i_n = i_o = 0$ i.e. the converter is switched off. The other solution is at $i_n = i_o = \frac{V}{R}$ which means that the converter is just a simple ideal switch where the entire source voltage is dropped across the load. One could have got the same result algebraically from solving equation 3 for i_o with $P_s = 0$ and formally replacing $i_n \rightarrow i_o$.

This implies that evolution along the line $i_n = i_o$ at any other point in the state space incurs a cost of having to store power.

4.1 Limits of series type Buck conversion

Considering the case that $i_o < \frac{V}{R} \implies v_o < V$. This is effectively a “buck” type converter. Note that *any* physically possible power converter which has the result that the output voltage is less than the input voltage is considered a “buck” type converter. A trivial example of a “buck” type converter would be a series resistor. From Figure 5, there exists a current $0 < i_o < \frac{V}{R}$ which has a maximum amount of power that must be stored, $\max P_s$, given that $i_n = i_o$. This is the worst case cost of using a series “buck” type converter. Finding this current, i_o is a constrained optimisation problem. The method of Lagrange multipliers is a very simple analytic technique which can find the maximum stored power, subject to the constraint that $i_n = i_o$. Firstly, define the extended storage power function F in equation 4, which can be maximised in the usual way, and then solve for the Lagrange multiplier λ using the constraint that $i_n = i_o$.

$$\begin{aligned} F &:= P_s + \lambda(i_n - i_o) \\ &= Vi_n - i_o^2 R + \lambda(i_n - i_o) \end{aligned} \quad (4)$$

Maximising F is done by setting all the partial derivatives to zero,

$$\frac{\partial F}{\partial i_n} = V + \lambda = 0 \quad (5)$$

$$\frac{\partial F}{\partial i_o} = 2i_o R + \lambda = 0 \quad (6)$$

$$\frac{\partial F}{\partial \lambda} = i_n - i_o = 0 \quad (7)$$

Solving equations 5 - 7 has the result that

$$i_n = i_o = \frac{1}{2} \frac{V}{R} \quad (8)$$

The amount of power stored in this condition is found using equation 3

$$\begin{aligned} \max P_s &= V \left(\frac{V}{2R} \right) - \left(\frac{V}{2R} \right)^2 R \\ &= \frac{V^2}{2R} - \frac{V^2}{4R} \\ &= \frac{1}{4} \frac{V^2}{R} \end{aligned} \quad (9)$$

Hence, given equations 9 and 8, the maximum amount of power stored will need to be a quarter of the power that would be supplied to the resistor if the full input voltage were dropped across it. This amount of power is stored whenever i_o and i_n are both equal to $\frac{V}{2R}$.

The efficiency of the series type buck converter is given by equation 14, where v_o is the output voltage and is always less than or equal to V . Hence, for a series only buck converter, the efficiency is exactly equal to the voltage gain ratio.

$$\eta = P_{out} P_n^{-1} \quad (10)$$

$$= (i_o)^2 R i_n^{-1} V^{-1} \quad (11)$$

$$= i_o^2 R i_o^{-1} V^{-1} \quad (12)$$

$$= i_o R V^{-1} \quad (13)$$

$$\therefore \eta = \left(\frac{v_o}{V} \right) \quad (14)$$

4.2 Limits of series type Boost conversion

It is somewhat serendipitous that equation 14 can be used to prove that series type boost conversion is impossible. Since both power and current conservation laws were used to find equation 14, it is physically impossible to manufacture a boost converter using only series components.

The proof is simple, a boost converter’s voltage gain ratio implies that $\frac{v_o}{V} > 1$. Since equation 14 relates efficiency to the voltage gain ratio, a series only boost converter would have an over unity efficiency, $\eta > 1$, which is impossible by the first law of thermodynamics. Hence, a series boost converter which conserves both power and current is impossible. QED.

The reader may be thinking that a series resonant circuit might be able to potentially contradict this proof. Namely that $v_o > V \implies \frac{v_o}{V} > 1$ at some time during a transient. This result would be an essential contradiction of equation 14. This is addressed next.

Consider the case of placing a series SPST switch, capacitor and inductor in the question mark in Figure 4. The situation under consideration is a SPST switch being suddenly closed at $t = 0$ producing a step input voltage $Vu_s(t)$. Note $u_s(t)$ is Heaviside's step function and $\delta(t)$ is the Dirac delta function. Using KVL equation 15 is arrived at, which may be differentiated, whilst substituting $v_o = iR$, to arrive at equation 17. Note that the output voltage is the voltage across the resistor, not the capacitor as is usually considered. The final time domain model of the efficiency is given by equation 18, if equation 14 is correct.

$$L \frac{di}{dt} + iR + \frac{1}{C} \int idt = Vu_s(t) \quad (15)$$

$$LC \frac{d^2i}{dt^2} + RC \frac{di}{dt} + i = CV\delta(t) \quad (16)$$

$$LC \frac{d^2v_o}{dt^2} + RC \frac{dv_o}{dt} + v_o = RCV\delta(t) \quad (17)$$

$$LC \frac{d^2\eta}{dt^2} + RC \frac{d\eta}{dt} + \eta = RC\delta(t) \quad (18)$$

Taking Laplace transforms of equation 18 results in equation 19, which is the impulse response of a second order system. The final value is zero, which is intuitive as the capacitor blocks DC.

$$\mathcal{L}\{\eta\} = \frac{RC}{LCs^2 + RCs + 1} \quad (19)$$

The second order prototype is given by equation 20, with gain K , damping co-efficient ζ and natural frequency $\omega_n = \frac{1}{T}$ rad/sec.

$$SO_p(s) = \frac{K}{((sT)^2 + 2\zeta(sT) + 1)} \quad (20)$$

The impulse response of equation 20 can be solved analytically and is given by equation 21 when $\zeta < 1$. The typical shape is  and is a decaying sinusoid.

$$so_p(t) = \frac{G}{T\sqrt{1-\zeta^2}} \sin\left(\frac{t}{T}\sqrt{1-\zeta^2}\right) e^{-\frac{\zeta t}{T}} \quad (21)$$

Using the result that $\sinh(x) = \frac{\sin(jx)}{j}$ where $j = \sqrt{-1}$, the analytic solution of equation 20 is valid when $\zeta > 1$ and results in equation 22. The typical shape is  and is a sum of two decaying exponentials.

$$so_p(t) = \frac{G}{T\sqrt{\zeta^2-1}} \sinh\left(\frac{t}{T}\sqrt{\zeta^2-1}\right) e^{-\frac{\zeta t}{T}} \quad (22)$$

The maximum value of both equations 21 and 22 is given by equation 23 and can be found with most modern

computer algebra systems.

$$so_{pmax} = \frac{G}{T\zeta\sqrt{\frac{(1-\zeta^2)}{\zeta} + 1}} \times \dots \exp\left(\frac{-\zeta \arctan\left(\frac{\sqrt{1-\zeta^2}}{\zeta}\right)}{\sqrt{1-\zeta^2}}\right) \quad (23)$$

Numerical plotting of equation 23 as a function of ζ reveals that the maximum value it attains is $\frac{G}{T}$ at $\zeta = 0$ and exponentially decays from there. This is the standard result from second order linear systems, the maximum amplitude of the impulse response occurs when there is pure resonance i.e. $\zeta = 0$. Using these results, the maximum value of η in equation 19 can be found. Firstly, matching co-efficients between equation 19 and 20 it can be shown that $G = 2\zeta T$, where $G = RC$ and $T = \sqrt{LC}$. Hence, the maximum value of η is governed by equation 24.

$$\eta_{max} = \frac{2}{\sqrt{\frac{(1-\zeta^2)}{\zeta} + 1}} \times \dots \exp\left(\frac{-\zeta \arctan\left(\frac{\sqrt{1-\zeta^2}}{\zeta}\right)}{\sqrt{1-\zeta^2}}\right) \quad (24)$$

A logarithmic plot of this maximum efficiency is depicted in Figure 6 and it can be seen that for large values of ζ the peak of the efficiency time curve approaches one. It could have been reasoned that there would be some value of ζ where $v_o > V$ in a series resonant circuit and hence contradict equation 14, since η and v_o are linearly related. The aforementioned analytical results clearly dispel this idea.

Note that Figure 6 does not imply that the efficiency is unity for all time for large ζ , just that at some point in the transient of the series RLC circuit, the ratio of power out against power in is one. A large damping coefficient implies a large load resistance in Figure 4 and a large capacitance to inductance ratio, both of which allow for a fast rise time and slow decay time in the impulse response, . The peak of the efficiency time graph, , is hence almost 1 for large ζ . Note that $\eta \rightarrow 0$ as time goes to infinity indicating that the output current eventually reaches zero. Again, this is due to the DC blocking of the series capacitor.

5. "T-NETWORK" CONVERTERS

A "T-network" converter is depicted in Figure 7. This circuit breaks the previous constraint whereby the input

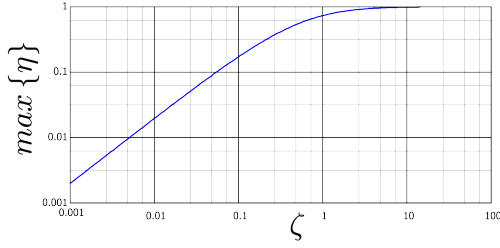


Figure 6: The maximum efficiency as a function of ζ in a series RLC circuit

current had to equal the output current. The act of placing a shunt path within the power converter has now resulted in extra freedom within the state space of Figure 5, specifically it is now possible to move off of the line $i_n = i_o$ since there is a shunt branch current i_B . This is the simplest non-trivial extension of the series only circuit in Figure 4.

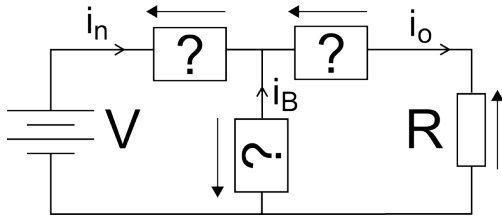


Figure 7: "T-network" converter circuit

The benefit of this extra freedom now is that it is possible that the system could evolve along the parabola $P_s = 0$ in Figure 2.

The reason for wanting to evolve the states along $P_s = 0$ is that this would then achieve a converter with 100% efficiency. Hence, a shunt path is a fundamental requirement to even have the possibility of 100% efficiency and Boost conversion. There are two regions of quadrant 1 of the state space in Figure 2 that are considered here: the "Buck" region which has positive values of $i_o < \frac{V}{R}$ and the "Boost" region where $i_o > \frac{V}{R}$. These regions are depicted in Figure 8.

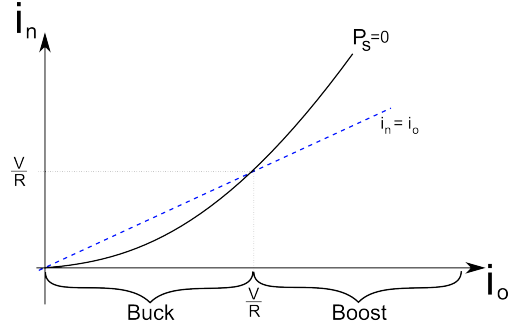


Figure 8: Buck and Boost regions in the state space of the power converter

5.1 T-network converter current relations

Consider operating at a steady-state value of $i_o = \frac{v_o}{R} \neq \frac{V}{R}$. Solve for the required input current using equation 3, given that the power being stored is zero and the result is equation 29.

$$V i_n = i_o^2 R \quad (25)$$

$$\Rightarrow i_n = \frac{1}{V} i_o^2 R \quad (26)$$

$$= \frac{1}{V} \left(\frac{v_o}{R} \right)^2 R \quad (27)$$

$$= \frac{v_o}{V} \left(\frac{v_o}{R} \right) \quad (28)$$

$$\therefore i_n = G i_o \quad (29)$$

Note that G is the voltage conversion ratio $\frac{v_o}{V}$. This neat result has non-trivial implications for the branch current in Figure 7. Performing KCL at the node of the T in Figure 7 and using equation 29 results in equation 33.

$$i_o = i_n + i_B \quad (30)$$

$$\Rightarrow i_B = i_o - i_n \quad (31)$$

$$= i_o - G i_o \quad (32)$$

$$\therefore i_B = (1 - G) i_o \quad (33)$$

Take special note of the direction of the branch current in Figure 7. Calculating the efficiency of this T-type converter using Ohm's Law and the definition of the voltage gain ratio results in an efficiency of one. This is achieved if and only if $i_n = G i_o$ and $i_B = (1 - G) i_o$.

$$\eta = P_{out} P_n^{-1} \quad (34)$$

$$= (i_o^2 R) (V i_n)^{-1} \quad (35)$$

$$= (i_o^2 R) (V G i_o)^{-1} \quad (36)$$

$$= \frac{i_o R}{G V} \quad (37)$$

$$\therefore \eta = \frac{v_o}{v_o} = 1 \quad (38)$$

Hence, it is fundamentally necessary to have a shunt path in a CIV converter in order to have the possibility of 100% efficiency as well as boost conversion.

5.2 T-network converter voltage relations

Given the current relations in equations 29 and 33, KVL will generate a set of further constraints which the converter in Figure 7 must adhere to. Using KVL in loop 1 results in equation 39, where v_l is the voltage across the component in the left arm of the T and v_B is the voltage across the branch component.

$$V = v_l - v_B \quad (39)$$

Using KVL in loop 2 results in equation 40, where v_r is the voltage across the component in the right arm of the T.

$$v_B + v_r + v_o = 0 \quad (40)$$

The final equation of constraint is that the power stored must be equal to zero, this is given by equation 41 which combined with equations 29 and 33 results in equation 43.

$$v_B i_B + v_l i_n + v_r i_o = 0 \quad (41)$$

$$\implies v_B (1 - G) i_o + v_l G i_o + v_r i_o = 0 \quad (42)$$

$$\implies [v_B (1 - G) + v_l G + v_r] i_o = 0 \quad (43)$$

Now equation 43 has two solutions, either $i_o = 0 \forall t$ or equation 44 is true.

$$v_B (1 - G) + v_l G + v_r = 0 \quad (44)$$

Simultaneously solving equations 39, 40 and 44 results in an infinite number of solutions with one of three voltages "independent" and the other two dependent. All possible solutions are in the equation sets 45 - 47.

$$\left. \begin{aligned} v_l &= v_l \\ v_B &= v_l - V \\ v_r &= -v_l + (1 - G)V \end{aligned} \right\} \quad (45)$$

$$\left. \begin{aligned} v_l &= V + v_B \\ v_B &= v_B \\ v_r &= -GV - v_B \end{aligned} \right\} \quad (46)$$

$$\left. \begin{aligned} v_l &= (1 - G)V - v_r \\ v_B &= -GV - v_r \\ v_r &= v_r \end{aligned} \right\} \quad (47)$$

5.3 Unit gain "T" converters

As an important check for correctness, consider the case with a gain of $G = 1$ and a short circuit in the left arm of the "T" i.e. $v_l = 0$. Hence, using the equation set 45 gives $v_l = 0$, $v_B = -V$ and $v_r = 0$. The currents using equations 29 and 33 are $i_n = i_o$ and $i_B = 0$. Hence, the "T" network

reduces to a series only system since the branch voltage is an open circuit and the arms of the "T" are short circuits, as one would expect.

Now consider a real component in the left arm of the "T" which has a small voltage drop, say δ . The gain is still maintained at $G = 1$. Using equation set 45 $v_l = \delta$, $v_B = \delta - V$ and $v_r = -\delta$. The currents are $i_n = i_o$ and $i_B = 0$. Looking at $v_r = -\delta$ with a current of i_o in the directions shown in Figure 7 means that the component in the right arm needs to be an ideal source with voltage enough to cancel the small drop across the left arm. Of course this is disallowed from the constraint that the only source of power is the input constant voltage source. The conclusion is hence that it is impossible to have a gain of $G = 1$ with a small voltage drop across the left arm component, it must be a perfect short-circuit or one will need to add a small ideal voltage source in the right arm to make up the drop in the left arm of the "T".

5.4 Impossibility of a perfect passive CIV power converter

Perfection here is an efficiency of one, passive power converter. Given the ideal current and voltage relations in equations 29, 33 and equation sets 45 - 47, it is a simple matter to prove that a passive converter with these current and voltage requirements is impossible. The important point is that no other power sources, other than the input voltage source are allowed. A component is considered to be a power source if the voltage and current are in the same direction. Again, no internal power sources are permitted in order to keep the "T" converter passive. Start with the left arm voltage v_l . This must be positive in order for the left arm component to be passive. Using the voltage relations in 45, the branch voltage v_B is negative if $v_l < V$. Hence the branch voltage must be a power source (keeping the branch current direction in mind) when $v_l < V$. This is expressly disallowed. Now consider the case that $v_l = (1 + \alpha)V \implies v_l > V$, where $\alpha > 0$ is the amount that the left arm voltage is greater than V . The implications for the right arm voltage are $v_r = (1 - G)V - (1 + \alpha)V = -(G + \alpha)V$. Both $G > 0$ and $\alpha > 0$ implying that $v_r < 0$ in this final case. Hence perfect passive power conversion is impossible with a positive voltage gain ratio, G . The proof for negative G involves looking at the reversed input current $i_n = G i_o$ and using the same argument as above to show that this too is impossible. Hence, the ideal "T" converter is impossible using only passive components. QED.

The result of this proof is that it is necessary to interrupt this passivity, either through the use of other power sources or through the use of a switch (as has been done for the last 50 years). It is hence a theoretical necessity that a CIV power converter have some form of switch.

6. APPROXIMATIONS OVER TIME

Even though it is impossible to satisfy the ideal current and voltage relations instantaneously, it may be possible to do this over a period of time. The required current relations, equations 29 and 33, dictate that “ G ” of the output current must come from the left arm and “ $(1 - G)$ ” must come from the branch. This could be done over a period of time by switching between the left arm and the branch. Consider now the inclusion of an SPDT switch in the “T” network of Figure 7. Here, the branch, left and right components have been made short circuits to illustrate the idea. The result is depicted in Figure 9. By leaving the switch connected to the left arm for “ G ” of the time and connecting it to the branch for “ $(1 - G)$ ” of the time, the result should (theoretically) be power conversion since the current relations are satisfied. The ideal current relations would only be upheld when averaging over the period considered, not instantaneously.

Of course there is no reason to stop with just one such period over time. It may be repeated and, provided that the correct proportions of time are allotted to the left arm and the branch, the resulting output current will be ideal (on average). This now is a theoretical justification for using PWM as a basic power converter. Note that it is no longer a happy accident that the buck voltage conversion ratio is equal to the duty ratio, it is out of theoretical necessity.

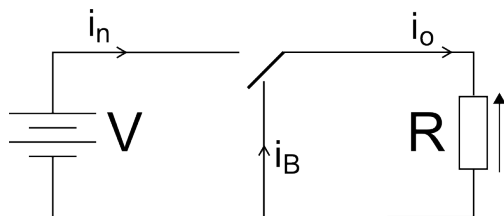


Figure 9: SPDT switch in T network

The circuit depicted in Figure 9 is often one of the first circuits introduced in power electronics as a simple buck converter. Using the results from Sections 3 - 5, it is shown here that this circuit can be found as a time domain approximation to the ideal CIV power converter.

7. RECOMMENDATIONS

Given the ideal voltage and current relations, it would be interesting to continue following the premise of approximating these ideal currents and voltages over time. It is worth looking at sinusoidal output currents and the implications on the ideal currents and voltages as a follow up to this work. Generalising these results to all four power conversion problems, using the same methodology, is a desirable future outcome of this work.

8. CONCLUSION

Using only power and current conservation the theoretical limits of CIV power conversion have been explored. Using only series components, the ideal efficiency is exactly equal to the voltage gain ratio. Furthermore, it was shown that series only boost conversion is fundamentally impossible. Hence, to allow for the possibility of 100% efficiency, even theoretically, as well as boost conversion, a “T” network converter can be used. It is the simplest non-trivial CIV power converter which has the possibility of being 100% efficient. From this premise, the fundamental voltage and current relationships which an ideal CIV power converter must obey have been developed. These are valid for either buck or boost power converters. The input and branch currents are fundamentally constrained by the required voltage gain ratio. The voltages are semi-free in that one of the “T” network voltages is arbitrary and the other two are then fully determined. This means that there are an infinite number of “T” network power converters. It was shown that it is fundamentally impossible to use only passive components in a “T” network power converter and achieve 100% efficiency. Hence, a switch is fundamental requirement in any CIV power converter. Recommendations for further work involve further investigation into achieving the ideal current and voltage requirements, on average. The investigation of the implications of sinusoidal output currents within this work’s paradigm are also worth looking into.

REFERENCES

- [1] K. Kit Sum. Remembering dr. middlebrook: Part 1 - 4. *PowerElectronics.com*, February 2012.
- [2] R.D. Middlebrook. Design of transistor regulated power supplies. *Proceedings of the IRE*, 45(11):1502–1509, Nov 1957.
- [3] G.W. Wester and R.D. Middlebrook. Low-frequency characterization of switched dc-dc converters. *Aerospace and Electronic Systems, IEEE Transactions on*, AES-9(3):376–385, May 1973.
- [4] Robert Erickson and Dragan Maksimovic. *Fundamentals of Power Electronics*. Kluwer Academic, 2nd edition, 2004.
- [5] Ned Mohan, Tore Undeland, and William Robbins. *Power Electronics: Converters, Applications and Design*. Wiley, 3rd edition, 2002.

DEVELOPMENT OF SMART CONTROLLER FOR FUEL CELL AND SUPERCAPACITOR APPLICATION IN ELECTRIC VEHICLES

H.J. Rautenbach^a, R. Gouws^a, D. Bessarabov^b, A. Kruger^b and G. Human^b

a School of Electrical, Electronic and Computer Engineering, North-West University Potchefstroom campus, 11 Hoffman Street, Potchefstroom, 2520, South Africa, E-mail: 22805184@nwu.ac.za.

*b Faculty of Engineering, HYSA Infrastructure CoC, North-West University Potchefstroom campus, 11 Hoffman Street, Potchefstroom, 2520, South Africa.**

Abstract: The growing demand for energy in the world causes a lot of pressure on the environment and the resources used to supply the energy. To ensure a continuous, more reliable and environmentally friendly energy supply system the world started to develop alternative technologies including photovoltaic panels, wind turbines and hydrogen fuel cells. The hydrogen fuel cell in combination with batteries has also been used in electric vehicles to minimize greenhouse gas emissions and the strain on crude oil. There is however no control applied on the different energy sources within the electric vehicle system. This project focused on developing a smart controller that would determine the energy source supplying the power demanded by the load. The energy sources include a hydrogen fuel cell, batteries and supercapacitors. The load for the system was simulated on an electronic load using a scaled profile of the power needed by an electronic motor that could be installed in a vehicle. The results showed that by using a smart controller in the system the motor can operate for a longer time than without the controller. Using a controller therefore resulted in increasing both the lifetime and energy supplying time of the energy sources within the system.

Keywords: Fuel cell, supercapacitor, controller , energy

1 INTRODUCTION

The world today relies on coal, natural gas and oil for more than 80% of its energy supply [1]. These resources are however depleted, non-renewable and causes a lot of pressure on the environment. In order to ensure a continuous more reliable and environmentally friendly supplying system, alternative resources should be used. In this paper a hydrogen fuel cell in combination with a supercapacitor and battery is used to supply energy to a load.

The hydrogen fuel cell is an electrochemical device that combines hydrogen and oxygen to produce electrical energy with water and heat as the by-products [2]. A single fuel cell consists of an anode, cathode and an ion conducting electrolyte [3]. The fuel cell used in this project uses a Polymer Exchange Membrane (PEM) as an electrolyte. One of the short comings of fuel cells however is there maximum voltage range of 0.2 V - 0.8 V per cell [4]. This challenge can be overcome by connecting multiple cells in series as was done in this project. Just like hydrogen fuel cells supercapacitors also have a low voltage range. The voltage per capacitor varies between 2.2 V and 2.7 V [5].

Like conventional capacitors, supercapacitors also store their energy in an electric field between two oppositely charged plates. However the plates of a supercapacitor are coated with activated carbon that enables the electrodes to have two layers of charge coating surfaces [6]. The low voltage range drawback for these devices can be overcome by connecting multiple supercapacitors in series. This typology would increase the voltage but would also decrease the total capacitance. Supercapacitors are capable of delivering a lot of power within a short amount of time and are thus known as power density devices. When compared to conventional

batteries the power density of supercapacitors can be 10 to 100 times greater than the power density of batteries.

Batteries on the other hand are known as an energy density device. This means that while a battery cannot supply energy to a load as quick as supercapacitors. They can however supply low power over a greater time period. The recharging time for batteries varies between minutes and hours whereas supercapacitors can recharge within a few seconds.

2 SYSTEM OVERVIEW

This section provides the building blocks for this project that include a controller, energy sources, electronic load, and sensors. The controller would measure the current drawn by the load and the voltage of each power source. Using these readings the controller would then determine which of the three energy sources or combination of energy sources should supply the power demanded by the electronic load. The electronic load would be programmed in order to simulate a scaled profile of an electronic vehicle driving at different speeds, accelerations, declines and inclines.

The main focus of this project is to use a reliable and environmentally friendly power source to supply the majority of the electrical power to a load. A controller would be designed to control the power distribution within the system and ensure that the battery is used to a minimum. The fuel cell would be the primary power source followed by the supercapacitors and then the batteries if needed. Figure 1 illustrates the conceptual design for this project and highlights the major components that would determine the success of the project. These components include the controller, energy source, sensors and the electronic load. Each building block would be discussed in the following chapter.

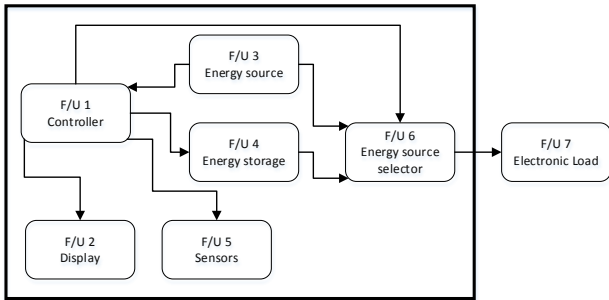


Figure 1: System conceptual design

3 DESIGN

The following section discusses the design of the basic building blocks as shown in Figure.1.

3.1 Controller

The Arduino receives the necessary input signals from the controller board discussed earlier. These signals are read by the Arduino as a value between 0 and 1023, where 0 indicates 0 V and 1023 indicates 5 V. For this reason the input values would first be converted to a 5 V value by dividing by 1023 and multiplying by 5. Depending on the type of reading, voltage or current, the 5 V value would then be multiplied by the necessary scale if it is the voltage reading of a power source. If the reading is a current reading the 5 V input value would be deducted by 2.5 and then divided by 0.04.

Using the voltage value the duty cycle of the PWM signal can be determined. This would ensure that no matter the input of the power source to the buck converter the output would be constant at 12 V. Using the current value the power source can be determine.

The current reading would be used to switch from the fuel cell to one of the other power sources. If the load current equals 3 A the Arduino would disconnect the fuel cell and either connects the supercapacitors or the battery based upon the voltage reading of the two. Should the current further increase to a value greater than 10 A the Arduino would shut down the system due to a current overload condition. Figure 2 illustrates the program flow diagram of the Arduino.

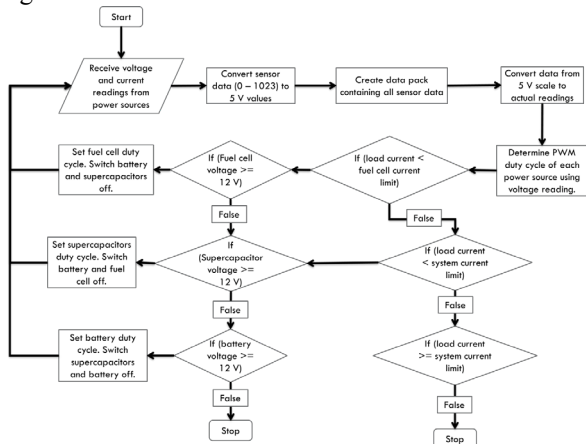


Figure 2: Arduino program flow diagram

3.2 Dc-Dc converter

Each power source has a different voltage. The fuel cell operates at a voltage of 56 V, the supercapacitors will be coupled in series to form a voltage of 16.2 V and the battery has a voltage of 16 V. In this project however the power sources should supply the same load so the voltages of each power source should either be amplified or dropped. The voltage drop of each power source would be accomplished by using a simple buck converter. The buck converter as illustrated in figure 3 would operate in discontinuous mode and would drop the voltage of each power source to 12 V. The transistor used in the buck converter is an IRG4PC50UD n-channel IGBT.

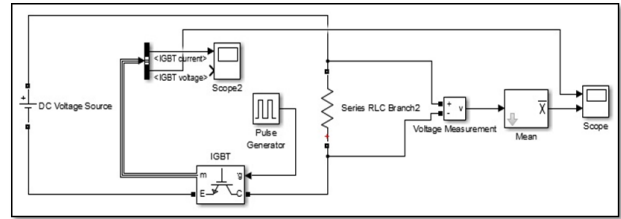


Figure 3: Buck converter

Figure 4 illustrates the simulated results with the PWM signal on the IGBT as 32 kHz signal and a duty cycle of 20%. The input voltage of the circuit is 16 V and it can be seen in the figure that the output voltage is about 3 V. By changing the duty cycle of the PWM signal of the IGBT the output voltage of the dc-dc converter can be controlled.

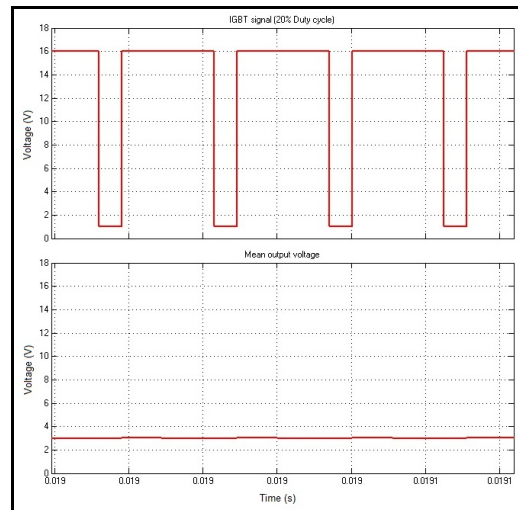


Figure 4: Buck converter simulation results

3.3 Sensors

Hall-effect current sensors were installed in series with the power source and transmitted a signal to the controller. The reading of each power source could then also be added in order to determine the total power demanded by the load. These readings would then be used to determine which power source should supply the power demanded.

Each power source voltage were scaled to a 5 V scale by a simple voltage divider circuit. The scaled voltage was then used as an input to the controller which determined the duty cycle of the PWM signal to the transistor. This would then ensure that each power source has the same voltage.

3.4 Load profile

The load profile used in this project simulates the power demanded by an electric vehicle during different situations. Due to the budget limit the profile is only a scaled version but would still test the concept of the controller. The profile used simulates a vehicle moving on various inclines, declines, and acceleration and deceleration levels and can be seen in figure 5.

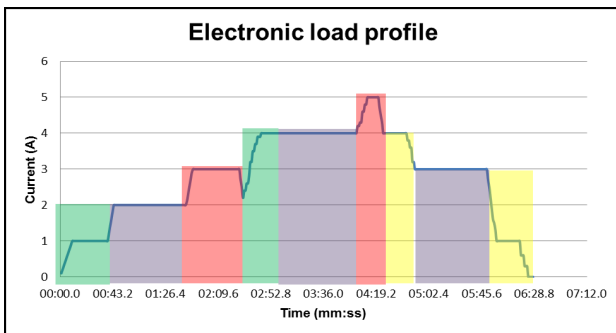


Figure 5: Load profile

The green areas on the graph indicate that the vehicle speed is increasing and simulates the current for the motor to deliver the necessary power. The purple areas simulate a situation where the vehicle drives at a constant speed for the given amount of time. The red areas simulate a situation where the vehicle overtakes another vehicle. Yellow finally indicates a situation where the vehicle speed is decreasing. This profile would test the capability of the controller to switch between power sources in order to supply the load with the required current.

4 IMPLEMENTATION AND EVALUATION

4.1 Hydrogen fuel cell performance characteristics

The fuel cell used in this project is a 300 W PEM fuel cell. The controller of the fuel cell was already designed and implemented in the system. The fuel cell controller is responsible for the purging and regulation of the hydrogen within the cell. Figure 6 illustrates the hydrogen consumption of the fuel cell at different power levels. If the fuel cell operates at 300 W the fuel consumption is 3.9 l/min.

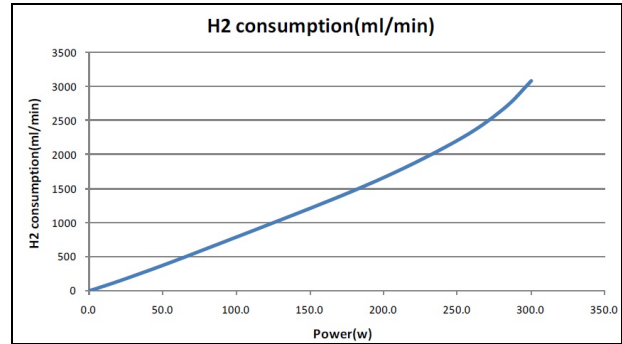


Figure 6: Hydrogen fuel cell fuel consumption

4.2 Supercapacitor charging and discharging profile

Six 3000 F supercapacitors were used in this project. Each supercapacitor has a rated voltage of 2.7 V and a continuous discharge current of 150 A. Connecting these capacitors in series adds up to a capacitor bank of 500 F with a rated voltage of 16.2 V, this voltage was also converted to a constant 12 V with a dc-dc converter. Table 1 shows the time it takes for the supercapacitors to fully charge from 8 V (minimum operating voltage) to 16 V with different current levels.

Table 1: Supercapacitors recharging time at different current levels

Charging current (A)	Time to recharge (min)
2	29
3	21
6	11
10	6
13	4

From the table it can be seen that the higher the current supplied the shorter the recharge time. If the trend in the table is followed it can be determined that with a current of 15 A the supercapacitors would take about 3 minutes to recharge. Due to the limited available current in the system, the supercapacitors cannot be charge within the system. Thus the supercapacitors were pre-charged before tests were done on the system.

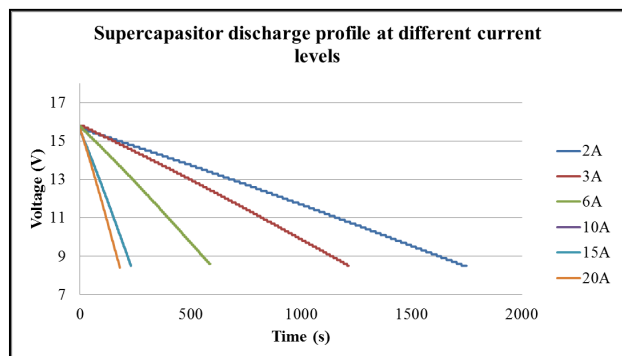


Figure 7: Supercapacitors discharge profile

Figure 7 illustrates the discharge profile of the supercapacitor bank. The graph is plotted with the

supercapacitor bank voltage versus time at varying recharging currents. From the figure it is evident that for the system to be properly tested, the current supplied by the supercapacitor bank should not be more than 10 A. this would allow the supercapacitors a discharge time of 192 seconds.

4.3 Battery charging and discharging profile

A 4000 mAh lithium-polymer battery was used in the system. The battery has a voltage rating of 16 V and a maximum continuous discharge current of 25 A. Table 2 shows the discharge time of the battery at different current levels. To ensure that the system is tested properly the maximum current that would be supplied by the battery was limited at 10 A to 15 A. As with the supercapacitors the battery was pre-charged before tests were done.

Table 2: Battery discharge data

Discharge current (A)	Current delivery time (min)
4	60
8	30
10	24
15	16
20	12

4.4 Supercapacitor test on electronic load

The supercapacitors were fully charged to a voltage of 16.2 V each time a test were done with them and they were used until the voltage drop over them were less than 12 V. Figure 8 illustrates the current demanded by the load (blue line) and the current supplied to the load by the supercapacitors (red line).

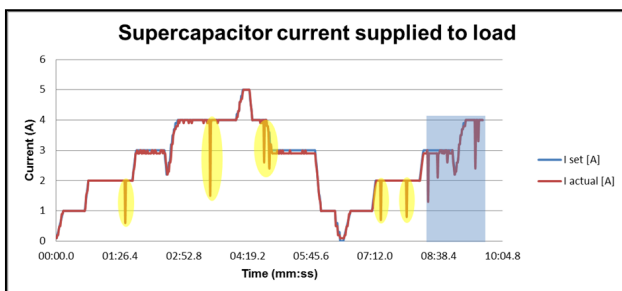


Figure 8: Supercapacitor test on electronic load

The yellow circles highlights instances where the voltage reading taken by the Arduino indicated that the supercapacitors voltages were too low to be used by the load. The Arduino then turned off the supercapacitors and since no other source were connected the current supply to the load were cut-off. This did however only last for a few milliseconds where after the voltage reading received by the Arduino was corrected and the supercapacitors were used to supply the load with the required current.

The blue block in figure 8 indicates a lot of voltage drops. At this point the voltage drop over the supercapacitors was starting to get smaller than 12 V and the Arduino

switched the supercapacitors of due to the low voltage drop over them.

4.5 Fuel cell test on electronic load

The fuel cell were started and allowed to operate for ten minutes before the electronic load was connected. This is to ensure that the fuel cell would supply the high current demand in the short amount of time without the fuel cell's controller from disconnecting the load. If the current demand is too high for the fuel cell the voltage drop over the fuel cell is less than 30 V and causes a voltage drop of less than 0.5 V per cell. The controller of the fuel cell is then programmed to disconnect the load in order to protect the fuel cell from permanent damage. Figure 9 illustrates the current supplied to the electronic load by the fuel cell and it should be noted that there was no current limit on the Arduino. This test was done to see how the fuel cell would react to the load profile by its own. The blue line illustrates the current required by the load and the red line indicates the current supplied to the load.

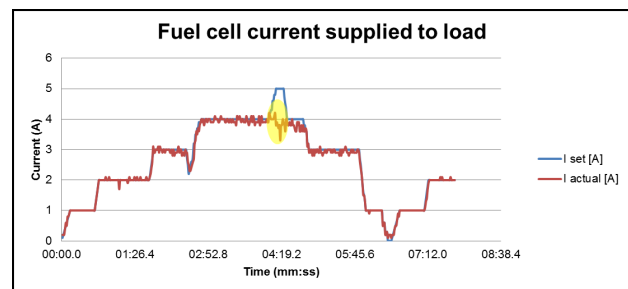


Figure 9: Fuel cell test on electronic load

4.6 Battery test on electronic load

The battery was charged to 15 V and as with the supercapacitors test and the load profile was also repeated. Figure 4-11 illustrates the current supplied to the electronic load by the battery (red line) and the current required by the electronic load (blue line).

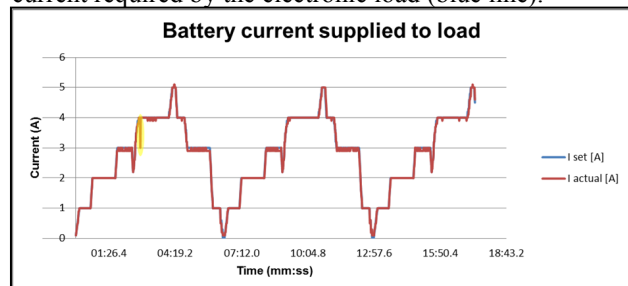


Figure 10: Battery test on electronic load

Figure 4-13 illustrates that the battery followed the profile for about two and a half cycles. After 17 minutes and 21 seconds the system was switched off. One cycle of the profile last for 6 minutes 28 seconds at the end of each cycle the battery has a voltage drop of 0.1 V. Using this information and the fact that for this system the battery can be discharged up to 12 V it can be calculated that the battery would be able to supply the necessary current to the electronic load for 4 hours 18 minutes 40

seconds. At this point the battery voltage would be less than 12 V and the Arduino would switch the battery off. The yellow circle on the graph highlights a current drop that occurred during the profile. The current drop occurred due to a false voltage reading given to the Arduino. The false reading caused the Arduino to think that the voltage of the battery was too low and caused the Arduino to switch the battery off. Since there is no other power sources the current to the electronic load also dropped. This did however only last for a few milliseconds where after the false reading was corrected and the battery was switched on to supply the current to the load. Due to the quickness of the switching the current did not completely drop to zero. It is also clear that during the two and a half load profile cycles the false voltage reading only occurred once.

4.7 Battery and supercapacitors test on electronic load

The following test was done using the supercapacitors and the battery. Before the test was done the supercapacitors were recharged to 16.2 V and the battery to 15 V. These two sources were then used to supply the required current to the load as required and it was up to the Arduino to decide which power source should supply the current to the load. Figure 11 illustrates the current supplied to the load by the power sources. The red line indicates the current supplied to the load while the blue line indicates the current requires by the load.

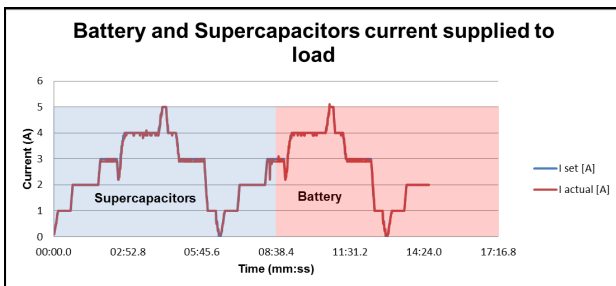


Figure 11: Battery and supercapacitor test on electronic load

The current supplied to the load was divided between the supercapacitors and the battery. The blue block indicates the time the supercapacitor was used to supply the current to the load and the red block indicates where the Arduino switched from the supercapacitors to the battery. The switching took place at 8 minutes 24 seconds at which point the supercapacitors voltage was too low to supply the current to the load and the batteries needed to take over. The system was again stopped to save time because the battery would just follow the profile until it has a voltage drop smaller than 12 V at which point the Arduino would switch off the battery

4.8 Fuel cell and supercapacitors test on electronic load

Figure 12 illustrates the current supplied to the electronic load by the supercapacitors and the fuel cell. The blue

line indicates the current required by the load and the red line indicates the current supplied to the load.

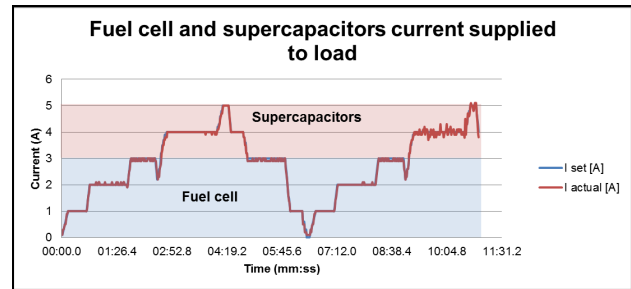


Figure 12: Fuel cell and supercapacitor test on electronic load

Analysing figure 12 the blue block indicates the current supplied by the fuel cell. If the current was equal or greater than 3 A the fuel cell was disconnected and the Arduino switched to the supercapacitors which are indicated by the red block in figure 12. At about 10 minutes 04 seconds the supercapacitors voltage started to get to low and could not continue to supply the system with the necessary current and the Arduino switched the supercapacitors off also since the current required by the load is greater than 3 A the fuel cell could not be switched back on again.

4.9 Fuel cell and battery test on electronic load

Figure 13 illustrates the current supplied to the electronic load by the fuel cell and the battery. The blue line indicates the current required by the load and the red line indicates the current supplied to the load.

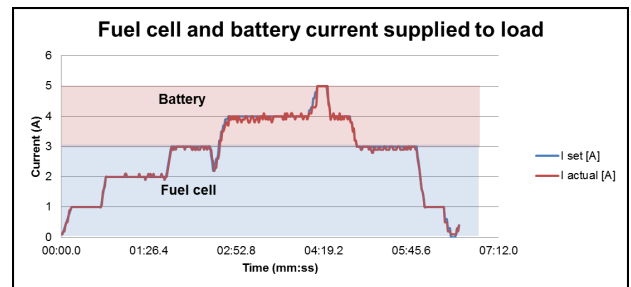


Figure 13: Fuel cell and battery test on electronic load

The fuel cell and the battery only supplied the load for one cycle of 6 minutes 33 seconds. The blue block indicates where the fuel cell supplied the current to the load and the red block indicates where the battery supplied the current to the load. The battery and the fuel cell would follow this profile for as long as the Arduino has power to do the switching. The other two factors that would cause the system to stop would be the hydrogen supply and the battery power.

The hydrogen supply available would last for two hours after which the fuel cell would shut down due to the lack of hydrogen. The battery would last for at least 5 hours which means that if the Arduino has enough power and the hydrogen is finished the battery would then supply the load with the remaining power.

4.10 Fuel cell, supercapacitors and battery test on electronic load

The final test was done by connecting the fuel cell, supercapacitors and the battery to the system. The Arduino would then be able to switch between these three sources as the load current varies. Figure 14 illustrates the current required by the load (blue line) and the current supplied by the system (red line).

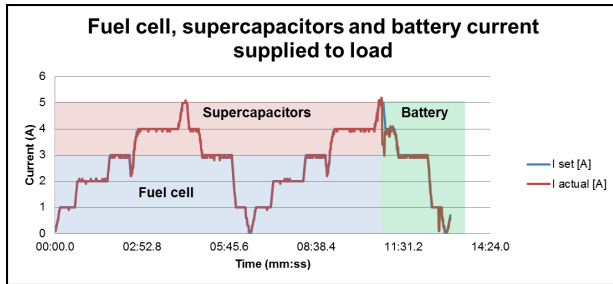


Figure 14: Fuel cell, supercapacitors and battery test on electronic load

The system provides power to the load for 13m05s. The blue block indicates the area where the fuel cell provided the power to the system, the red block is where the supercapacitors provided current to the load and the green block is where the battery provided current to the load. Analysing figure 14 it can be seen that the supercapacitors were able to provide current to the system up until 10m46s. The Arduino then switched to the battery in order to keep supplying the necessary current to the load. The remaining sources available is the fuel cell and the battery. Since the fuel cell in combination with the battery was tested already in figure 13 the fuel cell was not switched back on in order to illustrate that the Arduino would still draw power from the battery. The system would follow the course of the profile until the hydrogen supply is finished, battery supplying the load is discharged or the battery powering the electronics and the Arduino is discharged. In this case the battery supplying the power to the electronics would be discharged first and force the system to stop.

5 CONCLUSION

The use of the controller could extend the life time of each power source and the current delivering time of the system. Due to the budget limit the system could not be tested on a full scale vehicle. The alternative option was to use the three different power sources and connecting them to an electronic load. The load was then programmed to simulate a scaled version of the power needed by an electronic vehicle.

The electronic load simulated different conditions including varying accelerations, inclines and declines. The controller monitored the current delivered to the load and determined which power source should deliver the current to the load.

The tests done indicated that if the Arduino could switch between two power sources that the current supply to the load would be much smoother.

The second benefit would be that the one power source can supply energy to the system if the other is not able to do so. A third benefit when switching between more than two power sources is the current delivery time that is increased.

During the tests the battery and the fuel cell were not tested as to how long they could supply the system with power due to the fact that the battery would be able to supply the profile used to test the system for about 5 hours. The fuel cell would be able to supply the power to the system for as long as the fuel cell receives hydrogen. It was also not within the scope of the project to lengthen the range of the fuel cell, supercapacitors or battery. It was however the scope of the project to design a controller that can switch between the energy sources as the load current varies. The tests done indicate that the Arduino could switch between the energy sources as the demand varies. The tests also indicated that the Arduino would continue to supply energy to the system until all power sources were depleted.

6 ACKNOWLEDGEMENT

I would like to thank my family, friends and Dr. R. Gouws for the support and guidance given to me during this project. I would also like to thank HySA infrastructure for the financial support and guidance.

7 REFERENCES

- [1] John Browne. (2014, February) Global economic symposium. [Online]. <http://www.global-economic-symposium.org/knowledgebase/the-global-environment/the-energy-crisis-and-climate-change/proposals/the-energy-crisis-and-climate-change>
- [2] James Larminie and Andrew Dicks, Fuel cell systems explained, Second Edition ed. England: John Wiley & Sons Ltd., 2003.
- [3] Sossina M. Haile, "Fuel cell materials and components," Sciencedirect, p. 20, August 2003.
- [4] Dr. Colleen Spiegel, Renewable energy science education manue l, Stone Shen and Dane Urry Miro Zhang, Eds. Shanghai, China: Horizon fuel cell technologies, 2009.
- [5] (2013, December) Maxwell. [Online] <http://www.maxwell.com/products/ultracapacitors>
- [6] (2013, December) Gigaom. [Online]. <http://gigaom.com/2011/07/12/how-ultracapacitors-work-and-why-they-fall-short/>

Energy management system in autonomous microgrid

A.A. Aminou Moussavou**, M. Adonis**, AK. Raji**

***Centre for Distributed power and Electronics Systems, Dept. of Electrical, Electronic and Computer Engineering Department, Symphony Way, Bellville South Industrial, Cape Peninsula University of Technology, Bellville Campus, Cape Town 7530, South Africa E-mail: akdech80@yahoo.fr*

***Centre for Distributed power and Electronics Systems, Dept. of Electrical, Electronic and Computer Engineering Department, Symphony Way, Bellville South Industrial, Cape Peninsula University of Technology, Bellville Campus, Cape Town 7530, South Africa E-mail: AdonisMA@cput.ac.za*

***Centre for Distributed power and Electronics Systems, Dept. of Electrical, Electronic and Computer Engineering Department, Symphony Way, Bellville South Industrial, Cape Peninsula University of Technology, Bellville Campus, Cape Town 7530, South Africa E-mail: rajia@cput.ac.za*

Abstract: Renewable energy-based distributed generation (DG) has captivated the power generation sector and on a global scale has become a leading research area. Distributed generation using wind, solar energy or biomass as a source of energy can produce electricity on a small scale. However, a major problem facing renewable energies is that they are highly dependent on weather conditions. Since the power generated by distributed generation depends on the weather conditions, irregularity of production and consumption leads to frequency and voltage fluctuations, and it can become difficult to determine and monitor consumer usage at any given time. The development of a Logic Control Switch (LCS) is to ensure that a stable system is maintained under various loads and resource conditions. An LCS is used to continuously monitor and adjust the load through circuit breakers. It is a good alternative to load balancing for a cluster of villages in a rural area where a microgrid is operating in stand-alone mode. This LCS algorithm is based on the transition state flow chart and ensures the operation of the system within the limit to not cause instability of the system. The flow chart provides easy way using graphical transition state and state chart to establish a set of rules for the system.

Keywords: abc-dq0 transformation, Energy Management System (EMS), MATLAB/Simulink, microgrid, transition state flow, sensitive and non-sensitive loads, PI controller,

1. INTRODUCTION

One of the important characteristics of the modern world is the rapid increase of the population and the associated increase in the demand for electrical energy; this leads to increasing primary energy consumption (non-renewable energy) and consequently to depletion of fossil fuel reserves which are finite [1], [2]. As a result, end-users suffered severe blackouts and ever present electricity price hikes. The traditional power plants can no longer guarantee safe, reliable, and sustainable electricity supply. There is a strong focus on using renewable energy as a better alternative source of energy, especially since in the future it may play a dominant role in the world's energy production and help to tackle the increase of global warming caused by fossil fuel electricity-based production [3]. The concept of a DG was introduced in the late 1990s to overcome the multiple challenges faced by the centralised generation and has since gain popularity. DG generates electrical power from small energy sources (normally less than 50 MW) using non-traditional renewable energy source (RES) such as wind power, solar power, biomass. With this form of generation, transmission line losses are considerably reduced since the power plants are usually very close to

the consumer [4], [5]. Furthermore, the distributed power unit can be directly connected to the customer load or to support the distribution network by providing ancillary services [6], [7]. DG has the advantage that the power production process is very clean. One of the most popular renewable energy sources is solar energy because it is abundant, accessible and easily converted into electricity [8]. The demand for solar energy has increased by 20% to 25% per annum over the last two decades [9]. More importantly the PV system is one of the most efficient renewable energy technologies, especially in remote areas where electricity from the central grid is not available and alternative sources of electricity are expensive [10], [11]. The South African government is planning to provide power to 200000 homes, 100000 small businesses, 2000 clinics and 16800 schools, using PV or solar home systems, as a part of their off-grid electrification program [12].

However, a major problem facing renewable energies is that they are highly dependent on weather conditions. Since the power generated by DG, as well as consumption, depends on the weather conditions, irregularity of production and consumption leads to frequency and voltage fluctuations, and it can become difficult to determine and monitor consumer usage at any

given time. Distributed generation can then be subjected to discrepancies in consumer usage and this can lead to severe stability problem reducing the system reliability. As a result, microgrids powered by DG, operating in a stand-alone controllable system mode, face new challenges in terms of balancing a cluster of loads with the available weather-dependent power. Balancing a cluster of loads by making sure at all times that the entire system operates without overloading, is an essential requirement for the proper operation of a power system. The microgrid load considered in this project is the sum of sensitive and non-sensitive loads, respectively 5 kW and 100 kW, which constitute load requirement of one village; this total load required by a number of villages is called a cluster load.

2. MICROGRID SYSTEM DESCRIPTION

The model of the autonomous microgrid consists of a battery, an inverter, an LC filter and loads (sensitive load power and non-sensitive load power). The sensitive and the non-sensitive loads are both available within the system, the sensitive load power is permanently connected to the system, but the non-sensitive load power is initially disconnected from the system as shown in Figure 2.1. However, the connectivity of the non-sensitive load depends on the magnitude of the input voltage. The LCS monitors the system through the V_d component by determining whether or not the non-sensitive load will be connected to the system through a circuit breaker. This method tends to maintain the phase-to-ground V_{rms} at 230 V, which implies a peak output voltage waveform of 563 V. The size of the load and input power capacity affect the autonomous microgrid system operation; this interaction between load and power is analysed.

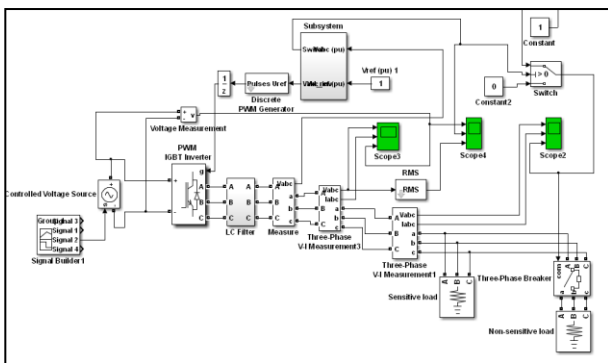


Figure 2.1: Microgrid system

In addition an EMS monitors and optimises the operation of a microgrid system, the system incorporated a dq0 transformation + PI controller; this is shown in Figure 2.2.

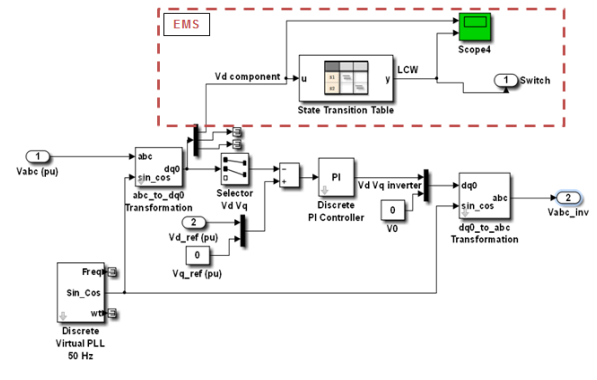


Figure 2.2: EMS integrated with a dq0 transformation + PI controller

3. CONTROL ALGORITHMS OF INVERTER OUTPUT VOLTAGE

3.1 Inverter control using the dq0 transformation + PI controller

The control method for regulating the inverter output voltage relies on the dq0 transformation and the PI controller. The three-phase signal voltage at the inverter terminal is fed to the transformation block $abc \rightarrow dq0$. This dq0 frame lessens the three-phase AC quantities V_a , V_b , V_c into two DC quantities V_d , V_q and in balanced systems, the 0-component is equal to zero. The DC quantities facilitate easier filtering and it is compared to a constant reference of value 1. The error sign from the comparator is passed through the PI controller block as seen in Figure 3.1 below. The controller used, is a combination of the discrete proportional gain k_p and an integral gain k_i , with fixed sample time. The output signal is the sum of the proportional gain, k_p and the integrator gain, k_i . The total signal and k_i and are limited by upper and lower values. Then the controlled signal is converted back to the inverse of the transformation block, $dq0 \rightarrow abc$. The virtual PLL block is connected to both transformation blocks in order to synchronize and maintain the frequency operation at 50 Hz.

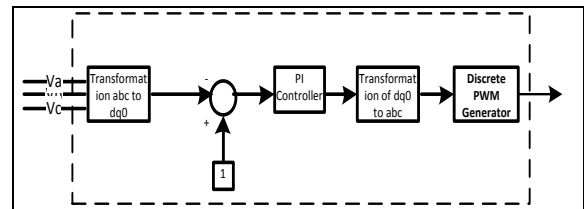


Figure 3.1: dq0 transformation + PI controller

3.2 Energy Management System Control algorithm

The energy management system (EMS) refers to the method of monitoring and optimizing the operation of the system. In practical applications SCADA/EMS is employed for monitoring and control functions. However the EMS is normally used for controlling energy generation and scheduling a programme for an ensemble

of power network applications. EMS can also be used to control the electrical loads in a microgrid. In order to improve the efficiency of the design control, an EMS called logic control switch (LCS) is added to the system grid to further stabilize voltage control.

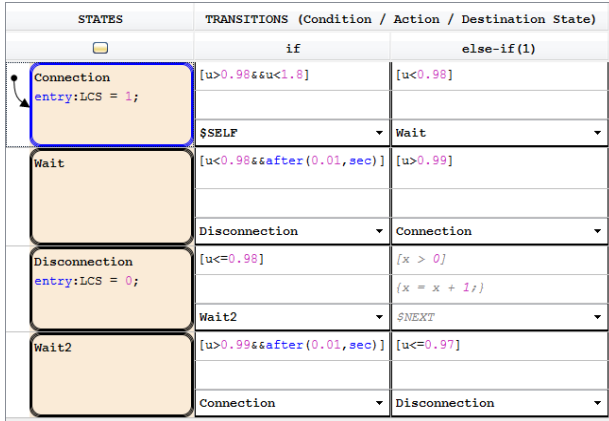


Figure 3.2: EMS transition state

EMS is implemented in MATLAB by developing an algorithm based on a flow chart as shown in Figure 3.2 above and Figure 3.3 below. This flow chart is developed to maintain further stability by automatically connecting and disconnecting non-sensitive loads. The flow chart transits from state-to-state according to the available input power in order to connect and disconnect the loads as seen in Table 3.1 below.

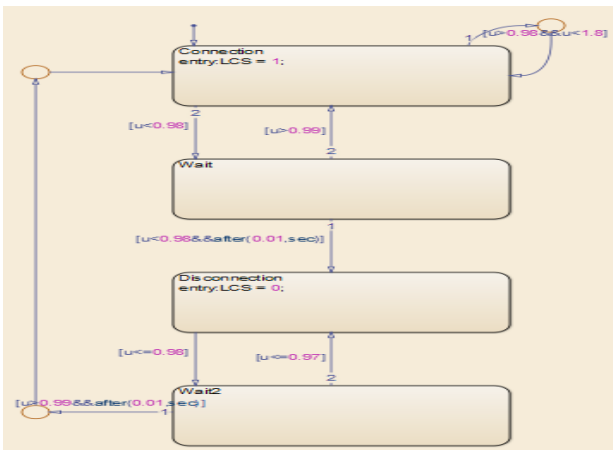


Figure 3.3: EMS flow chart

The EMS controls a breaker switch by connecting and disconnecting non-sensitive heavy load power according to the availability of the input battery voltage. The LCS monitors the system through the V_d component by determining whether or not the non-sensitive load will be connected to the system. When the V_d component from the abc to dq0 transformation and the logic control switch is at normal operation, the phase-to-ground V_{rms} is 230 V and $V_d = 1$. The logic control of the switch is based on the value obtained from V_d component. When V_d is less than 0.98 the switch is **off** and when V_d is greater or equal to 0.99 the switch is **on**.

Table 3.1: State transition matrix

		[u>0.98&&du<1.8]	[u<0.98]	[u<0.98&&after(0.01,sec)]	[u>0.99]	[u<0.98]	[u>0.99&&after(0.01,sec)]	[u<0.97]
1	Connection entry:LCS = 1;							
		Connection	Wait					
2	Wait			Disconnection	Connection			
3	Disconnection entry:LCS = 0;					Wait2		
							Connection	Disconnection
4	Wait2							

4. Simulation results

4.1 Inverter control operating with sensitive and non-sensitive loads and the EMS of the system activated

Figure 4.1 below shows the input voltage, logic control switch and phase to ground V_{rms} .

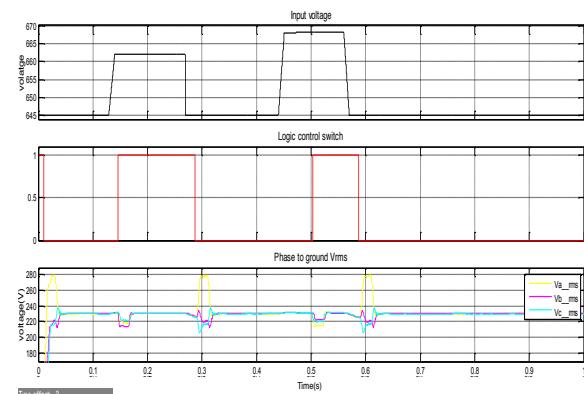


Figure 4.1: Input voltage, logic control switch and phase to ground V_{rms} of the total load with activation of the EMS of the simulated microgrid

The intervals in which the input amplitude voltage changes are 140 to 280 ms and 440 ms to 560 ms, the input voltage is respectively a voltage of 662 and 668 V. The rest of the intervals 0 to 140 ms, 280 to 440 ms, 560 to 1000 ms, the input voltage is 646 V.

The LCS is **on** during the time interval from 130 to 270 ms and 440 ms to 560 ms and it is **off** for the rest of the intervals. The nominal phase-to-ground V_{rms} is maintained at 230 V, the simulation shown on the graph in Figure 4.1 through the simulation except while the LCS changes its state, which occurred at 140 ms, 280 ms, 440 ms and 560 ms. The EMS improved the phase-to-ground V_{rms} value of the system by maintaining it at 230 V. Here, the EMS switches **on** and **off** the non-sensitive load depending on the magnitude of the input power, so that it maintains the V_{rms} value to 230 V except for minor oscillations at the time of LCS switching.

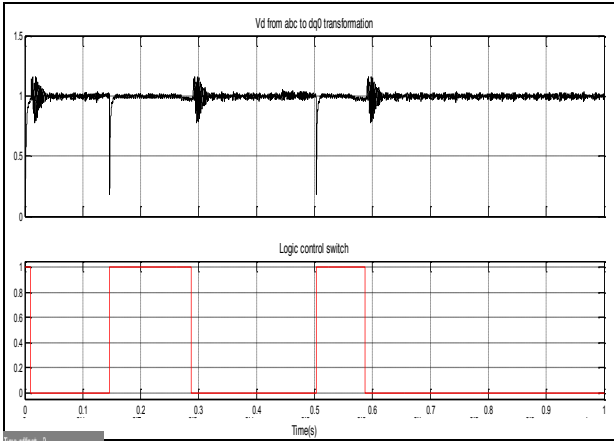


Figure 4.2: The V_d component of the dq0 transformation in the total load with activation of the EMS of the simulated microgrid

Figure 4.2 shows that the V_d component of the dq0 transformation is maintained at a constant value, despite the input voltage variation. The V_d component value of the transformation ranges between 0.99 and 1.01. In this case, the non-sensitive load is added to the system by the logic control switch, when the input voltage available can handle more loads. When the input voltage cannot handle an additional load, the logic control switch is activated to disconnect the non-sensitive load. Initially, both loads are connected to the system but, the LCS removes the non-sensitive load to keep the phase-to-ground V_{rms} at 230 V for each phase. Just after the non-sensitive load is removed at 10 ms, there is an overshoot during the transient period when the PI controller is applied to change the m_a value to effectively regulate the V_{rms} and the voltage at the inverter terminal. So, in the remaining simulation time the non-sensitive loads are connected during the intervals 140 to 280 ms and 510 to 560 ms. When, the non-sensitive load is added it causes a short and a quick voltage drop before the PI controller controls it. This explains the stability of the phase-to-ground V_{rms} as well as the peak output voltage waveform, because the EMS plays a bigger role.

Figure 4.3 presents the peak output voltage waveforms of the inverter terminals. Throughout the simulation, the output voltage presents stability except when the logic control switch changes its state.

When the LCS is switched the output voltage presents some voltage sags and voltage changes respectively at time 140 ms, 510 ms and at 140 ms and 510 ms. The peak current is very low at the time intervals corresponding to the *off* state of the logic control switch and the peak current is 220 A which corresponds to the *on* state of the logic control switch.

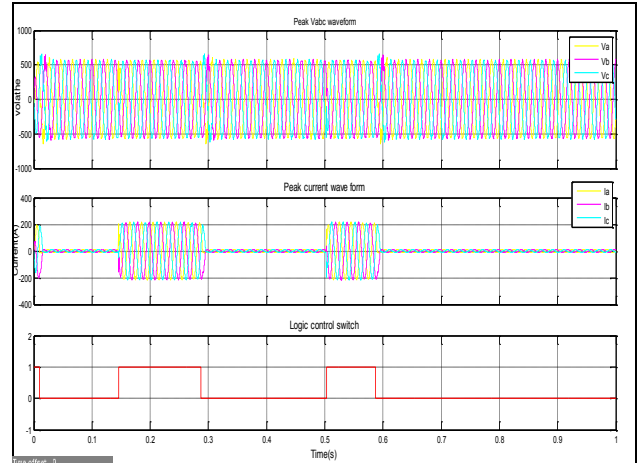


Figure 4.3: peak output voltage and current in the total load with activation of the EMS to the system

5. CONCLUSION

In conclusion the research work explored the modelling of a practical DG-microgrid based on photovoltaics within the MATLAB/SIMULINK simulation environment. The maximum capacity of the system was rated at 1 MW. The work presented focused on the operation of the microgrid in stand-alone mode.

The aim was to maintain the power generated equal to the load power; and to achieve this aim load balancing was found to be an essential requirement for the functionality of the power system by making sure that entire system works devoid of overloading.

Additionally, the stable system with different control mechanisms under various loads and resource conditions was presented.

The Stateflow logical programming environment was used to develop an algorithm for load balancing. The environment gives possibilities of modelling complex algorithms by combining graphical and tabular representations to make sequential decision logic based on state transition diagrams, flow charts, state transition tables, and truth tables.

LCS control is one of the ways of continuously monitoring and adjusting the load through circuit breakers, in accordance to the power generated by the DG-system. It is a good alternative to load balancing for a cluster of villages in rural areas where the microgrid operates in stand-alone mode.

For the simulation model, the sum of sensitive and non-sensitive loads is 5 kW and 100 kW respectively. The LCW control managed to balance the varying load quite well, however in some instances overloading did occur when the load value fell below the minimum load design value.

6. REFERENCE

- [1] B. K. Bose, "Global Warming: Energy, Environmental Pollution, and the Impact of Power Electronics," *IEEE Ind. Electron. Mag.*, vol. 4, no. 1, pp. 6–17, Mar. 2010.
- [2] P. K. Steimer, "Enabled by high power electronics - Energy efficiency, renewables and smart grids," in *Power Electronics Conference (IPEC), 2010 International*, 2010, pp. 11–15.
- [3] C. I. Buritica-Arboleda and C. Alvarez-Bel, "Decentralized energy: Key to improve the electric supply security," in *2011 IEEE PES Conference on Innovative Smart Grid Technologies (ISGT Latin America)*, 2011, pp. 1–6.
- [4] A. Anwar and H. R. Pota, "Loss reduction of power distribution network using optimum size and location of distributed generation," in *Universities Power Engineering Conference (AUPEC), 2011 21st Australasian*, 2011, pp. 1–6.
- [5] J. Martin, "Distributed vs. centralized electricity generation: are we witnessing a change of paradigm," *Introd. Distrib. Gener. Paris HEC* [Www Vernimmen NetftpAnintroductiontodistributedgeneration Pdf](http://www.Vernimmen.NetftpAnintroductiontodistributedgeneration.Pdf), 2009.
- [6] D. Isle, M. Vaziri, M. Zarghami, and S. Vadhva, "Review of Concepts to Increase Distributed Generation into the Distribution Network," in *2014 Sixth Annual IEEE Green Technologies Conference (GreenTech)*, 2014, pp. 118–125.
- [7] V. Bhadoria S., N. Pal S., and V. Shrivastava, "Review of DG definitions and its impact," *Scribd*, 2014. [Online]. Available: <https://www.scribd.com/doc/217615790/Review-of-DG-definitions-and-its-impact>. [Accessed: 29-Oct-2014].
- [8] M. K. I. MN Ambia, "An analysis & design on micro generation of a domestic solar-wind hybrid energy system for rural & remote areas-perspective Bangladesh," pp. V2–107, 2010.
- [9] J. Selvaraj and N. A. Rahim, "Multilevel Inverter For Grid-Connected PV System Employing Digital PI Controller," *IEEE Trans. Ind. Electron.*, vol. 56, no. 1, pp. 149–158, Jan. 2009.
- [10] G. E. Ahmad, H. M. S. Hussein, and H. H. El-Ghetany, "Theoretical analysis and experimental verification of PV modules," *Renew. Energy*, vol. 28, no. 8, pp. 1159–1168, Jul. 2003.
- [11] A. Chel, G. N. Tiwari, and A. Chandra, "Simplified method of sizing and life cycle cost assessment of building integrated photovoltaic system," *Energy Build.*, vol. 41, no. 11, pp. 1172–1180, Nov. 2009.
- [12] IEP, "Draft-2012-Integrated-Energy-Planning-Report-an-Executive-Summary.pdf." Department of energy, 2013.

EVALUATION OF SMART TECHNOLOGY FOR THE IMPROVEMENT OF RELIABILITY IN A POWER DISTRIBUTION SYSTEM

GC Dumakude*, AG Swanson**, R Stephen* and IE Davidson***

* Eskom Holdings SOC Ltd, Transmission, Block C 1st floor, 1 Langford road, Westville, 3630, South Africa

** Discipline of Electrical, Electronic and Computer Engineering, School of Engineering, University of KwaZulu-Natal, Durban, South Africa

*** Eskom Centre of Excellence in HVDC Engineering, HVDC/VRTC/Smart Grid Research Centre, School of Engineering, University of KwaZulu-Natal, Durban, South Africa

Abstract: This paper evaluates the application of smart technologies with the aim of improving the reliability of Eskom’s medium voltage (MV) networks. The intent is to reduce the outage duration, frequency of outages, maintenance costs, and operational expenditure while improving overall system performance. To achieve this, a methodology is developed and verified by comparing the calculated results with DigSilent PowerFactory simulations using a sample MV network. The reliability of a distribution system depends on a number of factors including the location (urban or rural), environment, the type of system and the type equipment installed. Events that affect the customer supply include failure rate of equipment and the duration of an outage. The outcome of the application of smart technology on MV network will influence on the availability of customer supply as the technology could not only be used to reduce the failure rate of the system but also decrease the time spent on fault finding and maintenance expenses due to greater visibility system wide.

Keywords: Network reliability, MV network, Distribution Automation (DA), smart technology, System Average Interruption Frequency Index (SAIFI), System Average Interruption Duration Index (SAIDI).

1. INTRODUCTION

The distribution system is an important part of the total electric system, as it provides the final link between the bulk system and the customer. In many cases, these links are radial in nature and therefore susceptible to outage due to a single event. It has been stated that most of interruptions that occurs in the power systems are due to failures in the distribution system [1].

An analysis of faults for the KwaZulu-Natal Operating Unit (KZN OU) MV network was conducted for the period January 2010 to January 2014 and the outcome of the analysis is summarised in Table 1 below.

Table 1: MV network fault causes

#	Cause of Outage	Frequency of Occurrence (%)
1	Transient or temporary faults, defined as greater than 2 minutes and less than 1hr long	25%
2	Conductor failures	15%
3	Jumper failures	14%
4	Transformer failure, pole mounted	9%
5	Structure failure e.g. pole , cross arm	8%
6	Insulator failure	4%
7	Isolators (links on the network)	3%
8	Fuse failure	2%

Currently the KZN OU has more than 1200 single MV feeders (i.e. 1 kV – 33 kV), which equates to 45 000 km of length supplying more than 805 000 customers, most of which has limited redundancy and back-feed capability. A test network model has been developed to validate the application of several smart technologies. This test network is small but representative of the radial MV network.

Eskom Distribution network topology, configuration, customer numbers and distribution on the network, operating environment and other network topology related variables are very different from that of utilities abroad, and hence other smart devices that work well in other countries may not be compatible for Eskom Distribution network. This is one of the findings that were distinguished as different technologies were being modelled. It should also be noted that the analysis involves unplanned outages only, planned outages does not form part of this study. The purpose of this study is to evaluate and recommend suitable technology for the existing infrastructure in the MV network for the purpose of enhancing overall system performance.

2. APPROACH

Historical and predictive approaches are the two power system reliability assessments that are predominantly used [1]. Both approaches are applied whereby expected

performance is modelled, given the specific network topology, past performance, customer numbers, operating environment, etc.

A number of specialised software packages are available in the market for reliability modelling of electrical networks including PowerFactory, ReticMaster, and PSS/E. These packages require detailed network models to model the expected reliability of power networks. KZN OU network engineers have introduced PowerFactory for the modelling of all MV networks. This is enabled by the Smallworld export to Powerfactory which was not available in the past. Furthermore there were other data incomplete issues that were experienced with Smallworld export to PowerFactory that were later resolved [2]. The accuracy of PowerFactory results were compared to calculations. Practical assumptions were made on the analytical approach with regards to failure rates, travel times to site; travelling speed for fault finding, repair times based on performance history of the feeders as well as interviews and interactions made with site engineers and operators.

Visits were made to different sites at Stanger Technical Service Centre (TSC) KZN OU to validate the information. A key assumption is that KZN OU MV networks are maintained and operated well according to Eskom maintenance standards and are fairly in a good condition. It was also noted that most substations have Remote Terminal Units (RTU), meaning that the fault finding and sectionalising time will be reduced through remote switching. Network control operators will be able to pick up equipment alarms which make the substation more visible, which is key to any smart technology.

A number of network components including transformers, lines, isolators, and fuses are used and applied in a systematic manner to calculate expected downtime experienced by the customer supplied on different connections of the network with different smart technology interventions. The focus of this study is on the MV feeders connecting the distribution substations to the customers. Customer, substation equipment and sub-transmission networks are excluded.

This approach recognises the fact that key network components such as length of line, number of transformers, location of fuses and breakers, etc. have a significant impact on the reliability of a feeder [8], [9]. Therefore the outcomes from this approach provide the intended “realistic anticipated” performance based on the application of different technologies on the MV network.

3. MODELLING METHODOLOGY

The distribution network modelling includes all feeders up to 33 kV. The detailed steps are described below.

3.1 List of smart technology evaluated

Table 1 presents a list of smart technologies that are currently available in the market to improve MV network reliability [5], [6]. Some of this technology is used already in utilities abroad. The combination of these smart technologies is commonly referred to as Distribution Automation (DA); which is one of the major aspects in smart grid [3].

Table 2: List of available smart technology [7]

Device	Impact on number of faults	Impact on duration	Impact on number of customer interrupted
Smart fuse saver	Will reduce number of faults by improving fuse failure rates, as a fuse tends to operate for temporary faults	Will reduce the outage duration where fuse has blown due to transient fault. Will also provide visibility to SCADA for all fuse operations without intervention from the customer.	No impact on number of affected customers
Transformer remote monitoring	No impact on number of faults	Will reduce the duration by a significant amount because it will provide visibility for all transformer interruptions without customer interventions.	No impact on number of affected customers.
Smart fault indicators	No impact on number of faults	Will reduce the outage duration by a significant amount	Will reduce the impact of number of customer affected, by quick identifying the faulted section. This will reduce the sectionalizing and fault finding time.
Automatic feeder switches	Will reduce the number of faults through self-healing	Will reduce the duration of the outage	Will reduce the impact of number of customers affected through self-healing
Fault Location Isolation & Service restoration (FLISR)	Will reduce the number of faults through self-healing and alternative source transfer	Will reduce the duration with a significant amount	Will reduce the impact of number of customers affected through self-healing
AMI & Smart meter for outage detection	No impact on number of faults	Will reduce the duration with a significant amount, by providing visibility all the way to the consumer.	No impact on number of affected customers.

3.2 Test network model used

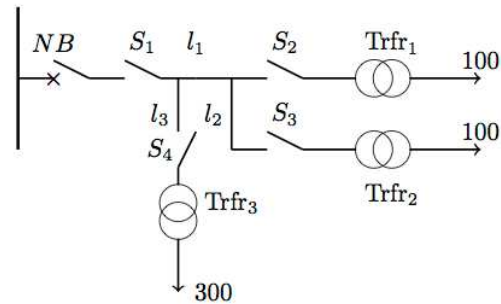


Figure 1: Test network

The network in Figure 1 was developed by the author and it resembles a typical radial network, the base network consist of disconnect switches. KZN OU is fusing their MV transformers and the intent is that for transformer faults the fuse should operate thus isolating the faulty transformer from the rest of the network [10]. Therefore all the different smart grid interventions will be evaluated on both a fused and an un-fused network

Table 3: Equipment details

Equipment count	
#Transformers	3
#Switches	4
#Overhead lines	L1 and L2 at 50km each, L3 at 20km
#Customers	500
#Breakers	1

3.3 Distribution network methodology

The methodology used to model the distribution network, (including all feeders up to 33 kV) is described below.

3.3.1 High level system model

The key is to analyse network's characteristics, configuration and customer type before implementing a specific technology.

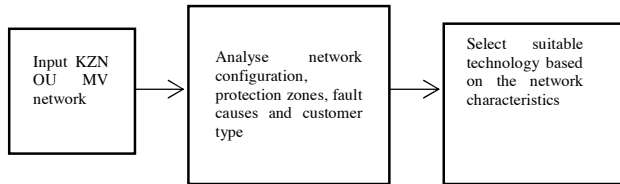


Figure 2: High level system model

KZN OU is divided into three zones i.e. Pietermaritzburg, Newcastle and Empangeni. The sample network that will be used will be taken from Pietermaritzburg zone since it consists of a combination of networks with different characteristics. Each zone consists of different components which can fail and result in an outage on a feeder.

3.3.2 Failure rates

Failure rates values used were taken from KZN OU. These assumptions were based on the historical analysis of the KZN OU MV network failures by the local engineers. High number of component exposure and long length of lines will have a higher exposure to faults hence

failure rates for lines and cables are assigned per kilometre.

3.3.3 Equipment exposure

The typical rural electrical network has long overhead line that covers large geographical area with a large number of components e.g. transformers, switches, fuses etc. It requires long travel and fault finding times during unplanned outages and also has a low customer density. Therefore requires a lot of expenditure to maintain while the revenue is low. The urban network consist of short overhead line or underground cable which covers a small geographical area with a small component count e.g. transformers, fuses etc. It has a short travel and fault finding times with high customer density. Both these networks will greatly benefit from smart technology application in terms of self-healing the network and isolate the faulted section from the rest of the network with a little or no human interventions. It has been observed that the number of equipment exposure, line length as well as number of customers plays a major role in network reliability.

3.3.4 Equipment distribution

The reliability modelling applied in this study does not take into account the actual contribution of customers along the length of the feeder due to the unavailability of this information at the time of this study. The homogenous model is therefore considered, meaning that all customers are evenly distributed beyond all transformers, as per the total number of customers on a specific feeder.

3.3.5 Reliability measures

The degree of reliability may be measured by the frequency, duration, and severity. It is fairly common practice in the electric utility industry to use the standard IEEE reliability indices such as Customer Average Interruption Duration Index (CAIDI), System Average Interruption Frequency Index (SAIFI), System Average Interruption Duration Index (SAIDI), etc. for reliability measures. Eskom also use these indices to track and benchmark reliability performance against other utilities abroad. There are also internal indices that Eskom is using such as SAIDI-N and SAIFI-N where transformer interruptions duration and frequency are measured [4]. Reliability indices also allow customers and investors to make an informed decision about the security of supply.

3.3.6 Unplanned Outage duration

The overall outage duration for each fault can be broken down into single steps of events as mentioned on figure 3. SAIDI and SAIFI values are calculated from the moment the fault is captured in the system. Each of these steps is further explained below.

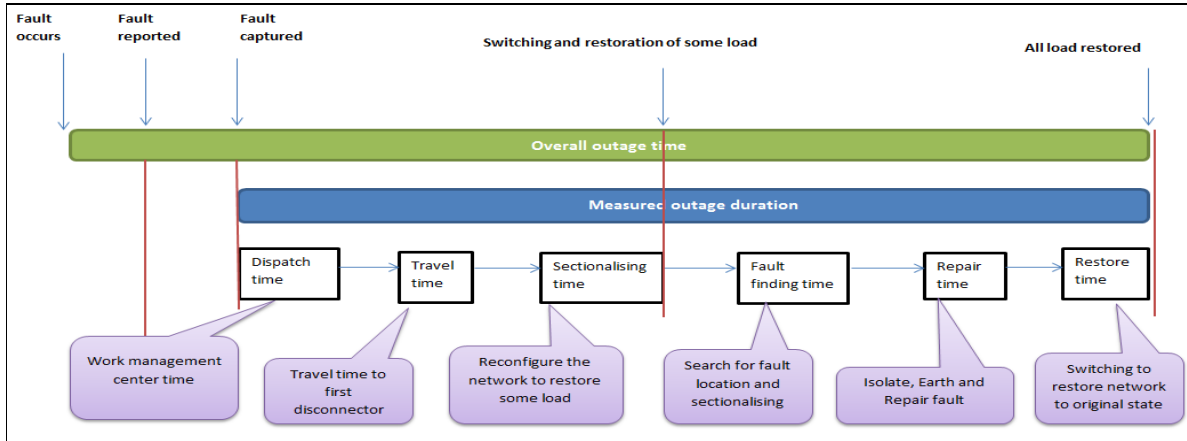


Figure 3: Key components for overall outage duration on MV network

Fault occurs: this is the time before the fault is reported and captured on the system, only known to the customer or through the RTU. To quantify the exact time depends on the individual customer reaction to report the fault or through network visibility on the RTU. Hence SAIDI and SAIFI are calculated based on the measured outage duration and not overall outage duration. Some of the smart grid benefits may be realised during the overall outage duration.

Dispatch time: the call has been logged on the system during this period through customer reporting or through Remote Terminal Unit (RTU) alarms at the station and the operator has been advised to travel to site.

Travel time: the time for an operator to travel to site to operate the first disconnector or isolator.

Sectionalising time: customers are partially restored during this period through back feeding and network reconfiguration. The operator is performing switching (opening and closing of breakers and disconnectors) on different locations along the network with the aim of isolating the faulted part of the network.

Fault finding time: the faulted section is already isolated from the rest of the network at this stage; an operator is doing a visual inspection on the components with the intent of identifying the faulted equipment.

Repair time: the faulted equipment is repaired at this stage and the customers affected are only those connected to that section. Fairly reasonable assumptions for different equipment's were made.

Restore time: after replacing or repairing the faulted equipment the network is returned to its original state.

The combination of these intervals represent the overall outage duration that is experienced by the customer from the moment the fault occurs. Planned outages are when maintenance work is being undertaken. Therefore the total outages that are experienced by the customer on the MV feeder include both planned and unplanned SAIDI.

$$U_D = SAIDI_{unplan} + SAIDI_{plan} \quad (1)$$

Where:

U_D = total outages experienced by the customer on the MV network

$SAIDI_{unplan}$ = unplanned SAIDI for a specific feeder

$SAIDI_{plan}$ = planned SAIDI for a specific feeder

3.4 Unplanned SAIDI and SAIFI approach

The methodology to determine unplanned SAIDI and SAIFI for a specific feeder was derived. The unplanned SAIDI algorithm for a feeder with fuses as well as smart technology interventions.

$$SAIDI = \frac{CID}{Cust_T} \quad (2)$$

$$CID = (line \times FR_L + Disc \times FR_D fuse \times FR_F) \times Cust_D + (line \times FR_L \times R_{imeL}) \times Cust_R + (fuse \times FR_F \times FR_F) \times Cust_R + (Disc \times FR_D \times R_{imeD} \times Cust_R) \quad (3)$$

The unplanned SAIFI algorithm is similar to SAIDI except that frequency is considered instead of duration. The SAIFI algorithm for a feeder with fuses as well as smart technology intervention is shown below:

$$SAIFI = \frac{CI}{Cust_T} \quad (4)$$

$$CI = (line \times FR_L \times Cust_D + fuse \times FR_F \times Cust_D) + (Disc \times FR_D \times Cust_D) \quad (5)$$

Where:

Line = total line length in km (km)

Fuse = total number of fuses on a feeder

Trfr = total number of transformers on a feeder

Disc = total number of isolators on a feeder

Cust_D = customer interrupted for dispatch, travelling and sectionalising time

Cust_R = customer interrupted for fault finding, repair and switching the line back to its original state

Cust_T = total number of customers in a specific feeder

CID = customer interruptions duration

CI = customer interruptions

FR_L = line failure rate (occ/km/a)

FR_D = Isolator failure rate (occ/a)

FR_F = fuse failure rate (occ/a)

FR_T = transformer failure rate (occ/a)

D_{time} = sum of dispatch, travelling and sectionalising time

R_{timeT} = sum of fault finding, transformer repair and switching the line back to its original state

R_{timeL} = sum of fault finding, line repair and switching the line back to its original state

R_{timeF} = sum of fault finding, fuse repair and switching the line back to its original state

R_{timeD} = sum of fault finding, isolator repair and switching the line back to its original state

3.5 Results of different reliability improvements interventions

During system modelling, it was evident that when fault occurs, the smart technology has the ability to analyse and restore supply to a healthy part of the network

without human intervention. Minimise operational costs and improve overall system efficiency.

Figure 4 and 5 below show the placement of automated feeder switches in different locations along the feeder. This is a crucial step as the position of automated feeder switches has a big impact on SAIDI and SAIFI values. It was also noted that network length as well as number of customer connected has a big impact on network reliability.

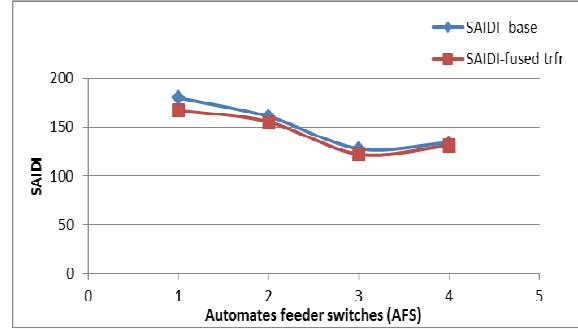


Figure 4: Automated feeder switches - SAIDI

Different SAIDI and SAIFI values with different position of automated feeder switches. In this network the best performance is achieved at point number 3 when the automated feeder switch is placed on line 2 (L2). Improved results are achieved on the network with fused transformers.

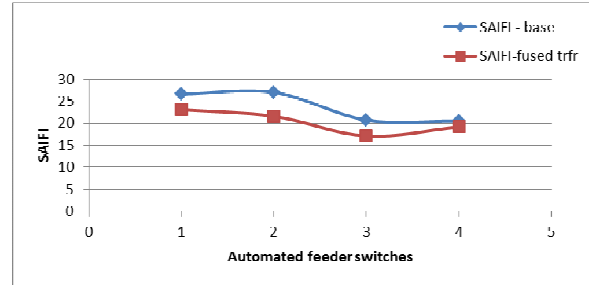


Figure 5: Automated feeder switches - SAIFI

Combination of smart technologies is applied in figure 6 and 7. For Distribution Automation only a certain number of technologies can be applied to improve network's reliability, thereafter it is not be financially viable to add more technologies as the performance is no longer improving. This is apparent on figure 6 below SAIFI values are staying constant between point number 3 and 4 regardless of additional technologies however on the same network SAIDI has improved as shown on figure 7. This demonstrates that some technologies improve SAIFI only and others improve SAIDI only while other technologies improve both indices.

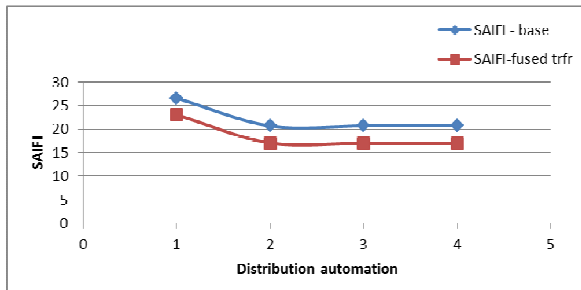


Figure 6: Automated feeder switches with Smart fault indicator and remote transformer monitoring – SAIFI

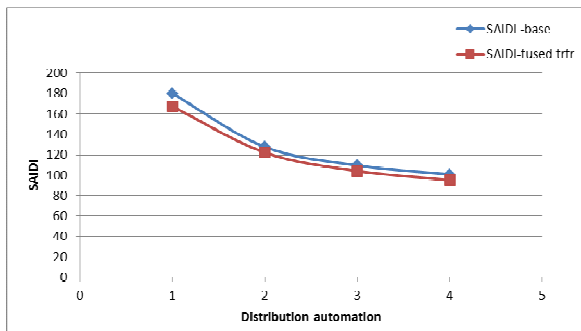


Figure 7: Automated feeder switches with Smart fault indicator and remote transformer monitoring – SAIDI

3.6 Discussion of different smart technology interventions

High level benefits of application of smart technology in MV network are discussed below. The impact of the combination of these technologies was also evaluated.

3.6.1 Application of Smart fuse saver

This device opens and clears a fault in as little as a half-cycle before the fuse operates for a transient fault as fuse is unable to distinguish between temporary and permanent faults, it blows on all faults. It can also be easily integrated with RTU to provide visibility for any operations taking place on the fuse. KZN OU is currently fusing the transformers only, by application of expulsion type fuse on medium voltage overhead line network.

The intention is that when a transformer fails, ideally the fuse should operate isolating the faulty transformer from the rest of the network. The installation of smart fuse saver in series with the fuse in this instance was evaluated. The benefits for this device are achievable when the fuse is applied as a spur line protective device. This device is therefore not a recommended solution as Eskom KZN OU is only fusing the transformers and not using fuse as a spur line protection.

3.6.2 Application of Transformer remote monitoring

During unplanned outages or interruptions when the network breaker trips, most of the time is being spent patrolling the lines and fault finding. The patrolman will first start by sectionalizing to isolate the faulted section from the rest of the network and back feeding some customers. If it is a transformer fault, then on the faulted section the patrolman has to drive on every single transformer to identify which one has faulted. The application of transformer remote monitoring device on the test network has reduced sectionalising as well as fault finding time during transformer faults as it provide visibility for any outages taking place in the transformer. The fault finding time contributes significantly on outage duration as the operator has to at least drive at 20km/h to perform visual inspection. In this instance fault finding time was eliminated as the transformer failure is visible to the RTU. Therefore this is the recommended solution for networks prone to transformer failures.

3.6.3 Application of Smart fault indicator

The integration of this device with RTU, remotely reports the passage of fault current. This has also reduced sectionalising as well as fault finding time by indication of where the faulted section is during unplanned outages. Two smart fault indicators are installed at line 2 and line 3. This is recommended for all networks as it indicates the section of the network where the fault is located.

3.6.4 Automatic feeder switching (auto reclosers and sectionalisers)

Integration of auto reclosers with RTU reduces sectionalising time by isolating the downstream network through the remote switching. All loads on upstream breakers remain supplied. This is recommended for all networks as it gives an indication of whether the fault is downstream or upstream. The position of these devices along the network is very important as it trips and isolates the downstream network during fault conditions. Different positions were modelled and verified that optimum performance is achieved when it is placed at Line 2.

3.6.5 Fault Location Isolation and Service Installation (FLISR)

This technology is ideal for the network with a back feed capability. It provides optimal feeder re-configuration during unplanned outages. It detects feeder faults; determine the fault location (between 2 switches), isolate the faulted section of the feeder (between 2 switches) and restore service to “healthy” portions of the feeder. It provides the facility of restoring some customers before patrolmen arrives to site. The network may require additional tie points to accomplish FLISR. This technology was not modelled in this case as it is best

suited for networks with an alternative source, it will however be modelled during the next phase of this research.

3.6.6 AMI and Smart meter for outage detection

Advanced Metering Infrastructure (AMI) is an integrated system of smart meters, communications networks, and data management systems that enables two-way communication and provides visibility between utilities and customers. It will reduce sectionalizing and fault finding time.

4. CONCLUSION

The optimum results are achieved when the smart technology is applied on the network with fused transformers. Figure 6 and 7 shows the 47, 2% and 35, 8% improvement on SAIDI and SAIFI respectively for Distribution Automation. It should be noted that results are network specific and only one automatic feeder is installed at this instance. Different results may be obtained for different network configurations. However to achieve maximum benefits of the smart technology, it is recommended to first analyse some key factors including network topology, configuration, customer type, number of customers per single breaker operation and history of faults of the network. A reliable communication link is needed for the effectiveness of a smart technology. These benefits include:

- Transformer remote monitoring for reduced sectionalising and fault finding time
- Automated feeder switches, solutions for a self-healing grid which reduce fault finding as well as maintenance costs. Also minimise number of customers exposed to a fault.
- Fault indicators for complete fault location and reduced fault-finding time

During the next phase of this research a more complex and interconnected sample network will be analysed.

5. ACKNOWLEDGEMENTS

The authors would like to thank Johanette van der Merwe for her support in modelling of smart technology on PowerFactory and Eskom for their support of the university through the Eskom Power Plant Engineering Institute programme.

6. REFERENCE

- [1] Roy Billinton and Ronald N. Allan, *Reliability Evaluation of Power Systems*. New York and London: Plenum Press, second edition, chapter 7, pp. 220 - 247, 1996.
- [2] Martin Cameron, Dieter Gutschow and Johanette van der Merwe, "Network segmentation and Reliability planning criteria," Cape town, pp. 1- 413, January 2014.
- [3] C Carter Brown, "Quantifying the reliability impact of Smart Grid Technologies on Medium Voltage overhead networks," *Proceedings: 7th Southern African Regional Conference - CIGRE*, Johannesburg, pp. 1- 11, 2012.
- [4] Nelson Nunes. Eskom Standard - Distribution Network Performance KPI definition, pp. 1- 29, August 2010.
- [5] Jarkko Holmlund. Practical experience of a self-healing grid, May 2013.
- [6] U.S. Department of Energy, "Reliability improvements from the application of Distribution Automation technologies," United States, pp. 1- 45, December 2012.
- [7] U.S Department of Energy. Smart grid.gov. [Online] "<http://www.smartgrid.gov>" "<http://www.smartgrid.gov>," December 2012.
- [8] Johanette van der Merwe and C Carter Brown, "Simplified sub-transmission reliability modelling as a basis to prioritise system level investment," in *CIGRE, 7TH Southern African Regional Conference*, Cape town, South Africa, pp. 1- 11, 2013.
- [9] Carter Brown C, Nunes N. and Cameron M.J, "Determining a relationship between Eskom Distribution network performance improvement and infrastructure investment cost," in *C I R E D, 20th International Conference on Electricity Distribution*, pp. 1- 4, June 2009.
- [10] Velosin Govender, "The application of expulsion type fuses on MV overhead line networks in KZN OU," *Eskom KZN OU, Durban, Technical Bulletin KZN13VGB020*, pp. 1- 8, August 2013.

COST EFFECTIVE SOLUTION FOR A SMART HOUSE ENVIRONMENT

D.Horne* , Q.Machin[†] , M.Shuma-Iwisi[‡] and I.Hofsajer[§]

Faculty of Engineering and the Built Environment, Private Bag 3, Wits 2050, South Africa

* *E-mail: daniel.l.horne@gmail.com*

[†] *E-mail: quinton.machin@students.wits.ac.za*

[‡] *E-mail: mercy.shuma-iwisi@wits.ac.za*

[§] *E-mail: ivan.hofsajer@wits.ac.za*

Abstract: An application, named Smarthome was designed and built as a low cost solution for a smart house environment. The system consists of two components, the back-end and the front-end. The front-end contains the power data storage, user interface, utilities override mechanism (UOM) and high usage warning system (HUWS). The back-end entails the construction on the power measuring unit, power supply, charging circuit and appliance control. The system developed met its basic requirements of user interaction and utilities control, however the algorithm developed for the UOM needs to be refactored to account for user preference. The power measuring chip (CS5463) inaccuracies were reduced from an average of 16.92% for voltage and 19.44% for current to 2.76% for voltage and 2.98% for current by placing the measuring circuit on vero-board. The product's aim at ease of use makes it a good candidate to install in low-cost housing to help educate the nation on cost effective power usage.

Key words: Smart energy, Smart house, Home automation

1. INTRODUCTION

Since the introduction of load shedding in 2008, South Africa has been in an energy crisis [1]. The price of fossil fuels continually increases which in turn increases living expenses [2]. In order to use energy more effectively the development and implementation of smart homes needs to become a focus of the country. The project objective was to develop a cost effective smart house environment. The developed system allows user control over appliances connected to the application. The system gave the utilities a high level of control as well as providing feedback to the via an interface and warning message system.

2. PROJECT BACKGROUND

In South Africa between 1994 and 2012 the number of households with access to electricity increased from 8.8 million to 13.2 million [3]. Though these numbers are a good indication of growth in South Africa, the effect on the power grid became prevalent in 2008. During 2008 the rolling blackouts that occurred because of the demand on the grid cost South Africa around R 50 bn [1]. This resulted in increases of the energy tariffs in order to fund the building of new power stations to meet South Africa's energy demands [1, 3]. With electricity access increasing making the South African population more conscious of their energy usage is vital. The new power stations namely Medupi and Kusile are still under construction and have an estimated time of completion in 2017 and 2019 respectively. Hence the demand in South Africa will not be resolved until the first of these power stations come online. The backlog of connections needing to be made totals 3,388,156 in Gauteng alone [3]. Therefore there is a need

to build new generating power stations and to instill energy efficient methods through the change of user behavior. The platform which will allow for the development of a more energy conscious nation is through the development and implementation of a smart house environment. A smart house environment is a home that uses information and communications technology (ICT) to control energy supply and demand. This can improve living standards by helping to reduce energy bills [4]. A smart house is equipped with a mechanism to visually display energy consumption which aids the resident to better understand their usage pattern as well as how to save energy more effectively [4]. Smart houses can also be equipped with energy storage units in order to facilitate efficient energy use [4].

3. SYSTEM OVERVIEW

The developed Smarthome application is made up of the front-end and back-end components as described by Table 1. The system was split in this way in order to separate the components of the system for easier development, debugging and modularity. Figure 1 gives a high level description of the functioning of the system. This diagram includes both the high usage warning system (HUWS) and the utilities override mechanism (UOM).

4. FRONT-END

4.1 Web-server and web-service

A web-server was setup on the Raspberry Pi so that the website and data could be remotely accessed. Nginx was

Table 1: System overview

Front-end	Back-end
Web-server, Web-service	Measuring Power
Storing Power Information	Feedback to the client via SMS
High Usage Warning System (HUWS)	Linking between The front-end and back-end
Utilities Override Mechanism (UOM)	Appliance Controls
User Interface	-
Appliance Control Page	-

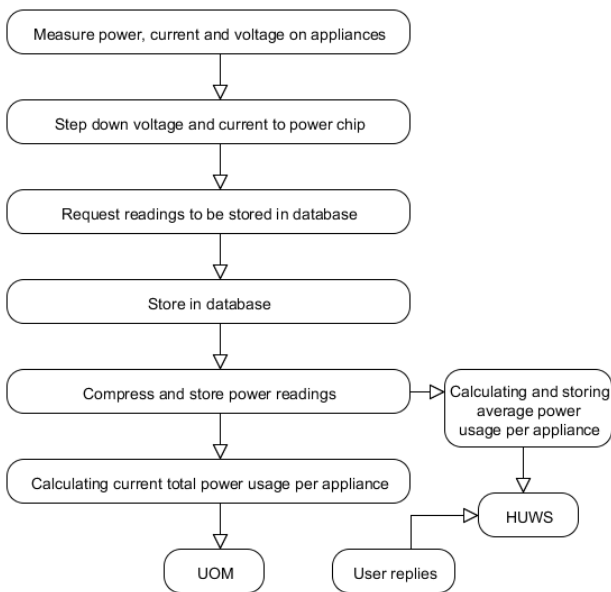


Figure 1: System overview

chosen as the web-server as this is lightweight web-server [5].

The communications from the website to the server were accomplished using as RESTful web-service. RESTful is an architectural styled web-service based on four principles; resource identification through URI, uniform interface, self-descriptive message and stateful interactions through hyperlinks [6]. The RESTful architecture has allowed for a modular and easily modifiable API so that new functionality can be added and old functionality removed in a systematic manner. The API was written using PHP.

4.2 Database

MySQL server was implemented as the database to store the power measurements of the appliances. Each appliance installed on the system has its own table for storing the power measurements received from the back-end. These

tables are central to the system as they provide the data for graphing power usage, average power usage and total power usage per appliance to be calculated.

4.3 Power storage

Eskom describes 5 power usage periods per day in average household [7]. Three low periods 12am-5am, 10am-4pm and 8pm-12am and two high periods 5-10am and 4pm-8pm. Appliances power usage would be stored as an average used in each period. The reason for doing so is to limit the amount of data that is needed to be stored per appliance as the Raspberry Pi has limited storage space. Algorithms for compressing incoming data and then calculating average and total usage were written.

Data compression: In the data compression algorithm the back-end writes power readings to the database every 7 seconds. This amount of data is not necessary to obtain information about basic power usage for each appliance, so the data is compressed. The system starts by checking what power usage period it is in currently. The system then takes an average of all the readings per appliance that are in the same power usage period. Finally the system converts these averages from Watts to kW/h and stores them. This compressed data is used for calculating total power usage, average power usage per appliance per month and data for graphing the power usage per appliance.

Calculating average power usage: The average power usage for each appliance per month calculated is used for checking conditions in the HUWS.

4.4 High usage warning and utilities override

A requirement of a smart home is to have remote feedback to the clients in the case of a change in system state. In the Smarthome application there is a High Usage Warning System as well as an Utilities Override Mechanism which can cause changes to the state of the system. If either system is activated a message is sent to the user by the back-end via GSM communications.

High usage warning system: The high usage warning systems algorithm is responsible for making sure that if an appliance goes over its average power use that the client is informed. The system first checks if the HUWS algorithm has already set the high usage warning and if it has been set, the system checks if the user needs to be sent the warning message again. The high usage warning system gets the latest calculated averages from the average_appliance_energy_readings_permonth table for each appliance. Then the current power usage per appliance is obtained from data_for_graphing for each appliance. The system makes sure that at least one appliance is on. The current power usage is checked against the average, if the current power usage is above the average power usage by a specified margin (2.5 kW/h)

then the high usage warning flag is set and the user is warned. If the user decides to give the system permission to automatically turn off the appliances, all appliances with high usage warning flag set will be turned off. However the user is able to turn these on again at any time.

Utilities override mechanism: A form of high level utilities control was implemented on the system. The utilities currently can control the house as a whole but has no access to power usage information nor to the individual appliances. The utilities override mechanism allows the utilities to request a percentage power usage drop from house in order to decrease demand on the grid during high usage periods. The software process for the utilities override is now explained. The system receives the instructions and starts off by checking what current usage period the system is in, it then calculates the total power usage for the period from the data_for_graphing table. Once this is obtained the system checks to see if any appliances are on. If not, all appliances are set to utilities override mode. The system calculates the power drop required by the utilities using the percentage drop requested as well as the current total power usage. Once this has been done the system starts by turning off lowest to highest usage appliances until necessary power drop has been attained. If an appliance has been turned off by the utilities override it cannot be turned on again until the utilities override has been shutdown. A relay on the current sensing unit is installed to physically stop the user from turning the appliances back on. Once the utilities override has been shutdown all appliances are turned back on as a safety precaution.

4.5 User interface

The website, which acts as the user interface, was designed with ease of use methodology in mind. A design principle like this results in a website which is user friendly to a broad spectrum of people. Bright colours and large writing were central to design making the website easy to read. The website consists of two pages the Graphing Power Usage page and the Appliance Control page. The navigation between the pages is done by a selection bar displayed at the bottom of the screen.

The interface is accessed via connecting to the Raspberry Pi either using the installed Wi-Fi dongle or through a router. During the development of the project a router was used to connect to the Raspberry Pi. In this case the Raspberry Pi is given a network specific IP address. The format `{ip address}/smarthome` was used to access the website stored on the web-server on the Raspberry Pi.

Graphing power usage page: The aim of the Graphing Power Usage page, as seen in figure 2, is to allow the user to easily access and view their power usage per appliance. A bar graph is used to display this information. The graph gives the information in an intuitive easy to read format. The graph displays kW/h versus time. The graph only

shows one appliance at a time, the user is able to change appliances using the select list. Another added feature is that the user can select a date range over which to view their power usage.

This date range stays constant as the user selects different appliances. This enables the user to compare the power usage of different appliances over the same date range. The user is able to gain insight into their power usage behavior per day, per week or per season. Combining this with knowledge of electricity tariffs the user can begin to make smart choices when considering efficient energy usage.

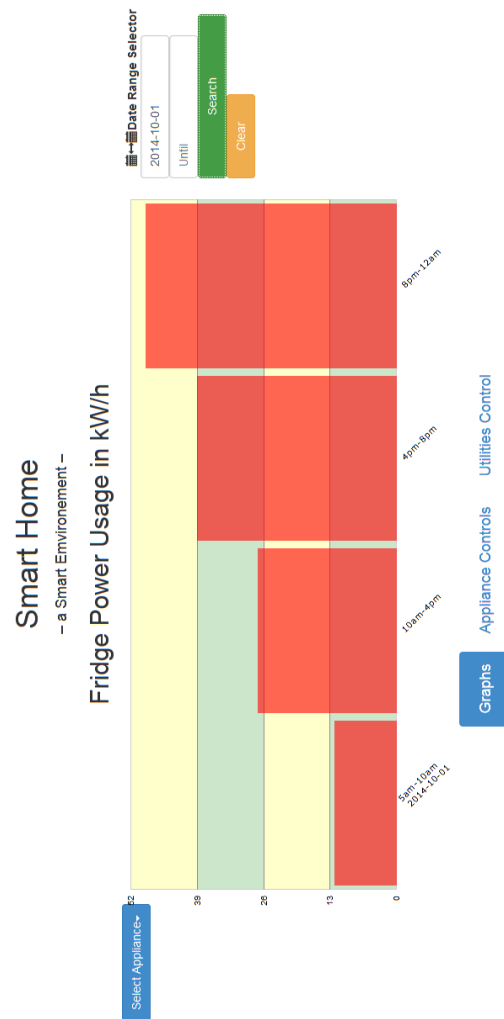


Figure 2: General layout of graphing power usage page

Appliance control page: When designing this page simplicity and speed were kept in mind. Efficient energy use is a key concern of the project therefore the user should be able to access the page and change the status of their appliances as quickly as possible. The user should not be deterred from taking part in smart power usage because of a complicated interface. The designed interface, as seen in figure 3, gives the appliance name and an on and off button in a list format. By simply tapping or clicking the button the user can change the state of their appliance.

The UOM has the ability to override this page. A device that is in utilities override has been shutdown to decrease demand on the grid. The system disables the on and off buttons on the interface. This stops the user from changing the status of the appliance. However the appliances state can be altered once the utilities override has been shutdown.

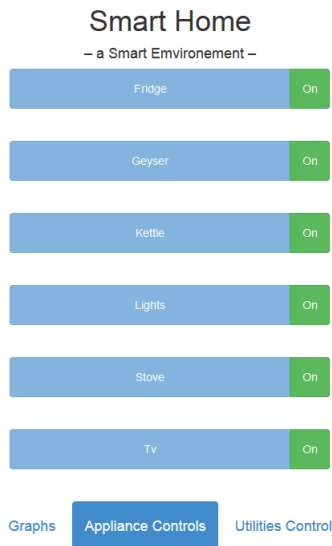


Figure 3: Appliance Control Page

5. BACK-END

5.1 STM board

The STM32F407 was selected as it has a wide user support group on Coocox forums as well as fairly easy to get up and running this would allow for minimal time spent installing.

5.2 Measuring power

The CS5463A chip is selected for power measuring as it can calculate power, voltage and current (for more readings refer to the datasheet of the CS5463A) over a specified number of cycles. The default is 4000 samples a second and with a 4Mhz clock it relates to 1 second per a reading. It has an 8bit interface and communicates via the SPI protocol, this allows for a N+3 approach for adding devices (1 device requires 4 pins, 2 devices requires 5 as this is the nature of SPI). To interface with the CS5463 a 8 bit command is sent and the chip replies with 24 bits of information if a request is sent.

In order to measure the AC voltage, the voltage needs to be stepped down either using a voltage transformer or a voltage divider as the CS5463 has a full scale input of 250mV. The current is also required to be stepped down with a current transformer or shunt resistor again as the CS5463 has a full scale current input of 250mV. The voltage divider and current transformer were

selected as it lowers the cost. The voltage divider and current transformer selected were 10000:1 and 1000:1 respectively. A low pass filter is also added for filtering out noise on each input.

The STM Board queries the status register on each of the CS5463 waiting for DRDY to be flagged, this means that a conversion is complete, once complete the STM then requests voltage, power and current. The STM board stores this data and waits for it to be requested from the Raspberry Pi.

5.3 Controlling appliances

In order to be able to turn appliances off and on a component that stops the power delivered to the appliance is required. A relay is selected as it separates the trigger from the high voltage connections. The selected relay triggers off 6VDC however each relay is driven by a 2N222A BJT as the STM board cannot supply the required current to drive each of the relays and hold the coil state. In order to minimize the PCB boards the relay is also inserted into the Power Measurement Unit.

5.4 Feedback to client

The selected method to provide feedback to the client is GSM communication as it is a low cost solution since majority of households are in the range of cell phone reception.

The SIM900 Module is a development board that communicates via USART at a baudrate of 19200 Kbps. It uses the AT library commands via USART to communicate.

5.5 Linking between front-end and back-end

SPI protocol is the communication used to link the STM (Back-End) and Raspberry Pi (Front-End). The Raspberry Pi continuously cycles through the following cycles:

- Control Appliances
- Request Readings
- Check Utilities Override
- Check High Usage
- Wait for Reply From High Usage

The first cycle **Control Appliance**, requests the status of each of the appliances in the appliance table from the MySQL database. If the status of the appliance changes the code then sends a command to the STM board which then either turns the appliance on or off.

Request Readings executes commands to obtain readings from each of the 6 appliances. The readings are requested in the following order; appliances 1 through 6 and for each appliance the voltage, current and then power readings.

Check Utilities Override, this checks if the Front-End has initialised a utilities override, if an override has occurred the status register for the override is flagged. The amount to reduce the power by is verified by sending a request and then a command is sent to the STM board with the reduced power amount. The STM board then sets up the SMS using the AT commands and sends a utilities override SMS with the set power amount. The method then sets the sent SMS override flag .

Check High Usage monitors a high usage flag which is flagged when an appliance uses more than the average amount of power. If the high usage flag is set the database is updated with the high usage warning flag set to 0, ignore warning flag set to 1, and the high usage resend time flag set to 4 hours later. A SMS command is then sent to the STM board which executes a send SMS method. If the appliance is still using more than its average after 4 hours the SMS is sent again.

Wait for Reply From High Usage checks and waits for a response from the STM board. If a response is triggered all the appliances in the database are set to off, while the STM board turns off the relays. In order for the STM board to notify the Raspberry Pi of a response it monitors the SIM900 receive register and waits for a receive command. If the command string contains a 'Yes', the next time the Raspberry Pi requests the receive register the STM board returns the yes command.

6. TESTING

6.1 Measurement unit

To test the accuracy of the measuring unit 230VAC was added to the input, the voltage after The voltage divided was measured to be 249mV. However when the voltage was removed 42.3mV still remained as noise. Similarly for current. A known current of 1A was set through the current transformer and an expected current of 15.62mV was required however measured results revealed that there was in fact 52.3mV on the line and with no current passing though again 46.6mV of noise on the line. Therefore the voltage has on error of 16.92% and a current error of 19.44%. Moving to vero-board lowered the error of the voltage to 2.76% and 2.98% for the current. However when connecting to the CS5463 the noise returned as the breakout board is connected to the bread board. In order to improve the noise, the CS5463 would have to be moved to PCB board as to negate the noise level produced whilst in the breadboard.

6.2 Test appliance controls

In order to test the appliance controls are working an LED was connected to each of the GPIO's that link to an appliance. The Raspberry Pi was set to only update the control sequence.

6.3 Testing features via SMS feedback

Test Utilities Override: To check the utilities override, the Front-End utilities override page was used. Once the override occurred the system should message the console on the Raspberry Pi as well as a message on the VCP, if these two message occur the sending is complete. During testing this part of the system worked.

Test high usage: In order to see if this feature of the project was working correctly, a MySQL injection was made into the high usage table, this then should trigger. The Raspberry Pi was programmed to just monitor the high usage flag, once the trigger is detected a note on the console displays the high usage warning. The VCP should also display a high usage message and finally a SMS should be received. This was not initially working as the protocol was misspelled, hence the correct command was not being transmitted.

Test for reply from high usage: Before this could be tested, a manual MySQL update had to be made into the database consisting of setting the sent SMS flag true. The STM then waited for a reply, and a note on the VCP is displayed, this then displays a note on the Raspberry Pi console and updates the database, the system is then stopped and the database checked. This operated correctly

6.4 TOTAL SYSTEM CHECK

All the features of the system were activated and then a full system check was performed, no errors were detected.

7. CONCLUSION

The aim of the project was to save power through the use of the developed system. The simplistic design of the user interface aimed at making the device easy to use. Doing so encourages the user to interact with the system. Their power usage information is readily available to them via the interface. They can then begin to understand the power usage behavior and become more energy conscious. With the ability to change the state of their appliances, the user is given the choice in creating an energy efficient environment. This is aided by the HUWS and the UOM. With correct social awareness and integration the Smarthome application has the future potential to increase power usage awareness in South Africa households.

REFERENCES

- [1] Rabobank. "Special report 2008/04." Date Accessed 21/10/14. URL https://economie.rabobank.com/PageFiles/3576/Energy%20crisis_tcm64-75053%5B1%5D.pdf.
- [2] R. H. Friis. *The Praeger Handbook of Environmental Health*. ABC-CLIO, LLC, 2014.

- [3] The Department of Energy. “A survey of energy-related behaviour and perceptions in South Africa.” Tech. rep., The Department of Energy, South Africa, 2012.
- [4] NEC. “Smart houses: smart Eenergy.” URL http://de.nec.com/de_DE/global/environment/energy/house.html.
- [5] P. Martin. “Joomla on raspberry pi (with nginx).”, Date Accessed 22/10/2014. URL <https://www.youtube.com/watch?v=u2MFQCoexD0>.
- [6] C. Pautasso and F. Leymann. “RESTful web services vs . big web services : making the right architectural decision categories and subject descriptors.” In *WWW 2008/Refereed Track: Web Engineering - Web Service Deployment*, pp. 805–814. Beijing, 2008.
- [7] Eskom. “Eskom homeflex.” URL <http://www.eskom.co.za/CustomerCare/TariffsAndCharges/Documents/EskomBooklet.pdf>.

A SYSTEMS ENGINEERING APPROACH TO ANALYSING MICRO-GRID CHALLENGES IN SUB-SAHARAN AFRICA

W. Doorsamy*, L. Lakay-Doorsamy† and W. A. Cronje*

* School of Electrical & Information Engineering, University of Witwatersrand, Johannesburg, South Africa

† Joy Global (Africa) (Pty) Limited, Johannesburg, South Africa

Abstract: Microgrids have been identified as a key instruments in solving the energy security, environmental sustainability and energy equity problems faced in Sub-Saharan Africa. In order to arrive at sustainable solution for practical application, these challenges must be addressed simulataneously. However, the vast majority of research and development in this area deals with technical challenges in isolation. This paper presents a systems engineering framework for assisting with the development of sustainable microgrid solutions. The framework deals with intialisation of the technical process in the life cycle of a microgrid system. The main elements of the stakeholders and requirements analysis are described within the context of microgrid systems.

Key words: Africa, Microgrids, Systems engineering, Requirements analysis, Rural.

1. INTRODUCTION

This paper proposes a framework to assist in the development of microgrids for Sub-Saharan Africa. The framework uses a systems engineering approach to analyse the requirements specific to non-integrated areas such in remote/inaccessible locations and rural communities. The challenges faced in the development and implementation of microgrids in Sub-Saharan Africa are not restricted to technical issues, but extend to social, environmental and economic challenges. In order to arrive at a sustainable solution, these challenges must be simultaneously addressed in the context of the application. However, the vast majority of research and development in this area addresses the technical issues in isolation. Futhermore, there is no practical framework available for contextualising development of microgrids.

The presented work describes how to properly contextualise and initialise the technical process within the system's life-cycle to ensure successful development and operation of microgrids. A detailed background of the problem is presented in the next section. Thereafter, the energy scene in Sub-Saharan Africa is briefly described in section 3. Section 4 then presents the framework and section 5 describes future plans before a brief conclusion.

2. BACKGROUND

2.1 The World Energy Trilemma

The World Energy Council has recognised the urgent need to address the aforementioned energy problems through provision of the "Agenda for Change", as a call for action from leaders and peers in the energy community [1]. The major energy challenges affecting all nations across the world have been identified and categorised within the three legs of the *Energy Trilemma*, as follows [1]:

- Energy equity - Task of providing accessible and affordable energy supply for the entire populace.
- Environmental sustainability - Issues relating to environmental impact such as supply and demand-side energy efficiencies, and utilisation of the renewable and low-carbon sources.
- Energy security - Challenges with reliability of the energy infrastructure, ability to meet current and future demands, and effective management of energy resources.

Although these are ubiquitous problems which are common knowledge, the concept of the *Energy Trilemma* conveys the importance of maintaining the balance of these three legs which is not always apparent. Simply put, a well-balanced solution must aim to address all of these issues. It is therefore essential for researchers and developers in the energy community to understand the relationship between the proposed technologies and the three aforementioned areas.

2.2 Microgrids

Through the widespread development and implementation of distributed energy resources (DER) which utilise technologies such as, *inter alia*, solar photovoltaic modules, small wind turbines, biogas digesters and storage devices, microgrids have been identified as key features of future power systems. Microgrids can be defined as LV distribution systems with DERs together with storage devices and flexible loads [2]. The IEEE standard 1547.4 uses the term "Distributed Resource Island System" to unambiguously describe microgrids [3]. Microgrids have demonstrated many benefits such as decentralised coordination of DERs, safe and efficient local distribution networks, and islanding capabilities amongst others. However, ongoing development and

diversification of application of microgrids consistently generates new challenges. As mentioned, these challenges are not restricted to technical issues and extend to social, environmental and economic issues.

Technical challenges vary with the microgrid’s capacity, topology, energy sources, physical size, existing infrastructure (if any) and load. Social, environmental and economic issues vary with government and/or utility policy, availability of funding, consumer profile and the physical location. These challenges are interrelated and must be considered during the planning stages. For example, policies issues such as tariffs and billing are not simply operational considerations, and affect the architecture of the system - i.e. topology and communications infrastructure of the system can directly affect accessibility to individual loads for efficient metering. This is one example of a number of interdependent components that affect the entire system and ultimately, the overall success of the microgrid. Hence, a systems engineering approach is to proposed as it provides a critical thinking framework when considering such a project [4].

2.3 Systems Engineering

A system is defined in [5] as, “a complex unity formed of many often diverse parts subject to a common plan or serving a common purpose”. In this case, a microgrid can be considered as a system of systems (SoS), as it consists of different interconnected or interrelated systems to produce results that cannot be achieved by the individual systems [6]. For instance, a typical microgrid is configured with the following: hardware, software, processes, procedures, policies, humans and the environment. Systems engineering concentrates on the design and application of the entire system as distinct from the parts which involves looking at a problem in its entirety, taking into account all the facets and all the variables and relating the social to the technical aspect [7]. It aims to capture stakeholder needs and objectives and to transform these into a holistic life-cycle balanced solution which both satisfies the minimum requirements, and maximises overall system effectiveness [8].

In general, failure of a project is defined as the inability to meet the time, cost and quality requirements [9]. Requirements analysis plays key role in a project as it benchmarks these deliverables. In this case, the quality of a microgrid must meet the requirements of *all the stakeholders*. Hence, a systems engineering approach is proposed here to ensure proper coordination of the development of microgrids from an African perspective. The overall systems engineering life-cycle process, as illustrated in Figure 1, consists of multiple iterative levels which generate information for decision makers and provides input for the next level of development [10]. The technical process in the life cycle is initialised with the stakeholder requirements definition and requirements Analysis. This is conducted before the actual design

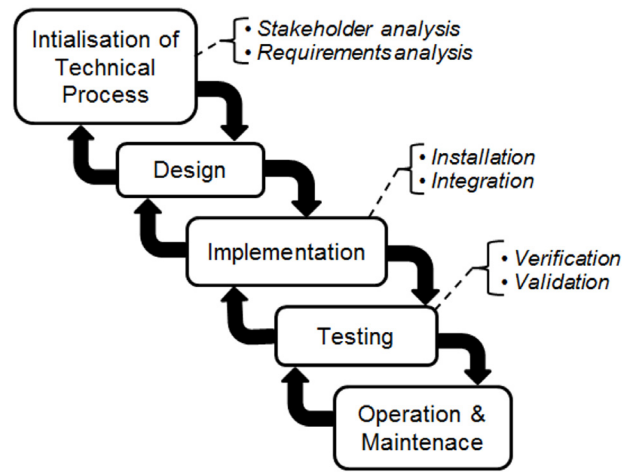


Figure 1: Overall systems engineering life-cycle process

process and involves the definition of an operational concept of the system (including usage scenarios), a description of the involvement of the system with other systems, and an objectives hierarchy of the stakeholders across all phases of the systems life cycle [12]. This paper concentrates on this aspect within the life cycle of the development of microgrids.

3. ENERGY SCENE IN SUB-SAHARAN AFRICA

In a global context, growth in the demand for primary energy is predicted between 27% and 67% through to 2050 [13]. There are currently an estimated 1.2 billion people who do not have access to electricity [14], of which over 550 million are African [18]. This tremendous rise in demand for energy has also been observed locally with recent stresses on the national grid. Furthermore, there are vast areas in sub-Saharan Africa which are still without access to electricity grids, with World Bank statistics placing more than 500 million people within this category [14]. Table 1 gives a comparison of the electrification rate for rural populations and places Sub-Saharan Africa with the lowest percentage in the world.

Table 1: Rural electricity access in 2009 - regional aggregate (information obtained from [15])

Region	Rural electrification rate (%)
Africa	25.0
North Africa	98.4
Sub-Saharan Africa	14.2
Developing Asia	73.2
China and East Asia	86.4
South Asia	59.9
Latin America	73.6
Middle east	71.8
Developing countries	63.2
World	68.0

The electrification challenge has a tremendous impact on the social and economic development of the countries in the Sub-Saharan region. However, there are positive aspects that can be taken from the lack of existing energy infrastructure. The power systems in advanced industrial countries are built around the conventional large-scale generation which rely primarily on fossil and nuclear sources [16]. Furthermore, these existing systems are supported by massive technological and regulatory infrastructures. The absence of the regulatory apparatus and existing infrastructures in developing countries in Africa offer the possibility of introducing renewable technologies at a fundamental level and the opportunity to lead the way for microgrid technologies.

4. INITIALISATION OF THE TECHNICAL PROCESS

The processes within a system's life cycle are typically grouped into two major categories - i.e. project/management processes and technical processes. The processes shown in Figure 1 fall into the category of technical processes. Technical processes are used to establish requirements for the system as the basis for the efforts to create an effective product or service (requirements analysis, design and testing); to sustain the system through its useful life (operation and maintenance); and to support retirement of the system (end of useful life and disposal - not shown in Figure 1) [7]. A process is defined in [17] as a "set of interrelated or interacting activities which transforms inputs into outputs".

In this case, the design process of the microgrid cannot be conducted successfully without suitable *inputs* obtained from the *outputs* of the requirement analysis. Furthermore, it is essential that errors be found in the early phases of the system's life-cycle to avoid unnecessary costs. Figure 2 gives an example of the average cost ratio for finding an error in the requirements analysis phase as compared to the later phases.

4.1 Stakeholder Analysis

In general, the term stakeholder refers to any entity (individual or organization) that is, directly or indirectly, affected by the existence of the system. Examples of stakeholders are the end-users of the system, managers of the organisations installing the system, external entities who have some kind of interest in the system, regulatory bodies, and engineers involved in the design, development and maintenance of the system [19]. The stakeholders' requirements are essential in clarifying the scope and governing the development of the system [7]. The requirements of a microgrid system must therefore be aligned with the expectations of the various stakeholders. This must be done iteratively at each stage of the technical process to ensure that the stakeholders remain supportive of the solution.

When defining the stakeholders' requirements for a

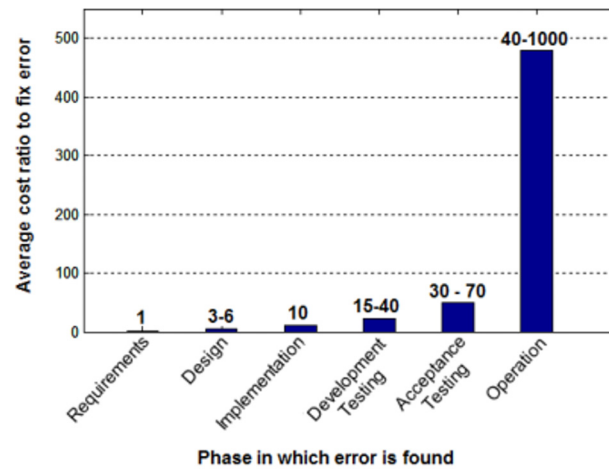


Figure 2: Example of the average cost ratio to fix an error when found in a specific phase of the systems engineering life-cycle process (information obtained from [11])

microgrid, the following should be considered (but is not limited to):

- Identification - All potential stakeholders throughout the life-cycle of the system must be identified. Some examples of stakeholders, in context of a microgrid system, are the users/community, municipality, operators, investors, maintenance personnel, local utility, equipment suppliers, engineers.
- Types of stakeholders - Each stakeholder has different levels of interest in the system and is affected either positively or negatively by the system. *Primary stakeholders* are directly affected by the system, *secondary stakeholders* are affected indirectly and *key stakeholders* are either or none of the previous two categories, but can directly affect the system in a positive or negative way.
- Elicitation - Information must be elicited from all stakeholders. This process may require interviews, research, analytical techniques. For example, the usefulness of the system is determined by the user and therefore interviews and behavioural studies should be conducted in this respect. If the user is not satisfied with the quality of the service provided by microgrid system, then he/she will revert to previous/alternative methods of cooking, heating and lighting. In the instance where stakeholders are not directly accessible, information can be researched or derived analytically.

4.2 Requirements Analysis

Requirements analysis is used to develop functional and performance requirements, that is, stakeholders' requirements are translated into a set of requirements that define what the system must do and how well it must perform [20]. This phase of the process is used to define

the functional requirements and design constraints in an understandable, unambiguous and comprehensive format. The following points must be considered during this stage:

- System boundaries and external interfaces - The interfaces and external boundaries of the microgrid system must be identified during the requirements analysis phase. This allows for the interactions between system elements and the system’s interaction with the other systems to be defined. For example, here the environmental factors influencing the system’s performance and vice versa are defined such as - insolation, if PV’s are used, and levels of the system’s carbon emissions. Context diagrams can be used to demonstrate these interactions as given by the example in Figure 3. Additionally, the different boundaries - i.e. 1-external systems level, 2-system level, 3-subsystem level, are illustrated in this figure.

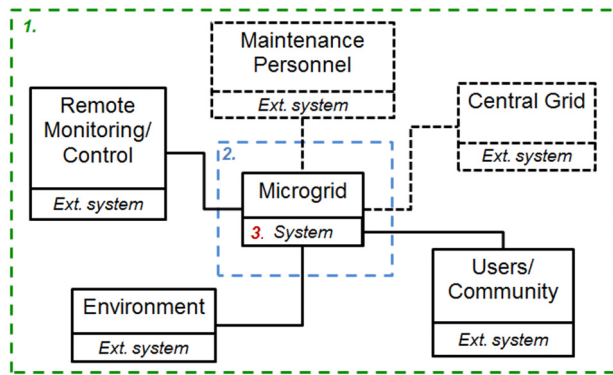


Figure 3: Example of a microgrid system context diagram

- Operational concept - The functional requirements of the system are also defined during this phase. The functions the system will perform, how it will perform those functions, and the standards to which it will perform are specified. Outputs here must be at a sufficient level of abstraction to avoid directing the design and implementation of the microgrid, but at the same time capture specific needs. One of the tools which assist with this is a scenario analysis. Two simple and contrived examples of scenario analysis diagrams for “store energy” and “supply energy” scenarios of a microgrid system are given in Figures 4 and 5 respectively. The scenarios given in these diagrams are decomposed into different levels corresponding the boundaries illustrated in Figure 3. For example, the controller and the batteries of the microgrid perform functions at a subsystem level.
- Design and implementation considerations - Assumptions and constraints are defined to inform, but not limit the scope, of the design of the system. These involve specification of factors such as legislation, development budget, total cost of ownership - i.e. cost to operate and maintain, timelines -i.e. actual project process, repair times and expected operational life.

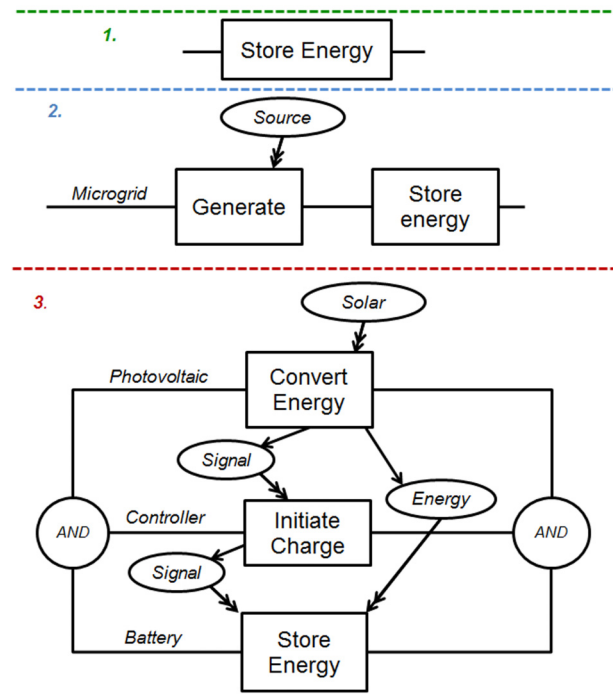


Figure 4: Example of a “store energy” scenario-analysis diagram for a microgrid system

This allows for upfront assessment of critical aspects such feasibility the lead-times for the replacement of parts - i.e. consideration of local versus overseas sourcing of parts.

- Standards - The standards, policies and legislation relating to microgrids must also be identified and/or defined. These factors are critical to the successful installation and operation of the microgrid. However, this is perhaps one of the most deficient areas of microgrid development and poses a significant challenge to the energy community in Africa. Standards specifying capacity, quality, safety, and disposal of the system must also be defined during the requirements analysis stage. Additionally, tariffs and billing policies must be considered which will determine the necessity and extent of load limiting policies.
- Ownership and responsibilities - Issues relating to the system ownership must be clarified upfront as this affects how roles and responsibilities are defined e.g. operational and maintenance responsibilities for the system. Roles and responsibilities of supply chain, contractors and the users should be considered. This will assist in determining if and what education and training is required.

In addition to the presented context and scenario analysis, the following techniques are included in a formal requirements analysis [22]:

- Context flow analysis - High level definition of the

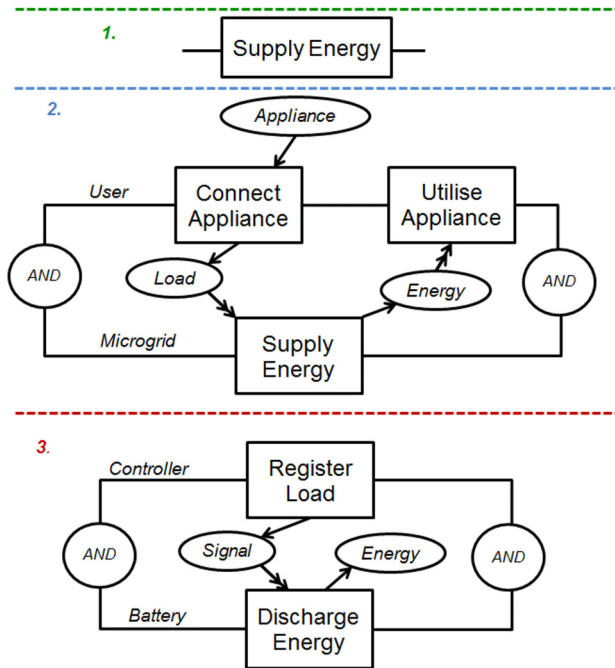


Figure 5: Example of a “supply energy” scenario-analysis diagram for a microgrid system

complete life of the system, - i.e. from manufacture to disposal, which all requirements are derived from.

- States and modes analysis - Expresses the requirements with respect to the time-varying behaviour of the system. The permitted or required conditions and the function sets of the system are specified. For example, this technique will be used to define the set of functions a microgrid is required to perform while in maintenance mode.
- Functional analysis - Models the functional aspects of the systems operational scenarios. This will include the scenario analysis as given by the examples in Figures 4 and 5.
- Parsing analysis - This technique is used to audit the overall requirements analysis by checking its completeness, clarity, consistency and feasibility. It is useful for the early identification of errors.
- Out-of-range analysis and measures of effectiveness - These techniques capture and validate any requirements relating to abnormal or unexpected inputs, outputs and system conditions. This is essential in determining how effective the system will be in the real world. For example, the microgrid must remain stable in the event of an unexpected load or weather fluctuation.

It should be highlighted that a stakeholders and requirements analysis for a system as complex as a microgrid, will be more comprehensive than the points listed here. The purpose of this deliberation is to give

an overview of the initialisation process and illustrate the importance of a formal requirements analysis in the life cycle of a microgrid system. For a more detailed treatment of systems engineering theory and practice, the reader is referred to [7], [5], [20], and the standard [10].

5. FUTURE PLANS

Application of the proposed systems engineering approach to initialising the technical process within a microgrid's life-cycle is the next step. At the University of the Witwatersrand, the School of Electrical Engineering's laboratory has recently undergone renovation, with the aim of developing and testing microgrid technologies [21]. The presented framework will assist in clearly defining strategies to best utilise the available infrastructure and future work for the microgrid research thrust. Additionally, the socio-technical and operational aspects of existing rural-microgrid installations are being studied to improve future design and development concepts.

6. CONCLUSION

A systems engineering framework for developing sustainable microgrid solutions in Sub-Saharan Africa is presented. The framework deals with the initialisation of the life cycle of microgrid systems. The main activities of the stakeholder and requirements analysis are presented together with specific examples pertaining to microgrids. The significance of these activities in the system's life cycle is also described. Although there is a multitude of installations across the globe, new challenges specific to the application constantly arise. From an African perspective, it is important to not only acknowledge lessons learnt from previous installations but to also determine the requirements specific to the continent. The presented framework is intended to assist with overcoming these contextual challenges and ensure that successful solutions are developed and implemented.

REFERENCES

- [1] P. Gadonneix, M. Nadeau, Y. D. Kim, L. Birnbaum, H. Cho, A. R. Choudhury, J. C. C. Neto, J. Dager, K. Meyers, A. Sambo, B. A. Statham, J. A. V. Lleras, G. Ward, W. Xinxiong, T. M. Zadari, and C. Frei: “World Energy Trilemma: Time to get real - the agenda for change”, *World Energy Council*, United Kingdom, 2013.
- [2] N. Hatziaargyriou: *Microgrids: Architectures and control*, John Wiley and Sons Ltd, IEEE Press, 2014.
- [3] IEEE Standards Association: *IEEE guide for design, operation, and integration of distributed resource island systems with electric power systems*, Institute of Electrical and Electronics Engineers (IEEE), No. IEEE 1547.4, 2011.
- [4] J. Kasser: “Holistic thinking and how it can produce innovative solutions to difficult problems”,

- Proceedings of the 7th bi-annual European Systems Engineering Conference (EuSEC)*, Sweden, pp. 1-17, 2010.
- [5] D. W. Oliver, T. P. Kelliher and J. G. Keegan Jr.: *Engineering complex systems with models and objects*, McGraw-Hill, 1997.
- [6] A. J. Krygiel: *Behind the wizards curtain: An integration environment for a system of systems*, National Defense University, DoD CCRP, 1999.
- [7] International Council on Systems Engineering: *Systems engineering handbook: A guide for system life-cycle processes and activities*, INCOSE, Version 3, 2006.
- [8] R. J. Halligan: "Requirements metrics: the basis of informed requirements engineering management", *Proceedings of Complex Systems Engineering Synthesis and Assessment Technology Workshop*, Calvados, USA 1993.
- [9] R. Atkinson: "Project management: cost, time and quality, two best guesses and a phenomenon, its time to accept other success criteria", *International Journal of Project Management*, Vol. 17, No. 6, pp. 337-342, December 1999.
- [10] International Standards Organisation: *Systems and software engineering - System life cycle processes*, ISO/IEC, No. 15288, 2008.
- [11] I. Hooks and K. A. Farry: *Customer-centered products: Creating successful products through smart requirements management*, AMACOM - Division of American Association, Business and Economics, 2001.
- [12] D. M. Buede: *The engineering design of systems: models and methods*, John Wiley and Sons Ltd, 2nd ed., 2009.
- [13] C. Frei, R. Whitney, H. Schiffer, K. Rose, D. A. Rieser, A Al-Qahtani, P. Thomas, H. Turton, M. Densing, E. Panos, and K. Volkart: "World energy scenarios: composing energy futures to 2050", *World Energy Council*, France, 2013.
- [14] S. G. Banerjee, M. Bhatia, G. E. Azuela, I. Jaques, A. Sarkar, E. Portale, I. Bushueva, N. Angelou, and J. G. Inon: "Global tracking framework: Sustainable energy for all", *World Bank*, Washington DC, Vol. 1, 2013.
- [15] International Energy Agency: *New electricity access database*, IEA - World Energy Outlook, 2011.
- [16] B. H. Krogh and H. R. Schmidtke: "Electrical power in Africa: Challenges and opportunities ", *IEEE Smartgrid Newsletter*, December 2012.
- [17] International Standards Organisation: *Quality management systems - Fundamentals and vocabulary*, ISO 9000, ISO/TC 176/SC 1, 2005.
- [18] D. Schnitzer, D. S. Lounsbury, J. P Carvallo, R. Deshmukh, J. Apt, and D. M. Kammen: "Microgrids for rural electrification: A critical review based on several case studies", *United Nations Foundation*, Washington DC, 2014.
- [19] I. Sommerville and P. Sawyer: "Viewpoints: principles, problems and a practical approach to requirements engineering", *Annals of Software Engineering*, Vol. 3, No. 1, pp. 101-130, 1997.
- [20] DOD Systems Management College: *Systems engineering fundamentals*, Department of Defence: Defence Acquisition University Press, Virginia, January 2001.
- [21] W. A. Cronje, I. W. Hofsajer, M. Shuma-Iwisi, and J. I. Braid: "Design considerations for rural modular microgrids", *IEEE ENERGYCON Conference and Exhibition - Future Energy Grids and Systems Symposium*, Italy, pp. 743-748, 2012.
- [22] R. Halligan: *Requirements analysis that works!*, Project Performance International (Pty) Ltd., PPI-005261-1B, 2012.

A DYNAMIC THREE-PHASE LOAD EMULATOR FOR DISTRIBUTED GENERATION STUDIES IN A MICROGRID LOAD TEST-BED

*T.K. Nkalai, *M.V. Mabuyakhulu and *W.A. Cronje

* Faculty of Engineering and the Built Environment, Private Bag 3, Wits 2050, South Africa

E-mails: 389114@students.wits.ac.za, 382310@students.wits.ac.za and willie.cronje@wits.ac.za

Abstract: The design, implementation and testing of a dynamic three-phase load emulator for distributed generation is presented. The emulator is implemented using an electromechanical drive system comprising of two mechanically-coupled induction machines rated at 2.2 kW that are controlled by two independent inverters. One machine operates as an induction motor and the other as an induction generator. The control signal which varies the speed set-point of the induction motor is the power profile of a user-specified three-phase load to be emulated.

Keywords: Emulator, Distributed Generation, Micro-grid, Power Factor, Slew Rate, Variable Speed Drive.

1. INTRODUCTION

In this paper, the design, implementation and testing of a dynamic load emulator is presented. The emulator is required to draw power from a grid in a manner that mimics a user-specified three-phase load. The emulation is to be realised using the equipment available in the Actom Energy Laboratory at the University of the Witwatersrand, Johannesburg.

2. BACKGROUND

Grid-function emulation is a useful tool for studying micro-grid systems [1]. The ACTOM energy laboratory is currently equipped to allow for the experimental study of micro-grids and smart-grids by allowing the basic functional blocks, present on a typical grid, to be emulated in hardware on a low power system. This allows for repeatable experimental studies at any convenient time without relying on the real loads, generators and other equipment to be present.

Figure 1 shows a typical micro-grid arrangement for such study through emulation of the generation, storage and load functions. Emulation of all these grid functions can now be used for controller design and to study interactions between electrical loads and sources under both transient and steady state conditions in a micro-grid. The campus grid fulfils the role of an infinite power source or sink, while the dynamics and behaviour on the micro-grid are studied.

Implementing an emulator for a PV source that can mimic a solar grid-tie feed-in has been reported previously [2]. Figure 1 shows a typical micro-grid that will be studied using the designed load emulator.

The required load emulator should be a dynamically-controllable three-phase power-sink which is capable of recreating practical power consumption patterns in a controlled laboratory environment [1-2]. The power demand profile of the emulator should preferably exhibit the exact same load attributes as the measured or user specified load that needs to be emulated

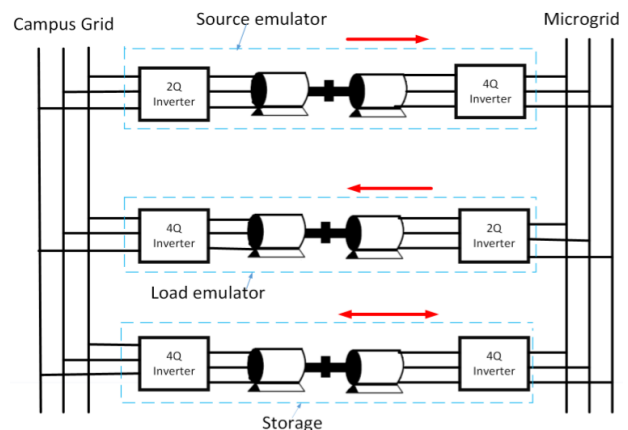


Figure 1 Three-phase laboratory based low voltage micro-grid using emulators to fulfill the various functions of generation, consumption and storage.

This implies that the load profile should be the same (although it might be scaled to a per unit level that can be accommodated by the equipment in the laboratory), the power factor should also be the same and ideally the load harmonics should be the same.

Research of the literature found various load emulation techniques and the one that is most relevant to the current set-up is [3], which uses an induction and dc machine set mechanically coupled together. The induction machine (motoring) is controlled using an inverter and the dc machine (generating) is controlled using a simple control scheme. The speed set-point of the induction machine is set constant using the inverter while the torque-speed characteristics of the dc machine are dynamically adjusted such that the dc machine draws more or less power as may be required. The decision to control the dc machine is motivated by the simplicity of control of a dc machine compared to an induction machine [3].

The load emulator to be implemented here falls in the same category as the above solution [3], however only induction machines and inverters are used. The power sunk by the induction motor-inverter combination from the micro-grid, will be sourced back into the campus grid by the induction generator and regenerating inverter.

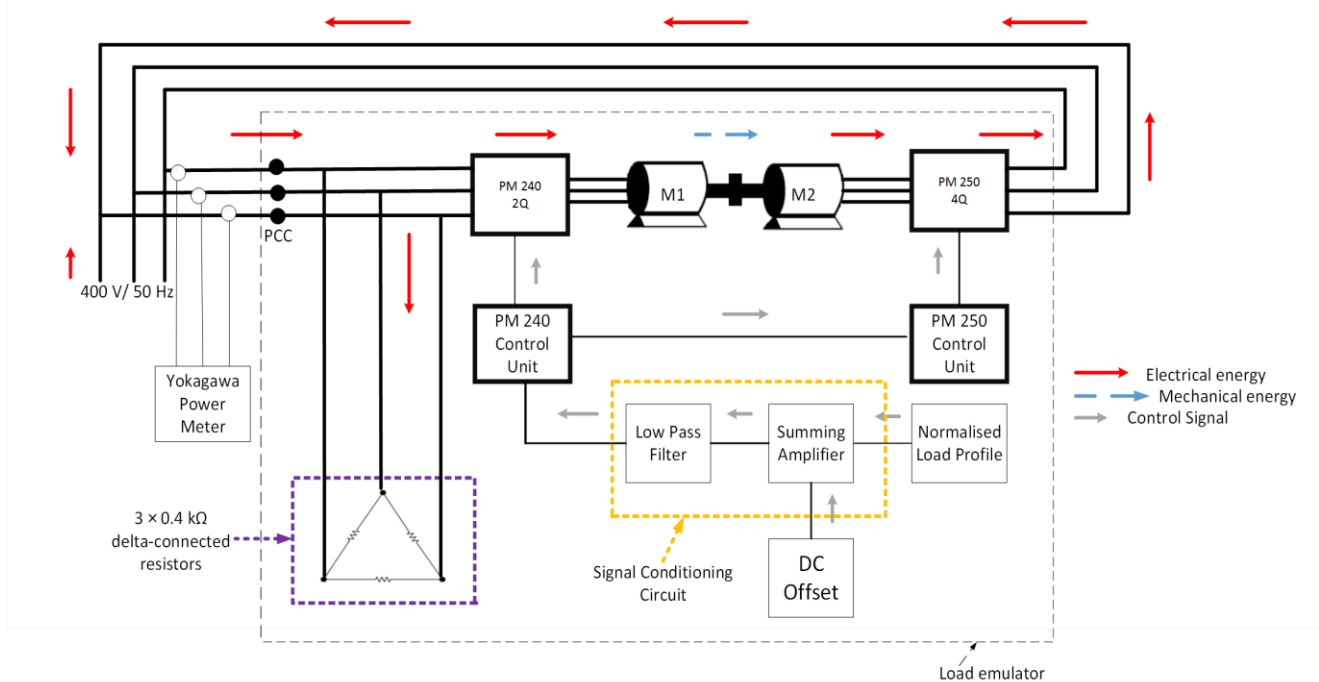


Figure 2: System block diagram of the proposed three-phase load emulator in a test setup. This setup only requires the losses in the system to be supplied from the main 400V supply.

3. SYSTEM OVERVIEW

The structure of the proposed load emulator with energy regeneration capability is shown in Figure 2. The implemented load emulation system uses the principles of electromechanical energy conversion to recreate power-consumption patterns of real electrical loads. These principles include speed-control, voltage-frequency (V/f) control, slip difference and power factor. Each of these determines the efficiency and accuracy within which load emulation can be achieved.

3.1 Electromechanical drive system

Central to the proposed emulator, is an electromechanical drive system composed of two mechanically-coupled induction machines rated at 2.2 kW, a 2 quadrant inverter and a 4 quadrant inverter. The electromechanical set-up is preferred for this system mainly because it provides galvanic isolation. One machine operates as an induction motor (M1) and the other as an induction generator (M2). The inverters used are SINAMICS G120 Power Modules (PM) designed for accurate and efficient speed-control of 3 phase induction machines. In the proposed system, as shown in Figure 2, the PM240 which is unidirectional controls the speed set-point of the induction motor and the PM250 controls the speed set-point of the induction generator.

As shown in Figure 2, the power drawn by the emulator-system is measured on the input side of the load emulator, at the Point of Common Coupling (PCC). This technique of measurement is dictated by the machine-drive set-up. The PM240 module only allows power flow

in one direction and therefore the power measured at the PCC can only be the power flowing from the grid into the system. If the rotor speed becomes greater than the synchronous speed of M2, PM250 allows power to flow back to grid. The adopted set-up allows power drawn, through the unidirectional inverter (2Q), by the system to be fed back to the grid through the bidirectional inverter (4Q). This regenerative capability of the system enables emulation experiments to be conducted in an energy-efficient way, the energy consumed by the system supplies only the losses.

The machines are set to operate under V/f control. This implies that the total air gap fluxes of the respective machines remain constant as the voltage and frequency increase or decrease proportionally [4].

Since power is a product of voltage and current, and voltage is fixed at 400 V on the input side of the load emulator, current must be varied to change the power drawn by the emulator from the grid. Therefore, since the machines are mechanically coupled together, there are essentially two methods which can be used to effectively vary the current drawn by the system. The acceleration and braking methods respectively can be used to vary the mechanical torque and since torque is directly proportional to the square of the current, the current drawn by the system will vary with changing torque [4].

Acceleration: On start-up, the speed set-points of both machines (M1 and M2) are equal and subsequently the slip of the induction machines will be equal as well. The set-point of M1 is then varied as per the control signal. Machine M1 whose set-point is being increased will therefore generate more torque to try and overcome the

opposing torque between the coupled rotors and subsequently increase the rotor speed. Since torque is directly proportional to current, the machine will therefore draw more current to accelerate the rotor thereby creating a unique and varying current profile.

Braking: Likewise, the speed set-points of both machines are the same on start-up. However, the set-point of M2 is then decreased as per the control signal and the machine will therefore draw more current from the grid to try and overcome the opposing torque and subsequently decelerate the rotor.

For the proposed emulator, the acceleration method was chosen. The synchronous speed of M2 is maintained at a constant set-point of 95% of the synchronous speed and the set-point of M1 is varied as per the control signal.

Speed range: For protection purposes, the maximum allowed slip difference between the machines is 2.5 Hz. At a supply frequency of 50 Hz, this slip corresponds to 75 rpm. This means that the difference between the synchronous speeds of the machines must not exceed 75 rpm otherwise the system trips. Since the induction machines used have a synchronous speed of 1500 rpm, the slip difference of 2.5 Hz translates to a control set-point range of 5% of the rated speed. Therefore, the speed set-point of M2 is kept constant at 95% of the synchronous speed while the set-point of M1 is varied by the control signal, which represents the load-profile to be emulated. The band of control is between 95% and 100% of the synchronous speed of the induction machine.

Frequency variation: The PM240 module is used to vary the frequency of power supplied to M1. It draws power from the grid at a power frequency of 50 Hz; varies that frequency based on a control signal and supplies power to the induction motor at a modified frequency, thereby changing the synchronous speed of the motor. The PM 240 control unit has an input range of 10 V, where 10 V corresponds to a set-point of 100% of synchronous speed. Therefore, to set M2 at a constant set-point of 95% of synchronous speed, a constant 9.5 V is supplied by the DC offset, as shown in Figure 2. The control signal must therefore vary between 0 and 0.5 V for speed-control.

3.2 Load data normalisation

Data for testing the system can be obtained from any electrical load. The load data used to test the emulator was obtained from the meters installed at The University of the Witwatersrand. The meters measure the average power consumed by the campus load in intervals of 30 minutes. From the data, the real power was retrieved in a form of an Excel file. The peak demand in the selected period is 1.61 MW and the base load is 0.53 MW. The induction machines used are rated at 2.2 kW. This implies that the campus load data must be normalised to be emulated by the system rated at 2.2 kW.

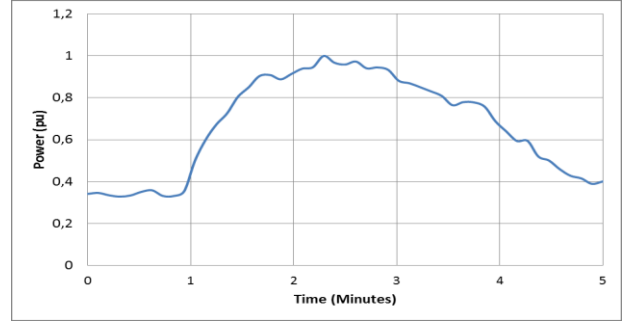


Figure 3: Three-phase load profile to be emulated in per unit.

Per unit: To convert the load power to per unit (pu), the peak demand in the measured data is selected as the base power and all other data points are normalised to a base of 1.61 MW. Therefore, the corresponding peak demand and base load are 1 pu and 0.32 pu respectively. The per unit load profile to be emulated is shown in Figure 3. Equation 1 illustrates the formula which is used to map load power to the corresponding system base power of 2.2 kW.

$$P_{system} = (P_{load} / P_{base (load)}) * P_{base (system)} \quad (1)$$

Where; P_{load} is the non-normalised real load power, P_{system} is the corresponding load power at the system base of 2.2 kW, $P_{base (load)}$ is the load power-base (peak demand) and $P_{base (system)}$ is the 2.2 kW system-base.

Time scaling: The measured-data profile was also compressed in time to enable multiple experiments to be conducted without having to use the real-time measured data. For testing the implemented load emulator, the data measured in intervals of 30 minutes over a 24-hour period was compressed to 5 minutes for experimentation. Compressing the control signal to five minutes increases the slew rate by 288 times and as a result; the load slew rate becomes 31.6 kW/s. The compression is achieved using a Matlab-implemented program. The program generates a WAV file from the Excel file containing the normalised load data. The WAV file is played using an audio MP3 player. Voltage is accessed from the laptop earphone-jack using earphones. This voltage is used as the control signal which must vary between 0 and 400 mV. The signal is fed into the signal conditioning circuit shown in Figure 4.

3.3 Signal conditioning

A signal conditioning circuit was implemented to condition the control signal to be compatible with the input requirements of the PM240 control unit. The signal conditioning circuit is made up of a summing amplifier and a low pass filter. The summing amplifier sums up the control signal and the DC offset. The low pass filter then filters out any unwanted noise that may be superimposed on the control signal. The filter is a second low pass filter with a cut-off frequency of 1 kHz. Figure 4 shows the signal conditioning circuit.

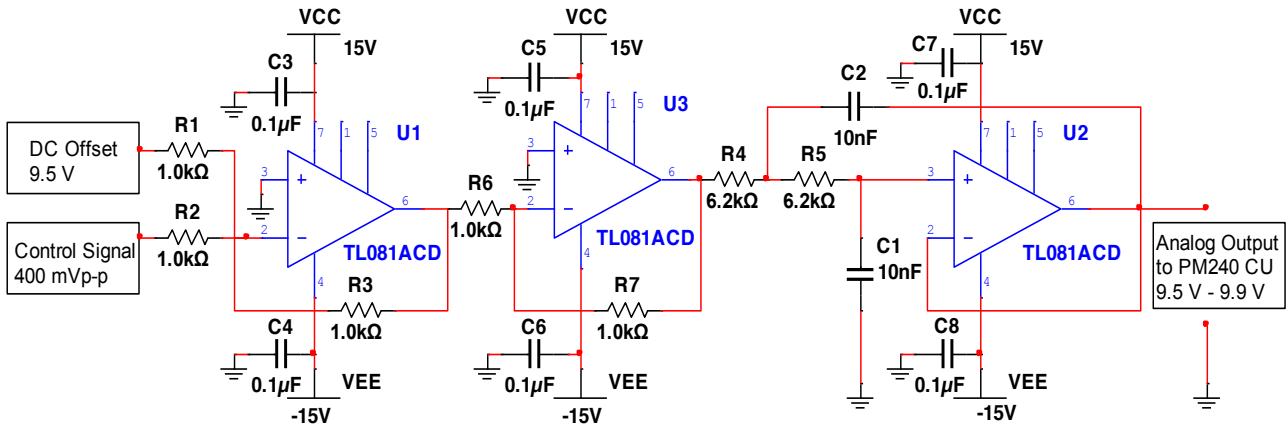


Figure 4: The signal conditioning circuit used to prepare the control signal for processing using the control units

3.4 System automation

Before the entire system is operated, the inverters are pre-loaded with the properties of the induction machine using the Starter software. The pins of the PM250 and PM240 control units are also configured to operate as analog and digital pins respectively.

4. EXPERIMENTAL TESTING AND RESULTS

In order to experimentally validate the performance of the proposed emulator, numerous experiments and tests were conducted during the development of the system.

4.1 System step response

To determine the response time of the proposed emulator, the system was tested with a step input generated using a signal generator. Generally, a faster slew rate is desired for any kind of a system. For the proposed emulator, a higher slew rate ensures that the system is able to trace all the switching dynamics of a load being emulated.

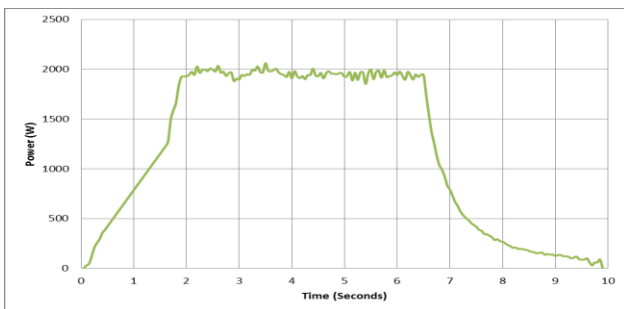


Figure 5: Three-phase load emulator system step response.

The system slew rate is 1.10 kW/s with the delay between maximum and minimum being 2 seconds. This delay is attributed to the inertia of the induction machines used. In terms of a real load, this implies an instantaneous switch-on of an electrical load rated at 1.106 kW. Therefore a change in the input signal which requires a change of more than 1.106 kW/s in the power drawn from the grid

by the system, will not be completely processed by the emulator.

4.2 Load emulation experiment I

The normalised profile shown in Figure 3 was used to test the emulation capability of the proposed system. The variation of power factor with power for this load is shown in Figure 6. The power factor varies between 0.8 and 1. This implies that the Wits campus load to be emulated is fairly resistive.

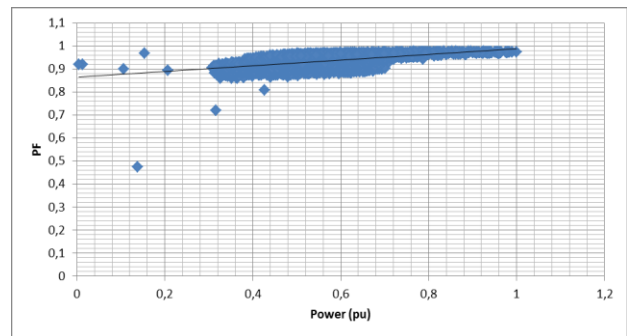


Figure 6: Load power factor (PF) vs three-phase power consumption for the West Campus at Wits University.

The block diagram of the experimental set-up used to conduct the emulation experiment is shown in Figure 2 without the three-phase bank. Both power and power factor were measured using a Yokagawa power meter and the results are shown in Figures 7 and 8.

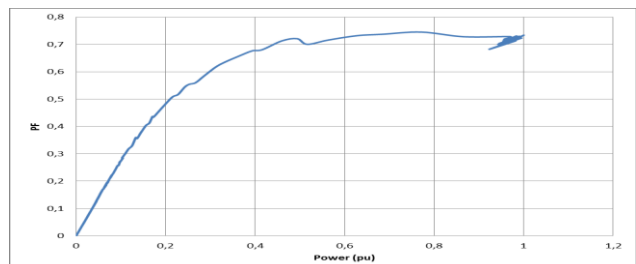


Figure 7: Three-phase load emulator system power factor (PF) as a function of varying emulator power.

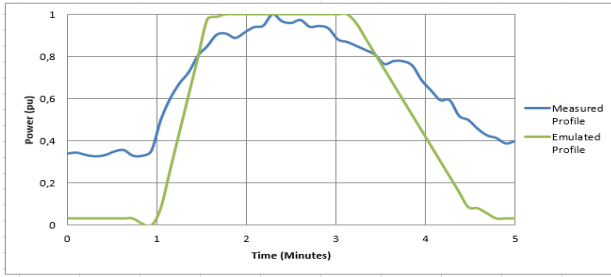


Figure 8: Emulated and measured Wits-campus three-phase load profiles.

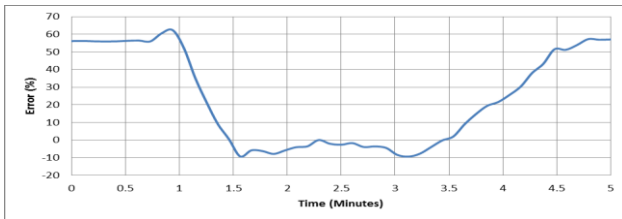


Figure 9 : Error in the response of the emulator system when emulating the Wits Campus load.

Of note in Figure 7 is that the power factor of the system on start-up is zero and increases gradually as the power drawn by the emulator increases. Figure 7 also shows a discrepancy between the base-loads of the emulator and the Wits campus load being emulated. The emulated base load is 0 pu whilst the base-load of the load being emulated is 0.31 pu. The error in the emulated profile is 63 %. To rectify the base-load error, a constant load of 0.31 pu must be added to the emulation system.

4.3 Power factor and base-load correction

To correct the base-load and the power factor, it was decided that a 3-phase resistive load must be added to the input side of the system. There were 3 sets of 3-phase resistors available for the project; three 1.2 kilo-ohm, three 0.8 kilo-ohm and three 0.4 kilo-ohm resistors. At the system power base of 2.2 kW and the system voltage of 400 V, the power dissipated by these resistors is 0.18 pu, 0.27 pu, and 0.43 pu respectively. The resistor bank dissipating 0.43 pu was therefore selected to provide the required system base-load. Since the power factor of a resistive load is one, adding the resistor bank into the system corrects the power factor as well. A delta-connected resistor bank was therefore added to the system as shown in Figure 2 and the load emulation experiment was conducted again.

4.2 Load emulation experiment II

For this experiment, the set-up is the same as that for Experiment I except that there is an added resistor bank into the system. The results are shown in Figures 10 and 11. It is clear from Figures 10 and 11 that the accuracy and performance of the emulator has been enhanced by the addition of the 3-phase resistor bank. When the system is switched on whereby the set points of both machines are at 95 % of synchronous speed, the electromechanical drive subsystems draws minimum power, almost zero.

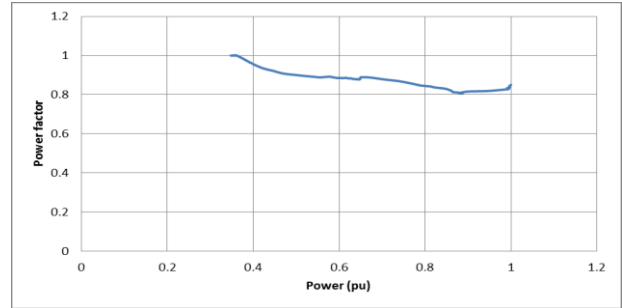


Figure 10: Emulator power factor variation with three-phase power.

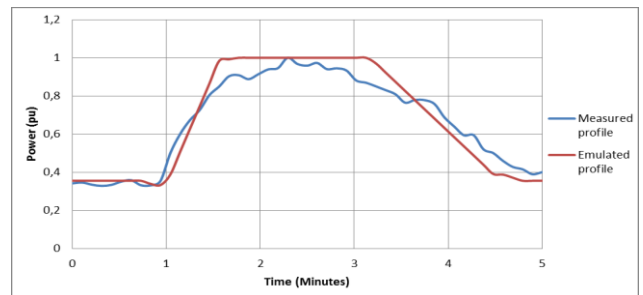


Figure 11: Emulated and measured Wits-campus three-phase load profiles with base-load added.

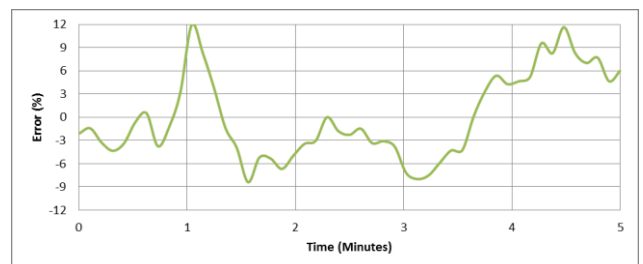


Figure 12: Error in the response of the emulator system when emulating the Wits Campus load. Addition of the resistor bank reduced the system error from 63% to 12%.

At this instance, the load seen by the grid is the resistor bank with a power factor of 1. This load dissipates energy in the form of heat. As the speed set point of M1 is increased by the control signal, the induction machines start drawing real and reactive power from the grid and as a result the power factor starts decreasing. However, it settles down to 0.8. Therefore, the addition of the resistor bank improves the performance and accuracy of the emulator-system, the error is reduced to 13 %.

5. DISCUSSION

5.1 Performance evaluation

The implemented load test-bed is able to recreate a practical power consumption pattern of a real electric load. As seen in Figure 9, the emulated profile is not an exact replica of the load profile. However from an energy point of view, the performance of the emulator is good because the areas under the emulated and the measured load profiles are almost equal. During testing of the system, it was observed that a smallest change in the

control signal causes the system to respond quickly thereby drawing more power from the grid. The slew rate of the load to be emulated and the duration of experimentation determine the performance of the emulator. For more accurate emulations, the system should run for longer periods. However, the resistor bank heats up excessively in seven minutes. Therefore, the system presents a trade-off between accuracy and time-efficiency.

Total Harmonic Distortion (THD): Non-linear loads form part of present electrical loads and these loads generate harmonic currents that affect the stability of power systems [5-6]. The developed load test-bed does not cater for the harmonic content inherent in non-linear loads. Therefore, the emulator can be further developed to cater for the dynamic behaviour of non-linear loads.

Power regeneration: The regeneration capability of the system which allows circulation of power with the grid enhances energy-efficiency while conducting the experiment. However, the addition of the resistor bank increases losses in the system because the energy dissipated by the resistive load is lost as heat. Nonetheless, this is a fair compromise because the added resistor bank improves the power factor of the system and provides a constant base-load required for accurate emulation. The added resistive load is based on the characteristics of the specific load tested. If a load with a different base-load is to be tested, a resistive load with different resistance would be required. To enable modularity, this suggests that the system requires a dynamic resistive bank for base-load and power factor compensation.

5.2 Recommendations

As mentioned, the system does not emulate non-linear characteristics of electric loads. It is recommended that for future work, the emulator must be improved to cater for harmonics inherent in electric loads. The load-data used to test the emulator was measured in intervals of 30 minutes. To validate the performance of the system, it is further recommended that the system be tested with data measured in intervals of seconds. This data will show the dynamic transient characteristics of the load.

6. CONCLUSION

In this report, a dynamic 3-phase load test-bed is presented. This emulator provides a platform for recreating practical 3-phase load-consumption patterns in

a controlled environment. The functionality provided by this test-bed allows for extensive experimentation of different kinds of 3-phase loads. Implementation of this emulator will assist future research on micro-grid stability. The emulator can be improved by investigating its capability to emulate non-linear loads with harmonics and possibly unbalanced 3-phase loads in the future.

ACKNOWLEDGEMENTS

ACTOM is acknowledged for the laboratory facilities. SIEMENS is acknowledged for the inverters and equipment.

ALSTOM Chair for Clean Energy Systems Technology is acknowledged for general support.

The authors would like to thank the School of Electrical and Information Engineering at the University of the Witwatersrand for sponsoring the project. Gratitude is extended to the manager of the Actom Energy Laboratory Mr. M. Goossens and the entire Laboratory staff.

REFERENCES

- [1] Rao, Y.S.; Chandorkar, M., "Electrical load emulation using power electronic converters," *TENCON 2008 - 2008 IEEE Region 10 Conference*, vol., no., pp.1,6, 19-21 Nov. 2008
- [2] Srinivasa Rao, Y.; Chandorkar, M., "Electrical load emulator for unbalanced loads and with power regeneration," *Industrial Electronics (ISIE), 2012 IEEE International Symposium on*, vol., no., pp.320,327, 28-31 May 2012
- [3] Kesler, M.; Ozdemir, E.; Kisacikoglu, M.C.; Tolbert, L.M., "Power Converter-Based Three-Phase Nonlinear Load Emulator for a Hardware Testbed System," *Power Electronics, IEEE Transactions on*, vol.29, no.11, pp.5806,5812, Nov. 2014
- [4] P.C. Sen, "*Principles of Electrical machines and Power Electronics*", p.220,221 Second edition, 1997
- [5] Darwish, A.; Abdelsalam, A.K.; Massoud, A.M.; Ahmed, S., "Single phase grid connected current source inverter: Mitigation of oscillating power effect on the grid current," *Renewable Power Generation (RPG 2011), IET Conference on*, vol., no., pp.1,7, 6-8 Sept. 2011
- [6] Wang Kui; Guan Shuhua; Hou Qian; Hou Yuanhong; Wu Qinfang, "Investigation of harmonic distortion and losses in distribution systems with non-linear loads," *Electricity Distribution, 2008. CICED 2008. China International Conference on*, vol., no., pp.1,6, 10-13 Dec. 2008

DYNAMIC POWER REQUIREMENTS FOR CONTROLLED ENERGY STORE USED FOR STABILIZATION OF THREE-PHASE LOW-VOLTAGE STANDALONE MICROGRID

N. Horonga* and W. Cronje

* Faculty of Engineering and the Built Environment, Private Bag 3, Wits 2050, South Africa. E-mail: nyasha.horonga@students.wits.ac.za and willie.cronje@wits.ac.za

Abstract: This paper investigates the dynamic power requirements for controllable energy storage systems used for stabilization of standalone three-phase low-voltage microgrids with high penetration of renewable energy. It uses recorded data for fluctuating power sources and fluctuating loads to determine how an ideal controllable energy store can be used to stabilize a microgrid with 100% renewable energy penetration. Simulations incorporating the measured data show that a Proportional Integral Derivative (PID) controller can be used to control the ideal energy storage device to ensure stability of the microgrid.

Key words: microgrids, energy storage emulation, Distributed Generation (DG), Microgrid emulation, remote communities, microgrid control.

1. INTRODUCTION

This paper focuses on understanding the dynamic power requirements for controllable energy storage systems to stabilize standalone three-phase low-voltage microgrids with renewable energy sources. This research is undertaken because in many countries, remote areas are unable to receive power from the utility grid and the use of a standalone microgrid is often considered as one of the solutions that can be used to address the problem. Renewable energy sources with large fluctuations are frequently the source of power for these standalone microgrids. The fluctuating nature of these renewable sources often lead to frequent blackouts. The remaining sections in this paper will discuss the background, problem statement and methodology for the research. A brief discussion on results for this research is also presented.

2. BACKGROUND

Figure 1 shows an example of a typical standalone microgrid. This standalone microgrid can be powered from Distributed Generation (DG) sources such as Photovoltaic (PV), wind or diesel generators. The renewable sources are influenced by natural conditions such as varying wind speed and cloud movements and cannot produce power continuously and steadily. This is illustrated by the measured insolation data ($P_{PV}(t)$) in figure 2 recorded on the roof of the Genmin building, University of the Witwatersrand. The insolation data was normalized to the insolation peak of 31.28 W/m^2 for the 5 days. The data was sampled at 5 minute intervals.

Fluctuating loads have always been present in power systems. Figure 3 shows the normalized recorded data for the power demand ($P_{load}(t)$) of a representative load. The load data was recorded for the Genmin building at

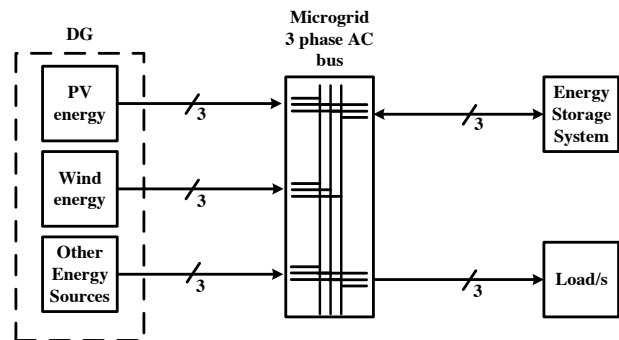


Figure 1. A single line schematic example of a three-phase low voltage standalone microgrid system.

the University of the Witwatersrand. The power demand values were normalized to the Genmin building load peak of 22 kW. The original data was sampled at 30 minute intervals and resampled at 5 minute intervals

Using fluctuating sources on a standalone microgrid

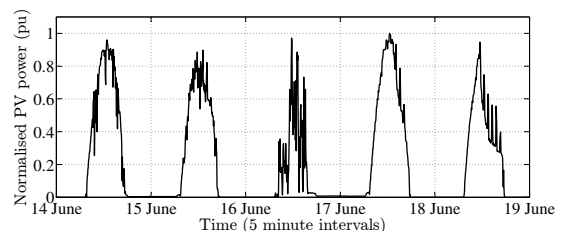


Figure 2. Normalized measured insolation (W/m^2) obtained at the Genmin building (Wits University) during the week of 14 - 20 June 2014.

which already has a fluctuating load can result in significant system power fluctuations. These fluctuations can negatively impact the microgrid operation because

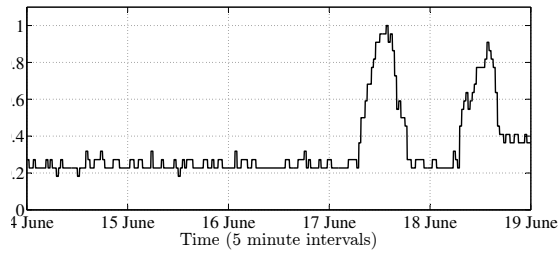


Figure 3. Normalized measured power demand for the Genmin building (Wits University) during the week of 14 - 20 June 2014.

they cause disturbances in the supply voltage. These disturbances includes voltage sags, transients, harmonics, dips and swells that can cause tripping or damage to sensitive appliances [1] [3].

Controllable energy storage can be used to compensate for the microgrid power fluctuations [4–9].

This study will focus on a simplified standalone microgrid that has a single source (in this case a PV source), a single load and a controllable energy store as shown in figure 4 to limit the complexity of the problem.

Depending on the requirements of the microgrid, different types of energy storage systems can be considered. These energy storage systems can be classified into short-term and long-term storage as shown in figure 5. Short-term storage is mainly applied to improve power quality, particularly to maintain the voltage stability during transients [10]. Long-term storage is deployed to contribute towards the energy management, frequency regulation and grid congestion management [10]. Choosing the appropriate energy storage system to stabilize a microgrid requires an understanding of the characteristics of existing energy storage systems. These characteristics includes ramp rate, charge rate, discharge rate, efficiency, energy and power density and response time and are explained in [12]. For the current paper, the most applicable dynamic characteristics are:

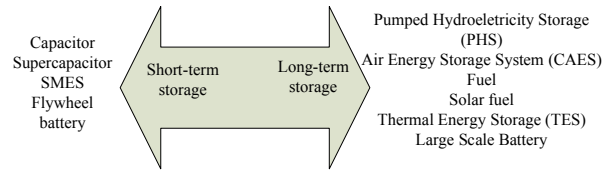


Figure 5. Energy storage classification [11].

- **Response time:** The amount of time the storage system requires to respond to a change in power power demand.
- **Ramp rate:** The rate at which the power flow can change and is sometimes known as the slew rate.

Although the current research is aimed at the dynamic behavior of a power network which strongly depend on DG (100% penetration), sizing of the storage is essential. It is important to note that the total energy supplied by DG and the total energy required by the load must always balance. Using the normalized data obtained from the Genmin building at the University of the Witwatersrand, the PV installation must be scaled by a factor of 1.6 pu for the system to meet the 5 day energy demand of the load. This value is obtained by integrating the normalised load consumed by the Genmin building over 5 days from 14th to 18th of June 2014. The result of the integration was then divided by the integrated normalised PV power over the same period of time. The factor 1.6 calculated above assumes that all the insolation energy is converted into energy required by the load with no losses. This is incorrect in real life and hence efficiency must be taken into account in future studies.

In addition, the PV system power must match the power demanded by the load and if there is any power imbalance, storage must supply the power or store the excess power as shown in equation 1.

$$P_{ES}(t) = P_{PV}(t) - P_{load}(t) \quad (1)$$

Figure 6 shows the overlaid profiles of power generation and load based on the data for the Genmin building on the

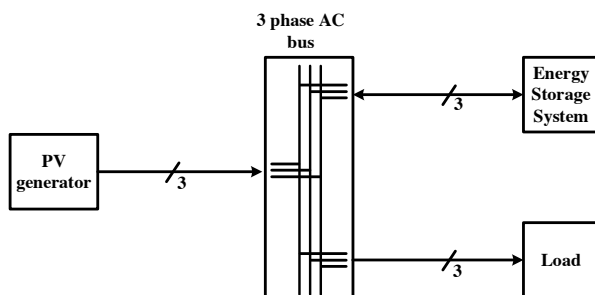


Figure 4. A single line schematic example of a three-phase low-voltage standalone microgrid system with only one power source (PV source).

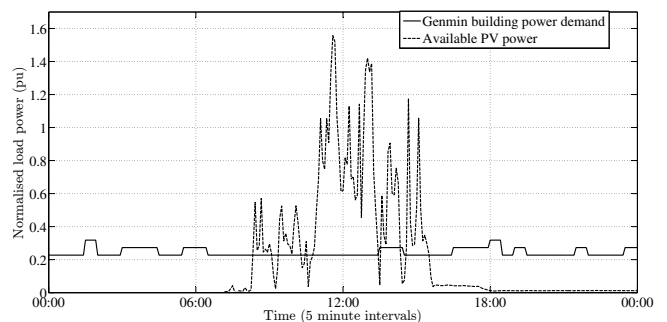


Figure 6. Measured PV and load profiles obtained from Genmin building (University of the Witwatersrand) on the 16th of June 2014

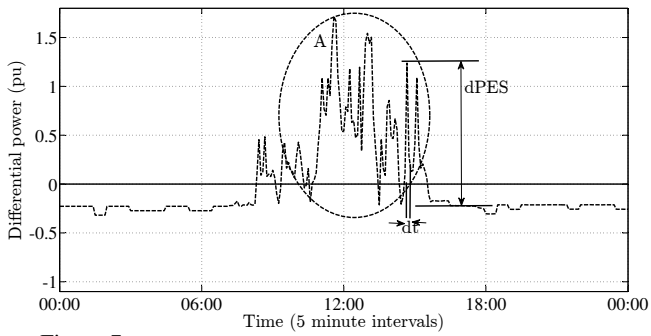


Figure 7. Calculated power difference between PV power and Genmin building load demand.

16th of June 2014. The data recorded on the 16th of June 2014 was selected because the insolation fluctuations were severe. This figure clearly illustrates that power generation does not always match the power demand.

Figure 7 shows the power difference (i.e. the difference between the potential power generation and power demand profiles). The data used as a representative case was obtained from normalized PV and Genmin building power demand data on the 16th of June 2014 at the University of the Witwatersrand. The graph also shows the power to be compensated by energy store and the study will mainly focus on the dynamic behavior of the system (i.e. region A). This power difference is seldom zero and hence the need for an energy storage system. The graph also shows that using the available data, the energy storage system must have a ramp rate (slew rate given by $\frac{dP_{ES}}{dt}$) of 0.1535pu/min. A new set of data with faster sample rate will be used in the future to represent the insolation and load demand data with better resolution and this will provide more accurate ramp rate.

Because the objective of this research is to investigate and determine the dynamic power requirements for using controllable energy stores to stabilize three-phase AC microgrids and ensure power balance, Simulations are conducted for the simplified microgrid in figure 4 to enhance understanding of the problem.

3. SIMULATIONS

The simulations are performed in Simulink[®], using idealised models to better understand the dynamic requirements for the controlled energy store. The simulations assume that the microgrid is a balanced three phase system and only one phase needs to be analysed. In these simulations, The PV source and the fluctuating load are modeled using norton equivalent circuits with controlled current sources.

The simulations are done with and without the controlled energy store. In these simulations the current sources representing the PV source and the load are controlled by the pre-recorded data shown in figure 2 and 3.

To better resemble the behavior of a real PV grid-tie inverter, the variable resistor value R_N in figure 8 and

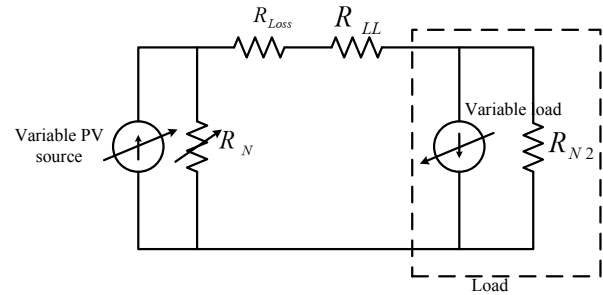


Figure 8. Simulation circuit for a standalone microgrid with 2 current sources modelling the PV source and the variable load respectively.

figure 11 is varied to keep the grid voltage within the acceptable range ($\pm 5V$ in this case). When the PV source current is high, the resistor value R_N is reduced and this will reduce the voltage on the microgrid. When the PV source current is low resistor value R_N is increased thereby keeping the grid voltage almost constant. If the PV source current is too low to sustain the voltage on the microgrid, the system blackouts.

3.1 Simulations without storage

In the absence of a controlled energy store, the grid voltage will fluctuate and these fluctuations can lead to problems on the microgrid. Figure 8 shows the simulation model for the microgrid without energy storage.

In a microgrid the voltage must be limited to the standardized voltage range. If the voltage is below 210V, the grid collapses and if the voltage is greater than 250V, the microgrid maintains the voltage of $230V \pm 20V$ as shown in figure 9. This figure also shows that, the absence of energy storage leads to frequent severe blackouts especially for days where there are high fluctuations in insolation.

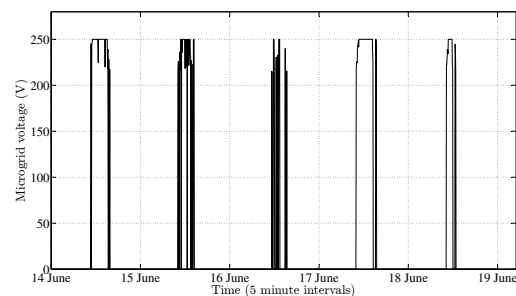


Figure 9. Simulation results for the PV supplied microgrid without storage with a PV inverter voltage controlled to $230V \pm 10\%$.

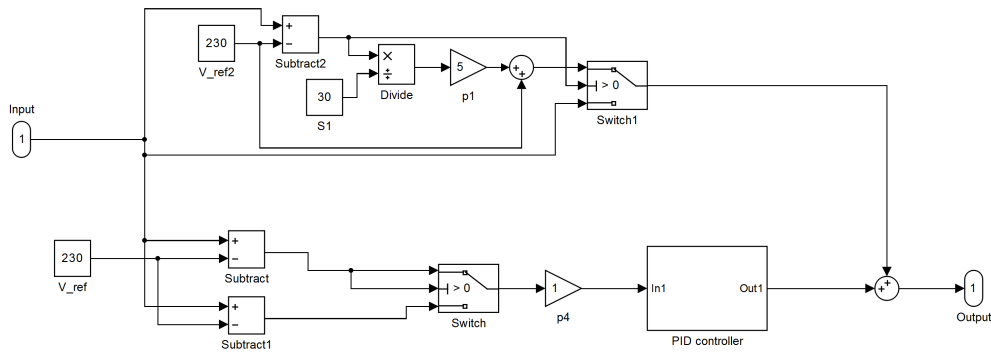


Figure 10. Simulink[®] circuit showing how the energy storage control signal is generated using the voltage and current signals.

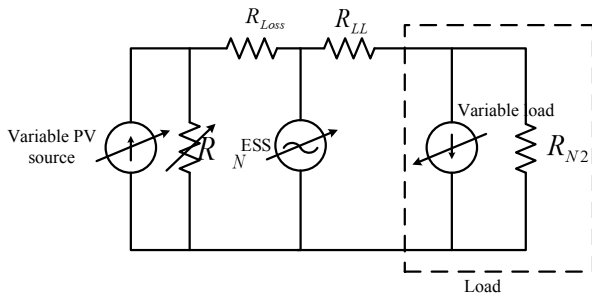


Figure 11. Simulation circuit for a standalone microgrid with current sources modeling PV source and variable load. A controlled voltage source is used to model an ideal energy storage system.

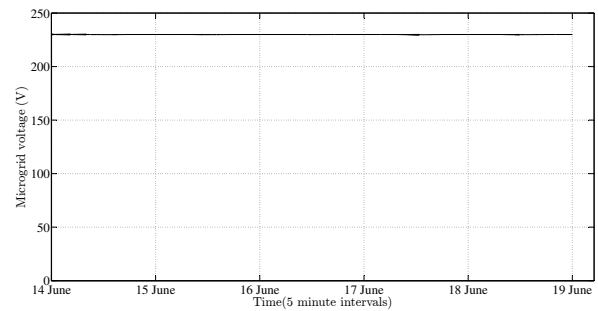


Figure 12. Simulation results of the microgrid with integrated controlled ideal energy storage system.

3.2 Simulations with storage

Subsequent to the simulations for a microgrid without storage, an energy store is introduced. The energy storage system is modeled using a controlled voltage source to regulate the microgrid voltage so that it remains almost constant at all time. By increasing or decreasing the voltage of the energy storage system, the direction of power flow can be changed as required. The energy storage system must maintain the voltage in the range of $230\text{ V} \pm 10\%$ [13]. Figure 11 shows the simulation model for the microgrid with ideal controllable energy store.

The block diagram in figure 10 shows how the energy storage control signal is generated in Simulink[®]. This control block has only one input at present (the microgrid voltage at the point of connection of the energy storage system). A PID controller is used to regulate the voltage. This PID controller uses the microgrid voltage and it assumes that the voltage is equal to the supply voltage of 230V plus an error ΔV (i.e. the difference between the measured microgrid voltage and 230V). The controller then responds to keep ΔV as close to zero as possible.

The results in figure 12 of this simulation for the microgrid with ideal energy storage shows that the voltage can be maintained in the range of $230\text{ V} \pm 1\text{ V}$, which is acceptable for most appliances.

4. DISCUSSION

The results in figure 12 shows that a controlled ideal energy store can be used to stabilize a microgrid with strongly fluctuating power sources and non-constant loads. The simulations do not yet take into account the state of the energy storage system and assumes that there is an infinite amount of energy stored.

The ramp rate and response time are not yet considered in this paper because of the idealized storage model used in the simulations. As part of the future work, an improved model for the energy store with all the required properties will be developed.

Data used in this paper was recorded at 5 minute and 30 minute intervals. There is a need to record the insolation data and load demand at a much faster sampling rate to establish if there is a change in the ramp rate as the

sampling time increases.

Experiments will be conducted on a microgrid testbed to verify the simulation results. The system block diagram shown in figure 13 shows the experimental setup that can be used to carry out the study. Sets of induction machines and variable speed drives will be used to emulate various DGs or energy storage systems as shown in figure 14 depending on the control signal used. Each emulator will receive a control signal that is used to generate a power profile resembling DGs or loads or energy storage system response.

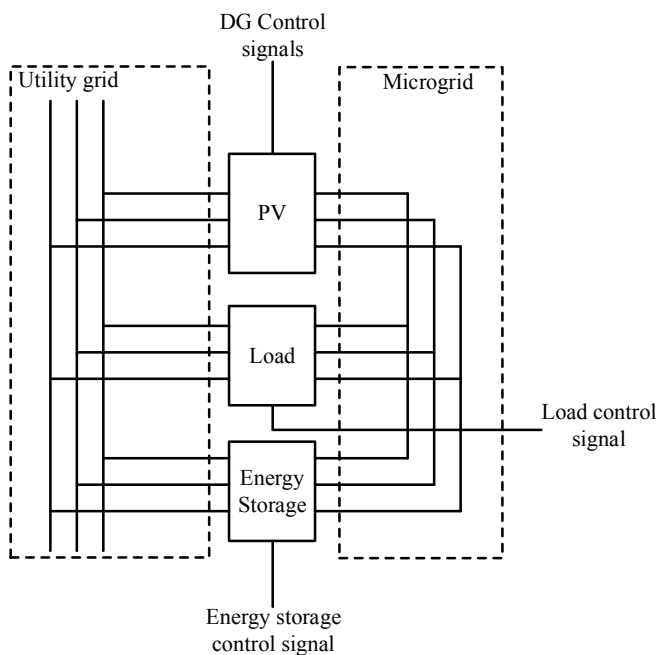


Figure 13. System block diagram of the microgrid testbed that will be used in this study.

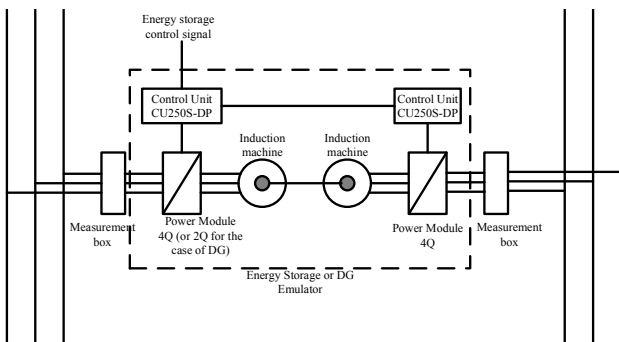


Figure 14. System block diagram of an emulator that can be used as PV source or load or storage depending on the control signal.

5. CONCLUSION

A Simulink® model of a standalone microgrid with and without integrated controlled energy storage was developed. This model can be used to determine the dynamic requirements for stabilizing a microgrid with controlled energy storage. Results from the simulations show that, a PID controlled ideal energy store will be used to stabilize a microgrid with intermittent sources and fluctuating load demand. The model can be further modified to incorporate the properties of a real energy store. Some of these properties include ramp rate and response time and finite energy storage capacity.

ACKNOWLEDGMENTS

The authors would like to thank the ALSTOM chair for clean energy system technology for funding the research. The author would also like to thank ACTOM for providing equipments used for the research investigations.

REFERENCES

- [1] X. Vallvé, A. Graillot, S. Gual, H. Colin: *Microgrid and demand side management in distributed PV grid-connected installations*, 9th International Conference on Electrical and power quality and utilization, Barcelona, 9 - 11 October 2007.
- [2] Robert G. Ellis: *A Reference Guide to causes, effects and corrective measures*, Power systems harmonics, Rockwell International Corporation, Canada, 2001.
- [3] W. Liang: *Determination of power system response during a small load fluctuations*, IEEE, 2009.
- [4] Mohd. Hasan Ali, Minwon Park, In-Ken Yu, Toshiaki Murata and Junji Tamura: *Improvement of wind generator stability by fuzzy logic-controlled SMES*, Proceeding of international conference on electrical machines and systems, South Korea, 8 - 11 October 2007.
- [5] G. Chen, Q. Yang, T. Zhang, Z. Bao, W. Yan: *Real-time wind power stabilization approach based on hybrid energy storage systems*, Sixth international conference on advanced computational intelligence, Hangzhou, China, 19 - 21 October 2013.
- [6] J. Kim, S. Kim and J. Park: *Contribution of an energy storage system for stabilizing a microgrid during standalone operation*, Journal of electrical engineering and technology, Vol. 4, No. 2, pp. 194 - 200, 2009.
- [7] R. Hesse, D. Turschner and H. Beck: *Microgrid stabilization using virtual synchronous machine*, International conference on renewable energies and power quality, Spain, 15 - 17 April 2009.

- [8] M.G. Molina: *Power flow stabilization and control of microgrid wind generation by superconducting magnetic energy storage*, special issue on power electronics for microgrids, IEEE, 2010.
- [9] A.A. Solomon, D. Faiman, G. Meron: *Properties and uses of storage for enhancing the grid penetration of very large photovoltaic systems*, Energy policy, Elsevier, 2010.
- [10] T.M. Masaud, K. Lee, P.K. Sen: *An overview of energy storage technologies in electric power systems: What is the future*, North American Power Symposium (NAPS), IEEE, 2010.
- [11] H. Chen, T.N. Cong, W. Yang, C. Tan, Y. Li, Y. Ding: *Progress in electrical storage systems: A critical review*, Progress in natural science 19, Elsevier Limited and Science in China Press, pp. 291 - 312 , 2009.
- [12] Supervised by: B. Espinar, D. Mayer : *The role of energy storage for mini-grid stabilization*, International Energy Agency Photovoltaic Power Systems Program, France, July 2011.
- [13] NRS: *Voltage characteristics, compatibility levels, limits and assessment methods*, Electrical supply-quality of supply, NRS 048-2:2003, South Africa, 2003

SMART MICROGRIDS FOR RURAL ELECTRIFICATION IN SOUTH AFRICA

R Chetty*

Raj Chetty, Chief Technologist, Eskom Research, Testing and Development (RT&D) E-mail: raj.chetty@eskom.co.za

Abstract: The energy poverty gap in South Africa affects approximately 3.3m million mainly rural households who do not have access to electricity. Energy poverty is a global issue and affects rural areas that are too far from the main grid and are too costly to electrify by extending the main grid. MicroGrids are emerging as an effective off grid solution that can close the energy poverty gap and can supplement existing electrification programs. Further research and development is required to ensure that these systems can be applied for rural electrification and can operate autonomously within specified limits whilst maintaining supply and demand. This study provides the basis for further research and development by simulating the requirements for a proposed hybrid off grid pilot site. The simulation is done using the HOMER simulation tool, the consumption data is sourced from the pre-electrification (PET) tool and the resource data is sourced from weather stations. This data will be used to develop a pilot site for the testing and development of 'smart' off grid solutions that can be used to support the current electrification program in South Africa and assist in reducing the energy poverty gap.

Keywords: Energy Poverty, Microgrids, Rural Electrification.

1. INTRODUCTION

There are approximately 3.3 million South African households who do not have access to electricity in 2014. The White Paper on Energy Policy of 2008 describes the universal access to electricity for all South Africans as a cornerstone for development and social upliftment. Since 1994 there have been a significant number of households that have been electrified by the state owned entity Eskom but there are several challenges that prevent the electrification of the remainder of mainly deep rural parts of the country. Amongst these challenges are the high cost of grid extension of the MV network to remote areas, the current low income levels of these communities, low density of rural populations and hard terrestrial conditions [1]. The social implications of not electrifying these communities far outweigh the challenges and the benefits to South Africa as a developing nation for closing the energy poverty gap and include poverty eradication, social upliftment and the impact on early childhood development, education and improving literacy in deep rural areas.

The current cost of grid extension exceeds approximately R200 000/km (\$20 000) and the breakeven point for grid extension compared to off grid systems is less than 35km [2]. The majority of deep rural communities however are in excess of 35km from the main grid and the high capital cost of grid extension is therefore uneconomical and delays the universal access policy for South Africans as set by Government. Energy poverty is regarded as global problem which not only hinders social development of communities but the absence of energy services, which is the 'lifeblood of economic and social development', and the lack of basic services often leads to social unrest and despair [3]. In Sub-Saharan Africa only 290 million of the 915 million inhabitants (31%) have access to

electricity and the numbers without access are increasing rather than decreasing due to increasing population numbers outpacing electrification programs [4].

2. BACKGROUND

South Africa is a developing country with a population of 54 million people. 38% of the population reside in rural areas and the remainder reside in the urban hubs of the country. The country produces 257 TWh of energy which is consumed by mainly the energy intensive large Industrial and Mining sector (59.5%), Residential consumers (19.7%), Commercial consumers (14.3%), the Agricultural sector (2.9%) and the Transportation sector (1.9%).

Eskom is the country's largest electricity producer (97%) with the rest been generated by municipalities. The generation capacity of Eskom is currently 41 GW and the majority of this capacity is derived from centralised coal fired thermal plants located in the eastern part of the country. The balance of the capacity is derived from nuclear, hydro, open cycle gas turbines (OCGT) and more recently added renewable generation from wind and Concentrated Solar Power (CSP) plants.

South Africa's electrification program commenced formally in the early 1990's. During this period, the country's economy was energy intensive due to mining and minerals and electricity supply was not constrained. There was excess capacity and the focus was mainly aimed at electrifying urban communities. Much of the barriers to widening the access to all communities were based on legacy political policies stemming from the Apartheid era. The democratic transition in the 1990's allowed for a dramatic shift in policy and provided the basis for the electrification program to be placed on the

policy agenda [5]. The scattered efforts of the late 1980's and early 1990's were replaced by institutional reforms in the late 1990's and early 2000 which culminated in the peak of electrification and reported the highest number of households electrified. Since then there has been a steady decline as all role-players in the electrification efforts.

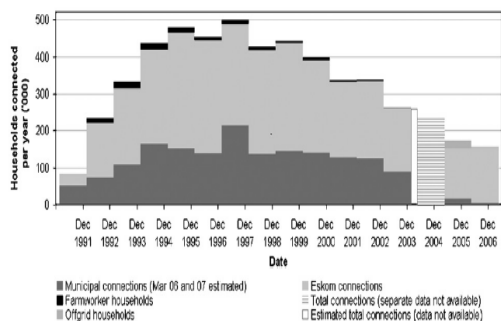


Figure 1: Annual new household electricity connections 1991-2006
(Source Bekker et al. (2006))

The incumbent years after the democratisation of South Africa did not lack the political will to deliver universal access to its people but there was several transitional phases during these years which ultimately resulted in the slow pace of electrification [5]. The focus began to shift to rural areas only in 2002 but this required funding for infrastructure to extend the grid to remote areas. The funding of the initial phases of the electrification program was based on the premise that the program could be self-funded and that capital and operational costs could then be recovered from the newly acquired revenue of electrified homes. Eskom played a role in obtaining funding in early 2000 from capital markets but the funding was derived mainly from the cross-subsidisation from its larger bulk industrial customers. The funding model for electrification has since shifted to Government as from 2001 via funds made available from National Treasury as indicated in the funding phases timelines from 1980 to 2007 [5].

The National Electrification Strategy was developed in 2002 in an effort to close the energy poverty gap in South Africa. The strategy combines current grid electrification and off grid systems into a single electrification strategy and program. This strategy was supported by the then Minister of Minerals and Energy, Phumzile Mlambo-Ngcuka, who, in an address to parliament in 2002 alluded to the high cost of grid electrification, the economic challenges in extending the grid to these communities in terms of the capital cost and due to the initial low consumption of rural communities and low population density rates. The minister also supported regulations to be developed by the then NER (National Energy Regulator) which was aimed at regulating off grid concessionaires to provide services supporting off grid communities in the most cost effective manner. However it was noted that simply providing the basic energy needs of communities such as lighting is not sufficient and

emphasis must be placed on providing power for sustainable economic activities as well in order to address the energy poverty problem in South Africa [1]. Several developing nations are exploring alternatives to conventional grid electrification and have made policy adjustments to encourage distributed generation (DG) and renewable resources that are available closer to the loads they may serve. Microgrids are emerging as effective options to centralised generation and grid electrification [9] & [10].

3. MICROGRIDS

Microgrids (MG) by definition are electricity distribution networks containing distributed energy resources (distributed generators and energy storage devices) and controllable loads that can be operated in a controlled way either connected to the power network or islanded (Cigrè C6.22) [6]. The definition of the term “MicroGrid” is currently been assessed by the Cigrè C6.27 (Hybrid Systems for Off-Grid supply) working group and for the purposes of this paper the term Microgrid is used as per the definition above.



Figure 2: Typical Microgrid configuration
(Source: Sbienergy)

Distributed generators (DG) may include combined heat and power (CHP), fuel cells, mini wind turbines and solar photo-voltaic (PV) and provide for the primary source by means of renewable energy. Energy storage systems maintain the balance between supply and demand in a MicroGrid by storing the energy to be later used during periods when renewable sources are at low levels. The storage system is important as it provides for the management of load fluctuations, provides ride through capabilities to compensate for the intermittency of DG's, especially wind, and allows for the seamless transition from grid tied to islanded modes of operation. Storage systems include batteries, fly-wheels and super-capacitors. Loads may be typically residential which are considered less sensitive than industrial or commercial loads and load segmentation through management systems play an important role in shedding load to 1) meet the net power of a grid tied system 2) stabilise the voltage, frequency and power quality of the system and

3) reduce the peak load in order to optimise the DG peak ratings and manage a ‘constrained’ supply [7] Loads can be segmented into critical or ‘must serve’ loads and non-critical or ‘shift table’ loads that can be supplied during different periods of the day as capacity becomes available or by means of the stored energy.

Microgrids can serve two purposes 1) provide power to off grid loads as a standalone network or 2) act as a generator for end of line grid strengthening when the MG is ‘grid-tied’. In grid tied mode the MG can provide power to and feed from the main grid and can separate from the grid or ‘island’ if the main grid has deteriorating power quality issues. When the MG is grid tied its primary function is to synchronise with the main grid and act as single controllable generation source and load. When the MG disconnects or ‘islands’ from the main grid the MG should act autonomously, maintaining frequency and voltage limits, shedding non-critical loads, providing the required reactive power and be able to supply the harmonics for non-linear loads. Communications networks should be reliable in order to provide for effective control and dispatching of DG sources, stored energy from the storage system and demand management in islanded mode.

4. SIMULATION STUDY

4.1. ESTIMATED CONSUMPTION

The RT&D MicroGrid research and development project was initiated by selecting a pilot site for the project. The pilot site chosen is an off grid rural community consisting based on the following selection criteria:

- An off grid rural customer base
- Optional close proximity to the MV grid for extending the R&D of grid tied microgrids
- Suitable sample size of rural homes

Based on the initial site survey, the customers were identified according to the LSM (Living Standards Measure) grouping. The LSM group was categorised as LSM1-2. The consumption and demand for this customer base was estimated using the PET (Pre-Electrification Tool) which estimated the demand based on the Herman-Beta method. The ADMD (After Diversity Maximum Demand) was estimated at 0.39kVA in year 1 increasing to 0.43 in year 15 and the total daily consumption was estimated at 148kWh/day. The following table shows the consumption (kWh) and demand (ADMD in kVA) for each year after electrification.

Year	Energy [kWh]	ADMD [kVA]	alpha	beta	Circuit Breaker
1	68.55	0.38	0.20	2.27	20.00
2	69.20	0.38	0.20	2.25	20.00
3	69.23	0.38	0.20	2.25	20.00
4	70.21	0.38	0.20	2.23	20.00
5	71.03	0.38	0.20	2.22	20.00
6	72.72	0.39	0.20	2.19	20.00
7	74.01	0.40	0.20	2.16	20.00
8	75.48	0.40	0.20	2.14	20.00
9	77.74	0.41	0.21	2.10	20.00
10	80.29	0.42	0.21	2.06	20.00
11	82.16	0.43	0.21	2.03	20.00
12	83.28	0.43	0.21	2.01	20.00
13	83.73	0.43	0.21	2.01	20.00
14	83.76	0.43	0.21	2.01	20.00
15	83.76	0.43	0.21	2.01	20.00

Table 1: Estimated consumption and demand per customer per month in a 15 year period

The PET data provided the primary load inputs and produced 8760 hourly load profile values for the typical LSM 1-2 customer and was estimated for a complete year accounting for seasonal variations in consumption (Figure 3).

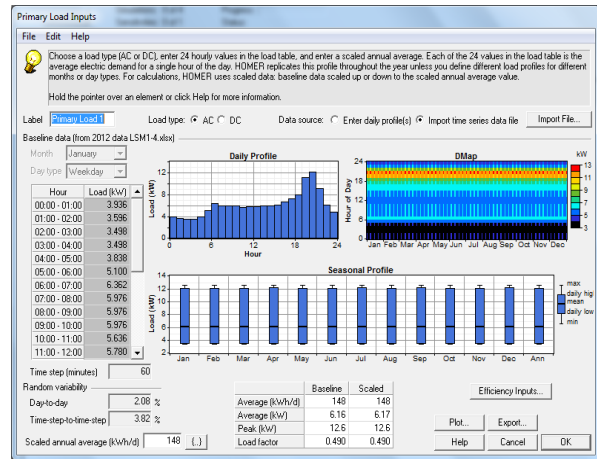


Figure 3: HOMER primary load input data for 34 customer pilot site

4.2. WEATHER DATA

The weather data was obtained from the closest weather station located at 50km from the site at Leander. The weather station provided solar irradiation data (kWh/m²/day) as well as temperature and humidity data. The solar irradiation data from the weather station was however replaced by data from HOMER¹ (Figure 4).

The HOMER modelling tool includes a database of resource data which is obtained from the HOMER website. The resource data provides the inputs for the modelling tool.

¹ HOMER (MicroPower Optimisation Model) originally developed by the National Renewable Energy Laboratory)

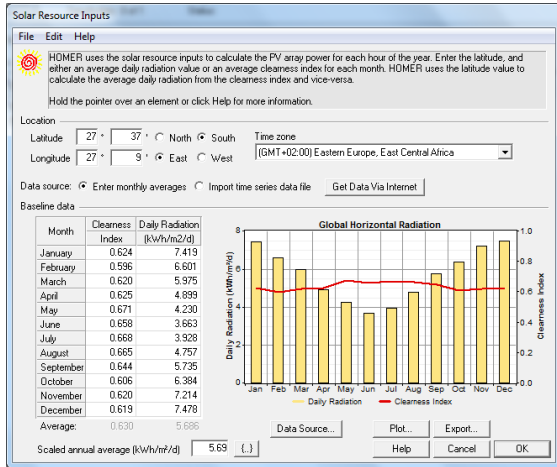


Figure 4: Resource data for pilot site using HOMER

4.3. SIMULATION RESULTS

The estimated consumption data and weather data was used as inputs in the HOMER simulation model. The model provided a basic configuration layout of the hybrid MicroGrid (Figure 5)

- 55kW of PV (Photovoltaic) distributed generation to supply primary power to the load
- 5000kWh of battery storage
- At the LCOE (Levelised Cost of Energy) of \$ 0.196/kWh

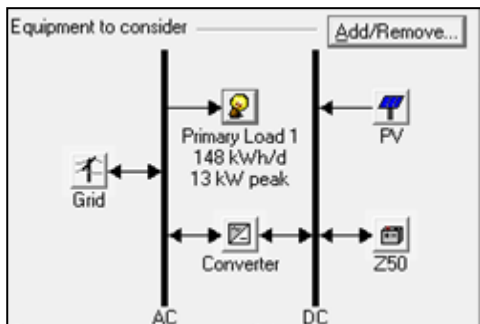


Figure 5: HOMER simulation of the Microgrid configuration

The Levelised Cost of Energy (LCOE) is the cost of a specific generation technology used in a project that will allow for a financial ‘break-even’ on the return on investment over the project lifecycle. LCOE is made up of the capital costs, operating costs, inflation costs and generally assumes a project life cycle of 20 years and serves as a useful comparison across different generation options. Grid electrification generally yields a low LCOE due to the large economies of scale provided by centralised generation however the LCOE of MicroGrids is expected to reach grid parity as the costs of the various distributed generation and storage technologies decrease and Microgrids may be a feasible option to grid electrification over the project life cycle (Figure 6).

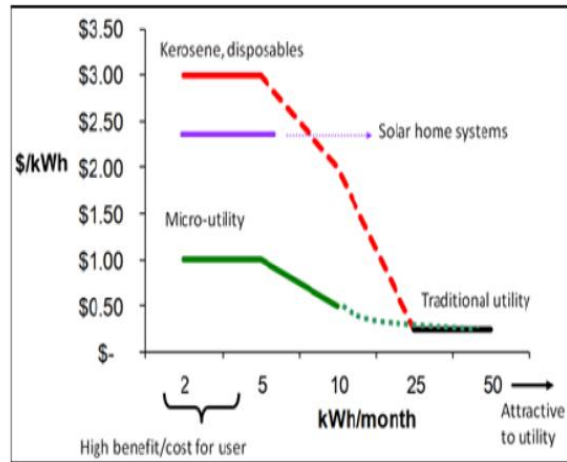


Figure 6: Cost benefit of Microgrids

In order to provide a wider research and development platform this site was also chosen due to the close proximity to the Eskom grid. It is proposed to operate the site in both off-grid and grid-tied modes. The grid tied configuration will require an inverter and due consideration to the design requirements for this configuration. Based on this, 25% of the supply will be delivered from the grid and 75% from the off grid PV system.

The control within a MG to balance supply and demand can be made autonomous for each of the DG sources which allows for modularity, flexibility and scalability without having to re-engineer the system. This design approach eliminates the need for a complex central controller [7], [8].

Much of the research on Microgrids by North American countries are focussed on the reliability of supply that can be provided by MicroGrids and operational systems are already been used in several military facilities to ensure continuity of supply after a catastrophic event. Europe and Asia are focussed on renewable energy and these are predominant in the test beds developed in these countries. The approach to MicroGrid design in North America deploys autonomous control whereas Asian countries are experimenting with central control. Common to both control approaches is the droop control method and observations indicate that droop control methods such as frequency-active power (P-f) and voltage-reactive (Q-V) power droop methods provides system stability [7].

The pilot project will provide a useful test bed for further MicroGrid research and Development. Several experimental microgrids and MicroGrid test beds that have been developed internationally and are been used to study the operational characteristics of microgrids [7].

These test beds aim to further the research and development of microgrids in relation to the IEEE 1547

Guide for Design, Operation and Integration of Distributed Resource Island Systems with Electric Power Systems. The key focus areas are the operating dynamics of MicroGrid systems in radial and mesh networks, the interoperability of the distributed generation sources such as PV, wind and fuel cells, energy storage technologies such as batteries and flywheels, various load types such as residential and commercial as well as the different MicroGrid control approaches such as central and autonomous control techniques.

5. CONCLUSION

This paper presents the basic concept design for a MicroGrid system as means to support current grid electrification particularly for customers too far from the main grid. Further research and development is required on Microgrids and off-grid solutions in South Africa and a proposed R&D pilot site will provide the basis for the research and development. The test site will allow for the analysis of a MicroGrid systems in terms of voltage and frequency stability of such systems when operated in grid tied and islanded (off grid) modes. A further understanding of the control methods is also required. Load management may play an important part in an off grid MicroGrid due to the systems limited capacity. The pilot will therefore provide useful data in terms of appliance control schedules and load limits levels. A thorough customer behaviour study is also required in order to understand the impact of Microgrids on customer acceptance, usage patterns and other social factors. These aspects will collectively assist in developing ‘smart’ microgrid systems which can be scale-able, modular and intelligent and can be deployed at a wider scale.

The HOMER simulation tool was used to estimate the basic components of the system using estimated consumption data and weather data for a pilot customer site. The next process of the pilot study will involve a more detailed design of a “Smart MicroGrid” taking the following into account:

- Detailed sizing of the PV system
- Detailed sizing of the battery storage system
- Intelligent and Optimal control system using either centralised or decentralised control
- Required load management of appliances specifically during peak consumption periods
- Required metering and revenue collection technologies
- Telecommunications requirements for the communication between the system components
- A customer behaviour and impact study
- Training and education of pilot customer on the efficient use of appliances.

6. REFERENCES

- [1] Department of Minerals and Energy (DME). 2008. Mini-grid hybrid viability and replication potential, The Hluleka and Lucingweni pilot projects, Final report, August 2008. Accessed 05 March 2014. Available at <http://nano.co.za/MinigridReplicationViabilityFinalReportAug08.pdf>.
- [2] O. M. Longe, K. Ouahada, H. C. Ferreira & S. Chinnappen. 2014. Renewable Energy Sources Microgrid Design for Rural Area in South Africa. University of Johannesburg.
- [3] Thompson, G. 2014. Democratization, Energy Poverty, and the Pursuit of Symmetry. Global Policy,. DOI: 10.1111/1758-5899.12103.
- [4] International Energy Association 2014. World Energy Outlook. Available at <http://www.worldenergyoutlook.org/>.
- [5] Bekker. B, Eberhard. A, Gaunt.T & Marquard.A. 2008. South Africa’s rapid electrification programme: Policy, institutional, planning, financing and technical innovations, Energy Policy. 36 (3115-3127). DOI:10.1016/j.enpol.2008.04.014.
- [6] Cigre SC C6 Distribution Systems and Dispersed Generation Available at <http://c6.cigre.org/WG-Area/WG-C6.22-Microgrids>.
- [7] Lidula, N.W.A & Rajapakse, A.D. 2011. Microgrids research: A review of experimental microgrids and test systems. Renewable and Sustainable Energy Reviews. 15(2011) 186-202 doi:10.1016/j.rser.2010.09.041. doi.org/10.1109/PES.2011.6039527
- [8] Olivares, D.E, Canizares, C.A & Kazerani, M. 2011. A Centralized Optimal Energy Management System for Microgrids. Power and Energy Society General Meeting IEEE.

A DATA VISUALISATION SOLUTION FOR SMART ENERGY MONITORING SYSTEMS

MC Geddes *, BE Phillips † and KJ Nixon ‡

* mcgeddes@gmail.com † b.phillips.za@ieee.org ‡ ken.nixon@wits.ac.za

School of Electrical & Information Engineering, University of the Witwatersrand, Private Bag 3, 2050, Johannesburg, South Africa

Abstract: A data visualisation solution for smart energy appliance usage behaviour and load profiling is presented. By using the MapReduce algorithm, a charting web application is implemented which allows the plotting of large datasets of electrical information without losing event information. The system is developed using a modular approach, allowing the MongoDB, charting library or other components to be replaced as required by other applications. The performance of back-end data management services and the web application is discussed, and it was found that the MapReduce algorithm facilitates charting large datasets and can provide more useful information than the original data. User interaction with the application is responsive with response times for data requests between 0.5 to 4 seconds if on-demand processing or preprocessing are used for the appropriate size datasets.

Key words: Load profiling, MapReduce, MongoDB, Usage behaviour, Visualisation

1 INTRODUCTION

In South Africa, the electricity public utility, Eskom, has prioritised efforts to reduce demand as peak demand exceeds supply. Being unable to service peak demand has several detrimental effects on the economy and the lives of South Africans. Also, the situation is further exacerbated as utilities are unable to be serviced as normal due to the struggle to service peak demand. Increasing and stabilising the electrical supply infrastructure remains an important goal, however, efforts to increase supply can prove expensive. A balance between supply and demand management must be obtained. In this way, strain on the national grid can be reduced to acceptable levels without compromising the stability of the national grid, the natural environment or the safety of the South African community [1].

By utilising the large amount of information available from local grids, it may be possible to selectively load-shed appliances, decreasing demand when required. For this purpose, technical analysis of smart grids and appliances is required so that state transitions can be identified. With this knowledge, it is possible to accurately describe usage behaviours. A visualisation framework which takes advantage of data aggregation (namely the MapReduce algorithm) is proposed in this document for technical users to observe the electrical behaviour of appliances.

The background to energy monitoring and data aggregation challenges is presented in section 2. The proposed system's implementation is discussed in section 3 with pertinent results and discussion in sections 4 and 5.

2 BACKGROUND

2.1 Appliance usage behaviour and load profiling

A graphing library could provide information on the usage of certain appliances in a grid. This information and presentation could be used to develop systems to intelligently control distribution for energy saving and smart grid management purposes. A common approach to obtaining the required appliance usage information is by observing daily behaviour-based usage patterns. With daily patterns, it is possible to determine appropriate schedules for selective load shedding of some appliances [2].

Load identification is essential so that the usage behaviour can be established. The proposed graphing library could provide the means for an engineer to profile appliances such that ON/OFF transitions can be identified. Some appliances can be identified in a smart energy metering system at sampling periods as high as 15 minutes. However, in a technical setting, away from the "smart home", sampling at a faster rate may provide more insight into the transient behaviour of appliances [3]. The monitoring and analysis of energy usage can create large volumes of data. This is apparent when attempting to initially identify appliances, where the required sampling rate is unknown. For example, it was observed that a sampling rate of 500 milliseconds over a 24 hour period produced 172 800 data points. Plotting this number of points in a useful manner is non-trivial.

2.2 Data aggregation and MapReduce

To aid in the processing and visualisation of the high volumes of data produced by load profiling and usage behaviour analysis, an appropriate data aggregation method must be employed. The type of data manipulation in the back-end has a direct impact on how the data

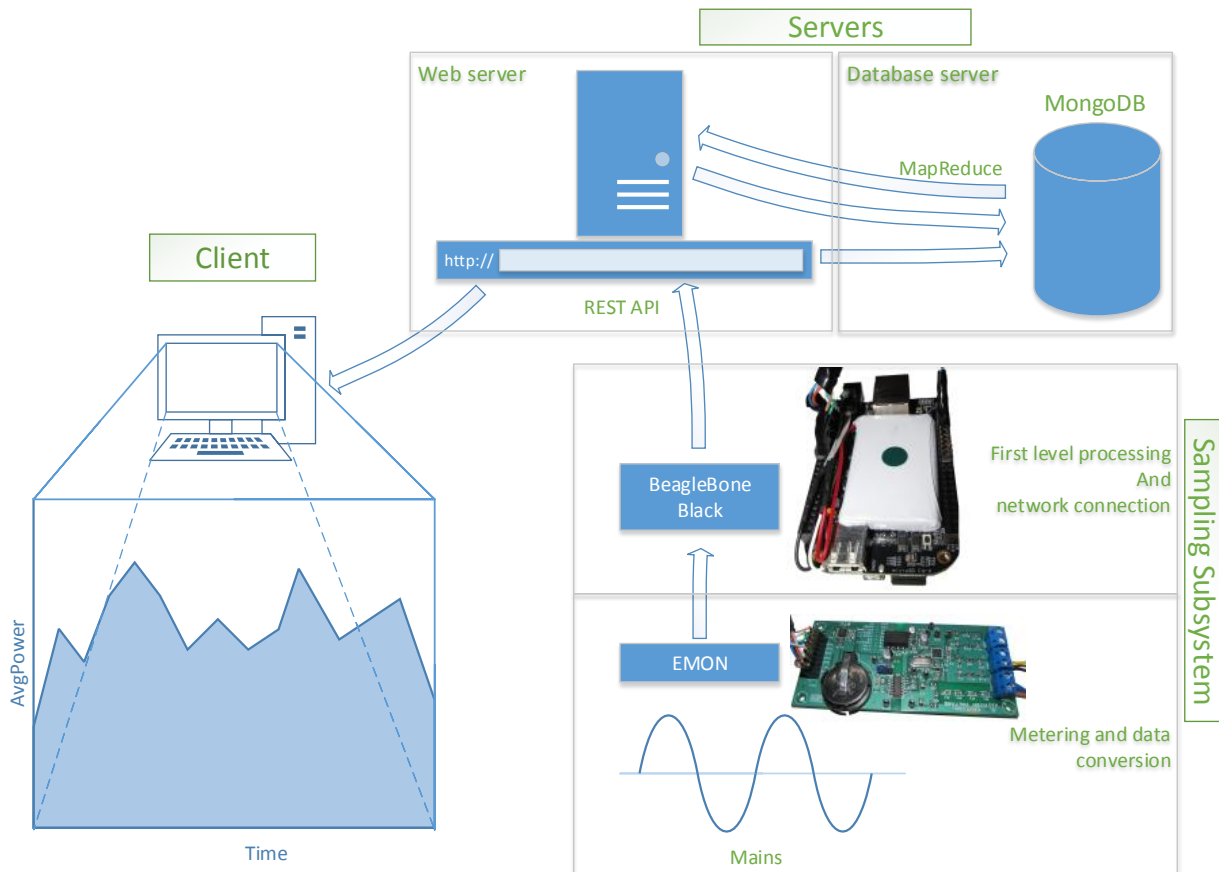


Figure 1: Example interactions in the system

can be visualised. In [4], the main approaches to processing big data are described. MapReduce algorithms process data in parallel but have the potential to retain event based information, essentially providing a filter for overwhelming information.

The data storage method is chosen based upon the findings that MapReduce is the main data aggregation method and also on the compatibility with the third party charting library as discussed in section 2.3. NoSQL databases have become a popular choice for the purpose of scientific data storage as they potentially provide faster read and write speeds for simple data with no relational properties. In [5], it was found that MongoDB was consistently among the fastest NoSQL implementations and therefore is the chosen data storage method. It is also noted that MongoDB provides a native MapReduce algorithm.

2.3 Third party charting libraries

The following libraries, extensions to existing libraries and programming frameworks were considered for the purpose of charting in the application (amongst others):

- JFreeChart, a Java chart library with support for many chart types [6];

- Dygraphs, a JavaScript library for large data sets with an emphasis on line charts (time series) [7];
- D3.js, a flexible JavaScript library providing extensible manipulation of the Document Object Model (DOM) [8];
- Cubism.js, a D3 plugin with emphasis on time series and realtime dashboards [9];
- R, a software framework for statistics with graphics support [10]; and
- Matlab, a popular framework for Mathematics and scientific computing with support for MapReduce [11].

The main focus is to provide an effective means of visualising electrical, time-based properties of appliances such that conclusions can be drawn for events in electrical grids. Therefore, the proposed solution prioritised time series support in the charting library. It was also found in preliminary tests that large amounts of data is collected while monitoring appliances (as discussed in section 2.1). As a result, Dygraphs was chosen as the main candidate for a third party charting library.

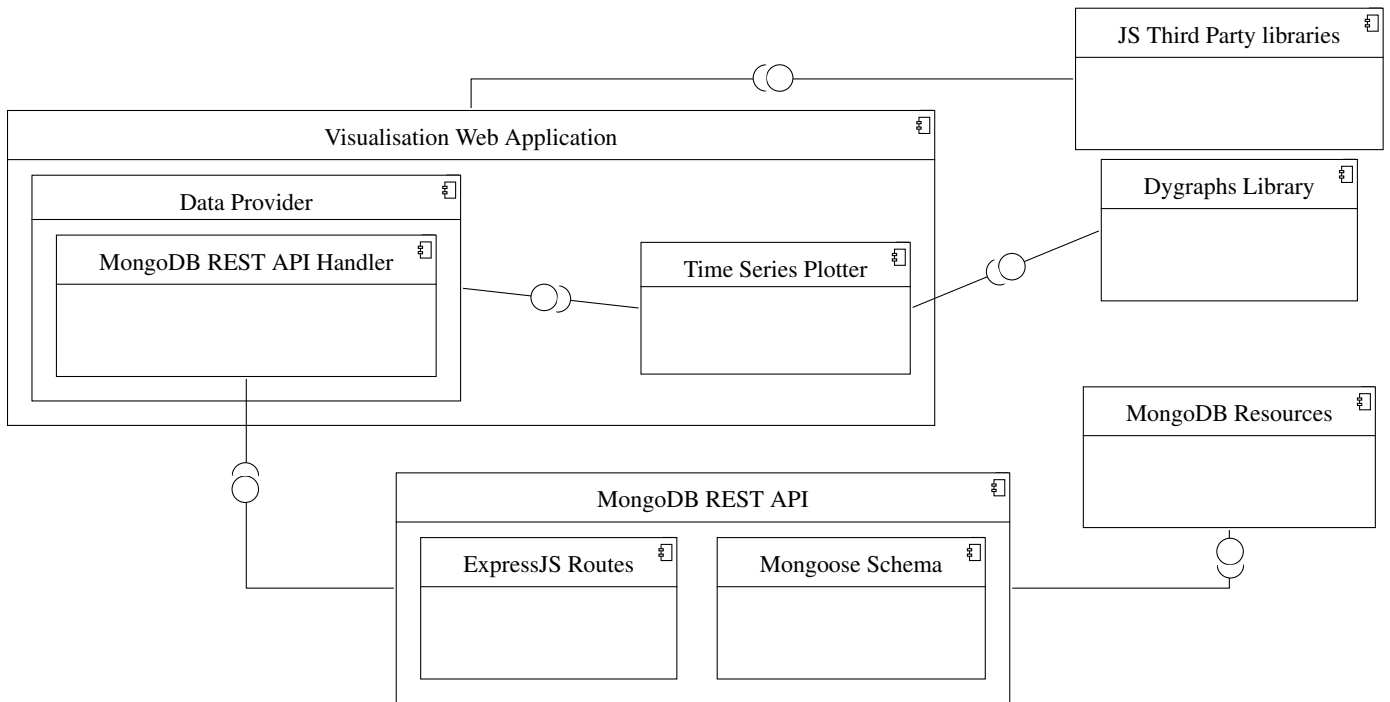


Figure 2: UML component diagram of software system architecture.

3 SYSTEM DESIGN

An example of interactions between all components in the system is presented in Figure 1. However, the layers on the system can be allocated in many configurations. It can also be noted that any hardware can be replaced with alternatives as a REST (Representational State Transfer) API provides a portable interface for database management. These flexible characteristics are discussed further in section 3.2.

3.1 Monitor subsystem

The Sustainable User Centred Smart Energy Systems (SUCSES) alliance has developed an energy monitoring board (EMON) based on the *Cirrus Logic CS5480* integrated circuit module [12]. The monitor subsystem is comprised of the EMON and a BeagleBone Black development board. The BeagleBone Black was chosen as it provides low level functionality out of the box and is sufficient for proof of concept.

3.2 Software framework

The proposed software system was implemented with interfaces defined as shown in the UML component diagram in Figure 2. The framework has three distinct layers as follows:

- Visualisation web application;
- MongoDB server; and
- MongoDB REST API server.

The layers can be separated between devices (client computers and servers) in all possible combinations, allowing for the framework to fit many scenarios. For example, this flexibility allows for easy off-line maintenance and testing when all layers can be run from one computer/device.

Visualisation web application: The web application provides a time series plotter which, amongst other features, provides a interaction model which allows data to be requested and map reduced on demand. The time series plotter and data provider are implemented so that the MongoDB REST API Handler can be replaced as long as some functions are provided. This allows the database framework to be reimplemented if it is found that a database infrastructure (such as Cassandra, CouchDB, HBase, Neo4j [5] [13]) is more suitable for a particular application. Indeed, the reimplementation could even make use of a relational database framework, such as a SQL implementation, if that proves useful. It has been shown that some SQL implementations can perform faster than some NoSQL solutions depending on the application [5].

MongoDB server: The MongoDB server hosts the MongoDB databases, which hold pure sampling data from the monitor subsystem described in section 3.1. Elaborating on the findings in section 2.2, the choice of MongoDB as the database implementation provides several opportunities. The native MongoDB query interface provides minimal yet scalable functionality such that the database can be separated and interacted with in

different ways. This allows a focused implementation, in this system the REST API server, of an extended query interface. However, other projects still have access to the same database and the application of such projects may require a different access method.

MongoDB REST API server: Fundamental to the flexibility of the framework is the REST API. There are two main interfaces to the REST API for the different accesses to the MongoDB databases. These are the monitor subsystem side and client web application side. The monitor subsystem is able to http POST readings to the server. The advantage to this approach is that only a basic implementation of http POST is required (which was provided by BSD socket API) which is a portability benefit [14]. The web application is able to request readings, and these readings can be provided at different levels of MapReduce as the web application determines appropriate. The use of CORS (Cross-Origin Resource Sharing) allows the database resources to be separated from the REST API as discussed, allowing the application to retrieve data from multiple sources [15].

4 RESULTS

4.1 Charting features

With all charts produced by the web application (Figures 3, 4, 5, 8 and 9) the dark lines represent the averages found by the MapReduce. The shaded areas represent the error bars, which are the minimum and maximum data points found in each mapped set.

In Figure 3, the average power consumption of a computer monitor is presented. With this type of appliance, usage behaviour is easily ascertained as the ON/OFF transitions are clearly visible. The error bars do reveal that the original data fluctuated around the trends to some extent, however, it is clear that sampling at a much slower rate would facilitate cheaper hardware while still being able to determine state (which appears to be binary with this limited dataset).

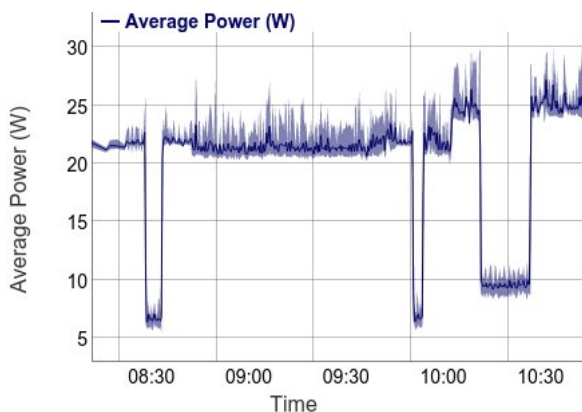


Figure 3: Average power measurements of computer monitor on 3 October 2014 (example application output).

Not all measurements provide clear ON/OFF transition patterns. In Figure 4, the average power consumption and power factor of a coffee machine is presented. The provided visualisation shows that both measures have a much wider spread than the computer monitor case in Figure 3. From the average data point lines in Figure 4 it is found that the MapReduce algorithm exposes events that may have otherwise been concealed if observing the original data.

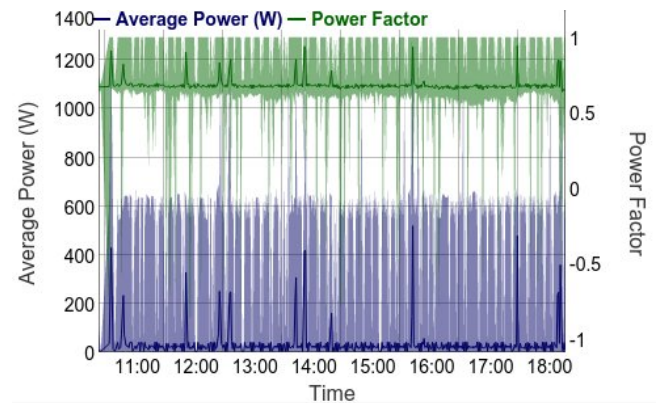


Figure 4: Average power and power factor measurements of coffee machine on 10 October 2014 (example application output).

The charting application allows the user to select a region of the graph to enlarge that region, but also to acquire a new map reduction of the dataset which provides a reduced set closer to the original data. This concept is presented with the coffee machine measurements in Figure 5. The time scale is reduced to approximately fourteen seconds, and as a result, the Map-reduce algorithm was configured to reduce the original dataset less. This is also apparent as the error bars on the average power have diminished almost completely. In this way, an engineer will be able to perform *load profiling* on this enlarged region, whereas the charts in Figures 3 and 4 provide the means to determine *usage behaviour*.

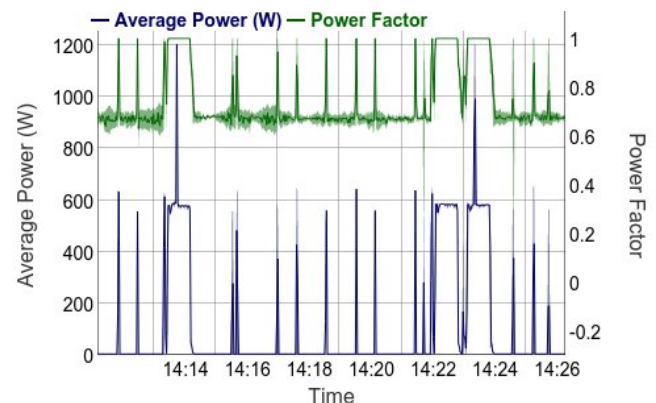


Figure 5: Average power and power factor measurements of coffee machine on 10 October 2014, closer inspection of spikes in average power (example application output).

4.2 MapReduce Performance

In Figure 6, the response time for the MapReduce algorithm with increasing number of samples is presented. It is apparent that the map function computation time increases with the size of the dataset and that this increase results in computation times that will greatly decrease the responsiveness of the charting application.

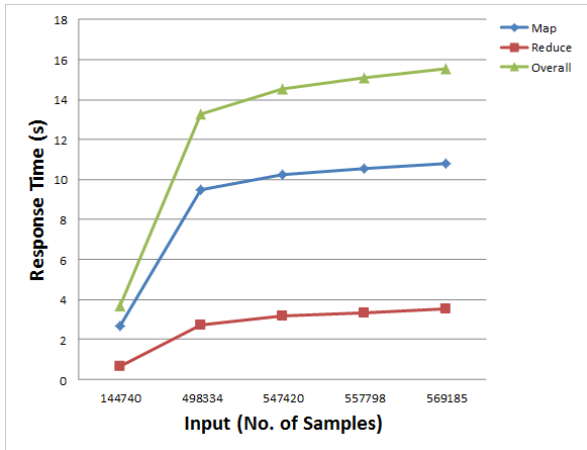


Figure 6: MapReduce response time for increasing number of samples.

Preprocessing the MapReduce algorithm may be a viable option such that response times for large datasets is in an acceptable range. In Table 1, the response times for the retrieval of MapReduced datasets by preprocessing and on-demand processing are compared. It can be concluded from the computation time that the charting application would benefit by using preprocessed data for datasets over approximately 145 000 (approximately 1 day in this application).

Table 1: Average response times (in ms) for preprocessing and on-demand processing of MapReduce.

No. Samples (Days)	On-demand	Preprocessed
569 158 (3.3)	15 560	527
498 334 (2.9)	13 257	447
144 740 (0.8)	3 650	163

Conversely, when dealing with smaller datasets where the reduction size request for MapReduce is small, the response time for the algorithm is as shown in Figure 7. The computation time greatly increases for reduction sizes of less than approximately 5 seconds. To alleviate this, the charting application may retrieve the original data without applying the MapReduce algorithm. In this way, the only computation cost will be the retrieval of the data.

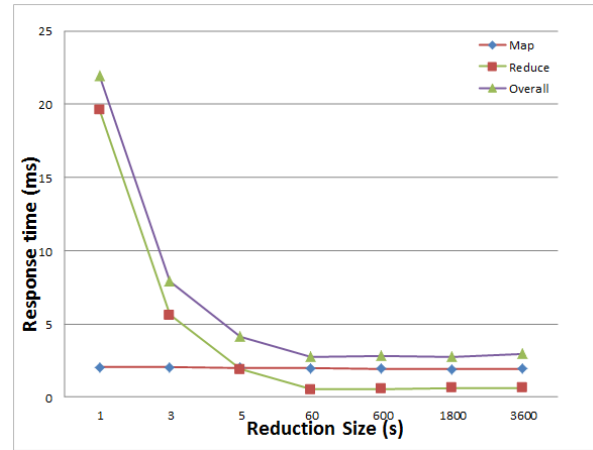


Figure 7: MapReduce response time for decreasing reduction sizes.

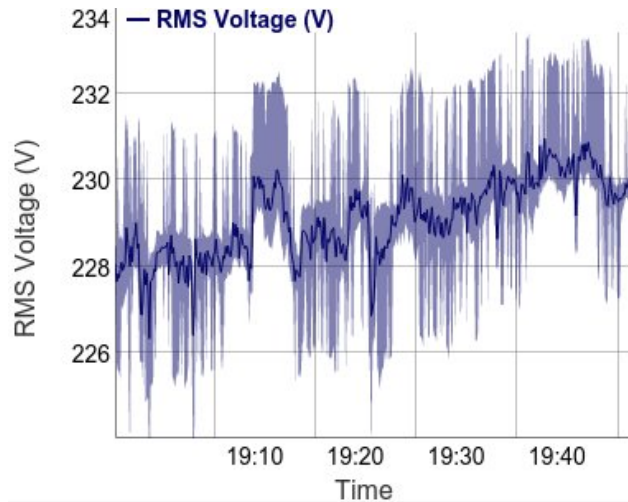


Figure 8: RMS voltage with minimum and maximum error bars for reduced sets (example application output).

4.3 MapReduce statistics

The MapReduce provides a generic, flexible algorithm for the purpose of reducing datasets. Neither the extent of the mapping for the reduction or the type of process used in the reduction is defined. This allows the selection of an appropriate technique on a per application basis [16].

For the purposes of the proposed application, the maximum and minimum in reduced sets is represented by the error bars (as discussed in section 4.1). This was compared with an implementation that uses standard deviation to fit the error to a normal distribution around a mean (the error bars represent 5 standard deviations around the mean). The minimum/maximum and normal distribution error bar methods are presented in Figures 8 and 9 respectively for the same original data. From the graphs, it is apparent the data may not fit the normal

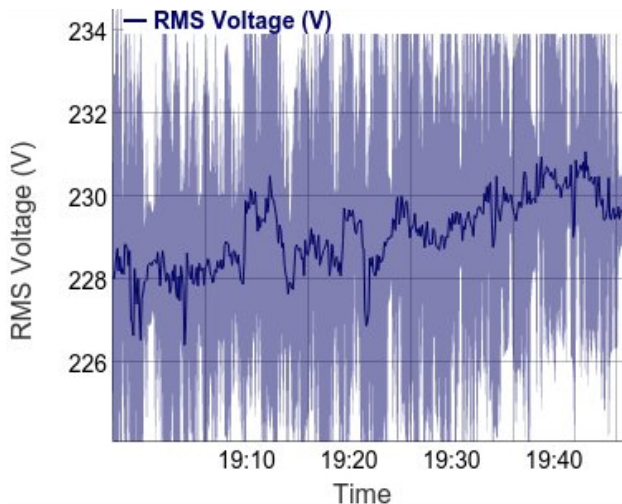


Figure 9: RMS voltage with error bars defined by the normal distribution span of five standard deviations for reduced sets (example application output).

distribution, which is a limitation of such an approach. For statistical analysis, all data would have to be fitted to an appropriate distribution [17].

5 DISCUSSION

It is important to emphasise that low-cost strategies are required to ensure a sustainable solution to excessive peak demand (as discussed extensively in [1]). Many strategies should be considered, but with the focus on smart energy systems, it can be found that rich usage behaviour data is available in local grids and the appliances that are being monitored and controlled.

The size of collected electrical data for smart energy systems has a large impact on not only the responsiveness of analysis applications but also on the type of information that is visible. In large datasets, event based information can be lost in the data. In some applications it is more appropriate to collect less data to alleviate this information overload, but without first profiling the application (in this case, an appliance), an engineer can not make informed decisions on hardware requirements and sampling rates. Therefore, this is the main motivation for the development of the application and framework presented in this document. The developed application could serve as an important technical analysis tool and building block in a programme to alleviate strain on the national grid by decreasing peak demand.

6 CONCLUSION

The background to the importance of data visualisation in smart energy systems has been presented. It was found that when appliances are monitored for usage behaviour and in an attempt to profile their loads, large volumes of data are produced which present computational challenges when visualising the data. To alleviate the computational strain

placed on charting applications, the MapReduce algorithm was employed. When monitoring for usage behaviour of an appliance, it was found that the MapReduce algorithm has benefits above its computational performance benefits. MapReduce allows charting applications to observe events which may otherwise have been obscured in the original measurements. A web application for charting was implemented and with the appropriate configuration of the MapReduce algorithm or other data aggregation technique, it was found that the application was responsive to user interaction with response times between 0.5 to 4 seconds.

ACKNOWLEDGEMENT

The authors would like to thank Eskom for their support of the Smart Grid research programme at the University of the Witwatersrand through the TESP. The authors would also like to thank Dan Vanderkam for providing the Dygraphs JavaScript charting library under a “MIT style” license. Joshua Sanderson also provided a framework under a similar license to perform data requests on graph interaction. The framework was modified extensively to perform similar interactions with the MongoDB REST API.

REFERENCES

- [1] Eskom Holdings SOC Limited. “2014 Integrated Report.” pp. 11–18. 2014.
- [2] Y. Chen, Y. Ko, and W. Peng. “An Intelligent System for Mining Usage Patterns from Appliance Data in Smart Home Environment.” In *2012 Conference on Technologies and Applications of Artificial Intelligence*, p. 320. Department of Computer Science, National Chiao Tung University, Hsinchu, Taiwan, 2012.
- [3] K. Basu, V. Debusschere, and S. Bacha. “Load identification from Power Recordings at Meter Panel in Residential Households.” In *Electrical Machines (ICEM), 2012 XXth International Conference*, p. 2098. 2012.
- [4] M. Riedel, M. Memon, A. Memon, G. Fiameni, C. Cacciari, and T. Lippert. “High Productivity Processing : Engaging in Big Data around Distributed Computing.” In *MIPRO 2013, May 20-24, 2013, Opatija, Croatia*, p. 147. Juelich Supercomputing Centre, Juelich, Germany. CINECA, Bologna, Italy, 2013.
- [5] Y. Li and S. Manoharan. “A performance comparison of SQL and NoSQL databases.” In *Communications, Computers and Signal Processing (PACRIM), 2013 IEEE Pacific Rim Conference*, pp. 16–18. University of Auckland, New Zealand, 2013.
- [6] Object Refinery Limited. “JFreeChart [Online 17/10/2014].” URL <http://www.jfree.org/jfreechart/>.
- [7] D. Vanderkam. “dygraphs [Online 23/10/2014].” URL <http://dygraphs.com/>.

- [8] M. Bostock. “D3, Data-Driven Documents [Online 23/10/2014].” URL <http://d3js.org/#introduction>.
- [9] Square, Inc. “Cubism.js, Time Series Visualization [Online 17/10/2014].” URL <https://square.github.io/cubism/>.
- [10] Free Software Foundation, GNU operating system. “What is R? [Online 17/10/2014].” URL <http://www.r-project.org/>.
- [11] Mathworks. “Big Data - MATLAB [Online 23/10/14].” URL <http://www.mathworks.com/discovery/big-data-matlab.html>.
- [12] SUCSES. “Energy Monitor [Online 30/10/2014].” URL http://www.suces.org/?page_id=17.
- [13] MongoDB, Inc. “NoSQL Databases Explained [Online 20/10/2014].” URL <http://www.mongodb.com/nosql-explained>.
- [14] S. McGuire. The Macintosh Development Group, MIT Information Systems. “BSD Sockets API [Online 31/10/2014].” URL <http://web.mit.edu/macdev/Development/MITSupportLib/SocketsLib/Documentation/sockets.html>.
- [15] A. van Kesteren. “Cross-Origin Resource Sharing [Online 31/10/2014].” URL <http://www.w3.org/TR/cors/>.
- [16] L. Bonnet, A. Laurent, B. Laurent, and N. Sicard. “REDUCE, YOU SAY: What NoSQL can do for Data Aggregation and BI in Large Repositories.” In *2011 22nd International Workshop on Database and Expert Systems Applications*, p. 486. 2011.
- [17] J. P. Bentley. “Principles of Measurement Systems.” pp. 99–101. Pearson Education Limited. Edinburgh Gate, Harlow, Essex CM20 2JE, England. Fourth Edition, 2005.

MODELLING AND PERFORMANCE ANALYSIS OF A MICRO-HYDROKINETIC RIVER SYSTEM AS COMPARED TO WIND SYSTEM

S.P. Koko*, K. Kusakana* and H.J. Vermaak*

* Dept. of Electrical, Electronic & Computer Engineering, Private Bag X20539, Central University of Technology, Free State, Bloemfontein 9300, South Africa, E-mail: skoko@cut.ac.za, kkusakana@cut.ac.za, hvermaak@cut.ac.za.

Abstract: Micro-hydrokinetic river (MHR) system is one of the promising technologies to be used for remote rural electrification. In rural areas with availability of both wind and flowing water resources, the potential benefits of generating electricity using flowing water is neglected while the wind generation is selected as a first priority. Hence, this paper presents the modelling and performance analysis of a MHR system as compared to wind generation system using MATLAB/Simulink software. These performances are compared while generating the same amount of electricity. A permanent magnet synchronous generator (PMSG) has been chosen or used to investigate the behaviour of each system under variable speeds. The MHR system model includes horizontal turbine model, drive train model and PMSG model. The simulation results illustrate the ability of a hydrokinetic turbine driven PMSG to generate electricity markedly better and cheaper than a wind driven PMSG. Hence, the MHR system presents a cheap electrification opportunity for poor rural households.

Keywords: Modelling, micro-hydrokinetic system, wind system, permanent magnet synchronous generator, rural electrification.

1. INTRODUCTION

Electrification can play an important role to support economic and social development of isolated rural societies. To improve the living conditions of poor rural households, it is important to provide the affordable and reliable electricity. A clean and sustainable solution for remote rural electrification is made possible by means of small-scale renewable energy sources. Among various renewable energy technologies, hydropower generation holds prime position in terms of the world's electricity generation [1, 2].

Some rural areas might be situated in close proximity to flowing water with little or no elevation at all. A conventional hydro generation system cannot be used in such rivers or water flow. This results in neglect of flowing water resource. Additionally, it has been proved that one-third of the world's population without electricity does have access to flowing water resource [3]. Apart from conventional hydropower generation, hydrokinetic is a new category of hydropower generation to be used in waterways with little or no elevation at all. It generates electricity by making use of underwater wind turbines to extract kinetic energy of flowing water instead of potential energy of falling water. Hence, no construction of dams or diversions is necessary. It means that theoretically there is huge number of potential sites available for micro-hydrokinetic power generation compared to conventional hydropower generation. The hydrokinetic technology is still in the development stage and lot of research still needs to be done. It has been

proved that there is still a lack of electrification applications in rural areas [4].

Hydrokinetic technology can be captured from waves, tides, oceans, marine thermal gradients, flow of water in rivers or artificial channels [5, 6]. Kinetic energy of flowing water is converted into electrical energy by making use of a turbine coupled to a generator via drive-train. Hydrokinetic turbines are available in either horizontal or vertical configurations.

This study focuses only on small-scale hydrokinetic system since it is suitable for low income remote rural residents. For small-scale electrification, free-flowing rivers/waterways are the possible sources. Small-scale turbines are generally available within power range of 1 kW to 10 kW [7]. In this study, a horizontal-axis turbine has been chosen due to its self-starting capability compared to vertical-axis turbines. A permanent magnet synchronous generator (PMSG) has been selected due to its high efficiency, reliability and capability of operating at low speeds [4].

This study aims to demonstrate the benefit of using the proposed off-grid micro-hydrokinetic river (MHR) system in remote areas with both wind and flowing water resources through the use of the developed model. The developed model has been applied in MATLAB/Simulink software. The performance of the proposed MHR system has been compared to the one of a wind system for generating the same amount of electrical power. Hence, the modelling of power electronic converter and storage devices is beyond the scope of the study.

2. PROPOSED HYDROKINETIC ENERGY CONVERSION SYSTEM

The modelled structure of MHR system consists of a horizontal turbine, mechanical drive-train, and PMSG components. Since a PMSG can operate at low speeds, the rotor shaft is coupled directly to the turbine. Hence, a gearbox is excluded. To measure the generated output voltage and current, a three-phase balanced resistive load is connected to the output of the generator.

Most of the available modelling and simulation tools used for mechanical and electrical systems are not equipped with hydrokinetic module. Hence, the mathematical model for each component of MHR system is developed using MATLAB/Simulink library. Hydrokinetic technology operates similar to wind technology in terms of operation and rotor blade configurations. The difference is that water is approximately 800 times denser than air while the wind speed is greater than the water speed [3].

2.1 Hydrokinetic turbine model

Zero head turbines are generally used to extract and transform the kinetic energy of flowing water into mechanical energy. The kinetic energy of flowing water is expressed as:

$$E_k = \frac{1}{2}mv^2 \quad (1)$$

Where:

m = water mass (kg)
v = water velocity (m/s)

Hence, the power of the flowing water (by assuming constant speed) is expressed as follows:

$$P_w = \frac{dE_k}{dt} = \frac{1}{2}\rho Av^3 \quad (2)$$

Where:

ρ = water density (1000 kg/m³)
A = swept area of turbine blades (m²)

The area of a horizontal-axis turbine is expressed as:

$$A = \pi r^2 \quad (3)$$

Where:

r = turbine blade radius in (m).

Hydrokinetic turbines can only harness a fraction of the total kinetic power due to losses entailed. So, the rotor power coefficient of the turbine is expressed using equation (4) below [8]. Based on Betz law, this power coefficient is limited to $16/27=0.593$ (59.3 %).

$$C_p = \frac{P_m}{P_w} \quad C_p < 1 \quad (4)$$

Where:

P_m = mechanical power captured by water turbine

By substituting equation (2) into (4), the mechanical power captured by water turbine from water flow is then expressed as:

$$P_m = \frac{1}{2}\rho Av^3 C_p \quad (5)$$

C_p depends on the tip-speed ratio, λ and the blade pitch angle, β (degrees) and can be expressed as follows [9, 10]:

$$C_p(\lambda, \beta) = c_1(c_2 \frac{1}{\lambda_i} - c_3\beta - c_4)e^{\frac{-c_5}{\lambda_i}} + c_6\lambda \quad (6)$$

Where:

c_1 to c_6 are the empirical power coefficients' parameters of the turbine.

In our case, $\beta=0$ degrees, in order to achieve maximum power extraction from a variable speed turbine. The empirical coefficients of a typical horizontal turbine c_1 to c_6 were 0.5176, 116, 0.4, 5, 21 and 0.0068 respectively [9, 11].

The parameter $\frac{1}{\lambda_i}$ can be solved by making use of the following equation [10, 12, 13]:

$$\frac{1}{\lambda_i} = \frac{1}{\lambda + 0.08\beta} - \frac{0.035}{1 + \beta^3} \quad (7)$$

The tip speed ratio can be determined as follows [12, 13]:

$$\lambda = \frac{\omega_m \cdot r}{v} \quad (8)$$

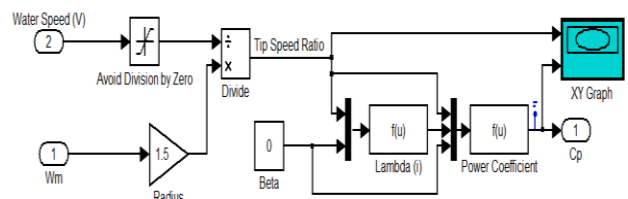


Figure 1: Simulink block diagram of a turbine power coefficient model

Where:

ω_m = mechanical angular speed of the turbine shaft in (rad/sec)

A water turbine power coefficient model is shown in Figure 1. Figure 2 shows that the maximum power coefficient of this turbine, $C_{p(max)}$ is found to be 0.48 at a tip-speed ratio (λ_{opt}) of 8.1, when $\beta = 0$ degrees. Hence, the value of $C_{p(max)}$ was entered as a constant to assume maximum power extraction at variable speeds. Mechanical torque of the turbine shaft can be expressed as follows:

$$T_m = \frac{P_m}{\omega_m} \quad (9)$$

2.2 Drive-train model

The role of the drive-train within hydrokinetic system is to enable the conversion of kinetic energy of flowing water into useful mechanical energy. Drive-train can either be geared or direct driven. The gearbox within the drive train connects the low speed shaft (on the turbine side) with the high speed shaft (on the generator side). This enables the provision of high rotational speed required by the generator to provide electricity up to certain level. A drive-train can be modelled by means of different methods such as three-mass, two-mass or one-mass drive train model [9]. Since the aim of this study is to see the interaction between water density and electrical output energy, the drive train was treated as a one-mass drive train model. This means that all inertia components are modelled as a single rotating mass.

The angular acceleration of the generator shaft can be expressed as follows [8]:

$$\frac{d\omega_g}{dt} = \frac{T_e - T_{w:g}}{J_{eq}} - \frac{B_m}{J_{eq}} \omega_g \quad (10)$$

Where:

T_e = electromagnetic torque in (N.m)

$T_{w:g}$ = mechanical torque from water turbine to the generator in (N.m)

J_{eq} = equivalent rotational inertia of the generator and turbine in (kg.m²)

B_m = damping coefficient in (N.m/s)

ω_g = rotor angular speed of the generator in (rad/sec)

One of the advantages of PMSG is that they are low inertia machines. Usually J_{eq} is almost equals to the turbine inertia since generator inertia is negligibly small [14]. The rotational damping coefficient was assumed to be equals to zero as shown in Figure 3.

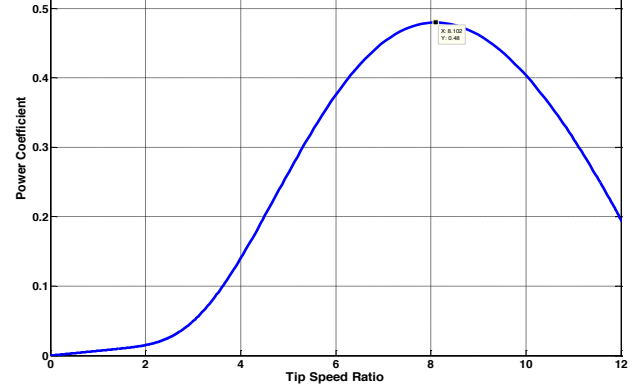


Figure 2: Power Coefficient versus tip-speed ratio of the turbine (with $\beta=0^\circ$)

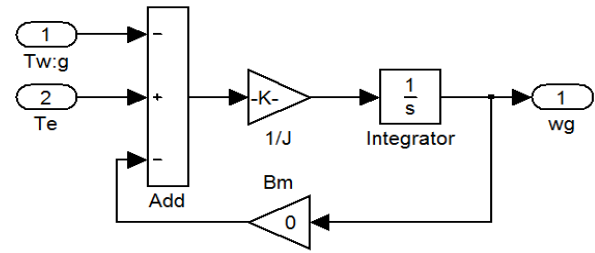


Figure 3: Simulink block diagram of a drive train model

By neglecting all inertia effects of the chain, the rotor angular speed of the generator can be expressed as follows:

$$\omega_g = \omega_m \cdot G \quad (11)$$

Where:

G = gear ratio

2.3 Permanent magnet synchronous generator (PMSG) model

A synchronous machine models for power systems are usually based on assumption such as damping effect is negligible (of both the rotor and the magnets), the magnetic flux distribution in the rotor is sinusoidal, magnetic circuit is unsaturated, iron losses are negligible and field current dynamics are absent [15,16].

The park transformation is a commonly used method for a three-phase machine modelling. It is used to transform the parameters and equation from the stationary form into direct-quadrature (dq) axis [17]. It converts the 3 phase alternating current quantities into direct current quantities, meaning ABC to dq transformation. The d & q voltage equations of the PMSG are expressed as follows [9,18]:

$$v_d = R_s \cdot i_d + L_d \frac{di_d}{dt} - \omega_e L_q i_q \quad (12)$$

$$v_q = R_s \cdot i_q + L_q \frac{di_q}{dt} + \omega_e \psi_{PM} + \omega_e L_d i_d \quad (13)$$

Where:

v_d and v_q = stator terminal voltages in the d, q axis reference frame in (V)

i_d and i_q = stator terminal currents in the d, q axis reference frame in (A)

L_d and L_q = d, q axis reference frame inductances in (H)

ω_e = electrical angular speed of the generator in (rad/sec)

ψ_{PM} = permanent magnet flux in (Wb)

R_s = stator resistance in (Ω)

The relationship between the electrical angular speed and rotor angular speed (ω_g) of the generator is expressed as follows:

$$\omega_e = p \cdot \omega_g \quad (14)$$

Where:

p = the number of pole pairs;

The equation for the developed electromagnetic torque is given as follows [19]:

$$T_e = \frac{3}{2} p (\psi_{PM} i_q + (L_d - L_q) i_d i_q) \quad (15)$$

3. RESULTS AND DISCUSSION

This paper provides an overview of the proposed MHR system model as implemented in MATLAB/Simulink. In this section, variable speed responses of the proposed system are presented. The main objective is to study the performance of the proposed MHR system as compared to the one of a wind generation system. The results highlight the system that generates electricity better than the other one for the same amount of electrical power generation. The block diagram of the developed MHR system model is shown in Figure 6 below. A 2 kW three-phase balanced resistive load is directly connected to the output of the generator to represent a full-load.

Simulink signal builder has been used for variable step input in order to see how the system responds to a change in water speed. The step input signal and the selected time range are only used for simulation purpose. The simulated parameters of the system components are shown in Tables 1 and 2 below.

Table 1: PMSG parameter list [20, 21]

Stator phase resistance	2 Ω
Number of pole pairs	8
d-q axis inductance	1 mH
Permanent magnet flux	0.46 Wb
Rated rotor speed	400 rpm
Rated Power	2 kW
Rated phase voltage	120 V
Rated phase current	17 A
Rated Frequency	50Hz

Table 2: Turbine and drive-train parameter list

Turbine blade radius	1.5 m
Blade swept area	7 m ²
Maximum C_p value	0.48
Optimal tip speed ratio	8.1
Gear ratio	1
Rotational damping coefficient	0
System total inertia	5 kg.m ²

3.1 Dynamic response of an off-grid hydrokinetic system

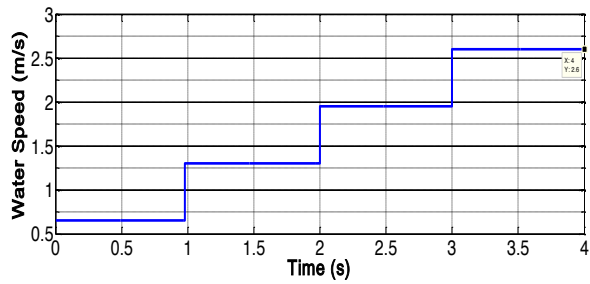
The step input representing variable water speed has been increased in steps of 0.65 m/s for 4 seconds as shown in Figure 4 (a). As the water speed increases, the generated voltage, load current, and frequency are gradually increasing as well. When the water speed increase from 1.95 m/s to 2.6 m/s (from t=3s to t=4s), the generator is rotating at its rated full-load speed. At that moment, the generated voltage, frequency and the load current were 126.6 V, 51.23 Hz and 17.58 A respectively. This demonstrates the effectiveness of the developed model since these parameters are close to the rated ones.

3.2 Dynamic response of an off-grid wind system

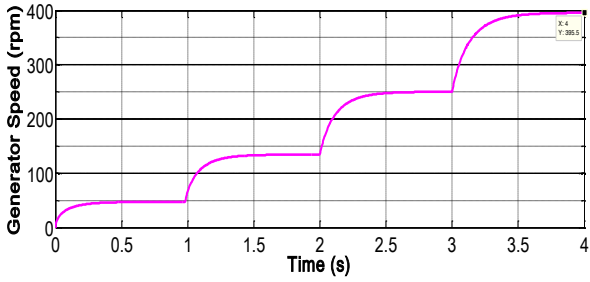
To study the response/performance of a wind system as opposed to the MHR system, the same system components parameters have been simulated. The air density was taken to be 1.225 kg/m³ during simulations. The step input representing variable wind speed has been increased in steps of 6.075 m/s for 4 seconds as shown in Figure 5 (a). To enable the same PMSG to rotate at its rated speed, the wind speed of 24.3 m/s is need. Such speed is practically impossible within South Africa (SA), since the average wind speed ranges between 4 to 7 m/s [22]. Hence, to enable a wind system to generate the same voltage as generated by the MHR system, techniques such as increasing the turbine blade size, considering a PMSG with larger number of pole pairs and/or adding a gearbox to the system can be applied. However, any of the above-mentioned techniques will results into high/extra additional costs. Furthermore, a gearbox will reduce the efficiency and reliability of the system due to regular maintenance requirement.

4. CONCLUSION

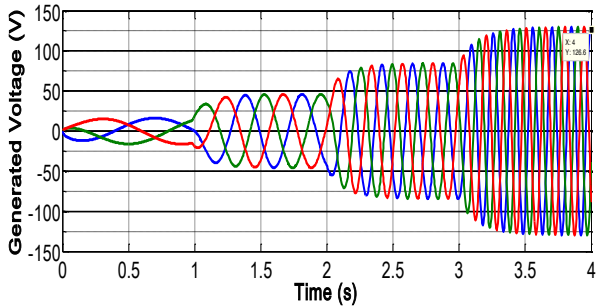
This paper presented the developed model for studying the performance of an off-grid MHR system as submitted to varying water velocity. The system consists of a horizontal turbine, drive-train and a PMSG. The performance of an off-grid MHR system as opposed to the one of a wind system has been revealed. The comparison results showed that due to high water density, a small-scale hydrokinetic river system generates electricity markedly cheaper than a small-scale wind system. This simply proves that in SA isolated rural areas with access to flowing water and adequate/inadequate wind resource, hydrokinetic power is the cheaper, reliable and efficient system to consider than a wind system.



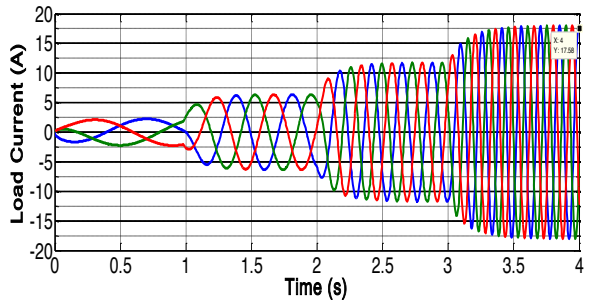
(a) Water speeds



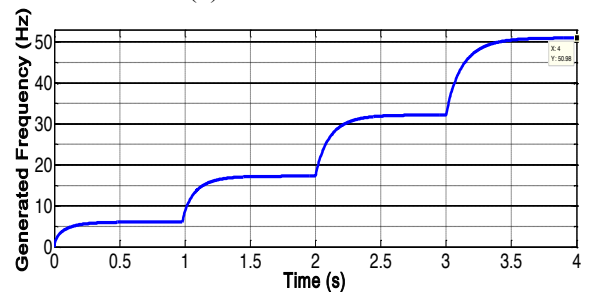
(b) Generator speeds



(c) Generated voltages

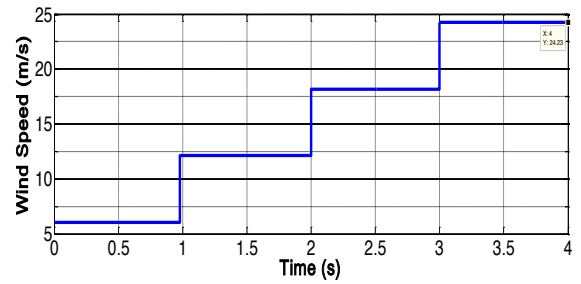


(d) Load currents

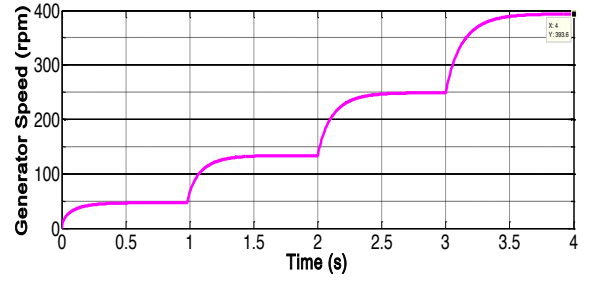


(e) Electrical frequency

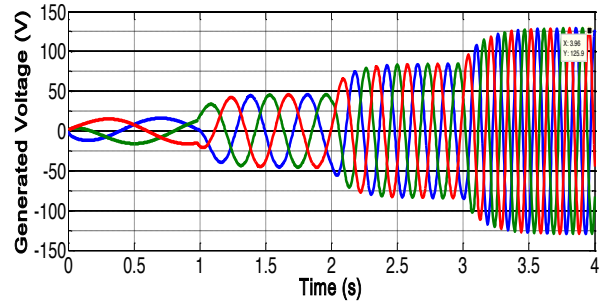
Figure 4: MHR system response for a step change in water speed from 0.65 m/s to 2.6 m/s.



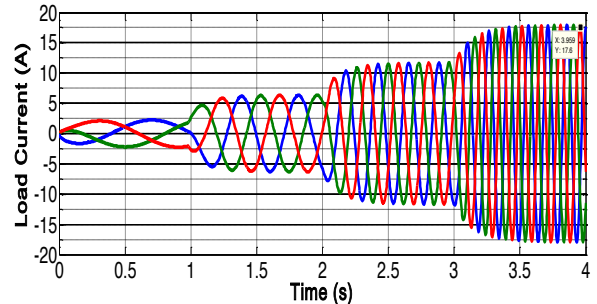
(a) Wind speeds



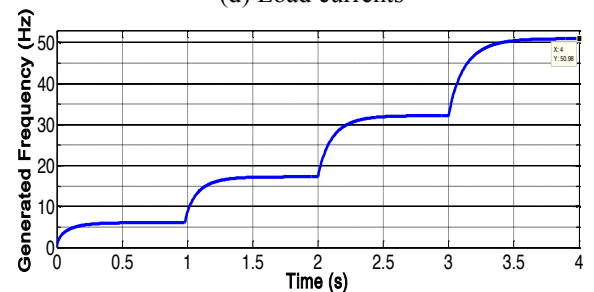
(b) Generator speeds



(c) Generated voltages



(d) Load currents



(e) Electrical frequency

Figure 5: Wind system response for a step change in wind speed from 6.075 m/s to 24.3 m/s.

- [15] M.G. Molina, A.G. Sanchez and A.M. Rizzato Ledo: "Dynamic Modeling of Wind Farms with Variable-Speed Direct-Driven PMSG Wind Turbines", *IEEE, Transmission and Distribution Conference and Exposition*, pp. 816-823, November 2010.
- [16] F. Zaiming: "Mathematical Modelling of Grid Connected Fixed-Pitch Variable-Speed Permanent Magnet Synchronous Generator for Wind Turbines", Master's Thesis, University of Central Lancashire, June 2012.
- [17] S.A. Khan, R.K. Rajkumar and C.V. Aravind: "Performance analysis of 20 Pole 1.5kW Three Phase Permanent Magnet Synchronous Generator for low Speed Vertical Axis Wind Turbine", *Energy and Power Engineering*, Vol. 5, pp. 423-428, July 2013.
- [18] F. Belloni, R. Chiumeo, C. Gandolfi and A. Villa: "Simulation model of a Permanent Magnet Synchronous Generator for grid studies". *International Conference on Renewable Energies and Power Quality (ICREPQ'14)*, April 2014.
- [19] M. Messaoud and R. Abdessamed: "Modeling and Optimization of Wind Turbine Driving Permanent Magnet Synchronous Generator", *Jordan Journal of Mechanical and Industrial Engineering*, Vol. 5 No. 6, pp. 489-494, December 2011.
- [20] L. Barote and C. Marinescu: "PMSG Wind Turbine System for Residential Applications", *IEEE, Power Electronics, Electrical Drives, Automation and Motion (SPEEDAM)*, pp. 772-777, June 2010.
- [21] L. Barote, C. Marinescu and I. Serban: "Energy Storage for a Stand-Alone Wind Energy Conversion System", *Rev. Roum. Sci. Techn. – Électrotechn. et Énerg.*, Vol. 55 No. 3, pp. 235-242, 2010.
- [22] N.A. Cencelli: "Aerodynamic Optimization of a Small-Scale Wind Turbine Blade for Low Wind Speed Conditions", Msc Thesis, University of Stellenbosch, December 2006.

ECONOMIC ANALYSIS OF A STAND-ALONE SOLAR PV SYSTEM FOR DIFFERENT SIZES OF MIDDLE INCOME RESIDENTIAL LOAD CLUSTERS IN SOUTH AFRICA

M. N. Martin*, C. Buque** and S. Chowdhury***

* University of Cape Town, Department of Electrical Engineering, Upper Campus, Rondebosch, Cape Town, 7701, E-mail: MRTMOG009@myuct.ac.za, Sunetra.chowdhury@uct.ac.za

** Mott MacDonald, Thermal and Renewable Energy Division, 25 Scott Street, Waverley, Johannesburg 2090, E-mail: claudiobuque@yahoo.com.br

Abstract: In this paper, a solar PV system comprises of PV panels, batteries, and inverters. The system is designed optimally and implemented using the HOMER software for varying load clusters. For modelling and simulation of the PV system in HOMER, the inputs provided to the software are various component parameters, ratings and costs, location, load profiles, economic parameters and system constraints. The main constraint considered is that the maximum annual capacity shortage is set to zero. Lastly, the load profile was taken as an input for each of the different cases studied with varying cluster sizes – a single household (Case 1), a five-household cluster (Case 2), a ten-household cluster (Case 3), and a twenty-household cluster (Case 4). The aim of the paper is to identify the most economically sound combination of cluster size PV system design to supply renewable energy to mid-income households in South Africa.

Keywords: Solar PV, residential load cluster, economic analysis, net present cost, cost of energy,

1. INTRODUCTION

Electrical energy has globally seen a dramatic increase in growth, and is now a basic requirement of life in all countries in the world, including South Africa. However, energy generation using fossil fuels which release greenhouse gases and particulate matter into the atmosphere, this large uptake of electricity usage has led to an increase in environmental pollution, global warming, and gradual depletion of fossil fuels. These factors have led to the research and development of alternative technologies for generating clean electricity in a manner that is less harmful to the environment and independent of fossil fuel. The most popular alternative energy source is solar energy. Solar energy captured from photovoltaic panels is seen to economically produce reasonable amounts of electrical energy when installed correctly. This, coupled with a battery unit, has the potential to become a reliable energy generation scheme for clusters of residential, commercial and industrial customers.

In order to become independent of the grid, people can implement a PV system locally to supply themselves with energy. This scheme can be used to feed an individual household or a cluster of households. However, the implementation of these schemes is highly dependent on the economic feasibility of the schemes. Thus, it is necessary to study solar PV schemes for different household cluster sizes, and compare them to the cost of buying electricity from the grid, in order to make an informed decision about whether these PV systems should be implemented or not, and if so, for which cluster sizes they should be implemented.

2. SOLAR ENERGY IN SOUTH AFRICA

2.1 The impact of solar energy to power low-cost housing
Installing solar PV panels on the rooftops of low-cost housing schemes would save the government money in the long run, as they could implement systems that run completely off-grid, while providing sustainable power to the poorer communities in the country. Implementing the technology would also improve the citizens' standard of living in these areas, leading to a better average quality of life, and improvement to the country's economy.

2.2 The impact of implementing solar farms
Building solar farms in South Africa would add much needed energy to the national grid, which could help to alleviate the grid by increasing the overall safety margin. The initial cost would be high, but cognisance should be taken that it is a form of renewable energy, which would be completely unaffected should the country's coal reserves run low.

3. ECONOMIC FACTORS OF PV SYSTEMS

It is important to be able to compare multiple projects on an economic level to decide which is more viable than the rest. For this reason, the economic terms and aspects of implementing a system of this type in South Africa are discussed in this section.

3.1 Cost of the PV System

The main contributors to the initial and recurring cost of the PV system are the battery banks, inverters, and the panels themselves [1]. It has been predicted that the cost of PV panels will decrease, and that the efficiency of these panels will increase as technology develops [2]. The main factors used to assess whether a project or system of

this type is economically worth pursuing is the Cost of Energy (COE) and the Net Present Cost (NPC) [1].

3.2 The cost of grid electricity

In order to compare the feasibility of implementing a stand-alone PV system for a middle-income household, it is important to compare the cost of the system to that of getting the electricity directly from the grid. The costs cannot be directly compared since the stand-alone system has the advantage of causing less harm to the environment than the coal-fired power stations which mainly power the grid. This environmental advantage does not constitute monetary value to the consumer, however, it is important to do a comparison nonetheless. A household consuming more than 450kWh per month from the City of Cape Town municipality will fall under the Domestic Tariff structure [3], as is the case with our average 774kWh per month household. The tariff block charges consumers 153.63c/kWh (\$0.14/kWh) for the first 600kWh used per month, and 186.81c/kWh (\$0.17/kWh) for any amount over 600kWh per month [3]. Thus, an average mid-income household would spend R1246.83 per month on 774kWh of electricity from the grid, if no other sources are considered. This is equivalent to \$116.43 per month, at the time of writing.

In order for a project to be considered viable by a person or company, the project has to be feasible. In the sense of this project, this means that the solar PV system that will be designed and tested, must be technically sound and profitable in the long run. That is, it should be able to supply a large enough amount of consumers with a good quality of energy supply, for the cost that the project will incur. The feasibility of the project will mainly be viewed from an NPC point-of-view as well as in terms of its environmental and social impacts.

To examine the impacts and economic feasibility of the project, the HOMER v2.81 software simulation package will be used. This software package allows the system to be modelled in its entirety, and optimized for different configurations. This will allow comparison of different cluster sizes, and will thus allow us to select the most feasible solution.

4. CASE STUDIES

In this paper, four case studies will be carried out for different load clusters consisting of a single household, 5 households, 10 households and 20 households followed by the economic comparison of these case studies. For generating the load profile for each cluster, the load profile of Table 1 is multiplied by the number of households in a specific cluster to get the total load demand for that specific cluster. Thus, it is assumed that there is no variation or diversity in load demand for each household, and that every household demands the same amount of electricity at each time during a day. The energy consumption and load summary for various load

clusters used in the case studies are listed in Table 2 below.

Table 1: Average Hourly Load Profile for a typical Mid-Income Household in South Africa [1][6]

Time of day	Load (kW)	Time of day	Load (kW)
00:00-01:00	0.670	12:00-13:00	1.210
01:00-02:00	0.630	13:00-14:00	1.200
02:00-03:00	0.590	14:00-15:00	1.200
03:00-04:00	0.600	15:00-16:00	1.180
04:00-05:00	0.620	16:00-17:00	1.180
05:00-06:00	1.090	17:00-18:00	1.370
06:00-07:00	1.290	18:00-19:00	1.325
07:00-08:00	1.320	19:00-20:00	1.250
08:00-09:00	1.330	20:00-21:00	1.180
09:00-10:00	1.320	21:00-22:00	1.100
10:00-11:00	1.300	22:00-23:00	0.910
11:00-12:00	1.250	23:00-00:00	0.780

Table 2: Energy Consumption and Load Summary for Various Load Clusters

Parameter	Case 1 – single household	Case 2 – cluster of 5 households	Case 3 – cluster of 10 households	Case 4 – cluster of 20 households
Average (kWh/day)	25.9	129	259	518
Average (kW)	1.08	5.39	10.8	21.6
Peak (kW)	2.42	12.1	24.2	48.4
Load Factor	0.446	0.446	0.446	0.446

It is to be noted that the load profile given above shows an average usage of 25.9kWh per day for a single household, resulting in a total monthly usage of 777kWh per month. This figure is very close to the average estimated 774kWh monthly average from [3].

5. NON-TECHNICAL INPUTS FOR HOMER

This section explores various non-technical inputs that are used for HOMER simulation of the solar PV system for various load clusters.

5.1 Economic inputs

Interest rates in HOMER are used to convert annual costs to once-off costs at the current value of money [4]. At the time of writing, the South African annual real interest rate was at 2.5% [5]. This value is used in the calculation of

the NPV within HOMER. It is also assumed that the project would run over the course of 25 years, as is the default in HOMER, and that this time period will be considered in all economic calculations within the software.

5.2 Emissions

The system has no harmful emissions throughout its 25 year life cycle while being operated. However, it should be noted that the production and disposal of the batteries, inverters, and PV panels after living out their useful lives would have some impact on the environment, though this will not affect the cost calculations in this paper.

5.3 System constraints

The following system constraints into account when calculating the most economical system as detailed below.

(i) Maximum annual capacity shortage

The maximum annual capacity shortage is the maximum capacity shortage the PV system is allowed to have [4]. Thus, setting this value to zero will result in the PV system meeting the entire yearly load. Increasing the amount of capacity shortfall the PV system is allowed will decrease the total cost of the system [1]. This can be seen from the fact that having to supply the full load of the household would require larger panels and battery banks, especially during the winter months when consumption increases. Since this paper is only considering standalone systems, as well as the fact that a mid-income homeowner would expect a constant supply of electricity, it will be assumed that no capacity shortfall is allowed, and the system has to constantly supply the load throughout the year.

(ii) Operating Reserve

The operating reserve is a certain amount of capacity that is kept available during normal operation, in case the load demand suddenly increases or the PV output decreases, and the system needs to keep up with the load demand. It acts as a safety margin to ensure the system is always able to keep up with the load demand. [4]

6. MODELING AND SIMULATION OF THE PV SYSTEM

The overall model for the system consists of an array of solar PV panels, the battery bank, inverters, and the load [1] for each cluster as shown in Figure 1. The inputs specified above are used in the HOMER simulation software for each of the different cluster sizes.

The input specifications for each system component are entered manually into the HOMER front end. Each component allows for a specific search space for that component to be defined [1]. The search space allows for different combinations and sizes of the components to be used when looking for the economically optimal system configuration [4]. Using the specified inputs and search

spaces defined above, the system gives the outputs described in the following section. These outputs are used to check which system configuration would be the most economically viable solution.

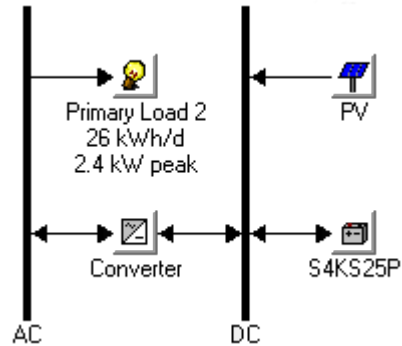


Figure 1: Overall PV system modelled in HOMER for a single household

7. PARAMETERS USED FOR ECONOMIC ANALYSIS

This section explores the various parameters to be calculated for economic analysis and comparison of the obtained from the simulations in HOMER.

7.1 The number of technical components required

The HOMER simulation specifies exactly how many PV panels, batteries, and converters will be needed to meet the specified load at the most economical cost, from within the given search space. The expected battery life considering the use of the batteries is also calculated and given as a simulation output.

7.2 Economic output parameters

The following costs are economically assessed by HOMER to find the optimal economic solution.

(i) Initial capital

This is the investment required at the start of the project [4]. It is the capital required to obtain and install the solar PV panel, the battery bank, and the converter [4].

(ii) Operating cost

This is the cost incurred from the yearly operation of the system, and includes all maintenance work and replacements required throughout the project [4]. It is measured in \$/year.

(iii) Total NPC

The total Net Present Cost is the total cost incurred by the system throughout its entire project lifetime, minus the salvage value and earnings at the end of the project, and thus takes the initial investment, operating costs, and replacement costs into account [4]. The future costs are converted to represent what they would be in terms of the current value of money, as the value of a given amount of money in the future is less than the value of that same amount of money, today, due to inflation. This is the

main parameter that is assessed by HOMER when deciding on the most economically feasible solution [4].

(iii) Cost of energy (COE)

This is the effective cost per kWh that is paid by the consumers or investors of the system, for electricity from the system [4]. This parameter takes the entire cost of the system throughout its lifetime into account, including replacement of components, and obtains an equivalent cost per kWh for the energy obtained from the system [4]. The aim is to keep this cost as low as possible, especially in the case of clusters being supplied by the system, in order to remain competitive with the cost per kWh from the grid. Having a competitive cost of energy compared to the grid would encourage more consumers to want to use solar PV systems, instead of electricity from the grid, which is generally produced in a much more environmentally harmful way in South Africa. A low COE would thus justify investment in the system.

(iv) Cash flow outputs

The cash flow forecasts are given as outputs, and summarised by total inflow or outflow of cash for a single year. The cash flow graph shows how the money flows through each year of the project lifetime.

In HOMER analysis, the cash flow summary is sorted by either by component or by cost type. When displaying the ‘by component’ summary, the cash flow summary summarises the cash flow spent on the PV panel configuration, the battery configuration, and the inverters [4]. All of these parameters are strictly positive cash flow, as it is money that is spent, not received. When displaying the ‘by cost type’ summary, the cash flow summary summarises the cash spent and received [4]. Cash is spent on the initial investment, replacement costs, operating costs, and fuel costs [4]. Cash received is the salvage value of the system, and thus takes a negative cash flow value, due to it being cash received, not cash spent.

Each of the two types of cash flow summaries calculated in HOMER can be given according to annualised cost, or NPC. The cash flow summary given according to the annualised cost shows the cash flow for every component for each year of the project, as if that cost were to occur in every year of the project lifetime, at the exact same value [4]. The cash flow summary given according to the NPC shows the total cash flow for each component throughout the project lifetime, in present value [4].

(v) Total salvage value

The total salvage worth of every component in the system, after the 25-year project life cycle, is also calculated by the software.

(vi) Total energy production and usage

The HOMER software also gives the total annual energy output of the solar PV panel, the total yearly load energy consumption, and the excess electricity produced by the system [1]. The system also gives time-series graphs of the energy produced and used in the system. The total

amount of kWh stored in the battery throughout its life cycle is also specified.

8. RESULTS

8.1 Case 1 – Solar PV system feeding a single household

Table 3: System Configuration for Case 1

	PV (kW)	Number of S4KS25P batteries	Converter size (kW)	Total NPC (\$)	Cost of energy (\$/kWh)
1	11	24	3	155,943	0.896
2	11	24	6	157,768	0.906
3	11	24	12	161,418	0.927
4	12	24	3	164,178	0.943

In Table 3, the most economic or optimal solution is shown in the first row, highlighted in orange. This solution is deemed the optimal solution due to its total NPC and COE being lower than that of the other solutions, thus making it the most economically feasible solution to implement for this case.

Table 4: Annual Electrical energy analysis for Case 1

	kWh/year	% of total production
Power Production (PV array)	16,472	100
Power Consumption (Household AC Load)	9,450	57.4
Excess Electricity	5,537	33.6
Unmet Electrical Load	3.18	
Capacity Shortage	4.55	

Table 4 shows that more than a third of the energy produced per year is ‘excess electricity’. This is electricity that is generated by the PV panel array cannot be absorbed by the batteries, due to them being fully charged, or the load, due to it being fully met already. This is an over-design and increases both the NPC and COE of the system.

Table 4 also shows that there is a small unmet load. The reason for this unmet load is that the energy in the battery and being produced by the PV panel array cannot fully satisfy the load at some instant in time, during the year. The time of occurrence of the unmet load and the time of occurrence of the excess electricity being produced do not overlap, thus explain the existence of the unmet load in spite of there being excess electricity being produced by the system.

8.2 Case 2 – Solar PV system feeding a cluster of five households

In Table 5, the most economic or optimal solution for case 2 is shown in the first row, highlighted in orange. This solution is deemed the optimal solution due to its total NPC and COE being lower than that of the other

solutions, thus making it the most economically feasible solution to implement for this case.

Table 5: System Configuration for Case 2

	PV (kW)	Number of S4KS25P batteries	Converter size (kW)	Total NPC (\$)	Cost of energy (\$/kWh)
1	64	120	16	854,440	0.985
2	64	120	32	864,173	0.996
3	64	160	16	960,325	1.107
4	64	160	32	970,058	1.118

Table 6: Annual Electrical energy analysis for Case 2

	kWh/year	% of total production
Power Production (PV array)	103,815	100
Power Consumption (Household AC Load)	47,085	45.35
Excess Electricity	49,701	47.9
Unmet Electrical Load	0.000607	
Capacity Shortage	0.00	

Table 6 shows that about 47.9% of the annual energy is ‘excess electricity’ indicating an overdesign while there almost no unmet electrical load that points to reliability of energy supply for this case.

8.3 Case 3 – Solar PV system feeding a cluster of ten households

Table 7: System Configuration for Case 3

	PV (kW)	Number of S4KS25P batteries	Converter size (kW)	Total NPC (\$)	Cost of energy (\$/kWh)
1	128	200	32	1,600,112	0.919
2	128	200	64	1,619,577	0.930
3	128	240	32	1,705,420	0.979
4	128	240	64	1,724,886	0.990

Table 8: Annual Electrical energy analysis for Case 3

	kWh/year	% of total production
Power Production (PV array)	207,631	100
Power Consumption (Household AC Load)	94,517	45.52
Excess Electricity	99,001	47.7
Unmet Electrical Load	17.8	
Capacity Shortage	21.1	

Table 7 shows the optimal solution for Case 3 in the first row, highlighted in orange. Table 8 shows that about 47.7% of the annual energy is ‘excess electricity’ in this case (similar to Case 2) while there is some unmet electrical load higher the previous two cases.

8.4 Case 4- Solar PV system feeding a cluster of twenty households

Table 9 shows the optimal solution for Case 4 in the first row while Table 10 gives the annual electricity analysis for the same. Table 10 shows that this case has the highest unmet electricity and excess electricity percentage slightly less than Case 2 and Case 3.

Table 9: System Configuration for Case 4

	PV (kW)	Number of S4KS25P batteries	Converter size (kW)	Total NPC (\$)	Cost of energy (\$/kWh)
1	250	400	64	3,150,812	0.905
2	250	400	128	3,189,743	0.916
3	500	240	64	4,788,377	1.375
4	500	240	128	4,827,308	1.386

Table 10: Annual Electrical energy analysis for Case 4

	kWh/year	% of total production
Power Production (PV array)	405,529	100
Power Consumption (Household AC Load)	189,002	46.6
Excess Electricity	188,245	46.4
Unmet Electric Load	67.6	
Capacity Shortage	91.8	

9. DISCUSSION OF RESULTS AND CONCLUSION

The four cases have been compared in terms of NPC and equivalent COE per consumer as summarised in Table 11. Table 11 indicates that Case 1 has the lowest NPC, with Case 4 costing only \$1597.6 more. Thus, it can be said that both of these cases exhibit very good NPCs, compared to the other observed cases. However, the NPC of every case is very high for a mid-income household owner to be able to afford without some sort of subsidy from the government. If these systems were completely funded by the government for economic upliftment of a specific community, it would become a lot more feasible. However, it is unrealistic for a middle-class household to invest in this sort of system when they have to pay for everything on their own. The results shown above are now condensed to a “per consumer” equivalent by dividing the NPC and COE by the number of consumers in a cluster. This can be done due to the lack of diversity in the clusters, and helps to better compare the cases on an equal base.

Table 11: Cost Comparison of equivalent Optimal Solutions for Each Case

Case	Number of households being fed	Equivalent total NPC per consumer (\$)	Equivalent cost of energy per consumer (\$/kWh)
1	1	155,943	0.896
2	5	170,888	0.197
3	10	160,011.2	0.0919
4	20	157,540.6	0.04525

The equivalent cost of energy per consumer obtained from Case 3 and Case 4 is extremely low compared to the City of Cape Town's current tariff, making these cases very attractive. Case 2 is also quite close to the City's current tariff, while Case 1 is extremely high compared to the City's tariff. The extremely high cost of energy obtained from the system in Case 1 makes Case 1 a very unfeasible solution. Case 4 exhibits the lowest cost of energy by a large margin. It should be noted that, due to there being no diversity in the loads in an individual cluster, the results tabulated above are actually quite conservative. This is stated due to the fact that some households might consume less energy than others, while others could consume more. Thus, if diversity of the households' loads were taken into account, the COE and NPC would both be lower and would thus reflect positively on the designed system. Thus, the absence of diversity in the loads could be thought of as an increase in the safety margin of the system.

It is seen that each of the systems exhibit an annual capacity shortage. However, these values are very small considering they are over an entire year, where a mid-income household is expected to consume 9453.5 kWh per year. The lower the electricity shortfall, the more desirable a case becomes. Case 2 has the smallest capacity shortage, and is almost non-existent, while Case 4 has the largest shortage, but is almost in line with Case 1. Each of the above cases shows a large amount of excess electricity being produced by the system. Case 1 shows the lowest amount of excess electricity being produced, with each of the other cases producing almost double the amount of excess electricity. The excess electricity can be used by the system as the demand of the household increases over time, and provides a safety factor should the actual load of a household exceed that of the load profile. The excess electricity cannot be exported to the grid due to the design being for a standalone system. However, if a connection to the grid ever becomes available, exporting the excess electricity to the grid could be considered. Following the trends in the past, it can be said that the cost of the solar PV and battery technologies will decrease as better technologies

and processing methods are discovered. It can also be said, based on past trends that the efficiencies of the PV panels will increase over time. All of these factors contribute to a forecast that the price of implementing a system of this type will decrease over time.

From the above results, it can be concluded that Case 4 offers the best economically feasible solution, especially considering that its NPC is very close to Case 1, but offers an extremely low effective cost of energy. This option seems to be the best as it would not be a single individual paying the cost for the project, but rather a company or municipality where the money is available, unlike in Case 1 where it would be an individual paying the entire cost of the system. The research done in this project sees promise in the sense that it can be used to help people become independent of the grid and provide electricity to people who are currently not connected to the grid, as well as shifting electricity generation sources away from fossil fuels, toward renewable, environmentally safe sources at a reasonable cost for organisations who have money available to spend to improve the organisation's public image. The system can also be implemented in business parks.

10. ACKNOWLEDGEMENT

The authors gratefully acknowledge the support and infrastructure provided by Electrical Engineering Department, University of Cape Town for carrying out this research work.

11. REFERENCES

- [1] J. February, W.N. Mbav and S. Chowdhury, "Economic analysis of a stand-alone residential solar PV system for a typical South African middle income household", *Proc. of 48th International Universities' Power Engineering Conference (UPEC 2013)*, Dublin, Ireland, pp.1-6, September 2013.
- [2] A.A. Lazou, A.D. Papatsoiris, "The economics of photovoltaic stand-alone residential households: A case study for various European and Mediterranean locations", *Solar Energy Materials and Solar Cells*, Vol. 62 Issue 4, pp.411-427, 2000
- [3] The City of Cape Town, "Residential Electricity Tariff Explanation". Internet: <https://www.capetown.gov.za/en/electricity/Elec%20tariffs%20201415/Residential%20Electricity%20Tariffs%20Explanation.pdf>, July 1, 2014 [Aug. 14, 2014].
- [4] HOMER v2.81 Help
- [5] The World Bank, "Real Interest Rate (%)". Internet: <http://data.worldbank.org/indicator/FR.INR.RINR>, Sept. 20, 2014 [Sept. 20, 2014].
- [6] City of Cape Town, South Africa, "Smart Living Handbook: Energy in your home", Available on: www.capetown.gov.za.

A customizable energy monitoring system for renewable energy systems

P.E. Hertzog and A.J. Swart

Department of Electrical, Electronic and Computer Engineering, Central University of Technology, Private Bag X20539, Bloemfontein, South Africa, 9300. Email: phertzog@cut.ac.za

Abstract: The installation of renewable energy systems is on the increase, as many seek to avoid the sharp rise in the cost of electrical energy as supplied by ESKOM in South Africa. Other reasons for the increase in installations of renewable energy systems include the decrease of carbon footprints, protection of the environment, sustainability, social responsibility and socio-economic development in rural areas. This paper aims to present a customizable energy monitoring system which may be used to analyse and evaluate the operation of a number of different photovoltaic modules (or arrays) which may be used in a singular photovoltaic system. Parameters which are monitored include the output voltage, current and temperature of three 10 W polycrystalline modules. The customizable energy monitoring system includes a data logging interface circuit, an ARDUINO MEGA 2560 data logger and a personal computer displaying a front panel of the recorded results which was developed in LabVIEW.

Keywords: Energy monitoring, LabVIEW, ARDUINO, logging interface, PV system

1. INTRODUCTION

“We're going to be able to ask our computers to monitor things for us, and when certain conditions happen or are triggered, the computers will take certain actions and inform us after the fact” [1]. These words uttered by Steve Jobs back in 1985 well illustrate the vision of having personal computers (PC) monitor and control specific events based on predetermined criteria. PC have become common place in all forms of society, and especially so within the field of scientific research. In fact, PC have become a fundamental part in the effective energy management of buildings and energy systems [2, 3].

Energy monitoring may be defined as a management technique that uses energy information as some feedback to reduce or eliminate energy wastage and control the current existing level of energy usage while improving the operating procedure [4]. Another definition states that energy monitoring is a technical and management function which provides the capability to monitor, record, analyse, examine, and control energy flow through systems [5]. Reasons for energy monitoring include verification of energy usage, determining where energy can be saved, avoiding maximum demand loads, increasing reliability of energy supply, verifying mathematical calculations of energy consumption, detecting faults, enabling effective intervention to minimize possible energy losses and for quality assurance purposes [6-11]. However, energy monitoring can be expensive due to the hardware requirements [12].

When considering renewable energy systems, energy monitoring becomes the first step towards a more complete diagnosis of photovoltaic (PV) modules and its prognosis regarding expected lifetime [13]. This is especially so when comparing the operation and

efficiency of different PV modules or arrays used within a specific PV system for large power generation.

The purpose of this paper is to present a customizable energy monitoring system which may be used by an end-user to analyze and evaluate the operation of a number of different PV modules (or arrays) which may be used within a singular PV system. The monitoring system is customizable in that various calculations can be included and specific log files can be generated that simplifies the analysis of the recorded data. The paper will firstly review some commercially available data loggers which form the backbone for energy monitoring. The practical setup used to validate the performance of the energy monitoring system is then provided. Results and discussions follow with some succinct conclusions.

2. COMMERCIALY AVAILABLE LOGGERS

A variety of commercial data loggers are available for purchase on the Internet today. Using Google Scholar to search for the exact phrase “data loggers” results in 38 000 hits [14] while the IEEE Xplore site reveals some 459 hits in total [15]. However, only 6 articles from the IEEE Xplore consider data loggers in the PV environment where the ARDUINO platform has been used.

A data logger, or energy meter, should be cost-effective, user-friendly, easily and quickly accessible and reliable [3]. [ENREF 5](#). Four commercially available data loggers in South Africa (SA) were reviewed as possible candidates for inclusion in an energy monitoring system for PV systems, and are given in Table 1 with selected advantages and disadvantages.

The ARDUINO MEGA 2560 is currently available from a number of distributors in SA and is

manufactured by SmartProjects in Italy [16]. They are currently the most cost-effective data loggers (approximately R 500) that simply require a permanent serial connection to a PC for data acquisition and storage.

Table 1: Data loggers with their advantages and disadvantages adapted from Swart et al. [3]

Data logger	Advantages	Disadvantages
Designed logger where ARDUINO MEGA 2560 was used as implementation platform	<ul style="list-style-type: none"> • Very cheap (R 500) • More functionality • More customizable • 16 I/O analogue channels • 54 I/O digital channels • Serial data communications to a PC • Repetitive unlimited samples with unique file names • Real time mathematical calculations • Remote access via network cable 	<ul style="list-style-type: none"> • Must be permanently connected to a PC • LaBVIEW software required for more functionality • Programming skills required
PICOLOG 1012	<ul style="list-style-type: none"> • Very user friendly interface • Repetitive unlimited samples with unique file names • Real time mathematical calculations • 12 input analogue / digital channels • 2 output digital channels • Remote access via network cable 	<ul style="list-style-type: none"> • Modestly priced (R 2500) • Time stamp per sample missing • Must be permanently connected to a PC
DAQPro 5300	<ul style="list-style-type: none"> • User friendly interface • On-board memory for medium data storage 	<ul style="list-style-type: none"> • Expensive (R12 000) • 8 input analogue channels • Limited number of samples • Mathematical calculations after data collection • One alarm output reduces input channels by 1 • No remote download
CAMPBELL Scientific CR800	<ul style="list-style-type: none"> • Medium user friendly interface • On-board memory for extensive data storage • Remote download via network cable • 4 output digital channels • Resistance measurements • Pulse counter 	<ul style="list-style-type: none"> • Very expensive (R18 000) • 6 single-ended analogue input channels • Mathematical calculations after data collection

The PICOLOG 1012 is manufactured by PICO Technology in the United Kingdom [17] and is available

from two local approved distributors in SA [18, 19]. They feature 12 single-ended input channels with a maximum input voltage of 2.5 V, but need to be permanently connected to a PC to enable data storage and analysis. A general purpose notebook (price of around R 4000 in SA) is the more logical choice, as it is portable, compact and provides battery backup in case of power disruptions.

The DAQPro 5300 is manufactured in the United States of America (USA) by Fourtec Fourier Technologies [20], and is available from a number of local suppliers in SA. They are rather expensive at around R 12 000 each, but do not require a permanent connection to a PC for logging purposes. They are limited to eight analogue input channels with a maximum input voltage of 10 V.

The CAMPBELL Scientific CR800 is the Rolls Royce of data loggers and is manufactured in the USA [21]. It has six single-ended analogue inputs with a maximum input voltage of 5 V. It can store data over an extended period of time and be remotely activated for data downloads.

The ARDUINO MEGA 2560 is the cheapest of the locally available microcontroller boards that was suitable for this project in SA, and has been used in 934 research projects according to Google Scholar. However, searching for the words “ARDUINO MEGA 2560” and “photovoltaic” returns 59 results, indicating its applicability as a data logger in PV systems. The ARDUINO MEGA 2560 is also very easily integrated into LabVIEW, where a customizable program can be developed according to end-user needs. Other reasons for choosing this platform for this research include [22]:

- It is an open-source project where the software/hardware is extremely accessible and very adaptable.
- It is flexible and offers a variety of digital and analogue inputs/outputs, serial interface and digital and PWM outputs.
- It is easy to change and update the program as it connects to a PC via USB and communicates using standard serial protocol.
- It is an inexpensive microcontroller for which the software is freely available.
- It has a large online community with a lot of references, example source codes and libraries to refer to.

3. LabVIEW

National Instruments LabVIEW is a graphical programming language that has its roots in automation control and data acquisition. Its graphical representation, similar to a process flow diagram, was created to provide an intuitive programming environment for scientists and engineers. The language has matured over the last 20 years to become a general purpose programming environment. LabVIEW has

several key features which make it a good choice in an automation environment. These include simple network communication, turnkey implementation of common communication protocols (RS232, GPIB, etc.), powerful toolsets for process control and data fitting, fast and easy user interface construction, and an efficient code execution environment [23].

4. ARDUINO

The ARDUINO is an electronic platform designed to simplify the process of studying digital electronics. According to one of its designers, David Cuartielles, in 2013 there were already some 700,000 ARDUINO boards in consumer's hands with at least the same amount of counterfeit boards. The ARDUINO comprises a microcontroller, a programming language and an Integrated Development Environment (IDE) [24]. ARDUINO was born to teach Interaction Design, a design discipline that puts prototyping at the centre of its methodology [25]. The designers attempted to design a user-friendly software and hardware interface, making freely available the necessary documentation to support it [26].

Two boards were considered, the UNO and the MEGA (Table 2 gives a brief specification breakdown). Figure 1 shows the ARDUINO MEGA 2560 that was used in this research due to its large number of input / output channels (see Table 1) and the relevant ease of connecting it to LabVIEW.

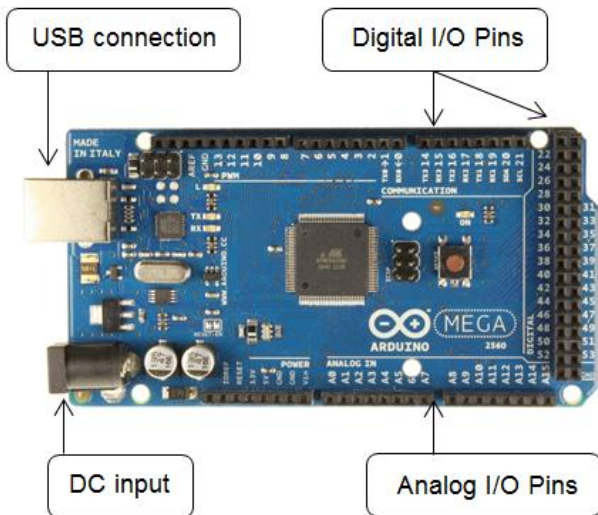


Figure 1: ARDUINO MEGA 2560

The cost of the hardware is relatively cheap (see Table 1) and the development software can be downloaded for free from the Internet. There are also a growing number of software examples which are freely available, making the implementation of ideas on these boards easier to achieve. Students from different fields make extensive use of these ARDUINO boards [27-29].

Table 2: UNO and MEGA specifications [30]

ARDUINO	UNO	MEGA
Microcontroller	ATmega328	ATmega2560
Operating Voltage	5V	5V
Input Voltage	7-12V	7-12V
Digital I/O Pins	14	54
Analog Input Pins	6	16
DC Current per I/O Pin	40 mA	40 mA
DC Current for 3.3V Pin	50 mA	50 mA
Flash Memory	32 KB	256KB
SRAM	2 KB	8KB
EEPROM	1 KB	4KB
Clock Speed	16 MHz	16 MHz

5. LabVIEW and ARDUINO

Before the ARDUINO can be used as a data logger in conjunction with LabVIEW, it needs to be flashed with the LabVIEW base software [31]. In the LabVIEW software the ARDUINO must be initiated, and again closed at the end of every session. Voltage readings are obtained from the ARDUINO by using the analog read function (see Figure 2). The value is then multiplied by a factor for calibration and to compensate for any interface losses. The immediate value is displayed on the front panel of the LabVIEW software visible on the screen of the PC. This value is then filtered by a Butterworth Filter before it is written into a matrix. The filter is used to filter out high frequency components that come from the ARDUINO's analog read circuit and any other noise present in the data logging system.

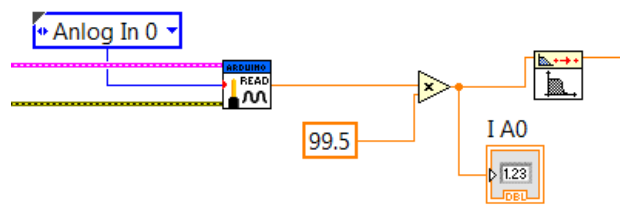


Figure 2: Analog read and conditioning functions used in LabVIEW

The functions in Figure 2 were duplicated for three voltage readings as well as for three current readings, as the output power of three different PV systems were being monitored (each comprising a 10 W polycrystalline PV module, data logging interface circuit and a fixed resistive load). The PV module was set to a tilt angle equal to latitude as suggested by Chinnery [32] and no batteries were included in the practical setup due to uncertain variations which may exist between batteries from the same manufacturer and with the same model number [33].

Temperature readings for the modules were obtained by a thermistor read function in LabVIEW (see Figure 3). The temperature value was also passed through a Butterworth Filter to eliminate any high frequency noise components. The temperature signal was multiplied by a calibration factor after which it is displayed on a graph on the front panel of the LabVIEW software program.

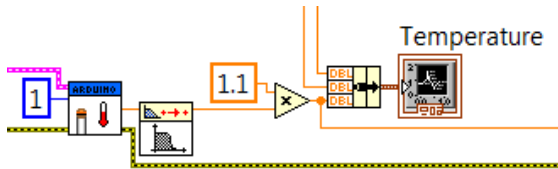


Figure 3: LabVIEW functions used for temperature readings from the thermistors

One way of comparing the performance of the three PV systems was to record the amount of samples where the output power of each module exceeded a set limit (3.5 W in this research). In order to have a record of the percentage of time that each PV module produced more than 3.5 W of power, a shift register was used in which the value was incremented each time a sample's value were above the set limit. The accumulation of these values was automatically written into a singular file at the end of each day. Figure 4 gives an indication of the implementation of the “samples above a certain level” method.

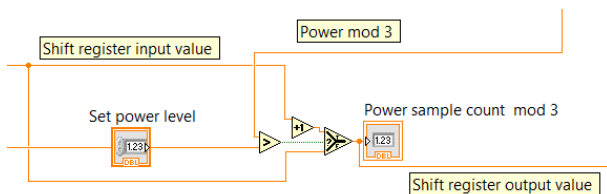


Figure 4: Process of incrementing the shift register for sample values above specified power

Another way to evaluate the performance of each of the three PV systems was to record the Watt hours (Wh) generated by each module. This was done by calculating the mean power for a specific number of samples and then multiplying that mean power with the time in hours represented by those samples (see Figure 5). This results in an instantaneous Wh value for a specific number of samples taken within a 24 hour period.

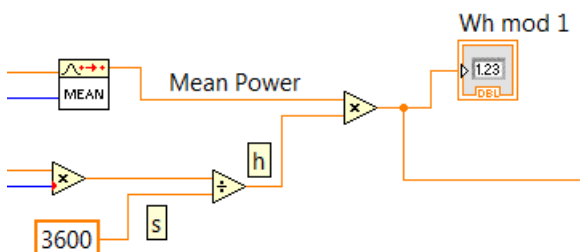


Figure 5: Calculation of Wh

At the end of each day a predefined file is opened and the collected data (number of samples above a set power limit, Wh, maximum temperatures and a date stamp) is added into the file (see Figure 6). This simplifies data analysis as one does not have to work through thousands of samples for each day to calculate the required data.

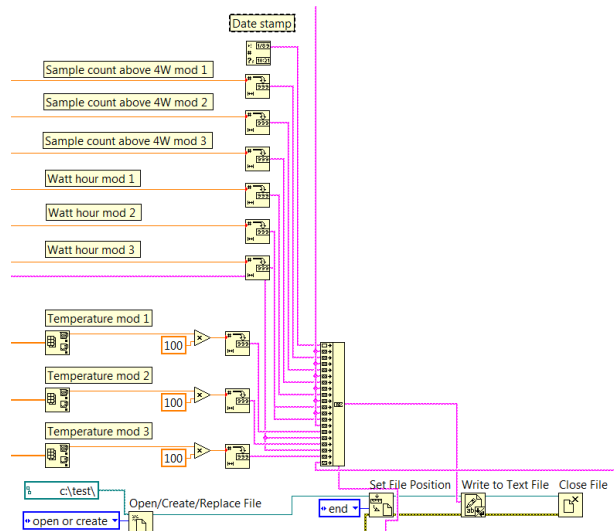


Figure 6: LabVIEW code for writing data to a file

Figure 7 is an example of the data file that is amended at the end of each day. Each row consist of the date, followed by the sample counts above 4 W, the total Wh for that day (which must be divided by 1000 as LabVIEW does not insert commas into the data) and lastly the maximum temperatures (must be divided by 100 to obtain the decimal separated value) during that day for each of the modules.

```
10/23/2014,2633,2552,2350,36610,36303,34972,5620,5405,5413
10/24/2014,2086,2076,1977,29546,29486,28947,5663,5328,5524
10/25/2014,2912,2890,2667,37937,37884,36944,5301,4902,5234
10/26/2014,2461,2420,2277,36569,36294,35090,4567,4384,4420
10/27/2014,3263,3160,2875,42205,41454,39852,4411,4254,4256
```

Figure 7: Example of data file where values need to

The LabVIEW front panel is shown in Figure 8 where the following is discernable:

- the total amount of samples that are to be recorded and written to a single file (see A);
- the Arduino board that is used for the sampling (see B);
- the power set limit for the sample count (see C);
- the calibration factor for the current (see D) and voltage of each module (see E);
- the instantaneous power for each module (see F);
- the accumulated Wh for each module (see G);
- a limited logged history as well as the instantaneous values of the current (see H), voltage (see I) and power (see J); and
- the total sample count which has been completed (see K).

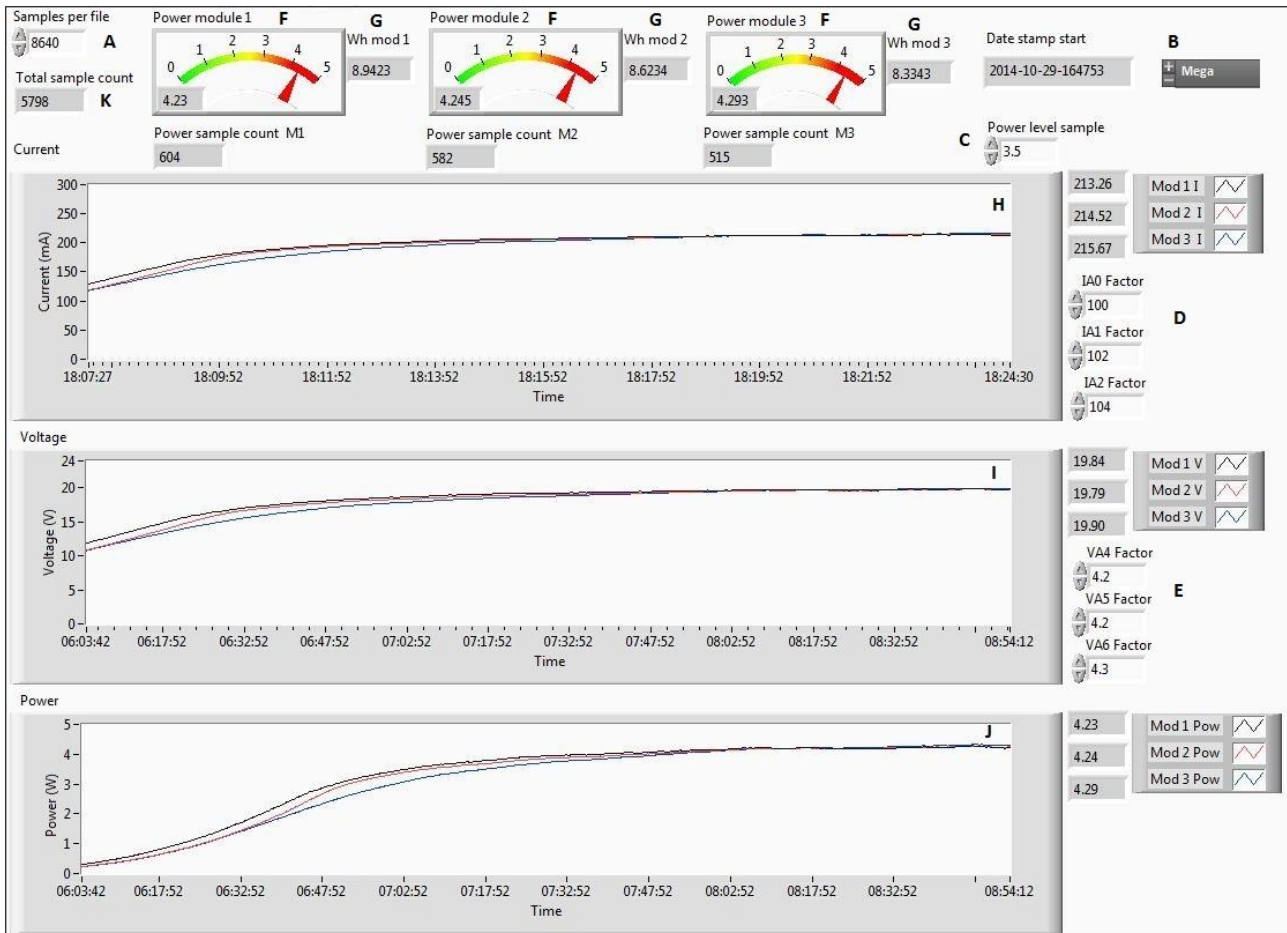


Figure 8: LabVIEW front panel

6. CONCLUSIONS

The purpose of this paper was to present a customizable energy monitoring system which may be used to analyse and evaluate the operation of a number of different PV modules. The output voltage, current and temperature of three 10 W polycrystalline modules were recorded using the ARDUINO MEGA 2560 data logger, with instantaneous power calculations being achieved and displayed on the front panel of the LabVIEW software program. Calibration settings and total sampling counts are accessible from the front panel. Specific data (number of samples above a set power limit, Wh, maximum temperatures and a date stamp) is added into a singular file at the end of each sampling period, which simplifies data analysis and PV system evaluation.

7. REFERENCES

- [1] Brainy Quote. Available: <http://www.brainyquote.com/quotes/>. Accessed: 01 October 2014.
- [2] C. Peng and K. Qian, "Development and Application of a ZigBee-Based Building Energy Monitoring and Control System," *The Scientific World Journal*, vol. 2014, 2014.
- [3] A. J. Swart, H. C. Pienaar, and R. M. Schoeman, "Cost-effective energy monitoring of domestic off-grid PV systems," presented at the APPEEC 2013, Beijing Yanshan Hotel, Beijing, China, 2013.
- [4] T. Bock, P. Kishore, T. Linner, and W. V. Lauer, "Mechatronics Assisted Architecture," presented at the 27th International Symposium on Automation and Robotics in Construction (ISARC 2010), Bratislava, Slovakia, 2010.
- [5] I. M. Saleh, "Energy Monitoring, Targeting and Waste Avoidance," in 4th IEEE-GCC International Conference, Manama, Kingdom of Bahrain, 2007, pp. 11-14.
- [6] N. Lemmer. (2012, June/July) Using energy meters as a tool to improve energy-efficiency. *25 Degrees in Africa*. 28-29.
- [7] S. C. Brofferio, A. Antonini, G. Galimberti, and D. Galeri, "A method for estimating and monitoring the power generated by a photovoltaic module based on supervised adaptive neural networks," in Smart Measurements for Future Grids (SMFG), 2011 IEEE International Conference, 2011, pp. 148-153.
- [8] D. Sera, R. Teodorescu, and P. Rodriguez, "Photovoltaic module diagnostics by series resistance monitoring and temperature and rated power estimation," in *Industrial*

- Electronics, 2008. IECON 2008. 34th Annual Conference of IEEE, 2008, pp. 2195-2199.
- [9] N. Pearsall and B. Atanasiu, "The European PV system monitoring guidelines - Modernisation under the PERFORMANCE project," in Photovoltaic Specialists Conference (PVSC), 2009 34th IEEE, 2009, pp. 256-261.
- [10] X. Jiang, S. Dawson-Haggerty, P. Dutta, and D. Culler, "Design and implementation of a high-fidelity ac metering network," in Information Processing in Sensor Networks, 2009. IPSN 2009. International Conference on, 2009, pp. 253-264.
- [11] R. Smutny, C. Neururer, and M. Treberspurg, "Sustainability evaluation of Viennese housing estates in the passive house standard—A post occupancy reflection of selected criteria," International journal of sustainable building technology and urban development, vol. 3, pp. 112-119, 2012.
- [12] J. W. Smith and I. Sommerville, "Workload Classification & Software Energy Measurement for Efficient Scheduling on Private Cloud Platforms," arXiv preprint arXiv:1105.2584, 2011.
- [13] J. Bastidas-Rodriguez, G. Petrone, C. Ramos-Paja, and G. Spagnuolo, "Photovoltaic modules diagnostic: An overview," in Industrial Electronics Society, IECON 2013-39th Annual Conference of the IEEE, 2013, pp. 96-101.
- [14] Google Scholar. *Data Loggers*. Available: <http://scholar.google.co.za/>. Accessed: 29 October 2014.
- [15] IEEE Xplore. *Data Loggers*. Available: <http://ieeexplore.ieee.org>. Accessed: 29 October 2014.
- [16] P. Vařacha, N. Mastorakis, R. Jašek, M. Pospíšilík, B. Chramcov, and D. Sámek, "Technical Devices for Supervising of a Household via Interned Based on Arduino Microcontroller," in 12th WSEAS International conference on Applied Informatics and Communications, Istanbul, Turkey, 2012.
- [17] PICO Technology. *Homepage*. Available: <http://www.picotech.com/index.html>. Accessed: 11 July 2012.
- [18] AP Electronics. *Homepage*. Available: <http://www.apelectronics.co.za/>. Accessed: 11 July 2012.
- [19] RS Components. *Homepage*. Available: <http://za.rs-online.com/web/>. Accessed: 11 July 2012.
- [20] Fourtec Fourier Technologies. *Homepage*. Available: <http://www.fouriersystems.com/>. Accessed: 17 July 2012.
- [21] Campbell Scientific. *Homepage*. Available: <http://www.campbellsci.com/>. Accessed: 20 July 2012.
- [22] A. Woodruff and B. Görmez, "Laser Music System: Implemented using lasers, infrared sensors, photocells and a Arduino Microcontroller," Bachelor Thesis, School of Information Science, Computer and Electrical Engineering, Halmstad University, Halmstad, 2012.
- [23] C. Elliott, V. Vijayakumar, W. Zink, and R. Hansen, "National instruments LabVIEW: a programming environment for laboratory automation and measurement," Journal of the Association for Laboratory Automation, vol. 12, pp. 17-24, 2007.
- [24] A. Martins, J. Lourenço, T. Patrício, and A. de Alexandria, "Sensor Kinect in a telepresence application," Computational Vision and Medical Image Processing IV: VIPIMAGE 2013, p. 151, 2013.
- [25] M. Banzi, Getting Started with arduino: " O'Reilly Media, Inc.", 2009.
- [26] L. Buechley and M. Eisenberg, "The LilyPad Arduino: Toward wearable engineering for everyone," Pervasive Computing, IEEE, vol. 7, pp. 12-15, 2008.
- [27] A. S. Rao, S. Marshall, J. Gubbi, M. Palaniswami, R. Sinnott, and V. Pettigrov, "Design of low-cost autonomous water quality monitoring system," in Advances in Computing, Communications and Informatics (ICACCI), 2013 International Conference on, 2013, pp. 14-19.
- [28] P. J. Gonçalves, P. Torres, and P. Lopes, "ROBIHO—A Robot Companion for Elderly People's Homes," Applied Mechanics and Materials, vol. 282, pp. 158-161, 2013.
- [29] S. R. Zeebaree and H. M. Yasin, "Arduino Based Remote Controlling for Home: Power Saving, Security and Protection," International Journal of Scientific & Engineering Research, vol. 5, pp. 266-272, 2014.
- [30] W. Chek and W. A. Khusairi, "PI voltage control technique for 3 phase induction motor using Simulink and Arduino," Universiti Tun Hussein Onn Malaysia, 2014.
- [31] A. Jamaluddin, L. Sihombing, A. Supriyanto, A. Purwanto, and M. Nizam, "Design real time Battery Monitoring System using LabVIEW Interface for Arduino (LIFA)," in Rural Information & Communication Technology and Electric-Vehicle Technology (rICT & ICeV-T), 2013 Joint International Conference on, 2013, pp. 1-4.
- [32] D. N. W. Chinnery, "Solar heating in South Africa," Pretoria CSIR-Research Report 248, 1981.
- [33] A. J. Swart and P. E. Hertzog, "Quantifying the Effect of Varying Percentages of Full Uniform Shading on the Output Power of a PV Module in a Controlled Environment," presented at the SATNAC 2014, Boardwalk Conference Centre, Nelson Mandela Bay, Eastern Cape, South Africa, 2014.

IMPACT OF PV GENERATORS ON POWER SYSTEM VOLTAGE REGULATION FOR DISTRIBUTION NETWORKS WITH VERY LONG BRANCH NETWORKS

M. Dlamini* and N Gule**

* Department of Electrical and Electronic Engineering, Universiteit Stellenbosch University, South Africa, E-mail: 19053541@sun.ac.za,

** Department of Electrical and Electronic Engineering, Universiteit Stellenbosch University, South Africa, E-mail: nathie@sun.ac.za

Abstract: This paper investigates the steady state impact of Distributed Generators (DGs), with major focus on Photovoltaic Cells (PV) on a real Swaziland distribution Network. The worst case scenario shall be analysed before the DG is connected to the grid to ensure that the network voltages operate within allowable ranges and then the voltage profile variation together with the steady state voltage regulation after the connection of the PV plant shall also be analysed. The impact of placing the generator at different locations within the network together with the penetration levels shall be studied and the optimal solution evaluated.

Keywords: PV Plant, DIGSILENT, IPP, Point of Common Coupling, Distributed Generators, Voltage Stability

1. INTRODUCTION

The power deficit and lack of energy self-sufficiency in a number of countries within the Southern African Power Pool (SAPP) member countries has forced utilities, including the Swaziland Electricity Company (SEC), to look into a number of options to arrest this problem. This drive has been further enhanced by the deregulation of the Electricity Supply Industry in most of these countries which have opened doors for partnering with independent power producers (IPPs). Moreover, with most governments becoming more inclined towards the development of renewable energy through providing support for renewable energy programs, there has been a high increase in the desire for integrating renewable energy into the grid. Furthermore, the establishment of policies to promote renewables, such as feed in tariffs as well as other financial and tax incentives in the forms of favourable loans and reduced corporate tax, to name but a few, have also encouraged individuals and companies to invest on green energy.

The influence of the above factors is more evident in the developed countries where there have been a large penetration of energy from other generators, mainly induction generators, into the power system and this has resulted in drastic changes to the system dynamics that had been previously determined by synchronous generators. Unlike the conventional synchronous generators, the power generated from induction generators is highly variable and therefore difficult to dispatch as a result of the stochastic nature of its prime movers i.e. wind speeds [1]. As a developing country whose energy supply industry has just been deregulated a few years ago, Swaziland has been found to be no exception from what most of the developed

countries have already experienced; hence this paper investigates the impact of integrating such systems into the Swaziland Electricity Network, especially on the distribution network.

Nonetheless, as a developing country, Swaziland is experiencing high development rates of its urban areas, which is likely to come with large structures that may impede the flow of wind in case of wind generation plants or may affect positioning of Photovoltaic (PV) plants and therefore influence the location of the generation plant. These unfavourable conditions can limit grid interconnection to radial feed for unidirectional power flow. This further implies that the power from these distributed generators may have to be evacuated through a weak and sometimes congested grid

Although, sometimes designed for ring feeds, distribution systems have been operated as radial feeds over the years for the best control and coordination of the protective devices. The radial or weakly meshed topological structure is characterised by a high resistance to reactance (R/X) branch ratios [3, 4, 5]. As a result, these networks are subjected to high power losses due to the very high line resistance which then result in poor voltage regulation thus making the study on the role of Distributed Generators (DGs) on the voltage regulation a very important area of evaluation. This is mainly because DGs have been recently proposed to minimise distribution power losses in the power network by improving the distribution system voltage at the load points, especially for those loads which are closer to the Point of Common Coupling (PCC).

Furthermore, the load of a distribution network is always changing due to the variations in consumer demands. The

distribution system sometimes experiences voltage collapse under critical loading conditions thus a need to further investigate the impact of distributed generation on the system voltage support. In [2], the connection of a generator to the distribution system has been found to affect the power flow and the voltage profiles of the power system and the profiles were found to be different for different types of loads.

To analyse the impact of DGs on the power system voltage stability, this paper shall focus on the considerations for generator placement, factors influencing generator sizing together with the impact of placing the generator at different locations within the network and the optimal solution evaluated.

2. DISTRIBUTION SYSTEM DESCRIPTION

In order to investigate the impact of the PV plant integration on the power system steady state voltage profile, a real radial distribution network located at the Malkerns Substation of the Swaziland Electricity Company Network is used. This network allows for the simulation and studying of the effects of the integration of PV plants into a radial distribution line with very long branch networks for voltage profile improvement. The single line diagram of the distribution system under the study, without DG, is presented in Fig. 1.

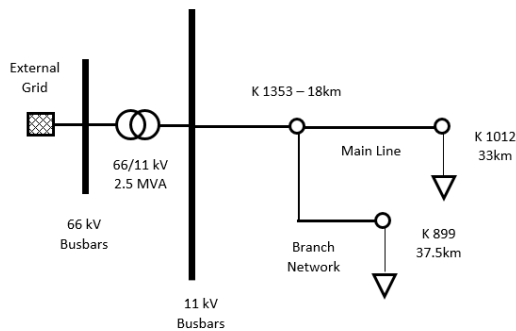


Figure 1. Simplified Radial feeder with long branch network single line diagram

The considered network consists of a 66 kV, 50 Hz transmission system which feeds an 11 kV distribution system through a 66/11 kV, DYN 11 transformer with rated apparent power of 2.5MVA. The primary substation transformer's tap is adjusted in order to maintain voltages at all buses within the allowable range for minimum and maximum demand without DG.

Only one feeder under this distribution network is covered in this study and consist of 38 nodes and 3 very long feeder branches that are heavily loaded. This feeder is composed of two major conductors; Mink which forms part of the main line together with a few branch networks and Gopher which is mainly used in the minor branch networks. Under normal operating conditions, the total network load during

maximum demand is 2.6 MW, with a total load is 0.8 MW experienced during the minimum demand period. The distribution lines and the feeder are modelled as series connection of resistance and inductance and the loads are represented by constant power model.

When load flow studies were carried out before the integration of PV generation, the network complied with the grid requirement up to 16% loading as shown in Table 1 below. Although the voltage drops tremendously at 20% loading, the effect of the distance from the supply is seen not have as much influence on the voltage as is with 30% and above loading.

To analyse the impact of the loading on the feeder voltage profiles, simulations were carried out in PowerFactory for the SEC distribution Network. These simulations were carried out for various feeder loading as depicted in Table 1

Table 1: Feeder voltage profile at various loading □No PV connected

	Source (1094)	K1353	K1012	K899
% Loading	Voltage p.u.	Voltage p.u.	Voltage p.u.	Voltage p.u.
10	0.98	0.96	0.95	0.97
16	0.97	0.94	0.92	0.95
20	0.97	0.92	0.90	0.94
30	0.95	0.87	0.84	0.90
40	0.93	0.77	0.81	0.85
41	0.93	0.80	0.76	0.85

3. GENERATOR SIZING IMPACT STUDY

Previous studies have shown that it may be desirable to have higher capacity generators connected to the distribution network to ease it from loading stress as well as have these generators positively contribute in the voltage regulation process. It has also been observed that the DG that can be installed on a distribution System is highly dependent on the circuit system voltage, the location of the DG generator on the circuit, the circuit configuration and characteristics, system protection issues, voltage regulation issues, as well as the DG characteristics [3]. As such, it has become paramount that these issues be considered in the study of the impact of DGs on the power system voltage stability.

In order to study the impact of integrating the PV plant into the distribution system, a PowerFactory PV model was evaluated for different penetration levels and their results compared. This was tested on the model of the network shown in Figure 1 and the PV plants were intentionally placed at the weak region of the network to simulate the worst case scenario.

4.1 Modelling Assumptions

When doing the analysis, the following assumptions were applied to the study:

- The maximum power output of the PV plants is at a power factor of between 0.975 inductive and 0.975 capacitive.
- A voltage regulation limit of +5% / -5% shall apply to the SEC network at the 11kV level.
- Maximum loading permitted for lines and transformers in the SEC network is 90%.
- The voltage of the 66kV Malkerns busbars will be controlled by the transformer tap changer(s) to 1.02p.u in accordance with the current operating philosophy for the Swaziland network.
- The effect of a generation plant on the network is proportional to the size of the generation plant i.e. the smaller the size of the plant the smaller the impact.

4.2 Methodology

The methodology applied to this project is summarised as follows:

- A DigSILENT PowerFactory model representative of an existing portion of the SEC distribution network at the study area was used as the basis for the capacity evaluation.
- Generation plants were operated in power factor control mode, with a power factor set point of 0.975 p.u. in the studies.
- The network capacity at the proposed point of connection was evaluated to determine the maximum amount of generation that can be connected at this point.

4. DISCUSSION OF RESULTS

Three case studies were carried out to evaluate the impact of installing PV generation on voltage stabilisation. A factor of the load around the area where the PV plant is to be installed over the complete feeder requirement was used to size the generators, in all the cases. Since the feeder maximum demand is 2.5MVA, the generation capacity was sized below this load and various loading were used per case, considering the effective load of the considered branch network.

To analyse the results, a voltage profile of the whole feeder is depicted in table 2 and the method used to obtain the results explained in the following Cases.

Case1: Placement of PV plant towards the tail of heavily loaded branch and the main line

In this case, voltage support can be achieved by installing one PV plant at the end of the network and another plant at the end of the branch network with the highest load. A 0.7MW PV plant was placed at node K1012 and a 1.1MW

PV plant placed at node K899 during the simulations and the following results were obtained as depicted in Scenario A of Table 2.

Table 2: Feeder voltage profile with PV plant connected at various nodes of the distribution lines

	Source (1094)	K1353	K1012	K899
Scenario	Voltage p.u.	Voltage p.u.	Voltage p.u.	Voltage p.u.
A	0.93	0.96	1.01	1.02
B	0.93	1.01	0.98	0.90
C	0.93	0.99	1.04	0.99

Scenarios:

- A. PV plant connected at nodes K1012 and K899
- B. PV plant connected at node K1353
- C PV plant connected at nodes K1353, K899 and K1012

This study revealed that placing PV generators at the end of the feeders and heavily loaded branch has a positive impact on the voltage profile. The voltage at the nodes where the plant is installed greatly improves and complies with the grid code. However, it was observed that there are areas where voltage sags and under voltage was experienced thus resulting in non-compliance with the Grid code.

Case2: Placement of PV plant at the Node where heavily loaded branch deviated from the main line

Case 2 investigates the impact of placing the PV plant at the central location that will provide voltage support to both the main line in the heavily loaded branch network and the results of the simulation are shown in scenario B of table 2. To achieve this objective, a PV plant is placed at node K1353 and then results of the generator integration investigated.

From this case study, it was observed that for optimum voltage support the plant size had to be confined to a maximum of 61% of the maximum feeder loading. When this limit was exceeded, voltage swells which could easily result in an overvoltage were experienced. However, even when the generation was increased beyond this optimum limit, it was observed that the power network still failed to comply with the Grid Code requirement. Although voltage swells were experienced very close to the injection point when the generation output was increased, it is also observed that this had little effect on the heavily loaded branch network as the voltage within this network remained below the 0.95p.u. Nonetheless, a positive impact was noted along the main line as the voltage at node K1012 was above the required 0.95p.u. and below 1.05p.u as specified in the grid code.

Case3: Placement of PV plant at the Node where heavily loaded branch deviated from the main line and at the tail of the main line as well as the heavily loaded line

Three PV plants are installed in this case. Two plants were installed at the end of the network and at the end of the branch network with the highest load. Another PV plant was also installed at the central location that will provide voltage support to both the main line in the heavily loaded branch network. This is achieved by placing 0.7MW, 0.8MW and 0.3MW PV plants at nodes K1012, K899 and K1353 respectively.

From this case study it was observed that better voltage support can be achieved with this method since the voltage levels were in compliance with the grid code at all levels of the network.

5. CONCLUSION

This paper presented the considerations and effects of integrating a PV plant into a distribution network with very long and heavily loaded branch networks. Part of the Swaziland distribution network was used in the study. It was observed that under such networks, dispersed generation offers adequate control on the voltage profile improvement.

It was further observed that for optimum voltage support, the placement of the generators is also greatly influenced by the loads and their distribution in the power network.

6. REFERENCES

- [1] S. Poal, A. Hanse, L. Jonosi, J. Bech and a. B. Bak-Jensen, □Simulation of interaction between Wind Farm and Power Systems, □Riso National Laboratory, Roskilde, 2001.
- [2] M. W. Davis, R. Broadwater and J. Hambrick, □Modelling and Verification of Distributed Generation and Voltage Regulation Equipment for Unbalanced Distribution Power Systems, □National Renewable Energy Laboratory, 2007.
- [3] N. Roy, M. Hossain and H. Pota, □Effects of load modelling in power distribution systems with distributed wind generation, □in Australian Universities Power Engineering Conference, Brisbane, 2011.
- [4] E. Salem, B. Mohammed and M. Joydeep, □Analytical aproach for placement and sizing of distributed generation on distribution system, □IET Generation, Transmission & Distribution, 2013.
- [5] M. Srinivas, □Distribution Load Flows: A brief review, □IEEE PES Winter meeting, 2000.

A PRELIMINARY STUDY TO ASCERTAIN THE TECHNO-ECONOMIC VIABILITY OF RESIDENTIAL AIR SOURCE HEAT PUMP WATER HEATER: FORT BEAUFORT, SOUTH AFRICA

Stephen L. Tangwe*, Michael Simon and Edson L. Meyer

*Fort Hare Institute of Technology, University of Fort Hare, Alice, Eastern Cape, South Africa

Phone: +27(0)406022086, Fax: +27 (0) 40 653 0665, E-mail: stangwe@ufh.c.za

Abstract:

The utilization of an air source heat pump (ASHP) to retrofit geyser can significantly reduce electricity consumption for sanitary hot water production. Furthermore, optimal operation of the system based on ambient conditions and capacity of hot water usage would enhance both achievable performance and payback time. The study focuses on using a data acquisition system to evaluate the performance of an efficiently installed ASHP water heater and hence determine the payback period of the system. Preliminary results depict that during the four months of performance monitoring of the system, the average month-day input energy, coefficient of performance and volume of hot water usage was 3.0 kWh, 2.2 and 260 L respectively. An average monthly energy saved of 125 kWh was achieved while the average ambient temperature and relative humidity of 24.6 °C and 64.2% were recorded for the entire time of operation of the system. Finally, using a multiple comparison test, it was demonstrated that no mean significant difference occurred in both the average week electrical energy and COP for each of the different months throughout the observations. The payback period of the ASHP unit was determined to be less than 6 years from a conservative approach method.

Keywords: Air source heat pump (ASHP); Sanitary hot water; Coefficient of performance (COP); Payback period, multiple comparison test, Data acquisition system (DAS).

1. INTRODUCTION

The commonly applicable type of heat pump heaters employed for sanitary hot water heating are the air source and the geothermal or ground source systems. These systems operate on the principle of vapor compression refrigerant cycle. The geothermal heat pump water heater possesses a better techno-economic potential to an ASHP water heater by virtue of its relatively constant and higher COP [1, 2]. Both systems can be classified as a renewable energy device, since all use one form of renewable energy from its immediate surroundings where its evaporator is located during the vapor compression cycle. The ground source heat pump water heater extract waste heat from underground in the form of geothermal energy while ASHP water heater utilized the heat from the air as aero-thermal energy. The capital cost of ground source heat pump water heater is much higher as compared to an ASHP water heater. ASHP water heat is fast gaining maturity in the market as sanitary hot water production constitutes a significant percentage of monthly energy consumption in the residential sector worldwide. In South Africa, residential hot water heating can contribute to more than 50% of the monthly energy utilization [3]. A far-reaching research conducted to justify in terms of energy usage revealed that the hot water contribution in the domestic sector of South Africa is between 40% to 60% on an average monthly basis [4, 5]. It is worth mentioning that despite the daunting electrical energy consumed for hot water production, not all the thermal energy gained by the hot water is effectively utilized.

There are always standby losses which are responsible for 20% to 30% of the total thermal energy gained by hot water contained in a storage tank [6]. Although, ASHP water heater coefficient of performance (COP) value can range from 2 to 4 [7, 8]; it is crucial to note that the system COP depends on the COP of the ASHP unit and the ambient climatic condition [9]. Clearly, the COP could be defined as the ratio of the useful thermal energy gained when water is heated to set point temperature and the electrical energy used by the system during the vapor compression refrigerant cycle. A salient and better understanding of refrigeration cycle of heat pump water heater was given by Ashdown *et al.* (2004) and Sinha and Dysarkar, (2008) [10, 11]. Heat pump water heaters also render an extra benefit of dehumidification and space cooling because they pull warm vapor from the air [12]. An efficiently installed residential ASHP water heater can guarantee an improvement on the system performance [13]. The study deal with an in depth performance monitoring of a residential split type ASHP water heater installed in a middle class home (containing 2 adults and a child) in Fort Beaufort in a bid to determine both the electrical energy saving from hot water production and payback period of the ASHP unit. The sanitary hot water set point temperature was 55 °C. The ASHP water heater and the metering equipments were installed in the month of January (2013) while the data collected for the analysis was from 01 st January - 30 th April 2014. These periods of monitoring were considered owing to minimal variability in climatic factors that can affect the system performance.

1.1 TYPES OF ASHP WATER HEATER

Residential ASHP water heaters in South Africa are divided into two categories, namely the integrated and the split type systems. The performance of the integrated system is better than that of the split type, albeit the latter is more stable [14]. In an integrated system, both the ASHP unit and the storage tank exist as a compact system. The condenser is usually immerse in the storage tank and act as the heat exchanger between the primary refrigerant in the close circuit of the heat pump and the water stored in the storage tank. The heat dissipated from the refrigerant is absorbed by the water to raise the temperature to the set point. Figure 1 shows a typical integrated system.

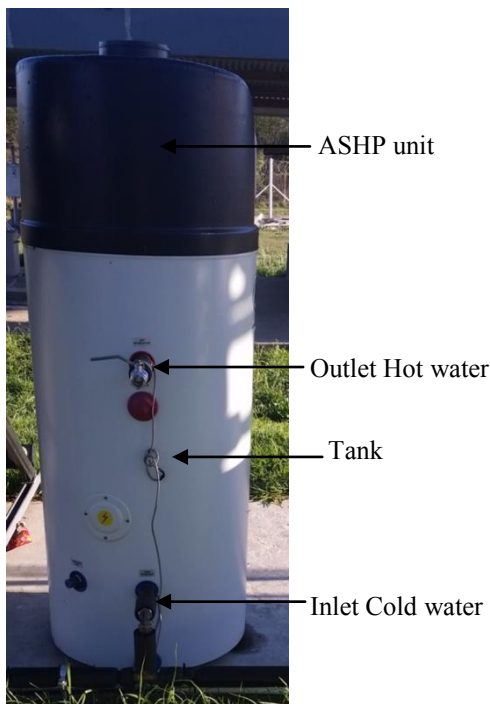


Figure 1: Shows an integrated ASHP water heater

The split type ASHP water heater is a retrofit system comprising of an ASHP unit and a storage tank connected by pipes. Split type system can either be a once pass or recirculation type. In a once pass type the inflowing water from the tank to the inlet of the ASHP unit is heated to hot water set point temperature before exiting via the outlet. This type of circulation is referred to as a single pass. A recirculation type is where there is continuous circulation of the water between the tank and the ASHP unit until the set point temperature of the water is attained. In a split type ASHP water heater the storage tank is usually above the ASHP unit and there are pipes connected from the inlet and outlet of the ASHP unit to the storage tank. More importantly, there is a water circulation pump connected via the ASHP inlet pipe and aid to provide sufficient pressure for the heated water to flow back to the tank. In addition to the water circulation pump, there exist other valuable components that make

up the close circuit of the vapor compression cycle. These include the evaporator, compressor, condenser and the thermal expansion valves. There are also a propeller axial fan, strainer, open and close valves. The connecting pipes are well insulated to prevent both reticulation and standby heat losses. Figure 2 shows a detail installation of a split type ASHP water heater.

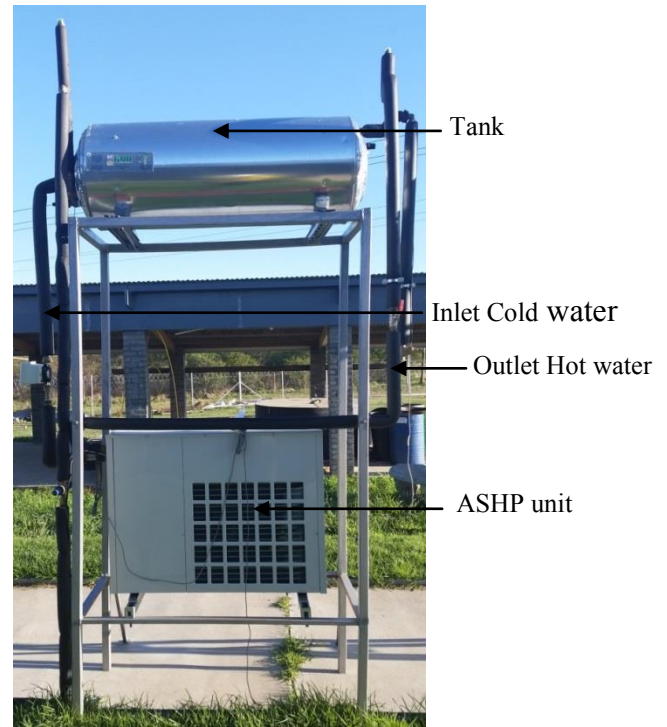


Figure 2: Shows a split type ASHP water heater

2. SYSTEM OVERVIEW

The system overview is break down into two; sensors and traducers use in the building of the data acquisition system and the full schematic layout of the ASHP water heater including the enclosure housing the data acquisition system.

2.1 DATA ACQUISITION SYSTEM

Table 1 shows the different components use in the building of the data acquisition system to monitor the performance of the ASHP water heater. All the sensors and the data logger were purchased from a single manufacturer (Hobo Onset Corporation). The sensors and transducer were all classified as class A and each come with its calibration certificate.

Table 1: show the equipment used to build DAS

Sensors	Quantity
U30-NRC (15 channels) data logger	1
T-VER-E50B2 power and energy meter	1
T-MINOL 130 flow meter	2
12 bits S-TMB temperature sensor	6
12 bits S-THB ambient temp and rel hum sensor	1
S-UCD electronic input pulse adapter	2
S-UCC electronic input pulse adapter	6
Protective fuse (50 A)	2
Current transformer (50 A)	2
4.5 V DC battery using a 240 V AC input	1

The U30-NRC was a robust and reliable data logger containing 15 digital smart jack ports. These ports are used to connect the sensors to the data logger to ensure measurement obtained from a specific sensor was recorded and stored in the data logger. The battery was used to power the U30-NRC data logger. The free end of the black and white twisted pair cable of the input pulse adapter (S-UCD) was connected to the output cable of the flow meter and was not polarity sensitive while the smart jack end was connected to one of the U30-NRC data logger ports [15]. The T-VER-E50B2 power and energy meter was connected with 3 S-UCC input pulse adapters from the Wh (active energy in watt hour), VARh (reactive energy in reactive volt-ampere hour) and Ah (current rating in ampere hour) ports to three ports in the logger via the smart jack ports [15]. 1 current transformer (CT) and 1 fuse were connected from the desired ports of the power meter (T-VER-E50B2) to the live cable powering the ASHP water heater. All the temperature sensors, the ambient temperature and relative humidity sensor were also connected to the U30-NRC data logger via the smart jack ports. The power meter was configured such that 1count equal 1 Wh and 1 VARh while 100 counts equal 1 Ah. The flow meters were configured such that 1 count equal 3.7854 liters [15]. The electronic input pulse adapters convert the analogue signal sense by the respective sensor to digital and hence eliminating errors in the measurement. The U30-NRC data logger was configured to log every five minute interval using the hoboware pro software which was also used to download the stored data obtained from the respective sensors for further analysis. It is important to note that due to the incorporation of the electronic input pulse adapter on the cable of the temperature sensors, flow and power meters the data store was an integral or average value for each logging interval (5 minutes). The figure 3 shows the schematic layout of the ASHP water heater and the enclosure accommodating the data acquisition system. And figure 4 illustrates the design configuration of the DAS built and used in the performance monitoring of the ASHP water heater.

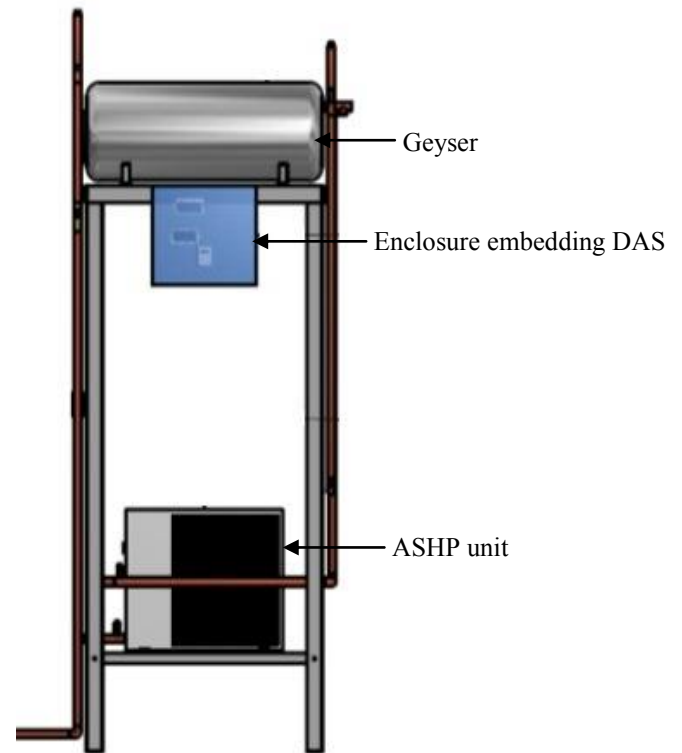


Figure 3: Shows the schematic diagram of the ASHP water heater and the enclosure housing DAS

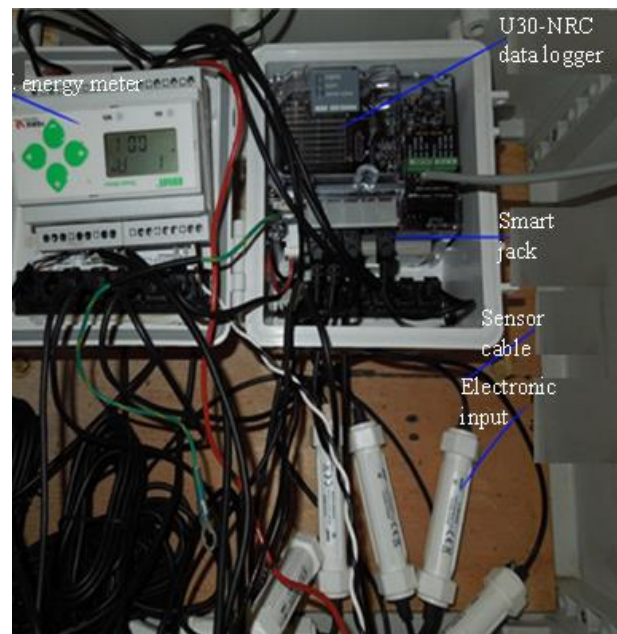


Figure 4: Shows the primary components of the designed and built DAS

3. THEORY AND CALCULATIONS

The set of equations given in the equation 1- 6 shown below were used to calculate the active power (kW); electrical energy (kWh), thermal energy gained by hot

water (kWh), the COP, the energy save (kWh) and the simple payback time (years).

$$E = \frac{Wh}{1000} \quad (1)$$

$$E = p \times t \quad (2)$$

Where E = electrical energy in kWh and t = time in hour
p = power in kW

$$Q = mc(T_o - T_i) \quad (3)$$

Where Q = thermal energy gain in kWh, m = mass of heated water = volume of water in litres heated by ASHP, c = specific heat capacity of water = 4.2 kJ/kg°C, T_o = ASHP outlet water temperature while T_i = ASHP inlet water temperature.

The COP of the system is given by the empirical equation shown in equation 4.

$$COP = \frac{Q}{E} = \frac{\text{output useful thermal energy gain}}{\text{input electrical energy}} \quad (4)$$

The energy saves (ES) is the difference between E and Q during a vapor compression refrigerant cycle assuming electrical energy consume by the power circuit of the control panel is negligible when heat pump unit is not running.

$$ES = Q - E \quad (5)$$

The simple payback time (SPB) is the ratio of capital cost of ASHP unit to the annual cost saving achieve from the technology.

$$SPB = \frac{\text{Capital cost}}{\text{Annual cost saving}} \quad (6)$$

4. RESULTS AND DISCUSSIONS

4.1. Average month-day comparative analysis of the ASHP water heater performance

Table 2 shows a detail analysis of the ASHP water heater performance for an average month-day over the monitoring duration (January-April 2014).

Table 2: Shows the average month-day performance

Parameters	Jan	Feb	Mar	Apr
Volume drawn (L)	258	271	263	253
Electrical energy (kWh)	2.93	2.94	2.93	3.22
Mean COP	2.18	2.17	2.25	2.08
Average ambient temp(°C)	25.3	24.2	26.0	22.7
Average Rel hum (%)	64.4	77.8	60.0	55.7
Average operating time(h)	2.27	2.08	2.23	2.73

Rel hum (relative humidity), temp (temperature)

It can be depicted that the hot water consumption based on the average month-day results were theoretically constants (slightly over 250 L). The systems COP on an average month-day were above 2 and in accordance with literature [16]. The COP is likely to increase with an increase in temperature. The COPs for the month of March and January were both 2.93 and the average ambient temperatures were 26.0 °C and 25.3 °C. Although there exist a negligible difference between the average ambient temperatures, the COPs have been constant since the average relative humidity which also influence COP was slightly higher for the month of January (as could be observed on table 2). On the contrary, the system COP was minimal for the April average month-day since its average ambient temperature was low (22.7 °C). It can also be elucidated that the better the COP, the smaller the electrical energy consumption and operating time for the ASHP water heater. The average operating time per day during the entire monitoring duration was more than 120 minutes but less than 180 minutes. Figure 5 illustrates two subplots that presented the variation of electrical energy consumption and operating time against the average month-day as well as the capacity of hot water usage per average month-day. From a comparative analysis using the two subplots, a noticeable increase in electrical energy consequently accompany an increase in the running time of the ASHP water heater. But an increase in the average daily electrical energy consumption might not lead to increase in the capacity of hot water drawn off, since not all drawn off leads to the running of the system and also the time taken for a specific heating cycle depends on the ambient temperature and relative humidity. The initial water temperature flowing into the ASHP inlet can also determine the electrical energy consumption.

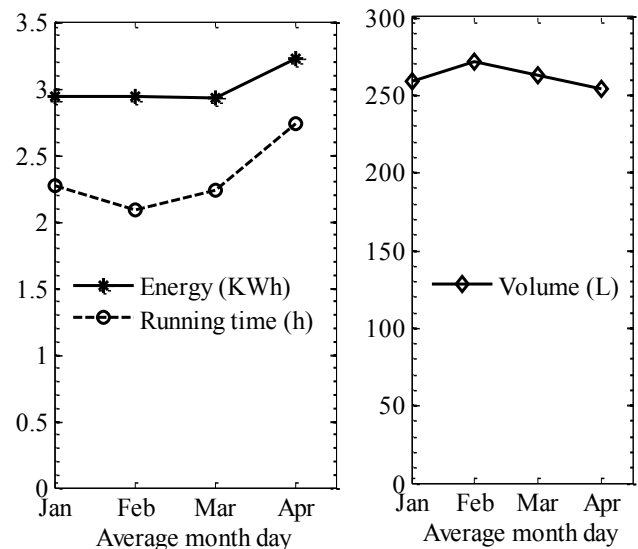


Figure 5: Variation of average heating up energy, time of operation and capacity of hot water usage (average month-day)

4.2. Monthly electrical energy consumption and thermal energy generated.

Figure 6 gives an illustration of the total electrical energy consume and the thermal energy gain for the four months (January-April). The thermal energy gain is the additional heat energy absorbed by stored water during the vapor compression cycle in a bid to attain the hot water set point temperature. The ratio of the thermal energy gain and the electrical energy consumption is the energy factor or COP. It can be deduced that the thermal energy gain by the storage tank were comparable (over 200 kWh) except for the month of February with less than 30 days. In a similar manner, the electrical energy consumption was about 75 kWh. It can therefore be delineated that on average per month the electrical energy saves by virtue of retrofitting of the geyser with an ASHP is 125 kWh. This saving is acceptable because geyser energy factor is very close to unity. Furthermore the geyser reactive power is practically negligible as the heating element is purely resistive. Hence the power factor is close to 1. Therefore, if the thermal energy contained in storage tank was 200 kWh, it corresponding electrical energy consumption by a geyser would also be 200 kWh.

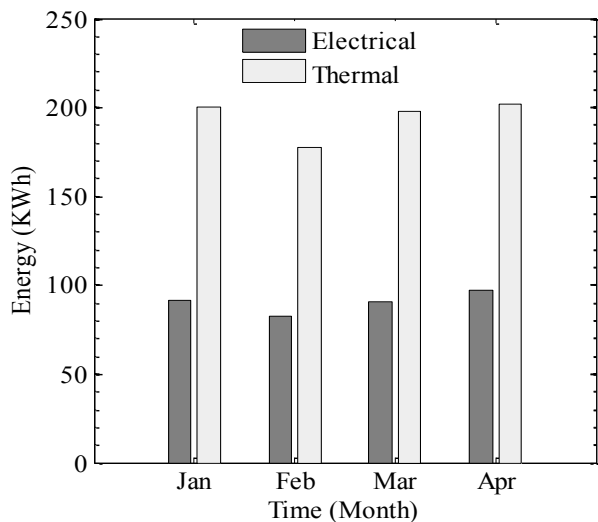


Figure 6: Show a bar plot of the monthly energies

4.3. Evaluation of the cost of energy consumption

The figure 7 revealed that there is a huge cost saving despite the environmental benefits just by retrofitting geyser with ASHP. Judging from the energies results in figure 6 and using it to predict the projected costs for the monthly energy consumption for hot water production, there are adequate reasons to motivate for a massive rollout of ASHP water heater in the residential sector. Furthermore, translating the thermal energy gain for the respective months to electrical energy for the scenario where geyser (old technology) was used and using an Eskom flat rate per kWh (tariff structure) of 1.20 Rands, the total energy consumption costing for hot water production is over 250 Rands. On the other hand, by retrofitting the system with an ASHP, the monthly energy cost of hot water production by the ASHP water heater

reduces to about 110 Rands. More generally, reporting on an average month cost saving for hot water production of 140 Rands and by assuming no increase in the Eskom tariff structure, the ASHP unit payback period can be estimated to be 5.4 years with the capital cost of the unit value at 9000 Rands. It is crucial at this junction to highlight that this payback duration can be far lower with some rebates or incentive from the Government to subsidies for the purchase of the system. And also in homes where there is huge demand for hot water usage.

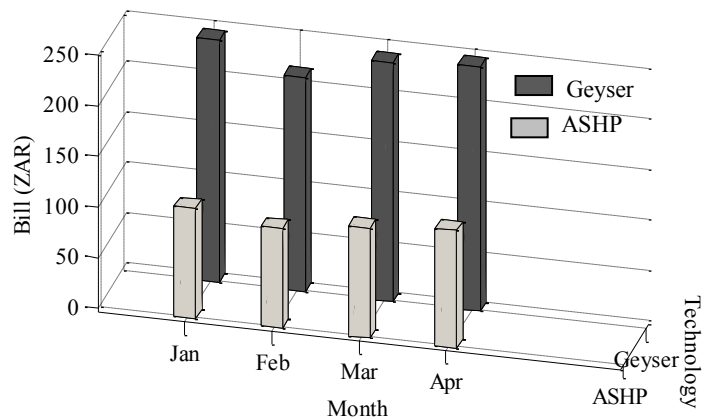


Figure 7: Monthly cost of hot water production for both technologies

4.4. Simple economic life costing of the ASHP

The ASHP unit comes with a manufacturer warranty of 15 years with no maintenance cost over this duration. Hence, without loss of generality and from a conservative calculation with a payback time of 5.4 years, a net accumulated cost saving of 16,000 Rands can be accrued. This net cost saving is over the remaining 9.6 years before the unit reaches its lifespan. It is worthy, to categorically highlight the fact that this analysis has been done without considering any inflation rate as well as any increase in the electricity cost per unit of electrical energy consumption. Furthermore, with an increase in the tariff structure, the accumulated cost saving would increase.

4.5. Multiple comparison tests for the COPs

A multiple comparison test was performed for the average month-day COP using the data for the four months monitoring period. This statistical test computes the mean COP of the ASHP water heater for specific month using the one way analysis of variance test and also checks for mean significant difference in the monthly COP through a visual plot [17]. The figure 8 shows the multiple comparison test of the COP for the respective monitoring months. It can be viewed from the simulation plots that the mean COP for each month was represented by a circle mark which is fixed on the respective line plot. The vertical broken lines reveal the upper and lower limit of the average COP for the whole week day in the month of January. Comparing the COP for the month of January to the other months, the

simulation plots show no mean significant difference as the rest of the COP line plots overlapped with that for the month of January.

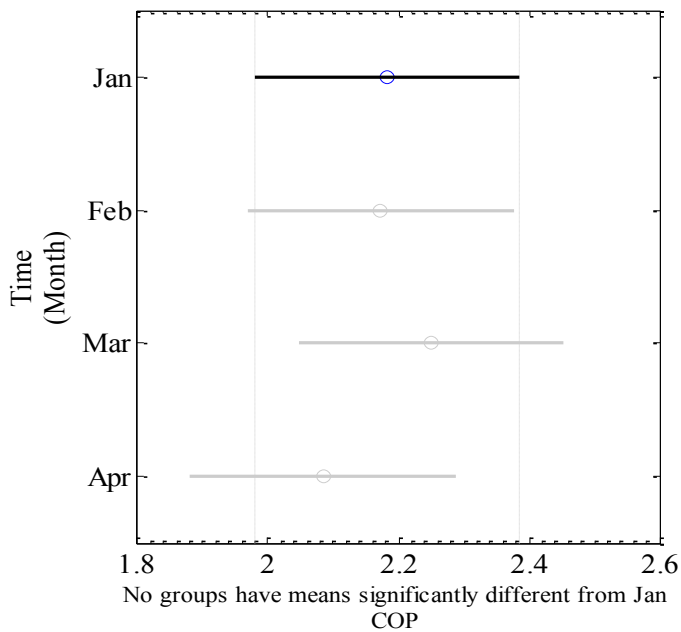


Figure 8: Multiple simulation plot of the week day COP

5. CONCLUSION

In conclusion, the data acquisition system (DAS) was used to evaluate the performance of an efficiently installed ASHP water heater. Based on the calculations from the obtained data, an average monthly energy saving of 125 kWh was achieved. There was no mean significant difference in the system COP for each of the monitoring months. A favorable increase in the fuel adjustment cost as well as progressive increase in the electricity tariff rate can also result in a payback time well below 5 years.

6. ACKNOWLEDGEMENT

We are delighted to acknowledge the financial supports from Eskom and the Fort Hare Institutes of Technology in a bid to enable us to purchase the equipments required to design and construct the data acquisition system, and also the geyser and the split type ASHP unit.

7. REFERENCES

[1] Esen, H., Inalli M, Essen M., A techno-economic comparison of ground coupled heat pump system for space cooling, *Building and Environment*, 42 (5), 1995-1965 (2007).

[2] Petit P.J, Meyer J.P. A techno-economic analytical comparison of the performance of air coupled and horizontal-ground coupled air conditioners in South Africa. *International journal of energy research* 1997:21 (11):1011-21.

[3] Meyer, J.P., and Tshimankinda, M. 1998. "Domestic Hot Water Consumption in South African Townhouses."

Energy Conversion and Management 39 (7): 679-84.

[4] Sustainable energy society South Africa. (www.Waterlite.co.za, 2013).

[5] Tangwe S L, M Simon and E Meyer. (2013) Experimental investigation to quantify the benefits of air source heat pump water heater in South Africa, Presented at the 5th International conference on applied energy, 1-4 th July 2013, Pretoria, South Africa, paper id 193.

[6] Van Tonder, J.C. and Holm, D. (2001). Measurement Based Quantification of storage water Heater losses and Benefit of Addition Thermal Insulation. *Domestic use of Energy Conference*. pp163-168.

[7] Levins, W.P. 1982. Estimated Seasonal Performance of a Heat Pump Water Heater Including Effect of Climatic and In-House Location. Oak Ridge National Laboratory, Oak Ridge, TN. National Technical Information Service. Vergina, USA. A03 Microfiche A01.Pp 24-36.

[8] Bodzin, S. (1997), "Air-to-Water Heat Pumps for the Home", *Home Energy Magazine Online*, July/August 1997.www.homeenergy.org/show/article/nav/hotwater/page/8/id/1315

[9] Tangwe.,S, M. Simon and E. Meyer, Computational approach to evaluate performance of split type residential air source heat pump water heater at different operational state, 12 th International conference on sustainable energy technology, 26-29 August 2013, Hongkong, paper id 317

[10] Ashdown, B.G., Bjornstad, D.J., Boudrean G., Laspsa M.V., and Schernayder S. 2004. "Shumpert Barry and Southworth Frank." "Heat pump water heater technology: Experiences of residential consumers and utilities." Oak Ridge, TN: Oak Ridge National Laboratory.

[11] Sinha, S.K., and Dysakar, A. 2008. United States Patent Application heat pump liquid heater. <http://appl.ft1.uspto.gov/netacgi/nph-parser>.

[12] Baxter, V. D., Tomlinson, J. J., Murphy, R.W., Ashdown, B.G.and Laspsa, M. V. (2005) Residential Heat Pump Water Heater Development Status USA. Oak Ridge, TN: Oak Ridge National Laboratory.

[13] Douglas, J.(2008). Demonstrations Encourage Wider Use of Efficient Technologies. *EPRI Journal*, 15-17.

[14] B. J Haung and F.H. Lin (1997), Compact and fast temperature response heat pump water heater, *American Society of Mechanical engineering* (paper) 97-AA-26.

[15] Tangwe, S, M. Simon and E. Meyer, Mathematical modelling and simulation application to visualize the performance of retrofit heat pump water heater under first hour heating rating, *Renewable energy* 72 (2014) 203-211

[16] Morrison, G.L., Anderson, T. and Behnia M.(2004). Seasonal performance rating of heat pump water heaters. *Energy Conservation & Management*. 76:147-152

[17] Hochberg, Y., and A. C. Tamhane. Multiple comparison procedures. Hoboken, NJ: John Wiley and Son, 1987.

A TECHNOLOGICAL AND PERFORMANCE COMPARISON OF WASTE-TO-ENERGY THERMAL TECHNOLOGIES

W. Maisiri*, L. Van Dyk* and J. De Kock**

* School of Mechanical and Nuclear Engineering, North-West University, Potchefstroom Campus

** School of Electrical, Electronic and Computer Engineering, North-West University, Potchefstroom Campus

Abstract: Economic growth and rapid population growth are a combination of factors that causes an increase in electric energy demand and municipal solid waste (MSW) generation. Interest in MSW as an alternative source of renewable energy has been growing and the global focus has shifted to waste management strategies that are harmonized with the goal of sustainable development through electrical power generation and minimization of adverse effects of landfill. Waste-to-energy (WtE) is proving to be a sustainable and successful alternative technology to treat residual MSW. The purpose of this study is to carry out a technological and performance comparison of proven WtE thermal technologies. The paper presents a comparison of four WtE technologies in the field of waste treatment, the thermal process and energy recovery options.

Keywords: Municipal Solid Waste (MSW), Waste-to-energy (WtE), Incineration, Gasification, Pyrolysis.

1. INTRODUCTION

Economic growth and rapid population growth are a combination of factors that are bound to increase the demand for electric energy and the generation of municipal solid waste (MSW). Strategies to de-couple economic growth from an increase in the rate of MSW generation have met with little success in developed countries, resulting in MSW management becoming a growing problem. Globally, the focus has shifted to waste management strategies that are harmonized with the goal of sustainable development through electrical power generation and minimization of adverse effects of landfill [1,2].

South Africa has been hit with a shortfall in electrical energy generation capacity due to an increase in demand and failure to invest in additional capacity since the onset of 2008 [3]. It has furthermore been projected that South Africa will experience a great risk of electrical energy supply interruptions between 2018 and 2024, fostering the need to moderate the anticipated supply interruptions by increasing the generation capacity [4].

Renewable energy is the fastest growing technology in the global energy mix, with a growing rate estimated at 8.2% by 2010 [4]. In a bid to align with global development, South Africa has adopted a policy that advocates renewable energy in mitigating the adverse impacts associated with its dependence on coal to meet the country's energy requirements [5]. South Africa is set to achieve a greener energy mix by 2030 through the contribution of independent power producers [6].

South Africa's renewable energy sources mix includes solar energy, biomass, wind and small-scale hydro generation. MSW is listed among the renewable energy

sources and it is estimated that the equivalent of 11 000 GWh per annum of MSW is sent to landfill sites [7]. This wasted energy can be harnessed through WtE thermal technologies and/or methane gas.

In South Africa, municipalities are regarded as the major consumers of electricity; their consumption percentage ranges roughly from 40 to 42% [8]. This can be supplemented by taking advantage of MSW as a source of energy.

WtE incineration technologies have been implemented in developed countries with overwhelming success to harness energy from MSW. In 2012, 472 European and 86 American WtE plants were in operation [9]. AEB, Amsterdam's WtE plant, the world's largest and cleanest plant, produces 1 million MWh/year of electricity and 300 million MJ/year of district heating through the incineration of 1.4 million tonnes of MSW [1].

The work presented in this paper forms part of an ongoing research project into technological and financial factors that influence the implementation of WtE thermal technologies in South Africa.

The paper presents a technological and performance evaluation of WtE thermal technologies. In this study four WtE thermal processes are compared in respect of classification, waste pre-treatment requirements and energy recovery options. The paper investigates technological performance in terms of capacity and scalability, energy production potential, flue gas and residual production and technological reliability.

This paper is organized as follows: a WtE overview, technological evaluation, comparison of technological

performance, technological cost evaluation and conclusion.

2. WASTE-TO-ENERGY OVERVIEW

WtE facilities convert MSW into gaseous, liquid and solid conversion products, simultaneously releasing heat energy, which is recovered through boilers. The recovered heat can be converted into electricity or directly exported to district heating systems [10].

About 50%-70% of the MSW stream sent to landfill sites as residual waste is of biogenic origin, such as food and garden waste, wood, paper and textiles. Therefore 50% of energy recovered from WtE incineration is regarded to be biogenic energy, hence contributing to renewable energy [1].

The efficiency of energy recovery in a WtE plant is influenced by factors such as the calorific value of the feedstock, losses in the combustion chamber and steam-water cycle, steam parameters and energy recovery process, which can be in the form of heat, power generation and combined heat and power generation (CHP) [11].

WtE thermal processes are classified as conventional and advanced technologies. Table 1 shows technologies discussed in this paper and their classification.

Table 1: WtE thermal technologies classification

Classification	Technology
Conventional	Grate incineration
	Fluidized bed incineration
Advanced	Gasification
	Pyrolysis

Figure 1 is a comparison of worldwide application of the WtE technologies mentioned in Table 1. Grate incineration is a commercially proven technology, with 90% of the WtE incinerators in Europe and more than 500 WtE plants worldwide using this technology. Fluidized bed incineration is commonly used for small throughput plants in Japan, with 50 plants operating on this technology worldwide [1,10].

Gasification is widely used in Japan, with 95 WtE plants using this technology. Pyrolysis is less proven on commercial scale with only 11 plants in Germany operating with this technology [1].

The process flow of conventional technologies, grate and fluidized bed incineration is shown in Figure 2. Figure 3 illustrates gasification and pyrolysis process flow.

In countries where WtE incineration has been implemented, it has been proved that WtE is compatible with high recycling rates [1, 12]. European countries such as Sweden, Denmark and the Netherlands make the highest

contributions to WtE, and concurrently show the highest recycling rates [13, 14]

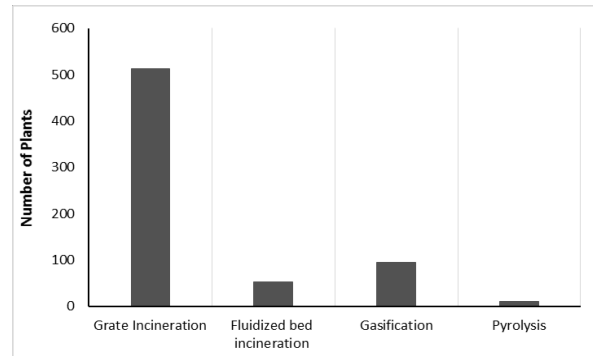


Figure 1: Worldwide operating WtE plants [1]

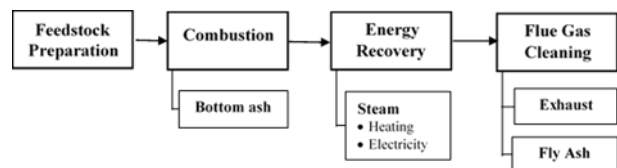


Figure 2: Conventional WtE overview [10]

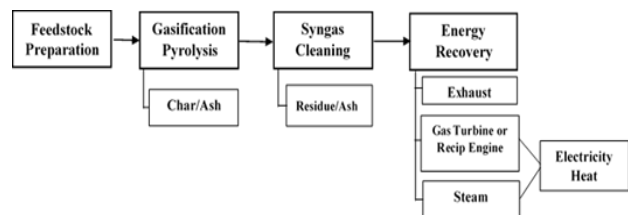


Figure 3: Advanced thermal treatment WtE [10]

Successful implementation of WtE has been driven by the desire to achieve sustainable development through elimination of landfill and improve on material and energy recovery. Countries that rely on landfill thus have greater potential to implement WtE [1].

3. WASTE-TO-ENERGY TECHNOLOGIES

This section evaluates four WtE thermal technologies namely grate incineration, fluidized bed incineration, gasification and pyrolysis. The technologies are evaluated on the basis of waste pre-treatment, the thermal process, energy recovery and management of residual waste from the processes. Table 2 is a summarized comparison of the above-mentioned four technologies.

3.1 Pre-treatment process

The first stage in a WtE plant is the storage and pre-treatment of the feedstock. Each technology has different feedstock quality and characteristics requirements, hence the objective of pre-treatment MSW is to ensure that waste is in an appropriate form for the combustion process [1, 10, 11, 15, 16].

Grate incineration processes MSW with minimum pre-treatment, such as the removal of recyclables, reusable material and bulky materials. Waste fuel is mixed and

homogenized with overhead cranes before being transferred into the incinerator hopper [1, 15, 16].

Fluidized bed incineration, gasification and pyrolysis handle waste fuel/feedstock of limited particle size and specific characteristics. These technologies are limited to

homogenous waste streams, hence effort is required in the waste pre-treatment process. Waste pre-treatment involves size reduction combined with removal of metallic species [1, 10, 11, 15, 16].

Table 2: Comparison of WtE thermal technologies

Parameter	Grate	Fluidized bed	Gasification	Pyrolysis
Waste type	Mixed waste from waste streams with no pre-treatment, LHV of 6 MJ/kg to 12 MJ/kg [1, 10]	Homogenized and pre-treated waste, specific particle size required, LHV of < 5 MJ/kg to >20 MJ/kg [1, 10].	Homogenized and pre-treated waste [1, 10].	Homogenized and pre-treated waste [1, 10].
Thermal process	Complete combustion in excess air [1, 10, 11, 16]	Complete combustion in excess air [1, 10, 11, 16]	Partial thermal degradation in limited oxygen [1, 11, 16].	Decomposition of organic substances in the absence of oxygen [1, 11, 16].
Operating parameters	Temperature – 800 °C to 1450 °C, pressure – 1 bar [1].	Temperature – 800 °C to 1450 °C, pressure – 1 bar [1].	Temperature – 500 °C to 1000 °C, pressure – 1 bar to 50 bar [1].	Temperature – 250 °C to 700 °C, pressure – 1 bar [1].
Energy recovery	Heat energy in off-gas of a combustion process is recovered in a boiler as process steam, heat and electricity [1, 11, 15, 16].	Heat energy in off-gas of a combustion process is recovered in a boiler as process steam, heat and electricity [1, 11, 15, 16].	Syngas either directly combusted and heat recovered in a boiler as process steam, and electricity or syngas processed into other fuels [1].	Syngas directly combusted and heat recovered in a boiler as process steam, and electricity or syngas processed into other fuels [1].

3.2 Thermal process

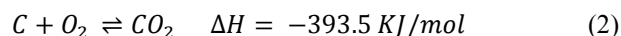
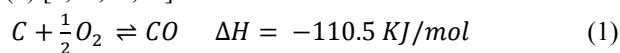
WtE thermal technologies are distinguished through the thermal process applied. Thermal processes are classified into three categories, namely combustion/incineration, pyrolysis and gasification. The principal distinguishing feature of these processes is the oxygen content in the process atmosphere and operating temperature range [1, 11, 16].

The pyrolysis process is the thermal decomposition or fragmentation of organic matter in a strictly inert atmosphere. The reaction temperature affects the proportion of gaseous, liquid and solid products. The temperature varies directly with the amount of gaseous products, whereas solid residues vary inversely with temperature. The pyrolysis gas produced is directly combusted to recover energy because of its complex composition, which requires extensive gas cleaning to remove sulphur compounds and other impurities [1, 11, 16].

The gasification process is the partial decomposition of feedstock in the presence of insufficient oxygen to oxidize the fuel. The main product of this process is synthetic gas, commonly referred to as syngas. Syngas from gasification of MSW is commonly used in a combustion chamber for energy recovery [1, 11, 16].

Grate incineration and fluidized bed incineration recover heat through complete combustion of waste fuel, an exothermic chemical process with the main energy

releasing chemical reactions, shown in equations (1) and (2) [1,10,11,16].



3.3 Energy recovery

Thermal process technologies that use MSW as feedstock are designed so that the chemical energy in the fuel is finally released into the off-gas of a combustion process and the energy is recovered in a boiler. The energy from waste, auxiliary fuels and pre-heated air is converted during the combustion process and transferred to a water steam circle [1, 11].

Gasification and pyrolysis of waste and waste-derived fuels are in principle two-stage processes designed to allow direct combustion of process products [1].

Recovered heat from the boiler can be used in three alternatives, namely direct export for district heating, conversion to electricity using turbines and combined heat and power. Figure 4 and Figure 5 show the hot water boiler circuit and the Rankine circuit used for heat recovery options [1, 11, 15, 16].

Factors that affect the choice of an energy cycle/circuit include the quality and quantity of waste, possibility of energy sales, water sources availability, acceptable noise levels and space available.

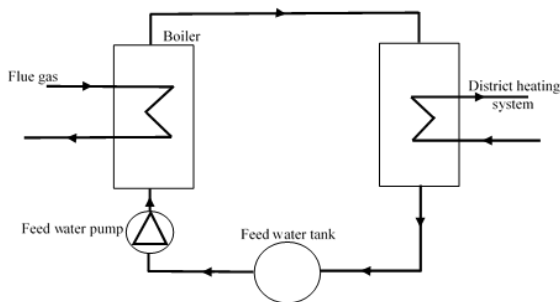


Figure 4: Hot water boiler circuit [15]

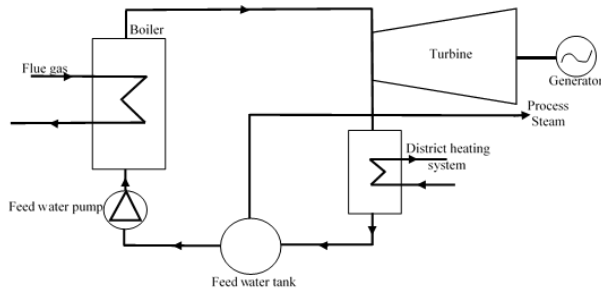


Figure 5: Rankine circuit [15]

3.4 Air pollution control

The removal of pollutants from the flue gas is one of the most important and most expensive process stages in a WtE plant. The design and operation of the air pollution control system technology is highly influenced by the required reduction in emissions to meet regulations, the compatibility of system components with one another, and investment, operation and maintenance costs [1, 10].

The air pollution control systems' components are classified according to their functions, namely removal of fly ash, removal of acid gases and removal of specific contaminants such as mercury and nitrogen oxides [1].

Combination of air pollution control components is determined by the system component to clean acidic gases, such as sulphur dioxide (SO₂), hydrogen chloride (HCl) and hydrogen fluoride (HF). Hence these components are selected first, then the selection of compatible and appropriate components to remove particulate matter, dioxins, mercury and NO_x follows [10].

Flue gas acidic compounds are cleaned using three options, namely dry/semi-dry scrubbing, wet scrubbing and semi-wet scrubbing systems. In this regard, there are three possible combinations of air pollution control system components [1, 10, 16].

Fly ash can be removed using cyclones; electrostatic precipitators (ESP) and fabric filters or bag house systems [1, 10, 16]. Cyclones have limited removal efficiency for fine particles and are not commonly used in modern WtE plants. ESP is the technique mostly applied owing to its design simplicity, low pressure loss and easy operation. The Morden ESP system can achieve dust removal efficiencies greater than 99% for particle sizes between

0.01 and >100 μm. The lowest emission, in a range of less than 1 mg/m³, is achieved through a fabric filter system [1].

Nitrogen oxide control is achieved through either non-catalytic removal (NSCR) or selective catalytic removal (SCR). NSCR uses the principle of injecting ammonia or another nitrogen-containing compound into the hot flue gases in the first flue of the boiler. SCR is done at the end of the gas-cleaning system at a temperature level of 250°C to 300°C [1].

3.5 Residue management

WtE facilities generate three categories of residue, namely bottom ash, fly ash and APC residues. Fly ash and APC residue are deposited into the landfill. Ferrous and non-ferrous metal can be separated from raw bottom ash for a further recycling process. Gravel size fractions of the bottom ash can be sieved and used in the construction industry, mainly road construction and brick pavement manufacturing [1, 15]

4. WTE TECHNOLOGIES PERFORMANCE

This section will evaluate the performance of four WtE technologies in terms of plant capacity and scalability, energy production, flue gas production, residual waste production and technological reliability. An analysis of potential revenue streams from each technology is carried out in this section.

Table 3 summarizes WtE thermal technologies' performance evaluation.

4.1 Plant capacity and scalability

WtE thermal technologies' capacity is measured in terms of the amount of waste that can be processed at any given time per individual line. A single installation can have a number of lines and the number of lines installed is directly proportional to overall size per installation.

Grate incineration records the highest capacities because of its ability to treat unprocessed waste. Single-line capacity ranges from 3 tonnes to 40 tonnes per hour. The technology can process waste with calorific values in the range 6 MJ/tonne to 12 MJ/tonne [1]. Grate incinerators can be scaled to various sizes, with a capability of multiple lines installation. However, only large installations of greater than 100 000 tonne/year can be economically viable.

Fluidized bed incinerators' single-line capacity ranges from 3 tonnes to 15 tonnes per hour. The technology can process waste with a calorific value of 5 MJ/tonne to 20 MJ/tonne [1].

Gasification has a processing capacity of 1 tonnes to 11 tonnes per hour for each single line. Gasification reactors

can have modularized designs, which are suitable for small installations [1, 10].

Pyrolysis thermal processing technology has the lowest capacity of 2.5 tonnes to 8.3 tonnes per hour. Annual installed capacity ranges from 28 000 tonnes to 140 000 tonnes [1].

Table 3: Technologies' performance evaluation

Parameter	Grate	Fluidized bed	Gasification	Pyrolysis
Capacity	3 tonnes to 40 tonnes/hr for a single-line, compatible with multiple lines [1].	3 tonnes to 15 tonnes/hr for a single line [1].	1 tonne to 11 tonnes/hr for each single line [1].	2.5 tonnes to 8.3 tonnes/hour [1].
Scalability	Various sizes, large installations of greater than 100 000 tonne/year can be economically viable [10].	Small installation [10]	Small installation with modularized designs [10]	Small installation [10]
Boiler efficiency	75% to 85%> [1].	75% to 85%> [1].	>80% [1].	75% to 85%> [1].
Power efficiency	Power only – 31 %, CHP - >70 % [1,10]	Power only – 25%, CHP - >70% [1,10]	Power – 20% to 22% [1,10]	Power – 15% [1,10]
Raw bottom ash	20% to 25% [10]	20% to 25% [10]	10% to 20% [10]	more than 30% [10]
Potential revenue streams	Electricity, heat and process steam, construction material, ferrous and non-ferrous metals [1, 10, 11, 15, 16].	Electricity, heat and process steam [1, 10, 11, 15, 16].	Combustion – process steam and electricity. Catalytic conversion – alcohols, chemicals, and synthetic diesel [1,10].	Combustion – process steam and electricity. Catalytic conversion – Pyrolysis oil, transportation fuel [1,10]

4.2 Energy production

The choice of a WtE thermal technology is influenced by the energy efficiency of a plant. Energy can be recovered as heat and/or electricity.

Grate technology has primary boiler efficiency in a range of 75% to greater than 85%. Modern facilities have power efficiencies that can reach as high as 31% and for heat only or combined power efficiency reach more than 70% [1]. Where grate incinerator plants are operated in combination with power plants, an efficiency of more than 40% can be reached.

Gasification in different types of reactors has boiler efficiency of more than 80%. Depending on plant size and waste, power efficiencies are found to be in the range of 22 % to 33% [1].

Fluidized bed incinerator boilers have primary efficiency of 80 % to more than 85%. The overall power efficiency reaches up to 25% and for heat and combined power it can surpass 70% [1].

Pyrolysis boiler efficiency can reach as high as that of grate incineration and the fluidized bed process. Power efficiency can be as low as 15% [1].

4.3 Flue gas production

The performance of a WtE plant can be measured in terms of the composition of the raw flue gas from the thermal process. The production of acidic substances, heavy metals and dust particulate are the best indicators in measuring the performance of a WtE plant.

Gasification and pyrolysis produce synthetic gases that are used in direct combustion for energy recovery or can be further cleaned and processed to be used in other applications. Pollutants of concern in these processes are HCl and SO₂ [1,10]. Gasification and pyrolysis aim to minimize gas cleaning obligations by lowering flue-gas volumes [16].

Grate and fluidized bed incineration produce raw flue gases that have a high margin of deviation from the minimum emission requirements. Conventional thermal process must be equipped with efficient air pollution control systems to meet emission requirements [1, 10].

4.4 Residual waste production

Grate and fluidized incineration produce bottom ash amounting to 20 % to 25% by weight of the incinerated waste. The bottom ash can be used in other applications, which can reduce residue disposed into the landfill to about 5% by weight of the incinerated waste. Grate and fluidized bed incineration conserve landfill capacity up to 90 % to 95% [10].

The gasification process is capable of minimizing bottom ash to about 10 % to 20% by weight of the incinerated waste. The bottom ash for gasification is highly marketable for other applications and residual disposal to the landfill can be minimized to 1% by weight of the incinerated waste. Gasification has the potential of reducing landfill capacity consumption by 90 % to 95% [10].

Pyrolysis produces residue of more than 30% by weight of the incinerated waste. However, if the residue can be treated, landfill disposal is reduced from 30 % to 10% by weight of the incinerated waste. Pyrolysis has the capability of conserving landfill capacity up to 90% [10].

4.5 Potential revenue streams

Potential revenue streams of a WtE thermal plant vary with applied technology. The common revenue stream is the sale of process steam, heat and electricity. Other streams of revenue include construction aggregate recovered from bottom ash, recyclable ferrous and non-ferrous metals recovered from bottom ash, syngas and pyrolysis oil [10].

Morden plants on grate incineration technology have electricity production rates of between 0.75 MWh and 0.85 MWh/annual tonne of MSW. Gasification and pyrolysis energy production is in the range 0.4 MWh to 0.8 MWh/annual tonne of MSW and 0.5 MWh to 0.8 MWh/annual tonne of MSW respectively [10].

Raw bottom ash from the incineration of mixed MSW contains huge amounts of ferrous and non-ferrous metals, amounting to about 10% by weight of the input incinerated waste. Post-processing of bottom ash, disposal and utilization depend on the total organic carbon of the ash [1].

4.6 Technological reliability

Grate technology is the oldest technology used in more than 500 plants worldwide, with proven operational success. The technology is commercially proven, operating with minimum challenges, with some plants having been in operation for 15 years to 30 years. Grate technology is reported to have both scheduled and unscheduled downtime of less than 10% of operating time. The technology is less complex in comparison with other thermal processes [1, 10]

Though commercially proven, fluidized bed incineration is faced with operational challenges with MSW as feedstock. About 50 plants worldwide use this technology, with many plants found in Japan for smaller throughputs [10].

Gasification has been used for more than a century with other fuels and recently MSW has been used as feedstock. The technology operates with scheduled and unscheduled downtime at approximately 20% [1,10]

Pyrolysis of waste is applied in only a few commercial-scale plants, hence there is limited information on the reliability of the process. The technology has limited capability to process MSW.

5. COST EVALUATION

WtE technology system component cost can be distributed as indicated in Table 4. Thermal processing equipment makes the highest contribution to the capital cost of a WtE thermal processing plant.

Table 5 is a comparison of estimated capital cost per installed tonne capacity and operating cost of a WtE thermal technology.

Table 4: Total WtE capital cost distribution of WtE [10]

System Component	Capital Cost % contribution
Thermal processing equipment (incinerator/boiler)	40%
Energy production equipment (turbines and generators)	10%
APC system (flue gas treatment)	15%
Building (civil works)	25%
Miscellaneous (approvals, general site works, ash processing, electrical transmission and interconnect etc.)	10%

Table 5: WtE facilities capital and operating Costs [10]

Technology	Capital Cost (\$/ton)	Operating Cost (\$/ton)
Conventional	775 +/- 50%	65 +/- 30%
Gasification	800 +/- 40%	60 +/- 45%
Pyrolysis	926	105

The capital cost per ton of installed capacity for gasification and pyrolysis is high owing to a front-end waste pre-processing system to achieve homogeneity, higher electrical energy and/or fossil fuel consumption to operate the facilities and decreased reliability of the technologies [10].

6. CONCLUSION

WtE thermal technologies stand to be a valuable alternative source of energy and a solution to ever-increasing MSW and other waste streams, such as medical waste and waste vehicle tyres. Experience from countries that have implemented WtE technologies proved that WtE it is compatible with high recycling rates.

The comparison of WtE thermal technologies indicates that grate incineration remains the preferred and economical thermal technology in view of its reliability, capability to incinerate assorted waste, lower operational complexity and higher power efficiency.

Advanced thermal technologies face both operational and economic drawbacks. Gasification and pyrolysis continue to experience certain limitations due to their complexity, difficulty in treating waste of various streams and lower net energy recovery.

7. REFERENCES

- [1] IEA Bioenergy: "Accomplishments from IEA Bioenergy Task 36: Integrating Energy Recovery into Solid Waste Management Systems (2007-2009)", *IEA*, pp 1-240, 2010.
- [2] S. Sethi, N. Kothiyal, A. K. Nema, M. Kaushik: "Characterization of Municipal Solid Waste in Jalandhar City, Punjab, India", *Journal of Hazardous, Toxic, and Radioactive Waste*, pp 97-106, 2012.

- [3] A. Pegels: “Renewable Energy in South Africa: Potentials, Barriers and Options for Support”, *Energy Policy*, 2010.
- [4] Y. Singh: “Johannesburg South Africa's Future Energy Mix and Role Out”, pp 1- 40, 2011.
- [5] Department of Minerals and Energy: “White Paper on Renewable Energy Policy of Republic of South Africa”, 2004.
- [6] A. Eberhard: “South Africa’s Renewable Energy IPP Procurement Program Success Factors and Lessons”, 2014.
- [7] Department of Energy: “South African Energy Synopsis”, 2010.
- [8] F. Caldo: “Eskom’s Power Crisis: Reasons, Impact and Possible Solutions”, *Centurion: Solidarity Research Institute*, 2008.
- [9] International Solid Waste Association: “Waste to Energy State of the Art Report”, pp 1-209, 2012.
- [10] Stantec Consulting Ltd: “A Technical Review of Municipal Solid Waste Thermal Treatment Practices”, pp 1-339, 2011.
- [11] S. Boehmer, M. Seidi, J. Stubenvoll, H. Zerz: “Waste to Energy in Malta: Scenarios for Implementation”, 2008.
- [12] DEFRA: “Incineration of Municipal Solid Waste”, 2013, 1-56.
- [13] Renewable Energy Association: “Energy from Waste: A Guide to Decision Makers”, 2011.
- [14] Eurostat: “Europe in Figures: Eurostat Yearbook 2009”, 2009.
- [15] The World Bank: “World Bank Technical Guidance Report: Municipal Solid Waste Incineration”, pp 1-111, 1999.
- [16] European Commission: “Integrated Pollution Prevention and Control - Reference Document on the Best Available Techniques for Waste Incineration”, pp 1-683, 2006.

PERFORMANCE PREDICTION OF WIND TURBINE BLADES: PRELIMINARY TESTING AND RESULTS

J. Braid*

* School of Electrical and Information Engineering, University of the Witwatersrand, Johannesburg

Abstract: This paper presents the methodology employed for predicting the performance of a turbine comprising a given set of blades, from which a series of physical measurements are taken. Using Blade Element Momentum (BEM) theory to analyse piece-wise elements of the turbine blade, a resultant Coefficient of Performance versus Tip-Speed-Ratio (TSR) is determined. The method is used to predict the performance of two sets of available blades, having unknown specifications. The preliminary results look promising, particularly centered around the maximum power point. However, additional research is required to refine the determination of the axial and angular induction factors, which, in this preliminary version, become highly inaccurate at low and high TSRs.

Key words: Aerodynamics, BEM theory, induction factor, Max C_p , Tip-Speed-Ratio.

1. INTRODUCTION

1.1 Blade Modelling and Design

Current day aerodynamic design makes extensive use of Computational Fluid Dynamics (CFD). Prior to the developments of CFD packages, BEM theory was the most widely used tool for the aerodynamic modelling and design of wind turbines, and is still commonly used today as the initial design step [1]. Consequently, and being relatively accurate, BEM theory is deemed suitable for the requirement of this application.

In general, the design process using BEM theory follows a straightforward approach, an example being [2]: for a required output power at a desired TSR, once a suitable airfoil profile is chosen, the blade's chord and twist along its radial length are determined. Since in this application, the design of the blade has already been undertaken by the manufacturer, the above methodology is reversed, to return the designed TSR and Coefficient of Performance.

1.2 Problem Statement

The need for performance curves of blades available in the author's laboratory, for the greater design process of wind turbine generators, necessitated this research. Two sets of available blades, one of 1.75m in diameter and another of 3.7m in diameter, both lack this vital information. The objective of this paper is therefore to present a simple methodology for predicting the performance of these blades from physical measurements taken from them.

2. BACKGROUND

2.1 Literature Survey

Extensive literature exists on the derivation of BEM theory and its use in blade design [3–5]; only a very brief overview together with the key equations are presented herein.

Effectively reversing the general design methodology, mathematical scripting software can be used to predict the performance of a wind turbine given the relevant blade data, such as in [6]. This paper shares the same objective.

Reference [7] presents the design of a 54m diameter wind turbine and provides detailed results for all parameters of the designed blades, thus making an ideal test-case for this work to develop the employed methodology.

A large volume of empirical data exists, primarily from the 1930s, on the testing of airfoils for aircraft wings. This has naturally been substantially used in the design of wind turbine blades too, [8] and [9] being examples used in this document. Other empirical data from wind tunnel tests, specifically for wind turbine blade research, such as [10], are also readily available from the large research organisations.

This work primarily follows the (reversed) design process of [2] to derive a suitable methodology to achieve the same objective as [6]; the parametric data found in [7] being used for verification purposes.

2.2 Extraction of Power from the Wind

The wind power P_∞ available in an unimpeded air-stream of velocity V_∞ far upwind of a turbine, having a circular cross-section with outer radius R [3], is given by:

$$P_\infty = \frac{1}{2} \rho V_\infty^3 \pi R^2 \quad \text{and} \quad P_{mech} = C_p P_\infty$$

Where ρ is the density of air $\sim 1.1 \text{ kg/m}^3$ and C_p is the normalised *Coefficient of Performance* which relates the extractable amount of mechanical power P_{mech} to the total power in the air-stream. From linear momentum theory, as energy is extracted from the air-stream by say an actuator disk (representing the turbine), the velocity of the downwind flow (called the *wake*) decreases as its cross-sectional area expands, in proportion to the

power extracted - the actuator disk can be envisaged as a power-dependent variable *impedance* to the airflow.

The relation of the upwind velocity V_∞ to that passing through the actuator disk (or turbine) V_t , and to that far downwind in the wake V_w , is respectively given by:

$$V_t = V_\infty(1 - a) \quad \text{and} \quad V_w = V_\infty(1 - 2a)$$

Where a is defined as the *axial induction factor* and represents the ratio by which the velocity is being retarded due to the power being extracted. The range of a is limited by: at $a = 0$ the air-stream sees no impedance corresponding to no power being extracted; at $a = \frac{1}{2}$ the air-stream is totally impeded and results in a downwind velocity $V_w = 0$, a condition not possible in reality.

After further analysis relating the extractable power to this induction factor [4], it is revealed that:

$$C_P = 4a(1 - a)^2 \quad \text{hence} \quad C_{Pmax} = \frac{16}{27} = 0.59$$

Which is a maximum when $a = \frac{1}{3}$ and is known as the *Betz Limit*. This returns a value of $C_{Pmax} \approx 0.50$ typical of large power-extracting horizontal axis wind turbines. Consequently, the velocity through the turbine is retarded to approximately $V_t \approx \frac{2}{3} V_\infty$.

2.3 Conservation of Momentum

Momentum theory is based on the conservation of momentum: the linear and rotational components, both upwind and downwind of the turbine, must be conserved. The momentum of the upwind air-stream can generally be assumed to comprise linear momentum only (unless the turbine is located in the wake of another turbine). However, since the blades gain angular momentum whilst extracting power, a wake must be induced, rotating in the opposite direction, to balance the acquired rotational momentum. This results in an angular component to the air-stream being developed across the blades, proportional to the speed of rotation but in the opposite direction. This is represented by an *angular induction factor* a' , the rotational component of the flow being $a' \Omega$. Typically, a' is highest (~ 0.5) in close proximity (within 10%) to the rotor hub and rapidly decays towards zero with increasing radius.

Using this Momentum theory (a comprehensive derivation can be found in [4, 5]), the thrust in an axial direction dF_A and torque dQ due to a thrust in a tangential direction dF_T , exerted on a differential element of annular section on the actuator disk is given by:

$$dF_A = 4\pi \rho r V_\infty^2 a(1 - a) F_{tip} dr \quad (1)$$

$$dQ = r dF_T = 4\pi \rho r^3 V_\infty^3 a'(1 - a) \Omega F_{tip} dr \quad (2)$$

Where r is the radius of the annulus being considered, and a and a' are the induction factors.

A *tip-loss correction factor* F_{tip} was derived by Prandtl [3] to adapt the disk-like actuator to one with discrete blades [2, 5], and is given by:

$$F_{tip} = \frac{2}{\pi} \arccos\left(e^{-\frac{B(R-r)}{2r \sin \phi}}\right) \quad (3)$$

Where the turbine comprises B blades and ϕ is the *angle of relative airflow* at radius r along the blade.

2.4 Blade Element Theory

By dividing the blade into a series of piece-wise airfoil sections and evaluating the aerodynamic forces on each element, the individual contributions can be summed to determine the resultant axial and tangential forces exerted on the blade. The axial force, in the direction of the rotor shaft, manifests in the bending of the loaded blade whilst the tangential force, orientated in the plane of rotation, is the direct producer of torque.

The aerodynamic forces exerted on a wing of area A , when incident with an airflow of velocity V_t , inclined at an *Angle of Attack* of α relative to the airflow, can be resolved into the two components *lift* L (perpendicular to the direction of the airflow) and *drag* D (parallel to the direction of the airflow) [11], given by:

$$L = C_L \frac{1}{2} \rho V_t^2 A \quad \text{and} \quad D = C_D \frac{1}{2} \rho V_t^2 A \quad (4)$$

Where the coefficients C_L and C_D are both functions of α .

Forces L and D can be further resolved into an axial F_A and tangential F_T component of thrust, similar to before, given by:

$$F_A = L \cos \phi + D \sin \phi \quad \text{and} \quad F_T = L \sin \phi - D \cos \phi \quad (5)$$

Where ϕ is the angle of the relative airflow to the plane of movement.

Since in this application, the wing is actually a blade rotating at an angular speed of Ω about the turbine's axis, the *relative velocity* V_{rel} of the airflow incident to the blade, relative to the plane of rotation, comprises two components: the axial V_t as before and a tangential Ωr ; the latter depending on the radial distance r from the axis of rotation. For a given Ω , for radii near to the hub, the tangential component is small and hence the resultant V_{rel} is dominated by the axial V_t . At large radii and/or high angular speeds, the resultant V_{rel} is large, being dominated by the tangential Ωr .

The TSR given by $\lambda = \frac{\Omega R}{V_\infty}$ can be directly used to determine the angle of the relative airflow over the blade, at any radius r , given the wind velocity V_∞ and angular speed (or alternatively given λ) [3], from:

$$V_{rel} = \sqrt{V_{\infty}^2 + (\Omega r)^2} = V_{\infty} \sqrt{1 + \left(\lambda \frac{r}{R}\right)^2} \quad (6)$$

$$\phi = \arctan\left(\frac{V_{\infty}}{\Omega r}\right) = \operatorname{arccot}\left(\lambda \frac{r}{R}\right) \quad (7)$$

Near to the hub of the rotor and for slow rotational speeds, ϕ will be nearly perpendicular ($\sim 85^\circ$) to the plane of rotation, whilst towards the tip and especially at high rotational speeds, ϕ will be close to parallel ($\sim 5^\circ$). This is the inherent reason for the blade requiring a twist, to maintain a constant angle of attack between the blade and relative airflow.

Equations 6 and 7 can be amended to include the axial and angular induction factors, representing the linear and rotational induced airflow components, for determining the relative airflow over the blade.

The magnitude and angle of the relative airflow are given by:

$$V_{rel} = V_{\infty} \sqrt{(1-a)^2 + \left(\lambda \frac{r}{R}\right)^2 (1+a')^2} \quad (8)$$

$$\phi = \operatorname{arccot}\left[\left(\lambda \frac{r}{R}\right) \frac{(1+a')}{(1-a)}\right] \quad (9)$$

Substituting the equations of (4) into (5) the differential axial thrust (dF_A) and torque ($dQ = r dF_T$) on each element at r with an effective area of $dA = c dr$, for B number of blades [3], is given by:

$$dF_A = B \frac{1}{2} \rho V_{rel}^2 [C_L \cos \phi + C_D \sin \phi] c dr \quad (10)$$

$$dQ = B \frac{1}{2} \rho V_{rel}^2 [C_L \sin \phi - C_D \cos \phi] r c dr \quad (11)$$

The above two equations represent the power extracted corresponding to the change in momentum of the same elements in equations 1 and 2.

2.5 Airfoils

Since the lift L is the only contributor to the torque dQ , to maximize L , the glide ratio $C_L : C_D$ must be a maximum. This occurs at a *best glide angle* and can be achieved by incorporating an efficient cambered airfoil section into the blade [3, 8].

A best glide of 50+ is typically obtainable just before the stall point ($\alpha \approx 15^\circ$) and at this corresponding angle of attack, will result in the highest possible lift, and hence torque, being produced by the blade.

One such series of the well-known NACA designed and tested airfoils is the "NACA 4-digit" series [8]. This is a relatively simple airfoil comprising some degree of camber. Airfoils of this series are characterised by having their thickest part located at 30% of their chord, from the leading edge. The classification takes the form of NACA XXXX where the first digit returns the maximum camber (as a percentage of chord), the second digit is the corresponding position of the maximum camber (in 10% increments of chord) and the last two digits are the maximum thickness (in percentage of chord) of the airfoil.

This is a particularly straightforward series of airfoil to identify from physical measurements: the maximum thickness is obtainable from direct measurement whilst the camber's maximum and corresponding position can be determined from a mean line plotted through the cross-section of the airfoil. Once the airfoil has been identified, empirical values of C_L and C_D at various angles of attack can be found in literature, such as [8] and [9].

2.6 Blade Element Momentum (BEM) theory

Both the Momentum theory and the Blade Element theory have their limitations. The former accounts for the power extraction from the total momentum by the induction of axial and angular flow components; the power extraction mechanism simply being modelled as an actuator disk through which the airflow passes. The latter determines the forces exerted on a blade element and hence torque and power, due to an incident airflow; the extraction of the power from the air-stream and hence resultant airflow not being accounted for in anyway.

As a result, the two theories were amalgamated to form the BEM theory [3]; consequently equations 1 and 10, and 2 and 11 are respectively equated to show the power extraction mechanism from the balance of momentum. This allows for the axial and angular induction factors to be solved for the relative airflow at each blade element [2, 5], as given by equations 12 and 13 respectively:

$$a = \frac{1}{1 + \frac{4F_{tip} \sin \phi}{\sigma(C_L \cot \phi + C_D)}} \quad (12)$$

$$a' = \frac{-1}{1 - \frac{4F_{tip} \sin \phi}{\sigma(C_L \tan \phi + C_D)}} \quad (13)$$

Where the *solidity factor* σ effectively normalizes the chord c of the blade at radius r by the corresponding swept arc length, hence given by: $\sigma = \frac{Bc}{2\pi r}$

The BEM theory relies on many assumptions, well detailed in the literature, but primarily: that there is no interference between the annulus under consideration and neighbouring annuli, and that the forces acting on the blade elements are entirely due to the lift and drag components only.

3. EMPLOYED METHODOLOGY

The air-stream is effectively divided into concentric annuli centered about the turbine's axis, of radius r , each having a cross-sectional area of $dA = 2\pi r dr$ where the power in each annulus is given by:

$$dP_\infty = \frac{1}{2} \rho V_\infty^3 dA \quad \text{where} \quad \sum_{r=0}^R dP_\infty = P_\infty \quad (14)$$

Similarly, the blades are divided into elements along their radial length, each element comprising a chord c , a twist β and an area $dA = c dr$. Furthermore, each element incorporates an airfoil section, assumed to be the same profile along the entire length of the blade.

In order to determine the aerodynamic forces exerted on each element (and hence torque and hence power), the relative airflow (described by equations 8 and 9) at each element r must first be determined, dependent primarily on the TSR λ . It must be noted that these two equations depend on the induction factors given by equations 12 and 13 which in turn depend on the relative airflow. To break the circular dependency, the direction of the airflow is initially determined from equation 9 using ideal values of $a = \frac{1}{3}$ and $a' = 0$ from theory and literature. This initial angle is then used to find the tip-loss correction factor F_{tip} using equation 3 which is substituted together with ϕ into equations 12 and 13 to refine the induction factor values. Subsequently, the velocity of the relative airflow is solved using equation 8.

With the relative airflow vector now determined, the coefficients C_L and C_D are required for equation 11. The angle of attack α at each element is the angle between the relative airflow ϕ and the blade's twist β , given by $\alpha = \phi - \beta$. Using empirical data for the airfoil incorporated, corresponding values of C_L and C_D can be interpolated for any angle of α .

The differential torque dQ on each element is now calculated; subsequently, the differential power, given by $dP = \Omega dQ$ is determined for each element. This can be normalised by the power in the corresponding annulus dP_∞ from equation 14, to find the Coefficient of Power at each element. Doing so proves beneficial when analysing the optimisation of power extraction along the length of the blade.

Finally, the Coefficient of Performance C_P is determined from the sum of power contributions from each element, normalised by the total wind power, as given below:

$$C_P = \sum_{r=0}^R dP \frac{1}{P_\infty}$$

To evaluate the turbine's performance over a series of TSR values, as is the objective of this work, the above methodology is repeated for each TSR, directly influencing the relative airflow at each element, and consequently resulting in corresponding C_P values. This relationship,

when plotted as the function $C_P(\lambda)$ can then be scaled by a set of wind speeds V_∞ to find absolute power-versus-speed curves etc.

The measurements required for the elemental analyses of a blade are the chord $c(r)$ and twist $\beta(r)$ along the length of the blade, from its root to tip R . The chord is simply the measured distance from the leading edge to the trailing edge, whilst the twist is measured by an inclinometer with the rotor disk lying in the horizontal plane. To determine the incorporated airfoil, a trial-and-error approach is used by trimming a cardboard template that slides over the airfoil profile at circa 50% radius, until a close fit is achieved. This assumes fundamentally that the same airfoil is used along the length of the blade, which for small turbine blades is a fair assumption. From the template, the mean line through the profile is drawn, the profile thickness is measured, and the maximum camber and its corresponding position are determined.

4. BLADE CHARACTERISATION

Comprehensive measurements (as above) of the two sets of blades were undertaken and are presented.

4.1 Blade #1: "3WT" Diameter 1.5 m

This three-bladed turbine features ground-adjustable pitch of the blades, set by indexed teeth in the rotor hub. For the purposes of this work, the pitch was set to -15° which is included in the twist angles measured below. The inner and outer radii of the rotor are 125 mm and 875 mm.

The blade was divided into 15 elements of $dr = 50$ mm each. The chord and twist of each element is plotted in Figures 1 and 2 respectively. This blade has a characteristic blunt tip evident in Figure 1.

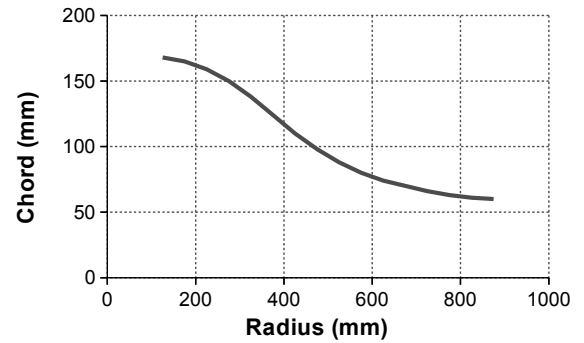


Figure 1: Measured $c(r)$ for "3WT" blade.

From the airfoil profile template at a chord of 124 mm ($\equiv 100\%$), a maximum camber of 4% at a position of 40% from the leading edge, and thickness of 9%, is determined. This identifies the airfoil as a NACA 4409 profile. Interpolated values for $C_L(\alpha)$ and $C_D(\alpha)$ are plotted in Figure 3 from empirical data published in [10].

4.2 Blade #2: "MS" Diameter 3.7 m

This is a larger three-bladed fixed-pitch turbine. The inner and outer radii are 300 mm and 1850 mm respectively.

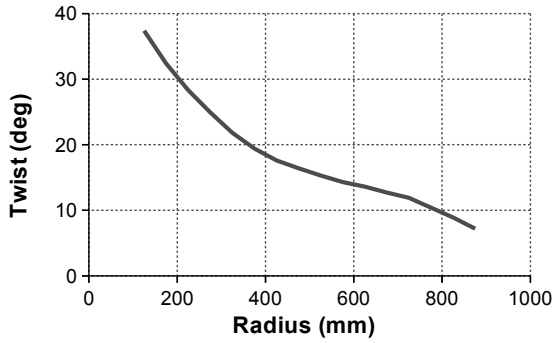


Figure 2: Measured $\beta(r)$ for “3WT” blade.

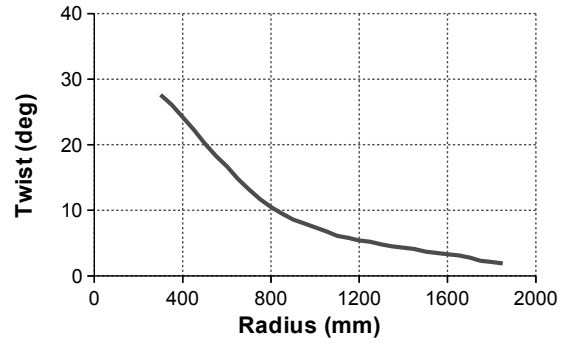


Figure 5: Measured $\beta(r)$ for “MS” blade.

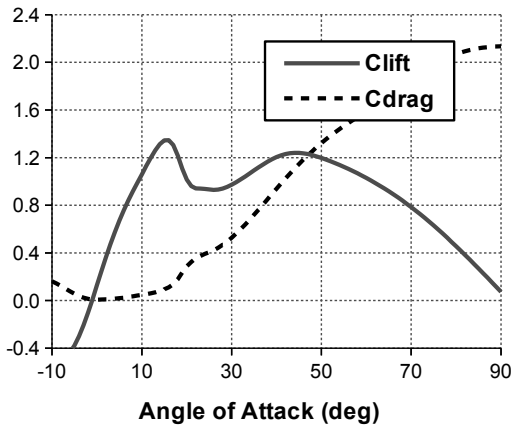


Figure 3: NACA 4409: Interpolated $C_L(\alpha)$ and $C_D(\alpha)$.

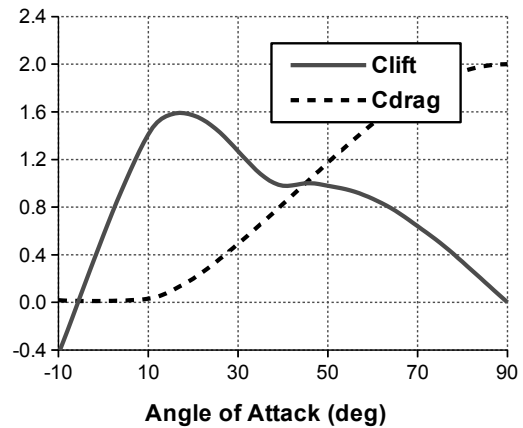


Figure 6: NACA 6415: Interpolated $C_L(\alpha)$ and $C_D(\alpha)$.

The blade was divided into 31 elements, each also spaced $dr = 50\text{mm}$ apart. The measured chord and twist along the length of the blade is plotted in Figures 4 and 5 respectively. This blade features a rounded tip which is evident in the figure.

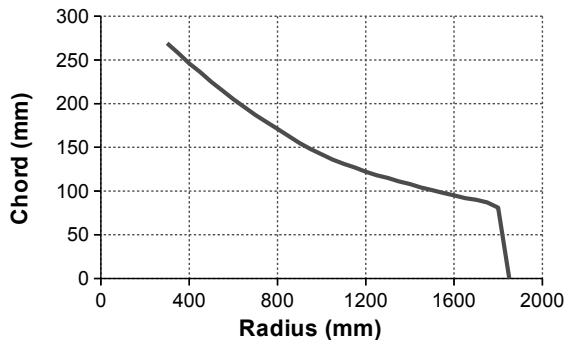


Figure 4: Measured $c(r)$ for “MS” blade.

At a chord of 136mm ($\equiv 100\%$), from the airfoil profile template a maximum camber of 6% at a position of 40% from the leading edge, and a thickness of 15% was determined, identifying the airfoil as a NACA 6415 profile. Interpolated values of $C_L(\alpha)$ and $C_D(\alpha)$ from [9] are plotted in Figure 6.

5. RESULTS

With the measured quantities of each blade presented in Sections 4.1 and 4.2, the method described is used to determine the desired $C_P(\lambda)$ relationships. These are respectively plotted in Figures 7 and 8.

5.1 Discussion of Results

The Coefficient of Performance for both sets of blades reach $C_{Pmax} \approx 0.42$ at a corresponding TSR of $\lambda \approx 7$, typical of small horizontal axis wind turbines i.e. despite their different diameters, they share the same maximum power points. Distinctly noticeable from the two graphs however is the shape of the curves, being inherently different due to the airfoils incorporated.

From detailed analysis of the power coefficients of each element along the length of the blade, it was noted that the accuracy of the induction factors a and a' diminished significantly at low and high TSR values and hence the plots have been limited to $1 \leq \lambda \leq 12$. The sources of the large errors introduced are due to the denominators of equations 12 and 13 tending towards infinity under certain combinations of σ , ϕ and C_L . Referring back to literature, this is a known shortcoming and stems from the fact that equations 12 and 13 are based on the notion that the turbine is operating under power-extracting conditions i.e. close

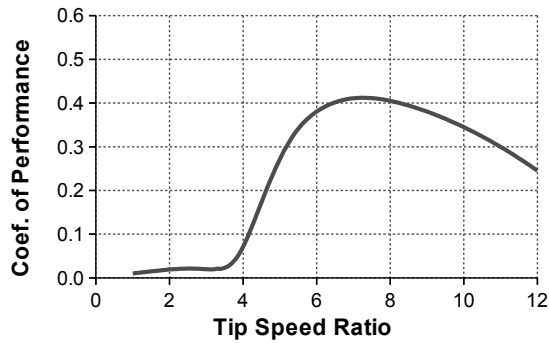


Figure 7: Predicted $C_p(\lambda)$ for 3-bladed "3WT" turbine.

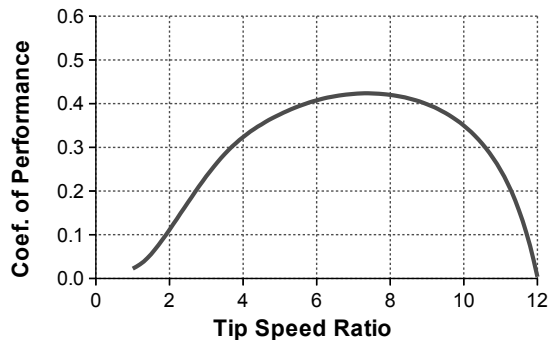


Figure 8: Predicted $C_p(\lambda)$ for 3-bladed "MS" turbine.

to C_{pmax} . At the time of writing an alternative method for the derivation of the induction factors had not been found, however [12] may offer a promising solution.

5.2 Future Work

An immediate improvement to be investigated is the accuracy of the induction factors at TSRs corresponding to standstill and to high speeds (say $\lambda \geq 20$).

Comparison of the predicted torque and power with experimental tests by means of coupling the turbines to a friction brake and adjusting the mechanical load, would be most valuable for the verification of the presented method.

6. CONCLUSION

This paper presents a methodology, using BEM theory, to predict the performance of a set of wind turbine blades, based on physical measurements of chord and twist. In combination with empirical data for the incorporated airfoil profile, the blade is divided into piece-wise elements and the differential torques and powers are computed along its length. Finally the overall Coefficient of Performance is determined and can be plotted against a range of TSRs. A weakness to the method employed arises due to the assumption that the turbine is operating under power-extracting conditions: at low and high TSR values, far from maximum power extraction, the induction factor equations become highly inaccurate and so too do the overall results. Despite this, two available sets of blades

were characterised and their predicted performance curves are successfully plotted.

REFERENCES

- [1] N. Mandas, F. Cambuli, and C. E. Carcangiu, "Numerical Prediction of Horizontal Axis Wind Turbine Flow," *EWEC 2006*, Feb. 2006. [Online]. Available: http://www.ewea.org/ewec2006/allfiles2/466_Ewecfullpaper.pdf
- [2] S. Gundtoft, "Wind Turbines," *Department of Mechanical Engineering, University College of Aarhus*, pp. 1–25, Jun. 2009. [Online]. Available: http://staff.iha.dk/sgt/Downloads/Turbines%20May4_2009_1.pdf
- [3] British Wind Energy Association, *Wind Energy for the Eighties*. Stevenage UK and New York: Peter Peregrinus Ltd., 1982, pp. 37–54.
- [4] J. F. Manwell, J. G. McGowan, and A. L. Rogers, *Wind Energy Explained*, 2nd ed. John Wiley & Sons, 2009, pp. 83–102.
- [5] E. Kulunk, "Aerodynamics of Wind Turbines, Fundamental and Advanced Topics in Wind Power," pp. 3–18, 2011. [Online]. Available: <http://www.intechopen.com/books/fundamental-and-advanced-topics-in-wind-power/aerodynamics-of-wind-turbines>
- [6] N. M. Mahmood and M. K. Abbas, "Computer Program to Predict Performance of Fast Running Horizontal Axis Wind Turbine to Reaching the Optimum Design," *Diyala Journal of Engineering Science*, vol. 04, no. 02, pp. 57–71, Dec. 2011.
- [7] A. Sedaghat and M. Mirhosseini, "Aerodynamic Design of a 300 kW Horizontal Axis Wind Turbine for Province of Semnan," *10th International Conference on Sustainable Energy Technologies (SET 2011)*, vol. 63, pp. 87–94, Nov. 2012.
- [8] I. H. Abbott and A. E. Von Doenhoff, *Theory of Wing Sections*, Dover, 1959, pp. 112–115.
- [9] E. N. Jacobs and R. M. Pinkerton. (1931, Dec.) Tests of NACA Airfoils in the Variable Density Wind Tunnel, Series 44 and 64. [Online]. Available: http://naca.central.cranfield.ac.uk/reports/1931/naca_tn_401.pdf
- [10] C. Ostowari and D. Naik. (1985, Jan.) Post-Stall Wind Tunnel Data for NACA 44XX Series Airfoil Sections. [Online]. Available: <http://wind.nrel.gov/public/library/2559.pdf>
- [11] E. H. Lewitt, *Hydraulics and Fluid Mechanics*, 10th ed. London: Sir Isaac Pitman & Sons, 1958, pp. 379–389.
- [12] V. L. Okulov and J. N. Sorenson, "Optimum Operating Regimes for Ideal Wind Turbine," *Journal of Physics: Conference Series*, vol. 75, no. 012009, pp. 1–9, 2007.

ECONOMIC FEASIBILITY ANALYSIS OF RURAL STANDALONE BIOFUEL-BASED ELECTRICITY GENERATION WITH AND WITHOUT ENERGY STORAGE

P. M. Seshabela* M. P. Nthontho* and S. Chowdhury*

*University of Cape Town, Dept. of Electrical Engineering, Cape Town, South Africa

E-mail: sshpor001@myuct.ac.za, nthpau005@myuct.ac.za, sunetra.chowdhury@uct.ac.za

Abstract: This paper investigates the techno-economic viability of a stand-alone biomass-based electricity generation with and without energy storage in Willary Farm in Matatiele village in Eastern Cape in South Africa. The test systems are modelled in HOMER Hybrid Optimization Modeling Software and consist mainly of a microturbine run from biomass-based fuel produced from the feedstock available in the farm and energy storage. The farm's potential to produce a large amount of feedstock capable of supplying sufficient biogas fuel is also assessed. Types of storage systems investigated in this work include lead acid battery, flywheel and flow battery and cost of the test system is compared with different forms of energy storage based on NPC, LCOE and operation and maintenance costs.

Keywords: Biofuel, Stand-alone, Energy Storage, Biomass, Net Present Cost, Cost of Energy

1. INTRODUCTION

The huge capital costs required for grid extension to areas that are particularly remote make it economically unattractive to connect these areas to the national grid. As a result, a large part of South African rural communities still lacks electricity supply from national grid. Therefore stand-alone electricity generation using locally available biofuel-based fuels becomes an attractive solution for supplying electricity to the South African rural communities. Animal waste is used to make biofuels in solid, liquid or gas form which can be effectively used to run small scale microturbine or small to medium range gas turbine systems [12, 13].

A major task associated with implementing such stand-alone electricity generation systems is to ensure that the system supplies quality and reliable power to the customers and at the same time become economically profitable in the long run. Energy storage forms a key component of stand-alone systems in order to maintain load-generation balance at all times to ensure energy security and power quality [14]. Hence, the economic feasibility should focus on comparing various types of available energy storage to be used in conjunction with biomass-based generation.

In this context, this paper presents an economic comparison of biofuel-based electricity generation system in Willary Farm in Matatiele village in Eastern Cape in South Africa with and without various forms of energy storage.

2. BIOFUELS IN SOUTH AFRICAN ENERGY MIX

South Africa's Department of Energy aimed to electrify 92% of formal South African households by the end of 2014. Currently, only 82% of these households have

been electrified. The remaining 18% is in the deep rural areas. One of major setbacks is due to large capital required for installation and supply of electricity to such locations [1]. Therefore off-grid or stand-alone electricity supply becomes the preferred solution to rural electrification. It has been found that the use of locally available biomass resources in a community such as plant and animal wastes, municipal solid wastes, etc. have the potential not only to produce electricity but also to reduce the harmful pollutants and greenhouse gas emissions.

2.1 Classification and Production of Biofuels

There are two main classes of biofuels. These are First generation and Second generation biofuels. The first generation biofuels are in liquid form. They are produced from plant based oils and starch such as food crops, oil seeds, sugar beet, etc. This type of biofuels has proven to run efficiently in Brazil and Germany [3]. The second generation refers to the liquid and gaseous forms of fuel from sources such as lignocellulose feedstock. These are generally feedstock from wood, grass and woody wastes. Another class referred to as the third generation biofuels are obtained from micro-organisms such as algae and other photosynthesising organisms [2]. Ethanol and Biogas are the most commonly used biofuels in the transportation and power generation industries [4]. Biomass is converted to biodiesel through a process called Trans esterification. Another method of biofuel production uses bio-digesters. Different types of bio-digesters are suitable depending on the state of the bio-fuel resource. Summary of different types of digester technologies can be found in [12].

2.2 Biofuels in South Africa

During the planning stage of biofuel-based rural

electrification, it is important to assess the biomass-based resource availability in any country including South Africa. This is important to make the generation systems feasible and sustainable for improving the community's socio-economic condition. The following sections discuss the potential of biomass, waste and landfill generated biofuels with reference to South Africa.

(i) Biomass from wood

The use of crop and wood as a form of biofuels requires large piece of land and large forestation. The figure below illustrates potential parts in South Africa where cultivation for crops and forestation of wood can be used for the production of biofuels [1]. Figure 1 shows that agricultural land covers 81% of the total land. Only 14.5% of this land has potential in growing crops. The total forest area that covers forestation is 9.2Mha and from that 1.3Mha can be used [6]. With this land agricultural and forestry activities are expected to produce food crops and be utilised for other industrial products. Thus creating problems such as loss of biodiversity through farming extension, food security issues, deforestation that partially contributes to soil erosion and of course the use of water growing crops for biomass production.

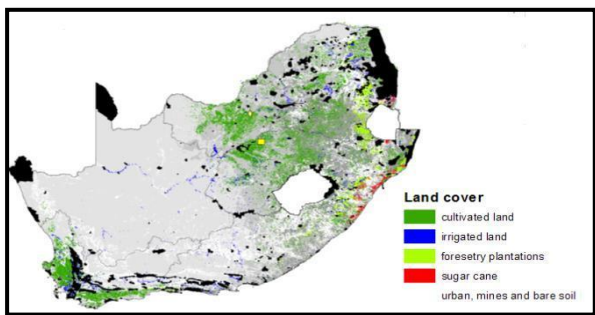


Figure 1: Agricultural and forestry land in South Africa

(ii) Biofuels produced from waste

Table 1: Waste products and their different methane production potential [7]

Biomass type	Specific methane potential m ³ CH/kgVS	Specific methane production m ³ CH/t
Cattle slurry	0.200	12.8
Mixed fruit residues	0.370	42.1
Fats	0.800	684.0
Household waste	0.400	102.0
Sewage sludge	0.400	30.0

Most of the waste product has the capabilities of producing methane gas. Although the gas is a greenhouse gas, if properly contained, it can contribute in producing power effectively. Table 1 illustrate different kinds of waste and their potential for producing methane gas. Fats and household waste are found to be large contributors of methane production.

2.3 Landfill and electricity production

The landfill gas emission presents health risks and environmental threat to the nearby communities, especially if proper waste management is not in place. Gases such as methane, nitrogen and carbon dioxide all contribute to global warming. Therefore to mitigate or alleviate such problems, biogas can be produced from this gases thus increasing energy supply [15]. The three biggest cities that have been identified as having proper waste management systems are Durban, Cape Town and Johannesburg. Durban landfill is currently producing electricity enough to supply 5000 to 6000 households by retrieving the biogas from the landfill [7]. Biogas from landfill is harvested by placing suction tubes horizontally aligned underneath the waste. These tubes capture the gas emitted from this waste.

3. REVIEW OF ENERGY STORAGE

Due to the unpredictable availability of biofuel resources, it is important to combine the biofuel-based generation with suitable energy storage for enhancing energy security of the system. For rural electrification in South Africa, it would be prudent to select a matured and well-known storage technology which need not be imported from abroad at high cost, can be incorporated in the system without too much technological challenge and for which replacement and maintenance would be easy. Hence, this section reviews three matured and proven energy storage technologies, such as lead-acid battery, flywheel and flow battery, for this work before carrying out the economic comparison of the stand-alone biofuel-based rural electrification system with different types of storage [11, 14].

3.1 Lead Acid Battery

Lead acid batteries are matured and proven and known for good energy density. However, their power density is limited and they might take a considerable time to charge. Still, with regard to cost, they are the best option. For implementing lead-acid batteries, it is important to select the right battery and the most suitable charge and discharge characteristic to suit the load profile of the target customer base [14].

3.2 Flywheel

Flywheels conserve energy in kinetic form and this stored energy is converted to electrical energy during periods of high energy demand. They can supply and store power at a very high rate, but energy needs to be stored within a vacuum which can be expensive to maintain. Flywheels have efficiencies between 80 and 90%, but incur large standby losses; therefore they are not economic for long term storage [14]. However, research is going on in South Africa to produce flywheels locally at a lower cost which will be helpful in the long run in using such products in rural electrification projects.

3.3 Flow batteries

A flow battery is another type of an electrochemical energy storage system. It has an ion or proton membrane that separates the two loops inserted in the electrolyte. The electrochemical reaction in this electrolyte releases or stores the electrical energy to the external electric circuit [11]. Popular types of flow batteries include the vanadium redox and the zinc bromide flow batteries. These batteries are mainly used in the application of power quality and management purposes. Their rapid response is one of the popular advantages over the lead acid batteries and also their energy storage capacity depends on the electrolyte content in the cell stack. They have longer lifespan and can also be fully discharged without being damaged as compared to normal batteries [17].

4. BIOMASS CAPACITY CALCULATION FOR WILLARY FARM

This section presents the biomass capacity calculation for Willary Farm in Ward 4 of Matatielevillage in Eastern Cape which is required for modelling and simulation of the biofuel-based stand-alone electricity generation system for the farm. The system is not connected to the grid and delivers the residential load for those households in the village who do not have access to electricity.

4.1 Willary farm parameters

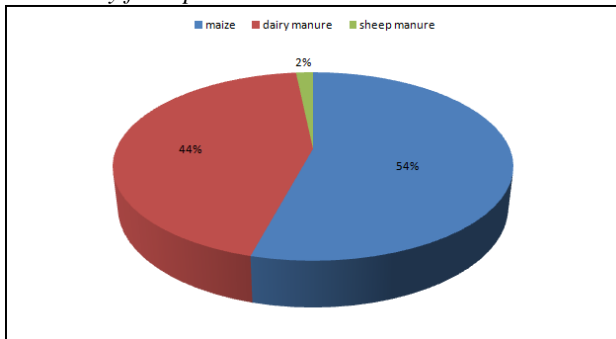


Figure 2: Available feedstock from Willary farm

Willary farm comprises of 130ha of dry land yellow maize and 20ha of silage maize, a dairy herd of 70 cows, 170 of beef herd and 160 sheep. The farm experiences a summer temperature of mid-twenties and maximum temperatures of 35 degrees [9]. The farm uses mainly yellow maize to feed the herds. Yellow maize was assessed to have a high volatile solid content and biochemical methane content. It is therefore found to be a potential feedstock for biomass production. The maize waste from the farm will be used in the anaerobic digester located in the farm. With this selection of wide variety feedstock, the methane yield is expected to increase. The owner of the farm keeps the farm's viability by making sure that the nutrients of the soil are in the correct margin. Furthermore, through correct use of fertilisers and diseases control for the livestock, the plant will constantly produce enough waste needed for the anaerobic digestion.

These precautions are important for sustainability of the plant. The feedstock that is available in the farm is shown in Figure 2.

4.2 Overview of the Willary farm plant

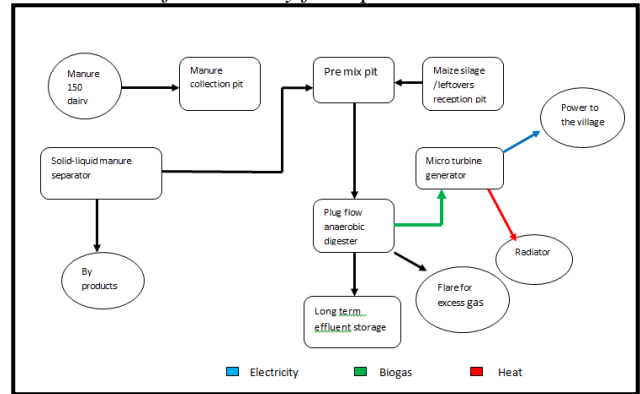


Figure 3: An overview of a proposed anaerobic digester configuration in the farm [10]

Figure 3 shows the schematic arrangement of Willary farm with the installation of the anaerobic digester system together with electricity generation system. The micro-turbine is placed closer to the anaerobic digester in order to reduce transportation costs of fuel produced by the anaerobic digester.

4.3 The Willary farm biomass capacity

Table 2: Annual waste and methane production from substrates in Willary farm

Substrate	Waste tonnage (tonnes/annum)	Methane production (m ³ /yr)
Maize silage	6500	684882
Sheep manure	197	11714
Dairy cow manure and left-over's	5298	73685
Total	11995	770281

Biowatts calculator online application was used to determine biomass yield from Willary farm. The application is an anaerobic digestion calculator which allows users to calculate the energy return of investment for the feedstock that is available in their feedstock database. It also includes a kinetic analyser that shows how parameters such as temperature and hydraulic retention time could have on the production of biogas [8].

Table 2 shows Biowatts calculator's results of the waste tonnage characteristics from Willary farm annually. The tabulated substrates in the table are the ones that are found in the farm and are also listed from the system's database. It is found from the results that the farm is capable of producing a 77021 volume per year of methane. This methane gas becomes a large contributor as source of energy for fuelling the generating system in the farm.

5. ECONOMIC ASSESSMENT OF BIOFUEL-BASED STAND-ALONE SYSTEM WITH AND WITHOUT ENERGY STORAGE

The economic assessment and cost comparison of the biofuel-based stand-alone electricity generation system is performed using the HOMER Hybrid Optimization Modeling Software, which is widely used for designing and analyzing hybrid power systems. The basic biofuel-based electricity generation system configuration consisting of a biofuel-based microturbine generator and converter, and the residential load profile for Ward 4 of Matatiele village remain common to all the four case studies conducted. The case studies vary in terms of different types of storage as follows: (i) Case 1 or Base case – system without energy storage, (ii) lead acid battery storage, (iii) flywheel storage and (iv) flow battery storage. The cases are compared in terms two economic parameters, Net Present Cost (NPC) and Levelized Cost of Energy (LCOE) discussed below.

(i) The Net Present Cost (NPC)

The NPC is defined as the present value of all costs associated with installations and operations of the system over the lifetime which the project will take place. [34] This is the main economic output when the user searches for results. Therefore in order for the project to be viable, it is required that the NPC be as minimum as possible. NPC calculation in HOMER considers cost factors such as (i) Initial capital, (ii) replacement cost, (iii) Operation and maintenance cost and (iv) Fuel cost.

The NPC is given by equation (1): [16]

$$NPC = \frac{\text{Total Annualised Cost}}{\text{CRF}(i,l)} \quad (1)$$

Here, CRF(i,l) is the defined as Capital Recovery Factor and it is a function of annualised interest rate of the country the project is implemented in and a function of lifetime of the project. In South Africa the year 2014 annualised interest rate is announced by the Reserve Bank to be 5.76%. The total annualised cost is summated cost of all components used in the biofuel-based electricity generation system [16].

(ii) The Levelized Cost of Energy (LCOE)

The levelized cost of energy (LCOE) in HOMER is defined as the cost per kWh that the micro power system has used whilst in operation. It is given by equation (2):

$$LCOE = \frac{\text{Annuliased total}}{I_{\text{prim}} + I_{\text{def}}} \quad (2)$$

I_{prim} and I_{def} are the primary load and deferrable load defined by the user respectively.

Table 3 lists the rating and cost of equipment and components for modelling the biofuel-based electricity generation system. Since HOMER works in US Dollars

(US\$), the equipment costs in Table 3 are in US\$. The current US\$ to South African Rand (ZAR) exchange rate of 1 US\$ = ZAR 11.61 can be used for converting the US\$ values to ZAR values.

Table 3: Economic data for equipment used

Equipment	Size	Capital Cost	Replacement Cost
Micro-turbine	10kW	US\$ 15000	\$15000
Converter	6kW	\$1135/kW	\$1135/kW
Batteries	1900Ah 4V (1-64 battery banks)	\$350/battery	\$320/battery
Flow batteries	-	\$700/battery	\$700/battery
Flywheel	20kW	\$300/kW	\$300/kW

5.1 Case 1: A biofuel-based system without energy storage (Base case)

In the base case, no energy storage is considered. System configuration is shown in Figure 4 and optimised system configuration is given in Table 4. The biomass resource required to fuel the 10kW micro turbine was calculated from Biowatts Online Calculator.

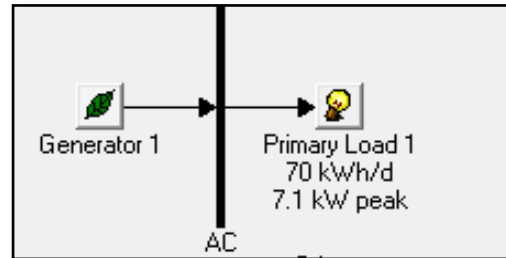


Figure 4: Case 1 system configuration

The primary load profile used for this case study is shown in Figure 5 it is assumed that this load is supplied by the 10kW microturbine continuously.

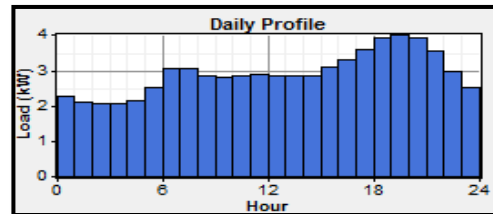


Figure 5: Load profile for Ward 4 of Matatiele

Table 4: Equipment Ratings and Specifications

Biofuel-based Microturbine(kW rating capacity)	Mean electrical efficiency (%)
Base case (10kW)	43.5
Case 2 (10kW)	46.7
Case 3 (10kW)	44.7
Case 4 (5kW)	48
Converter	
Nominal Power(kW)	
Base case	0
Case 2	6
Case 3	0
Case 4	6
Storage system	
Capacity	
Base Case	No storage system
Case 2	8 battery banks, 4V, 1900 Ah
Case 3	1 flywheel unit, 1000kW charge and discharge capacity and 1kW parasitic load
Case 4	3kW cell stack and 5kWh electrolyte

The expected operational lifespan of the micro turbine is ten years and that of the converter is fifteen years. In terms of each storage system, the lead acid expected throughput is 10,569kWh, the flywheel is 15 years and the flow battery’s cell stack is expected to last for a period of 15 years. The cash flow summary for this case is shown in Table 5. Exchange rate for Table 5 is 1US\$=ZAR11.61 as also indicated in Section 5.

Table 5: Cost Summary of Case 1 (Base Case)

NPC	US\$ 61,478
	ZAR 713,760
LCOE	0.184 US\$/kWh
	2,14 ZAR/kWh
Operating cost	US\$ 3,550/yr
	ZAR 41,216/yr

The cash flow summary for this case only includes the replacement of the microturbine twice in its 25 year lifespan, the replacements occurring on the tenth and nineteenth year of the project lifespan. The cost of fuel over the entire project life amounts to US\$ 31,903, i.e. ZAR 370,394. The salvage cost at the end of the project’s lifespan totals to an amount of \$4000, i.e. ZAR 46,440.

5.2 Case 2: Lead Acid Battery Storage

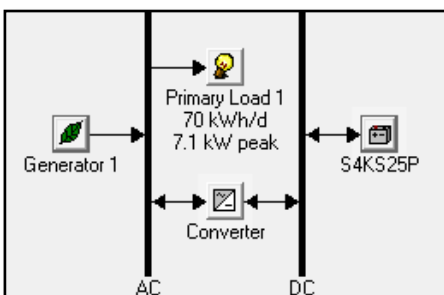


Figure 6: Case 2 system configuration

The system configuration for Case 2, as shown in Figure 6, includes 8 banks of Surrette 4KS25P 4V, 1900Ah and 7.6kWh lead acid battery as the storage for the primary load profile of Figure 5. The optimum configuration for this system also consists of 6kW converter. It is seen from HOMER analysis that this configuration is capable of delivering the entire load adequately. Cost summary of Case 2 as given in Table 6. Exchange rate for Table 6 is 1US\$=ZAR11.61 as also indicated in Section 5.

Table 6: Cost summary for Case 2

NPC	US\$ 66,925
	ZAR 777,000
LCOE	0.2 US\$/kWh
	2,32 ZAR/kWh
Operating cost	US\$ 3,233/yr
	ZAR 37,535/yr

In terms of the cash flow summary for this case, the generator has the largest capital, amounting to \$15,000. On the other hand the battery and converter have a much lower replacement and operating costs of \$2,860 and \$2,940 respectively whilst the microturbine requires an amount of \$6,375. The microturbine consumes a fuel of 1.358kg per kWh. These cost values have been retained in US\$ as these values are directly calculated from HOMER and can be converted to ZAR using the aforesaid exchange rate.

5.3 Case 3: Flywheel Storage

The optimal configuration for Case 3 includes a one unit of Powercorp flywheel as energy storage along with the 10kW biofuel-based microturbine, as shown in Figure 7. The flywheel has a charge and discharge capacity of 20kW and a parasitic load of 1kW. Table 7 gives the cost summary for this case. Exchange rate for Table 7 is 1US\$=ZAR11.61 as also indicated in Section 5.

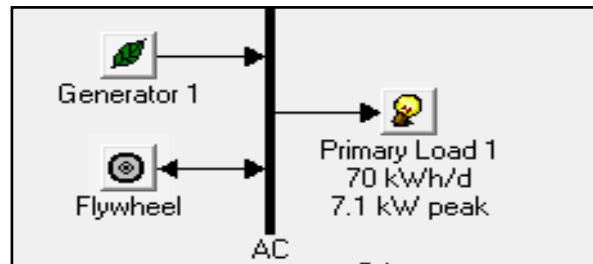


Figure 7: Case 3 system configuration

Table 7: Cost summary for Case 3

NPC	US\$ 74,766
	ZAR 868,033
LCOE	0.224 US\$/kWh
	2,6 ZAR/kWh
Operating cost	US\$ 4,107/yr
	ZAR 47,682/yr

It is seen that Case 3 records the highest NPC; however its operation and maintenance cost is ZAR 47,682 per year which is still considerably low.

5.4 Case 4: Flow Battery Storage

The optimal configuration for Case 4 includes a vanadium redox flow battery as the storage as shown in Figure 8.

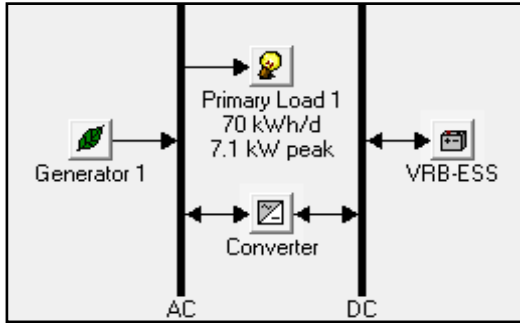


Figure 8: Case 4 system configuration

Unlike other cases, this configuration includes a 5kW microturbine. This is because the large size of electrolyte within the flow battery allows for greater storage capacity and the battery can be fully discharged without damage, therefore sustainably supplying electricity.

The cost summary in Table 8 shows that the NPC for this Case study is by far the least when compared to the previous three cases. The system uses a 5kW micro turbine that cost \$7,500 and VRB flow battery that cost \$3,600. The operation and maintenance cost for this micro power account for 1.4% of the total cost of this project's lifetime cost. Exchange rate for Table 8 is 1 US\$=ZAR11.61 as also indicated in Section 5.

Table 8: Cost summary for Case 4

NPC (US\$)	US\$ 50,328
	ZAR 584,308
LCOE	0.16 US\$/kWh
	1.86 ZAR/kWh
Operating cost	US\$ 2,691/yr
	ZAR 31,243/yr

The cash flow summary for this system includes a replacement cost for the 5kW microturbine for every twelve years in the systems life span and there is a replacement cost for the vanadium flow battery on the fifteenth year after operation. The salvage cost amounts to a total of US\$ 8000 i.e. ZAR 92,880.

6. ECONOMIC COMPARISON OF CASE STUDIES

This section presents the comparison of the four case studies in terms of NPC, LCOE and Operation and Maintenance (O&M) costs. Figure 9 shows that Case 3 has the highest and Case 4 the least NPC. Hence with respect to NPC, Case 4 is most viable economically; however this cannot be the only factor for selection of

storage. Maturity of technology and local availability of storage technology and suitability of its electrical characteristics to power quality and reliability requirements are also to be considered.

However, looking at the level of costs for all the cases with these costs, it can be commented that implementation of such projects will require substantial subsidy from the South African government until these become profitable.

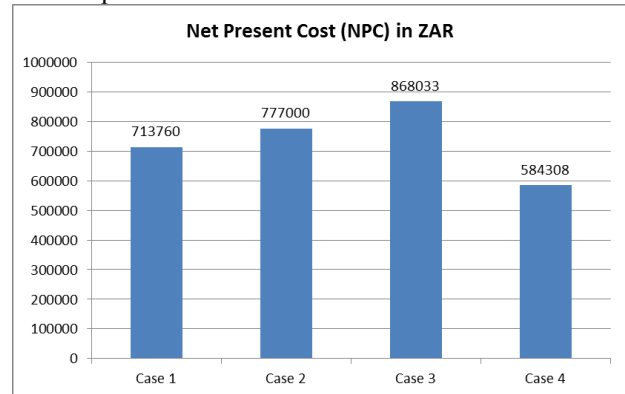


Figure 9: Comparison of NPC of the case studies

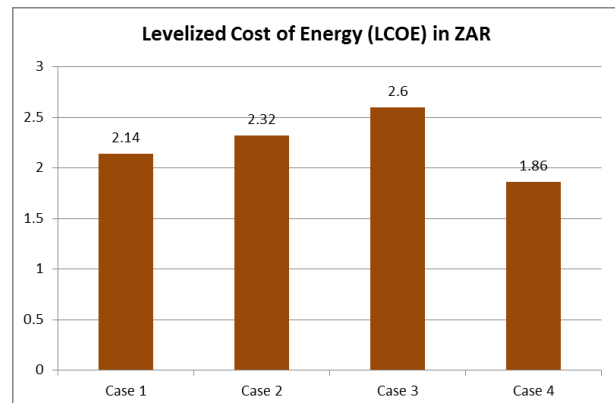


Figure 10: LCOE comparison for all case studies

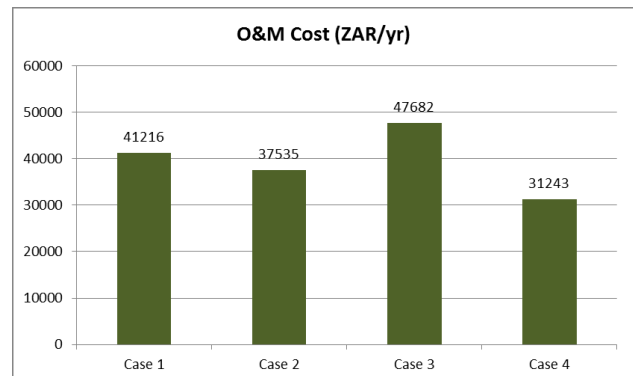


Figure 11: O&M cost comparison for all case studies

Figure 10 indicates that Case 4 has the least LCOE whilst Case 3 has the highest LCOE. A least LCOE is desirable as it means energy is produced at a lower cost and it has high return of investments for the investors concerned. Therefore with that, Case 4 is financially attractive to the investors as it has the least cost of electricity production

from its micro power system whilst on the other hand Case 3 which includes the flywheel storage has the highest LCOE.

For a standalone system located in a remote area, it is desirable to have a least operating and maintenance costs as possible, because the system needs to be independent. Figure 11 compares the O&M costs of all the cases reported in this paper. Therefore Case 4 is economically viable as it has the least operational and maintenance cost, and Case 3 is not financially viable as it has highest operational and maintenance cost.

The O&M cost of the base case is even more than cases with battery storage. Therefore not only is the storage technically competitive when compared with the case where there is no storage system, it also has less O&M costs. It is therefore recommended that the a biomass generation plant with a flow battery storage system be used to supply power to the village as it has minimum NPC, less cost of energy and it presents with the least operation and maintenance cost. Therefore in do so, we provide off the grid locations with secure electricity and at a minimum cost.

7. CONCLUSION

An economic comparison of biofuel-based electricity generation system in Willary Farm in Ward 4 of Matatiele village in Eastern Cape, South Africa without and with various forms of energy storage was investigated. An analysis of different case studies was conducted, such that we can observe the impact of storage system on the NPC, LCOE and O&M for the designed micro power system. Case 4 which incorporated a flow battery was the optimum case out of all the case studies conducted. It presented with a minimum LCOE of 0.16\$/kWh out of all the cases and also its NPC of \$53,451. These positive results from Case 4 are influenced by the fact that the micro power system used in this case includes a flow battery storage system. Flow batteries have an advantage over the lead acid battery in that they can discharge for longer periods without damage and they respond quickly when needed to operate. With these quality factors, the flow batteries contribute to increasing the quality of standalone electricity supply that is required for rural customers who do not have access to electricity from the grid. With that being said, it is therefore recommended that the a biomass generation plant with a battery storage system be used to supply power to the village as it has minimum NPC, less cost of energy and it presents with the least operation and maintenance cost.

8. ACKNOWLEDGEMENT

The authors gratefully acknowledge the support and infrastructure provided by Electrical Engineering Department, University of Cape Town for carrying out this research work

9. REFERENCES

- [1] (2012, Mar.) www.energy.gov.za. [Online]. www.energy.gov.za
- [2] (2011) energypedia.info. [Online]. www.energypedia.info.com
- [3] (2007, Jan.) IEA Energy Technology Essentials-Biomass for Power Generation and CHP. [Online]. www.iea.org
- [4] J. Nagi et. al., "Palm Biodiesel an Alternative Green Renewable Energy for the Energy Demands of the Future", ICCBT 2008, pp.79-94, 2008.
- [5] (2011) Centre for Climate Change and Energy Solution [Online]. www.c2es.org
- [6] B.Bolund et.al."Flywheel energy and power storage systems", *Renewable and Sustainable Energy Reviews*, Vol.11 Issue 2, pp.235-258, 2007.
- [7] IEA. Project summary document: Durban landfill gas to electricity project. [Online]. www.iea.org
- [8] (2013) Slideshare. [Online]. <http://www.slideshare.net/biowatts>
- [9] L. Phillips, "Mad about maize and working the soil", *Farmer's Weekly*, 2014.
- [10] J. Prontoand C. Gooch, "Greenhouse Gas (ghg) Emission Reductions Due to Anaerobic Digestion of Dairy Manure", *ASABE Annual International Meeting 2009*, Nevada, USA, pp.1-17, 2009.
- [11] P. Krivik & P. Baca, "Electrochemical Energy Storage" [online]. www.doi.org
- [12] A.Boadzo, S.P.Chowdhury and S.Chowdhury, "Modeling and assessment of dairy farm-based biogas plants in South Africa", *Proc. of IEEE Power and Energy Society General Meeting 2011*, Detroit, USA, pp.1-8, July 2011.
- [13] A.Boadzo, S. Chowdhury and S.P.Chowdhury, "Technical and Economic Assessment of Power Generation from Dairy Farm-based Biogas Plants in South Africa", *Proc. of 46th International Universities' Power Engineering Conference (UPEC 2011)*, Soest, Germany, pp.1-6, September 2011.
- [14] G.Copepez, S.Chowdhury and S.P.Chowdhury, "The importance of energy storage in Renewable Power Generation: A review", *Proc. of 45th International Universities Power Engineering Conference (UPEC 2010)*, Cardiff, UK, pp.1-5, September 2010.
- [15] K.Sekgoele, S.P.Chowdhury and S.Chowdhury, "Technical and economic assessment of power generation from landfill gas in South Africa", *Proc. of IEEE Power and Energy Society General Meeting 2011*, Detroit, USA, pp.1-8, July 2011.
- [16] Y. Maklad, (2014) "A Hybrid Renewable Energy System (Wind and solar) size optimisation and costing for residential buildings in Urban Armidale NSW", *Australia Bulletin of Energy Economics*, Vol.2 No.3, pp.50-61, 2014
- [17] D. Holzman, "The Vanadium Advantage: Flow Batteries Put Wind Energy in the Bank", *Environ Health Perspect.*, Vol.115 No.7, A358-A361, 2007.

The Characterization and Modelling of a Line Start Permanent Magnet Synchronous Machine

A.J. Grobler* and P. E. Platjie**

*Project supervisor at the North-West University Potchefstroom Campus, School for Electrical, Electronic and Computer Engineering, 25 Borchard Street, Potchefstroom 2520, South Africa. Email: www.AndreGrobler@nwu.ac.za

**Student at the North-West University Potchefstroom Campus, School for Electrical, Electronic and Computer Engineering, 25 Borchard Street, Potchefstroom 2520, South Africa. Email: www.ericplaatjie@gmail.com

Abstract: Line Start (LS) Permanent Magnet Synchronous Machine (PMSM) is a hybrid synchronous machine that has been designed to increase the efficiency of traditional induction motors. By introducing permanent magnets buried beneath the squirrel cage a hybrid motor is obtained that has a combination of asynchronous and synchronous capabilities. By implementing strong magnets in this machine the steady state performance (speed, torque and current) can be improved. The aim of this project is to characterize an existing LS PMSM by performing various laboratory tests to determine the machines parameters. Furthermore, the machine should be dynamically modeled to predict the dynamic behaviours of the machine. The procedures that were taken to solve this problem were to determine the machines parameters using no load, blocked rotor, stator resistance, slip and load tests. The parameters obtained are further used in equivalent circuits to analytically model the machine in dq rotor reference frame. The analytical model can be used to study the dynamic behavior of the LS PMSM. The block model approach in MATLAB/Simulink is used in the construction of the model that will allow the user to resolve reference frame theory issues.

Key words –Characterization, dynamic behavior, LS PMSM, MATLAB

1. INTRODUCTION

The first design of a Line-Start (LS) Permanent Magnet Synchronous Machine (PMSM) was suggested by F.W. Merrill in 1955, the idea was to combine induction motors (IM) and PMSM with the ability to start when connected to the voltage supply. This design at the time consisted of permanent magnets (PMs) with poor magnetizing properties, extra material costs when compared to IM, complex construction and design difficulties. All these difficulties prevented the idea to flourish amongst research groups [1].

With the advances in PM research, high performance rare earth magnets such as neodymium iron boron (NdFeB) bought upon more interest in the overall performance of the machine. The research focused on the machines steady- and transient-state behaviours, which are considered to be valuable information for designers. The steady state behaviour focused on the synchronisation of the machine which demonstrated higher efficiency capabilities and the transient state merely focused on analytical analysis based on the d - and q - axis reference framework in the late 1990s [2].

Since then, LS PMSM has grown in popularity due to their higher efficiency, reduced life cost and sensitivity to the environment. Various energy regulatory bodies internationally have started to set new higher minimum efficiency standards for these machines; this has increased investigations for newer designs with overall better performance to be presented by designers [1].

2. LITERATURE REVIEW

2.1 LS PMSM construction

Figure 1, illustrates a cross section of an LS PMSM with embedded permanent magnets in the rotor for excitation and a squirrel cage of an IM [3].

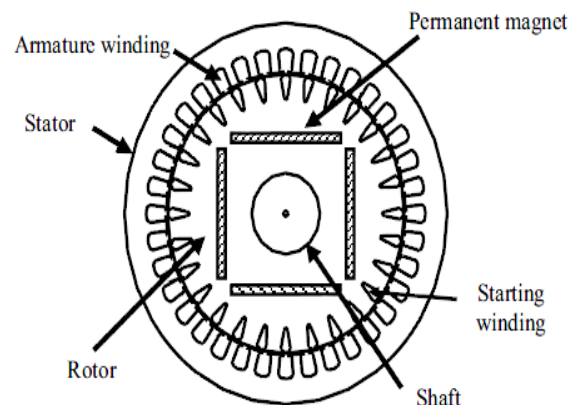


Figure 1: Cross Section of LS PMSM [3]

2.2 Machine nameplate specifications

The proposed machine to undergo testing and modeling has the following nameplate specifications listed in table 1.

Table 1: Proposed machine operating specifications

WEG W22 Top premium frame 132M IP55 (Radial flux)		
#	Star	Delta
V	525	550
Hz	50	50
kW	7.5	7.5
rpm	1465	1470
A	10.6	10.2
p.f	0,85	0.84
Duty	1.15	1.15
poles	4	4

The machine will operate under star configuration.

2.3 Methodology

The methodology used in this project focuses on the following aspects: parameter testing, speed versus torque characteristics, data capture, mathematical modelling, MATLAB Simulation and a verification process.

During testing the aim is to obtain all the necessary performance characteristics of an LS PMSM prototype. The torque under various loads, the speed and currents will be captured for further usage.

Further tests that need to be performed using the IEEE Guide [4] for parameter determination and analysis of machines include stator DC and inductance test, slip test, no load test, locked rotor test, load capability test and back-emf waveform test.

The parameters to be determined from the test mentioned will generalize an equivalent circuit for the proposed prototype. The equivalent circuit mathematical derivation consists of rotor and stator parameters in a specific reference framework. The mathematical equations will be implemented in a MATLAB/Simulink block approach to simulate the machines dynamic behaviours.

The verification process will require test results to be compared with the Simulink model simulated.

3. LS PMSM CHARACTERIZATION

The stator resistance of the machine is usually obtained by means of the DC test. Further the inductances L_{ds} and L_{qs} can be obtained by the slip test. The stator leakage reactance L_{ls} can be achieved by the blocked rotor test, and no load test.

The magnetizing reactance is obtained by keeping the rotor forced to rotate at synchronous speed, the inductance can be obtained by dividing the nominal voltage V_m [1] by the stator current I_s as follows:

$$X_m = \frac{V_m}{I_s} \quad (1)$$

With the rotor kept blocked and using induction motor equivalent circuit the rotor resistance and the rotor leakage reactance L_{lr} can be obtained [1].

3.1 Machine parameters

Additional machine parameters needed to dynamically model the LS PMSM are tabulated below:

Table 2: Additional machine parameters

Additional motor data			
RMS voltage Line - neutral	Vrms	V	525
Peak Voltage	Vm	V	430
Inertia	J	kg.m ²	0.0064
Flux	λ	Wb	1.31

Additional parameters will be obtained from the test performed on the proposed prototype .

4. LS PMSM ANALYTICAL MODEL

The analysis in this paper is based on the d-q equivalent circuit of an LS PMSM in the rotor reference frame shown as referred to the stator side. Note the subscript ‘k’ is similar to ‘r’ but only labeled in this literature article representing the rotor side [5].

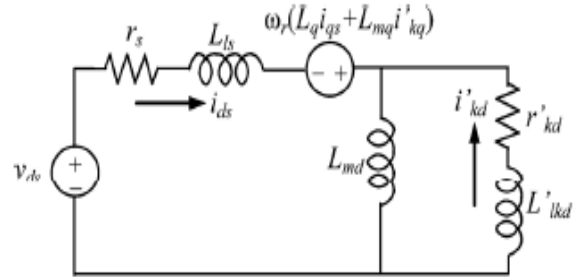


Figure 2: d-axis equivalent circuit of a three-phase LS PMSM in rotor reference frame [6].

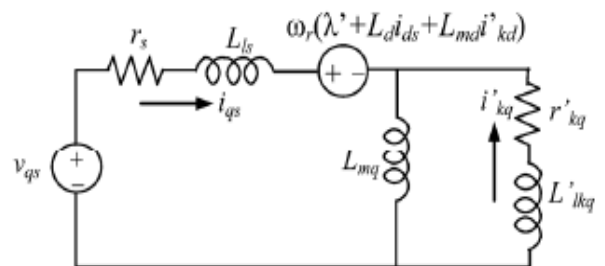


Figure 3: q-axis equivalent circuit of a three-phase LS PMSM in rotor reference frame [6].

The analytical model in d-q rotor reference frame, the voltage differential equations are as follows [3-5];

$$v_{qs} = r_s i_{qs} + \omega_r \lambda_{ds} + \frac{d}{dt} \lambda_{qs} \quad (2)$$

$$v_{ds} = r_s i_{ds} - \omega_r \lambda_{qs} + \frac{d}{dt} \lambda_{ds} \quad (3)$$

$$v_{qr} = r_r i_{qr} + \frac{d}{dt} \lambda_{qr} \quad (4)$$

$$v_{dr} = r_r i_{dr} + \frac{d}{dt} \lambda_{dr} \quad (5)$$

Whereby v, r, i, ω and λ are the voltage, resistance, current, electrical angular frequency and the flux linkages respectively. The subscripts "s" and "r" denote the stator and rotor quantities. The "d" is the direct axis and "q" the quadrature axis. The constant λ_{fo} denotes the flux generated by the permanent magnet. The currents are related to the flux linkages in these relations,

$$i_{ds} = \frac{1}{(L_{ds}L_{dr} - L_{md}^2)} (L_{dr}\lambda_{ds} - L_{md}\lambda_{dr} - (L_{dr} - L_{md})\lambda_{fo}) \quad (6)$$

$$i_{qs} = \frac{1}{(L_{qs}L_{qr} - L_{mq}^2)} (L_{qr}\lambda_{qs} - L_{mq}\lambda_{qr}) \quad (7)$$

$$i_{dr} = \frac{1}{(L_{ds}L_{dr} - L_{md}^2)} (-L_{md}\lambda_{ds} + L_{ds}\lambda_{dr} - (L_{ds} - L_{md})\lambda_{fo}) \quad (8)$$

$$i_{qr} = \frac{1}{(L_{qs}L_{qr} - L_{mq}^2)} (-L_{mq}\lambda_{qs} - L_{qs}\lambda_{qr}) \quad (9)$$

where

$$L_{ds} = L_{ls} + L_{md} \quad (10)$$

$$L_{qs} = L_{ls} + L_{mq} \quad (11)$$

$$L_{dr} = L_{lr} + L_{md} \quad (12)$$

$$L_{qr} = L_{lr} + L_{mq} \quad (13)$$

L_{ls} and L_{lr} are the leakage inductance of the stator and the rotor, whereas L_{mq} and L_{md} are the magnetizing inductances of the d-q axes.

The electromagnetic torque generated can be defined as follows [9]:

$$T_e = \left(\frac{3}{2}\right) \left(\frac{P}{2}\right) (\lambda_{ds} i_{qs} - \lambda_{qs} i_{dr}) \quad (14)$$

where P is the number of poles in the motor. The torque developed and the rated speed are related by [9],

$$T_e = J \left(\frac{2}{P}\right) \frac{d}{dt} \omega_r - T_L \quad (15)$$

where J the inertia of the rotor and the load is, T_L is the load torque. The angle θ_r is calculated by integrating the electrical angular frequency [9].

$$\theta_r = \int_0^t \omega_r dt + \theta_r(0) \quad (16)$$

The three phase voltage supply can be converted by means of park transformation to two phase voltages in stationary reference frame by using the following matrix equation:

$$\begin{bmatrix} v_{qs} \\ v_{ds} \end{bmatrix} = \begin{bmatrix} 1 & 0 & 0 \\ 0 & \frac{-1}{\sqrt{3}} & \frac{1}{\sqrt{3}} \\ 0 & 0 & 0 \end{bmatrix} \begin{bmatrix} v_{an} \\ v_{bn} \\ v_{cn} \end{bmatrix} \quad (17)$$

The relations can then be converted to synchronously rotating frame using the following matrix relation:

$$\begin{bmatrix} v_{qs}^r \\ v_{ds}^r \end{bmatrix} = \begin{bmatrix} \cos \theta_r & -\sin \theta_r \\ \sin \theta_r & \cos \theta_r \end{bmatrix} \begin{bmatrix} v_{qs} \\ v_{ds} \end{bmatrix} \quad (18)$$

Thus the current variable can be obtained by the following:

$$\begin{bmatrix} i_{qs} \\ i_{ds} \end{bmatrix} = \begin{bmatrix} \cos \theta_r & \sin \theta_r \\ -\sin \theta_r & \cos \theta_r \end{bmatrix} \begin{bmatrix} i_{qs}^r \\ i_{ds}^r \end{bmatrix} \quad (19)$$

$$\begin{bmatrix} i_a \\ i_b \\ i_c \end{bmatrix} = \begin{bmatrix} 1 & 0 & 0 \\ \frac{-1}{2} & \frac{-\sqrt{3}}{2} & 0 \\ \frac{-1}{2} & \frac{\sqrt{3}}{2} & 0 \end{bmatrix} \begin{bmatrix} i_{qs} \\ i_{ds} \end{bmatrix} \quad (20)$$

The above equations formulate the dynamic model prerequisites derived from LS PMSM equivalent circuit [5].

5. MATLAB/SIMULINK MODEL

The approach implemented in building the mathematical model on Simulink was the block type. To begin the construction of the LS PMSM, the equations (2-5), (6-9), (14), (15), (17), (18) and (19-20) were constructed by using subsystems.

Every MATLAB subsystem solves each equation in a manner that is easy to use and understand by dragging and placing operators such as sum, integrator, multiplier, etc. The blocks are a standard version included in the MATLAB SimPowerSystems library [10].

The subsystem that implements (2) is shown in Fig.4 a similar approach is taken for (3-5). The subsystem that implements (6) is given in Fig.5 and a similar approach was taken for (7-9). The subsystem that implements (14) is given in Fig.6 and (15) is shown in Fig.7. Further the subsystem that implements (18) is shown Fig.8 and (19 – 20) in Fig.9 uses the MATLAB Kabc matrix that can be defined in the editor.

6. SIMULATION RESULTS

6.1 Case study

The model will simulate the LS PMSM for the following case study: Under no load and load conditions (specifically torque ratings 35Nm and 50Nm below braking torque). The aim is to simulate the machines dynamic behaviours namely speed, torque and current transients against time.

6.2 Model parameters

Table 3: Machine parameters

Parameter	Description	Value
P	Number of poles (known)	4
Rs	Stator resistance	2.6933 Ω
λ	Permanent magnet flux linkage	1.31 Vs
Rr	Rotor resistance	3.994 Ω
Lds	Stator self-inductance in q-axis	0.15278 H
Lqs	Stator self-inductance in d-axis	0.2282 H
Lmd	mutual inductance in d-axis	0.1381 H
Lmq	mutual inductance in q-axis	0.20812 H
Ldr	rotor self-inductance in d-axis	0.15278 H
Lqr	rotor self-inductance in q-axis	0.2282 H
J	moment of Inertia	0.064 kg*m ²

6.3 Experimental results

The experimental results obtained from the TiePie scope when the machine is operating as LS PMSM. The torque versus speed data is plotted in Fig. 11,:

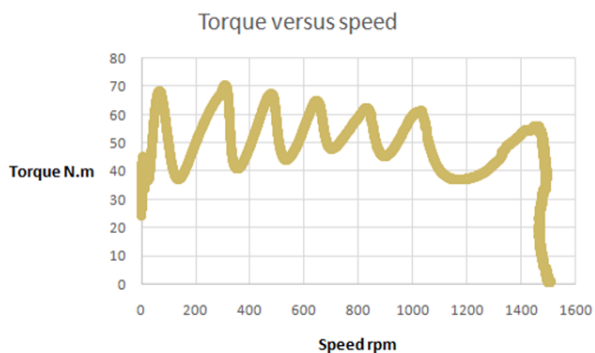


Figure 11: Experimentally measured Torque versus speed transient

It can be seen that the graph does represent the characteristics of a LS PMSM. At steady state the machines speed remains constant at 1500 rpm. Because the total torque production during this state is mainly influenced by the magnet torque the machine operates as

a PMSM. When the load torque is increased from zero up to braking torque (approximately 55N.m) the speed remains constant at approximately 1500 rpm and deviates due to the cage and magnet torque interaction as seen in Figure 11. Once the braking torque is exceeded the machine pulls out of synchronism hence the ripple seen towards a speed of zero rpm operating as an IM.

6.4 Simulation results

The simulations results below are obtained from Matlab Simulink scopes contained in the Mathworks library. Under no load conditions the speed, torque and current transient are as follows in Fig.12.

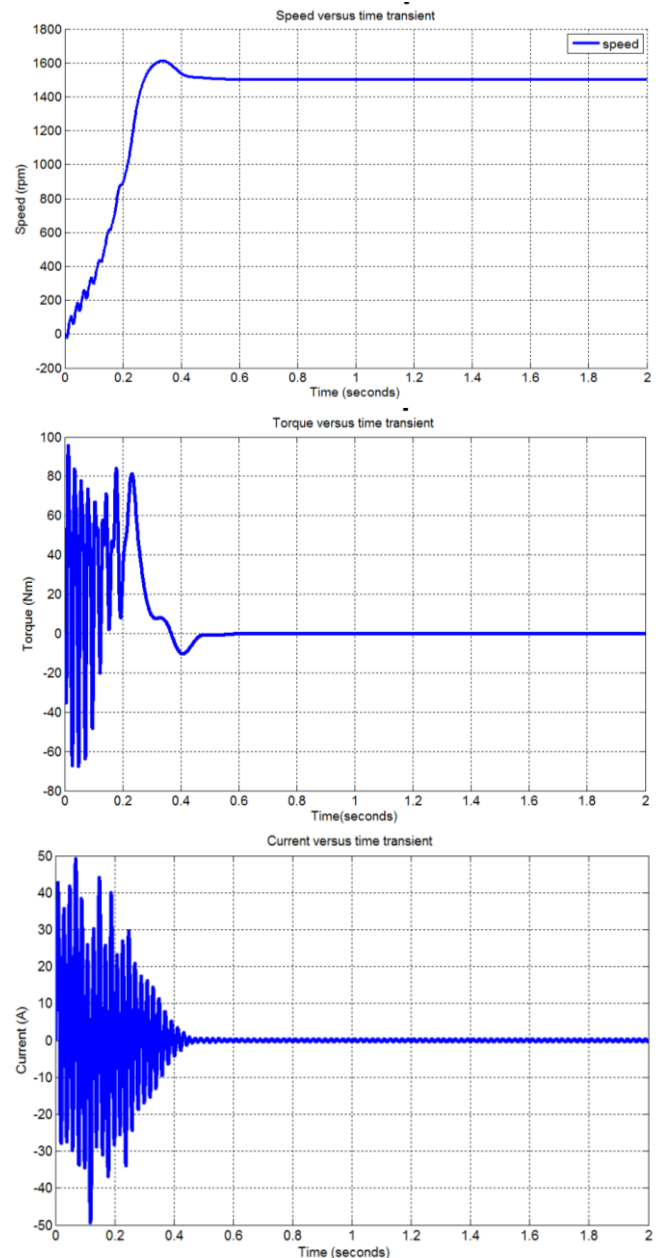


Figure 12: No load speed, torque and current transients

When a load of 35Nm is subjected to the model, the load is simulated as a step signal using a signal builder found in the simulink library. The step signal is drawn between 1 and 1.5 seconds to mimic a load (fan, pump, etc) in reality in Fig.13.

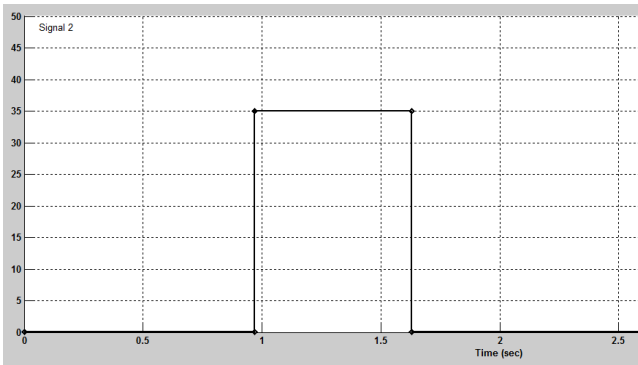


Figure 13: Load of 35N.m drawn on the signal builder

The following speed, torque and current transients are obtained under a load of 35N.m.

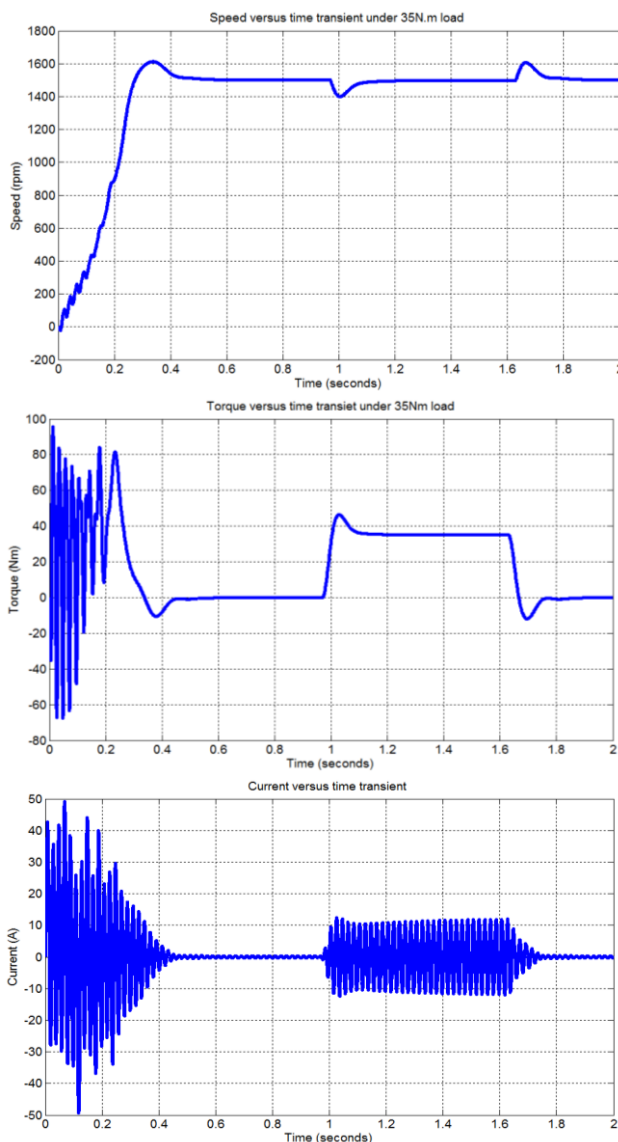


Figure 14: Speed, torque and current transients when a load of 35Nm is subjected to the machine

When a load torque of 35Nm is exerted on the machine just like in Figure 13, it can be seen in Figure 14, during time interval 0.9 seconds and 1.6 seconds the top transient

representing speed has not changed and the speed remains 1500 rpm also seen in Figure 11. It can be seen that based on literature LS PMSM are much more efficient than IM during steady state as the speed remains constant under load conditions. This was possible for load torques 0Nm to 39 Nm.

In Figure 15 below the signal is increased to mimic a load disturbance of 50 Nm the following speed, torque and current transients are obtained.

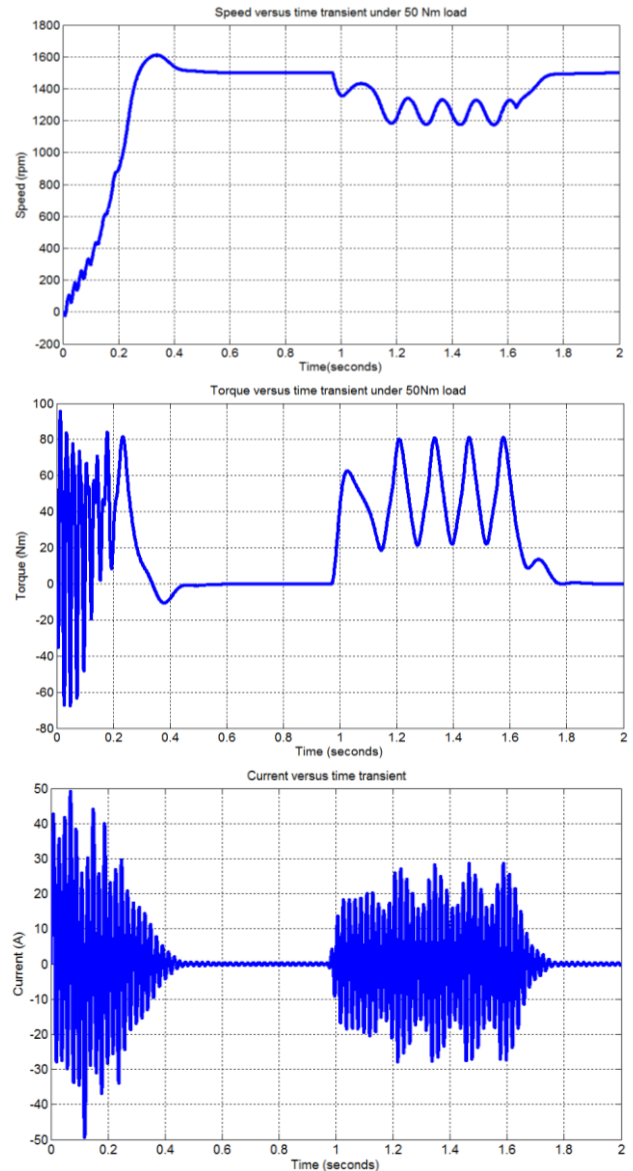


Figure 15: Speed, torque and current transients when a load of 50 Nm is subjected to the machine

In Figure 15, something abrupt occurs in the simulation of the LS PMSM at a load of 50N.m. It is expected from the simulation to show a constant speed up until 55N.m.

Here the in Figure 15 the machine is predicted to be out of synchronism before even reaching it braking torque, which is unlikely to happen with an LS PMSM. This can be explained according to literature that the reluctance torque (pulsating torque) in the middle transient may have a large saliency ratio which may cause the pull out effect

of synchronization. The components that may be accountable for this are X_{ds} and X_{qs} reactance's, measured and calculated during the slip test.

6.4.1 Comparison study

Percentage deviation validation experimental versus simulation results, shown in Fig. 16 below:

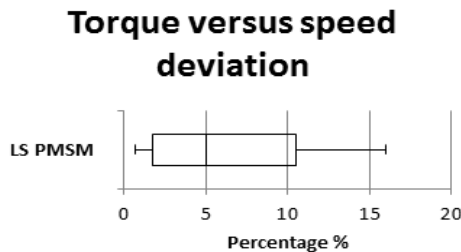


Figure 16: Box whisker plot percentage deviation

When median close to 1st quartile, it means half of the values are close to one another. And that the larger half of the values is scattered and distant from the others.

7. CONCLUSION

The characterization of LS PMSM has been proven to be a difficult task to undertake. The availability of a standard or literature articles on various ways to execute accurate measurements of LS PMSM should be researched. However the methods used in this project can also serve as a starting point to improvements in this regard.

The determination of X_{ds} and X_{qs} parameters has shown significant influences in the simulation of the speed and torque characteristics at certain load capabilities. Due to time constraints a much better method could have been investigated or various methods such as the FEM analysis method could have been used to compare the slip test analysis done in this project.

The characterization overall showed satisfying results when initialized in the MATLAB/SIMULINK simulation software. The parameters mimic the real life behaviour of the machine before any load capability tests were to be performed.

The equations obtained to analytically model the dq axis mathematical derivations according to various literatures have shown that the difference in IM and LS PMSM equations would be in the flux linkages. This is due to the additional permanent magnet component, the voltage and current equations are similar.

The MATLAB/SIMULINK Power System Block set has provided a cost effective approach to studying the dynamic behaviors of electrical machinery. The advantage is the ability to build the equations and connecting them to operate dependently. The results obtained by the MATLAB/SIMULINK model during IM state the simulated results mimicked the experimental

results sufficiently. However, the scope of the project was not to model an IM so the validation and verification process was only done for LS PMSM. It can be seen the transient mimic those of LS PMSM during steady state analysis but due to the pulling out of synchronism issue some parameters need to be thoroughly measured.

LS PMSM has been investigated to predict the dynamic behaviours of the. An analysis has been performed to better understand the dynamic modeling of the machine. The model was validated with the use of simulated versus experimental results and a deviation between 5% -11% was found

8. REFERENCES

- [1] R.T. Ugale, B.N. Chaudhari and A. Pramanik, "Overview of research evolution in the field of line start permanent magnet synchronous motor," in *IET Electrical Power Applications*, vol. 8, no. 8, pp. 141-154, April 2014
- [2] F.W. Merrill, "Permanent magnet excited synchronous motors," in *Electrical Engineering*, vol. 74, Issue: 2, Feb 1955
- [3] T. Modeer, "Modelling and testing of a line start permanent magnet motors," in *Licentiate thesis, monograph*, KTH, School of Electrical Engineering, Stockholm, pp.10-23, September 2007
- [4] IEEE Guide: Test procedures for synchronous machines, Part I— Acceptance and Performance Testing Part II—Test Procedures and Parameter Determination for Dynamic Analysis, IEEE Standard 115, 2009
- [5] Paul. C.K., Oleg, W., Scott, D.D.: "Analysis of electrical machinery", *IEEE Power Eng. Soc.*, 1995
- [6] Azari, M.N., Mirsalim, M.: "Line-start permanent motor synchronization capability improvement using slotted solid rotor". *IET Electr. Power Appl.*, 2013, 7, (6), pp. 462-469
- [7] A.W. Leedy and R.M. Nelms "Simplified Model of an Inverter-Fed Induction Motor for the analysis of a DC Power System", in the Proceedings of the 36th IEEE South-eastern Symposiums on System Theory, 2004, pp. 275-279
- [8] H. Karmaker, "Report on IEEE Standard Working Group P1812 on Guide for testing Permanent Magnet Machines" in *Energy Conversion Congress and Exposition (ECCE)*, 2012 *IEEE* . pp. 2326-2333. Sept 2012
- [9] S.V.Venna, "Mathematical modeling and simulation of permanent magnet synchronous motor" in *International journal of advanced research in electrical, electronics and instrumentation engineering*. Vol.2, Issue 8, August 2013
- [10] Author unknown, year unknown, Asynchronous machine. Available: <http://www.mathworks.com/help/physmod/sys/powersys/ref/asynchronousmachine>

POWER FACTOR CORRECTION AND REACTIVE POWER CONTROL OF A SLIP SYNCHRONOUS PERMANENT MAGNET WIND TURBINE USING VARIABLE FLUX.

A.S. Erasmus, L.L. Amuhaya and M.J. Kamper*

* Department of Electric and Electronic Engineering, Stellenbosch, South Africa.

Abstract: The slip-synchronous permanent magnet wind generator is a new concept wind generator that is able to directly connect to a power grid. In this paper the effect of implementing variable flux in the generator is investigated with regards to grid compliance of a Wind Energy Facility. The main focus of this paper will be the implementation of variable flux in the generator in order to achieve grid compliance in terms of power factor and reactive power control.

Key words: Variable flux, power factor correction, reactive power control, Q-Point control,

1. INTRODUCTION

There is a recent increase in electricity generated from wind turbines in the energy sector. Induction generators (IG) are popular choices among generator types for small scale wind farms. IGs however, have the disadvantage of requiring some form of power electronics to compensate for its power factor. Doubly Fed Induction Generator (DFIG) with a gearbox and a partially rated single stage converter (SSC) is the most common drivetrain technology used today [1]. The Slip-Synchronous Permanent Magnet Generator (SS-PMG) developed in [2] is an alternative, fixed speed wind turbine that doesn't require a gearbox or power electronics in order to be grid connected. The absence of power electronics and gearboxes makes the SS-PMG a robust and affordable generator for low to medium voltage use.

The SS-PMG in Figure 1 is a generator that originated from the PMIG concept of using multiple rotors and can be thought of as two separate PM generators linked by a freely rotating PM rotor. The SS-PMG's IG rotor is short-circuited and mechanically connected to the turbine blades. The generator's stator side directly connects to a 3-phase grid and is a synchronous generator (SG) operating at synchronous speed. The induction generator with its rotor connected to the turbine, operates at a slip speed relative to the synchronous rotor [3].

A performance evaluation of the SS-PMG with respect to the grid code in [4] shows that the voltage, frequency and low voltage ride through (LVRT) capability adheres to grid code standards. However, the SS-PMG doesn't have the required power factor at low loads and has no form of reactive power control, and is thus not completely grid compliant.

Due to the SS-PMG being a permanent magnet (PM) generator the flux is constant and cannot be used for power factor improvement. Hence, typical methods of improving the power factor is by either using an LC compensator or a static VAR compensator. These compensation techniques deliver or absorb reactive power depending on the power

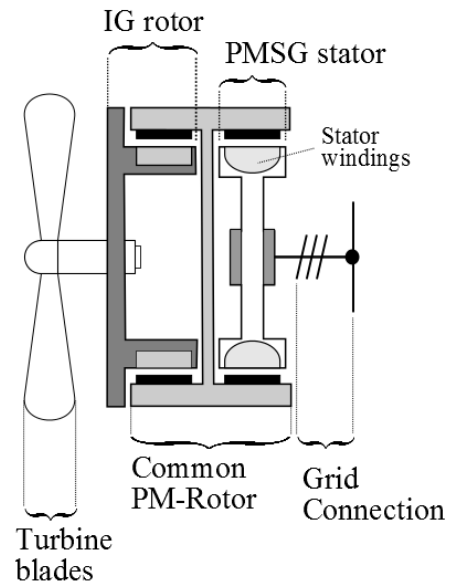


Figure 1: Cross section of SS-PMG

output of the generator.

The focus of this paper is to investigate a different approach to power factor correction with the use of variable flux in the PMSG side of the SS-PMG. Also investigated in this paper is if variable flux can be used as a reactive power control method to achieve complete grid code compliance of the SS-PMG.

Important questions arising with the use of variable flux in the SS-PMG include:

- Would the flux be adjusted physically in the generator?
- If it is possible to implement variable flux, how much should the flux be adjusted in order to make the SS-PMG grid compliant?
- How much reactive power would the variable flux compensate?
- If there is need of control systems or power electronics, how robust and cost effective would it be?

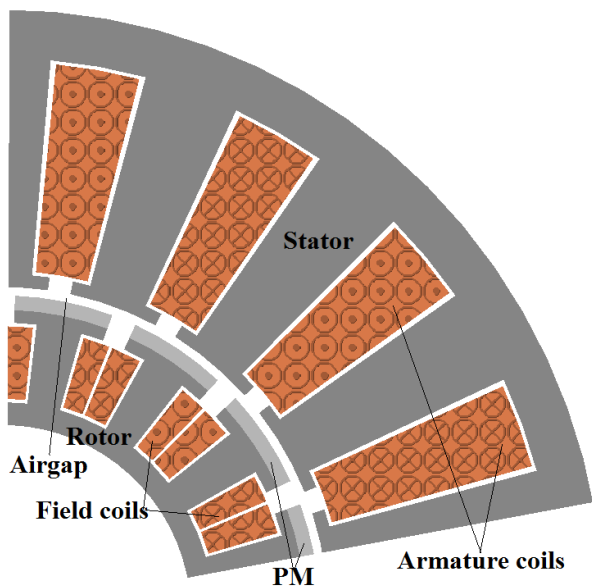


Figure 2: A double layer non-overlap synchronous generator capable of flux variation.

2. VARIABLE FLUX.

Electrically excited synchronous generators are widely employed due to their capability of flux variation. In the recent past permanent magnet synchronous generators (PMSGs) have been preferred options due to their efficiency, reliability, higher power density and size reduction as in the SS-PMG. PMs produce a constant PM excitation inhibiting their flux variation performance without the use of power electronics. Additional field coils can be included together with the PM excitation to have a double excited synchronous generator (DESG) as shown in Figure 2.

The magnetization sources of the PM and field coils are arranged in series, [5]. The PMs provide the constant flux to be used in normal operation of the generator, whereas the field coils provide means of flux variation using a simple 3 level switch. Depending on the direction of the DC field current, flux variation is achieved. The PMs and the field coils can either be located in the rotor, as shown in Figure 2, or in the stator. With excitations being located in the rotor, slip-rings and brushes are necessary, whereas for stator located excitations, the generator is brushless.

3. GRID CODE REQUIREMENTS.

In 2012, NERSA published a grid code [6], that provided a set of guidelines that all wind energy facilities (WEFs) must comply with in order to connect to the South African distribution system (DS) or transmission system (TS). The grid code specifies three categories of WEFs which are divided based on their power output. *Category A* (low voltage) includes facilities with a rated power of less than 1 MVA and *category B* (medium voltage) facilities with a rated power of more than 1 MVA but less than 20 MVA.

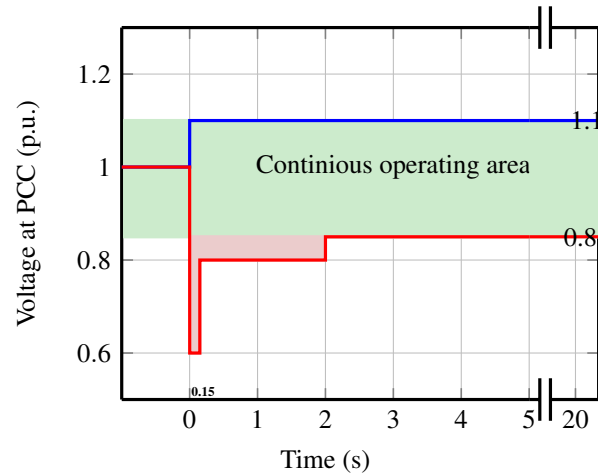


Figure 3: Fault Ride Through Capability for a category A WEF.

The grid code requirements are separated into six different categories but this paper will only focus on three, namely: (i) voltage and frequency requirements, (ii) power factor requirements and (iii) reactive power control requirements. These categories are selected because the SS-PMG lacks in meeting the requirements [6], of the grid code.

3.1 Voltage requirements

Normal or continuous operating conditions at the point of common coupling (PCC) is when the facility is connected to a stable power grid. Category A facilities should be capable of operating within a range of -15% to +10% of nominal voltage and within the network frequency range of 47 Hz to 52 Hz. Category B WEFs connected to the DS are required to operate within a range of $\pm 10\%$ of nominal voltage and also within the same frequency range as a category A facility.

3.2 Power factor requirements

Category A facilities have different requirements than category B facilities in terms of reactive power output. A category A facility is required to supply power with no less than 0.95 lagging and 0.95 leading power factor, whereas a category B facility is required to supply power with a power factor no less than 0.975.

When the WEF is starting up, it should supply reactive power no more than 5% of its rated power for 5 seconds. Both WEFs (A and B) should be able to supply the required power with the correct power factor from a minimum of 0.2 p.u. rated power up to full rated power output.

3.3 Reactive power control

Category B facilities are required to deliver an on-demand amount of reactive power (Q-point control), power factor and voltage if requested by the national service provider. The service provider can demand a steady supply of

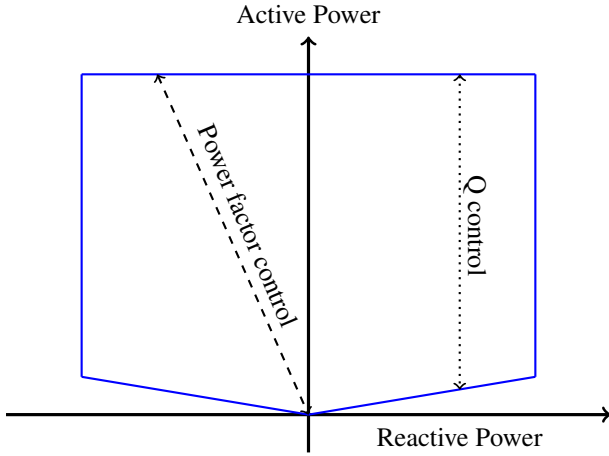


Figure 4: Q-point and power factor control.

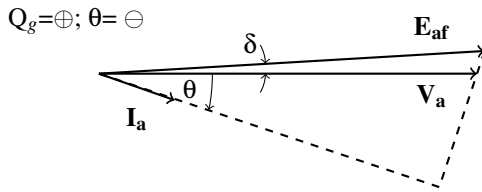


Figure 5: SS-PMG phasor diagram at 1.0 p.u. grid voltage and low torque loads.

reactive power to be supplied by the WEF with an accuracy of 1 kVAR and also demand either a leading or lagging power factor within the above mentioned grid code requirements shown in Figure 4. The service provider can also request a voltage value within range of the grid code requirement.

4. SLIP-SYNCHRONOUS OPERATION.

At a lagging power factor, the reactive power is positive and delivered to the network. Simulations show that the SS-PMG has a lagging power factor at low torque loads, delivering reactive power to the network. When the power factor is leading and has a positive current angle, the reactive power is negative and absorbed from the network. Figures 5 to 7 show the different power factor phasor diagrams and Figure 8 shows a single phase circuit of the grid connected SS-PMG.

Shown in Figure 5, at 1.0 p.u. grid voltage, the generator voltage E_{af} is designed to be the same magnitude as the line voltage V_a . Due to a varying grid voltage, E_{af} is slightly larger or smaller than V_a . At low torque load, the voltage angle δ is small and the generator has a low power factor, delivering reactive power ($Q_g = +$) to the grid because of a negative current angle ($\theta = -$), assuming $E_{af} > V_a$. The power factor at low torque loads will change greatly if the grid voltage changes slightly and the generator can suddenly go from a low lagging power factor to a low leading power factor. By reducing the

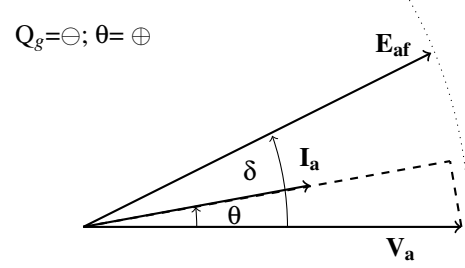


Figure 6: SS-PMG generator phasor diagram at 1.0 p.u grid voltage and high torque loads.

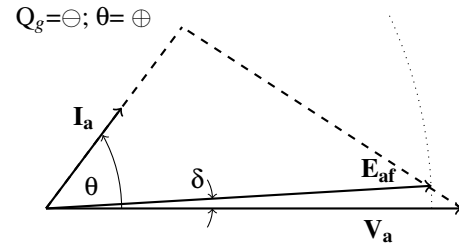


Figure 7: SS-PMG generator phasor diagram at 1.1 p.u. grid voltage and low torque loads.

generator voltage slightly, the power factor in this case can be corrected.

When the torque load is increased, as shown in Figure 6, together with the current, the voltage angle also increases. This results in the generator voltage being less than grid voltage ($E_{af} \cos(\delta) < V_a$), and the generator absorbs reactive power ($Q_g = -$) from the grid leading to a positive current angle ($\theta = +$). By increasing the generator voltage slightly, the power factor can be corrected.

At 1.1 p.u. grid voltage, as shown in Figure 7, the generator voltage remains the same but the line voltage is increased by 10%. At low torque loads and small current angles, the generator absorbs reactive power from the grid and has a positive current angle. At high torque loads the current is increased but its angle remains positive. Although the power factor has increased, the generator still absorbs reactive power from the grid. By increasing the generator voltage the power factor can be corrected.

At 0.9 p.u. grid voltage, the generator voltage yet again remains the same but the grid voltage has decreased by 10%. At low torque load the voltage angle is small and with the decreased grid voltage, the generator delivers reactive power. The current angle is now negative and the power factor is low. At a higher torque load the voltage angle increases with the current, still delivering reactive power at a negative current angle. By reducing the generator voltage the power factor can be corrected.

The effect of using double layer (DL) versus single layer (SL) non-overlap winding generators with a variation in grid voltage is given in Table 1. Non-overlap windings can be single or double layer and is shown in [3] and

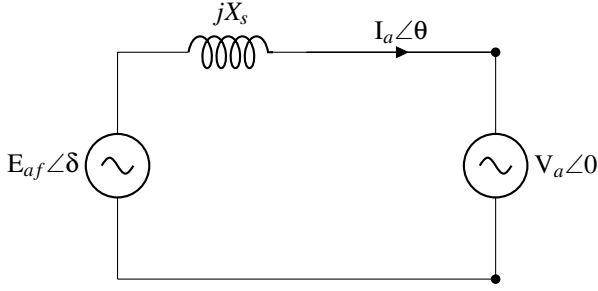


Figure 8: Per phase equivalent circuit diagram of the grid connected SS-PMG.

Table 1: Voltage and power factor angles at different grid voltages and different generator non-overlap windings.

V_a (p.u.)	X_s (p.u.)	θ	δ
0.9	0.5 (SL)	7.02°	33.74°
0.9	0.25 (DL)	-12.36°	16.127°
1.0	0.5 (SL)	15°	30°
1.0	0.25 (DL)	7.385°	14.47°
1.1	0.5 (SL)	24.7°	27°
1.1	0.25 (DL)	29°	13.14°

typically have reactance values of 0.5 p.u. and 0.25 p.u. for single and double layer respectively. With the active power ($P= 1.0$ p.u.) and generator voltage ($E_{af}= 1.0$ p.u.) fixed at rated values the voltage and power factor angle is calculated using

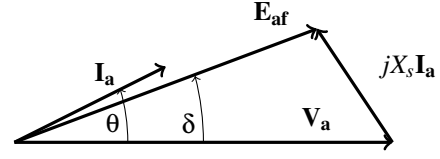
$$P = \frac{V_a E_{af}}{X_s} \sin(\delta) \text{ (p.u.)} \quad (1)$$

$$I_a \angle \theta = \frac{E_{af} \angle \delta - V_a}{jX_s} \text{ (p.u.)}, \quad (2)$$

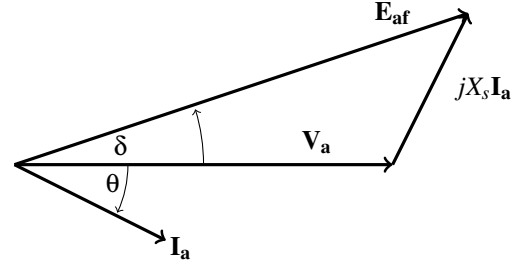
with the grid voltage varied by 10%. This shows a DL generator has a larger power factor angle, but has a smaller voltage angle than a SL generator.

5. SIMULATION RESULTS OF THE SS-PMG WITH VARIABLE FLUX

An SS-PMG model was developed using VHDL-AMS and simulated in ANSYS Simplorer. The simulations are based on the requirements for a category B facility as it requires reactive power control. Connecting the model with variable flux in a grid connected circuit can allow accurate dynamic evaluations of the generator output. Controlling the stator flux (λ_{ms}) of a synchronous generator effectively changes the magnitude of the generator voltage E_{af} . By decreasing the flux in this case, the generator voltage is less than the grid voltage $|E_{af}| < |V_a|$, thus the generator is under-excited and absorbing reactive power from the grid. By increasing the flux so that $|E_{af}| > |V_a|$, the generator is over-excited and delivering reactive power to the grid. Figure 9 shows the effects of variable flux on the generator voltage of a synchronous generator.



(a)



(b)

Figure 9: (a)Under-excited and (b)over-excited generator phasor diagrams using variable flux.

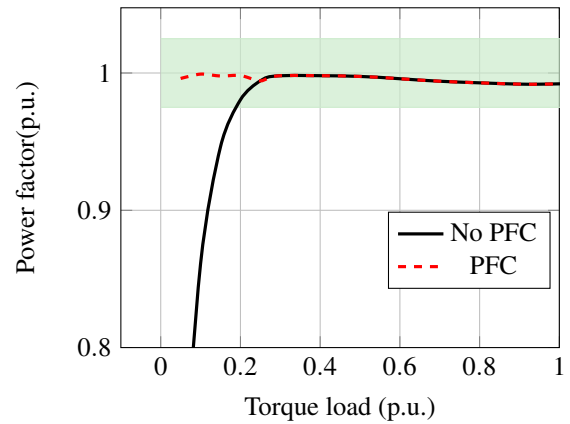


Figure 10: Simulated results of PFC at nominal grid voltage using variable flux.

5.1 Voltage control

Implementing flux control implies control of the generated voltage as shown in Figure 9. The generator voltage of a synchronous machine is expressed as a function of the stator flux and by varying the flux, the generator voltage is varied increased. This allows for effective voltage control of the SS-PMG.

5.2 Power factor control

Power factor control is where the service provider demands leading or lagging reactive power within limitations of the grid code (no less than 0.975) and can be implemented using variable flux. The power factor of the SS-PMG at low torque loads does not meet grid code requirements as it is less than 0.975 leading or lagging. Figure 10 shows that by using variable flux, effective power factor correction can be achieved.

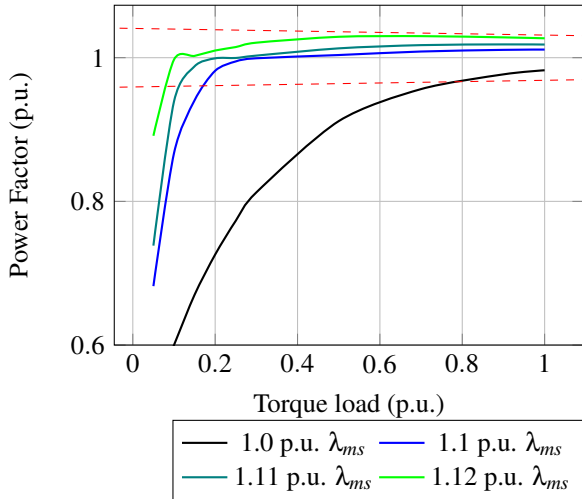


Figure 11: SL power factor at 1.1 p.u. grid voltage with variable flux as a parameter.

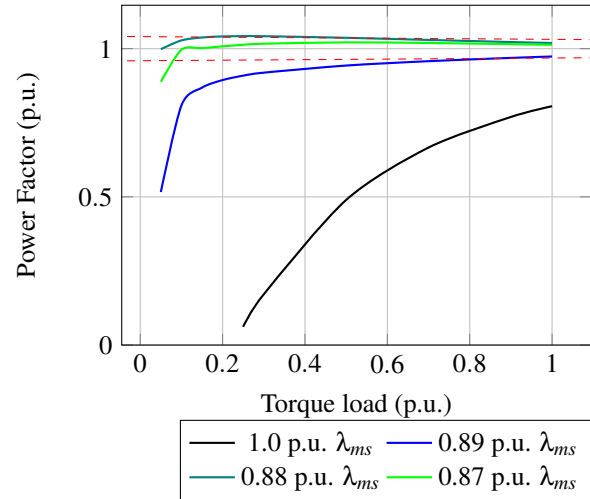


Figure 13: SL power factor at 0.9 p.u. grid voltage with variable flux as a parameter.

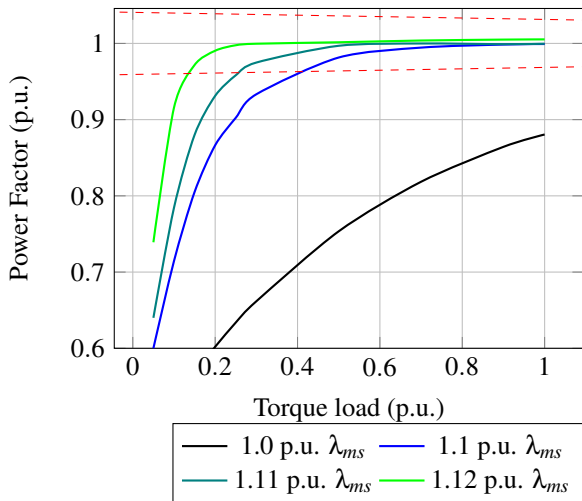


Figure 12: DL power factor at 1.1 p.u. grid voltage with variable flux as a parameter.

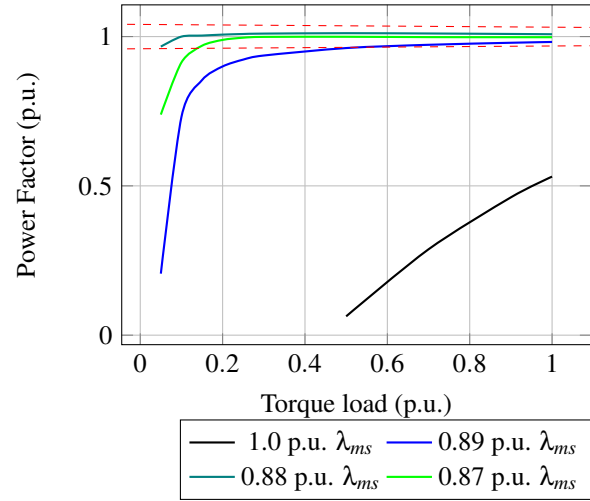


Figure 14: DL power factor at 0.9 p.u. grid voltage with variable flux as a parameter.

The generator model was simulated as both single and double layer non overlap winding models. The aim is to observe if the addition of only a constant flux value could improve the grid compliance of the generator.

The results of the simulations reveal the effectiveness of using variable flux to correct the power factor for both DL and SL non-overlap windings. Simulations at maximum and minimum grid voltages shown in Figures 11- 14 reveal a significant improvement of the SS-PMG's power factor with variation of the flux and also confirm that the DL has a lower power factor than the SL non-overlap windings.

At 1.1 p.u. grid voltage, the generator absorbs reactive power. By increasing the stator flux, the generator voltage is also subsequently increased. This results in a power factor improvement as seen by the network for both SL and DL non-overlap windings, as shown in Figures 11 and 12.

At 0.9 p.u. grid voltage the generator delivers reactive power and by reducing the stator flux the generator a better power factor seen by the network for both SL and DL non-overlap windings as shown in Figures 13 and 14.

If the generator is used with the a SL non-overlap winding, the generator power factor will be completely grid compliant if the flux can be adjusted between 0.87 and 1.1 per unit. For a DL non-overlap winding, the results show significant power factor improvement with variable flux. In order to meet grid code requirements, the double layer generator's flux should be able to be adjusted between 0.88 and 1.12 per unit.

5.3 Q-point control

Q-point control as explained in Figure 4 shows variable flux can enable the generator to supply a fixed amount of reactive power regardless of real power output. A simple

case where Q-point control is evaluated by varying flux for both DL and SL non-overlap windings. This maintains a reactive power output of 0.1 p.u. of the rated power with respect to an increasing torque load. Figure 15 shows that the DL requires less flux variation than a SL non-overlap winding.

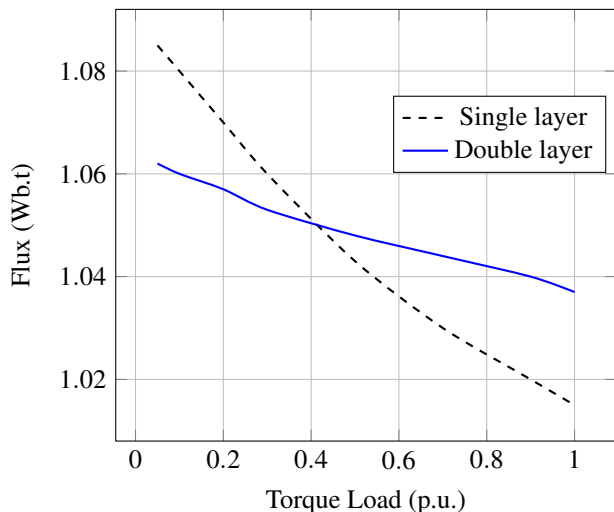


Figure 15: Q point control at $Q = 0.1$ p.u. using variable flux for SL and DL non-overlap windings

6. CONCLUSION

The flux variation can be achieved by having either a positive or negative field current produced by placing rotor field windings.

The simulation results indicate that by implementing variable flux on the SS-PMG allows for grid compliance for facilities of up to 20 MVA. All grid code requirements can be achieved by using variable flux of about $\pm 12\%$ to correct the power factor at low torque loads as well as allowing for reactive power control.

A simple and affordable three phase switch is used to switch between adding or reducing the flux by 12%. If the flux needs to be varied in smaller increments between 0 and 12% a power electronic circuit is used, making this method simple and cost effective.

Figure 15, shows that variable flux is an effective implementation of Q-point control, being able to compensate up to 1 kVAr of reactive power.

REFERENCES

- [1] Hansen, A. and Hansen, L.: Wind turbine concept market penetration over 10 years. *Wiley Online Library*, 2006.
- [2] Potgieter, J. and Kamper, M.: Design of new concept direct grid-connected slip-synchronous permanent-magnet wind generator. *IEEE Transactions of industry applications*, 2012.
- [3] J.H.J Potgieter, A.N Lombard, R.W. and Kamper, M.: Evaluation of a permanent magnet excited induction generator for renewable energy applications. *Southern African Universities Power Engineering Conference*, pp. pp. 299–304, 2009.
- [4] U. Hoffmann, P.B. and Kamper, M.: Direct-grid connection of a slip-permanent magnet wind turbine generator. *Energy Conversion Congress and Exposition (ECCE)*, 2011.
- [5] D. Fodorean, A.D. and Viorel, I.: A double excited synchronous machine for direct drive application design and prototype tests. *IEEE Transactions on Energy Conversion*, vol. 22, no. 3, pp. 656– 665, 2007.
- [6] Mchunu, T. and Magoro, B.: Grid code requirements for wind energy facilities connected to distribution or transmission systems in south africa. Tech. Rep., Nersa, 2012.

A HIGH PERFORMANCE CONCENTRIC MAGNETIC GEAR

A. Matthee*, S. Gerber* and R-J Wang*

* Dept. of Electrical and Electronic Engineering, Stellenbosch University, Stellenbosch 7600
E-mail: alexandermatthee@gmail.com; sgerber@sun.ac.za; rwang@sun.ac.za

Abstract: This paper is concerned with the design improvement of a previously designed magnetic gear with emphasis on performance optimization and the mitigation of end-effects. The performance analysis results show approximately 70% reduction in losses at full load and a 40% increase in maximum torque capability. New flux modulator manufacturing techniques, which yielded great results, are discussed.

Key words: Magnetic gears, end-effects, permanent magnet, design optimization

1. INTRODUCTION

Magnetic gears are receiving more attention in recent years. Among different types of magnetic gears, the concentric magnetic gear (MG) has been the focus of research and development. With a torque density comparable to mechanical gears, concentric MGs also demonstrate other distinct benefits such as high efficiency, low noise, low maintenance and overload protection. The potential applications for this novel gear technology include industrial drives, material handling, electric vehicles and wind turbine applications [1, 2]. This paper reports the design improvements of a previously designed concentric MG [3], which shows inferior torque and efficiency performance when compared with the design values. Design recommendations mentioned in [4] as well as other possible solutions will be investigated.

2. PRINCIPLE OF OPERATION

High-order magnetic flux harmonics are usually undesirable as they are the sources of torque ripple or loss, heating and decreased efficiency in electrical machines. In the case of the magnetic gear, harmonics are used to an advantage by making use of specific characteristics of these harmonics to realize a gear action between input and output rotors. Fig. 1 displays a cross-sectional view of a concentric-type magnetic gear, which consists of three concentric elements, namely, outer low-speed (LS) rotor, inner high-speed (HS) rotor and a flux modulator between them. If the flux modulator is kept stationary, the gear ratio G_r is governed by the following equation [5]:

$$G_r = \frac{q - p_h}{p_h} = \frac{p_l}{p_h} \quad (1)$$

where q is the number of modulator segments, p_l and p_h are the pole-pairs of the LS and HS rotors respectively. The fundamental operation principle of a magnetic gear is the modulation of fluxes from both high and low speed rotors. Fig. 2 shows the flux density waveform generated only by the magnets of the LS rotor in the HS side air-gap and its harmonic composition. It can be clearly seen that due to flux modulation there exists a prominent 2nd order space harmonic in the HS air-gap, which matches the HS

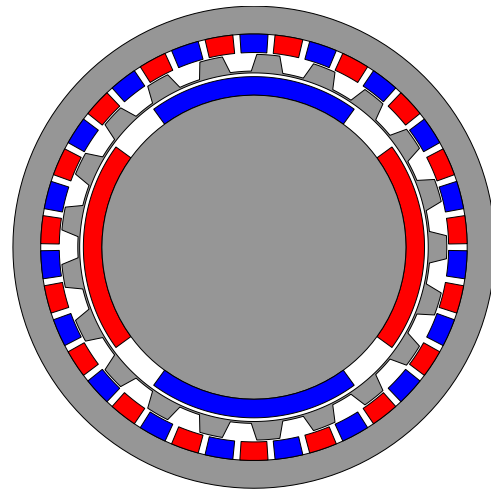


Figure 1: The layout of a concentric magnetic gear

pole pairs. Similarly the air-gap flux density waveform generated by only HS magnets in the LS air-gap and its harmonic composition is shown in Fig. 3. It can be observed that a large 21st order space harmonic, which corresponds to the LS pole-pairs, is present in the LS side air-gap as a result of flux modulation.

3. DESIGN IMPROVEMENTS

3.1 Problems with the Previous Design

The previously developed magnetic gear demonstrates relatively poor performance when compared with the calculated results. A recent study [4] shows that the performance reduction of the MG is mainly caused by the following design issues:

- the severe end leakage flux in the supporting structure not only reduces the magnitude of the torque producing harmonics, but also causes excessive eddy current loss in the end plates, which reduces the gear efficiency
- the stack length of the flux modulator is longer than the active PM length, which increases the flux leakage in the end region and reduces the peak torque capacity

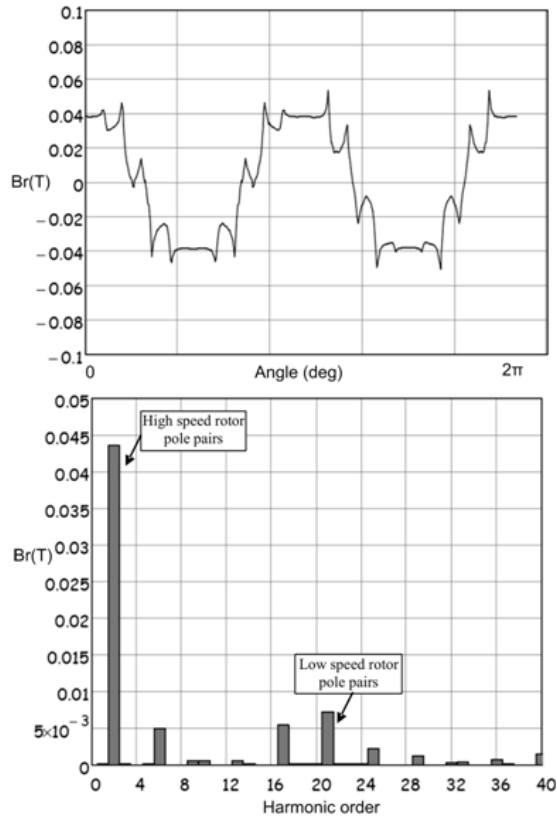


Figure 2: Flux density in HS Air-gap due to LS magnets [1]

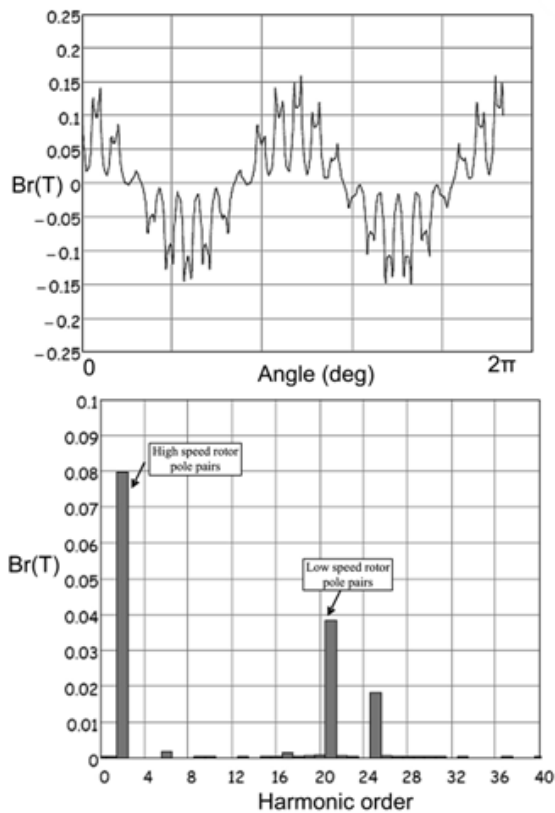


Figure 3: Flux density in LS Air-gap due to HS magnets [1]

Table 1 gives the key design specifications of the previously developed magnetic gear [3].

Table 1: Design specs of the magnetic gear prototype

Parameter	Value
Pole pairs on high speed rotor	2
Pole pairs on low speed rotor	21
Number of stator segments or pole-pieces	23
Outer radius of low speed yoke, mm	57.5
Inner radius of low speed yoke, mm	52.5
Outer radius of stator segments, mm	52
Inner radius of stator segments, mm	45
Outer radius of the high speed rotor, mm	44.3
Stack length, mm	40
Permanent magnet thickness, mm	5
Permanent magnet grade	N35

3.2 Objectives and Design Approach

The objective of the design improvements is to optimize the output torque capability of the previously developed magnetic gear. 2D FEM simulations have been applied to calculate the peak torque of the MG and analyze the flux distribution associated with different flux modulator designs. Several flux modulator topologies are evaluated and the most promising one is then selected for further design optimization. The optimum design obtained from 2D FEM optimization is modeled using 3D FEM for more accurate performance computation.

A commercial optimization software VisualDoc has been used together with SEMFEM, an in-house developed FEM package, for the optimization of the magnetic gear. A Python script is used to read the design variables and update the FE model. Fig. 4 shows the flowchart of the design optimization process. The optimized modulator design illustrated in Fig. 5 achieves a peak torque of 54.6 Nm (based on 2D FE calculation), which is about 2% improvement when compared with the previous design.

3.3 3D FEM Analysis

Since a typical magnetic gear exhibits no magnetic periodicity, a full FE model is required, which implies that FE modeling of an MG in 2D is already computationally expensive, not even to mention 3D FE analysis. 3D FEM simulation is used only to verify 2D FEM design as these can be very computationally expensive. Since 2D FEM simulations neglects end-effects of a magnetic gear, 3D FE simulations always result in a lower but more accurate torque output value. The 3D FEM model of the final design can be seen in Fig. 6. The previously constructed prototype has an extended stack length of 45 mm, which intensifies the flux leakage in the end regions, causing a reduction in the peak torque. The improved design, with an optimal stack length of 40 mm, increases the peak torque to 48.6 Nm (3D FE results), a 9.95% increase over the previous prototype.

4. CONSTRUCTION OF THE PROTOTYPE

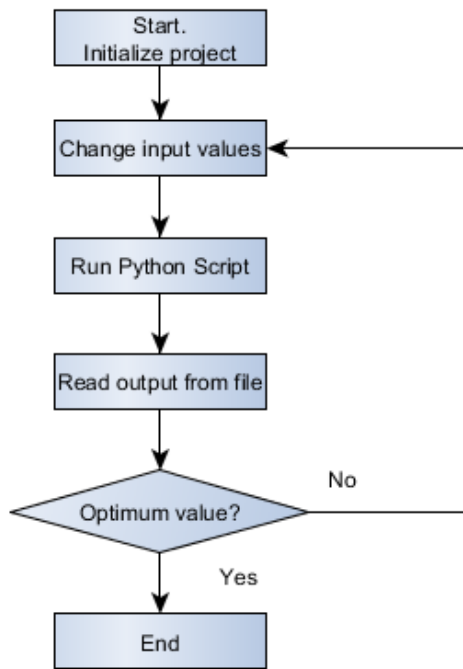


Figure 4: Flowchart of the optimization process

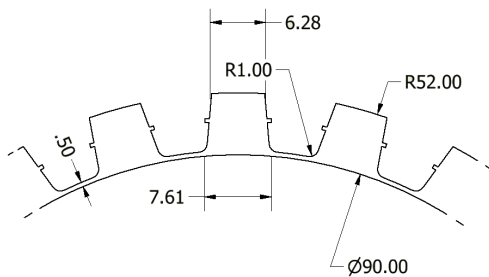


Figure 5: Section of the final modulator design

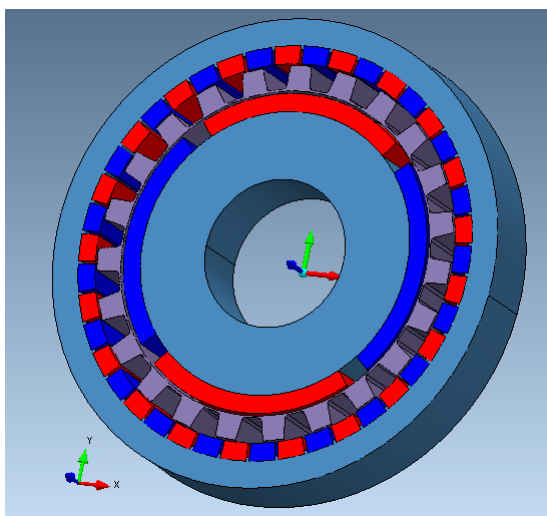


Figure 6: Auxiliary view of 3D FE model

The mechanical design changes have been effected with an aim to mitigate losses incurred in the gear due to end-effects. In the previous design the modulator was mounted directly on the mild steel high-speed cover plate as shown in Fig. 7, which has been identified as one of the major causes for excessive loss during high speed operation [4]. The new modulator design is constrained by the previous design's magnet layout. The magnets and shafts are re-used due to the limited time available to complete this project. The outer and inner radii of the modulator are therefore fixed but all other dimensions are free to be optimized. It has been shown in [4] that the thin bridges connecting the segments of the flux modulator increase the output torque and reduce unwanted harmonics. The final modulator retains this design feature.

In addition, a new casing is made from aluminum which has a much lower relative permeability. The cover plates of both high-speed and low-speed sides are remade using aluminum. The low speed side cover plate is slightly lengthened to better align the modulator to the magnets. This is necessary due to the newly added support ring. The low-speed yoke, which supports the low speed magnets, effectively shields the low speed cover plate from the majority of magnetic fields. The high speed cover plate and surrounding structure are the focus of the mechanical design improvement. As the casing has to support the modulator, which is a high flux density region, the casing is moved further away from the modulator segments by 15.5 mm. This increase in distance decreases the strength of magnetic fields that penetrate the casing (See sectional view of gear in Fig. 7).

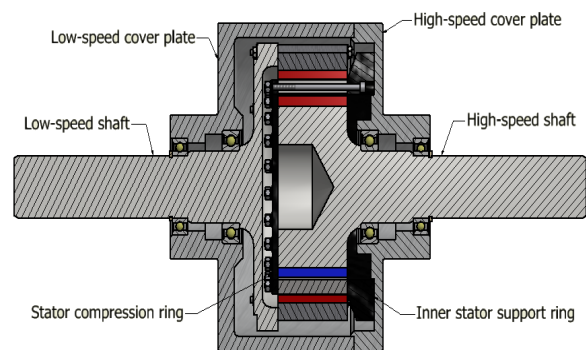


Figure 7: Sectional view of the final magnetic gear

The modulator, consisting of laminations, requires a mould to be positioned accurately. Previously the laminations were laser cut to specification and assembled on the mould before the epoxy bonding for added structural strength. A new process is followed whereby the lamination are cut larger than designed which allows a key groove to be added as shown in Fig. 8. This greatly simplifies the assembling process and allows the correction for possible dimensional imperfections. Once epoxy is applied and cured the entire modulator is machined to specification.

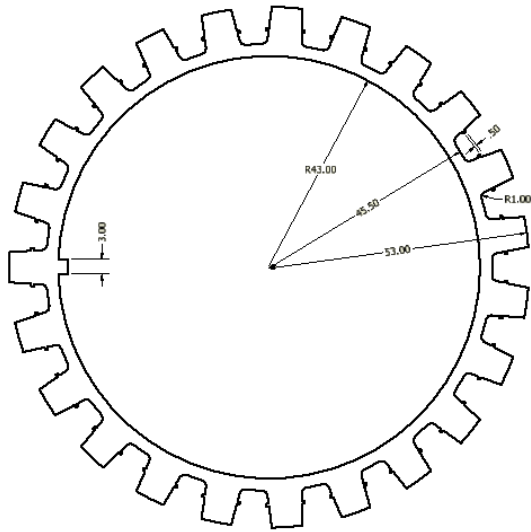


Figure 8: Cross-section of the final modulator design

The stainless steel rings previously used to compress and mount the modulator are replaced by Vesconite plastic supporting structures. Vesconite is a high load bearing plastic with dimensional stability but is also easy to machine. It is therefore chosen as the ideal non-magnetic material to use for supporting the modulator. The modulator inner support ring is mounted securely to the high-speed cover plate with 10 stainless steel bolts.

5. PERFORMANCE EVALUATION

In this section the experimental tests of the new magnetic gear prototype is described. Results obtained in these tests will be compared to those of the previously designed magnetic gear. Fig. 9 is a photo of the test setup.

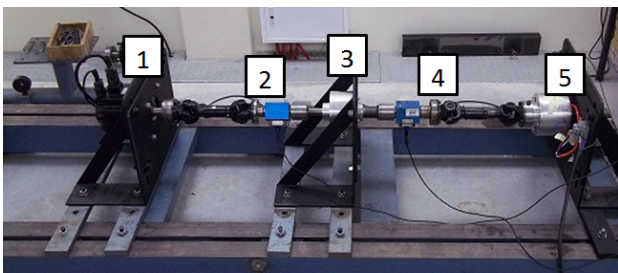


Figure 9: The test setup, where 1 - brushless DC motor drive, 2 - torque sensor, 3 - magnetic gear, 4 - torque sensor, 5 - pseudo direct drive generator as load machine.

5.1 No-Load Test

This test determines the no-load loss (including wind friction and core losses) in the magnetic gear. As shown in Fig. 10, the no-load loss of the previous magnetic gear is 157 W at 1700 rpm while this loss reduces to only 49 W at the same speed for the new gear design. This works out to be 68.7% reduction in losses at the mentioned speed. It is evident that the new magnetic gear prototype has much

reduced no-load loss when compared with the previously designed one.

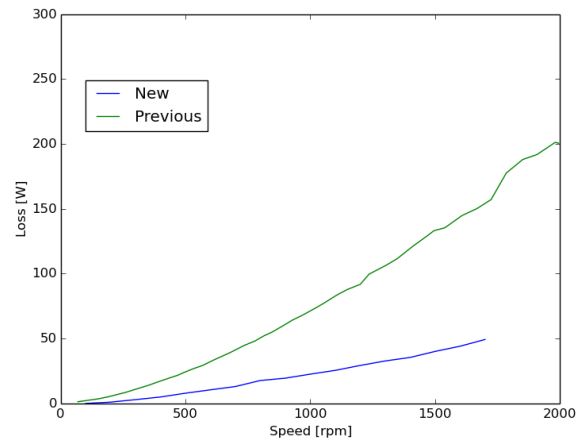


Figure 10: Comparison of no-load loss between the previous and the improved magnetic gears

5.2 Load Tests

The loss in a magnetic gear is mainly affected by its operation frequency and thus its rotational speed. The load placed on the gear has little effect on the losses of the gear. The load tests are performed at different speeds ranging from 100 rpm to 1700 rpm (on high speed side). At every speed interval the load is adjusted to vary the torque on the low speed shaft at intervals of 10 Nm starting at 10 Nm to a maximum value of 40 Nm. Fig. 11 shows the output power as a function of speed for different levels of output torque. The magnetic gear achieves a power output of 680 W at 160 rpm and 40 Nm torque.

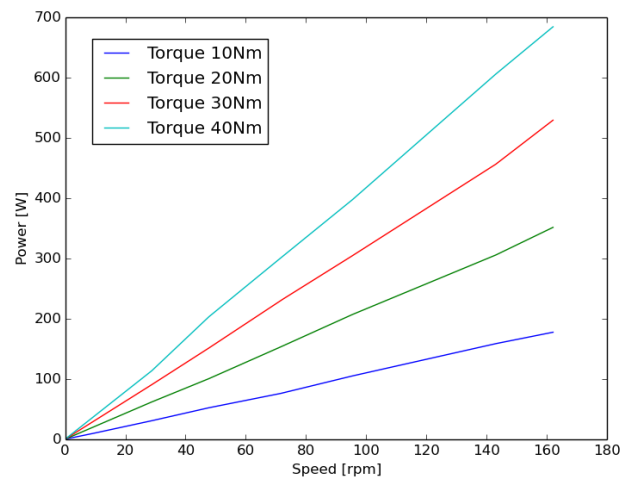


Figure 11: The output power of the magnetic gear as a function of speeds for different loads (on low speed side)

The efficiency map of the magnetic gear at different operation conditions is given in Fig. 12. It can be observed that the efficiency of the magnetic gear at 4 Nm and 1500 rpm (high speed side) is about 95%. Comparing with

the previous magnetic gear, the efficiency of the improved magnetic gear shows a marked improvement.

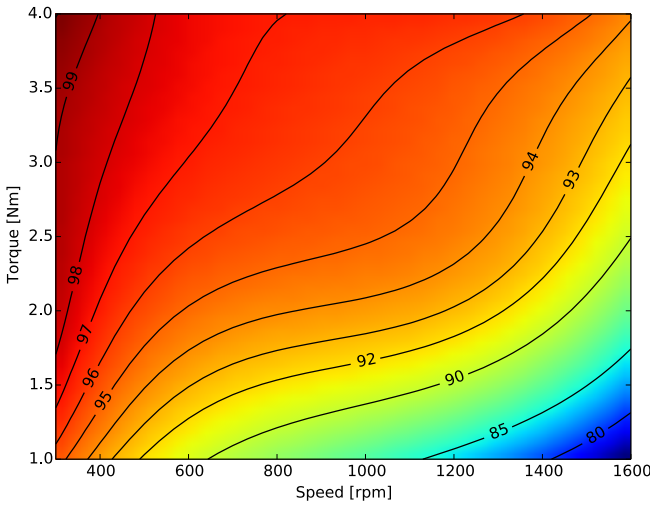


Figure 12: The efficiency map of the magnetic gear at different operation conditions (on high speed side)

5.3 Stall Torque

For the stall torque test the high-speed shaft of the magnetic gear is clamped and forced to a stationary position. A metal bar is attached to the low-speed side of the magnetic gear via a torque sensor to manually apply the torque. The stall torque is the maximum torque that can be transferred before the magnetic poles slip. This kind of pole-slipping under overload conditions offers inherent protection to a magnetic gear. The measured stall torque value of the new magnetic gear prototype is 46.2 Nm, which is about 13.2 Nm (or 40%) more than that of the previously designed magnetic gear [4]. Table 2 compares the measured and predicted stall torque values of the magnetic gear. It is clear that 3D FEM gives more accurate prediction than 2D FEM.

Table 2: Measured and predicted stall torque values

Method	Value	Diff%
Measured	46.2 Nm	-
3D FEM	48.6 Nm	5.2%
2D FEM	54.6 Nm	18.2%

6. CONCLUSION AND RECOMMENDATION

This paper describes the design improvements on a previously designed concentric magnetic gear. By optimizing the flux modulator and carefully considering the design aspects affecting 3D end-effects, the overall performance (efficiency and torque capability) of the magnetic gear has been significantly improved. The improved prototype has been constructed and experimentally evaluated. The measured results compare favorably with the predicted ones. The distinct features and high performance of magnetic gears make them an attractive alternative to conventional mechanical gears.

6.1 Recommendation for Future Work

Although the improved prototype shows a significant reduction in no-load loss, leakage magnetic fields are still present in the region of the high-speed casing that supports the modulator. Reducing this end leakage field will further improve the overall efficiency of the magnetic gear, especially at higher operation speeds. Possible solutions include increasing the distance between the modulator segments and the high-speed casing or constructing the entire high-speed casing from a non-magnetic material such as Vesconite.

Both 2D and 3D FEM simulations show that a slightly higher output torque can be achieved for the bridged modulator segments without the curved corners. These curved corners were added to the design to enhance the structural strength of the lamination, which in the end appears to be unnecessary.

For the previously constructed magnetic gear the N35H NdFeB magnets were used. Using stronger magnets in the design will easily improve the torque density of the magnetic gear by a significant margin.

ACKNOWLEDGMENT

This work was supported in part by Eskom Tertiary Education Support Program (TESP), Stellenbosch University and the National Research Foundation (NRF).

REFERENCES

- [1] R-J Wang, S. Gerber, "Magnetically geared wind generator technologies: Opportunities and challenges", *Applied Energy*, 136:817-826, Elsevier, 2014.
- [2] N. Niguchi, K. Hirata, M. Muramatsu, and Y. Hayakawa, "Transmission Torque Characteristics in a Magnetic Gear", *XIX International Conference on Electrical Machines (ICEM)*, 6p, Rome, Sept. 2010.
- [3] L. Brönn, R-J Wang, M.J. Kamper, "Development of a shutter type magnetic gear", *Proc. of the 19th Southern African Universities Power Engineering Conference*, pp.78-82, Wits University, Johannesburg, Jan. 2010.
- [4] S. Gerber and R-J. Wang, "Evaluation of a Prototype Magnetic Gear", *IEEE International Conference on Industrial Technology (ICIT)*, pp.319-324, Cape Town, Feb. 2013.
- [5] K. Atallah, S. Calverley, and D. Howe, "Design, analysis and realisation of a high-performance magnetic gear", *IEE Proc. Electric Power Applications*, 151(2):135-143, Mar. 2004.

IMPLEMENTATION OF A ROTOR ANGLE MEASUREMENT METHOD USING SYNCHROPHASOR TECHNIQUES

BWD Berry^{*,**}, MA Edwards^{*} and KJ Nixon^{**}

^{*} Operations Planning, Eskom Transmission, Corner of Lake and Power Roads, Germiston, 1400, South Africa E-mail: brian.berry@eskom.co.za, armien.edwards@eskom.co.za

^{**} School of Electrical and Information Engineering, Private Bag 3, Wits 2050, South Africa E-mail: ken.nixon@wits.ac.za

Abstract: The rotor angle metric of synchronous machines is used extensively in power system analysis in terms of angular stability. Whilst simple to observe this metric in simulations, it is difficult to measure in reality and is therefore not commonly done in practice. Whilst angular stability behaviour can be observed in the generators' terminal voltage phase and magnitude, the internal rotor angle (load angle) of a synchronous machine is useful for understanding the true severity and interaction of electromechanical oscillations in a power system. There is a proposed method of measuring the rotor angle using both a Phasor Measurement Unit (PMU) on the machine voltage terminals and a KeyPhasor which is a standard installation on most large generators. This research aims to determine the viability of such a method within both laboratory and simulation environments. The importance of monitoring rotor angle over wide areas is explored and the test environment is discussed in detail including the use of a PMU model constructed in Simulink and the results of various tests are presented and analysed.

Keywords: Phasor Measurement Unit (PMU), Wide Area Monitoring System (WAMS), synchrophasor, power system stability, IEEE C37.118, rotor-angle, Simulink, KeyPhasor

1. INTRODUCTION

The modern era of power delivery is faced with many challenges due to decreased reserves, increased use of renewable generation, Flexible Alternating Current Transmission System (FACTS) devices, and changes in customer/load behaviour. In order to manage the risks introduced by these challenges, it is important to have near real time observability of the health of the power system [1]. Synchrophasor technology provides high resolution, accurate measurement techniques which are useful for power system monitoring. Whilst Phasor Measurement Unit (PMU) metrics used over a wide area can show the interactions between synchronous machines, a direct rotor angle measurement could show these phenomena in a more reliable and quantifiable manner. Both the PMU standard of China and the current IEEE standard refer to a method of measuring the rotor angle by means of a KeyPhasor [2,3,4]. Whilst this is cited, it has not been explored nor documented adequately in practice. This paper details how the rotor angle is measured and tested using a PMU model created in Simulink to monitor a miniature synchronous generator under several operating conditions.

The structure of this paper is as follows: a brief overview of synchrophasor technology and rotor angle measurement techniques is presented then the general approach to this research is described. This is followed by an overview of the laboratory environment, the methodology used and results. Next, a design refinement is discussed and test results from using this in a simulation environment are presented. Finally, recommendations for further work are listed and conclusions are provided.

2. PMU MEASUREMENT TECHNOLOGY BACKGROUND

One of the key benefits of PMU measurement technology is the use of highly accurate GPS timing to measure phase angle which can be compared over a wide area. This is done in the following way: the GPS time is used to construct a time reference (this is essentially the same over a wide area due to the high accuracy of GPS timing). This time reference is transmitted to the PMU via a 1 Pulse per Second (PPS) signal which is used to define the start of each second. The phase angle is then measured as the angle difference between the start of the second and the peak of the wave as shown in Figure 1 [1].

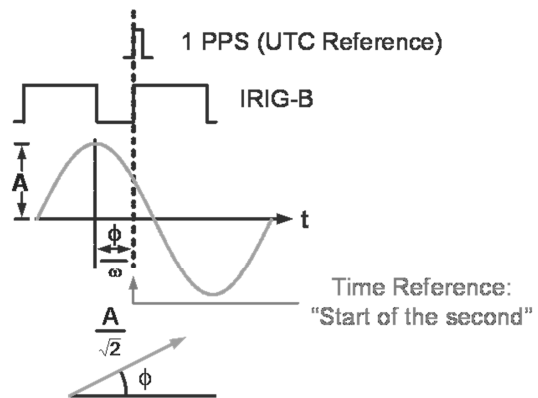


Figure 1: Phase angle measurement using a GPS time reference via the 1 PPS signal

This time reference can then be replicated over each sample so that a relative angle can be calculated per frame. Hence, if the voltage is at synchronous frequency (i.e. 50 Hz) and the frame rate is a factor of this frequency (i.e. 10, 25 or 50 Hz) then the phasor would remain stationary. However, if the frequency of the voltage signal is off nominal, the phasor would then rotate at a speed of $f_m - f_n$ where f_m is the measured frequency and f_n is nominal frequency [1,4].

This technique of phase angle measurement allows for the comparison of angles of a wide area since all PMUs share the same time reference. Combining this measurement with high resolution reporting (up to 50 frames a second), makes this data extremely useful for observing a power system's dynamic health [1].

The standard which defines PMU performance, known as IEEE C37.118, was revised in 2011 and is divided into two parts, the first (C37.118.1) dealing with PMU measurements and performance and the second (C37.118.2) focusing on the protocol for data transmission [4,5].

4. ROTOR ANGLE AS A POWER SYSTEM METRIC

4.1. Benefits of the Rotor Angle Metric

Angular stability in a power system refers the system's ability to return to equilibrium (synchronism) after large disturbances (transient stability) or oscillatory behaviour (small-signal stability). These phenomena are excited by deficits between electrical and mechanical power which inherently alter the rotor angle. Rotor angle is therefore a metric that is fundamental to understanding power system stability [6].

Whilst the terminal voltage angle of the synchronous machine is strongly related to the rotor angle, this changes under disturbed conditions and is also dependent on the voltage support surrounding the machine. Rotor angle which is determined from the physical position of the rotor represents a mechanical metric and therefore shows the stability phenomena in a more fundamental, independent and predictable manner hence the desire to measure and use it directly in Wide Area Monitoring System (WAMS) applications.

4.2. Rotor Angle Measurement

There are two common methods for measuring rotor angle: the first method estimates the rotor angle position from the terminal voltage and an equivalent model of the generator, the second method is done via physical measurement of the rotor relative to space. The preference would be to use the physical measurement since models inherently contain errors due to the assumptions used. These errors are particularly evident under dynamic conditions [2,4].

As per Annex F of the IEEE C37.118.1-2011 standard and other sources, there is a method for determining the rotor angle of a synchronous machine by using what is known a KeyPhasor pulse [2,3,4]. This is a pulse which is sent once per electrical revolution of a synchronous machine's rotor and is typically measured using a stationary electromagnetic sensor on the stator which pulses each time a slot (or ridge) on the rotor passes it. The number of slots is equal to the amount of poles on the machine therefore allowing for one pulse per electrical revolution, i.e. ± 50 PPS for a 50 Hz system [7]. When aligning this pulse with the 1 PPS signal from the GPS used to synchronise Phasor Measurement Units (PMU), the rotor position relative to time can be determined (angle α in Figure 2). By first observing the behavior of the generator under no load conditions, angle γ can be measured because at these conditions the terminal voltage is approximately equal to the excitation voltage. As seen in the bottom chart of Figure 2, once the machine is loaded, the rotor angle ($\delta = \alpha - \gamma - \beta$) can be determined since β is measured by the PMU and the other angles were determined during the no load condition.

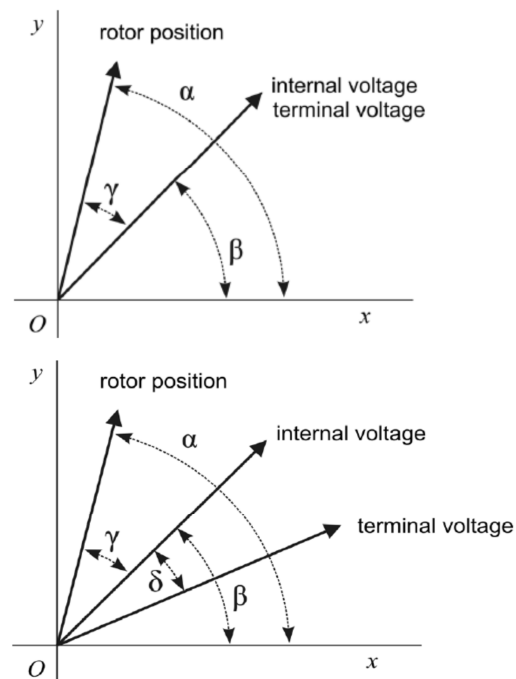


Figure 2: Top: Rotor position phasor diagram under no-load conditions, Bottom: Rotor position phasor diagram under loaded conditions [4]

5. APPROACH TAKEN

The aim of this research is to define and test an algorithm for measuring rotor angle on large synchronous machines. Since it is unsafe to implement this method directly on a large machine without having proven the concept, it is first attempted in controlled conditions. The approach taken is therefore to measure the rotor angle of a miniature synchronous machine using this method under several operating conditions. However, in order to

determine the accuracy of this measurement, the true value of the rotor angle must be known. Unfortunately, rotor angle is difficult to measure since it is defined by the relationship between the electrical and mechanical angles. This algorithm is therefore simultaneously tested in both simulation and laboratory environments. The simulation environment uses an Electromagnetic Transient (EMT) calculation program (DIgSILENT PowerFactory) and in this environment the measured rotor angle is easily validated because this can be directly compared to the simulated rotor angle metric. In the laboratory environment, this is not as easy because there is no true reference with which to compare. In order to provide some means of comparison, a traditional model estimation technique is used to determine the rotor angle. The estimation technique is done using terminal voltages and currents which were simultaneously measured by a commercial PMU. The PMU metric are accurate since it was tested to comply with the IEEE C37.118.1 standard [8,9]. Whilst this is not the best case, it is sufficient to draw conclusions and move to the next phase of testing, which is to implement this system on large generators which have rotor angle measurements that can be used as accuracy references.

6. TEST ENVIRONMENT OVERVIEW

The layout of both the laboratory and simulation environments is discussed in the following sections.

6.1. Laboratory Environment

The laboratory environment consists of a 20 kW, 2-pole, synchronous machine rotated by a drive-controlled induction machine. As shown in Figure 3, the stator voltages and currents are monitored by a commercial PMU via voltage and current transformers (CTs and VTs). The commercial PMU is also supplied with an accurate GPS unit which provides a 1 pulse-per-second (1 PPS) signal used to define its highly accurate time reference.

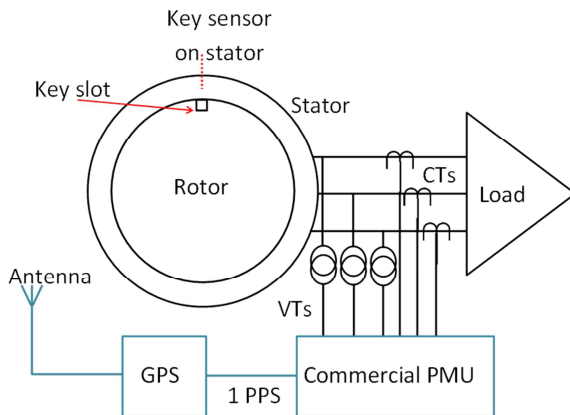


Figure 3: Physical connections from the synchronous machine to the commercial PMU used for accuracy validation

As shown in Figure 4, the PMU model mimics the commercial PMU setup using different CTs and VTs due to the lower input rating of the dSPACE system. The PMU model also uses the 1 PPS supplied from the commercial GPS unit via a fibre to copper converter. Rotor measurements are taken by measuring the field current via a Hall-effect transducer (since it is DC) and the KeyPhasor pulse. The KeyPhasor pulse is created by an electromagnetic sensor whose output changes significantly when a slot on the shaft passes by. In practice there would be a slot for each electrical pole pair, but since this is a 2-pole machine there is only one slot. Figure 5 shows a photograph of the physical KeyPhasor sensor that was made for this experiment.

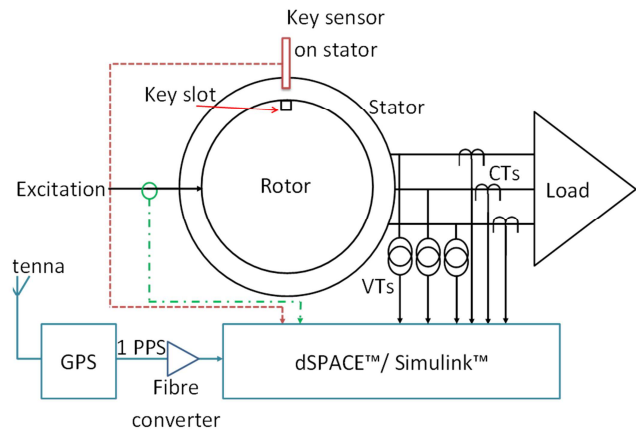


Figure 4: Physical connections from the synchronous machine to the dSPACE system

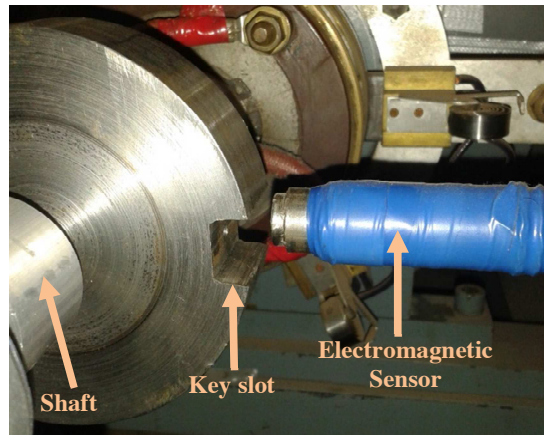


Figure 5: Photograph of the KeyPhasor measurement system used on the laboratory synchronous machine

6.2. Simulation Environment

DIgSILENT PowerFactory was used to do EMT studies for a small network. Two large synchronous generators were connected via long lines to represent a synchronous machine-infinite bus type system. The instantaneous voltage and current were measured on the generator terminals and the data exported to textfiles. The KeyPhasor pulse was created by monitoring the

instantaneous angle between the rotor's d-axis and a stationary reference. Events could then be simulated on this grid, i.e. tripping of lines, step changes to generators/load, etc. The data was then imported into Simulink in a format that is readable to the model.

7. PMU MODEL

The PMU model used in both the laboratory and simulation environments is constructed in Simulink and is made up of several functional blocks. Figure 6 shows an overview of the complete PMU model. Five inputs from the synchronous generator are injected into the model via the dSPACE system, namely the 1 PPS signal, instantaneous voltage and current waveforms, DC field current and the key pulse. The input data is scaled to the appropriate primary values and the field voltage (E') is determined based on the open circuit test results. The time module creates a time signal based on the 1 PPS signal (which is used to time stamp the data packets) and also subdivides the 1 PPS signal into a pulse per 20 ms (PP20ms). The PP20ms signal is used as an interrupt to trigger the capturing of the phasor angle, magnitude and frequency. The rotor angle is calculated by subtracting the key angle from the voltage angle. The reason that this is not done internally is because WAMS software allows this to be done over wide areas which means that the physical angles between two different generators can be monitored without the erroneous effect of the terminal voltage angle.

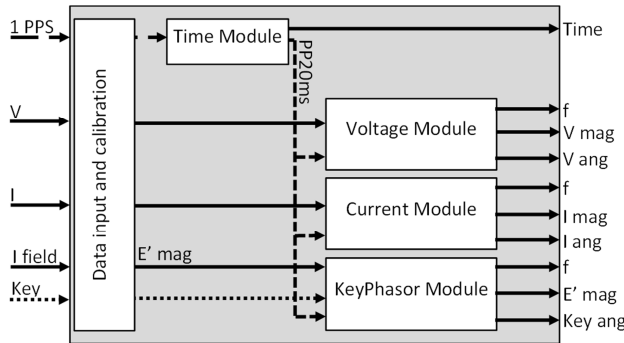


Figure 6: Overview of complete PMU model

Figure 7 shows a high-level breakdown of each phasor module. Whilst this example is shown for the voltage module, the module is almost identical for both the current module. For the laboratory environment, the KeyPhasor module has the same components except that the magnitude is simply passed through since it is a DC value. Fundamental to these modules is a phase-locked loop (PLL) which is used to track the frequency and produce an instantaneous angle (ωt). The frequency, angle and magnitude metrics are then compensated because of errors caused from various sources. The results are also time shifted to coincide with the correct time stamp since the frequency tracking causes delays to the output signal. The instantaneous values are then captured on the rising edge of each 20 ms pulse. This

produces a phasor quantity which is based on the nominal frequency of 50 Hz.

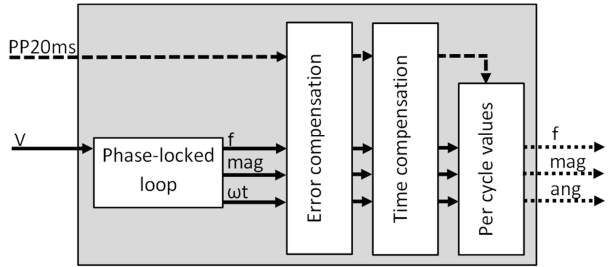


Figure 7: Phasor module breakdown

The time module is shown in Figure 8. The 1 PPS signal is used to create an accurate pulse every 20 ms. However, since the internal clock of the dSPACE unit drifts in time, this error must be compensated. The pulse generator is supplied by a clock source which is created by integrating to a value which is the sum of one and the time drift error per second. This essentially creates a new clock with little drift error. The time formatting block formats the clock signal into seconds and fractions of a second which is then directly usable for time stamping the phasor data packets.

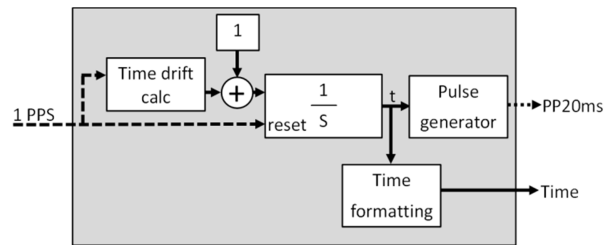


Figure 8: Time module breakdown

8. LABORATORY RESULTS

The PMU model was used in the laboratory environment where the miniature synchronous generator was monitored whilst increasing the stator current to approximately 15 A which is around half of the rated output of the machine. Figure 9 shows the errors on the terminal metrics when comparing the commercial PMU and the PMU model. The frequency error is between $\pm 25 \text{ mHz}$, the magnitude error between $\pm 0.7 \text{ V}$ and the angle error is between 0° and 4° . These equate to a Total Vector Error (TVE) of less than 8% which is much higher than the C37.118-1 requirement. The poor performance is attributed to the lack of filtering in the PMU model however the model is accurate enough to determine viability.

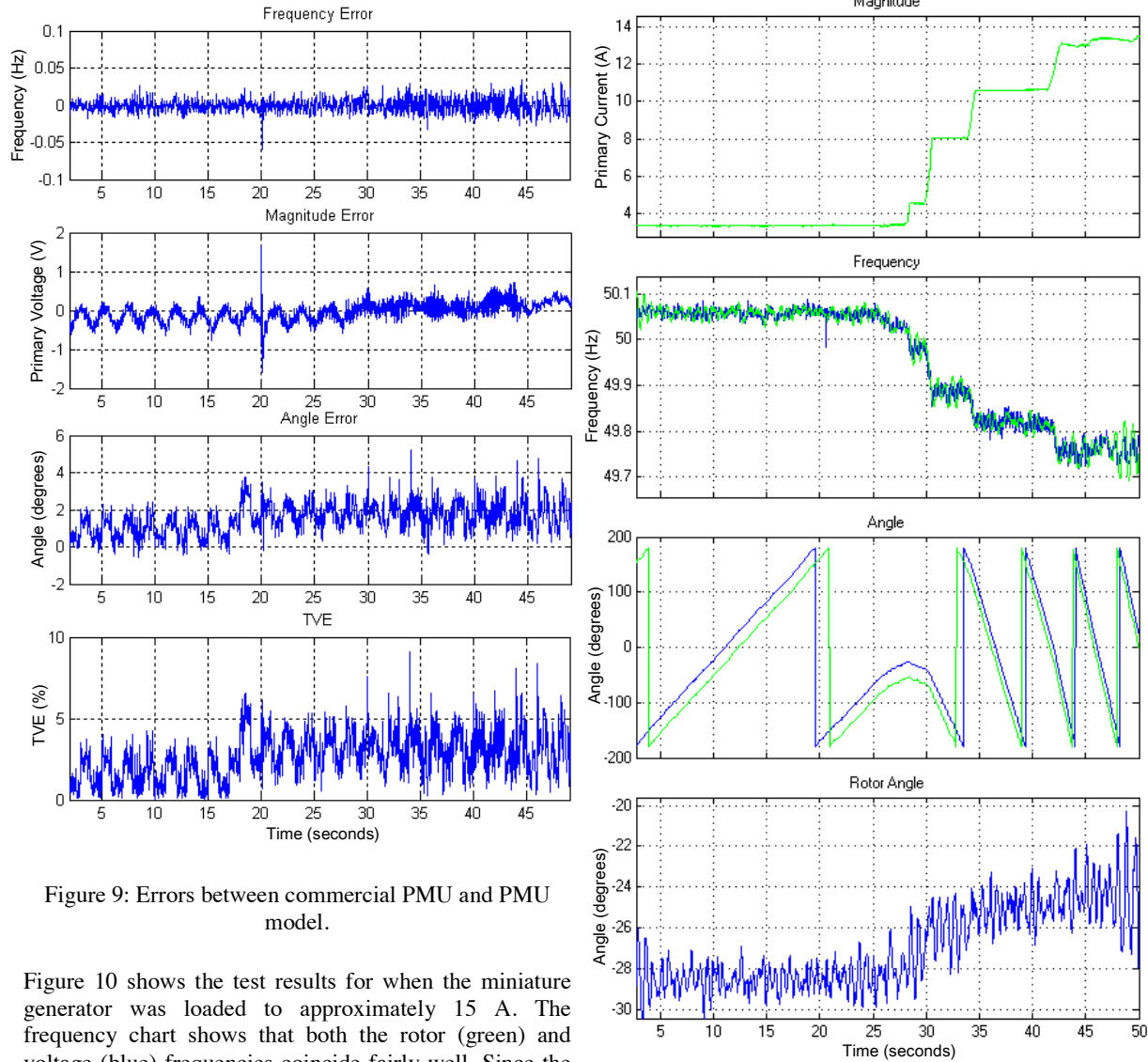


Figure 9: Errors between commercial PMU and PMU model.

Figure 10 shows the test results for when the miniature generator was loaded to approximately 15 A. The frequency chart shows that both the rotor (green) and voltage (blue) frequencies coincide fairly well. Since the terminal metrics tie up with the commercial PMU, this provides confidence in the rotor angle measurement (shown in the bottom chart). The rotor angle measurement shows an increase of approximately 5° when the machine is loaded to 15 A.

Figure 10: PMU model results from the miniature synchronous machine.

Figure 11 shows a comparison of the rotor angle as measured using the KeyPhasor technique and as estimated via the modelling technique. It is clear from this figure that the rotor angle is being tracked by the measurement technique but it is too noisy. The errors due to the noise are so significant that the measurements are deemed useless for practical applications. The measurement error is however due to a fundamental design issue.

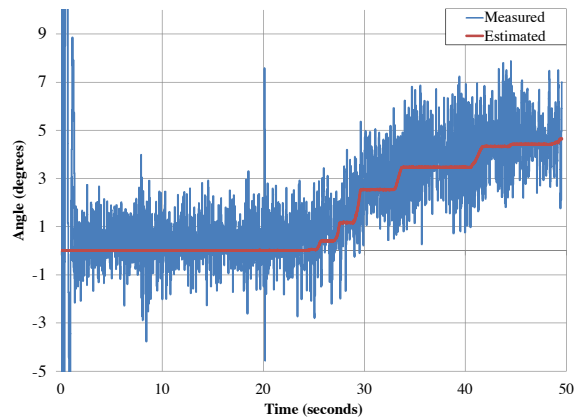


Figure 11: Comparison between the rotor angle as measured with the KeyPhasor technique and as estimated using modelling technique

The laboratory technique to calculate the KeyPhasor angle used the same algorithm as the voltage angle measurement, i.e. phase-locked loop to track speed and angle. This however failed due the low sample resolution which is typical of protection relays. These relays use low sampling rates (around 2.5 kHz) so an optimistic 10 kHz sampling resolution was used [10]. This low resolution poses a problem as presented in an example below:

- Period of key phasor pulse at 50 Hz: $1/50 = 0.02$ s
- Period of key phasor pulse at 50.1 Hz: $1/50.1 = 0.01996$ s
Rounded off to the nearest 0.0001 s (due to 10 kHz sampling), it becomes 0.02 s.

This is a problem because it means that the PMU will not be able to detect small disturbances. The equivalent frequency for 0.0199 s is 50.2513 Hz which means that sampling at 10 kHz results in a frequency resolution of around 0.25 Hz. This is inadequate since 0.25 Hz is substantial in power systems, for example: in the Eskom network, 250 mHz equates to around 350 MW of power [11]. The conclusion from this is that the KeyPhasor cannot simply be inserted into a PMU via an analogue input (which uses a similarly low resolution) but will require an intermediate step which translates the high resolution requirement of the KeyPhasor into one that is usable in a typical protection relay. Since this technique can be difficult to implement in the Laboratory environment due to limited resources and time, the technique was modelled in a simulation environment which is discussed in the next sections.

9. PMU DESIGN REFINEMENT

Due to the errors observed in the laboratory, a different technique was used for tracking the KeyPhasor angle in the simulation environment. The important part of the KeyPhasor signal occurs when its state changes. This means that a high resolution would be desired during this state change but not for the rest of the time. It also means that a PLL is not optimal for tracking its frequency and period. The result of this is that a high resolution input would be required but it is preferential that this module can output values that are still usable in numerical relays with a low sampling resolution. The proposed solution is shown in Figure 12, where a high speed oscillator/timer (represented by integrator blocks) is reset according to the KeyPhasor and PP20ms signals. To determine the mechanical speed of the generator, the timer is reset each time the KeyPhasor pulse occurs. This results in a time measurement for each mechanical revolution (period, T) and frequency is determined as $f=1/T$. To determine the rotor phase angle with reference to space, the timer is started each time the PP20ms pulse occurs and stopped when the KeyPhasor pulse is detected. This results in the phase measurement in time which must be converted to an angle which is done according to the following formula:

$$\alpha = \omega t = 2\pi f t = 360 f t^\circ$$

Where:

α is the phase angle of the rotor in space

f is the frequency of the waveform

t is the time between a particular reference (PP20ms) and a specific point on the waveform

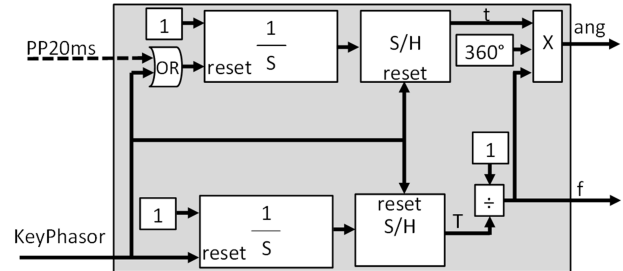


Figure 12: Functional diagram of the KeyPhasor module used in the simulation environment

10. SIMULATION RESULTS

Figure 13 shows plots of the refined PMU model in response to a simulated impedance step change. This was achieved by tripping a parallel line in the EMT simulation and was purposefully reduced to resemble a small disturbance in order to highlight the issue discovered in the laboratory tests. From comparing the mechanical speeds in the frequency chart (Blue – KeyPhasor frequency, Aqua – PowerFactory speed, Red – terminal frequency, and Green – PowerFactory frequency) it is clear that the tracking is good except for some oscillations observed on the measured speed curve. Similarly the rotor angle plots (Blue – measured, Green – PowerFactory angle) show good tracking with fewer oscillations. It is clear from both the frequency and rotor angle plots that the performance of the refined design far exceeds that of the one used in the laboratory tests. The oscillations that were observed on the frequency during times of transition are due to the high gain used on the PLL. The PLL, which uses a proportional-integral (PI) controller, was tuned according to the Ziegler-Nichols method [12]. Its high gain makes the output oscillate, however this is desired because the controller oscillation frequencies will not be near the electromechanical modes and it can be easily filtered away with a low-pass filter. The rotor angle plot of Figure 13 shows far less oscillations since it has been filtered as opposed to the frequency plot which has purposely been left unfiltered.

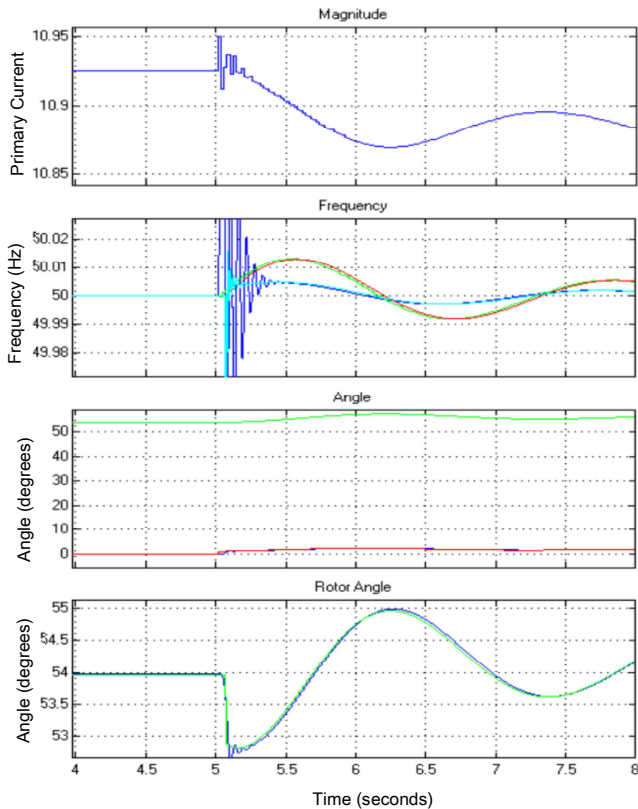


Figure 13: Results from the refined PMU model used in the simulation environment.

11. FURTHER WORK

It is clear from the results that whilst the technique is not easily implemented, there is a possible solution which looks promising in terms of viability of the method. To move to final implementation, the following still needs to be completed:

- *Test further with the EMT simulations*
Simulate out-of-step scenarios for when the zero point is both inside the machine and inside the network. This is a use-case for where this technology would be beneficial in practice.
- *Implementation on a large scale generator with a PMU vendor*
The final steps of this project would be to work with a vendor to get this technique implemented on a commercial PMU. During development, tests should be done on the relay by connecting it to a physical large synchronous machine.

12. CONCLUSION

The benefits of measuring the rotor angle of synchronous machines have proven this to be a useful metric for power system stability applications. A method for measuring the rotor angle via a KeyPhasor pulse is described and successfully tested in a simulation environment after the laboratory tests revealed the detrimental effect of using low sampling rates typical of modern numerical relays.

Providing the use of a high resolution oscillator module for tracking the KeyPhasor angle and frequency is possible practically, this technique shows promise in terms of being a viable method of measuring rotor angle.

13. REFERENCES

- [1] JS Thorp AG Phadke, *Synchronized Phasor Measurements and Their Applications*, 1st ed., A Stankovic MA Pai, Ed.: Springer Science+Business Media, LLC, 2008.
- [2] ZHOU Jie et al., "Rotor Position Measurement Method for Generator Power Angles," in *The International Conference on Advanced Power System Automation and Protection*, 2011, pp. 2196-2200.
- [3] Jingtao Wu, Ji Zhou, Daonong Zhang, Zhaojia Wang, and ShiMing Xu, "PMU Standard of China," IEEE, 2008.
- [4] Power System Relaying Committee, "IEEE Standard for Synchrophasor Measurements for Power Systems," IEEE Power & Energy Society, IEEE Std C37.118.1™-2011, Dec 2011.
- [5] Power System Relaying Committee, "IEEE Standard for Synchrophasor Data Transfer for Power Systems," IEEE Power & Energy Society, IEEE Std C37.118.2™-2011, Dec 2011.
- [6] P Kundur, *Power System Stability and Control*, 1st ed., MG Lauby NJ Balu, Ed.: McGraw-Hill, Inc., 1994.
- [7] Bently Nevada, "Specifications and Ordering Information - 3500/25 Enhanced Keyphasor Module," 2003.
- [8] B Berry, "Eskom Verification of the WAMS PMU FAT of the 72B Firmware – Steady State Results," Eskom, Oct 2012.
- [9] B Berry, "Eskom Verification of Dynamic Results of the WAMS PMU FAT for the 72B Firmware," Eskom, Oct 2012.
- [10] Alstom Grid, *Network Protection & Automation Guide*, 2011th ed.: Alstom Grid, 2011.
- [11] Edwards A, "Review of the Proposed UFLS Scheme," Eskom, Johannesburg, 342-156, 2013.
- [12] WY Svrcek, DP Mahoney, and BR Young, *A Real Time Approach to Process Control*, 2nd ed.: John Wiley & Sons, Ltd.
- [13] Bogdan Kasztenny and Mark Adamiak, "Implementation and Performance of Synchrophasor Function within Microprocessor Based Relays," in *Power Systems 2008 Conference*, Clemson, USA, 2008.
- [14] Performance & Standards Task Team (PSTT), "PMU System Testing and Calibration Guide," North American SynchroPhasor Initiative (NASPI), Dec 2007.
- [15] R Lira, D H Wilson, K Hay, and T Porrelli, "Performance Testing For Interoperability Of Phasor Measurement Units To Meet Application

- Requirements," in *International Protection Testing Symposium (IPTS)*, Brand, Austria, 2011.
- [16] Ghahremani E and Kamwa I, "Online State Estimation of a Synchronous Generator Using Unscented Kalman Filter From Phasor Measurements Units," *IEEE Transactions on Energy Conversion*, vol. 26, no. 4, pp. 1099-1108, December 2011.
- [17] Mazur DC, "Synchronized Rotor Angle Measurement of Synchronous Machines," Virginia Polytechnic Institute and State University, Blacksburg, MSc Dissertation 2012.
- [18] Moodley R and Berry BWD, "The Implementation of Phasor Measurement Technology in Eskom," in *Distributech Africa*, Cape Town, 2014.
- [19] H Saadat, *Power System Analysis*, 1st ed.: WCB/McGraw-Hill, 1999.
- [20] B Singh, NK Sharma, AN Tiwari, KS Verma, and SN Singh, "Applications of phasor measurement units (PMUs) in electric power system networks incorporated with FACTS controllers," *International Journal of Engineering, Science and Technology*, vol. 3, no. 3, pp. 64-82, 2011.
- [21] BWD Berry, MA Edwards, and KJ Nixon, "Implementation of a Rotor Angle Measurement Technique using Synchrophasor Techniques - Preliminary Investigations," in *Southern African Universities Power Engineering Conference*, Durban, 2014, pp. 19-25.
- [22] D de Canha, "The Analysis of Shaft Voltages in a Synchronous Generator with Various Induced Faults," University of the Witwatersrand, Johannesburg, MSc Dissertation 2008.
- [23] SJ Hoffe, "Synchronous Generator Fault Diagnosis using Shaft Signal Measurements," University of the Witwatersrand, Johannesburg, MSc Dissertation 2006.

OPTIMISATION OF A LINE-START PERMANENT MAGNET SYNCHRONOUS MACHINE FOR A LOAD SPECIFIC APPLICATION

A.J. Sorgdrager*, R-J Wang * and A.K Pfeffer

* Department of Electrical and Electronic Engineering, Stellenbosch University, Private Bag XI, Matieland 7602, South Africa E-mail: ajsorgdrager@gmail.com, rwang@sun.ac.za

Abstract: This paper presents the design, optimisation and prototyping of a 2.2 kW line-start permanent magnet synchronous motor. The initial design is done using analytical approach based on classical machine theory, which is then optimized. For the optimization, a gradient based Quasi Newton algorithm is used along with generic cost function methodology. The transient performance of the optimal design is evaluated by using transient 2D finite element (FE) time-step modeling. A prototype machine based on the optimal design is manufactured and experimentally evaluated. The simulated and measured results are compared. Relevant discussion and conclusions are drawn.

Key words: Line-start motor; permanent magnet; induction motor; design optimization; finite element method; transient performance; cage winding.

1. INTRODUCTION

Future energy challenges and global environmental concerns urge the world to focus on energy efficiency programs more than ever. Energy efficiency improvement is an important way to address these challenges. Since motor-driven systems are responsible for approximately 70% of all electricity consumption in industry, huge amount of energy saving can be realized by increasing electrical motor efficiency. Although the performance of induction motors have been significantly improved over years, the inherent limitation of induction motors such as relatively poor efficiency and power factor cannot easily be remedied. With the introduction of IEC 60034-30 standard, electrical motor manufacturers worldwide increasingly focuses on alternative motor technologies in an attempt to meet with the forthcoming IE4 standard. Amongst others, line start (LS) permanent magnet synchronous motor (PMSM) technology has received considerable attention. The distinct advantages of LSPM motors such as high efficiency, high power factor and high power density have made this new type of motor very attractive. This paper presents the design, optimisation and prototyping of an interior permanent magnet (PM) radial flux LS PMSM motor for fan-type loads applications.

2. DESIGN PROCEDURE

In this section the procedure of design is discusses. For cost saving purpose, an existing 2.2 kW, 4-pole, 525V, IE3 induction machine stator is used, whose key specifications are listed in Table 1. Essentially, this is a retrofit design with a main focus on the optimal design of the rotor.

2.1 Design Methodology

Fig. 1 illustrates the basic design methodology employed for the design process. The initial design is carried out by using the classical machine theory presented in [1–3].

Table 1: IE3 induction machine stator data.

Description	Specs
Outer diameter, mm	160
Inner diameter, mm	100
Stack length, mm	120
Number of slots	36
Number of turns per slot	81
Connection type	Delta
Air-gap length, mm	0.5
Lamination material	M400-50A

The optimisation criteria is implemented only on the rotor parameters subjecting to some dimension and topology constraints.

Essentially an LS PMSM contains two vastly different machines within one volume. The optimisation of its rotor is a rather complex process involving both cage and PM array design. The cage design mainly influences the transient (asynchronous) operation of the machine whereas the PM array (*PM components, duct and flux barriers*) design is responsible for the steady-state (synchronous) performance. The inherent competition of space between the cage slots and PM arrays often poses significant design challenges in the design of these machines. A simple two-step design approach is often adopted, i.e. (i) an analytical design analysis taking into account asynchronous operation to certain extent is first used to find a suitable design; (ii) after which a 2D FEM time-step analysis is applied to the candidate design to validate its starting and synchronization capability.

One important aspect of this design approach is that the accurate load characterization is necessary. By incorporating the dynamic response of an actual load, the transient performance of the machine can be better inspected and a more accurate comparison can be made once the machine has been experimentally tested against

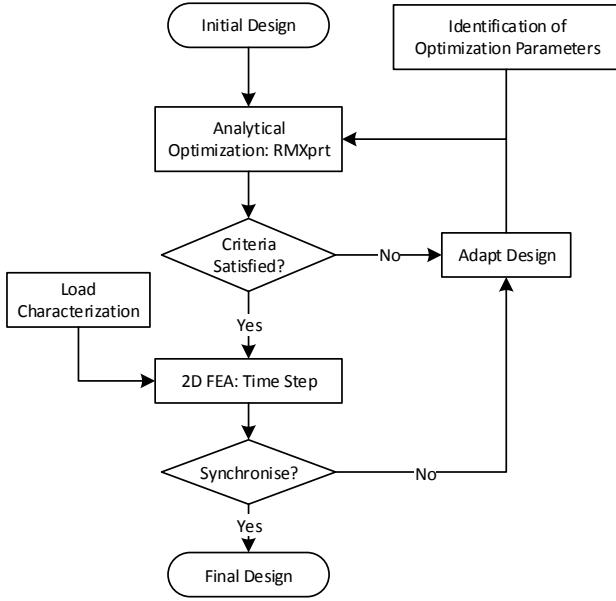


Figure 1: Flowchart of the design procedure

the same load. If the load connected machine synchronizes during the FEM time-step simulation, no further design changes is made and the machine can be manufactured. In the case that the machine fails to synchronize, the design is revisited and a further design iteration is required.

2.2 Optimisation Algorithm and Criteria

For the design optimisation, the gradient based Quasi Newton algorithm is employed to search for the minimum value of a defined cost function. The generic format of the cost function is given by (1). The cost value is the sum of the the normalized value around 1 for each performance objective that forms part of the optimisation criteria. The higher the deviation from the target value the higher the cost value. When minimising or maximising an objective, a theoretical limit is used as the target value .Each of the performance objectives is assigned a weight factor , K_i , according to its importance. Table 2 shows the objectives for the optimisation criteria along with their targets and weight values. It is clear that the ideal cost output will be 9.

$$\text{Cost} = \sum_i K_i [1 + |\text{Target Value} - \text{Actual Value}|^2] \quad (1)$$

By including the required rated output power (P_{out}) and

Table 2: Composition of the cost function.

Objective	Goal	Weight (K_i)
T_{rated}	14 Nm	1
P_{out}	2.2 kW	1
back-EMF (rms)	0.9 pu	1
PM mass	Min	2
T_{start}	Max	3
B_{ag}	0.55 T	1

rated torque (T_{rated}) in the cost function, it ensures that each machine during the optimisation is a valid design. The synchronous torque of an LS PMSM is calculated in the same manner as a PMSM and is the sum of the magnetic and the reluctance torque. The main torque (*magnetic torque*) is generated by the PM flux interacting with the stator coils. The higher the back-EMF the higher the torque. However, the magnitude of the braking torque developed during the transient operation is also directly proportional to the back-EMF and PM volume [4, 5]. By maximizing the back-EMF and minimizing the PM volume the PM leakage flux is reduced thus utilizing the maximum possible magnetic energy to achieve the desired performance. This prevents the optimizer from increasing PM volume for a higher back-EMF, which also in turn improves the transient performance. The target value for the back-EMF is set in the range as described in [2]. The target limit for the PM mass is calculated by determining the minimum BH operating point energy product to achieve the desired air-gap flux density [1].

Apart from achieving high efficiency and unity power factor at rated steady state condition with minimal PM volume, the motor needs to develop the highest possible starting torque. This is required to overcome the initial load and braking torque during transient operation. There is however no set criteria for quantifying the starting torque. A general assumption is that the higher the torque, the more likely machine is to synchronize. The starting torque of an LS PMSM is affected by the rotor slot profiles such as slot shape, depth, width and area.

The specific weight assigned to each objective is according to the importance each objective has on the overall optimisation criteria. By adding more weight to the PM volume and starting torque in the cost function, the optimisation is conducted with more consideration on the transient performance.

2.3 Optimisation Variables

As stated before, an LS PMSM has a hybrid rotor. In the rotor cage design, the total number of slots are selected as 28, which is the same as that of an IM with the same power rating. However a round slot is used as shown in Fig. 2 for the following reasons: (i) firstly, from a manufacturing point of view, if the rotor bars casting is not available, the round rotor bars can be easily manufactured and inserted into the slots; (ii) secondly, the number of variables to characterize a round slot in the optimisation is reduced to merely three.

Fig. 3 illustrates the different parameters that define the PM slot. The PM width (W_m) can vary within the width of the slot but its thickness (T_m) should match that of the slot. The gap between two PM slots (Rib) and the nearby cage slot bottom region form a flux saturation zone to limit the PM leakage flux. By optimally designing saturation zones, the magnet utilization factor can be much improved. By varying the depth of the PM slot (O1) along with the PM width, a suitable air-gap flux density can be realized [7].

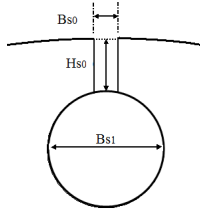


Figure 2: Rotor slot dimensions

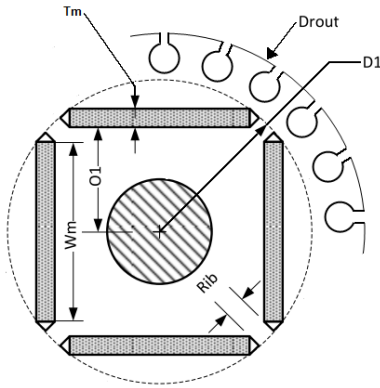


Figure 3: Magnet and PM slot dimensions

2.4 Optimized Design

Table 3 contains the relevant information of each variable. The starting values are the initial machine design that was calculated analytically as in [1]. The total number of simulations for the optimization is 408. Table 4 summarizes the change of each objective between the initial and optimized machines and Figs. 4 to 6 compare the different torque components. It is clear that optimized machine outperforms the initial design. The better utilization of the PM material increases both the air-gap flux density and back-EMF resulting in a higher maximum torque at steady-state as shown in Fig. 4. The higher back-EMF causes a higher braking torque, which is expected.

As the optimisation criteria is satisfied, the next step is to inspect the synchronization capability of the optimized machine with a specific load. For this project, a custom designed axial fan is used as the specific load, which provides a load torque of 14 Nm at the rated speed of

Table 3: Optimisation topology parameters.

Variable	Start Value	Min	Max
Bs0	1.5	1	3
Bs1	6.4	6	7
Hs0	3	1.325	3
D1	77	63	78
O1	24	23	27
Rib	2.5	2	4
T_m	6.5	4	7
W_m	30	28	35

1500 rpm. The fan's torque-speed curve, moment of inertia and damping coefficient are experimentally determined and implemented in ANSYS' Maxwell 2D FEM software. Fig. 7 is a flux density plot of the final design under full load condition at a certain time-step. Fig. 8 shows the

Table 4: Cost function objective comparison

Objective	Goal	Initial	Optimised
T_{rated} , Nm	14	14	14
P_{out} , kW	2.2	2.2	2.2
EMF (rms), V	370	330	341
PM mass, kg	Min	0.755	0.581
T_{start} , Nm	Max	47.89	54.56
B_{ag} , T	0.55	0.50	0.53

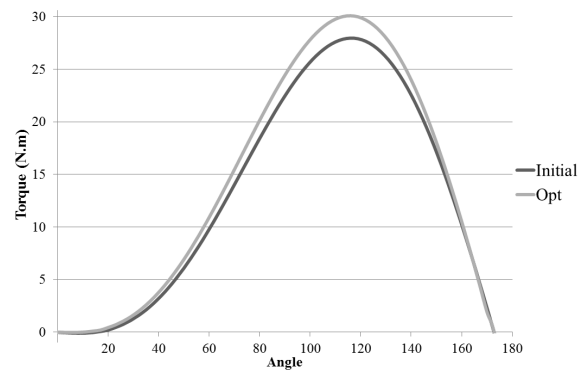


Figure 4: Comparison of initial and optimum steady-state torque

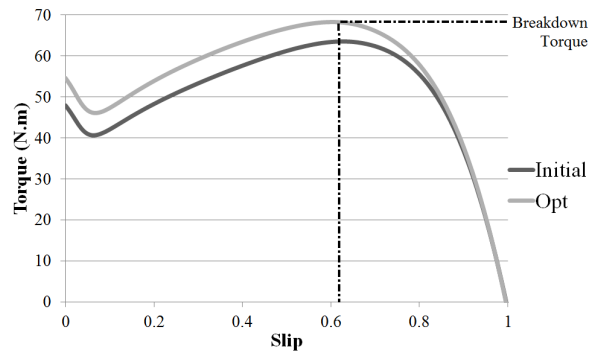


Figure 5: Comparison of initial and optimum torque-slip characteristics

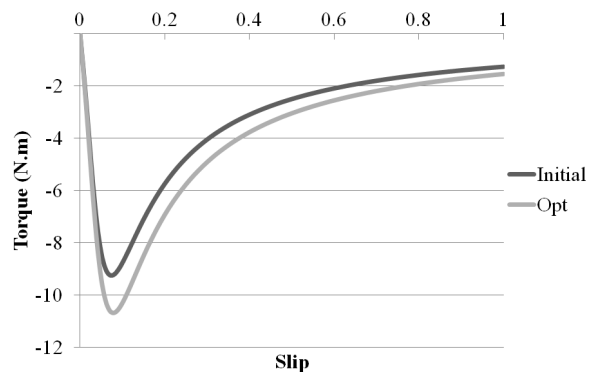


Figure 6: Comparison of initial and optimum braking torque

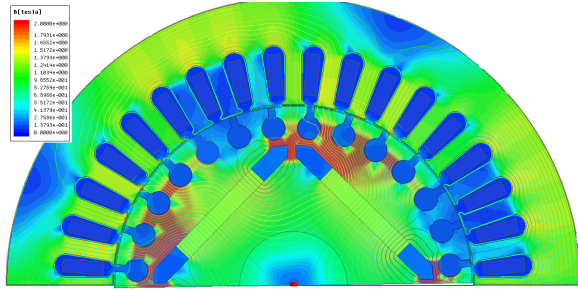


Figure 7: Steady-state flux density plot

transient synchronization performance of the optimized machine. From the figure it is clear that rated speed is reached at ± 0.8 s and the decision was made to manufacture the rotor.

3. SIMULATION AND EXPERIMENTAL RESULTS

This section compares the measured and simulated results of the machine in terms of the no-load, full-load and transit performance. Table 5 compares the simulated and the actual performance for both no-load and load test. The simulated performance shows high efficiency operating at a good power factor. The full load line current is also lower than an IE3 induction machine of the same rating.

It was possible during manufacturing to cast the rotor bars and end rings using gravity casting. The preferred method of casting, as used by electrical machine manufacturers, is vacuum pressure injection, but this is very costly for prototype manufacturing. To use gravity casting, the stack and casting jig have to be preheated before pouring in the aluminum. This is to prevent the aluminum from setting too quickly and creating air voids in aluminum bars. Once the aluminum cooled the stack can be removed from the casting jig and machined to provide the required air-gap. An image of the prototype rotor is shown in the Appendix

3.1 Performance Evaluation

To inspect the synchronization capabilities of the machine, the start-up test of the machine with the fan load is conducted in the laboratory. The machine failed to reach synchronization and settled at a sub-synchronous speed of 1290 rpm as seen in Fig. 8. The figure provides a comparison between the simulated and measured start-up performances. The measured results correlate well with the simulated ones up to 900 rpm where the two

Table 5: Comparison of measured and simulated results

Description	Simulated	Measured
Efficiency	94.6	-
Power Factor	0.91	-
$I_{\text{no-load}}$, A	2.2	2.96
$I_{\text{full load}}$, A	3.93	9.56
T_{average} , Nm	14	14.5
Speed, rpm	1500	1290

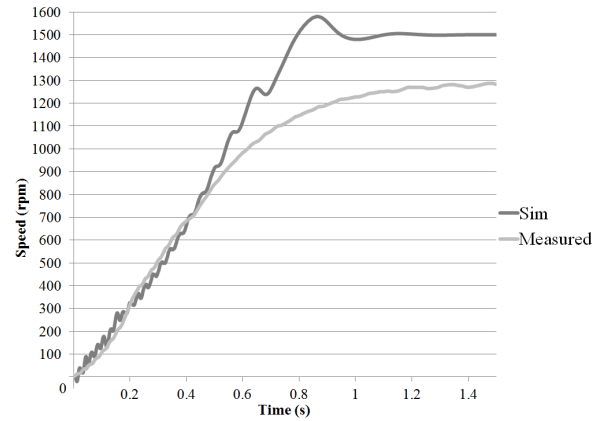


Figure 8: Comparison of measured and predicted start-up speed versus time characteristics of the LS PMSM

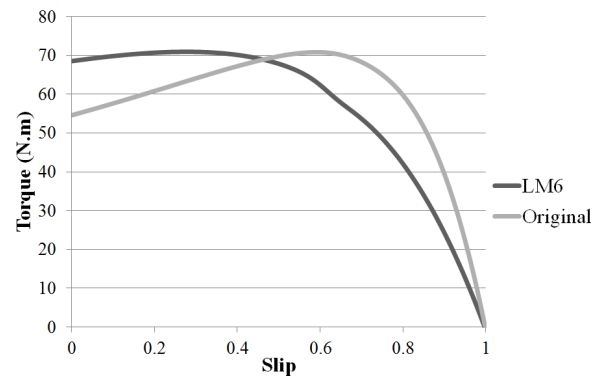


Figure 9: Torque curve deviation due to aluminium grades used

curves start to diverge. Upon further investigation it was determined that the main cause of the failed synchronisation is due to the aluminium grade used to cast the rotor cage, namely LM6. This aluminium grade has a lower electrical conductivity than the one selected during the design phase thus resulting in a higher resistance. This resulted in a change in transient torque as seen in Fig 13. A slight torque dip can also be seen between 0.6 to 0.7 which is around the diverge speed point. The increase resistance moved the breakdown torque point further away from $s = 1$ and as a result the PM cannot generate enough pull-in torque to bring the rotor into synchronization. As a result, the rotor operates at a sub-synchronous speeds. Under such an operation condition, the machine develops a pulsating torque and line current as shown in Figs 10-11.

Since the prototype machine failed to synchronize, the efficiency and power factor of the machine could not be determined for rated performance. The full load measurements could not be completed as the excessive line currents trip the protection breakers before the Watt-meters can be switched in. These Watt-meters cannot handle the high inrush starting currents so that they can only be switched in after the start up. In addition to the performance tests, the back-EMF waveform of the machine is also measured and compared to the simulation one. The measured and simulated waveform magnitude show significant discrepancy as seen in Fig. 12.

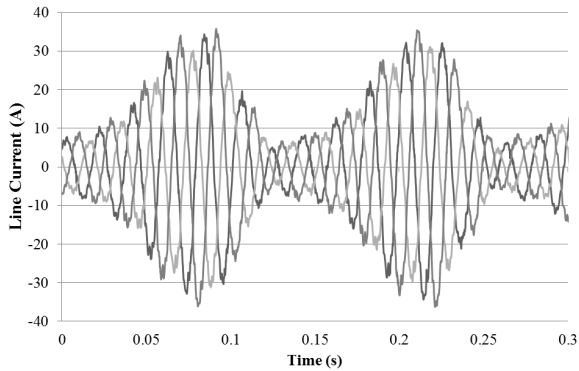


Figure 10: Instantaneous current waveform of LS PMSM under sub-synchronous speed

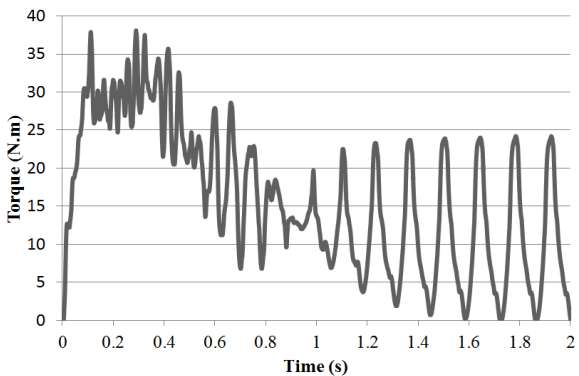


Figure 11: Instantaneous torque waveform of the LS PMSM under sub-synchronous speed

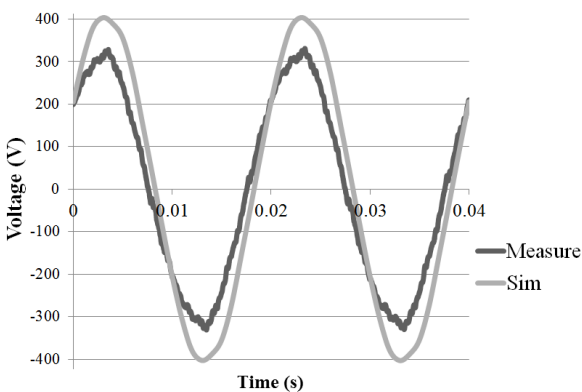


Figure 12: Measured and predicted back-EMF voltage of the LS PMSM prototype

4. CONCLUSION

The paper presents a design optimisation approach for an LS PSMS using a gradient based cost function to maximize starting torque and minimize PM volume whilst still adhering to a high steady state performance. The synchronization capability of the machine is checked using a 2D FEA time step simulation that incorporates the load parameters of the fan load set-up. The simulation results show good steady state and transient performance. The manufactured prototype machine was unable to synchronize when driving the load and as a result

the simulated and actual machine performance differed. Further investigation is still required into incorporating load parameters in a time step simulations approach before a conclusion can be made on the optimisation approach.

REFERENCES

- [1] A.J. Sorgdrager, A.J. Grobler, and R-J Wang, Design Procedure of a Line-Start Permanent magnet synchronous machine, in Proc. of the 22nd South African Universities Power Engineering Conference, 2014, vol.22, no.1, pp.307-314.
- [2] J. Pyrhonen, T. Jokinen and V. Hrabovcová, Design of rotating electrical machines, (1st ed.) West Sussex, United Kingdom: John Wiley & Sons, Ltd, 2008.
- [3] I. Boldea and L. Tutelea, Electric machines, (1st ed.) USA: CRC Press, 2010.
- [4] V.B Honsinger, "Permanent Magnet Machines: Asynchronous Operation", IEEE Trans. on Power Apparatus and Systems, vol. PAS-99, vol. 4, pp. 1503-1509, 1980
- [5] F.J.H. Kalluf, C. Pompermaier, M.V.F. Da Luz, and N. Sadowski, Braking torque analysis of the single phase line-start permanent magnet synchronous motor, in International Conference on Electrical Machines (ICEM), 2010, pp. 2011-2011.
- [6] A. Isfahani and S. Vaez-Zadeh, Effects of magnetizing inductance on start-up and synchronization of line-start permanent-magnet synchronous motors, IEEE Trans. on Magnetics, vol. 47, no. 4, pp. 823-829, 2011.
- [7] A.J. Sorgdrager and A.J. Grobler, Influence of magnet size and rotor topology on the air-gap flux density of a radial flux PMSM, 2013 IEEE Int. Conf. Ind. Technol., pp.337-343, Feb. 2013.

APPENDIX



Figure 13: Prototype LS PMSM rotor

ROTOR DESIGN OF A RETROFIT LINE START PERMANENT MAGNET SYNCHRONOUS MOTOR

K. Garner* and A.J. Grobler**

* School of Electrical, Electronic and Computer Engineering, North West University, Potchefstroom, South Africa, E-mail: karen.garner@sasol.com

** School of Electrical, Electronic and Computer Engineering, North West University, Potchefstroom, South Africa, E-mail: andre.grobler@nwu.ac.za

Abstract: The increasing need for energy and the lack of energy resources available has prompted designers to focus on improving the efficiency of equipment. Motors utilise a considerable portion of the electrical energy generated and thus improving the efficiency of these machines would reduce the overall power consumption. Research has indicated that permanent magnet synchronous machines (PMSM) offer improved efficiency when compared to induction machines. A retrofit design where the stator of an induction machine is kept intact and the rotor substituted with a permanent magnet core is proposed as a solution. A retrofit design is considered because of the ease of manufacturing for motor suppliers and the ability to apply the solution to existing operating induction machines. This paper focuses on the principles followed to design the permanent magnet rotor for a retrofit line start permanent magnet synchronous machine (LSPMSM).

Keywords: Rotor design, LSPMSM, PMSM, retrofit, permanent magnet, dimensions

1. INTRODUCTION

Our energy resources are under tremendous pressure with society's ever increasing need for electricity. There is an urgent need to look at how we are expending all the energy generated and to reduce our energy consumption. Studies have indicated that 65% of electrical energy is converted to heat and mechanical energy by electric motors [1]. Majority of these motors are three-phase induction motors and are mostly used in fan and pump applications [1]. Motors with a higher efficiency reduce energy losses, resulting in reduced operating costs. If designed correctly, a permanent magnet machine can be more efficient than an induction machine because permanent magnets eliminate the rotor excitation losses found in induction machines. A retrofit design of a three-phase induction motor is considered. The standard rotor of an induction motor is substituted with a rotor fitted with permanent magnets and the stator and frame of the induction motor is kept intact. The retrofit design is considered because a motor supplier will not need to replace its entire production line, but only replace its rotor design. The retrofit will also allow induction motors currently operating to be changed to a permanent magnet solution with minimal impact. A motor with increased efficiency can then be achieved without increasing the size of the motor.

An alternative solution is to construct a line start permanent magnet synchronous machine (LSPMSM) with a new rotor and stator. This allows the designer to manufacture a smaller machine able to deliver the same power output as an induction machine. The smaller construction is attributed to the fact that permanent magnet synchronous machines (PMSM) have lower operating temperatures because there are no rotor bar currents [2]. The lack of rotor bar currents means that the rotor losses are eliminated and hence the efficiency of the

machine is increased. The increased efficiency of the PMSM yields a higher power output than an induction machine of the same power rating [2]. Although a LSPMSM designed with a new rotor and stator will yield a smaller machine, it will not be feasible for replacing existing induction machines because of the impact on the installation.

2. ROTOR DESIGN

The following parameters have to be determined for the rotor of the retrofit LSPMSM:

- Direction of magnetisation
- Rotor slot dimensions
- Permanent magnet orientation
- Permanent magnet dimensions
- Flux barrier dimensions

A LSPMSM is a hybrid between an induction machine and a synchronous machine. The current densities for the retrofit design are chosen based on the suggested limits for the induction machine and the salient pole synchronous machine. The stator of the existing induction machine used for the retrofit design is developed for radial flux. Thus, a radial flux permanent magnet configuration is used. Embedded magnets are used for the prototype because the axial length of the machine is fixed. Using surface-mounted permanent magnets would lengthen the axial length of the rotor.

3. ROTOR SLOT DIMENSIONS

3.1. Slot area

The number of rotor slots is chosen by considering the number of poles and the number of stator slots. There are many requirements for choosing the rotor slot number, such as the rotor slot number must be as small as possible

to minimise asynchronous torques. Considering the requirements in [3] and that there are 48 slots in the stator, the number of rotor slots is chosen as 30. It is also important to keep the number of slots as low as possible to aid manufacturing. The rotor slot area is calculated by determining the stator and rotor currents. The stator current I_s can be calculated as follows

$$I_s = \frac{P}{m\eta V_{sph} \cos \varphi} \quad (1)$$

where P is the shaft power, m is the number of phases, η is the efficiency, $\cos \varphi$ is the power factor and V_{sph} is the stator phase voltage. The rotor current I_r is a factor of the stator current and is determined by [3]

$$I_r = \left(\frac{z_Q}{a} \right) \left(\frac{Q_s}{Q_r} \right) I_s \cos \varphi \quad (2)$$

where z_Q is the amount of conductors per slot, a is the number of parallel paths in the windings which is equal to 1 for a squirrel cage machine, and Q_s and Q_r represent the number of stator slots and rotor slots respectively. The area of the conductive material in the slot must be calculated in order to calculate the slot area. This is calculated using the current density J . Choosing a higher current density yields a smaller cross-sectional area of the conductive material and thus a higher resistance. A higher rotor resistance provides an increased starting torque because torque is proportional to the rotor resistance at low values of slip. The area of the rotor's conductive material A_{cr} is given by [3]

$$A_{cr} = \frac{I_r}{a_r J_r} \quad (3)$$

The area of the rotor slots A_{ur} is then calculated as

$$A_{ur} = \frac{z_Q A_{cr}}{k_{cu,r}} \quad (4)$$

where $k_{cu,r}$ is the space factor and is dependent on the conductive material of the machine. A space factor is a ratio of the area of conductive material in a slot and the area of the slot itself. Aluminium casted bars are intended for the design, making $k_{cu,r} = 1$.

3.2. Slot shape

The dimensions of the rotor slot need to be determined to form the appropriate shape. A circular slot shape was selected for this design. Most slot shapes are grouped into pear-shaped, trapezoidal or circular. Pear-shaped slots are more effective at weakening torque ripples, but the torque results between the three types vary marginally on the fundamental flux density [4]. The diameter of the slot is determined from the area, but the depth of the slot and the width of the opening required must also be determined to minimise the skin effect on the slots. The skin effect decreases a conductor's current-carrying capacity. It occurs in a rotor because at a low rotational speed, the rotor current frequency is increased and the current in the

rotor slots is displaced in a radial direction towards the air gap as depicted in Figure 1 [5]. The coil located deepest in the slot experiences a stronger leakage field and has the highest leakage inductance in comparison to the coils located close to the air gap. The rotor current concentrates in the upper coils. The conductive cross-section of the slot is decreased and the resistance of the rotor bar increases.

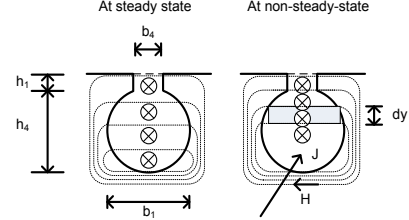


Figure 1: Skin effect on a rotor slot [5]

The correction coefficients for the slot resistance k_R and the slot inductance k_X are determined by [6]

$$k_R = \xi \frac{\sinh 2\xi + \sin 2\xi}{\cosh 2\xi - \cos 2\xi} \quad (5)$$

$$k_X = \frac{3}{2\xi} \frac{\sinh 2\xi - \sin 2\xi}{\cosh 2\xi + \cos 2\xi} \quad (6)$$

where ξ is the reduced conductor factor. To determine the best dimensions of the slot to minimise the skin effect, the correction coefficients should be 1. The reduced conductor factor, ξ , is then calculated and used to determine the slot opening for the various scenarios of slip. The depth of the slot δ_{skin} , or h_1 , is calculated by [7]

$$\delta_{skin} = \sqrt{\frac{2}{\omega \mu_0 \mu_r \sigma_{Al}}} \quad (7)$$

where ω is the frequency in radians, μ_0 is the permeability of free space, μ_r is relative permeability of the material and σ_{Al} is the electrical conductivity of aluminium.

4. PERMANENT MAGNET DIMENSIONS

Flux is the product of the flux density and the area of the material. The permeability of the core steel is assumed infinite compared to the permeability of the permanent magnet and the air gap. Deriving from this assumption, the permanent magnet's flux Φ_{mag} is equal to the air gap's flux Φ_g . This assumption neglects the effect of leakage flux and fringing and is a first order approximation [9]. The following can then be applied

$$A_{mag} B_{mag} = A_g B_g \quad \text{and} \quad (8)$$

$$B_g = \frac{A_{mag}}{A_g} B_{mag} \quad (9)$$

where A_{mag} is the area of the permanent magnetic material, B_{mag} is the flux density of the permanent magnet, A_g is the area of the air gap and B_g is the flux density of the air gap. In order to size the magnet appropriately a material and grade must be chosen for the

application. The selection is based on the typical flux density the magnet is capable of producing at 60°C which is the temperature the motor is designed to reach during operation. NdFeB 745TP is selected for the application. The operating point (B_{mag} , H_{mag}) of the permanent magnet must be calculated using the load line created by the magnet's remanence B_r and coercivity H_c . The load line is shown in Figure 2.

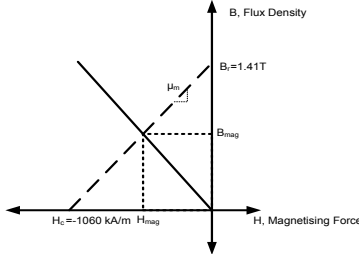


Figure 2: Load line of NdFeB Vacodym 745TP

The operating point of the material, B_{mag} and H_{mag} , is taken as the midpoint of the B-H curve in the second quadrant as indicated in Figure 2. B_{mag} is taken as half of B_r and the equivalent H_{mag} is then determined. The product of B_{mag} and H_{mag} yields the maximum energy product of the magnet. Using the maximum energy product yields the smallest volume of material able to produce the desired air gap flux density [9]. Drawing from the simplified magnetic circuit, the magneto motive force drop across the air gap and the permanent magnet is equal, but opposite in polarity as shown in [9]

$$\frac{H_{mag} h_{mag}}{H_g \delta} = -1. \quad (10)$$

where H_{mag} is the field intensity of the permanent magnet at maximum energy product, h_{mag} is the height of the permanent magnet, H_g is the field intensity of the air gap and δ is the thickness of the air gap. (10) can be solved for H_g and then for B_g as follows

$$H_g = -\frac{H_{mag} h_{mag}}{\delta} \quad (11)$$

$$\frac{B_g}{\mu_0} = \frac{H_{mag} h_{mag}}{\delta} \quad (12)$$

If (11) is multiplied with (12), then the following equation is obtained

$$B_g^2 = -\mu_0 \frac{h_{mag}}{\delta} \frac{A_{mag}}{A_g} H_{mag} B_{mag} \quad (13)$$

$$B_g^2 = -\mu_0 \frac{Vol_{mag}}{Vol_g} H_{mag} B_{mag} \quad (14)$$

where Vol_{mag} is the volume of the permanent magnetic material and Vol_g is the volume of the air gap. The required volume of magnetic material per pole Vol_{mag} is calculated from (14) and using the maximum energy product of the material as

$$Vol_{mag} = \frac{Vol_g B_g^2}{\mu_0 (-H_{mag} B_{mag})} \quad (15)$$

where Vol_g is volume of the air gap. The maximum volume of the magnetic material is then deduced as $50.960 \times 10^{-6} \text{ m}^3$. The equivalent BH product must be within the limit of the maximum BH of the material at the operating temperature. A rectangular shape is used for the permanent magnet and the depth is governed by the axial length of the rotor. The magnet thickness must be kept to a minimum to minimise the effect of the cogging torque and still provide enough flux [10]. As stated previously, the permeability of the core steel is assumed infinite. The following equation is obtained

$$\oint H dl = H_{mag} h_{mag} + H_g \delta = 0 \quad (16)$$

(11) is then rewritten to obtain the thickness of the magnet, h_{mag} [9]

$$h_{mag} = -\frac{(H_g \delta)}{H_{mag}} \quad (17)$$

The field strength of the air gap, H_g , is determined as follows

$$H_g = \frac{B_g}{\mu_r \mu_0} \quad (18)$$

The air gap flux density was chosen as $B_g = 0.85 \text{ T}$ and $\mu_0 \mu_r = 4\pi \times 10^{-7} \text{ H/m}$ which is the permeability of air. Substituting (18) into (17) gives

$$h_{mag} = -\frac{\frac{B_g}{\mu_r \mu_0} \delta}{H_{mag}} \quad (19)$$

The required area is known as well as the thickness of the permanent magnet, $h_{mag} = 6.5 \text{ mm}$. The required width of the permanent magnet is then calculated as 56 mm. The permanent magnets have been sized according to the application and corresponding magnetic circuit. The load line of the circuit is displayed in Figure 3 to indicate that the permanent magnets will operate within the designed operating point. The intersection of the load line of the magnetic circuit and the load line of the permanent magnet occurs at (0.789 T; -450 kA/m) at 60°C.

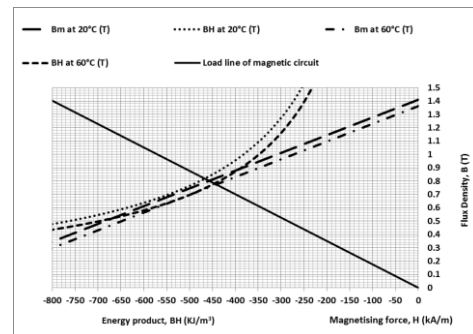


Figure 3: Load line of magnetic circuit intersecting with load line of the permanent magnet

5. FLUX BARRIER DIMENSIONS

Approximately 25% of the flux generated by an embedded permanent magnet is lost at the end points of a magnet [11]. Surface-mounted permanent magnets lose 5-10% of their flux. The literature on embedded permanent magnets does not give guidance on the lowest leakage flux obtainable, but it was decided to reduce the loss to 15%. In order to reduce the leakage flux, flux barriers are created at the ends of a magnet as depicted on the left of Figure 4. Air gaps are used as flux barriers in this design to channel more of the flux away from the magnet and towards the machine's air gap. The best solution for this application would be to join the flux barriers to the machine's air gap. This reduces the leakage flux to less than 10%, but splits the rotor laminations into four sections which are difficult to assemble. The design depicted on the right of Figure 4 was selected as the final design of the flux barriers to reduce the loss to 15%.

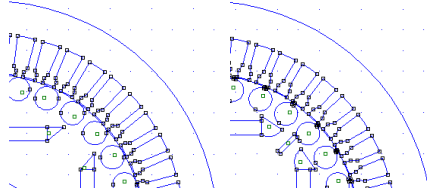


Figure 4: Model with original flux barriers on the left and final flux barriers on the right

6. TESTING

The prototype is tested in order to conclude if the machine can be used as a replacement for an equivalent induction machine. The 7.5 kW induction machine is tested first to establish a set of base parameters to be used for the comparison. The designed rotor is tested with and without the permanent magnets because the losses due to friction and windage are measured when the machine has no excitation. It is not possible to obtain zero excitation in a permanent magnet machine and hence the machine is tested without the permanent magnets [12].

The same tests are conducted on the induction machine and the LSPMSM. The tests are:

1. DC resistance test of the stator windings
2. Blocked rotor test
3. No load test
4. Back-emf (only for the LSPMSM)
5. Cogging torque test (only for the LSPMSM)
6. Final torque curve

6.1. Equivalent circuit parameter results

The equivalent circuit parameter results are displayed in Table 1.

Table 1: Equivalent circuit parameter test results in Ohms

Parameter	7.5kW Induction Machine	Retrofit LSPMSM Calculated	Retrofit LSPMSM Measured
R_1	2.383	2.383	2.423
X_1	5.748	5.748	5.551
R_2	1.622	2.122	2.281
X_2	7.722	8.01	7.743
R_{fe}	5349.904	3163.911	3809.28
X_m	195.908	247.714	204.241

There is a difference between some calculated and measured results. The rotor resistance is calculated by adding the resistance of the rotor bar, R_{rotor_bar} , and the resistance of the section of the end ring, R_{end_ring} , connected to the bar. When the rotor slots were designed, it was with the intention of casting the rotor bars and this decision was used to determine the rotor bar area and the rotor resistance. Casting was not possible during the manufacturing process and the bars were manufactured instead. This reduced the area of the rotor bars to allow for slotting of the bars into the lamination stack. The rotor bar resistance, R_{rotor_bar} , is determined as follows

$$R_{rotor_bar} = \rho_{Al} \frac{l'}{A_{ur}} \quad (20)$$

where l' is the equivalent length of the machine and ρ_{Al} is the resistivity of aluminium. It is clear that if the area is reduced, the resistance of the rotor bar increases. The profile of the rotor bar was decreased by 0.5 mm which reduced the area by 5% and increased the resistance by 7.5%. Similarly, this affects the rotor reactance.

The results obtained from the no load test do not correspond with the calculated results. There is also a difference in the no load test results between the retrofit design with and without the permanent magnets. This leads to the conclusion that the permanent magnets have an impact on the determination of the core resistance and magnetising reactance. Further investigation is required to determine how the effect can be accounted for during the design phase.

6.2. Back-emf results

The calculated back-emf is displayed in Figure 5. It was established during the testing that the calculated back-emf of the prototype is too high in comparison with the supply voltage which means that the machine will not operate correctly as a motor since the high back emf will keep it from synchronizing. The back-emf, E_m , produced by the permanent magnet is related to the permanent magnet flux Φ_{mag} , the winding factor k_w , the number of stator turns N_s and the number of magnets N_m , as follows

$$E_m = k_w N_s N_m \Phi_{mag} \quad (20)$$

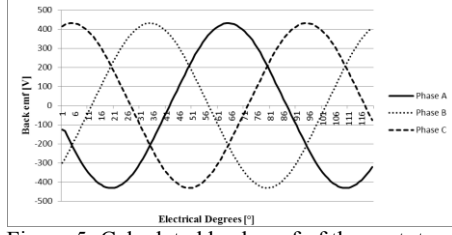


Figure 5: Calculated back-emf of the prototype

The flux generated by the permanent magnets is dependent on the flux density, B_r . This means that the magnet's flux density is too high for the application, though the operating point for the magnetic circuit is correct. However, if a permanent magnet with a lower B_r was selected the required magnetic material volume would increase to maintain the same flux. This would result in placement constraints. If a permanent magnet with $B_r = 1$ T was used, such as NdFeB Vacodym 688 AP, the required volume would be $102.08 \times 10^{-6} \text{ m}^3$. The required height to minimise cogging torque would then be $h_{mag} = 623$ mm which is impractical for the application. If a height of 10 mm is selected, the required width is 60 mm. This provides a better placement of the magnets, but increases the leakage flux because the magnet end points will be situated closer together than the current prototype.

The conclusion is that when a permanent magnet is designed for an application, the load line still applies, but the back-emf must be calculated at the same time in order to select the correct material grade. If the stator windings could be reduced, the back-emf would also be reduced because the induced emf is directly proportional to the number of turns in the stator coils. The original volume of permanent magnet material could be used. To reduce the back-emf of the prototype, only 105 mm of the 170 mm axial length of the permanent magnet material was placed into the rotor. This changed the RMS back-emf to $E_m = 303.23$ V. The recalculated and the measured back-emf curves are displayed in Figure 6. For display purposes, only Phase A is shown. The calculated and measured values correlate well.

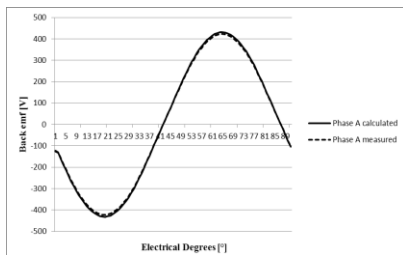


Figure 6: Re-calculated and measured back-emf of the prototype

6.3. Cogging torque results

Cogging torque requires the simulation of the machine at various positions of the rotor and is typically expressed as a Fourier series [13]. Calculating the theoretical cogging torque was not an objective of this design, but the measurement of the cogging torque is still required to

determine if it is within an acceptable range. The measured cogging torque is displayed in Figure 7. A small section is displayed for viewing purposes. According to [12] and [13], the measured cogging torque is within an acceptable range. The DC offset is a result of the friction the machine experiences. The oscillation frequency is a function of the stator turns and the number of poles as seen in (21) as follows [13]

$$T_{cogging} = N_p \sum_{k=1}^{\infty} T_{pN_s N_p k} \sin(N_s N_p \theta) \quad (21)$$

where N_p is the number of poles, $T_{pN_s N_p k}$ is the Fourier coefficient of the torque and θ is the angle of rotation.

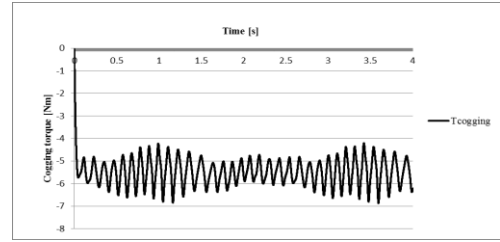


Figure 7: Cogging torque of the prototype

6.4. Final torque results

From [14], the electromechanical torque is derived by

$$T_{em} = \frac{m_s V_{sph}^2 (R_r' / s)}{(\omega_s / p) \left((R_s + (R_r' / s))^2 + (\omega L_k)^2 \right)} \quad (22)$$

where T_{em} is the electromechanical torque, m_s is the amount of phases in the stator, s is the slip, p is the amount of pole pairs, R_s is the stator resistance, R_r' is the rotor resistance referred to the stator and L_k is the machine's short-circuit inductance. The calculated, simulated and measured torque curves are displayed in Figure 8. The torque curve of the induction machine is also displayed. The torque curve of the LSPMSM correlates well with the induction machine and has a higher starting torque. The measured torque curve indicates the presence of the torque ripple as caused by the cogging torque. There is a maximum difference of 7 Nm between the calculated and measured torque curves. The difference between the curves is attributed to the discrepancy between the calculated and measured results of the rotor resistance. If the measured rotor resistance value is used in (22), the calculated torque curve then overlaps the measured torque curve.

Although only 105 mm axial length of the permanent magnet material was installed, this did not have a significant impact on the final torque curve because (22) is a function of the machine's equivalent electric circuit parameters. The stator and rotor resistances are not affected by the permanent magnets and the leakage inductances are dependent on the air gap, slot sizes, end windings and skewing [6]. The permanent magnets are sized to deliver the desired air gap flux density by the

area of the material and flux density. The volume of magnetic material was changed, but the thickness of the magnet in the radial direction did not change and still satisfied (8) and (16).

The efficiency of the prototype was calculated as 92.6% and measured as 91.8%. The equivalent induction machine used for the comparison has an efficiency of 90%. It is evident that the prototype is more efficient than the induction machine.

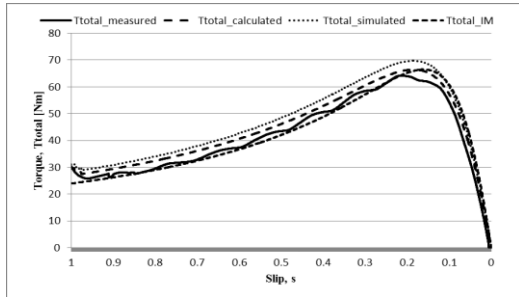


Figure 8: Torque comparison between design and performance test

7. CONCLUSION

Designing a rotor for a LSPMSM requires dividing the design into two sections: the induction machine where the cage or rotor slots are designed and the PMSM where the permanent magnets are designed. The rotors slots were designed by using standard induction machine equations and taking skin effect into consideration. The calculated and measured torque curves indicated that the cage was adequately designed to ensure a starting torque that would overcome the machine's inertia. The permanent magnets were capable of producing the required flux density but that back-emf of the selected material was too high for the prototype and hence less magnetic material was used in the final testing. It is important to perform the back-emf calculations together with the sizing calculations to ensure that the correct material is selected.

The LSPMSM compared well with the induction machine in terms of torque capability. The LSPMSM also proved more efficient than the induction machine, confirming that permanent magnets can improve a machine's efficiency.

8. REFERENCES

- [1] J. F. Gieras and M. Wing. "Introduction" in *Permanent Magnet Motor Technology*, second edition, volume 1. M. Wing, New York: Marcel Dekker Inc., 2002, pp. 12 – 13.
- [2] A. H. Isfahani, "Line start permanent magnet synchronous motors: challenges and opportunities", Elsevier: Energy, vol. 34, pp. 1755-1763, April 2009.
- [3] J. Pyrhönen, T. Jokinen and V. Hrabovcová. "Design Process and Properties of Rotating Electrical Machines" in *Design of Rotating Electrical Machines*, first edition, volume 1. West Sussex: John Wiley & Sons, 2008, pp. 307-342.
- [4] K. Zhang, X. Jiang, Y. Wu, L. Zhang and X. Wu. "Effect of slot shape in rotor of electrical motor with high-speed spindle on slot ripples" in *Proceedings of the 2010 International Conference on Modelling, Identification and Control*, Japan, July 2010.
- [5] M. Benecke, R. Doebbelin, G. Griepentrog and A. Lindemann. "Skin Effect in Squirrel Cage Rotor Bars and Its Consideration in Simulation of Non-steady-state Operation of Induction Machines" in *Proceedings of Progress In Electromagnetics Research Symposium*, Marrakesh, Morocco, March 2011.
- [6] J. Pyrhönen, T. Jokinen and V. Hrabovcová. "Flux Leakage" in *Design of Rotating Electrical Machines*, first edition, volume 1. West Sussex: John Wiley & Sons, 2008, pp. 243 – 253.
- [7] J. Pyrhönen, T. Jokinen and V. Hrabovcová. "Resistances" in *Design of Rotating Electrical Machines*, first edition, volume 1. West Sussex: John Wiley & Sons, 2008, pp. 256 – 259.
- [8] J. Santiago and H. Bernhoff. "Comparison between Axial and Radial Flux PM Coreless Machines for Flywheel Energy Storage", *Journal of Electrical Systems*, Issue 2, volume 6, June 2010.
- [9] A. E. Fitzgerald, C. Kingsley and S. Umans. "Magnetic circuits and Magnetic Materials" in *Electric Machinery*, sixth edition, volume 1. New York: McGraw-Hill, 2003, pp. 32 – 34.
- [10] D. C. Hanselman. "Design Variations" in *Brushless Permanent Magnet Motor Design*, first edition, volume 1. United States of America: McGraw-Hill, 1994, pp. 120 – 121.
- [11] J. Pyrhönen, T. Jokinen and V. Hrabovcová. "Design Process and Properties of Rotating Electrical Machines" in *Design of Rotating Electrical Machines*, first edition, volume 1. West Sussex: John Wiley & Sons, 2008, pp. 397-399.
- [12] H. Karmaker, "Report on IEEE Standard Working Group P1812 on Guide for Testing Permanent Magnet Machines" in *IEEE Transactions on Magnetics*, volume 46, pp. 2327 – 2333, 2012.
- [13] L. Dosiek, "Cogging Torque Reduction in Permanent Magnet Machines" in *IEEE Transactions on Industry Applications*, volume 43, pp. 1565 – 1571, 2007.
- [14] J. F. Gieras and M. Wing. "Design Process and Properties of Rotating Electrical Machines" in *Permanent Magnet Motor Technology*, second edition, volume 1. M. Wing, New York: Marcel Dekker Inc., 2002, pp. 330.

ROTOR DESIGN OF A LINE START PERMANENT MAGNET SYNCHRONOUS MACHINE USING THE TAGUCHI METHOD

A.J. Sorgdrager*, R. Smith* and R-J Wang*

* Department of Electrical and Electronic Engineering, Stellenbosch University, Private Bag XI, Matieland 7602, South Africa E-mail: ajsorgdrager@gmail.com, rwang@sun.ac.za

Abstract: This paper investigates the use of the Taguchi method for the design and optimization of a line-start (LS) permanent magnet synchronous machine (PMSM). The method is implemented separately for the steady-state and transient performance optimization. The optimized machine shows good transient performance as well as the steady-state performance that complies with IE4 efficiency standards. The main advantage of the Taguchi method is the large reduction in computational efforts when compared with traditional optimization methods.

Key words: Taguchi method, line-start motor, design optimization, transient performance.

1. INTRODUCTION

Induction motor (IM) drives have been widely used in a broad industrial drive application, of which a high percentage of the IM drive systems are line-start motors. These motors are of relatively poor efficiency, power factor and power density. The LS PMSM has been regarded as a promising alternative to traditional line-start IM. However, the design of an LS PMSM is rather complicated as it involves the design for both asynchronous and synchronous operation modes. This paper presents the design optimization of an LS PMSM by implementing the Taguchi method for robust design. The performance optimization considers both steady state and transient performance.

1.1 Taguchi Method Design Approach

Taguchi method is a modified and standardized form of design of experiments (DOE), which was proposed by Dr. Genechi Taguchi in 1957. This method is based on the DOE method developed by Sir R.A Fisher [1, 2] and was initially intended to increase quality control during the design phase for products and processes [3]. The main difference between the Taguchi method and DOE is the standardized application approach and methodology, which is done through the use of unique orthogonal arrays. The orthogonal arrays pre-define the conditions of each parameter in the array for each experiment or trail. Taguchi also introduced the use of the signal-to-noise (S/N) ratios to analyze the experiment results. Fig. 1 is a illustration of how the Taguchi method is used.

The orthogonal arrays trial results can be used to view the quality characteristics (QC) of the project, product or design depending on the desired result and the outcome of the QC. The three evaluations are *Bigger is Better* (QC = B), *Smaller is Better* (QC = S) and *Nominal is Better* (QC = N). In order to measure variation in a set of sample data the Mean-Squared Deviation (MSD) is calculated, which represents the deviation from the target. To calculate the MSD and then the S/N of a trial, each trial must be exposed

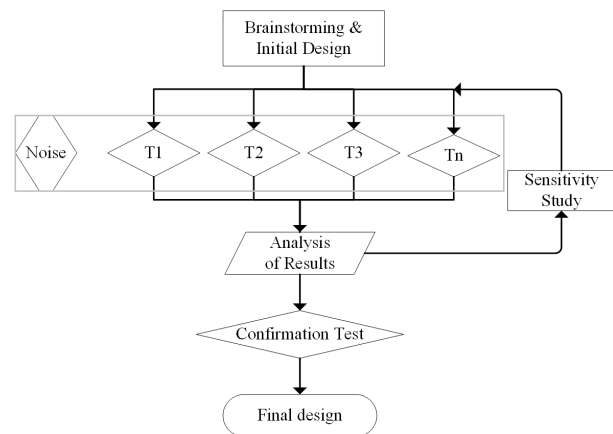


Figure 1: Flowchart of the Taguchi method design approach

to noise factors. By doing this, the robustness of the design is investigated. The noise factors are uncontrollable but known factors.

Once all the trials are performed, only then can the results be analyzed. The trial results are used to construct the S/N ratio plots of each factor used. From these plots the optimum conditions are determined. A conformation trial test is then done to ensure that the criteria is met. The optimum design as determined by the Taguchi method is not always the best performing design but rather the best performing consistent design within the noise exposure.

The Taguchi method has been used in some electrical machine designs in recent years. It has been used to reduce cogging torque and torque ripple in permanent magnet and synchronous reluctance machines. In one instance, the method was used to optimize a RSM. This was done by varying the parameters defining the flux barriers in the rotor to gain the highest possible saliency ration [4]. This design approach not only produces a design with an improved performance but also gives an insight on which topology factor influences the optimum conditions the most.

2. ROTOR DESIGN

For this study, an existing commercial 2.2 kW 4-pole induction motor stator is used as part of the design. The Taguchi method will only be applied to the rotor design of the machine. Table 1 gives the rated specifications of the proposed machine.

A comparative study [6] reveals that the LS PMSM rotor with an interior asymmetrical magnet array (shown in Fig. 2) demonstrates the best overall transient and steady state performance among different rotor topologies. This paper focuses on the further design analysis of this specific rotor topology. The objective is to search for an optimum design that is of high efficiency and power factor at steady-state and also a good starting performance. Considering the inherent conflict between magnetic and cage torques in an LS PMSM during asynchronous operation, a fine balance between the cage and PM array designs should be attained where the following favourable conditions are met: (i) under transient starting operation, the cage torque can sufficiently overcome the magnet's braking torque and accelerate the load to synchronous speed; (ii) under synchronous operation, the LS PMSM exhibits a good steady-state performance that a typical PM synchronous motor offers. Clearly, the design of an LS PMSM entails both steady-state and transient designs.

Table 1: Design specifications of the machine

Parameters	Value
Rated output power, kW	2.2
Rated voltage (line-to-line), V	525
Rated speed, rpm	1500
Rated torque, Nm	14

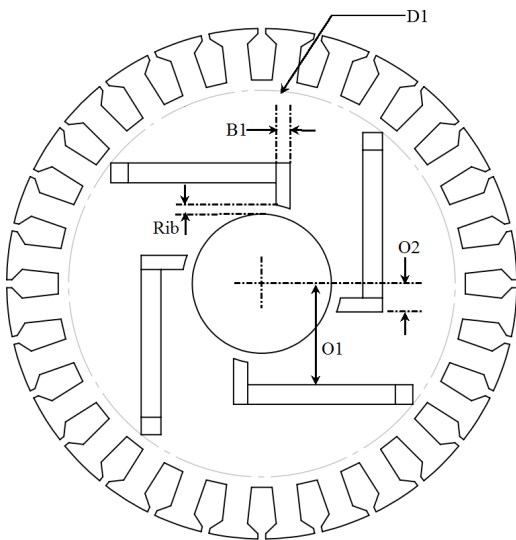


Figure 2: Interior asymmetrical PM array rotor topology

2.1 Steady State Design

The steady state design is of importance as it is the primary operation condition of the machine. Information from the steady state performance is also required for the rotor cage design as the cage produced torque needs to overcome the magnet braking torque and load inertia during transient operation. For this design, the PM dimensions, material and grade are fixed as an extra set of magnets was ordered for a previous project.

During steady state operation, the machine operates as a PMSM thus, the torque produced by the machine is the sum of the reluctance and PM torque. Fig. 2 illustrates the dimensions that are identified as design parameters for the steady state performance optimization. For all five design parameters an L16 inner array is required, which allows for the five parameters to be varied with four different states. Initially D1, Rib, O1, O2, B1 as in Fig. 2 is chosen for the inner array. As stated in Section 2, the use of an outer noise array is needed. To include this in the design, uncontrollable but known factors can be used. The PM property variation, PM thickness and shaft material are chosen as the outer array noise parameters. These parameters are chosen in order to account for manufacturing tolerances and the effect of material. For the outer noise array a L4 array is selected, which allows for three noise factors with two states. The final steady state array is indicated by Table 4 in the Appendix. The simulation process is given by Fig. 3, where T_x represent the main array, x is the 16 main designs that is individually exposed to the noise array N_y , y represents the four noise conditions. In total 64 simulations are required before the results can be analyzed and the five main array factors can be adjusted.

The area allocated for the PM slot is carefully selected so that all possible designs as per the L16 array is possible. From this the upper and lower limits for the initial design are defined and summarized in Table 2. The magnet slots

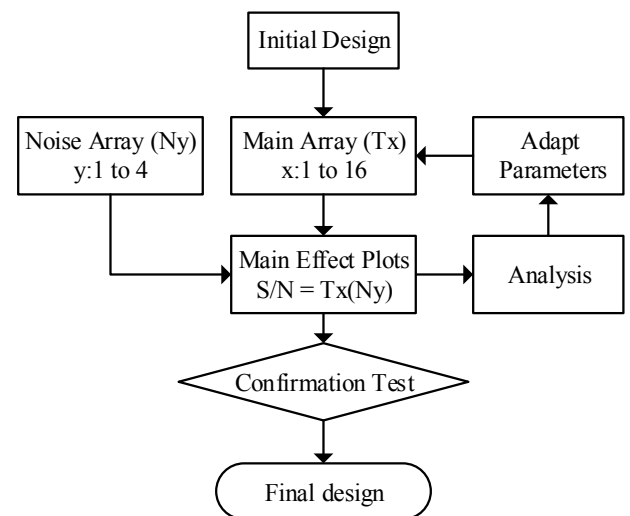


Figure 3: Taguchi steady state array simulations

have to be constrained to fit in the space available on the lamination while accounting for the rotor cage slots.

The four levels for each factor (D1, Rib, O1, O2, B1) in the main array are determined by dividing the lower and upper limits with equal increments. These states are then used to produce the first orthogonal array and design the first iteration of experiments. In theory the Taguchi method should provide the optimum result after one iteration. Since only four definite levels are selected for each factor the results may be non-linear between the different levels. To overcome this more than one iteration is done and after each iteration the worst performing level of each factor is reduced or eliminated with the aid of the main effects plot. As the maximum efficiency is desired a Bigger-is-better MSD is used to calculate the S/N results for the main effect plots. Fig. 4 contains the S/N plots of the first iteration and the final iteration of factor B1 and Rib. If focus is placed on the initial design it is clear that there is a big variance in performance as a result of factor change. By reducing the range of the levels after each iteration the final design resulted in a near horizontal plot, this is an indication that both B1 and Rib have reached its optimum level.

During the investigation it is found that by minimizing the two areas (A and B) as indicated in Fig 5 the steady state performance improves. Obviously, to minimize undesired leakage flux these areas need to be magnetically

Table 2: Upper and lower limits for magnet slots

Variables	Lower limit	Upper limit
D1	76	83
Rib	0.7	1.4
O1	15.2	23.2
O2	4	10
B1	4	7

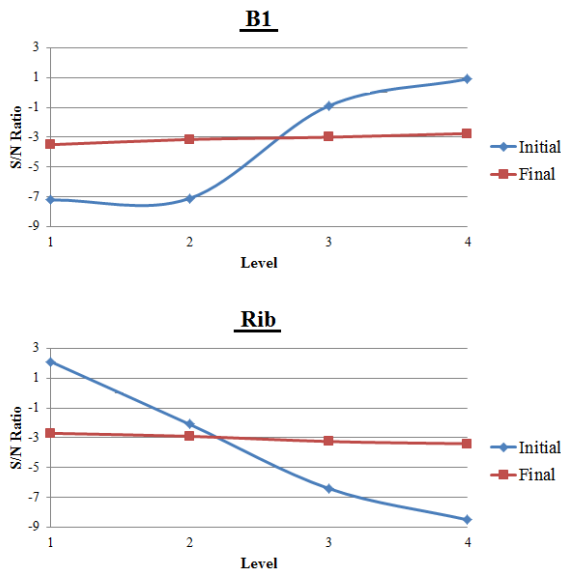


Figure 4: S/N ratio plots of two factors

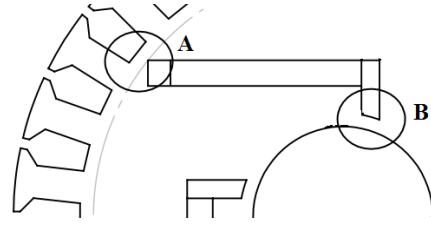


Figure 5: Saturation zones formed by D1 and Rib

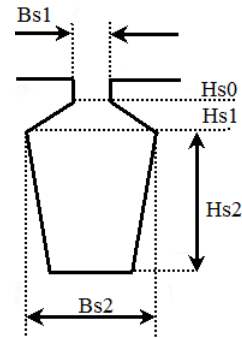


Figure 6: Rotor cage bar dimensions

saturated. With the knowledge of this, the two parameters characterizing these two areas, D1 and Rib, can be suitably chosen and fixed, which frees two factors in the L16 array. This opens the opportunity to incorporate two of the rotor slot factors as in Fig. 6. Since Bs2 and Hs2 influence the cross-sectional area the most, they are selected to replace D1 and Rib in the array. It can be observed that adjusting Hs2 leads to an change in distance between the rotor cage and the PM duct. Thus the following relation must be implemented to ensure that the distance is constant.

$$D1 = 2[(OD/2) - (Hs0 + Hs1 + Hs2 + 0.7)] \quad (1)$$

During steady state optimization it is found that minimizing Hs2 would result in optimal steady state performance. However, the excessive minimization of Hs2 would drastically decrease the transient performance of the machine. This shows a drawback of the Taguchi method as it can only consider a solitary output parameter during design and optimization. It is possible to use multiple criteria optimization, but this would require the knowledge of the interactions between the different performance criteria [1–3]. Having realized this, a reconsideration of the previous steps in the optimization process is necessary. A trade-off is needed between steady state and transient performances. An increasing of Hs2 results in a drop in efficiency. This efficiency decrease is attributed to the decrease in D1, which in turn reduces the size of the flux barriers and changes the pole arch coefficient. A change in pole arch coefficient affects the air-gap flux density [7, 8].

The larger the flux barrier is, the less the leakage flux becomes. The machine's efficiency also improves with larger flux barrier. However, there exists an optimum point where any further barrier size increase leads to negligible

efficiency benefits. This optimum point has been identified through several iterations of the L16 array and D1 is so constrained that the maximum allowable height of the rotor bar slots is subjected to (2)

$$Hs01 + Hs1 + Hs2 < D_{rotor} - D1_{optimum} \quad (2)$$

2.2 Transient Design

The rotor slot shape for the cage design is shown in Fig. 6. The slot has five parameters and a L16 array can be used for the simulations. Since FEM time-step simulations are computationally expensive, it is decided to fix one of the factors so an L9 array can be used. This will reduce the number of simulations by half. The L9 array allows for four, three-level factors, thus Bs1, Bs2, Hs1 and Hs2 are selected with Hs0 fixed at 0.3 mm. For the transient optimization no noise array is used. This again reduces the required number of simulations, but it also removes the option to use the S/N ratio main effects plot. To overcome this, three normalized performance objective is selected to quantify the transient performance. These objectives are the synchronization time, (τ_{synch}), settling time ($\tau_{settling}$) and speed overshoot as illustrated in Fig. 7. By normalizing the three objectives the MSD can be calculated. The final transit array is indicated by Table 5 in the Appendix.

3. SIMULATION RESULTS

This section contains the simulation results for both the steady state and transient operation as determined by ANSYS' Maxwell. The steady state performance of the machine is evaluated using ANSYS Maxwell RMXprt. Efficiency is the primary performance factor considered with some focus on the starting torque and back-EMF. In first iteration of the steady-state design experiments, the efficiency varies between 82% and 90% and for the final iteration the steady-state efficiency varies between 92% and 92.5%. Table 3 contains the steady-state performance of the final machine.

The transient simulations was done using ANSYS

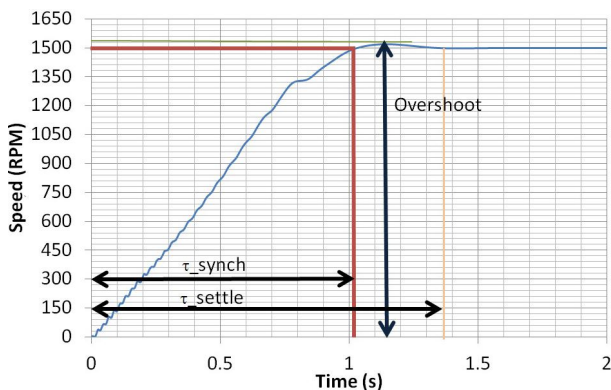


Figure 7: Illustration of transient parameters of interest

Table 3: LS-PMSM final design: steady-state performance

Parameter	Value
Efficiency	92.98 %
Power factor	0.954
Starting torque, Nm	43.55
Rated torque, Nm	14

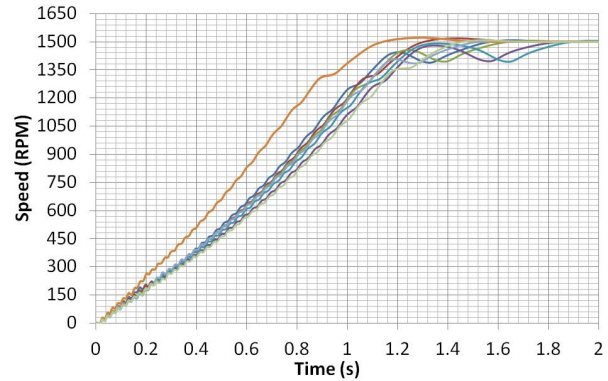


Figure 8: Initial transient performance

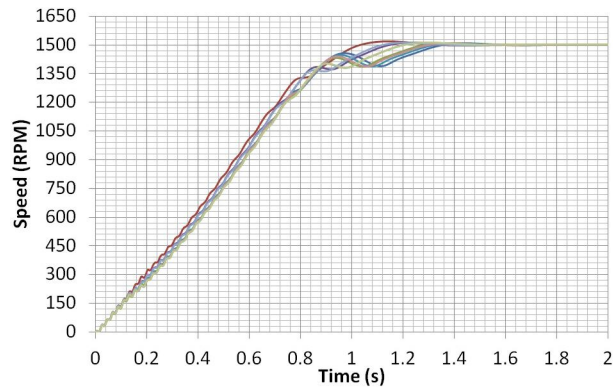


Figure 9: Final transient performance

Maxwell 2D FEM as time-step simulations is required. It is also possible to incorporate a load equation as part of a mechanical transient. The load characteristics of a custom designed fan is used in the simulations. Several iterations are carried out for the transient design. The results of the initial and final transient experiments can be seen in Figs. 8 and 9 respectively. The machine that delivers the shortest settling and acceleration time is used.

Figs. 10 to 12 indicates the transient performance of the designed machine when driving a fan load. The machine achieves synchronization within 0.9 seconds with negligible overshoot. Figs. 11 and 12 indicates the torque developed during this time.

4. CONCLUSION

This paper presented the design and optimization of an LS PMSM using the Taguchi method. For the optimization both steady-state and transient performance

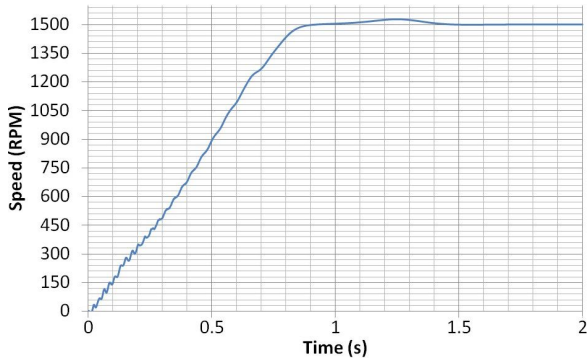


Figure 10: Final design: speed versus time plot

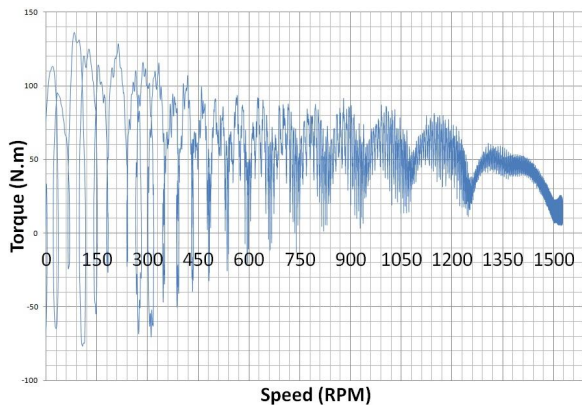


Figure 11: Final design: torque versus speed plot

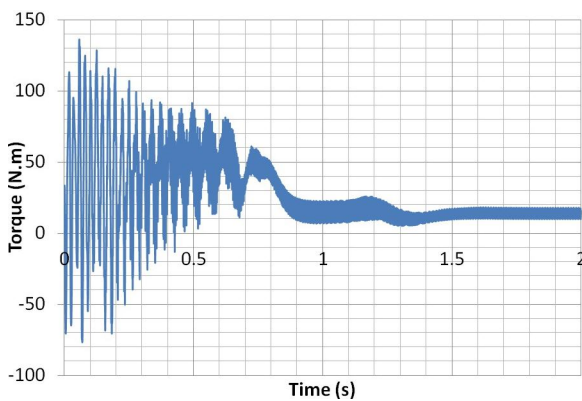


Figure 12: Final design: torque versus time plot

are individually considered. However, it is necessary to incorporate design constraints concerning the PM duct and rotor cage. This is to maintain a balance between the cage and PM array designs, which is important to realize acceptable transient and steady-state performances. The implementation of the Taguchi method to optimize the steady state performance has been a success. The use of the parameter interactions and how it can be used in the optimization of machine performance requires further investigation as some of the factors in the array moved to the optimum point within an iteration or two. With regards to transient optimization the Taguchi method proves to be

time efficient, which is one of the main advantages of the Taguchi method. The use of noise array also needs further study.

ACKNOWLEDGMENT

This work was supported in part by Eskom Tertiary Education Support Program (TESP), Sasol Technology Research and Development, and the National Research Foundation (NRF).

REFERENCES

- [1] R.K. Roy, A Primer on the Taguchi Method, 2nd Edition. Michigan, USA: Society of Manufacturing Engineers, 2010.
- [2] G. Taguchi, S. Chowdhury, Y. Wu, Taguchi's Quality Engineering Handbook, 1st Edition. New Jersey, USA: John Wiley and Sons Inc, 2005.
- [3] R.K. Roy: Design of Experiments Using the Taguchi Approach, Wiley-Interscience, 2001, New York, USA.
- [4] H. Azizi, A. Vahedi: "Rotor geometry parameter optimization of synchronous reluctance motor using Taguchi Method", *Przeglad Electrotechnical*, no. 1, pp.197-201, 2013.
- [5] M. Chowdhury, M. Islam, A. Gebregergis and T. Sebastian: "Robust design optimization of permanent magnet synchronous machine utilizing genetic and Taguchi's algorithm," *Energy Conversion Congress and Exposition*, vol., no., pp.5006,5012,15-19 Sept. 2013
- [6] J.P. Els, A.J. Sorgdrager and R-J Wang, "A Study of Rotor Topologies of Line-Start PM Motors for Cooling Fan Applications" in *Proceedings of the 22nd South African Universities Power Engineering Conference*, pp.284-289, Feb 2014.
- [7] C. Zhao, S. Li and Y. Yan, "Influence factor analysis of PMSM air gap flux density," *Electrical Machines and Systems*, 2005. ICEMS 2005. Proceedings of the Eighth International Conference on, vol.1, pp.334-339, 27-29 Sept. 2005
- [8] A.J. Sorgdrager and A.J. Grobler, "Influence of magnet size and rotor topology on the air-gap flux density of a radial flux PMSM," *Industrial Technology (ICIT)*, 2013 IEEE International Conference on, pp.337-343, 25-28 Feb. 2013

APPENDIX

Table 4: Steady state design array

L9	O1	O2	B1	Rib	DI	R1	R2	R3	R4	Mean	MSD	S/N
T1	1	1	1	1	1							
T2	1	2	2	2	2							
T3	1	3	3	3	3							
T4	1	4	4	4	4							
T5	2	1	2	3	4							
T6	2	2	1	4	3							
T7	2	3	4	1	2							
T8	2	4	3	2	1							
T9	3	1	3	4	2							
T10	3	2	4	3	1							
T11	3	3	1	2	4							
T12	3	4	2	1	3							
T13	4	1	4	2	3							
T14	4	2	3	1	4							
T15	4	3	2	4	1							
T16	4	4	1	3	2							
						PM	T	T	M	M		
						PM t	5	4.9	5	4.9		
						Shaft	M	nM	nM	M		

Table 5: Transient design array

L9	Bs1	Bs2	Hs1	Hs2	τ_{sync}	τ_{set}	Overshoot	Mean	MSD	S/N
T1	L1	L1	L1	L1						
T2	L1	L2	L2	L2						
T3	L1	L3	L3	L3						
T4	L2	L1	L2	L3						
T5	L2	L2	L3	L1						
T6	L2	L3	L1	L2						
T7	L3	L1	L3	L2						
T8	L3	L2	L1	L3						
T9	L3	L3	L2	L1						

- T Typical PM Magnetic Properties
- M Minimum PM Magnetic Properties
- M Magnetic Shaft
- nM non-Magnetic Shaft
- PMt PM thickness

THEORETICAL AND FINITE ELEMENT ANALYSIS OF A DOUBLE ROTOR RADIAL FLUX PERMANENT MAGNET EDDY CURRENT COUPLING

C.H.O. Lombard, S. Erasmus and M.J. Kamper

Department of Electrical and Electronic Engineering, Stellenbosch University, Stellenbosch, South Africa

Abstract: In this paper prove is given of the accuracy of a theoretical analysis approach in the performance calculation of double rotor permanent magnet eddy current coupling machines at low slip values. Analysis of permanent magnet eddy current coupling machines usually requires the use of finite element analysis for obtaining accurate calculated performance results. In this paper the calculated results of a theoretical analysis method are compared with the results obtained from finite element analysis. It is shown that the results of the proposed 3D theoretical analysis method at low slip values correlates well with the results obtained from complex 3D finite element analysis, given that the magnetic flux density within the air gap of the machine is exactly known. The calculated results are confirmed by measurements of a prototype permanent eddy current coupling.

Keywords: Eddy current coupling, permanent magnet, theoretical analysis, finite element analysis.

NOMENCLATURE

B	Magnetic flux density (tesla)
B_g	Magnetic flux density in the air gap (tesla)
e_θ	Induced voltage (Volt)
h_c	Radial height of the conductor (mm)
h_m	Radial height of the magnets (mm)
h_y	Radial height of the yoke (mm)
i_θ	Induced current (Ampere)
l	Length (m)
l_{le}	Axial length of the long overhang end (mm)
l_{se}	Axial length of the short overhang end (mm)
l_g	Radial length of the air gap (mm)
l_{pd}	Axial penetration depth of stator (mm)
l_{pm}	Axial length of the permanent magnet (mm)
l_s	Axial length of the stator (mm)
l_y	Axial length of the yoke (mm)
p	Number of poles
r_c	Radius of centre air gap (mm)
Theta_M	Magnet pitch (degrees or radians)
Theta_P	Pole pitch (degrees or radians)
v	Velocity (m/s)
α	Overhang factor
θ_e	Electrical angle (degrees or radians)
θ_m	Mechanical angle (degrees or radians)
τ_θ	Angular component of torque (Nm)
τ	Total torque (Nm)
ω_e	Electrical rotational speed (rad/s)

1. INTRODUCTION

The permanent magnet (PM) eddy current coupling machine is used in practice as an isolated coupling between two separate mechanical systems [1]. With this machine torque is transferred from one axis to another without any physical contact but by means of slip speed difference. There are numerous practical applications that require such a machine component, for example in wind generator systems [2]. The primary object of this study is to compare the accuracy of a purely theoretical approach in analysis as opposed to using the finite element method (FEM). The theoretical approach in electrical machine analysis and design optimisation is fast in terms of computation time. It is known that FEM is a very accurate and reliable method of analysis of machines such as the PM eddy current coupling studied in this paper. Finite element analysis (FEA), however, is expensive in terms of computational time and computer hardware required. The goal of this study is to document the accuracy by which the PM eddy current coupling can be analysed using a theoretical analysis approach based on the Lorentz and Maxwell laws [3].

The PM eddy current coupling machine analysed in this study was previously analysed using 2D and 3D FEM [2]. The same machine is re-analysed with FEM in this study, but with the addition of a theoretical 2D and 3D approach in the analysis. The results from the theoretical analysis in 2D are compared with the results from 2D FEA. It is furthermore possible to convert the 2D theoretical analysis to 3D by means of a theoretical 3D factor derived in [4]. The simulation time required for 2D FEA is less than 3D FEA, but the results are not as accurate as 3D FEA. Due to the fact that 2D FEA is based on much the same assump-

tions made in the proposed 2D theoretical analysis, the 3D factor should be able to convert inaccurate 2D FEA results to accurate 3D FEA. The results from the 3D theoretical analysis and the 3D FEA are compared with the measured results of an actual PM eddy current machine to validate both methods of analysis.

2. EDDY CURRENT COUPLING MACHINE

A 45° section of the PM eddy current coupling machine is shown in Figure 1 with the dimensions for the 2D analysis specified in Table 1. The actual PM eddy current coupling machine is shown in Figure 2.

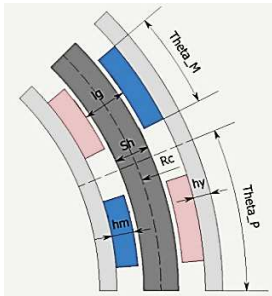


Figure 1: Cross section of the PM eddy current coupling.



Figure 2: PM eddy current coupling with hollowed aluminium cylinder stator (left) and double PM rotor (right) [2].

Table 1: Cross section dimensions of the PM eddy current coupling of Figure 1 in degrees and millimetres.

Theta_M	Theta_P	l_g	h_y	h_m	Sh	r_c	l_{pm}	p
13.34°	22.5°	10	4	5	8	76	35	16

It is important to understand the concept of slip or slip speed when referring to the eddy current coupling machine. The slip speed of the coupling is the relative speed between the PM rotor and the conductor cylinder stator. For the 16-pole PM machine of Figure 2 a 100 % slip is defined at 50 Hz as a slip speed of 375 r/min.

Using 3D analysis the axial dimensions of the machine are taken into account in the performance calculation. A 3D sectional model of the machine is shown in Figure 3, from which it is clear that some of the axial dimensions are chosen for mechanical simplicity. The rotor and the stator both require end-shells because they are fixed to separate axes.

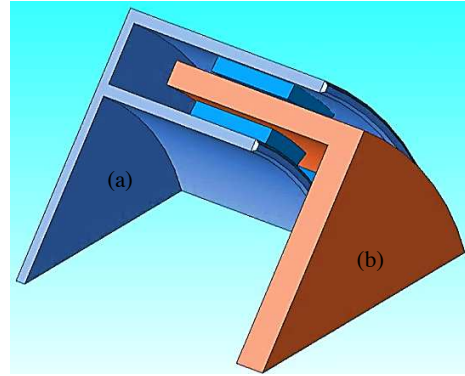


Figure 3: 3D sectional model of (a) the PM rotor and (b) the conductor stator.

When analysing a 3D model of the machine it is possible to simplify the model by ignoring the end shells of the rotor and the stator, as well as making use of angular periodicity. A model of the machine analysed in 3D is shown in Figure 4 for a single pole. In Figure 5 an axial section of the machine is shown indicating the axial dimensions needed for 3D analysis. The axial dimensions are specified in Table 2.

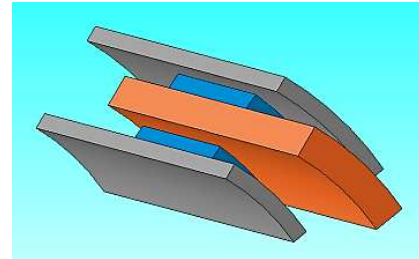


Figure 4: 22.5° periodic section of the PM eddy current coupling machine.

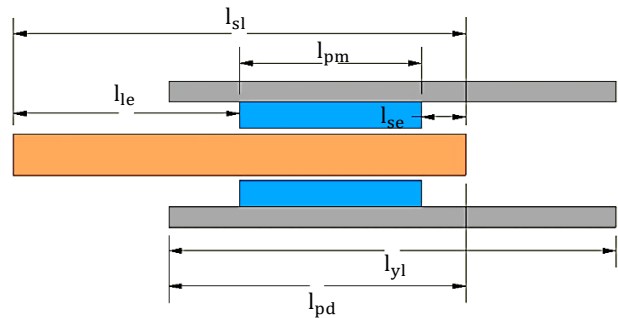


Figure 5: Axial dimensions of the PM eddy current coupling machine.

Table 2: Axial dimensions of the PM eddy current coupling in millimetres.

l_{sl}	l_{le}	l_{pm}	l_{se}	l_{y1}	l_{pd}
87	43.5	35	8.5	86	63

3. DERIVATION OF TORQUE EQUATION

By making use of Lorentz's force equation it is possible to calculate the 2D torque generated by the PM eddy current coupling machine. This analysis method requires the assumption that the magnetic flux density in the machine air gap has a sinusoidal shape in the angular direction and is constant in the axial direction. Torque in the angular direction is equal to the Lorentz force tangent to the circumference of the stator multiplied by the radial distance from the origin (radius) as

$$\tau_{\theta} = (Bl_{\theta})r_c, \quad (1)$$

where i_{θ} is the induced current in the stator segment. By assuming at a low percentage slip (low slip frequency) only a resistive load, the segment current can be calculated by

$$i_{\theta} = \frac{e_{\theta}}{R}. \quad (2)$$

Faraday's equation for calculating the EMF in a conductor segment moving through a magnetic field is given as

$$e_{\theta} = Blv, \quad (3)$$

where v is the velocity of the moving conductor given by

$$v = r_c \frac{d\theta_m}{dt} = r_c \frac{2 d\theta_e}{p dt}. \quad (4)$$

From Figure 6 it is possible to express the resistance in (2) of a segment of the stator as

$$R = \frac{\rho l}{A} = \frac{p}{2} \frac{\rho l_{pm}}{h_c r_c d\theta_e}. \quad (5)$$

By substituting (4) into (3) and then into (2), and also (5) into (2), a segment torque equation can be expressed from (1) and (2) as

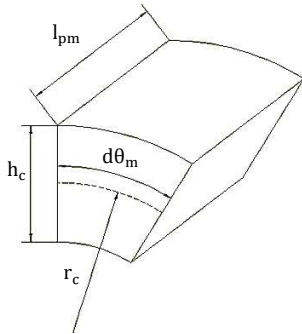


Figure 6: Segment of conductor cylinder stator.

$$\tau_{\theta} = \frac{4}{p^2} \left(\frac{r_c^3 B^2 l_{pm} h_c \omega_e}{\rho} \right) d\theta_e. \quad (6)$$

Equation (6) expresses the angular component of the torque and needs to be integrated over the entire circumference to obtain the total torque generated. It is important to note that it is assumed that the magnetic flux density in the air gap has a sinusoidal shape and can be expressed as $B = B_g \sin \theta_e$. Integration of (6) results in

$$\tau = \frac{2\pi}{p} \left(\frac{r_c^3 B_g^2 l_{pm} h_c \omega_e}{\rho} \right). \quad (7)$$

Equation (7) can be used to calculate the torque generated by the PM eddy current coupling based on 2D analysis. Note that (7) is reliant on having accurate information of the air gap magnetic flux density. This can be obtained from a 2D magnetic equivalent circuit solution or a static 2D FEM solution.

4. FINITE ELEMENT METHOD

It is widely known that FEM is an accurate method of analysis, especially in 3D. The FE analysis method is used in 2D and 3D to analyse the PM eddy current coupling machine investigated in this study. The results obtained from 3D FEA are used as the benchmark for accurate results.

2D FEA is not as accurate as 3D FEA when calculating the torque developed by an eddy current coupling machine as shown in [2]. In 2D FEA certain assumptions are made. The machine is only analysed as if at the centre of the machine stack, i.e. at the centre of the active region in the axial direction. It is then assumed that the magnetic flux density at the centre of the stack stays constant throughout the entire stack length. It also implies that the calculated induced current in the stator flows entirely in the axial direction of the machine. 2D FEA, thus, neglects all end effects on the magnetic flux density and the induced eddy currents in the stator conductor.

Analysis done in 3D can more accurately predict the induced eddy currents in the stator conductor. Also the variation of the magnetic flux density along the stack length of the machine is accurately taken into account. Although 3D FEM analysis is a more accurate analysis method, specifically for the PM eddy current coupling, it is a complex and computational expensive method. If however care is taken in optimising the amount of mesh elements used in the 3D FE transient calculation, it is possible to shorten the solution time substantially.

The induced current in the stator, according to 3D FEA, is shown in Figure 7. The magnetic flux density in the air gap from 3D FEA is shown in Figure 8 for the axial direction and in Figure 9 for the angular direction. It is clear that the assumptions made in 2D FEA regarding the in-

duced current and the constant magnetic flux density in the axial direction are incorrect. It is shown in Figure 7 that the induced eddy currents do not flow all along the axial direction but also in the tangential direction within the active magnetic field of the PMs.

The angular air gap magnetic flux density is shown in Figure 9 has a strong sinusoidal waveform. The fundamental sinusoidal component of this waveform can be obtained from a Fourier series to determine B_g in (7). Note that only one static 2D FE solution is required to obtain the waveform of Figure 9. The armature reaction effect of the eddy currents on the magnetic field in this case is ignored, but this is acceptable as the effect is very small due to the large air gap.

The torque output results from the 2D theoretical analysis (equation 7) as well as from 2D FEA and 3D FEA are shown in Figure 10. The results show that the 2D FEA and the 2D theoretical analysis correlate well, but that the torque results from the 3D FEA are significantly lower. The 3D FEA is more accurate than 2D FEA because of the incorrectly assumptions made in 2D FEA. In 2D theoretical analysis much of the same assumptions are made as in 2D FEA, thus their results should correlate well. At higher slip percentages (> 10 %) the correlation becomes less due to the assumption in 2D theoretical analysis of only a resistive load in (2).

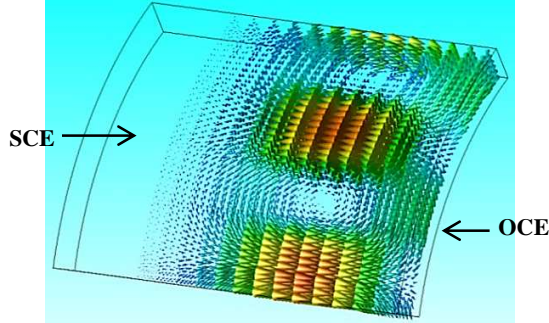


Figure 7: 3D FEA predicted induced eddy currents in the stator conductor.

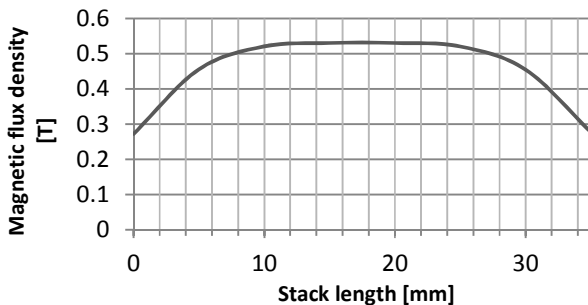


Figure 8: Magnetic flux density in the air gap in the axial direction of the magnet or stack length.

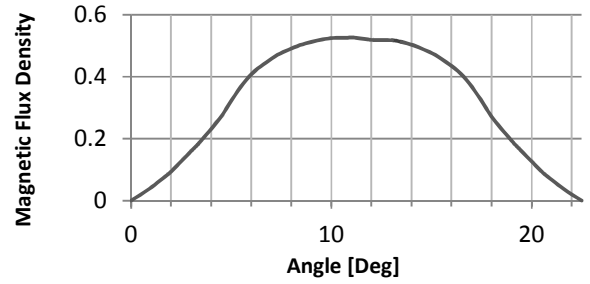


Figure 9: Magnetic flux density in the air gap in the angular direction.

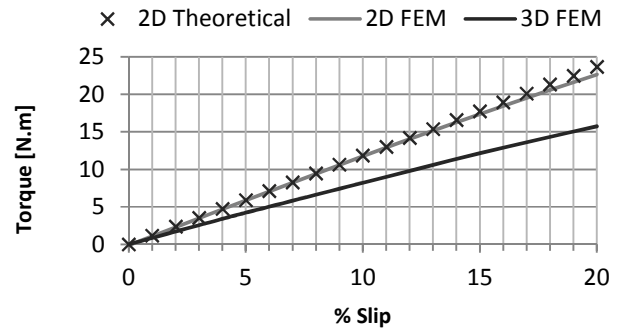


Figure 10: Torque versus percentage slip according to 2D FEA, 2D theoretical (equation 7) and 3D FEA.

5. 3D - FACTOR

In practice the stator of the PM eddy current coupling machine has overhangs beyond the magnetically active area. The stator conductor of the machine also has an open circuit end (OCE) on the one side and a short circuit end (SCE) on the other side as shown in Figures 7 and 11 (Figure 11 illustrates what is meant by an OCE and a SCE of the stator studied in this paper). This difference is necessary to define, because the stator needs to be mounted on an axis on the one end and slide into the double PM rotor on the other end. In the case of the prototype the SCE is far from the magnetically active area where the eddy currents do not flow anymore as shown in Figures 7 and 12(a). In this case thus the effect of the SCE becomes negligible and can this conductor end also be viewed as an OCE.

In [4] Russell defines a 3D factor that can theoretically be used to convert 2D calculated torque results to 3D torque results. This 3D factor considers the effect of having overhangs beyond the magnetically active area. The 3D factor is dependent on the length and type (SCE or OCE) of the overhang. For OCE the overhang coefficient is defined as

$$\lambda = \tanh\left(\frac{pl_{pm}}{2r_c}\right) \tanh\left(\frac{p\alpha l_{pm}}{2r_c}\right) \quad (8)$$

and for SCE as

$$\lambda' = \frac{\tanh\left(\frac{pl_{pm}}{2r_c}\right)}{\tanh\left(\frac{p\alpha l_{pm}}{2r_c}\right)}, \quad (9)$$

where α is an overhang parameter used to define the overhang length as $l_{overhang} = \alpha l_{pm}$.

For calculation simplicity both ends of the stator are analysed as OCEs with equal overhang lengths of 8.5 mm. The 3D factor K_s can then be calculated from [4] as

$$K_s = 1 - \frac{\tanh\left(\frac{pl_{pm}}{2r_c}\right)}{\left(\frac{pl_{pm}}{2r_c}\right)(1 + \lambda)}, \quad (10)$$

allowing the 3D torque to be calculated from (7) as

$$T = \tau K_s = \frac{2\pi}{p} \left(r_c^3 B_g^2 l_{pm} h_c \omega_e \right) K_s. \quad (11)$$

Multiplying the 2D FEM results with the 3D factor of (10) should also be able to convert the results to 3D FEM results. The successful conversion of 2D FEM to 3D FEM with Russell's 3D factor is shown in Figure 13.

A comparison between 3D theoretical analysis, 3D FEA and measured results from the PM eddy current machine is shown in Figures 14 and 15 for respectively aluminium and copper stators. The first observation is how accurate 3D FEA is, as it correlates almost exactly with the measured results. The second observation from Figures 14 and 15 is how accurate the 3D theoretical analysis predicts the torque outputs of the machine for both copper and aluminium stators for percentage slips of up to say 10 %.

The last experiment is done on a cylinder stator conductor with zero overhangs. The stator is machined in such a way that the induced current is limited from flowing past the magnet edges. This is done by machining a groove along the circumference of the stator as shown in Figure 16(d). It is however not possible to completely prevent the current from flowing past the magnet edges, as this would cause mechanical failure. Removing the overhangs would theoretically lower the torque output of the machine, as this limits the amount of induced eddy currents in the stator as shown in Figure 12(b). The machine with the zero stator overhangs is studied using 3D FEA and 3D theoretical analysis. The results of this experiment are shown in Figure 17. Here it is shown once again that the theoretical analysis correlates well with FEA. It is also seen that the measured results are slightly higher than the results obtained from 3D FEA. This is because of the mechanical construction that allows some eddy currents to still flow past the magnet edges. These measurements are, thus, not taken on a machine with completely zero stator overhangs.

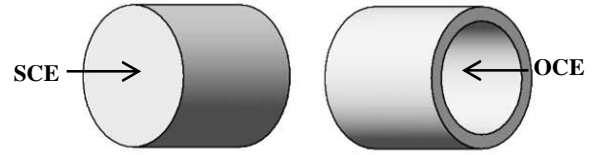


Figure 11: Illustration of stator OCE and SCE

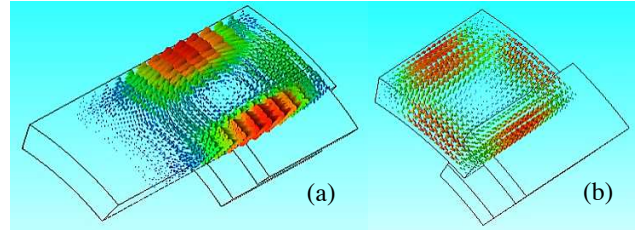


Figure 12: Induced eddy current of (a) normal stator and (b) stator with zero overhangs.

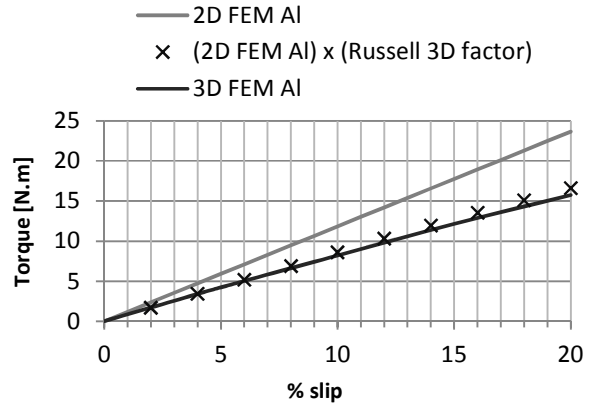


Figure 13: 3D factor tested on 2D FEM results.

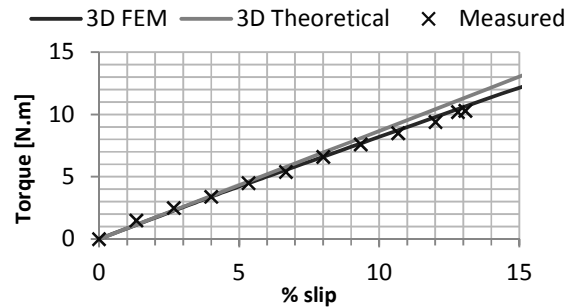


Figure 14: 3D FEA, 3D theoretical analysis and measured results for an aluminium stator conductor.

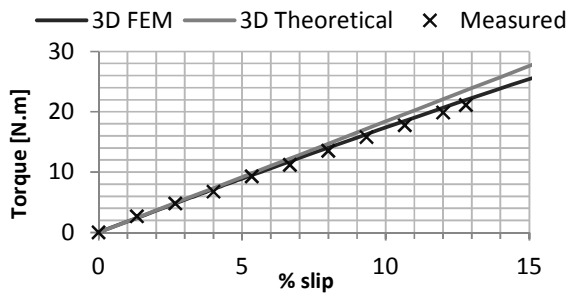


Figure 15: 3D FEA, 3D theoretical analysis and measured results for a copper stator.



Figure 16: (a) Normal aluminium stator, (b) normal copper stator, (c) equal overhang aluminium stator and (d) zero overhang stator.

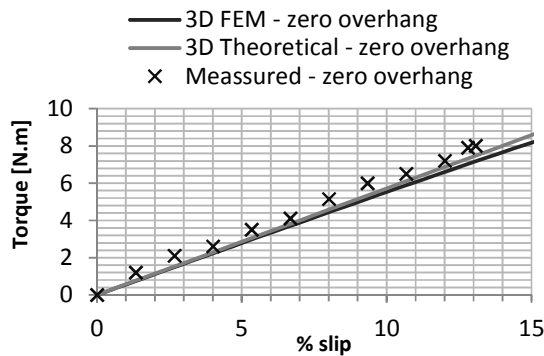


Figure 17: 3D FEA, 3D theoretical analysis and measured results for an aluminium stator with zero overhang.

6. CONCLUSION

It is shown in this study that a theoretical approach in analysis can be as accurate as the analysis done with FEM for the calculation of torque of a PM eddy current coupling machine at low slip values. The following conclusions are drawn from the analysis and measured results:

- The results of the derived 2D theoretical torque equation correlate well with the results obtained from 2D FEA, giving that the air gap flux density is known. The air gap flux density can be calculated by using a magnetic equivalent circuit method or from one static FEA solution.
- At higher slip speeds the percentage error between the 2D theoretical approach and FEA becomes larger. This is due to the theoretical torque equation that neglects the increasing reactance-impedance of the stator conductor with slip frequency. It is shown in this paper that very accurate results are obtained with the proposed theoretical analysis method for percentage slip values of up to say 10 %. This slip percentage is much higher than is required for performance calculations of most applications.
- To obtain the calculated torque value for a 3D PM eddy current coupling model requires the use of a 3D factor. A 3D factor converts the results from 2D to 3D by multiplying the 2D results with a 3D factor. It is found that the use of the 3D factor derived by Russell [4] gives extremely accurate 3D results. This is found for stators with zero and equal overhangs. It must be mentioned that [1] also found this for single rotor axial-flux PM eddy couplings. This finding significantly reduces computation time in the design optimisation of such a machine as 3D transient FEA is not necessary.

7. REFERENCES

- [1] Lubin, T.; Rezzoug, A., "Steady-State and Transient Performance of Axial-Field Eddy-Current Coupling," *IEEE Trans. on Industrial Electronics*, 2014 (in print and available on IEEEXplore).
- [2] Mouton, Z.; Kamper, M.J., "Design of an eddy-current coupling for slip-synchronous permanent magnet wind generators," *IEEE Trans. on Industrial Electronics*, vol. 61, no. 7, pp. 3367–3376, July 2014.
- [3] Houser, W.P., "Deriving the Lorentz force equation from Maxwell's equations", *Proceedings IEEE SoutheastCon 2002*, pp. 422-425, 2002.
- [4] Russell, R.L.; Norsworthy, K.H., "Eddy currents and wall losses in screened-rotor induction motors," *IEE proceedings—Part A: Power Engineering*, vol. 105, no. 20, pp. 163-175, April 1958.

LIGHTNING RETURN STROKE MODELLING WITH REFERENCE TO LIGHTNING ELECTROMAGNETIC FIELDS

C.W.I. McAfee and K.J. Nixon*

* *School of Electrical and Information Engineering, Faculty of Engineering and the Built Environment, University of the Witwatersrand, South Africa*

Abstract: The theory regarding lightning strokes, and return stroke models is presented along with the functions needed to model the return stroke. Three engineering models are presented: TLM, MTLE, MTLL. Three current impulse functions (required by the return stroke model) are also presented in detail: Double Exponential, Heidler and Terespolsky. The emphasis of the theory and models is focused towards future use in evaluating radiated lightning electromagnetic (EM) fields. Although no EM models or simulations are presented here, the use of the return stroke models is discussed with reference to a simplified electric field model. A comparison found that the Terespolsky function is better suited for modelling the return stroke for future use in EM models.

Key words: Return Stroke, Channel Base Current, Current Impulse Model, Induced Electromagnetic Fields

1. INTRODUCTION

In lightning protection the primary focus is often on direct lightning strikes attaching to ground objects. This is the most intuitive form of damage caused from lightning, and often results in serious property damage or loss of life [1]. However indirect (nearby) lightning is also responsible for property damage and needs to be designed for in lightning protection. There are a number of deleterious effects caused by indirect lightning, however the effect of lightning electromagnetic (EM) radiation is the primary focus presented here. During a lightning strike a large current flows in the leader channel. This moving current results in moving EM waves that propagate from the channel. When these EM waves move past electrical networks such as distribution lines, or telecommunications lines (or any conducting object) a current is induced in the network. Often these induced currents are large enough to result in damage to the network, or the electrical equipment attached to the network nodes [2].

A particular interest is the effect of a Lightning Electromagnetic Pulse (LEMP) inducing an overvoltage on a power distribution network. These overvoltages result in network damage, as well as interrupted energy delivery. In comparison, indirect strikes occur more frequently than direct strikes and are therefore more important [1] when considering the lightning protection of distribution lines (not transmission lines). In order to evaluate the induced overvoltages it is necessary to first evaluate the EM field that interacts with the line. In order to do this it is first necessary to develop a model that describes the current that flows in the lightning channel. This is referred to as the lightning Return Stroke model, and is attributed to causing the most damage to distribution networks [1–4]. Once a return stroke model has been developed it is then possible to use the model in conjunction with Maxwell's equations to evaluate the EM field in space and time [5].

Theory regarding return strokes is presented, and then the different modelling techniques are discussed. One of the aims is to simplify this topic for engineering applications. The different channel base current (current impulse) models are discussed, and simulated. The electromagnetic radiation theory of a lightning strike is briefly presented (without calculations) to show how the return stroke models will need to be evaluated in calculating electromagnetic fields. The results of these models, and decisions made are then discussed.

2. RETURN STROKE THEORY

There are four types of lightning as defined by Rakov [6], however only downward negative lightning will be discussed as it accounts for 90% of cloud to ground lightning globally. A lightning strike or lightning flash is composed of multiple lightning strokes. A lightning stroke is composed of a downward leader, followed by an upward return stroke [6]. For downward negative lightning, a stepped downward leader begins to travel downwards from the cloud to ground (due to a charge difference between the two locations). When the stepped leader gets close to ground (within a couple hundred meters) the electric field strength increases enough to cause upward leaders to form. When the upward leader connects with the downward stepped leader, the ground point that initiated the upward leader is "struck" by lightning.

As a stepped leader moves towards earth it leaves a conducting channel, as well as depositing negative charge. When the stepped leader connects to ground, the ground charge sees a conducting path to the cloud. Ground charge then moves into the channel to neutralise the negative charge. This flow of charge is called the return stroke, and it flows from ground to cloud. Under this situation both the leader and return stroke effectively transport negative charge to ground [6]. First strokes are often followed by subsequent strokes in negative downward lightning. A

subsequent stroke begins with the progression of a "dart" leader from cloud to ground (not necessarily along the initial stepped leader channel), and then followed by a return stroke from ground to cloud. It is also important to note that a return stroke may contain a low "continuing current" that follows a return stroke [6], however this will not be dealt with in the models. Subsequent return strokes will typically have less peak current than the first return stroke, therefore only the first return stroke will be modelled.

3. RETURN STROKE MODELS

Section 2. has discussed the theory of a return stroke from a physics viewpoint. Essentially a return stroke is a current that travels from the ground to a cloud. There are a number of factors that need to be considered when constructing a return stroke model:

- Path travelled by the return stroke.
- Channel height.
- Current impulse along channel.
- Current attenuation along the channel.
- Velocity of impulse moving upward in the channel.

Some of these model components are simple to define, however others can only be assumed. It is important to understand that a model is a mathematical construct which can be used to describe observed phenomena. These models are then used to understand variations of a phenomena under study [1]. This may seem obvious, but is important in understanding the meaning of the return stroke models being presented.

Measurements of return strokes have primarily been done through:

Optical/Photographic Measurements: Light intensity of a stroke indicating current density.

Channel Base Current Measurements: Current is measured at the base of a lightning channel which is initiated either by a tall conducting structure/tower, or rocket triggered lightning [1].

EM Field Measurements: The EM fields of a lightning stroke are measured, in addition to the stroke location [7].

It is important to note that none of these measurements can accurately describe the current throughout the leader channel, throughout time. Therefore all of these measurements are used to create models that are able to validate the measurements made, and infer the current distribution in the channel.

There are three main groups of return stroke models: *Electrothermodynamic models*, *RLC Transmission line models* and *Semi-Physical and Engineering models* [1]. However for the purpose of this paper only the Semi-Physical and Engineering models will be discussed. Both the Semi-Physical and Engineering approaches have adapted concepts from the RLC transmission line models. This group of models is better described in two different subcategories: *Current propagation models* (predominantly engineering models) and *Current generation models* (predominantly semi-physical models). As stated in Section 1., the main focus of this report is on engineering applications, and therefore only the Current Propagation models will be discussed in detail, however more information on the alternative models can be found in [1, 6].

3.1 Current Propagation (CP) models

In this approach the return stroke is modelled as a transmission line driven by a current source connected to the ground plane. In engineering models the current on the channel is described in space and time, and this is used to calculate remote EM fields. Figure 1 shows a visual representation of the model with a return stroke current impulse moving upwards from ground to cloud. The current impulse $I(h,t)$ is able to describe the current at any position (height, h) on the channel, at any time (t). This figure also shows that the stepped leader channel is modelled as a perpendicular uniform path on top of a perfectly conducting ground plane. These model components are not real representations of a lightning stroke. A stepped leader path down to earth is actually defined by multiple short paths that branch randomly in different directions (as seen in any typical lightning picture). The conducting path may vary due to the charge distribution, and the ground plane is never a perfect conductor due to ground loss and terrain layout.

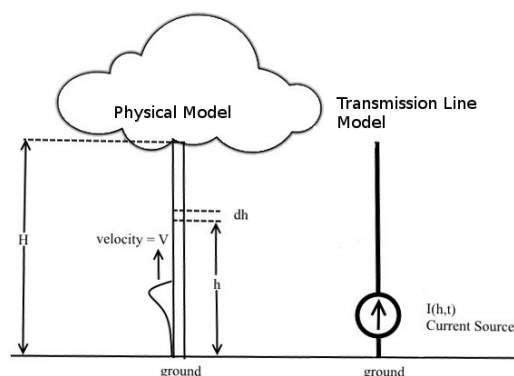


Figure 1: CP Return stroke model

Figure 1 also shows that the return stroke impulse travels up the channel at constant speed $v = 0.5 * c$ where c is the speed of light. In reality the velocity of the return stroke speed decreases with height, however for the purpose of simplifying the model the speed is considered constant between $0.8 - 2.8 * 10^8 m/s$ [1, 6].

Equations 1 to 3 show the three main mathematical equations used to model the current distribution along the return stroke channel. The left hand side of these equations shows that the current distribution is height and time dependant, however the right hand side shows the channel base current ($h = 0$). As the name would suggest, the channel base current is typically specified as the current measured at the base as a function of time ($I(t)$). In order to compensate for the displacement of the return stroke current pulse along the return channel the time variable is shifted: $t_o = t_n - \frac{h}{v}$ where t_o is the original time component, and t_n is the new time component simply referred to as t in the model. It is also important to note that channel base current only exists for $t \geq \frac{h}{v}$, which is mathematically included in the equations by using a unit step function $U(t_o)$.

$$\text{TLM: } I(h,t) = I(0, t - \frac{h}{v}) \cdot (U(t - \frac{h}{v})) \quad (1)$$

$$\text{MTLE: } I(h,t) = \exp(-\frac{h}{\lambda_c}) \cdot (I(0, t - \frac{h}{v})) \cdot (U(t - \frac{h}{v})) \quad (2)$$

$$\text{MTLL: } I(h,t) = (1 - \frac{h}{H}) \cdot (I(0, t - \frac{h}{v})) \cdot (U(t - \frac{h}{v})) \quad (3)$$

Equation 1 is the *Transmission Line Model* from Uman and McLain [1]. This model has an accuracy of about 20%, however it fails to account for the attenuation of the current along the channel. It has been observed that the current amplitude decreases as the return stroke current approaches the cloud (due to the charge in the corona sheath that forms around the leader channel [8]). In other words the problem with the TLM is that it does not account for charge neutralisation along the channel. To account for this the TLM was modified by decreasing the current amplitude while still maintaining the waveshape. Equation 2 is the *Modified Transmission Line Exponential* model proposed by Nucci *et al* [8]. As the name would suggest, the amplitude of the current decreases exponentially with height, where $\lambda_c = 2000m$. An alternative is to use Equation 3, which is the *Modified Transmission Line Linear* model, as proposed by Rakov *et al* [9]. With this model the current decreases linearly with height.

Both the modified models show an improvement with measured results as compared to the TLM. The main difference between the modified models is that the MTLL model is more accurate with measurements made near (50m) to lightning strikes.

4. CHANNEL BASE CURRENT MODELS

There are a number of different models used to represent the current of a lightning return stroke base current (Current Impulse Model). These models have been derived from measurements made at ground level, and attempt to account for the current wave shape, front rise time and peak current values (the characteristics of the wave). For this study the current impulse will be a 10/350 μs

waveshape with a peak current of 200 kA. These values were chosen from the IEC Std 62305-1 [10]. The choice of a 200 kA peak current was made for the worst case scenario (high level protection), however it is important to note that 50% of first return strokes have a value of 30 kA [6]. The choice of the waveshape was made due to the long duration of the 10/350 μs impulse, however there is no reason why another wave shape couldn't be chosen. This paper will discuss three current impulse models: *Double Exponential*, *Heidler* and *Terespolsky*.

4.1 Double Exponential Function

Equation 4 shows the mathematical equation for the double exponential function [11]. The parameters for the function were taken from [12] in order to achieve the required waveshape.

$$I(t) = I_p A \cdot (e^{-\alpha t} - e^{-\beta t}) \quad (4)$$

Where

A	=	Scaling Factor	=	1.025
I_p	=	Peak Current	=	200 kA
α	=	Time Constant	=	$2.05 * 10^3 s^{-1}$
β	=	Time Constant	=	$5.64 * 10^5 s^{-1}$

This function has been used in a number of lightning related research projects, however it does not accurately represent a physically realisable return stroke current waveform. As seen in Figure 2, the rise time of this function is instantaneous, which is not physically possible [6]. As the stepped leader approaches the ground during a lightning stroke, ground leaders start to form (causing a slow increase in current), and once the leader connects to upward leader, the current increases rapidly. In addition to this, due to the incorrect shape of the waveform there are incorrect representations of the radiated frequency components of the stroke. Even though the model does not accurately represent a lightning stroke, the mathematical properties of this function make it useful in preliminary modelling.

4.2 Heidler Function

The Heidler function (Equation 5) is another popular function used to model the return stroke current waveform. The parameters for the function were taken from [10] in order to achieve the required waveshape.

$$I(t) = \frac{I_p}{k} \cdot \frac{(\frac{t}{\tau_1})^n}{1 + (\frac{t}{\tau_1})^n} \cdot e^{-\frac{t}{\tau_2}} \quad (5)$$

Where

k	=	Scaling Factor	=	0.93
I_p	=	Peak Current	=	200 kA
n	=	Steepness Factor	=	10
τ_1	=	Time Constant	=	$19 * 10^{-6}$ s
τ_2	=	Time Constant	=	$485 * 10^{-6}$ s

This function is a closer approximation to the physical processes of a lightning stroke. As seen in Figure 2, shape of the waveshape as it rises is a better fit for the lightning stroke, and therefore overcomes the problems of the double exponential function. The problems associated with this function will be described in Section 5..

4.3 Terespolsky Function

Equation 6 shows the Terespolsky function. This function is an approximation to the Heidler function, and has less than 1.5% error [13] when adjusted to the IEC Std 62305-1 [10].

$$I(t) = \frac{I_p}{k} \cdot \left(1 - e^{-\omega_0 t} \left(\sum_{i=0}^n \frac{\omega_0^i t^i}{i!} \right) \right) \cdot e^{-\frac{t}{\tau_2}} \quad (6)$$

Where

k	=	Scaling Factor	=	0.93
I_p	=	Peak Current	=	200 kA
n	=	Steepness Factor	=	33
ω_0	=	Rise Time Constant	=	1768211
τ_2	=	Time Constant	=	$485 * 10^{-6}$ s

The advantage in using the Terespolsky function is that it is simpler to manipulate mathematically [13], and therefore simplifies lightning protection models. As seen in Figure 2 and 3 the Terespolsky function closely resembles the Heidler function, and although not yet accredited as an IEC standard, the Terespolsky function is a good approximation. This means that model results from this function should be comparable to those required by IEC Std 62305-1.

5. LIGHTNING ELECTROMAGNETIC PULSE EQUATION

Equation 7 shows a special case of the vertical electric field measured at a point on the ground plane a distance r from the return stroke channel (Figure 2.). The full electric and magnetic field equations can be found in [5, 7].

$$E_z(r,t) = \frac{1}{2\pi\epsilon_0} \left[\int_0^H \frac{2h^2 - r^2}{R^5} \left(\int_0^t I(\tau - \frac{R}{c} - \frac{h}{v}) d\tau \right) dh + \int_0^H \frac{2h^2 - r^2}{cR^4} \left(I(t - \frac{R}{c} - \frac{h}{v}) \right) dh - \int_0^H \frac{r^2}{c^2 R^3} \left(\frac{\partial I(t - \frac{R}{c} - \frac{h}{v})}{\partial t} \right) dh \right] \vec{z} \quad (7)$$

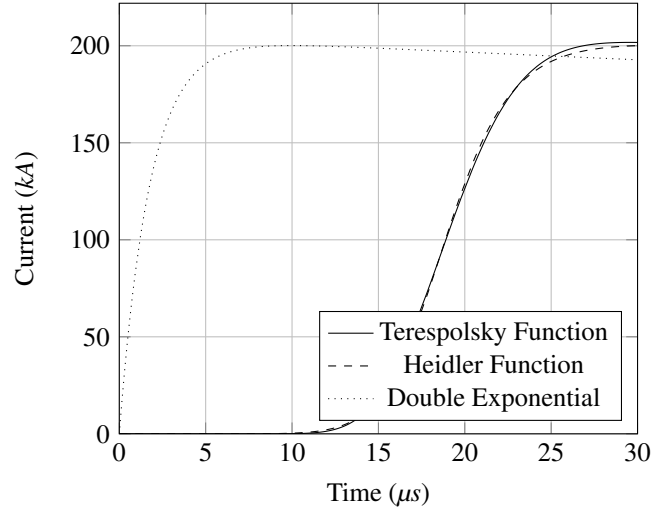


Figure 2: Rise Time - Channel Base Current Models

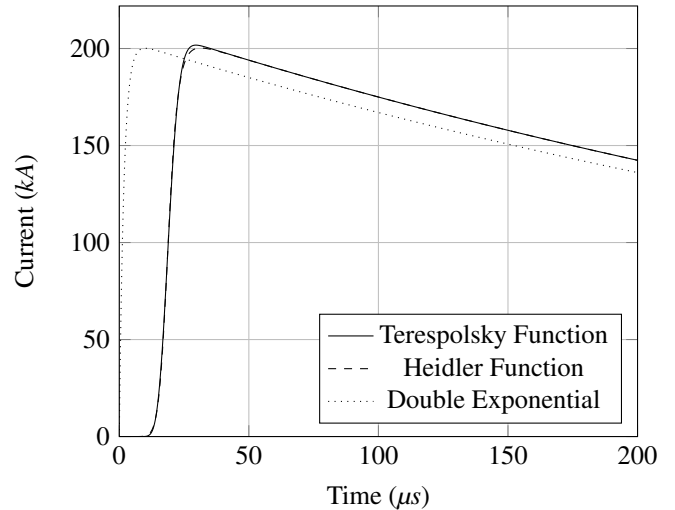


Figure 3: Channel Base Current Models

Where

H	=	Channel Height
R	=	$\sqrt{r^2 + h^2}$
h	=	Height of a point along the channel
r	=	Distance from channel base to point
ϵ_0	=	Permittivity of free space $4\pi * 10^7$

The purpose of including this equation here is not to simulate the electric field, but rather to emphasise the choice between the channel base current model chosen when modelling the EM fields. As seen in Equation 7, the return stroke current, $I(t)$, will need to be integrated twice, as well as differentiated. This is easily done when the double exponential function is chosen, however it is not an accurate model. It is however useful in understanding how a pulse propagates.

The next choice is to use the Heidler function, however after inspecting Equation 5 it should become clear that integrating this function is not a simple task. Different numerical techniques need to be used in order to achieve a result. This is where the Terespolsky function is most useful. Integrating and differentiating this function is far simpler, and easy to implement in a computer simulation [13].

6. CONCLUSION

The theory regarding lightning strikes and lightning return strokes has been presented, and the concepts necessary for understanding physical processes have been discussed. The different methodologies for modelling the return stroke current along the leader channel have been presented for engineering applications, and three mathematical models have been provided for future simulations. The return stroke channel base currents have also been described. The *Double Exponential*, *Heidler* and *Terespolsky* lightning impulse functions were presented along with practical constants that were used to model a 10/350 μ s waveshape with a peak current of 200 kA (worst case lightning stroke). An equation used to model the radiated lightning electric field was presented, and the benefits of using each of the respective current impulse models (in conjunction with the return stroke models) were presented. In this respect it was found that using the Terespolsky function to model the return stroke current would be the best option. This is because the Terespolsky function is simpler to manipulate mathematically than the Heidler function. In order to evaluate the EM fields radiated from a lightning stroke it is necessary to integrate the lightning current model. The theory presented in this paper should act as a guide in progressing to models involving EM radiation.

ACKNOWLEDGEMENTS

The authors would like to thank CBI-electric for funding the Chair of Lightning at the University of the Witwatersrand and for direct support of the Research Group. They would also like to thank Eskom for the support of the Lightning/EMC Research Group through the TESP programme. Thanks are extended to the department of Trade and Industry (DTI) for THRIP funding as well as to the National Research Foundation (NRF) for direct funding of the Research Group.

Special thanks to Brett Terespolsky for the help in implementing his new function, and to Darryn Cornish for graphical help.

REFERENCES

- [1] C. A. Nucci and F. Rachidi, *The Lightning Flash*, ser. Power Series 34, V. Cooray, Ed. Institute of Electrical Engineers, 2003.
- [2] M. Paolone, F. Rachidi, A. Borghetti, C. A. Nucci, M. Rubinstein, V. A. Rakov, and M. A. Uman, "Lightning electromagnetic field coupling to overhead lines: Theory, numerical simulations, and experimental validation," *IEEE Transactions on Electromagnetic Compatibility*, vol. 51, no. 3, pp. 532–547, August 2009.
- [3] P. Sewkumar, "Modeling the effect of adjacent lightning strikes to bare overhead medium voltage lines in south africa," Master's thesis, Faculty of Engineering and the Built Environment, School of Electrical and Electronic Engineering, University of the Witwatersrand, South Africa, 2001.
- [4] C. A. Nucci and F. Rachidi, *Lightning Protection*, ser. 58, V. Cooray, Ed. The Institute of Engineering and Technology, 2010, chapter 13.
- [5] M. A. Uman, D. K. Mclain, and E. P. Krider, "The electromagnetic radiation from a finite antenna," *American Journal of Physics*, vol. 43, pp. 33–38, January 1975.
- [6] V. A. Rakov and M. A. Uman, *Lightning Physics and Effects*. Cambridge University Press, 2004.
- [7] M. A. Uman, "Lightning return stroke electric and magnetic fields," *Journal of Geophysical Research - Atmospheres*, vol. 90, no. D4, pp. 6121–6130, June 1985.
- [8] C. A. Nucci, C. Mazetti, F. Rachidi, and M. Ianoz, "On lightning return stroke models for lemp calculations," *International Conference on Lightning Protection*, no. 4.7, pp. 463–470, 1988.
- [9] V. A. Rakov and A. A. Dulzon, "A modified transmission line model for lightning return stroke field calculations," *International Symposium on EMC*, no. 44H1, pp. 229–234, 1991.
- [10] *Protection Against Lightning - Part 1: General Principles*, IEC Std., 2006.
- [11] K. Berger, R. Anderson, and H. Kroninger, "Parameters of lightning flashes," *Electra*, no. 41, pp. 23–37, 1975.
- [12] W. Jia and Z. Xiaoqing, "Double-exponential expression of lightning current waveforms," *CEEM*, no. 3A1-09, pp. 320–323, 2006.
- [13] B. R. Terespolsky and K. J. Nixon, "Developing an approximation to the heidler function - with an analytical transformation into the frequency domain." *International Conference on Lightning Protection*, pp. 1134–1138, 2014.

CORRELATION BETWEEN IEC 60853 AND F.E. SIMULATIONS FOR TRANSIENT RATINGS OF BURIED CABLES.

B.J. le Roux* and J.J. Walker**

* Power Engineering, Vaal University of Technology, Vanderbijlpark, Gauteng South Africa E-mail: jolr@vut.ac.za

** Visiting Professor, Power Engineering, Vaal University of Technology, Vanderbijlpark, Gauteng South Africa E-mail:

Abstract: The purpose of this paper is to provide an easy-to-use Quickfield™ model to use to solve the computations for the transient rating of buried cables. Solving the heat transfer problem requires an iterative procedure, which is both time consuming and tedious. Even using a computer requires enormous data handling capacity. Once the model for the cable system has been set up it takes less than 4 minutes to solve the equations satisfactorily. The current ratings can be changed; the soil thermal conductivity can be changed, all with little or no effort. A daily load graph can be programmed with a few clicks of a button and the equation can be solved for the new values.

Keywords: Quickfield™, heat transfer, ampacity calculations, analytical solutions, emergency ratings.

1. INTRODUCTION

The most important tasks in cable current rating calculations are determination of the tolerable load current for a given conductor temperature. In order to perform these tasks the heat generated within the cable and the rate of dissipation away from the conductor, for a given conductor material and given load must be calculated.

The ability of the surrounding medium to dissipate heat plays a very important role in these computations and varies widely because of factors such as soil composition, moisture content, ambient temperature and wind conditions. The heat is transferred through the cable and its surroundings in several ways. For underground installations the heat is transferred by conduction from conductor to insulation, screens and other metallic parts.

It is possible to quantify the heat transfer process in terms of the appropriate heat transfer equation:

$$\frac{\partial^2 \theta}{\partial x^2} + \frac{\partial^2 \theta}{\partial y^2} + W_{int} \rho = \frac{1}{\delta} \frac{\partial \theta}{\partial t} \dots\dots\dots (1.1)$$

Where:

θ = unknown temperature

$\delta = \frac{1}{\rho c}$ thermal diffusivity of the medium (m²/s)

c = volumetric specific heat of the material (J/m³)

ρ = thermal resistivity of the material (K.m/W)

W_{int} = heat generation rate in cable (W/m)

Current rating calculations for power cables require a solution of the heat transfer equations which define a functional relationship between the conductor current and the temperature within the cable and its surroundings. The challenge in solving these equations

analytically often stems from the difficulty of computing the temperature distribution in the soil surrounding the cable. An analytical solution can be obtained when a cable is represented as a line source placed in an infinite homogenous surrounding medium. Since this is not a practical assumption for cable installations another assumption is often used; namely, that the earth surface is an isotherm. With the isothermal boundary, the steady-state heat conduction equations can be solved assuming that the cable is located in a uniform semi-finite medium. Methods of solving the heat conduction equations for steady state conditions are described in [1] and for transient (cyclic) conditions in [2] for most practical applications. When these methods cannot be applied as for many non-standard installation conditions the heat conduction equations can be solved using numerical approaches [3]. One such approach, particularly suitable for the analysis of underground cables, is the finite element method presented in this paper. Quickfield™ is the program used in this paper.

2. DEVELOPMENT OF THE FORMULAE

The boundary conditions associated with equation 1.1 can be expressed in two different forms. If the temperature is known along a portion of the boundary then

$$\theta = \theta_B(s) \dots\dots\dots (1.2)$$

where θ_B is the boundary temperature that may be a function of the surface length s . If heat is gained or lost at the boundary due to convection

$$h(\theta - \theta_B) \dots\dots\dots (1.3)$$

or a heat flux q , then

$$\frac{\partial \theta}{\rho \partial n} + q + h(\theta - \theta_B) = 0 \dots\dots\dots (1.4)$$

Where; n = the direction of the normal to the boundary surface,
 h = a convection coefficient, and
 θ = an unknown boundary temperature.

In cable rating computation, the temperature of the conductor is usually given and the maximum current flowing in the conductor is sought. Thus, when the conductor heat loss is the only energy source in the cable,
 $W_{int} = I^2 R$(1.5)
 and equation (1.1) is used to solve for I with the specified boundary conditions. For the purpose of introducing the method and explaining how it is used in cable rating computations the simplest and most common shape for two dimensional elements, the triangle, will be used.

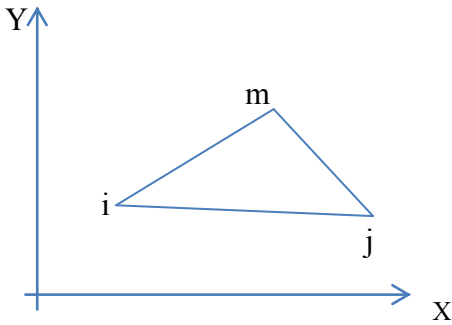


Figure 1: Area co-ordinates.

For this element, the temperature θ at any point inside can be uniquely specified as:

$$\theta = A\omega_i + B\omega_j + C\omega_m \dots\dots\dots (1.6)$$

Where $\omega_i, \omega_j, \omega_m$ = coordinates as shown in Figure 1. These area coordinates define uniquely the position of any point P inside the triangle ijm . To determine the constant A , the temperature at node i is written as $\theta_i = 1.A + 0.B + 0.C$ as per equation (1.6). This gives $A = \theta_i$. Similarly, for nodes j and m the following is obtained: $B = \theta_j$, and $C = \theta_m$. Therefore:

$$\theta = \omega_i\theta_i + \omega_j\theta_j + \omega_m\theta_m$$

$$= [\omega_i + \omega_j + \omega_m] \cdot \begin{bmatrix} \theta_i \\ \theta_j \\ \theta_m \end{bmatrix} = N^e \cdot \Theta^e \dots\dots\dots (1.7)$$

Assuming that the time derivatives are prescribed functions of the space co-ordinates at any particular instant in time, the time derivative for the temperature within each element is

$$\frac{\partial \theta}{\partial t} = \omega_i \frac{\partial \theta_i}{\partial t} + \omega_j \frac{\partial \theta_j}{\partial t} + \omega_m \frac{\partial \theta_m}{\partial t}$$

$$= [\omega_i + \omega_j + \omega_m] \cdot \begin{bmatrix} \frac{\partial \theta_i}{\partial t} \\ \frac{\partial \theta_j}{\partial t} \\ \frac{\partial \theta_m}{\partial t} \end{bmatrix} = N^e \frac{\partial \Theta}{\partial t} \dots\dots\dots (1.8)$$

Since N^e is a function of the co-ordinate system and not time. The relationship between area co-ordinates and Cartesian co-ordinates is:

$$\begin{bmatrix} x \\ y \\ 1 \end{bmatrix} = \begin{bmatrix} x_i & x_j & x_m \\ y_i & y_j & y_m \\ 1 & 1 & 1 \end{bmatrix} \dots\dots\dots (1.9)$$

The inverse relationship yields the coefficients of vector N^e :

$$\begin{bmatrix} \omega_i \\ \omega_j \\ \omega_m \end{bmatrix} = \frac{1}{2A} \begin{bmatrix} (y_j - y_m) & (x_m - x_j) & (x_j y_m - x_m y_j) \\ (y_m - y_i) & (x_i - x_m) & (x_m y_i - x_i y_m) \\ (y_i - y_j) & (x_j - x_i) & (x_i y_j - x_j y_i) \end{bmatrix} \begin{bmatrix} x \\ y \\ 1 \end{bmatrix} \dots\dots\dots (1.10)$$

Where; A = the area of the triangle. It can be observed from equations (1.7) and (1.10) that the temperature is a linear function in x and y . This means that the gradient in either x or y directions are constant. A constant gradient within any element means that many small elements have to be used to approximate a rapid change in the value of θ .

To obtain the node temperature, a property is used, known in the variational calculus, that states that the minimization of the functional over the area S bounded by the closed curve C , where the superscript t denotes the transposition and

$$\chi = \int_s \frac{1}{2\rho} \left[(\nabla\theta)^t \nabla\theta + \left(W_{int} - c \frac{d\theta}{dt} \right) \theta \right] dS$$

$$+ \int_c \left[q\theta + \frac{1}{2} h(\theta - \theta_{amb})^2 \right] dC \dots\dots\dots (1.11)$$

$$\nabla\theta = \begin{bmatrix} \frac{\partial \theta}{\partial x} \\ \frac{\partial \theta}{\partial y} \end{bmatrix} \dots\dots\dots (1.12)$$

Requires, that the differential equation (1.1), with the boundary conditions (1.2) and (1.3) be satisfied. Therefore the temperature distribution that makes χ a minimum also satisfies the governing differential equations and therefore is a solution to the problem being studied. Equation (1.11) is a starting point for determining the temperature at each node. It is minimised by using a set of element functions, each defined over a single element and written in terms of the nodal values. The nodal values θ_n are the unknown values in the formulation. These values are obtained by taking the derivatives of χ with respect to θ_n and equating them to zero. Recalling that functions θ are defined over each individual element, the integrals in (1.11) must be separated into integrals over the individual elements and the derivatives computed for each element; that is $\chi = \sum_{e=1}^E \chi^e$ (1.13)

Where
 χ^e = the functional defined for element e and
 E = the total number of elements.
 Consider a single element first. As any element contributes to only three of the differentials associated with its nodes, these contributions can be listed as;

$$\left(\frac{\partial \chi}{\partial \theta_n} \right)^e = \begin{bmatrix} \frac{\partial \chi^e}{\partial \theta_i} \\ \frac{\partial \chi^e}{\partial \theta_j} \\ \frac{\partial \chi^e}{\partial \theta_m} \end{bmatrix} \dots\dots\dots (1.14)$$

The derivatives in equation (1.14) cannot be evaluated until the integrals in equation (1.11) have been written in terms of the nodal values θ^e . This is done by first computing the derivatives of θ with respect to x and y. only two of the area co-ordinates are independent. Assuming that these are ω_i and ω_j it can be shown that:

$$\nabla \theta = \begin{bmatrix} \frac{\partial \theta}{\partial x} \\ \frac{\partial \theta}{\partial y} \end{bmatrix} = J \begin{bmatrix} \frac{\partial \theta}{\partial \omega_i} \\ \frac{\partial \theta}{\partial \omega_j} \end{bmatrix}$$

$$= \frac{1}{2A} \begin{bmatrix} (y_j - y_m) & (y_m - y_i) \\ (x_m - x_j) & (x_i - x_m) \end{bmatrix} \begin{bmatrix} \frac{\partial \theta}{\partial \omega_i} \\ \frac{\partial \theta}{\partial \omega_j} \end{bmatrix} \dots\dots\dots (1.15)$$

$$= \frac{1}{2A} \begin{pmatrix} b_i & b_j \\ a_i & a_j \end{pmatrix} \begin{bmatrix} \frac{\partial \theta}{\partial \omega_i} \\ \frac{\partial \theta}{\partial \omega_j} \end{bmatrix}$$

Where the Jacobian, J, is obtained by differentiating equation (1.10). Further, from equation (1.7) and the fact that

$\omega_i + \omega_j + \omega_m = 1$; the following is obtained:

$$\begin{bmatrix} \frac{\partial \theta}{\partial \omega_i} \\ \frac{\partial \theta}{\partial \omega_j} \end{bmatrix} = \begin{pmatrix} 1 & 0 & -1 \\ 0 & 1 & -1 \end{pmatrix} \begin{bmatrix} \theta_i \\ \theta_j \\ \theta_m \end{bmatrix} = \mathbf{V} \Theta^e \dots\dots\dots (1.16)$$

Thus for a single element we have:

$$\nabla \theta = \mathbf{J} \times \mathbf{V} \times \Theta^e \dots\dots\dots (1.17)$$

Substituting (1.17) into (1.11) with S and C corresponding to a single element, and differentiate with respect to Θ^e , after some routine but tedious computations, equation (1.14) can be written as:

$$\left(\frac{\partial \chi}{\partial \theta_n} \right)^e = h^e \Theta^e + q^e \frac{\partial \Theta^e}{\partial t} - k^e \dots\dots\dots (1.18)$$

By denoting d_{ij} , d_{jm} and d_{mi} the distance between the nodes ij, jm and mi the element conductivity matrix is equal to:

$$h^e = \frac{1}{4A\rho} \left\{ \begin{bmatrix} a_i^2 & a_i a_j & a_i a_m \\ a_i a_j & a_j^2 & a_j a_m \\ a_i a_m & a_j a_m & a_m^2 \end{bmatrix} + \begin{bmatrix} b_i^2 & b_i b_j & b_i b_m \\ b_i b_j & b_j^2 & b_j b_m \\ b_i b_m & b_j b_m & b_m^2 \end{bmatrix} \right\} \\ + \frac{hd_{ij}}{6} \begin{bmatrix} 2 & 1 & 0 \\ 1 & 2 & 0 \\ 0 & 0 & 0 \end{bmatrix} + \frac{hd_{jm}}{6} \begin{bmatrix} 0 & 0 & 0 \\ 0 & 2 & 1 \\ 0 & 1 & 2 \end{bmatrix} + \frac{hd_{mi}}{6} \begin{bmatrix} 2 & 0 & 1 \\ 0 & 0 & 0 \\ 1 & 0 & 2 \end{bmatrix}$$

$$a_i = x_m - x_j, a_j = x_i - x_m, a_m = x_j - x_i$$

$$b_i = y_j - y_m, b_j = y_m - y_i, b_m = y_i - y_j$$

$$\dots\dots\dots(1.19)$$

If there is no convective boundary along any segment of the element, the relevant term in (1.15) is omitted. The element capacity matrix is given by:

$$q^e = \frac{cA}{12} \begin{bmatrix} 2 & 1 & 1 \\ 1 & 2 & 1 \\ 1 & 1 & 2 \end{bmatrix} \dots\dots\dots(1.20)$$

And the element heat generator vector is equal to:

$$k^e = \frac{W_{int}.A}{3} \begin{bmatrix} 1 \\ 1 \\ 1 \end{bmatrix} + \frac{(h\theta_{amb} + q)d_{ij}}{2} \begin{bmatrix} 1 \\ 1 \\ 0 \end{bmatrix} + \frac{(h\theta_{amb} + q)d_{jm}}{2} \begin{bmatrix} 0 \\ 1 \\ 1 \end{bmatrix} \\ + \frac{(h\theta_{amb} + q)d_{mi}}{2} \begin{bmatrix} 1 \\ 0 \\ 1 \end{bmatrix} \dots\dots\dots(1.21)$$

Here again, the last three terms apply only if the appropriate boundary exists along the element edge. Factor $W_{int} \times A$ represents the total heat in W/m generated in the element. Performing computations given by equations (1.18) – (1.21) for each element, finally a set of linear algebraic equations for the whole region is obtained:

$$\frac{\partial \chi}{\partial \Theta} = \sum_{e=1}^E \left(\frac{\partial \chi}{\partial \theta_n} \right)^e = H\Theta + Q \frac{\partial \Theta}{\partial t} - K = 0 \dots\dots (1.22)$$

Where: H = heat conductivity matrix

Q = heat capacity matrix

Θ and $\frac{\partial \Theta}{\partial t}$ are the vectors containing the nodal temperatures and their derivatives.

K= vector expressing the distribution of heat sources and heat sinks over the region under consideration. In the steady-state analysis (1.22) simplifies to:

$$H\Theta - K = 0 \dots\dots\dots (1.23)$$

The set of ordinary differential equations (1.22) which define the discretised problem can be solved using one of many recursion schemes. It is proposed to use Lees' three-level, time-stepping scheme in which the discretised equation is replaced by a recurrent relationship:

$$\Theta^{n+1} = - \left[\frac{H^n}{3} + \frac{Q^n}{2\Delta\tau} \right]^{-1} \left[\frac{H^n \Theta^n}{3} + \frac{H^n \Theta^{n-1}}{3} - \frac{Q^n \Theta^{n-1}}{2\Delta\tau} - K^n \right] \dots\dots\dots(1.24)$$

Where the superscript n refers to the time level and $\Delta\tau$ is the time step. The procedure is unconditionally stable and has the advantage of producing the solution at time level n+1 without the need for any iteration as the coefficient matrices are evaluated at level n. the initial conditions have to be specified and the first time step iteration is performed by a modified version of (1.24) requiring only one previous time step solution.

3. QUICKFIELD™

This is the program used extensively at Vaal University of Technology (VUT) where a niche area exists for cable research. In [4] it was shown that simulations performed with Quickfield™ compare favourably with calculated results obtained in [5].

The challenge in solving equation (1.1) analytically stems mostly from the difficulty of computing the temperature distribution in the soil surrounding the cable. In the analytical methods used in [1], the case of group of cables is dealt with on the basis of the restricted application of superposition. This assumes that the presence of another cable, even if not loaded, doesn't disturb the heat flux from the first cable, nor the generation of heat within it. This allows separate computations to be performed on each cable with the final temperature-rise being the algebraic sum of the temperature rises due to the cable itself and the rise caused by other cables. Such a procedure is not theoretically correct and, for better precision, the temperature-rise caused by simultaneous operation of all cables should be considered. Direct solution of the heat conduction equation employing numerical methods offers such a possibility.

Numerical methods allow not only better representation of the mutual heating effects, but also permit more accurate modelling of the regions boundaries (e.g., a convective boundary at the earth surface, constant heat flux, circular boundaries for heat or water pipes in the vicinity of the cables, or an isothermal boundary at the water level at the bottom of the trench)

4. MODELLING THE CABLE

The chosen cable must be drawn to scale in the program and once this is done the constituent materials values must be added. The next step is to set the conditions for

each boundary in the model. The conductors must then be assigned as the heat source with the appropriate values; The heat source can also be assigned as a variable load of the cable and can be programmed as a step or impulse, exponential or sinusoidal forms to define the load curve.

The steady-state condition must first be solved to be able to have a starting point for the step function to be applied. This is then used to determine the time a certain overload can be applied before the maximum temperature of 90° C is reached. Figure 1 shows the temperature distribution at the start of the step load function with a conductor temperature of 74.3° C.

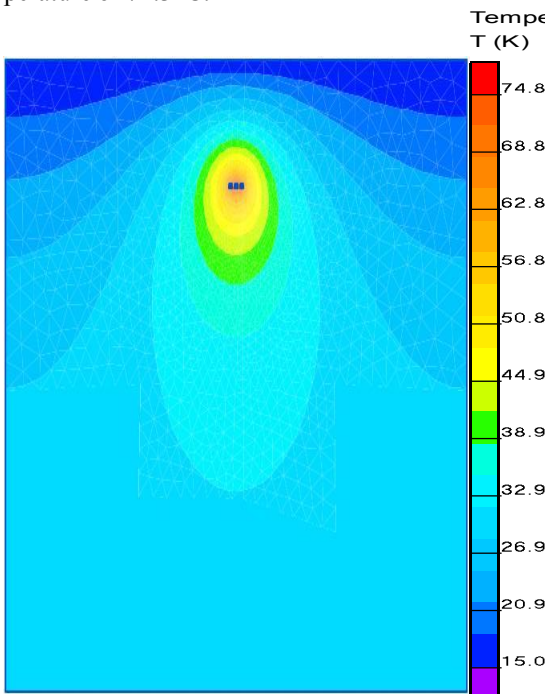


Figure 1: Quickfield™ solution and temperature Legend

The current used to determine the steady state temperature was 584 A. This steady state conditions are now linked to the starting conditions for the transient simulation.

5. LINKING THE MODELS

The steady state and transient problems must share the same geometric model and the results (data) from the steady-state problem must be imported to the transient problem as it will be used as the base to start from.

In this transient problem a step of twice the actual load current were used. This was done to determine the time that the cable can operate at this higher load without exceeding the maximum temperature rise. The equation (heat source step load) used in the transient problem were:

$$Q = 206e3 * \text{impulse}(t, 0, 86400) \dots\dots\dots (1.25)$$

Where

Q = the heat generated by the current and
t = time with starting at zero to 86400 seconds.

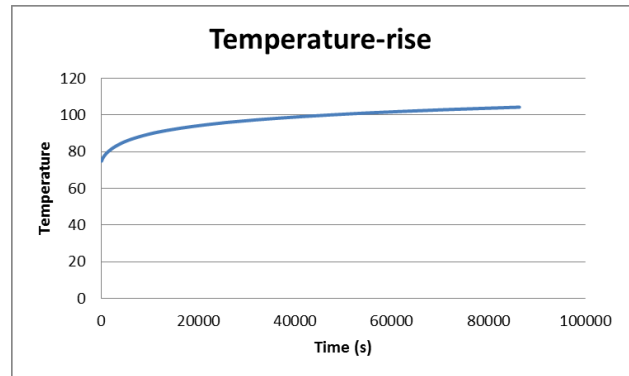


Figure 2: Quickfield™ graph of final temperature.

6. CONCLUSIONS

There are five important factors that the electrical engineer should take from this short discussion. Firstly, soil and backfill thermal properties must be known for a safe and successful buried cable installation. It is not good practice to assume a value of 0.9 mC/W. Secondly, density and water content play important roles in determining the thermal resistivity of the soil. Specify the density of the backfill material, and assure through proper design and management that the water content don't fall below the critical level. Thirdly, natural soil which supports plant growth will always have much higher resistivities than engineered materials because of their lower density and variable, but sometimes low, water content. Fourthly, engineered backfill materials are available which can assure adequate thermal performance under all conditions. Finally, there are several site specific issues such as depth of burial, vegetation and soil water management and avoidance of excessive drying and soil cracking that could lead to air gaps, all of which need to be taken into account when designing and implementing underground cables.

Figure 2 shows the temperature rise of the conductors when the load was applied for 24 hours (86400 seconds). From this figure the time taken to reach 90° C can be read of and that will be the time taken for the cable to carry double the current that resulted in a steady state temperature of 73.4° C. In this specific case the time taken to reach 90° C was ± 30000 seconds which is 8.333 hours.

From working with this program one cannot but marvel at the speed of the operation. It literally does thousands of calculations per second. The accuracy is exceptionally good and corresponds very well with any calculations done in [3] and [5].

7. REFERENCES

- [1] IEC 60287
- [2] IEC 60853
- [3] Technical Report IEC (TR 62095© IEC: 2003),

- [4] BJ Le Roux, JJ Walker: “Transient rating of underground cables a comparative study”, *Proceedings 6th International Conference on High-Voltage Engineering and Application, Poznan Poland (ICHVE)*, Paper A-3-4 8 – 11 Sept 2014.
- [5] G Anders, “Rating of electric power cables”, IEEE Press 1997

INVESTIGATING THE CONCEPT OF FRAUNHOFER LINES AS A POTENTIAL METHOD TO DETECT CORONA IN THE WAVELENGTH REGION 338.67NM – 405NM DURING THE DAY

N.Maistry, Dr J Van Coller and RA Schutz*

Faculty of Engineering and the Built Environment, Private Bag 3, Wits 2050, South Africa

*CSIR, SST, Meiring Naude Pretoria

Abstract: It is essential to detect corona discharge as a symptom of insulation breakdown in high voltage (HV) applications. However accuracy of such measurement is often degraded due to the existence of solar background noise in the signal. Fraunhofer lines in the solar spectrum are areas of the solar spectrum where the solar radiation is lower in intensity due to certain wavelengths of light been absorbed by gases. This paper will explore the potential of evaluating corona at these Fraunhofer lines and through signal processing optimise the signal to noise ratio. In addition the report will also provide a conclusion as to whether the Fraunhofer lines can be used as a potential detection method and recommendations for future research in corona detection.

Keywords: Fraunhofer lines, corona, solar spectrum, corona detection methods, SNR, signal processing, filters

1. INTRODUCTION

A corona discharge is a glowing partial discharge from conductors and insulators due to excitation of the air molecules, when the local electrical field exceeds a critical value. The excitation of the air molecules leads to the emission of ultraviolet (UV) radiation. Consequently a problem or defect on a component creating a local high electric field will produce corona activity. The early detection of corona is fundamental in preventing transmission line failures.

The corona discharge emits radiation in the 240 nm – 440 nm spectral range, mostly in the UV range and is therefore invisible to the human eye, though relatively weak emissions at around 400 nm might be observed at night under conditions of absolute darkness. Corona emission in the 280 nm – 405 nm spectral range cannot be detected during daytime due to the extremely disturbing solar radiation background [1].

UV cameras to detect corona in daytime are increasingly being used for periodic inspections. These cameras can provide information on the exact location of corona. Detection of corona using UV cameras currently is in the 240 nm – 280 nm solar blind UV range [2]. In this solar blind region, due to the ozone layer in the stratosphere, solar radiation is completely blocked and the background solar radiation at the earth's surface is zero. This absence of background solar radiation can be utilized to detect corona at extremely weak levels of UV emittance.

2. PROBLEM STATEMENT

Figure 1 shows the amount of absorption at different wavelengths by the atmosphere. It is presented in terms of the half-absorption altitude, which is the altitude (measured from the earth's surface) where half of the radiation at a given wavelength incident on the upper atmosphere has been absorbed.

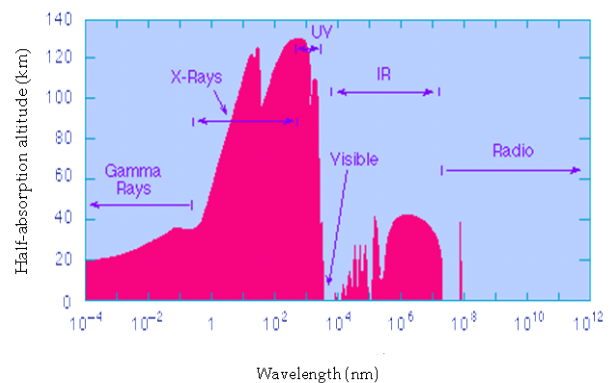


Figure 1: Absorption of solar radiation by the earth's atmosphere [3]

In the UV and X-ray portion of the electromagnetic spectrum almost no solar radiation reaches the earth's surface. This is known as the solar blind region. Detection of corona in daylight is feasible by utilizing the solar blind region and a solar blind filter (the blue line in Figure 2).

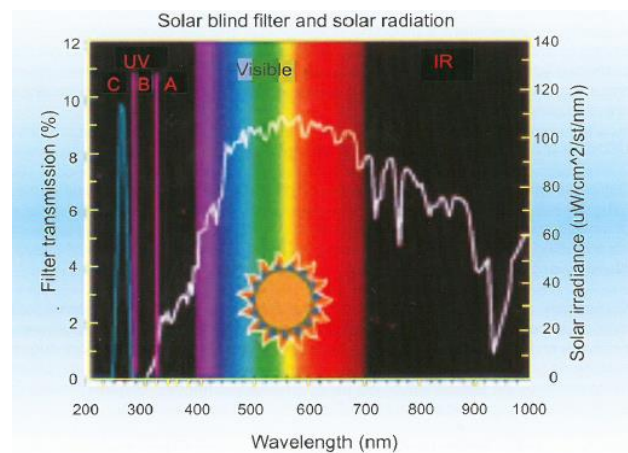


Figure 2: Visible solar spectrum [4]

Detection limited to this band has the advantage of a much better signal-to-background-noise ratio. The CoroCam and DayCor are examples of video cameras for viewing corona emittance in the solar blind region [2].

2.1 Possible solution to the corona detection problem

Solar radiation is a fundamental factor to consider when detecting corona. It is therefore important to understand the solar spectrum. Figure 3 is a standard spectrum of solar radiation.

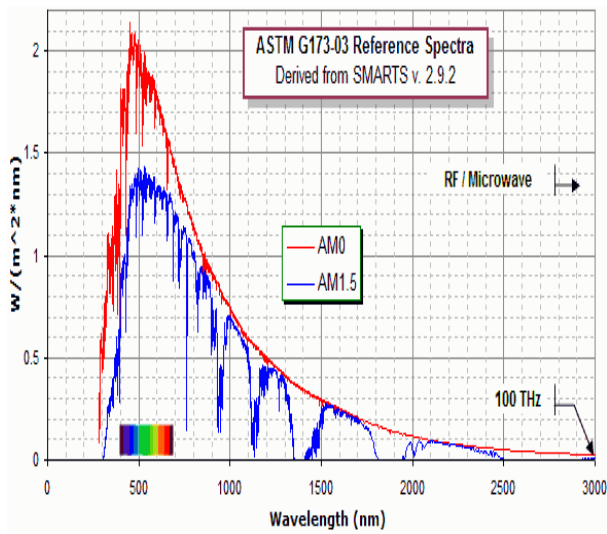


Figure 3: Solar spectrum [5]

Analysing the solar spectrum shows that the solar spectrum is interrupted by a large number of narrow dark lines as shown in Figure 4.

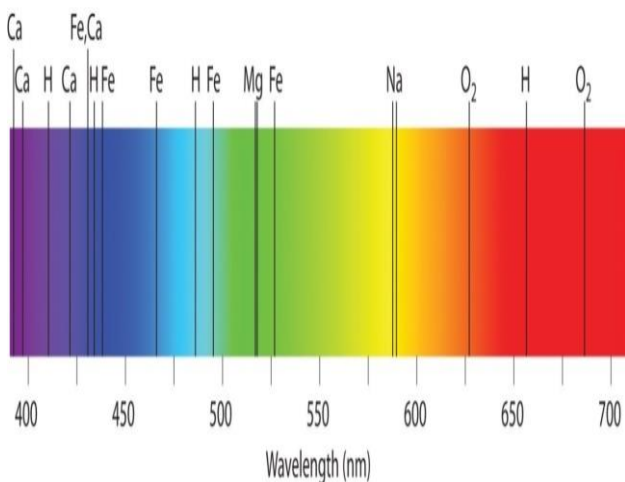


Figure 4: Spectrum showing absorption lines [6]

These lines are known as Fraunhofer lines. These lines represent the wavelengths of light that have been removed by gases present in the outer layers of the sun [7]. The effect of this is that there are a few regions of

solar radiation darkness at well-defined locations in the electromagnetic spectrum.

The major Fraunhofer lines are:

Table 1: Major Fraunhofer lines

Wavelength(nm)	Line due to
759.4	Telluric oxygen
686.7	Telluric oxygen
656.3	hydrogen, H
589.6	sodium
589.0	sodium
587.6	helium
527.0	iron and calcium
518.4	magnesium
486.1	hydrogen, H
430.8	iron (and calcium)
396.8	calcium
393.4	Calcium

The highlighted portion in Table 1 is the wavelength of the Fraunhofer line selected for further processing. One of the primary problems associated with observing corona UV radiation during daytime is that the wavelength corresponds directly to that of background solar radiation and therefore is masked from normal view [13].

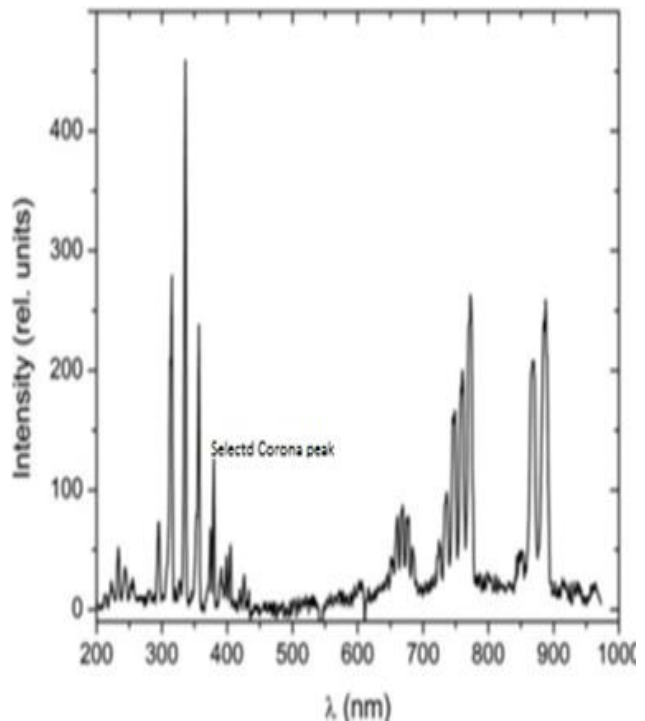


Figure 5: Corona spectrum [14]

From Figure 5 the strong emission bands lie between 300 and 400 nm. Fraunhofer lines are also present in this wavelength band.

Table 2 lists the overlap between the corona peaks and Fraunhofer lines.

Table 2: Overlap of corona and solar spectra at the Fraunhofer lines

Fraunhofer line (nm)	Line width (nm)	Corona peak (nm)
357.0134	0.1380	357.583
358.1209	0.2144	358.472
393.3682	2.0253	393.148
396.8492	1.5467	396.805

In theory if it were possible to match the corona peaks with the Fraunhofer lines then conceivably it would be possible to measure corona discharges in the presence of the solar radiation?

3. METHODOLOGY

Experimental tests were conducted to test hypotheses derived from theory and to explore certain concepts. In addition experiments were conducted to obtain absolute data on corona since this was not available in existing literature.

All the experiments were conducted in the CSIR Electro-optics (EO) lab with a 30 kV high voltage (HV) power supply and a rod-ball corona source. The primary variables were voltage, environmental parameters and the geometry of the corona source which contributed to the absolute intensity of the corona spectrum. The measurements were done using a Specline Avantes spectroradiometer and MATLAB software was used for the analysis of the results. The analysis method was to determine the signal to noise ratio (SNR) and thereafter optimize it through signal processing methods. The wavelength range 338.672nm – 405nm was chosen to achieve high resolution and to ensure that a corona peak and a Fraunhofer line overlapped.

After performing the experiments to investigate the filter efficacy in segregating the corona signal from the solar background, it was concluded that the purchased optical filter was not capable of detecting the corona peak at 393.148nm. Consequently it was decided that possibly the optical filter specifications were not ideal. Hence a new approach of simulating an optical narrow band-pass filter in MATLAB was executed to improve the SNR.

The bandwidth of the filter and the central wavelength (CWL) were adjusted and moved along the wavelength range 338.672nm – 405nm evaluating the SNR at each wavelength and CWL. The maximum SNR was thereafter displayed together with the wavelength and bandwidth of the filter. This new approach was intended to generate an ideal filter with an ideal CWL and bandwidth.

Table 3: Filter results

Tests	FWHM (nm)	CWL (nm)	SNR
Filtered signal using MATLAB simulated filter	0.05	357.455	2.1224
Filtered signal using purchased optical filter	0.3	357.455	0.0031
Filtered signal using purchased optical filter at selected Fraunhofer line	0.3	397.370	0.0026

NB: FWHM: Full Width Half maximum

From the results obtained it is evident the filter design is fundamental in improving the signal to noise ratio. Filtered results showed an improvement of the signal to noise ratio when compared with unfiltered results. In addition the newly designed narrow band-pass filter generated a much higher SNR when compared with the old filter (see Appendix Figure 6 for newly designed filter in MATLAB).

Thereafter cross correlation was investigated and this proved to be an extremely encouraging and promising area for corona detection.

Correlation can also be considered as a type of numeric band pass filter and thus can be used as a technique for extracting a signal from noise.

The results of cross correlation are shown in Table 4.

Table 4: Correlation results

$c \otimes \text{sun1}$	False
$c \otimes \text{sun2}$	False
$c \otimes (\text{sun1+noise})$	False
$c \otimes (\text{sun2+noise})$	False
$c \otimes (\text{sun1+corona})$	True
$c \otimes (\text{sun2+corona})$	True
$c \otimes (\text{sun1+noise+corona})$	True
$c \otimes (\text{sun2+noise+corona})$	True

NB:

- c is the corona spectrum
- sun1 is when the solar spectrum was recorded under intense sunlight.
- sun2 is when the spectrum was recorded under cloudy conditions.

It was noted that when the corona template was correlated with different solar spectra recorded at different times of

the day with different intensities, the same correlation coefficient resulted. Thereafter the corona spectra template was correlated with the solar + corona spectra. This resulted in different coefficients which was indicative that corona was present. To create a more realistic approach noise was included with the corona + solar spectra and correlated with the corona template and different correlation coefficients were generated.

In essence the results of cross correlation indicated that corona was present when the corona template was correlated with the solar+corona spectrum.

4. CONCLUSIONS AND RECOMMENDATIONS FOR FUTURE WORK

This paper has investigated Fraunhofer lines in the solar spectrum as a method to detect corona. The hypothesis was that there is an overlap between certain Fraunhofer lines and corona emission peaks which could conceivably be exploited as a way of detecting corona during daylight.

The Fraunhofer line at a wavelength of 393.13682nm and the corona peak at 393.148nm were chosen for the experiments. An optical band-pass filter with a central wavelength of 393.37nm with a bandwidth of 0.3nm was used for filtering of the signal. After performing the experiments and evaluating the results it was determined that the SNR had not improved sufficiently with the filter purchased and so a new band-pass filter was designed. The filter specifications that generated a higher SNR had a bandwidth of 0.05nm and a CWL of 357.4552nm which coincided with the wavelength of a different Fraunhofer line.

The results of cross correlation indicated that corona was present when the corona template was correlated with the solar+corona spectrum.

4.1 Recommendations for future work

1. Cross correlation has potential and is an area where more research and future work should be done.
2. An optical filter with the specifications generated in the MATLAB model should be purchased (if possible) and the previous experiment repeated.

5. REFERENCES

[1] L. Loeb, *Fundamental Processes of electrical discharge in gases*, London: John Wiley & Sons, 1939.

[2] W. L. Vosloo, R. Stolper and P. Baker, "Daylight Corona Discharge Observation and Recording system," *Proceedings of 10th International Symposium on HV Engineering*, vol. 6, pp. 161-164, 1997.

[3] B. A. a. E. P. Averill, *General Chemistry:*

Principles, Patterns, and Applications, v. 1.0 (2 Volume Set), 2007.

[4] S. P. Maruvada, *Corona in transmission systems: Theory, design and performance*, South Africa: Crown Publications, 2011.

[5] R. Bird, R. Hulstrom and L. Lewis, "Terrestrial solar spectral data sets," *Solar Energy*, Vols. Vol 30,, p. p 563., 1983.

[6] B. A. Averill and P. Eldredge, *General Chemistry: Principles, Patterns, and Applications*, 2007.

[7] W. H. Walloston, "A method of examining refractive and dispersive powers by prismatic reflection," *Philosophical Transactions of the Royal Society*, no. 92, pp. 365-380, 1802.

[8] L. Loeb, *Electrical Coronas: Their Basic Physical Mechanisms*, California: University of California Press, 1965.

[9] M. Goldman and R. S. Sigmond, "Corona and Insulation," *IEEE Transactions on Electrical Insulation*, vol. E, no. 2, pp. 1-17, 1982.

[10] S. P. Maruvada, *Corona Performance of High-Voltage Transmission Lines*, Baldock, Hertfordshire, England: Research Studies Press LTD, 2000.

[11] M. Bouchacourt, A. Bengston, A. Johann, E. Steers, V.-D. Hodoroaba and V. Hoffmann, "Glow discharge optical emission spectrometry: moving towards reliable thin film analysis," *Analytical Atomic Spectrometry*, no. 6, 2003.

[12] F. Peek, *Dielectric Phenomena in High Voltage Engineering*, New York: McGraw-Hill Book Inc., 1915.

[13] T. Czech, A. T. Sobczyk and A. Jaworek, "Optical emission spectroscopy of point plane corona and back - corona discharges in air," *The European Physical Journal D*, vol. D, no. 65, pp. 459-474, 2011.

[14] S. Chen, "Light spectra on AC Corona," in *International Symposium on Electrical Insulating Materials*, Japan, 1998.

[15] S. Y. a. C. Shixiu, "Light Spectra on DC Corona," in *International Symposium on Electrical Insulating Materials in conjunction with 1998 Asian International Dielectrics and Electrical Insulation and the 30th Symposium on Electrical Insulating Materials*, Toyohashi, Japan, 1998.

[16] S. Singh, *Electric Power Generation: Transmission and Distribution*, PHI, 2003.

6. APPENDIX

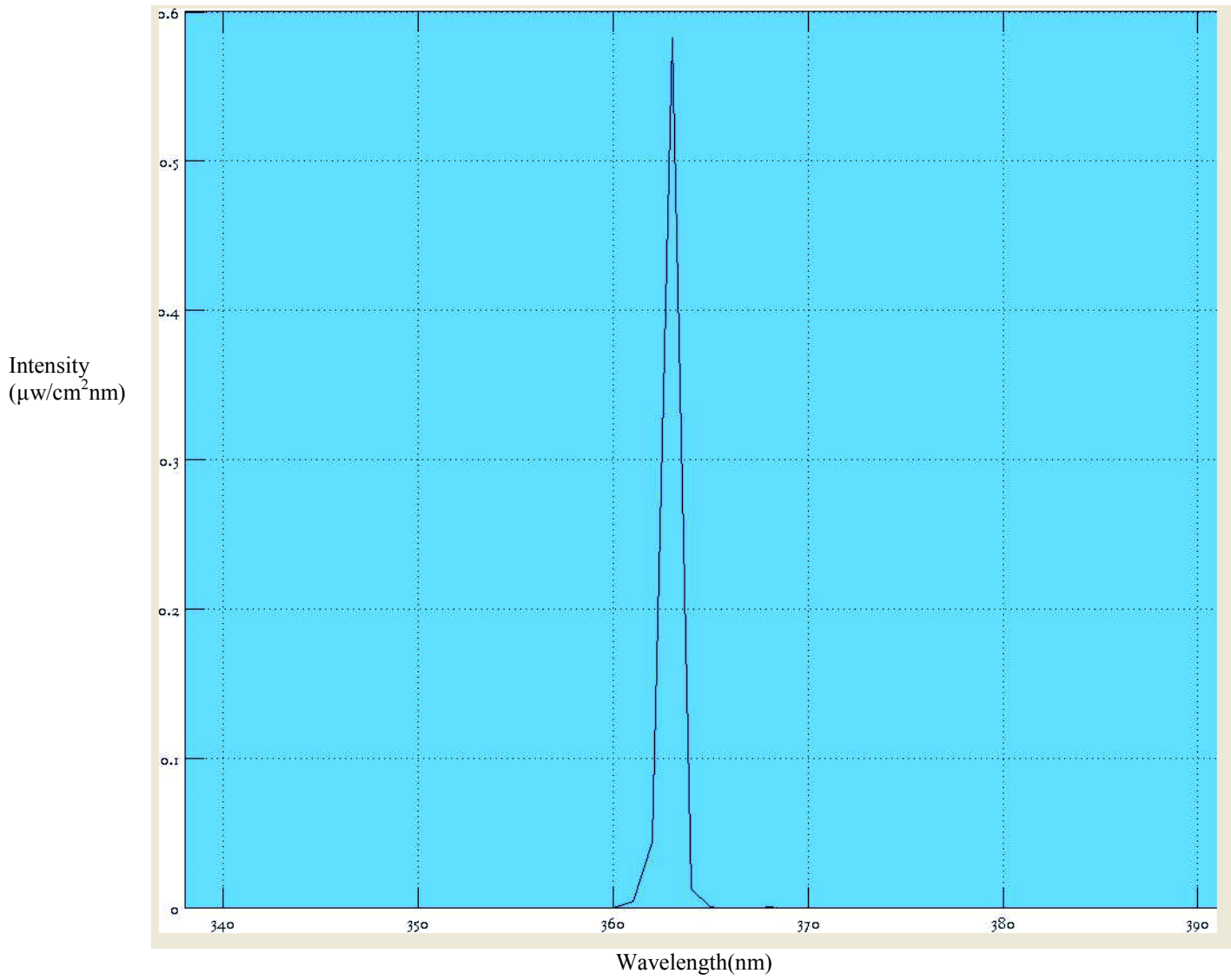


Figure 6: Matlab screen of new filter design

A COMPARATIVE STUDY OF SURFACE PARTIAL DISCHARGE PARAMETERS AT VERY LOW FREQUENCY (VLF) AND POWER FREQUENCY TEST VOLTAGES

S. Chimunda*, C. Chidzikwe**, C. Nyamupangedengu***

School of Electrical & Information Engineering, University of the Witwatersrand, Private Bag 3, 2050, Johannesburg South Africa

*E-mail: *samantha.chimunda@students.wits.ac.za **cliff.chidzikwe@students.wits.ac.za*

**** cuthbert.nyamupangedengu@wits.ac.za*

Abstract: Partial discharge (PD) tests on power cables are now conducted at Very Low Frequencies (VLFs) as it is technically and economically convenient, yet power cables operate and fail at power frequency. A comparative study is conducted in accordance with IEC 60270. Surface PD parameters in air at VLF (0.02 Hz and 0.1 Hz) and at power frequency (50 Hz) sinusoidal test voltages are presented. PD measurements were performed in a fairly constant temperature and humidity environment. Six polyethylene disk samples were prepared with a diameter of 132 mm and 4.25 mm thickness for each test frequency. The sample thickness was chosen to correspond to the insulation thickness of 6.35/11 kV XLPE insulated power cables. PD inception voltage and PD magnitude increased with frequency whilst PD extinction voltage showed no peculiar trend. Repetition rate increased with frequency and statistical operators such as kurtosis and skew of mean pulse height and pulse count of PD phase resolved patterns (PDPRPs) decreased with frequency. The findings are explained using the known theory of surface PD mechanism. Knowledge obtained from this work is used to qualitatively model the behaviour of surface PD parameters with frequency. Possible practical implications of the findings are also outlined.

Keywords: Surface PDs, very low frequency, power frequency, repetition rate, phase resolved patterns, kurtosis, skew

1. INTRODUCTION

Power cable diagnostic tests such as partial discharge (PD) techniques are conducted to investigate the state of dielectric material throughout its life [1]. Partial discharges occur due to enhanced localised stress at imperfections inside or on insulation surface [2]. In the past power cable diagnostic tests were performed using DC and after the introduction of synthetic insulation including polyethylene, XLPE and extruded rubber, DC tests proved to be destructive [3]. Testing at DC causes premature failure because the charge that is retained after the tests causes deleterious over voltages in the power cable on switching back to normal operation power frequency voltage [4,5]

Power cables are highly capacitive and therefore the size and power required for testing at power frequency become technically and economically a challenge. The apparent power rating of such diagnostic test equipment is a function of frequency given by Equation 1.

$$S = VI = 2 \pi f C V^2 \times 10^{-12} \quad (1)$$

Where:

S = apparent power in voltamperes

V = maximum test phase-to-ground voltage in volts

I = current in amperes

f = frequency in hertz

C = total capacitance of the cable in pF

Viable alternative techniques of testing power cables include the damped AC [6] and very low frequency (VLF) test voltage techniques [5]. VLF sinusoidal test voltages result in small apparent power ratings and consequently less costly diagnostic test equipment. For example the amount of power required when testing at 0.1 Hz and 0.02 Hz is 500 and 2 500 times less than that at 50 Hz respectively. The question and challenge associated with testing at VLF is whether or not surface PD parameters obtained at VLFs are comparable and can be inferred to the power frequency implications. The purpose of this document is to present results of a comparative study on surface PD parameters at VLF and 50 Hz test voltages.

2. BACKGROUND

Defects in insulation systems adversely affect insulation performance, reliability and consequently reduce life span of electrical equipment. Cavities in solid insulation are the most occurring defects and are known to be more harmful as stated in [7]. Surface discharge and corona are also common in solid insulation systems and especially on power cable terminations.

Surface PDs are localised discharge originating from a triple junction due to electric field enhancement [8]. Triple junction is the interface of an electrode and dielectric material in air. Electric field enhancement is aggravated by the differences in permittivity of air and dielectric [4]. At the triple junction with continually field

enhancement insulation degradation leading to insulation failure and then breakdown may result. Electrical stress in insulation systems are other forms of PDs [4]. In power cable installations, surface discharges are common problems on cable terminations and need to be correctly identified through techniques such as VLF PD diagnosis. An experimental study was conducted to investigate surface discharge characteristics at VLF test voltage in comparison with power frequency test voltage as presented in the rest of the paper.

3. INVESTIGATION METHODOLOGY

The steps taken to conduct the study at the different test frequencies include simulation, sample preparation, experimental set-up, measurement and analysis.

3.1 Simulation

To predict the inception voltage, experimental sample model was simulated using FEMM 4.2 software package. Figure 3 shows the simulation results. The test sample is polyethylene ($\epsilon_r = 2.3$) sheets between two brass electrodes. The bottom electrode is coated in epoxy ($\epsilon_r = 4$) to prevent surface discharges occurring at the interface of the bottom electrode and polyethylene sheets. Angle of contact and geometry of the electrode plays a critical role as it affects the electric field distribution [4]. It was assumed that the angle of contact between the top electrode and polyethylene surface is 90° .

An inception voltage of 6.7 kV was obtained from the simulations. This was determined by gradually increasing the electrode voltage until air at the triple junction reached a breakdown stress of 3 kV/mm.

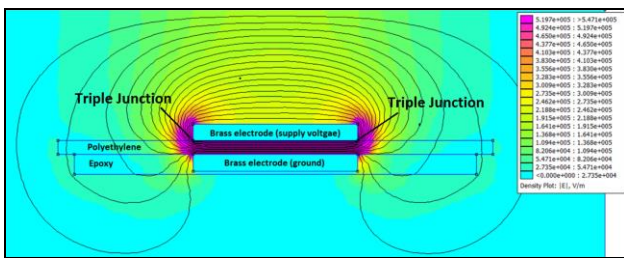


Figure 1: Simulation results to predict the inception voltage

3.2 Sample preparation

Six samples were prepared for each test frequency. Each sample was made of polyethylene sheets 4.2 mm thick (thickness of 6.3/11 kV XLPE insulated power cables), with a diameter of 132 mm. The diameter was selected to ensure that there was sufficient surface area for discharges to occur. Figure 2 shows the test sample indicating regions where surface discharge would occur. Test samples were cleaned with alcohol to minimize surface contamination and polished with Novus Scratch remover to ensure the surface did not contain defects, as

this could result in a lowered flashover voltage [4]-[5].

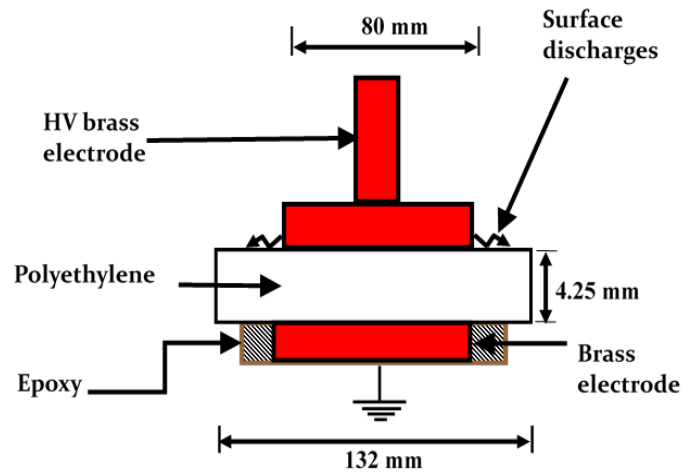


Figure 2: Test sample setup

3.3 The experimental setup

Figure 3 shows the experimental setup used for power frequency and VLF PD measurements in accordance with IEC 60270 PD detection method and guidelines in IEEE Std.400 and IEEE Std.400.2 for field testing and evaluation of insulation of shielded power cables for 50 Hz and VLF less than 1 Hz.

The 50 Hz test setup is fed from the mains 220 V/50 Hz supply through a 220 V/50 kV step up transformer whose output was controlled using a Variac. A 1 M Ω resistor of distilled water resistor was used to limit the fault current in case of breakdown. A voltage divider to step down the voltage to measurable values was used. A High Voltage Analyse (HVA60TM) was used to supply 0.02 Hz and 0.1 Hz sinusoidal test voltages of up to 60 kV. An isolation transformer was used to isolate mains noise from the VLF test circuit.

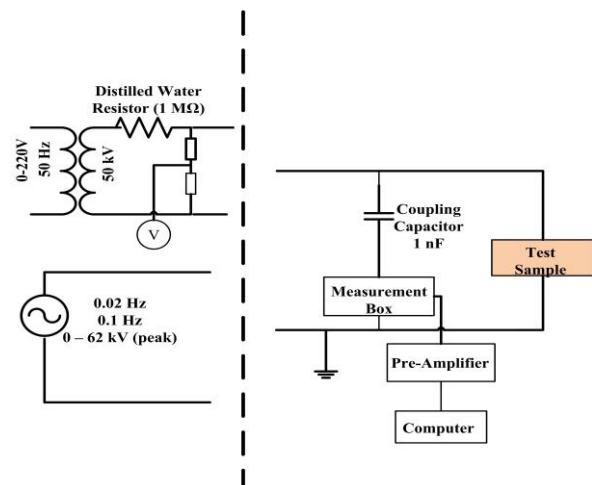


Figure 3: Experimental setup

Both test setups use a coupling capacitor which acts as a

charge current source in the PD current flow and for filtering out the test voltage frequency from the PD detection box. Detection box creates a PD voltage signal as PD current flows. The PD voltage is processed and displayed on the ICM Compact™ PD device.

3.4 PD measurements

Temperature and humidity were recorded prior to taking measurements. It was assumed that pressure was constant because the experiment was conducted at the same altitude. Measurements were conducted in a shielded high voltage laboratory environment. Prior to measurements, calibration was conducted by injecting a known charge magnitude and observing its response on the ICM compact device. The background noise was measured and showed a maximum of 0.83 pC. Inception voltage of each sample was determined by gradually increasing the supply voltage until repeatable surface discharges were observed.

PD phase resolved patterns (PDPRP) were recorded at 120 % of the inception voltage for 10 minutes. The data was obtained using the export function of the ICM compact software in text format for further analysis.

Cigre partial discharge recognition patterns (signatures) [10] were used to confirm that the discharges obtained were surface discharges which distinctively occur on the rise and fall edges of the sinusoidal waveform.

4. RESULTS

4.1 Inception voltage

PDIV is the applied voltage at which repetitive PDs are first observed in the test object, when the applied voltage is gradually increased from a lower value at which PDs are not observed [11]. PDIV increased with the supply frequency. The increase was however non-linear and also varied with temperature and humidity. Figure 4 shows the inception voltage at 21.7°C and 31.9 % RH and Figure 5 show the inception voltages at 22.8 °C and 59.1 % RH.

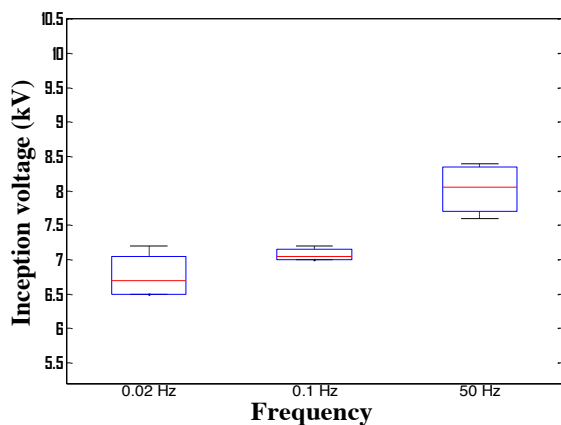


Figure 4: Inception voltage at 21.7°C and 31.9 % RH

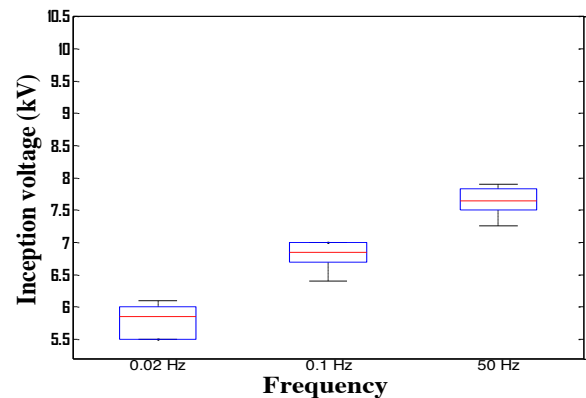


Figure 5: Inception voltage at 22.8 °C and 59.1 % RH.

Cavallini and Montanarri [12], and Hauschild [13] observed similar trends of increase in PDIV with the supply voltage frequency for spherical cavities in polyethylene, surface and corona discharges.

A crude estimate factor at which VLF and 50 Hz PDIVs are related can be determined, as an average of the ratios of the averages of PDIVs 50 Hz to 0.1 Hz. For example at 0.1 Hz and 50 Hz the calculated averages of PDIVs were 7.1 kV and 6.9 kV, 8.1 kV and 7.7 kV respectively. The average of the ratios of 8.1 kV and 7.1 kV, 7.7 kV and 6.9 kV is calculated to be 1.1. Thus PDIV at 50 Hz can be 1.1 times that at 0.1 Hz.

However, for cavities in epoxy as reported in [14] following work done by Pepper and Kalkner, PDIV at 50 Hz is about ~0.8 times that at 0.1 Hz.

4.2 PD magnitude

The actual partial discharge magnitude on the surface cannot be quantified; however the detection instrument detects the apparent charge within the dielectric [8]. Maximum PD magnitude increased with supply frequency with positive PD magnitudes relatively bigger than those of the negative PD magnitudes as shown in Figure 8.

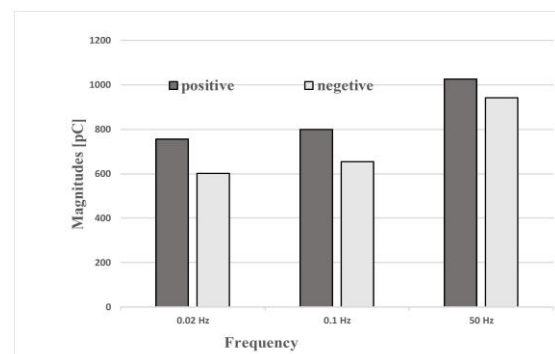


Figure 6: Maximum discharge magnitudes

Miller and Black in [15] also reported the increase of surface PDIV and PD magnitude with frequency in cavities and for surface discharges.

5. PHASE RESOLVED PATTERNS (PDPRP)

PDPRPs show the position of the discharges with respect to the angle on the sinusoidal voltage waveform. Figure 7, Figure 8 and Figure 9 shows the results of PDPRPs at 0.02 Hz, 0.1 Hz and 50 Hz. PDPRPs become more densely populated with increase in the supply frequency.

The average pulse count per cycle (repetition rate) [11] at 0.02 Hz is 4, at 0.1 Hz it is 10 and at 50 Hz it is 80. Skew, which measures symmetry with respect to the normal distribution [16] and kurtosis which measures the distribution sharpness were calculated and found to decrease with frequency. However, no literature was found which investigated effects of frequency on these statistical parameters.

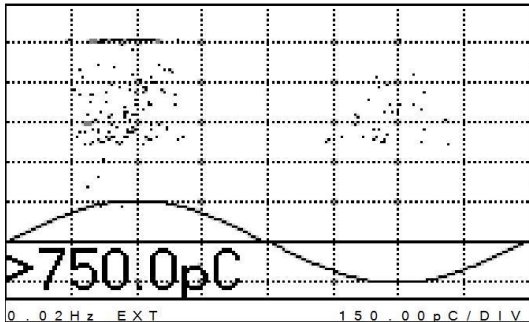


Figure 7: PDPRPs at 0.02 Hz

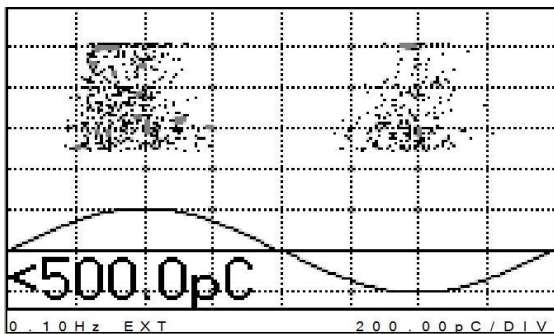


Figure 8: PDPRPs at 0.1 Hz

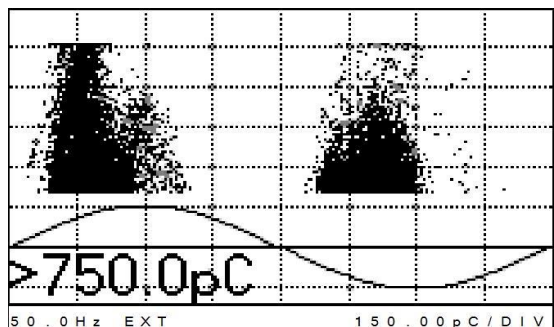


Figure 9: PDPRPs at 50 Hz

6. EXTINCTION VOLTAGE

Extinction voltage is the applied voltage at which repetitive PDs cease to occur, when the voltage applied to the object is gradually decreased from a higher value at which PD pulse quantities are observed [17]. The results did not show any peculiar general trend of the PDEV with frequency.

Behaviour of PDEVs with frequency in the range of 100 kHz and 3 MHz was studied in [17] for needle to plane configuration and no markedly trend was ascertained. PDEV was reported to be a reproducible quantity. This can be argued that the effect of frequency on PDEV is not fully known.

7. ANALYSIS OF RESULTS

The observed results are analysed and explained using known theory of surface PD mechanism. A discharge occurs when there is a free electron and the voltage is substantially high (inception electric stress) such that there is adequate field stress to propel a free electron to initiate ionisation avalanches. The probability of the presence of a free electron is directly proportional to time. Figure 10 shows the time delay in reaching theoretical inception voltage at VLF and 50 Hz test voltage frequencies. The time delay (Δt_1) at 50 Hz is much shorter than that at VLF (Δt_2), it is therefore more likely that a free electron is present by the time inception stress is reached at VLF than at 50 Hz. The overvoltage, defined as the difference in the actual and theoretical inception voltages [18], denoted as ΔV_1 and ΔV_2 in Figure 10 is directly proportional to the time delay in reaching the inception voltage.

This proportionality results in a lower actual inception voltage and magnitude at VLF than at 50 Hz test voltage frequency. The repetition rate increases with frequency because the charging time constant of the surface capacitance is smaller at power frequency than that at VLF [5].

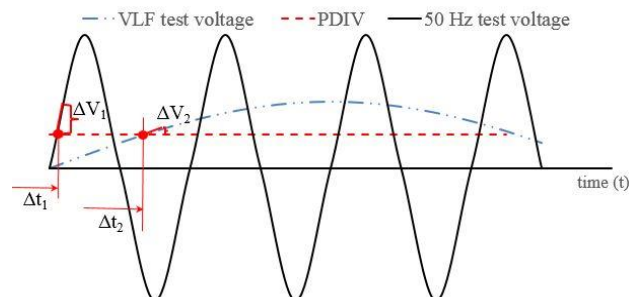


Figure 10: Time difference to reach inception voltage

The positive half cycle magnitudes are greater than those at the negative half cycle for all test frequencies as shown in Figure 7. This is attributed to the difference in mobility of the positive ions and electrons, which results in charge retention difference at VLF and 50 Hz. Positive ions have a lower mobility of $2.5 \text{ cm}^2/\text{Vsec}$ in comparison to

electrons with 10^2 - 10^3 cm²/Vsec [7]. At VLF the positive ions have ample time to disperse and move towards the cathode before the test voltage is in the negative half cycle, therefore the cathode fall phenomenon is less pronounced and negative half cycle magnitudes are lower. However the differences in magnitudes of the positive and negative half cycles at 50 Hz are due to cathode fall because there is pronounced surface charge retention (memory effect) [7]. An equation that relates surface discharge magnitude to background stress, main stress voltage, capacitance and the dimensions of the test sample is shown in Equation 2.

The nature of the test voltage affects the discharge mechanism [9,14]. According to Bartnikas and Novak [18] the extent of discharge augmentation is dependent on the overvoltage which in turn determines the residual voltage (voltage after a discharge). A higher overvoltage will result in ~15 % residual voltage, whereas a lower over-voltage retains ~98 % [18]. At lower frequencies the electric field is determined more by surface conductivity whereas at higher frequencies the capacitive component is more dominant; however the dielectric permittivity does not change at the test frequencies [5, 19].

$$q = \frac{A}{d} \varepsilon (\Delta U + \Delta U_q) \quad (2)$$

Where:

q = apparent charge

A = cross sectional area of surface discharge

d = insulation thickness

ε = surface permittivity

ΔU = overvoltage

ΔU_q = residual voltage

Temperature and humidity alter the surface and gas conditions. A higher humidity results in increased surface conductivity and air molecules have more energy at higher temperature. The environmental implication is that an increase in humidity suppresses discharges and more discharges occur at higher temperature. Furthermore the discharge mechanism is affected by the differences in the work function of the insulation and that of the electrode [12, 18].

8. POSSIBLE PRACTICAL IMPLICATIONS OF THE FINDINGS

PDIV: PDIV is attained easily at VLF. Thus during tests a cable can be failed at VLF yet the same cable will pass when tested at the normal service power frequency.

PD magnitude: At VLF resultant PD magnitudes of defects are small and could be below noise level and yet at 50 Hz the same defects produce larger PD magnitudes.

PDPRPs: Statistical and neural network analysis of PDPRPs to automatically identify types of defects is used

as presented in [16]. The automated techniques use statistical and mathematical methods such as skew and kurtosis to analyse the distribution of the patterns. The difference in skew and kurtosis of the PDPRPs observed at the different test frequency imply finger print variation with frequency.

The findings from this study also substantiate the fact that environmental conditions affect PDs, which can be argue that when conducting PD tests these effects should be considered as they have shown to be influential. Repetition rate increases with frequency, this implies the VLF tests may require more time to accurately describe the PD pattern is highlighted in [12].

9. CONCLUSION

Surface PD parameters were measured using IEC 60270 method at VLF and 50 Hz test voltages. PDIV increased with frequency, and at 50 Hz PDIV is estimated to be about 1.1 times that at 0.1 Hz. PD magnitude and repetition rate increased with frequency whilst PDEV showed non-peculiar trends. Skew and kurtosis for both positive and negative cycles decreased with frequency. The surface PDs parameters at 0.02 Hz and 0.1 Hz from this study are not comparable to those at 50 Hz. Possible practical implications of the findings are drawn from which it can be argued that PD tests at VLFs provide a conservative approach and safer operation margins for the tested equipment but at the expense of other factors like costs in the event of failed equipment.

10. REFERENCES

- [1] R. Bodega, P. Morshuis, M. Lazzaroni and F. J. Wester: "The effect of voltage frequency on partial discharge activity", *IEEE Annual Report Conference on Electrical Insulation and Dielectric Phenomena*, pp. 685 – 689, 2002.
- [2] Nyamupangedengu, C: "PD-type dependent spectral bandwidth in solid polymer dielectrics" PhD Thesis, University of the Witwatersrand, Johannesburg, South Africa, 2011.
- [3] M. Baur, P. Mohaupt and T. Schlick: "New results in medium voltage cable assessment using very low frequency with partial discharge and dissipation factor measurement", *CIGRE 17th International Conference on Electricity Distribution*, Barcelona, Paper No. 74, pp. 1- 5, 12 – 15 May 2003.
- [4] E. Kuffel, W.S. Zaengl and J. Kuffel: *High Voltage Engineering Fundamentals*, Butterworth-Heinemann, 2nd Ed, 2000.
- [5] IEEE Std 400-2001, *IEEE Guide for Field Testing and Evaluation of the Insulation of Shielded Power Cable Systems*, 2001.
- [6] C. Nyamupangedengu and I. R Jandrell: "Partial discharge spectral response to variations in the supply voltage frequency", *IEEE Transactions Dielectrics and Electrical Insulation*, Vol. 19, No. 2, pp. 521- 532, April 2012.

- [7] Y. Murooka, T. Takada and Hidaka: "Nanosecond surface discharge and charge discharge evaluation Part 1: Review and experiments", *IEEE Electrical Insulation Magazine*, Vol. 17, No.2, pp. 6 – 16, April 2001.
- [8] F. H. Kreuger: *Partial Discharge Detection in High Voltage Equipment*, Butterworths and Co, London, 1989.
- [9] R. A. Fouracre, E. Santos, M. J. Given and S.J. MacGregor: "Surface Discharge Propagation: The Influence of Surface Charge", *Power Modulator Symposium, 2006 Conference Record of the 2006 Twenty-Seventh International, Arlington VA*, pp. 39-42, 14 – 18 May 2006.
- [10] CIGRE: "Recognition of Discharges", Working Group No. 21, High Voltage Cables.
- [11] IEC – 60270: High Voltage test technique- Partial discharge measurements, 2000.
- [12] A. Cavallini and G. C. Montanari: "Effects of supply voltage frequency on testing of insulation system", *IEEE Transactions on Dielectrics and Electrical Insulation*, Vol. 13, No.1, pp 111-121, February 2006.
- [13] W. Hauschild: "Discussion: Effects of supply frequency on testing of insulation systems", *IEEE Transactions on Dielectrics and Electrical Insulation*, Vol. 13, pp 1189 – 1191, October 2006.
- [14] A. Cavallini, V. Krotov, G. C. Montanari, P. H. F. Morshuis and L. E. Mariut: "The role of supply frequency in the evaluation of partial discharge inception voltage in XLPE embedded cavities." *Electrical Insulation and Dielectric Phenomena (CEIDP), 2012 Annual Report Conference, Montreal, QC*, pp. 487-490, October 2012.
- [15] R. Miller and I. A. Black: "Partial discharge measurements over the frequency range of 0.1 Hz to 50 Hz". *IEEE Transaction on Electrical Insulation*, Vol. EI-12, No.3 June 1977.
- [16] E. Gulski and F.H. Kreuger: "Computer aided Recognition of Discharge Sources", *IEEE Trans. Electrical Insulation*, Vol. 27, No. 1, February 1992.
- [17] W. Pfeiffer & M. Paede: "About the influence of the environmental conditions on the partial discharge extinction voltage at higher frequency voltage", *Conference Record IEEE International Symposium on Electrical Insulation, USA*, pp 452–544, 2-5 April 2000.
- [18] R. Bartnikas and J.P. Novak: "Effect of over voltage on the risetime and amplitude of PD pulses", *IEEE Transaction on Dielectrics and Insulation*, Vol. 2 No.4, pp. 557-566, August 1995.
- [19] T. Joubert and J. J. Walker, "Influence of the permittivity and resistivity on the electrical stress in multilayer insulation systems at different frequencies", *Proceedings of the 22nd South African Universities Power Engineering Conference*, 2014.

A COMPARATIVE STUDY OF CAVITY PARTIAL DISCHARGE PARAMETERS AT VLF AND AT 50 Hz TEST VOLTAGES

K. Mosito*, M. Dlamini** and C. Nyamupangedengu***

School of Electrical & Information Engineering, University of the Witwatersrand, Private Bag 3, 2050, Johannesburg South Africa

E-mail: * katlego.mosito@students.wits.ac.za ** mlandeli.dlamini@students.wits.ac.za

*** cuthbert.nyamupangedengu@wits.ac.za

Abstract: In this paper a comparative study of cavity defect partial discharge parameters is performed at very low frequency (VLF) and power frequency test voltages. The parameters investigated are the Partial Discharge Inception Voltage (PDIV), Partial Discharge Extinction Voltage (PDEV), Partial Discharge Phase Resolved Patterns (PDPRP) and Partial Discharge charge magnitude. The study is conducted on polyethylene insulation discs and on nine 11 kV XLPE cables at 0.02 Hz, 0.1 Hz and 50 Hz test frequencies. A cavity of 1 mm diameter and 2 mm depth was introduced in all test samples. It was found that all the four PD parameters are affected by the test frequency and they all increase as the frequency increases. A mathematical model for PDIV was developed together with a pixel analysing software for analysing PDPRPs and PD charge magnitude. Pedersen's PD magnitude model proved to work only for 50 Hz and not VLF.

Key words: PDIV, PDEV, PDPRP, PD charge magnitude, Power frequency, VLF.

1. INTRODUCTION

Most defects in power cable insulation and especially accessories such as terminations and joints are diagnosed using partial discharge (PD) techniques. Air filled cavities in the insulation are among the common defects found in cable accessories due to ageing or installation flaws. PD activities occur in the gas trapped voids within the insulation and in insulation interfaces which with time, further erodes the cavity walls due to physiochemical processes and eventually completely bridge the cable insulation causing short circuits [1,2].

Diagnostic tests are performed on solid insulation cables to verify their manufacturing quality and determine whether they are suitable for installation and operation in the power grid according to the published cable standards SANS62067 and SANS60287. Most diagnostic tests are performed after transportation and installation. One of the diagnostic tests performed on cables on site is the Very Low Frequency (VLF) test. VLF tests are performed at frequencies within the range of 0.01 Hz and 0.1 Hz [3]. These frequencies are significantly lower than 50 Hz, hence VLF tests might not reflect the true conditions of the cable since the cable operates and fails at 50 Hz. This paper presents results of a comparative study of cavity defects PD characteristics at VLF and at power frequency.

2. BACKGROUND

VLF tests are performed on power cables because of the high capacitance of the cable given its installed length which increases the current required to energize it at the required voltage according to equation (1) below.

$$I = 2\pi fCV \quad (1)$$

From equation (1), for a given cable capacitance (C), in order to reduce the current (I) required to energize the

cable, either the frequency (f) or the voltage (V) of the supply source need to be reduced. Since the voltage is a set parameter in cable testing, the frequency is the parameter that is reduced to as low a value as possible which in this case is 0.01 Hz and 0.1 Hz. Reducing the frequency to this level allows for long lengths of cables to be tested on-site with relatively small testing equipment which reduces the cost and effort of cable testing. The problem with VLF testing is that partial discharge behaviour might be different than at the operating frequency hence this study aims at determining the relationship between the PD parameters at different test frequencies.

The PD parameters that are investigated in this paper are the Partial Discharge Inception Voltage (PDIV), Partial Discharge Extinction Voltage (PDEV), Partial Discharge Apparent Charge Magnitude and Partial Discharge Phase Resolved Patterns (PDPRP).

2.1. Partial Discharge Inception Voltage

Studies conducted by Miller and Black [4], show that the inception voltage remains constant as the frequency is varied from 0.1 Hz to 50 Hz and the PDIV parameter is also not affected by the source frequency [4]. Forssen and Edin [5], also found out that the inception voltage at VLF is relatively constant and only increases when increasing the frequency to 100 Hz due to the statistical time lag and the fast rate of change of the applied voltage [5]. The influence of frequency on this PDIV parameter is investigated in this paper to check on the existing knowledge.

2.2. Partial Discharge Extinction Voltage

After the PD activity initiates and the PDIV is recorded, the voltage at which the PD activity stops occurring as the applied voltage is reduced is termed the PDEV. The

PDEV just like the PDIV, depends on the electric field strength in the trapped insulation cavity and hence depends on factors such as cavity size, gas type and pressure in the insulation cavity [6]. Once the electric field is no longer strong enough for the PD activity to take place the extinction voltage is reached. With the cavity size, gas type and gas pressure in the cavity kept constant and hence constant electric field according to Paschen [6], the effect of the applied source frequency on the PDEV parameter can be investigated.

2.3. Partial Discharge Apparent Charge Magnitude

A study conducted by Cavallini and Montanari showed that PD apparent charge magnitude measured at high test frequencies will be less than that measured at low test frequencies [7]. Another study conducted by Miller and Black [4] showed that the PD apparent charge magnitude only depend on the cavity size at constant temperature and humidity and the change in frequency does not affect the PD charge magnitude [4]. There are therefore inconsistencies in the literature on the influence of the test voltage frequency on PD magnitude.

2.4. Partial Discharge Phase Resolved Patterns

Forsen and Edin [5] found out that PDPRPs get more irregular as the frequency increases and the discharges per cycle decrease as the frequency increases due to the increase in the cycles per second resulting in the inability to reach the required statistical time lag in the rising edge of the applied voltage waveform [5]. It was also found that PDPRPs shift both in time and phase at higher frequencies proving that they depend on the frequency of the applied test voltage [5]. This effect of the applied test frequency on the PDPRP parameter is also investigated further in this report.

3. INVESTIGATION METHODOLOGY

The investigation of the four PD parameters discussed previously is carried out in solid polyethylene insulation sheets and also in actual 11 kV XLPE power cables. The source test frequencies used to perform this study are 0.02 Hz, 0.1 Hz and 50 Hz. All the factors that influence PD parameters such as the cavity dimensions and the gas type in the cavity are kept constant with an assumption that the pressure of the gas in the cavity also remains constant at 1 bar. The influence of the applied test voltage frequency on PD parameters is then investigated.

3.1. Experimental setup

The experimental test circuit was constructed according to the IEC 60270 PD test setup shown in Figure 1. Two voltage sources were required, one to supply voltage at power frequency and the other to supply at VLF at different times during testing.

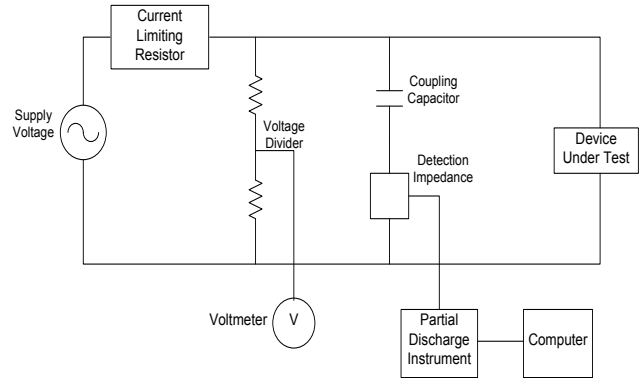


Figure 1: IEC 60270 PD test setup with all required apparatus.

For safety reasons a current limiting resistor was connected in series with the whole setup to limit the amount of current that would flow during an occurrence of a fault in the setup.

3.2. The test samples

Since the cavity wall conductivity changes and becomes more conductive as PD activity occurs, to get consistent results each test sample was only used once [4].

Each test sample comprised of a 4 mm stack of polyethylene discs. A disc shaped cavity of 1 mm diameter and 2 mm depth was punched in some polyethylene discs that would be sandwiched at either position A, B or C as shown in Figure 1. For the coaxial electrode setup, samples of 11 kV XLPE cables were used. Each sample was about 50 cm long and terminated on both ends to avoid discharges and flashover. A cavity would then be deliberately created by drilling a hole, 1 mm diameter x 2mm deep into the insulation from the interface with the outer semiconducting layer.

Figure 2 shows the void placement position for the parallel plate configuration.

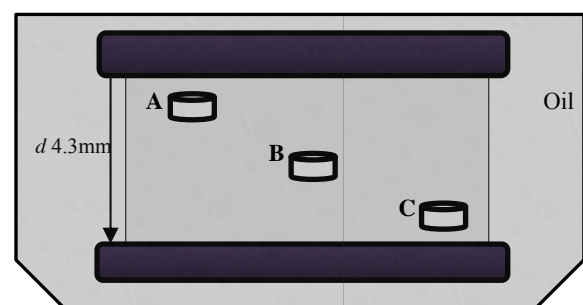


Figure 2: Parallel plate setup with different void position.

For defect A, a minimum of three samples per frequency were created and the same for defect B and C, this resulted in a minimum of 27 samples required in total. The setup was immersed in oil to avoid any surface discharges during testing.

The void dimensions were selected for easier construction using polyethylene sheets, and also easier drilling into the

cable insulation. The inception voltage would be above the rated voltage of a single phase 6.9/11 kV MV power cable and the charge magnitude would be above the noise level [8].

3.3. Test Methodology

The test procedure comprised of a sequence of activities as follows;

- The voltage is increased slowly while checking for any PD activity, if PDs occur the voltage is recorded as an PDIV.
- The voltage is raised to 10 kV_{rms} (≈ 1.55 U₀) for a minimum of 40 cycles to obtain a PDPRP. The PD charge magnitude is also taken at this point.
- After the PDPRP is obtained the voltage is decreased slowly until the PD activity stops and that voltage is recorded as the PDEV.
- The voltage is taken to 0 V and the test setup made safe and then the test sample replaced with another sample.

4. RESULTS

The expected results from the theoretical models as well as the actual obtained results from the investigation are presented for all four PD parameters that were investigated in the following subsections.

4.1. Partial discharge inception voltage

A gas filled cavity within an insulation results in an electric field enhancement within the cavity and once the electric field exceeds the breakdown strength of air, electronic ionisation avalanches are initiated in the cavity that leads to cavity breakdown [9, 10]. A free electron has to be available within the cavity to initiate the ionisation avalanche once the inception electric field has been reached [10]. The availability of a free electron introduces a statistical time lag parameter which can cause a delay in the inception of PDs. PDIV also depends on the size of the cavity, the gas trapped in the cavity and its pressure according to the Paschen curve [6].

Expected inception voltage results: Assuming the gas trapped in the cavity within the insulation is air at 20°C at a pressure of 1 bar (101×10³Pa) the Paschen curve can be used to determine the inception voltage of a 1 mm diameter cavity using equation (2) of the parallel electrode set up [9]. The inception voltage was then determined as 11 kV for a 1 mm void.

$$V_{inc} = \frac{\epsilon_2}{\epsilon_1} d_1 E_2 + d_2 E_2 \quad (2)$$

Where: V_{inc} = PD inception voltage
 ϵ_2 = permittivity of the gas trapped in the void
 ϵ_1 = permittivity of insulation, (2.3).

d_1 = thickness of the insulation
 d_2 = thickness of the void
 E_2 = Electric field in the void

For the coaxial electrode setup, Equation 3 is used and this gave an inception voltage (V_{inc}) of 6.75 kV for XLPE cables used in this work [].

$$V_i(rms) = 24.2p \left(r \ln \left(\frac{R_0}{R_i} \right) \right) \cdot \left(\frac{2\epsilon_r + 1}{3\epsilon_r} \right) \cdot \left(\frac{8.6}{\sqrt{(a+b)p}} + 1 \right) \cdot \frac{1}{\sqrt{2}} \quad (3)$$

Where: r = is the radial position of the cavity
 R_0 and R_i = are the outer and inner radius of the cable insulation
 ϵ_r = relative permittivity of XLPE
 a = radius of cavity
 b = depth of cavity
 B = constant, 8.6.
 p = pressure in cavity (101×10³Pa)

Experimental inception voltage results: The PDIV results obtained are presented in Figure 4 wherein it is evident that the PDIV increases as the frequency of the applied voltage increases. For the cable sample however, the PDIV at 0.1 Hz and at power frequency are in the same order of magnitude. The increasing trend of the PDIV with an increase in the applied test frequency can be generalised using Equation 4 for all cavity positions of the test samples. It is a straight line when plotted on a logarithmic scale.

$$V_{inc} = 0.5 \times \ln(f) + 7.51 \quad (4)$$

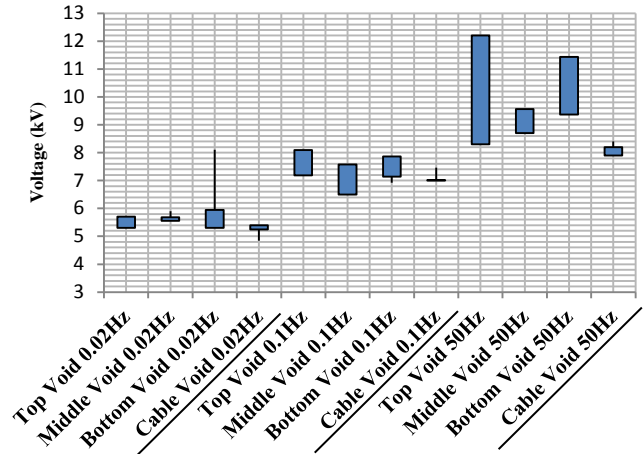


Figure 4: PDIV for all void positions and test frequencies

4.2. Partial discharge extinction voltage

The experimental results obtained for the PDEV parameter at different applied test frequencies for a middle cavity are presented in Table 1. It can be seen that the PDEV increases as the frequency increases but not as prominent as the PDIV.

Table 1: Average PDEV results for middle cavity

Frequency	0.02 Hz	0.1 Hz	50 Hz
Avg. PDEV	4.61 kV	7.63 kV	7.8 kV

4.3. Partial Discharge phase resolved patterns

The PDPRP is a pattern that is formed when the measured PD apparent charge magnitude is plotted against the phase of the applied test voltage resulting in a charge magnitude distribution as a function of phase. The PDPRP are also affected by all the factors that affect the PDIV since PD activity has to take place before the apparent charge magnitude can be plotted against the phase of the applied voltage. The PDPRP also depend on the length of time that the test object has been exposed to the test voltage as it is influenced by the ageing of the cavity in the insulation as PD activities occur and also due to the residual electric field and space charges in the cavity [10].

Expected PDPRP results: It was discovered that the phase position as well as the PD charge magnitude depend on the material type forming the boundaries of the cavity [10]. Bartnikas and Novak also reported that PD activities in insulation cavities are cathode emission-sustained discharges [12]. This means that the PDPRP on every half cycle of the applied voltage can be used to determine the cavity position within the insulation depending on which voltage half cycle contain more discharges at a higher magnitude. Hence for a cavity located where the insulation functions as the cathode (top cavity), in the positive half cycle, it is expected that more PD activities will take place on the positive half cycle at a higher magnitude than on the negative half cycle of the applied voltage. For a cavity located in the middle of the insulation, the PD activity is expected to be equal on each voltage half cycle and for a cavity near the bounded by the grounded electrode (bottom cavity) the negative half cycle is expected to have more PD activity at a higher magnitude than the positive half cycle.

Experimental PDPRP results: Figure 5, 6 and 7 are typical PDPRP results obtained on test samples with a cavity located on the top (bounded by HV electrode and insulation) at varying frequencies.

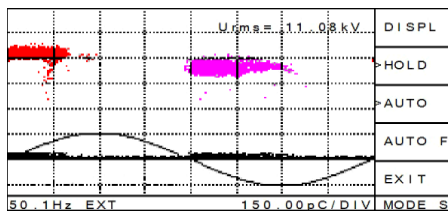


Figure 5: PDPRP for top cavity at 50 Hz test frequency.

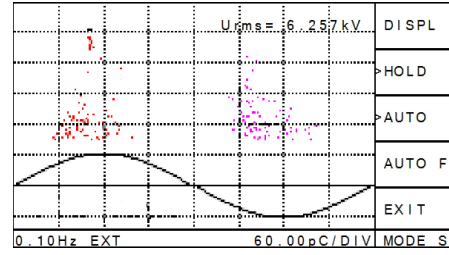


Figure 6: PDPRP for top cavity at 0.1 Hz test frequency.

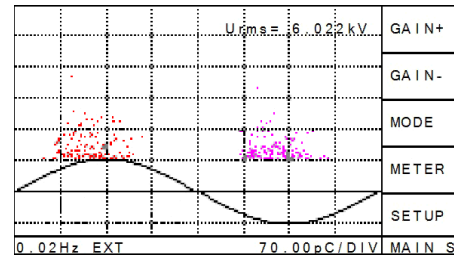


Figure 7: PDPRP for top cavity at 0.02 Hz test frequency.

As evident in the figures, cavities bounded by the HV electrode on one side and insulation on the other give PD signals such that the positive half cycle of the applied voltage has more PD activities at higher PD charge magnitude than the negative half cycle. This is as expected according to Bartnikas and Novak [12]. The other observation is that as the frequency decreases, the PD activity shift from the zero crossing to near the peak of the applied voltage. It can therefore be concluded that PDPRP also depend on the applied frequency.

4.4. Partial Discharge apparent charge magnitude

The PD apparent charge magnitude is the magnitude measured through the detection impedance and displayed on the PD instrument in pico Coulombs (pC) when a PD activity occurs in the test object [10, 11]. For a PD apparent charge magnitude to be measured a PD activity must take place in the test object, hence it depends on the same factors that affect PDIV.

Expected PD apparent charge magnitude: The PD apparent charge magnitude expected was calculated using Pedersen's quantitative model given by equation (5) [9]. The PD apparent charge magnitude that was determined at an inception voltage of 11.35 kV was 65 pC.

$$q = KV\varepsilon(E_i - E_f)\Delta\lambda \quad (5)$$

Where: V = cavity volume.

ε = insulation permittivity.

E_i = cavity minimum breakdown field.

E_f = field in the cavity after a PD activity.

$\Delta\lambda$ = $1/(\text{insulation thickness})$.

K = factor that is a function of cavity dimensions.

Experimental results for PD charge magnitude: After using the pixel analysing software that was implemented

to determine the PD charge magnitude from the PDPRP picture, the average charge magnitude for all void types at all test frequencies are plotted in Figure 8 and 9.

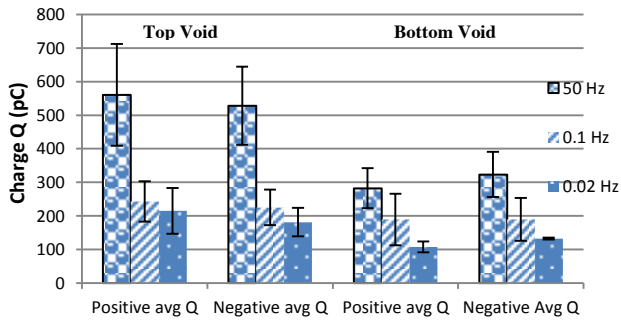


Figure 8: Average charge magnitude for Top Void and Bottom void samples for all frequencies.

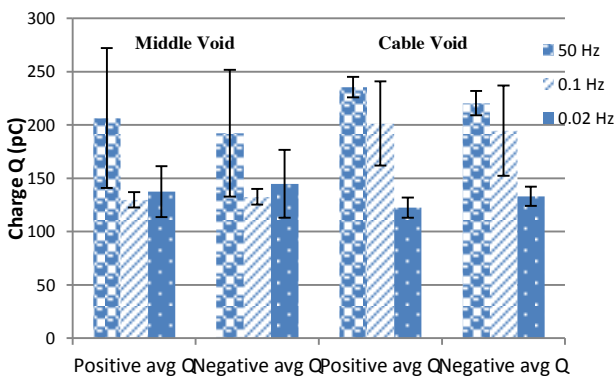


Figure 9: Average charge magnitude for Middle void and Cable void samples for all frequencies.

From Figure 8 it can be observed that the average charge magnitude for top void is greater than that of the bottom void at all frequencies and that the charge magnitude decreases with frequency. Figure 9 also shows that the charge magnitude in a cable with a void also decreases with frequency. This indicates that the PD charge magnitude depends on the test frequency. It is however notable that as with PDIV, the apparent charge magnitude for defects in the power cable samples are effectively the same at 0.1 Hz and 50 Hz. At 0.2 Hz however the magnitudes are much lower for all cases.

5. ANALYSIS AND DISCUSSION OF THE RESULTS

The PDIV increases with the increase in the source frequency as observed in the presented results and represented with the trend as given in Equation (4) also shows that PDIV is a function of frequency. The theoretical model which uses parallel plates and the Paschen curve is only applicable for modelling PDIV at 50 Hz and it does not apply to 0.02 Hz and 0.1 Hz together with Pedersen's quantitative model. Hence it is recommended that these two models be revised to include a frequency factor. The findings by Forssen and Edin [5] prove to be more accurate than that of Miller and Black [4]. The reason for the increase in PDIV as frequency increases is due to the fact that the rising slope of a 50 Hz waveform is greater than that of 0.1 Hz and 0.02 Hz

waveform, hence with an assumed constant statistical time lag, the discharge gap overvoltage at the moment of PD initiation in a 50 Hz waveform is greater than that of 0.1 Hz and 0.02 Hz resulting in a higher PDIV [12]. The other reason could be that at higher frequencies the fast rate of change of the applied voltage results in cycles with no PD activity hence increasing the PDIV [5].

The PDEV also increases with an increase in frequency since the PDIV also increases with frequency. The reason is that to sustain PD activity at higher frequencies requires higher voltage than at VLF hence resulting in higher PDEV at higher frequencies.

The PDPRP show a shift from the zero crossing toward the peak of the applied voltage phase as the frequency increases, this shows that the PDPRP depend on the applied test frequency as also reported by Forssen and Edin [5]. The shift in time and phase as the frequency increases is from the peak to the zero crossing of the voltage waveform. The reason why PD pulses occur on the rising and falling edges, and even around the zero crossings of the sinusoidal supply voltage, is because of the influence of the residual charge in the discharge area. At lower frequencies, the time interval between discharge pulses is much longer than at 50 Hz. The amount of residual charge is therefore less and the phase positions of the PD pulses consequently shift towards the crests as observed.

The PD apparent charge magnitude increases with an increase in frequency as can be observed in Figure 8 and 9. The discharge magnitude at 50 Hz is greater than that at 0.1 Hz and 0.02 Hz. This is due to the increased inception voltage at higher frequency than at VLF. This shows that the findings by Cavallini and Montanari [7] is inaccurate. Pedersen's quantitative model for apparent charge magnitude also needs to be remodelled to take the frequency factor into account.

6. PRACTICAL IMPLICATIONS OF THE RESULTS

The PDIV of a cable have to be greater than its operational phase voltage together with its PDEV for a cable to be considered healthy and fit for use. VLF testing gives a lower PDIV which in some cases is lower than the operational phase voltage of the cable which will suggest that the cable is poor and aged and hence will fail if put into use while when the cable operate at 50 Hz the PDIV and PDEV is within the acceptable range to prove the cable is still healthy. It is recommended that more tests like the resonance test be conducted together with VLF tests before making a conclusion on the condition of the cable.

The PDPRP results obtained at VLF resembles more of corona discharges than PD activities since they occur on the peak of the applied waveform. This could mislead the analysis of the type of defect in the cable during diagnosis which could be a different defect when tested or operating at 50 Hz. Hence for defect type diagnosis,

the VLF testing has to be supplemented with another test to confirm the type of defect present in the cable system.

7. CONCLUSION

The investigation of PD parameters at VLF and power frequency was successfully conducted. It was found that PDIV generally increases with frequency and this relationship was model using a mathematical equation with a frequency factor. It also implies that Pederson's model apply only to results of 50 Hz and not VLF. The PDEV also depends on the change in frequency since it is relative to the PDIV. The PDPRPs shift in phase when the frequency increases indicating frequency dependence as well. PD apparent charge magnitude decreases as the frequency decreases due to the high PDIV at higher frequencies than at VLF. These findings prove that the four PD parameters are affected by the testing frequency hence VLF testing should be supplemented by an alternative test before diagnosing a power cable on-site.

8. REFERENCES

- [1] N. Hampton, R. Hartlein, H. Lennartsson, H. Orton, R. Ramachandran. "Long-Life XLPE Insulated Power Cable". Jicable. 2007.
- [2] G. Paoletti, A. Golubev. "Partial Discharge Theory and Application to Electrical Systems". Cutler-Hammer Engineering services. IEEE IAS Pulp and Paper Industry Conference. 1999.
- [3] IEEE Standards Association. "IEEE Guide for Field Testing of Shielded Power Cable Systems Using VLF". IEEE Power and Energy Society. IEEE Std 400.2-2013.
- [4] R. Miller, I. A. Black. "Partial Discharge Measurements Over the Frequency Range 0.1 Hz to 50 Hz". IEEE Trans. Electr. Insul. Vol EI-12 No. 3, June 1977.
- [5] C. Forssen, H. Edin. "Modeling Partial Discharges in a Cavity at Different Applied Frequencies". IEEE Annual Report Conference on Electrical Insulation and Dielectric Phenomena. 2007.
- [6] PHYWE System GMBH. "Plasma Physics: Paschen Curve". PHYWE Series of Publications, Laboratory Experiments.
- [7] A. Cavallini, G. Montanari. "Effect of Supply Voltage Frequency on Testing of Insulation System". IEEE Transactions on Dielectrics and Electrical Insulation, Vol. 13, No. 1. February 2006.
- [8] C. Nyamupangedengu, I. R. Jendrell. "Sizing of Artificial PD Defects for an Accelerated Ageing Test of Power Cable Solid Dielectric Insulation". Southern African Universities Power Engineering Conference (SAUPEC), Capet Town 2008.
- [9] E. Kuffel, W.S. Zaengle, J. Kuffel. "High Voltage Engineering Fundamentals 2nd edition". Butterworth-Heinemann. 2000.
- [10] C. Nyamupangedengu, "Time-varying PD spectral characteristics in solid polymer insulation", *IET Journal of Science Measurement Technology*, Vol. 6, No. 2, pp. 85-95, 2012
- [11] C. Chan, P. Duffy, L.J. Hiiivala and J. Wasik (1991), Partial Discharge - Part VIII: PD Testing of Solid Dielectric Cable. *IEEE Electrical Insulation Magazine*, Vol. 7, No. 5, pp. 9-20, 1991.
- [12] R. Bartnikas, J. P. Novak. "Effect of Overvoltage on the Risetime and Amplitude of PD Pulses". IEEE Transactions on Dielectrics and Electrical Insulation. Vol. 2 No. 4, August 1995.

COGNITIVE EXPLORATION IN SUPPORT OF FORMULATING AN HYPOTHESIS TO EXPLAIN ANOMALOUS FLASHOVERS IN HVDC SYSTEMS

P. H. Pretorius

*University of the Witwatersrand, Faculty of Engineering and the Built Environment, School of Electrical and Information Engineering, Private Bag 3, Wits 2050, South Africa.
e-mail: pieter.pretorius@wits.ac.za*

Abstract: Unexplained flashovers associated with modern HVDC systems with reported occurrences of around ten per annum on one specific system remains a challenging problem to solve. Understanding the cause of anomalous flashovers will greatly assist in specifying design criteria supporting the improved performance of HVDC systems. A motivation particularly relevant to planned HVDC network expansion in South Africa. The following aspects are treated from an environmental perspective in an attempt to formulate a new hypothesis to explain anomalous flashovers in HVDC systems: the presence and contribution from an “Electrode Effect”; change in “Effective Permittivity”; the development of a “Maxwell Capacitor” and the formation of a “Double Layer”. Details are presented for each aspect in terms of its possible role and possible contribution to electric field enhancement acting as precursor to the breakdown of air.

Key words: anomalous flashover, HVDC, hypothesis, electrode effect, effective permittivity, double layer, Maxwell capacitor.

1. INTRODUCTION

The root cause of anomalous (unexplained) flashovers associated with modern HVDC systems remains a challenging problem to solve [1, 2, 3]. Since inception of Bipole I at full voltage, Manitoba Hydro has experienced numerous anomalous flashovers of the Nelson River HVDC transmission system. The cause of these flashovers is not understood and typical causes, such as, lightning and pollution have been ruled out [1, 2]. The problem translates into approximately ten unexplained events per year [2] with these events scattered over the northern 320 km section of the line [2]. Earlier attempts to identify the cause of the anomalous flashovers addressed the following [1]:

- Insulator pollution: Equivalent Salt Density Deposit (ESDD) tests yielded only light pollution levels; Large quantities of spruce pollen, found in the northern region, showed little impact as a possible contaminant.
- Birds (both streamers and nesting) did not correlate with any of the fault locations.
- Monthly and daily thunderstorm activity closely followed the pattern of anomalous flashovers but available evidence and engineering opinion favoured a mechanism involving common conditions rather than direct lightning strikes to the line.
- Space charge generated by relatively high electric fields near the guy wires of the towers was also considered.

- Detailed analysis of the locations where flashover occurred showed that all but three flashovers occurred far away from the towers and most occurred at relatively low points on the conductor catenary.
- Veld fires were also considered.
- Electric field enhancement by plants was considered as a possible contributor.
- The contribution by thunderclouds / storms to the change in electric field in the vicinity of the line was considered.
- Swarms of insects were also considered.

None of the above provided clear and conclusive answers that could explain the anomalous flashovers [1, 2].

In South Africa, the Cahora Bassa – Apollo HVDC lines, two monopolar lines designed to operate at $\pm 533\text{kV}$ and forming the 1 440 km long system link between South Africa and Mozambique, is currently the only HVDC system in South Africa [4]. Future network expansion may involve an extended HVDC network that will allow for the transport and injection of 2 500 MW power packages at selected sites in South Africa. A possible network to evacuate power from the north of the country is illustrated in Figure 1 [5]. The effective (fault free) operation of this network will be important to the reliable transmission of electric power in the country. The motivation to study anomalous flashovers and to better understand their cause/s and mechanism/s is therefore driven from a perspective of reliable energy transmission.

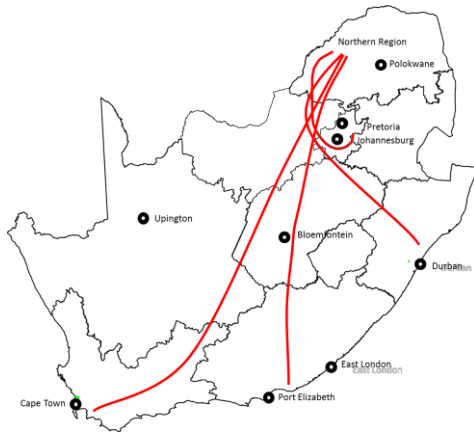


Figure 1: Possible future HVDC network in South Africa.

In this paper, a summary of observations from anomalous flashovers are presented. Specific consideration is then parted to conditions that may be set up, as a result of an existing or changing environment of the HVDC line or components of the HVDC system, that may act as electrical precursors to the insulation breakdown process. From these, a new hypothesis is developed in support of an explanation of the cause of anomalous flashovers and for further study.

2. APPROACH

The ultimate objective in studying anomalous flashovers is to better understand the phenomena and the mechanisms involved to allow for the setting of design criteria that can be used by the HVDC line designer to design a system reliable in the transfer of electric power. In working towards this objective, the approach followed was one that:

- Allowed a literature search from targeted literature associated with specific aspects noted or mentioned in reportings of observations associated with the anomalous flash-overs. The literature referenced in this paper is not exhaustive but is sufficient to support the technical arguments presented in this paper. More comprehensive literature surveys will form part of further studies. The literature targeted also came from study areas other than electrical engineering, such as, atmospheric physics, for example. These were explored for relevant knowledge already gained in those study areas (See list of References at the end of this paper).
- Differs from the conventional approach that addresses poor performance of a power line. The conventional approach may address, for example, pollution as a possible contributor to poor insulator performance. In this case, specific considerations were parted to aspects not usually addressed in evaluations of power line performance, such as, the four aspects discussed below.

- Did not address electric performance from a perspective of dry or wet conditions but rather to look at a condition in-between wet and dry, namely, a condition of high humidity, for example.

Specific aspects considered and covered in this paper include:

- Presence and contribution from an “Electrode Effect”;
- Change in “Effective Permittivity”;
- Development of a “Maxwell Capacitor”;
- Contribution from and formation of a “Double Layer”.

These are covered in more detail in the sections to follow and are contrasted in terms of their possible contribution to electric field enhancement as precursor to insulation breakdown.

3. OBSERVATIONS FROM ANOMALOUS PHENOMENA

3.1 Cahora Bassa - Apollo System

Cahorra Bassa - Apollo Line: Unexplained and increased corona activity on the HVDC line is covered in this section. During radio interference measurements conducted in the vicinity of the line (2012), particularly following a night of heavy rain, corona activity was strong in presence on the conductors of both Pole 1 and Pole 2. This was in effect contrary to the known and expected phenomenon of reduced corona activity during wet conditions on HVDC lines that results from the presence of space charge and that suppresses the corona activity during wet conditions [4, 6, 7].

The following postulate was formulated in an attempt to explain the observed phenomenon mentioned above [4]: The rain does not completely wash and clean the pole conductor from contaminants (small pieces of vegetation, insects, residue from wild fires and pollen) electrostatically attracted to the conductor but rather causes their rehydration. The rehydration of the surface contaminants, on the surface of the conductor, causes an increase in their conductivity and in turn increases the roughness of the conductor (lowers the roughness factor). With an increase in the conductor roughness, the corona inception level of the conductor is reduced [4].

The postulate was reflected against the following: “*Humidity may affect the level of corona activity. Leading to higher levels during high humidity*” [7, p262]. The authors of the EPRI report [7] believed that this may be due to debris on the conductor that becomes rehydrated by the high humidity resulting in increased corona activity. Further, “*Humidity may affect some of the ionisation parameters, such as , electron attachment but there is no clear evidence that relative humidity, in the absence of condensation on the conductor surface,*

has any measurable influence on the corona onset gradient” [6, p 70]. This is a point of further study [4].

The observations made during the measurement period strongly suggest that in dry conditions, the pole conductor performs below, but very close to the corona inception level. Under wet conditions (rain or high humidity) the electric field gradient on the pole conductor is then easily shifted to above inception because of an increase in conductor roughness, as explained above [4]. Gradient calculations and the corona observations made during the measurements (2011 and 2012 - little to no corona on the pole conductors of both poles during dry conditions and excessive corona during wet conditions on both poles), suggest that dry conditions is more representative of a roughness factor of 0,7 and wet conditions representative of a roughness factor of 0,6 or lower for the pole conductors and corona performance along the line in general [4].

Cahorra Bassa - Apollo Repeater Station Spark Gap: Unexplained flashover of the spark gap at the power line carrier repeater station of the HVDC line is covered in this section: The security guard at the repeater station reported frequent and loud bangs originating from the spark gap. These were taken as evidence of flashovers of the 2,5 m gap. Misty and fog conditions were likely to have been present during the flashovers, as verbally reported.

Figure 2 (a) illustrates the 2,5 m spark gap on the pole conductor at the Pietersburg Repeater Station fitted to protect the power line carrier (PLC) equipment.

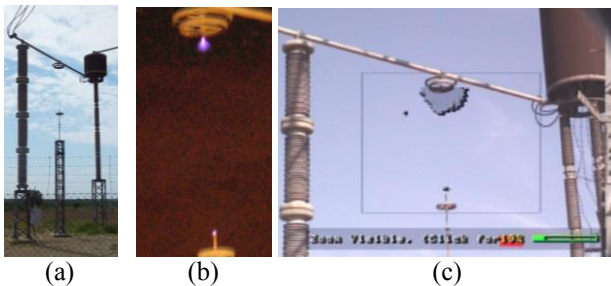


Figure 2: Spark gap on the pole conductor with corona present: (a) Spark gap with coupling capacitor and line trap; (b) Pole 1 (+503 kV); (c) Pole 2 (-370 kV) [4].

Figures 2 (b) and (c) show the presence of corona on the hardware of the spark gaps as captured during earlier measurements [4]. Distinct corona modes could be distinguished from the audible noise created by the corona. These mode changes are likely to be dictated by the presence of space charge [4].

Observed Arching on the Cahorra Bassa - Apollo Line: Unexplained arching was observed on the conductors and moved down the line, as verbally reported to the author by an observer residing close to the line. The arching was

only observed during the presence of fog covering the line.

3.2 Manitoba Hydro HVDC Scheme

Line Details: Figure 3 illustrates the pole configuration of the 2 x bipoles with details of the Manitoba Hydro HVDC line presented in Table 1 [1].

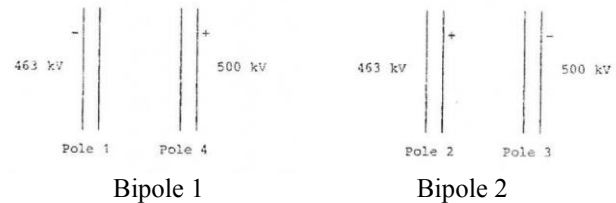


Figure 3: Pole configuration of the 2 x bipoles of Manitoba Hydro [1].

Table 1: Details of the Manitoba Hydro HVDC line [1]:

Scheme	2 x bipole lines
Connecting Points	Nelson River to Dorsey Station (Winnipeg)
Distance	890 km
Right of Way	Share common ROW
Line Spacing	65 m (South); 76 m (North) (Northern section carrier higher towers and longer spans).
Tower Type	Guyed, single mast, suspension type tower
Conductor Attachment	31 m to 37 m
Span Length	427 m to 488 m
Pole Spacing	13,4 m (based on corona losses)
Conductor	2 x ASCR 4,06 cm diameter, 72/7 strand, 934 mm ²
Sub-Cond Spacing	45,7 mm
Max Conductor Temp	Emergency loading of 3600 A at 40°C
Shield Wire	Single
Shielding Angle	35°
Shield Wire Height	9,94 m above pole conductors
Tower Head Clearance	3,5 m with 13,4 m pole spacing (not limiting even for max switching surge overvoltage in excess of 1,7 pu)
Wet CFO	1 240 kV (3 sigma withstand [5% standard deviation]) = 1 050 kV
Suspension Insulator Strings:	21 units (17,15 cm x 32 cm) 50,8 cm creepage distance
Total String Length	3,6 m
Total Creepage Length	10,7 m
Specific Creep	2,13 cm/kV at 500 kV DC (tested with cement contamination in fog chamber)

Line Operation: The line is operated in a cross-over mode with each tower carrying one 450 kV and one 500 kV pole. Negative poles occupy the outer positions. During the summer of 1988, poles on the west line were reversed with Pole 3 operating at - 250 kV. Only 1 anomalous flashover occurred with this configuration.

Soil and Rock: The northern 350 km section comprises of Precambrian Shield (characterised by granitic bedrock, glacio-lucastrine, thin glacial drift type soils, numerous lakes, extensive muskeg and peat deposits) forming part of the Discontinuous Permafrost Zone. The southern 540 km section comprises of predominantly flat terrain, thin glacial drift soils overlaying dolomitic limestone bedrock

Weather: Observations indicate that local weather conditions in the northern region can change rapidly and unpredictably during summer. Weather played a role in anomalous flashovers as they only occurred in summer, usually mid-afternoon on warm, sunny and calm days. The humidity when anomalous flashovers occur was typically low, but the anomalous flashovers often occurred after rain. The rain would provide a source of humidity through evaporation from the ground or swamps rising up towards the pole conductors [30].

Characteristics of Anomalous Flashovers on the Line: More details related to the characteristics of the unexplained flashovers on the HVDC line is covered in this section.

Table 2: Characteristics of the Anomalous Flashovers [1]:

First appeared	In 1970's; Both lines operated ± 450 kV;
Bipole II at ± 500 kV	In 1986
Favoured	- Negative Poles; - Seasonally, May to Sept; - Daily, noon to 16h00; - High ambient temperatures;
1986 and 1987	- 26 anomalous flashovers - Northern section of line - Several high resistance faults (not recorded as anomalous)

Observed Arching on the Line: Line inspectors reported what they described as “rolling fire” moving from one structure (from the source side) to another structure (towards the load) on both Pole 1 (-ve) and pole 4 (+ve) spanning about two spans [1]. The arcing appeared to “zig - zag” between the sub-conductors and was accompanied by a “roaring” sound. The arcing also appeared to discharge approximately every second about 4 units up the insulator string on one of the structures.

There appears to be some agreement between reports on arcing on the conductors if compared to that noted from the Cahorra Bassa - Apollo case. Any connection between the arching and the anomalous flashovers are unknown at this stage [1].

Figure 4 shows a frame of a video recording of a flashover captured on the Manitoba Hydro HVDC line in 1999 [2].



Figure 4: HVDC flashover captured on video [2].

4. FIELD ENHANCEMENT THROUGH SPECIFIC ENVIRONMENTAL PHENOMOMENA

4.1 Breakdown Process

Before embarking on specific environmental phenomena that may contribute to the enhancement of the electric field on hardware or the conductors, it is thought good to briefly review the classical mechanism of breakdown of large gapped air insulation comprising of streamer inception, streamer propagation, streamer-leader transition and leader propagation as covered in [8].

Streamer Inception: Following the appearance of an initial electron in a critical high electric field volume, an electron avalanche starts to develop. With a sufficient number of electrons (N_c) generated due to impact ionisation, a self-propagating streamer head develops. The (*streamer*) *inception criterion* is given by [8]

$$\int_{\gamma} \alpha_{\text{eff}}(E) dx = \ln(N_c) \quad (1)$$

where α_{eff} is the electric field dependent effective ionisation coefficient that includes ionization, electron attachment and detachment. The electric field $E = |\mathbf{E}|$ and the integration path integral- γ starting at the point of maximum field, follows the field line as long as $\alpha_{\text{eff}}(E) > 0$ and ends where the critical field value, E_{BD} given by $\alpha_{\text{eff}}(E_{\text{BD}}) = 0$ is reached (See Figure 5) [8].

Typical values are: $E_{\text{BD}} \approx 2,5$ kV/mm [8]. The inception voltage U_{SI} is based on the Laplacian background field, implicitly determined by the inception criterion. High voltage equipment usually contain additional solid insulation and the highest field values may occur away from electrodes, leading to “*electrodeless inception*” [8]. The underlying physics in this case differs from inception that occurs at an electrode. In particular, initiation is

assumed to be related to electron detachment, which occurs in normal bulk air at about 3,5 – 4 kV/mm [8]. Detachment from shallow surface traps at solid dielectric surfaces may happen at lower fields. The inception criterion to be applied in this case is not fully clear yet [8] (and may be applicable to the metal-oxide layer addressed later in this paper).

Streamer Propagation: The propagating streamer can be understood as a self-sustaining ionisation wave, which is driven partially by recombination-induced light-emission that leads to photo-electrons initiating avalanches and partially by the space-charge induced high electric field in front of the streamer head. In turn, these lead to the growth of the avalanches [8].

The streamer can reach the counter electrode only if the applied voltage is large enough to maintain the propagation process. An estimate of the distance d_s until a streamer stops is given by an equal area rule based on the hypothesis of constant field ($E_s \approx 0,5$ kV/mm for air) in the streamer channel, a reasonable assumption for electrode gaps from 5 cm to about 2 m [8].

Streamer-Leader Transition and Leader Propagation: Streamer-leader transition (Q in Figure 5) occurs when the current in the stem of the streamer bunch is sufficiently high to heat up this channel to more than 5000 K (~ 4700 °C) necessary for a thermal plasma with increased channel conductivity [8].

Leader transition is strongly influenced by capacitive coupling with the surrounding metal structures and dielectric bodies. A mature leader channel can carry a current of about 1 A at an electric field of about 0,1 kV/mm [8].

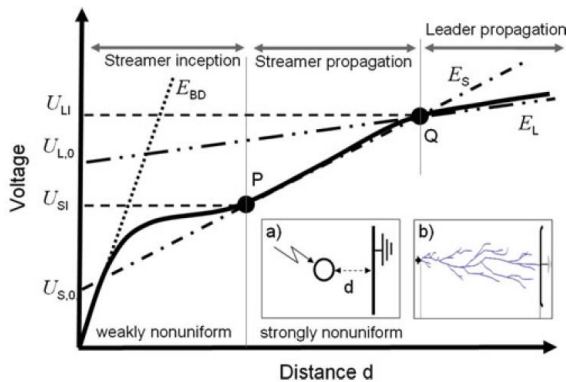


Figure 5: Summary of the breakdown process (Taken from [8]).

A summary of the breakdown process is illustrated in Figure 5 [8] that illustrates U_w (*thick curve*) in normal air as a function of the electrode distance for an inhomogeneous field configuration (for example, sphere-plate electrodes (inset a)). Gas breakdown field = E_{BD} ; Streamer inception voltage = U_{SI} (\approx voltage level at P); Streamer head voltage = $U_{S,0}$; Streamer propagation field = E_s (slope indicated by *dashed-dotted line*); Leader

inception voltage = U_{LI} (\approx voltage level at Q); Leader head potential = $U_{L,0}$; Leader internal field = E_L (slope indicated by *dashed-double-dotted line*). For weakly non-uniform fields, U_{SI} limits the withstand voltage (cross-over at P). The range relevant for streamer line modelling lies between P and Q. (Inset b is a sketch of a streamer bunch with many branches and connecting a tip electrode with a plate electrode [8]).

4.2 Electrode Effect

Ion Formation: The earth's atmosphere is slightly conducting due to the presence of small ions created by ionising radiation, such as, airborne and terrestrial radioactivity and cosmic rays [9]. Terrestrial radioactivity acting as main contributor to ionisation near the earth's surface. Cosmic radiation only accounts for about 10 % of the ionisation near the earth's surface.

Once created, an ion will attract water molecules to form a small cluster ion ~ 1 nm in size. Though many remain as small ions, some either recombine with a small ion of opposite polarity or attach to an aerosol altering its charge [9].

Primary free electrons, including positive and negative elementary ions are generated in the air at ground level. Various ion-molecular reactions then rapidly takes place (within about 10^{-5} s) resulting in the formation of stable ions (O^- , O_2^- , O_2^+ , NO^+ , CO_3^- , NO_2^- , NO_3^- , NH_4^+ and H_3O^+) near the earth's surface [11].

The mobility of negative ions, on average, is 1,3 to 4 times higher than the mobility of positive ions. The difference in mobility can be attributed to the asymmetry of the arrangement of ions with charge of different polarity with respect to an oxygen atom in a water molecule. Consequently, negative ions are characterised by lower energy, that is, by the smaller number of attached water molecules compared to positive ions. Negative ions can be assigned to the class of small to intermediate ions with mobilities of $0,05-5$ $cm^2V^{-1}s^{-1}$ [11].

Electrode Formation: Due to the differences in mobilities of ions with charges different in sign, under certain conditions, the atmospheric electric field may induce a non-compensated space charge near the surface of the earth during weak turbulent diffusion, when a cloud of radioactive gas spreads within a thin layer near the ground where the ions are produced [11].

Under the influence of the earth's natural electric field, the spatial distribution of charge near the earth's surface is presented: positive ions will drift towards the earth's surface where they will recombine. Their mobility is, however, low and as such, a spatial layer of positive ions form at the earth's surface. Negative ions will move vertically upwards (electrons are not considered since their concentration at the earth's surface is small) [11].

The “electrode layer” with a local electric field E_L will develop near the ground. This local field, E_L compensates (cancels) the basic natural field E . The field in the area above this layer will be amplified due to the presence of the non-compensated (superposed) negative charge (See Figure 6) [11, 12].

Turbulent and regular air flow can spread this spatial charge over the atmosphere, inducing an anomalous electrode layer over large areas. Apparently such a situation can occur only within short time intervals because the airflow destroys the electrode layer through ion mixing [11].

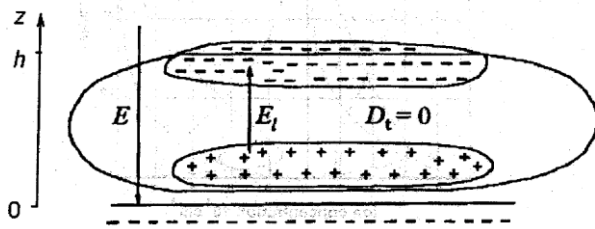


Figure 6: Near ground space charge formation - the “electrode effect” (D_t is the coefficient of turbulent diffusion) [11].

Using a new technique, as described by Kulkarni [13], it was shown that in the electrode layer, the space charge density varies exponentially in the vertical. Further, a new experimental method based on the surface measurements was discussed to determine all the characteristic scales and an average electrical and meteorological state of an electrode layer. The results obtained are in good agreement with previous studies [13]. These may be important to further studies related to anomalous flashovers.

Mareev, *et al*, (1996) [14], conducted outdoor experiments, using a metallic grid above the ground surface for electrode effect studies. The experiments yielded well-defined vertical profiles of the space-charge density and profiles showed strong evidence for the existence of an electrode effect. This experiment [14] can serve as a very useful and well-controlled model for the study of atmospheric electric processes in the atmospheric surface layer that may be associated with anomalous flashovers.

Mareev, *et al*, (1996) [14] further showed that the build-up or break-down of an electrode-effect layer occurred in a time of the order of 10 seconds under the experimental conditions of the time. The artificially generated electrode effect was dependent on the electric field strength generated, wind speed, turbulent mixing and ion mobilities [14]. Wind speed and ion mobility seemed to be the dominant factors that define the space-charge density profiles [14].

Bent, *et al*, (1966) [15] conducted space charge density measurements in fine and fair weather at 1 m, 2 m and 19

m above ground in addition to potential gradient measurements at the ground. Wind speed and temperatures at the various levels were also recorded. These measurements are considered important as they are associated with typical heights where information about space charge levels may be of interest below pole conductors of the HVDC line.

At 19 m the space charge density was usually considerably greater than that at 1 m and of the same sign as the potential gradient. Sometimes there were sudden changes of sign during the recording of space charge at wind speeds below 1 m/s [15]. These phenomena can be explained in terms of the electrode effect if regarded as general modification of atmospheric electric elements due to the presence of an earthed body that may be the earth’s surface itself, acting as an electrode [15].

The results from [15] further show that whereas direct measurements of space charge density near the bottom of a mast are satisfactory, near the top they may be unreliable in conditions of light wind or high potential gradient.

Bent, *et al*, (1966) [15] also noted that downwind of overhead electric AC power lines (66 kV and 132 kV) there is usually an excess of negative space charge during mist, sometimes persisting after the mist has cleared. Repetitive patterns in the courses of wind speed, temperature and humidity suggested that convection cells were moving past in the wind; the space charge records also showed these patterns [15].

How does Radon Contribute to the Electrode Effect?

Rn is a naturally occurring radioactive noble gas that is part of the $^{238}_{92}U$ decay chain and is the daughter of $^{226}_{88}Ra$. Similarly, $^{222}_{86}Rn$ and $^{220}_{86}Rn$ are in the $^{235}_{92}U$ and $^{232}_{88}Th$ decay chains and immediate daughters of $^{223}_{88}Ra$ and $^{224}_{88}Ra$ [10]. As radium decays, radon is formed and is released into small air or water-containing pores between soil and rock particles. If this occurs within radon’s diffusion length of the soil surface, the radon may be released to ambient air, with soil contributing the greater amount [10].

Radon is also released from the near surface water of oceans, tailings from mines (particularly uranium, phosphate, silver, and tin mines), coal residues and the combustion of fossil fuels (coal, oil, and natural gas) [10].

Alpha recoil is the process by which radon, when it is formed by radium emitting an alpha particle and occurs in the opposite direction from the path of particle ejection. Alpha recoil is important because this process dislodges radon from the edge of the soil mineral matrix and allows it to enter pore space between the soil grains [10].

After radon is released into the pore spaces, its ultimate release to ambient air is a function of the soil porosity, soil moisture content, and meteorological factors, such as

precipitation, atmospheric pressure, and the temperature versus altitude profile (including vertical temperature gradients and effects of wind) [10]. (These are all factors that appear to play a part in the anomalous flashovers).

Granitic rock is also associated with high radon levels [10]. Radon levels in ambient air vary with the type of soil and underlying bedrock of the area. The average outdoor radon concentration in the United States is about 0,4 pCi/L (14,8 Bq/m³) [10].

The transport of radon from subsurface soil to air is a complex process that is dependent upon characteristics of the soil and meteorological conditions, such as snow [10]. The rate of emanation (exhalation) is typically slower in very dry soils since alpha recoil may also result in moving the recoiled atoms into an adjacent wall of another soil particle rather than an open pore space [10]. On the other hand, if there is a small amount of water in the pore space, the kinetic energy of the recoiling atom can be dissipated and radon atoms can be slowed sufficiently before becoming embedded into an adjacent soil particle [10].

Soil moisture has an important but varying effect on radon release to the air. While lower levels of soil moisture greatly increase emanation by preventing recoil atoms from embedding into adjacent walls of soil particles as described above, saturated soil conditions in which the pores are filled with water tend to slow the rate of diffusion to the surface since the diffusion coefficient of radon is about 3 orders of magnitude lower in water as compared to air [10].

The influence of moisture and temperature on the radon exhalation rate in concrete, alum shale, and alum shale bearing soil was studied in laboratory experiments [10]. The results indicated that for each material, increasing the rate of moisture up to a certain point increased the radon exhalation rate from the material due to enhanced emanation.

For the alum shale, the maximum exhalation rate occurred at 10–15% moisture content and for the soil samples, the maximum exhalation rate occurred at 20–30% moisture content [10]. As the moisture content increased beyond these levels, a dramatic decrease in the exhalation rate was observed [10].

The above is relevant to the study of anomalous flashovers when noting the observations related to weather in the case of the Manitoba Hydro flashovers addressed earlier in this paper.

Vertical temperature gradients in the atmosphere can create slight vacuum conditions that “pull” radon from the soil, or temperature inversions that inhibit this movement. Therefore, meteorological events may both enhance and inhibit transport of radon from the soil into other media [10].

Diurnal and seasonal changes affect the behavior of radon at the interface between soil and ambient air by impacting temperature and atmospheric mixing [10].

Once radon reaches a height of approximately 1 meter above the soil surface, its dispersion is predominantly determined by atmospheric stability [10]. This stability is a function of vertical temperature gradient, direction and force of the wind, and turbulence. Temperature inversions in the early morning act to produce a stable atmosphere which keeps radon in the soil or near the ground or water surface [10].

Solar radiation breaks up the inversion, leading to upward dispersion of radon which reverses with radiant cooling in late afternoon. In general, radon levels in air typically decrease exponentially with altitude. In one particular study, outdoor radon concentrations at 1 meter above the ground were found to increase during the night, peak in the very early morning, and decrease during the day [10].

In the United States, radon concentrations typically reach their maximum in the summer to early winter, whereas from late winter to spring, concentrations are usually at a minimum as a result of meteorological changes and soil moisture conditions [10].

Figure 7 shows a radon potential map of Canada with higher levels (Zone 1) towards the northern parts of Manitoba [16]. Figure 8 shows a world map with mean atmospheric radon levels [17].

It is postulated by the author that through terrestrial ionisation, an electrode effect may be presented underneath or in close proximity to the HVDC line which in turn, through an “elevated earth plane” (Electrode Effect) may enhance the electric field gradient on the pole conductors, particularly nearer to the mid-span position, that acts as a precursor to the electric breakdown of the air insulation at this point.

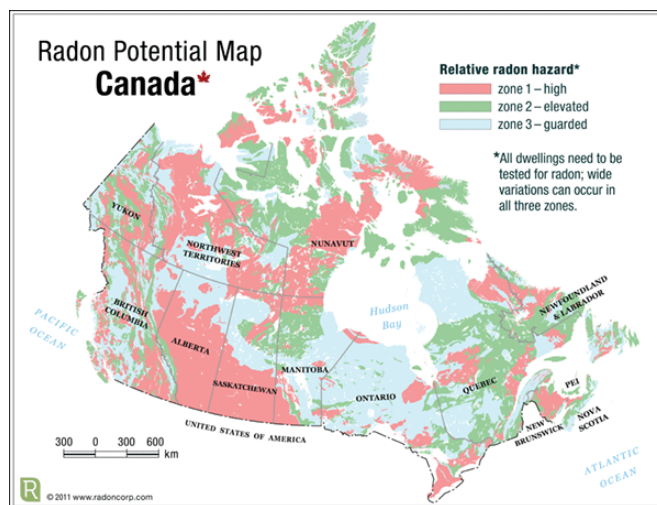


Figure 7: Radon potential map of Canada [16].

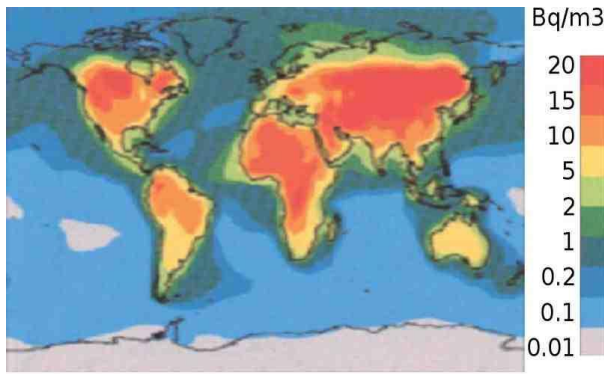


Figure 8: Mean Atmospheric Radon world map [17].

4.3 Effective Permittivity

Before addressing the concept of effective permittivity, it is perhaps necessary to consider fog as potential environmental mediator of effective permittivity.

What is Fog [18]: It is noted that the only difference between mist and fog is visibility [18]. The phenomenon is called fog if the visibility is about one kilometre or less otherwise it is known as mist [18]. Considering Figure 9, it is easy to imagine a power line passing through the mist / fog.



Figure 9: Mist lying in the folds of hilly terrain [18].

Can Electric Fields Affect Fog? From the work of Frost, *et al*, (1981) [19] it was noted that there is a general consensus that electric fields greater than 20 kV/m are required to influence significantly the stability of a natural fog. This is a typical electrostatic field level encountered in the vicinity of HVDC lines [20].

Frost, *et al*, (1981) [19], further indicated that an electric charge was imparted to the fog droplets, causing them to precipitate to the ground under the action of space charged induced electric fields or through enhanced coalescence and precipitation under gravitational forces [19].

Highly mobile electrons quickly move toward the grounded electrode and into a region of smaller electric field where they can no longer generate additional electrons. If electronegative molecules, such as O_2 , CO_2 , or H_2O are present, then the electrons attach themselves to these molecules forming stable ions (as noted earlier). Because of their considerably smaller mobility, the ions drift only slowly toward the grounded electrode (the earth) and a stable space charge is formed in the region

between the corona glow, which is close to the pole conductor and the surrounding electrode (the earth) [19] (See Figure 10).

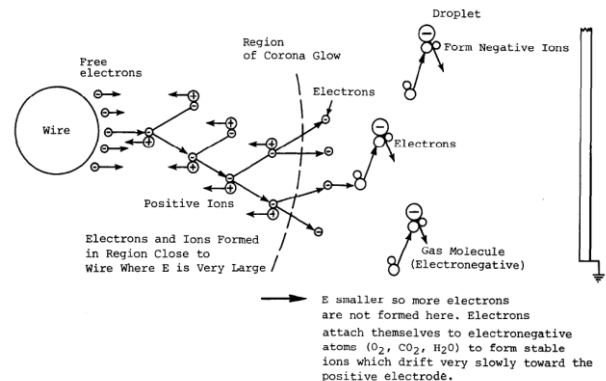


Figure 10: Physics of corona discharge [19].

If particles, such as water droplets, fog or mist, pass through the space charge, it is possible for these droplets to collect charges from the ions [19]. The process of charging a water droplet is complicated but it is common practice to simplify the analysis of the general process and distinguish between two main processes [19], namely: field charging and diffusion charging. Field charging accurately describes the charging of particles having a radius greater than 0,5 μm while diffusion charging is an approximate description of the charging of particles having a radius less than 0,2 μm [19]. The charging of intermediate-sized particles must be described by the combination of both types of charging (See Frost, *et al*, (1981) [19] for more details).

Can Fog Affect Electric Fields? Chalmers, (1952) [21] indicated that negative electric fields measured in mist / fog must be in some way associated with the mist / fog. It was found that the negative fields re-appear before fog or mist returns, for example negative fields of up to 500 V/m, were found during a fine evening after a morning with fog and intense negative fields and a fine afternoon with no negative field at all [21].

Chalmers also found that quite large effects extend to at least 3 km from the power lines down-wind; on one occasion with a south westerly wind when the field was -800 V/m at one location, it was found not long afterwards to be between -200 V/m and -300 V/m at locations over 3 km from the power lines [21].

From the work of Chalmers, 1952 [21], there is some evidence, though not quite conclusive, that the negative fields tend to keep to lower ground, in particular, the negative fields tend to follow valleys in the direction of the wind [21].

It is interesting to note the remark by Chalmers [21] that it seemed as if, in fine weather, the effects, which are then small, come more readily from nearby 66 kV lines than from a nearby 132 kV line [21].

Effective Permittivity: The dielectric constant of a material is the ratio of the permittivity of the material to the permittivity of free space and is an expression of the extent to which the material concentrates electric flux.

As the dielectric constant increases, the electric flux density increases, if all other factors remain unchanged, that enables objects of a given size, such as a set of metal plates, to hold their electric charge for long periods of time, and/or to hold large quantities of charge. In general, substances with high dielectric constants break down more easily when subjected to intense electric fields, than do materials with low dielectric constants. For example, dry air has a low dielectric constant but it makes an excellent dielectric material and acts as self-restoring insulation as in the case of power lines.

Kristensson, *et al.*, (1997) [22] describes the concept of effective, or macroscopic permittivity. Effective permittivity implies that a mixture (or an aerosol, such as, fog) responds to electromagnetic excitation as if it was homogeneous.

It may, however, be proper to remind that the dielectric constant (a term often used synonymously with permittivity) of a material very seldom is constant with respect to temperature, frequency, or any material property [22]. This view to the homogenisation of heterogeneous media is obviously not exact because by using electromagnetic waves of higher and higher frequency one can always “see” more accurately into the medium and probe its structural details. Therefore a quantity such as effective permittivity is only meaningful in the long-wavelength limit. This limit corresponds to low frequencies and indeed, the mixing rules are very often derived using static or quasi-static arguments. The size of the inclusions in the mixture and the spatial correlation length of the permittivity function need to be small with respect to the wavelength” [22]. Thus, the concept of effective permittivity is applicable in the context of HVDC systems.

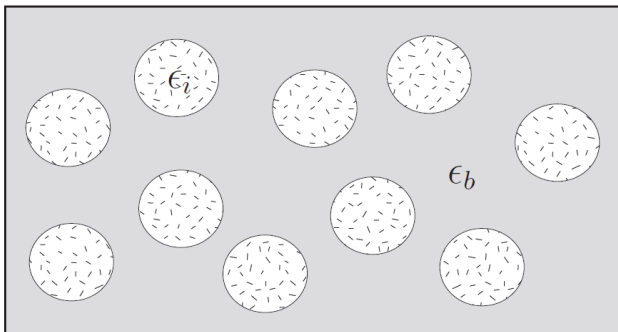


Figure 11: Schematic illustration of fog as an aerosol [22].

With fog as an aerosol represented schematically as illustrated in Figure 11, it is necessary to determine the effective permittivity of this aerosol. Perhaps the most

common mixing rule is the *Maxwell Garnett* formula which is the Rayleigh rule written explicitly for the effective permittivity [22, 23]:

$$\epsilon_{\text{eff}} = \epsilon_b + 3f\epsilon_b \frac{\epsilon_i - \epsilon_b}{\epsilon_i + 2\epsilon_b} \quad (2)$$

where $f = nV$ is a dimensionless quantity, the volume fraction of the inclusions in the mixture. Here n is the number density of dipole moments p in the mixture with unit m^{-3} . The volume of the sphere is V and ϵ_b and ϵ_i are respectively the permittivities of the background medium and the inclusion phase. Air and water in this case [22, 23].

Can Field Enhancement Occur? The fair weather electric field strength is on average about 120 V/m in clear atmosphere near ground level and it decreases quickly with altitude [24]. However, the presence of aerosols, fog or haze lowers atmospheric conductivity and strengthens the electric field locally [24]. Attachment processes in the atmosphere create large ions at the expense of small ions. Large ions have lower electrical mobility and thus decrease the electrical conductivity of the atmosphere [24]. Since the global ionospheric potential, which drives the fair weather atmospheric current, is relatively constant with diurnal variation caused by changes in global thunderstorm activity, a decrease in conductivity within the aerosol layer results in increased potential difference across it in accordance with Ohm’s law and hence in increased field strength [24].

Aerosols can also alter the atmospheric electric field directly if the aerosol is charged. Dust particles colliding between themselves and with the underlying surface become charged due to triboelectric effects [24]. This charge alone can produce a strong field within the dust cloud. It can be shown using Gauss’s law that the field near the bottom of a thin, uniformly charged layer at low altitude will be approximately $E = \Delta z \cdot \rho_c / \epsilon_0$, where Δz is the layer thickness, ρ_c is spatial charge density and ϵ_0 the permittivity of free space [24].

Measurements of the spatial charge density within dust clouds vary widely in magnitude; taking two examples, $3 \times 10^{-10} \text{ C/m}^3$ and $3 \times 10^{-8} \text{ C/m}^3$ yield field strength values of 3 kV/m and 300 kV/m, respectively, for a hypothetical 100 m layer [24]. Furthermore, the fields may be enhanced due to charge separation taking place as a result of size-dependent settling rates: it appears that larger dust particles tend to be charged positively, and since they settle out faster, a dipole can form irrespectively of the mechanism, observations show that normal atmospheric electric fields can become substantially increased in magnitude and reversed, depending on the horizontal position with respect to the cloud [24]. Field strengths as high as -20 kV/m have been observed at ground level during dust storms, in some cases tens of km from the source [24]. Similar values have been reported below volcanic plumes, and fields within the plumes can sometimes be high enough to initiate lightning [24].

4.4 Maxwell Capacitor

A Maxwell capacitor is a hypothetical configuration that describes the electrical phenomena at the interface between two different dielectrics (See Figure 12) [25].

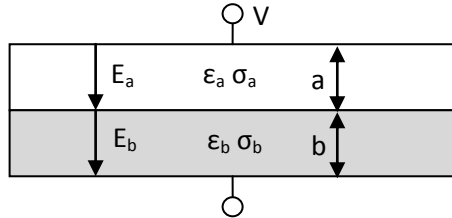


Figure 12: Maxwell capacitor that describes the electrical phenomena at the interface between two (or more) different dielectrics [25].

The Maxwell capacitor can be used to calculate and show the effect of the growth of surface charge at the interface between the two dielectrics. In addition, the Maxwell capacitor can be used to determine the change in dielectric behaviour from capacitive to resistive and to outline the conditions under which the dielectrics become overstressed and may result in breakdown. More details can be obtained from [25].

The author postulates that permittivity change introduced by a layer of fog may contribute to the development of a Maxwell capacitor between the pole conductor and the ground, with the fog (with effective permittivity higher compared to that of air) acting as one dielectric medium and the air acting as the second dielectric medium. The collation of space charge at the boundary between the two dielectrics drives the enhancement of the electric field gradient on the pole conductor up to a stage where the breakdown mechanism is initiated.

4.5 Double Layer

Water Vapour - Metal Oxide Interaction: Even when not in contact with bulk aqueous solutions, a metal oxide surface in air under ambient conditions is often covered by several to many monolayers of water, depending upon the relative humidity of ambient air. For example, gravimetric studies of water on $\alpha\text{-Al}_2\text{O}_3$ have shown that ~ 2 monolayers ($8,2 \text{ \AA}$) of water cover the surface at a relative humidity of 50%, whereas ~ 8 monolayers (32 \AA) are present at 80% relative humidity at 300 K ($27 \text{ }^\circ\text{C}$) (See Figure 13) [26].

Figure 13 shows elements of the Gouy-Chapman-Stern model, including specifically adsorbed anions and non-specifically adsorbed solvated cations. The metal oxide, or zero-plane, is defined by the location of surface sites which may be protonated or de-protonated. The inner Helmholtz plane, or β -plane, is defined by the centers of specifically adsorbed anions and cations. The outer Helmholtz plane, or d-plane, corresponds to the beginning of the diffuse layer of counter ions. Estimates of the dielectric constant, ϵ , of water are indicated for the first

and second water layers nearest the interface and for bulk water [26].

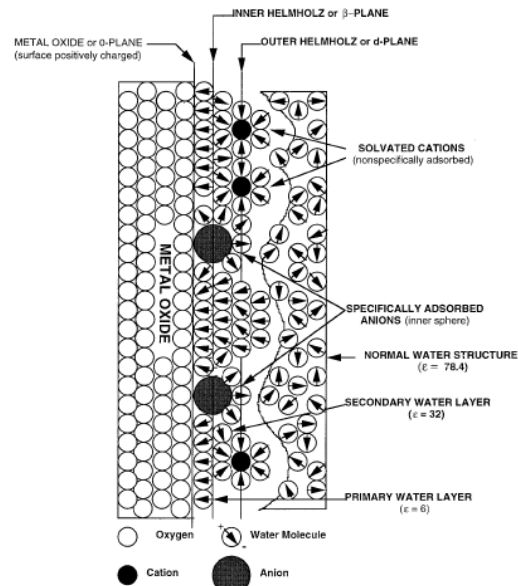


Figure 13: Schematic model of the electric double layer (EDL) at the metal oxide-aqueous solution interface [26].

Streamer Initiation at the Metal-Oxide-Water Interface:

Julliard, *et al*, (2000) [27] have shown that surface phenomena at electrodes play a major role in streamer inception. In this case the electrodes were covered with an oxide layer that affects the electrochemical structure of the metal-liquid interface. As the transport of charge carriers, from the electrodes to the fluid has to pass through the oxide layers, the electrical properties of the oxide-layers control the injected current in the initial phase of streamer inception [27]. Streamer inception modifies the structure of the surface layers and leads to a chemical reconstruction at the interface and in the liquid bulk [27].

In the case of aluminium (also brass, copper and steel electrodes), the passivation film developing at the metal surface consists of thick ($15 - 50 \text{ \AA}$; **Note:** $1 \text{ \AA} = 0,1 \text{ nm}$) coherent layers of inhomogeneous structure. The electrical properties of the oxide-layers are effectively representative of insulators with electron trap states with the electrode / fluid interface yielding semiconductor behaviour [27].

Julliard, *et al*, (2000) [27] presented a model for the behaviour of the metal-oxide-liquid interface based on percolation theory supported by experimental investigation of the surface structure of the electrode. Figure 14 shows the energy band model for the metal-oxide-fluid interface with and without an applied voltage.

By inserting the oxide-covered metal electrode into a liquid (or formation of a liquid layer on the aluminium conductor) causes formation of a double layer at the interface. In insulating liquid, the metal-side will carry space charge of positive polarity with ions of negative polarity attracted to the liquid side [27]. Thus, a double

layer structure is established with an inner Helmholtz plane at the oxide-metal interface and an outer Helmholtz plane at some distance away from the edge of the oxide-layer [27].

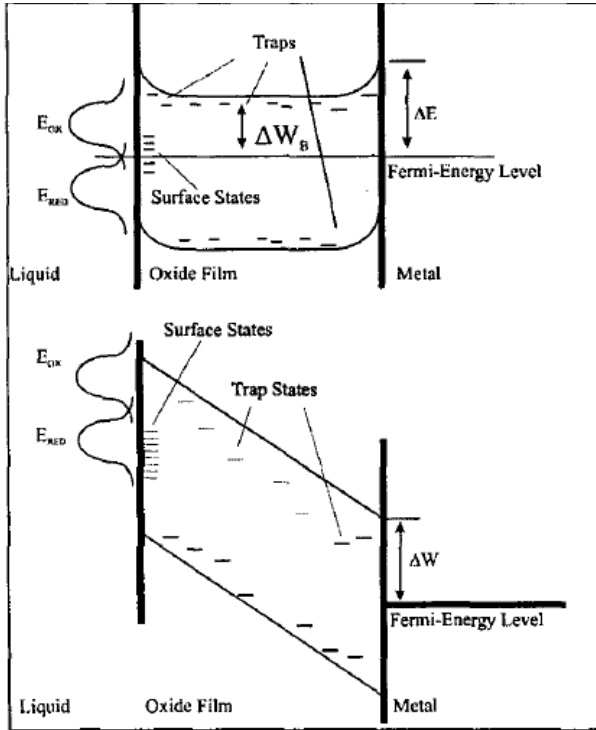


Figure 14: Energy band model for the metal-oxide-fluid interface with (bottom) and without (top) an applied voltage (From [27]).

The double layer structure affects the local order of the fluid in the vicinity of the electrode. Ions from the bulk liquid will be attracted and will establish a local order which extends into the liquid bulk. The local space charge induces clusters of liquid molecules in front of the electrode with the effect that the electrical properties change [27]. The local order of this double layer structure thus enhances the associated electron transport mechanisms as new electronic states are created through the interaction of liquid molecules with adsorbed ions in the double layer [27].

Electron Conduction through Oxide films: Electron tunnelling is typically associated with barriers less than 30 Å thick [27]. However, if there is a trapped charge state with an ideal energy level within the oxide layer, it could serve as a stepping stone for electron tunnelling advancing a trapped state to a free state in the liquid. Conduction resulting from this process will be weak [27].

In order to conduct current through the bands, the charge carrier must have sufficient energy to reach the conduction or valence band in order to cross the oxide layer without getting trapped. The oxide layer acts as an insulating film if the conduction band is significantly separated from the Fermi-Energy of the metal. Without any applied voltage to the conductor, the oxide layer

behaves as an insulator with anticipated behaviour of a back-to back-diode. This back-to-back diode blocks current flow from the conductor to the liquid [27].

With a voltage applied to the conductor and across the interface, electrons are likely to be injected into the oxide layer where they will be trapped due to the lower energies of trapped states. The trapped electrons will form a space charge that in turn will modify the electron structure of the oxide layer and with subsequent lowering of the trap depth [27].

With increasing voltage, trap controlled hopping may become possible and current flow (at rough edges or nicks) on the conductor is expected and will be localised at regions with high electric field gradient. In terms of percolation theory, the oxide layer itself is a prohibited region with the exception of localised areas where the field strength is excessively high [27]. Also with increasing voltage, more and more trap states will degenerate because of the lowering of the trap depth and the current flow mechanism shifts from trap controlled hopping to band conduction. At the same time, the metal-liquid interface shifts from an insulation state towards a conduction state [27].

A large number of charge carriers will be injected into the fluid. With the fluid behaving as an electrical insulator, the injected charge forms a space charge that lowers the electric field at the rough edges (nicks) on the conductor [27]. Should the space charge in the liquid exceed a critical value, the reverse process sets in with the metal-oxide-liquid interface finally reverting to an insulation state with back-to-back diode behaviour [27].

With high voltage applied and should the injected space charge be transported away from the conductor fairly quickly, then high current flow result with a non-reversible process setting in. In this case, the oxide layer will be damaged and part of the metal may be eroded. Following breakdown, the oxide layer establishes again as a result of reactive products, for example, free oxygen, Hydroxyl and Carbon-Radicals in the vicinity of the conductor [27].

Breakdown of Water: Water has been found to withstand electric fields up to 1 MV/cm for durations up to hundreds of nanoseconds but because of the longer residence time of ions on the conductor it is postulated by Schamiloglu, *et al*, (2004) that breakdown may be initiated [28].

Schamiloglu, *et al*, (2004) [28] argue that strong field enhancement at the liquid-metal interface, caused by changes in liquid polarizability, is an important universal mechanism that could be a source of electronic breakdown at high applied voltages. The presence of large electric fields at the liquid-metal interface should produce a realignment of the strongly polar water molecules due to electrostatic interactions [28]. Energy

minimization would then lead to the formation of an ordered molecular lattice over a few molecular monolayers of the interface. As is well known, dipolar ordering reduces the effective polarization [28]. This reduction should, therefore, work to further strengthen the electric field based on considerations of local continuity for the electric displacement vector and a potential positive feedback mechanism can thus be initiated near the electrodes under high-voltage stress [28].

Schamiloglu, *et al*, (2004) [28] further notes that phase transitions into a “solid water layer” close to electrodes have been reported at high electric fields and that collective experimental observations seem to suggest the following plausible scenario:

- Very high electric fields are capable of producing phase transitions and density variations in water. Since the fields are expected to be largest at electrodes and in the vicinity of the electrical double layer, tangible effects would be initiated and become observable at the contacts [28].
- The density and permittivity variations could lead to local opaque regions (due to refractive index variations), as have been reported in water breakdown experiments [28].
- The induced changes in dipole moments could produce strong ponderomotive forces [28]. In order to balance the ponderomotive forces, atomic displacements would then lead to internal stress and electrostrictive density variations. Pressure build-up is a natural consequence and could become manifested as a shock wave. Such shock waves have indeed been observed in high-voltage, water-filled systems [28].

In their contribution, (Schamiloglu, *et al*, (2004) analysed the electrical double layer at the electrode-water interface in high-voltage devices close to the breakdown point. They allowed for the inclusion of field-dependent permittivity and provided a self-consistent spatial distribution of the dipole structure, orientation, ionic concentrations and potentials. Dipole realignment effects, ion-ion correlation, finite-size effects, and other enhancements to the traditional Gouy-Chapman theory were all comprehensively included [28].

Their results showed that strong increases in the surface electric fields with concomitant lowering of the dielectric constant could lead to dramatic enhancements in Schottky injection at the contacts. This process could be a source for initiating electronic controlled breakdown and provide for carrier multiplication through impact ionization close to the metal surfaces [28]. Further analysis showed that high field regions with a sharp variation in permittivity can potentially be critical spots for instability initiation [28].

Movement of the Arc: Arroyo, *et al*, (1999) [29] have shown comparisons between theoretical results covering a wide range of particle sizes that demonstrated that the

Stern layer conductance always increases the magnitude of the low-frequency dielectric constant of suspensions, but its effect is less important the smaller the particle size and the larger the zeta potential for fixed ionic conditions in dispersion media [29].

Arroyo, *et al*, (1999) [29] further reported for electrokinetic phenomena, some discrepancies between theory and experiment can be explained by the existence of Stern layer surface conductance, that is, by using models in which the inner layer ions can undergo tangential transport under the action of external fields. This is more likely applicable for suspensions with large particles and / or high ionic strength [29].

The author is of the opinion that the effect described above by Arroyo, *et al*, (1999) plus the contribution of the electric field, tangential to the pole conductor (caused by the volt drop along the conductor), may be responsible for and may explain the movement of the arc along the line (the electric field is pointing in the direction of the conductor from the source to the load).

It is postulated by the author that the development of an electric double layer at the metal-oxide interface of the conductor under high humidity may enhance the electric field on the conductor surface, presenting a low pseudo-conductor-roughness-factor, acting as precursor to the electric breakdown of the air.

4.6 Space Charge - Power Line as Source

The contribution of AC power lines as anthropogenic sources of and to the development of space charge has been noted earlier in this paper. The effect of the space charge on the potential gradient downwind from the power lines with increasing wind speed, relative humidity and rainfall have been noted and warrant further investigation. The contribution of space charge from HVDC lines to anomalous flashovers is a topic of future study.

5. CONCLUDING REMARKS

Optimisation of air-insulation associated with power lines stems from maximisation of the dielectric withstand with respect to unwanted gas discharges. To prevent such discharges, both the electric field distribution and the critical failure mechanism must be known. In this paper, potential conditions that may influence the electric field distribution on and in the vicinity of the pole conductor that may initiate the failure mechanism and that may explain anomalous flashovers were covered.

Specific considerations were parted to the following aspects: the presence of an “Electrode Effect”, change in “Effective Permittivity” and the development of a “Maxwell Capacitor” below the pole conductors as well as the formation of a “Double Layer” on the pole

conductor. From these a new hypothesis is presented for future study. In particular, it is hypothesised that:

(1) Through terrestrial ionisation, an electrode effect may be presented underneath or in close proximity to an HVDC line that in turn, through an “elevated earth plane” (Electrode Effect), may enhance the electric field gradient on the pole conductors, particularly nearer to the mid-span position and that will act as a precursor to the electric breakdown of the air insulation at this location.

(2) Permittivity change introduced by a layer of fog may contribute to the development of a Maxwell capacitor between the pole conductor and the ground, with the fog (with effective permittivity higher than that of air) acting as one dielectric medium and the air acting as the second dielectric medium. The collation of space charge at the boundary between the two dielectrics drives the enhancement of the electric field gradient on the pole conductor up to a stage where the breakdown mechanism is initiated.

(3) The development of an electric double layer at the metal-oxide interface of the conductor, under conditions of high humidity, can enhance the electric field on the pole conductor surface, presenting a low pseudo-conductor-roughness-factor, that acts as precursor to the electric breakdown of the air.

(4) The electric field, tangential to the pole conductor (caused by the volt drop along the conductor), is responsible for and may explain the movement of the arc along the line where the electric field is pointing in the direction of the conductor from the source to the load.

Proper understanding how these aspects may contribute to possible flashovers will allow the establishment of design criteria for effective line operation. It is proposed that these hypotheses be studied further to ultimately arrive at specific design criteria that can be employed in the optimum performance of HVDC systems.

6. ACKNOWLEDGEMENT

This work was grant-funded by the Eskom Centre for High Voltage Engineering - Project No ECHV001 managed by the University of the Witwatersrand.

7. REFERENCES

[1] D W Miller, B D Rindall, O C Norris-Elye, “Anomalous Flashovers on the Nelson River HVDC Transmission Lines”, *Report 89-SP-166 presented to the Power System Planning and Operation Section*, Canadian Electrical Association, Toronto, Ontario, March 1989.

[2] R Wachal, “Unexplained Nelson River HVDC Flashovers”, *Manitoba HVDC Research Centre Journal*, Volume 11 Issue 4, Winter 2000.

[3] Personal e-mail correspondence with Mr Les Recksiedler, Senior Manager, Engineering and Business Development, Manitoba HVDC Research Centre, 17 Sep 2014.

[4] P H Pretorius, A C Britten, T Govender, K R Hubbard, N Mahatho, N Parus, “On the Electromagnetic Interference Associated with the Power Line Carrier System of the Cahora Bassa HVDC Line - A Hypothesis Based on Recent Investigations and Observations”, *Paper C4-111*, CIGRE Session, Paris, Aug 2012.

[5] P H Pretorius, P Goosen, G Bekker, R Vajeth, N Parus, T Govender, “Employment of Gold Mines in the Witwatersrand Area as Adjunct to the Establishment of a Deep Level HVDC Earth Electrode”, *Proceedings*, CIGRE Regional Conference, Somerset West, 7 - 11 Oct 2013.

[6] P S, Maruvada, *Corona in Transmission Systems - Theory, Design and Performance*, Eskom Power Series of Books, ISBN 978-0-620-49388-8, Crown Publications CC, Feb 2011.

[7] EPRI, *High Voltage Direct Current Handbook*, TR-104166, 1994.

[8] T Christen, H Böhme, A Pedersen, A Blaszczyk, “Streamer Line Modelling”, *Scientific Computing in Electrical Engineering*, B Michielsen and J R Poirier (Eds), *SCEE 2010*, Mathematics in Industry, 16, DOI 10.1007/978-3-642-22453-9__19, pp 173 - 181, 2012.

[9] J C Matthews, J P Ward, P A Keitch, D L Henshaw, “Corona Ion Induced Atmospheric Potential Gradient Perturbations Near High Voltage Power Lines”, *Atmospheric Environment*, 44, pp 5093 - 5100, 2010.

[10] ATSDR, Agency for Toxic Substances and Disease Registry, “Toxicological Profile for Radon”, Atlanta, GA: U.S. Department of Health and Human Services, Public Health Service. Toxicological Profile for Radon, May 2012, CAS#: 10043-92-2 and 14859-67-7 <http://www.atsdr.cdc.gov/toxpro/files/tp.asp?id=407&tid=71#bookmark16>, Last Accessed, 13 Sep 2014.

[11] K A Boyarchuk, A M Lomonosov, “Variability of the Earth’s Atmospheric Electric Field and Ion-Aerosols Kinetics in the Troposphere”, *Studia Geoph et Geod*, Vol 42, pp 197 - 210, 1998.

[12] W A Hoppel, “Theory of the Electrode Effect”, *Journal of Atmospheric and Terrestrial Physics*, Vol. 29, pp. 709-721, 1967.

[13] M N Kulkarni, “On the Modelling of Electrical Boundary Layer (Electrode Layer) and Derivation of Atmospheric Electrical Profiles, Eddy Diffusion Coefficient and Scales of Electrode Layer”, *J Earth Syst Sci*, Vol 119, No 1, pp 75 – 86, Feb 2010.

[14] E A Mareev, S Israelsson, E Knudsen, A V Kalinin, M M Novozhenov, “Studies of an Artificially Generated Electrode Effect at Ground Level”, *Ann Geophysicae*, Vol 14, pp 1095 - 1101, 1996.

[15] R B Bent, W C A Hutchinson, “Electric Space Charge Measurements and the Electrode Effect

- within the Height of a 21 m Mast”, *Journal of Atmospheric and Terrestrial Physics*, Vol 28, pp.53 to 73, 1966.
- [16] Radon Potential Map of Canada, <http://www.radoncontrols.com/>, Last Accessed 14 Sep 2014.
- [17] <http://arthurzbygniew.blogspot.com/2011/04/mean-atmospheric-radon-world-map.html>, Last Accessed, 13 Sep 2014.
- [18] <http://en.wikipedia.org/wiki/Mist>, Last Accessed 13 Sep 2014.
- [19] W Frost, F G Collins, D Koepf, “Charged Particle Concepts for Fog Dispersion”, *NASA Contractor Report 3440*, Contract NASS-33541, June 1981.
- [20] EPRI, “High Voltage Direct Current (HVDC) Transmission Reference Book”, *Report 1024318*, Dec 2012.
- [21] J A Chalmers, “Negative Electric Fields in Mist and Fog”, *Journal of Atmospheric and Terrestrial Physics*, Vol 2, pp 155 - 159, 1952.
- [22] G Kristensson, S Rikte, A Sihvola, “Mixing Formulas in Time Domain”, Department of Electrosience, Electromagnetic Theory, Lund Institute of Technology, Sweden, 25 February 1997.
- [23] A Sihvola, “Mixing Models for Heterogeneous and Granular Media”, <ftp://ftp.icess.ucsb.edu/pub/users/shi/RTbook/chapter5.5.pdf>, Last Accessed 14 Sep 2014.
- [24] Z Ulanowski, J Bailey, P W Lucas, J H Hough, E Hirst, “Alignment of Atmospheric Mineral Dust Due to Electric Field”, *Atmos. Chem. Phys*, 7, 6161 – 6173, 2007.
- [25] F H Kreuger, *Industrial High DC Voltage - Fields - Breakdown - Tests*, Delft University Press, ISBN 978-90-407-110-7 1995.
- [26] G E Brown, V E Henrich, W H Casey, D L Clark, C Eggleston, A Felmy, D W Goodman, G Maciel, M I McCarthy, K H Nealsen, D A Sverjensky M F Toney, J M Zachara, “Metal Oxide Surfaces and Their Interactions with Aqueous Solutions and Microbial Organisms”, *Chem Rev*, Vol 99, pp 77 - 174, (Page 82), 1999.
- [27] Y Julliard, K Kist, R Badent, A J Schwab, “Behaviour of the Metal-Oxide-Fluid-Interface”, *Annual Report*, Volume 2, pp 780 - 783, ISBN 0-7803-6413-9, Conference on Electrical Insulation and Dielectric Phenomena, 15-18 Oct. 2000.
- [28] E Schamiloglu, R P Joshi, J Qian, K H Schoenbach, “Microscopic Analysis for Water Stressed by High Electric Fields in the Pre-breakdown Regime”, *Journal of Applied Physics*, Vol 96, No 7, 1 Oct 2004.
- [29] F J Arroyo, F Carrique, T Bellini, A V Delgado, “Dielectric Dispersion of Colloidal Suspensions in the Presence of Stern Layer Conductance: Particle Size Effects”, *Journal of Colloid and Interface Science*, 210, pp 194 – 199, 1999.
- [30] K Laing, “Bipole I & II Anomalous Flashovers”, Correspondence from Manitoba HVDC Centre, 2014.

POWER SYSTEM TRANSIENT STABILITY ANALYSIS AND STABILITY IMPROVEMENT OF A LARGE MULTI-MACHINE HVAC NETWORK USING HVDC TECHNOLOGIES

K.N.I. Mbangula* and I.E. Davidson**

* *Electrical, Electronic & Computer Engineering Discipline, School of Engineering, Westville Campus, University of KwaZulu-Natal, Durban 4000, South Africa E-mail: 214584439@stu.ukzn.ac.za*

** *Eskom Centre of Excellence in HVDC Engineering, University of KwaZulu-Natal, Durban 4041, South Africa E-mail: Davidson@ukzn.ac.za*

Abstract: The last century has demonstrated that every facet of human development is woven around a sound and stable energy supply regime. Optimum operation of the power system depends largely on the operator's ability to provide reliable, stable and uninterrupted services to customers. Power system stability has been recognised as an important problem for secure operation. This paper presents a detailed analysis of the transient stability of a large HVAC power system. Expert system concepts were used to develop an appropriate research methodology and procedure for analysing transient stability of a multi-machine HVAC power system. Transient stability analysis of the generators in the power system was carried out by analysing the behaviour of the important variables of interest, which are used to determine the stability level of a generator in a large HVAC system. The stability level of the weakest generator in the network was analysed by determining the critical fault clearing time (CFCT) for the most severe fault in the network. It was found that the maximum time at which the most severe fault in the system should be cleared for generator NE_G8 to remain stable was 0.38 seconds. The objective of this investigation is to determine the impact of HVDC links on system stability, by comparing the critical fault clearing times of two system operational scenarios, namely: a network without HVDC links, and a network with HVDC links imbedded.

Keywords: Power system stability, Expert systems concepts, HVAC, HVDC.

1. INTRODUCTION

Successful operation of the power system depends largely on the operator's ability to provide reliable and uninterrupted services to customers. Ideally, the reliability of the power system implies that the loads must be supplied at constant voltage and frequency at all times. The first requirement of reliable service is to keep the synchronous generators running in parallel and within adequate capacity to meet the load demand with minimum interruptions over an extended period of time. If at any time a generator loses synchronism with the rest of the system, significant voltage and current fluctuations may occur, therefore lowering the standard of electrical service and affecting the power system reliability [1]. Power system stability has been recognised as an important problem for secure power system operation. Security of a power system refers to the degrees of risk in its ability to survive imminent disturbances (contingencies) without interruption of customer service [2]. Reliability is the overall objective in power system design and operation. To be reliable, the system must be secure most of the time. To be secure, the system must be stable but must also be secure against other contingencies that would not be classified as stability problems e.g., the fall of a transmission tower due to ice loading or sabotage. It is therefore important to ensure that the electric power system is stable at all times in order to allow for maximum power flow and the generation of voltage at system frequency and at the same phase angle for all the machines [3]. Transient stability analysis and assessment of the power systems involves a study of non-linear differential

equations. The solution obtained of the non-linear swing equation allows for the power systems engineer to determine the stability or instability of the power system [1]. Various methods and research procedures have been developed and used to determine the stability of a power system. The two main methods used for power system transient stability assessment are the traditional time-domain numerical integration method and the direct or energy function methods.

In this paper, the time-domain approach and expert system procedure has been used to analyse the transient stability of a large High Voltage Alternating Current (HVAC) system. The analysis is carried out on a 30 machine, 22-bus test system. The analysis is carried out to determine the critical fault clearing time for the most severe fault in the system. After determining the critical fault clearing time, further analysis is done to determine the effects High Voltage Direct Current (HVDC) links may have on transient stability of the network. The effects of HVDC links is analysed by doing a comparative analysis on the critical fault clearing times for a network without new HVDC and when new HVDC links are imbedded in the system.

2. LITERATURE REVIEW

2.1 Power system transient stability

The stability of an electric network can be classified into three main categories, namely: Steady state, small-disturbance (dynamic) and large disturbance (transient)

stability. Transient stability refers to the response of synchronous machines to large disturbances [4]. Large-disturbance and small-disturbance stability of a power system may further be classified as: rotor angle stability, frequency stability or voltage stability. The synchronous machine rotor angle stability is of interest in this study.

2.1.1 The inertia constant and swing equation

The angular momentum and inertia constant play an important role in determining the transient stability of a synchronous machine. The per-unit inertia constant H in MJ/MVA is defined as the kinetic energy stored in the rotating parts of the machine at synchronous speed per-unit MVA rating of the machine [5]. Under steady state conditions the corresponding input power (P_i) of the input torque provided by the prime mover at the generator shaft is equal to the output electromagnetic power (P_e), with the armature resistance neglected, therefore there is no net acceleration torque. If a departure from steady state occurs, such as a change in load or a major fault, the power in is no longer equal to the power out. Thus an acceleration power P_a comes into play. If P_a is the corresponding acceleration power, then

$$\frac{H}{180f} \frac{d^2\delta}{dt^2} = P_i - P_e = P_a \quad (1)$$

where: H = the inertia constant; f = the nominal frequency; δ = rotor angle with reference to synchronous reference; P_i = the input mechanical power; P_e = the output electromagnetic power

To investigate the stability of the machine or the stability of a particular power system after a disturbance, it is necessary to solve the dynamic equation describing the angle δ immediately following an imbalance or disturbance to the system [6]. A plot of $\delta(t)$ is known as the swing curve, a study of which often shows if the machine will remain in synchronism after a disturbance [5]. Time-domain numerical integration methods are used to solve the swing equation.

2.1.2 Power-angle characteristics and equal area criteria

During steady state, the per-phase power delivered by a salient-pole rotor synchronous machine as a function of the power angle δ is equal to the input internal mechanical power and is given by:

$$P_D = P_e = \frac{|E_g||V_t|}{X_d} \sin \delta + \frac{|V_t|^2}{2} \left(\frac{1}{X_q} + \frac{1}{X_d} \right) \sin 2\delta \quad \text{W/Phase} \quad (2)$$

where: P_D = the output power; P_e = the internal power developed; E_g = the internal voltage of the generator; V_t = the terminal voltage on load

X_d = direct axis reactance; X_q = quadrature axis reactance, and δ = the electrical power angle, which is the angle by which E_g leads V_t

Equation (2) is said to be a representation of the power-angle characteristics of a synchronous machine and it shows that the internal power developed by a synchronous machine is proportional to $\sin \delta$. From equation (2) it can be seen that the resulting power developed by a salient pole rotor synchronous machine is a sum of two power components. This is the power due to field excitation (the first term) and the power due to saliency (the second term). When $X_d = X_q$, the machine has no saliency and the second term reduces to zero.

2.1.3 System stability improvement using HVDC

Studies have been carried out on the performance enhancement of large AC grids using HVDC technology by previous researchers. Various power system models were used to carry out their investigations. For example, in [7] a study was done on the influence of Line Commutated Converter (LCC)-HVDC and Voltage Source Converter (VSC)-HVDC links on transient voltage stability of a Hybrid Multi-in feed HVDC power system (HMI-HVDC). The authors proposed a new voltage reference adjusting method that is used for transient voltage stability improvement. This method uses an improved reactive power control model at the grid side of the VSC. The VSC is then used as a source of reactive power compensation in order to keep the bus voltage at rated value after transient conditions. In [8], an investigation was carried out to demonstrate the stabilization of large power systems using VSC-HVDC links. Based on global power system measurements, a model predictive control (MPC) scheme manipulates the power injections of the HVDC links to damp oscillations in the ac system. The MPC grid controller explicitly accounts for constraints and the expected future behaviour of the system. Wide Area Measurement Systems (WAMS) are used to add a supervisory control layer to the system. This supervisory layer enables static optimization of the power system's load flow but it can also be used to enhance system stability during transients. It was found that in order to maintain stability, the ac power injections at the VSC-HVDC link's terminals have to be carefully manipulated.

Further research was carried out in [9], in which they proposed a control mechanism to augment the power system's rotor angle stability whereby P and PI controllers are used to alter power flow settings in the HVDC link by rapidly ramping down DC power injected into the AC system during transient disturbance to reduce the generation/load imbalance of the ac system on both sides of the converter. It was found that in some situations, it may be necessary to ramp up the dc power to assist system stability by taking advantage of the short-term over load capability of the HVDC system. Using a generic case study of a simplified model of South Africa's power system, [10]

presents an investigation into the upgrading of the existing HVAC power transmission circuits for higher power transfers using HVDC technologies. The proposed method uses one phase of the AC conventional line as the positive pole, another phase as the negative pole and the remaining third phase to be periodically swapped between positive and negative poles; yielding almost 2.5 times the power transfer capability of the conventional HVAC line. From this research it was found that for HVAC lines where the thermal capacity is close to surge impedance loading, no additional benefits would arise. Similarly for those lines that have higher capabilities for surge impedance loading but of small bundle configuration, the employment of Flexible AC Systems (FACTS) technology would be more cost effective. For those circuits having greater conductor bundle configurations, then the gap between thermal capacity and surge impedance loading is the largest and in these cases, the upgrade to HVAC to HVDC would have the most benefits.

2.1.4 Expert system concepts for stability analysis

The first step in power system stability studies is to make a mathematical model of the system during the transient. The elements to be included in the model are those effecting the acceleration or deceleration of the machine rotors. The complexity of the model usually depends on the type of transient and the power system being investigated. Generally, the components of the power system that influence the mechanical and electrical torques of the machine should be included in the model [1]. These components are:

- The network before, during and after the transient disturbance.
- The loads and their characteristics.
- The parameters of the synchronous machines.
- The excitation system of the synchronous machine.
- The mechanical turbine and speed governor.
- Other supplementary controls, such as tie-line controls, deemed necessary in the mathematical description of the system under investigation.
- Other important components of the power plant that influence the mechanical torque of the machine.

The work described in [11] was to develop expert system concepts for use with power system stability studies, and provide proof of the concepts in a computer prototype program. Expert systems are systems that requires a knowledge base, an inference engine, and a user friendly interface. The knowledge base contains the expertise to be applied to a particular problem. Akimoto [11] found that transient stability studies is suitable for the application of concept of expert systems for the following reasons. Expertise is required in several areas of transient stability such as:

- Selection of appropriate test cases and data sets to adequately test the performance of the system.
- Validation of the models and data to be used for the analysis
- Determination of system stability, will the system return to an equilibrium operating point?
- Determination of limits for pre-disturbance power transfer level
- Identification of the cause of particular system behaviour

According to [11], an analysis of the power systems transient stability problem solving process shows that it is an iterative design procedure, some portions of this procedure resemble a closed loop feedback control system. The main activities of power systems stability analysis and assessments are:

- Study organization,
- Time simulation,
- Output analysis,
- Problem cause identification,
- Specification of new test cases, and
- Remedial measures

3. NETWORK MODEL

The test network was modelled using the DIgSILENT PowerFactory software. The network consists of 30 machines and 31 bus bars, and it is made up of four main areas (zones), namely; area North-West, North East, South-West and South-East. Figure 4.1 depicts the over view of the power system under study. It can be seen that the four areas are interconnected by a number of AC transmission lines (tie lines), and there is a two-pole HVDC link which supplies power to an external area. The HVDC link is modelled with static generator elements. Areas South-West, North-West and North-East are closely interconnected by short lines, whereas area South-East is loosely connected to the rest of the power system with a very long tie transmission line. The area power interchange is controlled by means of a power controller which is named, Power Exchange Controller South-East.

3.1 Research procedure

The main steps of the procedure are as follows:

- Determine the variables of interest.
- Carry out system steady state analysis by analysing the network pre-fault conditions in order to determine the strongest and weakest machines in the network
- Determine the most severe system fault
- Develop a critical case list
- Carry out time-domain simulations for transient state analysis of the network
- Determine critical fault clearing times
- Determine the machine stability level

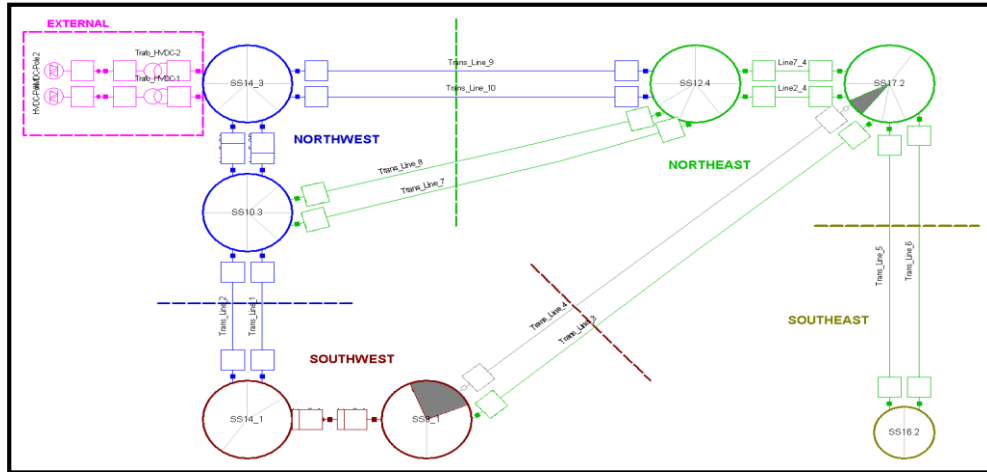


Figure 3.1: Multi-machine test network

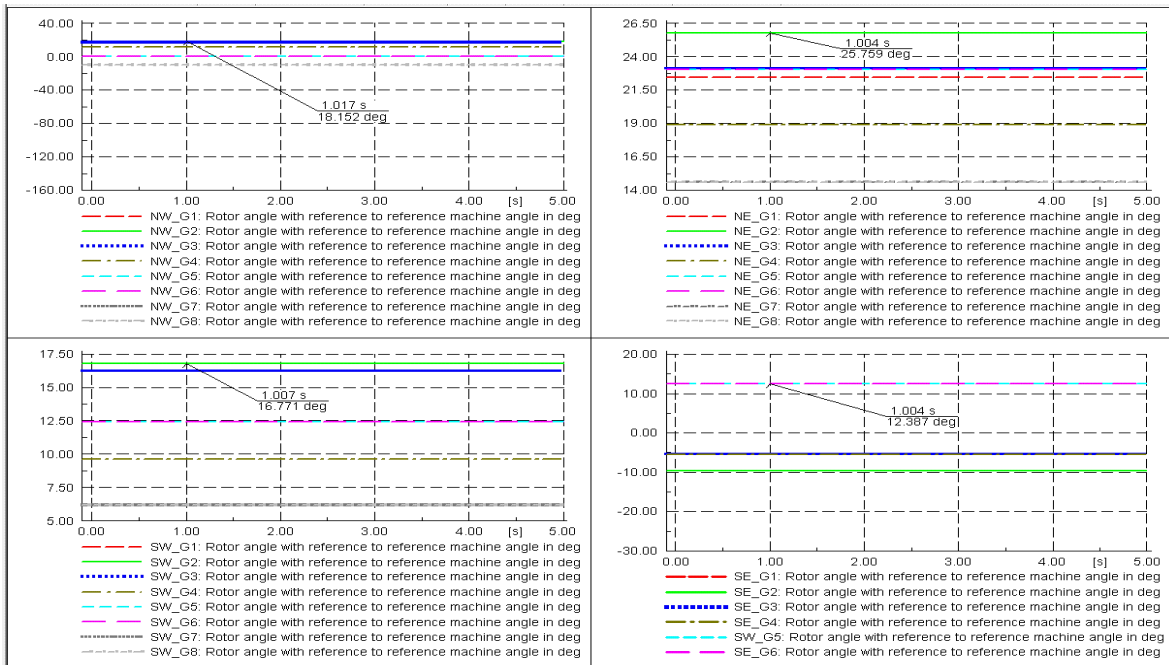


Figure 4.1: Machine rotor Angles with reference to the reference machine angle in degrees

Figure 4.1 shows the simulation results of the rotor angles of all the machines in the network.

4. SIMULATION RESULTS

4.1 Steady state results

In order to get a true sense of system transient stability, all the machine Automatic Voltage regulators (AVRs) and Power System stabilizers (PSS) were taken out of service. Generator NW_G6 was found to have the highest fault level. It was therefore set as the reference machine of the power system. The following result variables of interest have been defined for all the machines in the power system:

- Generator rotor angle with reference to reference machine angle, in degrees, c:firel
- Generator speed in p.u., s:xspeed
- Generator active power in megawatts, s:P1

Table 4.1: Critical case list

Pre-fault System Conditions	
Generator Controls	AVR and PSS neglected
System Loading	Full load
System Generation	All generators in service
Power Compensation	No reactive power compensation
Lines out of Service	Line_1, Line_4 and Line_10
Load Models	Voltage dependent
Simulated Fault Condition	
Fault Type	Solid three-phase short circuit
Fault Duration	100 milliseconds
Fault Location	End (99%) of line 3_4
Fault Impedance	0 ohms

4.2 Transient state results

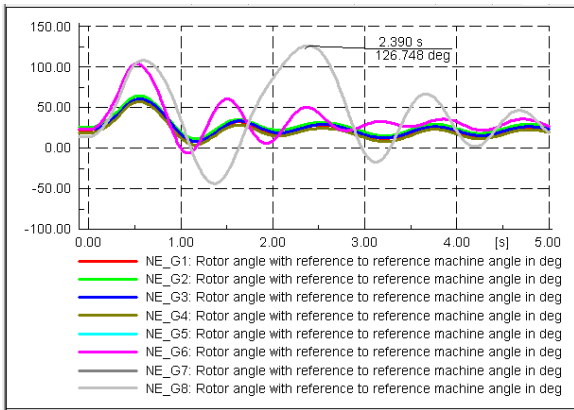


Figure 4.2: NE generator rotor angles in degrees

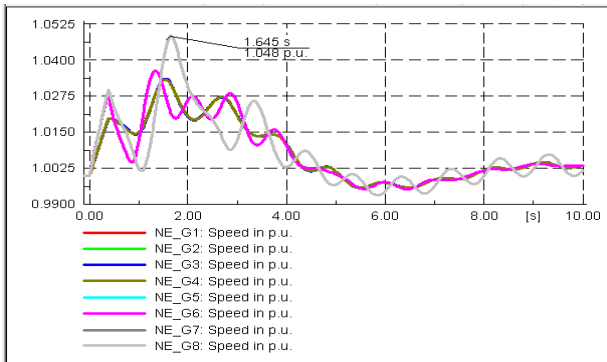


Figure 4.3: NE generator rotor speed in p.u.

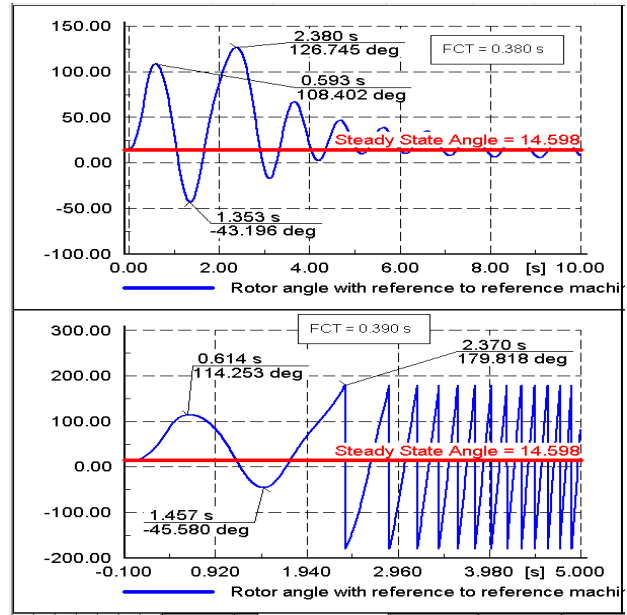


Figure 4.4: NE_G8 rotor angle in degrees

4.3 Discussion

4.3.1 Steady state results

Figure 4.1 illustrates the steady state simulation results of the rotor angle with reference to the machine angle, for all the machines in all the four zones of the power system. North-East have the highest rotor angle values. This is an indication that the generators in zone north east are the least stable in the power system. A transient state analysis was performed to determine the weakest generator.

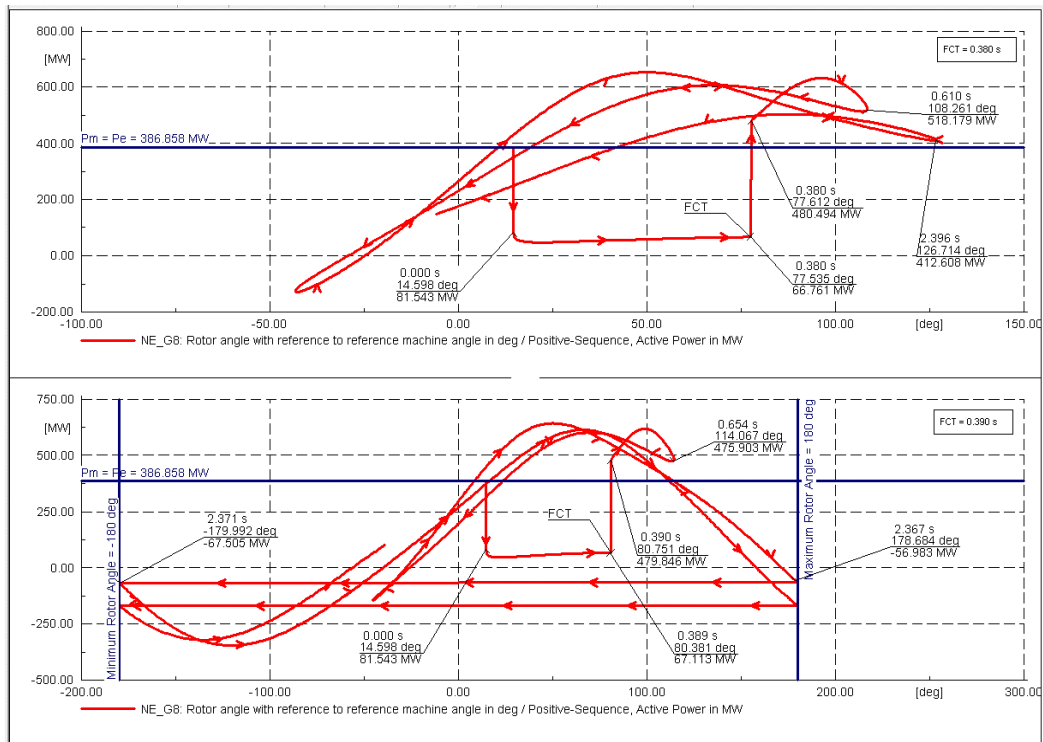


Figure 4.5: Power-angle characteristics of NE_G8

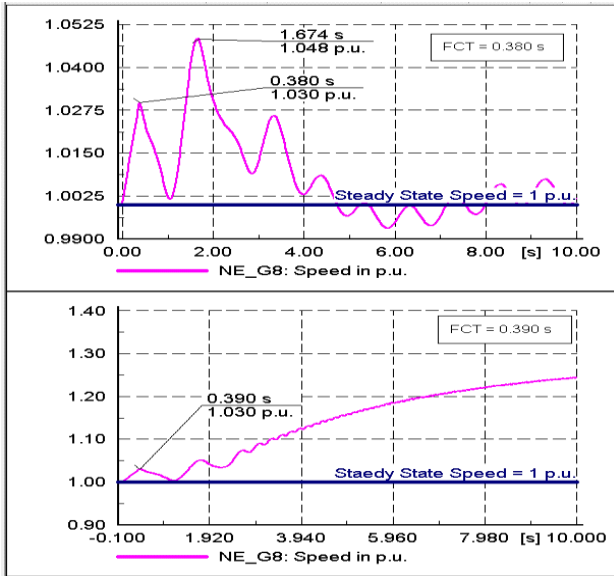


Figure 4.6: NE_G8 Speed in p.u.

4.3.2 Transient state results

Figure 4.2 shows the rotor angle simulation results for the machines in zone north east, when a three phase fault is simulated at the end of transmission line 3_4. NE_G8 has the highest rotor angle swing of 126.748 degrees. It can also be seen from figure 4.3 that, compared to the other machines in zone north east, the rotor speed of NE_G8 reaches the highest value of 1.048 p.u.. It was therefore concluded that NE_G8 is the weakest generator in area north-east. A detailed analysis was then carried to determine the stability level of NE_G8 by determining the maximum time at which the three-phase fault on line 3_4 can be cleared such that NE_G8 does not lose synchronism with the rest of the generators in the system (critical fault clearing time). Figures 4.4 - 4.6 present a comparative analysis of the behaviour of rotor angle, speed and the power angle characteristics of NE_G8 when the three phase fault line is cleared at 0.38 seconds and when it is cleared at 0.39 seconds. From figure 4.4 it can be seen that when the fault is cleared at 380 ms, the rotor angle oscillation amplitudes decrease with an increase in time and it eventually returns to its steady state value. It can also be seen that when the fault is cleared at 390 ms, the rotor angle runs off, it continues to oscillate between the peak values of 180 degrees and -180 degrees. This is an indication that the machine has lost synchronism due to pole slip. The power-angle characteristics are presented in figure 4.5 and based on the equal area criteria, the critical fault clearing time was determined.

5. CONCLUSIONS

NE_G8 was found to be the least stable machine in the network, so the stability level of the entire network under investigation was based on the stability of NE_G8. From the analysis done in section 4, it can be concluded that the maximum short circuit duration when NE_G8 remains in synchronism and no pole slipping occurs is 380 ms, which is the critical fault clearing time. The South African Grid

Code, The Network Code, Version 7.0 [12] states that, fault clearing times, including breaker operation time, shall not exceed 120 ms plus an additional 30 ms for DC offset decay. It can therefore be concluded that the system under investigation does not meet the fault clearing time requirements as stipulated in the grid code. This was expected because the network was considered to be a weak network.

6. REFERENCES

- [1] P. M. Anderson and A. A. Fouad: *Power system stability and control*, John Wiley & Sons Inc., Hoboken, chapter 1&2, pp. 3-48, 2003.
- [2] P. Kundur, J. Perseba, V. Ajjarapu, G. Andersson, A. Bose, C. Canizares, N. Hatziargyriou, D. Hill, A. Stankovic, C. Taylor, T. Van Cusem and V. Vittal: "Definition and classification of power system stability", *IEEE Transaction on Power Systems*, vol. 19, no. 3, pp. 1387-1401, August 2004.
- [3] C. A. Gross: *Power systems analysis*, John Wiley & Sons, Inc., London, second edition, 1986.
- [4] P. Kundur: *Power system stability and control*, McGraw-Hill Inc., New York, chapter 13, pp. 827-954, 1994.
- [5] S. A. Nasar and F. C. Trutt: *Electric power systems*, CRC Press LLC, Florida, chapter 6, pp. 169-196, 1999.
- [6] M. E. El-Hawary: *Electrical energy systems*, CRC Press LLC, Florida, chapter 8, pp. 326-333, 2000.
- [7] M. C. Nguyen and Z. A. Styczynski: "Improvement of stability assessment of VSC-HVDC transmission systems", *Proceedings: Critical Infrastructure (CRIS), 2010 5th International Conference*, Beijing, pp. 1-7, September 2010.
- [8] A. Fuchs, M. Imhof, T. Demiray and M. Morari: "Stabilization of large power systems using VSC_HVDC and model predictive control", *IEEE Transactions on Power Delivery*, vol. 29, no. 1, pp. 480-488, February 2014.
- [9] G. M. Haung and V. krishnaswamy: "HVDC controls for power systems stability", *Proceedings: Power Engineering Society Summer Meeting, 2002 IEEE*, pp. 597-602, Chicago, July 2002.
- [10] P. Naidoo, D. Muftic and N. Ijumba: "Investigations into the upgrading of the existing HVAC power transmission circuits for higher power transmission using HVDC technology", *Proceedings: Power Engineering Society Inaugural Conference and Exposition in Africa 2005 IEEE*, Durban, pp. 139-142, July 2005.
- [11] Y. Akimoto, H. Tanaka, J. Yoshizawa, D. B. Klapper, W. W. Price and K. A. Wirgau: "Transient stability expert system", *IEEE Transactions on Power Systems*, vol. 4, no. 1, pp. 312-320, February 1989.
- [12] "South African Grid Code," Johannesburg, 2008.

SOUTH AFRICAN LOAD MODELS FOR RESIDENTIAL ENERGY CONSUMPTION USING A BOTTOM-UP MODELLING TOOL

K.D Mutamba, M.T Samanga and K.J. Nixon *

* School of Electrical and Information Engineering, University of the Witwatersrand, Private Bag 3, 2050, Johannesburg, South Africa. E-mail: kd.mutamba@hotmail.com, malvinsamanga@gmail.com and ken.nixon@wits.ac.za

Abstract: Domestic energy usage patterns are highly coupled to occupant activities. This paper presents on the modelling of loads for residential energy consumption using a bottom-up modelling tool called Suricatta. The real and reactive power of 10 domestic appliances was measured in order to model the loads. The power drawn by each of these appliances was modelled using quadratic polynomial equations with a maximum error of 1.6% and an average deviation of 0.67% from the ideal curves of fit. Statistical data was obtained for use in the modelling of the appliance usage activity patterns and household active occupancy. A good correlation exists between behavioural simulations of energy use and actual data from an off-grid community in South Africa. An increase in the demand for apparent power during peak hours caused an increase in current flow and a decrease in the supply voltage on the network. Shifting of appliance use and turning off of appliances are viable Demand Side Management(DSM) strategies to prevent large supply voltage drops during peak hours.

Key words: load modelling, Suricatta, social behaviour.

1. INTRODUCTION

Suricatta is a Java application used to model and simulate an electrical distribution network in order to monitor the impact of human social behaviour on energy losses and voltage changes on the network [1, 2]. It is a bottom-up modelling tool which models how the power drawn by domestic appliances varies with the voltage supplied. It is still under development and was initially made to cater for United Kingdom appliances. Knowledge of how appliances operate at lower voltages is key to understanding voltage optimisation techniques to effectively reduce electricity usage. The monitoring of energy consumption by household appliances using software models is a cheap and effective way of acquiring information to help plan future power station construction, distribution network sizing and DSM schemes based on the energy usage forecasts. Appliance load models also form a basis in the research for smart appliance design which is key to understanding DSM strategies [3]. This helps create better customer service and enhances service efficiency and reliability.

This paper presents the development of South African load models for Suricatta. It takes into account the operation of appliances at different voltages. The effects of social behaviour on the demand of energy in homes is also explored through establishment of appliance usage patterns based on survey data previously collected from Khayelitsha and Devland [4, 5].

2. MODELLING TOOL ARCHITECTURE

The modelling tool requires two inputs: survey data and the power drawn by appliances. Figure 1 shows the system architecture with the grey boxes indicating the required inputs to suit typical South African loads. The survey data

is used to determine the probability of owning an appliance and the activity patterns based on a service model and an occupancy model which model the random nature of human behaviour.

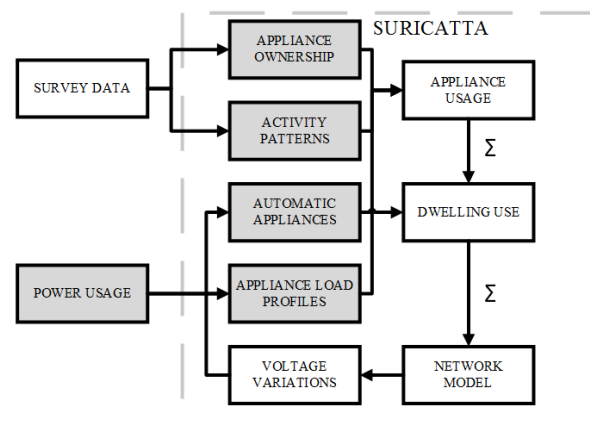


Figure 1: Suricatta design illustration showing the inputs needed for simulation and the outputs from the simulations.

The power drawn by each appliance is used to model the loads. This is dependent on the current and voltage levels on the network. The current and voltage demand on the network is attributed to the appliance usage in each dwelling in the community.

3. APPLIANCE OWNERSHIP

Statistical information was obtained from an off-grid community in South Africa which gave information about the appliances present in a particular household and also the number of rooms, adults and children present [6]. Each household had an average of four rooms which was

used as a basis to assume that four light bulbs exist per household given that each room had a functional light bulb (incandescent or compact fluorescent).

The appliance penetration indicates the average number of a specific appliance owned per household in a given household sample [7]. Equation 1 was used to calculate the appliance penetration (P) values shown in Table 1.

$$P = \frac{\text{number of devices in neighborhood}}{\text{total number of households in neighborhood}} \quad (1)$$

Table 1: Average number of appliances per household in the off-grid community.

Appliance	Appliance penetration
Television	0.79
Cellphone charger	2.00
Incandescent Light	1.94
CFL	1.94
Laptop	0.06
Kettle	0.35
Stove	0.71
DVD player	0.41
Fridge	0.74
Iron	0.38

4. MEASUREMENTS

A total of 10 appliances were acquired and measured based on the appliance ownership survey data. The voltage was varied from 170 V to 230 V in 10 V intervals for three repeat cycles. The current for a particular supply voltage was deemed correct provided that the calculated RMS current for the repeat cycles was within a 5% standard deviation.

The current drawn and the corresponding voltage were saved as Comma-Separated Value (CSV) files for analysis in MATLAB. The data collected from the measurements was stored in an electronic repository for future studies. The compact fluorescent had the highest harmonic content with the highest frequency at 6 kHz hence a sampling frequency of 20 kHz was chosen in accordance with the Nyquist sampling theorem. Figure 2 shows the setup of the measurement equipment.

5. DATA ANALYSIS

In order to analyse the data, scripts were made in MATLAB [8]. Firstly the current and voltage measurements were analysed at different harmonics in order to calculate the real and reactive power. The separation into harmonics was done through FFT filtering. The power factor was calculated from the phase differences of the voltage and current measurements. After calculating

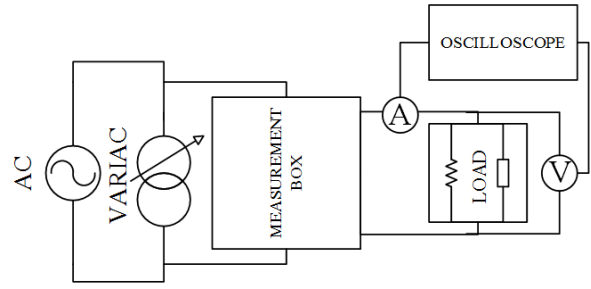


Figure 2: Measurements equipment setup used to measure the power drawn by appliances while varying the voltage.

the power values for each of the voltage levels, the three readings were averaged out thus giving the real and reactive power for the range 170 V to 230 V.

After averaging the values, lines of best fit were drawn through the collected points. A linear least squares fit was used in the approximation with polynomials of the second order. The coefficients of this line were then treated as inputs into Suricatta. Two sets of coefficients were calculated for the ranges 170 V to 230 V and also 200 V to 230 V. The worst error of fit was 1.6% for the incandescent light bulb in the range 200 V-230 V.

The equations used in calculating the real and reactive power for the appliances are as follows:

$$P = \sum_{n=1}^k V_n I_n \cos(\alpha_n) \quad (2)$$

$$Q = \sum_{n=1}^k V_n I_n \sin(\alpha_n) \quad (3)$$

$$S = V_{rms} I_{rms} \quad (4)$$

Where:

- V_n = Rms voltage of the n^{th} harmonic
- I_n = Rms current of the n^{th} harmonic
- α_n = Phase angle between the voltage and current
- S = Apparent power

The loads measured were split between those with harmonic content and those without. The non-harmonic loads noted were: iron, stove and incandescent light bulb. Those with harmonic content were: CFL, TV, DVD, kettle, fan, cellphone charger, laptop and fridge. The results for the kettle were an anomaly since a kettle should only contain a resistive heating element and therefore should produce any harmonics. Figure 3 shows the harmonic content of the TV measured at 230 V. It shows that the power drawn by the TV is affected mainly by the fundamental and third harmonic. The introduction of harmonics other than the fundamental can lead to undesirable effects such as increased heating in the TV.

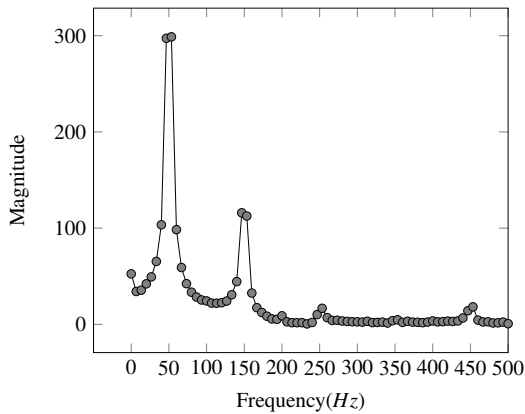


Figure 3: Harmonic content for a TV measured at 230 V.

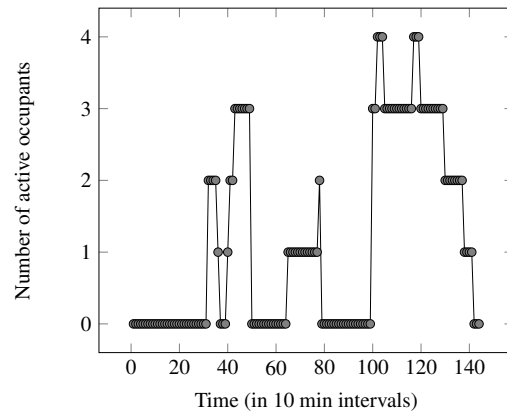


Figure 4: Active occupancy simulation output for a four person household.

6. HUMAN BEHAVIOUR

Some factors affecting human behaviour include income, poverty rate, inflation rate, economic stability, political stability, environmental quality, available appliances and personal unique habits. The modelling of human behaviour is thus complicated mainly because of the randomness in day-day activities attributed to the above mentioned factors.

6.1 Occupancy Model

The aim of the model is to represent the stochastic nature of human behaviour. It provides data on the number of active occupants as a variable over a day. Electricity consumption is highly coupled to the occupants' activities; thus taking into account the likelihood of using an appliance is of paramount importance within the Suricatta design. A good example is the household lighting in which knowledge of the number of active occupants helps to model the sharing of energy use since lighting is shared and not necessarily for individual use [9].

No time of use data was available for South Africa hence no correlation could be established between active occupancy and appliance usage. The already existing United Kingdom occupancy data within Suricatta was hence re-modelled such that the number of active occupants at a particular time was correlated to the energy demand profile, that is, minimal activity at night and peak activity in the morning, afternoon and in the evening. The established correlation can be seen from comparison between the randomly generated occupancy output for a four person household and a typical off-grid community load profile as shown in Figure 4 and Figure 5 respectively.

6.2 Service Model

The service model is used to refine the timing of occupancy activities together with the occupancy model [9]. An activity profile was assigned to each appliance such that the probability of an appliance being used throughout the

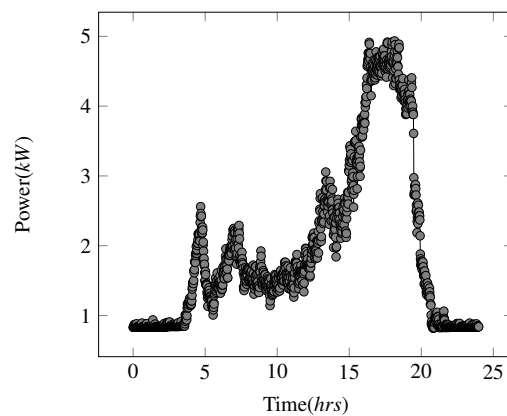


Figure 5: Typical load profile for an off-grid community in South Africa.

day was accounted for thus ensuring that appliances were activated at the expected times.

Time of use: A worst case approach was taken in which all appliances are used in a day. The following factors were used to determine the time of use: the frequency of appliance use in a day, the average number of hours that an appliance is used in a day and the typical times an appliance is used.

Frequency of use and average time of use The average hours of use and the frequency of use of an appliance per day were obtained from statistical data for Devland and Khayelisha respectively. This is tabulated in Table 2 [4]. Devland and Khayelisha were used as they have similar human behavioural characteristics to the off-grid community. The appliance ownership level, average income level and average household members are similar hence human behaviour in relation to appliance usage is expected to be the same.

Times of appliance usage The typical times that an appliance is used was deduced based on the load profile shown in Figure 5. Household loads are highly coupled

Table 2: Frequency of use of appliances and average hours of use per day for an off-grid community.

Appliance	Average hours of use/day	Frequency of use/day
Stove	2.5	4
Kettle	0.4	4
TV	3.0	2
Cellphone Charger	1.0	1
Laptop	2.0	1
DVD player	3.0	2
Iron	0.4	2

with the time of day hence the day was divided into two different periods.

On-peak : 4 am to 8 am and 12 pm to 8 pm
 Off-peak : 8 pm to 4 am and 8 am to 12 pm

The household was assumed to be completely unoccupied between 8 am and 12 pm as the power consumption was minimal which was assumed to be due to base appliances (fridge) drawing power while also assuming that stand-by losses were negligible. Between 8 pm and 4 am occupant activity is minimal since people are not using appliances even though they are present in the household.

The use of the appliances was further distributed into use in the morning (early morning and late morning), afternoon and evening peaks while making sure that the daily frequency of use of each appliance and the total average time of use per day was not exceeded. Table 3 shows the estimated time of use of each of the appliances in a day, assuming appliances other than the fridge are used during peak hours.

The time of use was used to set a threshold within a random profile generator in order to determine the service probabilities. This will be further discussed in the next sub-section.

Model implementation: A random activity profile generator was implemented in C++ which was used to generate half-hour probabilities of appliance usage by randomising the number of households using a particular appliance. The random process was used so as to model the stochastic nature of human behaviour. The probability of using an appliance at a specific 30 minute interval was calculated using:

$$P = \frac{\text{number of households using appliance}}{\text{total number of households in neighborhood}} \quad (5)$$

The total time of use of the appliance per service is

calculated using Equation 6:

$$t = \left(\sum_{i=1}^x p_i \right) T \quad (6)$$

Where:

- t = Total time of use per service
- T = Average daily time of use of the appliance
- $\sum_{i=1}^x p_i$ = Summation of the probability of use per interval within the time of the service

The calculated time of use per service had to be within 10% of the statistically obtained average time of use in Table 3 else the probabilities were re-calculated until they fell within range. The flowchart of the random demand profile generator is shown in Figure 6.

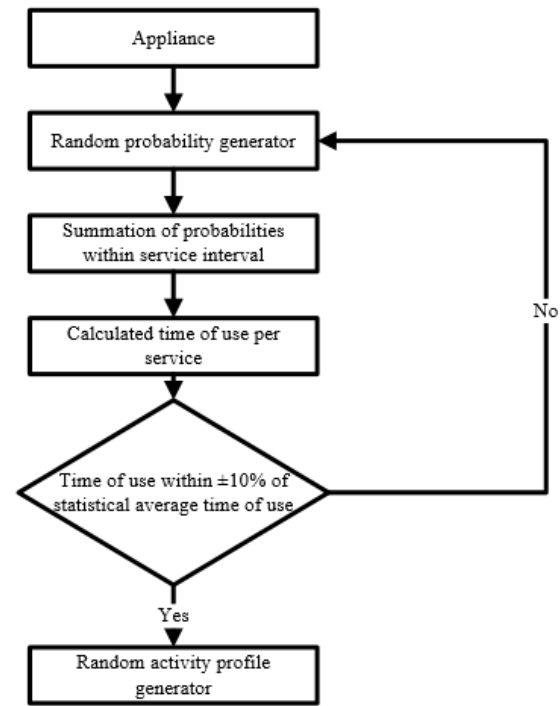


Figure 6: Random activity profile generator algorithm for each appliance over a day.

Model validation: Model was validated by visual comparison to see if a good correlation existed between the off-grid community load profile and the total activity pattern. The peak times were seen to resemble a good correlation as shown in Figure 7 and Figure 5.

7. DISCUSSION

The polynomial equations accurately model the power drawn by the 10 appliances. The quadratic polynomials used were sufficient to give good results with the maximum error being 1.6% (incandescent light bulb) for the reactive

Table 3: Average time of appliance use per day in off-grid community assuming appliances are only used during peak demand other than for the fridge.

Appliance	Early morning peak	Late morning peak	Afternoon peak	Evening peak
Stove	30 minutes	30 minutes	30 minutes	60 minutes
Kettle	3 minutes	3 minutes	3 minutes	3 minutes
TV	—	—	60 minutes	120 minutes
Cellphone Charger	—	—	—	60 minutes
Laptop	—	—	—	120 minutes
Iron	6 minutes	6 minutes	—	—

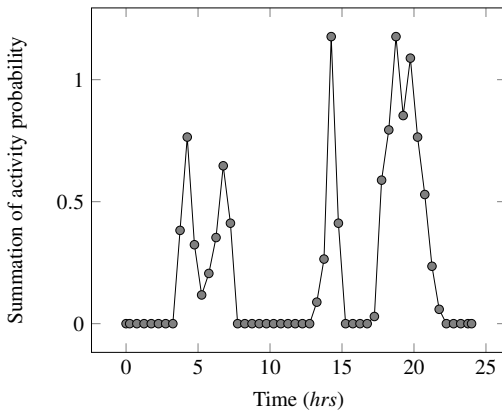


Figure 7: Daily total activity pattern for all appliances in the off-grid community obtained using the random activity profile generator.

power over a range of 200 V-230 V. The mean deviation of the polynomials from the real data was 0.76%. All the appliances behaved as expected except for the kettle which had harmonics even though it is a linear load. The harmonics introduced by appliances in the distribution network cause distortions in the current and voltage profiles and can lead to increased heating in appliances.

The simulations run using the statistical data show a high usage of appliances in the evening which has a very good correlation with most South African neighbourhoods. This increase in appliance usage will result in large currents flowing through wires. This results in an increase in I^2R losses and as a result lowers the voltage being transmitted to the consumers. Figure 8 shows the current-time simulation output illustrating the increase in current on the network during peak demand.

There is high energy demand between 6 pm and 9 pm. Schemes such as demand side management can be used to lower down this demand or the introduction of a pumped storage scheme can be used during these hours to take the voltage back up. Even though the statistical data used and appliances measured are from one community in South Africa, it is a very good representation of the effects of the social habits of the consumer on the distribution network.

Modelling and simulation tools are also important

for planning electrical distribution networks and their production capacity (transformer sizing). If the network is too big, large voltage drops are observed. Figure 9 and Figure 10 show a comparison of the voltage levels between a 10 house network and a 2 house network. This shows a 12 V difference in the voltage levels hence the required minimum voltage level and the particular maximum peak current values for each of the networks can be used for establishing the number of houses that can be supported on the network and the sizing of network conductors. The corresponding p-t characteristic can also be used to determine the required production capacity.

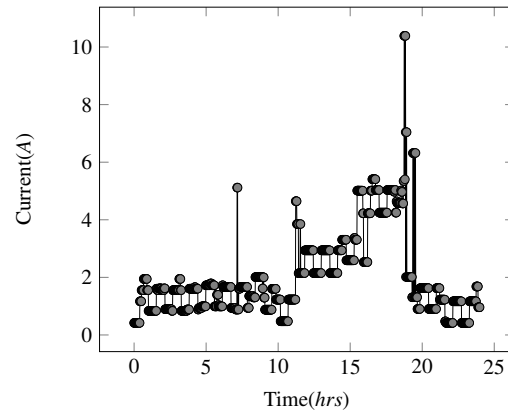


Figure 8: Current profile for a single day for a simulated network containing two houses.

A weakness in the system however is that it is not representative of a larger part of South Africa. The effect on distribution networks in high income areas or industries would give very different profiles to the one simulated using these models.

7.1 Preliminary validation of results

In order to perform a preliminary validation of the results obtained in the simulations the power usage data from the off-grid community was compared with the output from Suricatta which showed a good correlation. These results show that the peak use of electricity throughout the day occur between 6 and 7 am in the morning and after 6 pm in the evening. The simulations are representative of most low income communities in South Africa.

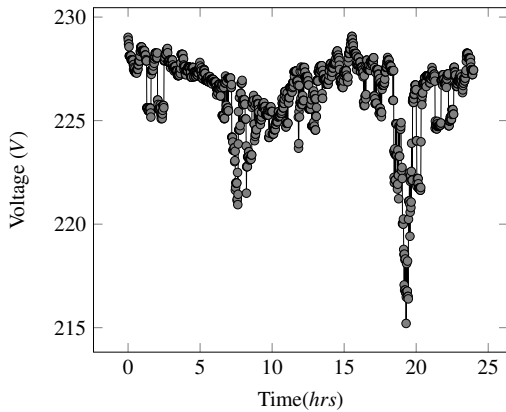


Figure 9: Voltage profile of a single day for a simulated network containing 10 houses.

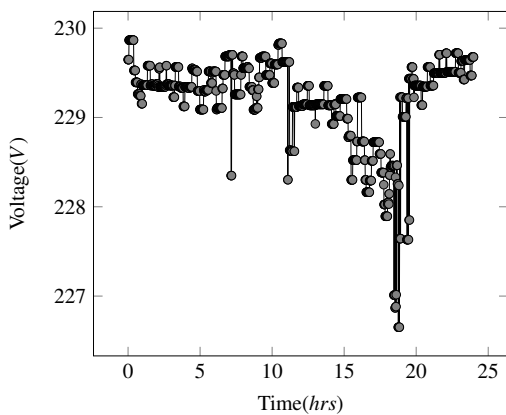


Figure 10: Voltage profile for a single day for a simulated network containing 2 houses.

8. RECOMMENDATIONS

Possible future improvements include conducting a survey to get more accurate statistical data and the modelling of standby losses for a more realistic load.

9. CONCLUSION

The modelling of loads for Suricatta was presented. A total of 10 domestic loads were modelled using linear least squares curve fitting of second order polynomials. The average deviation from the real data of the curves was 0.76%. The polynomials were therefore accurate enough to model the power drawn by the appliances. From the load models, appliances were seen to be either drawing a constant power or varying power with voltage.

The Suricatta model accurately simulated the activity patterns of an individual's use of household appliances and of a network based on stochastic statistical models of active occupancy and service probability. An off-grid community in South Africa was simulated and the output

validated using an available load profile. The number of active occupants was seen to be correlated to the number of appliances in use and hence the power consumption. An increase in the demand of apparent power due to simultaneous use of appliances was confirmed to be a cause for network losses and a reduction in the supply voltage levels. Most appliances were seen to have harmonic content which also contributed towards the resistive heating of the network conductors. Possible solutions to the problems include implementing DSM strategies and the proper design of distribution networks.

ACKNOWLEDGEMENTS

The authors would like to thank Eskom for their support of the Smart Grid research programme at Wits through TESP.

REFERENCES

- [1] James Gosling: JAVA, Oracle, Oracle Corporation, Redwood Shores, 2013, accessed from: <https://java.com/en/download/index.jsp>
- [2] M.D McCulloch: "Suricatta", [Online], accessed from: www.suricatta.org.uk, November, 2013, last accessed: 12 November 2014
- [3] T. Helfer: "Determining the power demand of domestic appliances", *4th year report Oxford University*, pp.6-7, May 2013
- [4] M. Shuma-Iwisi: "Estimation of standby power and energy losses in South African homes", *Proceedings of International Conference on Domestic Use of Energy*, Cape Town, South Africa, pp.18-27, 2009
- [5] E. Uken: "Energy usage in selected Cape Peninsula communities", *Sitshinga Energy Institute, Proceedings of International Conference on Domestic Use of Energy*, Cape Town, South Africa, pp. 2, 2012
- [6] M.V Shuma-Iwisi and E Trengove: "An off-grid community in South Africa: Survey response", 2013
- [7] G.J Gibbon and M.V Shuma-Iwisi: "Appliance standby power and energy consumption in South African Households", *Proceedings of International Conference on Domestic Use of Energy*, pp.1-2, 2009
- [8] MathWorks: MATLAB, MathWorks, 2013, Natick, United States, accessed from: www.mathworks.com/products/matlab/
- [9] I. Richardson, M. Thomson and D. Infield: "A high resolution energy demand model: Domestic electricity use", *Elsevier*, Vol. 42, Issue 10, pp. 1880-1883, October 2010

IMPACT OF SYSTEM EXPANSION ON SPECIFICATION OF PERSONAL PROTECTIVE EQUIPMENT: ARC FLASH ANALYSIS

D. Edwards* and P. Bokoro†

* Dept. of Electrical and Electronic Engineering Technology, University of Johannesburg, South Africa
E-mail: dwayne.edwards@norconsulafrika.com

† Dept. of Electrical and Electronic Engineering Technology, University of Johannesburg, South Africa
E-mail: pitshoub@uj.ac.za

Abstract: Electricity network expansion require the installation of new substations and switchgear equipment. This, in many cases, is intended to cater for electrical energy demand much needed for industrial operations. Such an increase in power available for use by consumers translates in high short circuit capacity or fault level of the network, which in turn causes the arc flash incident energy to be high in case of a fault. In this paper, the impact of network expansion on the arc flash incident energy is assessed using the digSilent software version 15.1. The influence of protective relays time setting on the reduction of arc flash energy, available during three-phase fault conditions, is also analysed for the purpose of PPE specification. The results obtained show that an increase in the short circuit capacity or fault level as well as in the fault clearing time, causes the arc flash incident energy to increase to higher level than the corresponding PPE prescribed.

Key words: Arc Flash Incident Energy, System Expansion, Short Circuit Capacity, Fault Clearing Time, Personal Protective Equipment.

1. INTRODUCTION

The South African industrial and mining sectors require greater demand for electricity as a result of economic growth and expansion [1]. This ultimately imposes the need for the development or upgrading of electricity infrastructure and network capable of conveying high energy demand from supply companies to consumers. However, this increases the risk of exposure to high dissipated arc energy during fault conditions, particularly for consumers with indoor switchgear which places operators in a close proximity to arc flash that may be created during switching.

In this article, an attempt to determine minimum personal protective equipment (PPE), as required for operators in close proximity to MV or LV switchgear, is undertaken on the basis of arc flash hazard analysis. Therefore, the arc incident energy and clearing time obtained by simulating a power network on the digSilent software version 15.1 are used to determine the optimum minimum required PPE. The results obtained indicate that an increase in the short circuit capacity or fault level as well as in the fault clearing time, causes the arc flash incident energy to increase to higher level than the corresponding PPE prescribed.

2. ARC FLASH ANALYSIS

Several contributing factors are usually regarded during arc flash analysis for the purpose required PPE determination:

2.1 Arc Flash Incident Energy

This is the amount of thermal energy which the operator's face and chest could be exposed to, at working distance in

case of an electrical arc event [2]. Three-phase fault level analysis is usually relied upon in a bid to estimate the fault current likely to be responsible for arc triggering [3]. The arc flash incident energy in a cubicle box could therefore be calculated on the basis of the following empirical equation:

$$E_i = 1038.7 \times d^{-1.4738} \times t_a (aI_F^2 - bI_F + c) \quad (1)$$

Where:

E_i = arc flash incident energy in J/m²

a = 0.0093

b = 0.3453

c = 5.9675

d = distance between arc electrodes in metres

t_a = arc duration time in second

I_F = fault current in kA

It is worth noting from equation 1 that the distance between the arc electrodes d is a constant parameter, and therefore the arc duration t_a as well as the fault current I_F are the key influencing factors of the arc flash incident energy.

Since system expansion or upgrading is meant to increase the amount of power, this will have no other effect than to increase the short circuit capacity (MVA_F) of the network, and hence the short circuit current (I_F). This could be observed in equation 2 and 3 expressed as follows:

$$MVA_F = \frac{MVA_b}{Z_{pu}} \quad (2)$$

Where:

MVA_b = base value of system capacity in MVA
 Z_{pu} = system impedance in per unit value

The resulting fault current is therefore:

$$I_F = \frac{MVA_F}{\sqrt{3} \cdot V_b} = \frac{I_b}{Z_{pu}} \quad (3)$$

Where:

V_b = base value of system voltage in kV
 I_b = base value of system current in kA

2.2 Arc Flash duration Time

The duration of an arc flash could be retrieved from a fault clearing process, as applicable to the conjunctive operation of protective relays and circuit breakers. This process commences with relay tripping command to the instant at which the arc extinction of the short circuit current is completed. The total fault clearing time is therefore the sum of the relay tripping time, the breaker opening time and the arcing time [4]. Figure 1 depicts the total fault clearing time.

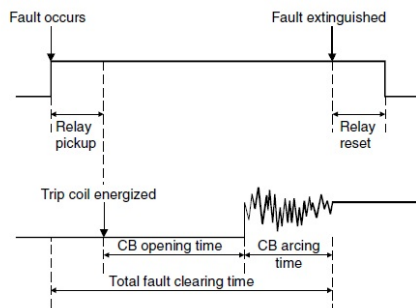


Figure 1: Total clearing time

The two tripping modes of protective relays namely: the instantaneous and time delay operation, as well as the speed of operation of circuit breakers could either increase or reduce the total fault clearing time. Instantaneous tripping of relays is usually recommended for differential protection of highly critical components such as: transformers, bus bars, feeders...

Protection settings are determined on the basis of the fault level as well as the prospective short circuit current of the network. Therefore, since network expansion increases the system fault level and the prospective short circuit current, the fault clearing time of the protection involved should be adequately selected.

2.3 Arc Flash Boundary and Working Distance

This is the maximum distance at which an operator will be exposed to an arc incident energy. To access the switchgear cubicle, the operator has no other choice than to encroach the arc flash boundary. Therefore, the distance between the

Table 1: Classes of equipment and typical working distances (IEEE-1584-2002)

Classes of Equipment	working distance in mm
15 kV Switchgear	910
5 kV Switchgear	910
Low voltage switchgear	610
Low voltage MCC and panel boards	455
Cables	455

arc flash and the body of the operator is normally referred to as the working distance.

The relationship between the incident energy and the arc flash boundary D is expressed as follows:

$$E_i = 2.142 \times 10^6 \times V \times I_F \left(\frac{t_a}{D^2} \right) \quad (4)$$

Where:

V = system working voltage in kV
 D = distance of the arc flash boundaries in metres

From equation 4, it could be observed that if network expansion could possibly have some influence on the arc flash boundary, but cannot be related to the working distance. Typical working distances based on classes of equipment are given on table 1.

3. PPE CATEGORIES

The five categories of required PPE are specified by the National Fire Protection Association (NFPA) standard 70. Each category corresponds to a determined value of an arc flash incident energy. This is shown in figure 2.

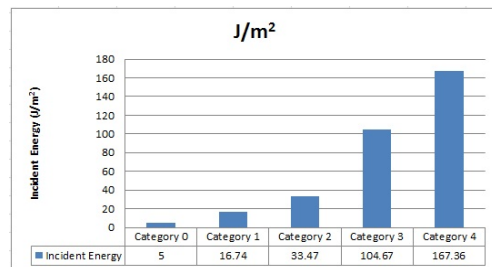


Figure 2: Arc flash incident energy versus PPE Category

As indicated above, expansion on the network will cause the prospective short circuit current to increase, and will therefore yield quite a significant amount of arc flash incident energy which should be cleared as quick as possible. The determination of the required PPE could be expected to vary as the network expands.

4. VARIATIONS OF ARC FLASH ENERGY RATINGS

Arc flash studies have been conducted on a power network built up on version 15.1 of the digsilent software. The applied network consisted of a 100 MVA/11 kV, star-connected and solidly earthed synchronous generator, supplying a 10 MVA, 11/88 kV power transformer with 0.1 pu impedance. The 11kV bus of the network is fed from a 88/11 kV transformer of similar power and p.u impedance ratings. Figure 3 shows the power network under study.

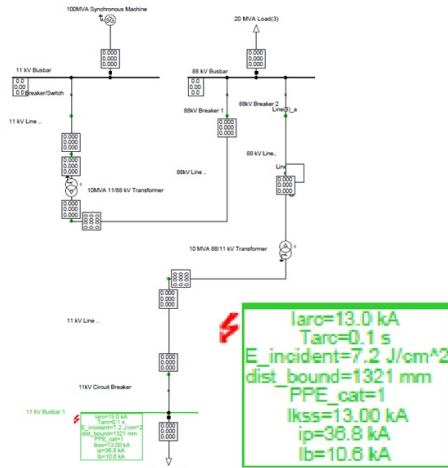


Figure 3: Power network under study

For the purpose of arc flash analysis on the power network depicted on figure 3, a steady state three-phase fault current of 13.00 kA is simulated on the 11 kV downstream bus bar. The fault clearing duration, obtained from the protection setting is taken to be 100 ms. The digsilent fault simulation run of the network points to the incident energy being 7.2 J/cm², with an arc flash boundary of 1.321 m. Based on figure 2, the minimum mandatory PPE required will be category 1 protection, which is also suggested by the simulation results.

The power network thus far described is now expanded in such a way that a steady state simulated three-phase fault current of 17.70 kA will be measured on the same bus bar under fault conditions. A resulting incident energy of 10.0 J/cm² is obtained with an arc flash boundary of 1.858 m. The required PPE corresponding to this incident energy is still category 1, although the results show 35 % increase in the energy dissipated during the fault. Figure 4 depicts the comparison between the two incident energies, and the expanded power network is depicted in figure 5.

Figure 5 implies that the expansion of the network has lead to the increase of the incident energy, which did not necessarily required a change in the PPE category, since the maximum energy required for category 1 of protection has not been exceeded.

However, if the expansion consists of downstream feeders

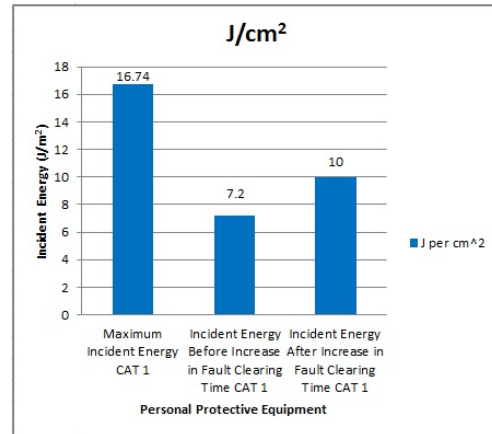


Figure 4: Comparison of Resulting incident energies

to the 11 kV bus, with graded protection being used. The fault clearing time is taken to be 400 ms with the grading margin of 300 ms. For a simulated three-phase fault of 13.00 kA on the same bus, the incident energy is risen to 28.7 J/cm², and the arc flash boundary distance increases to 5.474 m. In this case, the required PPE at the downstream 11 kV bus bar is category 2 of protection.

The grading margin selected implies that for a 3.4 kA three-phase fault on the downstream substation, the clearing time should be 100 ms. The simulation results point to an incident energy of 1.7 J/cm², with the arc flash boundary distance of 0.2 m. The required PPE specification will therefore be of category 0 of protection.

Figure 6 depicts the downstream feeders that form the expansion of the network.

Figure 7 shows the variations of the arc flash incident energy with the protection time grading.

Figure 7 implies that an increase in the fault clearing time causes the arc flash incident energy to increase, and this may lead to changes in the specification of the required PPE.

It could also be noticed that relay grading is significant contributory to the increase of arc flash incident energy since the upstream relays will experience longer fault clearing times, hence larger incident energy, arc flash boundary distance and probably higher category of required PPE as compared to the downstream protective relays.

5. CONCLUSION

The growth in economy imposes the need for industrial development which remains increasingly dependent on the availability of reliable electrical energy. Electricity network expansion is therefore unavoidable for industrial consumers. In such environments, employers are required by law to specify PPE requirements to employees or operators in a bid to adequately reinforce potential risk

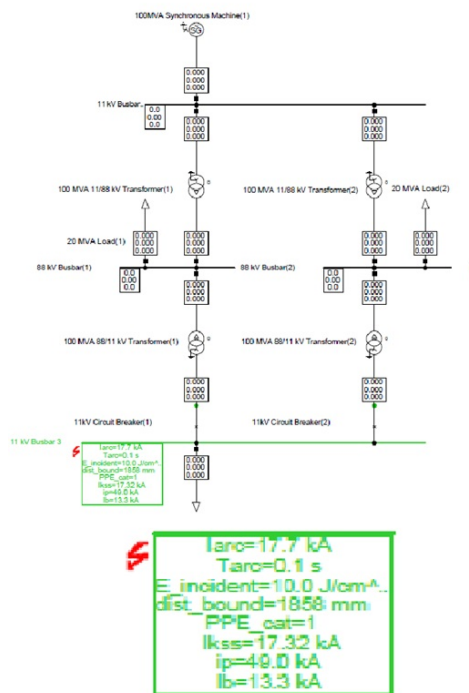


Figure 5: Expanded power network

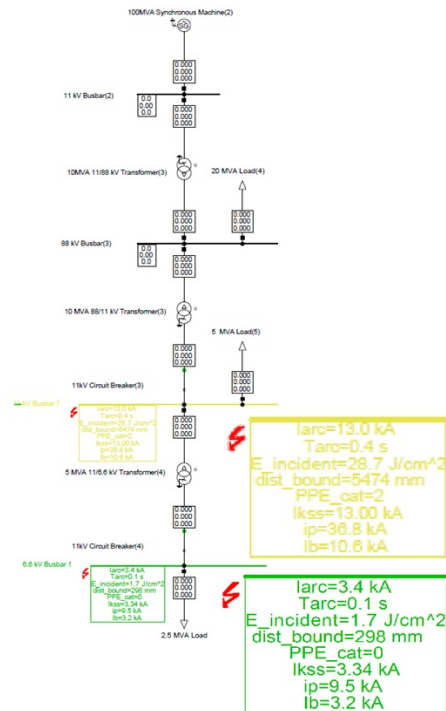


Figure 6: Feeder expansion of the network

prevention of arcing. Arc flash analysis on a network enable employers to quantify such potential risk of an arc flash. An increase of the network fault level, results in an increase of the incident energy likely to be produced by the arc during fault conditions. Similarly, an increase or delay in the fault clearing time of a relay will also prompt the arc flash incident energy to rise. Since power system expansion usually brings about an increase in the short circuit capacity or fault level, and the resetting of the protective relays. Arc flash analysis should also be conducted to determine whether or not the previously prescribed PPE is still valid with system expansion.

Bus zone and arc protection should be highly recommended over graded protection. This significantly reduces the incident energy level because of instantaneous tripping of protective relays. It is therefore of utmost importance that employers be clear in tune with the implications of arc flash incident energy related to system expansion for correct prescriptions of required PPE.

REFERENCES

[1] R. Inglesi-Lotz and A. Pouris: "On the Causality and determination of energy and electricity demand in South Africa: A review", *Department of Economics Working Paper Series*, University of Pretoria, March 2013.

[2] NFPA 70E Standard: "Electrical Safety Requirements for employees's workplace", *National Fire Protection Association*, Ed. 2000

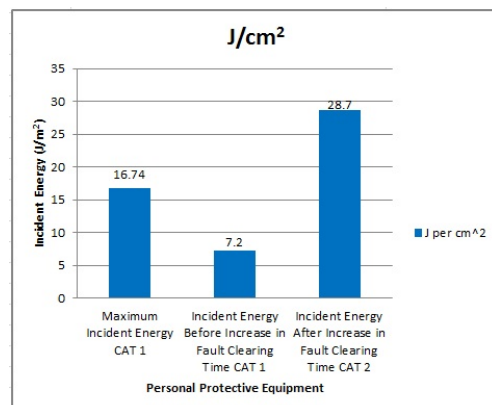


Figure 7: Arc flash incident variations with fault clearing time

[3] A. C. Parsons, B. Leuschner and K. X. Jiang: "Simplified Arc-Flash Hazard Analysis Using Energy Boundary Curves", *IEEE Transactions on Industry Applications*, Vol. 44, N0.6, pp. 1879-1885, November/ December 2008.

[4] ABB Power Transmission and Distribution Company: *Distribution systems division, medium voltage vacuum power circuit breakers*, January 1999.

A CASE STUDY OF INDUCED CURRENT UNBALANCE AS A RESULT OF CAPACITOR FAILURE

S. Zondi*, P. Bokoro[†] and B. Paul[‡]

* Dept. of Electrical and Electronic Engineering Technology, University of Johannesburg, E-mail: 201284239@students.uj.ac.za

[†] Dept. of Electrical and Electronic Engineering Technology, University of Johannesburg, E-mail: pitshoub@uj.ac.za

[‡] Dept. of Electrical and Electronic Engineering Technology, University of Johannesburg, E-mail: bspaul@uj.ac.za

Abstract: Capacitor banks rated 132 kV/ 72 MVar are installed at the Durban North Substation of Ethekwini municipality to compensate for inductive power losses. The POW or synchronous switching technique is used for on-line switching of these banks, in a bid to minimise high magnitude induced transient voltage and current. In this study, the voltage waveform records and the percentage current unbalance, measured on and six months post commissioning of the capacitor banks are analysed in order to test the effectiveness of POW switching method, when implemented with mechanically linked 3-phase, 3-pole SF₆ circuit breakers. The results obtained indicate that within 6 months of commissioning, capacitive impedance of the banks failed, as result of high magnitude induced transient current and voltage, and the percentage unbalance level observed in the neutral current grew from 2.3% to 5.7%.

Key words: Point on wave switching, capacitor bank, transient voltage, current unbalance, SF₆ circuit breakers.

1. INTRODUCTION

Capacitor banks are commonly used in electrical networks to provide leading reactive power [1]. This practice is fundamentally intended to provide compensation for inductive losses in order to improve the load system power factor, and thus to stabilise the bus voltage [2-3]. These units are automatically or manually switched on line during peak inductive load time. The continuous on and off switching of capacitor banks usually induces high magnitude transient current and voltage [4]. The point on wave (POW) switching technique, whereby capacitor banks are switched on line at or near zero crossing of the supply voltage waveform, is commonly applied for successful mitigation of induced switching transients.

In this case study, high voltage capacitor banks with POW on-line switching, installed at the Durban North substation of Ethekwini municipality, are tested to be aggravating current unbalance six months after commissioning. Voltage and current measurement records obtained on and after commissioning of capacitor banks at the substation are analysed. The results indicate that a shift on the mechanically linked 3-pole circuit breaker causes transient voltage to be induced, which in turn cause capacitor cans to fail and thus creating current unbalance in the system.

2. DESCRIPTION OF THE CAPACITOR BANKS

The capacitors connected at the Durban North Substation consist of 132 kV/ 72 MVar banks. Each capacitor bank is made up of 216 capacitor units or cans. The on-line switching is POW based. This is basically achieved using a 3-phase, 3-pole circuit breaker having a mechanical link

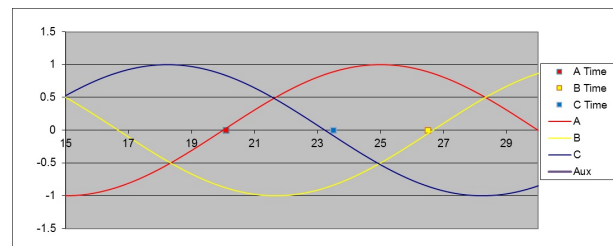


Figure 1: Ideal point on wave switching technique

staggered to satisfy 120 electrical degrees. The switching sequence is ideally meant to synchronise with the zero crossing instants of the 3-phase supply voltage. Therefore, considering the mechanical link as the horizontal axis, the first or reference pole is positioned at 27 degrees, while the second and the third ones are positioned at 88 degrees and 52 degrees of the horizontal axis, respectively. This setting ensures that all poles, and therefore capacitor banks are switched on line at zero crossing of the voltage waveform. The 3-pole SF₆ circuit breakers are used in this case study. Figure 1 depicts ideal POW or synchronous switching technique.

For the purpose of dampening the switching transient, some value of inductance and resistance are present in the switching circuitry of capacitor banks. therefore, 0.6 mH inductor and 10 Ω resistor are measured. The complete capacitor bank to be connected on each line is shown in figure 2. To monitor the level of current unbalance, the neutral current is constantly measured using a current transformer (CT) and an unbalance relay. The CT transforms the measured neutral current (I_n) to a lower

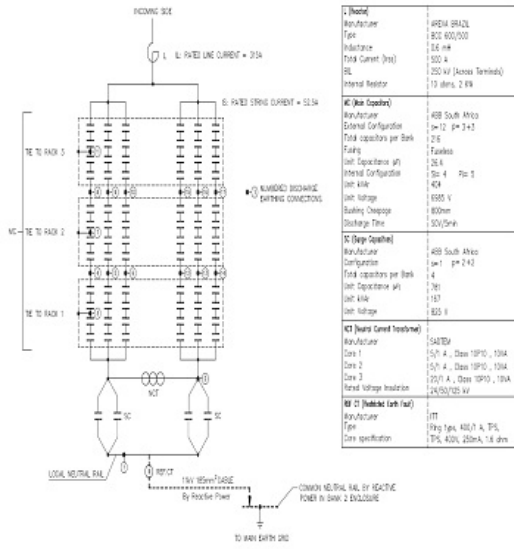


Figure 2: Line capacitor bank

scale, which is fed to the unbalance relay.

3. POINT ON WAVE SWITCHING AND CURRENT UNBALANCE

The POW switching of circuit breakers is mainly dependant on the breaker switch contact velocity, the time difference between contact closing and the breaking of the dielectric strength of the contacts' gap as a result of the applied voltage [5]. This could be expressed in terms of the following relationship:

$$\frac{U_m}{\sqrt{2}} \angle \phi = E \cdot v \cdot (t_s - t_b) \quad (1)$$

Where:

- $\frac{U_m}{\sqrt{2}}$ = rms value of phase voltage
- ϕ = phase angle
- v = switch contact velocity
- E = dielectric strength of the contact gap
- t_s = breaker's contact closing time
- t_b = time to overcome the dielectric strength of the contact gap

Successful implementation of this technique therefore requires the following conditions to be met:

1. The time difference ($t_s - t_b$) must be less than 5 electrical degrees: $(t_s - t_b) \leq 5$ electrical degrees
2. The switching phase voltage must be less or equal than the product of the dielectric strength and the velocity of the contacts: $E \cdot v \geq \frac{U_m}{\sqrt{2}} \angle \phi$

For the purpose of this study, the contacts of the SF₆ circuit breakers are mechanically linked and actuated upon reception of a closing command from a switching relay. The shift of the breaker's poles observed in this case study is shown in figure 4. This therefore results in transient voltages and current being induced, as well as steady state current and voltage unbalance in the system.

$$i(t) = \frac{u(t) - u(0)}{\sqrt{L_s C}} \cdot \sin \omega_0 t \quad (2)$$

Where:

- $i(t)$ = instantaneous transient current
- $u(t)$ = instantaneous transient voltage
- $u(0)$ = instantaneous transient voltage when $t=0$
- L_s = system inductance
- C = capacitance of the bank
- $\omega_0 = \sqrt{1/L_s C}$

Under steady state conditions, aggravated current unbalance is likely to emerge as an immediate consequence of transient voltage and current in this case study. Line or phase current unbalance occurs when the magnitude of line or phase currents becomes unequal as a result of change in the load phase impedance [6]. This results in the presence of negative and zero sequence in the system current. The percentage current unbalance factor (IUF) could be estimated using the ratio of the negative sequence to that of the positive components, given in equation 3:

$$IUF = \frac{I_2}{I_1} = \frac{I_R + a^2 I_Y + a I_B}{I_R + a I_Y + a^2 I_B} \times 100 \quad (3)$$

Where:

- I_2 = negative sequence component of the neutral current
- I_1 = positive sequence component of the neutral current
- I_R = rms magnitude of current in the red phase
- I_Y = rms magnitude of current in the white phase
- I_B = rms magnitude of current in the blue phase
- $a = 1 \angle 120^\circ$
- $a^2 = 1 \angle 240^\circ$

The neutral current (I_n) could therefore be expressed as follows:

$$I_n = 3I_0 + (1 + a^2 + a)I_1 + (1 + a + a^2)I_2 \quad (4)$$

The unbalance relay monitors the degree of current unbalance on the basis of the percentage IUF in the neutral current. Under tolerable unbalanced current condition, generally related to load imperfection, the percentage IUF should not exceed 5 % [7]. Therefore, the settings of the unbalance relay in this case study could be summarised as follows:

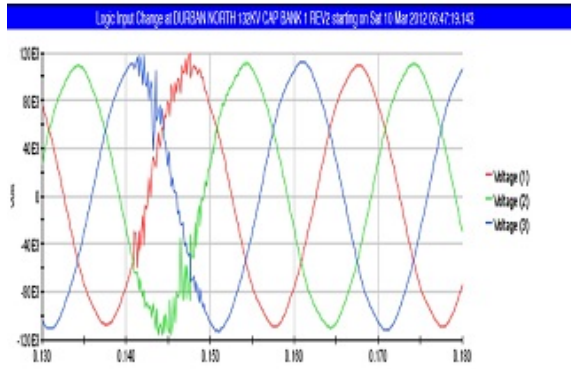


Figure 3: Transient voltage six months after commissioning

1. Unbalance relay trip condition: $IUF \{I_n\} > 5\%$
2. Unbalance relay restrain condition: $IUF \{I_n\} < 5\%$

The implementation of these relay setting conditions, on and after commissioning of the capacitor banks, are shown in figures 5 and 6, respectively.

4. RESULTS AND DISCUSSION

The voltage waveforms recorded six months after commissioning show the existence of transients in all the phases upon line switching of capacitor banks. This is shown in figure 3.

Since the presence of transients implies that the POW switching principle is either not or inadequately implemented, The switching positions or the closing positions of the 3-pole SF₆ circuit breakers are compared on and after commissioning. This reveals a position shift of about 15 or more electrical degrees (green arrow) from the initial position. This theoretically implies that the time difference ($t_s - t_b$), which in fact is the arcing time, has become too long than required, and thus causing the switching to take place beyond zero crossing. This is the basis of the transients induced in the waveform. Therefore, the transients observed in the voltage waveforms could be attributed to the displacement of the mechanical linkage between the circuit breaker poles, indicated in figure 4.

The neutral current measured after commissioning proved to have higher unbalance factor as compared to initial measurement. The results obtained are shown in figures 5 and 6. This relates to the fact that almost no transient voltage and current are induced on commissioning as compared to higher magnitude induced six months post commissioning of the capacitor banks.

The increase in the level of unbalance in the neutral current is a direct consequence of aggravated change in the impedance of capacitor banks, which are triggered by induced switching transients. This is indeed proven by testing the capacitance of the bank. This testing revealed

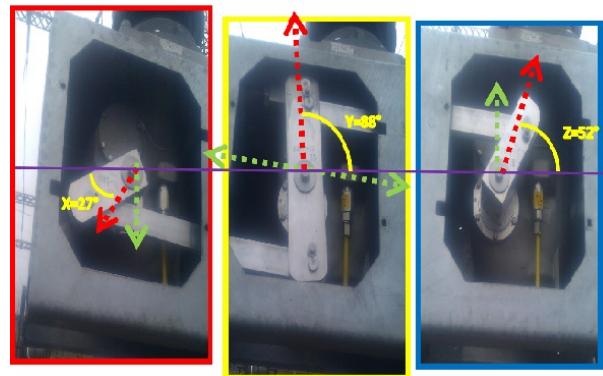


Figure 4: Shift of the mechanical linkage of the 3-pole circuit breakers



Figure 5: Current unbalance level on commissioning



Figure 6: Current unbalance level after commissioning

that seven capacitor units of the bank had failed due to resulting high magnitude transient voltage and current. Capacitor units failure occur as a result of increasingly high frequency voltage and current transient. This inrush amount of transient energy has the effect of causing the electrodes of the capacitor unit to short circuit. Since, the transient state lasts only for a few cycles, the resulting steady state overall capacitance and capacitive impedance of the capacitor bank will therefore be compromised. This implies therefore aggravated unequal current and voltage distribution across the phases. The level of unbalance measured in the neutral current in this study, happens to be 5.7% six months post commissioning, against 2.3% on commissioning of the capacitor banks.

It is worth noting that the root cause of induced transient voltage and current as well as current unbalance is the shift of the mechanical linkage between the poles of the circuit breaker.

5. CONCLUSION

The effectiveness of POW switching using mechanically linked 3-phase, 3-pole circuit breakers, for the purpose of transient voltage and current mitigation, when capacitor banks are switched on-line, is analysed in this case study. The voltage waveforms recorded and the level of unbalance measured in the neutral current, six months after commissioning, point to the following:

1. The transient voltage and current induced result from the shift of the mechanical link. This causes switching to take place beyond zero crossing.
2. The inrush transient energy into the bank is likely to damage capacitor units.
3. The increase in the neutral current unbalance level could be seen as the steady-state consequence of the damage effected on the bank as a result of high magnitude transient voltage and current.
4. The magnitude of the resulting transient current is dependent on the initial conditions of the contacts of the breakers.

These observations indicate that POW switching of capacitor banks using mechanically linked 3-phase, 3-pole SF₆ circuit breakers, is prone to induce transient current and voltage which in turn aggravate current unbalance resulting from capacitance failure in the bank. The fundamental source of these problems remains the shift of the linkage between the breakers which tends to occur in a very short period of time, and thus making this technique non effective.

Recent Developments in this field of study tend to promote electronic based POW switching technique of capacitor banks.

REFERENCES

- [1] T.E. Grebe: "Application of distribution system capacitor banks and their impact on power quality", *IEEE Transactions on Industry Applications*, Vol. 32 No. 3, pp. 714-719, May/June 1996.
- [2] E. Camm: "Shunt capacitor overvoltages and a reduction technique", *IEEE/PES Transmission and Distribution Conference and Exposition*, New Orleans, LA, April 1999.
- [3] T. Chen, C. Yang and T. Hsieh: "Case studies of the impact of voltage imbalance on power distribution systems and equipment", *Proceedings: 8th International Conference on Applied Computer and Applied Computational Science*, Athens, April 2010.
- [4] A.Iturregi, E. Torres, I. Zamora and O. Abarregui: "High voltage circuit breakers: SF₆ vs. Vacuum", *Proceedings: 9th International Conference on Renewable Energies and Power Quality*, Valencia, April 2009.
- [5] S. Kulas: "Capacitor switching techniques", *Proceedings: 9th International Conference on Renewable Energies and Power Quality*, Valencia, April 2009.
- [6] P. Pillay and M. Manyange: *Definitions of voltage unbalance*, IEEE Power Engineering Review, pp. 50-51, May 2001.
- [7] Power Quality Standards for electric service, 2008 issue: www.energy.com

RING MAIN PROTECTION

H. Sewnarain* and A.K. Saha**

* School of Engineering, Electrical, Electronic and Computer Engineering, Howard College Campus, King George V Avenue, University of KwaZulu-Natal, Durban, South Africa, E-mail: 211509679@stu.ukzn.ac.za, hansasewnarain@gmail.com

** School of Engineering, Electrical, Electronic and Computer Engineering, Howard College Campus, King George V Avenue, University of KwaZulu-Natal, Durban, South Africa, E-mail: saha@ukzn.ac.za

Abstract: This report entails the complete design process of a ring main protection system. Each design constraint has been outlined and achieved. A solution utilizing non-directional time overcurrent relays on the standard inverse setting was researched, conceptualised, and modelled. This solution encompassed 3 substations, which was a maximum for any given RSCAD rack. The software and hardware simulations are discussed and explained. The software simulations were very similar to the hardware simulations due to the time of operation for both the software and the hardware relays.

Keywords: Definite time relays, Instantaneous relays, RSCAD, RTDS, Standard inverse non-directional time overcurrent relays.

1. INTRODUCTION

Electricity is an essential commodity in the versatile 21st century that we thrive in. The modern age has come to depend heavily upon a continuous and reliability of electricity with an excellent quality of supply. Reducing faults and improving power system stability are the main aims of being an Electrical Engineer; however, no power system can be designed to ensure that it would never fail due to over loading, over voltages, power swings and faults. Therefore, different types of protection for different applications and their uses are vital.

The objective of power system protection is to isolate a faulty section of an electrical power system from the live system to ensure that the circuit can function satisfactorily without any severer damage due to fault current, and allows for normal operation from the load viewpoint [1]. This can be achieved by means of relays, which detect the fault and initiate the operation of the circuit breaker to isolate the defective element from the rest of the system.

Overcurrent exists in a power system where a current much larger than its rated value flows through the lines. This results in excessive power being generated and may cause equipment damage. Overcurrent results from short circuits, overloading or equipment failure. As a result of increasing energy demands and interconnections, the susceptibility of faults occurring is high. Faults pose a great threat to the operation and security of power systems. Power systems require an auxiliary system which is responsible for taking corrective actions on the occurrence of a fault [1].

Ring main protection systems are a form of protection where various substations are interconnected by the alternate routes and hence the overall system forms a closed path [1]. This ensures the continuity of the supply

to the healthy parts is unwavering, if any section is damaged and separated for repairs. The direction of power flow can be changed at will, when there are different sources supplying the ring main system, the current can be bi-directional.

The ring main system offers continuity of power in the event of a conductor failure or a fault in any section; this is due to the three feeders connected in different paths. This type of protection has various advantages over radial and parallel feeder protection, viz. it has two paths from the generating station to the load whereas, radial and parallel feeder only connects the source to the load [2]. It meets the requirements of two alternative feeds to give 100% continuity of supply, whilst saving in cabling compared to parallel feeders and radial protection [1], [2].

Due to the complexity of the possibility of power flow in both directions, as well as the interconnection of lines, it is extremely difficult to configure the protection required for ring main systems, whereas radial and parallel feeders offer a simplistic style of protection. The minimum number of relays and circuit breakers for a basic ring main system is 6 whereas the radial and parallel feeder circuits require a maximum of 4 relays and circuit breakers, this makes these protection methods much more cost efficient.

Contained in this report is a solution using mutually independent sources to supply three loads using time overcurrent non-directional relays.

2. BACKGROUND

In ring main systems, the various substations are interconnected by alternate paths in order to form a closed ring. The primary reason for its use is to maintain a continuous supply to consumers in case of fault conditions occurring on the interconnecting feeders.

Resulting in, if any section of the ring is disconnected for repairs, the supply to the other sections is not interrupted. The direction of power flow can be varied to suit the application.

The 230 V ring circuit was developed after the Second World War to minimise the use of copper in the massive reconstruction that followed the conflict [2]. This installation methodology was introduced in 1947 after a study led to the development of the Ring Circuit [2]. This study was remarkable due to the foresight of its authors, references to topics such as Energy Efficiency and Environmental Protection, which are more relevant now than they were in 1944.

During normal operation all the breakers are closed. When a fault is applied to the interconnecting lines the two breakers connecting the substations trips. During breaker maintenance the ring is broken but all the lines that are not undergoing maintenance remain in service. There are various advantages of a ring main system, low cost, flexible operation for breaker maintenance, any breaker can be taken out of service without interrupting load and power can be fed from both the directions.

There are two relays and two circuit breakers between each interconnecting transmission line. The relays used should be over current relays due to its ability to detect high fault current and isolate the faulty section. In actual power systems, the power station generates the electricity and then delivers it at a lower voltage level to the substation which steps up the voltage before it is sent to the distribution grid.

The main aim of this paper is to simulate and implement the protection for a ring main system making use of both software and hardware relays and comparing the simulated results for both. The ring main protection model will be developed using the RSCAD simulation tool. The RSCAD software interlinks the user to the simulator via a graphical user interface. The simulator used for this design is the Real Time Digital Simulator (RTDS). This models the exact operation of the ring main system as it would be in an actual scenario. The hardware relay will be connected to the digital input of the RTDS and the real scenario outputs will be given.

3. LITERATURE REVIEW

Overcurrent protection is the predominant type of protection in ring main systems. From 1890, when Thomas Edison patented the use of fuses in the electric distribution system, overcurrent protection was essential due to the high fault currents. High fault currents damage equipment connected the system, therefore electrical isolation is vital. The fuse was initially used to isolate the fault by sacrificing itself, however, fuses needed to be replaced every time there was a fault in the system. This proved expensive and inconvenient.

This was overcome by a boom in overcurrent protection devices in the power systems application. In South Africa, this boom was due to ABB and their invention of the time overcurrent relay in 1905. According to Lundqvist B [3], the development of relays can be divided into three eras, firstly, the era of electromechanical relays which started 100 years ago. The second era was the development of the static relays. Now, microprocessor based relays are used, such as the P122 MICOM non-directional time overcurrent relay used in this project.

According to Kundur P [4], the following are the main advantages of overcurrent protection:

- ❖ Detects abnormal conditions
- ❖ Isolates the faulty part of the system
- ❖ Fast Speed operation to minimize damage and danger
- ❖ Discrimination of relays
- ❖ Dependability / reliability
- ❖ Stability of the power system
- ❖ Cost of protection against cost of potential hazards

The ring main system overcomes drawbacks on the radial system by allowing one ring network of distributors to be fed by more than one feeder [5]. This is essential for uninterrupted power supply to the consumer, in addition, the system is also provided with different section which isolates at different suitable points.

4. RSCAD and RTDS

The ring main protection model will be developed using the RSCAD simulation tool. The RSCAD software interlinks the user to the simulator via a graphical user interface. The simulator used for this design is the Real Time Digital Simulator (RTDS); this software enables each increment of the design to be processed for a specified time step. The user models the network on the RSCAD software using predefined component blocks found in the users library [6]. The model is then compiled and downloaded, and then the application of faults and other system variables can be monitored on the runtime interface. This models the exact operation of the ring main system as it would be in an actual scenario. This simulator is essential in power systems as it allows the user to investigate the effects of disturbances on power system equipment and networks to prevent outages or complete failures.

The RTDS system may be interfaced with hardware such as relays, circuit breaks, generators etc. The interfacing requires GTA0 and GTFPI cards to be installed on the rack.

5. NON-DIRECTIONAL TIME OVERCURRENT RELAYS

A relay is a device which detects dangerous or abnormal conditions in a power system and initiates correct actions

(like opening the circuit breakers) to protect the equipment connected to the system.

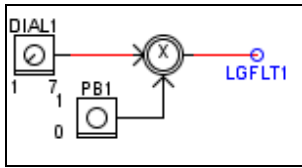


Figure 1: Fault logic

The fault logic is given in figure 1. The dial selects the type of fault, and the push button is pressed to apply the fault on the system. The output of this multiplication is the fault signal.

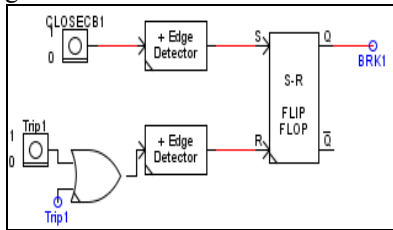


Figure 2: Relay and circuit breaker logic

The relay and circuit breaker logic is given in figure 2. The trip signal is outputted from the software relay which then gets inputted into the flip flop which produces the signal that opens the breaker (BRK1). CLOSECB1 serves as a reset, to reinstate the circuit breaker after it opens.

Non-directional time overcurrent relays on the standard inverse setting were used because of the presence of three sources; this caused current flow in both directions of the protection line. These relays were used to obtain proper selectivity due to the number of relays (6) used. These relays have a time of operation within 0.1 second of their time dial settings.

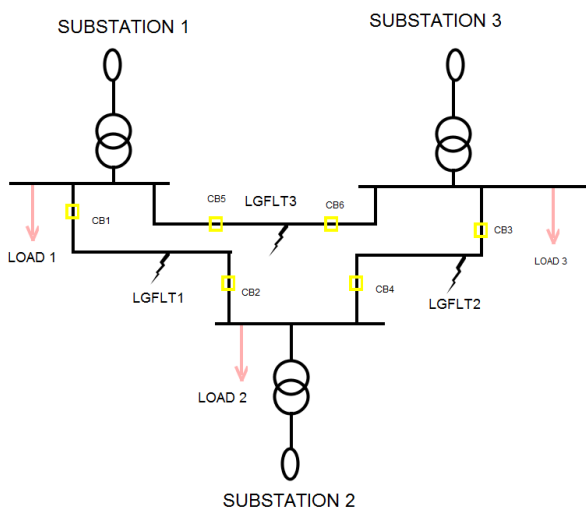


Figure 3: Runtime simulation diagram for ring main protection

Figure 3 refers to the Runtime diagram for this ring main protection. Fault 1 corresponds to relay and circuit breakers 1 and 2, fault 2 correspond to 3 and 4, and fault 3 corresponds to relay and circuit breakers 5 and 6.

6.1 Software relays response

The pickup settings as well as the time dial setting has to be configured for the relay. Figure 4 refers to the trip and breaking signals of the relays when fault 1 is applied. As observed, when fault 1 is applied, relays and circuit breakers 1 and 2 react to this fault.

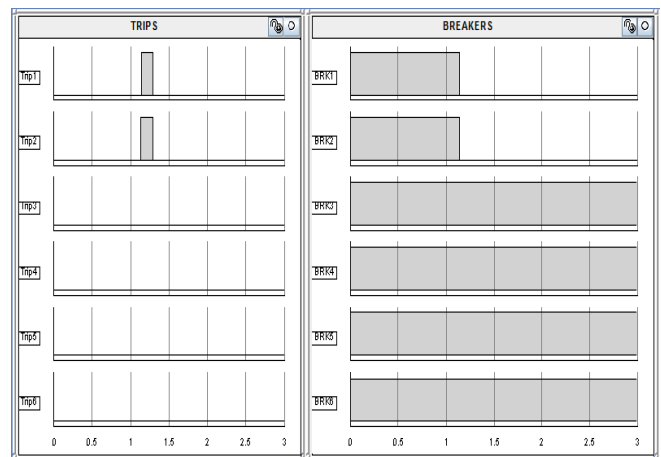


Figure 4: Trip and breaker signals for LGFLT1

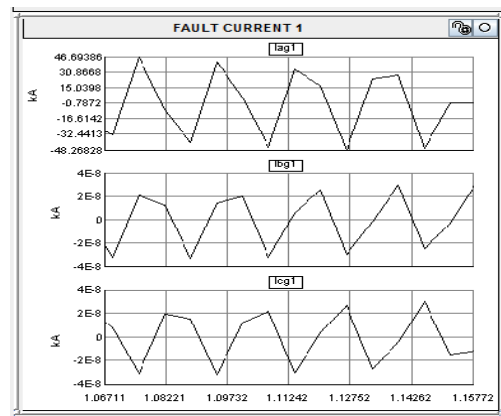


Figure 5: Fault currents for LGFLT1

Figure 5 depicts the fault currents that were obtained upon application of the first fault. It can be observed that only Iag1 is a high kA fault current, the other two phases have a 0 fault current. This shows that it was a single phase to ground fault, which was obtained by setting the fault dial to 1.

From figure 4, it can be seen the time of operation for the simulated relays is 0.49 s, this is within the 0.1 s specification. The calculated value, using the standard inverse characteristic is 0.46 s. There is a 0.03 second difference between the simulated values to the calculated; this is within the 0.5 second margin for standard inverse

non-directional time overcurrent relays. When the fault occurs on a specific interconnecting line, the relay and breakers on that line will detect the fault and trip.

6.2 Hardware relays response

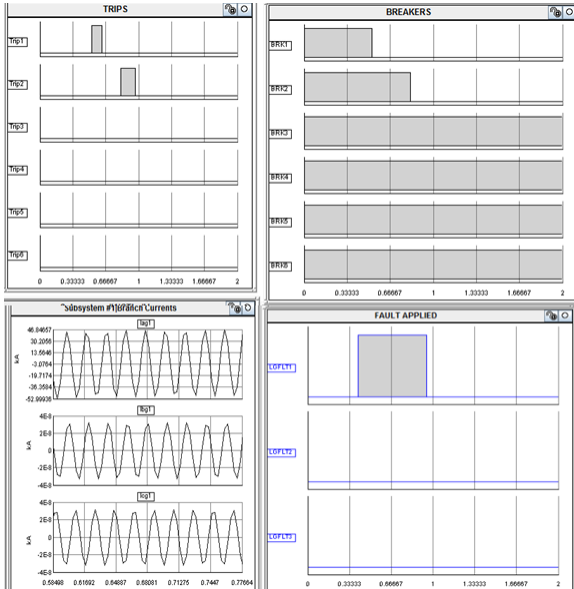


Figure 6: Hardware relay and software relay combination response

From figure 6, the hardware relay that is connected to the RTDS system trips first; this is due to the neutral overcurrent setting on the hardware relay. The software relay on the same line has to also trip as backup protection in order to isolate the fault from the loads and interconnected lines in both directions. The time of operation for the hardware relay was 0.11 s, this is due to the pick-up setting of neutral overcurrent to prevent damage to the hardware relay. The neutral overcurrent pick up settings were 0.005 A. The software relay 2 has a time of operation of 0.49 s.

6.3 Resulting conclusions

Since the software relay in the RSCAD component library is modelled after the hardware relay, it has the same features and operates exactly the same. This proves that the results that are obtained from RTDS from the software relays are a direct representation of the hardware response.

6. DISCUSSION

Standard inverse non-directional time overcurrent relays provide the best selectivity when the source impedance is less than the impedance of the protected line.

Instantaneous relays are only favoured over standard inverse time overcurrent relays in a ring main system when, there are procedures in place to decrease the flow of current in the protection lines during maintenance or

when the equipment attached onto the ring main system is "too valuable" therefore both relays trip for a much lower pick up current than the time overcurrent relay. This decreases the time of operation of the instantaneous relays.

7. CONCLUSION

The type of relay in the ring main protection system as well as the fault current and configuration determines the time of operation and the performance of the circuit.

If a mutual source is used in the ring main protection circuit, it is simpler to find the flow of current as it is predominantly straight from the source.

The fault current produced by specific faults in the circuit determines the type of relay that need to be used.

The type of relay in the circuit determines the time of operation of the relay.

Instantaneous, definite time and standard inverse relays are all suited for ring main protection depending on its operation.

If a practical, durable, reliable system needs to be built then standard inverse non directional time overcurrent relays may be used. This is due to these relays providing primary and back up protection as well as easy detection of fault currents.

8. REFERENCES

- [1] U. Bakshian and A. Bakshi. (2010). Protection of Power System.(1st Edition).[On-line]. Available: <http://books.google.co.za/booksProtection+of+Power+System+By+Uday+A.+Bakshi,+A.V.Bakshi&hl=en&sa=X&ei> [November, 10, 2014]
- [2] Institution of Electrical Engineers. (2010). Power System Protection 2: Systems and Methods. (1st Edition). [on-line], Available: <http://books.google.co.za/books?Power%20System%20Protection%20%3A%20Systems%20and%20Methods> [July. 30, 2014]
- [3] B. Lundqvist, "100 years of relay protection, the ABB relay history," *ABB Automation Products*, Sweden. November 2014.

- [4] U. Bakshi, M.V Bakshi (2006). Protection & Switchgear Engineering Protection & Switchgear Engineering. 4th ed. India: Technical Publications. Page 114-120 ISBN 8189411551.
- [5] Prabha Kundur: "Power System Stability and Control", page864 to page865, Tata McGraw-Hill, New Delhi, 1994
- [6] "Real Time Digital Simulator Power System Hardware Manual", RTDS Technologies, Winnipeg, Manitoba, Canada, January 2012

PRIME MOVER FAILURE PROTECTION FOR GENERATORS

D.N. Ngema* and A.K. Saha**

*School of Engineering, Electrical, Electronic and Computer Engineering, Howard College Campus, King George V Avenue, University of KwaZulu-Natal, Durban, South Africa, E-mail: *208528228@stu.ukzn.ac.za, **saha@ukzn.ac.za*

Abstract: The purpose of this paper is to look into loss of prime mover event as it is important to prevent any damage to turbine-generator set and protection of ac generators in case of loss of prime mover is implemented using both software and hardware relays. The simulation studies are done on real-time digital simulator in conjunction with commercial generator protection relay SEL 300G for hardware-in-loop testing. The relay settings used in this paper are according to IEEE standards for ac generators. The simulation results have been presented and analysed in the paper for both software and hardware relays.

Keywords: Prime mover failure protection, AC generator protection, real-time digital simulator (RTDS), multifunction generator relay, governor.

1. INTRODUCTION

In order to minimize disturbance on generating and distribution systems in a power system, protection schemes for each and every equipment/section are employed and configured in such a way to isolate only the affected plant area. The protection of generators is vital because the generators are very large and expensive machines that produce very high voltages and are linked with other equipment such as prime movers, excitation system, voltage regulators, cooling systems etc. In generator protection scheme individual parts of the generator are protected from various abnormal and fault conditions that might occur sooner or later [1].

There are many different types of faults that synchronous generators may experience and, therefore, many different types of protection in practical applications. These may include but not limited to: over current (51), stator ground fault (64), loss of field excitation (40), thermal overload (49) loss of prime mover (32), loss of synchronism (78), under voltage (27), overvoltage (59), negative sequence (46), voltage per hertz (24) etc. [2, 3]. For each fault type, there may be primary and backup protection applied to detect the fault and protect the generator. This paper focuses on prime mover failure on AC generators.

2. GENERATOR LOSS OF PRIME MOVER

This is classified as the loss of mechanical input, the steam flow to the turbine is interrupted by closing of the emergency stop valves or the governor valves. The remaining energy stored in the turbine-generator set is delivered to the system and the machine enters a motoring condition. The generator continues to remain synchronized with the grid, running as a motor. Once in this state, the machine draws a small amount of active power as compared to its active power rating from the grid in order to drive the turbine and meet the losses taking place in the machine keeping the machine at synchronous speed. At the same time, the machine

supplies reactive power to the grid since its excitation is intact. The magnitude of reactive power and resultant power factor for this operating condition are determined by the level of generator excitation when the loss of prime mover event occurs [2]. Running the generator in this mode is not really harmful to it but rather to a prime mover like a steam turbine. The loss of steam supply to the turbine can result in objectionable temperature rise as well as damage to the turbine blades. A reverse power relay is used to detect motoring condition of the generator. A separate reverse power relay may be used in the sequential trip logic scheme where motoring is allowed for a short time to ensure the prime mover has lost sufficient energy to prevent over speed following a turbine trip. The sensitivity and setting of the relays depend upon the type of prime mover involved [1, 2].

2.1 Turbine governor control

Turbine governor control may become an integral part of protection system to maintain acceptable system performance in the post disturbance period. The major role of the turbine governor control is to maintain proper speed regulation and load division for the generating units on the power system. Two types of controls are generally used depending on the units operation and control requirements: droop and frequency or isochronous (constant speed). Droop (speed/load) control behaves with a characteristic such that with increase in load speed decreases following a linear relationship. With synchronous machines, their operation is locked at system frequency. Therefore, the droop governor becomes a load controller. As load increases, the governor signals the governor valves to open to maintain the established speed setting and accommodate the additional system load. Governor droop control prevents one generator from trying to pick up the entire additional load. Important benefits are the load change being shared among units and better overall system stability [4]. In this paper the IEEE Type 1 turbine/ governor control is used in conjunction with IEEE type AC4 excitation system and

IEEE type 2 power system stabilizer which is a dual input stabilizer with bus voltage based output limiter [3].

2.2 RTDS/ RSCAD

Figure 1 shows the RTDS configuration used for the prime mover failure study. A real time digital simulator is a power system tool which provides facilities for simulations that takes place in real-time. Further, physical equipment such as relays, generator controls etc. can also be connected to a real-time simulator and tested before use on a real system and to observe the performance of the system and its components [6].

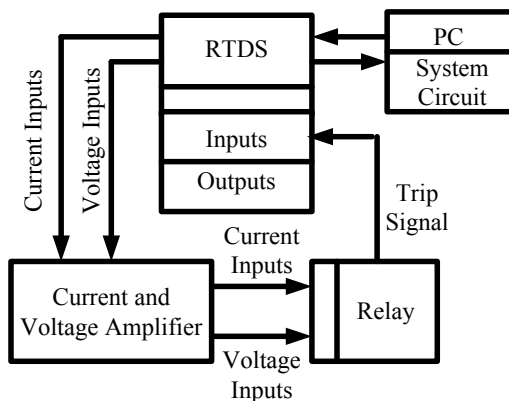


Figure 1: RTDS connection diagram [5]

The RSCAD software is used to build and compile models of a power system to be simulated using RTDS. It is the interface between the user and the simulator. System models are built in the sub-program DRAFT and monitored in another sub-program RUNTIME. Due to the accuracy of this simulator and the ability of it to interact with real equipment, control and power systems can be designed, modelled and tested realistically. The system is modelled on RSCAD and simulated on RTDS [3].

2.3 RSCAD software relay

The multi-function generator software relay is suitable for providing the protection function and has been in use on commercial synchronous machines. Differential elements for phase and neutral currents, 100% stator protection, loss of field protection, out-of-step, prime mover failure and other additional relay elements provide comprehensive protection for the generator in a multi-function generator protection relay. The relay provides an output trip signal used to control circuit breakers in a system in case of a fault of any type. There is a special output signal Info 1 in the software relay which has 32 relay word bit signals that enable the user to identify which relay has operated [3].

2.4 Hardware relay SEL 300G

The SEL 300G multifunction generator relay is used in the protection study and implementation of generator protection against prime mover failure. The primary

reason for hardware implementation using this relay is to verify the results found from the software simulation studies. The SEL-300G receives currents and voltage inputs at standard levels through protection transformers to provide suitable protection for generators. The relay front panel has LCD display showing all the metering and setting quantities and LEDs representing each protection element which in case of a fault will turn on as an indication.

3. SYSTEM UNDER STUDY

This paper uses a power system network rated at 1110 MVA, operating at 24 kV line-to-line voltage connected to an infinite bus through a step-up transformer and 400 kV transmission lines as shown in Figure 2 [7]. The generator is equipped with IEEE governor, exciter and power system stabilizer to ensure that the generator functions in a way that imitates the generator in power generating station.

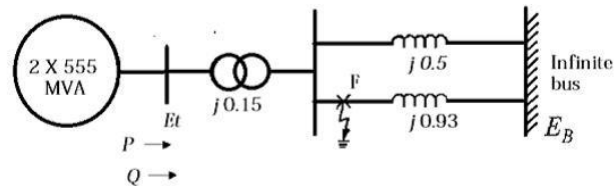


Figure 2: System under study [7]

4. PRIME MOVER FAILURE IMPLEMENTATION USING SOFTWARE RELAY

Two elements (32P1 and 32P2) are used to provide more or less sensitivity to reverse or low power flow in case of loss of prime mover. The relay calculates the instantaneous value of power from the phase connected current and voltage transformers and uses this value of power for the protection elements [3]. The instantaneous value of power is continuously compared to the setting thresholds.

4.1 Prime mover failure implementation

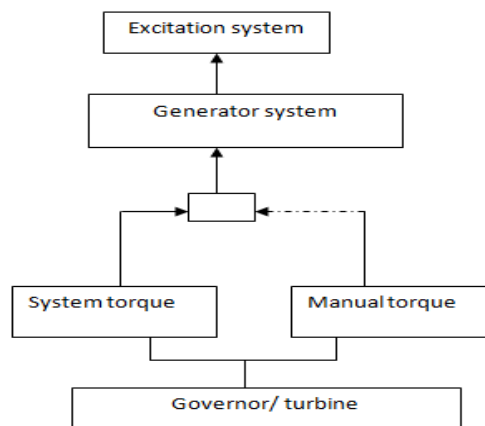


Figure 3: Prime mover failure implementation

Figure 3 is a simple block diagram showing the implementation of prime mover on RSCAD. The generator system is equipped with excitation and governor/turbine control. To implement prime mover failure, the torque of the system network is control manually through a switch. On normal operation the generator receives system torque (mechanical) from the governor. When switched to manual torque control, the mechanical torque from the governor to the generator is controlled there by reducing it to value less than the relay threshold setting, with this setup the prime mover is removed and therefore the relay operates to mitigate the consequences of such disturbance.

4.2 Relay settings

The RSCAD software relay has bit 18 inside info1 as the loss of prime mover trip signal. If this bit is set during the implementation of loss of prime mover, it means prime mover failure was detected. Steam turbine and hydro turbine units require small amounts of reverse power to spin the unit at synchronous speed with no prime mover. Typical values of reverse power are shown in percentage of nameplate ratings.

- Steam turbines, condensing types: 1–3%
- Steam turbines, noncondensing types: 3+%
- Hydro turbines: 0.2 – 2+%
- Gas turbines: 50+%

Ideally, the time delay can be set between 20.0 to 30.0 seconds to prevent tripping during machine paralleling operations and for this demonstration, a time delay of 20 s is chosen and a 0.7 to 0.5 multiplier offers secure detection of motoring conditions as low as 0.02 per unit [2]. In this study, 0.7 is used.

4.3 Software simulation results

The system is run and tested for stability before the element could be tested. Initially, the generator is operated at normal operating condition supplying 0.9 p.u. of active power, 0.436 p.u. of reactive power as shown in Figure 4. Mechanical torque supplied by the turbine in this operating condition found to be 0.9063 p.u. and terminal voltage of the machine is kept at rated voltage of 1 p.u. which are illustrated in Figure 4.

As the generator is running under normal operating condition, the generator breaker is found to be closed (level 1) as shown in Figure 5 with no trip signal from the relay. It is expected that during the loss of prime mover, the breaker status make a transition from high (1) to low (0) which implies opening so as to isolate the system before any further damages could happen.

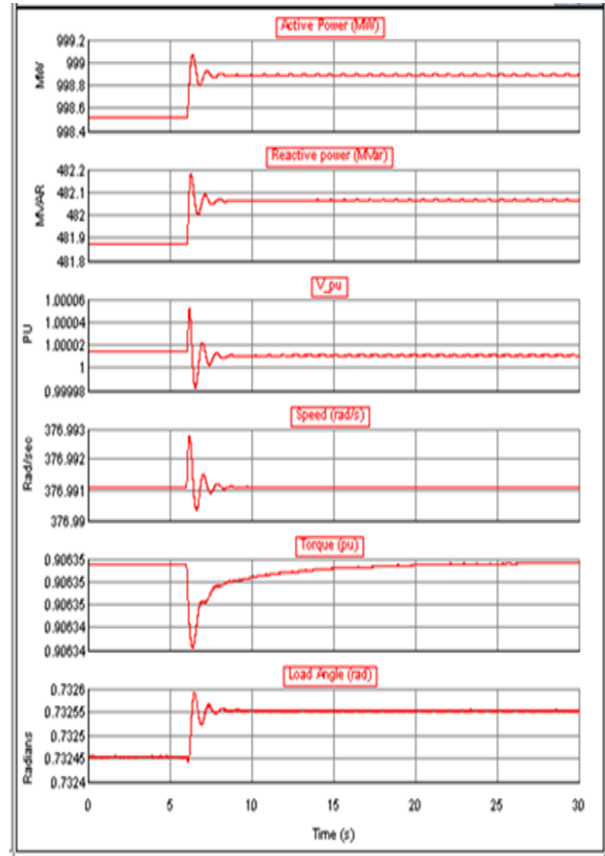


Figure 4: System prior to loss of prime mover

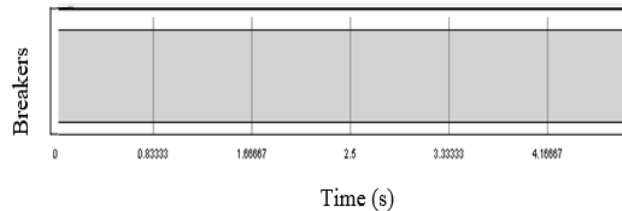


Figure 5: breaker status prior prime mover failure

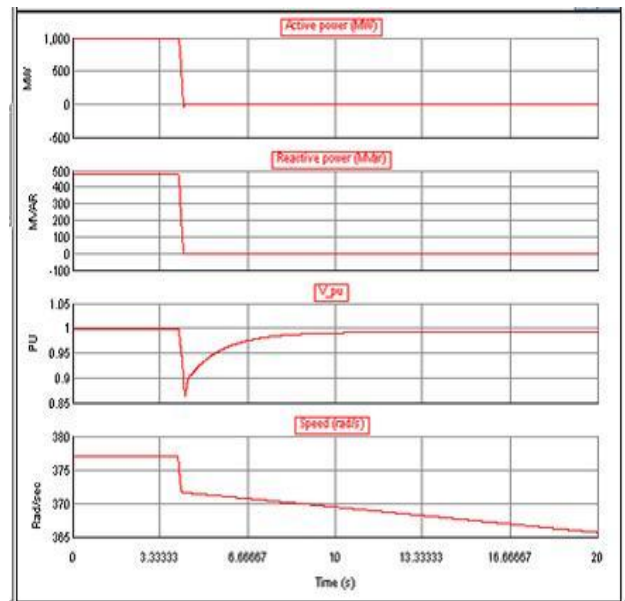


Figure 6: System behaviour after loss of prime mover

Figure 6 illustrates that when the prime mover is cut off from the system, the active power is reduced. As the active power reduces, it eventually reaches a point where the generator behaves like a synchronous motor drawing power from the grid instead of producing power. The field circuit is unaffected by the loss of the prime mover and as a result the terminal voltage remains unchanged straightway following the power reversal implying that the excitation of the system is stable. A significant reduction in frequency results in a decrease in speed, this is due to the fall of torque to values below that required to keep the machine spinning at a speed that is proportional to the grid frequency.

As the loss prime mover is detected by the relay, bit 18 of Info 1 inside the relay made a transition from 0 to 1 as shown in Figure 7, thereby, setting the relevant bit representing prime mover failure element. The bit is set at the same time as when the prime mover failure was detected by the relay.

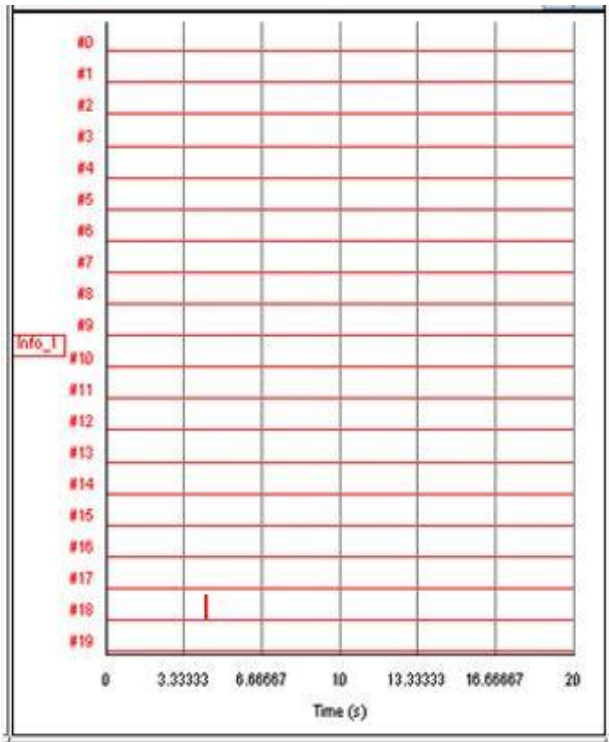


Figure 7: Bit trip signal

Under normal operating conditions, the trip signal is at zero and when the mechanical torque of the system is reduced below the relay setting threshold, the relay sends a trip command to open the circuit breaker and isolate the system. This is illustrated in Figure 8, immediately when the trip signal makes a transition from 0 to 1, the breaker opens (transition from 1 to 0) as expected.

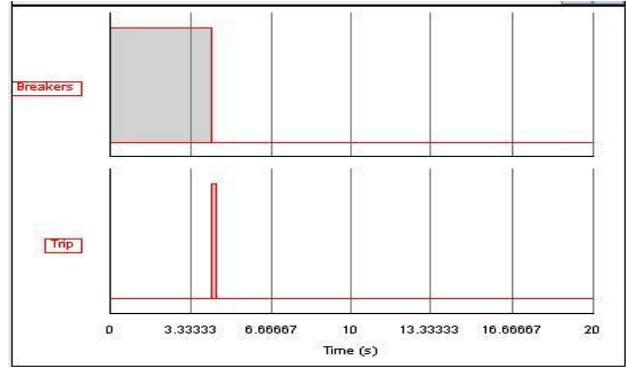


Figure 8: Breaker and trip signals

5. PRIME MOVER FAILURE IMPLEMENTATION USING HARDWARE RELAY

Anti-motoring protection in the SEL-300G is provided by a reverse/low-forward power element. This element measures the real-power flow from the generator. If the generator real-power output drops below the settings threshold, the relay operates [3]. Two reverse-power thresholds are provided but only level 1 is used in this paper.

The relay settings for this element are the same as the software relay. The idea is to verify the theoretical predictions as well as the software relay results. The same procedure is followed before testing the element on hardware. The relay is ensured to be operating at steady conditions imitating the normal operating conditions in actual power generating stations. Figure 9 shows the system parameters when the system was running under normal condition. The active and reactive power are found to be at their rated values as well as the primary current of the machine.



Figure 9: System under normal operation (SEL 300G)

Following the same procedure, the mechanical torque of the system was reduced to a value less than the pickup setting of the relay and change of active and reactive powers are illustrated in Figure 10. At that point failure of

prime mover was detected by the relay and a trip command was sent from the relay to open the circuit breaker and isolate the generator as shown in Figure 11.

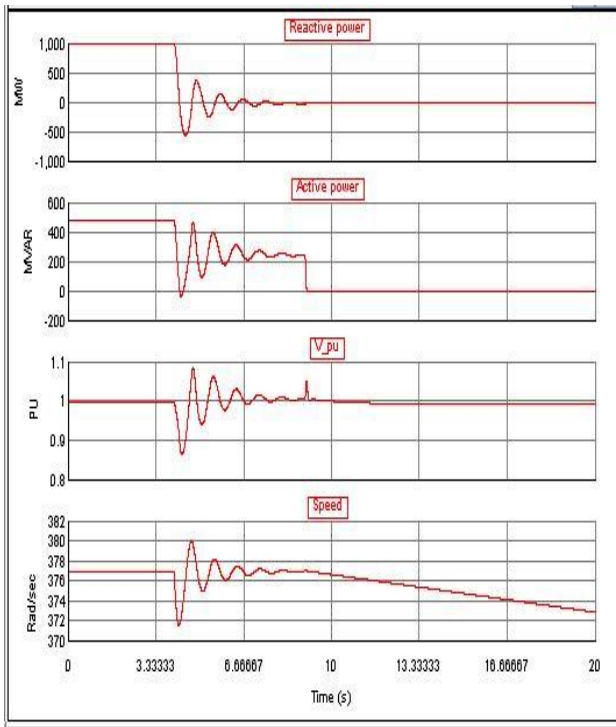


Figure 10: System behaviour after prime mover failure

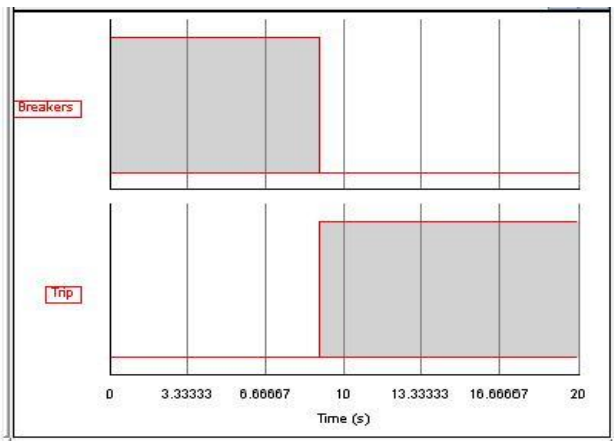


Figure 11: Circuit breaker and trip signals



Figure 12: Hardware relay operation

When the hardware relay is used to test prime mover failure, element 32 LED came on (Figure 12) to prove that prime mover failure was detected. In both software

and hardware relays, the relay operation can be shown by a trip and circuit breaker operation. When prime mover failure is detected by the relay, a trip command is sent and a circuit breaker opens to isolate the system before any damage can happen.

6. CONCLUSION

The paper examines causes of prime mover failure on ac generators, prime mover effects on the generators and protection scheme employed for prime mover failure. RSCAD software and RTDS are used to implement prime mover failure protection study. The results obtained using software relay were verified using the hardware relay and it can be concluded that the theoretical predictions were observed during the implementation of this fault condition and from that adequate protection was implemented and tested. The primary objective for this study is to provide learning opportunities as well as to promote the usage of RTDS in any power system especially, generator protection studies.

7. REFERENCES

- [1] U.A. Bakshi, and A.V. Bhakshi, "Protection and switch gear protection", *Technical publications*, pp. 114-120, ISBN 8189411551, 2006.
- [2] Power Systems Relaying Committee: "IEEE guide for AC generator protections – C37.102™ - 2006", IEEE Power Engineering Society, IEEE, 3 Park Avenue, New York, NY, 10016-5997, USA, pp. 1-177, November 2006.
- [3] RTDS: "Manual Set", *Real Time Digital Simulation*, pp. 1-517, November 2006.
- [4] Working Group J6 of the Rotating Machinery Protection Subcommittee, Power System Relaying Committee: "Performance of generator protection during major system disturbances", *IEEE Transactions on Power Delivery*, vol. 19, no. 4, pp. 1650-1662, October 2004.
- [5] A.K. Saha: "Simulation study of generator under-voltage and over-voltage protection", submitted for *Southern African Universities Power Engineering Conference*, 2015.
- [6] RTDS, Applications, closed-loop testing of physical devices, <http://www.rtds.com/applications/closed-loop-testing/closed-loop-testing.html>
- [7] P. Kundur: "Power system stability and control", *Electric Power Research Institute*, McGraw-Hill, Inc., New York, ISBN-13:978-0-07-035958-1.

STABILITY ENHANCEMENT OF HVAC NETWORKS USING HVDC LINKS

S M'builu Ives*, A Edwards*, AG Swanson**, and N Parus* & ***

*Eskom Holdings SOC Limited, Group Technology Engineering, South Africa E-mail: mbuilus@eskom.co.za.

** Discipline of Electrical, Electronic and Computer Engineering, School of Engineering, University of KwaZulu Natal, Durban.

*** School of Electrical and Information Engineering, University of the Witwatersrand, Johannesburg.

Abstract: This paper considers the basic principles of small signal stability and demonstrates the effect of using High Voltage Direct Current (HVDC) transmission to improve power system dynamic performance through case studies using DigSILENT PowerFactory. A four generator, two area AC network was developed showing the impact of the HVDC link on improving system stability. The damping ratios and the electro-mechanical oscillation modes, with emphasis on the inter-area mode, are presented for the different case studies. The results indicate that the damping ratio improved with the integration of the LCC HVDC link. The time domain simulations with faults introduced on the AC tie line demonstrate the improvement of recovery time of the active power. The results of this study indicate that parallel HVDC links could be used to improve dynamic system performance.

Keywords: LCC, Stability, PSS, SVC, POD, Surge Impedance loading, HVDC, Power angle, firing angle, Extinction angle

1. INTRODUCTION

It is known that the alternating current (ac) networks have various modes of oscillations due to the many interactions of different power system components [1]. The cumulative masses of the generator rotor swings, relative to one another, create small signal oscillations. The excitation of the inter area mode oscillations can cause the system to become unstable and lead to black-outs if their protection schemes operate.

Published literature indicates that High Voltage Direct Current (HVDC) links may be used to enhance power system stability. Due to the various benefits, Eskom is studying the impact of implementing more HVDC schemes in various areas of the country. Apart from bulk power transmission the added advantage of network stability enhancement and fault current limiting further contributes to the techno-economic feasibility.

This study investigates the use of HVDC to enhance small signal stability and presents the initial research. A two area ac network with an embedded Line Commutated Converter (LCC) HVDC link has been developed using DigSILENT PowerFactory and validated against literature [1]. The oscillation mode of interest is the inter-area mode to verify if HVDC can be used to enhance system stability of a two area network.

2. METHODOLOGY

The research methodology adopted for this study is as follows:

- A two area ac network as per [1] was designed and implemented,
- The performance specifications of this network were established by detailed modelling and represent the base case. The studies involved time domain fault analysis and modal analysis using the eigenvalue technique,
- A third parallel AC link was implemented and the change in damping was noted,
- The third ac link was replaced with a new HVDC link and the changes in damping were studied. This study also involved time domain fault analysis and modal analysis using the eigenvalue technique. A three phase fault was introduced and cleared in order to move the system out of steady state operating condition causing the rotors in the two areas to exchange the excess energy generated by the fault.

3. BACKGROUND

3.1 Stability and power system control

Stability of power system refers to the ability of the system to operate in a state of equilibrium under normal operating conditions. In the event of a disturbance, the system should return to a state of equilibrium within a specified time [1]. Stability in power systems is related to a condition where all the generators remain in synchronism with each other. Power systems are continually subjected to perturbations such as switching of transmission lines or loads and faults at different points on the system. The type of perturbation sub-divides stability into two categories, namely transient stability and steady state stability [2].

Power system control has a significant effect on the dynamic performance of the system after a disturbance therefore the dynamic performance of a system can be classified into [4]:

- Transient stability: the rotor angle instability after a major disturbance.
- Voltage stability: ability to maintain acceptable voltage levels leading to lack of reactive power.
- Frequency stability: Large deficits in generation and load resulting in large frequency excursions.
- Small signal stability: insufficient damping on rotor oscillations after a small disturbance.

3.2 Small signal stability

Small signal instability can exist after a loss of an interconnection resulting in rotor oscillations. Inter-area oscillation may occur where there are two areas of great inertia with a weak interconnection. In large power systems small signal stability problems may be either local or global in nature. The local problem is associated with oscillations between the rotors of a few generators close to each other (local mode) and the frequency of the mode of oscillation can be in the range from 0.7 to 2.0 Hz [1]. The global small signal stability problem is associated with a group of rotors in one area swinging against a group of generators in another area (inter-area mode) and the frequency of this mode of oscillation can be in the range from 0.1 to 0.7 Hz [1].

Small signal stability analysis is based on the eigenvalue technique which shows the small signal behaviour of the power system. This technique is used to investigate the problems related to oscillations with regard to their mode shape and relationship with different modes [2].

3.3 Mitigation of small signal instability

Devices that may be used for economic design and improvement of system stability without compromising system performance include Static VAR Compensator (SVC), Power System Stabiliser (PSS) and HVDC [1].

3.3.1 Static VAR Compensator with supplementary control

SVC has the ability to influence the voltage profile of a power system thus affecting the reactive and active power [2]. By accurately controlling the voltage and the reactive power, the SVC can enhance power system stability. The primary mode of operation is voltage regulation which improves transient and voltage stability. The SVC contribution to damping of system oscillation is however small and a supplementary control (or Power Oscillating Damper (POD)) is needed to achieve significant damping. The location of the SVC depends on the input signals used and the controller design [1]. The input signals used for the supplementary control must be responsive to the modes of oscillations to be damped.

This can be determined by the residues and observabilities of various input signal for both pre-fault and post-fault conditions [1].

3.3.2 Power System Stabilisers

The PSS function is to add damping to the generator's rotor oscillations. This is achieved by modulating the generator's excitation thus developing a component of electrical torque in phase with the rotor speed deviations [1]. Power system stabilisers are inexpensive and simple in design and can be the most effective power system damping controllers if setup correctly. Set up consists of two processes which include off-line analysis and on-line commissioning of the PSS.

The off-line analysis is essential because it is extremely difficult to simulate inter-area oscillations on line and the on-line commissioning is to determine if the models used for off-line analysis are accurate. The PSS must have phase lead requirements which are easily defined. The PSS phase lead characteristics are chosen to eliminate the lag between PSS input into the exciter and the generator rotor electrical torque with the generator at constant speed [2].

The performance of a PSS with regard to local modes is influenced slightly by the location of the PSS and the characteristics of the load. The PSS does however damp inter-area oscillations significantly by modulating the system loads. It is therefore evident that the mechanisms in which the PSS adds damping to local and inter-area modes are different [11].

3.3.3 HVDC links with supplementary control

Basic operation of the LCC HVDC: HVDC bridges convert ac power into dc power at the rectifier terminal and the inverse at the inverter terminal to allow power flow to the ac network. The advanced controls keep the direct voltage at specific levels for the transfer of power from or into the ac grid. The setting of the firing angle determines the size and polarity of the direct output voltage after rectification. The rectifier's output voltage differs to the inverter's input voltage due to a volt drop caused by the resistance of the transmission line [6].

HVDC control benefits: The HVDC control is the heart of the HVDC scheme as it is fast acting with controlled dynamics. HVDC control is more advanced than an AC system such as the control of electrical generators [6]. The correct design of HVDC control allows the fast acting control system to assist the weak ac network to recover from faults and as such avoiding voltage instability or voltage collapse as well as optimising the power flows within the network. The control requirement for HVDC power transmission related to control functionality is determined from the HVDC system objectives and varies between different projects. The control requirements include the following attributes [6]:

- Flexibility in the control of power,
- Fast control response,
- Stability under all operating conditions,
- Good transient recovery,
- Promotion of AC system performance,
- Robustness in the AC system events,
- Maintaining symmetrical valve firing in the steady state,
- Prevention of repetitive commutation failure in inverters,
- Reactive power control.

Power control using a Power Oscillating Damper: Damping of power oscillations can be achieved by using the ability of the HVDC scheme to control the active power accurately and fast. The HVDC link can be controlled by rapidly ramping the dc power down to reduce generation or load unbalance of the ac system on both sides. It can rapidly ramp up power through its overloading capabilities which can be used to assist to improve system stability [2]. A power oscillation damper, POD, can be used as a supplement control to modulate the HVDC power transmission to provide damping to the low frequency power oscillations. Power modulation function derives a measurement of the power oscillation in the connected ac system from the ac bus waveforms such as frequency and phase angle but the active power for the effective generator is the input signal selected in Figure 1.

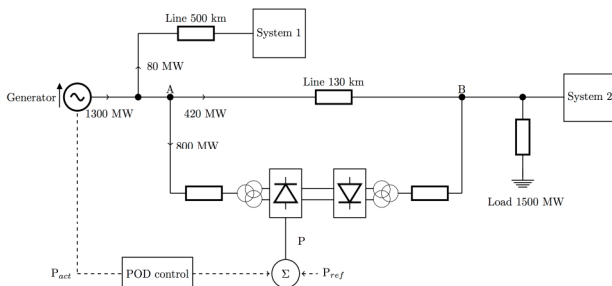


Figure 1: Test system for damping power oscillation using HVDC POD control [2].

In Figure 1, if a fault is applied on line A-B, the HVDC keeps its scheduled power without any additional measures introduced, and the power oscillation depends on the natural system damping. The gain and the phase angle as well as the limits are added to the system configuration and the output signal is the reference of the power controller. It is then emphasised that increased system damping can be introduced by the appropriate power modulation of a parallel HVDC link [2].

4. CHARACTERISTICS OF THE STUDY SYSTEM

4.1 The Two Area System Network

The network consists of two similar areas connected by weak parallel ac ties, as shown in Figure 2. Each area

consists of a set of coupled generator units, each having a rating of 900 MVA [1]. The generators, transformers and transmission system parameters are found in reference [1].

The system operating within area 1, exporting 400 MW to area 2 are electrically loaded according to reference [1]. The generators are equipped with an IEEE type DC1A DC excitation system model [1]. The loads of areas 1 (L_7) and 2 (L_9) are 976 MW and 1767 MW respectively.

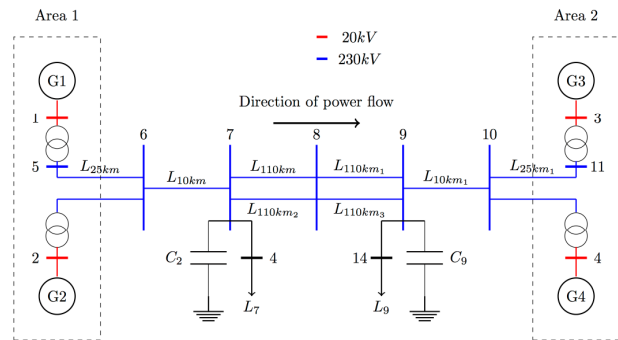


Figure 2: Two Area Network [1]

The load flow and eigenvalue analysis of the power system were performed where the inter-area and local modes were identified. Observability (mode shape) provides an indication of which generators are oscillating with each other. The state variable chosen is speed as it allows for identification of which generators are participating in the oscillatory modes. Their mode shapes as seen in Figure 3 a-c, show the eigenvector component corresponding to the rotor speeds of the four machines. The observability of the system exhibits three rotor angle modes of oscillations:

- Figure 3a shows that the inter area mode, with a frequency of 0.48 Hz, the generators G1 and G2 swinging against generators G3 and G4.
- In Figure 3b,c, the two local modes, with frequencies of 0.97 Hz and 0.99 Hz, as well as the G1 swing against G2 and G3 swing against G4 are evident.

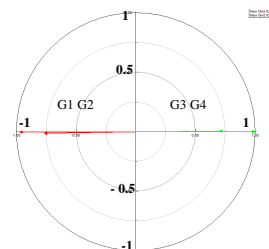
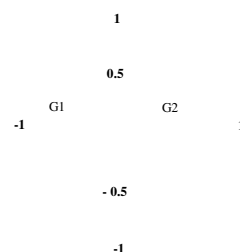


Figure 3 a: Mode shapes of generator speeds for the Two Area System (with an AVR) – Inter-area mode



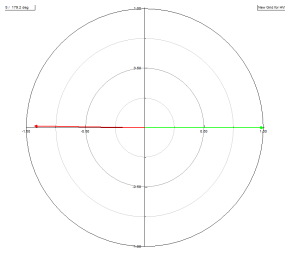


Figure 3 b: Mode shapes of generator speeds for the Two area system (with an AVR) – Local mode G1/G2

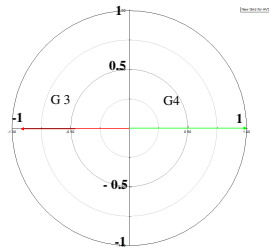


Figure 3 c: Mode shapes of generator speeds for the Two Area System (with an AVR) - Local mode G3/G4

Table 1: Damping ratios and Frequencies for Local and Inter-area mode (with an AVR)

Damped Frequency Hz	Damping Ratio	Mode shape
0.98889430402	0.093505871594	Local mode G3/G4
0.98889430402	0.093505871594	
0.96142066612	0.093978606936	Local mode G1/G2
0.96142066612	0.093978606936	
0.48374478077	0.025641683049	G1G2/G3G4 Inter Area mode
0.48374478077	0.025641683049	

Modes with a damping ratio of less than 3% can be accepted but with caution as it may lead to instability **Error! Reference source not found.** It is evident that the inter-area mode has poor damping of 2.5% as seen in Table 1. The local modes have significant positive damping of 9% which make those local modes more stable compared to the inter-area mode. A damping ratio of 5% means that in three oscillation periods, the amplitude is damped to about 37% of its initial value. The minimum acceptable level of damping is not clearly known but a damping ratio which is negative causes the mode to become unstable [1].

4.2 The LCC HVDC Model

The first Cigré LCC HVDC benchmark model as shown in Figure 4 was used. The model represents a monopolar 500 kV, 400 MW HVDC link with 12-pulse converters at both rectifier and inverter ends [3]. The DC side consists of smoothing reactors and a T-network equivalent of the DC transmission line. The DC line parameters could represent either a cable [5] or a monopolar equivalent of a bipolar overhead line [7]. The system parameters are shown in Figure 2 [5] although some changes in the filter parameters were proposed by

the Cigré at a later stage [7]. Further details of the converters, AC and DC sides are provided in [5, 7-9].

A generic primary control for LCC HVDC links was used here. Under normal condition the rectifier end operates in constant current control mode while the inverter controls the voltage/extinction angle. The roles could reverse under abnormal operating condition such as a fault on the rectifier bus. The current order is derived from the power order using the measured DC link voltage. A 10-15% margin is set between the current orders at the rectifier and inverter ends. Voltage dependent current order limit (VDCOL) is enabled to reduce with the current order under a drop in voltage conditions to prevent a run-away situation. The firing angle at the rectifier end was limited between 5° and 150° to allow reliable turn on of the valves and allow a change of mode i.e. inversion mode to clear faults in the DC link. At the inverter end, the firing angle was limited between 110° and 170° to reduce the possibility of commutation failure and avoid accidental switch over to rectification mode [1].

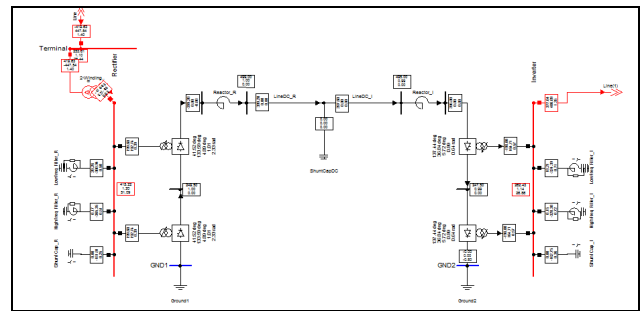


Figure 4: Cigré Benchmark Model for LCC HVDC

5. RESULTS AND DISCUSSION

Non-linear time domain simulations were performed to validate the dynamic response when a self-clearing fault is applied for a duration of 0.1 s on one of the tie lines connecting buses 8 and 9 (inverter end) for the following cases:

- The two area test system
- A third parallel ac tie line
- Embedded HVDC link

5.1 Case 1: A third AC line in parallel with the ac tie line connecting bus 7 and 9

The more lines that are connected in parallel reduce the Surge Impedance Loading (SIL) of the network. However, an AC line with specific power loading is connected between bus 7 and bus 9 to analyse the system behaviour. The three mode shapes that are seen in Table 1 are present in all the cases scenarios as seen in Table 2 but with different damped frequencies, however, this case study shows a damping ratio of 3.2% which is an improvement from the two area network. It is then noted that the power angle decreases as the load is distributed across all the transmission lines thus improving the damping ratio faintly.

Table 2: Damping ratios and frequencies for local and inter-area modes for Case 1.

Damped Frequency	Damping Ratio	Mode shape
Hz		Local mode G3/G4
0.99571558812	0.091537474825	
0.99571558812	0.091537474825	Local mode G1/G2
0.9664752374	0.092335641644	
0.9664752374	0.092335641644	G1G2/G3G4 Inter Area mode
0.5776000418	0.031778784573	
0.5776000418	0.031778784573	

The nonlinear simulation shows that the AC line experienced oscillations and the active power recovered after 30.4 s which is longer compared to Case 4, correlating the smaller damping ratio as seen in the modal analysis. It can be seen in Figure 5b that the additional AC line also is affected by fault with a sudden reduction in active power and generated oscillations which stabilises with the system natural damping.

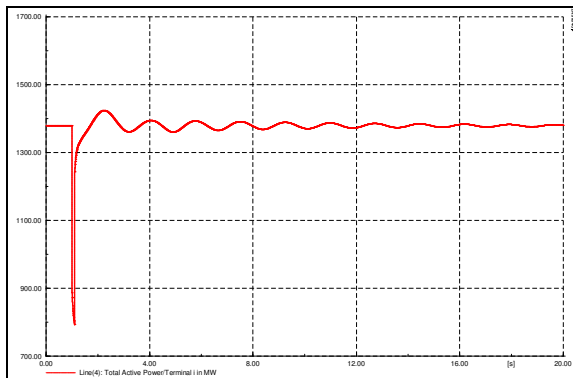


Figure 5 a: Time domain response of a fault for Case 1

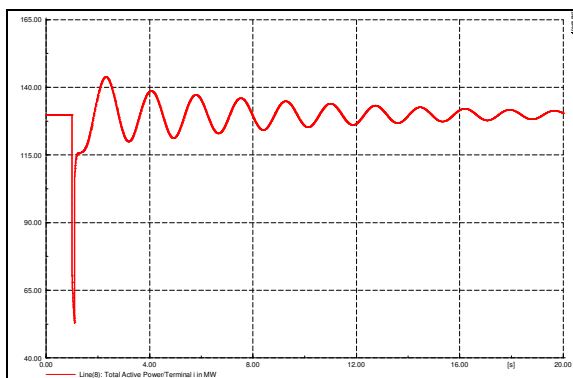


Figure 5 b: Time domain response of a fault for Case 1

5.2 Case 2: LCC HVDC integrated on the Network

The LCC HVDC link was integrated in the two area network -between bus 7 and bus 9 as shown in Figure 6. The modal analysis and simulation results are validated against certain parameters (e.g. for filters, capacitors, etc.) Some adjustments are made to adjust the power loading of the HVDC link rating to 0.45 A (to transmit 200MW). An LCC HVDC link is separately introduced

into the AC system in parallel with the AC corridor connecting the two areas in the power system.

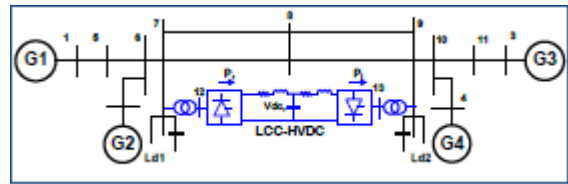


Figure 6: Two Area Network embedded with the LCC HVDC link [12]

Table 3: Damping ratios and frequencies for Local and Inter-area mode for Case 2

Damped Frequency	Damping Ratio	Mode shape
Hz		Local mode G3/G4
1.0492650868	0.058752627773	
1.0492650868	0.058752627773	Local mode G1/G2
1.0284085198	0.059550201582	
1.0284085198	0.059550201582	G1G2/G3G4 Inter Area mode
0.55948552244	0.049658546374	
0.55948552244	0.049658546374	

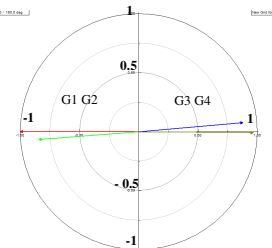


Figure 7 a: Mode shapes of generator speeds for Case 2 – Inter-area mode

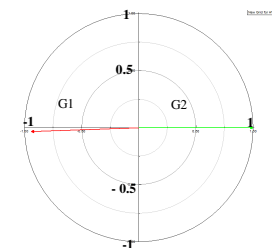


Figure 7 b: Mode shapes of generator speeds for Case 2 – Local mode G1/G2

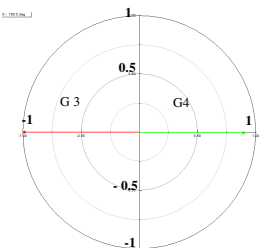


Figure 7 c: Mode shapes of generator speeds for Case 2 – Local mode G3/G4

The modal analysis was performed and the three mode shapes are also identified but at different damped frequencies. The local modes now represent a reduced

damping ratio of 6% and 5% respectively while the inter-area mode represent an improved damping of 5% as seen in Table 2. The mode shape is visible for all three oscillation modes as seen in Figures 7a,b,c. The integration of the HVDC link has increased the damping ratio of the inter-area mode as the AC tie lines are left to carry only 200 MW (instead of 400 MW) while HVDC link carries the other 200 MW. With a decrease in power over the AC tie line, the power angle across the corridor decreases which results in an increase in synchronising torque coefficient and therefore the frequency of oscillation [1].

If the network was heavily loaded, the inter-area mode will become unstable and the HVDC link will relieve the ac tie lines from carrying more power thus stabilising the inter area-mode. Changing the loading conditions has little impact on the local modes as they are faintly affected by line power flow [12].

5.3 Case 3: Fault on the Two Area Network without LCC HVDC link in the Time domain

Time domain results are effective in confirming small signal analysis results and it also shows how the system nonlinearities affect the mode of oscillations [2]. A three phase short circuit fault is simulated on the AC tie line connecting buses 8 and 9 for the duration of 0.1 s. It is monitored for 40 s to capture the damping of the power oscillation for the post-fault condition and pre-fault condition as shown in Figure 8.

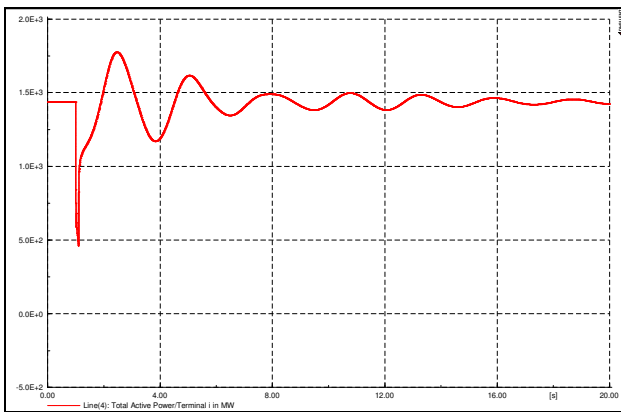


Figure 8: Time domain response for Case 3.

The active power at line 4 between bus 6 and 7 is monitored for the dynamic response of the fault on the system stability. The voltage and current network mode shape angles are not identical but the differences observed in the numerically computed solutions using algorithms arise as a result of the fact that the response of the network to a fault is directed by how long the fault acts on the network and the location of the fault within the network. These factors have an influence on the phase characteristics of the network because they directly impact the fault impedance and network stability. The system stabilised after a period of approximately 33.7 s and this is indicative of the system's natural damping.

5.4 Case 4: Fault on Case 2 Network in the Time domain with the LCC HVDC link connected between bus 7 and 9.

The case 1 network layout was used with the same fault and in the same location, i.e. midway along the line. Figure 9 indicates the results of this study.

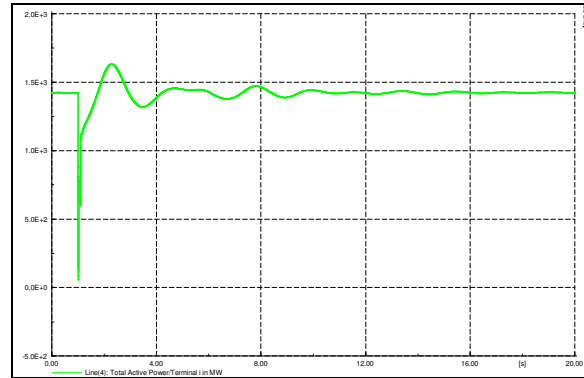


Figure 9: Time domain response of a fault for Case 4.

The active power did spike for the duration of the fault but the damping ratio was higher therefore the active power recovered quicker when compared with Case 3. The recovery time for the post fault condition was shortened to 19.5 s which correlates with the increased damping ratio as seen in Table 3.

The control action as seen in the responses is very fast and aims to maintain the accuracy of the controlled variable i.e. constant dc current and constant extinction angle. The presence of poorly damped inter-area mode is evident from the angular separation between G1 and G3 and the power flow in the line connecting buses 9 and 10 as seen Figure 10a. As seen in Figure 10c, the LCC HVDC link voltage drops sharply during the fault due to the reduction in inverter end AC voltage. With regard to inter-area oscillations as seen in Figure 10e, the rectifier switches between constant current and constant firing angle control and the power through the DC link drops during the fault as anticipated. The inverter moves to constant extinction angle control which is the measure of gamma, this is basically the period when the thyristor valve voltage is negative. As seen in Figure 10f, the gamma control element increases sharply during a fault but the controller reduces the value of gamma and operates in minimum extinction angle control thus reducing reactive power consumption and assisting in improving stability [12].

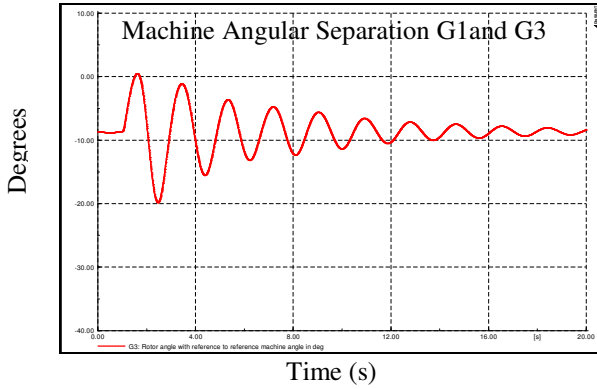


Figure 10 a Time domain response of the Rotor angle displacement when a fault is applied (with Reference slack bus G1)

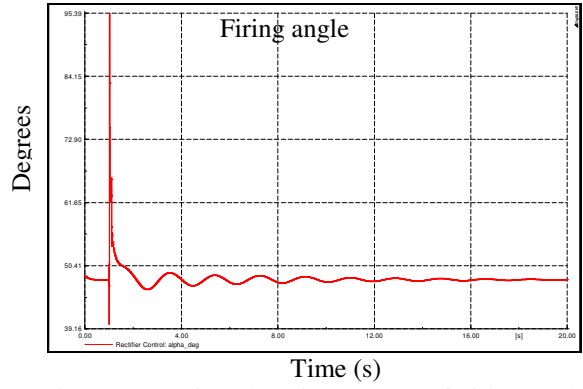


Figure 10 e: Time domain response of Firing angle

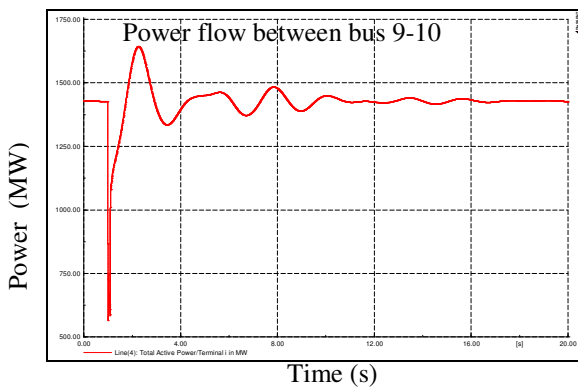


Figure 10 b: Time domain response of Active Power between buses 6-7

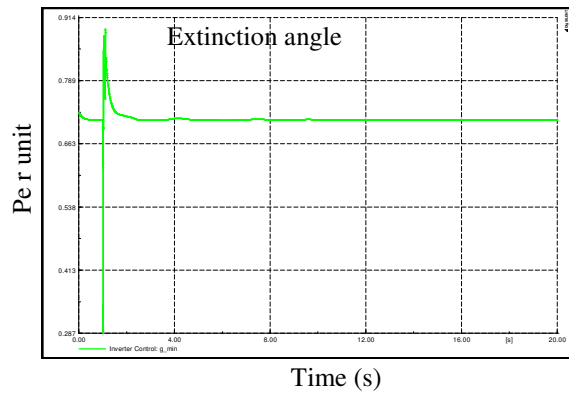


Figure 10 f: Time domain response of Extinction angle

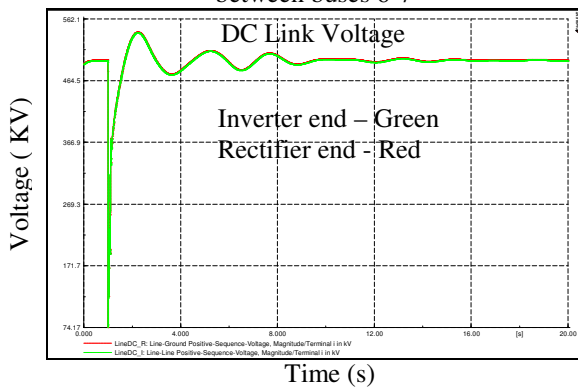


Figure 10 c: Time domain response of DC link Voltage

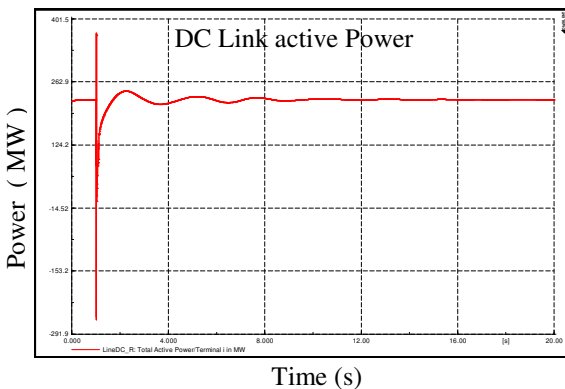


Figure 10 d: Time domain response of DC Link Active Power

5.5 Comparison of the Case study 3 and Case study 4

Figure 11 shows a comparison of the active power swing responses in Case 3 and 4 clearly, the behaviour of the active power and the rate of decay of the oscillations after the fault condition are visible. Case 3 which is red indicates the power swing with no HVDC link integrated and Case 4 which is green in colour indicates the power swing with an LCC HVDC connected. It can be clearly seen that the HVDC link enhanced the stability of the Network with the introduction of damping.

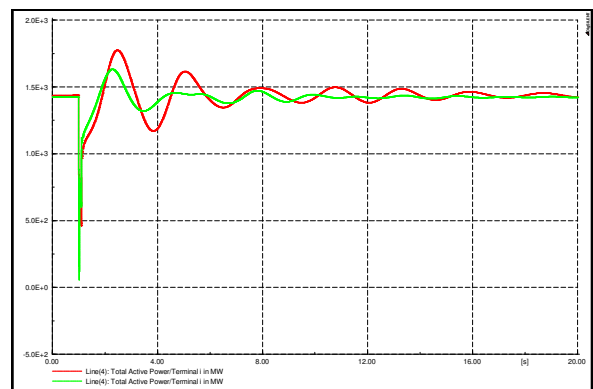


Figure 11: Time domain response of cases 2 and 3

6. CONCLUSION

This paper presented a power system modelling study of a two area AC network with an imbedded LCC HVDC scheme. The work was done in order to study the validity

of published literature with regard to power system stability enhancement through the use of parallel HVDC connections.

The results obtained were consistent and in good agreement with various literature. Although the two area AC network modified with an additional AC line (in place of the LCC HVDC link) became more stable with a slight increase in the damping ratio of the inter-area mode, the value was not large enough to contribute significantly to system stability. This slight increase in damping ratio is due to the fact that the additional AC tie results in a 'stronger' network and the power angle across the corridor decreases.

The integration of the HVDC link has increased the damping ratio of the inter-area mode. The presence of a poorly damped inter-area mode is evident from the angular separation between G1 and G3 and the power flow in the line connecting buses 9 and 10. Also, evident is the sharp drop in the LCC link voltage during the fault due to the reduction in the inverter end AC voltage. With regard to inter-area oscillations during fault conditions, the rectifier switches between constant current and constant firing angle control. As anticipated, the power through the DC link drops during the fault. The studies have also shown shorter recovery times after a fault or disturbance.

As Eskom is pursuing investing in HVDC lines at various locations, this analysis presented will be applied to those new cases so that all the advantages of HVDC links can be considered in the terms of the techno-economic feasibility. Eskom will then have the full advantage of transporting bulk power but at the same time mitigating the effects of small signal stability on the National grid and internationally (with the Southern African Power Pool (SAPP)).

7. FUTURE STUDIES

Further damping may be achieved with an adaptive control element using HVDC links. This research will involve developing detailed two area power system networks using power system modelling software. The Model predictive control will be developed for online corrective control. The benefits and factors affecting the adaptive control performance will be noted for possible future installations of HVDC schemes. The models will be validated against literature.

8. ACKNOWLEDGEMENTS

The authors would like to thank Eskom and the Eskom Power Plant Engineering Institute as well as Brian Berry for the knowledge and guidance provided.

9. REFERENCES

- [1]. P. Kundur. *Power system stability and Control*, 1st ed., McGraw-Hill, 1994
- [2]. Cigré task force 07 of advisory group 1 of study committee 38. Analysis and control of power system oscillation Cigré, Dec 1996
- [3]. M. Szechtman, T. Wess, and C.V. Thio. "A benchmark model for HVDC system studies". *International Conference on AC and DC Power Transmission*, pages 374–378. IET, 1991.
- [4]. B. Berry and A. Edwards "Control shift training presentation-Dynamic stability and WAMS: Small signal stability", Private Training Course, Eskom Holdings SOC LTD, Germiston, 2013.
- [5]. M. Szechtman, et al., "First benchmark model for HVDC control studies" in Cigré working group 02 (Control in HVDC Systems) of study committee, vol. 14, pp. 55-73, 1991.
- [6]. Eskom Power Series, *HVDC Power Transmission , Basic principles, planning and convertor technology*, Crown Publications, ISBN 978-0-9921781-0-9, Johannesburg, 2012.
- [7]. M. Szechtman, et al., "The Cigré HVDC benchmark model - a new proposal with revised parameters" Cigré working group 02 (Control in HVDC Systems) of study committee, vol. 14, pp. 61-66, 1994.
- [8]. M. O. Faruque, et al., "Detailed modeling of CIGRÉ HVDC benchmark system using-PSCAD/EMTDC and PSB/SIMULINK", *IEEE Transactions on Power Delivery*, , vol. 21, pp. 378-387, 2006.
- [9]. V. K. Sood, et al., "EMTP modelling of CIGRÉ benchmark based HVDC transmission system operating with weak AC systems "Proceedings of the 1996 International Conference on Power Electronics, Drives and Energy Systems for Industrial Growth, 1996. , pp. 426-432 vol.1,1996,
- [10]. E. KYRIAKIDESR. G. FARMER, "The modelling of damping for power system stability analysis", 2004
- [11]. M. Klein, G.J. Rogers S. Moorthy P. Kundur "Analytical investigation of Factors influencing Power system stabilisers performance", *IEEE Transactions on Energy Conversion*, vol. 7, No. 3, September 1992
- [12]. Adaptive HVDC control System and Power Oscillation Damping Methods: Theoretical Developments. EPRI, Palo Alto, CA:2012.1024321

SIMULATION OF 100 % STATOR WINDING INTERNAL GROUND FAULT PROTECTION IN RTDS

A. Gwala*, A.K. Saha**

* University of KwaZulu-Natal, School of Electrical, Electronic & Computer Engineering, Mazisi Kunene Rd, Glenwood, Durban, 4041

E-mail: 20950075@stu.ukzn.ac.za

** University of KwaZulu-Natal, School of Electrical, Electronic & Computer Engineering, Mazisi Kunene Rd, Glenwood, Durban, 4041

E-mail: saha@ukzn.ac.za

Abstract: Ground faults are the most common types of faults in generators and can damage the stator winding severely. 100 % stator winding ground fault protection therefore becomes one of the crucial protection functions in generator protection. The grounding method used plays an imperative role in determining which protection functions are to be employed on the generator. The new phase domain synchronous machine obtained in RTDS allows for the simulating of internal faults. 100 % stator winding ground fault protection is presented in this paper which is achieved using a multifunction generator relay.

Keywords: Generator stator winding protection, third harmonic voltages, ground faults

1. INTRODUCTION

Generators are a fundamental part of the power system. The fundamental role they play in the power system require their operation to not only be reliable but be supplemented by reliable protection system to protect the generator should any disruptions occur [1]. Despite monitoring systems, electrical and mechanical faults may still occur, therefore generators need to be equipped with protection schemes that will initiate a withdrawal of the machine and if, necessary, initiate a complete shut-down of the machine. The loss of one generator at an electricity utility can result in detrimental effects in the power system, increasing the load to be carried by other units which may cause more problems and also making the system prone to less revenue. The costs of repairing the damaged generator are very high. [2].

The most common faults reported on generators are ground faults. Stator ground faults may be triggered by the breakdown of insulation in the windings as well as environmental influences such as moisture or oil together with the dirt which accumulates on the coil surfaces outside the stator slots [3]. This paper serves to illustrate how 100 % stator ground protection can be achieved on a high impedance grounded generator.

2. STATOR GROUND FAULTS

For a single-phase to ground fault occurring at the generator terminals, the fault current is a result of two fault currents, one due to external sources and the other from the generator itself. The damage inflicted on the generator is related to the energy released at the arc in the fault during the duration of the fault [4]. When a ground fault occurs, the relevant protection scheme issues a trip signal to the generator breaker. However, the current in the generator is

not disturbed since the generator field remains excited. After the generator breaker has tripped, the excitation will then be reduced. The fault current continues to flow until the generator field demagnetises completely and because at this point the generator breaker is already opened the damage to the generator is unavoidable [5]. To reduce the amount of fault current the neutral point of the generator is grounded. There are various methods used for grounding practices. This study focused on ground fault protection of high impedance grounded generator. The type of grounding used determines the type of protection scheme to be used.

If a fault occurs near the neutral, the zero sequence voltage available in that region is too small to drive the current to a fault. This scenario does not impose damage on the generator. The uneasiness of this situation is however generated if a second ground fault occurs, whether at the same point, same phase or another creating a short circuit between the two points. Because of this second fault, severe damage may be sustained by the machine leading to a fault not restricted by the grounding impedance [6].

3. STATOR WINDING GROUND FAULT PROTECTION METHODS

Differential protection schemes are the primary protection used for asymmetrical faults in generators [7]. Overcurrent or over-voltage relays are also the fundamental protection relays used due to their reliability and simplicity. The drawback with these relays is that they cannot detect faults near the generator neutral in high impedance grounded generators. These methods include percentage phase differential protection, ground differential, ground time-overcurrent, instantaneous ground overcurrent, stator winding zero sequence neutral over-voltage protection and

wye-broken delta voltage transformer ground overvoltage protection. These entire protection schemes protect 5- 95% of the stator winding [8]. None of them achieve 100 % coverage of the stator winding. High resistance grounded generators requires more sensitive protection schemes. There are three most common methods used in industry to achieve 100 % stator winding protection:-

- Third harmonic neutral under-voltage scheme
- Third harmonic voltage ratio (differential) scheme
- Sub-harmonic injection scheme

A. Third harmonic neutral under-voltage scheme

This scheme includes a 27H under voltage relay accustomed to detect third harmonic voltage and a 59GN relay tuned to the fundamental frequency. The overlapping of the overvoltage/under voltage scheme provides 100% protection for generator stator ground faults by using two measuring functions that cover different portions of the machine winding [1,9]. The ground faults that occur in the stator winding from the generator terminals to within about 5 % of the neutral normally produce enough fundamental zero-sequence voltage to operate the 59 GN relay. Ground fault at the neutral will cause the third harmonic voltage to fall to zero triggering the 27H under voltage relay.

However, achieving appropriate settings for this relay is rather challenging. The 27H relay must be set sufficiently low to avoid dropout during periods of normal operation when third harmonic voltage is at a minimum. At the same time, the setting must be high enough to detect all the faults not seen by 59GN relay with the generated third-harmonic voltages at a maximum [1, 6].

B. Third harmonic voltage ratio scheme

The generator output voltage is not a perfect sinusoidal wave, it is distorted by harmonics and the third harmonic is the largest. The harmonics appear in each phase having similar magnitude and phase. They are found in the generator neutral and terminal as a zero-sequence quantity [10].The working principle of this method is to measure the harmonics either at the terminal, neutral or both for the protection of the generator. The third harmonic ratio scheme measures the third harmonic voltages both at the terminal and neutral of the generator.

Figure 1 illustrates the third harmonic distribution along the stator in different loading conditions. In the middle of the stator winding, the third harmonic has a null point (zero). When a fault occurs at the neutral of the generator, the third harmonic voltage at the terminal is increased to the maximum whereas at the neutral it is reduced to zero. This can be clearly seen in figure 2a. For a fault at the generator terminals, the opposite occurs, the third harmonic voltages at the terminal decreases to zero and the neutral now consists of the sum of the generated third harmonic voltages. This simple logic allows this protection scheme to detect ground faults at the terminal and neutral

of the generator. The decrease or increase in the third harmonic voltage will depend on where the fault occurs as well as the loading on the generator [5].

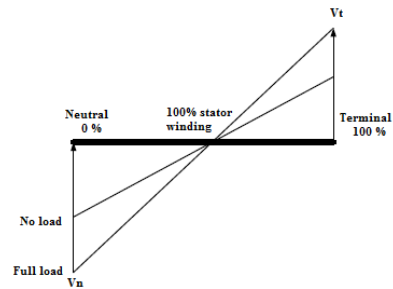


Figure 1: The distribution of the third harmonic at different loading conditions

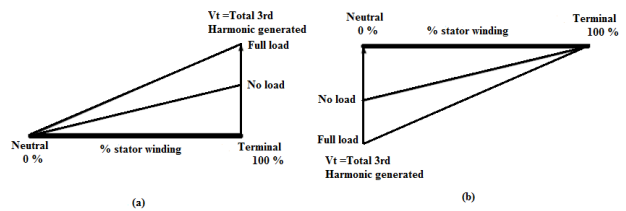


Figure 2: Third harmonic voltages distribution during a ground fault at the generator (a) terminals (b) neutral

To achieve 100 % protection of the stator winding, the third harmonic voltage ratio scheme is supplemented by a fundamental frequency 59GN overvoltage relay to provide protection around the null point which is at the middle of the winding. This also gives clarification to the previous section with regard to challenges faced when using overvoltage 59GN and under voltage 27H relays for stator winding protection, the discrepancies of the third harmonic voltages along the stator at different loading conditions. Therefore with the assistance of the over-voltage relay, this method becomes a better and more preferable method to use even at light loads.

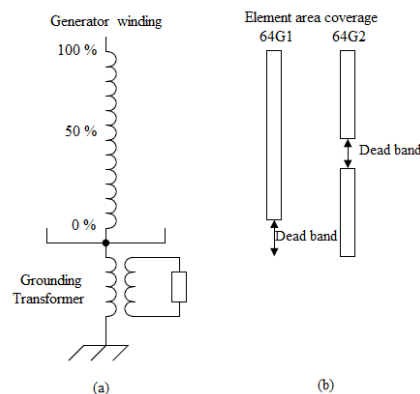


Figure 3: 64G element operating characteristics [12]

Figure 3 shows how these elements complement each other. Another imperative point to note is the failure of the overvoltage relay to operate for faults near the neutral and at this section the overvoltage relay is complemented by the third harmonic voltage ratio protection element.

Together these elements are referred to as 64G from generator protection elements list.

C. Sub-harmonic injection method

This method uses the injected voltage to detect ground faults along the stator. The voltage is injected with the use of a transformer between the grounding element and ground. The grounding element may be a distribution transformer, reactor or resistor. The injected voltage has a relatively low sub-harmonic frequency, usually a quarter of the system frequency is chosen. The currents that are caused by the injected voltage are continuously measured. During normal conditions, this current will flow through the stator winding shunt capacitances to ground, once a ground fault occurs, the shunt capacitances are short-circuited and as result the magnitude of the current rises. From this principle, the relay can detect occurrence of ground fault by the change in current magnitude. The advantages of this method are that the low injected frequency increases the impedance of the stator capacitance reactance thereby increasing the sensitivity of the protection scheme [13]. Furthermore, the current is measured for the full quarter of the system frequency (12.5 or 20 Hz cycles) that is used, and this method also uses a coupling filter to block the fundamental frequency component of the signal [5]. The drawback from using this method is that it is expensive due to the additional equipment it requires for the injection of voltage.

4. SYSTEM MODEL

The model of the system used in this study is well known model used mostly in stability studies. It consists of a 555 MVA generator connected to a step-up transformer which is also connected to an infinite bus through two parallel transmission lines as shown in figure 4. This model is generated from [14] where there are four 555 MVA generators, but for the purposes of this study only one generator was used. The real time digital simulator (RSCAD software) offers a new phase domain synchronous generator model which differs from other previous models in such that it allows the user to apply internal winding faults along the whole stator winding. Furthermore, the generator field circuit can be represented in detail with the use of power system components also allowing more realistic contingencies and fault scenarios which could enhance the results obtained from protection studies.

The generator is also connected to generator controllers and due to the effect of generator protection on system disturbances and vice versa, the simulation also made use of the power stabilizer and excitation control systems. Therefore, the generator has inputs for governor/turbine and exciter interfaces. For the user to be able to simulate for internal faults as mentioned above, the self and mutual inductances of the machine windings including the faulted windings must be computed as functions of rotor position and saturation. The model therefore uses two methods to compute the inductance matrix of the machine which are

the d-q and the modified winding function approach (MWFA) based methods. The D-Q based method which was used in this study is disadvantageous in such that it does not show the phase belt harmonics (3rd, 5th, and 7th harmonics) due to the non-sinusoidal distribution of the windings and permeance) [15].

The machine model is a two-axis model in which dynamics of all the stator and rotor electrical circuits are represented. The internal bus parameters and machine initial load parameters were used to specify the machine's initial operating conditions using the load flow tool in RSCAD. The load flow results were used to automatically set the inputs to the excitation and governor/turbine connected to the generator.

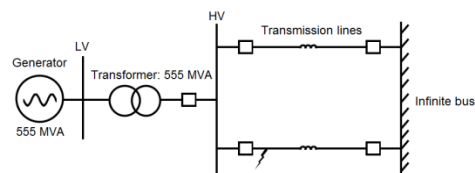


Figure 4: System model used for this study

A. Multifunction Generator Relay

The multi-function generator relay model is a full transient model that utilizes a threading technique developed by RTDS Technologies [15]. This relay consists of different protective functions employed for generator protection for numerous types of faults and abnormal conditions. Differential elements for phase and neutral currents, 100% stator protection, loss of field protection, out-of-step, volts per hertz, and other important additional relay elements which provide comprehensive protection for the generator [16]. The competency of the multi-function generator relay model to detect and clear synchronous machine ground faults is validated in this paper.

5. SIMULATION RESULTS

This study was based on the third harmonic voltage ratio method also known third harmonic differential method. This scheme is dependent on the availability of third harmonics in the generator. As mentioned in the previous section that the phase domain synchronous generator fault d-q based model used in this study does not generate the odd number harmonics, hence the first step was to artificially generate the third harmonics and add them to the neutral and terminal of the generator and pass them on to the multifunction generator relay. To realistically generate the third harmonic voltages, a logic which included all the factors that impact their production was created. The third harmonic voltages produced by the generator depend on the generator construction, generator excitation and loading on the generator [10, 17]. The grounding method was incorporated into the artificial third harmonic voltage generation method that was used. The generated third harmonic voltages both at the terminals and neutral of the generator also depend on the

capacitances and earthing resistances and therefore the stray capacitances were included to ensure that the model is as representative as possible [7, 17].

A grounding transformer was used which reduces the fault current to a range of 3 – 25 A [5]. The IEEE standard C37.101 [18] was used to calculate the size of the secondary resistor which limits the fault currents. The secondary resistor of the grounding transformer was calculated to be 0.271 Ω. Finding the exact value of this resistance is not critical since the equipment capacitive tolerances and resistances change due to temperature rise. The maximum stator-ground fault current that flows through the primary winding of the grounding transformer was found to be 5.11 A. The following results shows simulations where a ground faults were applied at different locations along the stator. Figure 5 presents a ground fault which was applied at 95 % of the stator winding.

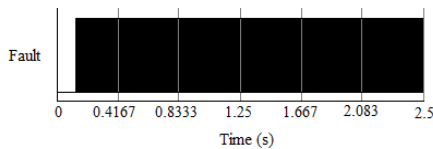


Figure 5: Fault logic

This fault is detected by the relay and both the 64G1 and 64G2 pick up for this fault and a trip signal is issued as seen in figure 6. The main generator breaker and the field breaker are opened to shut down the generator. As discussed in the previous section, when a fault is applied at the terminal, the third harmonic voltage at that point is reduced to zero and increased to maximum at the neutral. The info1 signal represents the generator protection elements signals and in this case bit 14 and 15 represents 64G1 and 64G2 respectively..

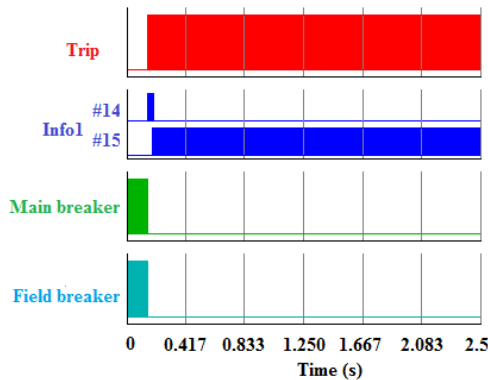


Figure 6: Relay and breaker signals

Figure 7 shows this phenomenon for a fault which occurs at 95 %. The same fault at figure 6 was also applied at 50 % of the stator winding. At this point, the reliability of the 64G2 element in detecting ground faults is dissatisfactory. Looking at the info1 signal in figure 8, one can clearly see the inadequate operation of 64G2 which is represented by bit 15. Since the two elements complement each other, overvoltage element 64G1 is more reliable and therefore

operates to ensure the respective breakers are opened and the generator is shut down.

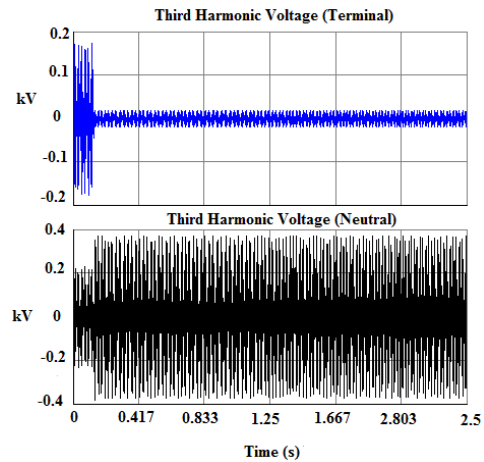


Figure 7: Measured terminal and neutral third harmonic voltages

As shown in figure 3, 64G2 element has a null point at the middle of the stator winding (around 50 %) which prevents this element from being effective. However, the operation of the 64G1 element at this point is exceptional due to the large neutral over-voltage which causes this element to trip. 64G1 detects the ground fault first. Figure 9 shows that there is not much change in the third harmonic voltage, therefore the operation of 64G2 which relies on this change (ratio) is affected.

To fully understand the 64G elements operating characteristics, a solid ground fault was also applied at 5 % of the stator winding. Again, as mentioned a fault occurring close to the neutral results in the third harmonic at that section increasing to maximum and another very important point about this region is the insufficient neutral over-voltage available to trip the 64G1 element during fault conditions.

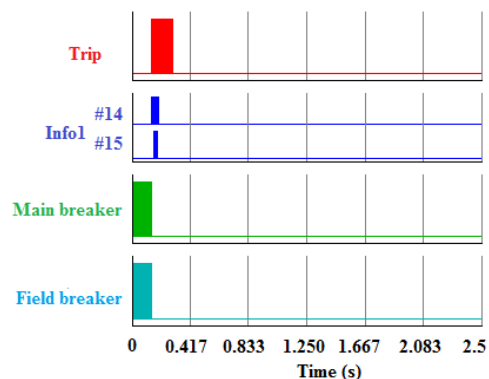


Figure 8: Relay and breaker response (fault at 50 %)

Figure 10 serves to show the operations of breaker and relay signals. The 64G2 element plays an efficient role in ensuring that faults at this point are detected and the generator stator winding remains protected. Figure 11

illustrates the reduction of third harmonic voltage at the neutral of the generator. This shows that 100 % of the stator winding is fully protected at all locations against solid ground faults. The operation of the 64G2 element also depends on the loading of the generator.

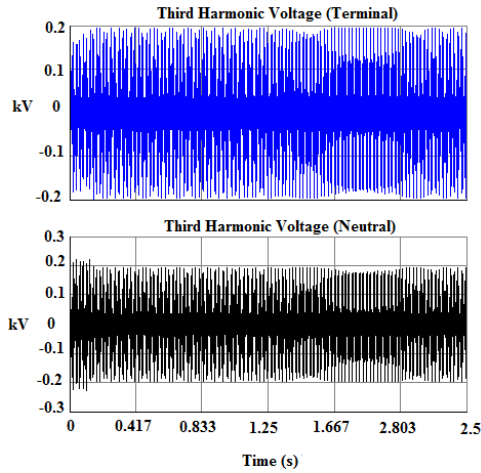


Figure 9: Neutral and terminal third harmonic voltage

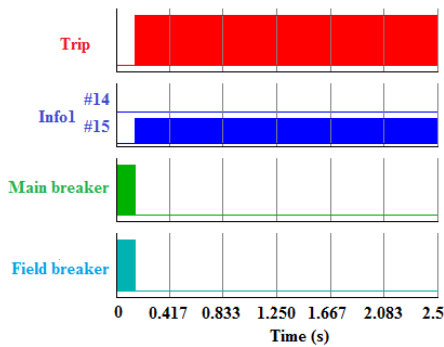


Figure 10: Breaker and relay signals during a ground a fault at 0 % of the stator winding

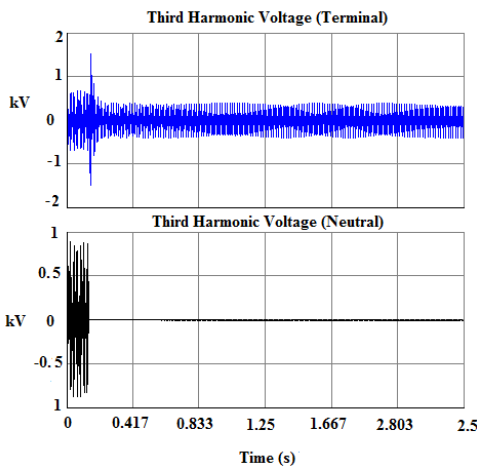


Figure 11: Variation of the neutral and terminal third harmonic voltage

The magnitude of the third harmonic voltages is highly affected by the loading of the generator. For this reason, the settings of this element require the protection engineer to know the magnitude of these harmonic voltages at zero

and full load conditions on the generator. Therefore, it was also investigated if the generator remains protected at 0 % and 100 % loading from 0% to 100 % of the stator winding. Solid ground faults were applied through the entire length of the stator, analysing the behaviour of both the 64G1 and 64G2 elements. The results obtained from these two cases were tabulated and recorded to table 1 and 2 as presented in the appendix.

6. CONCLUSION

Stator ground protection is a very critical protection function in generator protection. The occurrence of stator ground faults requires that the implemented methods provide 100 % stator ground protection at all times. This paper presented a new phase domain synchronous machine model which allows for internal faults to be applied along the stator winding. Differential protection is not adequate for the protection of the stator winding in high impedance grounded generators.

The multifunction generator model and the phase domain generator model demonstrated how the 100 % stator winding protection is achieved with the use of the 64G generator protection element which uses the third harmonic voltage ratio and overvoltage schemes. These scheme complement each ensuring that the stator winding is protected at all points. The dead bands of 64G1 and 64G2 were shown, with the 64G1 scheme failing to operate at lower percentages of the stator winding and the unreliability of the 64G2 scheme around the middle of the winding. Even with such catastrophes, both these schemes show to be a more reliable and cost effective method.

7. REFERENCES

- [1] Donald Reimert: *Protective Relaying for Power Generation Systems*, Taylor & Francis Group, New York, 2006
- [2] Power System Relaying Committee: "IEEE Guide for AC Generator Protection", IEEE Std C37.102-1995.
- [3] Fulczyk, M., Bertsch, J. (2002), Ground-fault currents in unit-connected generators with different elements grounding neutral, *IEEE Transactions on Energy Conversion*, Vol.17, No.1, March 2002, pp. 61-65
- [4] J. Lewis Blackburn, Thomas J. Domin: *Protective Relaying Principles and Applications*, Third Edition, Taylor and Francis Group, LLC, 2007.
- [5] IEEE Guide for Generator Ground protection, IEEE Standard C37.102TM-2006, Feb. 2007.
- [6] R.J. Marttila, "Design Principles Of A New Generator Stator Ground Relay For 100% Coverage Of The Stator Winding", *IEEE*

Transactions on Power Delivery, Vol. PWRD-1, No. 4, Oct. 1986, pp. 41 – 51.

- [7] Pope, J.W. (1984), A comparison of 100% stator ground fault protection schemes for generator stator windings, *IEEE Transactions on Power Apparatus and Systems*, Vol. PAS-103, No.4, April 1984, pp. 832-840.
- [8] Mieczyslaw, Zielichowski and Fulczyk (2003), Analysis of operating conditions of ground-fault protection schemes for generator stator winding, *IEEE Transactions on Energy Conversion*, Vol. 18, No.1, March 2003, pp. 57-62.
- [9] Schlake, R.L., Buckley, G.W, McPherson, G (1981), Performance of third harmonic ground fault protection schemes for generator stator windings, *IEEE Transactions on Power Apparatus and Systems*, Vol. PAS-100, No.7, July 1981, pp. 3195-3202
- [10] M. Fulczyk, R. Mydlikowski, “Influence of Generator Load Conditions on Third-Harmonic Voltages in Generator Stator Winding”, *IEEE Transactions on Energy Conversion*, Vol. 20, No. 1, March 2005, pp. 158 – 165.
- [11] Power System Relay Committee: “Coordination of Generator Protection with Generator Excitation Control and Generator Capability”, *IEEE Power Engineering Society General Meeting*, 2007.
- [12] “SEL-300G Multifunction Generator Relay Instruction Manual”, Schweitzer Engineering Laboratories, Inc., 2007.
- [13] Daquiang, Bi et al. (2001), Analysis and improvement on stator earth-fault protection by injecting 20 Hz signal, Tsinghua University, Beijing, China.
- [14] Prabha Kundur: *Power System Stability and Control*, McGraw-Hill Inc., New York, 1994
- [15] *RTDS User’s Manual*, RTDS Technologies Inc., Winnipeg, Canada, 2007
- [16] A.B. Dehkordi, D.S. Ouellette, P.A. Forsyth: “Protection Testing of A 100% Stator Ground Fault Using A Phase Domain Synchronous Machine Model in Real Time”, *IET International Conference on Developments in Power System Protection*, January 2010 Finney.
- [17] Y-T Huang, B S Rigby, A B Dehkordi: “Using a new faulted synchronous machine model for hardware-in-loop testing of a generator protection

relay”, *Southern African Power System Protection Conference*, 2012.

- 18. IEEE Guide for Generator Ground Protection, IEEE Standard C37.101, 1993

8. APPENDIX

Table 1: Results obtained for 64G operating characteristics for different fault locations full load

% of the stator winding	64G1	64G2
95	Tripped	Tripped
85	Tripped	Tripped
75	Tripped	Tripped
65	Tripped	Tripped
55	Tripped	Tripped
54	Tripped	Unreliable tripping
52	Tripped	Unreliable tripping
50	Tripped	Unreliable tripping
45	Tripped	tripped
35	Tripped	Tripped
25	Tripped	Tripped
15	Tripped	Tripped
10	Tripped	Tripped
5	Tripped	Tripped
0	No trip	Tripped

Table 2: Tabulated results obtained for 64G operating characteristics for different fault locations at zero loading

% of the stator winding	64G1	64G2
95	Tripped	Tripped
85	Tripped	Tripped
75	Tripped	Tripped
65	Tripped	Tripped
55	Tripped	Unreliable tripping
54	Tripped	Unreliable tripping
53	Tripped	Unreliable tripping
52	Tripped	Unreliable tripping
50	Tripped	Unreliable tripping
45	Tripped	Unreliable tripping
40	Tripped	Unreliable tripping
35	Tripped	Tripped
25	Tripped	Tripped
10	Tripped	Tripped
5	Tripped	Tripped
0	No trip	Tripped

SIMULATION STUDY OF OVERCURRENT PROTECTION COORDINATION OF DISTRIBUTION SYSTEM

A.K. Saha*

**School of Engineering, Electrical, Electronic and Computer Engineering, HC Campus, King George V Avenue, University of KwaZulu-Natal, Durban, South Africa, E-mail: saha@ukzn.ac.za*

Abstract: This paper presents simulation study of a distribution system protection using software over-current relays. The simulation study has been performed on a real-time digital simulation platform that enables studying power systems in real-time scenarios. The simulation results have been presented in this paper with analyses. The main aim of this paper is to encourage use of RTDS together with software relays that can be very useful particularly in education and training protection aspects and further in developing research case studies.

Keywords: Over-current, real-time digital simulator (RTDS), training and education, coordination

1. INTRODUCTION

Power systems comprise many items which are not only very expensive but must be utilised as much as possible within applicable constraints of security and reliability of supply. However, the fundamental requirement is that the power systems and their equipment must always be operated in a safe manner all the time irrespective of demand from the consumer side. To ensure this, power systems are always carefully designed and protected using proper schemes. Interestingly, no matter how well the power systems are designed, faults are obvious and they occur sooner or later [1]. Occurrence of faults due to insulation failure that might be exposed to some conductive parts may cause danger to electrical installations and human beings if they get involved anyhow [2]. Therefore, there must be some provision to detect fault conditions and disconnect elements to isolate faulty part/s of the system as quick as possible keeping the healthy part/s intact and distribution part/s of power system/s are of great importance as it is responsible for delivering power to consumer premises [1].

2. DISTRIBUTION SYSTEM PROTECTION

Overhead power distribution systems are normally subjected to transient faults because of phase-phase or phase-ground fault and permanent faults. The main aims of distribution system protection are to minimize: (a) the duration of faults and number of consumers affected by the fault and hence to eliminate safety hazards as quickly as possible (b) limit service outages (c) protect consumers' apparatus and system from unnecessary service interruptions and disturbances and (d) finally disconnect the faulty parts at the earliest [3, 4]. Distribution systems don't usually require fast fault clearance and hence are protected using time-graded systems and where fault clearance times are not critical time-delayed remote back-up protection may be adequate. However, knowledge of current and voltage distribution in a network during fault conditions are essential for setting up proper protection system. Time-graded method

uses appropriate time settings for each and every relay controlling the circuit breakers in the system that ensures that the breaker nearest to the fault opens first. The relay at the immediate upstream is set to have higher time setting as compared to first one and so on for the relays closer to the source side. This method, however, has the disadvantage that for a fault occurred at the farthest end of a feeder takes longest time to be cleared by the source end relay where the fault level is the highest when relays at the downstream fail to operate. Time-grading can also be obtained using standard inverse definite minimum time (IDMT) relays where current/time characteristics can be varied according to tripping time required. There are various such characteristics defined by IEC 60255, such as standard inverse, very inverse, extremely inverse. In most of the cases, standard inverse characteristics provide satisfactory results. However, if satisfactory grading is not achieved then other characteristics may be useful to solve the problem [1].

This paper utilized RTDS as a platform to simulate case studies in which there is a source representing a substation connected to downstream of a distribution system were simulated and tested with over-current software relays available at RTDS library.

3. REAL-TIME DIGITAL SIMULATOR

RTDS is special purpose computation facility that comes with a software suits and used to study electromagnetic transient phenomena in real-time. RTDS also includes accurate power system component models used for making a physical power system. Further, a powerful user friendly graphical user interface enables the user to construct, run and analyse power systems. It also allows the user to connect hardware such as power system controllers, protective relays etc. [5, 6]. Figure 1 shows the configuration that has been used for study of distribution system protection using software relay. The system under study is constructed on a computer using

RSCAD software which is simulated on RTDS processors and the results of simulation/s are sent back to the computer for analyses.

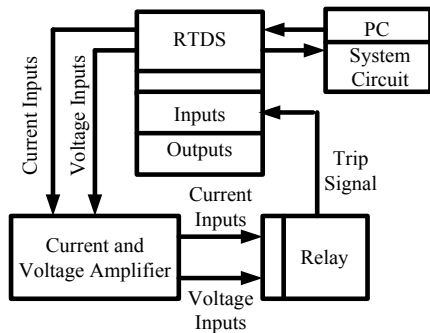


Figure 1: Use of RTDS for system under study

4. SYSTEM CONFIGURATION

The system under study is as shown in Figure 2 and has been adopted from [1] with little modification to make it suitable for training and education purposes, and also fuse protections have been replaced by relays as the main aim here to understand and apply the knowledge of over-current and earth fault protections using relays. Source at 88 kV is representing a power sub-station supplying load at 88 kV and transformers to supply load at loads at 11 kV as well as 0.4 kV levels. Three inverse time over-current relays having IEC standard inverse characteristics have been associated with three circuit breakers CB3, CB6 and CB7 for protection from over-current due to normal overloading and faults conditions F1, F2 and F3. Protection transformers were chosen based on the loading on the system and voltages at the buses from which the respective secondary current and voltage signals were sent to over-current relays. Also, other necessary logic circuits such as fault logic, circuit breaker control logic were developed using RSCAD control functions.

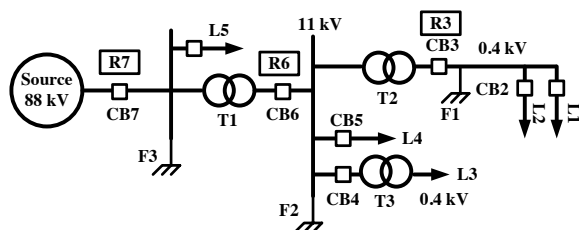


Figure 2: System under study

5. SIMULATION RESULTS AND ANALYSIS

5.1 Normal load change of L1

Figure 3 shows change in load demand L1 from 0.001 MW to 0.025 MW. The other loads L2-L5 are kept at their initial set value and hence they are not changed as evident from the plot. Figures 4, 5, and 6 illustrate that currents increase with increase in load L1. The corresponding changes in secondary currents are also shown Figures 4, 5, and 6.

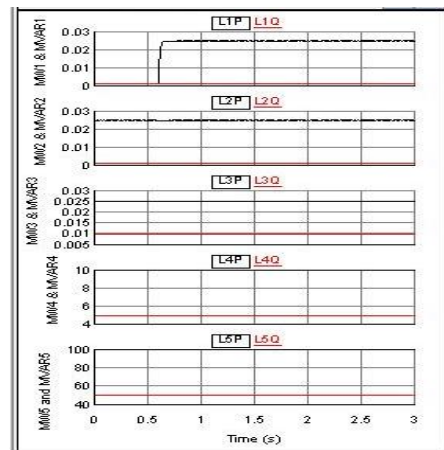


Figure 3: Change in L1

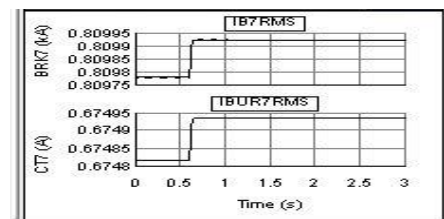


Figure 4: Currents (BRK7 & CT7)

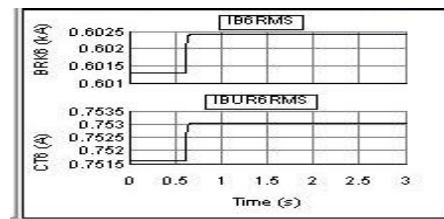


Figure 5: Currents (BRK6 & CT6)

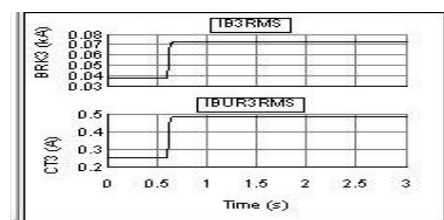


Figure 6: Currents (BRK3 & CT3)

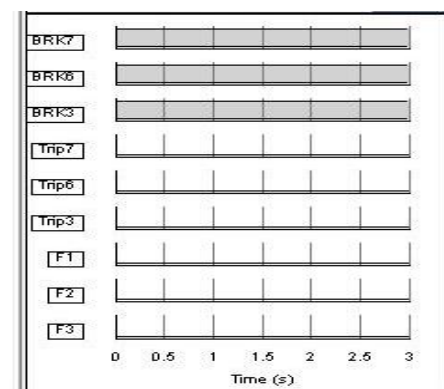


Figure 7: Breaker, trip and fault signals (load change)

Figure 7 represents breaker status signals which are at a value of 1 indicating the breaker on condition. The trip

signals issued by relays R3, R6 and R7 are also shown in Figure 7 indicating there is no such signal issued as there is no over-current condition persisting in the circuit. Further, the fault signals because of faults occurring at various locations at F1, F2 and F3 are shown in Figure 7 as well. There is no fault condition persisting and hence, all the fault signals are represented by zero.

5.1.2 Overloading by increasing L1

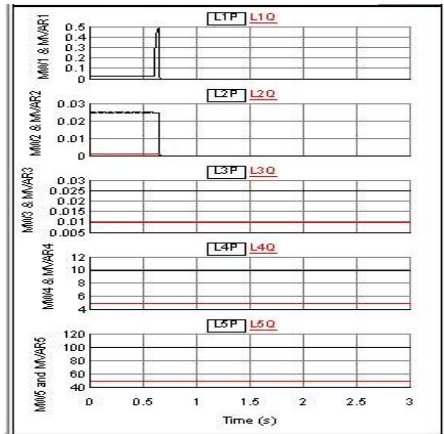


Figure 8: Load1 change (overloading L1)

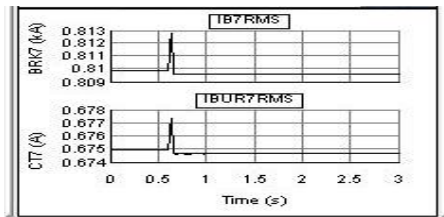


Figure 9: Currents (BRK7 & CT7 overloading L1)

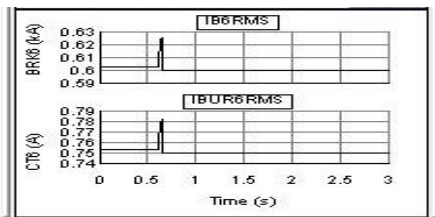


Figure 10: Currents (BRK6 & CT6 overloading L1)

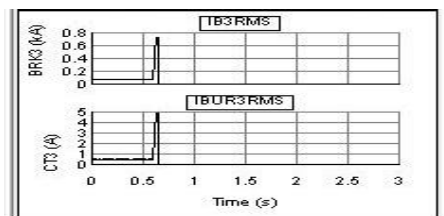


Figure 11: Currents (BRK3 & CT3 overloading L1)

In this case, Load L1 has been increased from its initial value to 0.5 MW to initiate overloading condition which is shown in Figure 8. Figure 8 is also showing other loads illustrating that there are no changes occurring in them. Because of this overloading condition, currents carried by upstream part of the circuit are shown in Figures 9, 10 and 11 together with currents seen by the respective relays. Because of over-current, relay R3 picked up and

issued a trip signal which is shown in Figure 12 that resulted in tripping of circuit breaker BRK3 that is associated with relay R3.

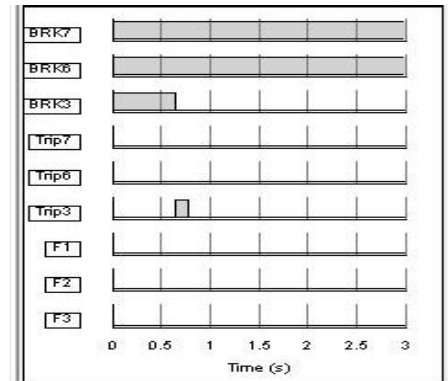


Figure 12: Breaker, trip and fault signals (overload L1)

5.1.3 Occurrence of fault at F1-R3 picks up

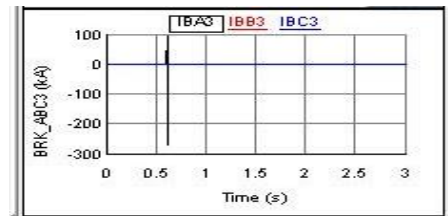


Figure 13: Phase-A to ground fault (F1)

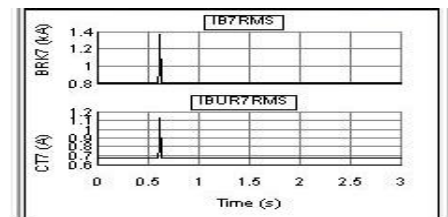


Figure 14: Currents (BRK7 & CT7 - F1)

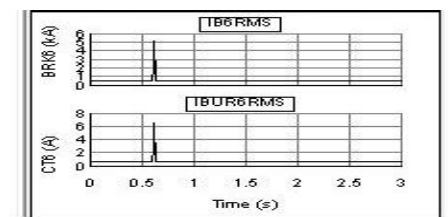


Figure 15: Currents (BRK6 & CT6 - F1)

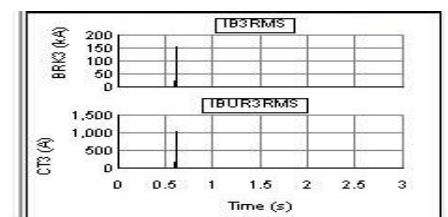


Figure 16: Currents (BRK3 & CT3 - F1)

A phase-A to ground fault is applied at location F1 and as a result phase-A current increases which is shown in Figure 13 and the resulting increase in currents in the circuit are shown in Figures 14, 15 and 16.

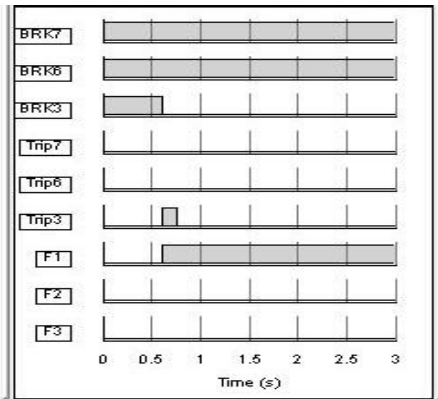


Figure 17: Breaker, trip and fault signals (F1)

The fault signal F1 is shown Figure 17 that causes relay R3 to pick up and issue the trip signal that in turn trips the circuit breaker BRK3 as shown.

5.1.4. Occurrence of fault at F1 – R3 fails to operate

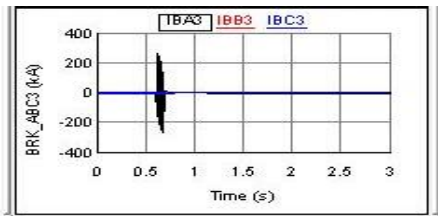


Figure 18: Phase currents (F1)

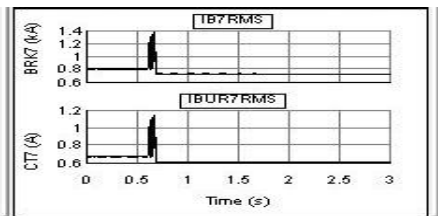


Figure 19: Currents (BRK7 & CT7 - F1- R3 blocked)

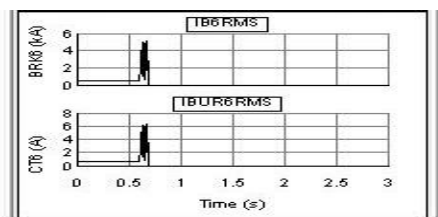


Figure 20: Currents (BRK6 & CT6 - F1- R3 blocked)

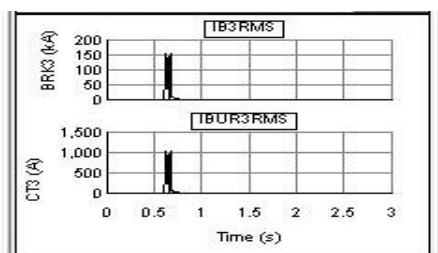


Figure 21: Currents (BRK3 & CT3 - F1- R3 blocked)

In this case, again the a phase-A to ground fault was applied at location F1, however, relay F3 was blocked to mimic the situation that it is not functional and hence will

not be able to pick up the faults occurring. Figure 18 shows the phase currents from which it is clear that because of phase-A to ground fault, the phase-A current increases as compared to other phase currents. Figures 19, 20 and 21 illustrate corresponding increase in currents. Figure 22 shows the associated signals from which is evident that relay R3 did not pick up the fault condition although F1 signal is present and hence, the relay R6 picked up and issued the trip signal to isolate the fault by tripping circuit breaker BRK6.

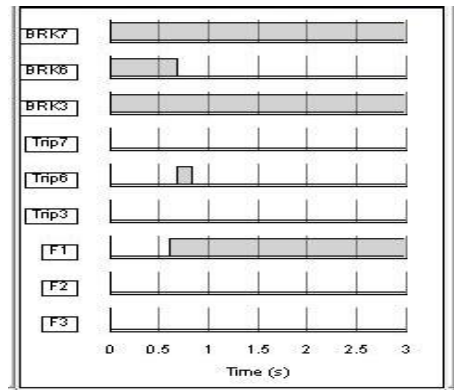


Figure 22: Breaker, trip and fault signals (F1-R3 blocked)

5.1.4. Occurrence of fault at F1 – R3 and R6 fail to operate

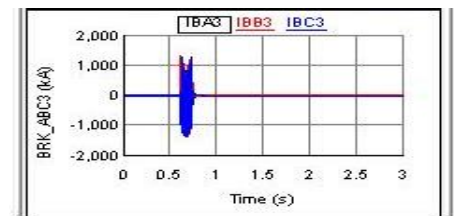


Figure 23: Phase currents (F1 - R3/R6 blocked)

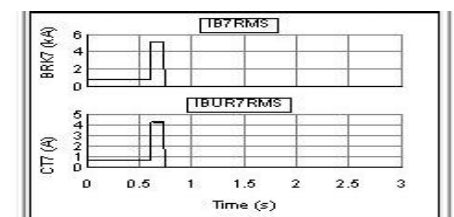


Figure 24: Currents (BRK7 & CT7 - F1- R3/R6 blocked)

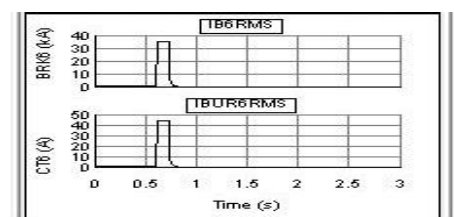


Figure 25: Currents (BRK6 & CT6 - F1- R3/R6 blocked)

In this case, a three-phase to ground fault was applied at F1 with relay R3 and R6 in blocked condition and increase in phase currents in the circuit are shown in Figure 23. Changes in currents in the circuit are shown in

Figures 24, 25 and 26 respectively. Figure 27 shows the presence of fault and at the absence of any trips signal issued by relays R3 and R6 while relay R7 has picked the fault condition up and issued the trip signal to cause circuit breaker BRK7 to trip.

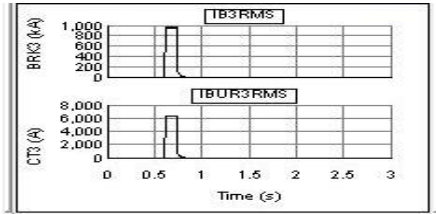


Figure 26: Currents (BRK3 & CT3 - F1- R3/R6 blocked)

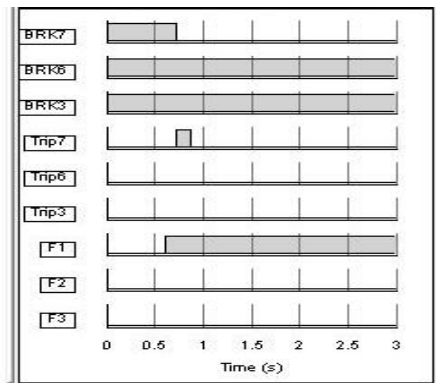


Figure 27: Breaker, trip and fault signals (F1-R3/R6 blocked)

5.2 Occurrence of fault at F2

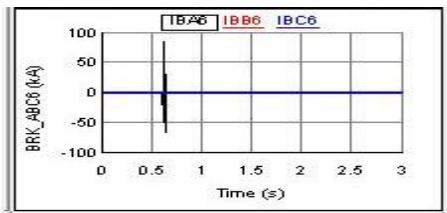


Figure 28: Phase currents (F2)

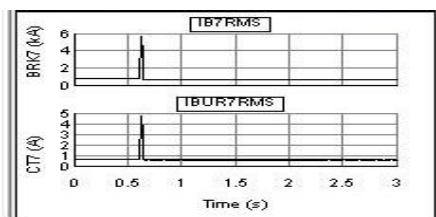


Figure 29: Currents (BRK7 & CT7 - F2)

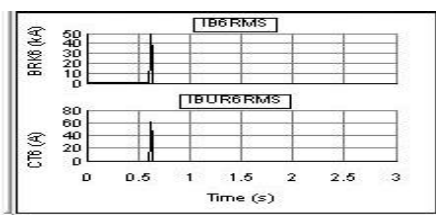


Figure 30: Currents (BRK6 & CT6 - F2)

In this case, a phase-A to ground fault was applied at F2 and the changes in phase currents is illustrated in Figure

28. The corresponding changes in circuit currents are shown in Figures 29, 30 and 31 respectively. Figure 32 shows that the fault condition was picked up relay R6 and a trip signal was issued causing circuit breaker BRK6 to trip.

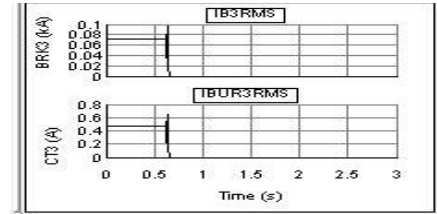


Figure 31: Currents (BRK3 & CT3 - F2)

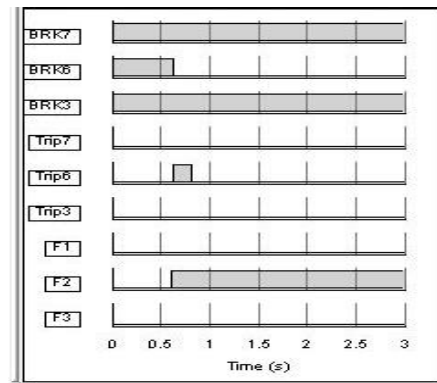


Figure 32: Breaker, trip and fault signals (F2)

5.2.1 Occurrence of fault at F2 - R6 fails to operate

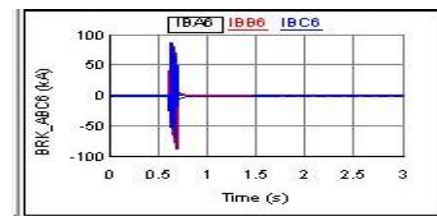


Figure 33: Phase currents BRK6 (F2 - R6 blocked)

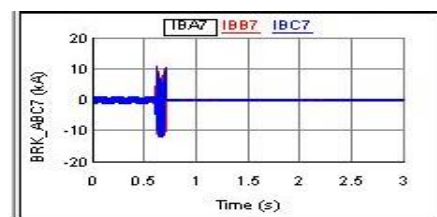


Figure 34: Phase currents BRK7 (F2 - R6 blocked)

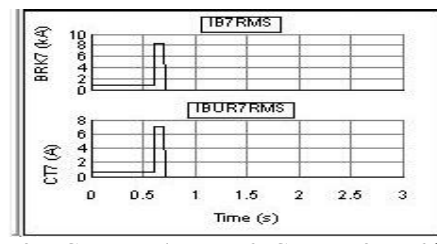


Figure 35: Currents (BRK7 & CT7 - F2 - R6 blocked)

In this case, a three-phase to ground fault was applied at F2 with relay R6 blocked. The increase in phase currents

are shown in Figures 33 and 34 respectively whereas the increases in currents in the system are shown in Figures 35, 36 and 37. Figure 38 shows the fault at F2 but the relay R6 failed to pick up while the relay R7 functioned properly backing up the protection for the system.

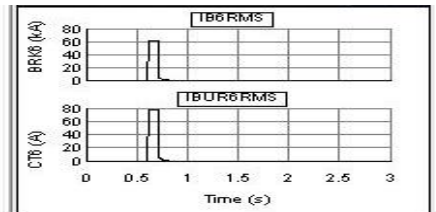


Figure 36: Currents (BRK6 & CT6 – F2 – R6 blocked)

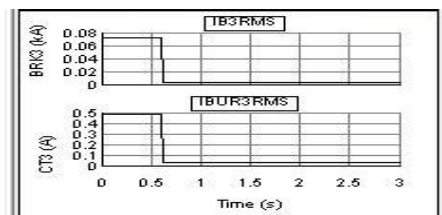


Figure 37: Currents (BRK3 & CT3 – F2 – R6 blocked)

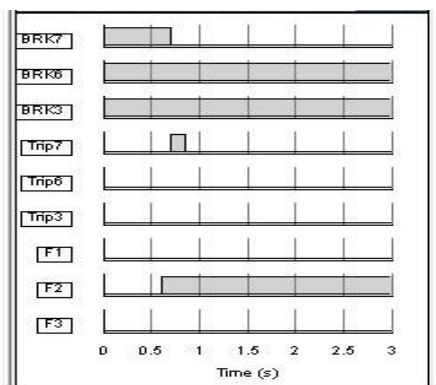


Figure 38: Breaker, trip and fault signals (F2-R6 blocked)

5.3 Occurrence of fault at F3

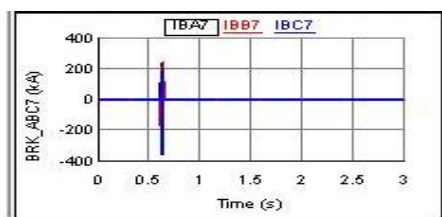


Figure 39: Phase currents BRK7 (F3)

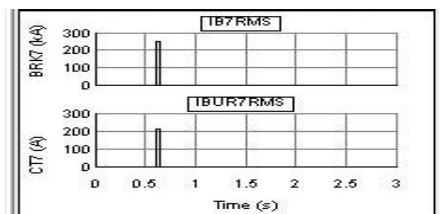


Figure 40: Currents (BRK7 & CT7 – F2)

In this case, a three-phase to ground fault was applied at F3 and the resulting increase in phase currents are shown Figure 39 whereas the increases in current seen by the part of the circuit are shown in Figure 40. The corresponding trip and circuit breaker signals are shown in Figure 41 that illustrates that the relay R7 picked up the fault condition and issued trip signal to circuit breaker BRK7 to trip and isolate the fault.

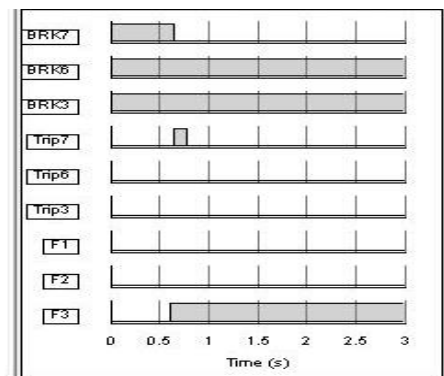


Figure 41: Breaker, trip and fault signals (F3)

6. CONCLUSIONS

The importance of power system and distribution system protection has been discussed and implemented on real-time digital simulation platform. Over-current protection using IEC standard inverse relay characteristics have been simulated for fault conditions at various locations of a radial distribution system and protection coordination have been implemented and demonstrated with the results obtained that could be helpful in teaching and education of over-current protection and protection coordination.

7. REFERENCES

- [1] Alstom Group: "Network protection & automation guide", *Alstom Grid*, pp. 1-476. May 2011.
- [2] ABB: "Distribution systems and protection against indirect contact and earth fault", *Technical Application papers*, pp. 1-56, April 2008.
- [3] H. Hosseinzadeh: "Distribution system protection", *University of Western Ontario*, pp. 1-16, May 2008.
- [4] J.J. Burke: "Characteristics of Fault Currents on Distribution Systems," *IEEE Transactions on Power Apparatus and Systems*, Vol. PAS-103, No. 1, January 1984
- [5] RTDS: "Manual Set", *Real Time Digital Simulation*, pp. 1-517, November 2006.
- [6] RTDS, Applications, closed-loop testing of physical devices, <http://www.rtds.com/applications/closed-loop-testing/closed-loop-testing.html>

REAL TIME SIMULATION AND TESTING OF LOSS OF FIELD EXCITATION EVENTS IN RTDS

A. Gwala*, A.K. Saha**

* University of KwaZulu-Natal, School of Electrical, Electronic & Computer Engineering, King George V. Rd, Glenwood, Durban, 4041

E-mail: 20950075@stu.ukzn.ac.za

** University of KwaZulu-Natal, School of Electrical, Electronic & Computer Engineering, King George V. Rd, Glenwood, Durban, 4041

E-mail: saha@ukzn.ac.za

Abstract: The impact of loss of field excitation in synchronous generators is one of the main causes of voltage instability. The large consumption of reactive power and rapid changes in the system components leads to severe damage of the generator and jeopardizes system stability. This paper looks into loss of field excitation events and how their impacts can be reduced by using the R-X protection scheme.

Keywords: Generator protection, Loss of Field Excitation (LOFE), synchronous generators

1. INTRODUCTION

The continually increasing power system has become a rising concern for power system stability and protection engineers. Loss of field excitation is a synchronous machine abnormal condition which results from unexpected tripping of the field breaker, short circuit fault in the field winding, exciter voltage regulator failure or loss of excitation supply [1]. This condition is likely to damage both the machine and the system. When loss of excitation occurs, the machine draws in a very high amount of reactive power which is supplied by the stator current.

In this condition, the machine runs at a speed that is higher than the synchronous speed operating as an induction machine and the stator is likely to be damaged due to overheating [2]. As the machine draws more reactive power from the system, neighboring machines in the system will be forced to increase their reactive power output which will result in deteriorating of voltage in the system. Weaker systems may fail due to the large voltage drop caused by this condition. In addition, the transmission protection relays may mal-operate due to overloading and isolate non-faulted sections of the power system [3]. For a large power system, voltage instability can cause a significant damage.

For cylindrical rotor synchronous generators the generator may lose synchronism instantly after loss of excitation even when the generator is operating at light loads [4]. Due to the mentioned reasons, protection engineers try to ensure that this condition is detected as early as possible. There are five protection schemes used to detect loss of excitation namely:- the U-I scheme based on the measurement of phase angle difference and between phase voltage and current, P-Q scheme which uses generator active and real power output, G-B scheme which is based on the generator terminal admittance. The

last two schemes are R-X schemes which are based on the measurement of impedance at the generator terminals. One of these two elements is supplemented by a directional element [5].

This paper focuses on the R-X protection scheme which is a negative MHO offset element. When this scheme is properly set, it can detect a loss of field excitation from full load down to no load [6].

2. GENERATOR OPERATING LIMITS

Each and every generator works according to a capability curve which is given by the manufacturer and limited by the rated MVA which represents the generator maximum continuous output in steady state without overheating [7]. During loss of field excitation, the machine will start operating in the under-excited operating limit region of the generator capability curve which is hazardous to the unit. The prime protection for this is the Under Excitation Limiter (UEL) control on the excitation system. The UEL's role is to prevent the excitation declining over the stator end region heating limit. For this reason it is very imperative that the settings of the UEL and the loss of field excitation protection should not overlap each other. If they overlap each other during the case of loss of field excitation than the leading reactive power should reach the UEL faster than the characteristics of the loss of field excitation protection elements [8].

3. NEGATIVE-OFFSET MHO

This element uses two circles which are formed using the generator's saturated direct axis transient reactance and a diameter for 1 per unit for the outer circle. Both these circles have a negative offset of half the saturated direct axis transient reactance. These two circles normally referred to as zone 1 and zone 2 together as shown in

figure 1 can detect loss of excitation occurring during light and heavy loads. When the measured impedance falls inside zone 1 or zone 2 (operating region), the relay will issue a trip signal and after a certain delay put to avoid tripping for scenarios such as power swings, the breaker will open to shut down generator [9].

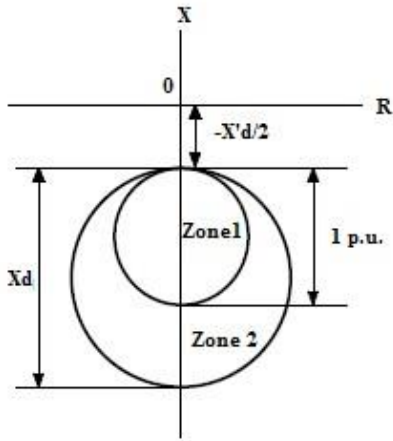


Figure 1: LOFE protection scheme with an offset mho element

4. SYSTEM MODEL

The model of the system used in this study is a well-known model used mostly in stability studies. It consists of a 555 MVA generator connected to a step-up transformer which is also connected to an infinite bus through two parallel transmission lines as presented in figure 2. This model is generated from [10] where there are four 555 MVA generators, but for the purposes of this study only one generator was used.

The real time digital simulator (RSCAD software) offers a new phase domain synchronous generator model which differs from other previous models in such that it allows the user to apply internal winding faults along the whole stator winding. Furthermore, the generator field circuit can be represented in detail with the use of power system components also allowing more realistic contingencies and fault scenarios which enhance the results obtained from protection studies.

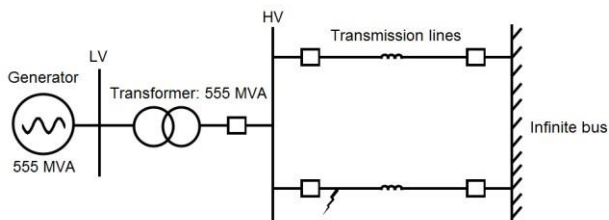


Figure 2: System model used for this study

The generator is also connected to generator controllers and due to the effect of generator protection on system disturbances and vice versa, the simulation also made use of the power stabilizer and excitation control systems. Therefore, the generator has inputs for governor/turbine and exciter interfaces [11].

5. CLOSE-LOOP TESTING OF HARDWARE PROTECTION RELAYS

Closed loop testing has made it possible for protection engineers to determine how the relay operates for a given fault condition. It allows one to analyze the behavior of the relay succeeding to initial operation (for reclosing strategies). With this arrangement, protection engineers can analyze the effect of the relay operation on the power system and its stability.

The interaction between the individual protection relays in a full protection scheme during the response to fault conditions and also consider the effect of inaccuracies, non-ideal characteristics or errors in measurement. Investigations and troubleshooting of field events where relays are found to operate differently in practice than expected can also be conducted using this arrangement [11]. Figure 3 shows the equipment and method of testing used in this study.

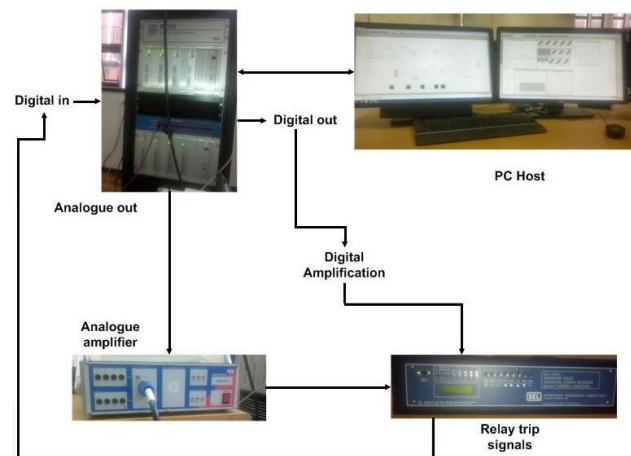


Figure 3: Closed loop testing of the SEL 300G generator protection relay using the RTDS system

6. SIMULATION RESULTS

When a generator loses excitation, it consumes a large amount of reactive power from the external power system in order to support its terminal voltage. The excessive reactive power drawn by the generator can harm the generator and cause instability of the whole system. To lower the damage that may be caused by this condition, loss of field excitation protection detects scenarios when the excitation is below the minimum excitation limit. A short circuit on the slip rings will reduce the excitation voltage down to zero. This will cause a gradual reduction of the excitation current and eventually a loss of excitation. An open circuit in the field circuit will also cause a total loss of excitation. When the field breaker is open, a high voltage is induced in field winding and there is a risk for damages to the discharge resistor [12]

For this study, loss of field excitation was investigated with:

1. Short circuit in the field winding
2. Open field breaker

6.1 LOFE Impact on Generator Parameters

Before the study was conducted, the hardware relay was verified if it was reading out the accurate system parameters before any disturbance could be applied. Figure 4 illustrates power output values, the power factor of the relay and the system frequency as taken from the display screen of the SEL 300G generator protection relay.

For the MHO negative offset element used, the relay settings were based on CT and VT secondary quantities, the impedances were calculated on the CT and VT secondary basis. The time delays were chosen so that zone 1 time delay is set to 0.05 seconds to prevent mal-operation during switching transients whereas a time delay of 0.5 seconds was used for zone 2 to avoid relay mal-operation during power swing conditions. Figure 5 shows the impact of LOFE on the generator parameters which resulted from a short circuit in the field winding. For the following results, the relay was deactivated so as to analyze the impact of LOFE events in the system.

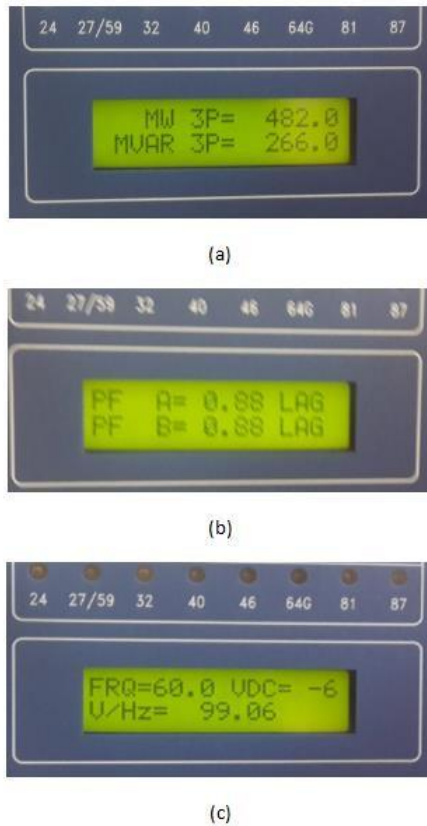


Figure 4: (a) Generator active and reactive power outputs, (b) machine power factor, and (c) system frequency

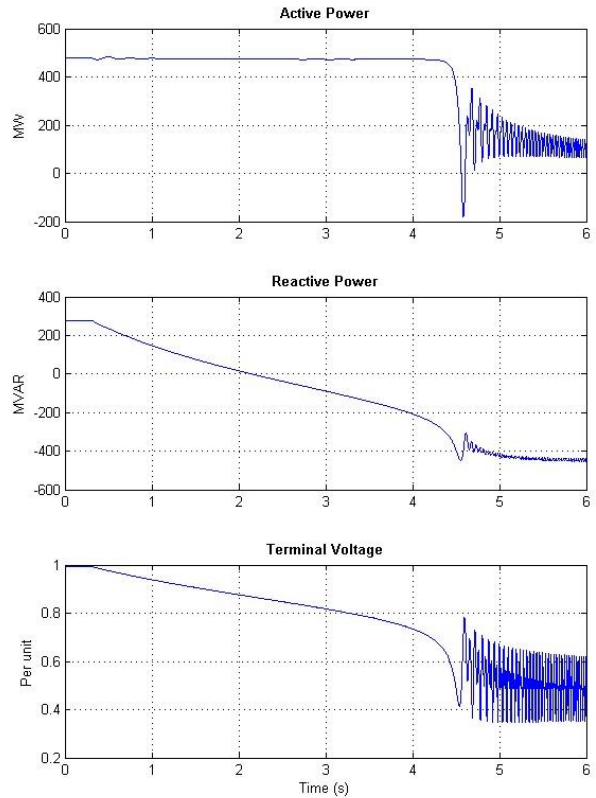


Figure 5: Effect of LOFE on generator parameters (short circuit in the field winding)

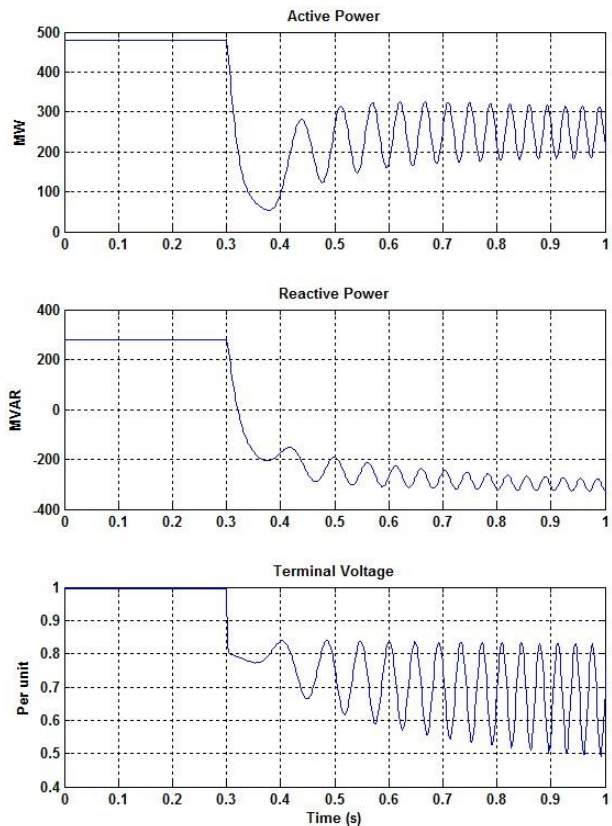


Figure 6: Drastic changes caused by the accidentally opening of the field breaker

The results shown in figure 5 also illustrates that during this condition, the mechanical power remains intact (active power remains at 482 MW) as the generator attempts to remain synchronized by running as an induction generator. As an induction generator, the machine speeds up and draws a lot of reactive power from the grid. The generator reactive power output is proportional to the internal generator voltage. Therefore, the terminal voltage of the machine also decreases at the same rate as the reactive power

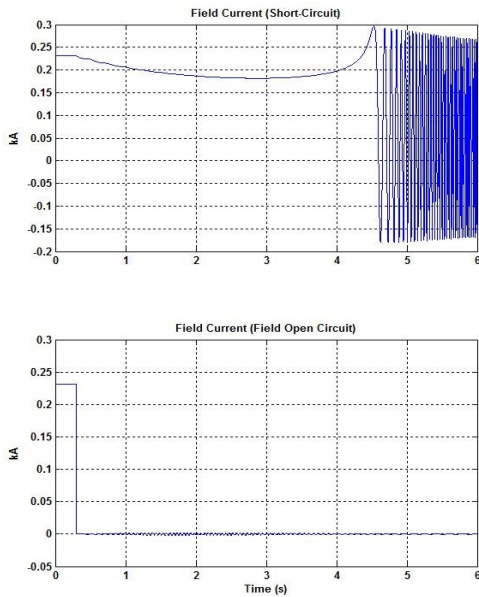


Figure 7: Field current during LOFE short circuit in the field winding and open field circuit

When a LOFE is caused by an open field breaker, the effect on the generator's parameters is more severe due to the impulsive change in the field current which in turn causes extreme fluctuations in the terminal voltage. Figure 6 illustrates the drastic changes in the generator parameters during open field circuit. The decaying of terminal voltage in both these conditions is due to the field current decaying at the field time constant rate. Figure 7 shows the behavior of field current for both the open field circuit and short circuit in the field winding.

6.2 Short – circuit in the field winding

Figure 8 shows the first event which was the short-circuit fault that occurs in the field windings that was investigated for this research, with the protection scheme enabled. A picture taken from the hardware relay showing that it has detected a LOFE condition and tripped with 40 element is shown in figure 9. Figure 10 illustrates the relay and breaker signal showing that the relay issued a trip signal at 4.494 seconds after the fault was applied. As mentioned previously, the relay uses the impedance measured from the generator terminal to detect LOFE events. Figure 11 illustrates the LOFE operating characteristics being overlaid by the impedance and the impedance locus enters zone 1 at 4.48 seconds giving a difference of 0.046 seconds which is approximately equal to the set time delay of zone 1.

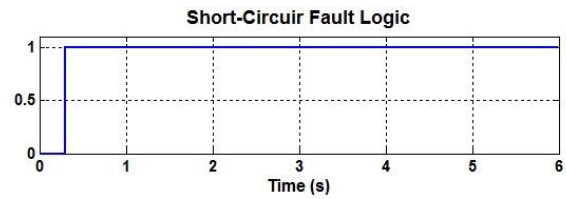


Figure 8: Short circuit fault logic

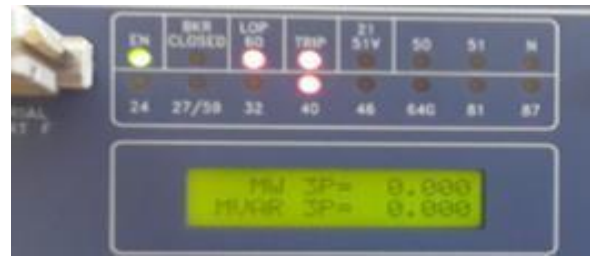


Figure 9: Response from hardware relay (SEL 300G)

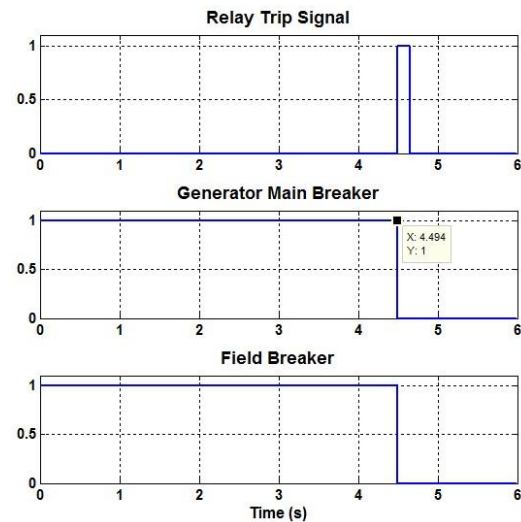


Figure 10: Relay and breaker signals (short-circuit fault)

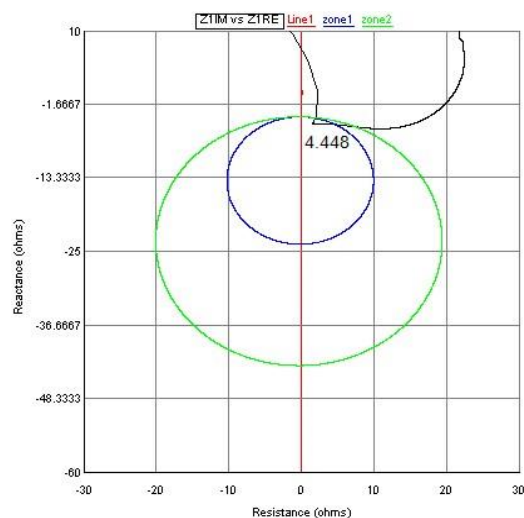


Figure 11: R-X diagram showing impedance locus during LOFE (from runtime interface in RSCAD)

6.3 Open field circuit

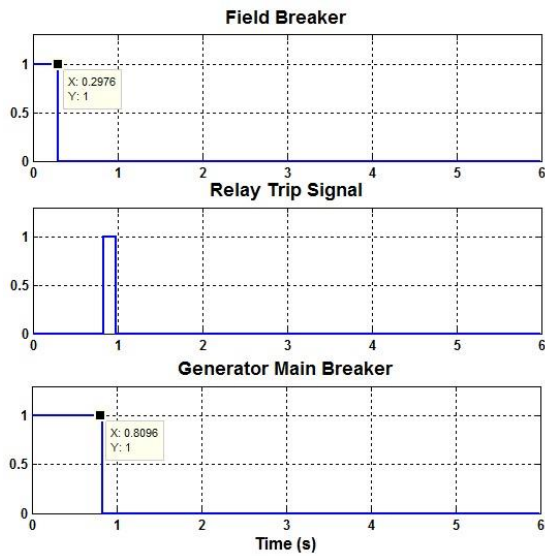


Figure 12: Response from breaker and relay

In this case the field breaker is intentionally opened at 0.2976 seconds as seen in figure 12. The relay picks up the fault as impedance locus falls on zone 2 of the 40 element characteristics. The generator was opened at 0.8096 seconds giving a difference of 0.512 seconds which can be accounted for time delay of 0.5 seconds in zone 2. The impedance locus in this scenario was more rapid compared to the short circuit fault condition making it challenging to prove that the relay had tripped at the appropriate time. Therefore, to successfully calculate the time of operation, the generator breaker was deactivated and the field breaker was opened for a better path of the impedance locus as demonstrated in figure 13.

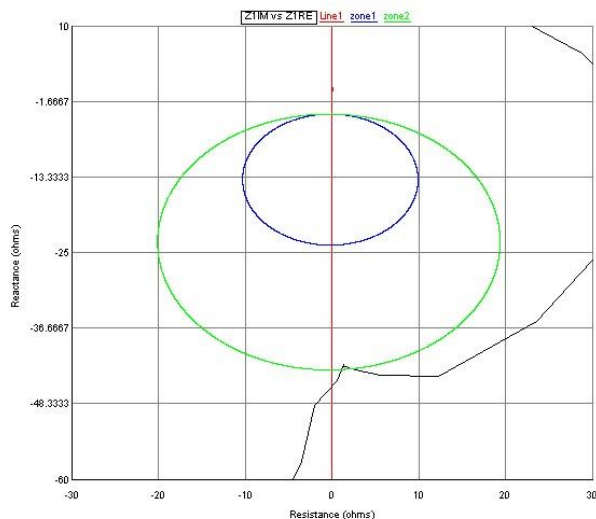


Figure 13: Impedance locus in R-X diagram



Figure 14: SEL 300G relay display screen

Figure 14 demonstrates the response from the hardware relay which indicates that the relay had detected LOFE event and issued a trip signal which was also sent back to the RSCAD software as seen in figure 12.

7. CONCLUSION

An undetected loss of field condition can lead to the decaying of voltage if the affected generator remains connected to the system. The pressure for neighboring generators to assist with the large reactive power drawn by the affected generator from the system can distress nearby voltage of the system rapidly and jeopardize voltage stability of the whole system. Furthermore, should this condition persist, severe damage to the generator due to the weakening of the magnetic coupling between rotor and stator, heavy loading on the armature windings, and thermal heating on rotor windings will occur. Hence to reduce all these impacts, LOFE events should be detected as fast as possible.

Two LOFE events were presented as well as the protection function used to protect the generator during these events. The R-X protection scheme used for the protection of LOFE in generators showed to be competent in protecting the generator during LOFE events and doing so at an appropriate time of operation.

8. REFERENCES

- [1] P. Kundur, A. Bose et al., "Definition and Classification of Power System Stability", *IEEE Trans. On PS*, Vol. 19, No. 2, pp. 1387-1401, May, 2004.
- [2] R. Sandoval, A. Guzman, H.J. Altuve, "Dynamic Simulations Help Improve Generator Protection", SEL 2006.
- [3] W.F. Mackenzie, J.A. Imhof, C. Dewey, E.J. Emmerling, F.H. Freer, S.H. Horowitz, C.L. Wagner, "Loss-of-field Relay Operation During System Disturbances Working Group Report", *IEEE on PAS*, Vol. 94, No. 5, pp.1464-74, 1971
- [4] Donald Reimert: *Protective Relaying for Power Generation Systems*, Taylor & Francis Group, New York, 2006.

- [5] Gabriel Benmouyal, *The Impact of Synchronous Generators Excitation Supply on Protection and Relays*, Schweitzer Engineering Laboratories, Inc.
- [6] Stanley H. Horowitz, Arun G. Phadke: *Power System Relaying*, Third Edition, John Wiley & Sons, Ltd., England, 2008.
- [7] IEEE Guide for Generator Ground protection, IEEE Standard C37.102TM-2006, Feb. 2007
- [8] Power System Relay Committee: "Coordination of Generator Protection with Generator Excitation Control and Generator Capability", *IEEE Power Engineering Society General Meeting*, 2007.
- [9] "SEL-300G Multifunction Generator Relay Instruction Manual", Schweitzer Engineering Laboratories, Inc., 2007.
- [10] Prabha Kundur: *Power System Stability and Control*, McGraw-Hill Inc., New York, 1994
- [11] *RTDS User's Manual*, RTDS Technologies Inc., Winnipeg, Canada, 2007.
- [12] A.B. Dehkordi, D.S. Ouellette, P.A. Forsyth: "Protection Testing of A 100% Stator Ground Fault Using A Phase Domain Synchronous Machine Model in Real Time", *IET International Conference on Developments in Power System Protection*, January 2010 Finney.

PROPOSED MODEL OF THE ELECTROMAGNETIC ENVIRONMENT IN TRACTION SYSTEMS TO PREDICT THE PATH OF RETURN

J. Clay^{1,2} and I. Hofsjager¹

¹ University of the Witwatersrand, Johannesburg, School of Electrical and Information Engineering.

² Transnet Freight Rail, Technology Management, Traction Technology, Johannesburg.

Abstract: The electric railway environment has long been considered electromagnetically unfriendly and has been plagued by electromagnetic interference. Recently, it has been found that a substantial percentage of return current flows through the couplers of moving trains. This paper presents a theoretical equivalent electrical circuit model of the wagon, railway infrastructure and locomotive in order to predict the coupler current. These models provide a theoretical approximation of the system and the contributing parameters. As a further development of the project, the model will be verified through in depth testing under various conditions. This testing will not only test the accuracy and reliability of the model, but will also refine it.

Keywords: Electromagnetic Compatibility, Model, Train, Wagon Current.

1. INTRODUCTION

Return current, or a portion thereof, to the substation from locomotives has been found to flow through the couplers of a train. This current, often referred to as “Wagon Current”, has been found to cause failures due to interference caused in systems located close to the couplers. Such an example is the Electronically Controlled Pneumatic (ECP) brake system which has a power and signal cable which runs the length of the train. This brake system is found on the South African Coal Line, which is one of South Africa’s heavy haul lines. It is suspected that the wagon currents cause interference through inductive coupling with such systems. The mechanism forming the wagon currents is not simple, and many parameters are suspected to influence the amount of current that flows through the couplers of the train. Some of these suspected parameters include the railway infrastructure, wagon design, line current, environmental conditions, train configuration and train location relative to the feeding substation to name a few.

In order to understand the mechanisms suspected to effect the current distribution along a train, an approximate circuit model of the system must be developed. This model will aid in theorizing the causes of the electromagnetic incompatibility, predict the effects, and also analyse the possible benefits of the presence of this coupling. Thus a model of the system is developed and proposed in the form of three sub-system models being the locomotive model, the supply model and the wagon model. The amalgamation of these models into the system model will expectantly allow for the simulation of the coupler currents.

2. THE SUPPLY INFRASTRUCTURE

2.1 The Ideal Supply Model

The power supply infrastructure to the locomotive can be modelled very simply, with only an ideal source, or with added levels of complexity. Each level of complexity that is added will result in a more accurate model. Initially, the simple ideal source model feeding power to the locomotive is proposed, as can be seen in Figure 1.

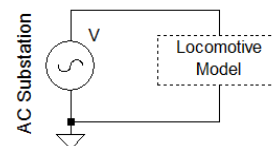


Figure 1: Diagram to show the Ideal AC Substation Supply Model.

This model means that the voltage supplied by the substation will be equal in magnitude and phase as the voltage supplied at the locomotive. This is clearly not the case, as the transmission line will cause a voltage drop as it is non-ideal and has impedance due to its physical attributes. It is for this reason that the lumped impedance supply model is proposed in section 2.2.

2.2 The Lumped Impedance Supply Model

The transmission line of any power transmission system will have a resistive, inductive and capacitive element to it. These attributes will result in the voltage magnitude and phase being altered. The impedance of the line will usually be specified per kilometer, thus a lumped model can be used such that the impedance is a function of the distance (d) of the locomotive from the substation. This model is shown in Figure 2.

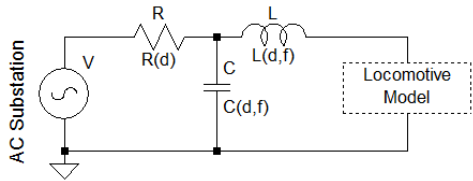


Figure 2: Diagram to show the Lumped Impedance Supply Model.

From Figure 2, it is clear that, depending on the transmission line parameters, there will be a voltage drop and phase shift along the transmission line. This means that the voltage at the output of the AC substation and the voltage at the input of the locomotive will be different in magnitude and phase; however they will be related through the parameters of the transmission line.

This model is a simple description of the power feeding circuit; however, there are multiple conductors as opposed to a single conductor carrying current to and from the locomotive. This means that the model must be extended in order to achieve an acceptable level of accuracy. In order to do this, the typical infrastructure layout must be considered as well as the electrical parameters of each conductor. Figure 3 shows the typical infrastructure layout that is found on the Coal Line.

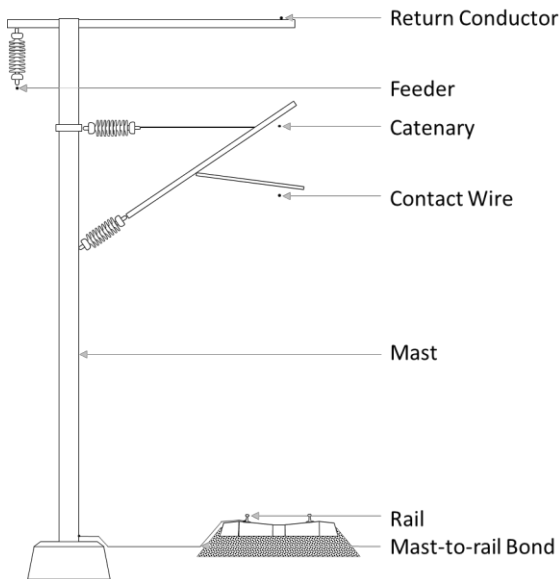


Figure 3: Diagram to show the Typical Supply Infrastructure Layout on the Coal Line.

The geometrical configuration of the conductors insinuates, that each conductor will have a self-inductance parameter as well as a mutual inductance parameter to every other conductor [1]. Although the current distribution in the conductors is considered to not be uniformly distributed over the conductor's cross-section due to the each conductors proximity to other current carrying conductors, the proximity effect is not considered to be pronounced as the conductors are a

substantial distance apart compared to their radii [1]. Figure 4 shows the typical conductor separation found on the Coal Line.

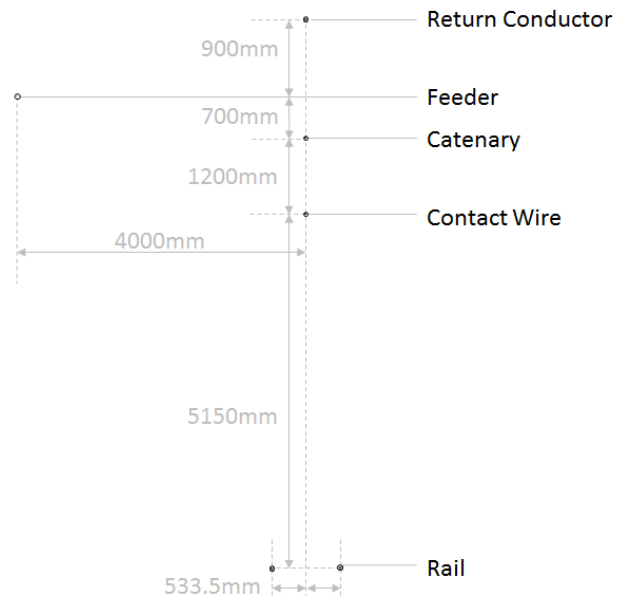


Figure 4: Diagram to show the Typical Conductor Separation on the Coal Line.

The conductors, although eventually forming a closed loop system, will be considered as partial inductances. The theory of partial inductance falls outside the scope of this paper, however the derivations are used. The details theory can be found in [1].

Since it is desirable to model the transmission line parameters as lumped parameters per meter, the self and mutual partial inductances will be specified per meter length.

Following complex mathematical derivations, the formulae for partial self-inductance and partial mutual inductance are found in equations (1) and (2) respectively [1].

$$L_p \cong \frac{\mu_0}{2\pi} l \left[\ln \left(\frac{2l}{r_w} \right) - 1 \right] \quad \text{for } l \gg r_w \quad (1)$$

$$M_p \cong \frac{\mu_0}{2\pi} l \left[\ln \left(\frac{l}{d} + \sqrt{\left(\frac{l}{d} \right)^2 + 1} \right) - \sqrt{1 + \left(\frac{d}{l} \right)^2} + \frac{d}{l} \right] \quad \text{for } d \gg r_w \quad (2)$$

where: L_p is the partial self-inductance of the conductor.

l is the length of the conductor/s.

r_w is the radius of the conductor.

M_p is the partial mutual inductance between two parallel conductors.

d is the physical distance between the two parallel conductors.

Due to the fact the orthogonal currents flowing along the mast structure travel a small distance in comparison to the transmission line, the coupling of these orthogonal currents is considered to be negligible.

The relevant physical parameters of each conductor described in Figure 3 and Figure 4 can be found in [2]. The rail, although not cylindrical is estimated to be cylindrical with a radius based on its cross sectional area.

Table 1: Table showing the Electrical and Physical Parameters of the Conductors Typically found on the Coal Line, [2].

	Units	Material	Ermelo - Vryheid	Vryheid - Richards Bay
Contact Wire	mm ²	HD Cu	107	161
Resistance	Ω/km		0.2186	0.1616
Catenary Wire	mm ²	HD Cu	65	80
Resistance	Ω/km		0.3230	0.2851
Return Conductor	mm ²	AAC	150	250
Resistance	Ω/km		0.2316	0.1574
Additional Return Conductor	mm ²	AAC	150	None
Resistance	Ω/km		0.2316	
Feeder Wire	mm ²	AAC	150	150
Resistance	Ω/km		0.2316	0.2316
Rail	mm ²	Steel	3853	3853
Resistance	Ω/km		0.04	0.04
Span Length	m		71	67
Contact Wire Height (Normal)	m		5.15	5.2

Using the parameters detailed in Figure 3, Figure 4 and Table 1, the partial inductances of the supply infrastructure can be calculated through the use of equations (1) and (2). The results of which can be seen in Table 2 where the partial mutual inductances between each pair of conductors is shown as well as a conductors partial self-inductance. All values are calculated for a length of 1 meter.

Table 2: Table showing the Partial Self and Mutual Inductance of the Conductors (per meter) Typically found on the Coal Line, [2].

(H)	Return	Feeder	Catenary	Contact Wire	Rail-Left	Rail-Right
Return	9.34E-07	2.43E-08	6.07E-08	3.53E-08	3.34E-08	3.34E-08
Feeder	2.43E-08	9.34E-07	2.45E-08	2.25E-08	1.27E-08	1.19E-08
Catenary	6.07E-08	2.45E-08	1.02E-06	7.93E-08	1.57E-08	1.57E-08
Contact Wire	3.53E-08	2.25E-08	7.93E-08	9.67E-07	1.93E-08	1.93E-08
Rail-Left	3.34E-08	1.27E-08	1.57E-08	1.93E-08	6.09E-07	8.82E-08
Rail-Right	3.34E-08	1.19E-08	1.57E-08	1.93E-08	8.82E-08	6.09E-07

The mast-to-rail bonding straps are typically installed on every fifth mast pole. If the assumption is that the impedance of the bond itself is negligible, then the parameter affecting the impedance between the rail and the return conductor is the impedance of the rail over the distance. The lumped impedance model of these bonds will need to be an oscillating function, as these bonds repeat every fifth mast pole. This oscillating function will be described using a Fourier series of sine waveforms and is approximated as follows:

$$Z_{bond} = Z_{rail} \left| \sin\left(\frac{180d}{5span}\right) - \frac{1}{9} \sin\left(\frac{540d}{5span}\right) + \frac{1}{25} \sin\left(\frac{900d}{5span}\right) \right|$$

where: d is the distance from the substation.
 $span$ is the distance between mast poles (either 0.071km or 0.065km).
 Z_{rail} is the impedance of the rail (0.04 + j0.95 Ω/km).
 Z_{bond} is the impedance of the bonding between the rail and the return conductor at distance d .

These parameters lead to an extended lumped impedance model which describes the parameters of each conductor as well as the bonding between the rail and the return conductor as can be seen in Figure 5. Z_{bond} consists of resistance R_{bond} and inductance L_{bond} . The resistive components are based in the physical resistivity of the materials as indicated in Table 1. The inductive components are based on the partial inductances of Table 2.

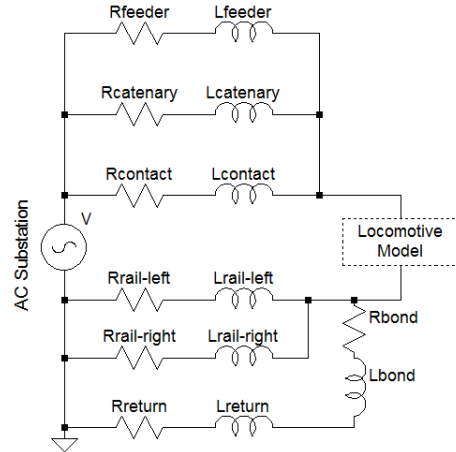


Figure 5: Diagram to show the extended lumped impedance supply model based on the parameters found in Figure 3, Figure 4, Table 1 and Table 2.

3. THE LOCOMOTIVE MODEL

3.1 The Single Source Locomotive Model

Due to the fact that modern locomotives have an approximated power factor of unity, stemming from the addition of advanced on-board power electronics, the locomotive can be simply modeled as a controlled current source as shown in Figure 6 below.

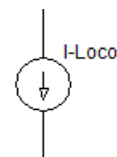


Figure 6: Diagram to show the simplified current source model of a modern locomotive utilizing on-board power electronics.

The instantaneous value of I_{Loco} , as depicted in Figure 6, can be determined by the rating of the locomotive, and the line voltage. This is assuming that the locomotive is operating continuously at full rating. This is assumed for the sake of simplicity, but can be extended further during the course of research to include operations at reduced power (lower traction command or coasting).

As an extension of this simple model, the regenerative braking function of the locomotive can be included. When a locomotive enters regenerative braking mode, the locomotive acts as a power source instead of a power sink or load. By simply inverting the current value of the locomotive model, I_{Loco} , to reflect $-I_{Loco}$, the locomotive itself becomes a power source.

Although this locomotive model is simple to use and understand, the effects of harmonics due to the use of the power electronics cannot be ignored and must be included in the locomotive model. Thus, the multiple source locomotive model is proposed in section 3.2.

3.2 The Multiple Source Locomotive Model

The on-board power electronics found in modern locomotives adds the benefit of simplifying the model of the locomotive as a power sink with unity power factor. However, this being said, the on-board power electronics also adds complexity due to the harmonic content that is introduced into the system. Table 3 shows the harmonic content measured from Transnet Freight Rail Class 19E locomotives which are the locomotives being used in the scope of this research.

Table 3: Table showing the approximated harmonic content of a class 19E locomotive, extracted from [3].

Harmonic order	Frequency [Hz]	Observed Current [A]	Percentage of Fundamental
Fundamental	50	180.00	100%
2	100	105.00	58%
3	150	7.00	4%
4	200	15.00	8%
5	250	1.50	1%
6	300	6.00	3%
7	350	0.90	1%
8	400	4.00	2%
9	450	0.70	0%
10	500	2.00	1%

From Table 3, it is clear that although the fundamental frequency, being 50 Hz, has the largest magnitude, there also exists substantial current magnitudes at higher frequencies. Thus, the single current source model will prove inadequate in modeling the higher frequency components found on the supply line. It is for this reason that the single current source model is extended to the multiple source current model. Each current source will be at the frequency and magnitude of a harmonic which is found through measured data as shown in Table 3. The multiple current source model can be seen in Figure 7.

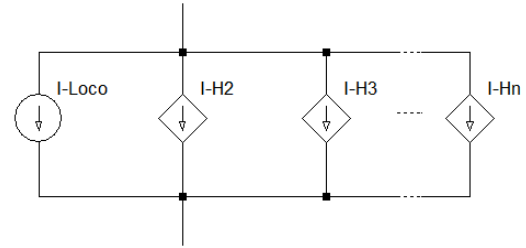


Figure 7: Diagram to show the simplified current source model of a modern locomotive utilizing on-board power electronics.

The number of sources can be varied depending on the level of accuracy required, however, for the purposes of this research the multiple source model will be limited to the 10th harmonic as per Table 3 and as depicted in Figure 8.

The return current leaves the locomotive through brushes on the axles on the wheels and into the rail which acts as the conductive path returning to the substation. This being said, the couplers on the locomotive can also act as a conductive path should another locomotive or wagon be coupled to it. This means that in a bo-bo configured locomotive (locomotive with four axles) such as the class 19E locomotive, the return current has the choice of six return paths, two couplers and four wheels. In the case of a co-co configured locomotive (locomotive with six axles), there will be eight return paths for current. However, for the scope of this research, only bo-bo configured locomotives will be considered. These return paths are added to the multiple source locomotive model as can be seen in Figure 8.

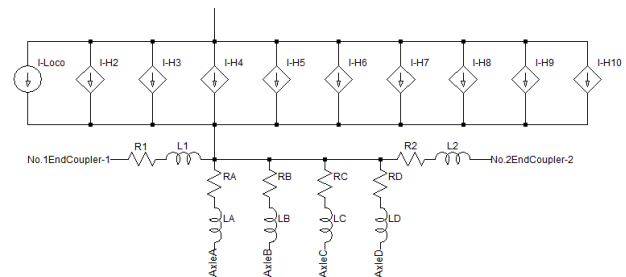


Figure 8: Diagram to show the simplified current source model of a modern locomotive utilizing on-board power electronics with various current return paths.

4. THE WAGON MODEL

4.1 The Ideal Wagon Model

Although not historically included in locomotive and supply system modelling, the wagon model must be included in this research as it is the crux of the return current distribution through a train.

In the ideal case the train of wagons could be modeled as another conductor to be included into the supply model. This additional conductor would also have a partial self-

inductance as well as a mutual partial inductance with every other parallel conductor.

4.2 The Distributed Parameter Wagon Model

Extending the ideal wagon model, we consider that the rail wagon generally has 10 points at which current can enter and/or exit the wagon. These paths are the eight wheels (four axles) and the two couplers. Similar to the various return paths seen in the locomotive model in section 3.2, the various paths are initially modelled as an arrangement of resistors and inductors.

It is expected that the values of the resistors and inductors will not be equal, and experimental research into the values of these parameters must be performed. In order to simplify the wagon model from the complex grid of resistors, assumptions regarding the symmetry of the wagons are made. It is assumed that the wheels and axle sets are symmetrical about the center of the wagon. This means that each axle with two wheels is considered a single node. For the purposes of this research, it is assumed, that the capacitive elements between the nodes of the wagon are negligible as the voltage that is expected between the nodes of the wagon should be very low. Thus the capacitive elements between the nodes of the wagon model are not included. The complex wagon model is described by Figure 9.

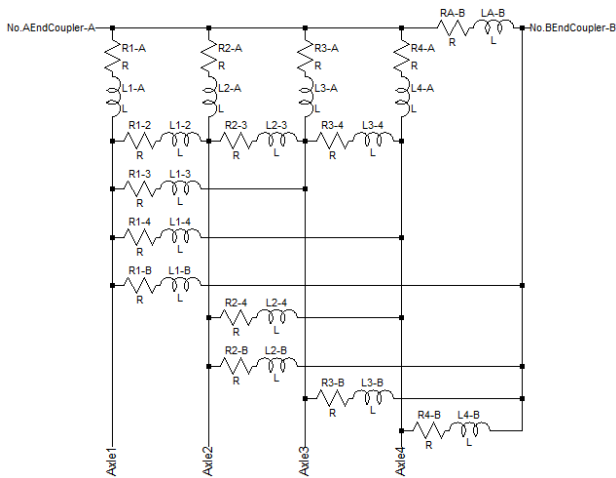


Figure 9: Diagram to show the reduced complex wagon model.

The inductive elements indicated in the model, will comprise of self partial inductance and mutual partial inductances with other conductors. The calculations of which are similar to those described in section 2.2.

5. EXPERIMENTAL VERIFICATION OF THE MODELS

In order to successfully use the models in simulations to determine the behavior of the system under varying conditions, the models must be verified and refined. This process is to be performed through experimental measurements.

5.1 The Supply Model Verification

The supply model must be verified by measuring the size of the components of the supply model. This will be performed by isolating a section of railway track whose configuration falls within the scope of research, and to supply a controlled (known) voltage and current and then to measure the voltage drop and phase shift at various distances from the supply. Analysis of the measurements will result in the sizing of the components in the supply model as well as model verification.

5.2 The Locomotive Model Verification

The locomotive model has been derived from the measured harmonic currents found on typical modern locomotives. This being said, the components constituting the current exit nodes must be sized through experimental verification. This will again be performed by applying a controlled voltage and current and measuring the magnitude drops and phase shifts at the various nodes of the model.

Again, analysis of the measurements will result in the sizing of the components in the locomotive model as well as model verification.

5.3 The Wagon Model Verification

The model of the wagon can be determined through the measurement of the voltage magnitude and phase at the various output nodes of the wagon whilst applying a set voltage, current and frequency to the physical wagon. Figure 10 shows the experimental setup.

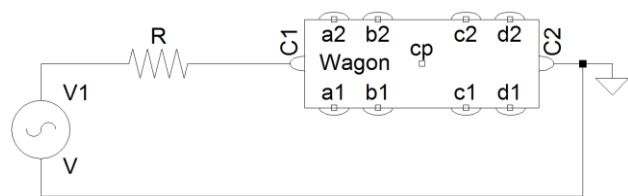


Figure 10: Circuit diagram showing the experimental setup to determine the wagon model.

- where: V is a frequency generator (variable frequency).
- R is a current limiting resistor.
- C1 is the No.1 end coupler.
- a1, a2, b1, b2, c1, c2, d1, d2 are wheel terminals.
- C2 is the No.2 end coupler.
- cp is a reference point.

Analysis of the measurements will be performed through the use of Nodal Analysis to obtain various complex simultaneous equations representing the circuit. These simultaneous equations will then be solved to size the components of the wagon model.

6. CONCLUSION

The unexpected distribution of return current, to the substation, through the train has resulted in component failures. In order to further understand the aspects influencing the return current distribution, as well as realize the value of the information obtainable by measuring the current through the couplers, a model of the system is necessary. Aspects of this model have been described in this document, the amalgamation of which provides a model which is sufficient to proceed with further investigation and research into the return current path through wagon couplers.

7. REFERENCES

- [1] C. R. Paul, *Inductance - Loop and Partial*. Hoboken, New Jersey: John Wiley & Sons, Inc., 2010, pp. 1-379.
- [2] R. S. Mann, "REPORT ON THE 25 kV AC TRACTION POWER SUPPLY REQUIREMENTS FOR THE TRANSPORT OF 30MTpa AND 40MTpa OF COAL BETWEEN ERMELO AND RICHARDS BAY.," p. 40, 1979.
- [3] H. Takahashi, M. Matsuoka, and F. Harano, "EMC Retests results: AC territory with locomotives coupled condition (2,3,6 July, 2009)," Ventersdorp, 2009.

CURRENT PROBE CALIBRATION FOR MEERKAT LIGHTNING INDUCED CURRENT MEASUREMENT

S.L. Combrink and P.G. Wiid*

* Dept. Electrical and Electronic, Stellenbosch University, Stellenbosch, South Africa, E-mails: 16030826@sun.ac.za, wiidg@sun.ac.za

Abstract: Measured and simulated results of a commercial calibration method for current probes with the focus on Rogowski coils is presented. An alternative current probe calibration method using a time domain approach is then presented. The research focuses on design and calibration of inexpensive current probes suitable for lightning induced current measurement. Preliminary test setups are discussed for measurement applications on the MeerKAT telescope.

Key words: Current measurement, Probe calibration, Lightning protection, RFI .

1. INTRODUCTION

The MeerKAT Telescope array will form part of the Square Kilometre Array which will be the world's most sensitive radio telescope [1]. To keep the system as sensitive as possible, studies have been devoted to keep the interference levels from radio frequency interference (RFI) sources as low as possible. However, environmental sources (such as lightning) can not be minimized since it occurs naturally.

Lightning protection is an important topic to consider for outdoor applications, especially in areas with active lightning activity. Currents and charge as much as 200 kA and 100 C, respectively can occur in a single short stroke [2]. Thus, it is important to not only evaluate the lightning current paths, but also induced currents which might interfere with or radiate to sensitive instruments. Lightning protection and lightning induced current mitigation is one of the main motivators of the research project. In order to evaluate mitigation an accurate measurement device is necessary.

Several ways of measuring lightning current exist with the preferred method being with a current transducer known as a Rogowski Coil (RC) [3] [4] [5]. The main advantage of a RC is the return winding which acts as a negative pick-up loop for stray fields, resulting in an output with a higher signal to noise ratio. RC's can also be designed to be larger than conventional current clamps, making them desirable when measuring currents in large conductors such as antenna struts. Figure 1 shows four RC's with one being intentionally large.

A main aim of the research project will be to set guidelines for delivering RC's with high sensitivity or high bandwidth, or to highlight restrictions on bandwidth due to physical dimensions. This will be achieved by developing and adjusting a theoretical model for the RC that will match the simulations and measurements in a time domain calibration technique. With this, a cost effective high bandwidth RC can be developed for specific RFI monitoring applications.



Figure 1: Different Rogowski Coils.

2. CURRENT PROBE CALIBRATION

2.1 Rogowski Coil theoretical model

Various sources consider the RC as a basic 2nd order filter with a series inductance and resistance and a shunt capacitance [6] [7]. Variations include terminating resistors and components for an integrator [8]. After some investigation it was found that this model is applicable to low bandwidth RC's. Work done by [9] introduces the RC as a distributed transmission line model with N sections (N being the number of windings). Although the theory and practical measurements correlate well, it is believed that the approach is application specific due to the constant capacitance introduced in calibration procedure which might not be present during a field measurement.

Our work aims to harmonise the approach in [9] with RC's of different physical dimensions. The model to be used will exclude inter-winding capacitance since simulations done by [10] and [9] have little effect over the working bandwidth and is therefore small enough to neglect. Some RC's include an electrostatic shield to counter a capacitive coupling component [11] [12]. Although a fair level of shielding is offered by this approach, the introduced capacitance will lower the RC's bandwidth

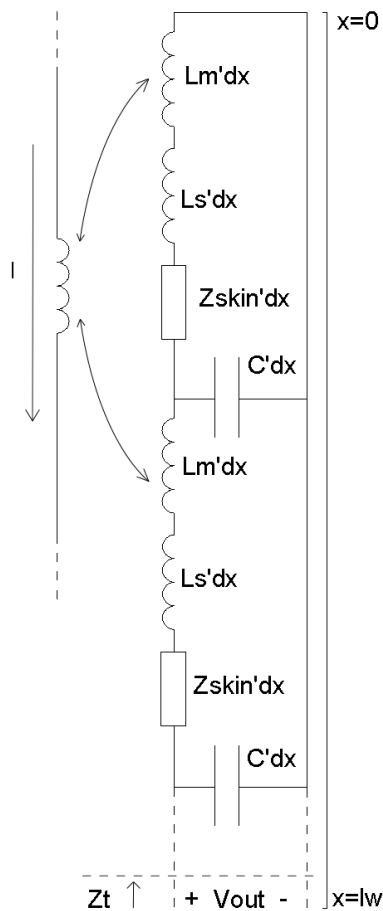


Figure 2: RC distributed transmission line model showing the transfer impedance Z_t as the induced voltage V_{out} from a current I on the enclosed wire being measured. This dependence is described by equation 1.

[11]. Therefore, the model currently only contains components for mutual ($L_m'dx$) and self inductance ($L_s'dx$), coil-to-return-winding capacitance ($C'dx$) and a resistive component due to the skin effect ($Z_{skin'dx}$). Figure 2 shows a transmission line model of the RC with mentioned components. The length lw is the total length of the wire used in the RC.

With the theoretical model still being investigated, another means of measurement verification was sought. FEKO, which is based on the Method of Moments approach, was used to simulate the calibration of the RC [13]. The setup is depicted in figure 3. The FEKO model for the fixture is a slightly simplified model of the actual calibration fixture which shortens the simulation time. Ports on the model correspond to the ports on the actual fixture and equation 2 is applied on the scattering parameters results from the simulation. The RC and fixture is discretized resulting in a mesh size of $\frac{\lambda}{25}$ at the highest frequency and simulated over the frequency band of 0.3-300MHz.

2.2 Conventional current probe calibration

For most applications, the current probe to be used is calibrated for the application. Usually in a partial discharge application the probe is calibrated with a current pulse with known characteristics. In some applications the probe's response is measured against another probe whose characteristics are known. The probe to be calibrated is then calibrated until the measured currents match to some extent. In the case where an integrator accompanies the RC, the integrator components are chosen for calibration. While the environment in such calibration setups is similar to those in an actual measurement, it may have noisy sources which will affect the calibration.

A calibration method commonly used by current probe manufacturers results in a transfer impedance for the RC. The transfer impedance is given by equation 1 which shows the relation of voltage and current depicted in figure 2. The conductor current to be measured is indicated by I , Z_t is the transfer impedance and V_{out} is the voltage of the RC's terminals.

$$Z_t = \frac{V_{out}}{I} \quad (1)$$

A calibration fixture is used in the transfer impedance method. The fixture (such as figure 4) needs to be physically small to ensure that resonances (due to quarter wavelength current paths) does not appear in the working bandwidth of the device under test. Unfortunately using a small fixture introduces a capacitance to RC's which might not be there during a normal measurement. To minimise the capacitance introduced, a larger fixture such as figure 3 is used. Since the current path of a quarter wavelength is longer with larger fixtures, the resonant frequency is lower and might fall in the working bandwidth of the RC, resulting in poor high frequency calibration. An advantage of this fixture is that it is relatively inexpensive and can accommodate RC's of different sizes.

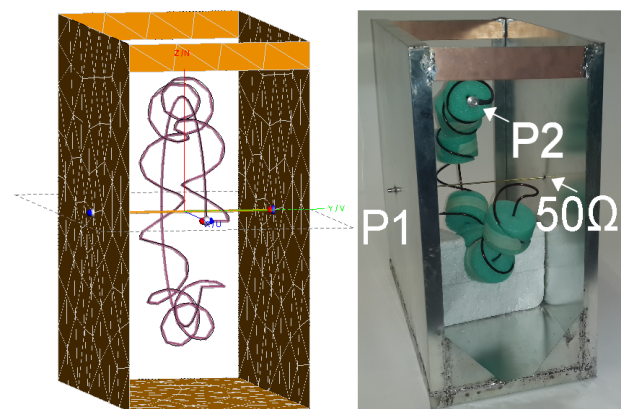


Figure 3: FEKO simulation and measurement of RC calibration fixture with the large RC. Port 1 is located on the visible fixture wall, port 2 is the RC output and port 3 is terminated with a 50Ω load.

The calibration method makes use of a calibrated Vector Network Analyser (VNA) and excites the centre conductor of a calibration fixture at selected pre-defined frequency points. The transfer impedance of a current probe is determined by equation 2 where S_{11} and S_{21} (reflection and transmission coefficients, respectively) are components of the scattering parameters received from a 2-port VNA measurement. VNA port one is the excitation port that is connected to the visible wall-port of the fixture in figure 3. VNA port two is connected to the RC. The second port of the fixture (not visible) is terminated with a 50Ω load.

$$Z_t = 50 \frac{S_{21}}{1 - S_{11}} \quad (2)$$

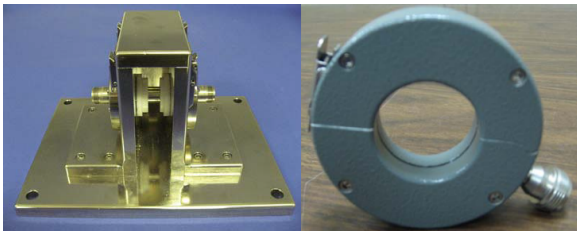


Figure 4: Fischer FCC-MPCF-3-32/71/1 calibration fixture and F-62 current probe [14]

2.3 Alternative calibration method

Some preliminary work has been done on a time domain calibration method which also makes use of a calibration fixture. The method entails sending a short pulse down the centre conductor of a physically long calibration fixture. The pulse contains the harmonically related frequencies of interest and by using Fourier theory, the RC can be calibrated over the desired frequency range through repeating pulses. To ensure that reflections do not interfere with the probe's response, the fixture needs to be long enough to clearly distinguish between the reflections and responses with sufficient time between them. The reflections of S_{11} and S_{21} is then gated out and equation 2 is used to calculate the transfer impedance. Currently a screened room is used as a calibration fixture. This is done to make use of a noise-free environment and to achieve acceptable fixture length. Figure 5 shows the reflection coefficient S_{11} of a TD approach in a screened room. The first reflection at 0ns originates from the step in impedances and the last reflection at 17ns is due to the short that is made with the screened room wall. With all the distances known, the expected response of the effect the RC has on the transmission line can be expected at $t_1 = \frac{2*w_2}{c}$ where c is the speed of light. Due to the large RC having only a small effect on the impedance of the line, minimal reflections are seen around $t=9$ ns.

2.4 Early results

The large RC was calibrated according to the method described in section 2.2. A simulation of the RC was also done in FEKO and the results are compared in figure 6.

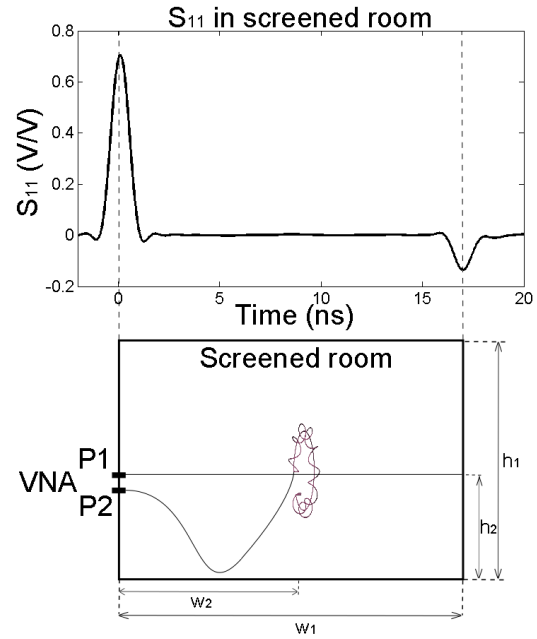


Figure 5: S_{11} and corresponding representation of screened room as calibration fixture. A thin wire is connected from port one to the opposing wall at a height h_2 . The RC is placed around this wire at a distance w_2 . The height and width of the screened room is indicated by h_1 and w_1 , respectively.

Figure 6 shows the transfer impedance of the large RC. Early measurements tie up well with simulations except for the resonance at 140 MHz. When the RC is measured without its supporting foam, a similar resonance occurs at a lower frequency. Future work will involve analysing the frequency difference in resonances. The measurement without the support structure brings forth an interesting aspect, namely a loss component in the foam. It is believed that a lossy substance can be used instead of a terminating resistance to dampen high frequency resonances and increase the working bandwidth of the RC [7]. Future RC work will involve explaining the frequency difference in resonances and also adjusting the model to tie up with measurements and simulations. Sensitivity and bandwidth widening will also be of interest.

3. MEERKAT LIGHTNING PROTECTION

3.1 MeerKAT preliminary test

The lightning protection system of the MeerKAT antenna consists of a lightning air termination rod (ATR) which connects to the lightning down conductors (LDC). The LDC relays current to the pedestal through conductive straps over the shoe-slip-ring assembly. Since the pedestal forms part of the LDC system, it needs to be connected to the earth termination system (ETS) to complete a low impedance path to ground. The pedestal is bolted to the ETS which has impedance to ground of 1Ω . Of 32 bolts, four is directly connected to the ETS. The bolts can be seen in figure 7 where two are circled and annotated as D .

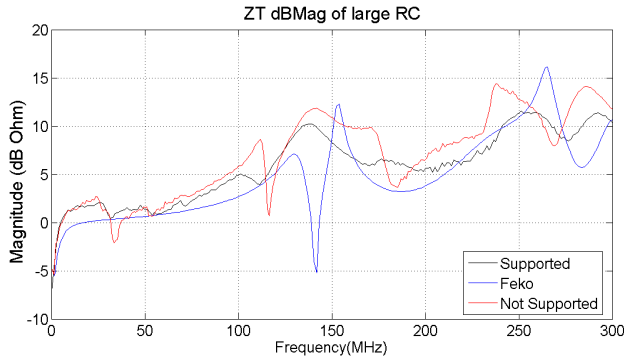


Figure 6: Transfer impedance of the large RC. Measurements of the RC with and without supporting foam structure (Supported and Not Supported, respectively) and a simulation done in FEKO is shown.

To keep the lightning current away from sensitive areas the mentioned connections must ensure a very low impedance path. For the MeerKAT antenna, some recommendations from academics and professionals for the KAT-7 project have been implemented. Per example, one of the recommendations was to make use of four instead of two conducting straps to relay current passing through delicate mechanical control infrastructure, resulting in a Faraday cage effect [16]. As part of a recent measurement campaign, preliminary measurements were taken in order to establish testing points and to prove our proposed measurement method using the RCs and current probe's. However, some tests could not be performed due to the antenna installation being finalized.

For the mentioned campaign three main areas of interest were investigated: The jack screw assembly, the conducting straps in around the shoe slip ring assembly and the pedestal to earth connections. These areas are circled in red in figure 7. The jack screw assembly is not part of the lightning protection system, but concern is raised since lightning currents might flow in the assembly, possibly damaging sensitive components such as bearings. Tests could not be done on the conducting straps since access was unavailable during the finalisation of the installation. Lastly the pedestal-to-earth connections were investigated. By measuring the current flowing through each connection, a comparison can be made of the current distribution and the relative impedance to earth.

To simulate a lightning strike without its severity, a pulse was injected onto the lightning ATR. Position A in figure 9 shows where the ATR is situated; being an earlier photograph, the actual ATR is not present. The current distributes and flows down the pedestal (figure 8 towards the lowest potential (earth)). The jack screw measurements were made with the large RC since it is the only device large enough to fit around the screw assembly.

For the pedestal-to-earth connections a small current probe was used, similar to that showed in figure 4. The results are shown in figure 9 and shows that the currents distribute more or less evenly between the four earth connections,



Figure 7: Earlier MeerKAT antenna photograph with circled points of interest: A: Current injection point, B: Jack screw assembly, C: Shoe-slipring assembly, D Pedestal-to-earth connections, E Isolation transformer.

due to the impedance paths being approximately the same.

Care was taken not to bias the current path that an actual lightning strike would take. To accomplish this both the pulse generator and the measurement device was powered from an inverter battery setup. The inverter unfortunately is a inherently noisy device and contaminated the measurements. Since the inverter battery setup was present in all the tests, it is constant in all the measurements and allows for comparable results. Another area of concern is the use of a long cable to connect to the lightning ATR. It was found that common mode currents exist on the cable and may illuminate the antenna, causing interference with the measurement.

3.2 Future work

Future campaigns may present opportunity to complete tests and attempts new tests. The results from the campaigns will need to be compared to simulations and a scaled model measurement. A simplified FEKO and a physical model of MeerKAT exists for these purposes. Three pulses will be defined for the simulations which will introduce different frequency content. The pulses will be made up of short or long stroke characteristics or a combination of both.

For one of the KAT-7 antennas an EMC gasket was

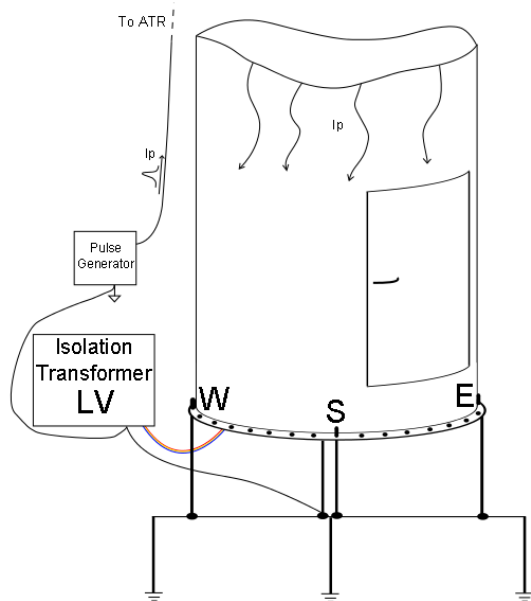


Figure 8: Diagram showing earth termination system, pulse generator setup and earth termination system with three measuring points (W,S and E). The current pulse (I_p) is injected on the air termination rod (ATR) and distributes along the pedestal, returning via ETS.

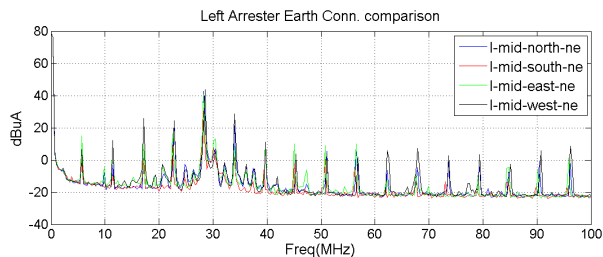


Figure 9: Current measurements at earth-to-pedestal connections

introduced, resulting in better shielding effectiveness [15]. Since the electronics for MeerKAT is fitted in a shielded cabinet, a shielded pedestal door is not required. However, investigations must be done to see whether lightning currents would find a path inside through the unshielded door.

Immediate work for the next campaign will involve investigation of the inverter. Either a quieter inverter or an EMC shielding enclosure will need to be added to the setup. Both options will be investigated along with the illumination from the common mode currents on the cable. A possible solution to the latter might be the use of RF chokes, also known as EMI suppression cores.

For the MeerKAT system an isolation transformer (point E in figure 7) is used to isolate it from the feeding ring's earth and neutral connections. The primary side connects to the feeding ring via delta connection although the feeding ring can supply a wye connection. On the secondary side the local earth of the antenna is connected along with the three

phases in a wye connection. For future measurements, the isolation transformer will allow access to the earth of the antenna to ensure an ideal common reference point. Figure 8 shows this proposed setup.

4. CONCLUSION

The research is ongoing and forms part of a Masters degree project. Acceptable simulated results have been obtained as compared to results measured with the conventional calibration technique used by current probe manufacturers. Preliminary work on an alternative calibration technique using time domain was presented. It is believed that this technique has great potential for faster wide-band calibration of current probes. With calibrated data on application specific designed Rogowski coils, lightning current paths for MeerKAT can be investigated in detail. From this, high-risk areas can be identified and appropriate mitigation measures proposed.

REFERENCES

- [1] South African SKA (Square Kilometer Array), <http://www.ska.ac.za/meerkat/>
- [2] South African National Standard: "Protection against lightning, Part 1: General principles", SANS 62305-1:2011, June 2011.
- [3] A.M. Hussein, W. Janischewskyj, M. Milewski, V. Shostak, W. Chisholm and J.S. Chang: "Current waveform parameters of CN tower lightning return strokes", *Journal of Electrostatics*, Vol. 60 Issues 2-4, pp. 149-162, February 2004.
- [4] J. Kato, T. Tominaga and N. Kuwabara: "Improved frequency characteristics of large Rogowski coil using lightning surges observation", *1999 International Symposium on Electromagnetic Compatibility*, NTT Multimedia Networks Laboratories, Tokyo, May 2007.
- [5] K. Yamamoto, N. Ueda, A. Ametani and D. Natsuno: "A Study of Lightning Current Distribution at a Wind Turbine Foot: Influence in Current Measurements Using a Rogowski Coil", *Electrical Engineering in Japan*, Vol. 180, Issue 4, pp. 10-17, September 2012.
- [6] G. Robles, M. Argüeso, J. Sanz, R. Giannetti, B. Tellini: "Identification of parameters in a Rogowski coil used for the measurement of partial discharges", *IMTC 2007 - IEEE Instrumentation and Measurement, Technology Conference*, Warsaw, Poland, May 2007.
- [7] M. Shafiq, M. Lehtonen, L. Kütt, G.A. Hussain and M. Hashmi: "Effect of Terminating Resistance on High Frequency Behaviour of Rogowski Coil for Transient Measurements", *Elektronika ir Elektrotechnika*, Vol. 19 No. 7, pp. 22-28, 2013.

- [8] W.F. Ray and C.R. Hewson: “High Performance Rogowski Current Transducers”, *SAIEE Africa Research Journal*, Vol. 95 No. 1, pp. 7-18, March 2003.
- [9] V. Dubickas and H. Edin: “High-Frequency Model of the Rogowski Coil With a Small Number of Turns”, *IEEE Transaction on Instrumentation and Measurement*, Vol. 56 No. 6, pp. 2284-2288, December 2007.
- [10] M. Rütshlin: *Aspects of modelling and metrology in EMC*, M.S. thesis, E.E. Dept., University of Stellenbosch, Stellenbosch, 1999
- [11] C. Hewson and W.F.Ray: “The effect of electrostatic screening of Rogowski coils designed for wide-bandwidth current measurement in power electronics”, *2004 35th Annual IEEE Power Electronics Specialists Conference*, Aachen, Germany, 2004.
- [12] C.D.M. Oates, A.J. Burnett and C. James: *The design of high performance Rogowski Coils*, Prentice-Hall Inc., USA, first edition, chapter 3, pp. 82-112, August 1989.
- [13] FEKO, www.feko.info/
- [14] Fischer Custom Communications, INC., www.fischercc.com/
- [15] J.S. van der Merwe: *Cabling and Interfaces for Karoo Array Telescopes: Modelling and Metrology*, Ph.D dissertation, E.E. Dept., University of Stellenbosch, Stellenbosch, 2011
- [16] P.G. Wiid: *Lightning Protection and Radio Frequency Interference Mitigation for the Karoo Array Telescope*, Ph.D dissertation, E.E. Dept., University of Stellenbosch, Stellenbosch, 2010

DESIGN AND IMPLEMENTATION OF A DATA ACQUISITION STATION

J. Joubert* and A.J. Grobler**

* Dept. of Electrical, Electronic & Computer Engineering, 11 Hoffman Street, North-West University, Potchefstroom 2531, South Africa E-mail: 22730893@nwu.ac.za

** Dept. of Electrical, Electronic & Computer Engineering, 11 Hoffman Street, North-West University, Potchefstroom 2531, South Africa E-mail: andre.grobler@nwu.ac.za

Abstract: The need for a system that obtains data from electronic sensors was identified at the North-West University. This article contains the designing process for a data acquisition station as such. The station is compatible with a variety of sensors, aiming to ease the process of utilising suitable electronic equipment by researchers from the North-West University. The station incorporates a developed electronic circuit as well as computer software.

Keywords: Data Acquisition; Analogue; Digital; Microcontroller.

1.1. INTRODUCTION

When conducting research in the field of engineering, electronic sensors such as tachometer and voltage meters are often used. For these sensors to be effective, a feasible method of acquiring data from the sensor and processing it into information is crucial. Data acquisition is the process where a physical phenomenon such as voltage, current, temperature, pressure or sound is measured and stored through use of a computer system [1]. Typical data loggers allow the connection of a variety of instruments and sensors.

The literature review contains a thorough study into the topology of data acquisition stations. Microcontrollers and controllers were examined as if suitable for the design of such a system. Different data communication methods were considered to ensure compatibility with most sensor types. Current practices in the data-acquiring field were investigated to ensure that the station can acquire both voltage and current waveforms.

The designing section includes the procedure to be followed for the electronics and the necessary software needed for the station.

Finally, the operational result of the project is discussed.

1.1 Design Criteria

Commercially available data loggers, capable of logging a variety of sensors simultaneously, are expensive with a price range of approximately R 3 000.00 – R 12 000.00 [2]. The development of a data acquiring station must therefore be of low cost. Since different electronic sensors have different output formats, the designed station must be compatible with the different types of sensor outputs. It must allow at least five simultaneous analogue and five digital connections. Electronic sensors do not output its measured value, instead it output an electrical impulse or waveform that relates to its measured value. The designed station must therefore allow users to input the data handling formula with which the sensor output will be

transformed into the physical value. It must display information using a user-friendly format like a graph.

Summary of design criteria:

- Low Cost (less than R 2 500.00);
- Compatible with current and voltage analogue waveform inputs;
- Compatible with digital inputs;
- At least five simultaneously connected analogue sensors and five connected digital sensors;
- Manage data according to user input (formula and frequency);
- Display acquired data to user on request.

2. LITERATURE REVIEW

Whenever a physical phenomenon is measured, such as the temperature of a room, the intensity of a light source, or the force applied to an object, a sensor is used. Sensors, otherwise called transducers, convert a physical phenomenon into a measurable electrical signal. Different sensors give different outputs such as a voltage, current, resistance, or another electrical attribute that varies as the physical measured value varies. In some cases additional components and circuitry is required to accurately measure the output of a sensor [1]. The supply voltage of sensors differ depending on the sensor. For sensors with a digital output, the supply voltage is usually between $3 V_{dc}$ and $5 V_{dc}$. For analogue outputting sensors the voltage can be $12 V_{dc}$, $25 V_{dc}$ and even higher. Most analogue outputting sensors used by the university requires a supply of $12-25 V_{dc}$ [3-7].

Typically, a data acquisition system consists of three major parts: an input system, which acts as the connection point for the sensors, a host computer, which provides processing power and controlling software. All three parts can be combined into one package such as a microcontroller, or be separate packages such as a microcontroller and a personal computer. If the parts are in separate packages, the packages require a way to

communicate with each other. Common data acquisition system interfaces include the Peripheral Component Interconnect (PCI) bus which is a parallel bus connection found on computer motherboards, the PCI eXtensions for Instrumentation (PXI) bus designed for measurement applications that require high performance and rugged industrial form-factor, Ethernet, Universal Serial Bus (USB) and serial input and output. Acquisition systems can be classified as “external box”, or internal plug-in board. Both configurations have certain advantages; the external box can be located closer to the measuring sensor and thus reduces noise due to shorter transfer cable between the sensor and the box while the internal board is closer to the functioning processor that increases the system speed. Ethernet and USB are external systems while PCI and PXI are internal [8].

The input part of the system functions as the interface between the computer and signals from the outside world. It digitizes incoming analogue signals and counts digital pulses before sending it to the computer [9]. The computer and software part is used for processing, visualizing, and storing measured data [1].

In order to satisfy the need of different research fields a variety of data acquisition systems have been developed. CAMAC is one of these systems. The Computer Automated Measurement and Control (CAMAC) system is a data acquisition bus used in nuclear and physics experiments [10]. Its function is to provide a scheme to allow a wide range of modular instruments to be interfaced with a computer. The CAMAC supplies 6 Vdc, 12 Vdc and 24 Vdc to the instruments. It can transfer data every 450 ns. The two greatest advantages of the CAMAC system is its flexibility and interchangeability. The system can be configured for different applications and the addition of different modules allow more sensors and sensor types to be connected to the system. The main problem with these commercial data acquisition systems is the high cost thereof. The system is also unnecessarily complex for intended use by the University.

Most data acquisition stations incorporate a microcontroller as either the input system or both the input and computer system of the station. A microcontroller is a compact microcomputer used in electronic embedded systems. A microcontroller contains a processor, storage, inputs and outputs. Software is used to program the function of the microcontroller in order to suite the specific need of the application [11]. A variety of microcontrollers exists such as programmable integrated circuits (PIC) and Arduinos.

Modern data acquisition stations incorporate a personal computer (PC) as controller of the system. PC-based data acquisition systems benefit from the ever-increasing performance of a PC's processor, hard-drive, display and peripheral bus. A PC can provide real-time visualization, user-defined functionality and network connectivity [12].

A system must be developed that can acquire different types of data simultaneously, handles and stores it and display the data to a user. Since this system can be achieved through a variety of designs, only a few of the most economical and practical designs will be discussed.

3. DESIGN

The first proposed design implements a single microcontroller to serve as both the collector and handler of the raw data collected from the sensors. Connected to the microcontroller will be an input interface for the user. This input will consist of the frequency of data collection, data handling formula and the selected data required for display. An output device such as a LCD screen should be connected to provide sensor information to the user. With this design, the microcontroller will require sufficient storage space since all data will be stored on the unit. Alternatively, an external storage support can be used.

The second proposed design incorporated Wi-Fi to maximize portability of the system. Each sensor will be equipped with its own Wi-Fi module at the installation location. The Wi-Fi module will then communicate wireless to a controller (Microcontroller or Personal Computer). This allows for sensors installed in inaccessible locations to communicate without the hassle of wiring the sensor to the controller. However, sensors need a power source, as do the Wi-Fi modules. Therefore, power should be available for the sensor. The controller will handle the processing of the raw data, the storing as well as the display thereof. The controller may provide a GUI on which the user can input unique data handling formula and data acquiring frequency for each sensor. The GUI will allow for the retrieval of previous data and display the data in a graph format.

The third proposed design incorporates both a collecting microcontroller and a separate controller (Personal Computer). All sensors are connected to the microcontroller, which will send data to the controller. The controller will handle the processing of the raw data, the storing of the data and the display. The controller may provide a GUI on which the user can input unique data handling formula and data acquiring frequency for each sensor. The GUI will also allow for the retrieval of previous data and display the data in a graph format.

Design 3 is most suitable for the project, as it is less expensive than design 2 and more user friendly and simplistic comparing to Design 1. Design 3 is also easy to upgrade and expand as explained later on in this document.

In order to design an effective, highly compatible data acquisition station, the proposed plan consists of two main components. First, the acquiring component. This unit will function as the collector of raw data from all the different types of sensors. The acquiring component needs to be able to receive both analogue and digital signals. It will then convey the data to the second component of the

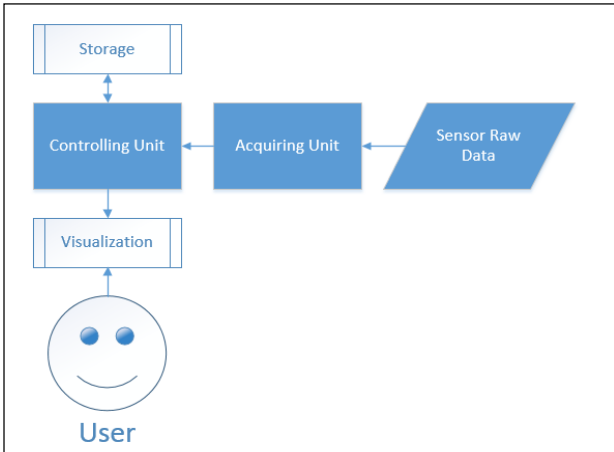


Figure 1: Proposed method

station, the control part. This component will function as the data-handling unit. The controlling component must be able to calculate information from the received raw data for use by different types of sensors. Since the conversion from raw data to usable information vary for different types of sensors, the controlling component must allow the user to set the way in which the data must be handled for each separate sensor. The controlling component should present a visual of data collected. It must also be able to store collected information in order for the user to view the data history. Figure 1 shows the diagram for the proposed method. This method provides for easy system expandability. Whenever more inputs are required, it is only the acquiring component that needs expansion. The use of a controller component ensures a high data handling capacity. Different types of controllers support a variety of capabilities in the case of data handling, processing, storing and visualization.

Since the acquiring component must allow at least five simultaneous connections, the use of a PIC microcontroller will be adequate. This microcontroller supports analogue to digital conversions, digital inputs as well as a variety of communication methods including serial and wireless communication. The microcontroller also has the ability to be added into a master - slave topology that allows a second microcontroller (slave) to adopt the characteristics of the first microcontroller (master). This allows the extension of the amount of inputs to the station by simply adding a second microcontroller to the system.

A personal computer (PC) is used as the controller component. Using a personal computer allows access to the computers storage and provides a GUI with which the user can interact. The computer's internal storage is expandable in order to store the data obtained from the sensors. Through testing, it was found that storing 10 000 data points require 300 kB of storage space. Thus, a computer with 120 GB storage space will be able to store 4 billion data points. For eighteen sensors simultaneously connected, each sensor will be able to store 200 million data points. If all sensors are set up to collect data every

second, the storage space will not be exhausted within a period of seven years. Therefore, it is safe to assume that the average storage capability of a computer will be sufficient for this project.

The first step in the design is the power supply. The microcontroller functions at a supply voltage of 3.3 V, while sensors may function from 3.3 V to 30 V and even higher. For this design, the station will supply 3.3 V, 5 V and 12 V. When a sensor requires a voltage higher than 12 V, an external power supply will be required. Since most sensors require less than 25 mA and the absolute maximum current rating of the microcontroller is 250 mA, the power required by the station will be less than 9 W. This design utilize two voltage regulators. The first regulates 220 V_{AC} to 12 V_{DC} and 5 V_{DC}. The second regulates 12 V_{DC} to 3.3 V_{DC}.

The second step in the design is the microcontroller. A programmable integrated circuit (PIC) is used due to the low cost of this microcontroller compared to other types of microcontrollers. The microcontroller consist of nine analogue input pins, master-slave configuration, serial communication (UART) and enough pins to allow for nine digital input pins. Figure 2 shows the connection diagram for the microcontroller. The microcontroller will communicate with the computer via a universal serial bus (USB).

Since the microcontroller and computer do not use the same language, communication between the two devices is obtained via an interpreter chip (UART to TTL converter).

The microcontroller can only sample voltage waveforms and since some sensors outputs a current waveform; a method is required to convert the current waveforms to voltage waveforms [13]. The simplest method is the use of an operational amplifier. The circuit consists of an operational amplifier with resistors. In order to ensure that the positive and negative terminals of the op-amp are at ground, the op-amp outputs a voltage equal to the voltage drop over the resistor connecting the negative terminal and the output. This ensures that the output voltage is

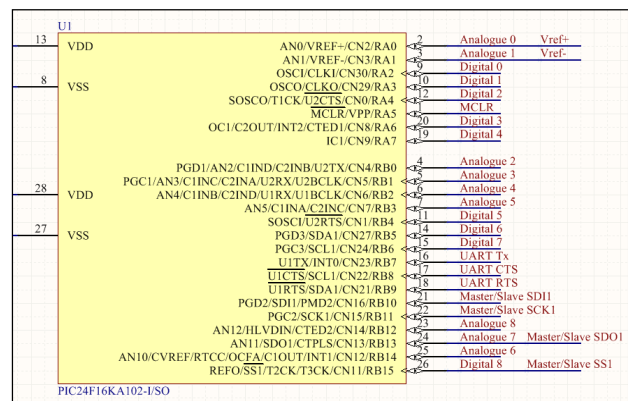


Figure 2: Microcontroller pin assignment

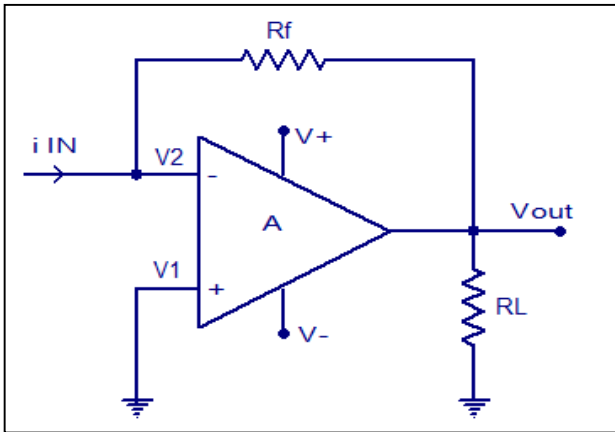


Figure 3: Current to voltage converter electrical circuit

proportional to the resistor voltage and therefore to the input current. The circuit for the current to voltage converter is shown in Figure 3 [14].

The third step in the design is the controller (Personal Computer). Designed software allows the user to set criteria for each sensor. Some of these criteria includes the frequency with which data should be sampled, the formula used to calculate information from the data and a sensor name and description. The computer receives the data from the microcontroller in one long string of characters at a regular interval. The computer selects the data of each sensor from the string, calculates the information by using the formula provided by the user and stores the value together with the current date and time. The computer allows the user to view real-time data, data history, data average for individual sensors as well as the data total for individual sensors over any given period. Figure 4 illustrates the design of the data acquisition station.

4. SOFTWARE DESIGN

Software is developed for both the computer software and the microcontroller.

4.1 Microcontroller Software

The microcontroller will start by initialising all necessary modules (Analogue to Digital Module; UART module). When one of the module initializations fails, the microcontroller will activate a warning signal and attempt to re-initialize that specific module. When all modules initialized successfully, any warning signals will be disabled and the coding will enter a loop in which the analogue and digital ports will be read and stored in temporary variables. This loop will continue until a counter reaches zero, causing all the temporary stored values to be combined into one string and be send via the UART module to the computer. The temporary stored values will be cleared in order to allow new data to be stored and the counter will reset. The microcontroller will continue functioning in this loop.

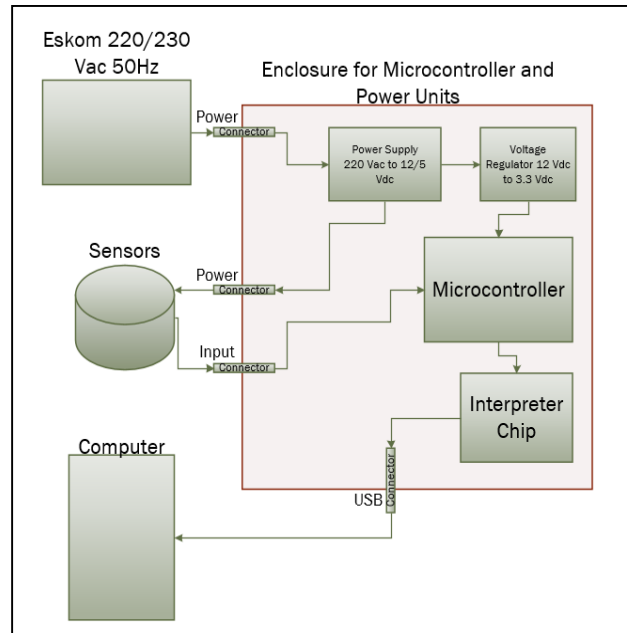


Figure 4: Data acquisition designed architecture

4.2 Computer Software

The developed computer software will initialize by creating and setting up all necessary timers, which is discussed below. Whenever data is send by the microcontroller it triggers an interruption in the software causing the specific communications port to be read. The values read from the communications port is stored in temporary variables. Each connected sensor has its own timer with its unique interval time, as set by the user. When the timers set up for the specific sensor reaches zero, the raw data stored in the temporary variable for that sensor is used to calculate the information by using the formula provided by the user. This new value is then permanently stored in a text-file.

The software allows the user to insert formulas used for calculating the correct values from the raw data received from the microcontroller. The user can choose at what frequency the sensor data must be sampled and stored – this changes the unique timer interval of that specific sensor.

The software is based on a GUI design and text files are used for storing each sensor's data. Using a GUI leads to user-friendly software and text files allow for easy transfer of data from one computer to another.

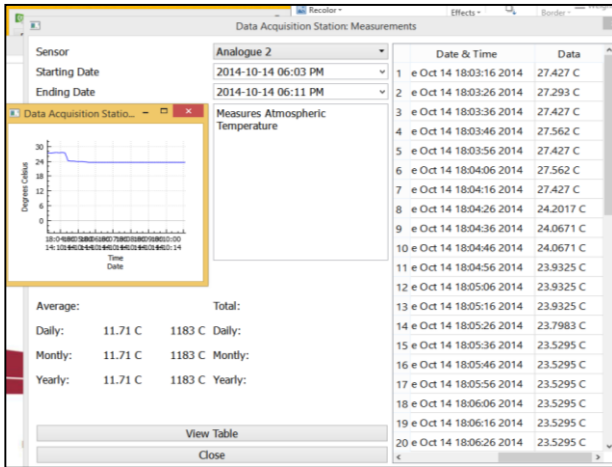


Figure 9: Computer software thermometer data review

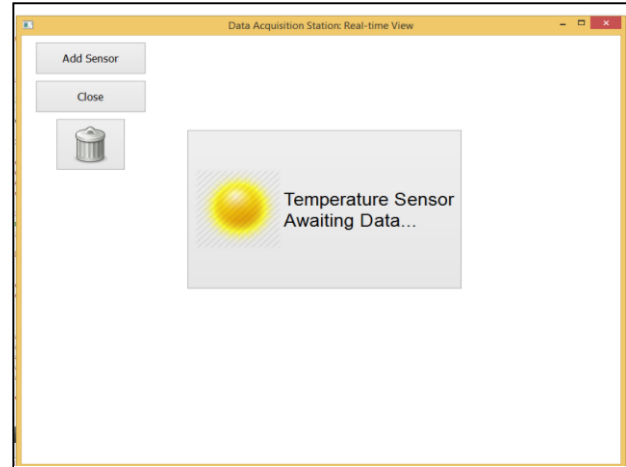


Figure 10: Computer software real-time

the programs real-time data view for the thermometer. The program retains all sensor information even when the program is not running. Therefore, whenever the program starts, it will continue collecting data from already set up sensors.

6. DESIGN CRITERION MET

- **Low Cost:** Since the entire budget of the project is R 2 500.00 the total cost of the development of the project is less than the budget of R 2 500.00. The estimate total cost of the project is R 1 500.00.
- **Compatibility:** The system is able to log current analogue signals, voltage analogue signals and digital signals successfully.
- **Amount of connections:** The system can support nine analogue and nine digital connected inputs simultaneously.
- **Handling of Data:** The system allows the user total control over the formula with which the data is handled as well as the frequency with which the data is sampled for each individual sensor.
- **Displaying of Data:** The system can display historical data over a period defined by the user in both table and graph form. Displaying Real-time data is also available.

7. CONCLUSION

The designed data acquisition station is capable of acquiring the data of eighteen simultaneously connected sensors. The station can collect analogue (voltage and current waveform) and digital data. Researchers have direct access to all historical and current data collected by the system. The user has full control over the data acquiring and handling capabilities of the data acquisition station. This station will dramatically reduce the effort to conduct research that utilizes sensors.

Overall, this solution is cost effective, practical and capable of logging a wide variety of sensor inputs.

8. REFERENCES

- [1] "What Is Data Acquisition?," National Instruments Corporation, 2014. [Online]. Available: <http://www.ni.com/data-acquisition/what-is/>.
- [2] "R.M. Young Company Price List," January 2013. [Online]. Available: <http://www.youngusa.com/products/5/>.
- [3] D. Poinsett, *MODEL 52202 / 52202H / 52203 datasheet*, Traverse City: R. M. Young Company, 2004.
- [4] D. Poinsett, *Model 41382LC2 RH/Temp Probe datasheet*, Traverse City: R. M. Young Company, 2004.
- [5] "VAISALA," 2014. [Online]. Available: <http://www.vaisala.com/en/products/windsensors/Pages/WA15.aspx>.
- [6] *WindSonic User Manual*, Hampshire: Gill Instruments, 2013.
- [7] J. P. Kerr, G. W. Thurtell and C. B. Tanner, "An Integrating Pyranometer for Climatological Observer Stations and Mesoscale Networks," *Journal of Applied Meteorology and Climatology*, vol. 6, no. 4, p. 688–694, August 1967.
- [8] "Data Acquisition Systems," United Electronic Industries, 2006. [Online]. [Accessed 2014].
- [9] "Introduction to Data Acquisition," OMEGA, 2014. [Online]. Available: <http://www.omega.com/prodinfo/dataacquisition.html>.
- [10] R. V. Ribas, "A camac data acquisition system based on PC-Linux," Universidade de Sao Paulo, Brazil, 2001.
- [11] A. Lindsay, "What's a Microcontroller?," Parallax Inc, 2009.

- [12] “Advantages of PC-Based Data Logging,” National Instruments Corporation, 2014. [Online]. Available: http://www.ni.com/data_logger/advantages.htm.
- [13] R. Kamal, Microcontrollers: Architecture, Programming, Interfacing and System Design, 2nd ed., V. Namboodiri, Ed., New Delhi: Pearson Education India, 2011, p. 888.
- [14] D. Neamen, Microelectronics, 4th ed., New York: McGraw-Hill, 2010.
- [15] S. Kundu, Analogue and Digital Communications, New Delhi: Pearson Education, 2010, p. 384.
- [16] L. Finkelstein, Pocket Book of Technical Writing for Engineers and Scientists, 3de ed., New York: McGraw-Hill, 2008.
- [17] P. Deitel & H. Deitel, C++ How to Program, 7th ed., New Jersey: Pearson Education, 2010.

SHORT TERM LOAD FORECASTING USING PSO AND ANN

E Shezi*, K A Folly**

**University of Cape Town, Department of Electrical Engineering, Rondebosch 7701.*

Email: sheziel@eskom.co.za

***University of Cape Town, Department of Electrical Engineering, Rondebosch 7701*

Email: komla.folly@uct.ac.za

Abstract: Short term load forecast is the forecast of electrical load for a period that ranges from minutes to days in advance. This paper presents a hybrid model made up of an artificial neural network (ANN) and particle swarm optimisation (PSO). Weather variables namely humidity and temperature are used in the model and are characterised as load affecting variables. A correlation study between these load affecting variables and load was conducted in order to determine the strength of their relationships. The PSO algorithm is used to reduce the forecast error by optimising the mean square error of the ANN. This model is used to forecast the next day's half hourly load profile for an area supplied by a South African power utility.

Key Words: Computational Intelligence, Artificial Neural Network, Particle Swarm Optimisation, Short term load forecasting

1. INTRODUCTION

Short term load forecasting plays an important role in the power system in terms of generation commitment as well as timely dispatcher information [1- 3, 7]. A forecast ranges from minutes up to several days. These forecasts are essential components of any energy management system. The forecasts of peak MW requirements for that period are used by system dispatchers and operation analysts to control and to plan power system operations. They are also very important for power system security studies such as contingency analysis and load management [1- 3].

Since the availability of electricity plays a vital role in the economic development of a country, it is imperative that an electrical utility be able to produce an accurate load forecast in order to meet the power requirements of that country as well as to support its development [4].

There have been a number of techniques that have been applied to the problem of load forecasting such as described by Moghram and Rahman in [4]. The authors reviewed Multiple Linear Regression, Stochastic Time Series, State Space Method, General Exponential Smoothing as well as Knowledge based approaches. Techniques used for short term load forecasting vary from the traditional Multiple Linear regression to the more recent Computational Intelligence (CI) techniques such as Expert Systems, Fuzzy logic, Artificial Neural Network (ANN), etc.

The traditional load forecasting tools utilised time series models which extrapolated historical load data to predict the future loads. These tools assume a static load series and retain normal distribution characteristics. Due to their

inability to adapt to changing environments and load characteristics, large forecasting errors would result when a deviation between historical load data and present conditions occurred [5].

CI techniques, on the other hand, are able to learn and adapt to changing environments and forecast accordingly with less forecasting errors as compared with the traditional forecasting tools [3].

This paper presents a combination approach known as hybrid method whereby two or more CI techniques are combined to bring about a load forecast. ANN is used in conjunction with Particle Swarm Optimisation (PSO) to forecast the next day's half hourly load.

2. ARTIFICIAL NEURAL NETWORKS

Artificial neural networks are a type of computational intelligence inspired by the way the biological systems of humans such as the brain, process information [6]. The human brain is made up of neurons which are interconnected by dendrites and collects information via this connection. ANNs are made up of a number of simple and highly interconnected processing elements called neurons [6]. An illustration of a neuron is shown in Fig. 1 below.

All the neurons in the brain work in unison to make sure that all the information that is received is processed as efficiently and accurately as possible. Therefore, the artificial neurons try to simulate this kind of behaviour displayed by the real neurons in the brain. ANNs learn by example and are configured for particular classes of problems or applications through a learning system [7].

The weights ($w_{j1} \dots w_{jn}$) in figure 1 depict the strength of the connection between the input variables and the output. The inputs ($x_1 \dots x_n$) together with the adjustable weights are then taken through a transfer function (f_j) and thereafter an output (O_j) is produced.

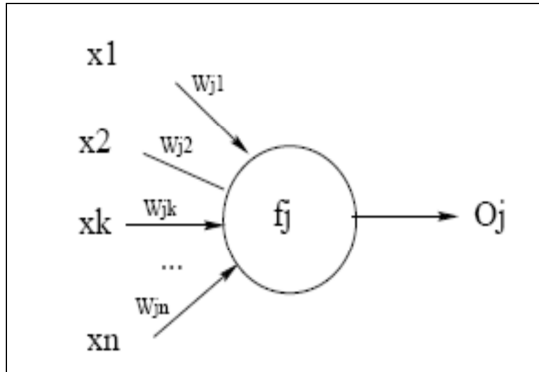


Figure 1: Structure of a neuron

There are a number of topologies that are utilized by the ANN such as feed-forward network which is commonly used. Feed-forward is basically the structure where the input signals are propagated from input neuron via a hidden layer to the output [7]. A feedback ANN also known as Recurrent Neural Networks (RNN) also exists where the networks have signals traveling in both directions within the network [8]. An example of these networks is the Elman Recurrent Network [9].

Figure 2 illustrates a feed-forward neural network which is the most commonly applied neural network architecture to short term load forecasting. It comprises of an input vector which would generally contain inputs made up of historical load data, historical and forecasted weather parameters, day types as well as other load affecting factors as determined by the engineer constructing the nature of the network [10]. It contains a hidden layer and then an output layer, usually one output is sufficient; however this can be configured as required.

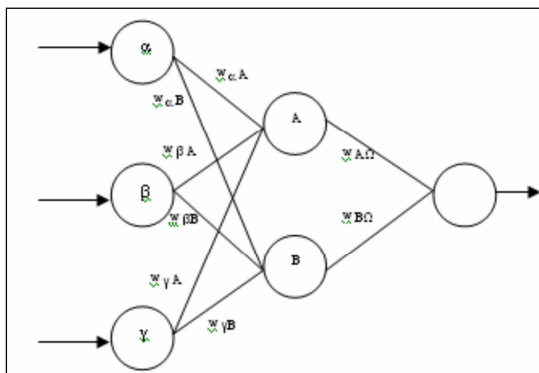


Figure 2: Feed-forward Network topology

A training algorithm such as back propagation is used for ANNs. It is basically a training method which finds the

difference between what the output is and what it was supposed to be, i.e. the reference or target output. The weights are then adjusted according to the errors and then propagated back into the system until the error is minimised [6].

The back propagation algorithm is excellent in its ability to accommodate load affecting variables. However; the main drawback with this training algorithm is that the training process can become very cumbersome and time consuming [11, 12]. Convergence also becomes a problem. Different proposals of dealing with the convergence problem are presented in [11] where the back propagation algorithm with a momentum factor is said to induce the neural network to converge much faster as well as introducing a new modified total error function within the algorithm.

Because back propagation is based on the gradient descent which is local search algorithm, the solution obtained with this method may not be optimal. Recently training methods based on Evolutionary Algorithms such as Genetic Algorithm (GA) and PSO have been proposed [13]. Quaiyum *et al* [14] uses PSO algorithm to train a Recurrent Neural Network with the result that PSO has a better convergence as compared to back propagation algorithm. GA and PSO training algorithms have a better convergence and search space capability [15].

3. PARTICLE SWARM OPTIMIZATION

Evolutionary Algorithms are search functions which operate on a population and take their inspiration from natural selection and survival of the fittest in the biological world [16]. Particle Swarm Optimization (PSO) is an evolutionary algorithm based on a model of social interaction between independent particles that use social knowledge (also called swarm intelligence i.e. the experience accumulated during the evolution) in order to find the global maximum or minimum of a function [17]. This method originates from the social behaviours such as those related to synchronous bird flocking and fish schooling.

In a PSO system, particles move around in a multidimensional search space with each particle adjusting its position in relation to its own experience as well as that of the adjacent particle. This helps make use of the best position of the particle encountered by itself and its neighbour. Thus, a PSO system combines local search methods with global search methods, attempting to balance exploration and exploitation [14].

The basic principle is described as follows [18]:

1. A particle i is associated with a current position in the search space w_i , a current velocity v_i and a personal best position p_i . A swarm s consists of particles i .
2. The personal best position p_i corresponds to the particles position in the solution space where

particle i presents the smallest error as determined by an objective function f .

3. The global best position p_g represents the position with the lowest error amongst all the p_i 's

The personal and global best positions are updated according to equations (1) and (2)

$$p_i(t+1) = \begin{cases} p_i(t), & \text{if } f(p_i(t)) \leq f(w_i(t+1)) \\ w_i(t+1), & \text{if } f(p_i(t)) > f(w_i(t+1)) \end{cases} \quad (1)$$

$$p_g \in \{p_0(t), p_1(t), \dots, p_s(t)\} \quad \text{and} \\ p_g = \min\{f(p_0(t)), f(p_1(t)), \dots, f(p_s(t))\} \quad (2)$$

Each particles velocity and position is updated using equations (3) and (5) as follows:

$$v_{i,j}(t+1) = \omega v_{i,j}(t) + c_1 r_{1,i}(t) (p_{i,j}(t) - w_{i,j}(t)) + c_2 r_{2,i}(t) (p_{g(i,j)}(t) - w_{i,j}(t)) \quad (3)$$

In equation (3), r_1 and r_2 are random values between 0 and 1 and are used to affect the stochastic nature of the algorithm. $w_{i,j}$, $p_{i,j}$ and $v_{i,j}$ are the current position, current personal best position and velocity of the j^{th} dimension of the i^{th} particle. The acceleration coefficients, c_1 and c_2 , control how far a particle can move in a single iteration. These are typically set to the value of 2 however they can be varied and range between 0 and 4.

The inertia weight ω is used to control the convergence of the PSO and is calculated as in (4).

$$\omega = \omega_{max} - \frac{\omega_{max} - \omega_{min}}{maxit} * iter \quad (4)$$

Equation (4) has ω_{max} and ω_{min} which signify the maximum and minimum inertia. The maximum number of iterations is denoted by $maxit$ and the current iteration value is represented by $iter$.

The new velocity is then added to the current position of the particle as follows in order to get its next position:

$$w_i(t+1) = w_i(t) + v_i(t+1) \quad (5)$$

The acceleration coefficients are typically set to the value of 2 however they can be varied and range between 0 and 4 [19]. These coefficients are called social and cognitive factors. The fitness of the i^{th} particle is measured by the optimisation function f which is configured according to

the problem that needs to be solved. The particle with the minimum error is chosen as the best particle.

In this PSO method, the objective is to obtain the particle with the lowest Mean Square Error (MSE) from a neural network. MSE is calculated as follows:

$$f(w_i) = \frac{1}{N} \sum_{k=1}^N \left[\frac{1}{O} \sum_{l=1}^O \{T_{kl} - P_{kl}(w_i)\}^2 \right] \quad (6)$$

Equation (6) is represented by the following elements:

- f is the fitness value
- T_{kl} is the target output value
- P_{kl} is the predicted output value based on the position vector w_i
- N is the number of training set samples
- O is the number of output neurons

The particle with the lowest fitness obtained in equation (6) is then utilised in the ANN to forecast the next day's half hourly load. The procedure is discussed in the next section.

4. PSO ANN MODEL

The following section describes the application of PSO in conjunction with ANN for short term load forecasting.

4.1 Data Analysis

The data set used for this analysis was obtained from Eskom Distribution. The area of study is a mainly residential area in the province of Kwa-Zulu Natal (KZN) for a 132/11 kV substation called Abattoir which supplies a portion of the Mkhambathini Municipality area. Weather data for the area was obtained from the South African Weather Services (SAWBS). The data sets for both weather and historical load were obtained for the period from 2009 – 2011. Data from the years 2009 to 2010 was used to train and validate the neural network. Select days in the year 2011 were then used to test the performance. The data was normalised between 0 and 1.

A correlation study to determine the weather variables that play a significant role in influencing the loading of the substation was conducted. The following variables were obtained from SAWBS: hourly humidity and temperature values as well as monthly rainfall measurements. Rainfall was removed from the correlation study and forecasting as some of the data for most months/days was incomplete or missing. Rainfall as a weather component plays a role in determining the load profile however the degree of influence would have to be determined by using of a correlation study. The lack of complete data was a limitation for this analysis.

The results of the correlation analysis contained in table 1 below shows that there is a strong linear relationship between load and temperature as well as between load and humidity. These parameters were included as part of the input vector to the neural networks.

Table 1: Correlation analysis

	Load
Temp	0.667544039
Humidity	0.563689217

4.2 ANN Model Design

The ANN network takes the following as inputs:

- Previous day half hourly load data
- Forecast and previous day type
- Forecast and previous day minimum and maximum temperature
- Forecast and previous day minimum and maximum humidity.

A total number of 58 neurons were required to form the input layer; each neuron corresponds to an input variable. The output layer consisted of 48 neurons which correspond to the half hour in a day. The number of hidden layer neurons was determined by trial and error whereby the numbers of neurons were increased iteratively from 5 to 100 in steps of 5. The network with the best performance in terms of mean square error was then utilised to forecast the next day's half hourly load.

4.3 PSO Design

PSO is used to alter the weights of the ANN such that the resulting MSE for the training data is reduced. This process runs until a stop criterion is met which in this case is until the maximum number of iterations has been reached. The particle position in the search space of the PSO corresponds to the weights of the ANN. The process flow is shown in figure 3.

The following PSO variables were used:

1. $c1 = c2 = 2$
2. w = reducing values from 1.0 to 0.4
3. $S = 20$ number of particles
4. Maximum iterations = 1000
5. $K = 0.729$ constriction factor
6. $r1$ and $r2$ are random values between $[0,1]$
7. $-0.4 < V_{max} < 0.4$

The fitness function f in (6) corresponds to the MSE of the ANN network. Each particle represents a possible solution of weights.

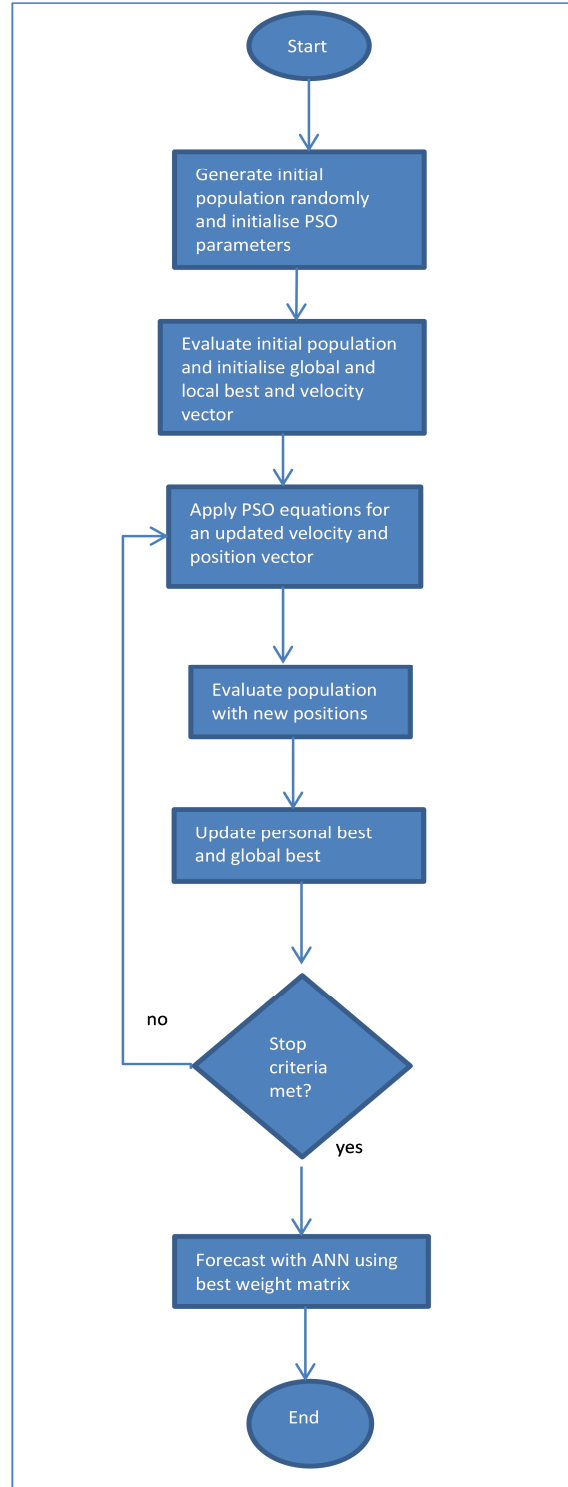


Figure 3: PSO-ANN optimisation process flow

5. SIMULATION RESULTS

In this paper, a forecast for weekdays only was conducted. Weekends, deemed as Saturday and Sunday, were removed during the training in order for the ANN to learn the weekday dependencies. The separation was

conducted as a result of the dissimilar weekday and weekend load profiles. The following figures 4 to 6 illustrate the predicted loads corresponding to 3 days in the month of March 2011.

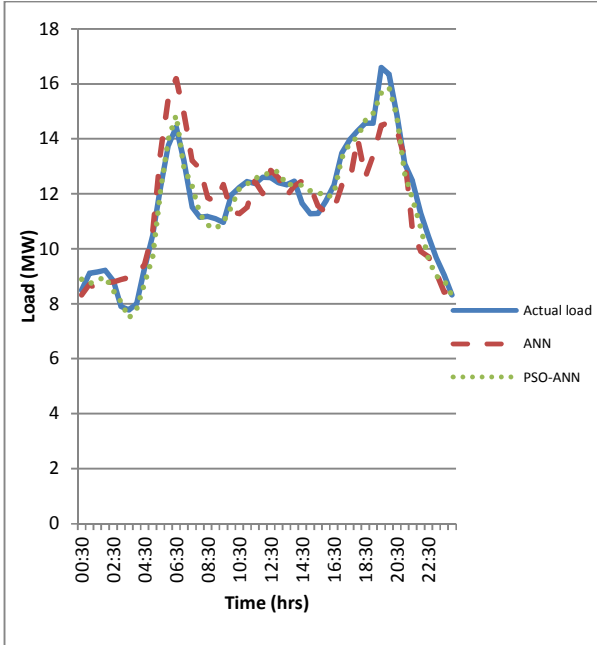


Figure 4: Load forecast for a Wednesday

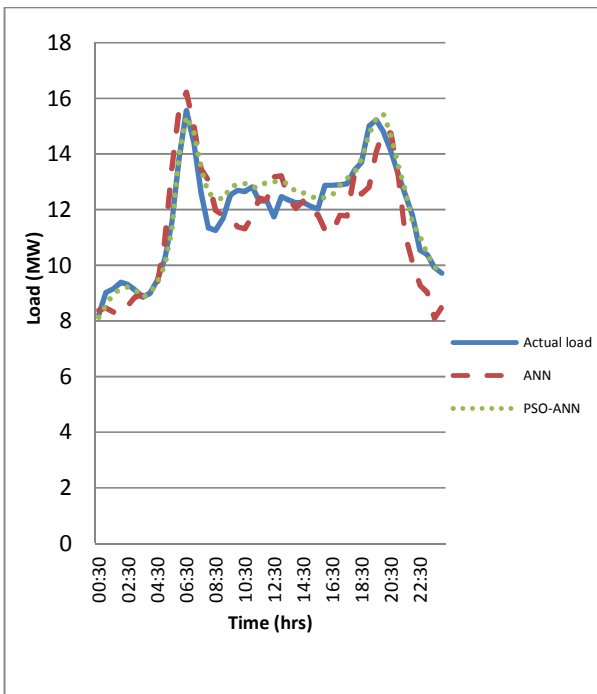


Figure 5: Load forecast for a Thursday

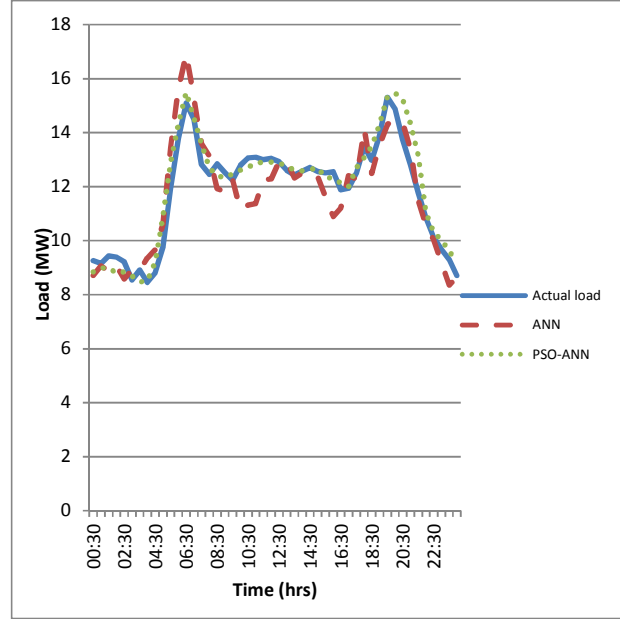


Figure 6: Load forecast for a Friday

The resulting Mean Absolute Performance Error (MAPE) given by equation 7 is shown in table 2.

$$MAPE = \frac{1}{N} * \sum_{i=1}^N \left| \frac{L_{ai} - L_{fi}}{L_{ai}} \right| * 100 \quad (7)$$

L_{ai} and L_{fi} are the actual and forecasted loads respectively. N is the number of data points which in this case is 48 since the forecast is for every half hour.

It can be seen that the overall performance of the ANN is vastly improved with the use of the PSO algorithm.

Table 2: Performance comparison of ANN and PSO ANN

Day	PSO-ANN	ANN
Wednesday	3.00%	5.98%
Thursday	2.84%	5.82%
Friday	3.32%	4.56%

6. CONCLUSION

This paper presented a hybrid method of PSO and ANN and produced acceptable results with a variation of $3 \pm 0.5\%$. It can be seen that an improvement in forecasting errors is obtained by combining PSO and ANN. This validates the hypothesis that the hybridization of computational intelligence techniques is effective in reducing forecasting errors.

7. REFERENCES

- [1.] F.D Galiana, G Gross, "Short term load forecasting", *Proceedings of the IEEE*, Vol 75, No 12, 1987
- [2.] A.D Papalexopoulos, T.C Hesterberg, "A regression based approach to short term load forecasting", *IEEE Transactions on Power Systems*, Vol 5 No 4, November 1990.
- [3.] W Charytoniuk, M Chen, "Very Short term load forecasting using Artificial Neural Networks", *IEEE Transactions on Power Systems*, Vol 15 No 1, February 2000.
- [4.] I Moghram, S Rahman, "Analysis and evaluation of five short term load forecasting techniques", *IEEE Transactions on Power Systems*, Vol 4, No 4, October 1989.
- [5.] M.A Farahat, M Talaat, "A New Approach for Short-Term Load Forecasting Using Curve fitting Prediction Optimized by Genetic Algorithms", *Proceedings of the 14th International Middle East Power Systems Conference (MEPCON'10)*, Cairo University, Egypt, December 19-21, 2010
- [6.] K.Y Lee, Y.T Cha, J.H Park, "Short term load forecasting using an artificial neural network", *Transactions on Power Systems*, Vol 7 No 1, February 1992
- [7.] E Banda, "Short term load forecasting using Artificial Intelligence techniques", *Department of Electrical Engineering*, University of Cape Town, Student Thesis, 2006
- [8.] J.K Mandal, A.K Sinha, G Parthasarathy, "Application of Recurrent Neural Network for Short Term Load Forecasting in Electric Power System", *IEEE International Conference on Neural Networks*, Vol 5, pp 2694-2698, 1995
- [9.] N Siddarameshwara, A Yelamali, K Byahatti, "Electricity Short Term Load Forecasting using Elman Recurrent Neural Network", *International Conference on Advances in Recent Technologies in Communication and Computing*, pp 351-354, 2010
- [10.] S Zhang, J Lian, H Xu, J Liu, "Grouping Model Application on Artificial Neural Networks for Short term Load Forecasting", *Proceedings of the 7th World Congress on Intelligent Control and Automation*, pp 6203-6206, 25-27 June 2008
- [11.] Y Riu, A.A El-Keib, "A Review of ANN-based Short Term Load Forecasting Models", *Proceedings of the 27th South Eastern Symposium on System Theory*, pp 78-82, 1995
- [12.] K Liu, S Subbarayan, R.R Shoultz, M.T Manry, C Kwan, F.L Lewis, J Naccarino, "Comparison of very short term load forecasting techniques", *IEEE Transactions on Power Systems*, Vol 11 No 2, May 1996
- [13.] P.K Sarangi, N Singh, D Swain, R.K Chauhan (DR), R Singh (DR), "Short Term Load Forecasting Using Neuro Genetic Hybrid Approach: Results Analysis With Different Network Architectures", *Journal of Theoretical and Applied Information Technology*, pp 109-116, 2009
- [14.] S Quaiyum, Y I Khan, S Rahman, P Barman, "Artificial Neural Network based Short Term Load Forecasting of Power System", *International Journal of Computer Applications (0975 - 8887)*, Vol 30- No.4, 2011
- [15.] K A Folly, G K Venayagamoorthy, "Performance Evaluation of a PBIL-Based Power System Damping Controller", 2010
- [16.] <http://www.cs.sandia.gov/opt/survey/ea.html>
- [17.] E Massio Grimaldi, F Grimaccia, M Mussetta, R E Zich, "PSO as an effective learning algorithm for neural network applications", *International Conference on Computational Electromagnetics and Its Applications Proceedings*, pp 557-560, 2004
- [18.] H. Shayeghi, H. A. Shayanfar, G. Azimi, "Intelligent Neural Network Based STLF", *World Academy of Science, Engineering and Technology* 52, pp 840-850, 2009
- [19.] www.swarmintelligence.org

HYDROCYCLONE SEPARATION EFFICIENCY ESTIMATION USING ARTIFICIAL NEURAL NETWORKS

S. van Loggenberg*, G. van Schoor**, K.R. Uren* and A.F. van der Merwe***

* School of Electrical, Electronic and Computer Engineering, North-west University Potchefstroom, Potchefstroom 2520, South Africa E-mail:21818347@nwu.ac.za/Kenny.Uren@nwu.ac.za

** School of Electrical and Electronic Engineering, North-west University Potchefstroom, Potchefstroom 2520, South Africa E-mail:George.VanSchoor@nwu.ac.za

*** School of Chemical and Mineral Engineering, North-west University Potchefstroom, Potchefstroom 2520, South Africa E-mail:Frikkie.VanDerMerwe@nwu.ac.za

Abstract: The hydrocyclone is widely used throughout the mineral processing industry when working with slurries for either classifying, desliming or dewatering. Hydrocyclones are inexpensive, application-efficient and relatively small to employ. In order to quantify its separation efficiency, models are incorporated to estimate the cut-size and sharpness of classification, usually in the form of a partition curve. Most models are based on experimentally obtained data and are therefore not universally applicable. Over the last decade researchers have started employing Artificial Neural Networks (ANN) in order to obtain just such a model. This study endeavoured to use experimentally acquired data to develop a model that predicts the cut-size and sharpness of classification. A control phase is also discussed.

Keywords: Hydrocyclone, Artificial Neural Network, partition curve, sharpness of classification, cut-size.

1. INTRODUCTION

Ever since the hydrocyclone became popular in the mineral processing industry, there have been researchers that worked on developing a model for it. In 1964 Bradley published a book in which the known hydrocyclone fundamentals and research of that time were documented. Bradley also compiled an extensive list of theoretical equations estimating the cut-size, among others. These equations however were not always relevant to industry type hydrocyclones [1], [2]. Lynch and Rao were the next researchers that made an important contribution to hydrocyclone modelling. The research was mainly focused around developing empirical equations for hydrocyclones used in industry [3]. In 1976 Plitt published a paper on his mathematical model. Up to this day it is seen as one of the most popular and widely referenced mathematical models. Plitt developed the model by utilising empirical data along with hydrocyclone variables that were deemed important in describing the hydrocyclone's operation [2]. Plitt and Flintoff revised the mathematical model and published a reviewed article on it in 1987 [4]. Throughout the literature mentioned, it becomes clear that because the process and fundamental principles of the hydrocyclone are so complex, the models that were developed were not always fully comprehensive.

With the computing power that is available presently, the modelling techniques have improved significantly, resulting in a better understanding of the hydrocyclone principles. These models now include Computational Fluid Dynamics (CFD), System Identification and statistical correlations. In 1997 H. Eren et al developed Artificial Neural Networks (ANNs) that were employed

to predict the Particle Size Distributions (PSD) and cut-size of various hydrocyclones [5], [6].

A hydrocyclone's separation efficiency is mainly described by the cut-size (d_{50}) and the sharpness of classification (m). These two parameters are used within a partition curve to quantitatively depict the separation efficiency of the hydrocyclone. Ideally a hydrocyclone is operated at conditions where a specific cut-size and sharpness of classification is achieved. These parameters cannot however be monitored in real-time. Thus this study aimed in developing an ANN, based on experimentally obtained data, which can predict the cut-size and sharpness of classification parameters at certain operating conditions.

This article will endeavour to describe some basic concepts of the hydrocyclone. A control perspective is briefly investigated. Next the developed Artificial Neural Network application and its specifics will be discussed. The results that were obtained is given and considered and finally a comprehensive conclusion binds the findings of the article.

2. HYDROCYCLONE OVERVIEW

2.1 A general description

A hydrocyclone is a stationary conical-apparatus that was developed to classify or separate solids from water, better known as slurries, and is generally used in mineral processing applications where classifying, dewatering or desliming is concerned. The separation of slurries within hydrocyclones is based on centrifugal sedimentation, where the necessary swirl motion is generated by the

slurry that is fed into the hydrocyclone by means of a pump [1]. A hydrocyclone is relatively small, inexpensive and efficient when used within specific conditions and applications. Over the years it has however become evident that the hydrocyclone and related investigations are very complex and therefore the analyses thereof is still not completely comprehensive [7].

2.2 Design and operating variables

Two groups of hydrocyclone variables exist. Design variables, which are dependent of the hydrocyclone size and proportions and the operating variables that are related to the operating conditions of the hydrocyclone and independent of its size and proportions. These variables however, cannot be considered separately because they interact with one another. Table 1 summarises the main variables that fall within the two groups mentioned [8]. Figure 1 depicts a hydrocyclone and its design variables.

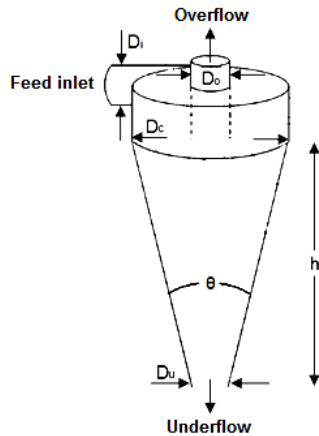


Figure 1: Graphical representation of a hydrocyclone with relevant design variables (adapted) [1]

Table 1: Hydrocyclone design and operating variables

Design variables	
Hydrocyclone diameter	D_c
Feed inlet diameter	D_i
Vortex finder diameter	D_o
Spigot diameter	D_u
Cone angle	θ
Free vortex height	h
Operating variables	
Hydrocyclone through-put	Q
Pressure drop	P
Solid concentration	ϕ
Solid density	ρ_s
Liquid medium velocity	V

2.3 Hydrocyclone performance

When describing the hydrocyclone's performance¹ the five major quantitative parameters are said to be [1], [2], [8]–[10]:

- Partition curves
- Cut-size (d_{50})
- Sharpness of classification (m)
- Pressure through-put relationship
- Split of water flow to products

For this study it was decided that only the cut-size, sharpness of classification and partition curves would be investigated. A brief discussion will follow describing these chosen parameters.

Partition curves: A partition² curve is a graphical and quantitative representation of a hydrocyclone's particle size separation performance. It usually describes the weight fraction (or percentage) of each particle size in the feed which reports to underflow, shown on the y-axis, to the particle size, shown on the x-axis. It is however assumed that a fraction of the fine particles completely bypasses the hydrocyclone's classification process. This is called the bypass and it explains why the efficiency curve does not have an asymptote at zero. It is generally assumed that the bypass is equal to the water that reports to the underflow. Thus the two types of partition curves that are generally discussed are the gross³ partition curve, which does not take into account the water recovery, and the reduced⁴ partition curve, which is adjusted to include the water recovery effects [10]. Figure 2 illustrates the two types of partition curves.

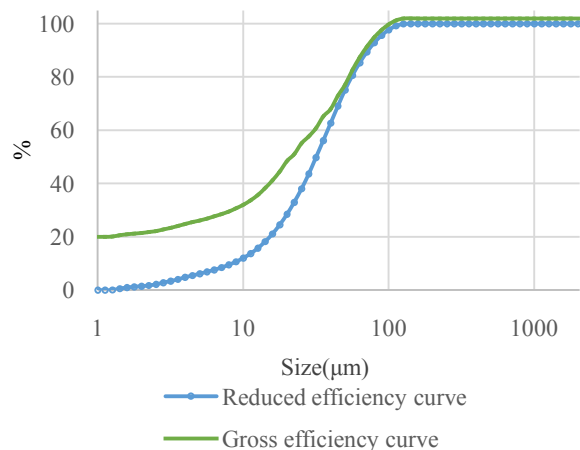


Figure 2: The two types of partition curves

¹ Performance refers to the hydrocyclones separation or classification efficiency.

² Also known as efficiency curves, performance curves or tromp curves.

³ Also called uncorrected partition curve.

⁴ The same as corrected partition curve.

Cut-size: The cut-size, also indicated as d_{50} , is said to be the size of the particle in the feed Particle Size Distribution (PSD) that has a 50% probability to either report to the underflow or the overflow of the hydrocyclone [1]. The cut-size is shown in Figure 3.

Sharpness of classification: The sharpness of classification is a parameter that is used to quantify the hydrocyclones classification or separation efficiency by supply a measure for the gradient of the partition curve. A $m < 2$ would signify poor classification and a $m > 3$ would imply good sharpness of classification [2].

Figure 3 also depicts the sharpness of classification indicated as m .

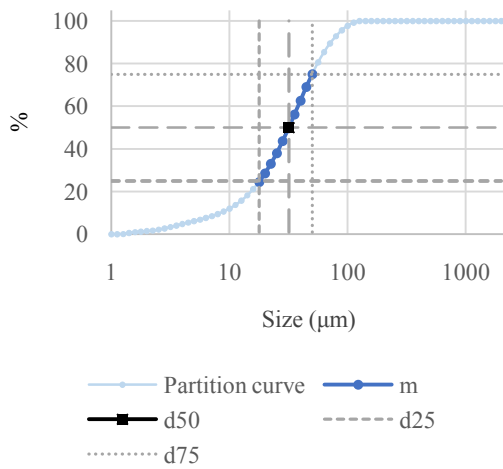


Figure 3: Partition curve displaying the d_{50} point as well as the m

In order to define the functionality of the partition curves there exist three distribution functions that closely fits the hydrocyclone's experimental performance. These distribution functions include the Exponential function, the Rosin-Rammler function as well as the Logistic function. The Rosin-Rammler function was said to deliver the best fit of the three [11]. Equation (1) shows the form in which the Rosin-Rammler function is used [2]. The sharpness of classification is also obtainable by using (2) [8].

$$y = \left[1 - e^{-0.693 \left(\frac{d}{d_{50}} \right)^m} \right] \times 100 \quad (1)$$

Where y is the distribution function, d is the PSD range in μm , d_{50} the cut-size in μm and m the sharpness of classification.

$$m = \frac{d_{75} - d_{25}}{2d_{50}} \quad (2)$$

Where m is the sharpness of classification, d_{75} the size of the particle that has a 75% probability of reporting to the underflow, d_{25} the size of the particle that has a 25%

probability of reporting to the underflow and d_{50} the cut-size.

2.4 A control perspective

There exist the need, especially within the industry, to optimise the hydrocyclone's performance so that it is operated as efficient as possible when referring to the cut-size and partition curve. Therefore a model will be very useful in a control applications where the cut-size and sharpness of classification needs to be optimised. Figure 4 shows a control scheme that could be implemented along with the developed model.

The hydrocyclone variables that might change during operation are the pulp density (ρ_p) and therefore the solids concentration (ϕ). The control system would have to account for these changes by adjusting the pressure and the flow rate so that the optimal cut-size and sharpness of classification is obtained.

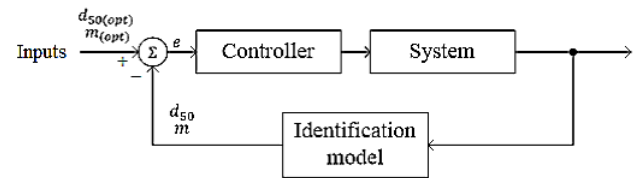


Figure 4: Control scheme

3. ARTIFICIAL NEURAL NETWORK INFERENCE MEASUREMENT

3.1 Artificial Neural Network overview

Artificial Neural Networks (ANNs) are used to describe input-output relationships of systems. Usually when using ANNs, there is no a priori knowledge needed of the system, which would make it an ideal modelling method to use with the hydrocyclone, because of the complex fundamentals that are involved. It also works very well when the model is solely based on experimentally acquired data, as with this study. Previous works have shown that the accuracy with which the ANN model predicts separation efficiency are comparable, in some cases even better, to the conventional models [6], [12]. ANN models are especially convenient should the model include alternative hydrocyclone variables, such as overflow and underflow flow rates and overflow density [6], [12].

3.2 The developed Artificial Neural Network

For this study a hydrocyclone's separation efficiency was predicted by developing an ANN model that is based on measurements obtained from experiments done on a hydrocyclone test-rig [2], [5], [12], [13]. The design configuration used for this study was fixed as portrayed in Table 2. A next phase would implement some sequential changes to the vortex finder diameter and spigot diameter.

Table 2: Experimental details

Design variable dimensions	
Hydrocyclone diameter	100 mm
Feed inlet diameter	48 mm
Overflow diameter	60 mm
Underflow diameter	15 mm
Free vortex height	700 mm

When investigating conventional models, it becomes evident that certain hydrocyclone variables are more influential than other in the estimation of the separation efficiency. The hydrocyclone variables that are seen as the most influential will be used as inputs to the ANN model along with the desired outputs.

Table 3 summarises the 8 hydrocyclone variables that were chosen as model inputs and Table 4 the 2 efficiency-indicating outputs.

Table 3: Artificial Neural Network model inputs

Design variables		
Hydrocyclone diameter	D_c	cm
Feed inlet diameter	D_i	cm
Overflow diameter	D_o	cm
Underflow diameter	D_u	cm
Free vortex height	h	cm
Operating variables		
Inlet flow rate	Q	l/s
Solid concentration	ϕ	%
Feed density	ρ_p	kg/m ³

Table 4: Artificial Neural Network model outputs

Hydrocyclone performance parameters	
Cut-size	d_{50}
Sharpness of classification	m

4.2 The Artificial Neural Network details

After the model inputs and outputs were determined and the experimental procedure was defined, the experimental sampling was done and analysed using a Malvern particle size analyser. In total 44 underflow samples were taken and analysed. Of these, 2 samples were withheld from the network development. The 2 samples were only used after the ANN was trained, validated and tested in order to have results that could be compared to the Malvern analysis results. Thus 42 samples were used for training, validation and testing purposes and 2 were used to depict the estimation of the ANN model in comparable output-parameters.

Using the nntool in Matlab® a feed-forward backpropagation network was used, employing the Levenberg-Marquardt training function. The Levenberg-

Marquardt training function uses the Levenberg-Marquardt optimisation technique to update the weights and bias values. It is one of the fastest backpropagation methods available although the memory requirements are somewhat high. Literature suggests that the number of neurons could be determined by using (3) [14],

$$\frac{\text{Number of samples}}{5} = (i + 1)N + (N + 1)o \quad (3)$$

where i is the number of inputs, N the number of neurons and o the number of outputs.

When applying (3) it was found that 2 neurons would be sufficient. After incorporating 2, 4, 5 and 10 neurons within the ANN, it became clear that the 5 neuron ANN delivered the best results for the configuration as summarised in Table 5. Figure 5 shows the network scheme diagram indicating the number of inputs, number of hidden layers, neurons used and the number of outputs that was used in the final ANN.

Table 5: Artificial Neural Networks specifics summary

Sample division %	Number of samples	Hidden layers	Neurons
Training	70	29	
Validation	15	7	1
Testing	15	6	5

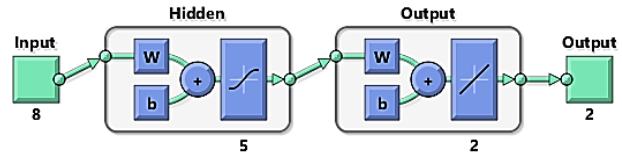


Figure 4: Artificial Neural Network diagram

4. EVALUATION

In order to evaluate the performance of the ANN the Mean Squared Error (MSE) plot and Regression plots were examined. The MSE plot, as depicted in Figure 6, shows how the MSE decreases for the three data sets (training, validation and testing) as the iterations proceeds. Training is stopped when the green validation line stops decreasing. This ensures that the network does not over-train. The red test line shows how well the network will generalise for new data.

Figure 7 shows the three data sets regression as well as the overall network regression. The regression plot illustrates the networks outputs versus the targets. The data markers should preferably be as close as possible to the dashed line. The regression lines (coloured lines) shows how well the network outputs are centred around the targets. The R-value states the average scatter around

the dashed line, of which the ideal R-value would be 1. From Figure 7 it is seen that the overall network R-value is 0.9979 and a very high correlation is achieved.

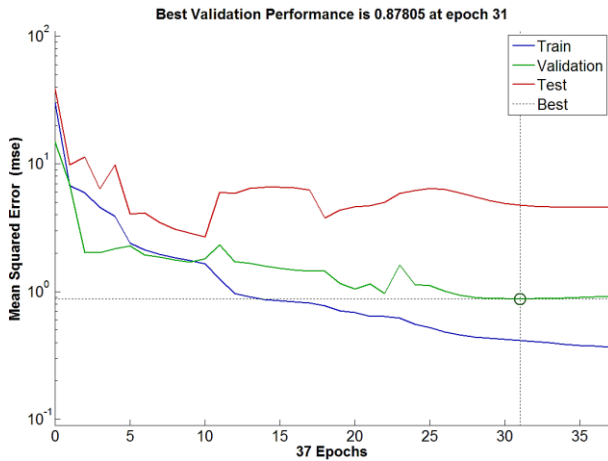


Figure 5: MSE performance plot

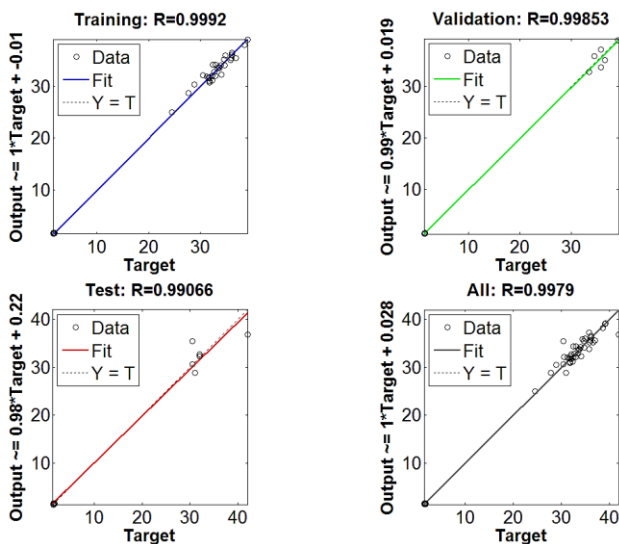


Figure 6: Regression plots

The 2 samples that were withheld from the network during development were now used to determine whether the network could accurately estimate comparable outputs when unknown inputs were introduced. Table 6 shows the 2 samples' experimental results; in other words, the ANN would be deemed accurate should it be able to predict these values with marginally small errors. Table 7 tabulates the predicted results that were obtained by simulating the ANN, the percentage error of the values are also given.

Table 6: The Malvern experimental analysis results

Experimental analysis	
$d_{50(1)}$	39.943
$d_{50(2)}$	30.636
$m_{(1)}$	1.4506
$m_{(2)}$	1.7454

Table 7: Artificial Neural Network estimation of the cut-size and sharpness of classification of the 2 samples

	Predicted value	error (%)
$d_{50(1)}$	35.0493	12.25
$d_{50(2)}$	32.3457	5.58
$m_{(1)}$	1.4263	1.68
$m_{(2)}$	1.5844	9.22

For each of the 2 withheld samples, the predicted values were plotted against the experimental analysis. The distribution function given in (1) was used along with the predicted sample values in order to obtain partition curves that could be compared to the experimentally obtained partition curves. The estimated samples deviate slightly as expected by the % error indicated. The overall shape however is satisfactory as shown in Figure 8.

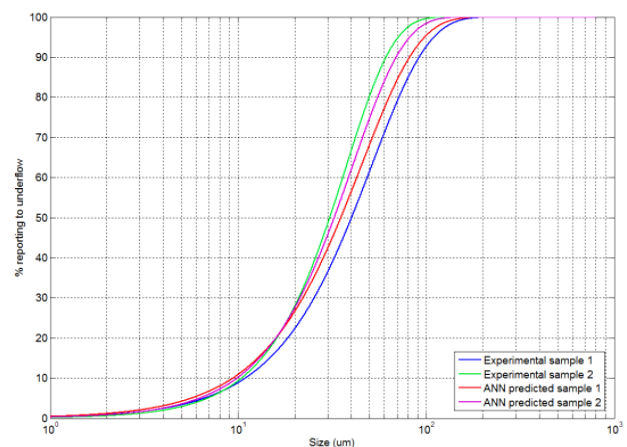


Figure 8: Experimental partition curve versus the predicted samples' partition curve

5. CONCLUSION

It was found that by using influential hydrocyclone variables as inputs along with a feed-forward backpropagation Levenberg-Marquardt ANN, a model could be developed that accurately estimated the separation efficiency parameters of a hydrocyclone. The ANN model errors were found to be marginally small, with an overall R-value of 0.9979. The next phase of the study would be to investigate the model estimations when compared to conventional models, the estimations when design variations are introduced and to determine the

application of the developed model when used for control purposes.

6. ACKNOWLEDGEMENTS

The authors would like to thank the School of Chemical and Mineral Engineering for the acquisition and analysis of the data, specifically R. Kok and H. Mulke.

7. REFERENCES

- [1] D. Bradley, *The Hydrocyclone - Bradley*. London: Pergamon Press Ltd., 1965.
- [2] L. R. Plitt, "A Mathematical Model of the Hydrocyclone Classifier," *CIM Bull. Miner. Process.*, vol. 69, no. December, pp. 114–123, 1976.
- [3] A. J. Lynch and T. C. Rao, "Modelling and Scale-up of Hydrocyclone Classifiers," *11th Int. Miner. Process. Congr.*, 1975.
- [4] B. C. Flintoff, L. R. Plitt, and A. A. Turak, "Cyclone modelling: a review of present technology," *CIM Bull.*, vol. 80, no. 905, pp. 39–50, 1987.
- [5] H. Eren, C. Fung, and K. Wong, "An application of artificial neural network for prediction of densities and particle size distributions in mineral processing industry," in *IEEE Instrumentation and measurement Technical Conference*, 1997, pp. 1118–1121.
- [6] H. Eren, C. C. Fung, and K. W. Wong, "Artificial Neural Networks in Estimation of Hydrocyclone Parameter 50 with Unusual Input Variables," *IEEE Trans. Instrum. Meas.*, vol. 46, no. 4, pp. 908–912, 1997.
- [7] E. G. Kelly and D. J. Spottiswood, *Introduction to Mineral Processing*. Australia: John Wiley & Sons, 1982.
- [8] B. A. Wills and T. J. Napier-Munn, *Wills' Mineral Processing Technology*, 7th Editio., no. October. Oxford: Butterworth-Heinemann, 2006.
- [9] H. Eren and A. Gupta, "Instrumentation an on-line control of hydrocyclones," in *International Conference on Control*, 1988, pp. 301–306.
- [10] M. Frachon and J. J. Cilliers, "A general model for hydrocyclone partition curves," *Chem. Eng. J.*, vol. 73, no. February, pp. 53–59, 1999.
- [11] S. Hore and S. Das, "Data-Based Performance Modelling of Hydrocyclone for Processing Iron Ore Fines," in *International Seminar on Mineral Processing Technology*, 2011, pp. 1–6.
- [12] H. Eren, C. C. Fung, and A. Gupta, "Application of artificial neural network in estimation of hydrocyclone parameters," in *Diversity, the key to prosperity: the AusIMM 1996 Annual Conference*, 1996, pp. 225–229.
- [13] H. Eren, C. C. Fung, K. W. Wong, and K. Street, "Back Propagation Neural Network in Determination of Parameter," in *IEE TENCON - Digital Signal Processing Applications*, 1996, pp. 163–166.
- [14] C. C. Klimasauskas, "Applying Neural Networks," *PCAI*, vol. 5, no. 3, pp. 20–24, 1991.

MINIMUM COST SOLUTION OF ISOLATED BATTERY-INTEGRATED DIESEL GENERATOR HYBRID SYSTEMS

K. Kusakana

* *Department of Electrical, Electronic and Computer Engineering, Central University of Technology, Free State, Bloemfontein, South Africa. kkusakana@cut.ac.za*

Abstract: The present paper develops a mathematical programming model to optimize the operation of a battery-integrated diesel generator hybrid system. The optimization approach is aimed at minimizing the cost function subject to the load energy requirements as well as to the diesel generator and the battery operational constraints. The main purpose of the developed control algorithm is to minimize the diesel generator operation cost in the electricity generation process. The non-linearity of the load demand, the non-linearity of the diesel generator fuel consumption curve as well as the battery operation limits have been considered in the developed model. The simulations have been performed using fmincon interior point in MATLAB, and the results obtained represent a helpful tool for energy planners and also justify the consideration of battery-integrated hybrid system in rural and isolated electricity generation.

Keywords: Battery-integrated, Diesel generator, Optimal operation control, Cost minimization.

1. INTRODUCTION

The lack of reliable electrical power supply, the high cost of AC grid extension and rough topography are some of the severe challenges faced in the rural electrification of a good number of developing countries. In most of the cases, loads in those rural areas are powered by small Diesel Generators (DGs) running continuously.

Compared to other supply options such as renewable energy sources, DGs have low initial capital costs and generate electricity on demand. They are easily transportable, modular, and have a high power-to-weight ratio. DGs can also be integrated with other sources and energy storage in hybrid system configurations making it an ideal option for standalone power generation.

However, due to the long running times and the highly non-linearity in the daily load demand profiles, DGs are usually operated inefficiently resulting in higher cost of energy produced. This overall cost includes the following:

- Operating cost which comes mainly from the direct fuel cost;
- Cost of the transportation of the fuel. This can be high depending on how the area to supply is remote or isolated;
- The maintenance and replacement cost of the generator.

In isolated power generation, battery storage systems are often used as back-up when the DG runs out of fuel, also during the DG start up or also to cover up the load when the generator is shut-down for maintenance.

By using battery integrated diesel generator hybrid systems in isolated power generation, significant savings can be archived in the overall DG running costs. In this configuration, the DG is used to recharge the battery when the load demand is low, and to balance the deficit of the power supply from the battery when the load

demand is high. This combination enhances the efficiency and the maximum output capability of the entire hybrid system.

Few research works have been conducted on the subject of optimal operation control of battery-integrated hybrid system in isolated electrification. In ref. [1] the authors have used the Hybrid Optimization Model for Electric Renewables (HOMER) for the feasibility study of a battery-integrated DG hybrid system for rural electricity supply. It has been noticed that even though adding batteries means increasing the initial cost of the system, the resulting cost of energy produced as well as the total net present costs are sensibly being reduced while using the hybrid system instead of the DG alone. However, for the optimal operation, some kind of rule-based (heuristic) algorithm is used by HOMER to solve the system's optimal operation control problem. Since no performance index is optimized, the solution provided by this method may lead to a very high running cost of the system.

In ref. [2] an optimization algorithm based upon the simulated annealing technique for a battery-integrated DG hybrid system have been presented. The developed algorithm provides optimal generator setting and battery charge/discharge schedules for a given daily load cycle. However, the developed model does not consider the non-linearity of the DG fuel consumption at different loading which was assumed to be linear.

Based on the shortfalls revealed in the papers above; the present paper reports on the development of a mathematical programming model to optimize the operation of a battery-integrated hybrid system. The optimization approach is aimed at minimizing the operation cost function subject to the load energy requirements as well as to the DG and the battery operational constraints. The main purpose of the developed control algorithm is to minimize the DG's operation cost in the electricity generation process. The

non-linearity in the fluctuation of the load demand, the non-linearity of the DG fuel consumption curve as well as the battery operation limits have been considered in the developed model. The simulations of two different load types have been performed using fmincon interior point implemented in MATLAB; the results have been compared with the case where the DG is used alone to supply the load.

2. HYBRID SYSTEM COMPONENTS AND OPERARTION DESCRIPTION

2.1. Diesel generator

A DG is normal diesel engine coupled to an electrical generator. DGs are usually designed in such a way that they always operate close to their power rating to achieve high efficiency; this condition can be used later as an operation constraint. With this operation strategy as well as operation constraint, the DG is expected to run at high load factors, which will result a decrease of the fuel consumption, of the Carbon footprint and increase of the DG lifespan [3].

The fuel cost (FC) for a day is given by the quadratic non-linear function below:

$$C_f \sum_{j=1}^N (aP_{DG(j)}^2 + bP_{DG(j)} + c) \quad (1)$$

N = the number of sampling intervals within the operation range or period of the system;

a, b, c = the fuel cost coefficients;

j = the j^{th} sampling interval;

$P_{DG(j)}$ = the output power from the DG at j^{th} sampling interval;

C_f = the price of one litre of fuel.

2.2. Battery storage system

The output power from the DG and the load demand at any given sampling interval j , determine whether the battery is charging or discharging. The dynamics of the battery state of charge (SOC) can be expressed in discrete-time domain by a first order difference equation as follows [4]:

$$SOC_{(j)} = SOC_{(0)} - \Delta t \frac{\eta_{Bat}}{E_{nom}} \sum_{i=1}^j P_{Bat(i)} \quad (2)$$

Where: SOC is the state of charge of the battery; η_{Bat} is the battery charging or discharging efficiency; E_{nom} is the battery system nominal energy, P_{Bat} is the power flowing from the battery system, Δt is the sampling time.

2.3. battery-integrated DG hybrid system

The schematic of a battery-integrated DG hybrid system's power flow is shown in Fig. 1. The system main

components are the DG operating and the battery bank used through a bi-directional converter. In this configuration, the battery is used to supply the load; and is allowed to be discharged within the preset operating limit. If the load demand is cannot be met by the battery, the then DG comes into operation either to supply the deficit of power from the battery needed by the load, or to supply the load and recharge the battery simultaneously.

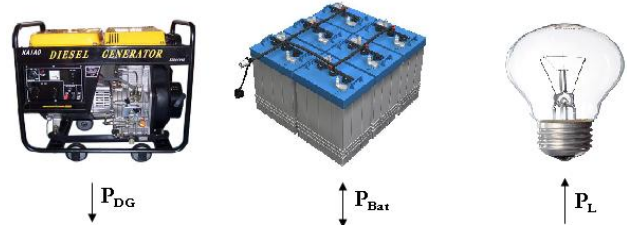


Figure 1: Hybrid system layout (power flow)

3. OPTIMIZATION MODEL AND PROPOSED ALGORITHM

The optimization problem addressed in this work aims at finding the daily optimal scheduling of energy production at any given time that minimizes the DG fuel expenses while totally responding to the load energy requirements within the system's operating limits and constraints. As stated in the introduction, the control of the hybrid system is implemented using the continuous operation control strategy.

3.1. Continuous operation control modeling

In this case the DG is always ON and its output power continuously controlled, depending on the demand, to minimize the fuel usage resulting in operation cost.

3.1.1. Objective function

The objective is to minimize the fuel consumption cost from the DG during the operation time. This can be expressed as:

$$\min C_f \times \sum_{j=1}^N (aP_{DG(j)}^2 + bP_{DG(j)} + c) \quad (3)$$

3.1.2. Constraints

The different constraints on the operation are as follows:

- Power balance:

At any sampling interval j , the sum of the supplied powers from the DG and from the battery must be equal to the demand. This can be expressed as:

$$P_{DG(j)} + P_{Bat(j)} = P_{L(j)} \quad (4)$$

- Variable limits:

The DG and battery modules are modelled as variable power sources controllable in the range of zero to their rated power for the 24 hour period. Therefore the variable limits are the output limits of these different power sources as well as of the battery storage system at any time t . These constraints depend on the characteristics of each power source and can be expressed as:

$$0 \leq P_{DG(j)} \leq P_{DG}^{\max} \quad (1 \leq j \leq N) \quad (5)$$

$$-P_{Bat}^{\text{rated}} \leq P_{Bat(j)} \leq P_{Bat}^{\text{rated}} \quad (1 \leq j \leq N) \quad (6)$$

- Battery state of charge:

The available battery bank state of charge in any sampling interval must not be less than the minimum allowable and must not be higher than the maximum allowable state of charge. This can be expressed as:

$$SOC^{\min} \leq SOC_{(j)} \leq SOC^{\max} \quad (7)$$

Equation (2) can be replaced in equation (7) to link the battery dynamics to its operation limits; this gives:

$$SOC^{\min} \leq SOC_{(0)} - \Delta t \frac{\eta_{Bat}}{E_{nom}} \sum_{i=1}^j P_{Bat(i)} \leq SOC^{\max} \quad (8)$$

3.2. Proposed algorithm

The objective functions have been modeled as a non-linear function of the DG output power. The non-linear optimisation problem can be solved using the “fmincon” function in MATLAB [5]. This function solves problems in the form:

$$\min_x f(x) \text{ Subject to: } \begin{cases} c(x) \leq 0 \\ c_{eq}(x) = 0 \\ A \cdot x \leq b \\ A_{eq} \cdot x = b_{eq} \\ l_b \leq x \leq u_b \end{cases} \quad (8)$$

Where:

x , b , b_{eq} , l_b , and u_b = vectors;

A and A_{eq} = matrices;

$c(x)$ and $c_{eq}(x)$ = functions that return vectors;

$f(x)$ = function that returns a scalar.

$f(x)$, $c(x)$, and $c_{eq}(x)$ can be nonlinear functions.

4. CASE STUDIES

4.1. 24 hours load demand

A typical South African rural household and a base transceiver system (BTS) daily load demands are selected

as two case studies to analyze the benefit of battery-integrated hybrid system compared to the DG alone [6-7]. The 24h demand for both cases are shown in Fig 2 and Fig 3. These data are used as input to the energy optimization model developed in section 3 above. It has to be noted that this household daily load profile can changes with the social habits on the occupants as well as with the seasons.

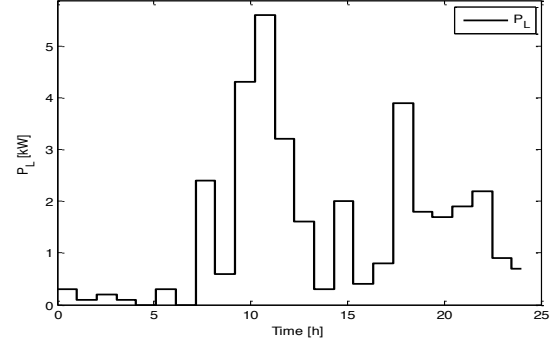


Figure 2: Household load profile

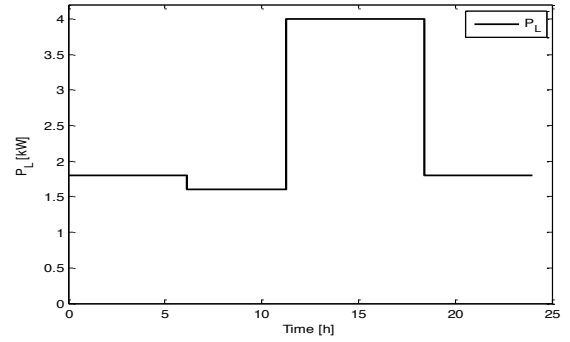


Figure 3: BTS load profile

4.2. Component size and model parameters

The components' sizes as well as the different parameters used in the simulations are given on the table 1.

Table 1: Simulation parameters

Item	Household	BTS
Sampling time (Δt)	15 min	15 min
Battery nominal capacity	5.6kWh	5.6kWh
Battery maximum SOC	95%	95%
Battery minimum SOC	40%	40%
Battery charging efficiency	85%	85%
DG rated power	5.6kW	2.6kW
Diesel fuel price	1.4\$/l	1.4\$/l
a	0.246	-0.0113
b	0.0815	0.3527
c	0.4333	1.1531

Using the sampling time in minutes, the daily number of sampling intervals used in the simulation can be calculated as:

$$N = \frac{24 \times 60}{\Delta t} \quad (9)$$

5. SIMULATION RESULTS AND DISCUSSION

5.1. Case 1: Rural household

Fig.4 shows the load demand, the DG output power, the battery power flow as well as the battery SOC during a 24h period. It can be noticed that during the night and early morning the load demand is low; therefore it is successfully met only by the DG which is at the same time charging the battery to its maximum SOC.

The load demand starts increasing, and the first peak demand occurs from 7h00 to 8h00, therefore the battery and DG output powers increase. After this first peak demand, the DG output power is kept constant to recharge battery system; this can be noticed on the top-left figure where the negative part of the battery power flow (P_B) represents the charging process.

From 9h00, the demand rises again, to reach a peak of 5.6kW, in this case the battery is extensively used and its SOC is reduces to the minimum operating limit at around 12h00 (40%). Therefore, after the peak, the DG produces more power than the load requirement to recharge the battery. This situation is also repeated during the evening peak.

Form the figure, it can be seen that neither the DG nor the battery reached their maximum operating power limits. The continuous operation control can allow a considerable reduction on the size or ratings of the DG and battery which can be lower than the one required during the peak demand. This can considerably increases the load factor as well as decrease the initial cost compared to the case where the DG is used alone.

5.2. Case 2: BTS Load

From figure 5, it can be noticed that the BTS load profile is generally flat, except during the daytime when the air-conditioning system is switched on giving a 4kW peak demand for six hour (from 12h00 to 18h00). During that peak demand, the battery system is operated first at its maximum limit to supply the load while the DG is kept low. The DG output power increases later, when the battery energy is depleted, to balance the deficit of energy needed by the load.

After the peak, the SOC of the battery is at its minimum operation limit (40%); therefore the DG produces more than the load requirement. This surplus is used to recharge the battery bank for future use as shown in Figure 5.

5.3. Daily operation costs summary

Table 2 shows how much fuel (cost) can be saved by using the hybrid system instead of the selected DG (only) in both the household and BTS cases. The results obtained from the simulation demonstrate the importance of considering the non-linearity of the DG fuel consumption curve as well as the one of the load when operating the hybrid system in order to minimize the daily operation costs.

It has to be highlighted that the amount of fuel saved is highly dependent of the type of DG (fuel consumption parameters) as well as on the battery operation settings (initial, maximum and minimum SOC).

Table 3: Daily fuel cost savings

	Household		BTS Load	
	Consumption (L)	Cost (\$)	Consumption (L)	Cost (\$)
DG only	19.06L	26.7\$	24.06L	33.7\$
Hybrid system	12.96L	17.8\$	18.47L	25.8\$
Savings	6.1L	8.9\$	5.59L	7.9\$

6. CONCLUSION

A mathematical model to minimize the daily operation of a battery-integrated DG hybrid system has been developed. This model aims to minimize the use of the diesel generator while optimizing the use of the battery storage system. As already mentioned, this work considers the non-linearity of the load demand as well as diesel fuel consumption resulting in uniform daily operational costs. The hourly load demand as well as the diesel generator fuel consumption curve parameters data has been used as input data for simulation purposes. The simulation results shows that by using the battery-integrated DG hybrid system and taking into account the non-linearity in daily load demand, more fuel (operation cost) can be saved compared to the case where the DG is used alone.

In this work, only the continuous control of the DG used in the hybrid system has been studied, therefore for future work, the ON/OFF operation control of the DG should also be studied and the results compared with the continuous control.

7. REFERENCES

- [1] K. Kusakana and H.J. Vermaak: "Hybrid Diesel Generator-battery systems for off-grid rural applications. *IEEE International Conference on Industrial Technology (ICIT)*, Cape Town, South Africa, pp.839-844, February 2013.
- [2] P. Arun, R. Banerjee and S. Bandyopadhyay: "Optimum sizing of battery-integrated diesel generator for remote electrification through design-space approach", *Energy*, Vol. 33, pp. 1155-1168, 2008.
- [3] K. Kusakana and H.J. Vermaak: "Hybrid diesel generator/renewable energy system performance modelling". *Renewable Energy*, Vol. 67, pp. 97-102, 2014.
- [4] M. Sechilariu M., B.C. Wang and F. Locment: "Supervision control for optimal energy cost management in DC microgrid: Design and simulation". *Electrical Power and Energy Systems*. Vol. 58, pp. 140-149.
- [5] A.S. Kumar and J.L. Munda: "Optimisation of voltage and frequency regulation in an isolated wind-driven six-phase self-excited induction generator", *Journal of the Energy Institute*, Vol. 87, pp. 235-245. 2014.
- [6] H. Tazvinga, X. Xia and J. Zhang, "Minimum cost solution of photovoltaic-diesel-battery hybrid power

systems for remote consumers”. *Solar Energy*, Vol 96, pp. 292-299, 2013

[7] K. Kusakana and H.J. Vermaak: “Hybrid renewable power systems for mobile telephony base station in developing countries”. *Renewable Energy*, Vol 51, pp. 419-425, 2014

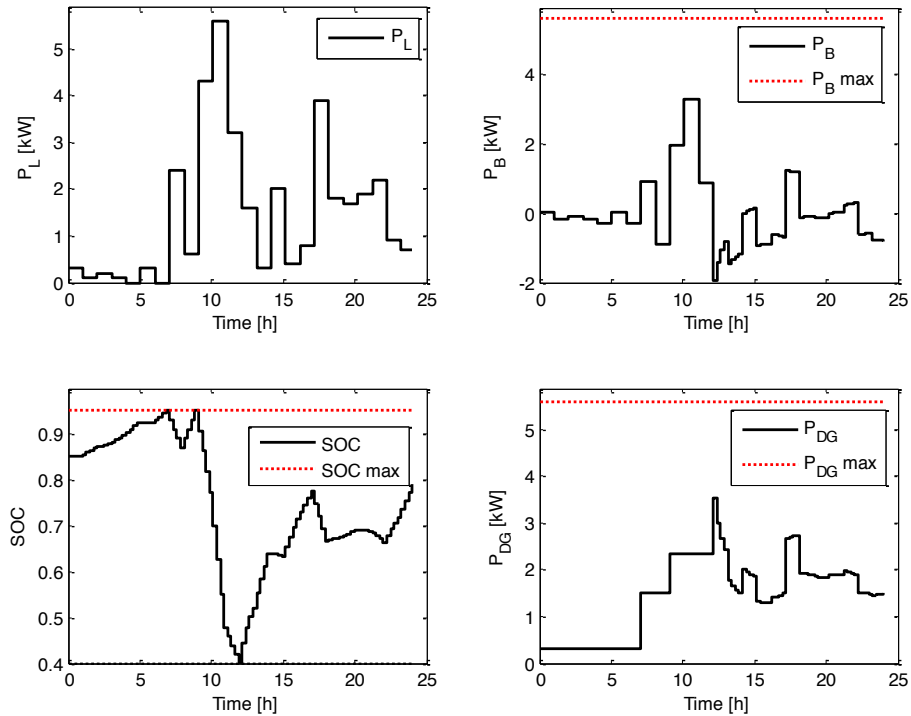


Figure 4: Daily load, DG, battery power flow and battery SOC (Household case)

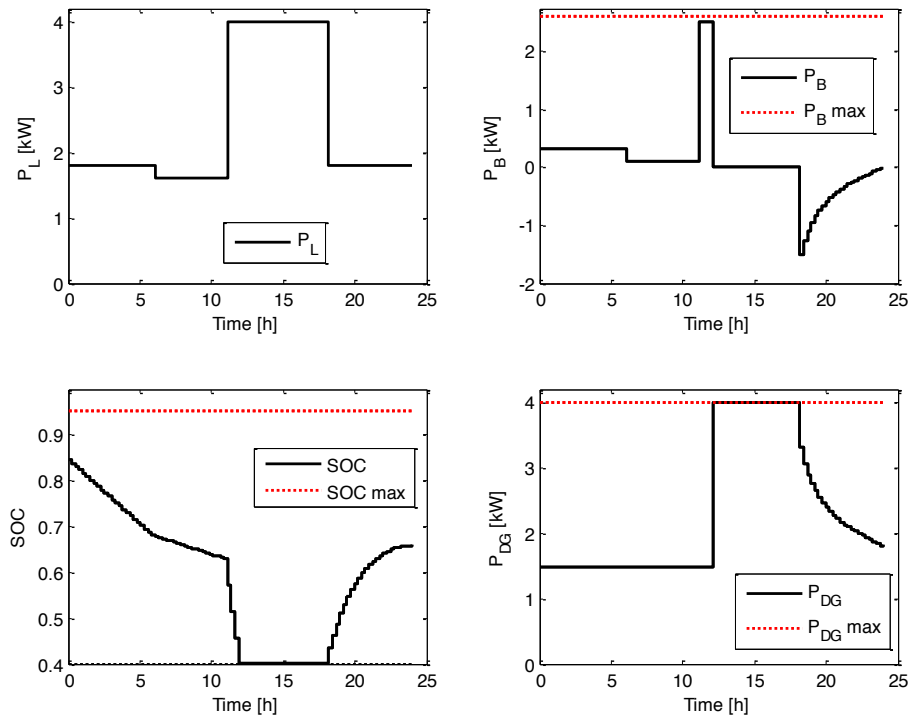


Figure 5: Daily load, DG, battery power flow and battery SOC (BTS case)

COMPARISON OF ECONOMIC LOAD DISPATCH OF NIGERIA THERMAL PLANTS USING GENETIC ALGORITHM AND DIFFERENTIAL EVOLUTION METHODS

O.O Awodiji* and K.A Folly**

* Department of Electrical Engineering, Faculty of Engineering and the Built Environment. University of Cape Town Private Bag X3, Rondebosch 7701 South Africa E-mail: awdolu002@myuct.ac.za

** Department of Electrical Engineering, Faculty of Engineering and the Built Environment. University of Cape Town Private Bag X3, Rondebosch 7701 South Africa E-mail: komla.folly@uct.ac.za

Abstract: This paper presents the solution of economic load dispatch problem using quadratic cost functions of Nigerian thermal power plants by means of Genetic Algorithm (GA) and Differential Evolution (DE). These techniques are particularly useful for optimization problems with non-convex, discontinuous and non-differentiable solution. The two techniques were tested and validated on the Nigerian Grid system. The results obtained by both techniques were compared with and without losses considered. It is shown that DE gives better results than GA. The results demonstrate the applicability of the two techniques for solving economic load dispatch problems.

Keywords: Economic Load Dispatch, Differential Evolution, Genetic Algorithm, Quadratic Cost Function.

1. INTRODUCTION

Economic load dispatch (ELD) is an important task in the power plants operation, which aims to allocate power generation to match load demand at minimal possible cost while satisfying all the power units and system constraints[1]. Its main objective is to minimize the total cost of generation and satisfy the system operation constraints of the different generation resources. Therefore, the ELD problem is a large scale constrained non-linear optimization problem.

For the purpose of economic dispatch studies, online generators are represented by functions that relate their production cost to their power output. Quadratic cost functions are used to model generators in order to simplify the mathematical formulation of the problem and to allow many of the conventional optimization techniques to be used. The ELD problem is traditionally solved using conventional mathematical techniques such as lambda iteration and gradient schemes [2]. These approaches require that fuel cost curves be increased monotonically to obtain the global optimal solution. The input-output of units are inherently non-linear with valve point loading or ramp rate limits and having multiple local minimum points in the cost function.

Techniques such as dynamic programming might not be efficient since they require too many computational resources in order to provide accurate result for large scale systems. But, with the advent of evolutionary algorithms which are stochastic based optimization techniques that search for the solution of problems using a simplified model of the evolutionary

process found in nature, ELD problems can be solved easily. The success of Evolutionary Algorithms (EAs) is partly due to their inherent capability of processing a population of potential solutions simultaneously, which allows them to perform an extensive exploration of the search space [3].

Evolutionary Algorithms includes Genetic Algorithm (GA), Simulated Annealing (SA), Particle Swarm Optimization (PSO), Differential Evolution (DE), Artificial Bee Colony (ABC) [2,3,4,5], etc. Genetic Algorithm methods have been employed successfully to solve complex optimization problems, though recent research has identified deficiencies in their performances which is apparent in applications when optimized parameters are highly correlated thereby, hampering crossover and mutation operations and compromising the improved fitness of offspring because population chromosomes contains similar structures.

SA is designed to solve the high non-linear ELD problem without restriction on the shape of the fuel cost function. EP also takes a long computation time to obtain solutions. PSO converges more quickly than EP, but has a slow fine tuning ability of the solution [3].

Differential Evolution (DE) is a recently developed heuristic evolutionary method for solving constrained optimization problems. DE is a powerful algorithm that improves the population of individuals over several generations through the operators of mutation, crossover and selection. DE offers great convergence characteristics and requires few control parameters which remains fixed throughout the solution process and requires minimal tuning.

2. PROBLEM FORMULATION

Consider an interconnected power system consisting of n thermal power stations as shown in Fig.1, the ELD problem seeks to find the optimal combination of thermal power plants that minimizes the total cost while satisfying the total demand and system constraints [8].

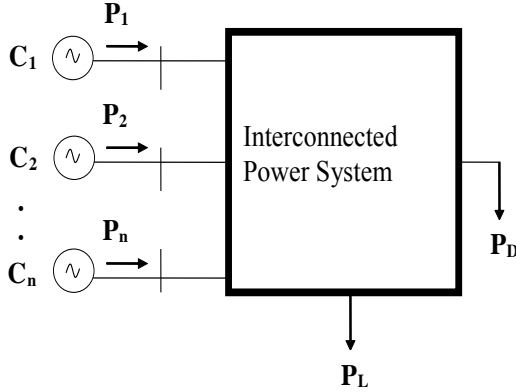


Fig.1: Interconnected power system

The ELD problem is formulated as follows:

$$\text{Min } C_T = \sum_{i=1}^n C_i(P_i) \quad (1)$$

Where:

$C_i(P_i)$ = Cost function of the i^{th} unit

$C_i(P_i) = \alpha_i + \beta_i P_i + \gamma_i P_i^2$ is a quadratic cost function as shown in Fig. 2. $\alpha_i, \beta_i, \gamma_i$ are cost coefficients of the i^{th} generator, which are found from the input-output curves of the generators and are dependent on the particular type of fuel used. P_i is the power output of i^{th} unit.

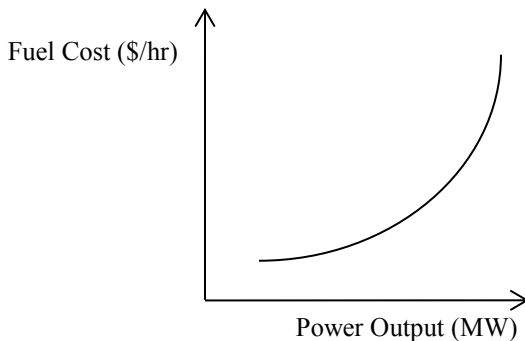


Fig.2: Quadratic cost function

The minimization is subject to the following constraints: The total power generated must be equal to the sum of load demand and transmission-line losses as given in eqn. (2):

$$P_D + P_L - \sum_{i=1}^n P_i = 0 \quad (2)$$

Where:

P_D = the power demand

P_L = the transmission loss

The transmission loss can be represented by the B-coefficient method as shown in eqn. (3):

$$P_L = \sum_{i=1}^n \sum_{j=1}^n P_i B_{ij} P_j \quad (3)$$

where B_{ij} is the transmission loss coefficient.

$$P_i^{\min} \leq P_i \leq P_i^{\max}$$

P_i^{\min} = the minimum power output

P_i^{\max} = the maximum power output

The above cast problem (1) is an optimization one. This will be solved using both genetic algorithm and differential evolution methods and demonstrated on Nigerian thermal power plants.

3. OVERVIEW OF GENETIC ALGORITHM

Genetic Algorithm searches a solution space for optimal solutions to a problem. The key characteristic of GA is how the searching is done. The algorithm creates a “population” of possible solutions to the problem and lets them “evolve” over multiple generations to find better and better solutions. The following steps were used to solve a problem using GA:

1. Create a population of random candidate solution named *pop*.
2. Until the algorithm termination conditions are met, do the following (each iteration is called a generation):
 - a. Create an empty population named *new-pop*.
 - b. While *new-pop* is not full, do the following:
 - i. Select two individuals at random from *pop* so that individuals who are more fit are more likely to be selected.

- ii. Cross-over the two individuals to produce two new individuals.
 - c. Let each individual in *new-pop* have a random chance to mutate.
 - d. Replace *pop* with *new-pop*.
3. Select the individual from *pop* with the highest fitness as the solution to the problem.

The population is the collection of candidate solutions that are considered during the course of the algorithm. Over the generations of the algorithm, new members are “born” into the population, while others “die” out of the population. A single solution in the population is referred to as an individual. The fitness of an individual is a measure of how “good” the solution represented by the individuals is. The selection process is analogous to the survival of the fittest in the natural world. Individuals are selected for cross-over based upon their fitness value- the fitter the individual the more likely the individual will be able to reproduce and survive to the next generation. The cross-over occur by mingling the solutions together to produce two new individuals. During each generation there is a small chance for each individual to mutate, which will change the individual in some small way.

Two GA methods were considered in this work which include the: micro-Genetic Algorithms (MGA) and the classical-Genetic Algorithm (CGA). The MGA is a “small population “ GA that operates on the principle of natural selection or “survival of the fittest” to evolve the best potential solution over a number of generations to the most-fit, or optimal solution. In contrast to the CGA, which requires a large number of individuals in each population (i.e., 30-200), MGA uses a population of five individuals.

4. OVERVIEW OF DIFFERENTIAL EVOLUTION

Differential Evolution (DE) is a relatively new evolutionary algorithm proposed by Storn and Price [7] which is simple, yet powerful, for solving complex, practical optimization problems. Practical optimization problems are often characterized by several non-linearities and competing objectives.

In a DE algorithm, candidate solutions are randomly generated and evolved by simple technique combining simple arithmetic operators with the classical events of mutation, crossover and selection. The basic evolutionary search mechanisms for DE are summarized in the following salient steps :

4.1 Initialization operation

In DE, a solution or individual i , in generation G is a multi-dimensional vector given by eqn. (4):

$$X_i^G = (X_{i,1}, \dots, X_{i,D}) \quad (4)$$

Where $X_{i,k}$ is given by eqn. (5)

$$X_{i,k} = X_{k \min} + rand[0,1] * (X_{k \max} - X_{k \min}) \quad (5)$$

$i \in (1, N_p)$ and $k \in (1, D)$

Where:

N_p = the population size
 D = the solution’s dimension i.e. number of control variables
 $rand[0,1]$ = a random number uniformly distributed between 0 and 1.
Each variable k in a solution vector i in the generation G is initialized within its boundaries $X_{k \min}$ and $X_{k \max}$.

4.2 Mutation operation

DE does not use a predefined probability density function to generate perturbing fluctuations. It relies upon the population itself to perturb the vector parameter. Several population members are involved in creating a member of the subsequent population. For every $i \in [1, N_p]$ the weighted difference of two randomly chosen population vectors, X_{r2} and X_{r3} , is added to another randomly selected population member, X_{r1} , to build a mutated vector V_i given as in eqn. (6).

$$V_i = X_{r1} + F * (X_{r2} - X_{r3}) \quad (6)$$

Where:

$r_1, r_2, r_3 \in [1, N_p]$ = integers and mutually different
 $F > 0$ = a real constant mutation rate to control the different variation $d_i = X_{r2} - X_{r3}$.

4.3 Crossover operation

The crossover function is very important in any evolutionary algorithm. In DE, three parents are selected for crossover and the child is a perturbation of one of them whereas in GA, two parents are selected for crossover and the child is a recombination of the parents. The crossover operation in DE can be represented by the following eqn. (7):

$$U_i(j) = \begin{cases} V_i(j), & \text{if } U_i(0,1) < CR \\ X_i(j), & \text{otherwise} \end{cases} \quad (7)$$

Where:

CR = the cross over rate of DE.

4.4 Selection operation

In DE algorithm, the target vector $X_{i,G}$ is compared with the trial vector $U_{i,G+1}$ and the one with the better fitness value is admitted to the next generation. The

selection operation in DE can be represented by eqn. (8):

$$= \begin{cases} U_{i,G+1} & \text{if } (U_{i,G+1}) < f(X_{i,G}) \\ X_{i,G}, & \text{otherwise} \end{cases} \quad (8)$$

Where:

$$i \in [1, N_p].$$

4.5 Verification of the stopping criterion

Loop to step 3 until stopping criterion is satisfied, usually a maximum number of iterations, G_{max} .

5. NIGERIAN GRID SYSTEMS

The Nigerian national grid belongs to rapidly growing power systems faced with complex operational challenges at different operating regimes. Indeed, it suffers from inadequate reactive power compensation leading to wide spread voltage fluctuations coupled with high technical losses and component overloads during heavy system loading mode. The standardized 1999 model of the Nigerian network comprises 7 generators, out of which 3 are hydro whilst the remaining generators are thermal, 28 bulk load buses and 33 extra high voltage (EHV) lines. The typical power demand is 2,830.1MW and bears technical power network loss of 39.85MW. The single line diagram of the 330kV Nigerian grid system is shown in Fig.3.

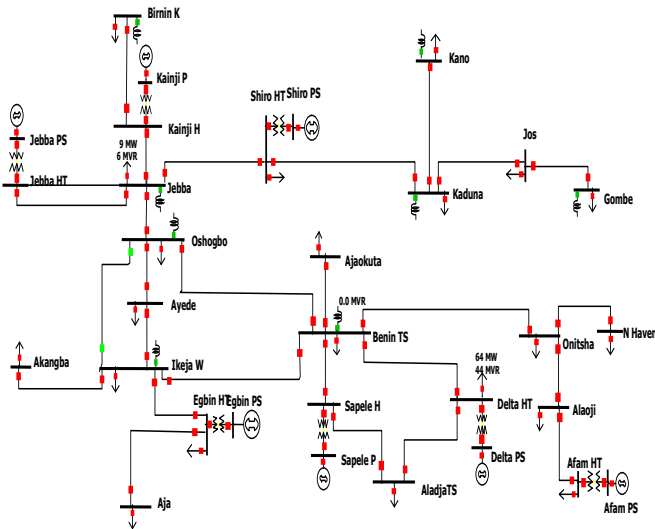


Fig.3: Single line diagram of Nigerian 330kV 31-bus grid systems

The Nigerian thermal power plants characteristics are shown in Table 1 with each plants cost coefficients and their corresponding minimum and maximum power outputs.

Table 1: Nigerian thermal power plants characteristics

Units	α	β	γ	P_i^{\min}	P_i^{\max}
Sapele	6929	7.84	0.13	137.5	550
Delta	525.74	-6.13	1.2	75	300
Afam	1998	56	0.092	135	540
Egbin	12787	13.1	0.031	275	1100

The Table 2 below shows the parameters setting for the minimization of the cost functions using GA and DE methods.

Table 2: Parameters setting for GA and DE

Control parameters	MGA	CGA	DE
Generation	200	200	200
Population	5	50	30
Crossover	0.85	0.85	0.8
Scaling factor for mutation			0.5

6. RESULTS

In this work, the ELD is applied to the four thermal plants of Egbin, Sapele, Delta and Afam. The results of the ELD with and without losses considered were shown in Table 3 and Table 4 respectively. With a total power generating capacity of 2823.1MW, the contribution of each thermal power plant to the total power generated and the cost of generation using GA and DE methods were shown. DE method produced the least cost of generation as compared to GA from the simulation results obtained for both cases that were considered.

Table 3: Solution of ELD without losses

	MGA	CGA	DE
Egbin	1075.71	937.5	1020.3
Sapele	174.81	227.88	263
Delta	79.59	81.03	81
Afam	202.99	289.68	168.8
Shiroro	490	490	490
Kainji	350	350	350
Jebba	450	450	450
P_G	2823.1	2823.1	2823.1
P_D	2823.1	2823.1	2823.1
Cost \$/hr	99818.29	101302.53	98380.05

Table 4: Solution of ELD with losses

	MGA	CGA	DE
Egbin	838.39	814.56	818.08
Sapele	345.35	457.79	365.93
Delta	68.48	69.51	68
Afam	320.46	230.82	318.36
Shiroro	490	490	490
Kainji	350	350	350
Jebba	450	450	450
P_G	2862.68	2862.68	2860.37
P_D	2823.1	2823.1	2823.1
P_L	39.58	39.58	37.27
Cost \$/hr	114521.33	116946.55	107430

7. DISCUSSION

The ELD was implemented on Mat Lab 2009 platform. The contributions of the hydro power plants to the load demand were fixed, while the least cost schedule of the online thermal power plants were determined. The minimum cost of production as shown in Table 3 without losses is \$98380.05 by DE method. Also, with losses considered in Table 4, DE gives the least cost of production of \$107430 and lowest transmission loss as compared to MGA and CGA. The generators schedule reflects the best possible contribution of the individual generators based on the demand. The MGA give a lower total cost compare to CGA, while DE gives an overall better cost minimization and losses for both cases.

8. CONCLUSION

In this paper, GA and DE methods have been applied to schedule online generators on the Nigerian thermal power plants. The results show that these methods are capable of being applied successfully to the economic dispatch problem of larger thermal power plants. The results of the two methods were compared and it is shown that DE gives a better cost minimization and reduced transmission losses.

9. REFERENCES

- [1] Y. Fang, M. Ke, X. Zhao, Y.D. Zhao, H. lu, J.H. Zhau and P.W Kit: "Differential evolution algorithm for multi-objective economic load dispatch considering minimum emission costs" *IEEE Power and Energy Society*, pp. 1-5, 2011.
- [2] R.E. Perez-Guerrero and J.R. Cedeno-Maldonado, "Economic power dispatch with non-smooth cost function using differential evolution," *IEEE Power symposium proceeding*, pp.183-190, 2005.
- [3] C. Thitithamrunehai and B.E. Arpon, "Economic load dispatch for piecewise quadratic cost function using hybrid self- adaptive differential evolution with augmented Lagrange multiplier method," *IEEE Power conference*, pp. 1-8, 2006.
- [4] C.L. Chang, "Genetic based algorithm for power economic dispatch. *IET Generation -Transmission distribution*, pp. 261-269, 2007.
- [5] J.S., Dhillion, J.S. Dhillion and D.P. Kothari "Generation pattern search for different kinds of load dispatch" *IEEE large Engineering system conference*, pp.250-255, 2007.
- [6] G.A. Bakare, G. Krost, G.K. Venayagamoorthy, Aliyu, U.O. "Differential Evolution Approach for Reactive Power Optimization of Nigerian Grid System". *IEEE Power Engineering Society Meeting*, pp.1-6, 2007.
- [7] K. Price and R. Storn, Differential Evolution – A simple evolution strategy for fast optimization. *Dr. Dobb's journal*. pp.18-78.
- [8] A.J. Wood and B.F Woolenberg. *Power Generation Operation and Control*. John Wiley and Sons, New York. Second Edition, Chapter 3, pp 29- 88. 1996.

MODELLING AND SIMULATION OF A FUZZY CONTROLLER FOR DOMESTIC BATTERY CHARGING APPLICATIONS

P. Lambert*, C. Buque** and S. Chowdhury*

* University of Cape Town, Department of Electrical Engineering, Upper Campus, Rondebosch, Cape Town, 7701, E-mail: LMBPAT003@myuct.ac.za; sunetra.chowdhury@uct.ac.za

** Mott MacDonald, Thermal and Renewable Energy Division, 25 Scott Street, Waverley, Johannesburg 2090, E-mail: claudiobuque@yahoo.com.br

Abstract: Energy storage systems such as batteries are an essential component to renewable energy generation. These batteries are generally expensive and it is important to make full use of their capacity. For this reason, effective battery charging control is applied to maximise the efficiency of the power supply system. The proposed control method in this paper is a fuzzy logic controller which will manage the state of charge of the battery.

Keywords: Domestic Battery Charging, Fuzzy Logic Controller, Lead Acid Batteries, Membership Function, State of Charge, Renewable Energy

1. INTRODUCTION

Gradual depletion of fossil fuel, environmental pollution caused by fossil-fuel energy generation and rising global energy demand has led to the harnessing of renewable energy resources such as wind, solar, marine, etc. Currently solar power is the leading renewable energy source in the world [1]. A commonly used set up for capturing solar energy is individual households having a separate battery and solar panel running the household appliances instead of the grid. Design of these stand-alone systems requires cost effective solutions. Fuzzy logic is a fairly new control strategy and it is currently being applied effectively to many classical control problems and finding more optimum solutions.

This paper will address the problem of intelligently managing batteries in order to reduce their required maintenance and increase their lifetime. It will also develop and simulate a battery management system for a stand-alone residential solar photovoltaic system.

This study will cover the battery charge control design whilst not including maximum power point tracking (MPPT).

The initial component of this paper will review lead acid battery management and operation, it will also review fuzzy logic and neural networks and how they can be applied to solar systems. Subsequently the paper will explain simulations and discuss results. Finally conclusions will be drawn and recommendations will be made.

2. LEAD ACID CELLS OPERATION

Lead acid battery cells are one of the first types of rechargeable battery cells to be produced. They consist of lead plates submerged in sulphuric acid and release energy through a chemical reaction.

2.1 Discharging the Cells

During the discharge of the battery the chemical process leads to lead sulphate forming and slowly building up on the plates. This causes the overall voltage that the battery can produce to drop. This can, however, be reconverted into lead and sulphuric acid if the battery is recharged immediately. If the battery is left in the discharged state, the lead sulphate will begin to crystallize which cannot be reconverted. Once every ten discharge cycles it is recommended to perform an equalizing charge which involves applying a certain voltage for a short period of time in order to equalize the chemical reaction and reduce the build-up of lead sulphate [2].

Lead acid batteries also experience self-discharging when left alone, which is usually around 1 percent of the state of charge per day [3].

2.2 Charging the Cells

During the charging process a certain voltage is applied to the battery. During the recharging process, electricity flowing through the electrolyte which consists of water and sulphuric acid, hydrogen and oxygen are formed from the water. This process is called gassing. This causes water loss and requires batteries to have water added to them periodically [2].

The most commonly used battery type is a lead acid battery which has long service time and good reliability, the batteries can be easily damaged by overcharging, [4] which is why it is important to implement a charging controller.

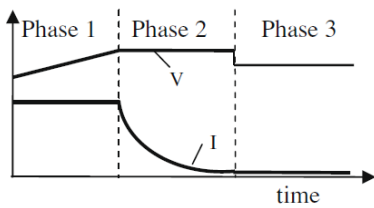


Figure 1: Charging process of lead-acid battery

Traditionally, as shown in the graph, the battery is directly charged from the solar panel, without any current control, until it reaches its overcharge point, at this point the battery has between 50-80 percent of its maximum capacity. During the second phase, the voltage is maintained while the current is gradually reduced, until the battery has reached its maximum capacity. Phase 3 reduces the voltage and current to avoid overcharge while still maintaining 100 percent voltage [4].

3. FUZZY LOGIC COONTROLLER MODEL

3.1 Creating the fuzzy rules

The fuzzy rules derived in this paper were created using Wang and Mendels' guide in [5], where labels are given as listed:

- S1 – Small 1
- B1 – Big 1
- CE - Centre

The rules that the controller uses are the same as normal logic in that it makes use of if statements to make its decision. For a battery controller this is simple as there are only the three states of charge (SOC) as pictured in Figure 1. The rules that were created in the simulation are as follows:

- If SOC is "S1" AND Voltage-Error is "S1" then PWM is "B1"
- If SOC is "S1" AND Voltage-Error is "CE" then PWM is "B1"
- If SOC is "S1" AND Voltage-Error is "B1" then PWM is "CE"
- If SOC is "CE" AND Voltage-Error is "S1" then PWM is "CE"
- If SOC is "CE" AND Voltage-Error is "CE" then PWM is "CE"
- If SOC is "CE" AND Voltage-Error is "B1" then PWM is "S1"
- If SOC is "B1" AND Voltage-Error is "S1" then PWM is "S1"
- If SOC is "B1" AND Voltage-Error is "CE" then PWM is "S1"
- If SOC is "B1" AND Voltage-Error is "B1" then PWM is "S1"

Table 1: Fuzzy Logic Rule Base

Voltage Error	State of charge			
	S1	CE	B1	
S1	B1	CE	S1	
CE	B1	CE	S1	
B1	CE	S1	S1	

The rules were derived in the same way any feedback set point tracking controller would apply rules by raising the voltage when the state of charge is below the set point, lowering the voltage when the state of charge is above the set point and maintaining the voltage when the state of charge is at in the region of the set point. The advantage of fuzzy logic is that these rules can be broadly applied. These rules can be more easily visualised in a rule base which is shown in Table 1.

3.2 Creating a membership function

The membership function is used to decide the weighting of each input based on its relative importance to the overall system. Membership Functions are generally triangular as this reduces computing complexity however Gaussian and other functions can be used if a more regularised output function is required. Due to the fact that the task of battery charge management does not require high precision, triangular membership functions will be used. The most commonly used and simplest membership function is also the triangular function. The membership functions were designed based on intuition and on the method described by Wang and Mendels [5]. The overall structure of the fuzzy logic controller can be seen in Figure 2. Figure 3 shows the input state of charge membership function and Figure 4 shows the input voltage error membership function. The output membership functions can be seen in Figure 6.

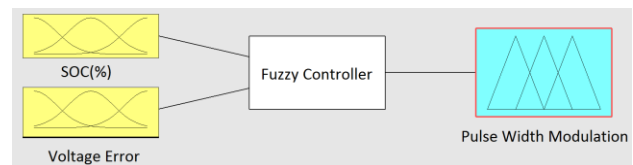


Figure 2: Overall structure of fuzzy controller

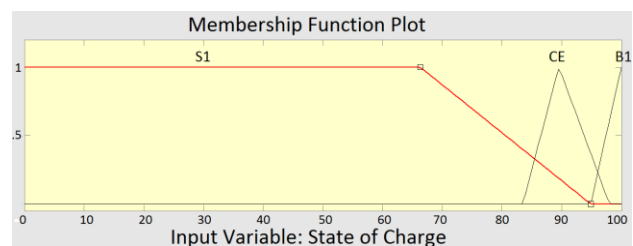


Figure 3: State of charge membership function

In the state of charge (SOC) membership functions the CE linguistic variable, which corresponds to the correct battery state of charge was given a membership function with outer points of 82 and 94 because this is what was determined to be an acceptable range of state of charge. The S1 and B1 variables will cause the controller to charge the battery or stop charging the battery respectively.

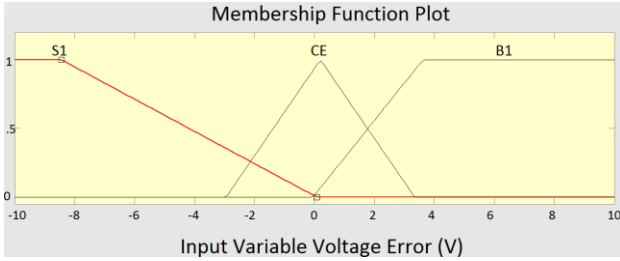


Figure 4: Voltage error membership function

In the Voltage error membership function the voltage error refers to how far away the regulator circuit voltage is away from the set point of 12.1 Volts. So the CE linguistic variable represents a near zero deviation from the set point whereas S1 and B1 variables represent voltages too low and too high respectively.

the fuzzy logic tool box in MATLAB in order to help understand how the controller is reacting. This can be shown in Figure7.

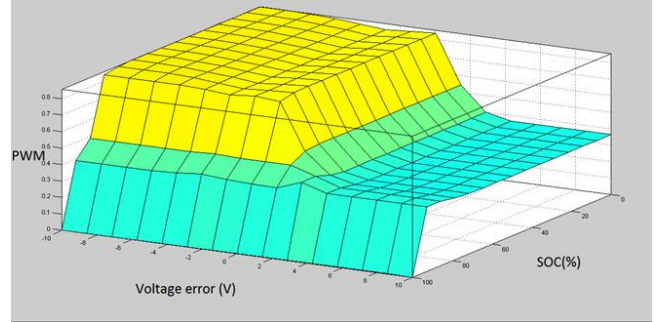


Figure 7: Surface relating input and output variable of fuzzy logic controller

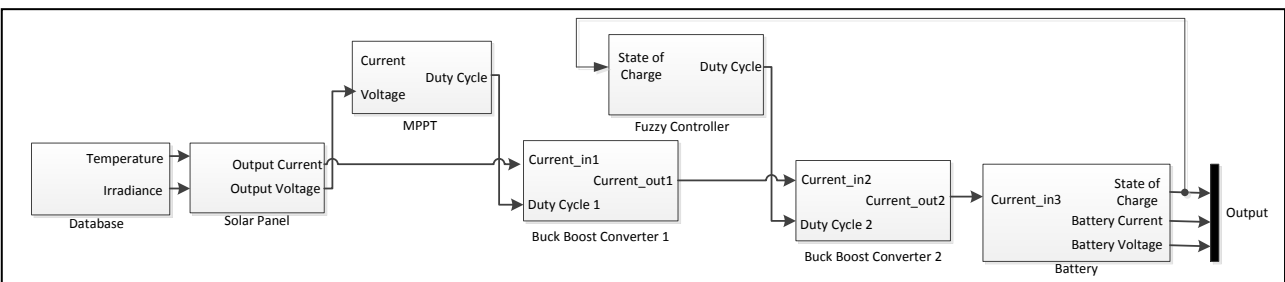


Figure 5: Overall circuit simulation

The function of the controller is to ensure that the voltage is reasonably close to this value in order to ensure gassing does not occur.

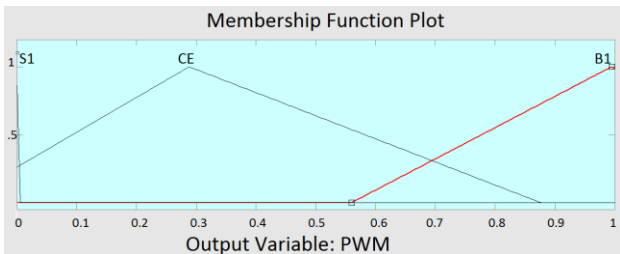


Figure 6: Pulse width modulation membership function

The output membership functions S1 variable ensures that the buck converter turns off so that the battery can reduce some of its charge into the load, the CE variable ensures that the battery will maintain its current state and the B1 variable causes the battery to charge.

For determining how to weight the pulse width modulated signals, the calculations of the buck boost designs maximum and minimum duty ratios were taken into account, the rate of change of the pulse width modulation required was designed by using narrower triangular membership functions near the set point for more precision.

4.3 Surface function

When the input and output membership functions are combined a non-linear surface function is generated by

4.4 Fuzzy logic controller implementation in Simulink

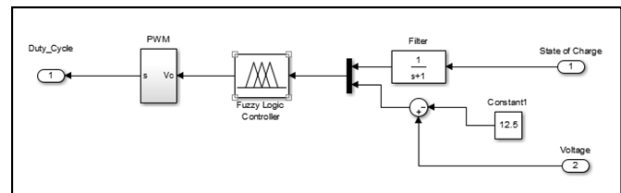


Figure 8: Simulation of fuzzy logic controller circuit

The filter from the state of charge is implemented so that the initial value that is fed into the controller is always 0. The voltage input error is generated by subtracting the measured terminal voltage of the battery by a constant value of 12.5

4. DOMESTIC SOLAR PV MODEL

The complete circuit simulated in Matlab Simulink is displayed in Figure 5. The solar PV model is based on the electrical data for Teneosolar PV modules as obtained from reference [6] and the lead acid battery electrical data is obtained from the data sheet for valve-regulated lead acid battery type LC-R127R2P manufactured by Panasonic [7]. Figure 5 shows an overview of the positioning of the different components in the scheme. In contrast to the usual domestic PV installations, the innovative installation proposed in this paper includes a fuzzy logic controller. The Fuzzy Logic Controller receives its inputs from the battery itself and uses it to

output an optimal duty cycle for the second converter in the circuit.

5. TESTING METHODOLOGY

A temperature and irradiance database for Cape Town, as shown in Figures 9 and 10 respectively, has been used to realistically simulate the output of the solar panels and the charge of the battery cells [8][9]. The following simulation conditions were run to obtain an understanding of the system operation during different conditions:

- No load Test
- Constant Load Test
- Sudden load change Test

From the results obtained in the different tests, a conclusion was derived on the efficiency of the system as described in the above sections.

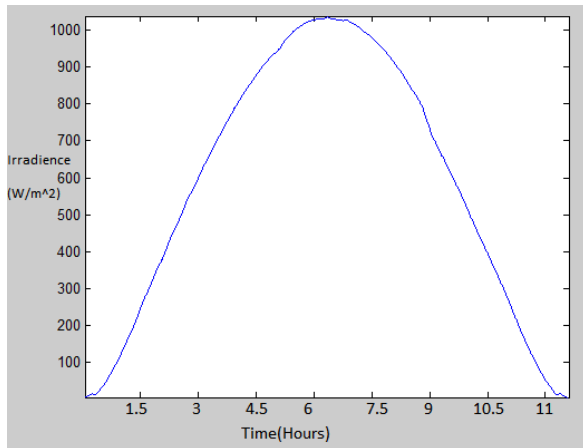


Figure 9: Average irradiance per square meter in Cape Town, South Africa during a 24 hour period [9]

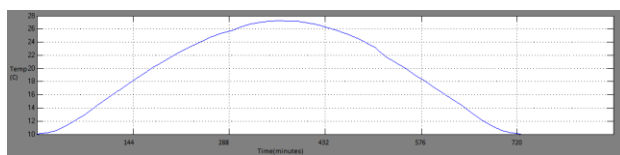


Figure 10: Average temperature in Cape Town, South Africa over a 24 hour period [8]

6. RESULTS

6.1 No load simulations

The first battery simulations were run without any load to determine how the controller charged the battery. Figures 11 and 12 show the battery charging with the solar panel set to a constant current and varying current respectively.

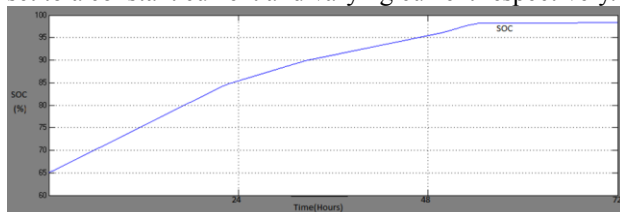


Figure 11: Battery charging with a constant solar panel current

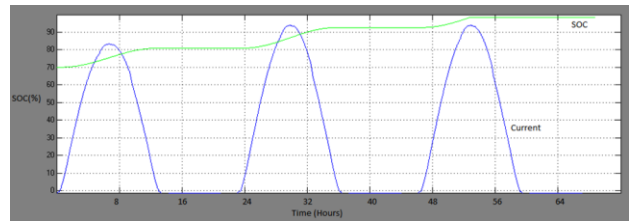


Figure 12: Battery state of charge over 3 days, with a varying solar panel current superimposed

6.2 Constant load battery charging

The subsequent battery simulations were run with a constant load. Figure 13 shows how the battery charged when there was a constant current supplied from the solar panel. Figure 14 shows how the battery charged with a varying current from the solar panel over a 3 day period.

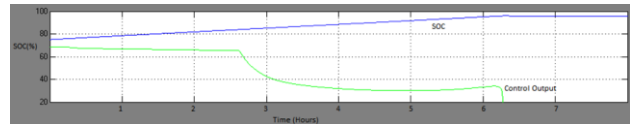


Figure 13: Battery charging with a constant load and constant solar panel current, controller output superimposed

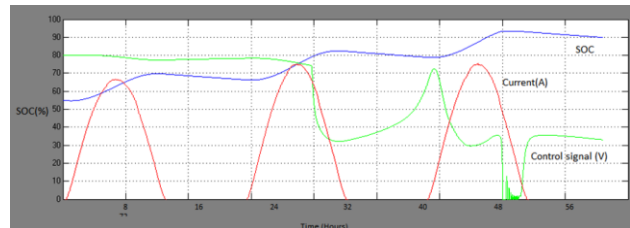


Figure 14: Battery SOC over three days with a constant load and varying solar panel current (superimposed) and control signal (superimposed)

6.3 Response to sudden addition of load

Figure 15 and Figure 16 show the response of the controller and the change in state of charge when the resistive load, varying in different manners, is added to the system. The pulse signal that connects the resistive load is also superimposed on this figure.

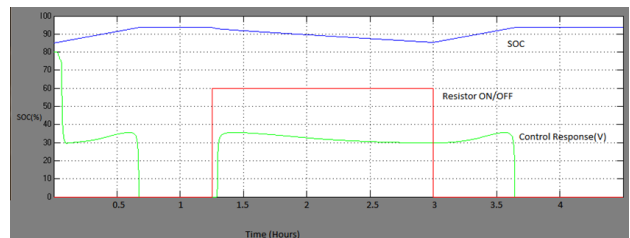


Figure 15: The change in state of charge when a resistive load is added as well as the controller response (superimposed)

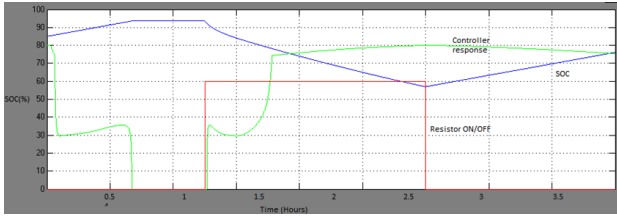


Figure 16: The change in state of charge when a higher varying resistive load is added as well as the controller response (superimposed)

7. CONCLUSION

The fuzzy logic controller proved that it could adequately charge the battery to the required battery state of charge with no overshoot and then stop the solar panel from charging the battery completely. This was tested with the solar panel generating a constant current due to it being fed a constant irradiance and temperature and also with the solar panel producing a varying current when the solar panels is fed time varying irradiance and temperature data for a three day period.

The simulations under constant current (no load) show that the controller managed to charge the battery to 98 percent charge and then cease charging. The controller effectively reduced the speed of the charge when the battery reached 85 percent. When the solar panel was given varying irradiance and temperature data in correspondence to 3 days' worth of sunshine and heat the batteries state of charge can be seen charging during the periods that the solar panel is active and remaining constant when there is no current supplied. During the third day it can be seen that the controller stops charging the battery when it reaches 98 percent charge.

During the constant load simulations the battery was connected in parallel with a constant load, the load was set as a constant resistance. During these simulations the battery took longer to charge due to the power loss in the load. As can be seen in Figure 13, under constant current, the controller charges the battery up to 98 percent charge and then stops charging it. Figure 14 demonstrates the circuit's ability to power the load whilst also charging the battery. During the periods when the solar panel is active, the battery is charging, and when the solar panel is not active, the power lost in the load can be seen reducing the batteries state of charge. When the battery enters the 80th percentile of charge the controller's voltage drops which reduces the current flowing into the battery. Finally when the battery state of charge reaches the 90th percentile the controller switches of the current to the battery completely. This simulation demonstrates that the controller is capable of effectively managing the state of charge of a battery which is having its power drained by a constant load.

In Figure 15, the controller's response to a resistor being added suddenly to the battery, this test gives a reasonable understanding of how the system would react to a constantly varying load that would be present in a real life

situation. As Figure 15 indicates, the battery charges to its full safe voltage in the 90th percentile of charge and the controller switches the buck boost circuit off, it remains in this state until the load is added, the charge is then drawn out of the battery and the controller quickly responds by turning the buck boost circuit back on. When the load is subsequently removed the controller continues to charge the battery until it is full and switches off afterwards. In Figure 16 the same experiment is repeated with a larger load which shows when the batteries state of charge drops below 80 percent the controller attempts to charge the battery at a greater rate.

Hence it is concluded that fuzzy controller can be effectively used for battery charge and discharge control in a stand-alone solar PV battery system. The authors recommend the development of other functionalities using fuzzy logic such as MPPT, taking into account seasonal variation of temperature and irradiance, and developing a laboratory set-up of the simulated circuits as a teaching tool for undergraduate students in Electrical and Electronic Engineering.

8. ACKNOWLEDGEMENT

The authors gratefully acknowledge the support and infrastructure provided by the Electrical Engineering Department, University of Cape Town for carrying out this research work.

9. REFERENCES

- [1] K.H.Solangi, M.R.Islam, R.Saidur, N.A.Rahim, and H.Fayaz: "A review on global solar energy policy", *Renewable and Sustainable Energy Reviews*, Vol. 15 No.4, pp.2149-2163, 2011.
- [2] Progressive Dynamics. Battery basics. <http://www.progressivedyn.com/batterybasics.html>
- [3] S. Oltman, "The super-secret workings of a lead acid battery explained", <http://www.batterystu.com/kb/articles/battery-articles/secret-workings-of-a-lead-acid-battery.html>
- [4] B.J.Huang, P.C.Hsu, M.S.Wu and P.Y.Ho: "System dynamic model and charging control of lead-acid battery for stand-alone solar PV system", *Solar Energy*, Vol. 84 No. 5, pp.822- 830, 2010.
- [5] L.-X.Wang and J.M. Mendel: "Generating fuzzy rules by learning from examples", *IEEE Transactions on Systems, Man and Cybernetics*, Vol. 22 Issue 6, pp.1414-1427, 1992.
- [6] Photovoltaic module TE 850-Ex, TE1300-Ex data sheet, Tenesol, www.photovoltaik-web.de
- [7] Individual data sheet for Valve-regulated lead acid batteries LC-R127R2P, Panasonic.
- [8] <http://www.accuweather.com/en/za/cape-town/306633/daily-weather-forecast/306633>
- [9] D.Ciolkosz: "SASRAD: An hourly-timestep solar radiation database for South Africa", *Journal of Energy in Southern Africa*, Vol. 20 No. 1, pp.25-34, February 2009.

QUADRUPLE TANK PROCESS DEMONSTRATOR

S. van Graan* , G. van Schoor† and K.R. Uren‡

* Department of Electrical Engineering, North-West University, Potchefstroom, 2520, South Africa. E-mail: shanevangraan@gmail.com

† Unit for Energy Systems, Department of Electrical Engineering, North-West University, Potchefstroom, 2520, South Africa. E-mail: george.vanschoor@nwu.ac.za

‡ Department of Electrical Engineering, North-West University, Potchefstroom, 2520, South Africa. E-mail: kenny.uren@nwu.ac.za

Abstract: A laboratory process demonstrator was constructed and can be used show how abstract control theory connects to real world systems. The process constitutes four interconnected tanks, two tanks are placed on top and two tanks are placed at the bottom. The system has two inputs and two outputs. The system has an adjustable zero, that can be placed in either the right or left-half of the s -plane by adjusting the position of a valve. A mathematical model of the system is derived and simulated in the Simulink[®] environment of MATLAB[®]. From the model, the system components can be specified. A decentralised PI controller is developed with the help of MATLAB[®] and implemented by making use of dSPACE[®]. The aim is to control the liquid levels in the bottom two tanks. The results show that this is possible and the physical results can be compared to the simulated results.

Key words: *Keywords* - Quadruple-tank process, dSPACE[®] software, multivariable control, adjustable zero

1. INTRODUCTION

Benchmark process control platforms are used to demonstrate the control dynamics involved in the system for the community that is interested in control. The platform can then be used to evaluate different control strategies. A benchmark control platform is very helpful to gain insight with respect to the actual system. A benchmark process control platform is also very useful in that it can be used for more than one study.

The benchmark control platform considered is a multi-variable system, thus the process should include more than one input and more than one output. With this multivariable system, the possibility of an adjustable zero originates. There are however not many processes that can demonstrate the effect of the adjustable zero's location [1]. The quadruple tank process was developed to demonstrate these effects [2]. Specifically the performance limitations that are associated with a zero in the right half of the s -plane are illustrated by this process.

The quadruple tank process constitutes four interconnected water tanks. The schematic diagram of the system is illustrated in Figure 1. The inputs to the system are the voltages to the two pumps and the outputs are the water levels in the lower two tanks. The system can be seen as an interconnection of two decoupled two tank subsystems [3].

There are two valves that control the percentage of flow to the lower tanks. The valve positions are not seen as inputs to the system but as parameters and are set prior to an experiment. In [1], it is shown that the positions of the valves determine whether the system is in a minimum or non-minimum phase condition. For this system, the minimum phase is when the flow to the lower tanks are

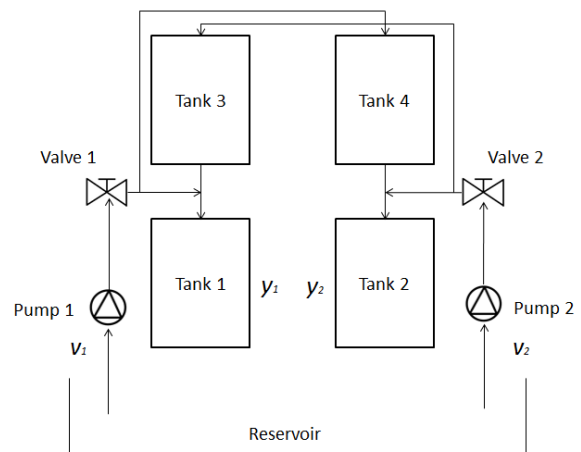


Figure 1: A schematic diagram of the quadruple-tank process

more than the flow to the upper tanks and the system is in non-minimum phase when the flow to the upper tanks is greater than the flow to the lower tanks [1].

The adjustable zero that has been mentioned above, can be located in either the left or the right half-plane just by changing the position of one of the valves. The quadruple tank process is a non-linear system and as the zero can be moved with the changing of a valve position, the valve position also affects the control performance of the system. Thus the platform can also show the sensitivity of the design method for a non-linear system [1]. The outline of this paper is as follows. An analytic model for the physical process will be derived in section II. The model will then be simulated in Simulink[®] environment

of MATLAB[®]. This will be given in section III. The simulation model is made to obtain practical parameters for the physical components and to later compare the simulation results with the physical results. Section IV discussed the practical implementation of the system and the use of dSPACE[®] to control the system. The results of the system will be discussed in section V and some concluding remarks will be given in section VI.

2. MATHEMATICAL MODEL

In this section a mathematical model of the system will be developed and linearised. A schematic layout of the system is shown in Figure 1. The aim is to control the water levels in the bottom two tanks which are given by y_1 and y_2 . This is achieved by controlling the voltages v_1 and v_2 to the pumps.

By applying Bernoulli's law [4] to a single tank one can obtain the velocity at the outflow of the tank which is given by:

$$V = \sqrt{2gh} \quad (1)$$

where g is the acceleration constant and h the liquid level in the tank. From the mass balances it is known that

$$Q_i - Q_o = A \frac{dh}{dt} \quad (2)$$

where

Q_i is the volumetric flow into the tank [m^3/s],
 Q_o is the volumetric flow out of the tank [m^3/s] and
 A is the cross sectional area of the tank [m^2].

By combining the above principles the height change in each tank is given by

$$\begin{aligned} \frac{dh_1}{dt} &= \frac{1}{A_1} \left(\left[k_1 N_{p1} \gamma_1 + a_3 \sqrt{2gh_3} \right] - a_1 \sqrt{2gh_1} \right), \\ \frac{dh_2}{dt} &= \frac{1}{A_2} \left(\left[k_2 N_{p2} \gamma_2 + a_4 \sqrt{2gh_4} \right] - a_2 \sqrt{2gh_2} \right), \\ \frac{dh_3}{dt} &= \frac{1}{A_3} \left(k_2 N_{p2} (1 - \gamma_2) - a_3 \sqrt{2gh_3} \right) \text{ and} \\ \frac{dh_4}{dt} &= \frac{1}{A_4} \left(k_1 N_{p1} (1 - \gamma_1) - a_4 \sqrt{2gh_4} \right) \end{aligned} \quad (3)$$

where A_i is the cross sectional area of tank i [m^2],
 a_i is the cross section area of the outlet hole [m^2],
 h_i is the water level in tank i [m] and
 γ_i is the setting between 0% and 100% of valve i .

The model is linearised by using the variables $x_i := h_i - h_i^0$ and $u_i := v_i - v_i^0$. A state space representation is thus obtained by differentiating (8) to h and v to obtain

$$\begin{aligned} \dot{X} &= AX + BU \\ Y &= CX, \end{aligned} \quad (4)$$

where

$$\mathbf{A} = \begin{bmatrix} -\frac{1}{T_1} & 0 & \frac{A_3}{A_1 T_3} & 0 \\ 0 & -\frac{1}{T_2} & 0 & \frac{A_4}{A_2 T_4} \\ 0 & 0 & -\frac{1}{T_3} & 0 \\ 0 & 0 & 0 & -\frac{1}{T_4} \end{bmatrix}, \quad (5)$$

with

$$T_i = \frac{A_i \sqrt{2h_i}}{a_i \sqrt{g}}, \quad (6)$$

$$\mathbf{B} = \begin{bmatrix} \frac{k_1 \gamma_1}{A_1} & 0 \\ 0 & \frac{k_2 \gamma_2}{A_2} \\ 0 & \frac{k_2 (1 - \gamma_2)}{A_3} \\ \frac{k_1 (1 - \gamma_1)}{A_4} & 0 \end{bmatrix} \text{ and} \quad (7)$$

$$\mathbf{C} = \begin{bmatrix} 1 & 0 & 0 & 0 \\ 0 & 1 & 0 & 0 \end{bmatrix}. \quad (8)$$

From the state space model a transfer function for the system can be obtained by using (9).

$$G(s) = C(sI - A)^{-1}B \quad (9)$$

The transfer function of the system is given by:

$$G(s) = \begin{bmatrix} \frac{c_1 \gamma_1}{(1+sT_1)} & \frac{(1-\gamma_2)c_1}{(1+sT_1)(1+sT_3)} \\ \frac{(1-\gamma_1)c_2}{(1+sT_2)(1+sT_4)} & \frac{c_2 \gamma_2}{(1+sT_2)} \end{bmatrix} \quad (10)$$

where $c_1 = T_1 k_1 k_c / A_1$ and $c_2 = T_2 k_2 k_c / A_2$.

By taking the determinant of the above equation, [2] states that the system has two zeroes, the one is always located in the left half-plane, and the other can be located in either the left hand or the right half-plane.

As previously stated, the position of the valves determine whether the system is in minimum phase or non-minimum phase. In minimum phase, the flow to the lower tanks are greater than the flow to the upper tanks. This is when

$$0 < \gamma_1 + \gamma_2 < 1.$$

In non-minimum phase, the flow to the upper tanks are greater than the flow to the lower tanks. This is when

$$1 > \gamma_1 + \gamma_2 > 2.$$

When $\gamma_1 + \gamma_2 = 1$ the zero is located at the origin. This is when the flow going to the tanks on the left is the same as the flow going to the tanks on the right.

In [1] it is stated that the system is more easily controlled in minimum phase and harder to control when the zero is located at the origin.

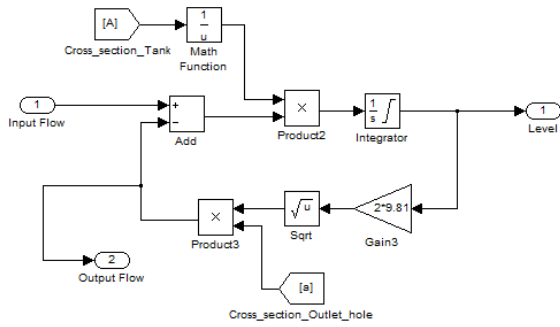


Figure 2: Model of a tank as given by Bernoulli's law and the mass balances equation

3. SIMULINK® MODEL

A simulation model is developed in Simulink®, an environment in MATLAB®. The simulation model is then used to obtain the physical parameters of the components.

In order to model the tanks, the mathematical equations as given in (1) and (2) are used. It can be represented by making use of mathematical Simulink® function blocks as seen in Figure 2. The model from Figure 2 is then used as a sub-system along with the models of a valve and a pump to model the full system as shown in Figure 3. A rough specification of the demonstrator size was given by the client as 1.5 m x 1 m x 0.5 m. Taking this into account along with the data from the simulation, the height of the tanks was chosen as 500 mm, the diameter as 200 mm and the outlet holes' diameter as 10 mm. By running experiments in the different modes with different parameters, it was estimated that a flow of at least 18 l/min or 0.0003 cm³/m was needed.

In order to vary the voltages to the pump, a signal with a variable duty cycle has to be given as input to the pump. There is however not a set relation between the duty cycle and the rotational speed of the pump, it differs for every pump, the situation the pump is used in and every operating point. Therefore special care must be taken when choosing the pump to make sure that the flow is sufficient for the system.

The total head loss is not included in the model but is present in the physical system. The characteristics of different pumps were considered at and the total head loss compared to the flow rate at that head loss. It was estimated that a centrifugal pump of 32 l/min will have a flow of 20 l/min at a head loss of 3 m [5]. The total head loss includes the pressure drop over the valves and the flow resistances of the pipes.

The following results were obtained by the simulation of the system in minimum phase (both valves set that 75% of the liquid flows to the bottom tanks) and non-minimum phase (both valves set that 75% of the liquid flows to the top tanks). The set points for both lower tanks are chosen as 15.24 cm. Figure 4 shows the water levels and output of the controller for minimum phase and Figure 5 shows the

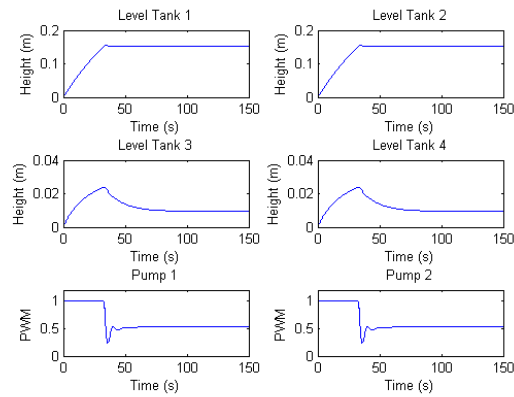


Figure 4: Minimum phase simulation results

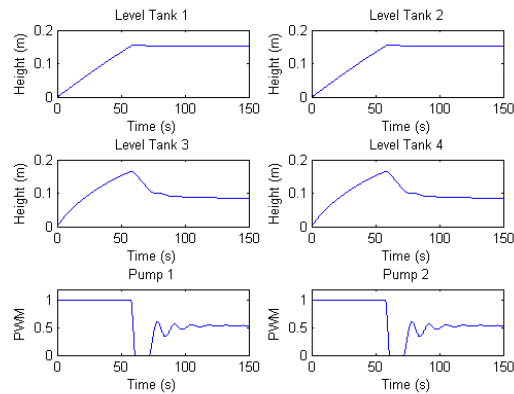


Figure 5: Non-minimum phase simulation results

water levels and controller output for non-minimum phase.

4. PRACTICAL IMPLEMENTATION

Once the parameters of the components were obtained in the simulation stage, the system was designed and constructed. As the system will make use of the dSPACE® environment for control, hardware and software will be discussed.

4.1 Hardware

The quadruple-tank process is a demonstrator. Thus it was decided to make use of perspex for the tanks so that the user can view the levels in the tanks. The tanks was mounted on a steel frame as can be seen in Figure 6. Two 32 l/min 12 V, 6 A, submersible in line pumps were chosen. Four two way ball valves were used to create the three way flow that is needed. The pipes used in the system are 20 mm see through flexible perspex pipes. It was decided to use an eTapeTM [6] as a sensor, a continuous fluid level sensor that looks like a ruler and makes use of pressure differences to estimate the liquid levels. The eTapeTM works as a variable resistor and is attached to the inside

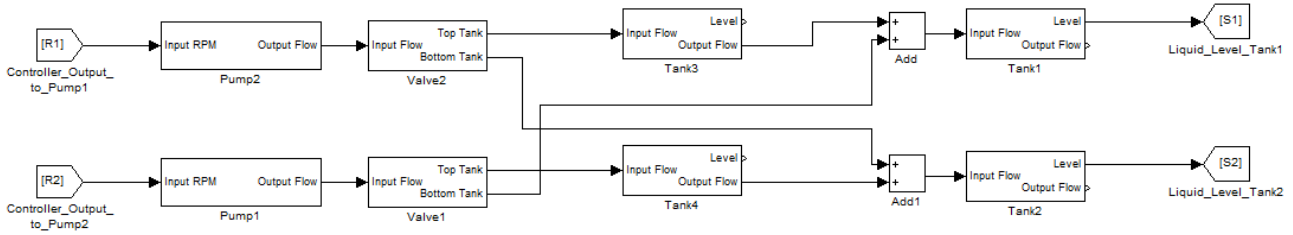


Figure 3: A model of the quadruple-tank process in Simulink®.



Figure 6: The physical system.

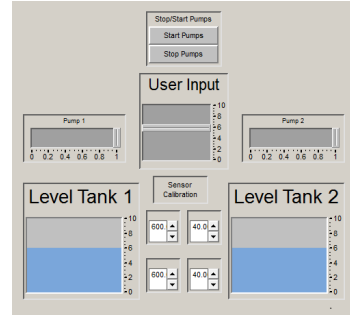


Figure 7: The graphic user interface that is used when an experiment is run.

of the tank. The higher the liquid level, the smaller the resistance. Several circuit stages had to be designed to ensure that the correct signal is sent to and from dSPACE® whilst making sure the dSPACE® hardware is protected. The outputs, namely the levels of the bottom two tanks are discussed first. A simple voltage divider is used to convert the varying resistance of the eTape™ to a voltage that can be measured. Then the signal is passed through a second order RC filter to eliminate noise and lastly through a protection circuit to ensure that the dSPACE® A/D does not receive a voltage greater than 10 V. 9.1 V Zener diodes will be used to accomplish the task.

To control the pumps a simple circuit is used, MOSFET technology was used along with an opto-isolator to isolate the software from the hardware and protect the dSPACE® hardware.

4.2 Software

As mentioned throughout, dSPACE® will be used to control the system. A graphic user interface is used so that the user can stop and start an experiment, display the water levels in the tanks and plot the liquid levels of the bottom tanks. The user interface can be seen in Figure 7. The bars at the sides make it possible for the user to specify the set point for a tank. The model that is used to control the

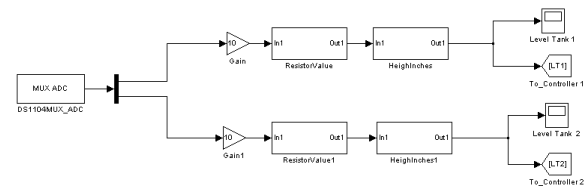


Figure 8: The Simulink® model used to measure the signal from the sensors.

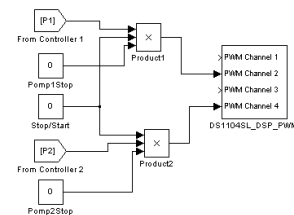


Figure 9: The Simulink® model used to provide output to the power circuit of the pumps.

system is designed in Simulink® and is shown in Figures 8 and 9. The RTI blocks are used to represent the inputs and outputs on the dSPACE card. Some of the blocks depicted are connected to the graphic user interface. For example the level of Tank 1 is connected to the tank in the user interface to show how the level varies. It was decided to make use of a decentralised PI controller. The controller model can be seen in Figure 10. The advantages for this method are a reasonable settling time, less percentage overshoot and a correct response even if disturbances are introduced in to the system [7].

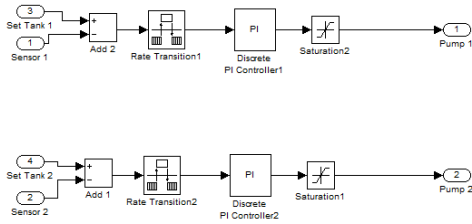


Figure 10: The decentralised PI controller that is used to control the quadruple-tank process.

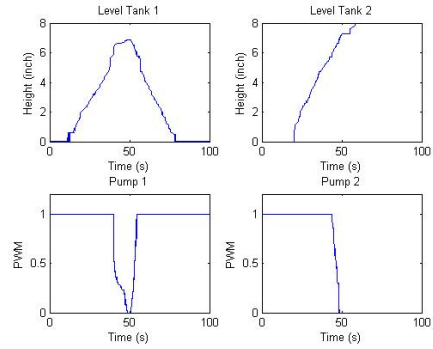


Figure 12: Non-minimum phase results

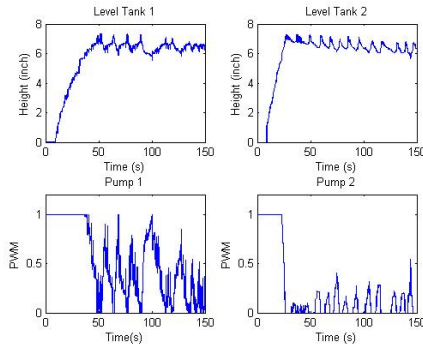


Figure 11: Minimum phase results

5. RESULTS

The results of the different experiments will be discussed in this section. As stated, the quadruple tank process has three different modes of operation, minimum phase, non-minimum phase and when the adjustable zero is at the origin. A practical experiment was conducted for each of the three modes. Only the results for the minimum and non-minimum modes are shown. The set points for the bottom tanks are chosen as 6 inches (the eTapeTM makes use of inches) or .1524 m.

5.1 Minimum phase

The system is in minimum phase when the flow to the bottom tanks is greater than the flow to the top tanks. The valves are turned accordingly so that 75% of the flow goes to the bottom tanks (tanks 1 and 2) and 25% to the top tanks (tanks 3 and 4). Figure 11 shows the results obtained by ControlDesk[®]. It can be seen that the simulation results, seen in the Simulink[®] model section, differ from the practical results. This means that the simulation model does not reflect the real-world system and should be adjusted. It can be seen however that if the fluctuations are ignored, the settling time of tank 2 is almost the same for both sets of results. Figure 11 illustrates that the flow to tank 2 is greater than the flow to tank 1. It was determined that this is due to the pumps that do not have the same flow rate.

5.2 Non-minimum phase

The system is in non-minimum phase when the flow to the bottom tanks is less than the flow to the top tanks. The valves are turned accordingly so that 25% of the flow goes to the bottom tanks (tanks 1 and 2) and 75% to the top tanks (tanks 3 and 4). Figure 12 shows the results obtained by ControlDesk[®]. It can be seen from Figure 12 that the system could not be practically controlled. The simulation results however show that it is possible. This reveals unmodelled effects in the simulation model.

5.3 Adjustments made to simulation

During the experiments, it was noted that the pipes took some time to fill (especially due to the vertical placement of the pipes). Thus there is a delay between the output to the pumps and the moment the tanks started filling with water. A delay was inserted into the model to simulate this delay. As it takes longer for the water to reach the bottom tanks, a longer delay is used for the bottom tanks in comparison with the top tanks.

The results of the adjusted model (in blue) are illustrated in Figure 13 along with the practical results (in green) it is seen that the practical results are closer reflected by the adjusted simulation results. The only adjustment made to the simulation is the delay time. The mean absolute percentage error (MAPE) for the levels in tank one is 15.2% and for tank two 6.7%. The discrepancy can be ascribed to external factors. The MAPE only used data points beyond 10 seconds. (Due to the inaccuracy of the sensor at very low water levels.)

When the graphs in Figure 14 are compared it is seen that the practical results (in green) are closer reflected by the adjusted simulation results (in blue). The delay time was adjusted as well as the positions of the valves. From the practical experiment it was clear that there was more flow to tank 4 than to tank 3. When the settings for valve one was adjusted to 0.3 and 0.7, the simulation results reflected the practical results more closely. The MAPE for the levels in tank one is 87.85% and for tank two 13.9%. The error for tank one is very large and is due to a small error at first that had an impact on the controller output and escalated

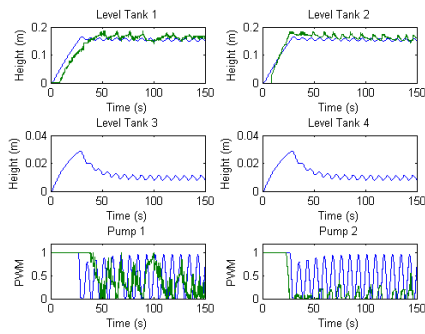


Figure 13: Minimum phase adjusted simulation and practical results

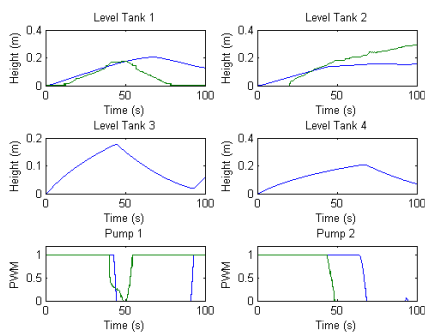


Figure 14: Non-minimum phase adjusted simulation and practical results

as the process continued. The discrepancy can also be ascribed to external factors especially the accuracy of the sensors. There is still a discrepancy in the results, but this can be ascribed to external components.

5.4 External factors

The external components referred to can be a slight difference in pipe lengths from the pumps, that the valves for tanks 1 and 4 are placed higher than the valves for tanks 2 and 3 or a slight difference in the outlet hole diameters. Furthermore when the experiment is practically run, and the water is lower than a certain level, a vortex is formed inside the tank. This is not included in the simulation model and can be a cause for the discrepancy. The inaccuracy of the sensors greatly effect the system. The sensor cannot measure the first 5 cm correctly and shows a value of 0 when the water level is below 5 cm. The sensors are not that accurate as they have to be calibrated before each experiment and this is done visually. The fault of parallax has an influence.

5.5 Discussion of the different modes

From both the practical and simulation results it can be seen that the system takes longer to stabilize in non-minimum phase than in minimum phase and the overshoot percentage is larger for non-minimum phase.

This confirms that there is limits in control performance when the system is in non-minimum phase as a larger amount of water is supplied to the top tanks.

6. CONCLUSION

As a laboratory demonstrator, the quadruple tank process is ideal to link the real-world system with the mathematics. The adjustable zero allows the system to operate in three different modes. The positions of the valves determine the mode. The position of the zero directly impacts the liquid level in the top tanks if the set points are the same for the different modes and only the valve positions are changed.

It was possible to control the system for two of the three modes namely in minimum phase and when the zero is located at the origin. The system could not be controlled in non-minimum phase. This is ascribed to inaccuracies in the hardware.

The Simulink[®] model is a reflection of the practical system and shows that it is possible to build a model of the system. The model can be updated to include the vortices that sometimes form inside the tanks. Future work is warranted in terms of improving the model as well as non-linear control techniques.

REFERENCES

- [1] K. H. Johansson, "The Quadruple Tank Process: A Multivariable Laboratory Process with an Adjustable Zero," *IEEE Transactions on Control Systems Technology*, vol. 8, pp. 456–465, 2000.
- [2] K. H. Johansson, "Relay feedback and multivariable control," Master's thesis, Department of Automatic Control, Lund Institute of Technology, 1997.
- [3] J. K. Johnsen and F. Allgower, "Interconnections and damping assignment passivity-based control of a four-tank system," *Lecture Notes in Control and Information Sciences*, vol. 366, pp. 111–122, 2007.
- [4] B. R. Munson *et al.*, *A brief Introduction to Fluid Mechanics*, J. Welter, Ed. John Wiley & Sons, 2011.
- [5] LVM. Congo submersible & in-line. [Online]. Available: <http://docs-asia.electrocomponents.com/webdocs>
- [6] M. Technologies. etape continuous fluid level sensor operating instructions and application notes. [Online]. Available: <http://www.mantech.co.za/datasheets/products/ETAPE>
- [7] R. S. M. Mular and T. Tyagarajan, "Design of Decentralized Fuzzy Pre compensated PI Controllers for Quadruple Tank System," *International Journal of Recent Trends in Engineering*, vol. 2, pp. 188–192, 2009.

NONLINEAR STATE SPACE MODELLING OF AN AXIAL-FLOW COMPRESSOR SYSTEM FOR ENERGY VISUALISATION

L.B. Fouché*, K.R. Uren*, G. van Schoor**

* School of Electrical, Electronic and Computer Engineering, North-West University, Potchefstroom campus, South Africa E-mail: 21620113@nwu.ac.za / kenny.uren@nwu.ac.za

** Unit for Energy Systems, North-West University, Potchefstroom, South Africa E-mail: george.vanschoor@nwu.ac.za

Abstract: Energy is associated with all engineering disciplines including electrical, mechanical and chemical engineering, and therefore a multi-domain concept. An energy visualisation for large-scale industrial systems can portray the system's steady state response from an energy perspective. If a controller can be based on the energy in a system, then any discipline can form a reasonable understanding of how to optimise a system from an energy perspective. This paper aims to derive a nonlinear model for an axial-flow compressor system similar to Greitzer (1986) in state space format. From the state variables the steady state energy flow rate in the system is calculated and visually presented. Evaluating the representation, a clear concept of the energy flow of the system is formed to determine the energy conversion at two different operating points.

Keywords: Axial-flow compressor, state space, nonlinear, energy, visualisation

1. INTRODUCTION

A model of a large-scale industrial system is most often derived from the conservation of mass, momentum and energy equations. Such a set of equations can either be linear or nonlinear depending on the complexity of the system. These equations are an accurate depiction of the system, but in most cases these models have been linearised at a certain operating point. The limitation of a linear model is that dynamics over a large operating range cannot be represented accurately.

Compressors form part of many of the systems found in the industry. One of the most common systems that includes a compressor is the Brayton-cycle. This system consists of a compressor, combustor and a turbine. Two types of compressors can be differentiated, namely positive displacement and dynamic compressors. Dynamic compressors are a type of continuous-flow compressors and unlike positive displacement compressors, they deliver a fixed volumetric flow [1]. Dynamic compressors can therefore be categorised into axial-flow compressors and centrifugal compressors. In axial-flow compressors the flow leaves the compressor in the axial direction and in the case of a centrifugal compressor the air leaves in a perpendicular direction with respect to the shaft [2].

Greitzer developed a nonlinear one dimensional lumped-parameter model for an axial-flow compressor in [3] to predict the transient response of a compressor system and to determine if compressor instability, rotating stall or surge will be encountered by operating the compressor near the stall line. In [4] and [5] a model was presented for the analysis of stall effects of a multi-stage axial compressor.

Considering literature focusing on the analysis of multi-domain nonlinear systems, passivity-based approaches

came out as the most prevalent. The underlying idea behind passivity-based techniques is the consideration of complex systems as energy manipulation devices. Lyapunov theory stemming from stability analysis also plays a vital role and is associated with energy analyses. Recent literature also considers complex systems in port-Hamiltonian framework which combines a bond-graph approach with theoretical mechanics. These approaches solely rely on energy principles [6].

In a multi-domain environment where thermal, hydraulic and the electric domains are present, a controller can be designed to control a nonlinear model from first principles of energy and to visually represent the energy and energy flow in the system.

An energy visualisation can be in the form of an energy signature for a system at a specified operation point. From a combination of these operating points it can be determined if the system is operating at maximum efficiency. Condition monitoring and fault detection and isolation (FDI) can be done on the system by using the energy visualisation.

The contribution of this paper is to describe the nonlinear, one-dimensional, lumped-parameter compressor model in state space format and to evaluate the energy flow with Bernoulli's equation for the flow and kinetic energy of the system from the state variables. The paper also focuses on visually presenting the energy flow of the system.

Section 2 of the paper starts with the derivation of the model for an axial-flow compressor system. In section 3 the state space model for the system is derived. Section 4 shows the simulation of the state space equations and the response of the state variables for different operating points.

An energy visualisation is depicted in section 5 for the compressor system for different operating points and the paper concludes with suggestions of possible future work to continue the research and a conclusion of the findings in this paper.

2. MODEL DERIVATION

From the conservation of the mass and momentum equations, the model consisting of the compressor, plenum and throttle for the compressor system is derived. Unlike more recent compressor models the equations are preserved in dimensional form and the derivation of the states is kept with respect to time. The compressor system for which the equations are derived is depicted in figure 1.

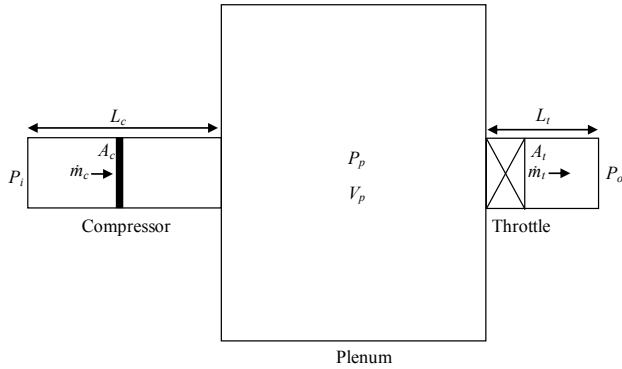


Figure 1 : Diagram of compressor system

A quadratic equation is used to describe the operation of the throttle and a cubic equation is used for the compressor's steady state response. This yields a nonlinear model for the compressor system. A result of the derivation is a one-dimensional, lumped-parameter model describing the response of the compressor system.

2.1 Mass and momentum equations

The first order state equations for the compressor's mass flow, throttle mass flow, plenum pressure and compressor's pressure rise are given by

$$\frac{d\dot{m}_c}{dt} = \frac{A_c}{L_c} (\Delta p_c - \Delta p), \quad (1)$$

$$\frac{d\dot{m}_t}{dt} = \frac{A_t}{L_t} (\Delta p - \Delta p_t), \quad (2)$$

$$\frac{dp_p}{dt} = \frac{a^2}{V_p} (\dot{m}_c - \dot{m}_t), \quad (3)$$

$$\frac{d\Delta p_c}{dt} = \frac{1}{\tau} (\Delta p_{c,ss} - \Delta p_c), \quad (4)$$

where A_c [m²] and A_t [m²] denote the active compressor and throttle area, L_c [m] and L_t [m] the length of the compressor and throttle duct, ΔP [Pa] the pressure

difference from the plenum to atmosphere, ΔP_t the pressure difference across the throttle, $\Delta P_{c,ss}$ the steady state compressor pressure rise, a [m/s] the speed of sound and V_p [m³] the plenum volume. The compressor's time lag τ is given by

$$\tau = \frac{2\pi RN_{Stall}}{U}, \quad (5)$$

with R [m] as the mean compressor radius, N_{Stall} as the number of revolutions required to develop a stall cell and U [m/s] as the mean rotor velocity.

2.2 Compressor characteristic

The compressor is modelled as an actuator disk, therefore energy is added to the system by the compressor in the form of a pressure rise in the working fluid. Equation (6) assumes a cubic equation to describe the compressor's steady state pressure rise for a given mass flow rate and rotor speed as

$$\Delta p_{c,ss} = \frac{C_0 (NR\pi)^2 \rho}{900} - H \left(\frac{15m_c^3}{\pi RN (\rho A_c W)^2} - \frac{3m_c^2}{2\rho (A_c W)^2} \right), \quad (6)$$

with C_0 as the shut off value, H and W as the compressor semi-height and semi-width respectively and N as the rotor speed.

2.3 Throttle characteristic

A quadratic equation is used to describe the throttle characteristic for a given mass flow rate and throttle position so that the pressure drop over the throttle is given by

$$\Delta p_t = \frac{u_t \dot{m}_t^2}{2\rho A_t^2}, \quad (7)$$

with u_t as the throttle position and ρ [kg/m³] as the density.

3. STATE SPACE MODEL

The states variables of the compressor system are chosen as follows:

$$\begin{aligned} x_1(t) &= \dot{m}_c(t), \\ x_2(t) &= \dot{m}_t(t), \\ x_3(t) &= p_p(t), \\ x_4(t) &= \Delta p_c(t). \end{aligned} \quad (8)$$

with \dot{m}_c [kg/s] as the compressor mass flow rate, \dot{m}_t [kg/s] as the throttle mass flow rate and p_p [Pa] as the plenum pressure of the system. The state differential equation [7] is then given by

$$\dot{\mathbf{x}} = \mathbf{A}\mathbf{x} + \mathbf{B}\mathbf{u}, \quad (9)$$

where the \mathbf{A} and \mathbf{B} matrices are given by

$$\mathbf{A} = \begin{bmatrix} 0 & 0 & -\frac{A_c}{L_c} & \frac{A_c}{L_c} \\ 0 & -\frac{x_2(t)}{2\rho L_t A_t} & \frac{A_t}{L_t} & 0 \\ \frac{a^2}{V_p} & -\frac{a^2}{V_p} & 0 & 0 \\ \frac{-15Hx_1^2(t)}{\tau\rho^2\pi R^3 W^3} + \frac{3Hx_1(t)}{2\tau\rho A^2 W^2} & 0 & 0 & \frac{1}{\tau} \end{bmatrix}, \quad (10)$$

$$\mathbf{B} = \begin{bmatrix} \frac{A_c}{L_c} & 0 & 0 \\ 0 & -\frac{A_t}{L_t} & 0 \\ 0 & 0 & 0 \\ 0 & 0 & \frac{C_0\pi^2\rho R^2}{900r} \end{bmatrix}. \quad (11)$$

It can be seen that the A-matrix contains some of the state variables and therefore the state space model can be considered as nonlinear. The output equation that relates the inputs of the system with the outputs of the system is given by

$$\mathbf{y} = \mathbf{C}\mathbf{x} + \mathbf{D}\mathbf{u} \quad (12)$$

4. SIMULATION

4.1 Initial values and parameters

The initial values for the states are given in (13) with the corresponding units of the state variables as discussed in (8).

$$\mathbf{x}_0 = [0.3 \quad 0.3 \quad 101700 \quad 1700]^T \quad (13)$$

The parameters used to describe the system are given in table 1. These parameters remain fixed for the duration of the simulation.

Table 1 : Simulation values

Parameter	Value	Parameter	Value
a	340 [m/s]	N_{stall}	2
A_c	0.1 [m ²]	p_i	100 [kPa]
A_t	0.1 [m ²]	p_o	100 [kPa]
C_0	0.3	ρ	1.15 [kg/m ³]
L_c	3 [m]	R	0.1 [m]
L_t	0.8 [m]	V_p	1.5 [m ³]
N	4591 [rpm]		

4.2 System response

The compressor system is started from a steady state operating point with a throttle position u_t of 4. Instantaneously the throttle position u_t is changed to 1 and a new steady state operating point is reached within a time window of 0.3 seconds.

In figure 2 the compressor pressure rise is superimposed on the compressor and throttle characteristics. The intersection of these two characteristics determines the steady operating point of the compressor system.

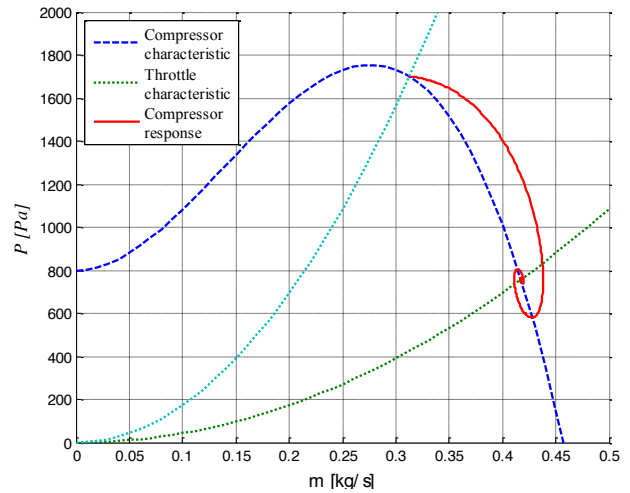


Figure 2 : Compressor pressure rise response superimposed on system characteristic

The response of the four states of the system with respect to time is shown in figure 3. It can be seen that all of the states settle to a new value when steady state is reached for the new throttle position.

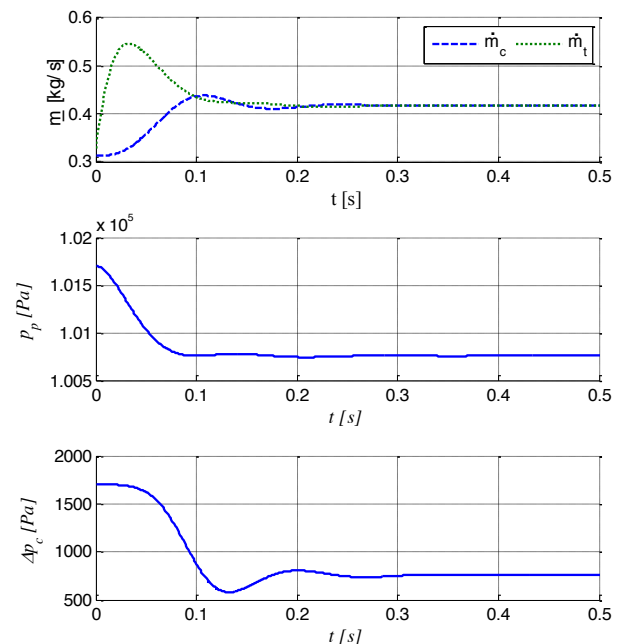


Figure 3 : Transient response of state variables

4.3 Model validation

Flownex[®] is a systems CFD software package capable of simulating thermo-fluid systems. Flownex[®] incorporates a variety of components and the components are validated.

The values for different steady state operating points for both the derived model and a Flownex[®] model are shown in figure 4. Only an operating range where the compressor is stable is shown in the figure.

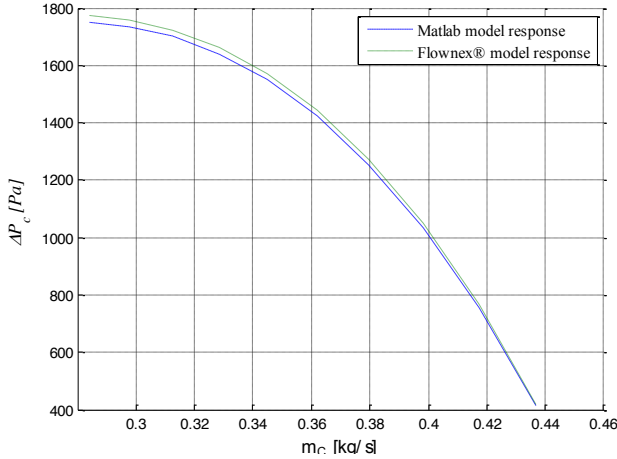


Figure 4 : Steady state response comparison of derived model and Flownex[®]

The percentage error for all operating points is calculated and shown in figure 5. The error is due to the fact that Flownex[®] takes temperature rise across the system into account, where the derived model neglects the temperature rise.

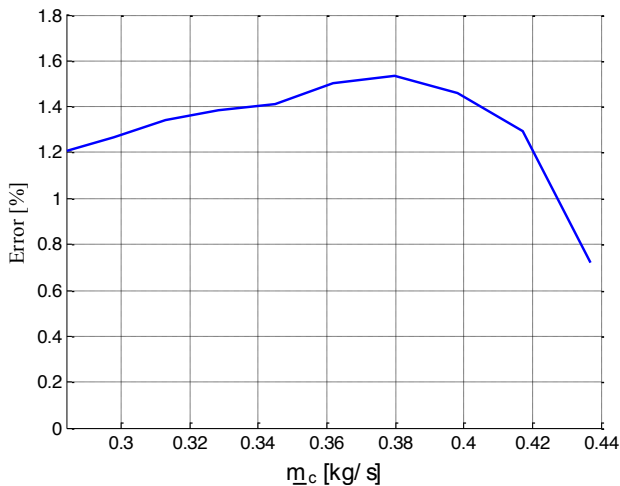


Figure 5 : Difference of the derived model and Flownex[®] model as a percentage error

5. ENERGY VISUALISATION

Energy is a fundamental concept in systems and can be used to describe multi-domain systems. It can therefore be seen to connect all domains and can depict a systems state using energy as the unifying domain [8].

5.1 Bernoulli equation

The Bernoulli equation is concerned with the conservation of kinetic, potential and flow energy to describe the mechanical energy of a particle in a streamline [9]. Bernoulli's equation is an approximate relation between the pressures, velocity and elevation. Bernoulli's equation is derived by using the conservation of linear momentum principle and can be evaluated at any point in a streamline where pressure, velocity, density and elevation are known for steady incompressible flow, and is given by

$$\frac{P}{\rho} + \frac{V^2}{2} + gz = const, \quad (14)$$

with P [Pa] as the pressure, ρ [kg/m³] as the density, V [m/s] as the velocity, g [m/s²] as the gravitational acceleration and z [m] as the height of a particle from a reference point. The first term P/ρ is recognized as the flow energy, $V^2/2$ as the kinetic energy and gz as the potential energy. The equation that relates the pressure to the energy flow rate can be calculated from the Bernoulli equation as

$$E_f = \dot{m} \left(\frac{P}{\rho} \right), \quad (15)$$

to obtain the flow energy flow rate or a type of potential energy flow rate due to pressure E_f [J/s]. The energy flow rate that relates to the velocity can be calculated by

$$E_k = \dot{m} \left(\frac{V^2}{2} \right), \quad (16)$$

to obtain the kinetic energy flow rate E_k [J/s]. The potential energy flow rate can also be calculated by multiplying the potential energy by the mass flow rate.

5.3 Node selection

The selection of nodes in the compressor system is done in such a way that each node can represent both the pressure and mass flow rate of the corresponding component at a node. The selection of nodes must also enable the evaluation of the flow energy rate at each node. The node diagram of the system is depicted in Figure 6.

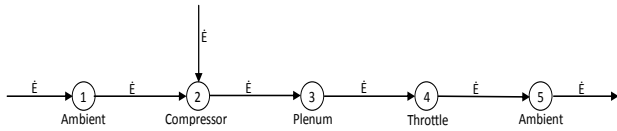


Figure 6 : Compressor system node diagram

Nodes 1 and 5 represent ambient conditions and nodes 2, 3 and 4 represent the compressor, plenum and throttle respectively.

Energy from node 1 as well as external energy converted to flow energy by the compressor on the working fluid, enter node 2. Because the model does not account for losses in the system, the energy that enters node 3 will flow through node 4 and exit at node 5. In the flow of energy through the nodes the energy is only converted to and from flow and kinetic energy.

5.3 Steady state energy flow rate

In this section the energy flow rate for the flow and kinetic energy of the compressor system at the nodes is graphically portrayed through bar graphs. The potential energy is disregarded because it is assumed that the height change is negligibly small. In steady state it is assumed that the mass flow rate is steady and the density at the different nodes is fixed, therefore the energy flow rate for a certain operating point of the system can be evaluated. A visualisation cannot be analysed with the standard Bernoulli equation when the compressor enters rotating stall or surge, since the flow is unsteady under these conditions and Bernoulli's equation does not hold in the case of unsteady flow.

The results are obtained for a pressure reference of 100kPa. The compressor system is initially set to a throttle position that restricts the mass flow of the system and results in a steady operating point. Figure 6 depicts the total energy flow rate entering and exiting each node.

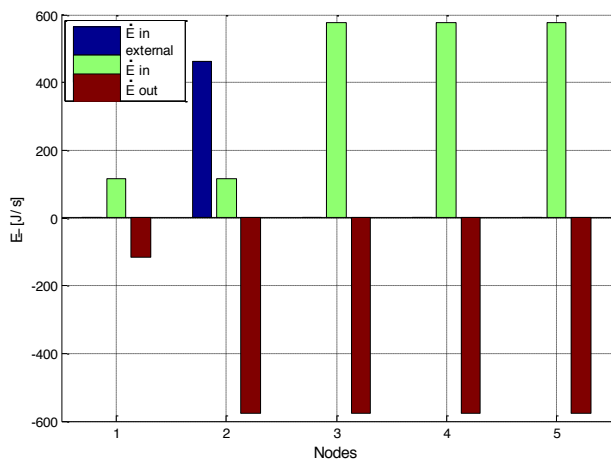


Figure 6: Total energy flow rate with a throttle setting of 4

The total energy flow rate for each node is discretised into the flow and kinetic energy components. This can be seen in figure 7 and how the energy is converted to and from flow and kinetic energy at nodes 2 and 4.

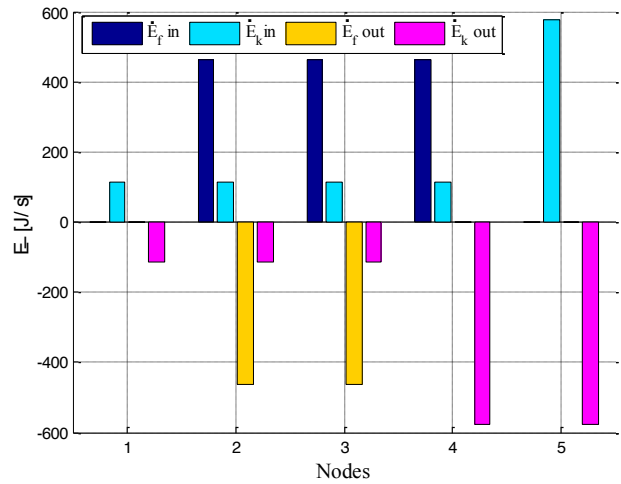


Figure 7: Energy flow rate with a throttle setting of 4 (discretised)

When the throttle position is changed, meaning that the throttle restriction of the flow changes, a new steady state operating point is reached within 0.3 seconds. This leads to a change in state variables, thus changing the energy flow rate.

The energy flow rate for the new throttle position is shown in figure 8.

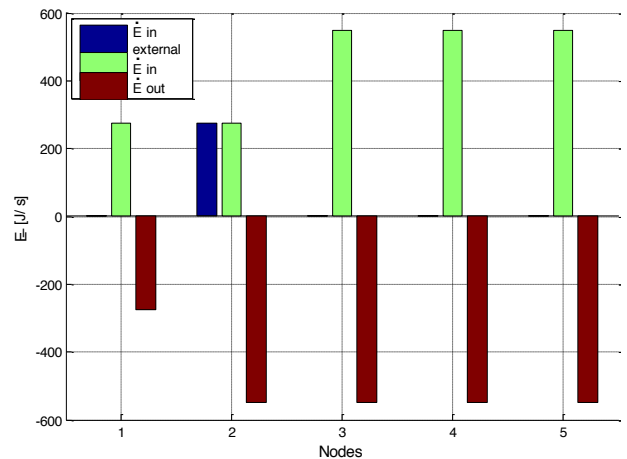


Figure 8: Total energy flow rate with a throttle setting of 1

Again the total energy flow for each node is discretised into the flow and kinetic energy. The new discretised energy flow rate for each node is shown in figure 9.

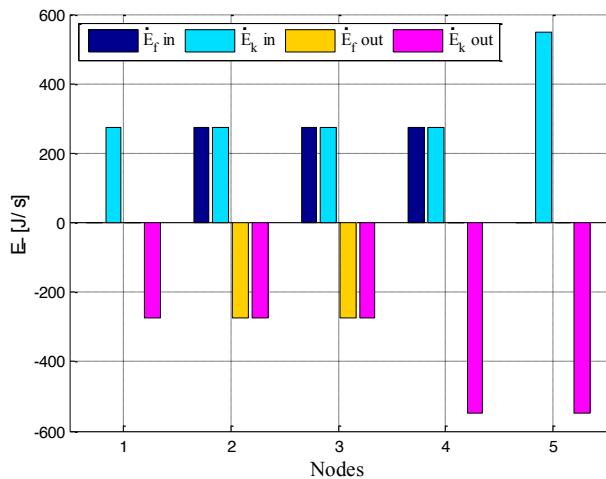


Figure 9: Energy flow rate with a throttle setting of 1 (discretised)

It can be deduced from the graph in figure 9 that the energy flow rate due to the work done by the compressor decreases and the energy flow rate due to the mass flow rate entering the compressor increases when compared to the energy flow rate of the initial throttle position.

The energy balance is achieved through the summation of the energy flow rate in and out of each node. Through this, possible energy lost at a node as well as the efficiency of a system can be determined.

6. FUTURE WORK

Future work includes adding a thermal domain to the compressor system and re-evaluating the representation at the different nodes for the flow energy rate. The future research also aims to evaluate the transient energy in each node with the extended Bernoulli equation and to describe the stored energy in each node.

The energy requirement to move from one operating point to another can be determined through this and it can suggest if the transition is energy efficient.

7. CONCLUSION

Energy visualisation seems relevant to use in research for alternative multi-domain system analysis and optimisation.

A nonlinear model for an axial-flow compressor system accurately depicts the response of the system and the flow and kinetic energy flow rates are determined with the Bernoulli equation from the state variables. From the steady state energy flow representation it is possible to

determine the amount of energy entering and exiting the system and how it changes at different operating points.

Another advantage seen in the visualisation is to distinguish between flow and kinetic energy flow rate and how energy is shaped from one sub-subsystem to another.

8. REFERENCES

- [1] S.L. Dixon and C.A. Hall: "Fluid Mechanics and Thermodynamics of Turbomachinery", Elsevier Inc., US, seventh edition, Chapter 5, 177-222.
- [2] J.T. Gravdahl: "Modeling and control of Surge and Rotating Stall in Compressors", Thesis, Norwegian University of Science and Technology, Norway, 1998.
- [3] E.M. Greitzer: "Surge and Rotating Stall in Axial Flow compressors Part I: Theoretical Compression System Model", *Gas Turbine Conference of the American society of mechanical engineers*, pp. 190-198, April 1976.
- [4] F.K. Moore: "A Theory of Rotating Stall of Multistage Axial Compressors: Part I - Small Disturbances", *Journal of Engineering for Gas Turbines and Power*, Vol. 106, pp. 313-320, April 1984.
- [5] F.K. Moore and E.M. Greitzer: "A theory of post-stall transients in an axial compressor system: Part I - Development of equations", *Journal of Engineering for Gas Turbines and Power*, Vol. 108, pp. 68-76, 1986.
- [6] D.J. Jeltsema and J.M.A. Scherpen: "Multidomain Modeling of Nonlinear Networks and Systems", *IEEE Control. Syst. Mag.*, vol. 29, no. 4, pp. 28-31, Aug. 2009
- [7] R.C. Dorf and R.H. Bishop: *Modern Control Systems*, Pearson, USA, twelfth edition, chapter 3, 183-193.
- [8] G. van Schoor, K.R. Uren, M.A. van Wyk, P.A. van Vuuren and C.P. du Rand: "An energy perspective on modelling, supervision, and control of large-scale industrial systems: Survey and framework", *Proceedings: 19th World Congress of The International Federation of Automatic Control*, South-Africa, pp. 6692-6703, August 2014.
- [9] Y.A. Cengel and A.J. Ghajar: *Heat and Mass Transfer: Fundamentals and Applications*, McGraw-Hill, fourth edition, chapter 5, 183-238.

AERIAL APE: INDUSTRIAL BRACHIATING POWER LINE INSPECTION ROBOT

J. Patel and Prof E. Boje

Dept. of Electrical Engineering, University of Cape Town, Private Bag X3, Rondebosch 7701, South Africa, E-mail: {ptljav001@myuct.ac.za, Edward.boje@uct.ac.za}

Abstract: This paper discusses engineering details of a brachiating robot for the industrial application of power line inspection. An Euler-Lagrange model with constraints is presented along with simulation of a brachiation manoeuvre. The mechanical design for the robot configuration and gripper mechanism are also presented.

Keywords: Brachiating robot, Power line inspection, Mechanical design

1. INTRODUCTION

The supply of electricity is crucial to the proper operation of an economy as it has an impact on nearly every sector. Both the high-voltage transmission and intermediate voltage distribution infrastructure requires regular inspection and maintenance to ensure reliability of the electrical network down to the reticulation level. The most common method for inspecting power lines is by a line crew walking along the line, which is labour intensive and not very reliable due to inconvenient access to servitudes and reliance on human judgment. An alternative or supplement to ground patrols is the use of fixed wing aircraft and helicopters to perform inspections. These are faster but significantly more expensive and also have limitations.

In recent years, a number of robotic platforms have been developed to perform autonomous inspection of power lines. Introducing a robot to perform power line inspection has a number of advantages such as:

- Faster and more effective inspection
- Cost-effectiveness
- Safety for operating crew

However, despite the number of robotic platforms that have been developed, very few are currently in commercial use, due to the challenges of operating in a real-world environment.

Among the most successful robotic platforms are the Expliner [1], LineScout [2], and the University of KwaZulu-Natal's Power Line Inspection Robot (UKZN PLIR) [3]. These robots have all been successfully operated in real-world industrial power line environments even if not commercially. Despite their success, they are either kinematically complex or rely on bulky, static schemes for obstacle navigation requiring high torque meaning bigger actuators and therefore bigger robots. Thus, a robot capable of operating in the real world while still remaining simple and compact is required.

This paper is focused on the design of a brachiating robot for industrial application to power line inspection. Brachiation allows for the design of a light-weight and compact robot which is capable of negotiating obstacles with less effort than current robotic platforms. The research presented in this paper builds on [4] in which the specifications of the brachiating robot were detailed. In this paper, an improved dynamical model of the robot is presented (in Section 2), followed by simulation results of a jumper-to-cable swing manoeuvre (in Section 3). The mechanical configuration design is then discussed in Section 4 and gripper design in Section 5. Finally, Section 6 concludes the paper and discusses future work.

2. DYNAMIC MODEL

The brachiating robot is modelled as a planar double pendulum, actuated at the elbow.

The generalised coordinates of the configuration are shown in Figure 1. θ_1 , is the angle of the first link with respect to the vertical and θ_2 is the angle of second link with respect to the first. The angle ϕ represents the angle of the slope and allows for brachiation on slopes to be simulated. Coordinates x and y are parallel and orthogonal distances, respectively, and allow for the imposition of constraints on the model.

The differential equations-of-motion are obtained using the Euler-Lagrange equation. The Lagrangian of the system is defined as,

$$L = T_1 + T_2 - (U_1 + U_2), \quad (1)$$

where T represents the kinetic energy and U , the potential energy of the system.

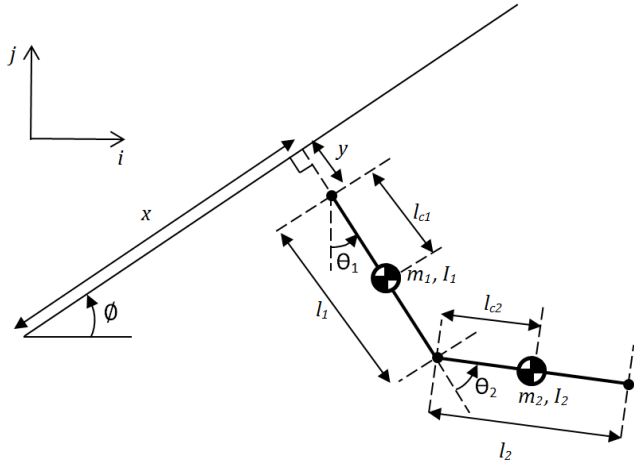


Figure 1: Generalised coordinates of robot

The kinetic and potential energies of the links are given respectively by,

$$T_1 = \frac{1}{2} m_1 [(\dot{x}\cos(\phi) + \dot{y}\sin(\phi) + l_{c1}\dot{\theta}_1\cos\theta_1)^2 + (\dot{x}\sin(\phi) - \dot{y}\cos(\phi) + l_{c1}\dot{\theta}_1\sin\theta_1)^2] + \frac{1}{2} I_1 \dot{\theta}_1^2 \quad (2)$$

$$T_2 = \frac{1}{2} m_2 [(\dot{x}\cos(\phi) + \dot{y}\sin(\phi) + l_1\dot{\theta}_1\cos\theta_1 + l_{c2}\cos(\theta_1 + \theta_2)(\dot{\theta}_1 + \dot{\theta}_2))^2 + (\dot{x}\sin(\phi) - \dot{y}\cos(\phi) + l_1\dot{\theta}_1\sin\theta_1 + l_{c2}\sin(\theta_1 + \theta_2)(\dot{\theta}_1 + \dot{\theta}_2))^2] + \frac{1}{2} I_2 \dot{\theta}_2^2 \quad (3)$$

$$U_1 = \frac{1}{2} m_1 g(x\sin(\phi) - y\cos(\phi) - l_{c1}\cos\theta_1) \quad (4)$$

$$U_2 = \frac{1}{2} m_2 g(x\sin(\phi) - y\cos(\phi) - l_1\cos\theta_1 + l_{c2}\cos\theta_2) \quad (5)$$

The generalised vector of coordinates, q , is defined as,

$$q = (x \ y \ \theta_1 \ \theta_2)^T, \quad (6)$$

By solving the Euler-Lagrange equations, the equation-of-motion can be written as,

$$M(q)\ddot{q} + C(q, \dot{q})\dot{q} + G(q) + F = B\tau + A(q)^T\lambda, \quad (7)$$

where,

$$B = \begin{bmatrix} 0 & 0 \\ 0 & 1 \end{bmatrix}, \quad (8)$$

and the constraint matrix A is,

$$A = \frac{\partial h}{\partial q} = \begin{bmatrix} 1 & 0 & 0 & 0 \\ 0 & 1 & 0 & 0 \end{bmatrix}, \quad (9)$$

A detailed derivation can be found in [4 & 5].

Finally, the torque output of the motor is modelled as

$$\tau = \eta(\sigma u) - \varphi\omega, \quad (10)$$

$$\sigma = \frac{Nk_M V}{R}, \quad (11)$$

$$\varphi = \frac{Nk_M^2}{R}, \quad (12)$$

where σ is the stall torque, φ is the back EMF coefficient, N is the gearbox ratio, k_M is the motor constant, R is the winding resistance, ω is the speed of the gearbox output shaft, η is the efficiency of the gearbox, V is the motor voltage and $u \in [-1, 1]$ is the control input.

3. SIMULATION

The robot was simulated in various brachiation scenarios to assess the feasibility of the concept and to gain insight into the dynamics. Simulations were performed in open loop with no disturbances, in order to determine the optimal trajectories. These trajectories will be used in the development of a minimum energy control scheme with a robust controller at a later stage in the research.

A constrained non-linear optimisation algorithm (Matlab's `fmincon` function) was used in order to determine these optimal trajectories. Details of the algorithm and the parameters used can be found in [4].

The most interesting brachiation scenario is the jumper-to-cable swing manoeuvre, shown in Figure 2. The ability to navigate jumper cables greatly increases the autonomy of the robot. This manoeuvre is particularly difficult as the robot must swing while on an incline while raising its centre of mass, which requires large actuation torque.

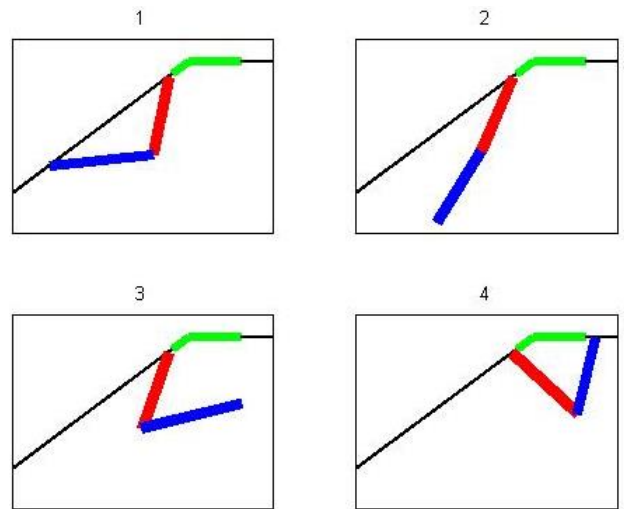


Figure 2: Jumper-to-cable swing manoeuvre

The parameters used for the simulation are presented in Table 1 and Table 2. The simulation results of the jumper-to-cable swing manoeuvre are also presented, where the jumper cable is inclined at 45° .

Table 1: Robot parameters

Link	Symbols (unit)				
	m_n (kg)	l_n (m)	l_{cn} (m)	I_n (kgm ²)	F_n (Nms)
n=1	5	1	0.5	1.67	0.1
n=2	5.2	1	0.5	1.73	0.1

Table 2: Motor parameters

Motor Parameters (unit)					
V (V)	N	R (Ohm)	k_M (mNm/A)	k_M (rpm/V)	η
24	51	0.341	13.5	705	0.7

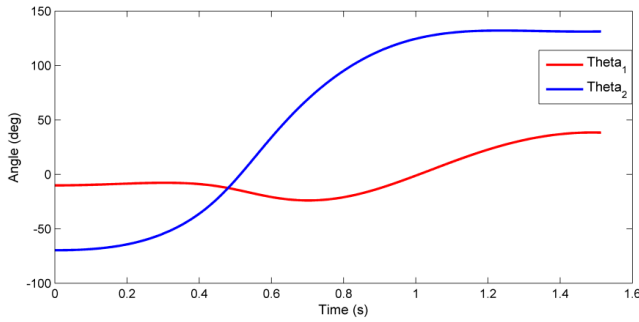


Figure 3: Trajectory of robot links

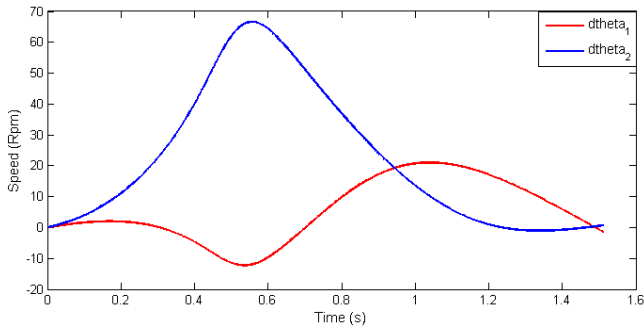


Figure 4: Speed of robot links

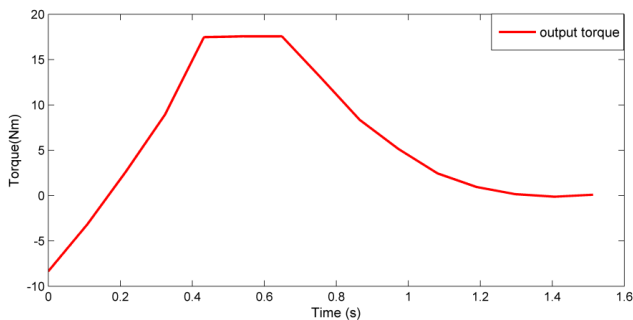


Figure 5: Torque output

4. MECHANICAL CONFIGURATION DESIGN

The mechanical configuration represents the way in which the major components namely, the arms, payload and grippers connect together. This has a direct influence on the way the robot achieves brachiation.

An optimal configuration is one which achieves brachiation but minimizes the associated mechanical and control complexities.

In [4] critical design factors for selecting an optimal configuration were discussed. Based on these design factors, 3 configurations were considered, namely:

- 2-link configuration, payload split equally onto each link, fixed payload
- 2-link configuration, payload split equally onto each link, moveable payload
- 3-link configuration, payload on central link, moveable payload

These configurations were simulated in various brachiation scenarios in order to assess their feasibility and allow for comparison between configurations.

Based on the simulation results and weighing up mechanical and control complexities, a 2-link fixed payload configuration is selected. This configuration offers the most simplistic and robust design, which is crucial for an industrial-level robotic platform.

4.1 Link actuation

In [4] two link actuation schemes are discussed, a traditional link actuation scheme and an energy storage scheme.

Traditional link actuation schemes offer mechanical simplicity and robustness, but suffer from higher power requirements. Conversely, energy storage schemes offer lower power requirements but are more mechanically complex and hence less robust.

A traditional link actuation scheme, shown in Figure 6, is selected as it ensures robustness and simplicity which is favoured above all else.

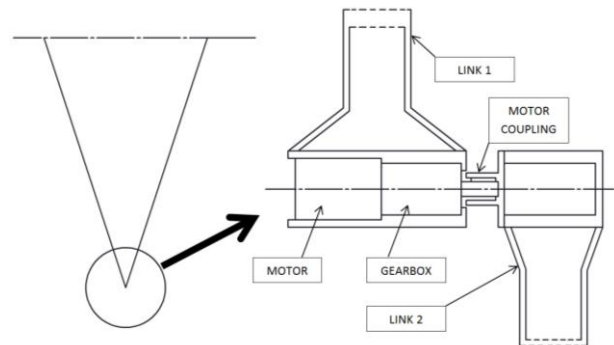


Figure 6: Schematic diagram of link actuation mechanism

5. GRIPPER DESIGN

The mechanical design of the gripper is critical to the success of the robot as it has a number of functions, namely:

- Opening and closing around/above the line quickly and with sufficiently precise timing
- Gripping onto the line, actively through a gripping mechanism or passively via friction between the gripper and line
- A drive mechanism for traversing the line
- A wrist mechanism, which allows the robot to perform out-of-plane manoeuvres

The initial gripper design was presented in [4] and is shown in Figure 7. The design of the gripper is simple, robust and light-weight. Details of the mechanical structure, drive mechanism and pulley design can be found in [4]. Although we present a design development below, it is instructive to note that in the initial design shown, the gripper arms and gears are attached to a common shaft and actuated by a motor via a pinion gear. Half-pulley profiles are attached to the ends of each gripper arm which form a wheel once the gripper is closed. A motor is attached to one of the half-pulleys to allow the robot to drive along the line.



Figure 7: Solidworks render of initial gripper design

5.1 Swinging on an incline

Swinging on a slope presents a challenging problem as a large actuation torque is required. Additionally, slipping, of the gripper attached to the line, while swinging is also a potential problem. If the gripper slips while swinging, the robot will slide down the incline and fail to brachiate successfully. This is especially the case for the gripper design presented in [4] as it relies on the friction between the pulleys and the line to avoid slipping while on a slope.

In order to determine whether the robot will slip, the dynamic reaction forces exerted on the gripper during a jumper-to-cable swing are analysed. By imposing constraints on the movement of the gripper in the Euler-Lagrange dynamic model, the attached gripper can be modelled as a pin joint and the dynamic reaction forces analysed as shown in Figure 8.

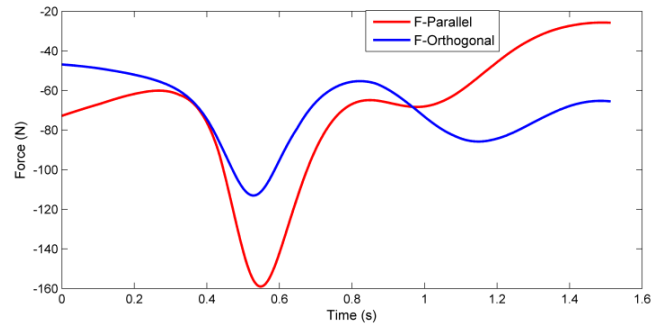


Figure 8: Reaction forces exerted on robot during jumper-to-cable swing

The frictional force acting against the force parallel to the slope can be defined as:

$$F_{fric} = F_{orthogonal} f_s, \quad (13)$$

where $F_{orthogonal}$ is the force acting orthogonal to slope cause by the weight of the robot and f_s is the static coefficient of friction between the gripper pulley and the line.

In Figure 9 the robot is simulated performing a jumper-to-cable swing manoeuvre with different friction coefficients to determine the minimum coefficient required to prevent sliding.

From Figure 9 it can be seen that a minimum friction coefficient of 1.6 is required to prevent the robot from sliding while brachiating on an incline.

Based on the simulation results, the robot will slip since the friction coefficient between the half-pulleys (aluminium) and the line (aluminium) is 1 [6] and a coefficient of 1.6 is required.

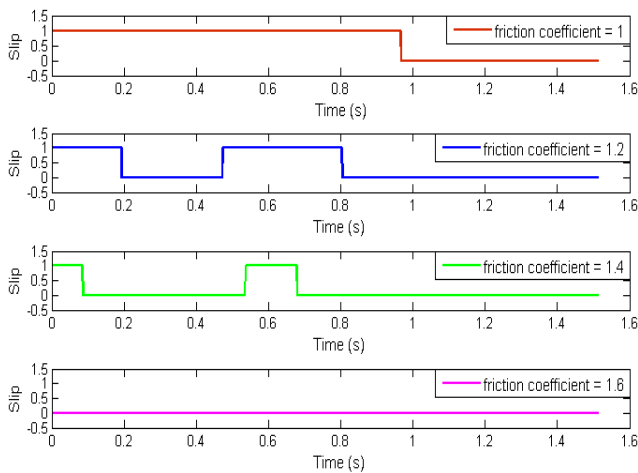


Figure 9: Slip conditions with various friction coefficients, where a 1 represents slip and 0 no slip

In order to prevent sliding, the gripper pulleys can be lagged (covered) with conductive rubber. The conductive rubber ensures that the robot remains at the line potential and also increases the friction coefficient between the pulley and the line.

The friction coefficient between the rubber and aluminium line is dependent on the surface roughness of the line and the surface free energy of the rubber. An increase in surface free energy of the rubber or surface roughness will result in an increase in the friction coefficient.

In [7] the kinetic friction coefficient between rubber and aluminium was found to range between 2 – 4.5, depending on the surface free energy of the rubber. The static coefficient of friction is usually greater than, or at least equal to, the kinetic friction coefficient. Therefore covering the pulleys with rubber will prevent the robot from sliding while brachiating on an incline as the friction coefficient is greater than the minimum required coefficient.

5.2 Re-designed gripper

A new gripper concept has been developed, shown in Figure 10.

The gripper is based on a 4-bar mechanism similar to the mechanism used in a vice grip. It allows the robot to drive along the line as well as actively grip onto the line. This offers the advantage of being able to use the pulley drive motor to assist in brachiation. In addition, by actively gripping onto the line the robot can perform an “inch-worm” manoeuvre [8] to navigate steep slopes that it would ordinarily not have been able to traverse.

The gripper arms are attached to gears which are driven by a worm, which is not back-driveable. This ensures that the gripper remains closed while performing a brachiation manoeuvre.

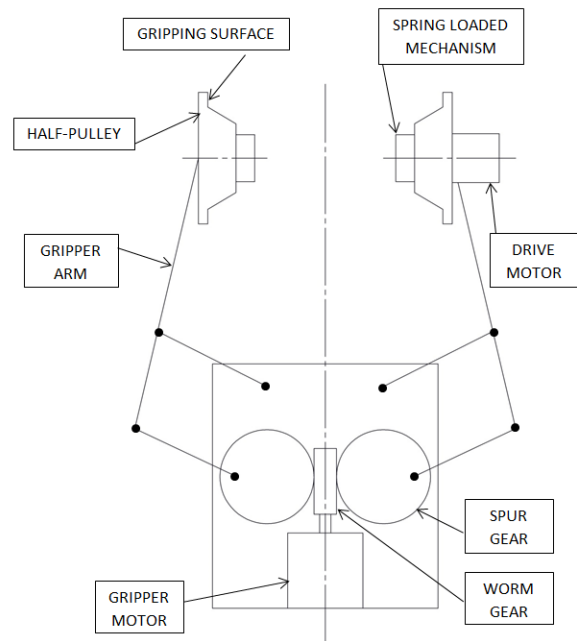


Figure 10: Schematic design of gripper mechanism

A spring-loaded mechanism is used to transmit torque between the two half-pulleys. This ensures that the maximum tractive force is achieved, which is essential for traversing steep slopes, such as on jumper cables.

The transmission of torque between the half-pulleys can be done via interlocking ends of the spring-loaded mechanism or by friction between the two ends of the mechanism.

6. CONCLUSION

This paper presented further work towards the development of a brachiating robot for power line inspection. A constrained Lagrange model was developed to simulate swinging on slopes and to analyse reaction forces during swings. Simulation results from a jumper-to-cable swing manoeuvre were presented and analysed. This provided insight into mechanical design of the robot configuration and its gripper.

Future work for this research project includes 3D-modelling of the gripper and mechanical configuration, and development of a minimum energy control scheme using a robust controller.

7. REFERENCES

- [1] P. Debenest, M. Guarnieri, K. Takita, E. Fukushima, S. Hirose, K. Tamura, A. Kimura, H. Kubokawa, N. Iwama and F. Shiga, “Expliner - Robot for Inspection of Transmission Lines,” *IEEE International Conference on Robotics and Automation*, 2008.

- [2] N. Pouliot and S. Montambault, "Geometric Design of the LineScout, a Teleoperated Robot for Power Line Inspection and Maintenance," *IEEE International Conference on Robotics and Automation*, 2008.
- [3] T. Lorimer, "The design and construction of a robotic platform for power line inspection," Cape Town, 2011.
- [4] J. Patel and E. Boje, "Brachiating Power Line Inspection Robot," *CARPI International Conference on Applied Robotics for the Power Line Industry*, 2014.
- [5] A. Meghdari, S. Lavasani, M. Norouzi and M. Mousavi, "Minimum control effort trajectory planning and tracking of the CEDRA brachiation robot," *Robotica*, 2013.
- [6] EngineeringToolBox, "The Engineering ToolBox," [Online]. Available: http://www.engineeringtoolbox.com/friction-coefficients-d_778.html. [Accessed November 2014].
- [7] B. Persson, "On the theory of rubber friction," *Surface Science*, 1997.
- [8] N. Morozovsky and T. Bewley, "SkySweeper: A Low DOF, Dynamic High Wire Robot," *IEEE/RSJ International Conference on Intelligent Robots and Systems (IROS)*, 2013.

8. ACKNOWLEDGMENTS

This work was supported in part by the South African National Research Foundation and the Eskom Tertiary Education Support Programme. This support is gratefully acknowledged.

COMPUTER VISION FOR A POWER LINE INSPECTION ROBOT

B. Morarjee*, F. Nicolls* and E. Boje*

* University of Cape Town, Dept. of Electrical, Electronic and Computer Engineering, Rondebosch 7700, Email: bhavani.morarjee@gmail.com

Abstract: This paper reports on a study to provide a reliable, low-cost reconstruction of a 3D model of a transmission tower from 2D images. The model is intended for later use for object tracking and robotic localization. The tower is considered to be a wiry object and a 3D reconstruction method, based on state-of-the-art work, is investigated and successfully reproduced with modifications. The algorithm coded in this research is capable of reconstructing 3D models, from 2D images, up to scale. Reconstruction is based on using multiple images of the target, robust 2D line detectors, and pinhole camera models in order to triangulate corresponding lines into 3D hypotheses. These 3D hypotheses are subsequently scored and clustered to remove spurious lines. Finally, a wiry reconstruction is achieved which preserves the geometry of the wiry object and is more compact than point cloud representations.

Key words: 3D reconstruction, pin hole camera models, line segment detection, multi-view geometry.

1. INTRODUCTION

Image processing can be integrated into a multitude of scenarios, one of which is in the growing power sector in South Africa. South Africa has around 30 000 km of transmission-level lines, and internationally, there is more than a million km of lines at and above 220 kV. Risk, cost and reliability are among the reasons to look for ways of automating the inspection of the integrity and condition of transmission line components. Current inspections are performed manually by flying helicopters and fixed-wing aircraft over the lines, and by ground patrols. The maintenance task can be streamlined if attention is focussed on problematic equipment. In response, computer vision strategies for power line inspection are currently being studied for both aerial and line-based platforms. Examples of robots that are capable of live line inspection include PLIR [1] and the LineScout [6]. Image processing for these types of



Figure 1: Power Line Inspection Robot developed at UKZN [1].

platforms have mostly focused on processing information from 2D images. Most of the work is concentrated around what the robot is *expected* to see when placed on a transmission line. The problem of ambiguity, poor lighting, occlusion and other unforeseen circumstances in the outdoor environment makes it difficult to rely on 2D

information alone. The present work aims to construct a 3D model of a transmission tower which can be used for localization by an inspection platform as the first step in high resolution inspection tasks. The model must be compact and encapsulate the geometry of the underlying structure.

2. LITERATURE REVIEW

To understand how computer vision and image processing tools for a power line application may be used, state-of-the-art research is acknowledged. These can be separated into two broad categories i.e. a) shape primitives (line, circles and ellipses) which are detected in images and are used to infer the presence of specific components – e.g. dampers and insulator strings [4], conductor cables [5] and spacers [3], and b) 3D models of objects acquired through laser scanners. The work of [1] used Sobel edge detection to parametrize image lines in order to suggest the presence of cable and damper-ends. The experiments in [1] revealed that the overall approach was vulnerable to lighting changes and occlusion, and broken image lines were detected. In [3], a two-step approach involved the use of image-filters to first locate conductor cables before attempting to detect spacers. However, the intrusion of background clutter was unavoidable and resulted in false positives.

For 3D modelling, Hydro-Québec has recently incorporated a LIDAR device on their robot, the LineScout [7]. The UTM-30LX device was selected for its detection range and price. Their goal is to equip the robot with this small scanner and detect objects in 3D. Experiments conducted in [8] showed that in order to detect splices, dampers and clamps, operational problems included waiting for the scanner to warm up.

Stand-alone point clouds of transmission towers also exist and are further examples of 3D models, but they are stored in files that often take up hundreds of megabytes

of disk space. They also require specialised software and hardware.

An interesting approach is to construct a 3D tower from 2D images. The tower is regarded as a ‘wiry’ object due to its lack of solid texture and the dense configuration of beams. This was exploited in [9], where a camera moved around a real transmission tower and 106 images were captured. Mathematical models of cameras (for each of the images), called pinhole camera models, were obtained using automated tools. This resulted in camera models which did not cater for scale and therefore scale had to be known *a priori*. Thereafter, between image-pairs, lines were then detected using a robust line segment detector (LSD) [11] and triangulated into 3D. These 3D lines (or hypotheses) were scored in order to remove spurious lines, and the final phase of the algorithm, the clustering phase, ensured that the reconstructed tower had representative line segments that preserved scale and angles. In the present work, 3D models are shown to be reconstructed from images using the approach followed in [9]. Changes made in the experiment work are explained.

3. PROJECTIVE GEOMETRY

To perform the 3D reconstructions from 2D images, first the pinhole camera model needs to be understood. This mathematical model is made up of camera intrinsics (\mathbf{K}) and extrinsics (\mathbf{R} and \mathbf{t}). The intrinsics (internal

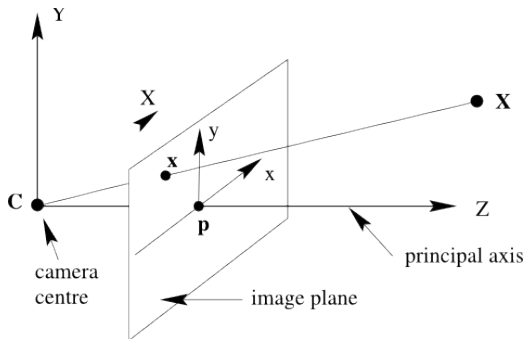


Figure 2: Conceptual 3D-2D projection [12].

parameters) describe attributes such as focal length and optical centre, thus describing how a 3D point is projected onto a 2D image plane, as shown in Figure 2. These quantities are represented in a matrix as:

$$\mathbf{K} = \begin{bmatrix} f & & p_x \\ & f & p_y \\ & & 1 \end{bmatrix}. \quad (1)$$

Extrinsic parameters describe the pose (3×3 rotation matrix \mathbf{R}) and position (3×1 translation vector \mathbf{t}) of the camera sensor. Combining both intrinsic and extrinsic parameters, the pinhole camera model (3×4 matrix, \mathbf{P}) may be denoted as

$$\mathbf{P} = \mathbf{K}[\mathbf{R} | \mathbf{t}] \quad (2)$$

where intrinsic parameters may be found by performing standard calibration. In this work, extrinsic parameters are found by manually establishing point correspondences in different views. This was to alleviate the need for scale correction after reconstruction. Ultimately, a (homogeneous) point in 3D, e.g. $\mathbf{X} = [X, Y, Z, 1]^T$ in Figure 2 which is a 4×1 vector, may be mapped to its image equivalent, $\mathbf{x} = [x, y, w]$ – also homogeneous – as:

$$\mathbf{x} = \mathbf{P}\mathbf{X}. \quad (3)$$

Homogeneous coordinates are used so that a linear formulation of the projections may be used.

3.1 Multi-view geometry

Understanding of one camera may be extended to the scenario where different cameras observe the same object from different positions. Note that this is equivalent to a single camera taking pictures at different locations around the target. The principles of *epipolar* geometry relates these cameras. An illustration of this concept is shown in Figure 3 for two cameras, where a crucial observation is that P3D points \mathbf{X} , \mathbf{X}_1 and \mathbf{X}_2 project to the same image point, \mathbf{x} , in the left image plane, but to a line l' in the right image. Line l' is the *image* of the line-of-sight that exists between the left camera and 3D point \mathbf{X} . The fact

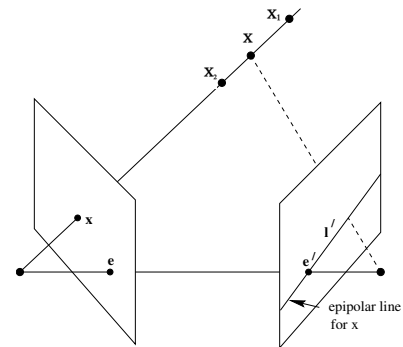


Figure 3: A visualization depicting how two cameras view the same point [12].

that epipolar geometry maps points to lines, allows for corresponding points (across different images) to have a 1D search space (line l') and not a 2D one (the entire image plane). This is exploited in the hypothesis-generation phase (Section 4.1) of the reconstruction scheme pursued by [9] and this work.

4. LINE RECONSTRUCTION

The method of reconstructing a wiry model, as presented in [9], is reproduced here. The three phases — hypothesis generation, scoring and clustering, are presented with modifications. Changes are made based on computational runtime and in an effort to understand the nature of the algorithm.

4.1 Hypothesis Generation

For line detection, the line segment detector was used as it was more robust than the Hough transform. Figure 4 shows a comparison between the two line detection schemes. Even though some lines are not detected by the LSD algorithm, there are fewer spurious lines produced than the Hough transform. The output of the LSD algorithm are

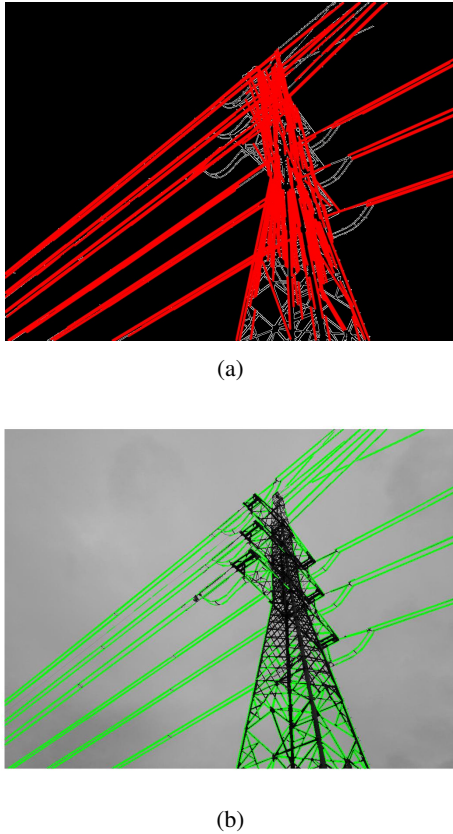


Figure 4: Hough (4a) vs LSD (4b) on a tower image provided by [2].

line-endpoints. Consider a pair of images, I_i and I_j , in Figure 5 and a single, detected line l_i . The two epipolar lines (green) are generated in image I_j thanks to the knowledge of I_j 's pinhole camera model. A corresponding line in image I_j would ideally start and end between the epipolar lines. The LSD algorithm is also applied to image I_j and all lines between the green epipolar lines are accepted as possible matches for line l_i . In this case, the two blue candidates will each be triangulated to form 3D hypotheses. If a line, l_i , proposed by the LSD in image I_i , has k candidate matches in image I_j , k pairs of endpoints are triangulated into 3D. At most, the candidate set contains one correct solution but it is possible that all candidate lines are false positives. This process is repeated for every line the LSD finds in image I_i and subsequently, every image. At this point, the algorithm cannot discriminate between good and false candidates. After processing all lines in all images, the scoring process is applied to the set of 3D hypotheses, $\{S\}$.

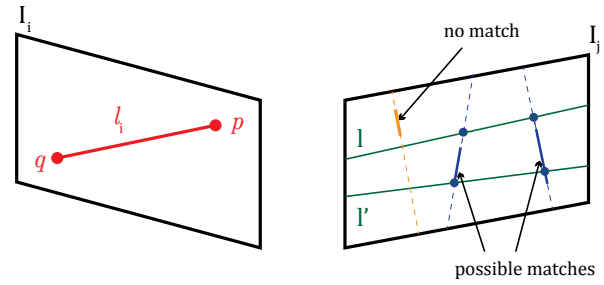


Figure 5: An illustration to show line matching is performed [9].

4.2 Scoring

Scoring aims to quantify how meaningful each of the 3D candidate lines are. Neighbouring views of a valid line segment on a wiry object should be similarly visible (but not identical), and adhere to the pinhole camera models at those locations i.e. obey Equation. 3. In contrast, spurious, unwanted lines would not be consistent with projections by pinhole camera models at the varying locations around the target. To formulate this concept, the scoring measure relies on the construction of image neighbourhoods, where each neighbourhood, N_i , consists of a fixed number of frames (or cameras) that are close to each other — within d_c metres — and have similar lines-of-sights i.e. within d_{ang} degrees. For each image neighbour (in a given neighbourhood) the set of 3D hypotheses, $\{S\}$, are reprojected onto this image. The scoring process makes use of line-pixel intensities, which is why image gradients are used. The boundaries of wiry objects are prominent. Candidate L_m is scored as proposed by [9],

$$s(L_m) = \frac{1}{|N(I_i)|} \sum_{I \in N(I_i)} \sum_{\mathbf{x} \in \mathbf{M}(I)} \frac{\|\nabla I(\mathbf{x})\|}{|M(I)|} e^{-\left(\frac{\lambda \cdot \text{dist}(\mathbf{x}, L_m)}{2 \cdot \text{dist}_{\max}(L_m)}\right)^2} \quad (4)$$

where $\|\nabla I(\mathbf{x})\|$ is the pixel's image gradient (magnitude), M is measurement pixels, and N_i is the neighbourhood. The $e^{-\left(\frac{\lambda \cdot \text{dist}(\mathbf{x}, L_m)}{2 \cdot \text{dist}_{\max}(L_m)}\right)^2}$ term places more weight on measurement pixels closer to the reprojected line. This weighting scheme is done because of the Gaussian-like roll-off of e^{-x^2} which weights far pixels smoothly. (If these calculations are onerous, a reasonable approximation near e^{-x^2} — for small x — is $(1+x)(1-x)$ and this be used in parallel computing strategies).

In Figure 6, L_m will receive a high score from this image neighbour since there is significant overlap between the reprojected line and the underlying image gradient. Measurement pixels, M , are used to measure the amount of overlap. Figure 6 shows red measurement pixels and the reprojected version of L_m (blue), with underlying image gradient content. Finally, the overall score for candidate L_m is averaged over all other neighbours and eventually, all other neighbourhoods. Scores of hypotheses

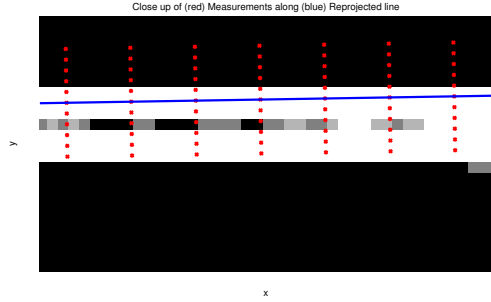


Figure 6: In this example, L_m projects well onto the image gradient.

are independent of each other. An outline of the scoring process is provided in Algorithm 1. Furthermore, if a

Algorithm 1 Iterative scoring

```

1: procedure SCORING( $\{S\}$ )           ▷ Read hypotheses
2:   for <Each Neighbourhood  $i$ > do
3:     for <Each Neighbour  $n$ > do
4:        $pts2D \leftarrow 3D - 2D$  projections of  $\{S\}$ 
5:       for <Each hypotheses  $L_m$ > do
6:          $Gmag \leftarrow$  image gradient of  $n$ 
7:          $score(L_m) \leftarrow score(L_m) +$  update
8:       end for
9:     end for
10:  end for
11:  return  $score$            ▷ vector of cumulative scores
12: end procedure

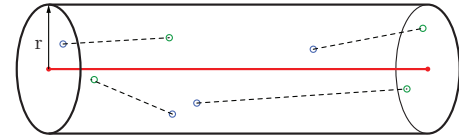
```

line segment is occluded, the score does not update until the line segment comes into view again. Due to the iterative nature of the algorithm (consultation of every neighbourhood), the scoring phase is extremely slow. MATLAB was chosen to facilitate the understanding and development of the algorithm, but no optimization was implemented. Execution (scoring) of code i.e. processing 18000 lines took 5 hours on a i7 16GB Machine.

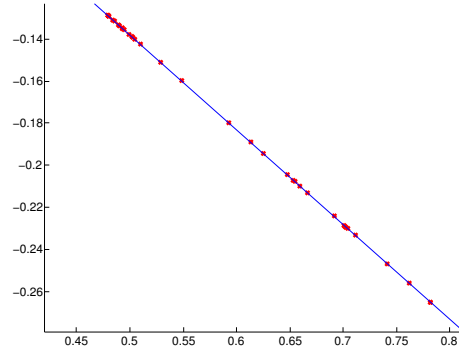
4.3 Clustering

After scoring all lines, representative line segments are required. In order to minimise repeated line segments, and filter out noisy lines, clustering is performed on scored candidates. Starting with the highest scoring line, line L_m is extended by 10% on either side and forms the principal axis for a cylinder with radius r . All other line segments are checked to see if their endpoints fall within this cylindrical volume. If there are at least H_{min} line segments in the cylinder, this volume is a successful cluster (see Figure 7a). All lines that were accepted are removed from the list of candidates so that they do not form nuclei of cylinders themselves. If the number of lines does not meet the minimum requirement, L_m is discarded. This process is repeated for all scored lines.

After establishing successful clusters, each cluster is generalised so as to have a single line segment with length



(a) A cluster with all endpoints.



(b) All endpoints projected onto the direction vector. Length spanned by two-outermost points.

Figure 7: All lines accepted in a particular cylinder collapse onto a final line segment.

and direction. It is the aggregated line segments that make up the end reconstruction. To further illustrate how a successful cluster is generalised into one line segment, consider the set of endpoints $\{S_m\}$ in a 3D cylinder. By performing a singular value decomposition on the endpoints, the largest eigenvalue corresponds to an important eigenvector, the direction of this model line segment. Subsequently, all endpoints in the cylinder are projected onto this vector, and the two outermost points determine the length of the model line segment (Figure 7b). This process is repeated for all successful clusters.

5. EXPERIMENTS AND RESULTS

5.1 Lab test on simple polygons

To test the reconstruction approach outlined above, 100 images of simple wiry polygons were taken in an indoor environment. In Figure 8, the area within the red square

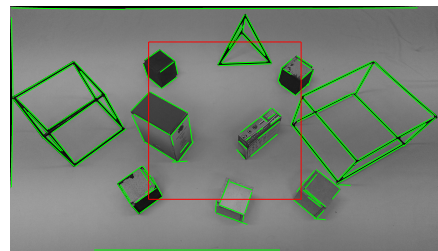
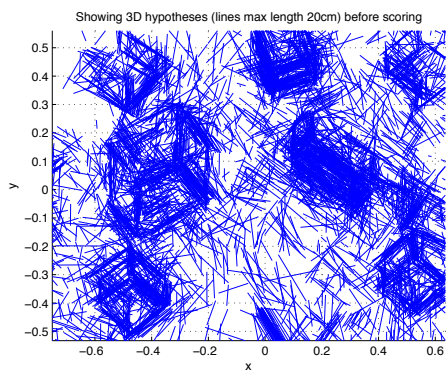


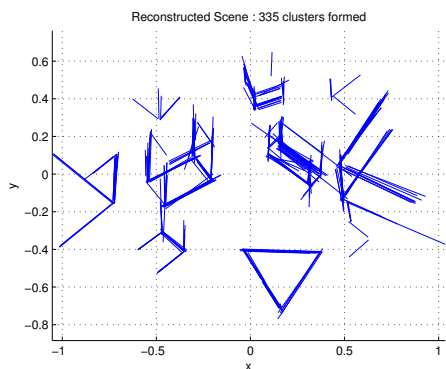
Figure 8: Green lines are detected by the Line Segment Detector algorithm.

was calibrated (to find the internal parameters of the

pinhole camera model). Thereafter a single camera was moved in a circular trajectory, and for each of the frames a pinhole camera model was devised. The camera matrices were refined via bundle adjustment, so as to provide a best joint-estimate for the set of cameras. This step deviated from the way camera models are estimated in [9]. The approach followed in this work meant that it was more tedious to estimate camera models, but scale was accounted for in the final reconstruction i.e. no known marker had to be accounted for. After establishing camera models in this way, the algorithm proposed by [9] was implemented and this allowed for comparison between physical and virtual bodies.



(a) After creating 3D hypotheses.

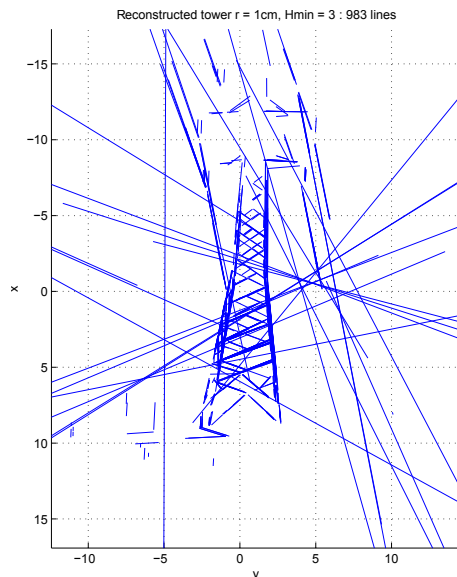


(b) After the clustering process in the algorithm, the final reconstructed scene is shown.

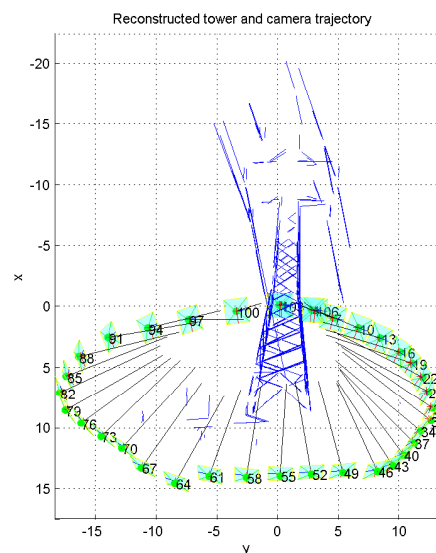
Figure 9: The total number of lines decreased from 1800 to 335.

For the experiment consisting of simple wiry polygons, r was set to 2.5 cm and H_{min} was set to 15. These values were selected by trial and error which indicates a downside to the method proposed by [9]. It was observed that the clustering parameters had an influence on the final reconstruction. Setting the cylinder radius, r , to a small value, while increasing H_{min} , decreased the number of spurious lines in the reconstruction, as these effects impose stricter criteria about which lines constitute a cluster. However, the final reconstruction preserves the scale and structure of the objects.

Having performed tests on simple objects, the same code was applied to a dataset provided by [10], that consisted of 106 images and the associated 106 pinhole camera models. From 106 images, 524700 hypotheses in 3D were formed. Scoring was deliberately performed on one neighbourhood because of how slow the scoring process was. Both the reconstructed tower and cameras are shown in Figure 10b. From 524700 hypotheses, 983 lines were



(a) A result resembling the tower obtained in [9] but with spurious lines.



(b) Reconstruction after using one neighbourhood.

Figure 10: Even after scoring 1 neighbourhood, a tower can be visualized.

arrived at even though only one scoring neighbourhood was used. However, unwanted lines were also produced (Figure 10a). The tower has a height of approximately 30 m, thus conforming to the structure of a real tower.

6. PARAMETER SELECTION

This algorithm is severely dependent on a wide range of parameters that are fixed by trial and error. Parameters d_c and d_{ang} are not automatically derived while clustering parameters r and H_{min} are not adaptive. Increasing H_{min} and decreasing r indicates a strict requirement on the error-tolerance of 3D lines. These values depend on the context of the object, and to some extent, on how well the pinhole cameras are modelled. For the experiment consisting of simple polygons, the d_c parameter was set to 1 m and d_{ang} was 50°. For the reconstruction of a real transmission tower, d_c was set to 30 m and d_{ang} was 30°. The reconstruction itself is promising in its ability to encapsulate the underlying geometry of a wiry object. The changes between the work in [9] and this study is in the number of neighbours (for image neighbourhoods) and how camera models are arrived at. In [9], a neighbourhood of size 20 was used while experiments for this work used a neighbourhood consisting of 9 images.

7. CONCLUSION

The algorithm proposed by [9] is novel because it applies fundamental aspects of multi-view geometry to both propose and prune line-hypotheses. This method of reconstruction does not require expensive equipment such as laser scanners and specialised software, and the compact models arrived at are quantifiable and measurable. The reconstruction is formed from 2D images which can serve as records themselves. However, the shortcomings of this algorithm are based on the non-adaptive parameter selection (d_c , d_{ang} , r and H_{min}), as well as the slow runtime of the scoring phase, suggesting that this reconstruction is best performed offline. To set these parameters would require some manual intervention and a known context (expected size of the tower height, for example). The pinhole model must also be well estimated.

8. FUTURE WORK

Adaptive clustering parameters should be investigated to speed up (and automate) the model generation process. A more important objective, however, would be to use the final reconstruction of the tower (its 3D coordinates) in order to track the target, from 2D images, in real time. Doing this would allow the robot to determine its position and orientation (relative to the tower). This aspect of robot localization would be a primary step in visual inspection. This ability would allow a robot to search for a known target, rather than ‘blindly process image feeds in order to infer the presence of components. Subsequent to localization, the robot can zoom in on specific hardware in order to inspect for defects.

REFERENCES

- [1] T. Lorimer: “Masters Dissertation: The Design and Construction of a Robotic Platform for Power Line Inspection”, *University of KwaZulu-Natal*, 2011.
- [2] T. Lorimer: “Personal communication”, March 2013.
- [3] W.H. Li, A. Tajbakhsh, C. Rathbone and Y.Vashishtha: “Image processing to automate condition assessment of overhead line components”, *Proceedings: 1st International Conference on Applied Robotics for the Power Industry (CARPI)*, Montreal, pp. 1-6, 2010.
- [4] S. Fu, L. Weiming, Y. Zhang, Z. Liang, Z. Hou, and Tan, M. Tan, W. Ye, B. Lian and Q. Zuo: “Structure-constrained obstacles recognition for power transmission line inspection robot” *IEEE/RSJ International Conference on Intelligent Robots and Systems (IROS)*, Beijing, pp. 3363-3368, 2006
- [5] Q. Zuo, Z. Xie, Z. Guo and D. Sun: “The obstacle recognition approach for a power line inspection robot” *International Conference on Mechatronics and Automation (ICMA)*, Changchun, pp. 1757-1761, 2009
- [6] K. Toussaint, N. Pouliot and S. Montambault: “Transmission line maintenance robots capable of crossing obstacles: state of the art review and challenges ahead”, *Journal of Field Robotics*, Vol. 26 No. 5, pp. 477-499, 2009.
- [7] N. Pouliot, P. Richard and S. Montambault: “LineScout power line robot: Characterization of a UTM-30LX LIDAR system for obstacle detection” *Proceedings: IEEE/RSJ International Conference on Intelligent Robots and Systems (IROS)*, Vilamoura-Algarve, pp. 4327-4334, 2012.
- [8] P. Richard, N. Pouliot S. Montambault: “Introduction of a LIDAR-based obstacle detection system on the LineScout power line robot” *Proceedings: IEEE/ASME International Conference on Advanced Intelligent Mechatronics (AIM)*, France, pp. 1734-1740, 2014.
- [9] M. Hofer, A. Wendel and H. Bischof: “Line-based 3D reconstruction of wiry objects” *Proceedings: 18th Computer Vision Winter Workshop*, Hernstein, pp. 78-85, 2013.
- [10] M. Hofer: “Personal communication”, August 2013.
- [11] R. Gioi, J. Jakubowicz, J. Morel and G. Randall: “LSD: a Line Segment Detector” *Image Processing On Line*, Vol. 2, pp. 35-55, 2012.
- [12] R. Hartley and A. Zisserman: “Two View Geometry” *Multiple View Geometry in Computer Vision*, Cambridge University Press, UK, second edition, chapter 9, pp. 239-261, 2003.

DEMYSTIFYING INTERCONNECTION AND DAMPING ASSIGNMENT PASSIVITY-BASED CONTROL

P. J. Kruger* K. R. Uren* and G. van Schoor†

* School of Electrical, Electronic and Computer Engineering, North-West University, Potchefstroom Campus, South Africa E-mails: krugerpetrus@gmail.com and kenny.uren@nwu.ac.za

† Unit for Energy Systems, North-West University, Potchefstroom Campus, South Africa E-mail: george.vanschoor@nwu.ac.za

Abstract: Due to the vague description in the literature, the learning curve for Passivity-based control is particularly steep from an engineering perspective. In this article, the authors attempt to offer a layman's guide to Interconnection and Damping Assignment Passivity-based Control (IDA-PBC) that may ease the demystification of the technique for other researchers. Through thorough discussion, the application of this theory is demonstrated for a parallel RLC circuit and a magnetic levitation system. Both examples feature prominently within popular literature. This article is therefore meant to be a valuable companion guide to material on the subject of IDA-PBC. Simulation parameters and results are included for comparison by researchers who may be interested in duplicating the results. The simulation results for the RLC system show the quality of the controller as well the improved energy dissipation obtained by implementing the control. The MAGLEV system simulation shows how different response characteristics may be obtained with the free parameters in the control law.

Key words: IDA, PBC, examples, RLC, MAGLEV, nonlinear, control system.

1. INTRODUCTION

In the experience of the authors, the greatest challenge to Passivity-based control is the understanding and then reproducing of the controller design process. One reason for this challenge is the cryptic and sometimes mistaken description of certain critical steps within the calculation procedure as discussed in literature. Although many steps such as the solving of partial differential equations may seem relatively intuitive, the authors had spent much time understanding how the prominent researchers of IDA-PBC have worked toward the mathematical steps that were just briefly noted within articles. The authors also found it necessary to cross-reference between several articles before certain steps were completely understood. Motivated by this challenging experience with the understanding of the IDA-PBC technique, the authors have made it their goal to write a companion guide to material on the subject of IDA-PBC. It is expected that this material will be especially valuable to engineers who do not have the extensive experience with the application of partial differential equation solutions for control problems.

One of the primary reasons for the interest of the authors in this technique is its ability to control nonlinear systems. PBC is in fact known to simplify the controller development strategy. Ortega *et al.* [1] state that monolithic theory for the nonlinear control problem is simply too difficult for the vast and varied array of nonlinear systems. Passivity-based control has at least served for some form of unification for nonlinear control theory of passive systems. A vast array of systems have been controlled with Passivity-based control [1,2]. Control of these varied systems may at least be approached with a similar set of effective tools.

PBC also allows the designer to do the modelling and control from a framework that is commonly understood over various disciplines of engineering. Ortega and Van der Schaft [2] called energy concepts the “*lingua franca*” among various engineering disciplines. According to [2] and [3], the design of controllers become more intuitive when viewed from an energy-shaping perspective, which allows one to move away from approaching controllers as signal processors. In some cases, it can be beneficial to see how the controller effects the stability of the system when viewed as an energy-transforming system [2, 4]. The benefits of approaching the controller design from the energy system perspective over the energy processing perspective is elaborated upon in [2].

2. BASIC THEORY

2.1 Preliminary assumptions and recommendations

Since this article focuses on the applications of IDA-PBC rather than the mathematical proof of the technique, stability proofs are not included within this article. However, a concerted effort was made to include all the practical computations necessary to understand the application of IDA-PBC to control problems. While an understanding of the basic state-space representations of systems and the computation of partial derivatives are assumed, the reader does not require any prior experience in the solution of PDEs. Neither is an understanding of Hamiltonian mechanics required. An effort was made to discuss all the practical theory within the sections below. Researchers who are interested in additional properties and proofs for this technique are encouraged to study [2, 5, 6].

Both the RLC circuit example and the MAGLEV example are discussed within [2], albeit not with simulation results. The article does offer additional insight into theory that

could not be discussed within this article due to space constraints. Readers are also recommended to study the work in [7] for clear discussions and excellent examples.

2.2 Port-Hamiltonian representation

IDA-PBC is based upon the port-Hamiltonian representation of systems. This is simply an alternative representation of the a linear or non-linear state-space system as given by:

$$\dot{\mathbf{x}} = \mathbf{F}(\mathbf{x}) + \mathbf{G}(\mathbf{x})\mathbf{u}. \quad (1)$$

Instead, the equations of motion are described by:

$$\dot{\mathbf{x}} = [\mathbf{J}(\mathbf{x}) - \mathbf{R}(\mathbf{x})] \frac{\partial H}{\partial \mathbf{x}}(\mathbf{x}) + \mathbf{g}(\mathbf{x})\mathbf{u} \quad (2)$$

where:

\mathbf{x} is the state vector.

$\mathbf{J}(\mathbf{x})$ is called the interconnection matrix used to indicate the interconnection between states; it is typically composed of the terms -1 , 0 or 1 .

$\mathbf{R}(\mathbf{x})$ represents the damping matrix and includes all the dissipation terms, usually in the form of resistances or damping constants.

$\frac{\partial H}{\partial \mathbf{x}}(\mathbf{x})$ is the gradient of the Hamiltonian function. The Hamiltonian function is composed of the sum of the energies of the system.

$\mathbf{g}(\mathbf{x})$ is the regular input gain matrix.

\mathbf{u} is the regular input matrix.

The simplest way to understand the port-Hamiltonian representation of a system is to review an example of system modelled in this form. Readers are encouraged to study the modelling of the RLC circuit example in section 3 for a concise description that represents the intuitive nature of this representation.

2.3 IDA-PBC matching equations

As a preliminary, it is necessary to define the concept of the left annihilator and the Moore-Penrose inverse of the term $\mathbf{g}(\mathbf{x})$. The left annihilator $\mathbf{g}(\mathbf{x})^\dagger$ of $\mathbf{g}(\mathbf{x})$ is the solution to the equality $\mathbf{g}(\mathbf{x})^\dagger \mathbf{g}(\mathbf{x}) = \mathbf{0}$. $\mathbf{g}(\mathbf{x})^\dagger$ is not necessarily uniquely determined by $\mathbf{g}(\mathbf{x})$. This is illustrated in the two examples below. Suppose that $\mathbf{g}(\mathbf{x}) = [0 \ 0 \ 1]^T$, then:

$$\mathbf{g}(\mathbf{x})^\dagger \mathbf{g}(\mathbf{x}) = [0 \ 1 \ 0] \mathbf{g}(\mathbf{x}) = \mathbf{0}, \text{ and}$$

$$\mathbf{g}(\mathbf{x})^\dagger \mathbf{g}(\mathbf{x}) = [1 \ 1 \ 0] \mathbf{g}(\mathbf{x}) = \mathbf{0}.$$

Generally, to solve the matching equations defined below, the inverse of $\mathbf{g}(\mathbf{x})$ is required. However, $\mathbf{g}(\mathbf{x})$ is rarely a square matrix, and therefore a different form of the inverse is used. The Moore-Penrose inverse given by $[\mathbf{g}(\mathbf{x})^T \mathbf{g}(\mathbf{x})]^{-1} \mathbf{g}(\mathbf{x})^T$ is selected throughout [3, 5] and [6].

The objective of the matching equations of IDA-PBC is to add control terms in the form of $\beta(\mathbf{x})$ to the system

given by (2) so that the integrated system demonstrates new behaviour. This objective is stated in:

$$[\mathbf{J}(\mathbf{x}) - \mathbf{R}(\mathbf{x})] \frac{\partial H}{\partial \mathbf{x}}(\mathbf{x}) + \mathbf{g}(\mathbf{x})\beta(\mathbf{x}) = [\mathbf{J}_d(\mathbf{x}) - \mathbf{R}_d(\mathbf{x})] \frac{\partial H_d}{\partial \mathbf{x}}(\mathbf{x}). \quad (3)$$

The desired forms of the terms on the right side of the above equation serve to assign specific qualities to the interconnection and damping structures. Also, the desired Hamiltonian should have at least an isolated local minimum at the desired equilibrium point \mathbf{x}_* [2, 5, 7]. In order to alter the Hamiltonian of the system from $H(\mathbf{x})$ to $H_d(\mathbf{x})$ an additional function $H_a(\mathbf{x})$ is added to $H(\mathbf{x})$. Therefore, $H_d(\mathbf{x}) \triangleq H(\mathbf{x}) + H_a(\mathbf{x})$. One may substitute $\mathbf{J}_d(\mathbf{x}) \triangleq \mathbf{J}(\mathbf{x})$ and $\mathbf{R}_d(\mathbf{x}) \triangleq \mathbf{R}(\mathbf{x})$ into (3), such that:

$$[\mathbf{J}(\mathbf{x}) - \mathbf{R}(\mathbf{x})] \frac{\partial H}{\partial \mathbf{x}}(\mathbf{x}) + \mathbf{g}(\mathbf{x})\beta(\mathbf{x}) = [\mathbf{J}(\mathbf{x}) - \mathbf{R}(\mathbf{x})] \frac{\partial H}{\partial \mathbf{x}}(\mathbf{x}) + [\mathbf{J}(\mathbf{x}) - \mathbf{R}(\mathbf{x})] \frac{\partial H_a}{\partial \mathbf{x}}(\mathbf{x}), \quad (4)$$

The terms $[\mathbf{J}(\mathbf{x}) - \mathbf{R}(\mathbf{x})] \frac{\partial H}{\partial \mathbf{x}}(\mathbf{x})$ cancel, such that:

$$\mathbf{g}(\mathbf{x})\beta(\mathbf{x}) = [\mathbf{J}(\mathbf{x}) - \mathbf{R}(\mathbf{x})] \frac{\partial H_a}{\partial \mathbf{x}}(\mathbf{x}). \quad (5)$$

This is precisely the PDE that [2] posed to solve for $\beta(\mathbf{x})$. However, being able to select $\mathbf{J}_d(\mathbf{x}) \neq \mathbf{J}(\mathbf{x})$ and $\mathbf{R}_d(\mathbf{x}) \neq \mathbf{R}(\mathbf{x})$ allows for additional degrees of freedom when solving for $\beta(\mathbf{x})$. Indeed, the MAGLEV example from [2] illustrates that in some cases, the unmodified interconnection matrix will cause the controller to be unstable. The energy-shaping objective is not altered if one were to set $\mathbf{J}_d(\mathbf{x}) \neq \mathbf{J}(\mathbf{x})$ and $\mathbf{R}_d(\mathbf{x}) \neq \mathbf{R}(\mathbf{x})$. If one sets $\mathbf{J}_d(\mathbf{x}) \triangleq \mathbf{J}(\mathbf{x}) + \mathbf{J}_a(\mathbf{x})$ and $\mathbf{R}_d(\mathbf{x}) \triangleq \mathbf{R}(\mathbf{x}) + \mathbf{R}_a(\mathbf{x})$, then (3) may be simplified as given by (6).

$$[\mathbf{J}(\mathbf{x}) - \mathbf{R}(\mathbf{x})] \frac{\partial H}{\partial \mathbf{x}}(\mathbf{x}) + \mathbf{g}(\mathbf{x})\beta(\mathbf{x}) = [\mathbf{J}(\mathbf{x}) + \mathbf{J}_a(\mathbf{x}) - \mathbf{R}(\mathbf{x}) - \mathbf{R}_a(\mathbf{x})] \frac{\partial H_d}{\partial \mathbf{x}}(\mathbf{x}),$$

$$[\mathbf{J}(\mathbf{x}) - \mathbf{R}(\mathbf{x})] \frac{\partial H}{\partial \mathbf{x}}(\mathbf{x}) + \mathbf{g}(\mathbf{x})\beta(\mathbf{x}) = [\mathbf{J}(\mathbf{x}) + \mathbf{J}_a(\mathbf{x}) - \mathbf{R}(\mathbf{x}) - \mathbf{R}_a(\mathbf{x})] \left[\frac{\partial H}{\partial \mathbf{x}}(\mathbf{x}) + \frac{\partial H_a}{\partial \mathbf{x}}(\mathbf{x}) \right],$$

$$\mathbf{g}(\mathbf{x})\beta(\mathbf{x}) - [\mathbf{J}_a(\mathbf{x}) - \mathbf{R}_a(\mathbf{x})] \frac{\partial H}{\partial \mathbf{x}}(\mathbf{x}) = [\mathbf{J}(\mathbf{x}) + \mathbf{J}_a(\mathbf{x}) - \mathbf{R}(\mathbf{x}) - \mathbf{R}_a(\mathbf{x})] \frac{\partial H_a}{\partial \mathbf{x}}(\mathbf{x}). \quad (6)$$

With appropriate $\mathbf{J}_a(\mathbf{x})$, $\mathbf{R}_a(\mathbf{x})$ and $H_a(\mathbf{x})$ terms, one is able to solve for the control law $\mathbf{u} = \beta(\mathbf{x})$. These three free parameters are calculated from the definitions for $\mathbf{J}_d(\mathbf{x})$, $\mathbf{R}_d(\mathbf{x})$ and $H_d(\mathbf{x})$. One can conclude that one needs to understand how to select the desired matrices to design an

IDA-PBC with this technique.

2.4 Alternative form of matching equations

Dorfler *et al.* [7] make use of (3) together with the left-annihilator and Moore-Penrose inverse defined earlier to derive two alternative matching equations as defined in (7) and (8). These are included for the reader's reference, though they are not applied within this article.

$$g^\dagger(\mathbf{x})[\mathbf{J}(\mathbf{x}) - \mathbf{R}(\mathbf{x})] \frac{\partial H}{\partial \mathbf{x}}(\mathbf{x}) = g^\dagger(\mathbf{x})[\mathbf{J}_d(\mathbf{x}) - \mathbf{R}_d(\mathbf{x})] \frac{\partial H_d}{\partial \mathbf{x}}(\mathbf{x}) \quad (7)$$

$$\beta(\mathbf{x}) = \mathbf{g}^{-1}(\mathbf{x}) \left([\mathbf{J}_d(\mathbf{x}) - \mathbf{R}_d(\mathbf{x})] \frac{\partial H_d}{\partial \mathbf{x}}(\mathbf{x}) \right) - \mathbf{g}^{-1} \left([\mathbf{J}(\mathbf{x}) - \mathbf{R}(\mathbf{x})] \frac{\partial H}{\partial \mathbf{x}}(\mathbf{x}) \right) \quad (8)$$

2.5 Solving of the partial differential equations

The most complex task of the IDA-PBC design is to obtain an appropriate solution of $H_d(\mathbf{x})$ for the matching equations. The use of computational tools such as MapleTM greatly ease this process, but in many cases, MapleTM includes an arbitrary differential function $\mathcal{F}(z)$ in the solution. Here z is a combination of several states. Any function of z will be sufficient as long as it is differentiable. However, very few functions will satisfy the additional requirements posed by the IDA-PBC technique.

In order to enforce passivity, IDA-PBC also requires that $H_d(\mathbf{x})$ has at least a local minimum, and preferably a global minimum, at the desired equilibrium point \mathbf{x}_* . Therefore, $\mathcal{F}(z)$ should be selected such that $\frac{\partial H_d}{\partial \mathbf{x}}(\mathbf{x}_*) = \mathbf{0}$ is satisfied. The examples within this article will clearly illustrate how these conditions are met for the controller design. One final comment about $\mathcal{F}(z)$ is necessary. Generally, the function $\mathcal{F}(z)$ will be in one of two forms [7]:

$$\mathcal{F}(z) = -\frac{K_p}{2}(z - z_d)^2 + \phi \quad \text{or} \quad \mathcal{F}(z) = K_p(z - z_d \ln z) + \phi. \quad (9)$$

Here, z_d has the same form as z , but instead of the states, z_d incorporates the desired value for each respective state. ϕ represents the additional terms necessary to ensure that $\frac{\partial H_d}{\partial \mathbf{x}}(\mathbf{x}_*) = \mathbf{0}$. The squared and \ln forms are chosen specifically because they both have global minimums. The proportional constant K_p offers an additional degree of freedom. The z_d term provides the reference term necessary to force the minimum of $H_d(\mathbf{x})$ to occur at \mathbf{x}_* .

The final step in the design procedure is to write out the control law. The nature of the matrix $\mathbf{g}(\mathbf{x})$ from (2) introduces both zero and nonzero gain factors that are multiplied with the system input. For this reason, (5) will produce both homogeneous and nonhomogeneous matching equations. The nonhomogeneous matching equation will be used to solve for the control input $\beta(\mathbf{x})$

while the homogeneous equations are used to determine the arbitrary differential function $\mathcal{F}(z)$. This will once again be illustrated best within the examples below.

2.6 General Algorithm

The general procedure for IDA-PBC design may now be summarised. Assuming that the system model is already in port-Hamiltonian form and that desired equilibrium point \mathbf{x}_* is known:

1. Determine the most appropriate form of the matching equations to be used. This may require trial and error.
2. Solve the homogeneous matching equation to determine the form of the arbitrary differential function $\mathcal{F}(z)$.
3. Ensure that the choice of $\mathcal{F}(z)$ satisfies the condition $\frac{\partial H_d}{\partial \mathbf{x}}(\mathbf{x}_*) = \mathbf{0}$.
4. Use the entire homogeneous solution to solve the nonhomogeneous matching equation for $\beta(\mathbf{x})$.

The control input $\beta(\mathbf{x})$ may then be used within a simulation of the system.

3. RLC EXAMPLE

The port-Hamiltonian model of the circuit in Figure 1 is wholly based upon Kirchhoff's current and voltage laws. The important differences within this model are that the states are not the voltage and current of the circuit. Instead, they are the charge accumulated in the capacitor, q_C , and the flux flowing through the inductor, ϕ_L . Of course, flow of the charge, \dot{q}_C , is current. So is the term $\frac{1}{L}\phi_L$. Similarly, the flow of flux, $\dot{\phi}_L$, induces a voltage and the voltage across the capacitor terminals is given by $\frac{1}{C}q_C$. Therefore, the state-space model from KVL and KCL is given by (10).

$$\begin{aligned} \dot{x}_1 = \dot{q}_C &= -\frac{1}{RC}x_1 + \frac{1}{L}x_2, \\ \dot{x}_2 = \dot{\phi}_L &= -\frac{1}{C}x_1 + u. \end{aligned} \quad (10)$$

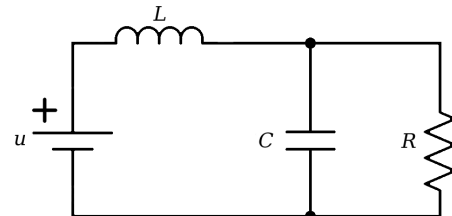


Figure 1: RLC circuit layout

To obtain the port-Hamiltonian model as defined by (12), the Hamiltonian should be defined as the sum of the individual energies:

$$H(\mathbf{x}) = \frac{1}{2C}x_1^2 + \frac{1}{2L}x_2^2. \quad (11)$$

$$\mathbf{x} = \left\{ \begin{bmatrix} 0 & 1 \\ -1 & 0 \end{bmatrix} - \begin{bmatrix} 1/R & 0 \\ 0 & 0 \end{bmatrix} \right\} \begin{bmatrix} \frac{\partial H}{\partial x_1}(\mathbf{x}) \\ \frac{\partial H}{\partial x_2}(\mathbf{x}) \end{bmatrix} + \begin{bmatrix} 0 \\ 1 \end{bmatrix} \mathbf{u}. \quad (12)$$

Readers may easily confirm that (10) and (12) represent the same system.

Ortega and Van der Schaft [2] started with the following matching equation:

$$[\mathbf{J}(\mathbf{x}) - \mathbf{R}(\mathbf{x})] \frac{\partial H_a}{\partial \mathbf{x}}(\mathbf{x}) = \mathbf{g}(\mathbf{x})\beta(\mathbf{x}). \quad (13)$$

From (12) the above matching equation may be expanded to:

$$\begin{aligned} -\frac{1}{R} \frac{\partial H_a}{\partial x_1}(\mathbf{x}) + \frac{\partial H_a}{\partial x_2}(\mathbf{x}) &= 0, \\ -\frac{\partial H_a}{\partial x_1}(\mathbf{x}) &= \beta(\mathbf{x}). \end{aligned} \quad (14)$$

The authors used Maple™ to obtain that:

$$H_a(\mathbf{x}) = \mathcal{F}(Rx_1 + x_2), \quad (15)$$

with $\mathcal{F}(\cdot) : \mathbb{R} \rightarrow \mathbb{R}$ is the differentiable function that is left to the choice of the designer. Let $(Rx_1 + x_2) = z$. For the purpose of passivity-based control $\mathcal{F}(z)$ should be chosen such that $H_d(\mathbf{x})$ has a minimum at the desired equilibrium point \mathbf{x}_* . If the desired source input is given by u_* then $\mathbf{x}_* = [Cu_* \quad \frac{L}{R}u_*]^\top$ which may be readily confirmed by recalling the definitions for the charge in a capacitor and the flux in an inductor, $q_C = CV_C$ and $\phi_L = LL_L$ respectively.

From [2] it was shown that $\mathcal{F}(z)$ was chosen to be a quadratic function such that:

$$H_a(z) = \frac{K_p}{2} [z - z_d]^2 - Ru_*z. \quad (16)$$

However, by substituting $H_a(z)$ into $H_d(\mathbf{x})$ and solving for $\frac{\partial H_d}{\partial \mathbf{x}}(\mathbf{x}_*)$, it may readily be seen that this form does not satisfy the equilibrium conditions:

$$\frac{\partial H_d}{\partial \mathbf{x}}(\mathbf{x}_*) = \begin{bmatrix} K_p R [(z_*) - (z_d)] - u_* R^2 + \frac{Cu_*}{C} \\ K_p R [(z_*) - (z_d)] - u_* R + \frac{L}{R} u_* \end{bmatrix} \neq \mathbf{0}. \quad (17)$$

Instead, a slightly different form for $H_a(z)$ is proposed:

$$H_a(z) = \frac{K_p}{2} [z - z_d]^2 - \frac{u_*}{R} z. \quad (18)$$

In this case, $\frac{\partial H_d}{\partial \mathbf{x}}(\mathbf{x}_*) = \mathbf{0}$ is satisfied:

$$\frac{\partial H_d}{\partial \mathbf{x}}(\mathbf{x}_*) = \begin{bmatrix} K_p R [(z_*) - (z_d)] - u_* + \frac{Cu_*}{C} \\ K_p R [(z_*) - (z_d)] - \frac{u_*}{R} + \frac{L}{R} u_* \end{bmatrix} = \mathbf{0}. \quad (19)$$

From (14) one can solve for the control law:

$$\beta(\mathbf{x}) = -K_p R [R(x_1 - x_{1*}) + (x_2 - x_2)] + R^2 u_* - \frac{x_1}{C}. \quad (20)$$

4. MAGLEV SYSTEM

Due to space constraints the model for the MAGLEV system shown in Figure 2 is not discussed in great detail here. Instead the reader is referred to [2] and [8]. It is believed that the reader will be able to confirm the port-Hamiltonian model. Kirchhoff's voltage law for the coil of the electromagnet and Newton's second law was used to derive the model. The coil has a resistance R and an inductance $L(\theta)$. The force of the electromagnet is given by (21):

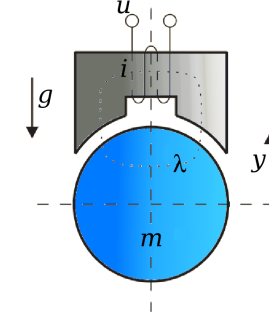


Figure 2: MAGLEV system layout

$$F = \frac{1}{2} \frac{\partial L}{\partial \theta}(\theta) i^2. \quad (21)$$

θ is the distance of the ball from the nominal position. The inductance may be suitably approximated with:

$$L(\theta) = \frac{k}{c - \theta}, \quad (22)$$

where the nominal position has been set equal to c and k is positive constant. This approximation is valid for the interval $-\infty < \theta < 1$.

If one selects the states as the flux through the electromagnet λ , θ and $m\dot{\theta}$, then $\mathbf{x} = [\lambda, \theta, m\dot{\theta}]^\top$. Once again, the Hamiltonian is given by the sum of the system energies:

$$H(\mathbf{x}) = \frac{1}{2k} (c - x_2) x_1^2 + \frac{1}{2m} x_3^2 + mgx_2.$$

The port-Hamiltonian model may then be stated as given in (23).

$$\mathbf{x} = \left\{ \underbrace{\begin{bmatrix} R & 0 & 0 \\ 0 & 0 & 1 \\ 0 & -1 & 0 \end{bmatrix}}_{\mathbf{J}(\mathbf{x}) - \mathbf{R}(\mathbf{x})} \right\} \frac{\partial H}{\partial \mathbf{x}}(\mathbf{x}) - \underbrace{\begin{bmatrix} 1 \\ 0 \\ 0 \end{bmatrix}}_{\mathbf{g}(\mathbf{x})} \mathbf{u}. \quad (23)$$

The chosen equilibrium points are selected to be $\mathbf{x}_* = [\sqrt{2kmg}, x_{2*}, 0]^\top$. x_{2*} is a setpoint that is left to the choice of the designer.

In [2] it is shown that by investigating the Hessian of $H_d(\mathbf{x})$ above, it may be shown the system is sign indefinite for

all $H_a(x_1)$. This will cause instability of the IDA-PBC controller. In order to solve the problem, which apparently stems from the lack of effective coupling between states, [2] propose a new form for $\mathbf{J}(\mathbf{x})$.

$$\mathbf{J}(\mathbf{x}) = \begin{bmatrix} 0 & 0 & -\alpha \\ 0 & 0 & 1 \\ \alpha & -1 & 0 \end{bmatrix},$$

where $\alpha > 0$ is a constant. Note that later within [2], a shuffling of the damping matrix $\mathbf{R}(\mathbf{x})$ is also done to simplify the control law. It is important to take note that such simplifications and adaptations may be made, but these adaptations are not the focus of this article.

The resulting matching equations for the new $\mathbf{J}(\mathbf{x})$ are then given by:

$$\begin{aligned} -R \frac{\partial H_a}{\partial x_1}(\mathbf{x}) &= \frac{\alpha}{m} x_3 + \beta(\mathbf{x}), \\ \frac{\partial H_a}{\partial x_3}(\mathbf{x}) &= 0, \\ \alpha \frac{\partial H_a}{\partial x_1}(\mathbf{x}) - \frac{\partial H_a}{\partial x_2}(\mathbf{x}) &= -\frac{\alpha}{k} (1 - x_2) x_1. \end{aligned} \quad (24)$$

Solving the last of these in Maple™ results in a solution for $H_a(x_1, x_2)$:

$$H_a(x_1, x_2) = \frac{1}{6} \frac{x_1^3}{\alpha k} + \left(\frac{1}{2} \frac{x_2}{k} - \frac{1}{2k} \right) x_1^2 + \mathcal{F}I \left(\frac{x_1 + x_2 \alpha}{\alpha} \right). \quad (25)$$

The arbitrary differentiable function $\mathcal{F}I \left(\frac{x_1 + x_2 \alpha}{\alpha} \right)$ is given by [2] as (26).

$$\begin{aligned} \mathcal{F}I \left(\frac{x_1 + x_2 \alpha}{\alpha} \right) &= mg \left[-x_2 + x_{2d} - \frac{x_1 - x_{1d}}{\alpha} \right] \\ &+ mg \left[\frac{1}{2} b \left(x_2 - x_{2d} + \frac{x_1 - x_{1d}}{\alpha} \right)^2 \right] \end{aligned} \quad (26)$$

By substituting (26) into (25) and then solving for $H_d(\mathbf{x}) = H(\mathbf{x}) + H_a(\mathbf{x})$, one can test whether the equilibrium conditions $\mathbf{x}_* = [\sqrt{2kmg}, x_{2*}, 0]^\top$ will satisfy the requirement that $\frac{\partial H_d}{\partial \mathbf{x}}(\mathbf{x}) = \mathbf{0}$.

Again, Maple™ was used to determine that

$$\frac{\partial H_d}{\partial \mathbf{x}}(\mathbf{x}) = \begin{bmatrix} mg \left(-\frac{1}{\alpha} + \frac{b}{\alpha} \left(\frac{x_1 - x_{1d}}{\alpha} + x_2 - x_{2d} \right) \right) + \frac{1}{2} \frac{x_1^2}{k\alpha} \\ mg + mg \left(-1 + b \left(\frac{x_1 - x_{1d}}{\alpha} + x_2 - x_{2d} \right) \right) \frac{x_3}{m} \end{bmatrix}.$$

By substituting $\mathbf{x}_* = [\sqrt{2kmg}, x_{2*}, 0]^\top$ into the above, it may be seen that the choice of (26) is correct. It may be reasoned that with a little trial and error, the reader could also arrive at this choice of (26).

According to [2], both $\alpha, b > 0$. It was confirmed within the simulations that $\alpha < 0$ or $b < 0$ produce unbounded outputs.

The first condition from (24) was solved with Maple™ to

produce the control law given by:

$$\begin{aligned} u &= -R \left(\frac{1}{2} \frac{x_1^2}{\alpha k} + \frac{(x_2 - 1)x_1}{k} \right) \\ &+ mgR \left(-\frac{1}{\alpha} + \frac{b}{\alpha} \left(x_2 - x_{2d} + \frac{x_1 - x_{1d}}{\alpha} \right) \right) - \frac{\alpha x_3}{m}. \end{aligned} \quad (27)$$

With some rearrangement of the terms as given below, one may arrive at the form of u given in [2].

$$\begin{aligned} u &= -\frac{R}{\alpha} \frac{x_1^2}{2k} + \frac{R}{k} (-x_2 + 1)x_1 \\ &- mg \frac{-R}{\alpha} - \frac{mgRb}{\alpha} \left(x_2 - x_{2d} + \frac{1}{\alpha} x_1 - x_{1d} \right) - \frac{\alpha x_3}{m} \end{aligned} \quad (28)$$

Notice that K_p would then be set equal to $\frac{mgRb}{\alpha}$. The authors found that by simply selecting $K_p > 0$ as suggested by [2], the system would not necessarily stabilise for too large a value of K_p .

5. SIMULATION RESULTS AND DISCUSSION

5.1 RLC example

The systems described in sections 3 and 4 were simulated within MATLAB® SimuLink™ using the parameters as defined by:

$$\begin{aligned} u_d &= 12 \text{ V} & R &= 200 \text{ } \Omega \\ C &= 625 \text{ } \mu\text{F} & L &= 10 \text{ mH} \\ K_p &= 24.96 \end{aligned}$$

Figure 3 shows the response of the system for the capacitor charge q_C , both for the controlled and uncontrolled voltage sources. The values for R and C were specifically selected to produce a response with a poor damping constant so as to evaluate the controlled response. A strongly damped system will show considerably less difference between the controlled and uncontrolled responses.

Figure 4 displays the cumulative energy dissipation within the resistor of Figure 1. It may be clearly seen that the oscillatory response of the uncontrolled system adds excessive energy dissipation.

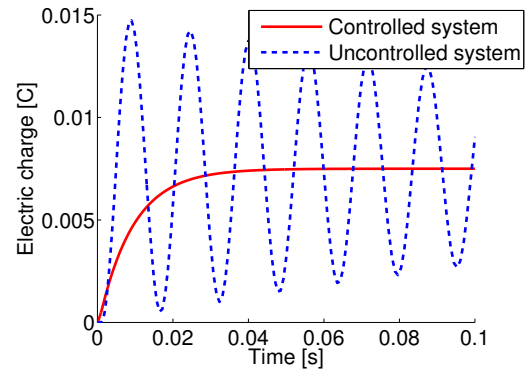


Figure 3: Capacitor charge over time

5.2 MAGLEV example

The MAGLEV example was simulated using the parameters from [8] as defined by:

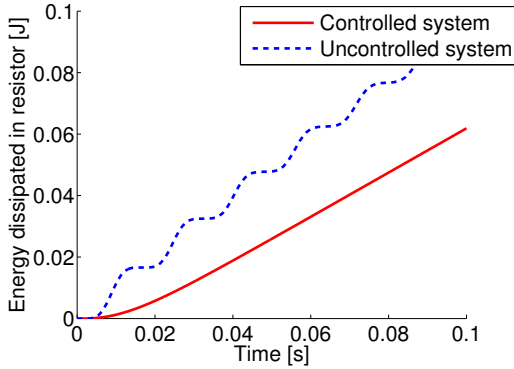


Figure 4: Energy dissipation of circuit over time

$$\begin{aligned}
 c &= 5 \times 10^{-3} \text{ m} & k &= 6.4042 \times 10^{-5} \text{ H}\cdot\text{m} \\
 R &= 2.52 \text{ } \Omega & m &= 0.0844 \text{ kg} \\
 K_p &= 3.16 & g &= 9.81 \text{ m/s}^2 \\
 x_{1d} &= 0.0103 \text{ Wb} & x_{2d} &= -3 \times 10^{-3} \text{ m}
 \end{aligned}$$

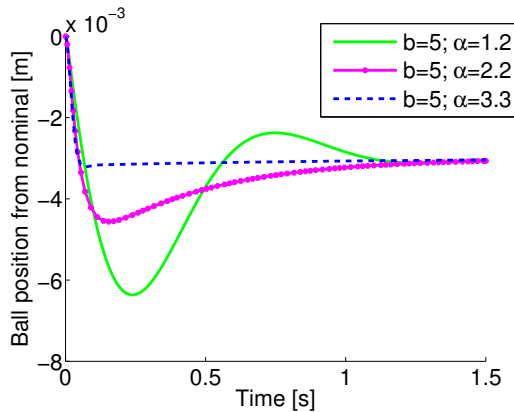


Figure 5: $H_{a1}(x)$: Sweep of the α -parameter, MAGLEV system

Figure 5 shows a sweep of the α parameter for the control law of (28). Sweeping the parameters in this way allowed the authors to change the response of the system to the reference input. The final simulation with the parameters $b = 5$ and $\alpha = 3.3$ allowed for the shortest settling time and least overshoot of the ball position from its reference point. The b parameter may be swept in a similar manner to obtain the response desired for the particular control problem.

6. CONCLUSIONS

Within this article, the port-Hamiltonian theory and matching equations that form an integral part of the IDA-PBC methodology have been discussed thoroughly. The authors have also given a clear discussion of two popular examples of IDA-PBC to control problems. Simulation results with practical system parameters were included to demonstrate the effect of the controllers produced with this technique.

The results for the above simulations should be simple for the reader to reproduce with the parameters given in sections 5.1 and 5.2. Working through these examples should give readers a clear introduction to the technique, allowing them to apply the principles to other control problems and further research.

Figures 3 to 5 show that high quality controllers may be developed with the IDA-PBC technique. Also, energy dissipation may be lowered. The system output may be controlled to stabilise at a set equilibrium point with minimal overshoot and a short settling time. When the control law contains several free parameters as in (28), the designer has more control over the shape of the response.

Testing the hypothesis that lowered energy dissipation will reduce maintenance costs in systems could constitute future work. Similarly, investigating the effect on energy dissipation of the various forms of the controlled response as for the MAGLEV system invites several more research questions. One would expect a more stringent response to dissipate more energy within the electromagnet, but initial investigations have proposed that the total energy dissipation of the system may be less for more stringent control laws even though the energy dissipation in the electromagnetic field may be larger.

REFERENCES

- [1] R. Ortega, A. Loría, P. J. Nicklasson, and H. Sira-Ramírez, *Passivity-based Control of Euler-Lagrange Systems*, ser. Communications and Control Engineering. London: Springer London, 1998.
- [2] R. Ortega and A. Van der Schaft, "Putting energy back in control," *Control Systems*, vol. 21, no. 2, pp. 18–33, 2001.
- [3] J. A. Naudé, "Control Design Using Energy-Shaping Methods," Ph.D. dissertation, University of the Witwatersrand, 2012.
- [4] A. Y. Mersha, R. Carloni, and S. Stramigioli, "Port-based Modeling and Control of Underactuated Aerial Vehicles," in *2011 IEEE International Conference on Robotics and Automation*, Shanghai, China, 2011, pp. 14–19.
- [5] R. Ortega, A. V. D. Schaft, B. Maschke, and G. Escobar, "Interconnection and damping assignment passivity-based control of port-controlled Hamiltonian systems," *Automatica*, vol. 38, pp. 585–596, 2002.
- [6] R. Ortega and E. García-Canseco, "Interconnection and Damping Assignment Passivity-Based Control: A Survey," *European Journal of Control*, vol. 10, no. 5, pp. 432–450, Jan. 2004.
- [7] F. Dörfler, J. K. Johnsen, and F. Allgöwer, "An introduction to interconnection and damping assignment passivity-based control in process engineering," *Journal of Process Control*, vol. 19, no. 9, pp. 1413–1426, Oct. 2009.
- [8] H. Rodriguez, H. Siguerdidjane, and Ort, "Experimental Comparison of Linear and Nonlinear Controllers for a Magnetic Suspension," in *Proceedings of the 2000 IEEE International Conference on Control Applications*. Anchorage, Alaska (USA), 2000.

THERMAL-FLUID STATE SPACE MODEL OF A COUNTER-FLOW SINGLE PHASE HEAT EXCHANGER FOR ENERGY VISUALIZATION

S.B. Smuts*, G. van Schoor† and K.R. Uren*

* North-West University, Potchefstroom Campus, School of Electrical, Electronic & Computer Engineering, South-Africa email: 21796432@nwu.ac.za / kenny.uren@nwu.ac.za

† Unit for energy systems, North-West University, Potchefstroom Campus, South-Africa email: george.vanschoor@nwu.ac.za

Abstract: In the current world energy saving has become more important due to the vast increase in consumption. Heat exchangers have become important components in terms of energy transfer and efficiency. This paper proposes a multi-domain thermal-fluid state space model to investigate the transient response of a counter flow heat exchanger. The fundamental laws of conservation of energy, moment and mass are used to derive the state space equations. The state space model is simulated in MATLAB® and the model results are compared to a Flownex® simulation as validation. The power transferred between the fluids and the power stored are discussed with an analysis of the influence of a change in pressure on the energy stored in the heat exchanger.

Key words: Counter flow heat exchanger, heat exchanger model, fluid dynamic, thermodynamic, state space model, energy analysis

1. INTRODUCTION

Heat exchanger technology has rapidly advanced in the last century due to the increase in complexity of industrial processes that requires higher efficiency heat exchangers to meet the industrial processes' demand at an acceptable cost [1]. Heat exchangers are widely used in many energy conversion applications ranging from process, power, transportation and air-conditioning to heat recovery, alternate fuels and manufacturing industries [2]. Heat exchangers is therefore an important component that warrants optimisation in terms of energy efficiency.

In the present world where energy consumption is significantly rising due to an increasing demand, energy efficiency has become more important [3]. With this in mind the importance of heat exchangers in energy transfer and efficiency has become even more apparent [2]. It is therefore advantageous to describe the heat transfer process that occurs inside a heat exchanger by means of energy due to: (1) heat exchangers relation to energy and (2) the conservation and management of energy gaining much more importance at the present.

When the overall energy of a heat exchanger is evaluated for the purposes of energy visualization, the fluid dynamic effects have to be taken into account. This study aims to provide a combined thermal-fluid state space model of a heat exchanger with the focus on using this model to characterize the energy representation or visualisation. In turn this understanding of the energy in the heat exchanger can lead to control, optimization, fault identification and prevention.

This paper will discuss a combined thermal and fluid dynamic state space model of a counter flow heat

exchanger. The model results will be compared to a Flownex® model in order to verify and validate the results. An energy representation will then be derived from the model results in order to gain insight into the current operating conditions and efficiency of the heat exchanger by analysing the energy.

In section 2 an overview of counter flow heat exchangers are described and section 3 describes the derivation of the thermal-fluid state space model. Section 4 lists the results of the state space model including the Flownex® simulation model. Section 5 describes the energy visualization of the heat exchanger system and section 6 concludes the paper.

2. COUNTER-FLOW HEAT EXCHANGERS

A heat exchanger is a device used to efficiently transfer heat between two fluids that are at different temperatures and usually separated by a solid wall [4]. Heat exchangers are classified into several categories depending on the flow arrangement. Typical flow arrangements include parallel flow, counter flow and cross flow [5]. Heat exchangers can be operated in two different operating conditions; (1) steady state conditions where mass flow rate and temperatures are constant and (2) transient conditions where there are changes in the temperatures and mass flow rate [5]. Figure 1 shows a basic illustration of a counter flow heat exchanger.

The heat exchanger of interest in this paper is a counter flow double-pipe heat exchanger. In a counter flow heat exchanger the hot and cold fluid flows in opposite directions to achieve better heat transfer since the difference between the hot and cold fluid temperature (δT) remains mostly constant with respect to the length (x) of

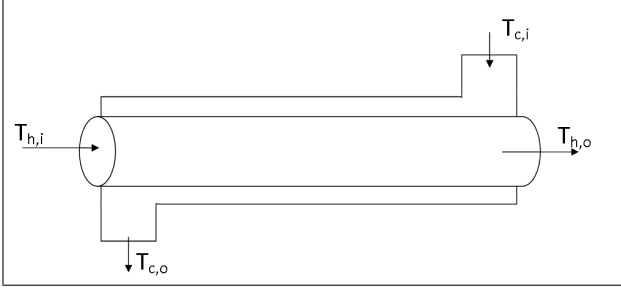


Figure 1: Basic illustration of a counter flow heat exchanger

the heat exchanger. The overall heat transfer rate of a heat exchanger is mostly dependent on ΔT . For a counter flow heat exchanger ΔT varies little with x resulting in more heat transfer than a parallel flow heat exchanger.

3. STATE SPACE MODEL

Figure 2 shows a segment of a double-pipe counter flow heat exchanger. From the figure, one can see that the heat

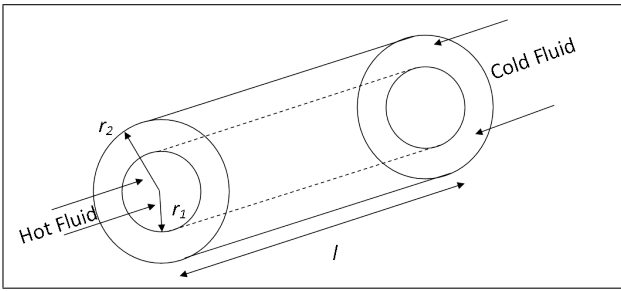


Figure 2: A segment of the counter flow heat exchanger

exchanger segment consists of 2 pipes. The inner pipe has a radius of r_1 and the outer pipe has a radius of r_2 . The hot fluid will flow in the inner pipe, whereas the outer pipe will house the cold fluid. The length of the pipe is denoted by l and the fluids are separated by a wall of thickness d . The purpose of the double-pipe setup is to maximize the heat transfer area between the two fluids. In order to derive the model of the heat exchanger, the system will be divided into a node and element network. Figure 3 shows this nodal network. Each node represents a temperature and pressure whereas each element represents a mass flow rate and energy transfer. The network constitutes of two control volumes for each of the hot and the cold fluid. The control volumes are based on the node centred approach. This implies that pressure and temperature is constant within the control volume and mass and thermal energy enters the control volume from the adjoining elements.

The system inputs are given by $P_{c,i}$ and $P_{h,i}$ denoting the inlet pressures and $P_{c,3}$ and $P_{h,3}$ the outlet pressures with the subscripts h and c referring to the hot side and cold side respectively. $T_{c,i}$ and $T_{h,i}$ are the inlet temperatures whereas the system outputs is given by $T_{h,o}$ and $T_{c,o}$ which is the outlet temperatures. Energy is exchanged with the conductive separation wall via convection. Conduction

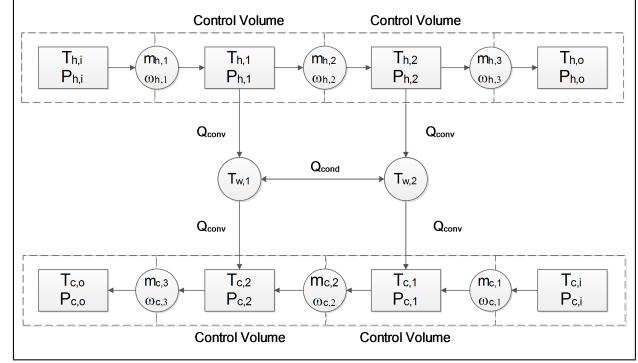


Figure 3: The element and nodal diagram of a counter flow heat exchanger

transfer occurs between the two wall elements with temperatures denoted by $T_{w,1}$ and $T_{w,2}$. The state space model can now be derived by applying the conservation of mass and energy laws to each node and the conservation of momentum law to each element.

3.1 Conservation of mass

The conservation of mass equation states that the rate of change of mass in the control volume is zero. The conservation of mass for a control volume as shown in (1). The first term indicates the change of mass in the control volume while the second term indicates the mass flow through the control surface [6].

$$\frac{\partial}{\partial t} \int_{CV} \rho dV + \int_{CS} \rho \mathbf{v} \cdot \mathbf{n} dA = 0 \quad (1)$$

Replacing the integrals with summations, introducing a change of variable from mass to pressure and simplifying in order to solve numerically, yields (2).

$$\frac{dP_j}{dt} = \dot{m}_{j-1} - \dot{m}_{j+1} \quad (2)$$

P is the pressure [Pa] in the element, \dot{m}_{j-1} is the mass flow rate [kg/s] of the node preceding the element and \dot{m}_{j+1} is the mass flow rate of the node after the element. (2) thus relates the pressure in a element with the mass flow rate entering and leaving the element.

3.2 Conservation of momentum

The conservation of momentum equation states that the time rate of change of the momentum of the fluid in a control volume is equal to the sum of all the external forces acting on the fluid. This governing equation is shown in (3) [6].

$$\frac{\partial}{\partial t} \int_{CV} \mathbf{v} \rho dV = - \int_{CS} \mathbf{v} \rho \mathbf{v} \cdot \mathbf{n} dA + \int_{CS} \boldsymbol{\tau} dA + \int_{CV} \beta \rho dV \quad (3)$$

The term on the left represents the rate of change of linear momentum of the control volume. The first term on the right represents the rate of linear momentum flow through the control volume. The second term gives

the total surface-force distribution on the control surface. Surface-force is force that arises from direct contact between the fluid and the control surface. The main contributor to this force is the force needed to overcome the friction cause by a fluid flowing in a non-smooth pipe. The last term represents forces acting on the fluid due to non-contact. The most common non-contact force is gravity. Integrating, simplifying and taking note that the effect of gravity is neglected because $\Delta z = 0$, (3) yields,

$$\frac{d\dot{m}_j}{dt} = \frac{A}{l}(P_{j-1} - P_{j+1}) - \frac{f}{2\rho DA}|\dot{m}_j|\dot{m}_j, \quad (4)$$

with \dot{m}_j the mass flow rate [kg/s] through the node, A the pipe surface area [m²] and l the distance [m] between nodes. P_{j-1} and P_{j+1} is the pressure [Pa] in the element before and after the node respectively. The Darcy-Weisbach friction factor is denoted by f while ρ represents the fluid density [kg/m³] and D is the hydraulic diameter [m] of the pipe.

3.3 Conservation of energy

The law of conservation of energy states that the change in stored energy with respect to time, in a control volume must be equal to the energy entering the control volume minus the energy leaving the control volume plus the energy entering the control volume due to heat transfer and work transfer. The conservation of energy law is shown in (5) [6].

$$\frac{\partial}{\partial t} \int_{CV} \rho p dV = - \int_{CS} \rho \mathbf{v} \cdot \mathbf{n} dA + \dot{Q} + \dot{W} \quad (5)$$

The term on the left is the time rate change of stored energy in the control volume. The first term on the right is the energy entering and leaving the control surface. The heat transfer rate, \dot{Q} , represents all the ways in which energy enters the control volume due to heat transfer and \dot{W} represents the rate of work done on the control volume. Integrating, simplifying and noting that all work energy is negligible, (6) yields,

$$V\rho c_p \frac{dT_j}{dt} = \dot{m}c_p(T_{j-1} - T_j) + \dot{Q}, \quad (6)$$

with V the volume [m³] of the element, c_p the specific heat [J/kg.K] of the fluid, T_j the temperature [K] of the element and T_{j-1} the temperature [K] of the element preceding this one. A few points need to be noted. Firstly the fluid is assumed to be an ideal gas and thus $h = c_p T$. Secondly the only heat transfer effect of interest in this paper is convection heat transfer and, in the case of the separation wall, conduction heat transfer.

3.4 State space model states

The states of interest can be defined by figure 3. Two state space matrices will be used, one modelling the thermodynamic effects and one the fluid dynamic effects. The reason for this is that the fluid dynamic time constant is much smaller than the thermal time constant implying

that the dynamic effects of the fluid dynamic model can be ignored for the thermodynamic model. Table 1 lists the states of the thermodynamic model and Table 2 list the states of the fluid dynamic model.

Table 1: List of the thermodynamic states of the heat exchanger system

$x_1 = T_{h,1}$	$x_2 = T_{h,2}$	$x_3 = T_{c,1}$
$x_4 = T_{c,2}$	$x_5 = T_{w,1}$	$x_6 = T_{w,2}$

Table 2: List of the fluid dynamic states of the heat exchanger system

$x_1 = P_{h,1}$	$x_2 = P_{h,2}$	$x_3 = \dot{m}_{h,1}$
$x_4 = \dot{m}_{h,2}$	$x_5 = \dot{m}_{h,3}$	$x_6 = P_{c,1}$
$x_7 = P_{c,1}$	$x_8 = \dot{m}_{c,1}$	$x_9 = \dot{m}_{c,2}$
$x_{10} = \dot{m}_{c,3}$		

3.5 Fluid dynamic state space equations

The state space equations for the fluid dynamic model can be derived by applying the (2) to each node and (4) to each element. The state space equations of states x_1 to x_{10} for the fluid dynamic model are shown in (7) to (16).

$$\dot{x}_1 = \frac{B_h}{\rho_h V_h}(x_3 - x_4) \quad (7)$$

$$\dot{x}_2 = \frac{B_h}{\rho_h V_h}(x_4 - x_5) \quad (8)$$

$$\dot{x}_3 = \frac{A_h}{l_h}(P_{h,in} - x_1) - \frac{f_h}{2\rho_h D_h A_h}|x_3|x_3 \quad (9)$$

$$\dot{x}_4 = \frac{A_h}{l_h}(x_1 - x_2) - \frac{f_h}{2\rho_h D_h A_h}|x_4|x_4 \quad (10)$$

$$\dot{x}_5 = \frac{A_h}{l_h}(x_2 - P_{h,out}) - \frac{f_h}{2\rho_h D_h A_h}|x_5|x_5 \quad (11)$$

$$\dot{x}_6 = \frac{B_c}{\rho_c V_c}(x_8 - x_9) \quad (12)$$

$$\dot{x}_7 = \frac{B_c}{\rho_c V_c}(x_9 - x_{10}) \quad (13)$$

$$\dot{x}_8 = \frac{A_c}{l_c}(P_{c,in} - x_6) - \frac{f_c}{2\rho_c D_c A_c}|x_8|x_8 \quad (14)$$

$$\dot{x}_9 = \frac{A_c}{l_c}(x_6 - x_7) - \frac{f_c}{2\rho_c D_c A_c}|x_9|x_9 \quad (15)$$

$$\dot{x}_{10} = \frac{A_c}{l_c}(x_7 - P_{c,out}) - \frac{f_c}{2\rho_c D_c A_c}|x_{10}|x_{10} \quad (16)$$

3.6 Thermal state space equations

The state space equations for the thermodynamic model can be derived by applying (6) to each node. The state space equations of states x_1 to x_6 for the thermodynamic

model is shown in (17) to (22).

$$\dot{x}_1 = \frac{\dot{m}_{h,1}}{\rho_h V_h} (T_{h,in} - x_1) + \frac{h_h A_h}{\rho_h V_h c_{p,h}} (x_5 - x_1) \quad (17)$$

$$\dot{x}_2 = \frac{\dot{m}_{h,2}}{\rho_h V_h} (x_1 - x_2) + \frac{h_h A_h}{\rho_h V_h c_{p,h}} (x_6 - x_2) \quad (18)$$

$$\dot{x}_3 = \frac{\dot{m}_{c,1}}{\rho_c V_c} (T_{c,in} - x_3) + \frac{h_c A_c}{\rho_c V_c c_{p,c}} (x_6 - x_3) \quad (19)$$

$$\dot{x}_4 = \frac{\dot{m}_{c,2}}{\rho_c V_c} (x_3 - x_4) + \frac{h_c A_c}{\rho_c V_c c_{p,c}} (x_5 - x_4) \quad (20)$$

$$\dot{x}_5 = \frac{h_h A_h}{\rho_w V_w c_{p,w}} (x_5 - x_1) + \frac{h_c A_c}{\rho_w V_w c_{p,w}} (x_5 - x_4) + \frac{k A_w}{\rho_w V_w c_{p,w}} (x_6 - x_5) \quad (21)$$

$$\dot{x}_6 = \frac{h_h A_h}{\rho_w V_w c_{p,w}} (x_6 - x_2) + \frac{h_c A_c}{\rho_w V_w c_{p,w}} (x_6 - x_3) + \frac{k A_w}{\rho_w V_w c_{p,w}} (x_5 - x_6) \quad (22)$$

By constructing the state space model of the state equations listed in (7)-(22) in the form shown in (23),

$$\dot{\mathbf{x}} = \mathbf{A}\mathbf{x} + \mathbf{B}\mathbf{u} \quad (23)$$

with \mathbf{x} containing the states, \mathbf{A} and \mathbf{B} are coefficient matrices and \mathbf{u} is the system inputs. For the thermodynamic model \mathbf{x} is a 6x1 vector, \mathbf{A} is a 6x6 coefficient matrix. \mathbf{B} is a 1x6 vector and \mathbf{u} is a 6x1 vector. For the fluid dynamic model \mathbf{x} is a 10x1 vector, \mathbf{A} is a 10x10 coefficient matrix, \mathbf{B} is a 10x1 vector and \mathbf{u} is a 10x1 vector.

4. SIMULATION RESULTS

This simulation was conducted with a counter flow heat exchanger with pure water as the hot fluid and unused engine oil as the cold fluid. Table 3 shows the heat exchanger characteristics and table 4 lists the simulation conditions.

4.1 Fluid dynamic model results

Figure 4 shows the results of the mass flow rate in the centre element (\dot{x}_1 and \dot{x}_6) and figure 5 shows pressure in the outlet nodes (\dot{x}_4 and \dot{x}_9) for the hot and cold fluid. The oscillations in figure 4 and 5 in the pressure and mass flow rate is due to the sudden addition of high pressure to a system already in steady state, causing a sudden increase in mass flow rate and results in a back pressure forcing the mass flow to change flow direction until the pressure has reduced. This is known as the water hammer effect.

4.2 Thermodynamic model results

Figure 6 shows the output temperatures of the hot and cold fluid (states \dot{x}_2 and \dot{x}_4). It is important to note the difference in time scale between the fluid dynamic domain (figures 4 and 5) and the thermal model (figure 6).

Table 3: List of the simulation parameters

Name	Symbol	Value	Unit
Geometry			
Inner pipe radius	r_1	0.008	m
Outer pipe radius	r_2	0.016	m
Inner pipe thickness	d	0.00175	m
Pipe length	l	2	m
Friction factor	f	3	
Hot fluid - at 300K			
Specific heat	$c_{p,h}$	1909	J/kg.K
Density	ρ_h	884.1	kg/m ³
Convection coefficient	h_h	800	W/m ² .K
Bulk modulus	B_h	2.2×10^9	Pa
Cold fluid at 300K			
Specific heat	$c_{p,c}$	4186	J/kg.K
Density	ρ_c	1000	kg/m ³
Convection coefficient	h_c	900	W/m ² .K
Bulk modulus	B_c	2.2×10^9	Pa
Separation Wall			
Specific heat	$c_{p,w}$	421	J/kg.K
Density	ρ_w	8933	kg/m ³
Conduction coefficient	k_w	421	W/m ² .K

Table 4: List of the simulation conditions

Name	Symbol	Value	Unit
Cold Side			
Inlet Pressure	$P_{c,i}$	300	kPa
Outlet Pressure	$P_{c,o}$	190	kPa
Inlet Temperature	$T_{c,i}$	290	K
Hot Side			
Inlet Pressure	$P_{h,i}$	300	kPa
Outlet Pressure	$P_{h,o}$	150	kPa
Inlet Temperature	$T_{h,i}$	330	K

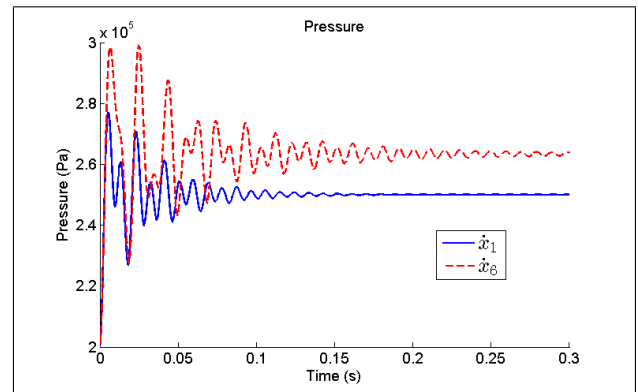


Figure 4: The results of the fluid dynamic state space model - Pressure

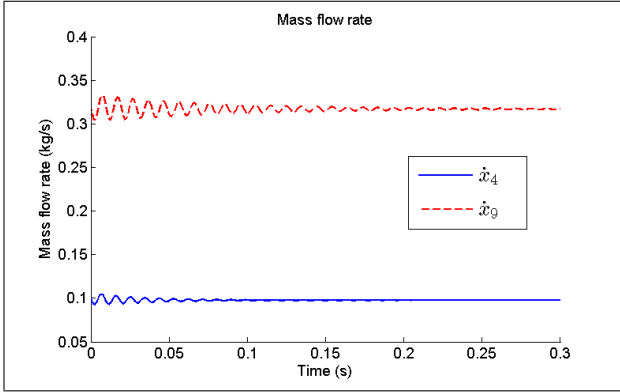


Figure 5: The results of the fluid dynamic state space model - Mass flow rate

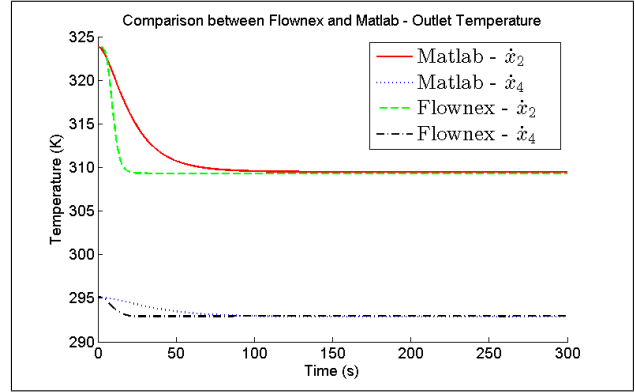


Figure 7: The comparison between the output temperature results of Flownex[®] and MATLAB[®]

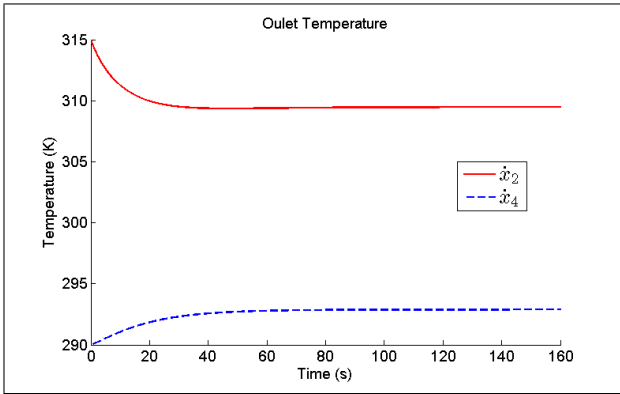


Figure 6: The output temperatures of the heat exchanger

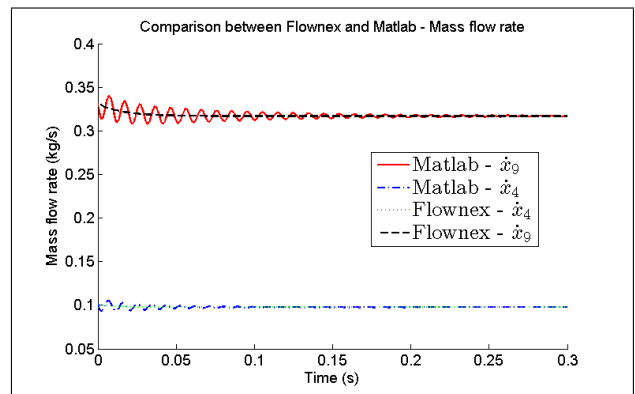


Figure 8: The comparison between the mass flow rate results of Flownex[®] and MATLAB[®]

The decrease in hot fluid temperature is significantly more than the increase in cold fluid temperature due to the differences in characteristics of the fluids mainly the specific heat and mass flow rate.

4.3 Model validation

Flownex[®] is validated simulation software that specializes in simulations where fluids are the driving factor. Figure 7 shows the comparison of the output temperature of the thermal model to the output temperatures of the Flownex[®] model. The difference in settling time of the temperatures is attributed to the way and extent to which the thermal capacitance is modelled. In the thermal model the wall capacitance is more accurately modelled for a better energy representation. Figure 8 shows the comparison of the mass flow rate (\dot{x}_4 and \dot{x}_9) of the fluid dynamic model to the output of the Flownex[®] model.

The different oscillations present results can entirely be attributed to the difference numeric solution techniques. Although oscillations is present in both simulations, the difference in magnitude of the oscillations is due to the numeric techniques.

5. ENERGY VISUALIZATION

When an energy visualization of a heat exchanger is considered, the dominant factor of importance is the energy transferred between the hot and cold fluids. Another important factor often omitted in heat exchanger analysis is the energy storage effect the separation wall has on the heat exchange process. The wall is an important part of the energy analysis as it acts like a thermal capacitor, storing energy. Thermal energy is transferred from the hot side to the cold side via the wall. The rate of energy transfer is given is (24),

$$\dot{Q} = \dot{m}c_p(T_i - T_o) \quad (24)$$

with \dot{Q} the rate of energy transfer [J/s], \dot{m} the mass flow rate [kg/s], c_p the specific heat of the fluid [J/kg.K] and T_i and T_o the inlet and outlet temperatures [K] respectively. Figure 9 shows the power transferred from the hot side, the power absorbed and stored and the power transferred to the cold side.

It can be seen from figure 9 that the storage element gains less energy as more energy is transferred to the cold side increasing until such a point where the energy storage element is saturated and all the energy transferred from the hot fluid goes to the cold fluid. The energy

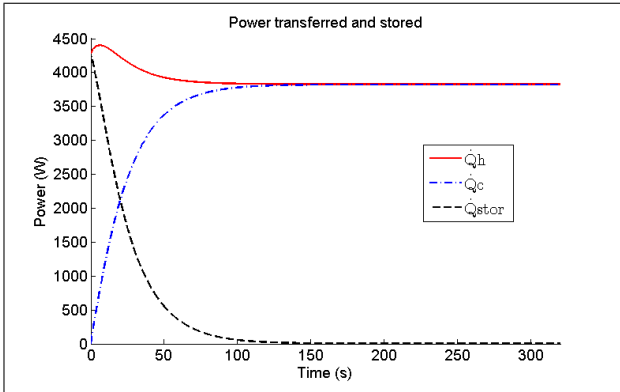


Figure 9: The power transferred and stored in the heat exchanger

approach includes the effects of the thermodynamic and fluid dynamic domains. To illustrate this, figure 10 shows the same results as figure 9 but with an increase in $P_{h,i}$ of 50kPa to 350kPa.

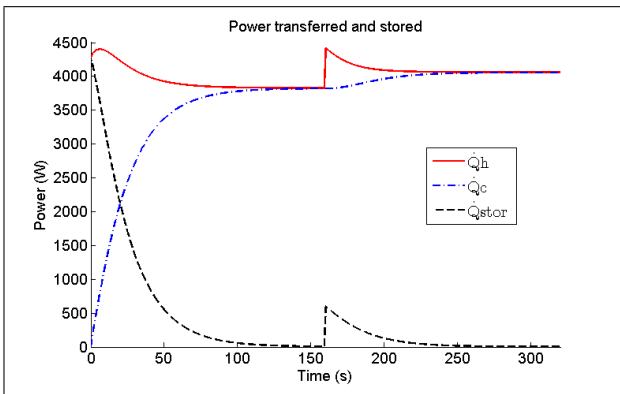


Figure 10: The changes in power stored and transferred for a step input in pressure at the hot side

One can see that the effects of the fluid domain is important in heat transfer analysis as it affects the heat transfer rate of the heat exchanger. Since there is a change in the power transferred when an increase in pressure is applied, the consequence of this increase in pressure on energy stored can also be observed. Figure 11 shows the energy stored in the system, including the increase in energy stored due to the change in pressure. From figure 11 on can see that the change in the energy stored is influenced by a change in pressure. This indicates that occurrences such as a leak or a pressure drop, due to a for instance a defective pump, can be seen in an energy effect. The energy approach gives a more universal representation of the system status using energy transferred, absorbed and stored.

6. CONCLUSION

This paper discussed the process followed to derive a fluid dynamic as well as a thermodynamic model of a counter flow heat exchanger. The models were derived by applying the principles of conservation of mass, momentum and

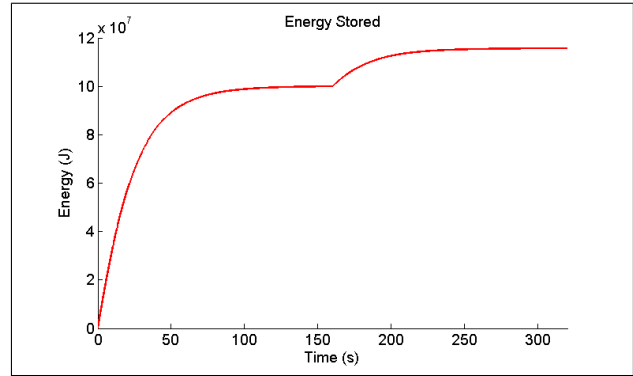


Figure 11: The changes in energy stored for a step input in pressure at the hot side

energy to the heat exchanger. Both models were simulated and an energy analysis was done on the results.

The thermal-fluid domain approach gives a more exact representation of a heat exchanger by including an additional domain (fluid dynamic domain) of the heat exchangers' behaviour. This leads to a more accurate energy representation which in turn can be used to make a more informed decision regarding the heat exchanger's current operating conditions or efficiency. The additional information provided by the multi-domain model and the energy representation can lead to efficiency optimization as well as fault detection and isolation of a heat exchanger.

REFERENCES

- [1] B. I. Master, K. S. Chunangad, A. J. Boxma, D. Kral, and P. Stehlik: Most Frequently Used Heat Exchangers from Pioneering Research to Worldwide Applications, *Heat Transf. Eng.*, Vol. 27 No. 6, pp. 4-11, June 2006.
- [2] Q. Wang, M. Zeng, T. Ma, X. Du, J. Yang: Recent development and application of several high-efficiency surface heat exchangers for energy conversion and utilization, *Applied Energy*, Vol 135, pp.748-777, December 2014
- [3] J. Rose, T. R. Nielsen, J Kragh, S. Svendsen: Quasi-steady-state model of a counter-flow air-to-air heat-exchanger with phase change, *App Energy*, Vol. 85 No.5, pp. 312-325, May 2008
- [4] F.P. Incropera and D.P. DeWitt: *Fundamentals of heat and mass transfer*, 5th ed. John Wiley Sons Inc., 2002.
- [5] S.E. Chouaba, A. Chamroo, R. Ouvrard, T. Pointot: A counter flow water to oil heat exchanger: MISO quasi linear parameter varying modelling and identification, *Simulation Modelling Practice and Theory*, Vol. 23, pp. 87-98, April 2012
- [6] Y.A. Cengel and A.J. Ghajar: *Heat and Mass Transfer: Fundamentals and Applications*, 4th ed. McGraw-Hill.

Efficiency Benchmarking and Evaluation of Coal Fire Power Stations using Data Envelopment Analysis

A. de Villiers* and H. J. Vermeulen**

* Dept. of Electrical and Electronic Engineering, Stellenbosch University, Private Bag XI, Matieland, 7602, South Africa
Email: almerod@sun.ac.za

** Dept. of Electrical and Electronic Engineering, Stellenbosch University, Private Bag XI, Matieland, 7602, South Africa
Email: vermeuln@sun.ac.za

Abstract: South Africa's current rate of increase in energy demand brings with it a need for optimized efficiency in existing power plants. Tracking plant efficiency can be troublesome, as traditional methods rarely include all relevant factors. This paper proposes Data Envelopment Analysis (DEA) as a diagnostic tool to assist in interpreting the efficiency performance of power stations. DEA is a non-parametric linear programming process used for calculating comparative efficiencies that can be adapted to encompass any factors deemed relevant. Results are presented for DEA Energy Efficiency (EE) case studies performed for a local coal-fired power station. The performance of the station is comparatively evaluated on a month-to-month basis and against similar US plants. Results from these analyses are analysed and explained. DEA is found to have potential as a viable M&V comparison tool, but is dependent on the availability of accurate data.

Keywords: Data Envelopment Analysis, Power Plant Efficiency, Performance Benchmarking, Coal Fire Power Stations, Measurement and Verification.

1. INTRODUCTION

The South African power grid has been experiencing severe capacity constraints in generation and transmission in recent years. This has given rise to major efforts to implement Energy Management (EM) initiatives in all load sectors, including the industrial, commercial and residential all load sectors. These efforts are supported by the construction of multiple new power plants, both thermal and renewable. Additionally, the Energy Efficiency (EE) of existing plants is being optimized, which requires performance evaluation and benchmarking as part of Measurement and Verification (M&V) exercises.

Traditional methods of evaluating power plant efficiency, such as heat-rate monitoring, are difficult and often produce inconclusive results due to a lack of online data and the complex nature of factors, such as environmental conditions, that determine the overall efficiency of the plants. Furthermore, the savings impacts of many individual EE interventions are small compared to the plant ratings, resulting in difficulties in extracting the savings impacts from the noisy baseline. High noise levels in trying to extract them may also be too rigid in structure to allow for use in both comparative benchmarking between individual plants and a time-based evaluation of a single plant e.g. month-to-month or year-to-year.

This paper applies Data Envelopment Analysis (DEA) as a means to gain some insight into the EE performance of power stations by tracking a metric of performance efficiency over a given timeline or comparing the relative

efficiencies of similar stations. The results do not represent a direct measure of efficiency for M&V purposes, but can assist in gaining insight into the relative efficiency over time and between plants. DEA is a widely used, non-parametric, linear programming process used for calculating comparative efficiencies in Decision Making Units (DMUs) [1]. The DEA process can also be adapted to incorporate almost any factor deemed relevant, thus making it useful for determining the effect of such a factor on overall performance. This can, in principle, assist in the M&V process.

DEA have been used extensively to comparatively benchmark power stations [2] [3] [4]. In this paper a the EE performance of single coal fired plant is evaluated on a month-to-month basis, with the view to get an idea of the effects of changing input parameters on the performance over time, as well as comparatively to 19 similar plants.

2. DATA ENVELOPMENT ANALYSIS

DEA is a non-parametric, non-linear benchmarking technique that utilizes linear programming as its basis [5]. The process comparatively evaluates individual DMUs based on the inputs and outputs provided. As these inputs and outputs can consist of any measurable values, the process can include almost any factor deemed relevant. Unlike a simple efficiency ratio, the analysis can have any number of inputs and outputs, yet still return a useful result [5]. Results are returned as an overall efficiency, as well as a combined weight, thus creating a hypothetical compound DMU, highlighting specific inefficiencies.

Inefficient DMUs can thus benefit from following the practices found in efficient DMUs.

The initial DEA model was first proposed by Charnes, Cooper and Rhodes in 1978 [1]. This model was developed as a way to evaluate non-profit and public sector operations [5] and became known as the CCR model (after their respective names). Their work was a continuation of that by that of Farrell (1957), who attempted to develop a more effective productivity evaluation method [6]. Presently there are numerous variations on the CCR, such as the Banker, Charnes and Cooper (BCC) model that attempt to expand various aspects of the original model [6]. In this paper the CCR model is used in an expanded form,

2.1 Mathematical Formulation of DEA

Efficiency is usually calculated as a ratio of total output to total input, as shown in Equation 1:

$$\theta = \frac{\sum \text{output}}{\sum \text{input}} \quad (1)$$

where θ represents total efficiency. Thus, a higher efficiency is achieved but increasing the output and/or decreasing the input. Complex systems may have multiple Input and Output (IO) categories. By associating weights with each IO category, the DEA process manipulates the relative contributions of the individual input and output parameters on the efficiency metric θ . Weights also allow each DMU to become more efficient in the most suitable manner [7].

When evaluating the j^{th} DMU of a total number of k DMUs, efficiency can be calculated using the relationship

$$\theta = \frac{\sum_{r=1}^s u_r y_{rj}}{\sum_{i=1}^m v_i x_{ij}} \quad (2)$$

where

x_{ij} denotes i^{th} input value of the j^{th} DMU,

y_{rj} denotes the r^{th} output value the j^{th} DMU,

u_r denotes the weight of output parameter y_{rj} ,

v_i denotes the weight of input x_{ij}

and

m and s denote the number of input and output parameters respectively.

The DEA process maximises objective function represented by Equation 2, subject to the following constraints:

$$\frac{\sum_{r=1}^s u_r y_{rk}}{\sum_{i=1}^m v_i x_{ik}} \leq 1 \quad (3)$$

$$u_r \geq 0, \text{ with } r = 1, 2, \dots, s \quad (4)$$

$$v_i \geq 0, \text{ with } i = 1, 2, \dots, m \quad (5)$$

Equations 2 to 5 represents the original form of the CCR model [1]. In order to solve the constrained optimisation problem by conventional linear programming methods, Equation 3 is written in standard mathematical notation as follows [7]:

$$\sum_{r=1}^s u_r y_{rk} \leq \sum_{i=1}^m v_i x_{ik} \quad (6)$$

This gives rise to a simplified objective function given by

$$\sum_{r=1}^s u_r y_{rj} \quad (7)$$

with constraints given by

$$\sum_{r=1}^s u_r y_{rk} - \sum_{i=1}^m v_i x_{ik} \leq 0 \quad (8)$$

$$\sum_{i=1}^m v_i x_{ij} = 1 \quad (9)$$

$$u_r \geq 0, v_i \geq 0 \quad (10)$$

The mathematical model represented Equation 1 to Equation 10 is known as the primal model. It treats the rows of the linear programming problem as the model and seeks to maximize the output defined by Equation 7. In this paper a second model, known as the dual model, is utilized. This differs from the primal as it rather strives to minimize the input. Also, the columns of the linear programming problem are used to represent the model, rather than the rows. This method only requires a single weight in the form of λ , as input and output variables are no longer mixed [6].

Applying the dual model Equation 8 to 10 produces Equation 11 to 13, where the objective is to minimize inputs. Also, from Equation 11 and Equation 12 it can be seen that input and output variables (x and y) are not mixed, thus the linear programming model is now considered in terms of its columns.

$$\sum_{k=1}^s \lambda_k x_{ik} \leq \theta x_j \quad (11)$$

$$\sum_{k=1}^s \lambda_k y_{rk} \geq y_{rj} \quad (12)$$

$$\lambda_k \geq 0 \quad (13)$$

From a computational perspective, the dual model is simpler compared to the primal model. Since the input is being minimized, the resulting λ values can be interpreted as a hypothetical compound DMU, showing what

percentages of relatively efficient DMUs inputs can be used by an inefficient DMU to produce the same output.

3. CASE STUDY: COAL-FIRED POWER STATION

The case study is performed for a coal-fired power station commissioned in the 1960s. The station is rated for a total installed capacity of 1200MW, consisting of six 200MW units. The dataset used in the study consists of daily coal usage [ton], daily coal calorific and total moisture content values, daily fuel oil consumption [kg] and monthly generated and sent-out energy [MWh] for the timeline from 1 January 2012 to 31 December 2012.

3.1 Comparative Monthly Analysis.

In the first case study the DEA analysis is performed on a month-to-month basis, using the individual months as the DMUs. The same efficiency metric can thus be tracked over time and seasonal changes in inefficiency can be identified. The practical usefulness and interpretation of DEA results are largely dependent on the nature of the IO categories that are chosen for analysis. As the focus of the investigation is on EE performance, the following parameters are chosen:

Inputs:

- Coal consumption [kg] or [MJ]
- Fuel oil consumption [kg] or [MJ]
- Auxiliary plant energy consumption [MJ]

Outputs:

- Sent out energy [MJ]

The available dataset does not contain calorific values for fuel oil and coal calorific data is incomplete. Thus two separate analyses are performed. The first analysis uses the mass of coal and fuel oil as inputs (in tons and kilograms respectfully). The second analysis uses the calorific values for coal where available, with a monthly average when data is incomplete. Fuel oil energy is calculated using the supplied average value. Auxiliary plant energy and sent out energy are used in mega joules in both analyses.

3.2 Comparative Monthly Analysis Results

The DEA is performed using Microsoft Excel's SIMPLEX Solver add-on. The results are summarised in Table 1 to Table 3, while Figure 1 shows a plot of relative efficiency over the analysis timeline. The results show that May, August, September, November and December are the most efficient months in both analyses.

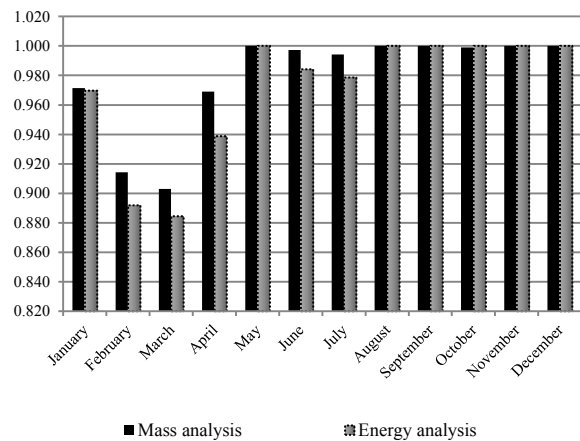


Figure 1: Relative efficiency vs. month for 2012

Table 1: Monthly efficiencies for 2012

Month	Efficiency (mass)	Efficiency (energy)
January	0.971	0.970
February	0.914	0.892
March	0.903	0.884
April	0.969	0.939
May	1.000	1.000
June	0.997	0.984
July	0.994	0.979
August	1.000	1.000
September	1.000	1.000
October	0.999	1.000
November	1.000	1.000
December	1.000	1.000

Table 2: Lambda values for mass analysis

	Lambda Values				
	May	Aug	Sep	Nov	Dec
Jan	0.200	0.251	0.550		
Feb		0.450		0.299	0.250
Mar		0.410		0.114	0.475
Apr		0.551			0.449
May					
Jun		0.957			0.043
Jul		0.866			0.134
Aug					
Sep					
Oct		0.587			0.413
Nov					
Dec					

Table 3: Lambda values for energy analysis

<i>Lambda Values</i>				
	<i>May</i>	<i>Aug</i>	<i>Sep</i>	<i>Dec</i>
<i>Jan</i>	0.311	0.119	0.570	
<i>Feb</i>		0.063	0.705	0.232
<i>Mar</i>		0.190	0.373	0.437
<i>Apr</i>		0.378	0.247	0.374
<i>May</i>				
<i>Jun</i>	0.225	0.592	0.183	
<i>Jul</i>		0.775	0.131	0.094
<i>Aug</i>				
<i>Sep</i>				
<i>Oct</i>				
<i>Nov</i>				
<i>Dec</i>				

It can be seen from Table 1 and Figure 1 that there is not a large variation in efficiency from month to month, with March 2012, the least efficient month, reaching 88.4% of the efficient months. However, by following processes used in these months the stations output can be kept at current levels, but inputs decreased by a significant portion. Table 2 and Table 3 show the lambda values for each inefficient month. This data can serve as a guide to help M&V personnel identify the efficient processes in efficient months to be emulated in inefficient months.

During the months January to April, the station’s relative efficiency is lower than in the later months. This is due to scheduled unit maintenance during these months, which reduced overall productivity of the plant. In addition, the summer months bring a greater average rainfall, increasing coal moisture content and thus lowering efficiency. The drier winter months can be seen to be more efficient. Figure 2 shows the monthly average moisture content for 2012. This data has a -54.6% correlation with the mass analysis in Figure 1, which supports the above speculations. It should be noted that no moisture content data was available the month of July in Figure 2, thus the yearly average was used.

Comparing the first analysis to the second, one can see that calorific value plays a major role in energy efficiency processes. Despite having a 98% correlation, the energy analysis’s inefficient values are significantly lower. This means that monthly inefficiencies cannot be attributed to lower quality coal. This is supported by Figure 3, which shows average coal calorific content with very little variation between months. It should be noted however that the previously mentioned inaccuracies in the data used could greatly affect the results of the analysis.

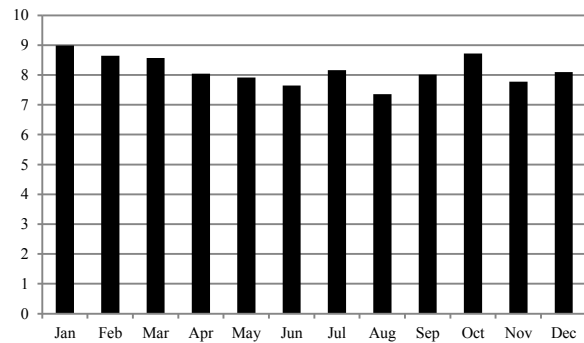


Figure 2: Average coal moisture per month

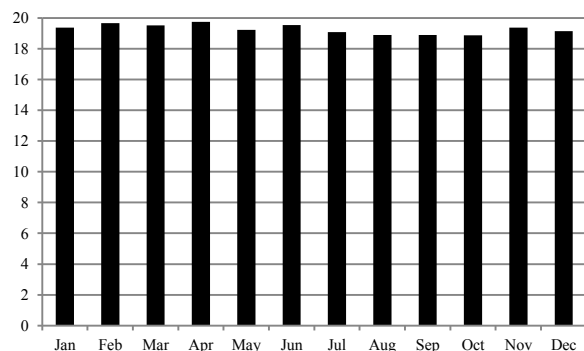


Figure 3: Average coal calorific content per month

3.3 Plant Comparison Analysis

The objective of second case study is to perform a more conventional benchmarking analysis of the target power station, by comparing the performance metric to those of other similar plants. These plants consist of 19 coal-fired power plants of varying capacity from a number of different states in the US. The plants were selected to use similar quality of coal, as the calorific content of this fuel plays a large role in efficiency. All plants in question primarily use sub-bituminous coal, which has an average calorific content of between 19 and 26 MJ per kg [8]. The plants are also, approximately, of the same age as the target station. The dataset used in the analysis ranges from 1 January 2012 to 31 December 2012 was used. This data is freely available from the US Energy Information Administration website (<http://www.eia.gov>).

Only location, capacity, fuel input and energy output are available and, as such, the analysis does not include all IO categories considered in the first case study. The following input and output parameters are used:

Inputs:

- Plant capacity [MW]
- Energy input [MJ]

Output:

- Energy output [MJ]

The input energy input is the combined input of all fuels used. The missing calorific data for the target station is handled as in section 3.1. The output energy output is the total energy supplied to the grid by the station.

3.4 Plant Comparison Analysis Results

Table 4 shows the results of this plant comparison analysis.

Table 4: Plant comparative analysis results

Plant Name	Location	Efficiency
Target plant	South Africa	0.899
Platte	Nebraska, USA	1.000
Whelan Energy Center	Nebraska, USA	1.000
Aurora Energy LLC Chena	Alaska, USA	1.000
Escalante	New Mexico, USA	0.938
Holcomb	Kansas, USA	0.986
Cholla	Arizona, USA	1.000
Oklunion	Texas, USA	0.977
Apache Station	Arizona, USA	0.942
Grand River Dam Authority	Oklahoma, USA	0.903
Limestone	Texas, USA	0.991
Joliet 29	Illinois, USA	0.940
Arapahoe	Colorado, USA	0.870
Comanche	Colorado, USA	1.000
Bridgeport Station	Connecticut, USA	1.000
E D Edwards	Illinois, USA	0.956
Coffeen	Illinois, USA	0.920
Crawford	Illinois, USA	0.901
Waukegan	Illinois, USA	0.939
Burlington	Iowa, USA	0.930

Table 4 shows 6 different plants identified as efficient, Platte and Whelan Energy Centre in Nebraska, Aurora in Alaska, Cholla in Arizona, Comanche in Colorado, and Bridgeport in Connecticut. The target plant is seen to be the second least efficient plant in the analysis. The efficiency of all plants is compared in Figure 4.

4. CONCLUSIONS

When using DEA to evaluate the performance of a single power plant over time, it is easy to identify inefficient periods (in the case of this case study, these time periods are individual months). The results give an indication of the overall effect of the various parameters that define the metric and can be evaluated. Plant processes and operations for efficient time periods can be used as

benchmark to improve the performance for inefficient time periods, thus increasing overall performance.

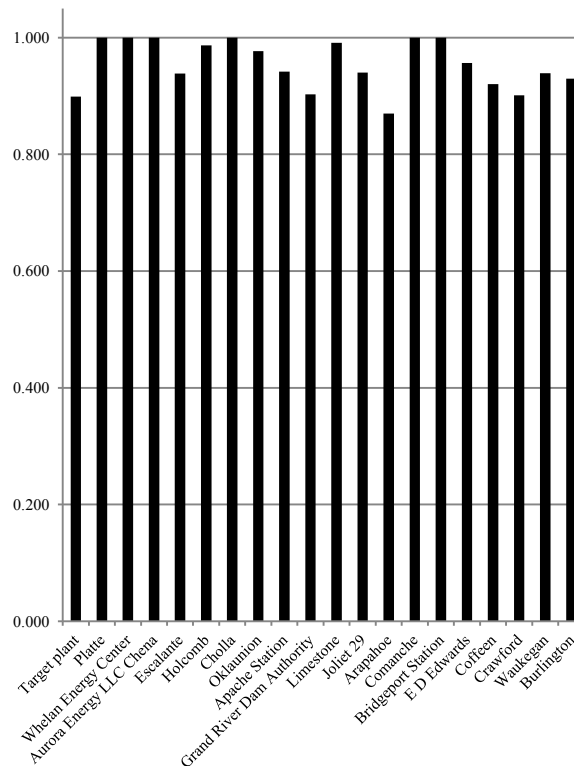


Figure 4: Relative efficiency per plant

Additional input and output parameters can be incorporated, such as CO₂ emissions, man-hours worked, etc., in order to gain insight into the effects of these parameters on the performance metric.

This paper serves as an exploratory study into DEA’s usefulness for M&V application. However, further research is required to exploit the process’s potential. While DEA is not a replacement for heat rate calculations, it can in principle be a valuable diagnostic tool in performing M&V activities and to interpret the results and difficulties associated with M&V of power station efficiency.

When using DEA to comparatively evaluate a number of plants, the sources of inefficiencies are also easily identified. The efficient plants’ practices can be considered for use in inefficient plants as a means of increasing productivity. The process can also be expanded to include additional relevant factors such as station age, station employees or CO₂ emissions. M&V teams can use the process to gain a general insight into the overall efficiency of a single plant.

DEA requires the availability of quality input data. This is often, as for the case studies performed in this investigation, a major problem in practice. It is

difficult to make an assessment of the impacts of missing and inaccurate data on the overall results.

5. ACKNOWLEDGEMENTS

The authors wish to thank Eskom for their help in the procurement of the data used in this study, as well as the Eskom Tertiary Education Programme for financial support.

REFERENCES

- [1] A. Charnes, W. Cooper and E. Rhodes., "Measuring Efficiency of Decision Making Units," *European Journal of Operational Research*, vol. II, pp. pp.429-444, 1978.
- [2] I. Or and K. Sarica, "EFFICIENCY ANALYSIS OF TURKISH POWER PLANTS USING DEA," in *Proceedings of the Fifth Asia Pacific Industrial Engineering and Management Systems Conference*, Queensland, Australia, 2004.
- [3] M. Hosseini and J. Hasanpour, "Evaluating the efficiency changes of the Thermal Power Plants in Iran and Examining its Relation with Reform using DEA Model & Malmquist Index," in *3rd International Conference on Information and Financial Engineering*, Shanghai, China, 2011.
- [4] S. Behera and P. Dash, "Performance Analysis of Coal fired Power Plants in India," in *Proceedings of the 2010 International Conference on Industrial Engineering and Operations Management*, Dhaka, Bangladesh, 2010.
- [5] S. H. D. and J. Zhu, *Service Productivity Management*, Springer, 2006.
- [6] W. W. Cooper, L. M. Seiford and J. Zhu, *DATA ENVELOPMENT ANALYSIS : History, Models, and Interpretation*, Springer, 2011.
- [7] S. Yokota and T. Kumano, "Mega-Solar Optimal Allocation Using Data Envelopment Analysis," in *EA4EPQ International Conference on Renewable Energies and Power Quality*, Santiago de Compostela, Spain, 2013.
- [8] "Subbituminous coal," *Encyclopædia Britannica, Inc.*, [Online]. Available: <http://global.britannica.com/EBchecked/topic/570576/subbituminous-coal>. [Accessed 30 10 2014].

VOLTAGE PROFILES IMPROVEMENT WITH WIND ENERGY CONVERTER CONNECTED TO A DISTRIBUTION NETWORK

Ayodeji Stephen Akinyemi * and Kehinde Awodele**

Department of Electrical Engineering, University of Cape Town, South Africa
Email: * aystevo@gmail.com, **kehinde.awodele@uct.ac.za

Abstract: The quality of power delivered to the consumers by the utility determines the functionality and performance of the most sensitive equipment or appliance. For an equipment or appliance to function and perform well, the voltage level of the distribution network must not exceed the acceptable limit or range. When DGs are connecting into the network, the voltage profile of the network may be altered above the standard limit, thus, the impacts of DGs on a network depend on the placement of such DGs in the network. The voltage profile of a network may not be influenced if the DG's power injected into the network is very small compared to the load, otherwise, if the injected power by the DGs are more than the loads connected to the network, the grid voltage of such network can exceed an acceptable range of the grid code act or international standard specification. This paper presents the voltage profile of a distribution network under static loads and the percentage bus voltage drops along the network, it investigates the impacts of wind energy conversion system (WECS) (different power rating in kVA and MVA), the penetration level, the effects of WEC location and the level of common coupling. It showcases the comparison of the impacts of WEC on the voltage profiles in determining the maximum penetration level on the selected buses on IEEE 13 test feeder using SIMULINK package in MATLAB. Based on the simulation results, recommendation are given to the utility or independently owned generating units on the suitable/wrong location of WECs in the network.

Keywords: voltage profiles, WECS, grid code, location and point of common coupling

1. INTRODUCTION

The introduction of DGs into the power system has benefits, but it causes the system to be more complicated. For instance, with large central generating units, the system operators are aware of the condition and security level of the arrangement while the situation is not applicable in case of the introduction of DGs into the network; the units are totally out of control of the system operator. For DGs with renewable energy sources like wind and solar, their productions are intermittent and fluctuating with time and it is hard to predict, which make power system planning and operation more complicated. The principal goals of the power system are the reliability of power supply and good power quality, DGs can play vital parts in reaching them. The voltage range within low and medium voltage networks of the power system determines how efficient and durable an equipment or appliances connected to the network can be [1], [2]. With the conventional generator, and small amount of DG power, voltage rise may not be a serious issue, but with the growth in the DGs penetration level in the network, voltage rise may need to be monitored [3]. In terms of network protection, there may be an economic optimisation for small DGs owners in installing a control and protective device in the course of electricity production to minimize the contribution of DGs into a fault. At that point, there is no important direct increase in the number of voltage dips with the distributed generation; otherwise, DG strengthens the grid, which can result in the number of dips experienced by the local customer being decreased. The impacts of the renewable

DGs connected to the distribution network are investigated in this paper

2. GRID CODE REQUIREMENT

With the rapid growth in penetration of wind power in the power system, a number of transmission system operators issued grid codes imposing specific requirements concerning grid support during steady-state functioning as well as grid faults or disturbances. It becomes necessary requirement for wind farms to behave as much as possible as conventional power plants to sustain the network voltage and frequency. Due to this demand, the utilities in many countries have recently built or are developing grid codes for operation and grid connection of wind farms. The aim of these grid codes is to ensure that the continued growth of wind generation does not compromise the power quality as well as the security and reliability of the electric power system [4], [5], [6]. The grid code act is also utilized by the South African power utility to determine the minimum technical and design grid connection requirements for renewable energy connected to or seeking connection to a distribution system. The compliance with this grid connection code is applicable to the DG, depending on its rated power, and the nominal voltage at the point of connection (POC).

2.1 Classification by category

The integration of WEC or DG into the South African distribution network is divided into three categories based on the size of the facility and the connection voltage.

According to the South African grid code rules [7], Table 2.1 gives details.

Table 2.1 WECs classification into distribution network

Sub-categories of Renewable power plant (RPP)	Power Range	Connect ion Voltage	Voltage limits %
A1	$0 < x \leq 13.8$ kVA	LV	-15+10
A2	$13.8 \text{ kVA} < x < 100$ kVA	LV	-15+10
A3	$100 \text{ kVA} \leq x < 1$ MVA	LV	- 15+10
B	$1 \text{ MVA} \leq x \leq 20$ MVA, $0 < x < 1$ MVA	MV	± 10
C	$x \geq 20$ MVA	HV	± 10

2.2 Grid connection of WECs

The voltage at the point of connection according to the South Africa grid connection code must be in the range of -15 % to +10 % (0.85 to 1.1 pu) for low voltage network and ± 10 (0.9 to 1.1 pu) for medium and high voltage networks around the nominal voltage [7]. This condition is put into consideration in this paper

2.2.1 WEC penetration level

The bases for choosing WEC rated power and penetration level shall be according to the WEC categories mentioned in the Table 2.1 above. Wind penetration level can be defined thus:

Wind capacity penetration level =

$$\frac{\text{Installed Wind energy capacity (MVA)}}{\text{Total load demanded (MVA)}} \times 100 \dots \dots \dots (1)$$

Penetration levels will vary as the total load demand in the network varies.

3. THE TEST SYSTEM DESCRIPTION

To demonstrate the impacts of a WEC on a distribution network, the wind energy converter to be considered in this paper is a doubly fed induction generator (DFIG) and set to voltage control mode. DFIG is a wound rotor induction generator with voltage source converter connected to the slip-rings of the rotor; it interacts with the grid through the rotor and stator terminals. This character of wind turbine has been designed to increase the aerodynamic efficiency in several ranges of wind velocities. Their electrical system is more complex than the fixed-speed wind turbines. Better power quality,

higher amount of energy extracted and less mechanical stress on the turbines are the main benefits.

IEEE 13 bus test system is considered as a standard test system to be used [8], [9], as shown in the figure 3.1, which has challenging voltage management task, as it exhibits extreme voltage issues. It is made of medium (1 kV to 44 kV) and low voltage (50 V to 1 kV). The test feeder is short and relatively highly loaded for a 4.160 kV feeder, it has several key distribution system components such as overhead lines, underground cables, distributed loads, substation transformers, step down transformer between the buses 633 and 634, mixture of constant kW and kVAr loads, capacitors bank and voltage regulator etc. Only bus 634 receives 480 V, all other buses receive 4.16 kV.

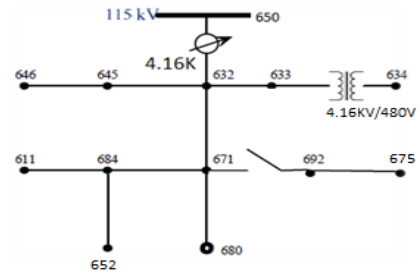


Figure 3.1 IEEE 13 Node feeder test system

4. SIMULATION

For the simulation work presented in this paper, this test system (IEEE 13-bus Test Feeder system) is modified and modelled in MATLAB/SIMULINK according to the following cases

- The unbalanced loads were made balanced (balanced network), this was achieved by extending the total loading 3.27 MW, 1.99 MVar to 3.561 MW, 2.310 MVar (total loading of 4.3 MVA) and make each load balanced, underground cables are modelled as overhead lines and bus 634 is made overloaded since is the only low voltage bus, so that WEC can be connected to the bus.
- Single and double phase lines were replaced with three-phase lines, installed capacitor bank at buses 675 and 611 are removed.
- The voltage regulator at the bus 650 is removed

4.1 Purpose of the network modification

- The network is made balanced in order to eliminate the unbalanced voltage drop, reduction in network losses and harmonic generation
- The network loading is extended to ensure that loads are connected into all the buses. Since the network is taking balance load, it is obvious that all the single and double phase lines must be replaced by the three phase lines
- The installed capacitor bank and the regulator were removed to monitor the original network nominal voltage from the substation to the farthest bus on the network without any compensation or voltage

regulation, this is because the voltage profile of the network must be drawn and monitored with/without wind power integration

5. SIMULATION RESULTS AND DISCUSSION

Various simulation cases are investigated and the results obtained are discussed below:

5.1 Voltage profile of the modified IEEE 13 node test system

The network was designed, tested and simulated in MATLAB/SIMULINK; the voltages are measured at each bus bar of the network, the results obtained are depicted in Table 5.1, which is used to plot the network voltage profile in Figure 5.1, from the voltage profile plotted, the power flow through the feeder results in a smooth voltage drop from the beginning to the end of the feeder, i.e., the voltage drops along the feeder are within an acceptable limit in compliance with the normal permissive ($\pm 10\%$) drop in the nominal voltage of any standard network and with South Africa Grid code for a distribution network except that there is a voltage dip in bus 634 which is the weakest bus. The transformer located at the bus was a step down transformer which stepped down 4.160 kV to 480 V (the load on the bus is the only load that is supplied by 480 V), it is found that the transformer was overloaded; the power rating of the transformer is 500 kVA while the load connected to the bus is 550.7 kVA. The voltage obtained at the bus is 0.8359 V or has a drop of voltage 16.41 %, which is not acceptable (less than acceptable range).

More also, there is a voltage drop (9.7 %) at the bus 652 which is the second weakest bus compared to other buses in the network, this is because, the bus 652 is connected to a huge amount of load (about 1.2 MVA) that is almost two times that of any other bus in the network. Also, the voltage drop at bus 652 may be related to the line length and load current. When the length of the network line increases, the percentage of the voltage drop will also increase, this is due to the increase in the voltage drops along the network as the power flows from the source to the terminal end of the network. Bus 680 may be expected to be the weakest bus being the farthest bus, but it is not so because the load connected to the bus is not huge (very light load, which draw little power from the network) compared to buses 634 and 652 that have peak loads and draw more power in the network (Table 5.1)

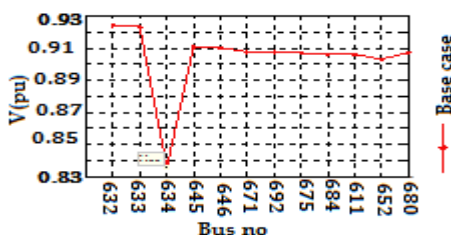


Figure 5.1 voltage profile of the modified IEEE 13 node test system without WEC

Table 5.1 buses voltage measurement

Bus Number	Base Voltage (pu)	Voltage drop (%)
632	0.9242	7.58
633	0.9232	7.68
634	0.8359	16.41
645	0.9107	8.93
646	0.9101	8.99
671	0.9076	9.24
692	0.9076	9.24
675	0.9070	9.30
684	0.9061	9.39
611	0.9060	9.4
652	0.9030	9.7
680	0.9071	9.29

5.2 Connection to the farthest bus

The impacts of the wind energy integration on the voltage profile of a distribution network are demonstrated in the simulation of a modified 4.160 kV test feeder. Different generation scenarios (WECs range of 13.8 kVA, 100 kVA, 300 kVA, 600 kVA, 1 MVA, 2 MVA and 2.8 MVA) are considered to know the impacts of WEC in the network, to investigate the maximum penetration level of the WEC in the network without grid code act violation (-10%) as stated in the sections 2.1 and to determine the impacts of WEC on the voltage profile along the feeder. Bus 680 is considered to be the point of integration into the network; this location is chosen because it is very far to the substation.

When a 13.8 kVA, DFIG (0.3 % penetration level) is connected to the network at the bus 680 in relation to the category B as mentioned in Table 2.1, to supply the local load, the impact is negligible on the network voltage profile as shown in Figure 5.2 below. This is because the ratio of the 13.8 kVA wind power integrated into the network that consist of 4.3 MVA is 1:312, therefore, more wind power is required for the network voltage profile to be improved. At 2.3 % WEC penetration level, the network profile increased slightly, but a voltage dip is still noticed on the bus 634. From 7 % WEC penetration level, decrease in the voltage drop occurred, which brings about the increase in the voltage level of the network.

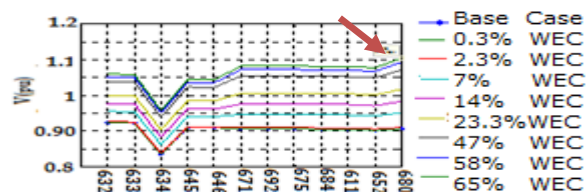


Figure 5.2 voltage profile of the farthest bus

Further increasing the injection of the size of WEC (14 %, 23.3 %, 47 %, 58 % and 65 %) penetration levels, the network profile improved; at bus 680 with 58 % injection scenario, it has an additional voltage of 0.0929 (pu) i.e, $(1.0929 \text{ pu} - 1 \text{ pu} = 0.0929 \text{ pu})$ or $(+ 9.29\%)$

which is within an acceptable range in relation to the grid code act and is the best simulation result for the bus 680. Injection of WEC to 65 % penetration, the additional voltage on that bus is 0.1041 pu or +10.41 %, which is not acceptable in relation to the grid code act ($\pm 10\%$), i.e., the bus voltage is more than 1.1 pu voltage required. But this over voltage is only noticed at the point of PCC of the WEC (bus 680), while other voltages are still within an acceptable range, meanwhile, the penetration level cannot be increased further beyond this point.

5.3 Determination and comparison of the maximum penetration level on other selected buses

Having shown in the section above that the WEC can improve the voltage profile of a distribution network, it is necessary now to determine and compare the integration of WEC into different buses of the network to really know the bus that can take the highest WEC penetration level without violating the grid code act, when WEC is connected to buses 633, 652, 675, 611 and 646. The simulation results are depicted in the figures 5.3 (a) to (e) below. The maximum penetration level at each of the buses are shown in Table 5.2

Table 5.2: Penetration level at each bus

Bus no	Highest penetration level without grid code violation	Figure 5.3
633	81 %	(a)
652	93 %	(b)
675	70 %	(c)
611	70 %	(d)
646	70 %	(e)

Buses 675, 646, and 611 accept 70 % WECs penetration level; beyond this may lead to the grid code act violation. Integration of WEC into a distribution network by selecting a different location within the network bus confirm that its voltage profile can be improved, meanwhile, the penetration level may vary depending on the type of load connected to a particular bus (light or heavy load), and the distance of the bus bar from the substation. Some of the benefits of choosing the weakest bus for WEC integration in any network is that, voltage dips can be minimized, voltage drop can be reduced, more WECs penetration can be attained without the fear of an over voltage and the weaker network can be strengthened. Buses 633 and 652 (Figures 5.3 (a) and (b)) have the highest penetration levels of the WEC in the network. However, as observed in the previous section, bus 680 which is the farthest bus takes only 65 % WEC penetration level which is lower compared to buses 675, 646, 611, 652 and 633. This may be because it is lightly loaded.

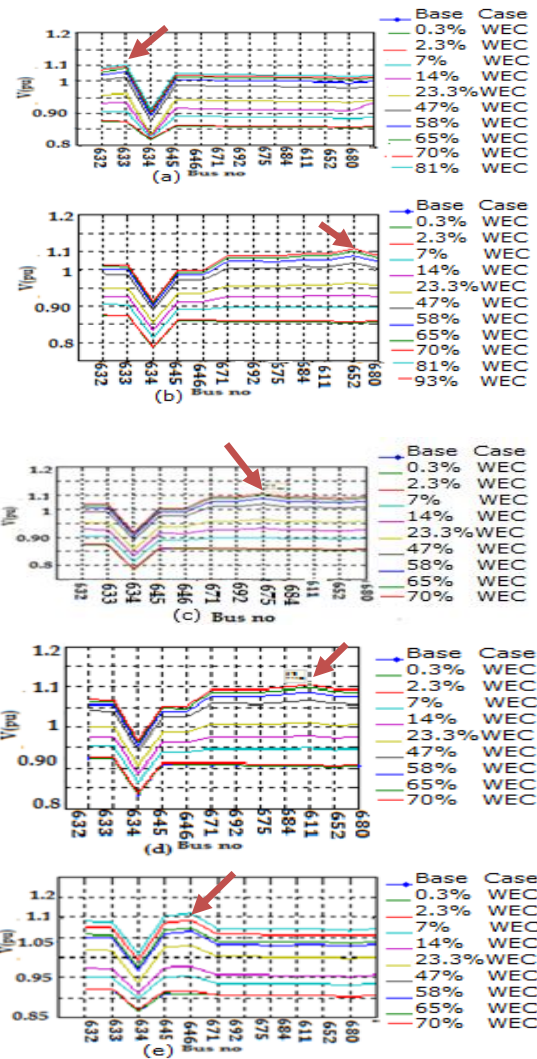


Figure 5.3: System voltage profile at different penetration level with WECs connected (a) bus 633 (b) bus 652 (c) bus 675 (d) bus 611 (e) bus 646

Immediately a WEC is connected to a particular bus in a network, increase in the penetration level of the WEC will bring about an increase in voltage and the active power generated at the bus. As a result, it will turn the weak bus to an active bus compared to any other buses on the network. This increase in voltage at the point of common coupling should be monitored so that it does not go above the permissible range of the grid code act and the WEC should be designed in such a way that existing levels of voltage variations do not lead to premature failure or disconnection of the unit [11]. In the same vein, an increase in the voltage at the PCC should allow easy flow of power in both directions in the network.

5.4 Impact of location of WEC on a low voltage network

The previous section showed in details, the WEC penetration level comparison at different buses. In this section, the impacts of WEC location shall be considered. Bus 634 is the only bus that received low voltage (low voltage is within 50 V to ≤ 1 kV), and the maximum

WEC integration into the low voltage network cannot more than 1 MVA as already stated in the Table 2.1 above. Bus 634 has the total loading of 550.7 kVA and has the highest voltage drops (13.41 %) according to the voltage profile in Figure 5.1 and Table 5.1, which can be regarded as the weakest bus in the network, the transformer of the bus is overloaded, the power rating of that transformer is 500 kVA.

When WEC of different power rating (13.8 kVA, 100 kVA, 300 kVA, 600 kVA, and 1 MVA) is connected to the bus, the impact of WEC till 7 % penetration level connected to the bus is accepted in relation to grid code act, but the impact is slightly felt on all other buses in the network (Figure 5.4). When the penetration level exceeds the 7 %, voltage rise occurs (The receiving end voltage on the bus is more than the sending end voltage therefore, the load connected to the bus will behave as a capacitive load), between the buses 633 and 634 which result in an unacceptable voltage profile and the grid code act is violated (Figure 5.4 indicated by the green arrow) while all other bus voltages in the network remained unaffected. This occurs as a result of reversed power flow, which is a function of the power generated by the WEC and the short-circuit power of the network at the point of interconnection. This reversed power flow effect gets stronger as the WEC injects more active power into the network, by this investigation, which means that bus 634 is not the best location for WECs integration, as it cannot accept more WECs power. Bus 652 can be considered to be a very good location of WEC integration because it can take more WEC penetration level without the fear of over voltage. Also buses 633,675, 680,646 and 611 can also be considered as a point of WEC integration into the network, but in this case, it can be so when two or more WECs are to be connected to the network either by the utility or independently own generating units.

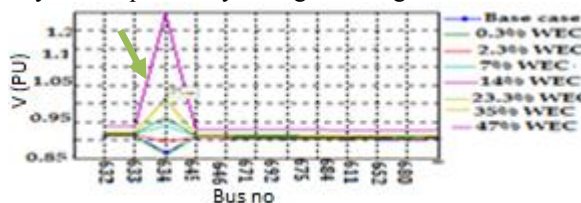


Figure 5.4: Bus 634 voltage profile with WECs penetration level

5.4.1 Effect of WECs penetration level on bus loading at low voltage bus

If bus 634 is to be considered for point of WEC integration, the rated power of such WEC must not be more than 500 kVA, any wind power more than that, a voltage rise may occur which can cause an unnecessary damage to the power equipment and the load connected to the network. Connection of WEC to a lightly loaded network can cause reverse power flow, which can cause the voltage at the WEC connection point to rise and the supply voltage of the customers connected to nearby WEC units may start to rise as well. As a result of this effect, energy flow may be interrupted, leading to rapid

buildup of heat, machine over speed, damage the transformer coil, insulation breakdown, large over voltage and tripping of multiple generators can occur when the level of the voltage quality variation (imbalance) reaches [2], [10]. This voltage rise is a steady state effect that depends on the resistance and the reactance ratio, load feeder and the power injection by the WEC units.

WEC will trip for extreme levels of voltage quality variation and severe event in the network, the generator connected to the same part of the network will experience a similar disturbance thereby resulting into the tripping of multiple units [11]. Furthermore, a higher level of over voltage can cause faster power component aging, immediate disconnection of the generation from the network and damage to the customer equipment.

5.4.2 Voltage rise at the bus 634

- Inability of the power to flow back to the rest of the network because there is step down transformer between buses 633 and 634.
- The WEC power injected into the bus is more than the load demanded or connected to the bus

5.5 Methods of keeping the voltage within an acceptable limit in a distribution network

- To avoid voltage rise problem, the Voltage of a distribution network can be kept to the allowed limits without violating the lower voltage limit by reducing the primary substation voltage, as this can work well for those feeders with the DGs connected to the same substation. But without the DGs, it may result into too low voltage at the substation; while in some cases, the voltage can be reduced to some extent without violating the lower voltage limit.
- By increasing the conductor diameter of the specific feeder to which the DG unit is connected. It is possible when the distribution grid has to be extended due to the connection of the DG units [12].
- Reactive control in the network is also an alternative method. DG units, e.g. synchronous machine can absorb reactive power which helps to reduce the voltage rise or by using compensation device such as STATCOM.
- Generation curtailment approach [13]

5.6 The impact of WEC at the point of common coupling in the distribution network

Haven successfully investigated the impact of WEC (different power ratings) on a voltage profile of a distribution network; the comparison has been made between different buses in relation to the penetration level, grid code act violation, implications of choosing the weakest and wrong location for WEC integration into the network. This section investigates the impact of WEC

at the point of common coupling or point of connection of WEC into the network. From the simulation results, in the figures 4.3 shown above, it can be noticed that the voltage on the bus where WEC is connected is slightly increased or higher than any other voltage of the bus of the network, but they are still within an acceptable range in relation to the grid act code as indicated by a red coloured arrow in each graph. This is because the integration of WEC at any point of common coupling to the network will inject active and reactive power at that point, there is no doubt that the voltage at the point of common coupling will be slightly more than any other bus that is not taking as the POCC

6. SUMMARY AND FUTURE WORK

In general, it can be seen that the connection of WEC to distribution network have the potential benefits of improving and supporting the voltage profile of the network. It also shows the negative impacts that the ranges of WEC penetration levels can have on a distribution network. The voltage profile graphs also revealed that at any point of WEC integration (point of common coupling) into a network, the voltage of that point is usually higher than the voltage of all other buses in the network. It is also observed that a small amount of WEC penetration level, e.g., below 14 % (500 kVA) installed in the wrong location (Figure 5.4) can cause unacceptable voltage profiles, at the same time very large amount of WEC that is close to 81 % penetration level installed with adequate strategy improved the voltage profile without grid code act violation and enabled acceptance of good operating condition (see Figure 5.3 b). It is found that the over generation or higher penetration level of WEC in a localized area can cause an overvoltage or a voltage rise, which may cause the tripping of the network protection.

The original voltage profile of any network should be a guide in determining the point of connection and strictly followed by the utility before DGs are considered for integration, which requires the cooperation between the network operators and the independently owned generator units. The impacts of WEC under variable loads, additional control mechanism for DG shall be considered for future work and research.

7. REFERENCES

- [1] C.G. Carter-Brown and C.T. Gaunt: "Model for apportionment of the total voltage drop in combined medium and low voltage distribution feeders", *South Africa Institute of Electrical Engineers*, vol. 97, No 1, pp. 66-73, March 2006.
- [2] P.K. Ainah and . K. Folly: "Voltage rise issue with high penetration of Grid connected PV", *international federation of Automatic control*, Cape Town, pp. 4959-4966, 2014.
- [3] M.A. Mahmud, M.J. Hossain, and H.R. Pota: "Analysis of voltage rise effect on distribution network with distributed generation", *IFAC World*

Congress, Italy, pp. 14796-14801, 2011.

- [4] W. Qiao and R.G Harley: "Grid Connection Requirements and Solutions for DFIG Wind Turbines", *IEEE Energy 2030 Conference*, pp. 1– 8, 2008
- [5] I. Erlich, F. Shewarega, C. Feltes, F.W. Koch, and J. Fortmann: "Offshore Wind Power Generation Technologies", *IEEE Proceedings*, vol. 4, pp. 891 - 905, 2013.
- [6] I. Erlich and U. Bachmann: "Grid code requirements concerning connection and operation of wind turbines in Germany", *IEEE Power Engineering Society General Meeting*, vol. 2, pp. 1253 - 1257, 2005.
- [7] B. Magoro and T. Khoza: "Grid Connection Code for Renewable Power Plants Connected to the Electricity Transmission or Distribution System in South Africa", *RSA Grid Code Secretariat*, Vsn 2.6, 2012
- [8] W.H. Kersting: "Radial distribution test feeders", *IEE Power Engineering Society Winter Meeting*, vol. 2, pages 908 - 912, 2001.
- [9] W.H. Kersting: "Radial distribution test feeders" *IEEE Transactions on Power Systems*, vol. 6, issue 3, pages 975 - 985, 1991.
- [10] R. Schainker, "Effects of Temporary Overvoltage on Residential Products", Electric Power Research Institute, California, USA, Final Report, pp. 6-11, March 2005.
- [11] M. J. Hossain, H. R. Pota, M. A. Mahmud: "Analysis of Voltage Rise Effect on Distribution Network with Distributed Generation", *18th IFAC World Congress*, pp 14796 -1480, 2011
- [12] E.J Coster, J.M.A Myrzik, B. Kruimer and W.L Kling: "Integration Issues of Distributed Generation in Distribution Grids", *JPROC*, vol. Vol 99, pp. 28-39, 2011
- [13] H.J Math Bollen and F. Hassan: *Integration of distributed generation in the power system*, John Wiley & Sons, Canada Inc, 2011, chp. 6, pp 223– 266.

8. APPENDIX

Load parameters: bus 632 = 200 + j 116 kVA, bus 633 = 170 + j 100 kVA, bus 634 = 480 + j 270 kVA, bus 645 = 170 + j 110 kVA, bus 646 = 230 + j 132 kVA, bus 671 = 300 + j 200 kVA, bus 692 = 170 + j 151 kVA, bus 675 = 375 + j 202 kVA, bus 684 = 118 + j 93 kVA, bus 611 = 270 + j 80 kVA, bus 652 = 950 + j 770 kVA, bus 680 = 128 + j 86 kVA. **Transformer data:** substation 115/4.16 kV, X/R is 8/1, in line transformer is 4.16 kV/480 V, X/R is 2/1.1, and frequency is 50Hz. **DFIG data:** 13.8 kVA, 100 kVA, 300 kVA, 600 kVA, 1 MVA and 2 MVA, PF = 0.98, stator resistance = 0.00706 Ω, stator inductance = 171 mH, magnetizing inductance 2.9 H, rotor resistance 5 m Ω, rotor inductance 0.156 H, pole pair of 0.013

Wind capacity penetration level =
$$\frac{\text{installed Wind energy capacity (MVA)}}{\text{Total load demanded (MVA)}} \times 100 = \frac{0.1}{4.3} \times 100 = 2.3 \%$$

AN INTELLIGENT GEYSER WITH WI-FI ACCESS TO SUPPORT DEMAND-SIDE MANAGEMENT

J.W.K. Brown and M.J Booyesen*

* Department Electrical and Electronic Engineering, Private Bag XI, Matieland 7602, South Africa.
Email: mjbooyesen@sun.ac.za

Abstract: In the current climate of energy shortages and attempts to reduce electricity consumption, demand-side management has proven to be effective and popular. One implementation of demand-side management has been to provide the end-user with control over the ubiquitous household water heater (called geysers in South Africa). This paper presents a novel way to interact with water heaters, in which water heater control and monitoring is provided on a website that is accessible through a Wi-Fi hotspot interface. Both of these are hosted by the processor that controls electricity supply, tank temperature, and water supply; and monitors electricity consumption, water consumption, inlet, outlet and tank temperatures. The proposed system also provides protection against inevitable mechanical failure of the water heater, by detecting leaks and bursts, and by stopping water and electricity supply in such scenarios. This paper shows that the proof of concept is realisable in terms of cost, functionality, and energy savings.

Key words: Demand-side management, intelligent control, user interface, water heater, geyser, power saving.

1. INTRODUCTION

The demand for electricity in South Africa is rising and rapidly approaching generation capacity. Incidences where demand had the potential to exceed generation capacity have been evidenced in recent years by the institution of rolling blackouts, in an effort to maintain grid stability [1]. Currently, at peak load, South Africa is operating at a surplus capacity of just 8% - just over half of the typical international minimum of 15% [2]. When power generation plants are taken offline for necessary maintenance or repair, this can drop even further.

This situation has resulted in Eskom having to take measures to increase the generating capacity, in order to maintain stability of the power system. These measures included the reopening of power plants that were mothballed in the 1990s, the construction of open cycle gas turbine plants, and the construction of two new power stations. Medupi and Kusile stations add a capacity of 9564MW to the national grid, an additional 21.6% [3] [4]. However, all of these methods take time to implement. Returning a mothballed power station to a completely operational state takes approximately three to four years. While the construction of a new coal power station typically takes eight years [3] [4].

Eskom has instituted the shorter term solution of Demand Side Management (DSM) in the interim. DSM can be summarised as reducing the demand for power through a change in consumer behaviour. This is achieved by causing the consumers to use less power by providing them with the incentive and means to do so. The incentive is provided through the implementation of power tariff increases of 78% between 2008 and 2011, to fund the the production of the aforementioned additional generation

capacity. Additionally, power tariffs are set to further increase by 8% per annum [1]. So far, implementations have included the installation of Compact Fluorescent Lights (CFLs) and solar water heaters in many homes and workplaces, as well as pilot schemes to reduce power use during times of peak load.

Applications that aid in the implementation of DSM have the greatest potential to alleviate the situation of excess demand in the short term. Water heating is the area of greatest electricity consumption in the residential sector. It offers the greatest opportunity for overall power usage savings and peak power use reduction [5]. Applications that focus on this area will offer the greatest per-unit return.

One of the suggested implementations of DSM has been to retrofit a control system to the to existing water heater installation [6]. Water heating contributes 35% of residential electricity consumption [5], and is mostly uncontrolled. The solution proposed in [6] provides both control and metering information to the user. This monitoring and control enables the user to implement usage strategies that make more efficient use of electricity. Another advantage of targeting this source of power use is that water heaters have the ability to store energy in the form of heat. This can be leveraged to shift power use away from times of peak load to times of typically low consumption, 2AM for instance, which reduces the peak load on the the power system.

1.1 Contribution

This paper presents a novel way to interact with the ubiquitous household water heater control system, such as the one in [6], and also proposes novel control strategies that leverages the novel interface. The system allows the

user to interact with the water heater through an interactive and user-friendly web site, hosted by a Wi-Fi access point (hot-spot) that is hosted by the control system. The user connects to the Wi-Fi hot spot with any Wi-Fi enabled device (e.g. smartphone, tablet, laptop) in-range of the water heater, and uses any browser to access the features of the geyser that are presented as an interactive web site. The web site gives the user control over the element state (on/off), set temperature, control scheme, and water supply (on/off). The user is also able to monitor various indicators, including element state (on/off and power), water flow rate (litres/minute), tank temperature, inlet temperature, outlet temperature, daily power consumption, daily water consumption.

Through providing this interface, the user is empowered to apply their own supply-side management in an easy way with immediate feedback. The results from the tests of the unit and the unit itself demonstrate both the feasibility and the benefits of intelligent control.

The rest of this paper is structured as follows: Section 2 summarises the research that was done to contextualise the work done in this paper. Section 3 records the design process that was followed to create the unit. Section 4 provides the systems tests results as applied to the water heater used. Finally, in section 5, a conclusion is reached as to whether the unit met the objectives and possible further work that could be done is suggested.

2. RELATED WORK

The authors of [6] analysed the data from water heater control units installed in several homes to determine the potential energy savings of installing a control unit. The energy savings from operating a geyser on a timer was proven theoretically and validated empirically. It was found that, not only does the installation of a control unit result in reduced energy usage, it also changes the behaviour of the user. This behavioural change results in a further reduction in energy usage and is driven by the feedback that a control module can provide [6]. The control unit used for this study did not include a method of measuring the water consumption and did not include ease of installation and user interaction as a focus. Both of these could adversely affect the wide scale acceptance of the unit.

In [7], Müller et al. presents the implementation of a water consumption measurement and control solution, to enable remote utility monitoring and control. This was done through the inclusion of a solenoid valve in the water supply and the design of an orifice flow meter. It was determined that the meter operated to within 3% accuracy and provided an accurate indication of water consumption rates [7]. However, the orifice flow meter uses a pressure differential to measure water flow rate, which makes it unsuitable for volumetric metering (any meter inaccuracies will integrate over time). Moreover, the unit was not specifically designed for geyser control but

rather as a proof of concept for the control and monitoring of general utilities.

Nel et al. [8] implemented a smart phone application that enabled users to monitor the status of a water heater with the aim of informing the user of their historical and near real-time water consumption. The application takes the form of an application for Android-enabled devices. The application is highly intuitive and the custom GUI presents the information in a manner that is easy to assimilate [8]. A drawback of this system is that it relies on pre-installed hardware and the assimilation of separate monitoring systems which increases the complexity and cost. Moreover, the system relies on cellular networking and cloud-hosted services.

3. SYSTEM DESIGN

This section describes the system presented in this paper. The system diagram shown in figure 1 shows the relationship between the various parts of the system, hereafter referred to as the intelligent geyser module.

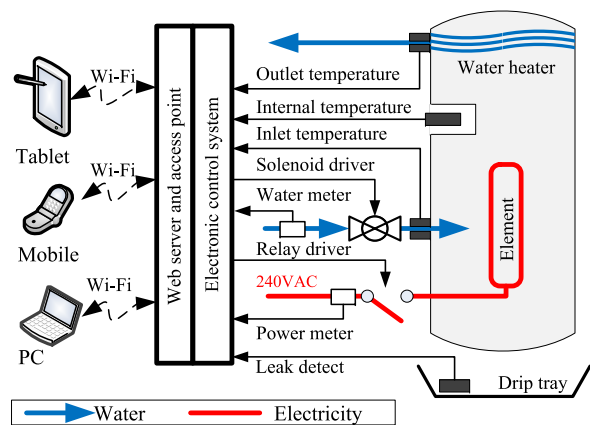


Figure 1: System diagram

3.1 Processing

The Beagle-bone Black was chosen to provide the necessary processing capacity for the intelligent water heater module. The Beagle-bone Black is a single board computer that is approximately the same size as a credit card. It typically runs a version of the Linux kernel. The Debian operating system was used. Hardware Input/Output functionality is provided by two pin headers, which include dedicated serial and analogue input pins.

3.2 Sensors

Temperature sensors that provide analogue output (10 mV for degree Celsius) were chosen as the temperature sensor to measure the temperature of the water heater at the inlet, outlet and internally. The sensors were secured to copper pipe at the inlet and the outlet to the water heater and to the rear face of the element flange. In the case of this system the legs of the sensors were electrically insulated

before the sensors were secured. This output monitored by the Beagle-bone.

The water meter chosen to measure the water usage was the Elster Kent V100T PSM volumetric water meter [9]. This meter has an optional reed switch that outputs a pulse every half litre. These pulses were input counted by the Beagle-bone and were used to determine the water flow and usage.

The power was measured by means of a specialised system-on-chip measurement IC which communicates with the Beagle-bone via a serial connection. The power measurement IC (PMIC) used for the measurement was the CS 5490 by Cirrus Logic. This PMIC is powered by 3.3V and can accurately measure voltage, current and power factor [10]. Complete isolation from the 220V AC supply was desired for the PMIC, so the voltage and current were measured through voltage and current transformers respectively. This unit draws its power from a 3.3V voltage rail on the Beagle-bone and communicates with the Beagle-bone via a serial connection.

A switch was included that is used to detect structural failures of the water heater. In its current form, it is manually activated but can be easily adapted to close if a burst or leakage is detected in the drip tray. The switch is connected to the Beagle-bone. Closing the switch activates the water cut off valve, cuts off power to the element and alerts the user by means of the user interface.

3.3 Actuators

The element was controlled using a solid state relay from ECE [11]. A drawback of using solid state relays is that they can overheat if not properly cooled. To provide sufficient cooling the relay was bolted to an aluminium heat-sink. As an additional protection measure the relay was fitted with a thermal fuse. The fuse is placed in series with the control signal to the relay and fastened to the heat sink to be at the same temperature as the relay. The necessary 4V and current to switch this relay and the mechanical relay used to switch the solenoid valve, was provided by means of a Darlington pair switched by one of the general Input/Output pins on the processing unit.

Water flow control was implemented using a valve activated by a solenoid. The valve requires a 24V AC voltage in order to be switched on. This voltage was provided by the voltage transformer that was used as part of the power supply for the system.

3.4 Power supply

The Beagle-bone and the much of the circuitry associated with the sensing and actuation require a power supply of 5V to operate. The power measurement IC (PMIC) requires 3.3V and a scaled AC voltage to measure. Finally, the solenoid valve requires 24V AC to operate. The power supply was designed to supply all the required voltages

in such a way that additional supplies will not be needed and the intelligent water heater module can draw its power from the supply for the water heater itself.

3.5 Software

The programming language chosen to implement the control system was JavaScript. This was done for several reasons. The first of these was the presence of several libraries and modules that would be invaluable in the development of a web server that would also have the ability to manipulate the hardware on the Beagle-bone Black.

3.6 User interface

The user interface for the unit was provided by means of an interactive website hosted on the Beagle-bone and accessed through a Wifi access point created by the module. The wireless access point was implemented by using the TPlink Wireless N Nano Router. The router was connected to the Beagle-bone via an Ethernet cable and supplied with power via a USB cable connected to the USB port on the Beagle-bone.

The website for the UI was implemented in three pages. The pages were Status, Graphs and Control panel. These pages were written in html 5. JavaScript was used to provide dynamic content and communication with the server.

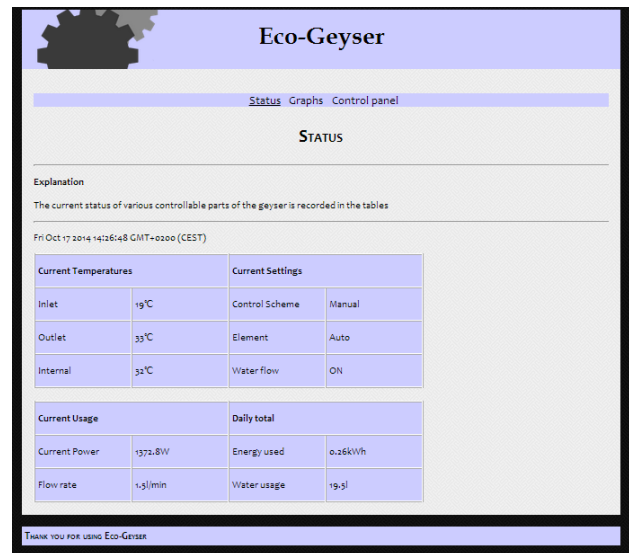


Figure 2: Status page of the website

The status page was designed to give the user an indication of the most important parameters of the intelligent water heater system at a glance. These parameters are current values being measured and the active control scheme. The three temperature measurements, current water and power usage and daily totals for water and energy usage are given. This page can be seen in figure 2.

The Graphs page displays the current temperature values, water usage and power usage. For each data point the graph indicates the value and the time at which the value was recorded. This will save the user from having to determine the time that the datum was recorded using the update interval. This page is shown in figure 3.



Figure 3: Graphs page of the website

The control page presents the user with the option to select one of the three different control schemes; Manual, Temperature and Eco. The user is also given the option to override control of the geyser element - turning it either on or off. The water cut off control is also available on this page. This page is shown in 4.

3.7 Control schemes

The three control schemes available to the user are Manual, Temperature, and Eco.

Manual control places all control of the heating element



Figure 4: Control panel page of the website

of the water heater with the thermostat. Water heater operation in this mode is identical to that of a water heater without a control module. The only benefit of the intelligent water heater module in this mode is the feedback that it provides.

In the Temperature control scheme, the control module cuts power to the element when it reaches a desired temperature. The user can set the desired temperature on the interface.

The Eco scheme operates in the same way as the Temperature Control scheme with the addition that users are able to specify a times at which they desire hot water. The system will then determine when the water heating needs to begin to provide hot water at the desired time and only switch on at that point.

3.8 Demonstration unit

Once completed the system was installed on a ten litre geyser as a test and demonstration set up which can be seen in figure 5.

4. RESULTS

The test and demonstration set up was used to test the performance of the unit. Various aspects of the unit were tested: the accuracy of the sensors, the potential energy savings for the given test water heater, power usage of the system, and finally we give an estimate of the cost of the system.

4.1 Sensor tests

The power measurement and temperature sensors were tested against the measurements obtained using a commercially available power measurement unit and



Figure 5: Control module installed on demonstration and test setup

thermometer respectively. From this test it was determined that the Power measurement was accurate to within 3% accuracy and the temperature measurement was accurate to within 9%. As a comparison the built in thermostat of the water heater was only accurate to within 5%. The reason for the inaccuracies of the temperature sensors is that they are decoupled from the water. These inaccuracies can, however, be overcome by modelling the heat transfer between the water and the sensor, to accommodate the differences.

According to the SABS, the water measurement unit is accurate to within 2% at the flow rates experienced.

4.2 Power saving tests

The potential of the unit to save power was tested by comparing the consumption of the unit under the Manual control scheme with the consumption when controlled by the Temperature and Eco control schemes. The Temperature control scheme was tested at a 15°C reduction in temperature from nominal. This resulted in a 30% power saving during a single heating cycle. Similarly, a timed test of the Eco control setting at nominal temperature resulted in a 30% saving in power when compared to the consumption of the unit under Manual control.

The results of these tests, particularly the second test, are highly dependent on several different factors; size of the geyser, use cycle, hot water consumed during the use cycle, etc. However the results are more than sufficient to prove that an Intelligent water heater unit such as this has the potential to affect significant power savings.

4.3 Power use

The power consumed by the control module alone is approximately 9 W when the unit is under power, hosting the access point, measuring the power and water flow, and monitoring the three different temperatures, which is roughly 5% of the daily consumption of a household water heater. The system can be significantly optimised, by reducing the processing power of the Beagle-bone black, and by using switch-mode regulators. The power consumption increases to approximately 24 W when the solenoid valve controlling the water flow is activated. It is therefore recommended that a normally open water flow control is implemented in future, to further save energy.

4.4 Unit cost

The prototype module, which can be reasonably expected to be compatible with any domestic geyser unit, was assembled for a price of approximately 2250 ZAR. If components were to be sourced in bulk and more cost effective suppliers were located, this figure could drop to an estimated price of 1550 ZAR.

This initial outlay, even with the added installation cost, is expected to be recovered in the first year of operation in the form of reduced electrical bills. A deliberately pessimistic test designed to isolate the effect of reducing the operating temperature in a water heater resulted in estimated savings of 2300 ZAR over an operation period of a year.

5. CONCLUSION

Further work that could be done on the intelligent water heater module could include the following. Wi-Fi access to the unit could be provided using a USB dongle instead of using a router. This will make the unit more cost effective and reduce the footprint of the unit. Additionally, data logging could be implemented in order to provide the user with monthly or even yearly totals for power usage.

Conversely the unit could be simplified - if the user interface is modified control could be provided by a micro-controller. This would provide a smaller, cheaper unit at the expense of the user interface but theoretically none of the functionality. The user interface would be provided by means of a GSM modem which uploads the data to a central server. This would enable the user to control the unit as long as they have internet access. This adaptation is currently under development.

REFERENCES

- [1] N. Fisher, “Balancing South Africa’s Energy Poverty and Climate Change Commitments,” 2014.
- [2] Eskom. Load management: Surplus capacity. [Date Accessed: 2014/10/06]. [Online]. Available: http://www.eskom.co.za/Whatweredoing/ElectricityGeneration/LoadManagement/Pages/Surplus_Capacity.aspx
- [3] B. Majola, “Newly re-opened Grootvlei Power Station contributes to keeping the lights on,” 2013.
- [4] Eskom, “COP 17 fact sheet: Kusile and Medupi,” 2011.
- [5] S. de la Rue du Can, V. Letschert, G. Leventis, T. Covary, and Xia, “Energy efficiency country study: Republic of South Africa,” 2013.
- [6] M.J. Booyesen, J.A.A. Engelbrecht, and A. Molinaro, “Proof of concept: Large-scale monitor and control of household water heating in near real-time,” in *International Conference of Applied Energy: (ICAE 2013)*, Jun 2013.
- [7] R. Müller and M. Booyesen, “Household electricity and water monitor and control with cellular communications and web interface,” in *South African Universities Power Engineering Conference (SAUPEC)*, Jan 2014.
- [8] P.J.C. Nel, M.J. Booyesen, A.B. van der Merwe, “ICT-enabled solutions for smart management of water supply in Africa,” in *International Conference on the Use of Mobile Information and Communications Technology in Africa (UMICTA 2014)*, Dec 2014.
- [9] Elster Kent Metering, *ELSTER KENT V100T PSM Volumetric Water Meter*, 2009.
- [10] Cirrus Logic, *Two Channel energy measurement IC CS5490*, 2013.
- [11] ESR, *Solid state relay*, 2002.

DESIGN OF AN INTELLIGENT CONTROLLER FOR A RENEWABLE ENERGY EFFICIENT BULK STORAGE TANK

W.A. Pelser* and R. Gouws*

* North-West University, School of Electrical, Electronic and Computer Engineering, Potchefstroom, Email: 22704515@nwu.ac.za

Abstract: The national electricity supplier in South Africa is experiencing difficulty in providing the required electricity, due to compliance with environmental regulations and the continuous price increase of commercial fuels. Making use of renewable energy solutions and energy efficient systems in everyday applications would address this problem. This project focusses on cooling systems, and illustrates an energy efficient cooling system by making use of a pre-cooler for a bulk storage tank. The cooling tank uses thermoelectric cooling modules (TECMs) to cool the milk before it is added to the actual bulk tank, and is controlled by a programmable logic controller (PLC). A small scale model of an actual tank was used to perform tests, which indicated the abilities of the cooling system. Further Solidworks® simulations were done by implementing the measured results, where after it was decided to make use of a pre-cooler, instead of adding the system to a traditional cooling system. A solar power system to power the TECMs was also designed by making use of PVSyst® simulations.

Keywords: renewable energy; energy efficiency; PLC; TECM; bulk storage tank; cooling system; solar power design.

1. INTRODUCTION

South Africa has been reported to be entering a dark age in terms of the availability of electrical energy, resulting in regular and unexpected power outages [1, 2]. By implementing more energy efficient systems in everyday life, and additionally making use of renewable energy sources, a great deal of the strain to provide electricity can be relieved from Eskom.

This study focuses on making cooling systems more energy effective, and it was decided to demonstrate such a system by making use of a bulk tank's cooling system, used on dairy farms. The lifetime of the milk that is stored in the tanks is shortened by power outages, causing losses for the farmer. The cost of electricity for cooling the milk and keeping the temperature constant is another problem for the farmers. These increased costs are a great threat to the agricultural sector, as the number of dairy farmers in South Africa has decreased by about 5 000 in the past 10 years [3, 4]. A solution which reduces the cost of providing milk, and simultaneously reduces the strain on the national electricity supplier to provide electricity would be a promising development in the field.

There are already several cooling methods available for use in bulk tanks which works very sufficiently, but not necessarily energy efficiently. It was thus decided to make use of TECMs as the cooling mechanism and testing it as the sole cooling device in a small-scale model of an actual tank. TECMs have also been used as part of an air-conditioning system in a previous project in [5], and a TECM holder for vaccines in [6]. Further relevant research that has been done with regards to this project is all of the research on developments in the solar power industry. Results from such research are used to design the solar power system needed to operate the TECMs in the cooling system.

Past research has focused on the use of cooling units and making it more energy efficient, as well as on renewable energy sources. The research discussed in this article focuses on the combination of all of the different technologies, and makes use of practical tests on a small scale to validate simulation results before making final assumptions. The PLC is also used as a control device, which is not used in traditional milk cooling systems. The farmer will benefit by this, as it intelligently controls the energy sources for TECMs, as well as ensures that the TECM does not use unnecessary power. The PLC will further measure the capacity of the tank's content, ensuring accurate measurements.

Against this background, it is seen that the main problem to be addressed is the implementation of energy efficient products in everyday life, with support from renewable energy sources. This will be done by investigating generally used cooling systems, with specific focus on bulk tanks used in dairies. Research in this field would thus benefit the dairy farmer, as well as the agricultural sector of South Africa. The design of the intelligent, energy efficient bulk tank was done by first building a small-scale model of an actual tank, and performing various tests on it to verify the simulated results. These results were used in further simulations to design the actual tank, while a solar power system was also designed for this system. The modified system making use of the TECMs and solar power has to be compared to the traditional cooling system of a bulk tank, in order to observe its effect. It is important to find the balance between cost and effectiveness of the TECMs, and to determine up to which point its implementation would still be useful and economically feasible.

The remainder of this paper will discuss a literature review of some of the main components that were used in the system, as well as the methodology that was followed

in the pursuit of finding a solution to the stated problems. The results obtained from testing the small scale model and the design decisions made from it will then be given, followed by a discussion summarising the findings of the study.

2. LITERATURE REVIEW

This literature review will only highlight the main critical components that were used in the design of the system. These components are the renewable energy source, controller, and cooling device. Other components that were also investigated in the original literature study for this project is the storage batteries, charge controller, additional energy source, holder, temperature sensors, and liquid level sensor. The literature study investigated a variety of different products that are available for use as a certain component in the system. This literature review will, however, focus only on the products that were chosen for each component, and will thus not discuss all of the alternative options.

2.1 Renewable energy source

South Africa as a whole has been reported to be responsible for approximately 2% of the greenhouse gas emissions in the world, even though it only has about 1% of the population [7]. This emphasises the need for the implementation of more renewable energy sources in the country. The intended operating environment and implementation of the energy source also has to be considered, implying that the choice is not only made by choosing the most cost-effective and environmentally-friendly solution. For the environment of a dairy farm, and the relevant size of the system, it was decided that a solar power solution would be the most effective choice.

Figure 1 shows the global horizontal irradiation map for South Africa [8]. This is reported to be the most important parameter to be used for the evaluation of solar energy use in a specific region, and is also the most basic value used when doing photovoltaic (PV) simulations [8]. As can be seen in Figure 1, most parts of South Africa have a very high average irradiation, as the standard measurement is expected to be about 1000 W/m^2 . The average daily irradiation of the Earth is approximately 250 W/m^2 for an entire year [9]. This is due to the fact that irradiation is lower in winter months, causing a decrease in the yearly average. The map in Figure 1 shows the irradiation for South Africa in terms of the average annual sum over seven years. When converting the general average of 250 W/m^2 to an annual sum, by multiplying it with the number of hours in a year (8760 hours), it can be seen that the average annual sum is about 2190 kWh/m^2 .

In Figure 1 all of the regions that is an orange colour is above the average of 2190 kWh/m^2 . When viewing the map, it can be seen that more than half of the country has an above average annual irradiation, making it a potential

area for the implementation of solar power. The Potchefstroom area, where the project was completed, falls inside an orange area, implying that solar power is a viable choice for use as a renewable energy source. Additional to the irradiation, the air mass (thickness and clarity of the air) and the temperature of the module is also taken into account when deciding whether or not solar power is an appropriate solution [9]. Different manners for generating electricity by means of solar power are with single-crystalline PV panels, polycrystalline PV panels, and amorphous silicon panels.

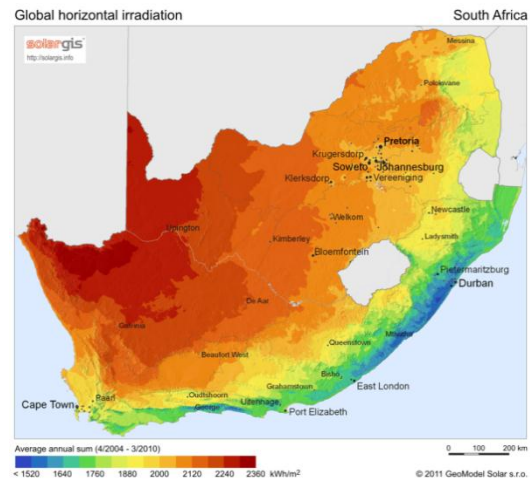


Figure 1: Global horizontal irradiation in South Africa [9]

The final decision was to make use of poly-crystalline PV panels, based on criteria that includes, but are not limited to, the initial cost, and small-scale efficiency. The polycrystalline cells that are used to construct these panels are made from numerous silicon crystals of varying size (as shown in Figure 2), that is melted, poured into a mould, and crystallised in an imperfect manner. This process of construction makes the manufacturing of the polycrystalline PV panels less expensive than the single-crystalline PV panels. These panels are, however, only about 12% effective in converting solar power to electricity, making it less efficient than the previously mentioned panels [10, 11].



Figure 2: Silicon crystals to be melted [12]

2.2 Controller

In this specific system, the controller receives inputs such as the level of the milk inside the tank, and the temperatures of several thermometers. Depending on the level of the milk inside the tank, the controller will determine which sensor should be used as the critical sensor to indicate the temperature of the milk. The level of the milk will also activate and deactivate certain aspects of the system, for example when the level of the milk is very low, the milk mixer would not be effective and is deactivated. The volume of the contents of the tank is also determined in litres from the level of the milk, and it is displayed to the operator.

The controller further has to be able to switch intelligently between the renewable energy source and the solar power, and be able to switch the cooling system on and off, depending on the temperature measured by the critical sensor. A dairy is typically situated and operated in quite harsh conditions, implying that the controller should be able to handle such conditions. Among the controllers that were considered for use were a PLC, Arduino, Raspberry PI, Panda board, and Beagle board. It was decided to use the PLC as the control unit, as it is easy to use and implement, and it would be sufficient for the system and applicable to the conditions.

A PLC is reported to be a compact, universally applicable, easy to operate control device that is easy-to-use and can control any simple control task without any effort. The “Siemens LOGO!” module that was used is convenient and user-friendly for simple open- and closed-loop control tasks, but can be implemented universally. This module has a number of built in basic functions that can be easily accessed, with new functions and programs that can be generated with the use of PC software. The module can also be connected to a PC to demonstrate the working of the control unit, and even to obtain required measurements [13].

2.3 Cooling device

TECMs were suggested by the client as cooling devices and have been used in previous final year projects [5] and [6] - in 2012 as part of a “TECM holder” for vaccines, and in 2013 as part of a “Mini TECM Solar Air Conditioning System”. The devices will thus not be investigated in full again, as the same TECM devices are to be used for this project, and has already been purchased. The TECM to be used is a modified version for liquid cooling and will also be customized for simulation purposes.

TECMs are small devices based on the “Peltier effect”. Peltier, a scientist, found that if a voltage is applied to a thermocouple, a temperature difference can be found between the junctions. The working of a TECM is shown in Figure 3 in a very simplified form. This image shows that when DC power is applied to the device, the one side

of the device will become warmer, and the other side will cool down. This results in a specific temperature difference, depending on the module chosen from the available variety [14].

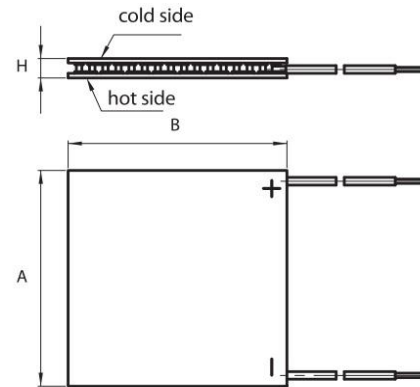


Figure 3: Working of a TECM [14]

2.4 Remaining components

The remainder of the components that were used in the project were also discussed in the literature study, and the desired products were chosen based on specified criteria for each component. The component choices are listed in Table 1.

Table 1: Component Choices

Component	Chosen product
Renewable energy source	Poly-crystalline solar panels
Alternative energy source	Eskom power grid
Controller	PLC
Cooling device	TECM
Holder	Bulk storage tank
Temperature sensor	Thermistor
Liquid level sensor	eTape
Storage battery	Lead-acid battery
Charge controller	PWM charge controller

3. METHODOLOGY

The method that was used to achieve the completion of this project and to be able to obtain the required results is the typical engineering design process. This included identifying the problem; deciding on- and confirming the specifications with the client; doing research to decide upon the best choice of components for each element of the system; designing and simulating the end product; testing the system; and processing the obtained results. This section of the paper will, however, focus on the designing, building, and testing methods that were used to obtain the results that will be discussed in the following section.

After conducting the literature study and deciding upon the components in Table 1 to be used in the system, the detail design of the end product had to be initiated. This required choosing the exact components to be used in the tank, and how it would be implemented. The tank that was used is a 25:1 scaled model of an actual 1500 l bulk storage tank. The Laird Technologies LA-115-24-02-0710 liquid cooled TECM assembly [15] was used as the cooling device, with pipes being placed in direct contact with the milk inside the tank for better efficiency. 99.7% pure ethanol was circulated through the pipes and cooled by the TECM. LM35 temperature sensors were modified to be waterproof by making use of the method described in [16], as well as a PT100 sensor which was already available and is much more accurate. The eTape was applied to the side of the tank as a liquid level sensor as instructed in [17], and connected by making use of a voltage divider circuit.

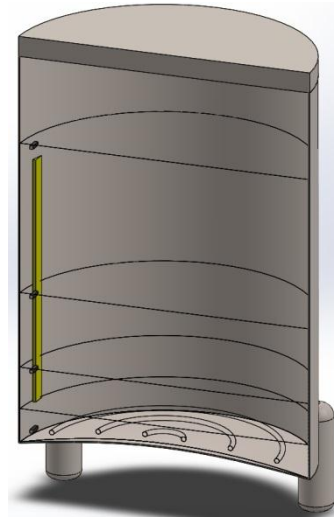


Figure 4: Inside of tank with relevant components

The basic setup of the inside of the tank, including the pipes for circulation, is shown in the simulated representation of Figure 4. The lines in the cross-section of the tank indicate four different levels at which the tank was simulated, and where the critical sensors were placed. During the initial simulations, assumptions about the operation of the TECM setup was made, and simulations were done at different levels, for different numbers of TECMs in the system. These simulations are, however, omitted from this paper, as it was redone later in the redesign with more accurate losses included from the test results, as in Figure 10.

The Siemens LOGO! 0BA6 PLC was used as the controller, and the flow diagram for the control of the level- and temperature sensors is shown in Figure 5. A flow diagram for the switching between the two energy sources was also drafted, but is not presented in this paper, as the solar panels were merely simulated, and not implemented in the actual system. After all of the subsystems were in separate working conditions, they were added together to represent the small-scale prototype for testing.

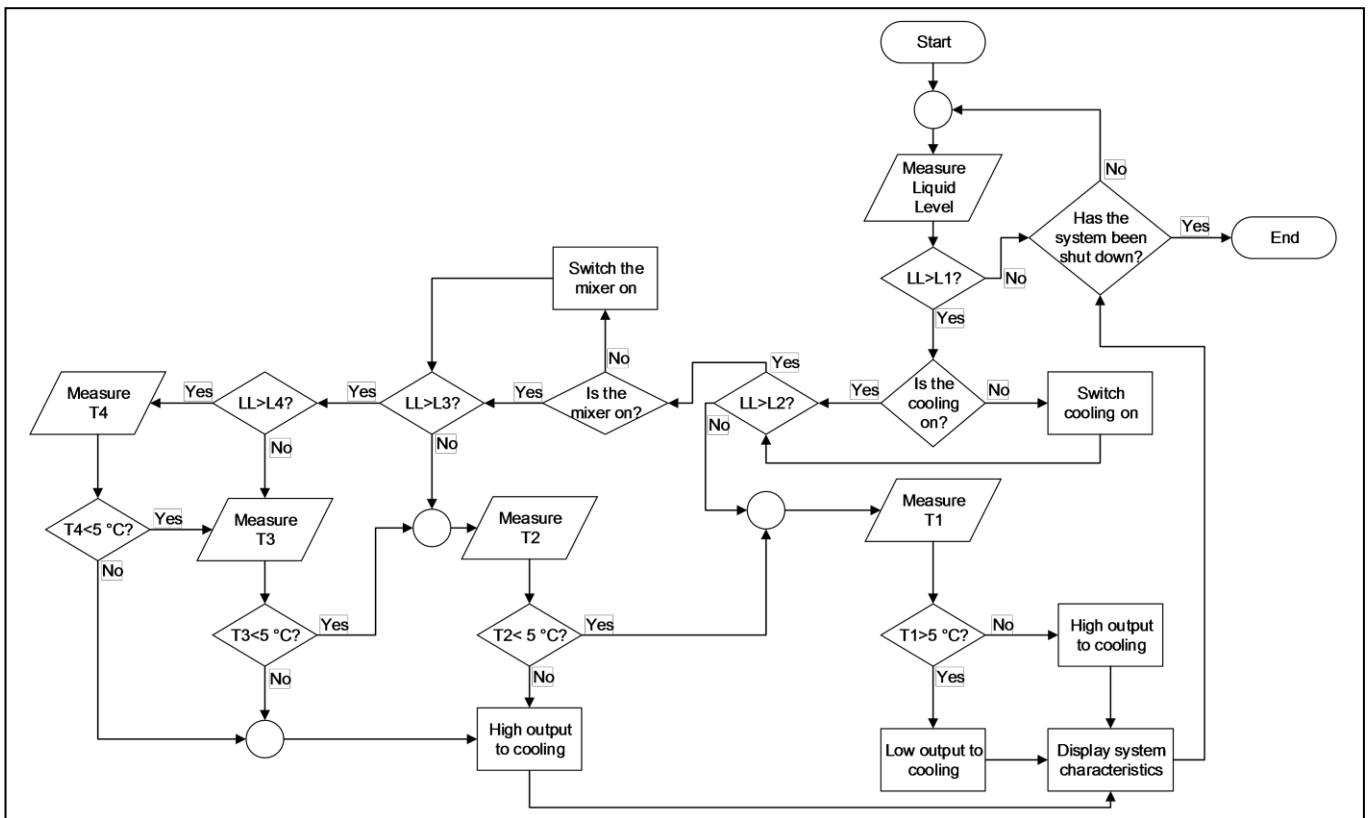


Figure 5: Sensors and outputs flow diagram

The circuitry included 5 V and 9 V voltage regulators, as the temperature sensors requires 5 V for operation and the milk mixer and eTape requires 9 V. The rest of the system was operated at 24 VDC.

After all of the components were added together, the testing of the tank could begin. Two main tests were performed to determine the effectiveness of the cooling system in the tank, in order to simulate the tank correctly. According to the “Agricultural Products Standard Act of 1990” [18], the milk has to be cooled to a temperature of below 5 °C within a period of 3 hours. The milk is expected to enter the tank at a temperature of about 38 °C, which is the body temperature of the cow [19]. During the performing of the tests, the current was measured in order to generate graphs of the energy used by the system. This made it possible to determine the required characteristics of the solar power system. The two tests that were performed are listed below.

- Test 1: The first test was to determine within which period of time, and to what temperature the system is able to cool the milk from a starting temperature of 38 °C. While performing this test, two different methods of operating the system were also tested, in order to determine which method is more effective in terms of cooling capabilities, and comparing it to the energy efficiency of one another. The first method was to keep all components of the system active during the entire process. The second method was to switch the circulation of the ethanol through the pipes on for 1.5 minutes, and then off for 3.5 minutes, while simultaneously switching the milk mixer on and off for 5 minutes at a time. These tests had to be performed for a minimum time duration of 3 hours.
- Test 2: The second test the was performed was to determine the ability of the system to keep the temperature below the required 5 °C, but still above -0.5 °C, which is the freezing point of milk [19]. This test was performed by adding milk to the tank at a temperature of below 5 °C, and observing the temperature change and power dissipation for a period of at least 2 hours.

4. RESULTS

This section discusses the results of the two tests that were performed, as described previously. The tests were performed on the small-scale prototype, as shown in Figure 6. This figure shows the inside of the tank, containing the coil through which ethanol was pumped for the liquid cooling, the eTape liquid level sensor, temperature sensors, and the mixer for the milk. The sensors are exported to the outside of the tank through a small hole, and connected to the relevant circuitry. The circuitry is again connected to the PLC, in order to provide all of the necessary inputs to the control system.



Figure 6: Inside of physical tank that was tested

The result of the first test is shown in Figure 7. As can be seen, the two methods give a very similar temperature drop from 38 °C, and both methods were only able to cool the temperature to about 15 °C after 4 hours. This indicates that it does not matter which method is used in terms of the change in temperature. These results will also be implemented in the simulations. The one liquid cooled TECM setup that was used in the system was very effective in cooling the temperature from 38 °C to about 20 °C, where after the fall in the temperature became very slow. The tests were conducted at liquid level 1. The graph also shows a third order polynomial trendline for the results, accompanied by a representing equation. The R^2 value of the trendline is also given as 0.998, which indicates that the line is an appropriate representation of the data, as the value is close to 1.

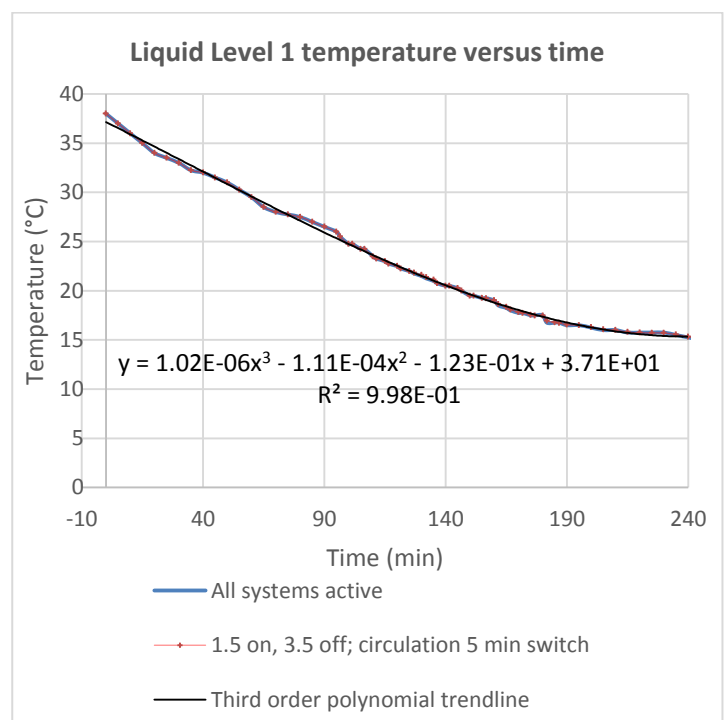


Figure 7: Test 1 temperature comparison

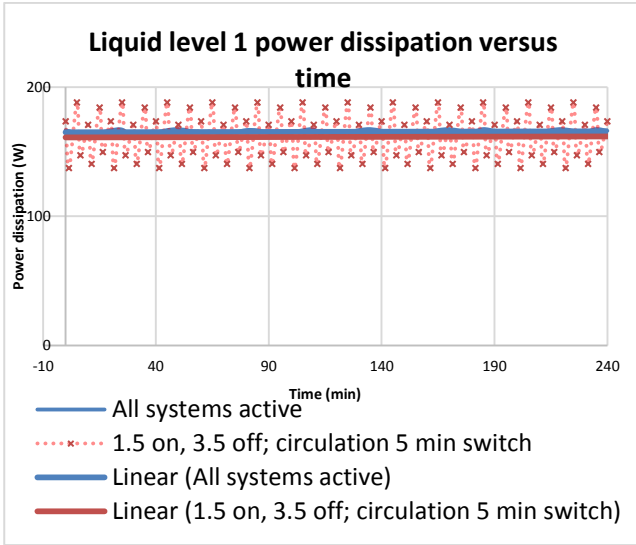


Figure 8: Test 1 power dissipation comparison

The comparison in the power dissipation of the two methods of test 1 is shown in Figure 8. As can be seen in this figure, the power dissipation of the second method changes periodically. A trend line representing the average power dissipation of this method has, however, also been drawn, indicating that the second method requires less power on average to operate than the first method. The power dissipation of the first method was determined as 165 W for the experiment, while the average power dissipation for the second method was determined to be 161 W during the test period. This indicates that the second method is more energy efficient, and is thus the method that will be implemented in the final design.

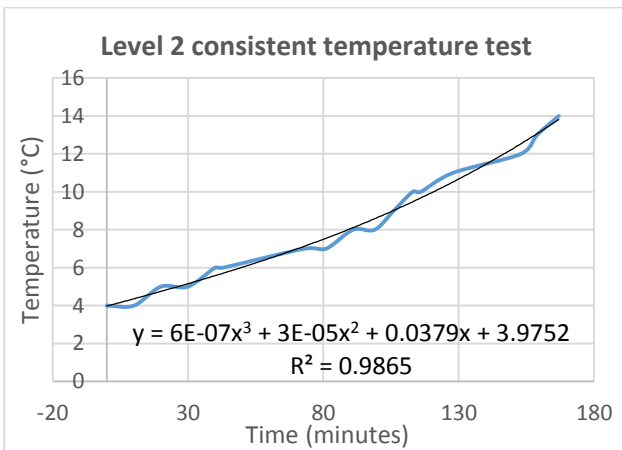


Figure 9: Test 2: Consistent temperature test

The second test that had to be done was the consistent temperature test. The test was conducted as described in the previous section, with an initial temperature of 4 °C, and the tests being conducted at liquid level 2. The resulting temperature of this test is shown in Figure 9. The test was conducted for a period slightly shorter than 3 hours, and indicated that one liquid cooled TECM setup

will not be able to keep the temperature of the milk below 5 °C. The temperature rose above 5 °C after about 30 minutes, where after it continued to rise as shown in the graph. It was found that a third order polynomial equation fits the plot, and is added as a trendline in Figure 9, accompanied by the relevant equation. The R² value of 0.9865 proves that the equation is an acceptable representation of the data. The power dissipation for this test is about the same as that shown in Figure 8 for method 2, as the switching of the system components was done in the same manner.

5. DISCUSSION

The results can be interpreted to design a supporting cooling system for an actual tank by making use of simulations. The small-scale model was simulated for various numbers of TECM assemblies at different liquid levels, and it was decided that the most effective implementation would be to make use of the tank as a pre-cooler for an actual bulk tank, implementing six liquid cooled TECM assemblies. The pre-cooler would be able to reduce the temperature of the milk by 10 °C before it enters the bulk tank, with sufficient time left for the traditional cooling methods to further cool the milk to the required temperature. The resulting simulation with the six liquid cooled TECM setups is shown in Figure 10(a) and Figure 10(b).

The pre-cooling system in the design would only make use of solar power to operate, thus eliminating a great deal of strain from the electricity supplier. The results in Figure 9 proved that the system will not be able to keep the temperature below 5 °C. It is thus estimated that the system will only be active for about 6 hours per day: 3 hours per session with two sessions per day. The daily energy requirement of the tank is thus about 5.8 kWh for six TECM assemblies.

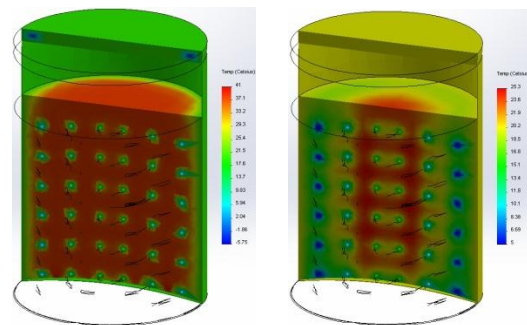


Figure 10: Simulation with six TECM setups: (a) after 5 minutes; (b) after 3 hours

The battery capacity was chosen to be for 12 hours in the simulations, in order to be able to operate the system for two days without charging the batteries from the solar panels. The minimum requirements for the solar panels and storage batteries were determined from the winter months (specifically June), when the solar irradiation is at its lowest. From the PVSyst[®] simulation results shown in

Figure 11, it is seen that the solar power needs to be able to provide 1271 W, and the 24 V batteries should have a capacity of 142 Ah.

The total estimated cost for the year 2014 for the solar panels is about R 16 253.22 [20], and about R 7 678.00 [20] for the lead-acid storage batteries. A liquid cooled TECM assembly would cost about R 4 000.00 [5], resulting in a cost of about R 24 000.00 for six assemblies. Other costs that also have to be taken into account is that of the temperature sensors, liquid level sensor, PLC, and mixer, which adds an amount of about R 4 550.00 to the total, as determined in the year 2014, and implemented in the test model of figure 6. The total cost to implement this system in the tank as shown in Figure 10 would thus be about R 52 481.22.

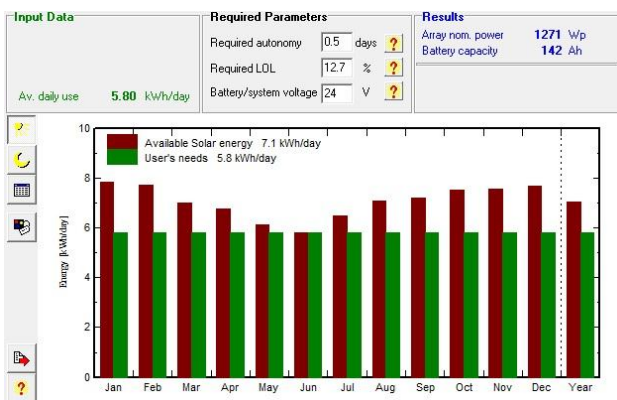


Figure 11: PVSyst[®] simulations for solar panel size and batteries

6. CONCLUSION

The main purpose of this project was to design an energy efficient cooling system, that would make use of a renewable energy source and thus relief strain from Eskom to supply electricity. The cooling system that was used as demonstration is a supporting cooling system for a bulk storage tank, which was tested practically in order to adapt the simulation to a more practical situation, and to take actual losses into account during the redesign process.

It was determined that by making use of six TECMs in a 60 litre tank as a pre-cooler for an actual bulk tank, the milk could be cooled by 10 °C from its initial temperature, and still leave sufficient time for a traditional bulk tank to cool the milk to the required temperature. This would however require an initial cost of about R 52 481.22 (estimated from prices received during the year 2014) to equip the pre-cooler and purchase solar panels and storage batteries. As each situation is unique in terms of how much milk is produced, etc. it has to be determined how many pre-cooling systems are required for each situation. The number of pre-coolers in the system can be adjusted by

the dairy farmer, depending on the initial amount he is willing to pay.

7. REFERENCES

- [1] L. Buthelezi and D. Pressly, "SA faces 'dark age' as Eskom struggles," *Business report*, 3 December 2013.
- [2] H. Grover and M. Pretorius, "The technology assessment of demand side bidding within the South African context," in *AFRICON 2007*, Windhoek, 2007.
- [3] A. Janeke, "Melkbedryf verloor 'n boer per dag," *Lanbou.com*, 16 July 2013.
- [4] A. Stuijt, "Are S.A dairy farmers going extinct?," *Censorbugbear reports*, 17 July 2013.
- [5] B. de Waal, "Mini TECM Solar Air Conditioning System," North-West - University Potchefstroom Campus, Potchefstroom, 2013.
- [6] H. Eilers, "Thermoelectric (TECM) Cooling Holder," North-West - University Potchefstroom Campus, Potchefstroom, 2012.
- [7] A. Meyer and D. Dintchev, "South Africa's electrical energy economy: environmental impacts, future developments and constraints," *Engineering Science and Education Journal*, vol. 7, no. 5, pp. 227 - 232, 2002.
- [8] 2014 GeoModel Solar, "Solar radiation maps: Global Horizontal Irradiation (GHI)," Solar GIS, 2010-2014. [Online]. Available: <http://solargis.info/doc/71>. [Accessed 9 March 2014].
- [9] R. F. Pantelimon, M. Adam, M. Andrusca and C. Pancu, "Aspects Regarding Solar Battery Charge Controllers," Faculty of Electrical Engineering, Department of Power Engineering "Gheorghe Asachi" Technical University of Iași, Iași, Romania, 2013.
- [10] D. Chiras, *The Homeowner's guide to renewable energy*, Canada: New Society Publishers, 2006.
- [11] Dako Power cc, "Three Photovoltaic Technologies: Monocrystalline, Polycrystalline and Thin Film," Dako Power, 2008. [Online]. Available: http://www.dako.co.za/photovoltaic_types.html. [Accessed 9 March 2014].
- [12] Ridders-Solar BVBA, "Polycrystalline Silicon," Ridders-Solar, [Online]. Available: <http://www.ridders-solar.com/poly.shtml>. [Accessed 12 April 2014].
- [13] Siemens AG Industry Sector, "LOGO! logic modules," Siemens, 2008. [Online]. Available: <https://eb.automation.siemens.com/mall/catalog/products/5000562>. [Accessed 17 March 2014].
- [14] M. Deng, A. Inoue and S. Goto, "Operator based Thermal Control of an Aluminum Plate with a Peltier Device," in *Innovative Computing, Information and Control, 2007. ICICIC '07. Second International Conference*, Kumamoto, 2007.
- [15] Laird Technologies, "LA PowerCool Series, LA-115-24-02 Thermoelectric Assembly," 2010. [Online]. Available: www.lairdtech.com/WorkArea/DownloadAsset.aspx?id=5308. [Accessed 11 May 2014].
- [16] "Waterproof DS18B20 Digital temperature sensor + extras," Adafruit, 2014. [Online]. Available: <http://www.adafruit.com/products/381>. [Accessed 25 May 2014].
- [17] Milone Technologies, Inc., "eTape Operating Instructions and Application Notes," New Jersey, 2009.
- [18] Dairy Standard Agency, "Code of practice for milk producers," [Online]. Available: http://www.landbou.com/content/uploads/ArticleDocument/COP_for_Milk_Producers_Oct_2013_s.pdf. [Accessed 24 January 2014].
- [19] S. Rath, *About Cows*, Minocqua: Heartland Press, 1987.
- [20] Imperial Crown Trading, "Solar Panel prices," Sustainable.co.za (Pty) LTD - Online Eco Store, 2014. [Online]. Available: <http://www.sustainable.co.za/catalogsearch/result/?q=poly>. [Accessed 26 May 2014].

DESIGN A THERMOELECTRIC COOLING HOLDER SUPPLIED BY PHOTOVOLTAIC PANELS

N. Zabih^{*} and R. Gouws^{**}

^{*} School of Electrical, Electronic & Computer Engineering, North-West University, Potchefstroom Campus, South Africa E-mail: nima.z.sh@gmail.com

^{**} School of Electrical, Electronic & Computer Engineering, North-West University, Potchefstroom Campus, South Africa E-mail: Rupert.Gouws@nwu.ac.za

Abstract: In this paper, the development of a portable solar power vaccine carrier box for local usage in Africa and South Africa is described. The purpose is to provide guidance to the design of a thermoelectric cooling holder. An overall design of a cooling holder was done in SolidWorks[®] and a thermal analysis of the complete systems was done in Flow Simulation. The thermal analysis was done to simulate the cooling capacity of the Thermoelectric Cooling Module (TECM) heat exchanger. Design of the solar power supply including photovoltaic panels, charge controller, and batteries were also done.

Keywords: Cooling holder, Thermoelectric Cooling Module (TECM), photovoltaic panels.

1. INTRODUCTION

Infectious diseases are the main course of deaths or disabilities among infants and young children in rural parts of Africa. The most effective and cheapest method to prevent infectious diseases is vaccine [1]. These vaccines are administered into the body of patients during routine immunization programs. The most important part of these immunization programs is the cold chain system. This system implies the storing and transporting of vaccine from the manufacturer to the patient in a certain temperature in order for it to stay in a potent state. All vaccines lose their potency if exposed to heat or when it is frozen. Obviously it is pointless to immunize with vaccine which has lost its potency [1]. The storing standards of vaccine set out by the World Health Organization (WHO) state that vaccine should be stored within 2 - 8°C [2]. In order to deliver vaccine to patients in a potent state, the most important tool is functioning freezers and refrigerators. These cooling containers must also be rugged and find a mean to power itself as it will be used in rural parts of Africa where no electricity is available.

In this paper, the design and development of a portable solar powered vaccine carrier box is described. In order to successfully design a vaccine cooling holder, that utilizes thermoelectric technology as a heat pump, it was necessary to determine if the cooling power of this type of technology would be satisfactory for the application. Thermoelectric Cooling Module (TECM) with different voltage, current and heat pumping capabilities are available and that is why it is important to determine the correct heat pumping capability needed for a given application. The hot side of the cooling holder is cooled by using a heat sink and fan assembly, due to the size and complexity when compared to water cooling. A heat exchanger with a very high efficiency should be used to cool the hot surface of a TECM. A design for the solar power supply including photovoltaic panels, charge

controller and batteries were done. An overall design of the cooling holder was constructed in SolidWorks[®] and a thermal analysis of the complete system was done in Flow Simulation. These simulations ensure that the results are optimum and that a proper prototype of the design can be implemented. The simulation results were used to construct a prototype cooling holder with the exact dimensions as the designed cooling holder. The design of the model in SolidWorks[®], a thermal analysis performed of the model in Flow Simulation and the design of the control circuit in OrCAD[®], forms all part of the simulations.

2. DESIGN CONSIDERATIONS

The proposed design of this paper is to design and implement a cooling system for the storage of vaccine for the use in Africa. The efficiency of the cooling holder will be evaluated under normal operating conditions to determine if its cooling capacity is aliquant. In figure 1 all sections of the system are shown. The most important components of the project are the photovoltaic panel, charge controller, battery, cooling holder, temperature control circuit and the thermoelectric cooling modules. This is the functional architecture of the preliminary design of the project.

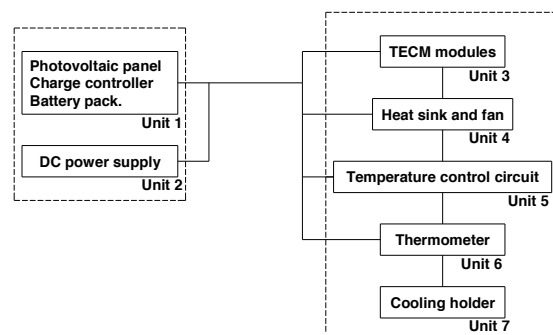


Figure 1: Preliminary design functional architecture

2.1. Photovoltaic panels

The rated power output is used to classify photovoltaic panels and it is measured in watts (W). It is expected of the photovoltaic panel to produce its rated amount of power in one peak hour of sun [3]. When making calculation the geological location must be kept in mind as it will affect the peak sun hours. In figure 2 the average annual solar radiation falling on one square metre surface from 2004 to 2010, measured in kilowatt hours is illustrated [4]. There is more than 2000 kWh/m² of energy available in the mid region of Africa to generate power. This justifies the use of solar energy to power the cooling holder.

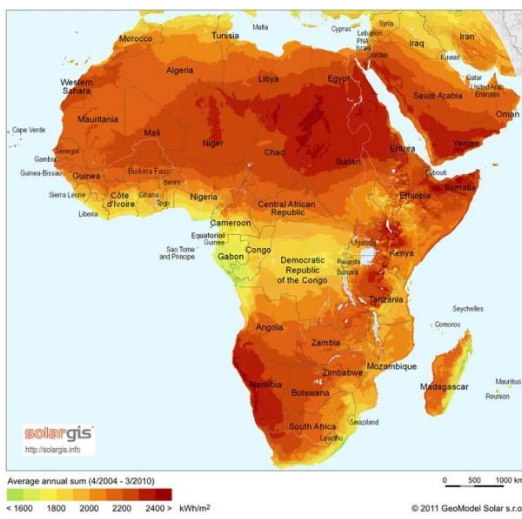


Figure 2: Average solar radiation in Africa [4]

In figure 3 the average annual solar radiation falling on one square metre surface from 1994 to 2010, measured in kilowatt hours is illustrated [4]. There is more than 2000 kWh/m² of energy available in the Potchefstroom region to generate power.

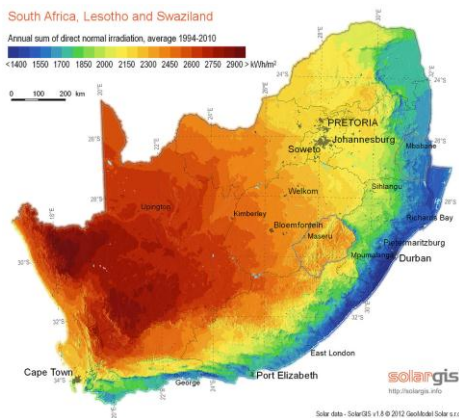


Figure 3: Average solar radiation in South Africa [4]

Photovoltaic panels can be wired in series or in parallel, to increase voltage or current respectively. When photovoltaic panels are wired in series the output voltage is increased and when they are wired in parallel the output current is increased [5]. Photovoltaic panels are rated according to their peak power (W), with the associated voltage (V) and the current (A) at this point of peak power. Photovoltaic panels normally have a rated terminal voltage of 17 V, while the cell operating temperature affects the output of the photovoltaic panel. Twenty five degrees Celsius is the nominal temperature at which the panels are rated, while their output can vary by up to 2.5% for every 5 degrees increase in temperature. The output of the photovoltaic panel decreases, as temperature increase [6]. It should be kept in mind when sizing a photovoltaic panel that the output is affected by the temperature. The output of the photovoltaic panel can be increased up to 25% above its nominal rated current with the increase in temperature. Due to this fact, the charge controllers must be sized to account for this increase in the output of the photovoltaic panels, hence it can withstand the increase in the short circuit current. Charge controllers are rated 125% higher to ensure that it can handle the short circuit [7].

2.2. Solar Power Supply

In order to provide power to the complete cooling holder, a solar panel, charge controller and battery are used. The size of the power supply is determined by the power consumption of the system. The total power consumption of the system is the sum of the power consumption of the TECMs with the two fans (P_1) and the temperature control circuit (P_1).

$$P_{total} = P_1 + P_2 = 134 + 1.2 = 135.2 W \quad (1)$$

The exact size of the photovoltaic panels, charge controller and batteries are determined in the rest of this section.

Determine the DC Load: The total load of 135.2 W will be operated for 24 hours per day, resulting in 3244.8 Wh per day. There will be energy losses to account for and therefor 20% has to be added to the load. The total load is therefor:

$$P_{load} + P_{losses} = 1.2 P_{load} = 3893.8 Wh/day \quad (2)$$

Sizing the photovoltaic panels: Due to weather conditions in Africa a peak sunshine period of 6.6 hours is available. In order to determine the required solar panel input power, the total load must be divided by the peak sunshine period as follow:

$$P_{solar\ panel\ input} = \frac{3893.8 Wh}{6.6 h} = 589.97 W \quad (3)$$

This implies that solar panels that will generate 589.97 watts are needed.

Selecting the photovoltaic panels: A combination of photovoltaic panels must be selected to provide at least 589.97 W. Five 130 W photovoltaic panels will be used to generate 650 W. Each photovoltaic panel will provide an output of 130 W (P_{max}) at 7.7 A (current at P_{max}). It should be noted that any configuration of solar panels can be used to generate at least 600 W of power. In the Potchefstroom region there is more than 2000 kWh/m² of solar energy available to generate power, as it is mentioned above.

Selecting the charge controller (solar regulator): Charge controller is rated by the amount of current they can receive from the photovoltaic panels. Therefore it is necessary to know the exact rated short circuit current of the photovoltaic panels. The panels that are selected in the previous step, each has a rated short circuit current of 8.1 A. The charge controller should be capable of handling the total short circuit current. Thus the total short circuit current is:

$$I_{Total.s.c} = 5 \times 8.1 = 40.5 A \quad (4)$$

The output of photovoltaic panels vary with temperature and due to this an additional 25% must be added to the total short circuit current rating to allow for growth and the fact that the solar panels may exceed their rated output.

$$I_{Total.s.c} = 1.25 \times 40.5 = 50.63 A \quad (5)$$

This implies that a charge controller of at least 50.63 A is needed for the design. There is not a standard size of 50.63 A and due to this the developer propose the use of a 60 A charge controller. The charge controller must have a voltage rating of 24 Vdc as this is the operating voltage of the TECMs.

Sizing the batteries: It is recommended to shallow cycle batteries so that it last longer. This implies that the batteries are discharged to only 20% of its capacity. A conservative design will save the deep cycling for occasional usage, like when it is raining or cloudy. This implies that the battery bank should be about five times the daily load. This also means that the system will be able to provide power continuously for five days without any sun or recharging. The total battery amp-hours (Ahs) required is determined by the daily watt-hour requirements and the desired number of days of storage capacity required and the assumption that the battery will never be discharged more than 20% of its capacity. First the average Ahs per day are calculated by dividing the average daily load with the system voltage.

$$Average AH/day = \frac{3893.8 Wh}{24 V} = 162 Ah/day \quad (6)$$

The number of batteries connected in parallel (N) is determined by multiplying the average Ah per day with the number of battery storage days and dividing that with the battery discharge limit and the battery ampere

capacity of the batteries that was chosen. The batteries must have two days of storage capacity and the discharging limit is 0.8 and the batteries to be used are 100 Ah batteries.

$$N = \frac{(162 AH/day)(2 days)}{(0.8)(100)} = 4 \text{ batteries in parallel} \quad (7)$$

In order to get a system voltage of 24 Vdc it will be required to connect two 12 Vdc batteries in series.

Power supply requirements table: The design of the solar power supply was discussed in this section. The design decision requirements for each of the units in the solar power supply are summarized in the table 1. In the table the requirements for each unit is given as well as the quantity needed. There are many quality brands for each unit and the decision on which brand to use will be determined by each person's requirements; like cost, quality, availability ext. It is however important that the selected brand for each unit must adhere to the requirements as determined in table 1.

Table 1: Power supply requirements

Unit	Quantity	Requirements
Photovoltaic panel	5	130 W at 7.7 A
Charge controller	1	24 Vdc, 60 A
Battery	4	12 Vdc, 100Ah

Power supply connection diagram: The power supply must provide two output voltages, a 24 Vdc output for the TECMs with fans and a 12 Vdc output for the temperature control circuit. A graphical illustration of the power supply is shown in figure 4. This diagram illustrates the connection of the separate units.

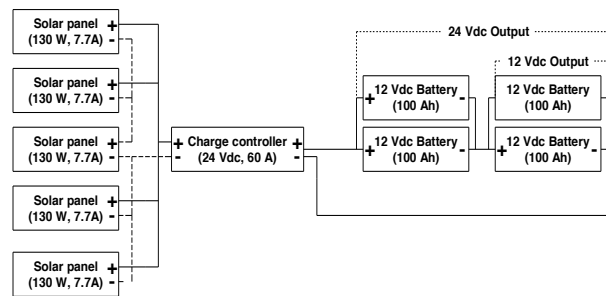


Figure 4: Power supply concept

2.3. Temperature Control

In order to regulate the temperature between 2 °C and 8 °C the KEMO M169 temperature switch supplied by Communica is selected. This temperature switch is the on/off cycle type temperature controller. This temperature switch, switches according to a pre-set temperature value a relay on or off. When the measured temperature is below the pre-set value the temperature switch, switches off the TECMs and when the measured temperature is above the pre-set value the temperature switch, switches

on the TECMs. In this design the pre-set temperature value will be set at 5 °C. This allow for a temperature hysteresis band of 3°C below and above the pre-set temperature value. The temperature switch has a temperature range of 0°C to +100°C, which cover the full range of temperature for the project. The output relay is able to switch 5 A at 25 V. The current rating is however to low as the TECMs will occupy 6.6 A starting current and 5.6 A running current at 24 V. This requires for an extra power switching stage to be built, ensuring that the TECMs get enough power to function properly. The output relay of the KEMO M169 temperature switch is used to switch another relay with ratings of 10 A at 24 Vdc. This relay is able to handle the amount of current needed by the cooling unit. In figure 5 the KEMO M169 temperature switch is illustrated [8].

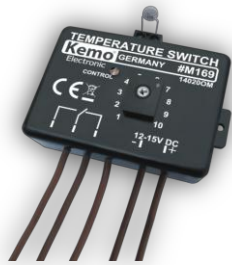


Figure 5: KEMO M169 temperature switch

In figure 6 the wiring diagram of the complete temperature control circuit is illustrated. Internal Relay is the internal relay of the KEMO M169 temperature switch and External Relay is the relay that has been added to compensate for the current used by the TECMs.

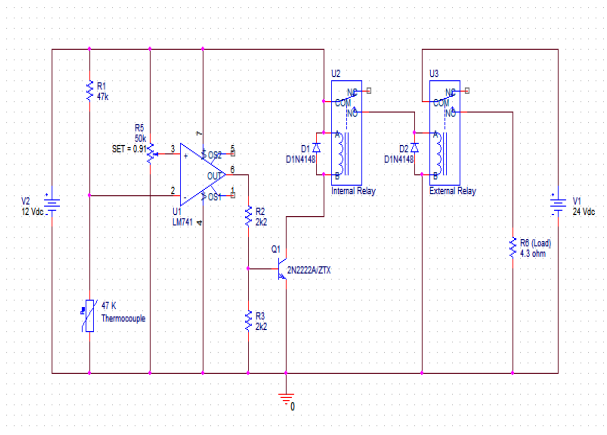


Figure 6: Wiring diagram of temperature control circuit

In order to evaluate if the temperature control circuit will be able to control the temperature of the refrigeration compartment between 2 °C and 8 °C a temperature sweep of the complete circuit was done in OrCAD®. The switching graph is illustrated in figure 7. This graph illustrate that the output of the control circuit is 0 Vdc for all the temperature values below 5 °C and the output is 24 Vdc for all the temperature values above 5 °C.

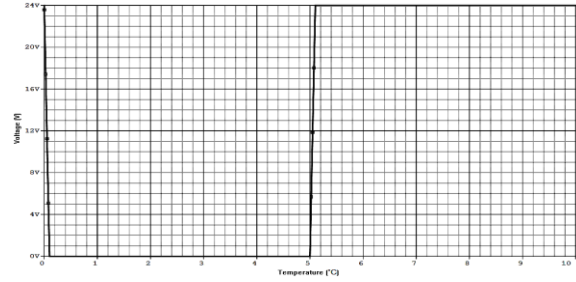


Figure 7: Switching graph of temperature control circuit

3. SOLIDWORKS® MODEL DESIGN

The design and construction of an accurate model for the cooling holder as well as the TECM and heat sink fan units was the first part of the SolidWorks® simulation. These models will then be used to perform a thermal analysis for the cooled operating condition of the cooling holder. In figure 8(a) the model designed for the cooling holder in SolidWorks® is illustrated. The main objective was to create an accurate model to be able to perform an accurate thermal analysis of the refrigeration compartment temperature of the cooling holder. The cooling holder consists of two layers of temperature isolation material that is covered in a thin layer of metal sheet to protect it. The temperature isolation material is polyurethane foam with a thickness 15 mm and polystyrene with a thickness of 35 mm, as indicated in figure 8(b). The polyurethane foam forms the outside layer and polystyrene form the inside layer. The combined thickness of the isolation is 50 mm. The reason for the choice of the two materials is that they have the lowest thermal conductivity values. The thermal conductivity of polyurethane foam is 0.039 W/m°C and for polystyrene is 0.037 W/m°C. To enhance the efficiency of the cooler box, it was decided that a top loading entry door to the cooler box would be used. This does not allow the heavy cool air to be drained from the cooler box each time the door is opened, as is the case with vertical cooler doors. The volume of the inside area of the cooling holder is 0.27 m³. The total capacity of the cooling holder is 27 litres.

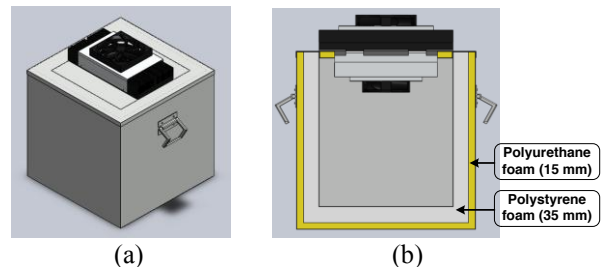


Figure 8: (a) Final design of cooling holder; SolidWorks® model, and (b) Cooling holder enclosure.

Vaccine storage shelves for the cooling holder are designed as shown in figure 9(a). These storage shelves make it possible to store a total of 400 vaccine bottles, 100 on each shelf. Each one of the vaccine bottles is

able to store 20 ml of vaccine. This count up to a total of 8 litres of vaccine. In figure 9(b) the position of the shelves inside the cooling holder's refrigeration compartment is shown.

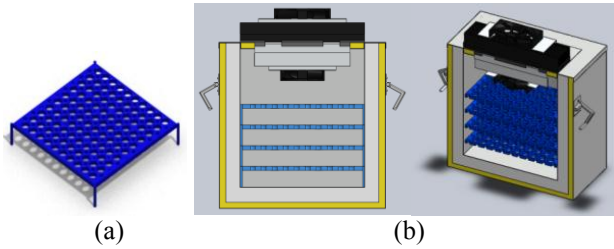


Figure 9: (a) Vaccine storage shelf and (b) Position of vaccine storage shelves in cooling holder

4. SIMULATION AND RESULTS

The aim of this simulation is to verify whether the design cooling holder has the necessary cooling capacity for an ambient temperature. As an example in this simulation the ambient temperature is considered 20 °C. The time period that the designed cooling holder takes to reach the desired temperature in the refrigeration compartment of the cooling holder is also determined through this simulation. The no-load simulation is done at temperature 20 °C. The results for these simulations are illustrated in three different formats: a table format, temperature profile format and graph format. The table format illustrates the minimum, average and maximum temperature of the surface and volume goals. The temperature profile gives a visual illustration of the temperature on the inside of the cooling holder. The graph format illustrates the temperature at a specific time period and this also shows the amount of time that the cooling holder takes to reach 5 °C on the inside of the cooling holder. The values shown in table 2 are the results for both the volume and surface goals of the thermal analysis at an ambient temperature of 20 °C while the TECMs are not in operation. The temperature throughout the cooling holder is uniform 20 °C as illustrated by the numerical results in table 2. It is important to ensure that the temperature in the cooling holder is at the same temperature as the ambient temperature at which the test is done to test the cooling power of the heat pumping unit correctly.

Table 2: Numerical results; No-operation of TECMs at 20 °C

Volume Goals	Value (°C)	Surface Goals	Value (°C)
Min air temp.	20.05	Min air temp.	20.05
Ave. air temp.	20.05	Ave. air temp.	20.05
Max air temp.	20.05	Max air temp.	20.05

The values obtained from the volume and surface goals show that the ambient temperature remains constant at 20.05 °C. In figure 10 the temperature profile of the cooling holder at ambient temperature of 20 °C is illustrated.

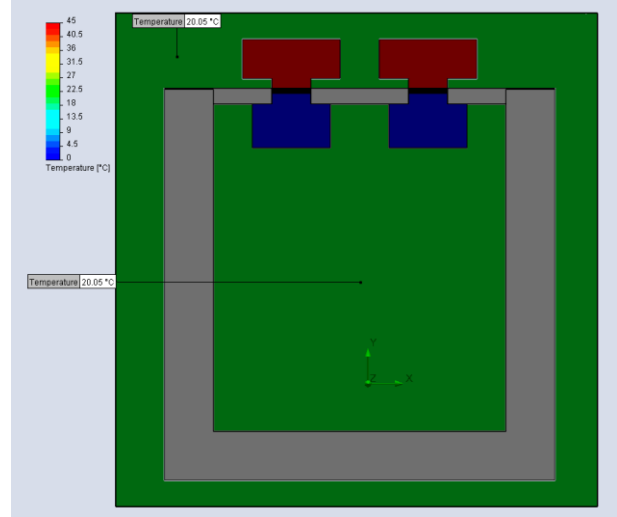


Figure 10: Temperature profile; No-operation of TECMs at 20 °C

The values shown in table 3 are the results for both the volume and surface goals of the thermal analysis at an ambient temperature of 20 °C, while the TECMs are in operation.

Table 3: Numerical results; Full operation of TECMs at 20 °C

Volume Goals	Value (°C)	Surface Goals	Value (°C)
Min air temp.	3.857	Min air temp.	3.999
Ave. air temp.	4.814	Ave. air temp.	4.603
Max air temp.	5.770	Max air temp.	5.206

In figure 11 the temperature profile of the cooling holder at ambient temperature of 20 °C is illustrated. Figure 12 illustrates that the design cooling holder takes about 17 minutes to reach 5 °C on the inside of the cooling holder when the ambient temperature is 20 °C.

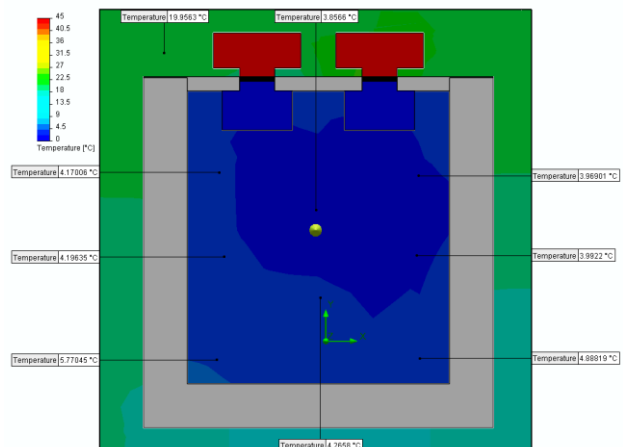


Figure 11: Temperature profile; Full operation of TECMs at 20 °C

The results of the no-load simulation verify that the design cooling holder has the necessary cooling capacity

to cool the refrigeration compartment of the cooling holder to 5 °C while the ambient temperature is 20 °C. The time in which the desired temperature on the inside of the cooling holder is reached show a linear relationship with the ambient temperature, due to the increase in the heat load on the inside of the cooling holder when the ambient temperature increase.

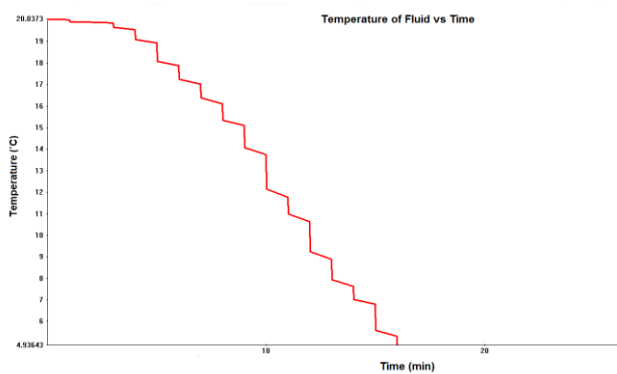


Figure 12: Time graph; Full operation of TECMs at 20 °C

The actual constructed model of the complete cooling holder system is illustrated in figure 13(a). This model was fabricated by making use of the designs done in SolidWorks®. The AA-100-24-22 thermoelectric heat pumping assembly is illustrated in figure 13(b). The heat sink fan assembly is illustrated in the top picture. The cold sink fan assembly is illustrated in the down picture. It is directly related as to the design module done in SolidWorks®. This prototype was tested at different conditions.



Figure 13: (a) Actual constructed model and (b) AA-100-24-22 thermoelectric heat pumping assembly

5. CONCLUSION

The detail design of the thermoelectric cooling holder was discussed in this paper. The design of the solar power supply was also discussed. The calculation for the sizing of the photovoltaic panels, charge controller and batteries were done. It was concluded that five 130 W photovoltaic panels must be used to provide 650 W of power in order to charge the batteries during the day and provide power

to the cooling unit. The simulation that was done in OrCAD® on the KEMO M169 temperature switch was discussed. The results of the simulation validate that this temperature switch will be able to control the temperature in the refrigeration space between 2 °C and 8 °C. The design of the cooling holder is done in SolidWorks®. Thermal simulations of the cooling holder were performed in Flow Simulation. A thermal analysis of the complete cooling holder was done in Flow Simulation at the ambient temperature of 20°C, for no-operation and full operation of the TECMs in order to test their cooling performance. The results reveal that the cooling holder takes about 17 minutes to reach 5°C in the refrigeration space when the ambient temperature is at 20 °C. A prototype cooling holder was build based on the design done. This design and investigation is very important to show if a cooling holder for the storage of medication can be made from using thermoelectric cooling modules instead of the normal compression cycle as used in normal refrigerators.

6. REFERENCES

- [1] L. Arevshatian, C.J. Clements, S.K. Lwanga, A.O. Misore, P. Ndumbe, J.F. Seward, and P. Taylor, "An evaluation of infant immunization in Africa: is a transformation in progress?" *Bulletin of the World Health Organization*, Vol. 85, pp. 449-457, June 2007.
- [2] World Health Organization homepage (2011), Available: <http://www.who.org/>
- [3] A.O. Dieng and R.Z. Wang, "Literature Review on Solar Adsorption Technologies for Ice-Making and Air Conditioning Purposes and Recent Developments in Solar Technology," *Renewable and Sustainable Energy Review*, Vol. 5, Issues 4, pp. 313-342, 2010.
- [4] Solargis homepage, (2012), Available online: <http://solargis.info/doc/28>
- [5] Solar Total homepage (2012), Available Online: <http://www.solartotal.co.za/?gclid=CJTPkeHU0rACFUcKfAodvwzN2Q>
- [6] R.E. Critoph, "An Ammonia Carbon Solar Refrigerator for Vaccine Cooling," *Renewable Energy*, Vol. 5, Issues 1-4, pp.502-508, 1994.
- [7] Y.J. Dai, R.Z. Wang, and L. Ni, "Experimental investigation and analysis on a thermoelectric refrigerator driven by solar cells," *Solar Energy Material & Solar Cells*, Vol. 77, pp. 377-391, 2003.
- [8] KEMO M169 temperature switch thermostat on Communica homepage (2012), Available Online: http://www.comunica.co.za/ProductDetails.aspx?DataLink=P_100271108981.

IN-LINE WATER HEATING SYSTEM FOR INDUSTRIAL APPLICATION

O. Dobzhanskyi*, R. Gouws*, N. Zabihi *

* O. Dobzhanskyi, R. Gouw, and N. Zabihi are with the Department of Electrical, Electronic and Computer Engineering, North-West University, Potchefstroom 2520, South Africa, E-mail: 24881902@nwu.ac.za, Rupert.Gouws@nwu.ac.za, nima.z.sh@gmail.com.

Abstract: Due to the increase of electricity prices in South Africa and the World, there exists the need for energy efficient water heating systems. The authors of this paper conducted a literature study on existing water heating systems. The study shows that there is a possibility of designing more efficient water heating system at lower cost. An in-line water heating system for industrial applications was designed and tested. Before the system was designed a Finite Element Method analysis of the system was carried out to predict the systems' pressure and temperature. During a physical model test the energy consumption was measured and compared to a conventional storage water heating system. The designed in-line water heating system is shown to be more energy efficient than the conventional storage water heating system. It also had a variety of advantages such as: size, adaptability to a variety of locations, and robustness.

Keywords: Energy consumption, temperature controller, water heating system.

1. INTRODUCTION

Tankless electric water heaters have become more popular in industrial use due to their advantages over conventional water heating systems. Tankless electric water heaters are not harmful to the environment and require less space for installation, since there is no water tank.

A consumer can receive hot water instantaneously at any time. Tankless water heating systems are more durable than the conventional water heating tanks. The absence of the water tank significantly simplifies maintenance (no rust, corrosion, flooding or bursting of a tank, etc.). The disadvantages of electrical water heating systems are: electronic failure, and trouble shooting.

Almost one third of electricity bills in the industrial sector are towards hot water energy consumption. There are therefore always room for improvement in the water heating field, which will save money, water and preserve the environment.

After exploring alternative methods of increasing the efficiency of water heating systems [1-4], a design of an in-line water heating system was performed. Literature study shows that some of the water heating system manufactures do not consider temperature controllers in their products [5-6]. There is therefore the possibility of pressure and temperature build up in the system which can end up with significant power losses. The main focus of this paper is to design an energy efficient instantaneous water heating system including controller. The project is also oriented on minimizing the cost of the system, and avoiding any complexity in manufacturing. The designed in-line water heating system includes affordable components available in the market in South Africa.

2. CONCEPTUAL DESIGN

In-line electric water heaters usually consist of two coils. The first is the water carry coil. It carries the cold water into the system, heats it and then warm water is sent through the same coil as output to the user. The second coil is better known as the heating coil. With a swirling motion it is twisted around the carrier and heats the water as it passes through. The water unit system consists of different types of sensors to ensure correct and efficient operation. When the hot water faucet is turned open, two sensors are activated: the pressure and temperature sensors. The pressure and temperature of the incoming cold water are measured and the data is sent to a microprocessor for calculations. The microprocessor compares the calculated values with the pre-programmed data, and adjusts the heating coil as needed [7-8]. Figure 1 shows the conceptual design of the in-line water heating system.

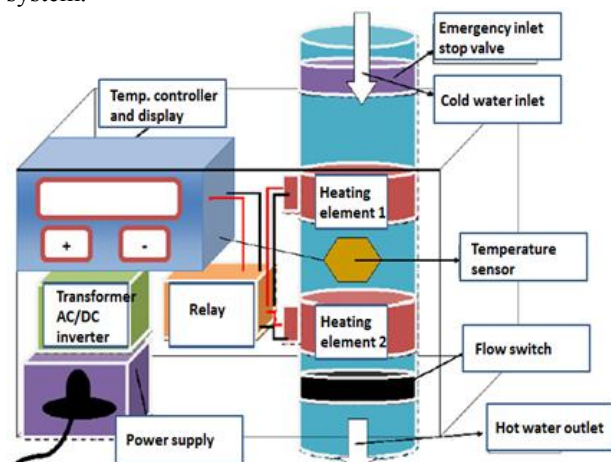


Figure 1: Conceptual design of the in-line water heating system

The components are as follows: temperature controller, transformer or AC/DC inverter, relay, heating elements, emergency input valve, temperature sensor, flow switch, outside enclosure containing all the components, outlet valve, power input inlet, and heating pipe. The system is designed to provide reliable operation with maximum efficiency at minimal cost.

Cold water fills the pipe which can be copper or galvanize pipe. The flow switch detects the water flow in the system and turns on the heating elements. The temperature sensor sends a signal to the temperature controller which in turn correlates the received temperature with the pre-programmed temperature. The controller also sends a signal to the relay that conveys the essential power to the heating elements. The heating elements heat the pipe with the power reviewed from the relay. The heated water reaches the outlet. As soon as the inlet faucet is turned off the flow sensor opens and the system turns off.

3. DETAILED DESIGN

The detailed design of the system is shown in figures 2 and 3.

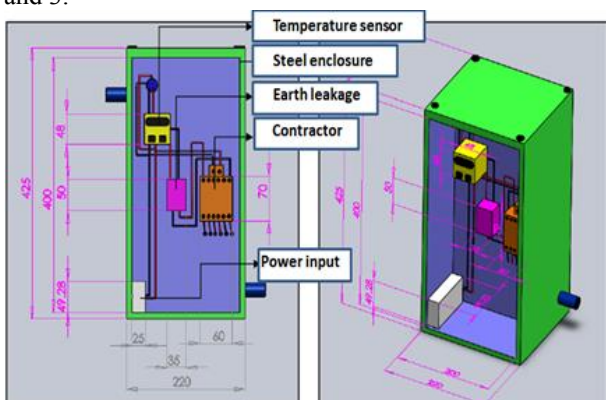


Figure 2: Designed in-line water heating system with all necessary components

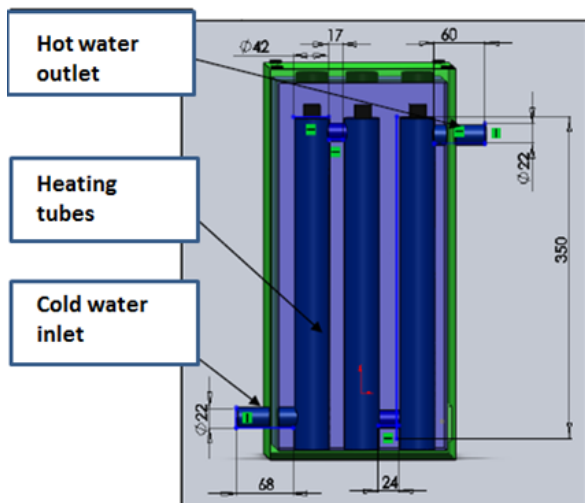


Figure 3: Water circulating component of the system

The design consists of a 230 VAC PID controller, power inlet at 230 VAC, electromechanical relay, contractor, three 4 kW screw type stainless steel geyser elements, a PT 100 temperature sensor, cold water inlet with pressure reducing valve, and a warm water outlet faucet with a flow switch mounted inside the outlet pipe.

The main task of the project is to provide the system with optimal control in order to increase efficiency of the system. The temperature controller can either increase or decrease efficiency of the system depending on how it is used. On/off control would be the most uncomplicated mode to select, but the water heating system should be energy efficient and more advanced than existing water heaters. The PID control option is selected for the project. The reason for this is because PID control takes present, future and past errors in consideration to assure efficient working of the system. PID control improves the speed of the response, suppress disturbances and reduce oscillations. Control accuracy is dependent on the signal from the temperature sensor. PT 100 (platinum resistant thermometer) temperature probe was implemented in the design. In most heating water systems a basic geyser thermostat is used. However, the temperature controller is not adjusted to the thermostat input. The PT 100 temperature probe is another critical integration. The output of the system is dependable on the temperature sensor. The PT 100 ranges from $-199.99\text{ }^{\circ}\text{C}$ to $500\text{ }^{\circ}\text{C}$. The probe sends a temperature input to the temperature controller. If the process value reaches the set value (in a particular case $40\text{ }^{\circ}\text{C}$) the heating unit should switch off. The temperature probe is located in the second heating tube. This is done in order to make the process less flexible and the output more stable. The measured hot water output was adjusted by a couple of degrees Celsius for the measurement to be accurate.

CN-40 temperature controller was used to display both the process and set values of the system. The output of the system is dependable on the programmed settings of the controller. Most of the settings on the controller are pre-programmed. The controller receives 220 V and data from the PT 100 sensor and the in-line Flow/Pump flow switch. The Flow/Pump flow switch is the critical component which makes the heating system an in-line or instantaneous system. The switch enables the system to switch on as soon as enough water passes through the normally open switch. The pressure allows the switch to close, which in return activates the controller and energizes the contractor. When the contractor is de-energized the heating elements switch off. Each of the three stainless steel heating elements is mounted in a stainless steel heating tube.

The heating elements are connected to the contractor as well as to the earth connection in the casing. This is required by safety standard for electrical products. The CN-40 temperature controller, flow switch, contractor, and heating element are shown in figure 4.

To calculate the efficiency of the in-line water heating system, the Watts hour have to be measured and

compared to existing systems. A kWh counter was integrated for this purpose. An identical unit was also connected to a conventional geyser in order to be able to make a comparison. The counter has a green light if zero or minimal energy is drawn, a flashing red light during normal load operation and a green/red flashing when a fault occurs. The counter is shown in figure 5 a).

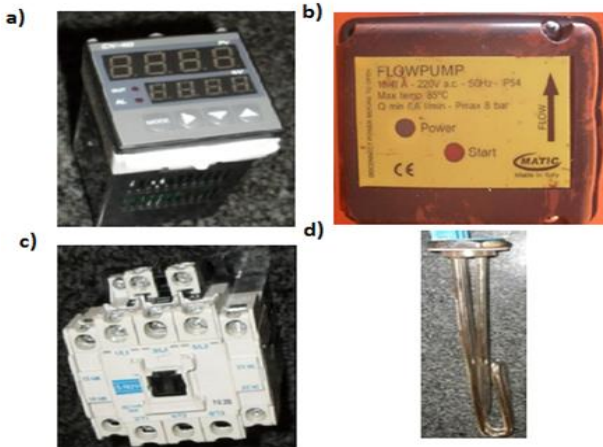


Figure 4: In-line water system components: a) CN-40 temperature controller, b) Flow/pump switch, c) contractor, d) heating element

Earth leakage connector can also be seen as one of the main safety devices in the heating system. The earth leakage will trip for several reasons. If any of the electrical wiring or devices receives water damage the earth leakage will trip. The earth leakage connector is shown in figure 5 b).

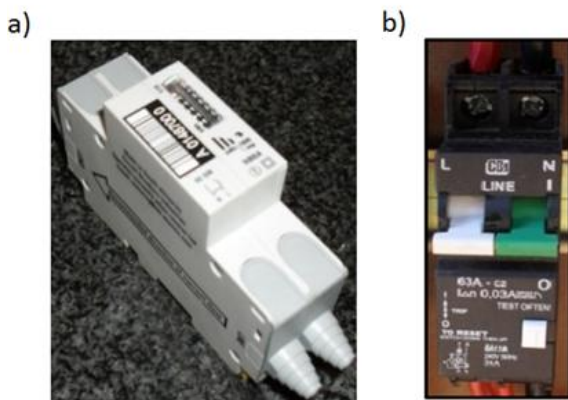


Figure 5: a) single-phase kWh counter, b) earth leakage connector

All the individual units come together in a 600 mm x 400 mm x 200 mm steel enclosure. The enclosure is waterproof and will protect the electrical units from dust and water particles. Both plumbing and electrical devices are mounted inside the enclosure. The controller is mounted in the door, with the display facing outwards for easy accessibility. This enclosure is smaller than

conventional water heating systems presented in the market.

The completed system is shown in figure 6.

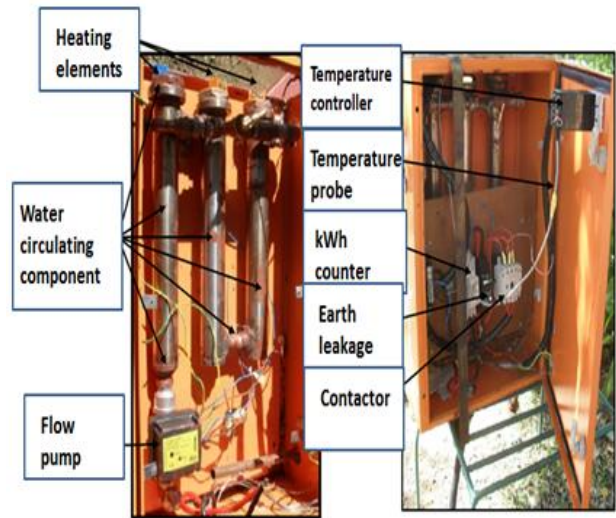


Figure 6: Completed in-line water heating system

4. SIMULATIONS AND PRACTICAL RESULTS

The system was simulated for a variation of inputs in order to predict system behaviour before testing. From the flow lines in figure 7 a) is clearly visible how the 20 °C input cold water heats up with three separate 4 kW heating element in each heating tube to obtain an average output value of 34 °C when the water flows at 0.1333 kg/s (8 l/min).

Figure 7 d) shows the temperature simulation results where input flow rate of the water has been reduced, while figure 7 c) shows the result for an increase in flow rate. By reducing the speed of the water flow inside of the heating tubes a more suitable and stable output can be achieved.

Figure 7 b) shows the simulation results in terms of pressure for a cold water input value of 20 °C at flow rate of 0.1333 kg/s. The results show a decrease in pressure during the flow in each heating tube. If the faucet at the outlet is turned off the pressure in the system will increase.

The practical tests were performed in the laboratory. Two systems: 1) conventional and 2) in-line water heating systems were tested and the results were compared. The conventional geyser used power of 10.5 kW and two and half hours to heat 150 litres of water from 15 °C to 60 °C. This means that the geyser takes 70 Wh to heat a single litre of water. The in-line water heating unit consumed the same amount of energy of half of the time, but provided more than twice as much hot water.

The instantaneous geyser takes 24.9 Wh to heat a single litre of water. This is 36.9 Wh per litre difference compared to the conventional geyser. Figure 8 shows

conventional geyser versus the in-line water heating systems energy consumptions.

From figure 8 it is visible that in both systems kWh rating is directly growing to the time for which the system is running. With a high current rating the in-line water heating systems takes only seconds to reach the process value, while the conventional heating system takes hours.

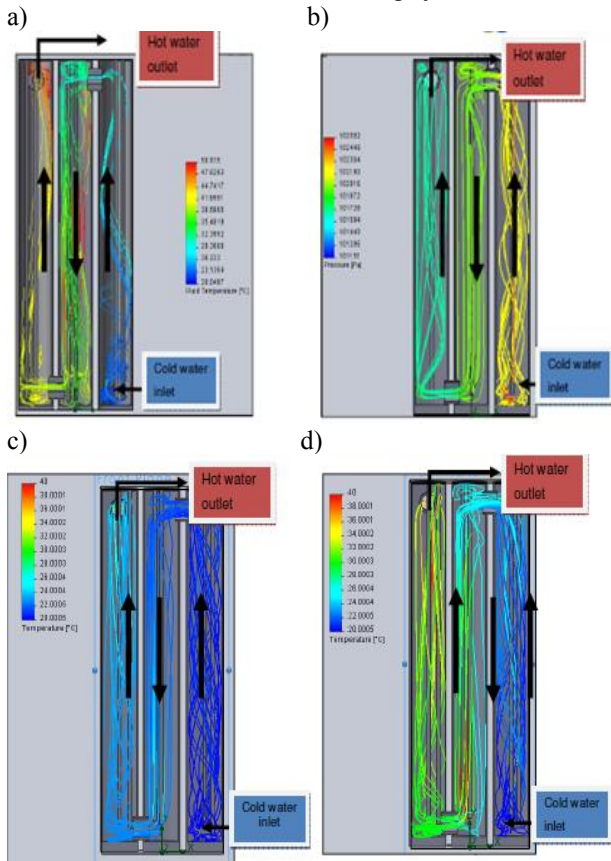


Figure 7: In-line water system simulation: a) temperature analysis for 12 kW at 0.1333 kg/s, b) pressure analysis for 12 kW at 0.1333 kg/s, c) temperature analysis for 12 kW at 0.66 kg/s. d) temperature analysis for 12 kW at 0.233 kg/s

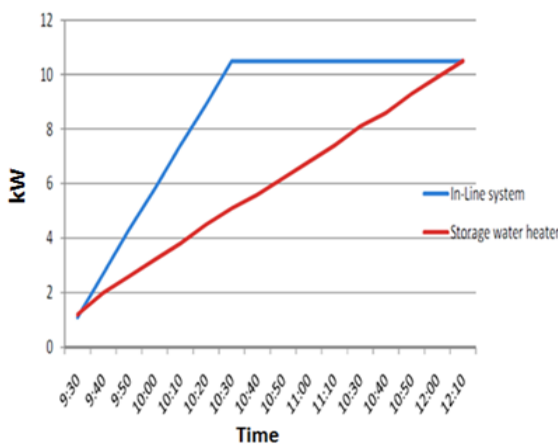


Figure 8: Energy consumption of a conventional and in-line water heating systems

Figure 9 shows the in-line temperature measurements over the energy consumed every ten minutes the system is running. During the first twenty minutes the temperature shows a fluctuation, thereafter the process temperature shows increase up until 45 °C. For the last twenty minutes the process stabilizes at 45 °C.

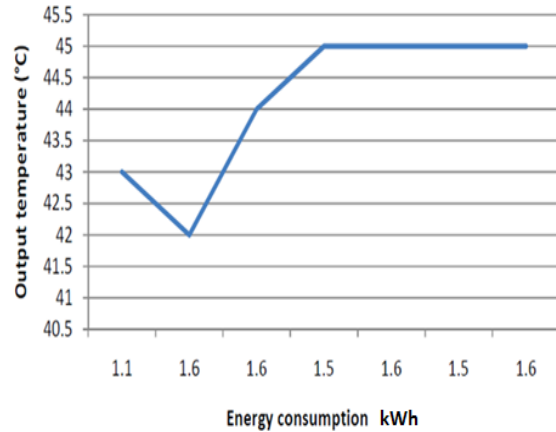


Figure 9: Energy consumption with output temperature of the in-line water heating systems

5. CONCLUSIONS

Energy savings in industry are becoming a problem in South Africa. The authors of the paper conducted a literature study to find possible ways to minimize the energy consumption in industry by maximizing efficiency of electro-technical processes. One of these processes was water heating.

An efficient in-line water heating system with a controller is designed and tested. The energy consumption was measured and compared to a conventional storage water heating system. After a variety of tests and measurements the in-line water heating system appeared to be more energy efficient. The system can supply hot water within 35 seconds from turn on at a flow rate of 7 litres per minute. Ideally in any hot water system the flow rate should be unlimited, but in comparison to existing water heaters in-line water system performed better.

Apart from unlimited hot water supply the in-line heating has a number of advantages such as: size, adaptability to a variety of locations, and robustness. The system is a right solution for industries where instantaneous flow of hot water is required.

6. REFERENCES

[1] C. A. Duff, C. Bradnum, "Design of domestic water heating system to save water and electricity," Proc. of Domestic Use of Energy Conf. (DUE), Cape Town, South Africa, 2013, pp.: 1- 6.

[2] L. Jiayou, Z. Yanxin, "Techno-economic analysis on water source heat pump system," Int. Conf. on Energy and Environment Technology (ICEET), Guilin, Guangxi, Oct. 16-18, 2009, pp.: 385-387.

[3] H. Thybo, L. Larsen, "Control of a water-based floor heating system," IEEE Int. Conf. on Control Applications (CCA), Singapore, Oct. 1-3, 2007, pp.: 288-294.

[4] L. Jinhai, F. Lide, C. Suosheng, Kong Xiangjie, "Analysis of dynamic model of heating system after step change of water supply temperature," 10th Int. Conf. on Control, Automation, Robotics and Vision, (ICARCV), Hanoi, Dec. 17-20, 2008, pp.: 1924-1928.

[5] "Instant Shower Heater," [Online]. Available: <http://www.gosurfonline.co.za/instantwaterheater.html>. [Accessed: Apr. 24, 2014].

[6] "Shower Heater," 2008. [Online]. Available: <http://www.zj-zhenhua.comuctid=1087>. [Accessed: Apr. 24, 2014].

[7] "Compare Electric Tankless Water Heaters," [Online], Available: <http://www.e-tankless.com-tankless-water-heaters.php>. [Accessed: Apr.1, 2014].

[8] W.J.Baily, "Advantages of an Instant Water Heater," [Online]. Available: <http://ezinearticles.com>. [Accessed: Apr. 2, 2014].

BAYESIAN PARAMETER ESTIMATION FOR POWER ENGINEERS

W. Doorsamy*, J. Naude*, W. A. Cronje*, and I. Hofsjer*

* School of Electrical & Information Engineering, University of Witwatersrand, Johannesburg, South Africa

Abstract: In recent times, there has been an increase in the application of Bayesian methods in various branches of electrical engineering, such as power systems, machine learning, signal processing, and control. This growing interest comes from the need for methods which provide statistical inference and decision making under uncertainty. However, there is a deficiency in simple, illustrative and contextual material for teaching and learning purposes. This paper provides such material in the form of a tutorial to assist students, teachers, researchers, and practitioners in the field of electrical engineering. Two examples demonstrating the practical application of basic probability theory and Bayesian parameter estimation are presented.

Key words: Bayesian methods, Electrical engineering, Probability, Tutorial.

1. INTRODUCTION

This paper presents a tutorial on the application of probability as extended logic. Two illustrative examples of how probability theory is applied in electrical engineering are given. The first example determines the unknown value of a resistor using basic probability theory and the second deals with the application of Bayesian theory in estimating the parameters of an unknown linear time-invariant (LTI) system. In general, the field of statistics is based on two major paradigms namely, frequentist and Bayesian. Bayesian methods provide a complete paradigm for both statistical inference and decision making under uncertainty [1]. These methods are widely utilised in various branches of science and engineering. More specifically, in electrical engineering, Bayesian methods are applied in *inter alia*, machine learning [2], control systems [3], signal processing [4], power systems [5], and instrumentation and measurement [6]. However, the growing requirement for probability theory in electrical engineering has surpassed the availability of simple, illustrative, and contextual information. An extensive review of literature confirms this deficiency in suitable teaching and learning material. This paper demonstrates the practical application of probability theory and provides material which will assist students, teachers, researchers and practitioners in the field of electrical engineering.

2. PROBABILITY AS EXTENDED LOGIC

Probability theory has a rich history. The initial motivation for probability theory was a means to characterize games of chance and was first described by Cardano in the 16th century [7]. Mathematicians and physicists, such as Poisson, Poincare, Gauss, Laplace and Euler have all had an influence on its development as a body of knowledge. Laplace was the most influential in the early analytical development with the work, *Théorie analytique des probabilités*, which gave useful and important results [8]. This work was challenged by Venn, Nyman and Pearson and eventually marginalised to make room for

what would become known as orthodox or frequentist statistics [9]. Harold Jeffreys, Richard T. Cox and Edwin T. Jaynes were responsible for reviving Laplace's work, which included Bayes theorem [10]. Jaynes showed that probability is a natural extension of Aristotelian logic and that the axioms of frequentist probability are actually derivable as a logical consequence of key desiderata of rational thought [11]. Moreover, given that orthodox statistics was not derived from these logical desiderata, it is a mathematical fact that there is a pathological inconsistency in the reasoning of orthodox statistics. Probability represents a rational agents state of knowledge and is numerically equal to a frequency of some repetitive experiment only under very special circumstances. It can be chosen to be represented by the real numbers between zero and one. Instead of stating whether a proposition is true or false, the probability represents a degree of truth given some information [11].

All probability is dependent on what is actually known. For instance, let A be some definite logical proposition say - "the earth is flat" - then $p(A)$ would be the probability that "the earth is flat" [11]. The statement $p(A)$ is meaningless as it does not state which background information has been used to draw the conclusion on the probability. A probability always needs conditioning information (even if it is just background information) and is denoted in equation (1). Equation (1) is read as, "*the probability of A, given X*". It should be noted that A does not have to be random at all, it is simply a proposition which one would like to infer the degree of truth of.

$$p(A|X) \quad (1)$$

There are two important rules for probability theory as extended logic, the "sum" and the "product" rules [11]. The product rule allows the expansion of the *AND* operator in a logical proposition. For example the probability that "the earth is flat" - A *AND* "the sky is falling" - F , given the background information - X , is written as $p(A, F|X)$. The comma notation for logical *AND* will be used throughout

this paper. The product rule which expands these sort of logical propositions is given by equations (2) and (3) [11].

$$p(A, B|X) = p(A|X)p(B|A, X) \quad (2)$$

$$= p(B|X)p(A|B, X) \quad (3)$$

The sum rule is given by equation (4), where \bar{A} is the logical NOT of the proposition A . Essentially the sum rule states that it is a certainty that a logical proposition is TRUE or FALSE [11].

$$p(A|X) + p(\bar{A}|X) = 1 \quad (4)$$

A simple derivation using De Morgans' law and equations (2) - (4) results in the extended sum rule in equation (5) [11].

$$p(A \text{ or } B|X) = p(A|X) + p(B|X) - p(A, B|X) \quad (5)$$

Consider the case of multiple logical propositions H_i , where i is an integer in $[0, N]$. If the propositions are mutually exclusive, this implies $p(H_i, H_j|X) = 0 \forall i \neq j \in [0, N]$ which means that it is impossible for both H_i and H_j to be true simultaneously. Additionally, if the propositions are collectively exhaustive, meaning that it is a certainty that at least one of the hypothesis is true, implies that $p(H_0 \text{ or } H_1 \text{ or } \dots H_N|X) = 1$. Finally, if the propositions are both mutually exclusive and collectively exhaustive (MECE), then using the extended sum rule in equation (5), the MECE probability sum is arrived at in equation (6) [11].

$$p(H_0 \text{ or } H_1 \text{ or } \dots H_N|X) = \sum_{k=0}^N p(H_k|X) \quad (6)$$

The suite of tools needed for applying and manipulating logical propositions using probability are all available in equations (2) - (6). For instance, Bayes' theorem is simply the equality of the two representations of the product rule in equations (2) and (3). This derivation is done in equations (7) - (9) with Bayes theorem resulting in equation (9).

$$p(A, B|X) = p(B, A|X) \quad (7)$$

$$p(A|X)p(B|A, X) = p(B|X)p(A|B, X) \quad (8)$$

$$\implies p(B|A, X) = \frac{p(B|X)p(A|B, X)}{p(A|X)} \quad (9)$$

Furthermore, equations (5) - (9) are special results from repeated application of the sum and product rules. It should be noted that there are important conditions which need to be true for equation (6) to be valid. All other equations in the set between (2) - (9) are unconditionally true [11]. To wrap up the theory, some terminology is needed for Bayes theorem in equation (9). There is the posterior probability, the prior probability, the likelihood and the normalisation constant. Rewriting equation (9) using this terminology results in equation (10) [11].

$$\text{posterior} = \frac{\text{prior} \times \text{likelihood}}{\text{normalisation}} \quad (10)$$

All probability calculations begin with answering the following set questions:

1. What do you know now?
2. What do you want to know?
3. What do you know before the experiment?
4. What model are you going to use for the likelihood?

Generic answers to these questions are:

1. X is known now. This is a collection of all the user's knowledge up to this point.
2. The probability of a hypothesis H , given some measured data D , and background knowledge X - i.e. $p(H|D, X)$
3. The prior is what is known from the background information - i.e. $p(H|X)$
4. The model which represents how likely the data are, if you accept the model as true $p(D|H, X)$.

A number of significant mistakes have been made in court rooms, in the financial world, and in science and engineering by failing to strictly adhere to the rules of probability. A common mistake is unconditional multiplication of probabilities as presented in equation (11). The only time this is allowed is when A and B are logically independent [11].

$$p(A, B|X) \neq p(A|X)p(B|X) \quad (11)$$

Another common mistake is assuming the equality given in equation (12).

$$p(A|B) \neq p(B|A) \quad (12)$$

3. EXAMPLE 1: AN UNKNOWN RESISTOR IN A BOX

The E6 series of resistors is a set of resistors which have 20% tolerance, as stated by the colour bands on the resistor. There are 6 values per decade, which is the reason for naming it the E6 series. For 6 decades worth of resistors, there are exactly 36 possible colour band combinations on the resistors. Consider the problem of trying to identify which of the 36 possible E6 resistors is within a black box. It is emphasised that this experiment is not about finding the resistance, it is about identifying which of the possible colour bands are actually on the resistor in the box. The experimental setup is depicted in Figure 1. The background information X is usually implied, but not explicitly stated. Here X is the knowledge that: the DC voltage is V_{dc} ; the E6 resistor series has a 20% tolerance; there is definitely one and only one of the E6 series in the box; the ammeter has a maximum current measurement

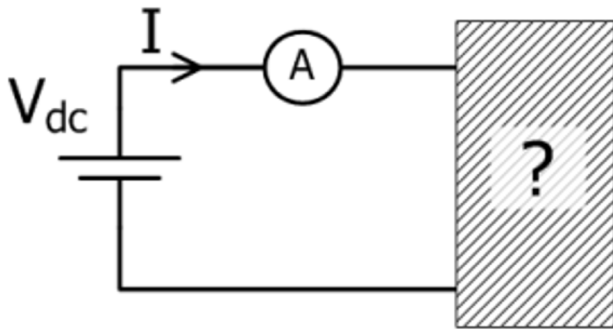


Figure 1: Circuit configuration of experiment with an unknown E6 resistor in a box

of I_{max} and a resolution of δI . Note that I is measured by the ammeter in Figure 1 and is not known before the experiment whereas X is known before the experiment is conducted. In this experiment, the desired quantity is the probability for each of the resistors, given: the measured current I and the other relevant knowledge X . This quantity is written as $p(R_i|I, X)$, where R_i is the label on the i^{th} resistor. Using the presented Bayesian theory, the calculation for finding each of the 36 probabilities is:

$$p(R_i|I, X) = \frac{p(R_i|X)p(I|R_i, X)}{p(I|X)} \quad (13)$$

There are a number of parts to the right-hand side of equation (13) - i.e. the prior probability, the likelihood and the normalisation. Each of these will be addressed separately before continuing.

3.1 Prior Probability - $p(R_i|X)$

The prior probability is the knowledge of which resistors are more or less likely before the experiment is conducted. Given that nothing is known before the experimental results, to claim that any one resistor in the set of 36 is more likely than another requires additional knowledge not present in X . The most honest reflection of the state of knowledge that is captured by X and most non-committal stance is to make all of the 36 resistors equally likely. Written mathematically, this is reflected in equation (14).

$$p(R_i|X) = p(R_k|X) \quad (14)$$

Equation (14) is valid for all $i, k \in [1, 36]$. Since X dictates that one and only one of the resistors in the E6 resistor series must be in the black box, it is a certainty that either R_1 or R_2 or...or R_{36} is in the box. Written mathematically, this is expressed in equation (15).

$$p(R_1 \text{ or } R_2 \text{ or } \dots R_{36}|X) = 1 \quad (15)$$

Furthermore, since X stipulates that the probability of having two resistors in series is zero - i.e. $p(R_i, R_k|X) = 0$, the modified sum rule can be applied to the logical

proposition in equation (15) resulting in equation (16).

$$\sum_{k=1}^{36} p(R_k|X) = 1 \quad (16)$$

Combining the facts of equation (14) and (16), the sum of 36 equal terms results in equation (17).

$$\begin{aligned} 36 p(R_k|X) &= 1 \quad (17) \\ \implies p(R_k|X) &= \frac{1}{36} \quad (18) \end{aligned}$$

It is worth mentioning that although this is a labourious derivation of what was intuitive from the information given, equation (17) is derived from the axioms of probability and is not a definition of probability [11].

3.2 Likelihood - $p(I|R_i, X)$

The likelihood is literally the probability of the current measured, I given the label on the i^{th} resistor. This is not a question of the current given the resistance as Ohm's law gives that unambiguously. Simply put, it is asking about the possible current measurements given the *label* on the resistor. Given that the resistors have a tolerance, there will naturally be a tolerance on the possible currents that can be measured, even if V_{dc} is known absolutely and is perfectly constant. To make this worked example simple, the likelihood function is somewhat contrived. A Gaussian-like function with two standard deviations placed at the edge of the tolerance envelope is used. The reader is free to use other probability functions which may represent the situation more accurately when applying this methodology to real problems.

The IEC 60063:1963 standard stipulates the preferred numbers for resistors and capacitors how the tolerance envelopes should overlap [14]. It has been reported that during the manufacturing of resistors, any out-of-specification resistors are placed into the next tolerance band. For example, if 1% tolerance 100 Ω resistors are being manufactured, and a resistor happens to be 105 Ω or 95 Ω , then it is not scrapped but is placed among the 5% tolerance resistors. The consequence is that for low tolerance resistors, the measured resistance value will almost never be the value that is stated on the component. This information is not taken into account to simplify this example. Additionally, it should be noted that the ammeter in Figure 1 is digital in the presented case. As a result, there is a finite resolution in both time and amplitude. Hence, the likelihood function is discretised to within the digital ammeter's resolution, δI . Analog ammeter's have a finite measurement resolution (given by the markings on the instrument). For this specific example, the possible values of I are given by equation (19).

$$I = k\delta I \quad (19)$$

where k is an integer and the absolute maximum value it could be is given by equation (20).

$$|k_{max}| = \frac{I_{max}}{\delta I} \quad (20)$$

Maximum entropy distributions: What likelihood function should be used for $p(I|R_i)$? In this case, using a discrete Gaussian is a good assumption provided that *all* that is known are the mean and variance [11]. If more than this is known, then a Gaussian distribution is too conservative and more information can be gleaned from the experiment [11]. A discrete Gaussian distribution is a maximum entropy distribution when all that is known are the first two moments. If entropy measures uncertainty (which a number of researchers believe to be true) then maximum entropy distributions, subject to the known constraints, represent the extreme of ignorance one can be in, knowing only the mean and variance [12]. Using any other distribution, when all that is known is the mean and the variance, would in effect be claiming something one does not know. The maximum entropy principle subject to given known constraints, is a generalisation of the argument in Section 3.1. In fact, the mathematical machinery of maximum entropy, subject to the constraint that there only 36 possible values and *no other information is known*, lead exactly to equation (17).

In other words, there is a combinatorial reason for using a Gaussian distribution. The distribution is what one would get if choosing “randomly” amongst all the possible distributions which have a fixed mean and variance, which numerically match the known values. This is one of the interpretations of the derivation of the maximum entropy distribution. A maximum entropy distribution with finite states k , with a known mean $\langle k \rangle$, and second moment $\langle k^2 \rangle$ is given by the following set of equations [11]:

$$MaxEnt = \frac{1}{Z} \exp \{ -\lambda k - \eta k^2 \} \quad (21)$$

$$Z = \sum_{k=k_{min}}^{k_{max}} \exp \{ -\lambda k - \eta k^2 \} \quad (22)$$

$$-\frac{\partial \ln Z}{\partial \lambda} = \langle k \rangle \quad (23)$$

$$-\frac{\partial \ln Z}{\partial \eta} = \langle k^2 \rangle \quad (24)$$

Maximum entropy distributions are typically solved numerically for the free parameters [11], λ and η in this case. For the problem at hand, the expected current that we will measure is the result of Ohm’s law if the value of the resistor is what is printed on the label R_i . In other words, the average current is:

$$\langle I \rangle = \frac{V_{dc}}{R_i} \quad (25)$$

since the expected value of the resistor is what is printed on it. The variance depends on the tolerance of the resistors, which is 20% in this case. Note that the standard deviation

(square root of variance) is related to the second moment and average value via equation (26).

$$\sigma^2 = \langle I^2 \rangle - \langle I \rangle^2 \quad (26)$$

The maximum entropy distribution for the current is then given by the set of equations (27) - (30), which is numerically solved as follows:

$$p(I|R_i, X) = \frac{1}{Z} \exp \{ -\lambda I - \eta I^2 \} \quad (27)$$

$$Z = \sum_I \exp \{ -\lambda I - \eta I^2 \} \quad (28)$$

$$-\frac{\partial \ln Z}{\partial \lambda} = \frac{V_{dc}}{R_i} \quad (29)$$

$$-\frac{\partial \ln Z}{\partial \eta} = \sigma^2 + \left(\frac{V_{dc}}{R_i} \right)^2 \quad (30)$$

The final piece of the model is the standard deviation σ , given what is known. For explanatory purposes, two standard deviations are placed at 20% of the average value. When applying this methodology to real world problems, if it is known that the manufacturing plant that produces the resistors is a “six sigma” manufacturer, then the 20% tolerance can be made to occur at three standard deviations. As an alternative to numerically solving equations (27) - (30), one may directly use the definition of a Gaussian as shown in equation (31).

$$p(I|R_i, X) = \frac{1}{Z_i} \exp \left\{ -\frac{1}{2\sigma_i^2} \left(I - \frac{V_{dc}}{R_i} \right)^2 \right\} \quad (31)$$

$$Z_i = \sum_I \exp \left\{ -\frac{1}{2\sigma_i^2} \left(I - \frac{V_{dc}}{R_i} \right)^2 \right\} \quad (32)$$

The difference now is that a new normalisation condition must be fulfilled in equation (32). This summation is over $I = -I_{max} + k\delta I$, with k as an integer between $[0, 2k_{max}]$. Finally, the two standard deviations at 20% of the average value results in equation (33).

$$2\sigma_i = 0.2 \frac{V_{dc}}{R_i} \quad (33)$$

This second parameterisation of the maximum entropy distribution (equation (32)) will be used due to its simplicity. An arbitrary likelihood appears, as in Figure 2, with important states highlighted - namely the average value and the first standard deviation away from the average.

3.3 Normalisation Constant - $p(I|X)$

The normalisation constant $p(I|X)$ can be rewritten, using simple logic, as equation (34).

$$p(I, true|X) = p(I, (R_1 \text{ or } R_2 \text{ or } \dots \text{ or } R_{36})|X) \quad (34)$$

Any logical proposition of $A \text{ AND } TRUE$ is true - i.e. $A, true = A$. It is true that one of the resistors must be in the box in the circuit of Figure 1, so the sequence of *or* propositions may be substituted for *true* on the left-hand

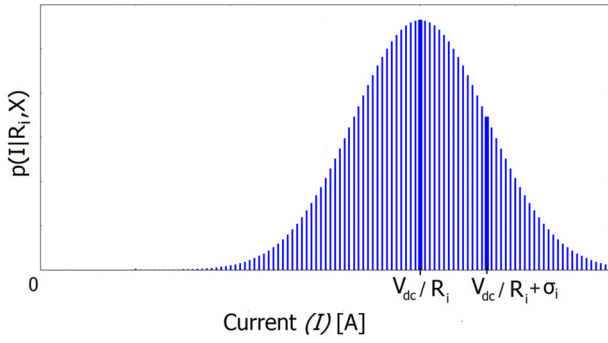


Figure 2: Likelihood function for all possible currents, given a fixed resistor - R_i

side of equation (34). Finally, since the set of propositions involving the resistors is mutually exclusive and collective exhaustive, equation (36) is the ultimate result of logically decomposing the normalising constant.

$$p(I, (R_1 \text{ or } R_2 \text{ or } \dots \text{ or } R_{36})|X) = \sum_i p(I, R_i|X) \quad (35)$$

$$= \sum_i p(R_i|X) p(I|R_i, X) \quad (36)$$

Hence, $p(I|X)$ is the marginalisation over all possible resistors.

3.4 The Final Calculation

The Bayesian machinery has been set-up and the final algorithm for calculating the probabilities for each of the resistors in the E6 series is given by equation (38). It should be noted that the uniform prior probabilities $p(R_i|X)$ have been cancelled out of the top and bottom of equation (13).

$$p(R_i|I, X) = \frac{p(I|R_i, X)}{\sum_i p(I|R_i, X)} \quad (37)$$

$$= \frac{\frac{1}{Z_i} \exp\left\{-\frac{1}{2\sigma_i^2} \left(I - \frac{V_{dc}}{R_i}\right)^2\right\}}{\sum_i \frac{1}{Z_i} \exp\left\{-\frac{1}{2\sigma_i^2} \left(I - \frac{V_{dc}}{R_i}\right)^2\right\}} \quad (38)$$

The remaining tasks are to conduct the experiment in Figure 1, measure I , and plot the probabilities for each of the resistors using equation (38) for each resistor. To elucidate this procedure, a few explicit calculations will be done to illustrate the use of equation (38). Firstly, assume it is known that $V_{dc} = 10V$, $I_{max} = 5A$ and $\delta I = 1mA$. The first decade of E6 resistors is the set $\{10\Omega, 15\Omega, 22\Omega, 32\Omega, 46\Omega, 68\Omega\}$. Now consider the case where exactly $1A$ is measured by the ammeter - i.e. $I = 1A$. At first inspection, the resistor within the box is most likely to be the 10Ω , since $\frac{10V}{10\Omega} = 1A$. Using

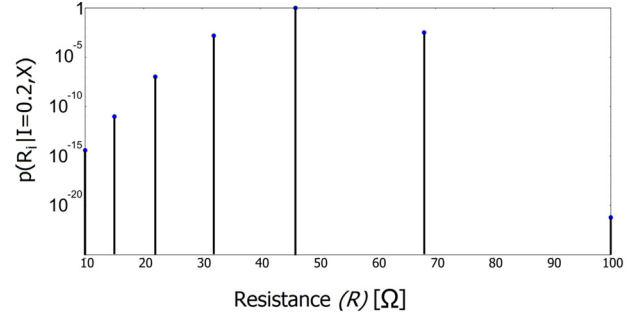


Figure 3: Probability of E6 resistor given a measured current of $I = 0.2A$

equation (38):

$$p(R = 10|I = 0.8, X)$$

$$\approx \frac{\frac{1}{250} \exp(0)}{\frac{1}{250} \exp(0) + \frac{1}{167} (10^{-6}) + \frac{1}{113} (10^{-32}) + \frac{1}{78} (10^{-106}) + \dots}$$

$$= 0.9999985\dots \quad (39)$$

which is almost certainty. Calculating the probability that $R = 15\Omega$, the next resistor in the E6 series, when $I = 1A$ gives:

$$p(R = 10|I = 0.8, X)$$

$$\approx \frac{\frac{1}{250} (0.135)}{\frac{1}{250} (0.135) + \frac{1}{167} (0.135) + \frac{1}{113} (10^{-13}) + \frac{1}{78} (10^{-53}) + \dots}$$

$$= 0.4004\dots \quad (40)$$

and doing the same probability calculation for $R = 15\Omega$ gives:

$$p(R = 15|I = 0.8, X)$$

$$\approx \frac{\frac{1}{167} (0.135)}{\frac{1}{250} (0.135) + \frac{1}{167} (0.135) + \frac{1}{113} (10^{-13}) + \frac{1}{78} (10^{-53}) + \dots}$$

$$= 0.5995\dots \quad (41)$$

The conclusion drawn here is that it is more probable that the resistor inside the black box, when $I = 0.8A$, is 15Ω . Equation (38) is also useful because a computer can be used to automatically plot the probability distribution for each of the resistors in the set, for a given current measurement. An example is shown in Figure 3 which depicts a logarithmic plot of the E6 resistor probabilities when $I = 0.2A$.

4. EXAMPLE 2: A FIRST ORDER LTI SYSTEM RESPONSE

As a final example, consider the case of a sampled time domain signal, $y(t)$ presented in Figure 4. For this signal, the sampling time $T_s = 1sec$ and the signal in Figure 4 was simulated using equation (42).

$$y(k) = 6 \left(1 - \exp\left(\frac{-kT_s}{3}\right) \right) + n_k \quad (42)$$

Note that n_k is zero mean, variance 1 Gaussian noise and k is an integer in $[0, 19]$.

4.1 Model Problem Statement

A number of working assumptions are needed to begin modelling the data in Figure 4. Firstly, the assumption of additive noise. Note that y_k is measured data, s_k is the signal or model function and n_k is noise in equation (42). This assumption may be tested by zeroing the signal (if possible). If the data captured during the times of zero signal is not zero but instead is constantly changing, then this adds evidence that the noise is probably additive. The signal part can be any reasonable model which looks like it could fit the data, even piecewise approximations. Typically, there will be some model function which is a result of the known physics of the problem considered. For this case, the step response in Figure 4 looks like a noisy first order or second order step response. For brevity's sake, the first order approximation will be used. This is trivially generalised to an arbitrary model function that the reader would like to use. Lastly, it is known that: any time constant cannot be smaller than 0.5sec due to the Shannon-Nyquist sampling theorem; the noise has unit variance and a mean of zero; the maximum time constant τ_{max} is 15 seconds; the gain cannot be larger than 10 and must be positive ($G_{max} = 10$), and finally that the gain and time constant are discretised with resolution δG and $\delta \tau$ respectively. Hence, this subsection defines the background information X .

4.2 First Order Model

The goal is to model the salient features of the data using a function of the form given in equation (43). This model looks similar to the signal used to generate the data in Figure 4, only so that the technique of finding the parameters can be measured against the truth. An arbitrary model parameter with an arbitrary number of parameters may be used, for example - a straight line with unknown slope and intercept.

$$s(k) = G \left(1 - \exp\left(\frac{-kT_s}{\tau}\right) \right) \quad (43)$$

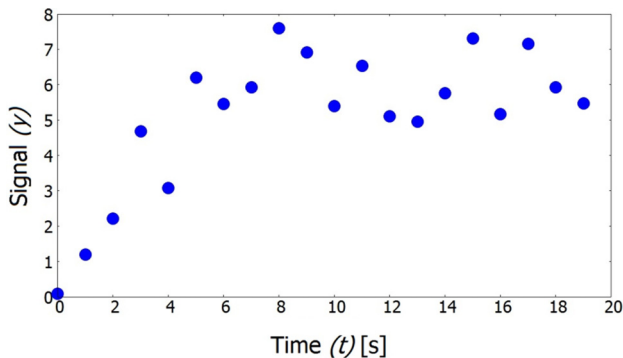


Figure 4: A sampled time-domain signal representing the measured step response of an unknown LTI system

4.3 Probability Calculation

The probability calculation that needs to be performed is the probability for the gain and the time constant, given the data and the background information. Let the data collected be D . The result of applying Bayes' theorem is given by equation (44).

$$p(G, \tau|D, X) = \frac{p(G, \tau|X)p(D|G, \tau, X)}{p(D|X)} \quad (44)$$

The only difference between this problem and the previous example is that there are two parameters to consider in the prior and more importantly, there is more than a single datum to be taken into account in the likelihood. The product rule can be used on the prior, which results in equation (45).

$$p(G, \tau|X) = p(G|X)p(\tau|G, X) \quad (45)$$

At this point, it must be decided whether the time constant depends on the gain in any way at all. It might, if there is some physical knowledge about the system under test. The place to put this interdependency is in the $p(\tau|G, X)$ term. For this example, the gain and time constant are made to be logically independent. Hence, the prior splits into two independent pieces in equation (46).

$$p(G|X)p(\tau|G, X) = p(G|X)p(\tau|X) \quad (46)$$

Again, uniform priors are used over the possible space of gains and time constants. Given the background information, the priors are given by equations (47) and (48).

$$p(G|X) = \frac{\delta G}{G_{max}} \quad (47)$$

$$p(\tau|X) = \frac{\delta \tau}{\tau_{max} - 0.5} \quad (48)$$

As before, these constant priors will cancel out with the normalisation of equation (44). However, this is not always the case. In fact, for this parameter estimation problem, if more data were subsequently taken in another experiment, the outcome of this present calculation would be used as a prior. In that case, there would be additional complexity but the inference would be more accurate as some values must become more unlikely as a result of the present calculation. The likelihood in equation (44) can easily be found using a simple trick. The trick is to work out the probability of the noise first, and then re-write the noise in terms of the signal and the output using equation (42) [13]. Firstly, the probability of having 20 samples of noise, in the order of appearance, must be split using the product rule.

$$p(n_0 n_1 \dots n_{19}|G, \tau, X) = p(n_0|G, \tau, X) p(n_1|n_0, G, \tau, X) \dots p(n_{19}|n_0 n_1 \dots n_{18}, G, \tau, X) \quad (49)$$

If there is any known interdependence between noise samples, then this can be fully taken into account using

equation (49). A typical assumption in other parameter estimation problems is that the noise is identically distributed (same probability function) and logically independent (the samples do not depend on each other). When it is known that the samples are not independent, then the inference can be achieved by assuming they are sub-optimal. In this case, it is clear where the known correlations could be placed between noise samples. For the presented calculation, the noise is considered to be identically distributed and logically independent for the sake of clarity. The result of this knowledge is given by equation (50).

$$p(n_0 n_1 \dots n_{19} | G, \tau, X) = \prod_{k=0}^{19} p(n_k | G, \tau, X) \quad (50)$$

The mean and the standard deviation are all that is known about the noise thus the maximum entropy distribution is a Gaussian. The probability for a single noise sample is given by equations (51) and (52).

$$p(n_k | G, \tau, X) = \frac{1}{Z_\sigma} \exp \left\{ -\frac{n_k^2}{2\sigma^2} \right\} \quad (51)$$

$$Z_\sigma = \sum_k \exp \left\{ -\frac{n_k^2}{2\sigma^2} \right\} \quad (52)$$

In the normalisation, equation (52), the sum is taken over all possible noise samples. This will depend on the resolution and quantisation of the measuring instrument as some values of the noise will be impossible (outside of maximum sensor readings for example) and hence must have a probability of zero. The noise also has a set of discrete levels since the sensor has finite resolution. For these two reasons, equations (51) and (52) are used to represent our uncertainty about the noise samples. Substitution of equation (51) into (50) and using the fact that a product of exponentials is equivalent to the sum of the arguments resulting in equation (53).

$$\begin{aligned} p(n_0 n_1 \dots n_{19} | G, \tau, X) &= \prod_{k=0}^{19} \frac{1}{Z_\sigma} \exp \left\{ -\frac{n_k^2}{2\sigma^2} \right\} \\ &= Z_\sigma^{-19} \exp \left\{ -\frac{1}{2\sigma^2} \sum_{k=0}^{19} n_k^2 \right\} \end{aligned} \quad (53)$$

The final part required to get the likelihood of the data is to transform the noise into the subtraction of the data and the signal - i.e. equation (42). Hence, the likelihood of the data given the model parameters is calculated using equation (42) with (53) to produce (54).

$$p(D | G, \tau, X) = Z_\sigma^{-19} \exp \left\{ -\frac{1}{2\sigma^2} \sum_{k=0}^{19} (y_k - s_k)^2 \right\} \quad (54)$$

In order to find the maximum likelihood of equation (54), the argument of the exponential should be as close to zero as possible. The noise variance σ is fixed and known and cannot be altered and the data captured y_k are similar measured and fixed values. Hence, the parameters of s_k ,

which are samples of equation (43), should be chosen such that the overall sum is as small as possible. The reader will notice that this is exactly the least squares problem. Hence, for a known Gaussian model of noise, maximum likelihood estimation and least squares produce the same result [13]. More importantly, these techniques are both contained as subsets of the full Bayesian analysis. This is only true for this set of assumptions (uniform constant priors, additive noise, gaussian noise model, noise is uncorrelated) and in other cases, MLE and least squares may produce different results with different confidence. Finally, the normalisation of equation (44) is given by equation (55), which is the summation over all possible gains and time constants and is the same process followed in Section 3.3.

$$p(D | X) = \sum_G \sum_\tau p(D, G, \tau | X) \quad (55)$$

Again, the priors cancel due to being constant and the final algorithm to be implemented is given by equation (56).

$$\begin{aligned} p(G, \tau | D, X) &= \frac{p(D | G, \tau, X)}{\sum_G \sum_\tau p(D | G, \tau, X)} \\ &= \frac{\exp \left\{ -\frac{1}{2\sigma^2} \sum_{k=0}^{19} (y_k - s_k)^2 \right\}}{\sum_G \sum_\tau \exp \left\{ -\frac{1}{2\sigma^2} \sum_{k=0}^{19} (y_k - s_k)^2 \right\}} \end{aligned} \quad (56)$$

Recall that $G = m\delta G$ where m is an integer which belongs in $[0, m_{max}]$. The maximum integer with $m_{max} = \frac{G_{max}}{\delta G}$. Similarly, $\tau = 0.5 + p\delta\tau$ with p as an integer running from $[0, p_{max}]$ and $p_{max} = \frac{\tau_{max}-0.5}{\delta\tau}$. The probability distribution given in equation (56) is two dimensional and exists in a space of all possible G and τ . It is also a probability mass function and as such, the discrete values of G and τ may be inserted which results in a probability for those parameters. Selection of the parameters that one will use as the model \hat{G} and $\hat{\tau}$ is discretional. One may use the averages, the median values or the mode of the distribution for each of the parameters. Also, marginalisation can be used to reduce the dimension of the problem. For example, if one is only concerned about the probability for G then marginalising equation (56) involves summing both sides over all possible τ . The result is given by equation (57).

$$\begin{aligned} p(G | D, X) &= \sum_\tau p(G, \tau | D, X) \\ &= \frac{\sum_\tau p(D | G, \tau, X)}{\sum_G \sum_\tau p(D | G, \tau, X)} \end{aligned} \quad (57)$$

This can be simply thought of as taking into account all possible values of τ and what remains is the probability for G only. It is identical to what was done in the normalisation value in Section 3.3. The marginalised gain is presented in Figure 5. Note that the mode of the marginalised gain is exactly the truth, $\hat{G} = G = 6$. The average of the distribution in Figure 5 is $\langle G \rangle = 6.26$. The marginal probability for τ is depicted in Figure 6. Again, the mode of the probability distribution in this figure is the truth, $\hat{\tau} = \tau = 3$. The average value of τ in the distribution depicted in Figure 6 is $\langle \tau \rangle = 2.63$. The comparison between the model

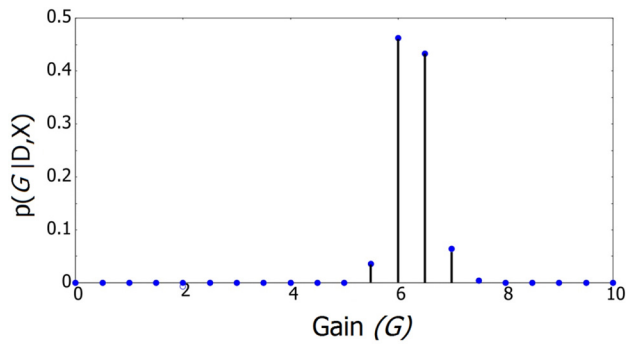


Figure 5: Marginalised probability distribution for the gain G , of the LTI system

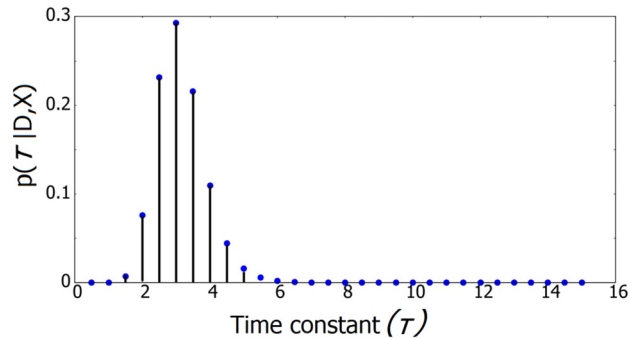


Figure 6: Marginalised probability distribution for the time constant τ , of the LTI system

and the truth, with two sets of single point estimates, is depicted in Figure 7. The two sets of single point estimates of the marginalised posterior distributions in Figures 5 and 6 are: the modes \hat{G} and $\hat{\tau}$; and the averages $\langle G \rangle$ and $\langle \tau \rangle$.

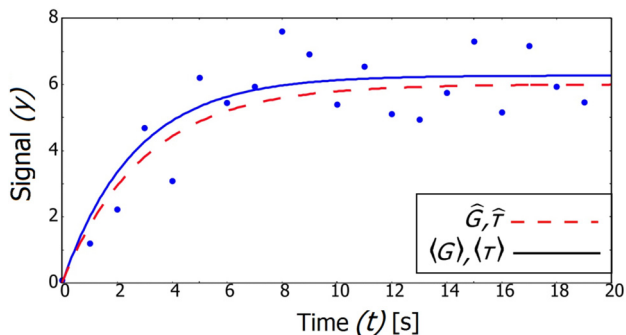


Figure 7: Comparison of the measured step response of the LTI system with various single point estimates

5. CONCLUSION

A tutorial demonstrating the application of basic probability theory and Bayesian parameter estimation is presented. This tutorial is intended as teaching and learning material on the application of Bayesian methods in electrical engineering. Fundamentals of probability are given and thereafter two novel examples are presented. The first example shows how an unknown resistor can be

identified using basic probability theory. Thereafter, a more advanced example on parameter estimation is given. In this example, the parameters of a first order LTI system are determined from a measured step response.

REFERENCES

- [1] J. M. Bernardo: "Bayesian Statistics", In: R. Viertl (ed.), *Probability and statistics, Encyclopedia of Life Support Systems*, EOLSS Publishers, Oxford, 2003.
- [2] W. Lam: "Bayesian network refinement via machine learning approach", *IEEE Transactions on Pattern Analysis and Machine Intelligence*, Vol. 20, No. 3, pp. 240-251, March 1998.
- [3] E. Vargo and R. Cogill: "An argument for the Bayesian control of partially observable Markov decision processes", *IEEE Transactions on Automatic Control*, Vol. 59, No. 10, pp. 2796-2800, April 2014.
- [4] K. Copsey, N. Gordon, and A. Marrs: "Bayesian analysis of generalized frequency-modulated signals", *IEEE Transactions on Signal Processing*, Vol. 50, No. 3, pp. 725-735, March 2002.
- [5] D. C. Yu, T. C. Nguyen, and P. Haddawy: "Bayesian network model for reliability assessment of power systems", *IEEE Transactions on Power Systems*, Vol. 14, No. 2, pp. 426-432, May 1999.
- [6] B. Saha, K. Goebel, S. Poll and J. Christophersen: "Prognostics methods for battery health monitoring using a Bayesian framework", *IEEE Transactions on Instrumentation and Measurement*, Vol. 58, No. 2, pp. 291-296, 2009.
- [7] R. A. Epstein: *The theory of gambling and statistical logic*, Academic Press, first edition, 2012.
- [8] P. S. marquis de Laplace: *Théorie analytique des probabilités*, Ve. Courcier, Paris, 1814.
- [9] N. D. Singpurwalla: *Reliability and risk: A Bayesian perspective*, John Wiley & Sons, 2006.
- [10] P. Damien, P. Dellaportas, N. G. Polson, and D. A. Stephens: *Bayesian theory and applications*, Oxford University Press, first edition, January 2013.
- [11] E. T. Jaynes: *Probability theory: The logic of science*, Cambridge University Press, 2003.
- [12] A. Caticha: *Lectures on probability, entropy and statistical physics*, arXiv.org/0808.0012, 2008.
- [13] G. L. Bretthorst: *Bayesian spectrum analysis and parameter estimation*, Springer-Verlag, 1988.
- [14] International Electrotechnical Commission: *Preferred number series for resistors and capacitors*, IEC Standards Publications, No. IEC 60063, Second Edition, 1963.

ON THE ADEQUACY OF ELECTRICITY RELIABILITY INDICES IN SOUTH AFRICA

R. Herman*, C. T. Gaunt* and L. Tait**

* Dept. Electrical Engineering, University of Cape Town, Private Bag, Rondebosch 7600. E-mail: hermantek@mweb.co.za and ct.gaunt@uct.ac.za

** Energy Research Centre, University of Cape Town, Private Bag, Rondebosch 7600. E-mail: louise.tait@uct.ac.za

Abstract: This paper investigates ways of describing the reliability performance of an electric power grid. Traditional indices such as SAIDI, SAIFI and MAIFI are inadequate for many comparisons and assessments of reliability. They do not reflect financial, economic or socio-political effects of poor reliability. Southern African decision makers in the supply industry, in the national regulator and among customers urgently need clarity on the subject of reliability and guidance on appropriate methods to manage it. This paper examines the extension of existing approaches to reliability indices and describes alternatives based on recent research in the areas of reliability assessment, costs of interruptions and social response to interruptions.

Keywords: Reliability indices, power system reliability, cost of interruptions.

1. INTRODUCTION

In November 2014 the financial analysts, Moody's, downgraded the South African economy citing among its reasons the threat of electrical power shortfall. Also in November, a collapsed coal silo at an Eskom power station lead to load shedding. Clearly, the electrical supply structure in South Africa is weak and vulnerable. In this paradigm it is vitally important to use accurate, effective and appropriate grid performance indicators for making management decisions. These decisions have significant financial implications. In an economy that is already strained by world markets, labour issues and huge debts it is imperative that decisions are made that will result in the greatest benefit for all the stakeholders. These include the users of electricity, from which wealth is derived and the power supply entities, including Eskom. To lend confidence to investors and local industry the supply should be seen as both sustainable and of an acceptable quality. The South African Regulator has the responsibility to monitor the supply and issue regulations, and for this purpose indicators must be employed to monitor both sustainability and quality. In this case the mechanism is the regulation of tariffs and some cases the imposition of penalties. To compound the problem energy theft and non-payment of electricity bills is still rampant in South Africa.

In this paper we look at traditional grid performance indicators, or reliability indices, and examine their usefulness in guiding decisions relating to grid operation and planning. We refer to research done and some publications that suggest a fresh approach that is probabilistic and time-dependent. It combines both frequency and duration of failures resulting in a measure that is amenable to interpretation by non-technical financial managers. The proposed reliability index

expresses the expected performance at load points in the system in terms of value at risk.

2. INTERRUPTIONS: STAKEHOLDERS AND ROLE PLAYERS

Faults on power systems affect the consumer as well as the supplier and also involves body responsible for monitoring and regulating the supply process – the national regulator.

Figure 1 shows the entities affected by and contributing to the overall reliability of the power delivery system. In the past the generation and transmission in South Africa were closely linked and operated by Eskom, while the distribution to industrial, commercial and residential customers was shared by municipal undertakings and Eskom. Generation now includes independent power producers, especially employing wind and solar energy sources, while non-traditional distributors serve some customers.

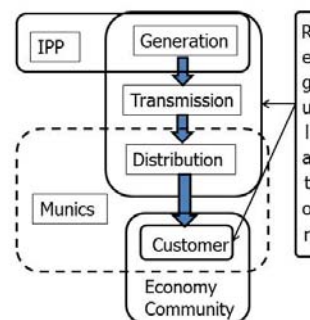


Figure 1. Stakeholders and role players in power system reliability.

The following causes of faults have been identified and characterised for failures on transmission lines in South Africa [1]:

- Lightning
- Fires
- Pollution
- Bird streamers
- Wind storm damage
- Other

However, interruptions can occur in generation simply through inadequacy to meet the load demand, or through external causes or equipment failure throughout the system of generation, transmission and distribution. These interruptions affect the utilities, the customers, the economy and the society.

The utilities experience loss of revenue through energy not served and incur expenses in repairing or replacing damaged equipment. The National Regulator monitors the supply process and responds to complaints about continuity and quality. It regulates tariffs and might also impose penalties for failure to meet supply agreements.

Irrespective of the cause of the outages, the customers suffer loss through damage or lost production and/or sales. Certain customers are more heavily affected than others due to the nature of their application of electrical energy. The effects of the disruption of supplies to customers can be measured by evaluating customer interruption costs (CIC).

A host of associated infrastructure functions that serve a society, such as transport, water supplies, sewerage, emergency services etc. are directly dependent on electrical power. When there are frequent and/or lengthy disruptions the community and the society are very severely affected. This problem is universal and has been widely reported [2, 3].

Lower voltage distribution lines operated by utilities and municipalities in both urban and rural environments are vulnerable to faults caused by weather, birds and animals and even by unintended human interference like vehicle accidents. However, other sources of disruption include theft of energy (illegal connections) and of conductors.

3. CONVENTIONAL RELIABILITY INDICES

A wide variety of indices has been defined to measure the adequacy and interruptions of electricity supplies [4]. In this section we examine only the most common reliability indices based on the following definitions [4] for interruptions of different durations:

- Momentary Interruption – A single operation of an interrupting device that results in a voltage zero
- Momentary Interruption Event – An interruption duration limited to the period required to restore service by an interrupting device. This must be completed in 5 minutes

- Sustained Interruption – Any interruption not classified as a momentary event.

3.1 SAIDI, SAIFI and MAIFI

System Average Interruption Duration Index (SAIDI) indicates the total duration of interruptions for the average customer during a given time period, usually on a monthly or yearly basis. Each interruption to a customer during a sustained interruption is multiplied by the duration experienced and then summed to give the total customer minutes (or hours) during the basis period. It is then divided by the total number of customers on the system. Thus, SAIDI (in minutes) can be expressed as:

$$SAIDI = \Sigma(r_i \times N_i) / N_T \quad (1)$$

Where

r_i = Restoration time in minutes

N_i = Total number of customers interrupted

N_T = Total number of customers served

Only the sustained interruptions are considered, i.e. those longer than 5 minutes, to allow the utility time for automatic restoration [4]. However, short interruptions can never-the-less adversely affect the customers although the duration is excluded from the index.

The System Average Interruption Frequency Index (SAIFI) describes the average number of times a system customer is interrupted during a given period of time and is expressed as:

$$SAIFI = \Sigma(N_i) / N_T \quad (2)$$

In essence SAIFI expresses the probability of customers experiencing an outage within a given time frame.

Since customers can be adversely affected by momentary interruption events the Momentary Average Interruption Frequency Index (MAIFI) was introduced, defined in the same way as SAIFI, but only for the momentary interruption events excluded from SAIFI

These three indices may be applicable to the whole power system or any part of it.

Two similar indices, CAIDI and CAIFI, are customer-based instead of system-based. They and others that reflect power or energy interruptions are used widely in reliability analysis.

3.2 Discussion of conventional indices

Some reliability indices are used to compare the performance of the electricity systems of various utilities or countries in so-called 'benchmarking' surveys. In practice, the indices are difficult to compare because they refer to networks with different customer densities, constructed using different technologies, and/or in regions exposed to different intensities of the conditions

causing the faults. The disparities between indices can be so large, with ratios of up to 60 between indices for different systems, that it is possible even to confuse comparisons based on annual values of SAIDI expressed in minutes and hours.

Most conventional indices are based on average values. These averages (means) give no indication of the dispersion of the interruption data or the extreme values experienced by the worst served customers. Average value indices can be misleading when used in applications sensitive to the full probabilistic spread of the data. Minnaar *et al.* [1] analysed transmission system fault data and concluded that faults were often time, region and season dependent. For example, in South Africa, outages caused by lightning in the summer rainfall area are most likely to occur during the summer months between 12:00 and 18:00. They also showed that the statistical distributions of fault frequency and duration were often skew with large dispersion and could be modelled with a Beta PDF. A probabilistic approach that includes both a specified level of risk in specific time windows of occurrence, which can be paired with the power or demand on the system, provides a more realistic measure of the likelihood of events on the power system and how serious they might be.

A separate problem arises in the under-reporting of momentary events. MAIFI is not often reported in reliability data because it is difficult to know when the short interruptions occur and, where reported, the index is generally only measured at the substation level. Faults on medium and low voltage feeders could go unrecorded and, importantly, a large number of affected residential and small commercial, industrial and agricultural customers could be ignored. These customers may form a significant component of the community and excluding their reliability assessment can exacerbate negative social sentiments.

Recent research has addressed some of these issues and provides approaches to applying reliability indices in small and large power systems and from high voltage to low voltage. Three of these approaches are described in the following sections:

- Considering the probability density functions (PDFs) of the interruption statistics leads to a time dependent probabilistic approach to reliability analysis.
- Factoring the economic costs of interruptions to customers (CIC) into the reliability analysis leads to estimates of the value at risk, a term widely used in the risk sector.
- Surveying the customers' perceptions of interruptions leads to a different, non-technical view of reliability in terms of social acceptance.

4. TDPA ANALYSIS

Most quality of Supply indices are not averages but 5% or 10% risk values or limits, as for example in respect of

voltage magnitude and voltage dips. Edimu *et al.* developed a time-dependent probabilistic approach (TDPA) to reliability analysis of a power system subjected to interruptions caused by the various causes of faults listed in section 2 [5,6]. By taking cognizance of the time and seasonal dependence of faults, a 16-cell time matrix proposed by Herman and Gaunt [7], is used to describe frequency and duration of various fault categories, as shown in Table 1.

Table 1. A 16-cell time matrix with Beta PDF shape parameters defined for all or a specified sub-set of faults

Period or season	Daily time intervals (hrs)			
	0000 - 0600	0600 - 1200	1200 - 1800	1800 - 2400
1	$\alpha_{11} \beta_{11} C_{11}$	$\alpha_{12} \beta_{12} C_{12}$	$\alpha_{13} \beta_{13} C_{13}$	$\alpha_{14} \beta_{14} C_{14}$
2	$\alpha_{21} \beta_{21} C_{21}$	$\alpha_{22} \beta_{22} C_{22}$	$\alpha_{23} \beta_{23} C_{23}$	$\alpha_{24} \beta_{24} C_{24}$
3	$\alpha_{31} \beta_{31} C_{31}$	$\alpha_{32} \beta_{32} C_{32}$	$\alpha_{33} \beta_{33} C_{33}$	$\alpha_{34} \beta_{34} C_{34}$
4	$\alpha_{41} \beta_{41} C_{41}$	$\alpha_{42} \beta_{42} C_{42}$	$\alpha_{43} \beta_{43} C_{43}$	$\alpha_{44} \beta_{44} C_{44}$

Adopting the approach of modelling only the down states of the power system in a Monte Carlo simulation, it became possible to reduce the calculation time for a system reliability study by more than a factor of 30 compared with the conventional approach [5]. Within any 6-hour window of Table 1, probability-based indices may be calculated for any chosen level of risk (or confidence) for use in operational procedures. The application is similar to that of a contingency analysis, except that in contingency analysis a different level of risk is associated with each fault possibility. Deterministic contingency analysis, assessing the effects of an (N-1) event, is appropriate for small systems, but as systems increase in size and complexity the possibilities of concurrent failure of more than one element, and risk of failure of parts of the system, become realistic, and can only be modelled probabilistically. The same TDPA can also be used for planning by extending the window of analysis from 6 hours to a full year, thereby correlating the seasonal and time-of-day availability of generation, likelihood of faults and load demand of the customers. Further, because a probabilistic method is used, selected levels of risk can be included by assigning a level of statistical confidence to the resultant PDFs of system failure.

5. COST OF INTERRUPTIONS

The financial impact of interruptions was briefly mentioned in section 2. Dzobo *et al.* examined the effects of interruptions on various types of customers as well as at different times of the day and season of the year [8]. As in the case of the reliability assessment it was found that the Beta PDF could be used to describe CIC and that the time 16 cell time matrix was appropriate for explaining the variability in cost. Dzobo *et al.* went on to demonstrate that customers could be categorised into segments, each with its characteristic CIC description [9].

Now, by combining the TDPA reliability analysis and the CIC concepts it is possible to consider a geographically located load bus within a power system, calculate the probabilistic frequency and duration statistics of likely faults, aggregate the load types and determine the likely cost of outages. This value at risk can be expressed in monetary terms for a specified level of risk, for example in South Africa as Rands at risk: R@R.

Various combinations of the cost of interruptions to the economy as a whole, a utility's loss revenue, or the costs seen by customers allow the consequences of a probability-based loss of reliability to be assessed. Such information expressed in monetary terms is useful for decision-making in financial and regulatory management.

6. SOCIO-POLITICAL EFFECT

The financial impact of interruptions on industrial and commercial customers can be assessed probabilistically using the R@R measure. When interruptions are long and frequent the collective impact affects the economy of the community. This leads to dissatisfaction with the services followed by the threat of disinvestment and can spill over into the socio-political area. However since there are more individual residential customers the socio-political impact on poor service is even greater. This has been demonstrated in South Africa where protests and even riots have erupted.

In a case study, approximately 230 households were surveyed in two low-income settlements in South Africa. One settlement comprised formal housing and the other only shacks, and both were fully electrified. Households were surveyed about a range of issues related to their energy use, one of which was their perceptions of the number of interruptions they experienced and overall satisfaction with the reliability of their electricity supply. Residents in the communities estimated the typical number of interruptions during winter months as 1.8 to 2.6 incidents per month. Virtually all households reported that there were more frequent interruptions in winter than during summer months. In contrast, data provided by the utility indicates there were only 1 and 3 incidents *per year*, the average values over several years being 1.4 and 2.2 interruptions per year. The average duration of interruptions was 2.7 hours and 2 hours respectively.

More than 90% of respondents in the poorer area expressed dissatisfaction with the reliability of their electricity supply. In comparison, only 25% of the sample in the formal housing settlement expressed dissatisfaction with their supply.

The seeming disparities between the perceptions of survey respondents and the utility's data may arise from a number of reasons. First, the accuracy of self-reported data on recollections about past events in surveys is affected by recall bias. This is especially true for emotive topics, of which the quality of service delivery in South

Africa is one. This information error could lead to respondents overestimating the number of outages they experience. Secondly, the utility collects data on interruptions at sub-station level, thus excluding low voltage incidents. Typical events affecting low voltage systems include weather related events, trees or vegetation interfering with lines, theft/vandalism, meter failures and other technical faults. Thirdly, the utility data does not reflect momentary interruptions; only those of longer duration. The utility's measured data could therefore under-estimate the number of interruptions, although the extent of such potential under-estimation cannot be determined. The omission of low voltage system and momentary interruptions from reliability indices is not unusual in South Africa.

Poor reliability may compromise (to a degree) the beneficial societal outcomes of having access to an electricity supply for low-income customers. For low-income residential consumers some of the potential impacts of unreliability may be direct financial loss where it interrupts economic activities, spoilage of food, inconvenience, increased feelings of vulnerability and crime on dark nights. Perhaps most significantly an unreliable electricity supply may increase the usage of and consequent risks associated with alternative fuels like paraffin and candles. Understanding the societal and economic impacts (for all sectors) may give more insight into what appropriate thresholds for an acceptable minimum level of utility's reliability performance may be.

7. DISCUSSION

Conventional reliability measures based on deterministic methods using average values of fault duration and frequency have limitations. Generally, they provide indices that are compared with standards adopted from historical performance or derived from other power systems. Such indices do not reflect the basic purpose of power systems to supply electricity economically or to meet social requirements.

In conventional long term planning approaches, known component failure rates are used in deterministic reliability analyses to predict SAIDI and SAIFI and indices of the energy not supplied, but these are average values and do not indicate the possible extremes that can arise. Similarly, contingency analysis for (N-1) events to examine the operational risk of system interruptions compares possibilities with different probabilities of occurrence.

These approaches may no longer be useful decision guides for more complex systems.

The TDPA to reliability analysis incorporates both the dispersion of fault data and presents a range of outcomes according to the risk levels needed by system planners and operators. Adding CIC data allows a value index,

R@R, to be derived, which is consistent with other financial indicators associated with investment and risk exposure decisions. The same analytical approach for system operations analysis is appropriate to system planning and is based on consistent data sets and confidence levels.

Even as simple measures of system performance, SAIDI, SAIFI and MAIFI do not adequately reflect the perceptions of customers, partly because some of the interruption data are omitted from the indices by definition. Surveys of the social responses to interruptions indicate discrepancies between utility reliability indices and customer perceptions. It appears more research is needed in this area to inform utilities and regulators, and to establish objective standards of performance. Bringing together the technical and societal elements of reliability poses some interesting problems for researchers and regulators.

In this last respect, there could be a requirement for inexpensive interruption monitors suitable for low voltage feeders. Such monitors would be consistent with the concept of smart grids and fill the data gap not met by smart meters with a sampling cadence of only 15 minutes. The monitors should measure and distinguish between momentary and sustained interruptions as presently defined.

8. RECOMMENDATIONS AND CONCLUSION

The conventional indices for reporting the reliability of electricity supply appear to be inadequate for decision making in modern power systems.

It is recommended that indices more closely related to value-based decision making are needed, and the R@R index derived from the TDPA reliability analysis should be considered in more detail for application in South Africa.

Value based reliability measures will need to be supported by more comprehensive CIC data than already collected by researchers at UCT from residential, commercial and industrial customers, but the techniques for collecting the data efficiently have already been developed and published.

At the same time, utility and regulatory staff will need to be trained in probabilistic reliability assessment.

It also appears that broader assessment of the social and political responses of communities to interruptions is

desirable, especially in the context of the present attitudes to electricity supply utilities in South Africa.

9. REFERENCES

- [1] U.J. Minnaar, C.T. Gaunt and F. Nicolls: Characterisation of power system events on South African transmission power lines. *Electr. Power Syst. Res.*, Vol 88, 2012, pp 25-32. doi:10.1016/j.epsr.2012.01.015
- [2] <http://www.energyathaas.wordpress.com/2012/11/04/measuring-the-economic-costs-of-electricity-outages/> (Accessed 14 Nov 2014)
- [3] <http://www.enca.com/coverage/power-outages-sa?gclid=CIaCy4O2-cECFRMatAod0DsAjA> (Accessed 14 Nov 2014)
- [4] IEEE Power Engineering Society. *IEEE Std 1366:- 2003 IEEE Guide for Electric Power Distribution Reliability Indices*. New York: Institute of Electrical and Electronics Engineers, Inc. 2014. 35 pages.
- [5] M.Edimu, C.T. Gaunt and R. Herman: "Using probability distribution functions in reliability analyses", *Electr. Power Syst. Res.*, Vol 81, I (4), April 2011, pp 915-921.
- [6] M. Edimu, K. Alvehag, C.T. Gaunt and R. Herman: "Analyzing the performance of a time-dependent probabilistic approach for bulk network reliability assessment", *Electr. Power Syst. Res.*, Vol 104, year 2013, pp. 156 – 163.
- [7] R.Herman and C.T.Gaunt: "Probabilistic Interpretation of Customer Interruption Cost (CIC) Applied to South African Systems", *PMAPS2010*, Singapore, June 2010.
- [8] O. Dzobo, C.T. Gaunt and R. Herman, "Investigating the use of probability distribution functions in reliability-worth analysis of electric power systems", *International Journal of Electrical Power and Energy Systems*, Vol 37, May 2012, pp110-116.
- [9] O. Dzobo, K. Alvehag, C.T. Gaunt and R. Herman: "Multi-dimensional customer segmentation model for power system reliability-worth analysis", *International Journal of Electrical Power & Energy Systems*, Nov 2014, pp 532–539.

INTRA-BUILDING POWER NETWORK NOISE MODELLING IN SOUTH AFRICA

A. M. Nyete, T.J.O. Afullo and I.E. Davidson

Discipline of Electrical, Electronic and Computer Engineering

University of KwaZulu-Natal

Durban, South Africa

Email: 212536330@stu.ukzn.ac.za, afullot@ukzn.ac.za, davidson@ukzn.ac.za

Abstract: The study of the power line network as a communications medium has been going on for a long time. Powerline communication technology is mainly used in last-mile and last-inch communication applications; that is, from the medium voltage transformer to the premises, and within premise communications. Even though this channel has its own challenges as a communication medium, research efforts are on-going that are geared towards the elimination of many of the channel impairments, or at least to mitigate their effects to acceptable levels. Most recently, there has been renewed interest in the use of the power line for the delivery of broadband services. However, the channel noise remains the greatest hindrance towards the realization of this dream. To that effect, in this paper, we study the channel noise in a broadband environment. We present broadband noise measurements and then develop a model that can be applied in optimizing the channel for communication purposes.

Keywords: Power line communication, noise, broadband, alpha stable distribution, McCulloch's method.

1. INTRODUCTION

The possibility of using the power line channel for the transmission of voice and data services has received a lot of interest in the recent past. This interest is driven by the ubiquitous nature of the power network and the fact that the infrastructure is already in place. But, the usage of the power network as a communications medium is not a new idea at all. In fact, power lines have been used in low data rate transmissions for supervision, control and management functions in power grid. These low data rate applications have been utilized in the monitoring of power equipment, remote metering, and lighting control. However, the current research activities in the use of the power grid for communication purposes are geared towards provision of high data rate services. This means that the channel characteristics have to be adapted to accommodate the high data rate requirement. Thus, studies to develop models of the channel frequency response and channel noise are a very essential step towards the optimization of the power line channel for the delivery of high speed broadband services. These high speed broadband services include home equipment networking, fast internet access and voice over IP [1-5].

However, the realization of high speed power line communications (PLC) is not a trivial thing to do. This is a task that requires a full understanding of the channel characteristics, which tend to be completely different from those of their radio counterparts. The PLC channel is a very horrible channel for communication purposes since its channel frequency response is very dynamic and there is a lot of noise in the channel. The greatest impairments in the PLC channel are attenuation, multipath and noise effects. Multipath effects are caused

by the back and forth reflections of the signal at the different nodes (cable joints) which produces echoes. Thus, different versions of delayed signal components will arrive at the receiver through different paths [2, 3, 6].

Noise in power line networks is very different from the additive white Gaussian noise (AWGN) found in many other communication systems. The noise in PLC systems is non-white, non-Gaussian but additive. The noise manifests itself in two broad categories: background noise and impulsive noise. Background noise comprises of two main types, which are: coloured background noise and narrowband noise. Impulsive noise components are on the hand categorised as follows: noise that is non-periodic and asynchronous to the mains frequency, noise that is periodic and synchronous to the mains frequency and finally noise that is periodic but whose repetition rate is different from that of the mains. Impulsive noise is the greatest cause of both bit and burst errors in data transmission. It is usually characterized by a short duration of occurrence but high power spectral density [6-8].

Different research works have reported on PLC noise both in the time and frequency domain. Most of the models are developed from measured data. For example, Zimmermann and Dostert [7] have developed an impulsive noise model based on partitioned Markov chain from channel measurements. Also, Esmailian *et al.* [1] have also developed separate models for the background and impulsive noise.

In this paper, our focus is to develop a channel noise model for application in broadband PLC networks. This model is developed using frequency domain data

collected through a noise measurement campaign lasting over six months. The average indoor supply voltage in South Africa is 240 V at 50Hz. These measurements were carried out in different rooms at the department of Electrical, Electronic and Computer Engineering, Howard College, University of KwaZulu-Natal. The models are developed for the measured power spectral density (PSD) using alpha stable distribution. The choice of this statistical tool is informed by the long-tail characteristic of the measured PSD probability density function, and the fact that most natural and manmade phenomena are not necessarily Gaussian.

2. ALPHA STABLE DISTRIBUTION

Impulsive signals/noise are inherent in many communication and radar systems. Such signals are usually characterized by many spikes, which in turn translate to a heavy-tailed non-Gaussian probability density function. In all of these applications therefore, it is very important that the distributional properties of the signal be properly characterized before any digital signal processing technique can be applied, such as detection and filtering. The stable distributions family has been shown to be an appropriate model for long-tailed distributions. Since the stable distribution contains the Gaussian distribution as a limiting case, it is applicable for signals that are impulsive or not [9].

The stable distribution is preserved under convolution such that the sum of two independent random variables from a common stable distribution retains the same distribution [9, 10]. The closed form expression for this distribution does not exist, and therefore its formulation is given in terms of its characteristic function, given by [9-11]:

$$\phi(t) = \begin{cases} \exp\{i\delta t - \gamma^\alpha |t|^\alpha [1 - i\beta \operatorname{sgn}(t) \tan \frac{\pi\alpha}{2}]\}, & \alpha \neq 1 \\ \exp\{i\delta t - \gamma |t| [1 + i\beta \frac{2}{\pi} \operatorname{sgn}(t) \ln |t|]\}, & \alpha = 1 \end{cases} \quad (1)$$

Where

$$\operatorname{sgn}(t) = \begin{cases} 1 & \text{for } t > 0 \\ 0 & \text{for } t = 0 \\ -1 & \text{for } t < 0 \end{cases}$$

$$-\infty < \delta < \infty, \gamma > 0, 0 < \alpha \leq 2, -1 \leq \beta \leq 1$$

α is the characteristic exponent, δ is the location parameter, γ is the dispersion parameter and β is the skewness parameter. The parameters α and β determine the rate at which the tails of the distribution decay. Thus, they determine the shape of the characteristic function. On the other hand, γ simply expands or dilates the characteristic function magnitude. It is analogous to the variance in the Gaussian distribution.

The four-parameter alpha-stable family of distributions is a rich class, which includes three special limiting subclasses [12]:

- 1) The Gaussian distribution, where, $\alpha = 2$ and $\beta = 0$.
- 2) The Cauchy distribution, where, $\alpha = 1$ and $\beta = 0$
- 3) The Levy distribution, also referred to as the Inverse Gaussian or Pearson V, where, $\alpha = 1/2$ and $\beta = 1$.

Only for the above three special subclasses of stable distributions does a closed form of the density function exist. Usually, a stable distribution model is constructed by first estimating the four parameters that define it from a set of data [9].

There is an increasingly important and broad class of many manmade and natural phenomena found in many applications that is non-Gaussian and can be generally classified as impulsive. Many signals and noise that belong to such a category are sharp spiked and experience occasional bursts of outlier observations than those expected in a normal distribution of signals. Consequently, their tails decay at a slower rate than those of the Gaussian density function. Low-frequency atmospheric noise, underwater signals, lightning in the atmosphere, accidental hits in telephone lines and noise in power lines are just but some examples of impulsive phenomena that clearly deviate from the normality observed in the distribution of many other random variables. Middleton [13] has proposed some statistical-physical models of electromagnetic interference, which are based on filtered-impulse mechanism. These models are however quite limited in that mathematical approximations have to be employed in the derivation of the model, which equates to changing the assumption that was made on the physics of the noise and this leads to ambiguities between the mathematical formulae and the physical scenario relationship. Thus, a better alternative to the Middleton's models for electromagnetic interference would be the alpha stable family of distributions which are justified by the Central Limit Theorem, just like the Gaussian distribution. Also, the stable distribution is the only distribution that obeys the stability property. The stability property states that the summation of two independent stable random variables with the same characteristic exponent results in a random variable that is again stable and has the same characteristic exponent. Intuitively therefore, the stability property makes stable distributions very suitable especially in the modelling of random noise and uncertain errors [11-14].

3. NOISE MEASUREMENT METHODOLOGY, RESULTS AND DISCUSSION

Comprehensive frequency domain power line noise measurements were carried out in an indoor network environment at the department of Electrical, Electronic and Computer Engineering building at the University of KwaZulu-Natal, Howard College. The noise measurements were carried out over period of six months.

These measurements were carried out using a Rhode and Schwarz FS300 spectrum analyzer. Some of the captured noise waveforms are shown in Figure 1 below.

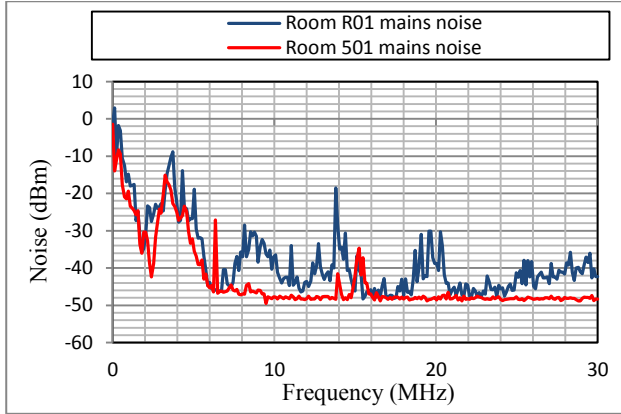


Figure 1: Noise spectrum captured in two separate rooms

From this figure, we see that the noise captured in room R01 is more impulsive than that captured in room 501. In fact, much of the noise captured in room 501 is background noise whose floor is around -49 dBm. From the many noise waveforms that were captured, we developed a probability density function for the noise power. This is shown in Figure 2 below.

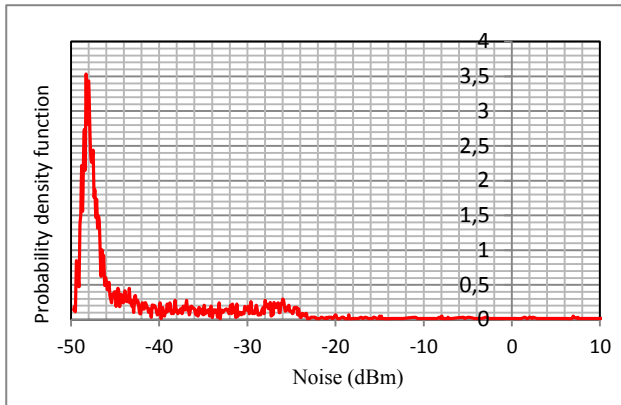


Figure 2: Measured noise power probability density

From Figure 2 above, we notice that the probability density function of the measured noise power possesses a long-tailed characteristic, an indication of the impulsive properties of the measured noise. This means that the noise distribution deviates from the Gaussian distribution. Thus, for the reasons explained above, we applied the alpha stable distribution to develop a noise model for the indoor PLC network using the measurements obtained.

4. NOISE MODELING WITH ALPHA STABLE DISTRIBUTION

As stated above we need to start by first estimating the four parameters of the stable distribution before we can come up with a model for the measured noise. Different numerical techniques have been fronted in literature to solve this problem. They include the methods proposed by Tsihrintzis *et al.* [13] that are based on fractional lower order moments, extreme value theory and order statistics, the empirical characteristic function (ECF) based methods found in [9, 15], and the quantile based methods, like that proposed in [16]. Quantile based methods are computationally less intensive and for this reason, we have chosen the method proposed in [16] for finding the parameters of the noise model in this paper. The parameter estimation procedure is explained next.

McCulloch's method [16] has less computational intensity when compared with empirical characteristic function (ECF) based Fourier methods. For this method, five pre-determined sample percentiles, that are accompanied by tables, for β (-1, 1) and α (0.6, 2.0), are used to consistently estimate the four parameters of the stable distribution.

First we estimate the characteristic exponent α and the symmetry parameter β using the percentiles of the empirical distribution. We define:

$$v_\alpha = \frac{x_{0.95} - x_{0.05}}{x_{0.75} - x_{0.25}} \quad (2)$$

And,

$$v_\beta = \frac{x_{0.95} + x_{0.05} - 2x_{0.25}}{x_{0.95} - x_{0.05}} \quad (3)$$

Where x_p is the empirical distribution p th percentile, having $v_\alpha = \phi_1(\alpha, \beta)$ and $v_\beta = \phi_2(\alpha, \beta)$, or by way of inversion, $\alpha = \psi_1(v_\alpha, v_\beta)$ and $\beta = \psi_2(v_\alpha, v_\beta)$. Also,

$$\psi_1(v_\alpha, v_\beta) = \psi_1(v_\alpha, -v_\beta) \quad (4)$$

Bi-linear interpolation to estimate α and β is then carried out using tables developed for the functions $\psi_1(\cdot)$ and $\psi_2(\cdot)$ for different values of v_α and v_β . Similarly, the location parameter δ and the dispersion parameter γ are estimated using the corresponding tabulated functions and the previous estimates for α and β .

The four parameters obtained are shown in Table 1 below and the resulting model in Figure 3. From this model we see that the long-tailed characteristic of the measured noise pdf is very well captured.

Table 1: Alpha stable noise model parameters

Method	Characteristic exponent (α)	Symmetry Index (β)	Scale parameter (γ)	Location parameter (δ)
McCulloch	1.72	1	4.29	-45.69

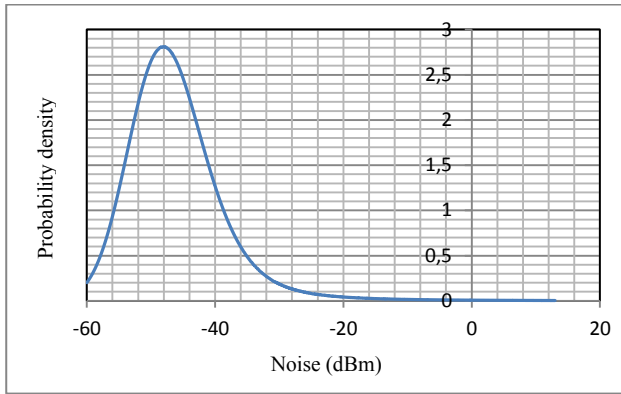


Figure 3: Alpha stable PLC noise model.

Also, the measured noise pdf is fully skewed to the left and this is well captured as can be seen in Figure 3 and Table 1 ($\beta = 1$). Also, the location of the pdf is very well approximated going by the location parameter in Table 1 and referring back to Figures 2 and 3. However, we note that the sharp peaked characteristic of the measured noise pdf is impossible to capture fully. All in all, we can comfortably say that the noise model obtained is a good fit for the measured noise characteristics.

5. CONCLUSION

In this paper, we have presented an alternative technique for the characterizing and modelling of the noise in indoor power line networks. The measured noise characteristics have been found to be long-tailed, an indication that the noise is impulsive and the tails decay at a slower rate than those of the Gaussian distribution. Possible avenues for future research would involve more noise measurements and alternative modelling techniques, as well as the application of the noise model in the design of a more robust PLC system.

6. REFERENCES

- [1] T. Esmailian, F. R. Kschischang, and P. G. Gulak, "Characteristics of in-building power lines at high frequencies and their channel capacity", *Proceedings of the IEEE ISPLC 2000*, Limerick, Ireland, pp. 52-59, 2000.
- [2] M. Gotz, M. Rapp, K. Dostert, "Power line channel characteristics and their effect on communication system design", *IEEE Communications Magazine*, Vol.42, No.4, pp.78-86, Apr 2004.
- [3] A. M. Nyete, T.J.O. Afullo and I. Davidson, "On Rayleigh approximation of the multipath PLC channel: Broadband through the PLC channel", *In 2014 SATNAC Proceedings*, Port Elizabeth, South Africa, pp. 265-270, 31 August-3 September 2014.
- [4] T. Esmailian, F. R. Kschischang, and P. G. Gulak, "In-building power lines as high-speed communication channels: channel characterization and a test ensemble", *International Journal of Communication Systems*, pp. 381-400, 2003.
- [5] L. Di Bert, P. Caldera, D. Schwingshackl, and A.M. Tonello, "On noise modelling for power line communications", *IEEE International Symposium on Power Line Communications and Its Applications (ISPLC)*, pp.283-288, 3-6 April 2011.
- [6] Y.H. Ma, P.L. So, E. Gunawan, "Performance analysis of OFDM systems for broadband power line communications under impulsive noise and multipath effects", *IEEE Transactions on Power Delivery*, vol.20, No.2, pp.674-682, April 2005.
- [7] M. Zimmermann and K. Dostert, "Analysis and modeling of impulsive noise in broad-band powerline communications", *IEEE Transactions on Electromagnetic Compatibility*, Vol. 44, No. 1, pp. 249-258, November 2002.
- [8] A. M. Nyete, T.J.O. Afullo and I. Davidson, "Performance evaluation of an OFDM-based BPSK PLC system in an impulsive noise environment", *PIERS Conference Proceedings*, Guangzhou, China, pp. 2510-2513, 25-28 August 2014.
- [9] S.M. Kogon and D.B. Williams, "On the characterization of impulsive noise with α -stable distributions using Fourier techniques", *Proceedings of the ASILOMAR-29*, pp. 787-791, 1996.
- [10] M.J. Lombardi, "Bayesian interference for α -stable distributions: A random MCMC approach", *Computational Statistics and Data Analysis*, Vol. 51, pp. 2688-2700, 2007.
- [11] M. Shao and C. L. Nikias, "Signal processing with fractional lower order moments: Stable processes and their applications", *Proceedings of IEEE*, Vol. 81, pp. 986-1010, 1993.
- [12] J.P. Nolan, "An Algorithm for evaluating stable densities in Zolotarev's (M) parameterization", *Mathematical and Computer Modelling*, Vol. 29, pp. 229-223, 1999.
- [13] D. Middleton, "Statistical-physical models of electromagnetic interference", *IEEE Transactions on*

Electromagnetic Compatibility, Vol. EMC-19, No. 3, pp. 106-127, 1977.

- [14] G. A. Tsihrintzis, and C. L. Nikias, "Fast estimation of the parameters of alpha-stable impulsive interference," *IEEE Transactions on Signal Processing*, Vol. 44, No. 6, 1996.
- [15] I.A. Koutrouvelis, "Regression-type estimation of the parameters of stable laws", *Journal of the American Statistical Association*, Vol. 75, No. 372, pp. 918-928, December 1980.
- [16] J.H. McCulloch, "Simple consistent estimators of stable distributions parameters", *Commun. Stat.-Simula.*, Vol. 15, No. 4, pp. 1109-1136, 1986.

DISTANCE TO FAULT ACCURACY IN AN ESKOM DISTRIBUTION NETWORK

C. Snyman* and A. Marks**

* Eskom Distribution, Control Plant Maintenance, Protection Department, 7-8th Milestone Macleantown Road, Eskom Ducats Engineering Complex, Beacon Bay, East London, 5241, South Africa E-mail: charlene.snyman@eskom.co.za

** M.Ed. (CIE); Faculty of Engineering, the Built Environment and Information Technology, PO Box 77000, Nelson Mandela Metropolitan University, Port Elizabeth, South Africa E-mail: anthony.marks@nmmu.ac.za

Abstract: After permanent faults occur on the Eskom Distribution network fault analysis will be done by the Operator on site or by the Protection Technician in order to determine the physical location of the fault. This is done using the software provided for the Protection device or additional recording equipment that has been installed in the substation. Over the past five years a trend has been developing where the distance to fault information supplied to assist in finding the fault is inadequate. This paper seeks to solve the inaccurate display of the distance to fault calculation on radial feeders with YNd1 TRFRs on the remote side within the Eastern Cape in order to improve fault location times. Fault simulation testing was performed to prove the relay settings and masking. A comparison will be done on three different devices that provide distance to fault.

Keywords: Distance to fault; DTF; Zero sequence current flow; Radial feeders; Earth return path.

1. INTRODUCTION

1.1 Problem Statement

Protective relays are installed throughout the Eskom network to remove faulty equipment from service as fast and as accurate as possible when a fault condition occurs. A well-known protective philosophy that is applied in the Eastern Cape Operating Unit on the distribution lines is distance/impedance protection. After a permanent fault has tripped and locked out a feeder breaker, there are facilities available on the relay to assist the field technicians with identifying the fault location which speeds up the “locate and repair” process.

Calculated values for the distance to fault (DTF) values on “Glenden – Fort Beaufort” 66kV feeder is giving incorrect fault locations. This line is currently protected by the Asea Brown Boveri (ABB) REL511 relay.

After faults have occurred the calculated DTF provided by the relay is either 0% or 100%.

After considering the implications of what 0% or 100% of the line is, it is clear that the fault would either be directly after the CTs on the local site towards the remote side or just before the CTs on the remote side. This scenario seems rather unlikely.

1.2 Sub Problems

Sub Problem 1: Incorrect DTF values result in unnecessary delays when patrolling the line in order to locate and repair the fault which negatively impacts on System Average Interruption Duration Index (SAIDI) and System Average Interruption Frequency Index (SAIFI) statistics. The additional time spent looking for

the fault also impacts negatively on the safety of Field Staff.

Sub Problem 2: The three pieces of equipment to be investigated are manufactured by three different companies and use different algorithms for calculating DTF:

Sub Problem 3: Control Officers at the Control Centre who monitor the Eskom network do not have direct access to DTF values.

2. OUTLINE OF THE STUDY

The existing ABB REL511 relay will be investigated to determine whether there are any errors in the settings or the masking that has been applied.

As a relay will only perform the job it has been assigned in the logic or masking, the most probable cause of the relay incorrectly displaying the DTF is incorrect settings, disabled logic, disabled masking settings or even malfunctioning of the relay.

3. FAULT TYPE FOCUS AREA

Up to 85% of all faults on the Eskom Network are single phase to earth faults [1]. For the purpose of this study the focus will be on this type of fault.

4. CIRCUIT DIAGRAM OF NETWORK

The line in question is the “Glenden – Fort Beaufort” 66kV feeder and is shown in Figure 1. The line is fed from Poseidon Substation (S/S).

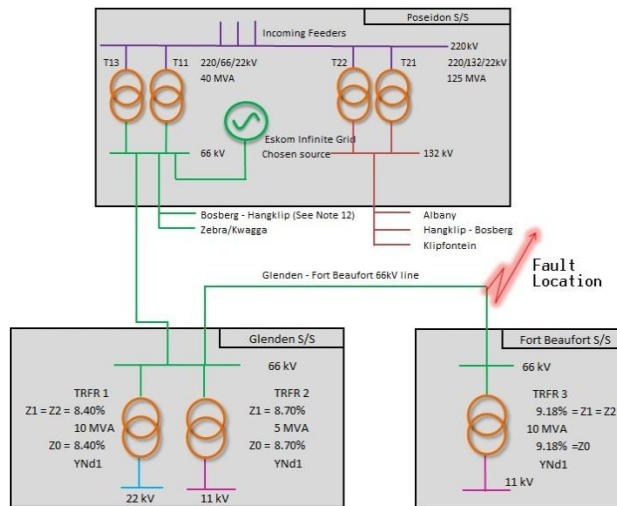


Figure 1: Circuit diagram of network feeding Fort Beaufort S/S

5. NORMAL OPERATION OF DISTANCE PROTECTION

When rated load flows through a line the relay uses the measured currents and voltages to calculate the impedance from the CTs to the load [1]. This impedance will fall within the load area as shown in Figure 2 which is considered as normal operation. The reactance and resistances can be represented as secondary or primary ohms.

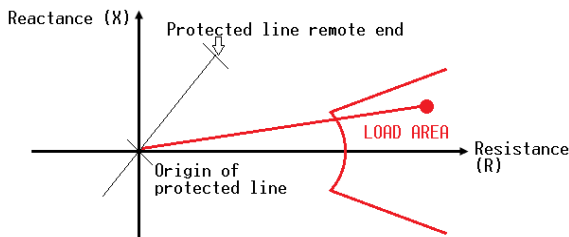


Figure 2: Load seen by distance protection

6. DISTANCE TO FAULT

When a fault occurs the secondary measured impedance will be converted to a DTF value either in kilometres or percentage of the line. The distance to fault is seen as the distance from the CTs to the physical permanent fault.

7. CIRCUITS FOR CALCULATION OF ASYMMETRICAL FAULT

When an asymmetrical single phase to earth fault occurs a single line makes contact with the general mass of earth. The positive, negative and zero sequence networks are considered for asymmetrical faults.

The impedance networks are connected in series [2] in order to analyse single phase to ground asymmetrical faults as shown in Figure 3.

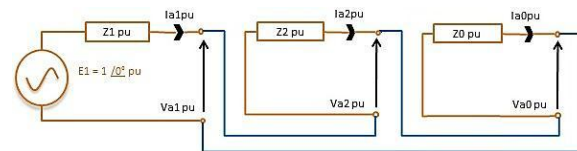


Figure 3: Generic sequence impedance networks

Considerations are to be made for the zero sequence circuit of the transformers in circuit. The „a” legs are closed when that side of the TRFR is an earthed Star (Y) connection. In Figure 4 the „a” leg on the Primary side of the TRFR is labelled as „Aprim” and on the Secondary side as „Asec”. The „b” legs are closed when the connection is Δ. In Figure 4 the „b” leg on the Primary side of the TRFR is labelled as „Bprim” and on the Secondary side as „Bsec”.

The transformers found at Glenden and Fort Beaufort Substations are YNd1 which will affect the zero sequence current flow during earth faults. For all these transformers the „Aprim” and „Bsec” links will be closed as shown in Figure 4.

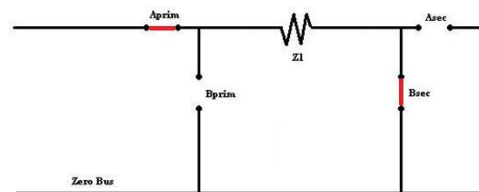


Figure 4: Zero sequence circuit of TRFRs

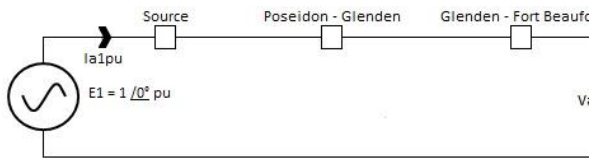


Figure 5: Positive sequence impedance network

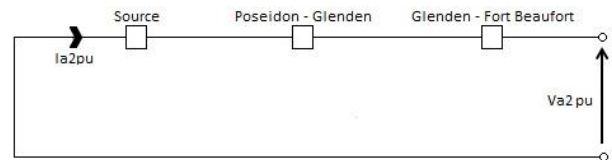


Figure 6: Negative sequence impedance network

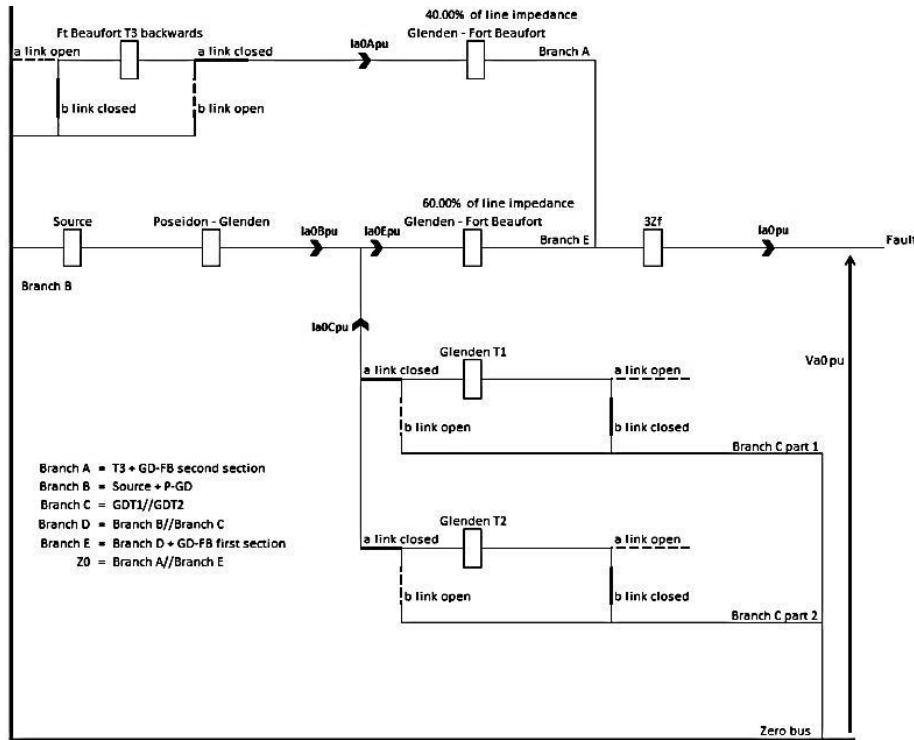


Figure 7: Zero sequence impedance network with fault located 60% of line

8. CALCULATION OF ASYMMETRICAL FAULTS

The current distribution principle that will be experienced during a fault on the “Glenden – Fort Beaufort” 66kV line on the red phase is shown in Figure 8. The generic asymmetrical fault calculations do not consider this zero sequence circulation path created by the TRFR at Fort Beaufort S/S resulting in zero fault current in the unfaulted phases.

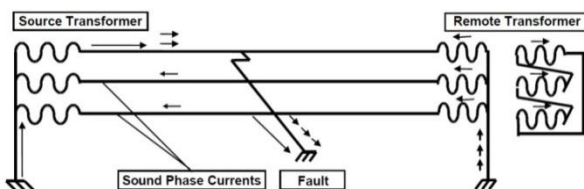


Figure 8: Current distribution for earth fault [1]

The sequence fault current is calculated with Formula 1:

$$I_{a1pu} = I_{a2pu} = I_{a0pu} = \frac{E}{Z_1 + Z_2 + Z_0} \quad (1)$$

In order to calculate the voltage drops across items of plant in the zero sequence impedance network as well as the fault current in the white and blue phases, the current divider rule is used to calculate the branch currents. See Figure 7 for the circuit diagram.

$$\text{Branch E: } I_{a0Epu} = I_{a0pu} \frac{Z_{\text{Branch A}}}{Z_{\text{Branch A}} + Z_{\text{Branch E}}} \quad (2)$$

$$\text{Branch A: } I_{a0Apu} = I_{a0pu} - I_{a0Epu} \quad (3)$$

As seen in the zero sequence network in Figure 7, current will flow through Branch A which is the neutral of the Fort Beaufort TRFR. This current will be flowing out of the red phase of the TRFR at Fort Beaufort S/S towards the fault. This current will cause a circulating current in the Delta secondary winding. As the TRFR must maintain ampere-turns balance [3] there will be a resulting current flowing out of the white and blue phases

of the Star primary winding. Due to the current convention of the arrows drawn it can be seen that when describing the current at the “Glenden – Fort Beaufort” relay the current is 180° out of phase. The angle of both the white phase and blue phase currents will have 180° added to them. The red phase current is calculated with Formula 4:

$$I_{ANF} = 3 * I_{a1pu} * I_{base} \quad (4)$$

The calculated fault current on the red phase contains three different elements:

- The zero sequence current from the red phase winding at Fort Beaufort S/S.
- The white and blue phase currents from the TRFR at Fort Beaufort via Glenden S/S.
- The earth fault current supplied from the source.

In order to calculate the current that will be flowing through the red phase at Glenden S/S, the fault current will need to subtract the current that joins at the point of the fault from the red phase winding of the TRFR at Fort Beaufort.

Fault sequence voltages are described by Formulas 5 to 7.

$$V_{a1pu} = E - I_{a1pu} * Z_{1pu} \quad (5)$$

$$V_{a2pu} = 0 \angle 0^\circ - I_{a2pu} * Z_{2pu} \quad (6)$$

$$V_{a0pu} = 0 \angle 0^\circ - I_{a0pu} * Z_{0pu} \quad (7)$$

With $V_{base} = \frac{V_L}{\sqrt{3}} = \frac{66000}{\sqrt{3}} = 38105 V$ and α as 120° the fault voltages at the point of the fault are calculated with Formulas 8, 9 and 10.

$$V_A = V_{a1} + V_{a2} + V_{a0} \quad (8)$$

$$V_B = \alpha^2 V_1 + \alpha V_2 + V_0 \quad (9)$$

$$V_C = \alpha V_1 + \alpha^2 V_2 + V_0 \quad (10)$$

In order to test this fault condition at Glenden S/S the voltage drop across the impedance of the circuit has to be considered. The derived formulas used are:

$$V_{1relay} = E - I_{a1pu} * (Z_{1source} + Z_{1P-GD}) * V_{base} \quad (11)$$

$$V_{2relay} = \left((I_{a2pu} * (Z_{2source} + Z_{2P-GD})) \right) * V_{base} \quad (12)$$

The volt drops due to fault impedance and line impedance:

$$V_{a0Relay} = V_{a0pu} + I_{a0Epu} * Z_{GD-FBA} + I_{a0pu} * 3Z_f \quad (13)$$

$$V_{0relay} = V_{a0relay} * V_{base} \quad (14)$$

The voltages that need to be used for testing at Glenden Substation are calculated with Formulas 8, 9 and 10 with the sequence voltages calculated with Formulas 11, 12 and 14 for the primary values.

To obtain the secondary injection values the primary values are multiplied with the CT/VT ratio [4, 5]. For the “Glenden – Fort Beaufort” 66kV Feeder the CT ratio is 200/1 A and the VT ratio is 66kV/110V.

The CT/VT ratio is $\frac{I_P/I_S}{U_P/U_S} = \frac{200/1}{66000/110} = 0.333$.

The resulting current flow is shown in Figure 9. The positive and negative sequence current is shown separately in order to prevent confusion with the zero sequence current flow.

For this specific current flow diagram it is assumed that most of the zero sequence current will flow up the neutral at the Fort Beaufort TRFR. When this assumption is no longer valid, the current flow diagram becomes a lot more complex due to the current splitting up the neutrals of the TRFRs at Glenden as well as the TRFR at Fort Beaufort S/S.

The positive and negative sequence current in Figure 5 and Figure 6 show that the current can only flow through the source impedance, where the zero sequence current is shown to flow through many parallel paths in Figure 7.

9. FAULT DESCRIPTION SUMMARY

In order to simulate various fault conditions on this line the required secondary voltages and currents were calculated and are summarised in Table 1, for the following fifteen fault locations. RWB is a symmetrical fault; R-E is a red phase to earth fault.

Test 1 - RWB no fault resistance 73.21% of the line

Test 2 - RWB no fault resistance 95.79% of the line

Test 3 - RWB fault resistance 3.05254 ohm 73.21% of the line

Test 4 - RWB fault resistance 3.05254 ohm 95.79% of the line

Test 5 - RWB double fault resistance 95.79% of the line

No remote TRFR at Fort Beaufort S/S:

Test 6 - R-E no fault resistance 73.21% of the line

Test 7 - R-E no fault resistance 95.79% of the line

Test 8 - R-E fault resistance 3.05254 ohm 73.21% of the line

Test 9 - R-E fault resistance 3.05254 ohm 95.79% of the line

Test 10 - R-E double fault resistance 95.79% of the line

Remote TRFR in circuit:

Test 11 - R-E no fault resistance 73.21% of the line

Test 12 - R-E no fault resistance 95.79% of the line

Test 13 - R-E fault resistance 3.05254 ohm 73.21% of the line

Test 14 - R-E fault resistance 3.05254 ohm 95.79% of the line

Test 15 - R-E double fault resistance 95.79% of the line

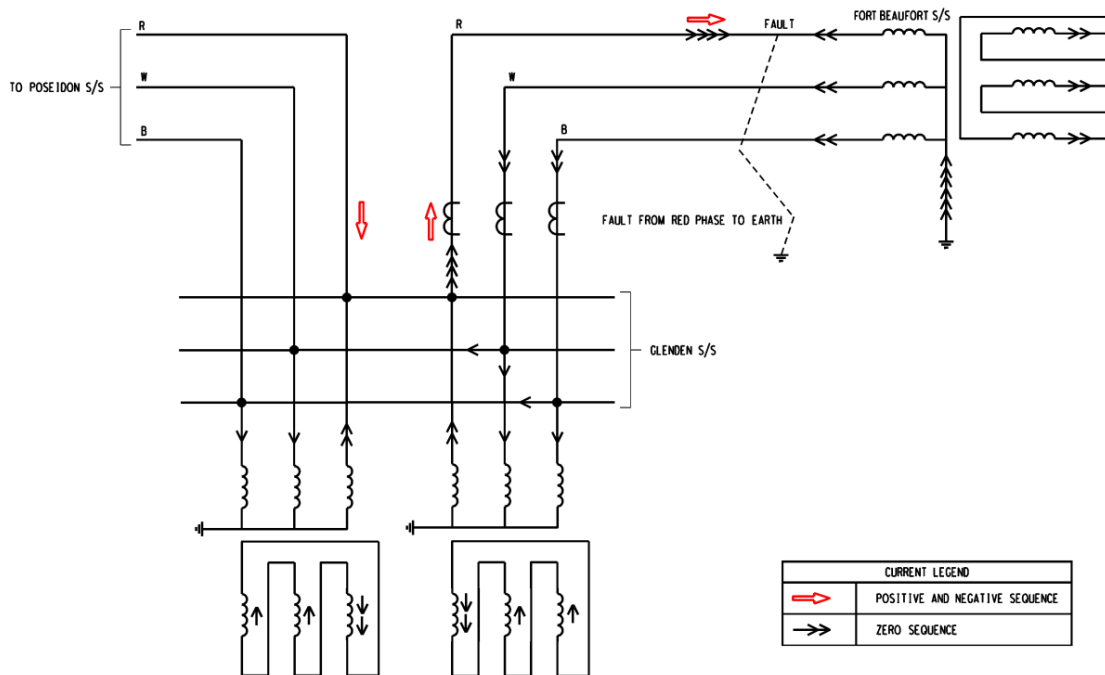


Figure 9: Sequence current flow during Red phase earth fault on “Glenden – Fort Beaufort” line

Table 1: Test currents and voltages summary

Test	IA (A)	IB (A)	IC (A)	VAN (V)	VBN (V)	VCN (V)
1	4.99 ∠ -54.67 °	4.99 ∠ -174.67 °	4.99 ∠ 65.33 °	23.79 ∠ -10.85 °	23.79 ∠ -130.85 °	23.79 ∠ 109.15 °
2	4.48 ∠ -53.55 °	4.48 ∠ -173.55 °	4.48 ∠ 66.45 °	27.95 ∠ -9.73 °	27.95 ∠ -129.73 °	27.95 ∠ 110.27 °
3	4.76 ∠ -51.10 °	4.76 ∠ -171.10 °	4.76 ∠ 68.90 °	26.40 ∠ -14.58 °	26.40 ∠ -134.58 °	26.40 ∠ 105.42 °
4	4.29 ∠ -50.38 °	4.29 ∠ -170.38 °	4.29 ∠ 69.62 °	30.07 ∠ -12.33 °	30.07 ∠ -132.33 °	30.07 ∠ 107.67 °
5	4.10 ∠ -47.48 °	4.10 ∠ -167.48 °	4.10 ∠ 72.52 °	32.16 ∠ -14.02 °	32.16 ∠ -134.02 °	32.16 ∠ 105.98 °
6	4.49 ∠ -60.56 °	0.00 ∠ 0.00 °	0.00 ∠ 0.00 °	31.50 ∠ -7.33 °	64.96 ∠ -115.43 °	58.18 ∠ 118.57 °
7	3.90 ∠ -59.59 °	0.00 ∠ 0.00 °	0.00 ∠ 0.00 °	35.78 ∠ -6.36 °	64.67 ∠ -116.00 °	58.90 ∠ 118.70 °
8	4.33 ∠ -57.10 °	0.00 ∠ 0.00 °	0.00 ∠ 0.00 °	33.19 ∠ -9.97 °	64.59 ∠ -115.52 °	58.47 ∠ 118.33 °
9	3.77 ∠ -56.60 °	0.00 ∠ 0.00 °	0.00 ∠ 0.00 °	37.06 ∠ -8.13 °	64.41 ∠ -116.07 °	59.13 ∠ 118.52 °
10	3.65 ∠ -53.81 °	0.00 ∠ 0.00 °	0.00 ∠ 0.00 °	38.39 ∠ -9.49 °	64.16 ∠ -116.16 °	59.36 ∠ 118.38 °
11	4.72 ∠ -58.68 °	0.96 ∠ 113.12 °	0.96 ∠ 113.12 °	28.52 ∠ -7.15 °	61.54 ∠ -110.35 °	56.19 ∠ 112.28 °
12	4.22 ∠ -57.49 °	1.08 ∠ 112.14 °	1.08 ∠ 112.14 °	31.98 ∠ -6.03 °	60.95 ∠ -110.13 °	56.49 ∠ 111.70 °
13	4.50 ∠ -54.38 °	0.91 ∠ 117.43 °	0.91 ∠ 117.43 °	30.84 ∠ -11.02 °	60.84 ∠ -110.91 °	57.13 ∠ 112.21 °
14	4.04 ∠ -53.49 °	1.03 ∠ 116.14 °	1.03 ∠ 116.14 °	20.34 ∠ -9.04 °	60.30 ∠ -110.71 °	57.40 ∠ 111.69 °
15	3.85 ∠ -49.83 °	0.98 ∠ 119.80 °	0.98 ∠ 119.80 °	21.54 ∠ -11.08 °	59.79 ∠ -111.31 °	58.22 ∠ 111.80 °

10. TEST RESULTS

10.1 REL511 from ABB

Settings had to be changed within the REL511 General Fault Criteria (GFC) settings in order to provide accurate DTF values. The existing relay situated on the Fort Beaufort 66kV feeder could not provide an accurate DTF

when an earth fault occurred with the remote TRFR in service due to the relay selecting the wrong fault loop with which to perform DTF calculations.

By disabling the “Z>” setting and enabling the “I>” setting, the GFC would determine what kind of fault had occurred by only using current levels.

The test results are summarised in Table 2 and it can be seen that good accuracy is achieved for Tests 1 through

13, but during faults at the far side of the line with high fault impedance, the DTF becomes less accurate. E.g.: This line is 31km long in total and for Test 15 the relay will indicate that the fault occurred at 58.4% (or 18.1km), even though it occurred at 95.79% (or 29.69km).

Table 2: Test results for REL511

Test	Simulated DTF	Relay DTF
1	73.21%	72.7%
2	95.79%	95.1%
3	73.21%	69.4%
4	95.79%	91.9%
5	95.79%	100%
6	73.21%	78.5%
7	95.79%	100%
8	73.21%	73.3%
9	95.79%	100%
10	95.79%	100%
11	73.21%	71%
12	95.79%	95.5%
13	73.21%	73.8%
14	95.79%	57.9%
15	95.79%	58.4%

10.2 SEL321

By setting up a SEL321 to mimic the settings of the REL511, the results obtained are summarised in Table 3. The SEL321 was found to be consistently accurate in providing DTF, but it would trip in the incorrect distance zone for most faults which is a concern.

Table 3: Test results for SEL321

Test	Simulated DTF	Relay DTF
1	22.7 km	22.65 km = 73.1%
2	29.69 km	29.63 km = 95.6%
3	22.7 km	22.66 km = 73.1%
4	29.69 km	29.64 km = 95.6%
5	29.69 km	29.66 km = 95.7%
6	22.7 km	22.69 km = 73.2%
7	29.69 km	29.65 km = 95.6%
8	22.7 km	22.68 km = 73.2%
9	29.69 km	29.65 km = 95.6%
10	29.69 km	29.65 km = 95.6%
11	22.7 km	22.02 km = 71%
12	29.69 km	17.85 km = 57.6%
13	22.7 km	22.69 km = 71%
14	29.69 km	29.68 km = 95.6%
15	29.69 km	29.69 km = 95.6%

10.3 Sherlog recorder from KoCos

Accurate DTF obtained for symmetrical faults, but the recorder could not be set up for providing earth fault DTF, hence only Tests 1 through 5 results are tabulated in Table 4.

Table 4: Test results for Sherlog recorder

Test	Simulated DTF	Sherlog DTF
1	22.7 km	22.97 km = 74.1%
2	29.69 km	29.31 km = 94.5%
3	22.7 km	26.73 km = 86.2%
4	29.69 km	29.88 km = 95.8%
5	29.69 km	29.42 km = 94.9%

11. CONCLUSION

After testing the REL511, SEL321 and Sherlog recorder it has become clear that the settings applied to these devices within the Eastern Cape Operating Unit do not take the zero sequence impedance circuit into consideration. The required settings that are considered only involve the line parameters.

11.1 Accuracy comparison

The test results obtained show that the DTF accuracy provided by all three devices are accurate for symmetrical faults but have the following issues:

- REL511 is inaccurate for earth faults once the TRFR at Fort Beaufort is introduced unless the “Z>” setting is disabled. This forces the relay to recognize the fault loop by fault current alone. This may not be the best solution, as it would be preferable to define the faulty phase by impedance measured.
- SEL321 is accurate for all fault types to provide DTF, but operates in the incorrect zone.
- Sherlog recorder zero impedance setting could not be set to provide DTF for earth faults.

The REL511 is the best performing relay in the regard that it operates in the correct zones and provides a relatively good DTF function.

11.2 Prefault conditions

While testing all three devices it was noted that the REL511 and SEL321 require a few seconds of healthy voltages and currents before it provides a stable DTF value.

It is therefore important to note that all the tests performed had to be done using a State Sequencer test module within the Omicron Test Universe 2.41 SR 1 software which is set up to provide 5 – 15 seconds of nominal voltage and a three phase load of about 70A which simulates normal load conditions.

11.3 Hypothesis

The original hypothesis suggests that the most probable cause for the inaccurate DTF is incorrect settings, disabled logic, disabled masking settings or malfunctioning of the relay. It has now been proven that the faulty DTF is a direct result of incorrect settings on the relay. The hypothesis has thus been proven.

12. RECOMENDATION

The testing performed on the REL511, SEL321 and Sherlog recorder has made it evident that the settings applied are not considering the zero sequence impedance circuit in order to provide an accurate DTF for earth faults. Further recommendations per device are given below:

12.1 REL511

GFC settings to be redone taking zero sequence impedance circuit in consideration. When the settings can accurately predict the DTF, the “Z>” setting will have to be switched back on.

In order to obtain correct DTF values the following GFC settings were changed:

IP> 110% IN> 120%

Switch Operation I> on and switch Operation Z> off.

12.2 SEL321

Initiate investigation into the incorrect tripping as subsequent simulations performed in DIgSILENT indicate that the relay should have tripped in the correct zones, but during testing the relay did not behave in this manner.

12.3 Sherlog Recorder

Sherlog Recorder – Engage KoCos technicians further and determine zero impedance setting for radial feeders with YNd1 transformers. This will have to be taken up by the Settings Department within Eskom in order to find and apply the required settings.

Sherlog recorder zero impedance setting cannot be accurately set, further investigation is required as the scope of this paper was to fix the DTF on the REL511 and time constraints limited the function checking of the Sherlog recorder.

15. REFERENCES

- [1] Eskom, "Protection guide: *Line distance Protection up to and including 132kV*," vol. SCSAGAAI0, ed, 2003.
- [2] A. E. Guile and W. Paterson, *Electrical Power Systems*: Pergamon Press, 1977.
- [3] *Eskom Power Systems Skill Program Module 3 - Power Transformers*: Netgroup Academy, 2010.
- [4] G. Alworthy, "Eskom Manual Compilation: Impedance Protection," ed, January 1999.
- [5] ABB. (2007). *Application manual: Line distance protection terminal REL 511*2.5*. Available: <http://www.abb.co.za/product/db0003db004281/b9a37ab9e515e64dc1257a7200451594.aspx>

MEASUREMENT OF SWITCHING SURGES AND RESONANCE BEHAVIOUR IN TRANSFORMER WINDINGS

Cedric. A Banda^{a*} and Dr John M. Van Coller*

^{a*} School of Electrical and Information, Private Bag 3, Wits 2050, South Africa E-mail: cedric.banda@students.wits.ac.za & john.vancoller@wits.ac.za

Abstract: Internal winding resonance is a phenomenon which can lead to overvoltages within transformer windings. This paper will address resonance behaviour in transformer windings using the Multi-conductor Transmission Line (MTL) model. The aim in using the MTL model is to determine the turns between which insulation breakdown can occur due to internal winding resonances. Since an internal winding resonance can be excited when a frequency component of an incoming surge equals a resonance frequency of the transformer, measurement of the switching surges generated when switching a transformer with a vacuum circuit breaker were conducted. Results of the pre-strike behaviour also indicated high du/dt which could lead to stressing of the end-turn insulation of the transformer.

Key words: MTL model, pre-strike, resonance over-voltage.

1. INTRODUCTION

Switching transients due to vacuum circuit breakers can lead to resonant over-voltages in wind turbine step-up transformers. In medium voltage networks the switching of vacuum circuit breakers [1], [2] can result in re-ignitions and pre-strikes. These can lead to high-frequency oscillations with also high du/dt resulting in stressing of the end-turn insulation of the transformer. A more prominent problem is resonance phenomena in transformer windings which can be classified as either internal resonance or external resonance. External resonance occurs due to cable and transformer interaction such that the natural frequency of the supplying cable matches the natural frequency of the transformer. This is more common in wind turbine transformers where energization may result in cable-transformer resonant transients [3]. Onshore wind farms can have a vast cable network with lengths of up to 600m. If the quarter wave frequency of such cables is in the vicinity of the resonant frequencies of wind turbine transformers, resonant overvoltages may occur on the LV terminal of step-up transformers and inside HV windings [3]. Internal resonance occurs when a frequency component of the incoming surge equals a resonance frequency of the transformer winding. These resonant over-voltages can result in a flashover from the windings to the core or between the turns [4]. However it should be noted that internal winding resonances will not necessarily result in immediate breakdown, but may result in partial discharges, which will further aid in insulation degradation and ultimately failure [1]. Measurement of resonance overvoltages cannot be done at the transformer terminals since they occur inside the windings. Special prototype transformers are usually constructed for the measurement of these overvoltages or through an analytical high frequency model of a transformer. In the literature, two high frequency modelling techniques are usually employed which are the Multi-conductor Transmission Line (MTL) model and the RLC ladder equivalent circuit [5], [6], [7], [8]. The MTL model is usually used for analysis

of fast transients with frequency components above 1 MHz whereas the RLC ladder equivalent circuit for transients up to 1 MHz [8]. In [9], a special prototype wind turbine step-down transformer was designed for the purpose of analysis of resonant overvoltages in wind turbine transformers. The special prototype transformer was a 11/0.24 kV 500 kVA transformer with three different winding designs which are pancake, layer and disc winding [3]. Results show that a layer winding is more likely to have a higher transferred overvoltage to the LV terminal than disc and pancake windings. However the layer and pancake windings have lower values with regards to resonance over-voltages inside the windings compared to the disc winding. This paper deals with the calculation of the inter-turn overvoltage using transformer parameters from [6] and the measurement of switching transients obtained at wind farm.

2. BACKGROUND THEORY

Analysis of the voltage distribution within the transformer windings can be represented by a group of interconnected and coupled transmission lines as shown in Figure 1.

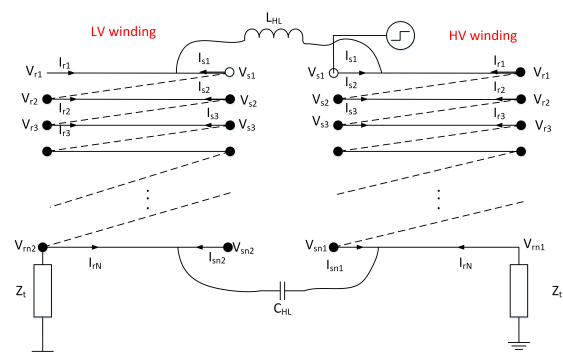


Figure 1: Multi-conductor Transmission Line model

Figure 1 shows a model representation of the HV and LV

windings. With reference to SANS 60076-3, transferred voltages have both a capacitive and inductive character which are presented by C_{HL} and L_{HL} respectively in Figure 1. The coupled transmission lines can be described by the Telegraphers equations: Equation 1 and Equation 2:

$$\frac{d^2 \mathbf{V}}{dx^2} = -[\mathbf{Z}][\mathbf{Y}] \quad (1)$$

$$\frac{d^2 \mathbf{I}}{dx^2} = -[\mathbf{Z}][\mathbf{Y}] \quad (2)$$

where \mathbf{V} and \mathbf{I} are the incident voltage and current vectors respectively. \mathbf{Z} and \mathbf{Y} are the impedance and admittance matrices of the line respectively. The Telegraphers equations can be solved to find the voltages and currents at a distance x as shown in Equation 3 and Equation 4 [10].

$$V_x = V_1 e^{-[P]x} + V_2 e^{[P]x} \quad (3)$$

$$I_x = Y_o \left(V_1 e^{-[P]x} - V_2 e^{[P]x} \right) \quad (4)$$

Applying boundary conditions to the solution of Equation 3 and Equation 4 it is possible to express the sending end (S) and receiving end (R) voltages as shown in Equation 5 [6]:

$$\begin{bmatrix} I_S \\ I_R \end{bmatrix} = \begin{bmatrix} A & -B \\ -B & A \end{bmatrix} \begin{bmatrix} V_S \\ V_R \end{bmatrix} \quad (5)$$

where:

$$A = YS\gamma^{-1} \coth(\gamma l) S^{-1} \quad (6)$$

$$B = YS\gamma^{-1} \operatorname{cosech}(\gamma l) S^{-1} \quad (7)$$

and I_R and I_S are the current vectors at the receiving and sending end respectively. V_R and V_S are the voltage vectors at the receiving and sending end respectively. In Equation 6 and Equation 7: S is the matrix of eigenvectors and γ^2 is the matrix of eigenvalues of the matrix ZY . l is the length of the line. Further simplification of Equation 5 results in the following:

$$\begin{bmatrix} I_{S1} \\ I_{S2} \\ \vdots \\ I_{Sn} \\ I_{R1} \\ I_{R2} \\ \vdots \\ I_{RN} \end{bmatrix} = \begin{bmatrix} A & -B \\ -B & A \end{bmatrix} \begin{bmatrix} V_{S1} \\ V_{S2} \\ \vdots \\ V_{Sn} \\ V_{R1} \\ V_{R2} \\ \vdots \\ V_{RN} \end{bmatrix} \quad (8)$$

From Figure 1 it is possible to apply the following identities to Equation 8 [11]:

$$\begin{aligned} I_{r1} &= -I_{s2} & I_{r2} &= -I_{s3} & -I_{rn} &= V_{rn}/Z_t & V_{rl} &= V_{s2} \\ V_{r2} &= V_{s3} & \dots & & & & & \end{aligned}$$

This will enable matrix reduction techniques to be applied without altering the system equations. The result is Equation 9.

$$\begin{bmatrix} I_{S1} \\ 0 \\ \vdots \\ 0 \\ 0 \end{bmatrix} = \begin{bmatrix} & & & & \\ & & & & \\ & & & & \\ & & & & \\ & & & & \\ & & & & \\ & & & & \\ & & & & \\ & & & & \\ & & & & \end{bmatrix} Y \begin{bmatrix} V_{S1} \\ V_{S2} \\ \vdots \\ V_{Sn} \\ V_{Rn} \end{bmatrix} \quad (9)$$

where Y is an $n \times n$ matrix. The termination impedance for the transformer winding Z_t in Figure 1 is assumed to be $10^{-9} \Omega$ [12]. If the current I_{S1} is eliminated from Equation 9 then Equation 9 can be re-written as shown in Equation 10 to solve for the voltages at any arbitrary turn k .

$$\begin{bmatrix} V_{S2} \\ V_{S3} \\ \vdots \\ V_{Sn} \end{bmatrix} = \begin{bmatrix} H_1 \\ H_2 \\ \vdots \\ H_{n-1} \end{bmatrix} \begin{bmatrix} V_{S1} \\ 0 \\ \vdots \\ 0 \end{bmatrix} \quad (10)$$

where the magnitude of the transfer function at turn k relative to the input can be calculated as [5]:

$$H_k = \frac{YY^{(k+1,1)}}{YY^{(1,1)}} \quad k = 1, 2, \dots, n-1 \quad (11)$$

YY is the inverse matrix of the matrix Y in Equation 9 and H is a square matrix of order $(n-1) \times (n-1)$. It should be noted that surge transference from HV to LV winding as depicted in Figure 1 will not be the focus in this paper.

3. PARAMETER CALCULATION OF A TRANSFORMER WINDING

In [6] and [13] Liang showed how to model transformer windings for the analysis of resonant overvoltages. A core-type transformer was used and the winding parameters shown in Table 1 will be used in this paper [13].

The impedance $\mathbf{Z} = \mathbf{R} + \mathbf{j} \omega \mathbf{L}$ and admittance $\mathbf{Y} = \mathbf{G} + \mathbf{j} \omega \mathbf{C}$ matrix of Equation 1 and Equation 2 are calculated as:

$$\mathbf{Z} = \left[\mathbf{j} \omega \mathbf{L} + \left(\frac{1}{2(d_1 + d_2)} \right) \cdot \sqrt{\frac{\pi f \mu}{\sigma}} \right] \quad (12)$$

$$\mathbf{Y} = (j\omega + \omega \tan \delta) \mathbf{C} \quad (13)$$

where μ and σ are the permeability and conductivity of the conductor. d_1 and d_2 are the diameter of the conductor.

Table 1: Main Parameters of the winding

Number Of discs	18
Turns per disc	10
Conductor width [mm]	6.95
Conductor height [mm]	11.2
Average turn length [m]	1.4828
Thickness of inter-turn insulation [mm]	3.00
Relative permittivity of inter-turn insulation	3.5
Conductor conductance [$s \cdot m^{-1}$]	3×10^7
Inter-turn capacitance (C_k) [$pF \cdot m^{-1}$]	120
Inter-section capacitance (C_s) [$pF \cdot m^{-1}$]	10
Turn to core capacitance (C_g) [$pF \cdot m^{-1}$]	15

In (12) the real part takes into account the skin effect at high frequencies [13]. The real part of Equation 13 represents the dissipation factor ($\tan \delta$) or dielectric losses [5], [12]. It should be noted that $\tan \delta$ is frequency, moisture and temperature dependent and will influence the admittance matrix greatly at higher frequencies. An approximate equation for $\tan \delta$ (Equation 14) was used to model the frequency dependency of the transformer insulation [3].

$$\tan(\delta) = (1.082 \times 10^{-8}) \cdot 2\pi f + 5.0 \times 10^{-3} \quad (14)$$

The capacitance and inductance matrix were calculated as follows:

3.1 Capacitance

The capacitance matrix \mathbf{C} was formed as follows in [12]:

- $C_{i,i}$ capacitance of layer i to ground and the sum of all other capacitances connected to layer i
- $C_{i,j}$ capacitances between layers i and j taken with negative sign ($i \neq j$)

It should be noted that the capacitance matrix is crucial especially for the determination of the transient voltages between the turns.

3.2 Inductance

The inductance matrix is calculated from two parts. The first is directly from the capacitance matrix \mathbf{C} if the following assumptions are made [11]:

1. High frequency magnetic flux penetration into the iron laminations and transformer core is negligible.
2. The magnetic flux will be constrained within the paths of the insulation.

The first inductance matrix can then be obtained using Equation 15:

$$L_n = \frac{\epsilon_r}{v^2} \cdot \mathbf{C}^{-1} \quad (15)$$

where v is the velocity of light in vacuum and ϵ_r is the relative permittivity of the insulation (in this case equivalent permittivity of the air and paper combination). The second part of the inductance takes into account the flux internal to the conductor [13]. It is given by:

$$L_i = \frac{\mathbf{R}}{f} \quad (16)$$

where \mathbf{R} is from the real part of Equation 12. The total inductance matrix can be expressed as:

$$\mathbf{L} = L_n + L_i \cdot E_n \quad (17)$$

where E_n is a unit matrix of size $n \times n$.

4. COMPARISON WITH PREVIOUS WORK

As previously mentioned, this work was done by Liang in [6] and [13]. The aim of redoing Liang work was to validate the work that was done earlier and test the validity of the developed algorithm. From then on the algorithm will be applied to transformers at a wind farm to try to explain if failure could be caused by resonance behaviour. Resonance phenomena in transformer windings is usually brought about if the frequency components of the switching surges matches one of the resonant frequencies of the transformer winding. The high frequency components lead to destruction of the insulation and breakdown tends to occur in the turns close to the led-in end [13].

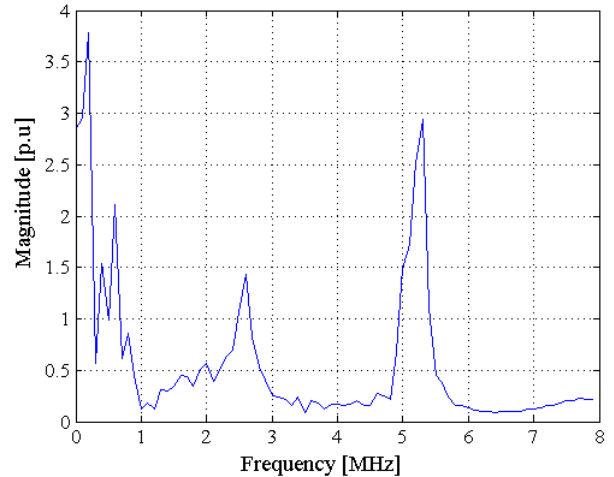


Figure 2: Magnitude of the transfer function of turn 20 relative to the input

Figure 2, Figure 3 and Figure 4 show the magnitude profile at different turns. An important characteristic to note from the waveforms is that the magnitude of the high frequency components decreases as the number of turns increase down the transformer winding. The waveforms

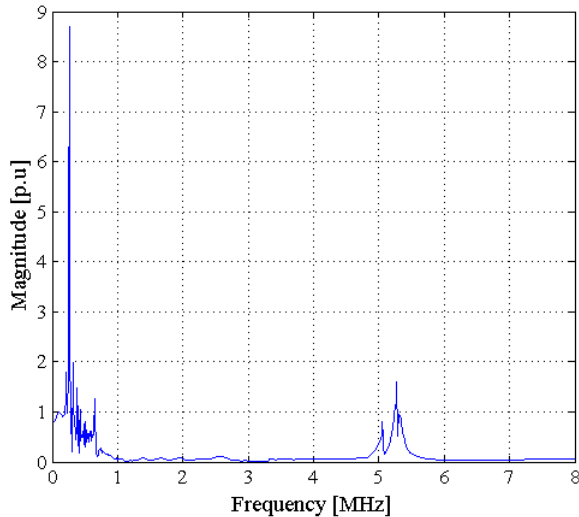


Figure 3: Magnitude of the transfer function of turn 40 relative to the input

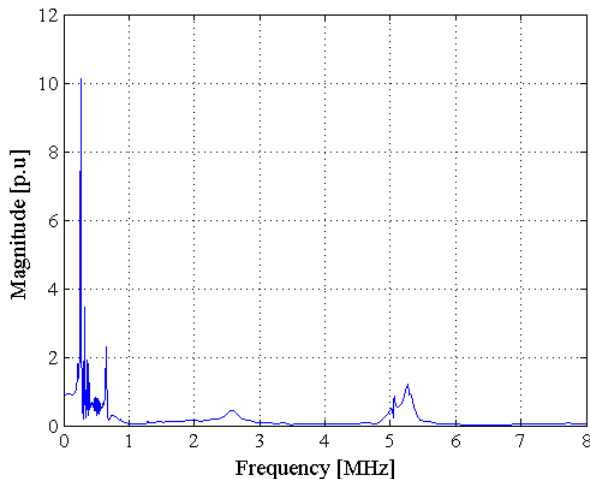


Figure 4: Magnitude of the transfer function of turn 60 relative to the input

produced show a resonant frequency around 5 to 6 MHz. Comparison with the results obtained by Liang in [13] reveal that the waveforms follow the same profile although the magnitude of some frequency components do not correlate. This could be as a result of the approximation for the calculation of $\tan(\delta)$ and also the assumed termination impedance of $Z_t = 10^{-9}\Omega$. However the results of Figure 2, Figure 3 and Figure 4 are a good enough approximation to visualize the resonance phenomena in transformer windings and the possible determination of inter-turns breakdown.

4.1 Measurement of switching transients

As discussed earlier, internal resonance occurs when one of the frequency components of the incoming surge equals a resonance frequency of the transformer winding. Switching transients tests were conducted on a Wind

turbine transformer. The tests involved the following:

1. Energizing the transformer during no-load.
2. Disconnecting the transformer during no-load.

Measurement of the three MV phase-to-earth voltages were made by use of a capacitive voltage divider on each phase. The MV bushing screen had a measured capacitance of 32 pF and an additional capacitance of 10 nF was externally mounted in series with the bushing screen terminal and the transformer tank which provided local earth. The resulting voltage division ratio was 313. Figure 5 shows the measurement setup with the FLUKE 1750 connected to the phase conductors.

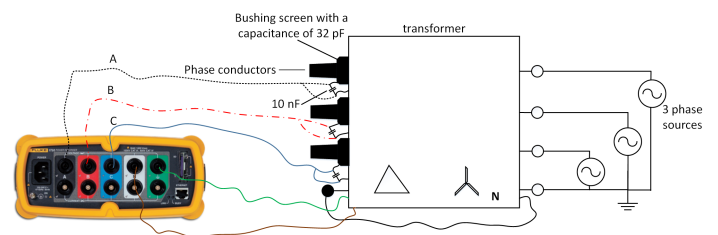


Figure 5: Measurement setup for recording transients

4.2 Energizing the transformer during no-load

Energization of the transformer from always results in at least one pre-strike per phase [14]. During the contact making process of the vacuum circuit breaker, generation of high du/dt transients can occur at the transformer terminals leading to over-voltages within a few milliseconds [15]. This behaviour can be observed from the measured transients in Figure 6. Analysis of the waveform in Figure 6 reveals a pre-strike behaviour with high du/dt which could result in the development of resonance overvoltages within the transformer winding.

4.3 Disconnecting the transformer during no-load

On disconnection of the VCB higher over-voltages can occur if the arc re-ignites after the first current interruption [16]. If the VCB is not able to quench the arc, multiple re-ignitions can occur and with each re-ignition, the voltage escalates resulting in higher over-voltages. No significant over-voltages were measured on de-energizing of the transformer.

5. DISCUSSION

In this paper a study into resonant overvoltages has been presented. White box models such as the MTL model and RLC model require the precise geometry of the transformer windings. In this paper since the actual parameters of the wind turbine transformers were not known, external transformer parameters were chosen to illustrate resonance phenomena in transformer windings. However the model has several limitations. Firstly an

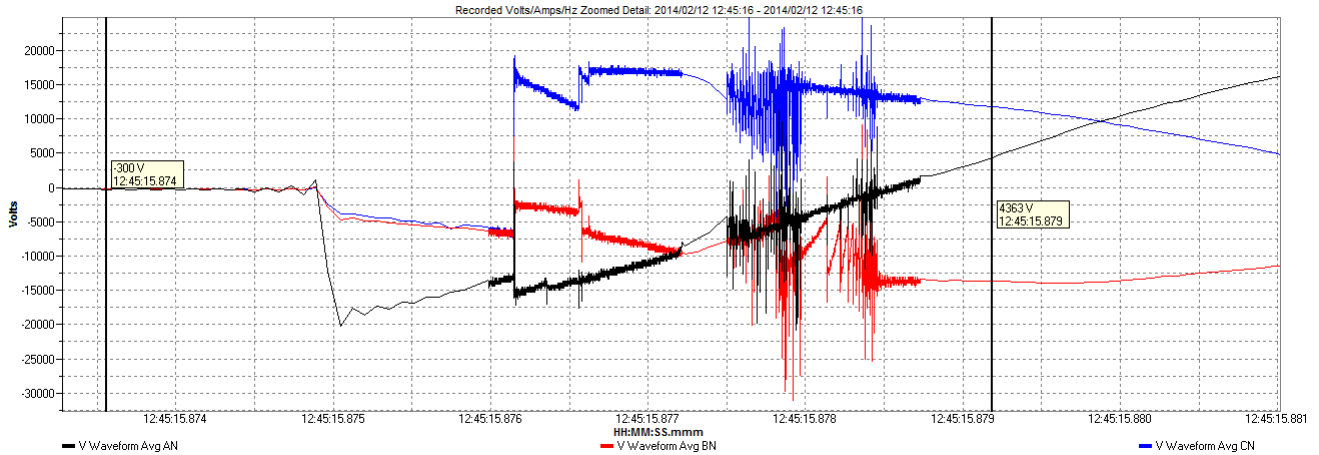


Figure 6: Measured pre-strike behaviour on closing of the vacuum circuit breaker

assumed value of the termination impedance was used. According to [12], to eliminate the divergence of the computations, a small impedance: $Z_t = 10^{-9}\Omega$ must be used. This value may be different from the termination impedance used by Liang in [6], [13].

As previously mentioned $\tan(\delta)$ is frequency, moisture and temperature dependent and Equation 14 is an approximate equation. Thus at frequencies above 1 MHz, Equation 14 will not take into account the detailed frequency dependency of the dissipation factors of the transformer insulation, which is crucial for accurate modelling using the MTL model [3].

The next issue which warrants a discussion is the resistance calculation. In [13], Liang calculated the resistance by taking into account the skin effect at high frequencies as shown in Equation 12. However, another way of calculating the impedance is shown in Equation 18.

$$Z = \left(j\omega + \sqrt{\frac{2\omega}{\sigma\mu_0 d^2}} \right) \mathbf{L} \quad (18)$$

where the real part takes into account the skin effect and proximity effects of the conductor and its dependency on frequency [12]. In Equation (18), d is the distance between the layers and σ is the conductivity of the conductor. According to [3], the total resistance is dominantly affected by the proximity effect for frequencies above 4 MHz. Neglecting the proximity effects as done by Liang in [13] and only taking into account the skin effect in the resistance calculation can result in resonant frequencies below 1 MHz with quite high amplitudes [3] as shown in Figures 2, 3 and 4. To illustrate Hans Kristian Hidalen point [3], the magnitude of the transfer function at turn 20 is re-calculated taking into account proximity effect. The results of the MTL model with the impedance Equation (18) is shown in Figure 7. Analysis of Figure 7 shows that the magnitude of the resonance frequencies below 1 MHz which had quite high amplitudes have diminished considerably compared to the original waveform in Figure

2. Not taking into account the proximity effects can lead to calculated results which have a poor agreement with measurements as shown in [3].

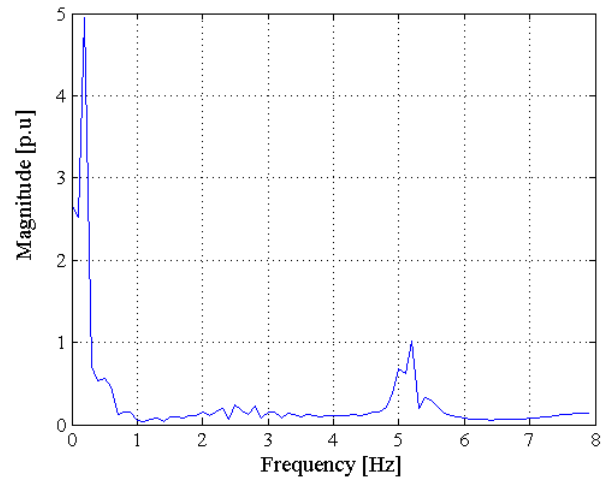


Figure 7: Magnitude of transfer function of turn 20 relative to the input (taking into account proximity effects)

6. CONCLUSION

In this paper, resonance phenomena in transformer windings and the measurement of switching transients have been presented. The MTL model has been used to calculate the magnitude of the resonant over-voltages within the turns and the possibility of breakdown between turns. Although the model has several shortcomings, the qualitatively good agreement of the calculated waveforms with the measured results can help understand the phenomena of internal winding resonance in transformers windings.

ACKNOWLEDGEMENT

This work is in partial fulfilment towards an MSc in Electrical Engineering and the author would like to thank

the Eskom Power Plant Engineering Institute (EPPEI) and Dr John Van Coller for their support and funding of the research program. Also the engineers from the transformer factory and at the wind farm who made all the measurements possible.

REFERENCES

- [1] T. Craenenbroek, J. D. Ceuster, J. P. Marly, H. D. Herdt, B. Brouwers, and D. V. Dommelen. "Experimental and numerical analysis of fast transient phenomena in distribution transformers." in *IEEE Power Engineering Society Winter Meeting, Singapore*, vol. 3, no. 1, pp. 2193–2198, Jan. 2000.
- [2] M. Popov and L. van der Sluis. "Improved calculations for no-load transformer switching surges." in *IEEE Transactions on Power Delivery*, vol. 16, no. 3, pp. 401–408, Jan. 2001.
- [3] A. H. Soloot, H. K. Hidalen, and B. Gustavsen. "Modeling of Wind Turbine Transformers for the Analysis of Resonant Overvoltages." in *International Conference on Power Systems Transients IPST2013 in Vancouver, Canada*, pp. 1–7, Jul. 2013.
- [4] M. Popov, L. V. der Sluis, G. C. Paap, and H. D. Herdt. "Computation of Very Fast Transient Overvoltages in Transformer Windings." in *IEEE Transactions on POWER DELIVERY*, vol. 18, no. 4, pp. 1268–1274, Oct. 2003.
- [5] M. Popov, L. V. der Sluis, R. P. P. Smeets, and J. L. Roldan. "Analysis of Very Fast Transients in Layer – Type Transformer Windings." in *IEEE TRANSACTIONS ON POWER DELIVERY*, vol. 22, no. 1, pp. 238–247, Jan. 2007.
- [6] H. Sun, G. Liang, X. Zhang, and X. Cui. "Analysis of Resonance in Transformer Windings under Very Fast Transient Overvoltages." in *17th International Zurich Symposium on Electromagnetic Compatibility*, vol. 22, no. 1, pp. 432–435, Jan. 2006.
- [7] J. Du, G. Liang, H. Sun, X. Liu, and X. Liu. "Lumped Parameter Modeling of Transformer windings under VFTO." in *17th International Zurich Symposium on Electromagnetic Compatibility*, pp. 258–261, Jan. 2011.
- [8] S. Hosseini, M. Vakilian, and G. Gharehpetian. "Comparison of transformer detailed models for fast and very fast transient studies." in *IEEE Transactions on Power Delivery*, vol. 23, no. 2, pp. 733–741, Apr. 2008.
- [9] A. H. Soloot, H. K. Hidalen, and B. Gustavsen. "Upon the Improvement of the Winding Design of Wind Turbine Transformers for Safer Performance within Resonance Overvoltages." in *Tenth Deep Sea Offshore Wind Research and Development Seminar*, pp. 1–7, Jan. 2013.
- [10] S. N. Hettiwatte, P. A. Crossley, Z. D. Wang, A. Darwin, and G. Edwards. "Simulation of a transformer winding for partial discharge propagation studies." in *IEEE Power Engineering Society Winter Meeting*, vol. 2, no. 1, pp. 95–101, Jun. 2002.
- [11] J. Guardado and K. J. Cornick. "A Computer model for calculating Steep-Fronted Surge Distribution in Machine Windings." in *IEEE TRANSACTIONS ON Energy Conversion*, vol. 4, no. 1, pp. 95–101, Mar. 1989.
- [12] M. Popov, L. V. der Sluis, and R. P. P. Smeets. "Evaluation of surge-transferred overvoltages in distribution transformers." in *Electric Power Systems Research 78 (ELSEVIER)*, vol. 78, no. 3, pp. 441–449, May 2007.
- [13] H. Sun, G. Liang, X. Zhang, and X. Cui. "Modelling of Transformer Windings under Very Fast Transient Overvoltages." in *IEEE Transactions on Electromagnetic Compatibility*, vol. 48, no. 4, pp. 621–627, Nov. 2006.
- [14] L. Liljestrand, E. Lindell, D. Bormann, C. Ray, and E. Dullni. "Vacuum circuit breaker and Transformer interaction in a cable system." *CIGRE 22nd International Conference on Electricity Distribution Stockholm*, , no. 0412, pp. 1–4, Jun. 2013.
- [15] D. Smugala, W. Piasecki, M. Ostrogorska, M. Florkowski, M. Fulczyk, and P. Kyles. "Distribution transformers protection against High Switching Transients." *Przegląd Elektryczny (Electrical Review)*, pp. 296 – 300, Jan. 2012.
- [16] A. Mueller and D. Saemann. "Switching phenomena in Medium Voltage Systems - Good Engineering Practise on the application of Vacuum circuit breakers and contractors." pp. 1–9, Mar. 2011.

ADVANCEMENTS IN DISTRIBUTION TRANSFORMER ELECTRICAL TRANSIENTS AND POWER FREQUENCY SIGNAL MONITORING

F. A. Netshiongolwe¹, R. Cormack², J. M. van Coller¹

¹*Eskom Power Plant Engineering Institute (EPPEI)-High Voltage (HV), School of Electrical and Information Engineering, University of the Witwatersrand, Private Bag 3, Wits 2050, South Africa Email: netshifa@eskom.co.za, John.VanColler@wits.ac.za*

²*Eskom, PO Box 1091, Johannesburg, 2001, South Africa Email: CormacR@eskom.co.za*

Abstract. This paper presents the use of a designed Rogowski coil current sensor and a capacitive voltage divider for both transient and power frequency monitoring in distribution networks. Limitations to presently available monitoring systems that use conventional ferromagnetic core current transformers are presented. The designed 875 turns coil was used in successfully measuring currents rated up to 600A. The integrated output of the designed Rogowski coil was consistent with measured 6 kA 8/20 μ s impulse current. An embedded screen on a 24 kV rated bushing was used in capturing power frequency voltages ranging from 1 kV up to 27 kV. Non-linearity have however been observed when measuring 1.2/50 μ s impulse voltage beyond 80 kV.

Key Words: Rogowski coils; capacitive voltage divider, impulse current, impulse voltage

1. INTRODUCTION

Advancements in the distribution network have resulted in the need for increased electrical monitoring. The increased use of compact fluorescent lamps, computers and PV generation sources with power electronic interfaces have also led to an increase in the level of harmonics at the distribution level [1]. Transients introduced by faults and lightning strikes can cause significant damage to distribution transformers. Failed surge arrestors on pole-mount transformers are often not identified in time, resulting in premature transformer failures [2]. All this highlights the need to have reliable monitoring that enables effective management of distribution-level equipment.

Monitoring technology applied to distribution transformers is often limited due to the unavailability of low cost sensors. This paper presents a low cost approach to monitoring distribution transformers using an existing bushing screen and a Rogowski coil embedded in the bushing. An overview of the potential electrical stresses observed at distribution level is given. The operating principles of the capacitive voltage divider and the Rogowski coil are given. Both the power frequency and the transient measurement capabilities of the above sensors are evaluated.

2. BACKGROUND

2.1 Electrical stresses

The premature failure of distribution transformers (rated up to 2 MVA) has led to the use of current and voltage monitoring systems on the low voltage (LV) side of Eskom distribution transformers [3]. The use of such monitors coupled with temperature sensors has shown that some transformers are subjected to severe system faults, severe overloading and load unbalance. Such stresses often lead to transformers operating at significantly higher temperatures

resulting in insulation damage. Overloading has been shown to have the following effects on transformers [4]:

- Damage to tap changers and bushings
- Paper insulation degradation when the winding temperature (i.e hot spot temperature) is in excess of 90^oC. Observations show that paper insulation life is halved for every 6^o C the hot spot temperature exceeds 98^o C

Non-linear loads such as compact fluorescent lamps (CFLs) battery chargers, uninterruptable power supplies (UPSs), television sets, inverter-controlled air conditioners and refrigerators are becoming more common in South Africa. Such non-linear loads cause harmonic currents that also produce harmonic voltages that increase the losses in the utility equipment. Sharengi et al. showed that the loading capacity of a transformer had to be reduced by 35 % when supplying CFLs compared to linear loads such as incandescent lamps [5]. Monitoring harmonics at transformer level can thus lead to more accurate derating of such transformers.

Electrical stresses in the form of lightning transients also contribute towards premature failure of transformers. In Eskom, pole-mounted transformers are protected using fuses and surge arresters. Fuses isolate faulty transformers. Surge arrestors offer protection against lightning or switching transients. Table 1 shows lightning related transformer failures that were reported in the Eskom Free State Operating Unit. Such a failure rate highlights the need for monitoring systems capable of quantifying these stresses.

Monitoring systems developed within Eskom for pole-mounted transformers currently measure only the power frequency stresses on the LV side of pole-mounted transformers. The developed system already has a communication infrastructure that sends

measured parameters to the network operators. The MV side is not monitored. Transients are also not monitored. This paper looks at the use of Rogowski coils and bushing screen capacitive voltage dividers for wideband monitoring on the MV side of distribution transformers.

Table 1: Financial year 2013/2014 MV/LV pole-mounted transformer equipment failures in the Free State Operating Unit [2]

Average failures (per year)	Total	Due to lightning	Percentage
MV fuses	7895	6160	78%
Pole-mounted transformers	638	497	77.9%
MV surge arrestors	2312	2312	100%

2.2 Rogowski coil current monitoring

Saturation and limited bandwidth have led to the switch from using ferromagnetic core current transformers to air-cored Rogowski coils. Rogowski coils such as the one depicted in Figure 1 sense the current flowing through the conductor. A Rogowski coil with physical properties shown in Table 2 was designed and studied. The 875-turn coil was terminated with a 179 Ω resistor. Rogowski coil operation is based on Ampere's law, where the coil senses the magnetic field around the conductor. The respective equation is [6]:

$$i = \oint H \cos \alpha \cdot dl \quad (1)$$

Where:

- i = primary current [A]
- H = magnetic field strength [A/m]
- dl = small element along the coil path [m]
- α = angle between the magnetic field and the element

The flux linking the entire coil given by [7, 8]:

$$\varphi = \int d\varphi = \int \mu_0 n A H \cos \alpha dl = \mu_0 n A i \quad (2)$$

Where:

- φ = Total flux linkage [Wb]
- $d\varphi$ = Flux linkage within a section dl
- $\mu_0 = (4\pi \times 10^{-7} \text{ [H} \cdot \text{m}^{-1}]$, Permeability of air
- n = Number of turns per metre [m^{-1}]
- A = coil cross-sectional area [m]

The voltage induced in the coil is a function of both the time derivative of the measured primary current and the mutual inductance of the coil as expressed in equation (3) below [7,8]:

$$V_c = \frac{d\varphi}{dt} = -\mu_0 n A \frac{di}{dt} = -M \frac{di}{dt} \quad (3)$$

Where

- V_c = Coil voltage [V]
- M = Mutual inductance [H]

The corresponding mutual inductance based on the parameters in Table 2 can be calculated as [9]:

$$M = \mu_0 \frac{N_2}{L} A \quad (4)$$

The current in equation (3) is obtained by integrating the coil output voltage using active integration circuits [6, 10]. The current can also be calculated using numerical integration techniques [11]. In this study, numerical integration techniques are used for both power frequency and transient measurements.

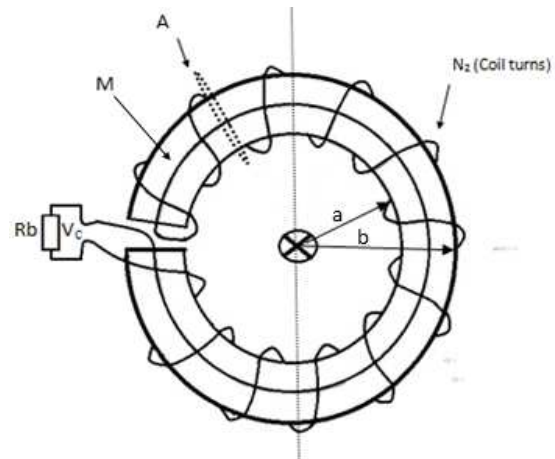


Figure 1: Rogowski Coil: the current to be measured flows through a conductor centrally located at X

Table 2: Designed Rogowski coil specification

Parameter	Parameter description	Value
d_w [mm]	Wire diameter	0.375
R [Ω]	Wire resistance	18.66
a [mm]	Toroid inner radius	33.5
b [mm]	Toroid outer diameter	57.5
L [m]	Wire length	65
A [mm ²]	Coil area	452.39
N_2	Number of turns	875
M [nH]	Mutual inductance	497

The Rogowski coil designed in this study will be embedded in 22 kV bushing. The power frequency performance of the Rogowski coil was evaluated as

shown in Figure 2 below. The transient performance was evaluated using an 8/20 μ s current impulse generator as shown in Figure 3. A wideband current monitor was used as a reference in both the power frequency and the impulse measurements. Both coil voltages were integrated numerically so as to evaluate the primary current.

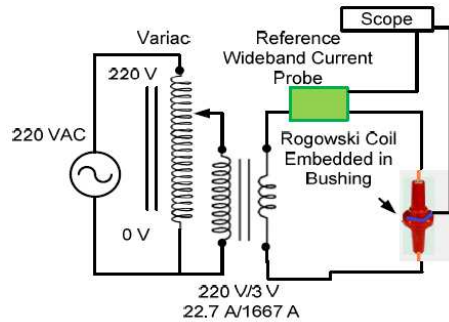


Figure 2: Power frequency test circuit

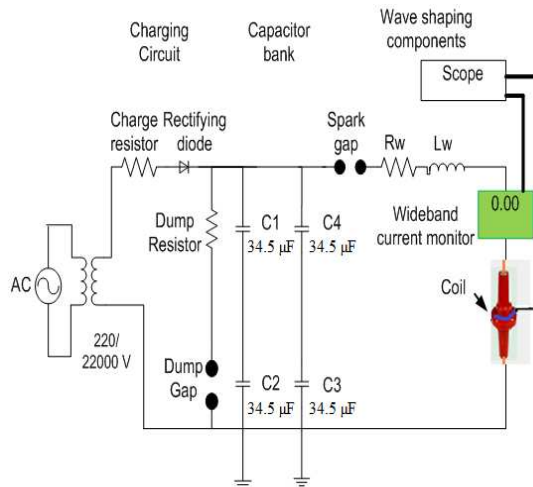


Figure 3: Impulse current test circuit

2.3 Screened bushing voltage monitoring

The 22 kV epoxy resin bushing with embedded screen for internal electric field control is shown in Figure 4 and has been successfully used for measuring power frequency voltages [11]. In this study the performance of the bushing was evaluated for measuring both power frequency and impulse voltages. A comparison between the voltage obtained using the bushing screen and a wideband 1000/1 capacitive probe for power frequency measurements was made. The capacitance between the bushing conductor and the screen was measured as 22 pF.

Both the power frequency and the transient output voltages were measured across the external capacitor connected between the screen and earth. The ratio of the bushing divider was determined by varying the input voltage from 1 kV up to 22 kV. Impulse voltages were also applied using a 1.2/50 μ s voltage impulse generator. If the insulation conductance can be ignored

$$V_{out} = \frac{C_1}{C_1 + C_2} V_{in} \quad (5)$$

Where:

C_1 = Capacitance between the bushing screen and the bushing MV conductor [F]

C_2 = External Capacitor [F]

V_{in} = Input voltage [V]

V_{out} = Output voltage [V]

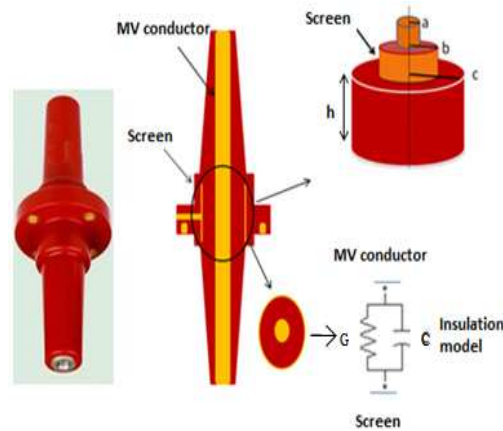


Figure 4: Cross-sectional view of a 22 kV epoxy resin bushing with embedded screen with emphasis on the position of the screen relative to the MV conductor [14].

The external capacitor had a value of 47 nF. Based on equation 5, the voltage division ration was

$$\frac{V_{out}}{V_{in}} = \frac{1}{2137.36} \quad (6)$$

3. CURRENT MEASUREMENT RESULTS

3.1 Power frequency current measurement

Low range and high range currents measured with the Rogowski coil are shown in Figure 5 and 6 respectively. The corresponding scaled numerically integrated current shown in Figure 7 and 8 respectively and is compared with the reference wideband current monitor. Kojovic however suggests that numerical integration is not necessary for power frequency measurement since it is known that the measured signal is shifted by 90° [9]. Though numerical integration is performed in this study, analysis of measured coil data can also be done without going through the complexities of integrating provided power frequency signals are the only signals of interest. The measured voltage signal would simply be related to the primary current through a scaled multiplying factor.

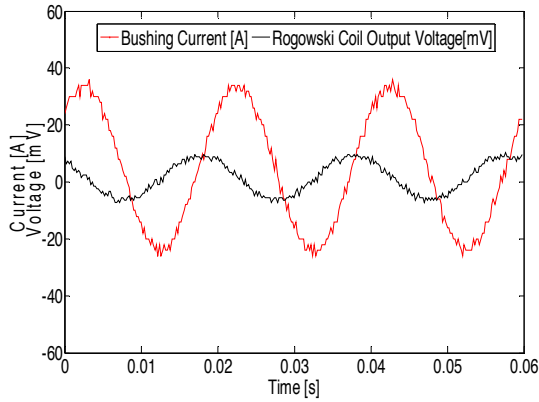


Figure 5: Unintegrated low range 50 Hz current signal

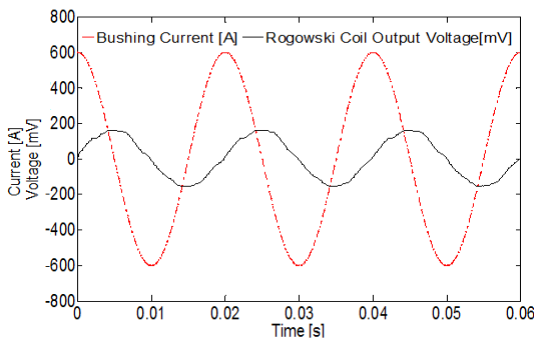


Figure 6: Unintegrated high range 50 Hz current signal

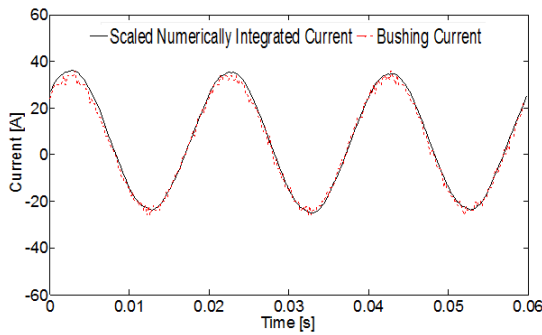


Figure 7: Integrated low range current 50 Hz

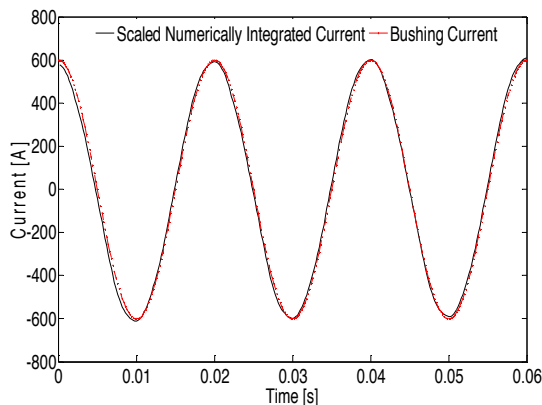


Figure 8: Integrated high range current 50 Hz

3.2 Impulse current measurement

The output voltage of the Rogowski coil when subjected to a 6 kA current impulse is shown in Figure 9. The measured signal was taken with a 10/1 passive probe with the Rogowski coil terminated with the same resistor used in power frequency measurement. Figure 10 shows the current signal that was measured with a wideband current monitor and the corresponding scaled numerically integrated signal based on the output in Figure 9. There is however a $4\mu\text{s}$ time shift introduced by the numerically integrated signal with the reference wideband current monitor output.

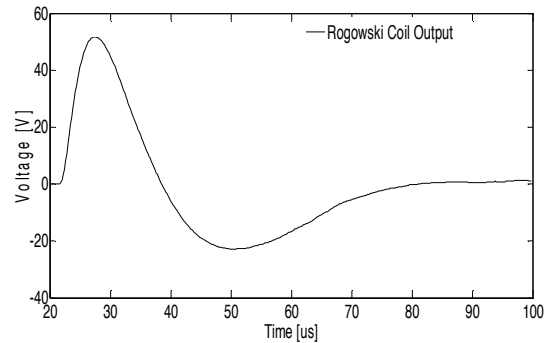


Figure 9: Rogowski coil voltage output under impulse current measurement conditions

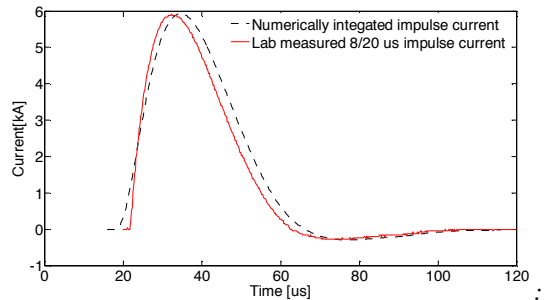


Figure 10: Integrated impulse current signal

4. VOLTAGE MEASUREMENT RESULTS

4.1 Power frequency voltage measurement

Comparison between the measured output voltage of the reference wideband capacitive divider probe and the bushing voltage divider are shown in Figures 11, 12 and 13. Figure 11 shows the use of the bushing divider in measuring a 1.5 kV power frequency voltage. The corresponding bushing voltage divider output in this case was 0.7 V. A scaled version of the bushing voltage divider output termed Scaled CVD shows that the measured waveform is in phase with the wideband capacitive probe output. The division ratio is consistent with the calculations in equations 5 and 6. The scaling factor used for the Scaled CVD signal is 2.137 instead of 2137 so as to match with

the division by a factor of a 1000 introduced by the wideband capacitive voltage probe.

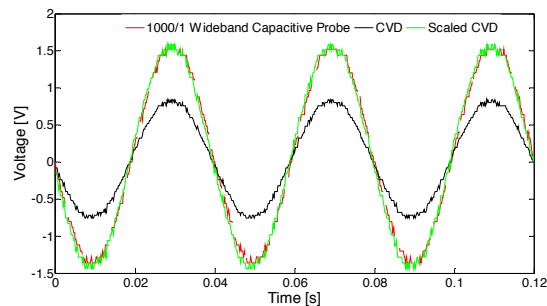


Figure 11: Low range 50 Hz voltage measurement. Measured signal in green has a magnitude of 1.5 kV scaled by a factor of 1000 which enables comparison with the measured bushing voltage divider output termed CVD.

Analysis of the measured waveforms shows that the ratio given in equation 6 is still applicable at a midrange voltage of 13 kV as well as at 27 kV with the bushing voltage divider output equal to 6 V and 12.6 V respectively. The output voltages of both the reference capacitive divider and the bushing voltage divider are shown on the Figures 12 and 13 below.

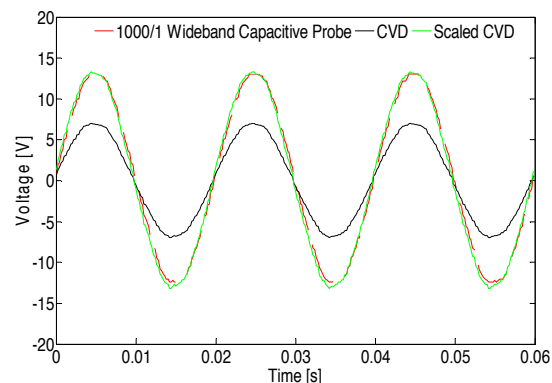


Figure 12: Mid-range 50 Hz voltage measurement. Measured signal in green has a magnitude of 13 kV scaled by a factor of 1000.

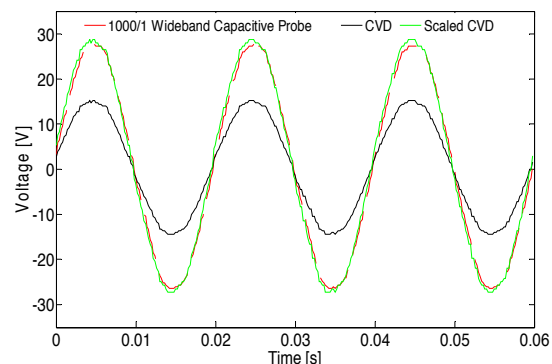


Figure 13: High range 50 Hz voltage measurement. Measured signal in green has a magnitude of 27 kV scaled by a factor of 1000.

4.2 Impulse current measurement

The measurement of voltage transients using the same bushing screen divider was also evaluated where voltage transients up to the Basic Insulation Level (BIL) of 125 kV is of interest. A comparison of the bushing divider and a reference resistive divider showed that 1.2/50 μ s lightning voltage impulses can also be measured with the bushing divider. The bushing divider has the capability of accurately measuring both the rise time and the fall time of the 54 kV impulse shown in Figure 14 below. Non-linearity is however observed when the impulse voltage is increased beyond 80 kV. Laboratory results also showed that earthing and shielding play an important role in obtaining accurate results. Further investigations will revolve round identifying parameters responsible for the observed nonlinearities as suggested in [13].

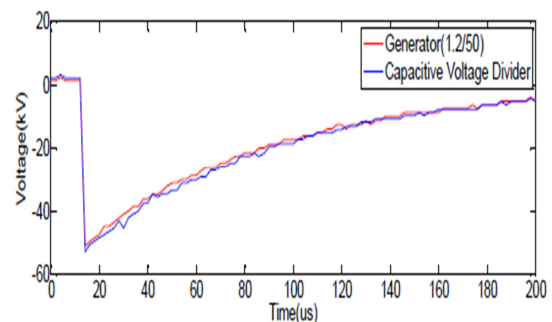


Figure 14: Impulse voltage measurements

5. Conclusion

The presence of both power frequency and transient electrical stresses leads to premature failure of distribution transformers. Both low range and high range currents were successfully measured with the designed embedded Rogowski coil. The current obtained by numerically integrating the output voltage of the Rogowski coil gave results that were consistent with both the power frequency and the transient primary current captured by the reference wideband current probe. Low range and mid-range voltage measurements taken with the bushing divider were consistent with the output of the reference divider. Further work will involve investigating possible causes for nonlinearities of the bushing divider.

REFERENCES

- [1] MAS Masoum, PS Moses and S Deilami, "Load Management in Smart Grids Considering Harmonic Distortion and Transformer Derating", *Proc. Int. Conf. Innovative Smart Grid Technology*, pp. 1-7, 2010.
- [2] WJD Van Schalkwyk and J van Coller, "An Investigation into a More Optimal Choice of BIL

- on MV Feeders”, *Cigré 7th South African Regional Conference*, 2013.
- [3] R Kleinhans, “Current and Voltage Monitors Combat Theft and Improve Supply Quality”, *Energize: Transmission and Distribution*, pp. 41-45, 2011.
- [4] NL Meyer, *Distribution Guide-Part 1: Network Planning Guideline for Distribution Transformers*, Eskom Distribution, 2010.
- [5] M Sharengi, B Phung, M Naderi, T Blackburn and E Anbikairajar, “Effects of Current and Voltage Harmonics on Distribution Transformer Losses”, *International Conference on Condition Monitoring and Diagnosis(CMD)*, Bali, 2012
- [6] WF Ray and RM Davis, “High Frequency Improvements in Wide Bandwidth Rogowski Transducers”, *EPE 99 Conference Proc.*, Lauzanne. 1999.
- [7] DA Ward and J La T Exon, “Using Rogowski Coils for Transient Current Measurements”, *Engineering Science and Education Journal*, pp 105-113, 1993.
- [8] A Phillips, G Grobbelaar, C Pritchard, R Melaia, and I Jandrell. “Development of a Rogowski Coil to Measure Lightning Current Impulses”, *SAIEE Transactions*, 1996.
- [9] LA Kojovic, “Rogowski Coil Transient Performance and ATP Simulations for Applications in Protective Relaying”, *Conference on Power Systems Transients, IPST’05*, Montreal, Canada, 2005.
- [10] SJ Petting and J Siersema, “A Polyphase 500 kA current measurement system with Rogowski coils”, *IEE Proc. B*, Vol. 130, No. 5, pp. 360-363, 1983.
- [11] K Schon and W Schuppel, “Precision Rogowski Coil used with Numerical Integration”, *13th ISH*, Ljubljana, paper T10-130, 2007.
- [12] FA Netshiongolwe, J Van Coller and R Cormack, “Development of Electrical Stress Monitoring Transducers Applicable to Distribution Transformer,” *SAUPEC*, UKZN, 2014.
- [13] JA Martinez-Velasco, *Power System Transients: Parameter Determination*, CRC press, pp. 111-115, 2009.

INVESTIGATION AND ANALYSIS OF THE CAUSES OF 11kV/400V DISTRIBUTION TRANSFORMERS' HIGH FAILURE RATE: CASE STUDY-SWAZILAND ELECTRICITY COMPANY

M.T. Maziya* and K. Awodele**

* Swaziland Electricity Company, Mhlambanyatsi Rd, Swaziland

E-mail: Mphumuzi.maziya@sec.co.sz

** University of Cape Town, Faculty of Engineering and the Built Environment, Department of Electrical Engineering

E-mail: kehinde.awodele@uct.ac.za

Abstract: This paper presents a study on the high failure rates of pole mounted distribution transformers on the 11 kV network of the Swaziland Electricity Company (SEC). The hypothesis is that when exposed to lightning impulses, the likely point of failure is the windings or bushings. Currently, SEC spends a lot of money especially in the summer months on maintenance of 11 kV network, with a large portion of the money spent on replacement of faulty pole mounted distribution transformers. For each distribution depot in the four geographic regions of Swaziland, failed transformers were noted as well as the weather when the transformer failed over a period of approximately two years. A common trend of failure was observed on the failed transformers, where damages included failure of the neutral bushing especially in the summer months. The Highveld and Middleveld recorded the highest failures of pole mounted distribution transformers. The consequences of not having a surge arrester were then simulated in Matlab 2009b as well as the effects of resistivity on the performance of surge arrestors.

Keywords: pole mounted distribution transformer, root causes, distribution depot

1. INTRODUCTION

The Swaziland Electricity Company has a lot of pole mount distribution transformers at distribution level. These consist mainly of 16kVA single phase and 25 kVA three phase transformers, which are often connected at long distribution lines. Due to these sizes, the pole mount distribution transformers have a low kVA rating and a small core area which result in low leakage impedances [1], hence increased fault levels on the secondary.

Throughout its useful life, a pole mount distribution transformer is exposed to a number of factors which stress it mechanically, electrically, chemically and thermally [2], thereby deteriorating its condition. Repeated exposure to stressors reduces the transformer withstand capabilities to lightning and switching impulses, through faults and overloads. Being an open field transformer, moisture ingress is imminent and affects the dielectric system of the transformer [2], and a content as small as 50 parts per million is capable of causing a breakdown strength to drop from 50 to 23kV/mm [3]. The oil condition of such transformers is not monitored and maintenance is only limited to replacing damaged surge arrestors. Without maintenance, and the stressors playing their part, three modes of failure can be identified [2]; partial failure of insulation by localised high temperature overheating, total insulation failure due to severe insulation ageing, and failure of the windings mechanically.

Seasons seem to have a significant impact on the performance of open field transformers, especially in the summer months. In summer months, there is a lot of

tripping and closing of 11 kV switchgear, resulting in inrush currents as the transformers are energized. Transient faults also cause inrush currents in transformers. Inrush currents may contain harmonics and dc offsets. Over-excitation due to repeated lightning strikes in summer may lead to saturation of the transformer core. A saturated core does not provide the least reluctance path for the flux [4], hence stray flux on tank walls resulting in additional heating internally of the transformer. A majority of the transformers fail when there are thunderstorms, although a certain number fails in winter due to overload related incidences.

Swaziland has four geographic regions with unique climatic conditions. The Highveld [5] receives the highest rainfall through thundershowers, and further records the highest failure rate of transformers. Swaziland is a severe lightning area with lightning ground flash density of above 5 per square kilometre per year [6].

Surge arrestors are used to protect transformers against lightning impulses, so the option of having secondary surge arrestors was explored further, in trying to reduce the high failure rates.

2. METHODOLOGY

The failed transformers were sampled and visually inspected to see if there were any patterns in the nature of the failure. The weather was noted on any day there was a significant number of failed pole mount transformers.

Lightning effects were further explored through simulation using Matlab 7.9.0 (R2009b). The simulation

was aimed at showing arrester operation during lightning strikes. Shown below is the simulation arrangement that was used

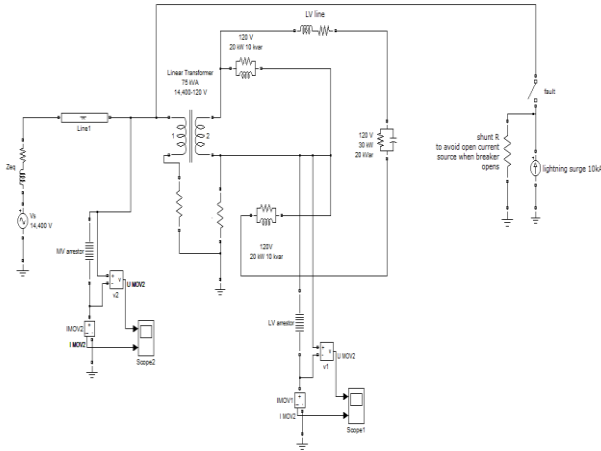


Figure 1: Primary and secondary neutral lightning arrester operation

Currently, the pole mount distribution transformers at the Swaziland Electricity Company network do not have a secondary surge arrester.

The above network is made up of a 75kVA transformer which steps down 20.4kV to 120V, a voltage source at 20.4kV and some loads on the secondary of the transformer. The loads are resistive and inductive/or capacitive. Surge arrestors are then connected on either sides of the transformer, and finally a current source which will be used to simulate a lightning surge into this network. The simulation aimed to find out the following:

- Effect of varying soil resistivity. Soil resistivity in Swaziland is generally higher [7][8], although earthing methods can be applied to alter these values.
- Effect of surges entering primary side of the transformer and those entering the secondary side of the transformer.

Model used to show effects of varying resistivity is shown below:

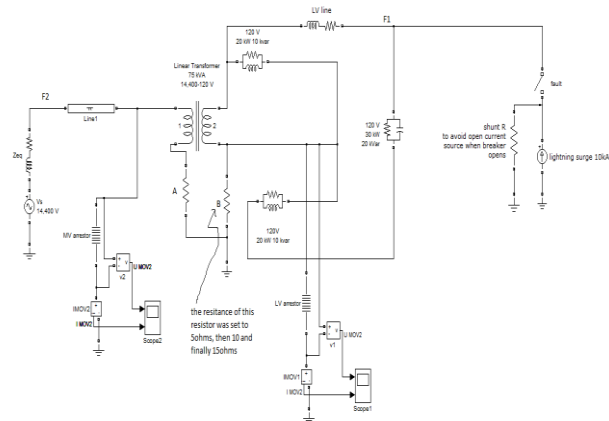


Figure 2: earth resistivity effects

The earthing resistance B of the secondary side was set to 5Ω, 10Ω and lastly 15Ω. As this resistance was varied, a

fault was applied at points F1 and F2. Scope1's output will be used to monitor the output across the LV surge arrester.

To view effects of lightning entering primary and secondary side of the transformer, the resistors A and B were both set to 10Ω, then the surge was set to 10kA and applied to F1 and F2. Scope1 and scope2 were then monitored to see what happened during MV or LV lightning strikes. With the same arrangement, the lightning surge was decreased to 5kA, and the output on the scopes was then monitored.

Based on the simulation results and the information gathered from field data, secondary neutral surge arrestors were practically installed on site. The chosen sites were transformers on feeders which have a number of transformers failing whenever there is a thundershower. In the selection of a suitable neutral surge arrester, the figure below was used:

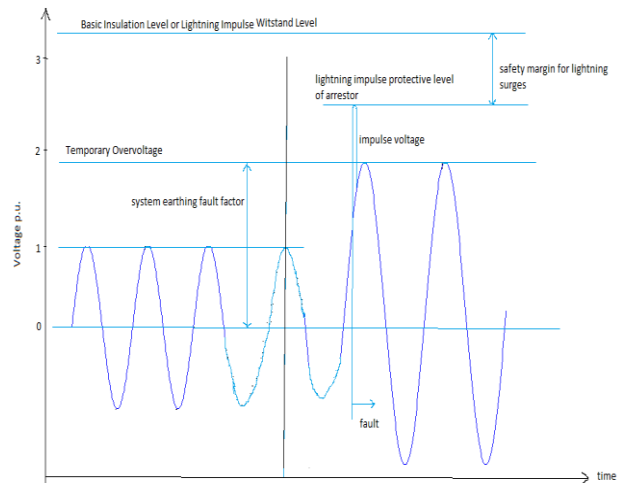


Figure 3: Factors considered when choosing neutral surge arrester

The specifications for the chosen arrester are as follows,

Table 1: Neutral Surge arrester Specifications

Rated Voltage	6 kVrms
Continuous Operating Voltage	4.8 kVrms
Lightning Impulse Residual voltage under nominal discharge current	≤18 kVp
Creepage Distance	240mm
2ms square wave Impulse Current Withstand	250A
4/10μs high current Impulse Withstand	100kA

Most of the pole mount distribution transformers are from the same manufacturer, and they are the Swaziland

Electricity Company's stock item. Therefore, the connection shown below is based on the design of these transformers,

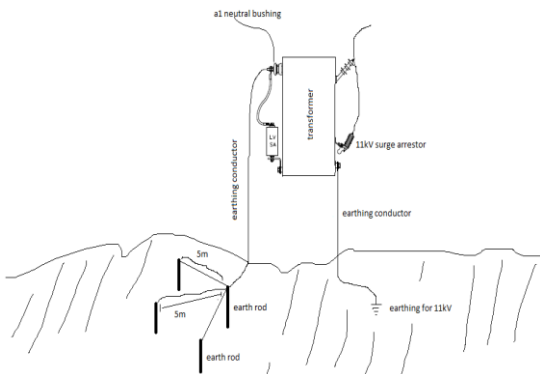


Figure 3: Connection and earthing of neutral arrester

The crowfoot method of earthing was used to ensure low earthing values for effective surge arrester operation. Other material required: 35 square millimetre lugs, earth spike clamps, earth rod and gopher conductor.

A contractor was engaged for the practical installation of the neutral surge arresters. The performance of this system was then monitored for effectiveness.

3. RESULTS AND ANALYSIS

The visual inspections revealed that there was a pattern in the failure of the transformers. The LV neutral winding/insulator was damaged in most instances. It failed together with another winding/bushing either on the secondary or primary side. Pole mounted distribution transformers are often damaged by surge currents which enter through the unprotected secondary (LV windings) side [9]. The current surges on the LV side are non-destructive, but may induce destructive over-voltages on the primary side [9]. The 16kVA transformers have the secondary windings thinner in cross sectional area than the primary windings due to the high LV currents.

It can therefore be said that the use of primary arresters on their own does not protect the transformer from lightning surges, as they can enter through the secondary windings and then be induced into the primary windings. Lightning may enter the transformer LV through direct strikes [9], or through a primary strike which has some surge diverted to the neutral of the secondary which is connected to ground.

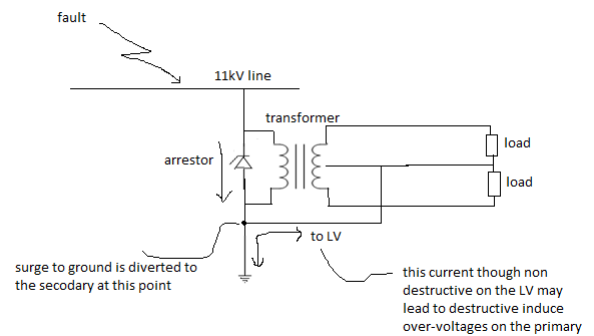


Figure 4: Neutral without a surge arrester

When earthing resistance values are varied from 5Ω to 15Ω and a fault applied on the LV side, the voltage and current across the neutral surge arrester increases with increasing earthing resistance. The distortion of the current and voltage waveforms worsens with increasing earthing resistance values.

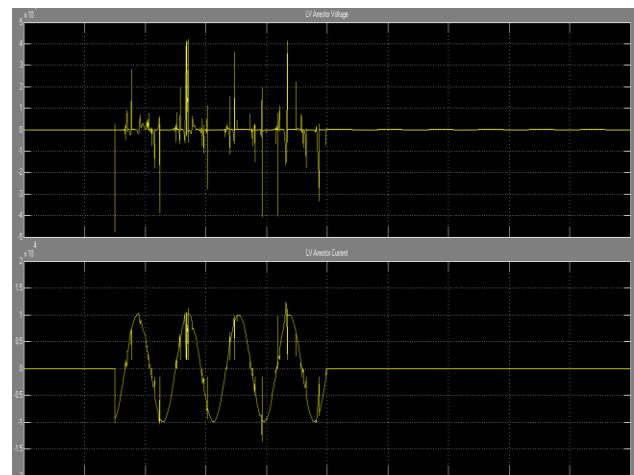


Figure 5: Current and voltage waveforms with 5Ω earthing resistance

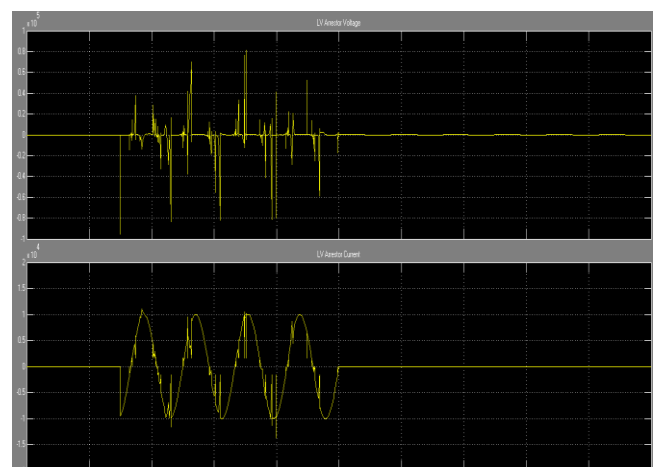


Figure 6: Current and voltage waveforms with 10Ω earthing resistance

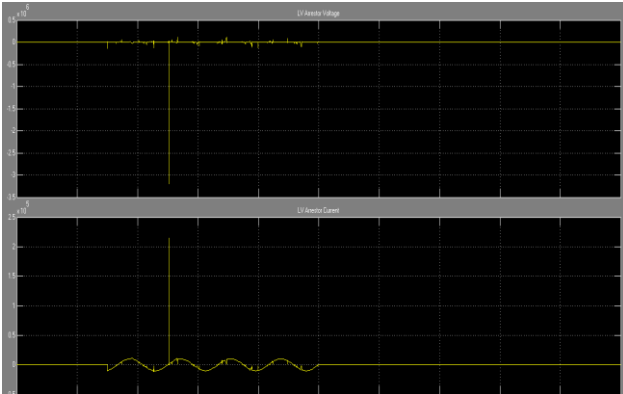


Figure 7: Current and voltage waveforms with 15Ω earthing resistance

Earthing values of above 10Ω are very detrimental to pole mount distribution transformers. So whether the surge is on the primary or secondary side, with high earthing values, the surge arrestors are likely to be damaged leaving the transformer vulnerable to strikes.

When lightning strikes are simulated on the secondary of the transformer, the primary surge arrester also operates when a 10kA fault is applied. The current surges on the LV side are non-destructive, but may induce destructive over-voltages on the primary side [9].

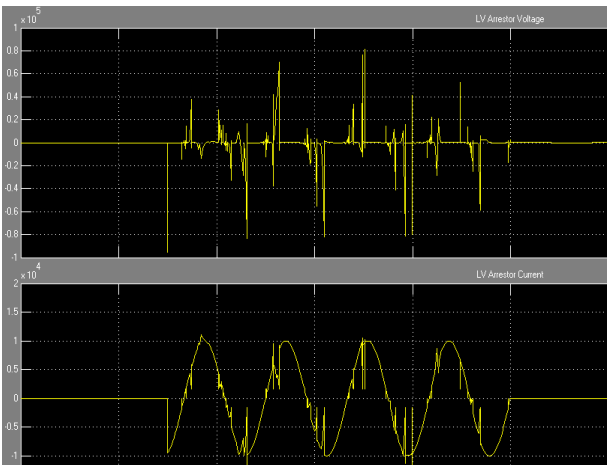


Figure 8: Neutral surge arrester response to LV surge



Figure: Primary side arrester response to LV surge

Without the neutral surge arrester, all the LV surges appear on the primary side and appear as very high over-voltages, as evident in the conduction of the primary surge arrester.

The field data of monitoring the effects of practically installing neutral surge arrestors to pole mount distribution transformers is ongoing and will be concluded soon.

4. CONCLUSION

The collected data shows that the failure of a number of pole mount distribution transformers is due to lightning strikes during the summer months. A sample is shown in the table below,

Table 2: Lightning activity and transformer failures

DATE	WEATHER	FAILED TRANSFORMERS
22 Nov 2013	Thunderstorm, windy	9x16kVA, 1x50kVA, 1x100 kVA
24 Nov 2013	Thunderstorm	3x16 kVA
26 Nov 2013	Thunderstorm	1x16 kVA, 1x100 kVA
30 Nov 2013	Lightning, windy, hailstones	9x16 kVA, 1x50 kVA, 1x100 kVA
3 Dec 2013	Thunderstorm	3x16kVA
5 Dec 2013	Thunderstorm	2x16 kVA, 2x50 kVA

A relationship was also found between lightning activity and transformer failures as most failures were discovered after there had been a thunderstorm.

It has also been shown that primary surge arrestors alone are not sufficient in the protection against lightning strikes.

Surges entering through the LV neutral can cause detrimental effects in transformers. Surges on the LV can enter directly through LV strikes or through primary surges diverted to the secondary, which then appear on the primary as over-voltages. These over-voltages can damage windings and/or the bushings.

The installation of neutral surge arrestors throughout the entire SEC network will help a great deal in reducing lightning related failures, especially as a result of LV surges.

The hypothesis therefore holds in that whenever a pole mount distribution transformer is exposed to lightning, the likely point of failure is the windings or bushings.

5. REFERENCES

[1] Lunsford, J.M., "Overcurrent protection of pole top distribution transformers that have tank mounted lightning arresters," *Transmission and Distribution Conference, 1996. Proceedings., 1996 IEEE*, vol., no., pp.586,590, 15-20 Sep 1996

[2] Hongzhi, D.; Heywood, R.; Lapworth, J.; Ryder, S., "Why transformers fail." *Euro TechCon*, 2009

[3] Sabiha, Nehmdoh A.; Lehtonen, M., "Lightning-Induced Overvoltages Transmitted Over Distribution Transformer With MV Spark-Gap Operation—Part II: Mitigation Using LV Surge Arrester," *Power Delivery, IEEE Transactions on*, vol.25, no.4, pp.2565,2573, Oct. 2010

[4] Molinski, T.S., "Why utilities respect geomagnetically induced currents," *Journal of atmospheric and solar terrestrial physics*, 2002

[5] Matondo, J. I., and K.M. Msibi. "Estimation of the impact of climate change on hydrology and water resources in Swaziland." *Water international* 26, no. 3 (2001): 425-434.

[6] Stringfellow, M.F.; Met, F.R., "Overhead distribution lines and surge arrestors for severe lightning areas," *South African Institute of Electrical Engineers*, Lightning performance of overhead lines, 1982

[7] Mswane, L. M., and C. T. Gaunt. "Lightning performance improvement of the Swaziland electricity board transmission system (66kV & 132kV lines)-results of the pilot project." In *Power Engineering Society Inaugural Conference and Exposition in Africa, 2005 IEEE*, pp. 364-370. IEEE, 2005.

[8] Monadjem, Ara. "Geographic distribution patterns of small mammals in Swaziland in relation to abiotic factors and human land-use activity." *Biodiversity & Conservation* 8, no. 2 (1999): 223-237.

[9] Goedde, G.L.; Kershaw, S.S.; Schettler, R.N., "Low Voltage, High Energy Arrester for Secondary Applications," *US Patent* 5, 220,480, 1993-Google patents.

WIDE BAND ANALYTICAL INDUCTANCE CALCULATIONS FOR LARGE POWER TRANSFORMERS USING WILCOX'S APPROACH

B.J van Jaarsveld

*Dept. of Electrical Engineering Technology, Faculty of Engineering and the Built Environment, Johannesburg University, PO Box 17011, Doornfontein 2028 Johannesburg, South Africa
E-mail: barendvj@gmail.com*

Abstract: This paper presents the application of an analytical inductance calculation method applied to a large power transformer winding. This type of inductance parameter calculation is exceptionally useful in the electromagnetic modelling used for the wide-band frequency studies. The methodology reviewed in this paper is applied to calculate the self-inductance of the secondary winding of a large power transformer. The results of the analytical calculation are compared to the results obtained using finite element modelling methods. The difference between the two values are approximately 2%. This preliminary finding seems to indicate that the analytical methodology is suitable for the context of the application. Future work requires the validation of the methodology over a wider frequency range and different geometries.

Keywords: Inductance, Electromagnetic modeling, Electromagnetic coupling

1. INTRODUCTION

The electromagnetic modelling of power transformers for high frequency studies has been a field of interest for more than a century. Abnormal power network conditions and exposure to lightning events spurred the curiosity of many authors to analyse the behaviour of a power transformer when excited with surges having a high frequency content [1] [2] [3].

The most common approach in these investigations is to model the transformer's winding structure using a circuit equivalent model of either lumped- or distributed form. In this manner, the transformer can be represented with a RLCG network [2] [3] [4] [5] [6]. The characteristic equations of the model parameters with reference to their response to current and voltage are then used to set up a mathematical model that could be formulated in a suitable form such as a state space or modal representation [7] [8].

The parameters pertaining to these models naturally represent the inductive, capacitive and lossy nature of the transformer windings. When a winding is excited at very high frequencies such as those found in steep fronted voltage waves, it has a trait similar to that of a capacitor [9]. However, the high frequency inductive behaviour of the transformer windings has remained a controversial topic in many studies [10] [11].

In essence the matter in question is the degree to which the magnetic flux is able to penetrate the iron core surface during high frequency excitation. The premise in many studies is that eddy currents are set up on the core surface which inhibits the flux penetration [10] [12] [13] [14].

Based on this line of reasoning, the self- and mutual-inductances of the windings are calculated often assuming an air core [2] [10] [13]. In many of these calculations, Maxwell's inductance formula, or a modified derivative thereof, is used [15] [16]. However, the use of an air-core model are challenged in studies where the effect of the presence of the iron core is evident up till 1 MHz [17].

Another reason for using an air core model is the fact that these models are usually used for simulating the transformer's response during standard factory acceptance testing. During these tests, the non-impulsed terminals are grounded [18] causing flux cancellation in the core. This configuration is not representative of the transformers terminal conditions during network operation and would render a model based on this assumption ill-suited for network studies.

It is therefore necessary to take into account the effect of the iron core when calculating the inductive parameters of the electromagnetic model. This paper reviews an analytical calculation method to determine the inductance parameters suitable for wide-band modelling of a power transformer's windings with the iron-core taken into consideration.

2. THEORY OF INDUCTANCE

The inductance of a winding is governed by the distribution of magnetic flux in the region enclosed by the winding. A current flowing along a closed contour produces a magnetic flux \bar{B}_1 in the enclosed surface a as presented in Figure 1 [19]. The self-inductance L_{11} of the contour having N_1 turns is defined by the relation:

$$L_{11} = \frac{N_1}{I_1} \int da \cdot \bar{B}_1. \quad (1)$$

The magnetic field can also be influenced by nearby ferromagnetic material. If a ferromagnetic material is placed in the magnetic field enclosed by the current contours, the magnetic domains of the material will line up with the magnetic field. This causes the magnetic material to act as an induced magnetic source further enhancing the magnetic field. Hence the presence of the magnetic material will cause the inductance of the circuit to increase since the total magnetic flux in the enclosed region increases. It is therefore critical to evaluate the magnetic flux behaviour in and around the winding-block of a power transformer when determining the inductance parameters.

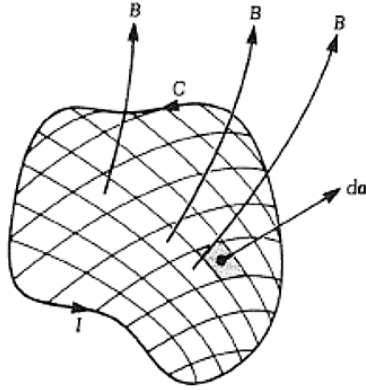


Figure 1: Flux enclosed by a current carrying contour

What is of particular interest is the relation between the magnetic field density \vec{B} and the magnetic field strength \vec{H} . This is quantitatively defined by the relative permeability μ_r of the core material. However, this relationship is highly non-linear. The permeability is affected by the rate of change of the magnetic field as well as its magnitude. In addition to this, the stacking factor, conductivity and laminated nature of the core also determines the relationship between the magnetic field density and the magnetic field strength.

It is not the purpose of this paper to discuss this particular parameter in depth. It is however very important to take note of this very matter. The reason for this is that there is a very thin line where the model parameter and the model synthesis start address the same observed phenomena. As an example of this; it is possible to assume that the permeability of the material is an absolute constant. The effect of the conductivity of the material on the relationship between the magnetic field strength and density could then be added in the model. Alternatively, the model could be developed assuming that the permeability is an input variable. It is clear that this could be a pitfall if validation is done by comparing various models with each other.

The following section will review a modelling method proposed by Wilcox [20] [21]. In this very approach, the relative permeability of the core as well as its conductivity is regarded as variable inputs that is predetermined at the desired excitation frequency, magnitude and core characteristics.

3. A REVIEW OF WILCOX'S METHOD

In the work done by Wilcox et al, the total impedance between two current carrying sections as shown in Figure 2 consists of the impedance due to the air-core inductance L_0 and the complex impedance Z_c as presented in the following relation:

$$Z = j\omega L_0 + Z_c. \quad (1)$$

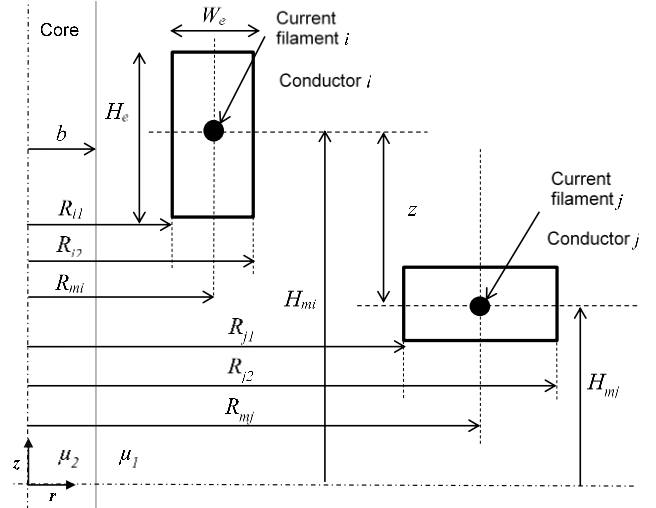


Figure 2: Current filament approximation of winding conductors

The real part of the complex impedance represents the resistance between the conductors, while the imaginary part represents the reactive impedance between them. This reactive impedance is for all practical purposes purely inductive. Since the focus of this paper is on the inductive behaviour of the windings, the resistive component will be ignored and thus equation (1) can be rewritten as:

$$X = j\omega(L_0 + L_c). \quad (2)$$

3.1 Air-core inductance

The air-core inductance term L_0 in equation (2) represents the inductance of the current carrying turn without the presence of the iron core. The self-inductance of each current carrying turn in a winding can be calculated using the traditional Maxwell equation [22]:

$$L = 4e^{-7}\pi R_m \left(\log \left(\frac{8R_m}{GMD} \right) - 1.75 \right). \quad (3)$$

where R_m is the radius of the centre of the conductor. Since the winding conductors in power transformers are often rectangular, the geometrical mean distance (GMD) of each conductor can be approximated by [23]:

$$GMD = 0.2235(H_e + W_e). \quad (4)$$

With K and E representing the elliptic integrals of the first and second kind respectively of modulus k , the mutual inductance between the conductors can be calculated using the following expression [24]:

$$M_{ij} = 4e^{-7}\pi\sqrt{R_{mi}R_{mj}} \left[\left(\frac{2}{k} - k \right) K - \frac{2}{k} E \right] \quad (5)$$

where

$$k^2 = \frac{4(R_{mi}R_{mj})}{((R_{mi}+R_{mj})^2 + z^2)}. \quad (6)$$

3.2 Iron-core contribution

In Figure 2, the relative permeability of the core and the surrounding medium are μ_2 and μ_1 respectively. In the context of the application, the surrounding medium will always have a relative permeability of 1. It should also be noted that the permeability of the core is isotropic and has thus two components in the Cartesian plane namely in the axial direction, μ_{2z} and in the radial direction μ_{2r} . For the sake of simplicity of this study, it is assumed that $\mu_{2z} = \mu_{2r}$. Hence the permeability of the core will simply be μ_2 . The correction term in equation (2) can be defined as:

$$Z_c = Z_{c1} + Z_{c2}. \quad (7)$$

Defining I_0 and I_1 as the modified zeroth and first order Bessel functions respectively of the first kind, Z_{c1} is expressed as:

$$Z_{c1} = j\omega N_i N_j \frac{\pi b^2}{l} \left[\frac{2\mu_2 I_1(mb)}{mb I_0(mb)} - \mu_1 \right] \quad (8)$$

where

$$m = \sqrt{j\omega\mu_2\sigma_2}. \quad (9)$$

with l as the mean magnetic path length of a core as seen in Figure 3 having a conductivity of σ and a radius of b . The second term of equation (7) is a summative operation with β_n as a transformation parameter defined as:

$$\beta_n = \frac{2\pi n}{l}. \quad (10)$$

With K_1 as the modified first order Bessel function of the second kind, Z_{c2} is expressed as:

$$Z_{c2} = j\omega N_i N_j \frac{\pi}{l} \cdot \frac{4}{W_{ei} W_{ej} H_{ei} H_{ej}} \cdot \sum_{n=1}^N \left(P_1(\beta_n R_{i1}, \beta_n R_{i2}) \cdot P_1(\beta_n R_{j1}, \beta_n R_{j2}) \cdot Q_1(\beta_n W_i, \beta_n W_j) \cdot \frac{I_1(\beta_n b) \cdot F_1(\beta_n b)}{K_1(\beta_n b)} \cdot \cos(\beta_n z) \right) \quad (11)$$

where

$$P_1(x, y) = \frac{1}{\beta_n^2} [p_1(x) - p_1(y)] \quad (12)$$

with

$$p_1(\alpha) = \frac{\pi\alpha}{2} [K_1(\alpha)L_0(\alpha) - L_1(\alpha)K_0(\alpha)] \quad (8)$$

in which L_0 and L_1 represent the modified Struve functions. The function $F_1(\beta_n b)$ is defined by the following expression:

$$F(\beta_n b) = j\omega\mu_1 \left[\frac{f(\beta_n b) - \frac{\mu_1}{\mu_2} f(\Gamma_n b)}{g(\beta_n b) + \frac{\mu_1}{\mu_2} f(\Gamma_n b)} \right], \quad (9)$$

where f and g are the auxiliary functions:

$$f(x) = x \left[\frac{I_0(x)}{I_1(x)} \right] \quad (10)$$

and

$$g(x) = x \left[\frac{K_0(x)}{K_1(x)} \right], \quad (11)$$

where K_0 is the modified zero order Bessel function of the second kind. The complex quantity Γ_n is specified as:

$$\Gamma_n = \sqrt{c\beta_n^2 + m^2}, \quad (12)$$

where c is the ratio of the core permeability in the z and r direction with reference to Figure 1 and specified as:

$$c = \frac{\mu_{2z}}{\mu_{2r}}. \quad (13)$$

As mentioned earlier, $\mu_{2z} = \mu_{2r}$ and thus $c = 1$. The function Q_1 is defined as:

$$Q_1(x, y) = \frac{2}{\beta_n^2} \left[\cos\left(\frac{x-y}{2}\right) - \cos\left(\frac{x+y}{2}\right) \right] \quad (19)$$

The relations above can be used to correct both self- and mutual-inductance. For self-inductance, z is set to 0. Since for self-inductance $R_{mi} = R_{mj}$, R_{mi} is set to $R_{mi} = R_{mi} - GMD$ to ensure that $R_{mi} < R_{mj}$. The imaginary part of Z_c is used to obtain the inductance L_c that should be added to the air-core inductance L_0 . Thus,

$$L_c = \text{imag}(Z_c)/(\omega). \quad (20)$$

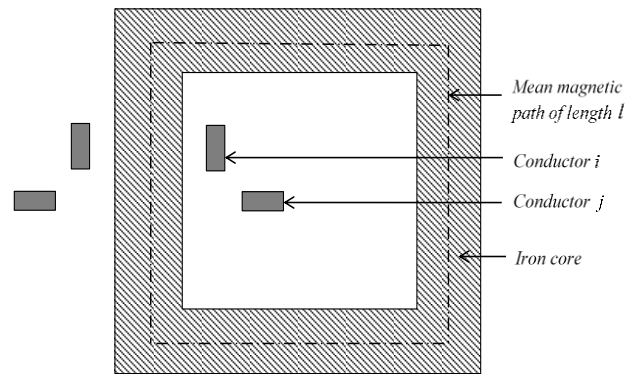


Figure 3: Mean magnetic path of a closed iron-core

4. APPLICATION AND RESULTS

In this study, this methodology was applied to determine the self-inductance of the low-voltage winding of a three-limb, three phase power transformer as illustrated in Figure 4. The secondary windings are fitted closest to the core and connected in delta.

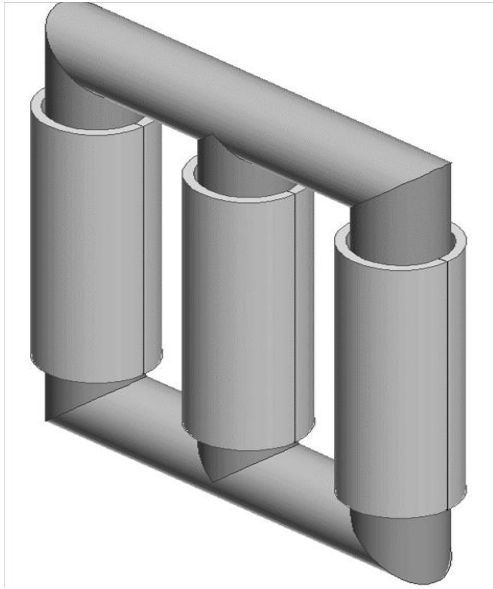


Figure 4: Secondary windings on a three-limb three phase power transformer

4.1 Transformer core and LV winding description

The secondary low voltage windings are disk-type windings with 504 turns. The winding dimensions are presented in Table 1. The core was manufactured from electrical steel of grade 30H105. The geometric detail with reference to Figure 5 is presented in Table 2.

Table 1: Winding dimensions (mm)

Winding height	1637
Number of disks	126
Turns per disk	4
Inner diameter	456
Outer diameter	550
Conductor width	11,1
Conductor height	10,4
Spacer thickness	2

Table 2: Core dimensions (mm)

Limb height	1830
Limb pitch	893
Diameter (D)	420

4.2 FEM simulation

The geometry was created in ANSYS MAXWELL. A transient solver was used in conjunction with an external circuit. Each winding was specified to have 504 turns with an external excitation. The material type selected for the windings was pure copper with default values in the material library. The core material however had to be user defined. From the material specifications of the grain orientated core steel supplier, the BH curve values were entered.

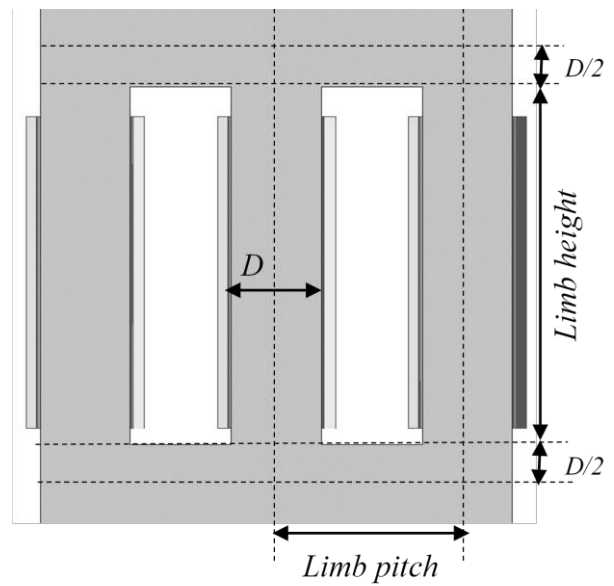


Figure 5: Secondary windings on a three-limb three phase power transformer

The relative permeability in the linear region of the BH curve was approximately 51000. The conductivity of the core steel was set to 204 S/m. The 50 Hz excitation voltage on the windings was set to be 1000 volts with a 120° phase shift between each windings terminal voltages. The calculated self-inductance of the LV winding on the centre limb was 246 Henries.

4.3 Analytical model simulation

The relations presented in section 3 was implemented in MATLAB where the readily available native “BESSELI” and “BESSELK” functions were used with ease. The mean magnetic core length with reference to the centre limb is approximately 4.4 meters. Relation (7) was applied for each turn of the LV winding resulting in a 504 by 504 inductance matrix as shown in Figure 6. To get the self-inductance of the winding, all the matrix elements must be added together yielding 236 Henries.

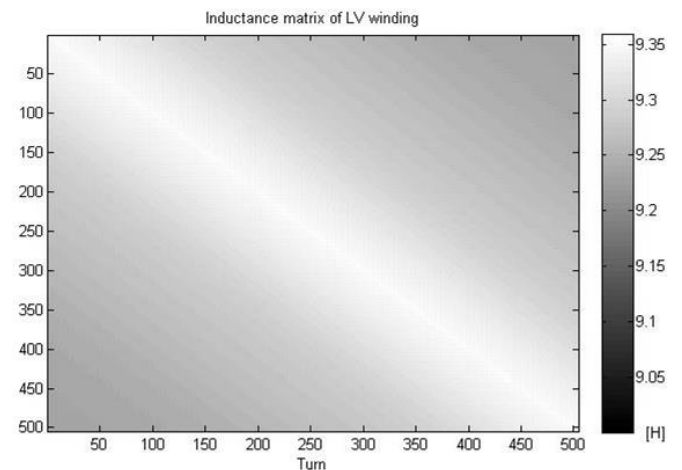


Figure 6: Inductance matrix of LV winding using WILCOX’s model

5. CONCLUSIONS

This paper presents the application of WILCOX's analytical model to calculate the inductance of a LV transformer disk winding fitted to a three-limb three phase core made from highly permeable grain-orientated steel. The geometry was also created in ANSYS MAXWELL and the calculated self-inductances of the LV winding on the centre limb were compared. The difference between the two values are approximately 2%. Hence, the values obtained using both methods agrees well.

Future work could entail a sensitivity study to determine which parameters of the analytical model plays the dominant role. In addition to this, the suitability of the model still needs to be evaluated over a wide range of frequencies and geometries.

6. REFERENCES

- [1] J. M. Weed, "Abnormal voltages in transformers," *AIEE Trans. Power App. Syst.*, vol. 34, no. 2, pp. 2197 - 2236, 1915.
- [2] L. F. Blume and A. Boyajian, "Abnormal voltages within transformers," *AIEE Trans. Power App. Syst.*, vol. 38, no. 1, pp. 577 - 620, January 1919.
- [3] B. Heller and A. Veverka, *Surge phenomena in electrical machines*, J. S. Vosper, Ed. London: Iliffe, 1968.
- [4] M. D. Loose, "Lumped parameter based transformer analysis: Modeling, reduction, time and frequency domain solutions," Rensselaer Polytechnic Institute, New York, Ph.D dissertation 2003.
- [5] B. J. van Jaarsveld, "Wide band modelling of an air-core power transformer winding," Department of Electrical and Electronic Engineering, Stellenbosch University, Stellenbosch, M.Sc Thesis 2013.
- [6] B. J. van Jaarsveld and H. J. Vermeulen, "Implementation and evaluation in MATLAB of Dommel's method for a lumped parameter model of a power transformer," in *South African Universities Power Engineering Conference*, Cape Town, 2011.
- [7] P. I. Fergestad, "Transient oscillations in transformer windings," Ph.D dissertation 1972.
- [8] H. W. Dommel, "Digital computer solution of electromagnetic transients in single and multi phase networks," *IEEE Trans. Power App. Syst.*, vol. 88, no. 4, pp. 388 - 399, April 1969.
- [9] F. F. Brand and K. K. Palueff, "Lightning studies of transformers by the cathode ray oscillograph," *AIEE Trans. Power App. Syst.*, vol. 48, no. 3, pp. 998 - 1008, July 1929.
- [10] R. Rudenburg, "Performance of traveling waves in coils and windings," *AIEE Trans. Power App. Syst.*, vol. 59, no. 12, pp. 1031-1040, 1940.
- [11] P. A. Abetti and F. J. Maginniss, "Natural frequencies of coils and windings determined by equivalent circuit," *AIEE Trans. Power App. Syst.*, vol. 72, no. 2, pp. 495 - 504, January 1953.
- [12] X. M. Lopez-Fernandez, C. Alvarez-Marino, D. Couto, R. Lopes, and A. Jacomo-Ramos, "Modeling and insulation design methodology in power transformer under fast transients," in *16th International Conference on Electrical Machines*, 2010, pp. 1-6.
- [13] G. Hoogendorp, M. Popov, and L. van der Sluis, "Computation of inter-turn voltages in transformer windings with interconnected distribution cable," in *International Conference Power System Transients*, Delft, 2011.
- [14] Y. Shibuya, S. Fujita, and N. Hosokawa, "Analysis of very fast transient overvoltages in transformer winding," in *IEE Proceedings on Generation, Transmission and Distribution*, vol. 144, September 1997, pp. 461 - 468.
- [15] W. Grover, *Inductance calculations*. New York, United States of America: D. Van Nostrand Co., 1946.
- [16] F. W. Grover, "The calculation of the inductance of single-layer coils and spirals wound with wire of large cross section," *Proceedings of the Institute of Radio Engineers*, vol. 17, no. 11, pp. 2053 - 2063, 1929.
- [17] S. D. Mitchell and J. S. Welsh, "Permeability and its influence on the broadband frequency response of a power transformer," in *Asia-Pacific Power and Energy Engineering Conference*, 2009.
- [18] "Power Transformers - Part 3: Insulation levels, dielectric tests and external clearances in air," IEC, 60076-3, 2000.
- [19] L. C. Shen and J. A. Kong, *Applied electromagnetism*, 3rd ed.: PWS Publishing Company, 1995.
- [20] D. J. Wilcox, W. G. Hurley, and M. Conlon, "Calculation of self and mutual impedances between sections of transformer windings," in *IEE Proceedings*, vol. 136.
- [21] D. J. Wilcox, M. Conlon, and W. G. Hurley, "Calculation of self and mutual impedances for coils on ferromagnetic cores," in *IEE*, vol. 135, 1988, pp. 470 - 476.
- [22] T. R. Lyle, "On the self-inductance of circular coils of rectangular section," *Philosophical Transactions of the Royal Society of London*, vol. 213, pp. 421 - 435, 1914.
- [23] E. B. Rosa, *The self and mutual inductances of linear conductors*, Bulletin of the Bureau of Standards, Ed.: U.S. Dept. of Commerce and Labor, Bureau of Standards, September 1907, vol. 4.
- [24] C. Snow, *Formulas for computing capacitance and inductance*, 544th ed. Washington, United States of America: National Bureau of Standards , 1954.

APPLICATION OF KEY FAULT GASES AND OIL TESTING FOR EVALUATION OF TRANSFORMER CONDITION AND ITS MAINTENANCE REQUIREMENT

G. K. Irungu*, A. O. Akumu**, J. L. Munda*** and B. Lubisi****

Faculty of Engineering and the Built Environment, Department. of Electrical Engineering, Tshwane University of Technology, Private Bag X680, Pretoria 0001, Republic of South Africa

* kimaniirungu@yahoo.com

** akumuao@tut.ac.za

*** mundaji@tut.ac.za

**** *Department of Asset Management, ESKOM, P.O Box 2199, Witbank 1035, Republic of South Africa , E-mail: lubisitb@eskom.co.za*

Abstract: Critical power transformers require special attention because of the role they play in power system reliability. The generator step-up (GSU), transmission line and high voltage direct current converter (HVDC) transformers must be monitored closely. Various monitoring tools like dissolved gas, partial discharge and temperature monitors have been deployed over the years with the aim of getting data for fault diagnostics. This paper uses key gases dissolved in oil generated by electrical and thermal faults plus some oil characteristics to evaluate the transformer health status. In the analysis, the dissolved gases and oil testing parameters are first normalized and then transformed into fuzzy membership functions. This information is then transformed into a multiple-attribute decision making (MADM) problem which can be applied in transformer condition evaluation for maintenance planning. Finally, this MADM is synthesized to transformer condition assessment under an evidential reasoning (ER) framework. A case study is evaluated using actual field data to verify the methodology.

Key words: Basic Belief Assignment (BBA), Dissolved Gas Analysis (DGA), Dielectric Strength (DS), Evidential Reasoning, Power Transformer, Reliability.

1 INTRODUCTION

The operation of key strategic power transformers is a factor of major technical and economic significance in utilities. In the present economic scenarios, industries and electric power supply utilities are tightening their spending and making cutbacks in maintenance budgets. Greater emphasis is placed on the reliability, availability and optimization of the existing equipment [1]. Consequently, the loading is increased on current units, as this will defer purchasing additional plant capacity. This leads to the increase of transformer operating stresses. These stresses are; electrical, mechanical, thermal and chemical [2]. The electrical stresses arise from the applied normal operating voltage, lightning and switching surges, fault transients and ferro-resonance voltages. On the part of mechanical stresses, the transformer may experience such problems from short circuit within the transformer itself, heavy through fault or an earthquake. These abnormalities can disturb the windings and core configurations. This may lead to change in capacitance, inductance and resistance of the active part of the transformer [3].

Another key stress a transformer is exposed to is the thermal arising from the operating temperature rise due to the core hysteresis and eddy current losses plus the winding ohmic losses. The last stress is chemical in nature emanating from the combined effect of electrical and thermal stresses acting individually or collectively.

All these stresses leads to insulation degradation occasioned by partial discharge, sludge formation, increase in oil acidity, formation of gases in oil, reduction in insulation dielectric strength and finally transformer failure [4]. The data gathered from monitoring these stresses can be applied to assess the transformer health status.

Section two looks at the fault analysis using dissolved gases in transformer oil and other byproducts of chemical decomposition of oil-paper insulation system. Part three highlights the assessing hypothesis development and evaluation methodology. Part four deals with the normalisation and fuzzification of field data. The last two portions entail the actual evaluation and conclusion.

2 FAULTS DETECTABLE BY DGA

Many faults occurring in a power transformer can be detected by dissolved gases in oil. This has been nicknamed the transformer 'blood test', in comparison to human blood test. It is the most sensitive and reliable technique used for evaluating the health status of oil filled electrical equipment. The chemical decomposition of transformer oil-paper insulation whenever subjected to electrical and or thermal stresses generates some chemical byproducts. Notable among these are the gases which if generated by incipient faults dissolve in oil.

The dissolved gas magnitude, type and rate of generation have been used for many years to diagnose the type and

3 TRANSFORMER ASSESSING GRADE TECHNIQUE

severity of faults [5]. The main gases generated as results of the oil-paper decomposition are; hydrogen, methane, ethane, ethylene, acetylene, carbon monoxide and carbon dioxide [1], [5]-[9].

Many numerical tools are available for classifying and analyzing faults using dissolved gases [5]-[12]. These tools fall into two broad categories. The first is the key gas method which looks at the amount and type of gases present to deduce the fault. The second is the ratio-based tool which include but not limited to; Duval triangle, Rogers ratio and Doernenburg ratio. The key gas method relates key gases to different faults mainly identified as follows;

- Oxygen and nitrogen: non-fault gases.
- Hydrogen and methane: caused by corona or partial discharge. These are low energy electrical discharge faults.
- Carbon monoxide and carbon dioxide: produced by overheating of cellulose solid insulation.
- Ethane and ethylene: caused by overheating of oil.
- Acetylene and hydrogen: due to arcing, that is high energy electrical discharge fault.

Since the key gas method does not give numerical correlations between fault types and gas types directly, the diagnosis depends greatly on experience. On the other hand, the gas ratio methods are coding schemes that assign certain combinations of codes to specific fault types. The codes are generated by calculating ratios of gas concentrations and comparing the ratios with predefined values, which have been derived from field experience and are modified continually. A fault condition is detected when a gas combination fits the code pattern of a particular fault [5]-[12]. The ratios used are;

$$\frac{CH_4}{H_2}, \frac{C_2H_2}{C_2H_4}, \frac{C_2H_2}{CH_4}, \frac{C_2H_6}{C_2H_2}, \frac{C_2H_4}{C_2H_6}.$$

One key point to remember when using ratio-based diagnostic tools is that minimum gas levels are required and are generally defined in the IEEE C57.104, 2009. The separation, identification and quantification of the dissolved gases require the use of sophisticated laboratory equipment and technical skills and therefore can only be conducted by a suitably equipped and competent laboratory. Currently, there are several dissolved gas extraction techniques; these are [11];

- Gas chromatography
- Hydrogen on-line monitoring
- Photo-acoustic spectroscopy
- Infrared spectroscopy
- Array type gas sensor method

Other than the dissolved gases in oil, oil testing can also be done to detect the presence of other chemical byproducts of oil-paper insulation degradation. This entails checking the oil colour, acidity, dielectric strength, dielectric loss, interfacial tension, specific gravity, moisture content, furanoids, oil quality index etc. This has been done over the years and is well documented in literature [1], [13]-[15]. Both the dissolved gases and oil test parameters can be used to estimate the oil-paper insulation life and thus ascertain transformer health status.

The transformer condition assessment is evaluated using indices from three factors; thermal fault gases, electrical fault gases and oil test parameters. This is illustrated pictorially by Fig. 1.

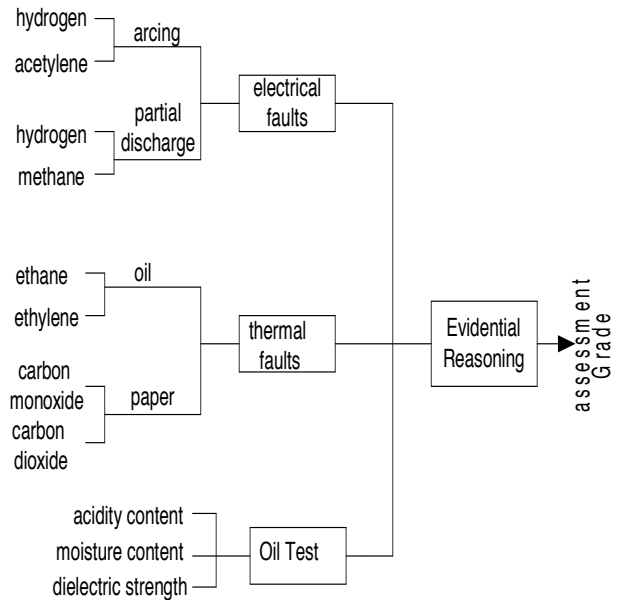


Fig.1 Transformer condition assessment tree model

This is a two-level model structure which can be viewed as a decision-making tree shown in Fig. 2. Level-one synthesizes transformer condition based on individual parameters and level-two combines the three factors assessment to an overall assessment. The model output is quantified by an assessing grade that an engineer can use to plan when maintenance is to be done.

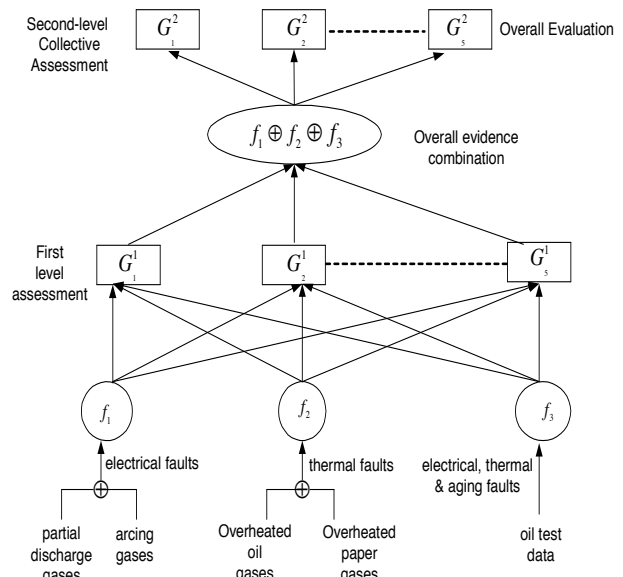


Fig. 2 Two-level model for transformer condition-based maintenance assessment

Suppose G_n ($n = 1, 2, \dots, N$) represents an assessing grade such as excellent or poor, then a set of assessing grades can be represented as;

$$G = \{G_1, G_2, \dots, G_n, \dots, G_N\} \quad (1)$$

Where N is the total number of assessing grades, in this work $N = 5$. Therefore,

$$G = \{\text{excellent}, \text{good}, \text{average}, \text{poor}, \text{critical}\} \quad (2)$$

This ideology of assessing transformer condition and subsequently its maintenance needs is summarized in table 1 and offers a logical way of planning the maintenance strategy.

Table 1. Maintenance schedule as related to assessing grades

Grade assignment	G_1	G_2	G_3	G_4	G_5
Assessing grade	excellent	good	average	poor	critical
Maintenance attention	delay	normal	prior	sooner	immediate

4 NORMALIZATION AND FUZZIFICATION OF PARAMETERS

In order to transform the dissolved gases and oil parameters into fuzzy membership functions they are normalized first. Equation (3) is used for normalizing cost parameters.

$$x_{rm} = \frac{E_{rm} - E_{rm0}}{E_{rma} - E_{rm0}}, \quad E_{rm0} \leq E_{rm} \leq E_{rma} \quad (3)$$

Where E_{rm0} is the minimum threshold parameter value below which the transformer is considered normal. The variable E_{rma} is the maximum threshold of the parameter above which the transformer is considered to be in critical state and its failure is imminent [8]. The measured parameter value is given by E_{rm} . The normalization of benefit attribute like oil dielectric strength is given by (4).

$$x_{rm} = \frac{E_{rmN} - E_{rm}}{E_{rmN} - E_{rmx}}, \quad E_{rmx} \leq E_{rm} \leq E_{rmN} \quad (4)$$

Where E_{rmN} is the new oil dielectric strength and E_{rmx} is the minimum dielectric strength below which the transformer is considered to be in critical state and it can fail any time [7]. The normalized values are then transformed into fuzzy membership functions. After fuzzifying the indices for the electrical and thermal faults, the outcome is the fuzzy assessing intermediate values expressed mathematically as;

$$M_i(G) = \sum_{m=1}^2 w_{im} P_i(G) \quad i = 1, 2, 3 \quad (5)$$

Where $P_i(G)$ is the fuzzy membership matrix, $m = 2$ gives the number of parameters in each sub-factor of electrical and thermal faults. The w_{im} is the weighting

matrix which takes into consideration the fact that each parameter has different significance level in the assessment. The weights can be subjectively or objectively derived. Numerous subjective weighting approaches are available like Delphi and analytic hierarchy process (AHP). Also several objective weighting criteria such as entropy and Ma et al are found in literature [13]. In this work the subjective approach using the analytic hierarchy process (AHP) is applied [16].

5 EVIDENTIAL REASONING: DEMPSTER-SHAFFER THEORY

This is a mathematical theory of evidential reasoning that allows one to aggregate evidence from different sources and arrives at a degree of belief that takes into account all the available evidence. The Dempster-Shafer Theory (DST) is well-known for its usefulness to express uncertain judgments of experts. It has been used widely as a realistic approach to handle problems with fuzziness and uncertainty [1], [13], [17]-[18].

Using this theory, a frame of discernment is defined as Ω and a basic hypothesis is denoted by G_n that is $G_n \subseteq \Omega$. All the hypotheses jointly make up a set $G_n = \{G_1, G_2, G_3, G_4, G_5\}$. In this research, the five assessing grades ($G_1 - G_5$) form the frame of discernment. DST makes it possible to model several single pieces of evidence within single or multi hypothesis relations as uncertain assessments of a system in which exactly one hypothesis is objectively true. Let $m(\Psi) = [0 \ 1]$ denote the basic belief assignment to the subset Ψ of Ω , which measures the extent to which the evidence supports Ψ and the total belief is one. The basic belief assignment for an empty subset of Ω is denoted as $m(\Phi)$. Then, it follows that;

$$\sum_{\Psi \subseteq \Omega} m(\Psi) = 1, \quad 0 \leq m(\Psi) \leq 1 \quad (6)$$

$$m(\Phi) = 0 \quad (7)$$

Let the quantity $m(\Omega)$ measure the portion of the total belief that remains unassigned after commitment of belief to all subsets of Ω . The core of the D-S theory of evidence is the combination rule that will be applied to aggregate the different sources of evidence. The three evidence sources are denoted as f_1 (electrical), f_2 (thermal) and f_3 (oil test). The multiple-evidence combination rule for $f_1 \oplus f_2 \oplus f_3$ is defined as;

$$m(\Psi) = \sum_{f_1 \cap f_2 \cap f_3 = \Psi} \frac{m_1(f_1)m_2(f_2)m_3(f_3)}{1-K} \quad (8)$$

Where

$$K = \sum_{f_1 \cap f_2 \cap f_3 = \Phi} m_1(f_1)m_2(f_2)m_3(f_3) \quad (9)$$

And K gives a measure of the degree of conflict among the multiple sources of evidence.

6 DETERMINATION OF WEIGHTS OF INDICES AND FACTORS

The weighting for the electrical and thermal fault gases as well as the factors was made based on expert AHP subjective judgment. The weight reflects the relative importance of each element or factor in the assessment process. The various weighting comparison matrices are as elaborated in this section.

For gases generated by overheating oil (C_2H_4 to C_2H_6);

$W_o = \begin{bmatrix} 1 & 3/4 \\ 4/3 & 1 \end{bmatrix}$ from which the normalized eigenvector gives the weight of ethylene as 0.5714 and that of ethane as 0.4286.

For gases generated by overheating of paper (CO to CO_2);

$W_p = \begin{bmatrix} 1 & 2/1 \\ 1/2 & 1 \end{bmatrix}$ from which the weights are 0.6667 and 0.3333 for carbon monoxide and carbon dioxide respectively.

For gases produced due to arcing (H_2 to C_2H_2);

$W_A = \begin{bmatrix} 1 & 1/5 \\ 5/1 & 1 \end{bmatrix}$ from which the weights are 0.1667 for hydrogen and 0.8333 for acetylene.

For gases produced due to partial discharge (H_2 to CH_4);

$W_{pd} = \begin{bmatrix} 1 & 1/2 \\ 2/1 & 1 \end{bmatrix}$ from which the weights are 0.3333 for hydrogen and 0.6667 for methane.

The oil testing parameters possess the same level of significance and they have close correlation. Therefore have equal weights.

$$w_{or} = \begin{bmatrix} 1/3 & 1/3 & 1/3 \end{bmatrix} \quad (10)$$

For the three factors electrical, thermal and oil test, the comparison matrix is;

$$W_{ETO} = \begin{bmatrix} 1 & 1/1 & 2/1 \\ 1/1 & 1 & 2/1 \\ 1/2 & 1/2 & 1 \end{bmatrix}$$
 from which the weights are 0.4,

0.4, 0.2 for electrical, thermal and oil test respectively.

6.1 Practical Case Study

Data from two different generating station transformers was used for validation. Table 3 shows the data for those two transformers under consideration. Calculation for only T₁ 22/420 kV, 700 MVA transformer is shown here using the IEEE gas limits [7]. The oil test crucial limits for the oil parameters are as shown in table 4 [19].

Table 4. Oil Testing Limits

Oil Parameter	Normal Value	Critical Value
Acidity (mgKOH/g)	<0.01	>0.25
H_2O (mg / kg)	<5	>20
Diel. Strength (kV)	87>	75<

6.2 Evidence Evaluation & Combination

The evidence from thermal and electrical factors is computed first by aggregating the information from the faults gases associated with each of them. Thus for thermal faults in oil and paper whose evidence is given by (11), the aggregate basic belief assignments (BBAs) is given by (12). The same applies to the electrical factor whose evidence from the partial discharge and arcing fault gases is given by (13) and its BBAs by (14).

$$M_{op}(G) = \begin{bmatrix} G_1 & G_2 & G_3 & G_4 & G_5 \\ 0.3886 & 0.1828 & 0 & 0 & 0.4286 \\ 0.6667 & 0.3333 & 0 & 0 & 0 \end{bmatrix} \quad (11)$$

$$M_T(G) = \begin{bmatrix} G_1 & G_2 & G_3 & G_4 & G_5 \\ 0.8097 & 0.1903 & 0 & 0 & 0 \end{bmatrix} \quad (12)$$

$$M_{pda}(G) = \begin{bmatrix} G_1 & G_2 & G_3 & G_4 & G_5 \\ 1 & 0 & 0 & 0 & 0 \\ 1 & 0 & 0 & 0 & 0 \end{bmatrix} \quad (13)$$

$$M_E(G) = \begin{bmatrix} G_1 & G_2 & G_3 & G_4 & G_5 \\ 1 & 0 & 0 & 0 & 0 \end{bmatrix} \quad (14)$$

The BBAs for the oil test is given by (15).

$$M_{or}(G) = \begin{bmatrix} G_1 & G_2 & G_3 & G_4 & G_5 \\ 1 & 0 & 0 & 0 & 0 \end{bmatrix} \quad (15)$$

Table 3. Transformer in Service DGA and Oil Testing data

Tx.	Fault gases dissolved in oil in ppm							Oil Test Parameters		
	H_2	CH_4	C_2H_6	C_2H_4	C_2H_2	CO	CO_2	Acidity (mgKOH/g)	H_2O (mg / kg)	Diel. Strength (kV)
T ₁	23	159	154	74	0	435	4319	0.01	4	92
T ₂	34	22	6	11	0	519	1787	0.05	18	78

Having computed the BBAs for each factor, the next step is calculation of the overall evidence combination. Due to measurements errors arising from imperfect sensors and other associated equipment; a degree of belief coefficient $\beta_r = 0.90$ (based on 90% confidence level) is introduced to calculate the final BBAs before evidence combination. Because the thermal and electrical factors are the key factors, we first normalize the factor weights. This new factor weight is given by (16).

$$\bar{w}_i = [1 \quad 1 \quad 0.5] \quad (16)$$

The final factor weights after introducing the uncertainty are as given by (17).

$$\alpha_i = \beta_r \bar{w}_i = [0.9 \quad 0.9 \quad 0.45] \quad (17)$$

The degree of unbelief assignment for thermal, electrical and oil test is 0.1, 0.1 and 0.55 respectively as given by (18).

$$m_i(\Omega) = [0.1 \quad 0.1 \quad 0.55] \quad (18)$$

The final weighted BBAs for the three factors from (12), (14), (15) and (17) are given by (19).

$$m_i(G) = \begin{bmatrix} G_1 & G_2 & G_3 & G_4 & G_5 \\ 0.7287 & 0.1713 & 0 & 0 & 0 \\ 0.9 & 0 & 0 & 0 & 0 \\ 0.45 & 0 & 0 & 0 & 0 \end{bmatrix} \quad (19)$$

The evidence combination table 5 is formed from the matrix of (18) and (19) for two factors, thermal and electrical. From table 5, the following can be calculated for $f_1 \oplus f_2$; the degree of conflict from (9);

$$K = 0.15417, \Rightarrow 1 - K = 0.84583$$

Using (13),

$$m(G_1) = 0.967925, \quad m(G_2) = 0.02025$$

$$m(G_3) = m(G_4) = m(G_5) = 0, \quad m(\Omega) = 0.011823$$

Likewise combining $f_1 \oplus f_2$ evidence with the oil test BBAs we get $f_1 \oplus f_2 \oplus f_3$ as;

$$m(G_1) = 0.98218, \quad m(G_2) = 0.0112679$$

$$m(G_3) = m(G_4) = m(G_5) = 0, \quad m(\Omega) = 0.0065498$$

Therefore, the overall transformer condition assessment can be summarised by the matrix below.

$$m(G) = \begin{bmatrix} G_1 & G_2 & G_3 & G_4 & G_5 & m(\Omega) \\ 0.9822 & 0.0113 & 0 & 0 & 0 & 0.0065 \end{bmatrix}$$

6.3 Application of Evidential Reasoning Criterion

The Dempster-Shafer evidential decision-making criterion is used to locate the assessing grade with the maximum value of basic belief assignment. This should satisfy the following three conditions.

- The located grade should have BBA greater than that of other grades by a certain amount in this work 0.001.
- The BBA for the unassigned belief should be as small possible in this work 0.1 or less.
- The located assessment grade should have greater BBA than the unassigned belief.

Applying the criterion to the above case study we have; Condition 1:

$$m(G_{N_0}) - m(G_{N_1}) > 0.001 \\ \Rightarrow m(G_1) - m(G_2) = 0.9707 > 0.001 \quad \text{satisfied}$$

Condition 2: $m(\Omega) < 0.1 \Rightarrow m(\Omega) = 0.0065 < 0.1$ satisfied

Table 5. Evidence combination table for thermal and electrical factors

		Thermal f_2						
		G_1	G_2	G_3	G_4	G_5	$m_1(\Omega)$	
Electrical f_1	G_1	0.9	0.7287	0.1713	0	0	0	0.1
	G_2	0	0	0	0	0	0	0
	G_3	0	0	0	0	0	0	0
	G_4	0	0	0	0	0	0	0
	G_5	0	0	0	0	0	0	0
	$m_2(\Omega)$	0.1	x_2	x_3	0	0	0	x_5

Condition 3: $m(G_{N0}) > m(\Omega) \Rightarrow m(G_1) > m(\Omega)$
satisfied

Therefore the transformer condition assessing grade is $m(G_1)$ excellent and from table 1, the maintenance should be delayed. If the California State University Sacramento (CSUS) [1] gas limits are used, the evidence for paper and oil (thermal factor) will be uncombinable. Likewise the BBAs for transformer T₂ 22/11 kV, 40 MVA, using IEEE gas limits are;

$$m(G_1) = 0.9920, m(G_2) = m(G_3) = 0, m(G_4) = 0.0010$$

$$m(G_5) = 0.0010, m(\Omega) = 0.0060$$

The application of DST criterion to T₂ gives the assessing grade as excellent.

7 CONCLUSIONS

Transformer condition assessment using three sources of evidence has been presented. More sources can be added if data is available. Nevertheless, the gases dissolved in oil and oil test form crucial sources of evidence pertaining to transformer health status. Their evaluation outcome in this work is in agreement with the inspection report. The report indicated that the transformer condition to be normal. If more data from different test condition could be available it can be added since the DS evidential reasoning is flexible. The case analyzed shows that the transformer T₁ condition is excellent with a degree of belief of 98.22%. This can be translated to mean that the transformer condition is excellent with a minimum probability of 98.22% and a maximum probability of 98.87%. This methodology can be applied to many units and then an engineer can rank them for maintenance purposes accordingly. Therefore, it can be concluded that evidential reasoning can be applied for condition-based maintenance assessment for a transformer of any size given its operational data.

8 REFERENCES

- [1] I. A. R. GRAY: "A Guide to Transformer oil Analysis", Transformer Chemistry Service.
- [2] W. H. TANG & Q. H. WU: *Condition Monitoring and Assessment of Power Transformers Using Computational Intelligence*, Springer-Verlag Limited. London, UK2011.
- [3] M. BAGHERI, M. S. Naderi, B. Trevor & P. Toan: "Frequency Response Analysis and Short-Circuit Impedance Measurement in Detection of Winding Deformation Within Power Transformers", *IEEE Electrical Insulation Magazine*, Vol. 29 No. 3, PP 33-40, May/June 2013.
- [4] J. B. DIGIORGIO: "Dissolved Gas Analysis of Mineral Oil Insulating Fluids", *Northern Technology and Testing*, 2014. [Available]: <http://www.nttworldwide.com>.
- [5] CIGRE Technical Brochure 248. Economics of transformer management, June 2004.
- [6] M. DUVAL & A. DEPABLO: "Interpretation of Gas-in-Oil Analysis Using New IEC Publication 60599 and IEC TC10 Data Bases", *IEEE Electrical Insulation Magazine*, Vol. 17 No. 2, pp. 31-41, March/April 2001.
- [7] C. E. Lin, J. M. Ling & C. L. Huang: "An Expert System for Transformer Fault Diagnosis Using Dissolved Gas Analysis", *IEEE Trans. on Power Delivery*, Vol. 8 No. 1, PP. 231-238, Jan. 1993.
- [8] *IEEE Guide for the Interpretation of Gases Generated in Oil-Immersed Transformers*. IEEE std. C57.104-2008. New York, USA, 2009.
- [9] *IEC Guide to the Interpretation of Dissolved and Free Gases Analysis-Mineral Oil-Impregnated Electrical Equipment in Service*. IEC60599, Geneva, Switzerland, 1999.
- [10] A. ABU-SIADA & S. ISLAM: "A New Approach to Identify Power Transformer Criticality and Asset Management Decision Based on Dissolved Gas-in-Oil Analysis", *IEEE Trans. on Dielectrics and Electrical Insulation*, Vol. 19 No.3, pp. 1007-1012. 2012.
- [11] A. SIADA, S. Islam & B. N. Abu: "A Review of Dissolved Gas Analysis Measurement and Interpretation Techniques", *IEEE Trans. on Dielectrics and Electrical Insulation*, Vol. 30 No. 3, pp. 39-49, May/June 2014.
- [12] M. DUVAL & J. DUKARM: "Improving the Reliability of Transformer Gas-in-Oil Diagnosis", *IEEE Electrical Insulation Magazine*, Vol. 121. No. 4, pp. 21-27. 2005.
- [13] R. LIAO, H. Zheng, S. Grzybowski, L. Yang, Y. Zhang, & Y. Liao: "An Integrated Decision-Making Model for Condition Assessment of Power Transformers Using Fuzzy Approach and Evidential Reasoning", *IEEE Trans. on Power Delivery*, Vol. 26 No. 2, pp.1111-1118, April 2011.
- [14] T. Cargol. "An Overview of Online Oil Monitoring Technologies", 4th Annual *Weidmann-ACT Technical Conference*. San Antonio, 2005.
- [15] Transformer: Basics, Maintenance and Diagnostics. *US Department of the Interior Bureau of Reclamation*. April, 2005.
- [16] T. L. SAATY. *The Analytic Hierarchy Process*. New York, USA: McGraw-Hill.1980
- [17] W. H. Tang, K. Spurgeon, Q. H. Wu, & Z. J. Richardson: "An Evidential Reasoning Approach to Transformer Condition Assessments", *IEEE Trans. on Power Delivery*, Vol. 19 No. 4, pp. 1696-1703, October 2004.
- [18] U. RAKOWSKY: "Fundamentals of the Dempster-Shafer Theory and its Applications to Systems Safety and Reliability Modelling", RTA (3-4) - special issue. December 2007.
- [19] T. H. DALTON; *Insulating Oil Management Training Manual*: ESKOM.

MODELLING AND EVALUATION OF SINGLE-PHASE OPTIMISA POWER TRANSFORMER

A. Coetzer and M.J. Kamper

Department of Electrical and Electronic Engineering, Stellenbosch University, Stellenbosch, South Africa

Abstract: As the cost of electricity continues to rise, electrical energy saving technologies are becoming more popular. In this paper the working principle of the energy optimisation technology developed by Power Optimisa is investigated. A novel tap-changing power transformer is used to control the varying supply voltage. The load voltage is also controlled to create a more energy-efficient load. The transformer working principles are determined and a computer model is developed to simulate the transformer's behaviour. Tests are conducted to determine the efficiency and voltage regulation versus load of a 30 kVA single phase Optimisa transformer.

Keywords: Power transformer, voltage management, transformer efficiency, voltage regulation

1. INTRODUCTION

The electricity supply to low voltage networks can range from 207 to 253 V phase to neutral. All electrical equipment must be able to function within this voltage range [1]. It is normal for electricity to be supplied at voltage levels slightly towards the higher end of the allowed voltage range (higher than 230 V). Most electrical equipment, however, will function more efficient at a slightly lower voltage, say 220 V. Voltage management technologies such as the Optimisa power transformer can be used to lower the incoming supply voltage levels to increase the energy-efficiency of loads.

The Optimisa power transformer was developed by Power Optimisa, a South African company based in Cape Town. The company specialises in supply-side energy-efficiency by using a technique referred to as voltage power optimisation [2]. The voltage can either be controlled automatically by the unit's control system or manually by the user. The single phase Optimisa unit has three different tap settings namely a 0 %, -3 % and -6 % tap setting. The incoming supply voltage can thus be lowered by either 3 % or 6 %, or kept the same with the 0% tap setting.

The exact internal working principle of the Optimisa power transformer is generally unknown. The objective, hence, of this paper is to determine the transformer's working principle by conducting various tests. From these tests and measurements a computer simulation model for the transformer is developed. The performance of the transformer and the transformer model are evaluated in terms of efficiency and voltage regulation.

2. TRANSFORMER WORKING PRINCIPLE

The Optimisa transformer working principles can be described in terms of its different tap settings. From an in depth investigation and numerous tests it was found that the Optimisa transformer with its tap settings can be represented by the simple circuit diagram shown in Figure 1. If the 0 % tap setting is selected in Figure 1, the

transformer functions as a current transformer [3]. In this case the volt drop across the primary winding in Figure 1 is almost zero due to the very low equivalent series impedance. The flux in the core in this case is also almost zero due to current transformer action. Hence the core losses in the transformer with the 0 % tap setting are for all practical purposes zero.

If either the windings of the -3 % or -6 % tap settings are connected to the primary winding the transformer functions as an autotransformer [4] as shown in Figure 1. In autotransformer mode, as is commonly known, the power efficiency and voltage regulation of the transformer are again very good. The core losses in this case, however, cannot be ignored as the core goes through full flux variation.

To model the power transformer the number of turns on each winding have to be determined as well as the winding resistances. The magnetic hysteresis curve of the transformer is also required for the modelling of the non-linear magnetic behaviour of the transformer core.

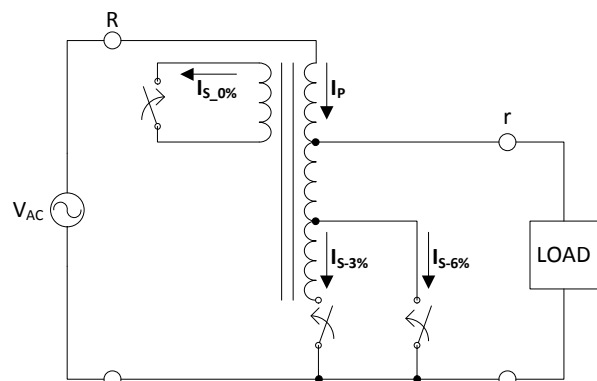


Figure 1: Equivalent circuit diagram of the Optimisa power transformer with its three tap settings.

2.1. Primary winding configuration

The primary winding consists of four coils as illustrated in Figure 2, which are wound on a common core shown

in Figure 3. The polarities of the coils are also indicated in Figure 2. The equivalent primary winding is defined as

$$X_{LP} = \frac{X_{LR1} \times X_{LR2}}{X_{LR1} + X_{LR2}} + \frac{X_{LT1} \times X_{LT2}}{X_{LT1} + X_{LT2}}. \quad (1)$$

Due to the design and layout of the transformer the different primary windings could not be tested separately. All tests involving the primary windings were conducted with respect to the equivalent primary winding.

The number of turns on the equivalent primary winding was determined by adding a separate winding around the transformer core with a known number of turns. Thin copper wire was used to carefully construct eight turns around the transformer's iron core as shown in Figure 3. With this secondary winding shorted a variable voltage was applied to the primary circuit and the currents in both the primary and secondary windings were measured. In this way the primary to secondary winding ratio was determined from the current measurements as

$$\frac{I_s}{I_p} = \frac{N_p}{N_s} = 2.626. \quad (2)$$

The number of turns on the primary winding is thus

$$N_p = \frac{I_s}{I_p} \times N_s = 2.626 \times 8 = 21. \quad (3)$$

The same method is used to determine the number of turns of the secondary windings. The equivalent primary winding resistance is measured as 0.02Ω .

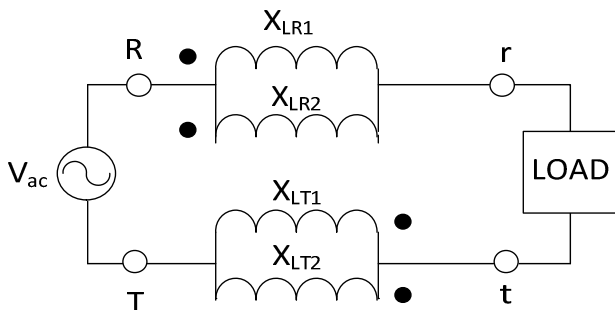


Figure 2: Equivalent circuit diagram of the primary winding coil configuration.

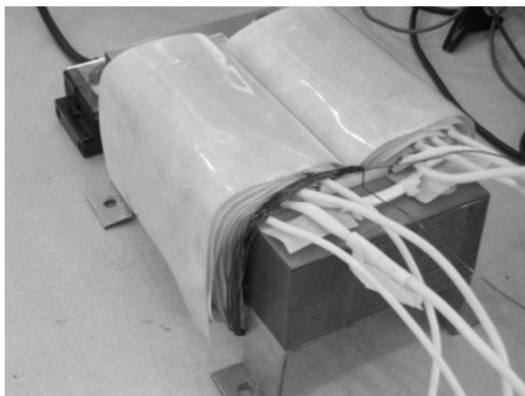


Figure 3: Photo of the 230 V, 30 kVA Optimisa transformer coils wound on a common core. In front, on the left core-leg, the added secondary winding is visible.

2.2. Saturation current

The saturation current through the transformer core is determined by replacing the load in Figure 2 with a short circuit. A 15 V voltage was applied between the terminals labelled R and T in Figure 2. This voltage and the resulting magnetising current are shown in Figure 4.

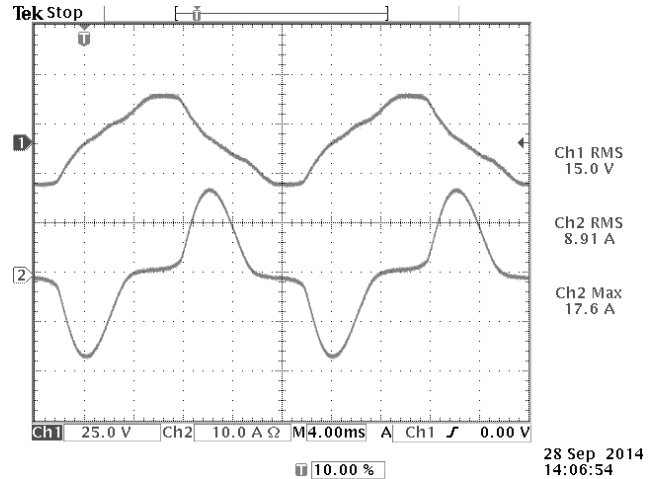


Figure 4: Measurements of applied voltage (Ch1) across the primary winding coils and magnetising current (Ch2).

2.3. Secondary winding ratios and resistances

The primary-to-secondary winding ratios were determined for all the different tap settings by measuring the currents of the primary and secondary windings. The current ratios determine the winding ratios as from equation (2). With $N_p = 21$ from (3) the number of turns of the different secondary tap windings were determined. The results of these calculations are given in Table 1. The measured resistances of the different tap setting windings are also given in Table 1.

Table 1: Current ratios and number of turns and resistances of the different tap winding coils.

Tap Setting	I_p/I_s	N_s	$R_s (\Omega)$
0 %	16.66	350	2.9
-3 %	35.64	749	2.1
-6 %	16.76	352	1.0

3. MODELLING AND SIMULATION

The ANSYS SImplorer simulation program was chosen for the modelling and simulation of the Optimisa power transformer. This ANSYS package is developed specifically for the modelling and simulation of electromagnetic systems. In the next sections the SImplorer models are described.

3.1. Simplorer models

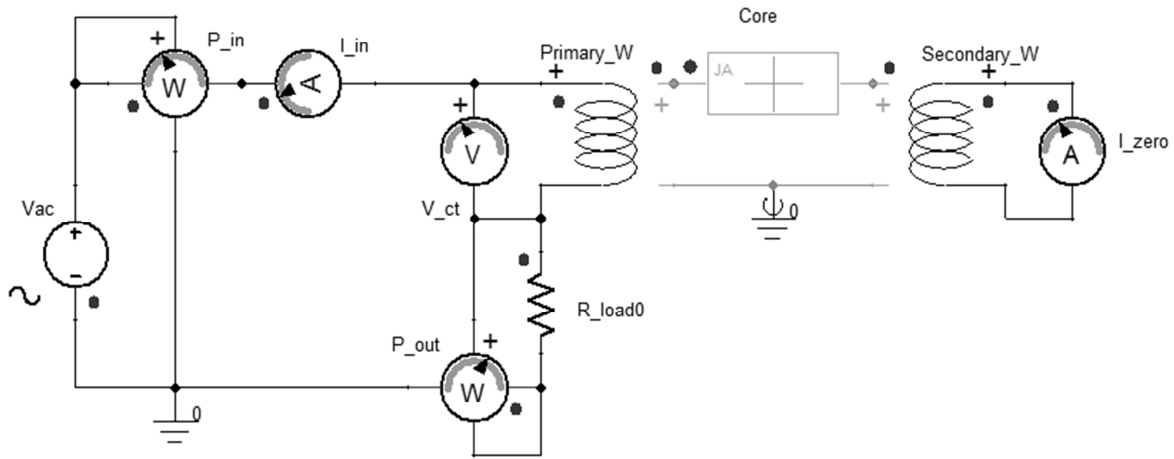
The different tap settings were all modelled individually. The Simplorer model for the 0 % tap setting is shown in Figure 5(a). The 0 % tap setting was modelled as a current transformer as shown.

The Simplorer model used for the -3 % and the -6 % tap settings is shown in Figure 5(b). Both these tap settings are connected as autotransformers, thus their simulation models look identical and only one model is shown. The only difference between the -3 % and the -6 % tap setting models is the resistance and number of turns of the secondary winding.

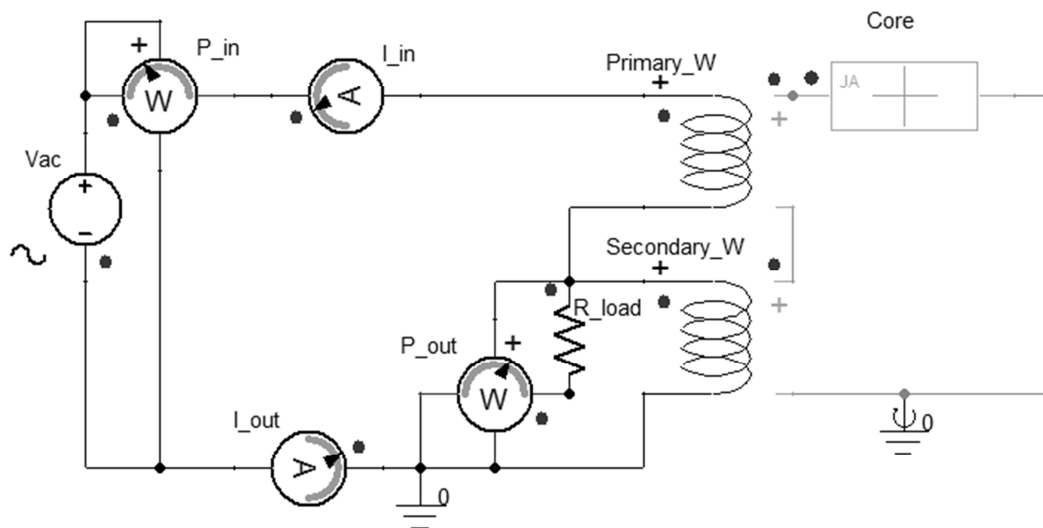
3.2. Non-linear modelling of the transformer

The non-linear behaviour of the Optimisa transformer core was also included in the Simplorer simulation models. The Jiles-Atherton theory of ferromagnetic hysteresis [5], [6] was used to model the non-linear behaviour of the transformer core. All the parameters of the Jiles-Atherton hysteresis model were determined experimentally. This hysteresis model is created in Simplorer with the BH magnetic hysteresis curve shown in Figure 6.

The simulated magnetising current according to the Simplorer model is shown in Figure 7. It closely matches the measured magnetising current shown in Figure 4. In this way, thus, the transformer core saturation and hysteresis core losses are accurately simulated.



(a)



(b)

Figure 5: Simplorer models for (a) the 0 % and (b) the -3 % and -6 % tap settings.

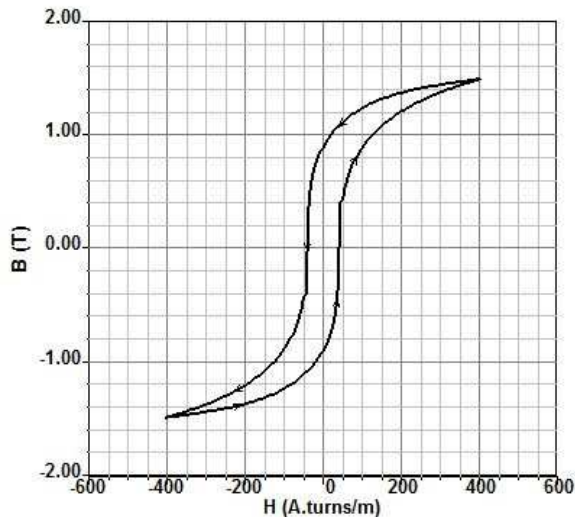


Figure 6: Simplorer magnetic hysteresis curve.

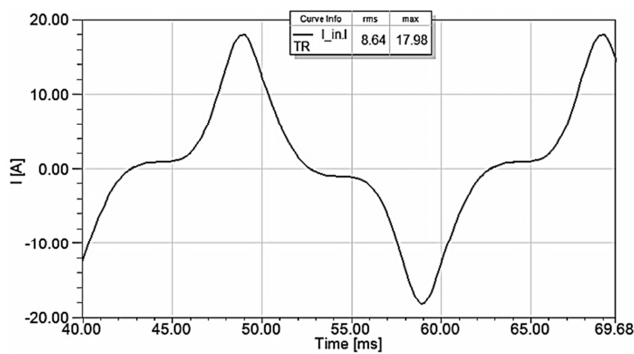


Figure 7: Simulated magnetising current.

4. TRANSFORMER TESTING AND EVALUATION

The transformer is rated at 230 V, 30 kVA. To truly test the transformer’s capabilities, load currents as high as 100 amps are required. A special test setup is used to load the transformer to such high current. The transformer is evaluated in terms of efficiency and voltage regulation. The simulated efficiency and voltage regulation are compared with measured results.

4.1. Test setup

The test setup is shown in Figure 8. Inside the safety box the three phase supply voltage connection is separated and only a single phase connection is used for the rest of the test circuit. A switch is located inside the box to turn the power on and off for the test circuit.

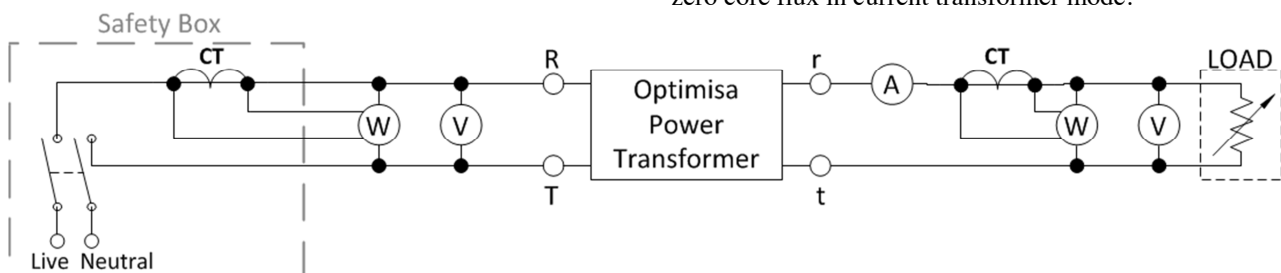


Figure 8: Schematic of the high-current single phase test setup.

All the meters that were used are analogue meters. Two current transformers with a ratio of 20:1 were used to lower the current for the watt meters that are rated at 6.5 A.

The variable load shown in Figure 8 is a resistor bank which consists of nine 18 Ω resistors. Four sets of parallel resistors were made, each with an equivalent resistance of 9 Ω. These four sets together with the last 18 Ω resistor functioned as the load for the test setup. By connecting the parallel sets in parallel with each other and using the 18 Ω load separately, the load can be varied between 18 Ω, 9 Ω, 4.5 Ω, 3 Ω and 2.25 Ω. This created load currents that vary from 12 to 97 A.

4.2. Transformer efficiency

The transformer efficiency is calculated by

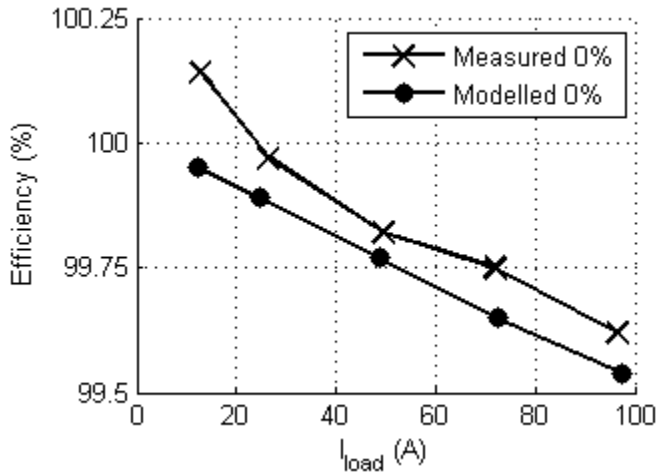
$$\eta = \frac{P_{out}}{P_{in}} \times 100\% . \quad (4)$$

The measured efficiencies only include the efficiency of the transformer itself. The efficiency of the complete Optimisa unit will be slightly less due to the power losses of the electronic and power electronic components.

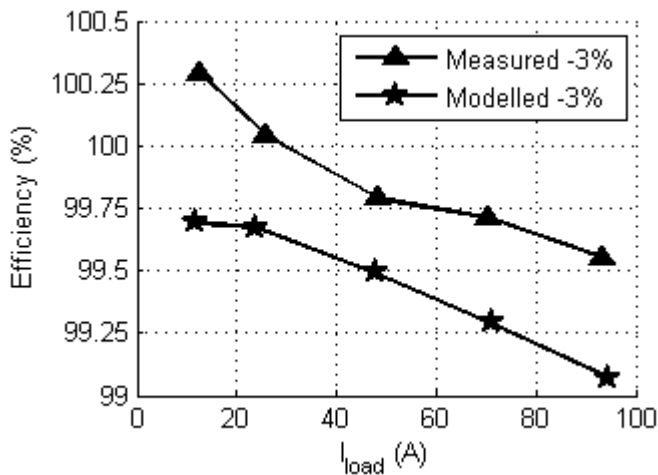
The measured and simulated efficiencies for the three different tap settings are shown in Figure 9. Note that at a load current of 90 A the transformer is only at 0.69 p.u. load current. From Figure 9 it can be seen that there is a decrease in efficiency as the load current increases for both the simulated and measured efficiency. This is expected since the power loss over the primary winding resistance will increase as the load current increases.

The efficiencies determined from the test measurements indicate that the transformer has an efficiency of just over 100 % for load currents less than 25 A. This discrepancy is caused by the measuring-equipment (i.e. the current transformers and analogue watt meters), which are not absolute identical and introduces a small measuring-error.

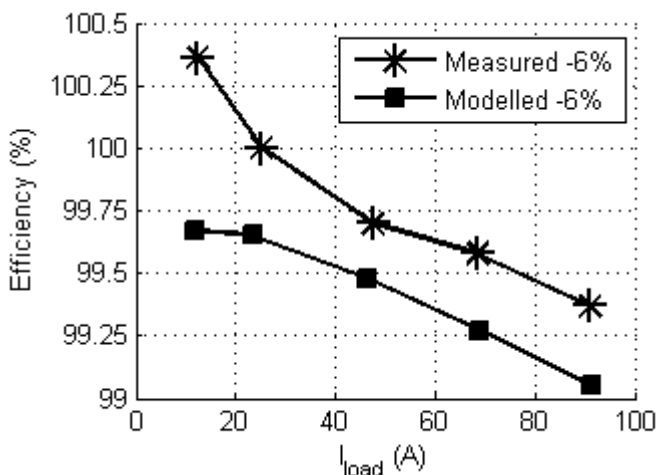
The simulated efficiency for the 0 % tap setting decreases perfectly linearly with the load current while the -3 % and -6 % tap setting does not. This is due to the hysteresis core losses that are included in the -3 % and -6 % tap setting models. For the 0 % tap setting model the core losses are for all practical purposes zero due to the almost zero core flux in current transformer mode.



(a)



(b)



(c)

Figure 9: Optimisa transformer efficiency for (a) 0 % tap setting, (b) -3 % tap setting and (c) -6 % tap setting.

The maximum errors between the measured and simulated efficiencies are given in Table 2. The maximum measured efficiency in this error calculation is considered to

be 100 %. The transformer has an efficiency of 99.9 % for load currents less than 26A.

Table 2: Maximum error between measured and modelled efficiencies

Tap Setting	Error
0 %	0.1%
-3 %	0.48%
-6 %	0.35%

4.3. Percentage voltage regulation

The percentage voltage regulation is calculated by

$$\%SR = \frac{V_{no_load} - V_{load}}{V_{load}} \times 100\% . \quad (5)$$

The measured and simulated voltage regulations are shown in Figure 10 with V_{no_load} in (5) taken as $V_{no_load} = V_{supply}$. The measured voltage regulation of the 0 % tap stays constant as shown in Figure 10; this is probably a measuring-error. The simulated voltage regulation of the 0 % tap setting shows a very low regulation. This is expected since with the 0 % tap setting the transformer acts as a current transformer with a very low internal voltage drop.

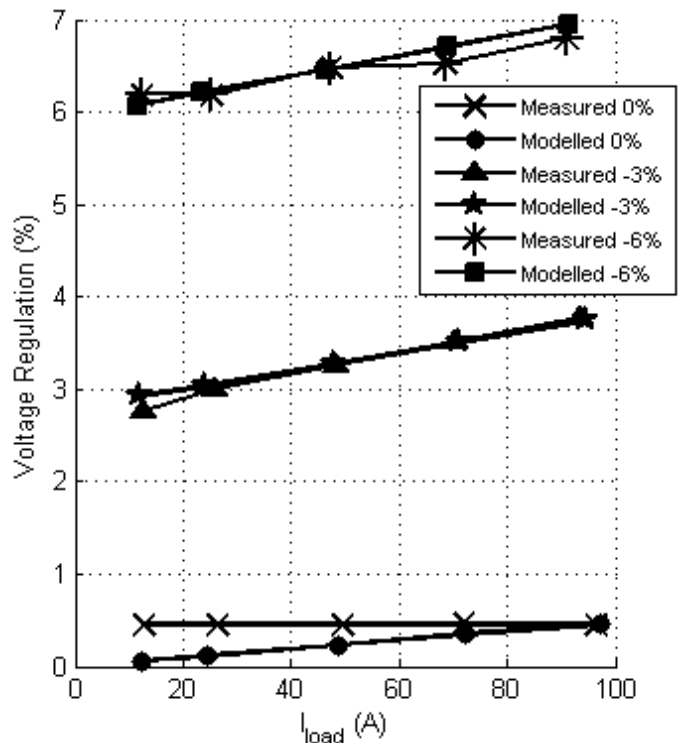


Figure 10: Percentage voltage regulation of the Optimisa transformer for three tap settings with V_{no_load} equal to the input voltage that varied slightly with load current.

The simulated and measured voltage regulations of the -3 % and -6 % tap settings show an increase of about 1 % with load. This is due to the equivalent series impedances of the autotransformer connections. In this case good matching is obtained between the simulations and measurements. The maximum error between the measured and simulated output voltages for the same input voltage is only 0.32 %. Hence, the Simplorer's simulated model can be used to determine rather accurately the voltage regulation of the real transformer.

5. CONCLUSION

The working principles of the Optimisa power transformer, which were unknown at the beginning of the study, were determined successfully. It was found that the Optimisa transformer acts as a current transformer when the 0 % tap setting is connected. If the -3 % or -6 % tap setting is connected the Optimisa transformer functions as an autotransformer.

The transformer was modelled successfully in Simplorer. The three different tap setting (0 %, -3 % and -6 %) were modelled individually. The Jiles-Atherton theory of ferromagnetic hysteresis was used to model the non-linear behaviour and losses of the transformer core accurately. The maximum error found between the measured and simulated efficiency is only 0.48 %. Also the maximum error between the measured and simulated output voltage is 0.32 % at a load current of 91.41 A (0.7 p.u.). Thus, the simulated model of the transformer is accurate and can be used to predict the behaviour of the transformer.

The measured transformer efficiency shows that at an input voltage of 220 V the transformer is 99.9 % efficient for load currents less than 26 A (0.2 p.u.). At full load the efficiency of the transformer is estimated to be just less than 99 %. Hence, the Optimisa power transformer has an extremely high efficiency under normal loading conditions. Furthermore, the full-load voltage regulation for the different tap settings is found to be within 1 %. Both the high efficiency and very good voltage regulation can be explained by the functioning of the transformer as either a current transformer or an autotransformer.

6. REFERENCES

- [1] Technology Standardization Department, "Rationalized User Specification, Electricity Supply - Quality of Supply Part 2," Eskom, Johannesburg, Rep. 0-626-15179-1, 2003.
- [2] A. Palmer, "Efficiency, Control Over Received Power," *EE Publishers Vector*, June 2012. [Online]. <http://www.ee.co.za/article/power-optimisa-200.html>
- [3] C.A. Castro and C.A.F. Murari, "A Lecture on Autotransformers for Power Engineering Students," *IEEE Transactions on Education*, vol. 46, no. 3, pp. 373-378, Aug. 2003.
- [4] S.D. Umans, "Transformers," in *Fitzgerald & Kingsley's Electric Machinery Seventh Edition*. Singapore: McGraw-Hill Education, 2014, ch. 2, pp. 63-100.
- [5] D. L. Atherton and D. C. Jiles, "Theory of Ferromagnetic Hysteresis," *Journal of Magnetism and Magnetic Materials*, no. 61, pp. 48-60, Jan. 1986.
- [6] D. C. Jiles, J. B. Thoeke, and M. K. Devine, "Numerical Determination of Hysteresis Parameters for the Modelling of Magnetic Properties Using the Theory of Ferromagnetic Hysteresis," *IEEE Transactions on Magnetics*, vol. 28, no. 1, pp. 27-35, Jan. 1992.